MALLA REDDY ENGINEERING COLLEGE

(Autonomous) - Main Campus

(A UGC Autonomous Institution, Approved by AICTE, New Delhi & Affiliated to JNTUH, Hyderabad).
Accredited by NAAC with 'A++' Grade (Cycle- III),
NIRF Rank Band 101-150, ARIIA Band Performer,
NBA Tier-I Accredited (B.Tech- CE, EEE, ME, ECE & CSE, M.Tech - CSE, EPS, TE)
Maisammaguda, Medchal-Malkajgiri District, Secunderabad– 500100,
Telangana State. www.mrec.ac.in

LIST OF SCOPUS JOURNALS IN THE CALENDAR YEAR-2022

MALLA REDDY ENGINEERING COLLEGE (AUTONOMOUS)
(UGC Autonomous Institution, Approved by AICTE, New Delhi & Affiliated to JNTUH, Hyderabad). Accredited by NAAC with 'A++' Grade, Maisammaguda (H), Medchal-Malkajgiri District, Secunderabad, Telangana State – 500100, www.mrec.ac.in

Faculty Research Publication in the Calendar Year - 2022

LIST OF SCOPUS JOURNALS

S.No	Department	No.of Journals
1	Civil Engineering	16
2	Electrical and Electronics engineering	01
3	Electronics and Communication Engineering	06
4	Computer Science and Engineering	08
5	CSE-CS&IOT	01
6	CSE-DS	03
7	Information Technology	01
8	Humanities and Science	26
9	Master of Business Administration	01
10	Mechanical Engineering	04
Total		**67**

MALLA REDDY ENGINEERING COLLEGE (AUTONOMOUS)

(UGC Autonomous Institution, Approved by AICTE, New Delhi & Affiliated to JNTUH, Hyderabad). Accredited by NAAC with ‘A++’ Grade,

Maisammaguda (H), Medchal-Malkajgiri District, Secunderabad,

Telangana State – 500100, www.mrec.ac.in

Sl. No	Title of paper	Name of the author/s	Department	Name of journal	Year of publication	ISSN number
1	Outdoor air pollution and respiratory health: A bibliometric analysis	C.M. Vivek Vardhan	Civil Engg	International Journal of Health Sciences	June, 2022	2550-6978
2	Outdoor air pollution and respiratory health: A bibliometric analysis	V Ravindra	Civil Engg	International Journal of Health Sciences	June, 2022	2550-6978
3	Prediction Of California Bearing Ratio (Soaked) And Unconfined Compressive Strength Values With Index Properties Of Different Stabilised Soils Of Medak District Region Of Telanagana State	M.Prashanth	Civil Engg	NeuroQuantology	7/1/2022	1303-5150
4	Silicafume Based Geopolymer Concrete-Durability Properties For M60 Grade	M. Uday Bhaskar	Civil Engg	NeuroQuantology	7/1/2022	1303-5150
5	Silicafume Based Geopolymer Concrete-Durability Properties For	M.Uday Bhaskar	Civil Engg	Neuro Quantalogy	6/1/2022	1303-5150

	M60 Grade					
6	Seismic Analysis Of Steel Plate Shear Wall And Concentric Braced Frames	M.Uday Bhaskar	Civil Engg	Neuro Quantalogy	6/1/2022	1303-5150
7	Seismic Analysis Of Steel Plate Shear Wall And Concentric Braced Frames	S.Manasa	Civil Engg	Neuro Quantalogy	6/1/2022	1303-5150
8	Study Of Compressive Strength & Tensile Strength Of Concrete By Using Glass Waste & Geogrids	S.Manasa	Civil Engg	Neuro Quantalogy	6/1/2022	1303-5150
9	Evaluation Of Strength Characteristics And Identifying The Optimum Dosage With The Impact Of Partial Replacement Of Recycled Fine And Coarse Aggregate From Construction And Demolition Waste	C. Bala Krishna	Civil Engg	Materials today Proceedings	5/1/2022	2214-7853
10	Applying ANN – PSO Algorithm To Maximize The Compressive Strength And Split Tensile Strength Of Blended Self Curing Concrete On The Impact Of Supplementary Cementitious Materials	J.S.S.K.Vasa	Civil Engg	International Journal on Interactive Design and Manufacturing (IJIDeM)	6/1/2022	1955-2505

11	Effect Of Fibre Mixing And Nano Clay On The Mechanical Properties Of Biodegradable Natural Fibre - Based Nano Composites	Dr. Selin Ravi Kumar	Civil Engg	Hindawi: Journal of Nano-materials	9/1/2022	1687-4129
12	Analysis Of BIM Use In Green Construction	Dr. Selin Ravi Kumar	Civil Engg	Neuroquantology	9/1/2022	1303-5150
13	Seismic Analysis Of A Reinforced Concrete Structure With And Without Shear Wall At Zone-II With Etabs	Ms. K. Harshada	Civil Engg	Indian Journal of Natural Sciences	8/1/2022	0976 – 0997
14	IOT In Civil Engineering: State Of Art	Dr.J.Rex	Civil Engg	Neurquantology	8/1/2022	1303-5150
15	Performance Of Hybrid Columns Subjected To Axial, Eccentric And Cyclic Loading	Mr.T Ram Prasanna Kumar Reddy	Civil Engg	Indian Journal of Natural Sciences	August, 2022	0976 – 0997
16	Development Of Low Calcium Fly-Ash Based Geopolymer Concrete Using Marble Powder	Dr.J.Rex	Civil Engg	Materials Science Forum	Nov, 2022	1662-9752
17	A Novel Efficient Adaptive Neuro Fuzzy Interfaced System Control Based Smart Grid	D.Chandra Sekhar	EEE	International Journal of Electrical and Computer Engineering (IJECE)	August, 2022	2722-2578

	Enhance Power Quality					
18	Mitigating The Challenges Of Online Learning And Conduct Of Examinations-From Faculty Perspective To Student Satisfaction	Shankaranand Jha, Santosh Kumar Choudhary, Ritesh Kumar	ECE	Journal of Engineering Education Transformations	2022	2394 - 1707
19	Deep Learning-Based Image Processing Approach For Irradiance Estimation In MPPT Control Of Photovoltaic Applications	J. Shirisha, C. P. Thamil Selvi, S. Saru Priya, V. Saravanan, B. Sakthivel, R. Surendiran	ECE	SSRG International Journal of Electrical and Electronics Engineering	Sept 2022	2348 - 8379
20	Challenges In Internet Of Things Towards The Security Using Deep Learning Techniques	K.C. Ravikumar, Pandi Chiranjeevi, N.Manikanda Devarajan, Chamandeep Kaur, Ahmed I. Taloba	ECE	Measurement: Sensors, Science Direct, Elsevier	10.10.2022	2665-9174
21	Implementation Of Multi Bit Error Detection And Correction Using Low Density Parity Check Codes	Dr.M.Jagadeesh Chandra Prasad	ECE	IEEE	2022	2168-2216

22	Plant Leaf Classification Though Deep Feature Fusion With Bidirectional Long Short Memory	Dr G prasanna Kumar	ECE	IEEE	2022	2168-2216
23	Detection And Prediction For Obstructive Sleep Apnea Recognition	Dr. T. Srinivas Reddy	ECE	IEEE	2022	2168-2216
24	Emerging Challenges In Iot,Blockchain And Data Mining For Effective Treatment Of Covid And Flu Diseases Through Telemedicine Process	Dr.Manyam Thaile	CSE	NeuroQuantology	22-Sep	1303-5150
25	Detection Of Cyber Hacking Breaches Using Machine Learning Algorithm	Dr. A. Rama Swamy Reddy1 , Talasila Alekhya2	CSE	NeuroQuantology	22-Aug	1303-5150
26	Hate Classify A Service Framework For Hate Speech Recognition On Social Media Network	Uppitarla Shireesha 1* , Dr. S. Shiva Prasad2	CSE	NeuroQuantology	22-Aug	1303-5150
27	Stress Detection In It Professional By Machine Learning	ABDUL GAFFAR KHAN1 , DR. D. KRISHNA MADHURI2	CSE	NeuroQuantology	22-Aug	1303-5150
28	A Light Weight Convolution Nural Network For Realtime Facial Expression Detection	Dr.B Hari Krishna	CSE	NeuroQuantology	22-Aug	1303-5150

29	Plant Disease Prediction Using Transfer Learning Techniques	Dr. N.Supriya	CSE	IEEE	22-Jul	
30	Big Data Processing Using Mining Algorithm In Data Set For Data Base Systems	Ms.Akankasha,Mr.P V Ramana Murthy,Dr.P Srinivas	CSE	IJCRT	22-Jun	2320-2882
31	Analysis Of Influencing Features With Spectral Feature Extraction And Multi-Class Classification Using Deep Neural Network For Speech Recognition System	Dr.J.Anitha	CSE	International Journal of Speech Technology	22-May	https://doi.org/10.1007/s10772-022-09974-9
32	Life Expectancy Prediction Through Analysis Of Immunization And HDI Factors Using Machine Learning Regression Algorithms	Dr.K.Vasanth Kumar	CSE-CS&IOT	International journal of online and biomedical engineering	2022	26268493
33	IOT For Analyzing And Investigating Digital Forensics Toools Using Cloud Computing	S.Shivaprasad	CSE-DS	IJHS	2022	2550-6978
34	Hate Classify A Service Framework For Hate Speech Recognition On Social Media	S.Shivaprasad	CSE-DS	NEUROQUANTOLOGY	2022	1303-5150

35	Hate Classify A Service Framework For Hate Speech Recognition On Social Media	SHIREESHA	CSE-DS	NEUROQUANTOLOGY	2022	1303-5150
36	Assessing Deep Neural Network And Shallow For Network Intrusion Detection Systems In Cyber Security	Dr.Deena Babu Mandru	IT	Computer Networks and Inventive Communication Technologies	2022	2193-1801
37	Developing English Communication Skills For Non- Native English Speaking Engineers: A Challenage And A Proposed Approach	R. Raga latha	English	DICKENSIAN JOURNAL	6-Jun-22	Dec-40
38	Exfoliation Of Mos2-RGO Hybrid 2D Sheets By Supercritical Fluid Process	Murthy Muniyappa1,, Mahesh Shastri1,2,, Manjunath Shetty3, Vinay Gangaraju1,, Jagadeesh Babu Sriramoju4, Sindhushree Muralidhar1,, Manikanta P. Narayanaswamy1,, Mudike Ravi1, Navyarani	Department of PHYSICS	Asian Journal of Chemistry	2022	0975-427X

		Marlingaiah5, , Prasanna D. Shivaramu1,, Ananda Kumar C S1, and Dinesh Rangappa1,*,				
39	Radiation, Radiation Absorption, Chemical Reaction And Hall Effects On Unsteady Flow Past An Isothermal Vertical Plate In A Rotating Fluid With Variable Mass Diffusion With Heat Source	Dr.G. Rami Reddy	H&S MATHS	*Neuroquantology*	2022	1303-5150
40	Dufour And Chemical Reaction Effects On Two Dimensional Incompressible Flow Of A Viscous Fluid Over Moving Vertical Surface	Dr.G. Rami Reddy	H&S MATHS	*Neuroquantology*	2022	1303-5150
41	Heat Transfer of A Peristaltic Electro - Osmotic Flow of A Couple Stress Fluid through an Inclined Asymmetric Channel with Effects of Thermal Radiation	Dr.K. Rama Krishna Reddy	H&S MATHS	*Indian Journal of Natural Sciences*	2022	0976 – 0997

42	Heat Transfer of A Peristaltic Electro - Osmotic Flow of A Couple Stress Fluid through an Inclined Asymmetric Channel with Effects of Thermal Radiation	M.Srikanth	H&S MATHS	*Indian Journal of Natural Sciences*	2022	0976 – 0997
43	Heat Transfer of A Peristaltic Electro - Osmotic Flow of A Couple Stress Fluid through an Inclined Asymmetric Channel with Effects of Thermal Radiation	Dr.K.Venugopal Reddy	H&S MATHS	*Indian Journal of Natural Sciences*	2022	0976 – 0997
44	AN ANALYTICAL STUDY OF CHEMICAL REACTION EFFECT ON MHD FLOW IN A VERTICAL SURFACE FILLED WITH POROUS MEDIUM	Ms. S Saroja	H&S MATHS	Journal of Positive School Psychology	2022	2717-7564
45	Radiation And Chemical Reaction Effects on Unsteady Flow Past an Accelerated Infinite Vertical Plate with Variable Temperature and Uniform Mass Diffusion Through a Porous Medium	Dr. P Sarada Devi	H&S MATHS	Journal of Positive School Psychology	2022	2717-7564

46	Topological Rank of (-1, 1) Metabelian Algebras	Dr. K. Hari Babu	H&S MATHS	Bol. Soc. Paran. Mat	2022	2175-1188
47	Numerical Study of Hall Current Effect on MHD Nanofluid with Inclined Plates in the Presence of Brownian motion and Thermophoresis	G.GANGADHAR	H&S MATHS	*Mathematical Statistician and Engineering Applications*	2022	2094-0343
48	Recent Development of Heat and Mass Transport in the presence of Hall, ion slip and thermo diffusion in radiative second grade material	N.Ravi Kumar	H&S MATHS	*Micromachines*	2022	2072-666X
49	Testing Of Multivariate Nonlinear Regression Hypothesis Using Nonlinear Least Square (Nls) Estimation	Dr. V. Pavankumari	H&S MATHS	International Journal of Mechanical Engineering	2022	0974-5823
50	Groundwater quality assessment by Water quality index (WQI) and Multivariate statistical analysis (MSA) for coastal zones of Srikakulam district, Andhra Pradesh	Dr. V. Pavan Kumari	H&S MATHS	*Journal of Applied NaturalScience*	2022	2231-5209
51	Model specification test against non-nested univariate and multivariate nonlinear	Dr. V. Pavankumari	H&S MATHS	Journal of Mathematical Problems, Equations and Statistics	2022	2709-9407

	regression models					
52	Magnetic Field And Chemical Reaction Effects On Unsteady Flow Past A Stimulate Isothermal Infinite Vertical Plate	V.NagaRaju	H&S MATHS	*Neuroquantology*	2022	1303-5150
53	Radiation and Mass Transfer effects on MHD mixed convective flow from a vertical surface with heat source and chemical reaction	Ashfar ahmed	H&S MATHS	*Neuroquantology*	2022	1303-5150
54	Chemical Reaction And Mhd Effects On Free Convection Flow Of A Viscoelastic Dusty Gas Through A Semi Infinite Plate Moving With Radiative Heat Transfer	M.Chitra	H&S MATHS	*Neuroquantology*	2022	1303-5150
55	The prediction of CO2 adsorption on rice husk activated carbons via deep learning neural network.	Dr.K.SUBBA RAO	chemistry	Materials Today:Proceedings	2022	2214-7853
56	“Promotional effect of Ce on catalytic performance for the glycerol hydrogenolysis over Ni–Ce/RSAC catalyst”.	Dr.K.SUBBA RAO	chemistry	Materials Today:Proceedings	2022	2214-7853

57	Preparation of Activated carbon from Rice husk for CO2 adsorption : Isotherm and artificial neural network modeling	Dr.K.SUBBA RAO	chemistry	MRS communications(research letters)	2022	2159-6867
58	Comparative study of Adsorption Isotherms on Activated carbons synthesized from Rice husk towards Carbon dioxide adsorption	Dr.K.SUBBA RAO	chemistry	Chemical Papers	2022	0366-6352
59	Titanium Dioxide Electrospun Nanofibres For Dye Removal - A Review	Dr. Madhavi Konni	chemistry	Journal of Applied and Natural Science	2022	2231-5209
60	Hydrogen Sorption Behaviors on Lithium Doped MIL@53-Al at Non - Cryogenic Temperatures	Dr. Madhavi Konni	chemistry	International Journal of Surface Engineering and Interdisciplinary Materials Science	2022	2166-7225
61	Surface investigation on aluminium composite by additive manufacturing process	CH.LDS. Narayana Gupta	chemistry	Materials Today: Proceedings	2022	2214-7853
62	Effect of parameters and surface analysis on eglin steel by shot blasting method	CH.LDS. Narayana Gupta	chemistry	Materials Today: Proceedings	2022	2214-7853
63	People Behaviour on savings and Investment after COVID-19	Dr.N.Ramanjaneyulu ,Dr.M.Rajesh & Mr.A. Sarveswar	MBA	The Sey Bold Report	Dec-22	1533-9211

		Reddy				
64	Designing a face shield frame in PTC Creo and printing it in a 3D printer	A.Raveendra	Mechanical	AIP	2022	0094243X
65	Floorplanning for Thermal Consideration: Slicing with Low Power on Field Programmable Gate Array	Subbulakshmi N, M. Pradeep, Patter Sampath Kumar, Megavath Vijay kumar, Rajeswaran N	Mechanical	*Measurement: Sensors*	October, 2022	2665-9174
66	one dimensional numerical simulations of single cylinder spark ignition engined fuel H2o based emission fuel ,methonal blends and gasoline conventional	Ufaith Qadiri	Mechanical	Material science for engineering technologies	2022	155-160
67	A Study on Tribological Properties of different Nanoparticles as additives in various Lubricants	M. V. Varalakshm	Mechanical	International Journal of Mechanical Engineering	2022	ISSN: 0974-5823

How to Cite:
Vardhan, C. M. V., Bhomesh, S., Ravindra, V., & Ramaganesh, M. (2022). Outdoor air pollution and respiratory health: A bibliometric analysis. *International Journal of Health Sciences*, *6*(S3), 11240–11249. https://doi.org/10.53730/ijhs.v6nS3.9240

Outdoor air pollution and respiratory health: A bibliometric analysis

Dr. C. M. Vivek Vardhan*
Professor, Department of Civil Engineering, Malla Reddy Engineering College, Maisammaguda, Hyderabad

Mr. Shyamala Bhomesh
Professor, Department of Civil Engineering, Malla Reddy Engineering College, Maisammaguda, Hyderabad

Vempati Ravindra
Professor, Department of Civil Engineering, Malla Reddy Engineering College, Maisammaguda, Hyderabad

M. Ramaganesh
Assistant Professor, Department of Mechanical Engineering, Kalasalingam Academy of Research and Education

***Abstract*---**Outdoor air pollution is a major threat to global public health that needs responsible participation of researchers at all levels. Assessing research output is an important step in highlighting national and international contribution and collaboration in a certain field. Therefore, the aim of this study was to analyze globally-published literature in outdoor air pollution – related respiratory health. Outdoor air pollution documents related to respiratory health were retrieved from Scopus database. The study period was up to 2017. Mapping of author keywords was carried out using VOSviewer 1.6.6. Search query yielded 3635 documents with an h-index of 137. There was a dramatic increase in the number of publications in the last decade of the study period. The most frequently encountered author keywords were: air pollution (835 occurrences), asthma (502 occurrences), particulate matter (198 occurrences), and children (203 occurrences). The United States of America ranked first (1082; 29.8%) followed by the United Kingdom (279; 7. 7%) and Italy (198; 5.4%). Annual research productivity stratified by income and population size indicated that China ranked first (22.2) followed by the USA (18.8). Analysis of regional distribution of publications indicated that the Mediterranean, African, and South-East Asia regions had the least contribution. Harvard University (92; 2.5%) was the most active institution/organization followed the US Environmental Protection

Manuscript submitted: 18 Feb 2022, Manuscript revised: 27 April 2022, Accepted for publication: 9 June 2022

Agency (89; 2.4%). International collaboration was restricted to three regions: Northern America, Europe, and Asia. The top ten preferred journals were in the field of environmental health and respiratory health. Environmental Health Perspective was the most preferred journal for publishing documents in outdoor pollution in relation to respiratory health. Research on the impact of outdoor air pollution on respiratory health had accelerated lately and is receiving a lot of interest. Global research networks that include countries with high level of pollution and limited resources are highly needed to create public opinion in favor of minimizing outdoor air pollution and investing in green technologies.

***Keywords*---**outdoor air pollution, respiratory health, bibliometric analysis.

Introduction

Outdoor air pollution is defined as the presence of one or more substances in the atmospheric air at concentrations and duration above the natural limits [1]. Such substances include ozone [O3], airborne lead [Pb], carbon monoxide [CO], sulphur oxides [SOx] and nitrogen oxides [NOx] [2]. Recently, air pollution with particulate matters (PM), especially those with less than 2.5 µm, has been the focus of most outdoor air pollution studies due to its ability to penetrate the lung tissue and induce local and systemic effects [2]. Air pollution has been described as one of the “great killers of our age” and as “major threat to health” due to its tremendous and various health effects on humans of all ages and in both genders [3, 4]. In 2014, the World Health Organization (WHO) estimated that 92% of the world population was living in places with less than optimum outdoor air quality. Furthermore, WHO reported that in 2012, outdoor air pollution caused around 3 million deaths worldwide and 6.5 million deaths (11. 6% of all global deaths) were associated with indoor and outdoor air pollution together [5].

Air pollution was linked to cancer, respiratory diseases, negative pregnancy outcomes, infertility, cardiovascular diseases, stroke, cognitive decline, and other adverse medical conditions [6–13]. Nearly 90% of air-pollution-related deaths occur in low- and middle-income countries, with nearly 2 out of 3 occurring in South-East Asia and Western Pacific regions. The problem of outdoor pollution is not a new one, but the rapid urbanization, particularly in Asia, made the problem of air pollution more visible and its health burden more tangible [14–17]. Bibliometric analysis is the application of statistical methods on published literature to analyze publication trends with time and to shed light on influential researchers, countries, and institutions in the field. In the past decade, at least seven bibliometric studies on air pollution were published [18–24]. However, none of the published bibliometric studies have shed light on the air pollution - related respiratory health. Therefore, in the current study, we aim to analyze literature pertaining to outdoor air pollution and respiratory health. The size of the literature and research productivity in this field is a good indicator of national and international efforts to improve air quality and to decrease the health and economic burden of air pollution. Furthermore, the quality of the air we breathe is the responsibility of everyone including researchers and academics. This study comes in line with perceived personal responsibility toward better air quality.

Method

Search strategy This study aimed to analyze the documents about outdoor air pollution – related respiratory health. Scopus database was used to retrieve relevant documents because of its advantages over other databases [25–28]. The search strategy developed for this study consisted of nine steps (Additional file 1). The first six steps utilized various keywords and search queries to retrieve the maximum number of documents. Keywords included in search queries were those found in recent relevant systematic reviews [6, 12, 13, 29, 30].

Data analysis and visualization

In this study, Hirsch-index (h-index) was used as a measure of impact of publications [36]. Graphs were created using Statistical Package for Social Sciences (SPSS). Hirsch - index is defined as the number of articles (n) that have received at least n citations [36]. VOSviewer software was used to create visualization maps while ArcMap 10.1 was used to create geographical distribution of the retrieved documents [37–39]. For VOSviewer mapping of most frequent author keywords, a minimum occurrence of 10 was used as a cut-off point for inclusion of the keyword in mapping analysis. Analysis also included distribution of publications based on World Health Organization (WHO) regions.

Types and growth of publications

The search strategy yielded 3635 documents. The earliest document in this field was published in 1943 in American Journal of Epidemiology [40]. The analysis of the types of documents showed that research articles (2935, 80.7%) were the most common type followed by review articles (359; 9.9%). The remaining documents (341; 9.4%) were conference papers, letters, editorials, short surveys, and notes. English (2923, 80.4%) was the primary language of documents followed by French (156; 4.3%) and German (124; 3.4%). The subject areas of the documents were medicine (2772; 76.3%) followed by environmental science (1038; 28.6%) and biochemistry/ genetics/ molecular biology (317; 8.7%) with the possibility of overlap among different subject areas. The growth of publications showed a dramatic increase in the past decade. Figure 1 shows the annual growth of publications. There was a 72% increase in number of publications in 2017 compared to that in 2008.

Author keywords

Analysis of author keywords showed that the most frequently encountered author keywords were: air pollution (835 occurrences), asthma (502 occurrences), particulate matter (198 occurrences), and children (203 occurrences) (Fig. 2a). Further mapping of types of pollutants most commonly encountered in author keywords showed that particulate matter (198 occurrences), ozone (192 occurrences), nitrogen oxide (95 occurrences), PM10 (75 occurrences), PM2.5 (57 occurrences), and Sulfur dioxide (54 occurrences), were the most frequently encountered author keywords (Fig. 2b).

Discussion

Growth of publications

In this study, we analyzed global research output in outdoor air pollution – related respiratory health. The results showed a noticeable increase in the number of publications in the last decade of the study period. This indicates that the level of air pollution and its health consequences reached serious levels. In 2012, air pollution was responsible for 3 million deaths, representing 5. 4% of the total global deaths. In the same year, about 25% were due to lung cancer deaths, 8% were due to chronic obstructive pulmonary disease (COPD) deaths, and about 17% of respiratory infection deaths were caused by outdoor air pollution [41]. A study indicated that the contribution of outdoor air pollution to global premature mortality could double by 2050 [42]. Another study concluded that outdoor air pollution contributes to the increase in global burden of COPD and that an increase of 10 μg/m(3) in PM10 produced significant increase in COPD deaths and exacerbations that can be substantially reduced by controlling air pollution [43]. A cohort Chinese study concluded that the risks of mortality and years of life lost were elevated corresponding to an increase in current ambient concentrations of the air pollutants [44]. The contribution of researchers from /ifferent scientific fields led to an acceleration in the growth of publications in this field. Scientists in the fields of the environment, respiratory health, public health, and even molecular biology/genetics contributed to the retrieved documents [45–49]. The fact that air pollution is a multidisciplinary field created a large number of readers from different scientific fields and thus leading to large number of citations, reflected in the relatively high h-index value of documents. For example, the h-index of literature in global carbapenem resistance was 102 and that for literature in resistant tuberculosis was 76 [50, 51].

Active countries and institutions

Our results showed that China had the highest research productivity in terms of GDP per capita per year. In China, air pollution was previously estimated to contribute to 1.2 to 2 million deaths annually [52]. In its list of the world's deadliest countries for air pollution, the WHO ranked China first followed by India, Russian Federation, Indonesia, Pakistan, Ukraine, Nigeria, Egypt, USA, and Bangladesh [53]. Out of the top 10 countries that have high total annual number of deaths from PM2. 5 and PM10, only China and USA were among the top ten active countries in research output. The deadliest effects of air pollution in China led to the adoption of the Ambient Air Quality Standard in China in 2012 [54]. This system started a national Air Reporting System that now includes 945 sites in 190 cities.

Highly cited documents

The top cited documents in the field was about the relationship between outdoor air pollution and lung cancer; and received a large number of citations suggestive of great importance. The International Agency for Research on Cancer [60], which is part of the WHO, has classified outdoor air pollution, as a whole, as a cancer-causing agent (carcinogen) [60]. The International Agency for Research on Cancer (IARC) concluded that outdoor air pollution causes lung cancer and is associated with increased risk for bladder cancer. Urgent action to minimize level of outdoor air pollution and exposure of population to such carcinogenic pollutants is necessary, particularly in cities with high levels of outdoor air pollution [61, 62].

Analysis of Author Keyword Co-Occurrence

In bibliometric research, topic mapping is critical. Figure 1 illustrates all of the issue categories related to the keywords of scientific literacy in general. In the bibliometric analysis, VOSviewer may give six unique mapping visualisations. The thickness of the connecting line represented the strength of a pair of topic areas or keywords.

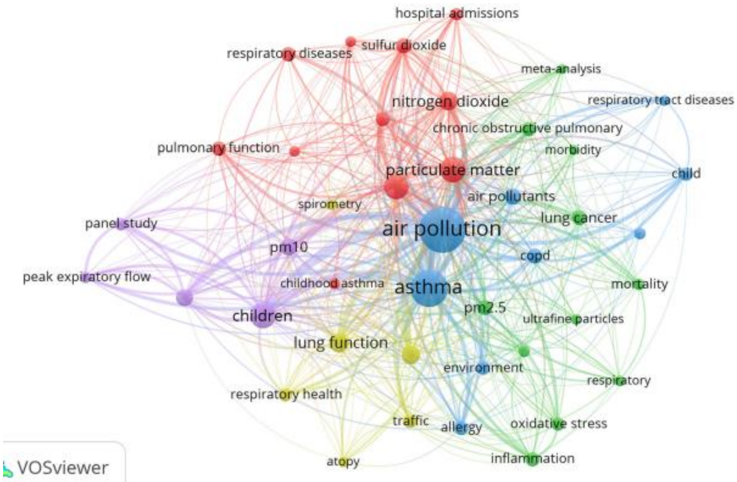

Fig. 1. The Network Visualization of Literacy Topic Area

In terms of country, co-authorship is as follows

Countries having an emphasis on scientific literacy research are depicted in Figure 2. The United States and India have the most scientific literacy research studies, followed by Canada, Australia, and Turkey, according to the data. Meanwhile, as the VOSviewer mapping results reveal, scientific literacy research in Indonesia is still in its infancy.

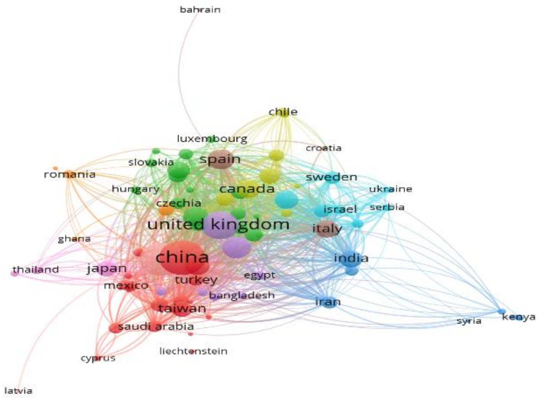

Fig. 2. The Visualization of Countries Related to Scientific Literacy Research

Co-authorship in terms of Authors

This analytical parameter is considered with 04 additional parameters. This parameter considers the word, authors, organisations, and countries. This research does not include documents with a large number of authors. This number is considered to be 13. For the author's minimum number of documents, the barrier is set at 4. It should be highlighted that 328 of the 1549 writers met the requirements from the scopus and web of science databases.

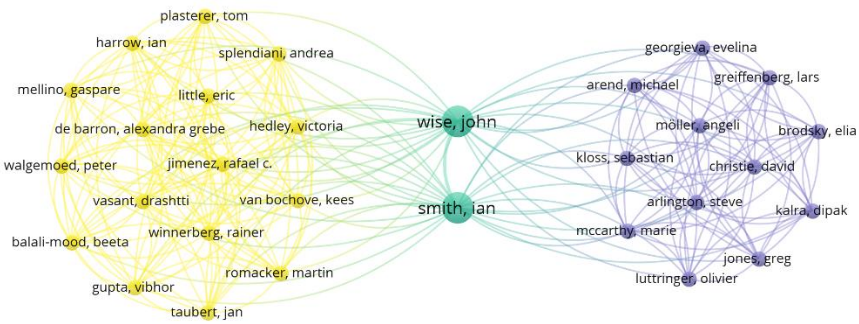

Fig. 3. Network Analysis of Co-authorship in terms of authors

CO-authorship in terms of Organizations

Co-authorship in the unit of organisations is calculated by disregarding the citation of at least two publications in organisations; 45 organisations meet the condition out of the total of 1426 displayed in the image. Stony Brook University (SBU),NY,United States has the highest link strength of 5 and the highest number of citations of 154. (with 2 documents).

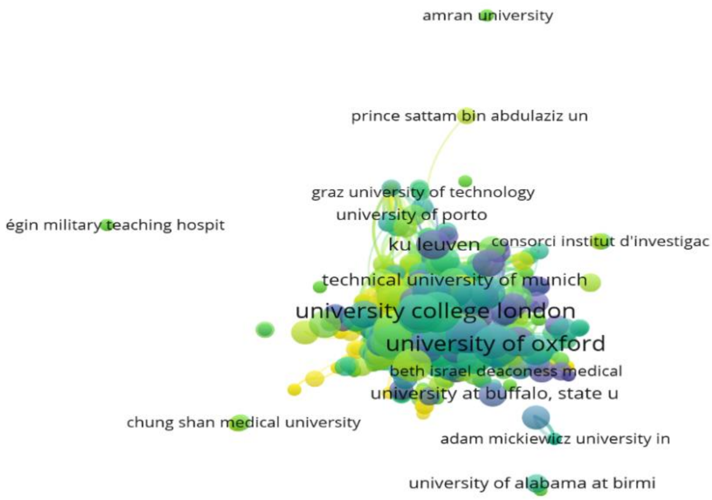

Fig. 4. Network Analysis of Co-authorship in terms of organizations

Conclusions

Growth of publications in outdoor air pollution – related respirator health is rapidly increasing. However, limited research output and international collaboration were seen in world regions such as the Middle East, Africa, and South-East Asia. International multidisciplinary research network, involving countries with high levels of air pollution and limited resources, are needed. Research in atmospheric pollution should also be directed toward prevention of air pollution problems by investing more in green technology. The results presented in this study are indicative of how research activity is interacting with the urgent acceleration of the air pollution crisis at the global level. Furthermore, the research activity is indicative of the response rate adopted by certain countries to face this global problem in a responsible way. Pressure groups can use the research activity to enforce certain environmental and industrial agendas on politicians and political campaigns. Countries with high levels of outdoor air pollution, and therefore, poor air quality, need to get engaged in research pertaining to this field to provide health policymakers with baseline data for future action. Establishing research center for monitoring national air quality and level of air pollution is a step forward that needs to be adopted by all countries.

Such centers could include scientists from different disciplines who can collaborate to convert research findings into national agendas and policies. At the national levels, different world countries need to adopt strict guidelines for air quality. Collaboration between industry and health authorities is needed to implement measures that could significantly reduce the levels of particulate matter. The outdoor air pollution is a global public health and therefore research networking between developed countries and developing countries with high levels of air pollution should be prioritized. The Chinese model in controlling air pollution and minimizing its health consequences could be of a global benefit. Finally, since the respiratory effects of air pollution are affecting children, there is a need to educate and increase the awareness of parents regarding this issue.

References

1. Seinfeld JH, Pandis S. Atmospheric chemistry and physics: from air pollution to climate change. Volume 2nd ed. New York: John Wiley; 2006.
2. Nemmar A, Holme JA, Rosas I, Schwarze PE, Alfaro-Moreno E. Recent advances in particulate matter and nanoparticle toxicology: a review of the in vivo and in vitro studies. Biomed Res Int. 2013;2013:279371.
3. Venkatesan P. WHO report: air pollution is a major threat to health. Lancet Respir Med. 2016;4(5):351.
4. Landrigan PJ. Air pollution and health. Lancet Public Health. 2017;2(1):e4–5.
5. World Health Organization (WHO). WHO releases country estimates on air pollution exposure and health impact. [cited 2018 March 12]; Available from: http://www.who.int/mediacentre/news/releases/2016/air-pollution-estimates/en/
6. Khreis H, Kelly C, Tate J, Parslow R, Lucas K, Nieuwenhuijsen M. Exposure to traffic-related air pollution and risk of development of childhood asthma: a systematic review and meta-analysis. Environ Int. 2017;100:1–31.
7. Bloemsma LD, Hoek G, Smit LA. Panel studies of air pollution in patients with COPD: systematic review and meta-analysis. Environ Res. 2016;151:458–68.
8. Checa Vizcaino MA, Gonzalez-Comadran M, Jacquemin B. Outdoor air pollution and human infertility: a systematic review. Fertil Steril. 2016;106(4): 897–904. e891
9. Zanoli L, Lentini P, Granata A, Gaudio A, Fatuzzo P, Serafino L, et al. A systematic review of arterial stiffness, wave reflection and air pollution. Mol Med Rep. 2017;15(5):3425–9.
10. Power MC, Adar SD, Yanosky JD, Weuve J. Exposure to air pollution as a potential contributor to cognitive function, cognitive decline, brain imaging, and dementia: a systematic review of epidemiologic research. Neurotoxicology. 2016;56:235–53.
11. Siddika N, Balogun HA, Amegah AK, Jaakkola JJ. Prenatal ambient air pollution exposure and the risk of stillbirth: systematic review and metaanalysis of the empirical evidence. Occup Environ Med. 2016;73(9):573–81.
12. Orellano P, Quaranta N, Reynoso J, Balbi B, Vasquez J. Effect of outdoor air pollution on asthma exacerbations in children and adults: systematic review and multilevel meta-analysis. PLoS One. 2017;12(3):e0174050.
13. Jacobs M, Zhang G, Chen S, Mullins B, Bell M, Jin L, et al. The association between ambient air pollution and selected adverse pregnancy outcomes in China: a systematic review. Sci Total Environ. 2017;579:1179–92.
14. Air and Waste Management Association. Asia renews commitment to fight air pollution at the 2014 better air quality conference. EM: Air and Waste Management Association's Magazine for Environmental Managers [Conference Paper] 2015 [cited 2018 February 12]; Available from: http://cleanairasia.org/wp-content/uploads/portal/files/documents/17_asia_renews_commitment_to_fight_air_pollution_-_february_2015.pdf.
15. Vichit-Vadakan N, Vajanapoom N, Ostro B. The Public Health and Air Pollution in Asia (PAPA) project: estimating the mortality effects of particulate matter in Bangkok, Thailand. Environ Health Perspect. 2008; 116(9):1179–82.

16. Wong CM, Vichit-Vadakan N, Kan H, Qian Z. Public Health and Air Pollution in Asia (PAPA): a multicity study of short-term effects of air pollution on mortality. Environ Health Perspect. 2008;116(9):1195–202.
17. Lelieveld J, Crutzen PJ, Ramanathan V, Andreae MO, Brenninkmeijer CM, Campos T, et al. The Indian Ocean experiment: widespread air pollution from South and Southeast Asia. Science. 2001;291(5506):1031–6.
18. Brimblecombe P, Grossi CM. The bibliometrics of atmospheric environment. Atmos Environ. 2009;43(1):9–12.
19. Wang F, Jia X, Wang X, Zhao Y, Hao W. Particulate matter and atherosclerosis: a bibliometric analysis of original research articles published in 1973-2014. BMC Public Health. 2016;16(1):348.
20. Kolle SR, Thyavanahalli SH. Global research on air pollution between 2005 and 2014: a bibliometric study. Collect Build. 2016;35(3):84–92.
21. Nykiforuk CI, Osler GE, Viehbeck S. The evolution of smoke-free spaces policy literature: a bibliometric analysis. Health Policy. 2010;97(1):1–7.
22. Andrade A, Dominski FH, Coimbra DR. Scientific production on indoor air quality of environments used for physical exercise and sports practice: bibliometric analysis. J Environ Manag. 2017;196:188–200.
23. Zell H, Quarcoo D, Scutaru C, Vitzthum K, Uibel S, Schoffel N, et al. Air pollution research: visualization of research activity using density-equalizing mapping and scientometric benchmarking procedures. J Occup Med Toxicol. 2010;5(1):5.
24. Jia X, Guo X. Bibliometric analysis of associations between ambient pollution and reproductive and developmental health. Zhonghua Yu Fang Yi Xue Za Zhi. 2014;48(6):521–6.
25. Falagas ME, Pitsouni EI, Malietzis GA, Pappas G. Comparison of PubMed, Scopus, Web of Science, and Google Scholar: strengths and weaknesses. FASEB J. 2008;22(2):338–42.
26. Bakkalbasi N, Bauer K, Glover J, Wang L. Three options for citation tracking: Google Scholar, Scopus and Web of Science. Biomed Digit Libr. 2006;3:7.
27. Kulkarni AV, Aziz B, Shams I, Busse JW. Comparisons of citations in Web of Science, Scopus, and Google Scholar for articles published in general medical journals. JAMA. 2009;302(10):1092–6.
28. De Groote SL, Raszewski R. Coverage of Google Scholar, Scopus, and Web of Science: a case study of the h-index in nursing. Nurs Outlook. 2012;60(6):391–400.
29. Abdo N, Khader YS, Abdelrahman M, Graboski-Bauer A, Malkawi M, Al-Sharif M, et al. Respiratory health outcomes and air pollution in the Eastern Mediterranean region: a systematic review. Rev Environ Health. 2016;31(2): 259–80.
30. Zhao L, Liang HR, Chen FY, Chen Z, Guan WJ, Li JH. Association between air pollution and cardiovascular mortality in China: a systematic review and meta-analysis. Oncotarget. 2017;8(39):66438–48.
31. Gearing RE, Mian IA, Barber J, Ickowicz A. A methodology for conducting retrospective chart review research in child and adolescent psychiatry. J Can Acad Child Adolesc Psychiatry. 2006;15(3):126–34.
32. Kimberlin CL, Winterstein AG. Validity and reliability of measurement instruments used in research. Am J Health Syst Pharm. 2008;65(23): 2276–84.

33. Banks NJ. Designing medical record abstraction forms. Int J Qual Health Care. 1998;10(2):163–7.
34. Allison JJ, Wall TC, Spettell CM, Calhoun J, Fargason CA Jr, Kobylinski RW, et al. The art and science of chart review. Jt Comm J Qual Improv. 2000;26(3): 115–36.
35. Hallgren K. Computing inter-rater reliability for observational data: an overview and tutorial. Tutor Quant Methods Psychol. 2003;8(1):23–34.
36. Ellegaard O, Wallin JA. The bibliometric analysis of scholarly production: how great is the impact? Scientometrics. 2015;105(3):1809–31.
37. van Eck NJ, Waltman L. Software survey: VOSviewer, a computer program for bibliometric mapping. Scientometrics. 2010;84(2):523–38.
38. Van Eck NJ, Waltman L. Text mining and visualization using VOSviewer. arXiv preprint arXiv:11092058 2011 [cited 2018 March 12]; Available from: https://arxiv.org/abs/1109.2058.
39. van Eck NJ, Waltman L. VOSviewer manual. Leiden: Univeristeit Leiden; 2013. [cited 2018 March 12]; Available from: http://www.vosviewer.com/documentation/Manual_VOSviewer_1.5.4.pdf
40. Mills CA. Urban air pollution and respiratory diseases. Am J Epidemiol. 1943; 37(2):131–41.
41. World Health Organization (WHO). Mortality and burden of disease from ambient air pollution. Global Health Observatory (GHO) data 2012 [cited 2018 March 15]; Available from: http://www.who.int/gho/phe/outdoor_air_pollution/burden_text/en/.
42. Lelieveld J, Evans JS, Fnais M, Giannadaki D, Pozzer A. The contribution of outdoor air pollution sources to premature mortality on a global scale. Nature. 2015;525(7569):367–71.
43. Suryasa, I. W., Rodríguez-Gámez, M., & Koldoris, T. (2022). Post-pandemic health and its sustainability: Educational situation. *International Journal of Health Sciences*, *6*(1), i-v. https://doi.org/10.53730/ijhs.v6n1.5949
44. Suryasa, I.W., Sudipa, I.N., Puspani, I.A.M., Netra, I.M. (2019). Translation procedure of happy emotion of english into indonesian in kṛṣṇa text. *Journal of Language Teaching and Research, 10*(4), 738–746

PREDICTION OF CALIFORNIA BEARING RATIO (SOAKED) AND UNCONFINED COMPRESSIVE STRENGTH VALUES WITH INDEX PROPERTIES OF DIFFERENT STABILISED SOILS OF MEDAK DISTRICT REGION OF TELANAGANA STATE

* **Miryala Prashanth**
Assistant professor, Civil Engineering Department, Malla Reddy Engineering College (MREC),(Autonomous), Mysammaguda, Secunderabad, Telangana, India, 500100
** **Shantala.T**
Assistant Professor, Civil Engineering Department, Srinivasa Ramanujan inistitute of Technology (Autonomous) , Anantapuramu
*** **Pathangi Eswanth**
Assistant Professor, Civil Engineering Department, G.Pulla Reeddy Engineering College (Autonomous), Kurnool.

Abstract
Thickness of the Pavement Affects the Subgrade Strength in The Design of Flexible Pavements. California Bearing Ratio (CBR) Is One of The Methods to Determine the Subgrade Strength. The Conventional Soaked CBR Testing Method Is Expensive, Laborious and Time Consuming, So Here an Attempt Was Made for Correlating CBR Values as Well as UCS (Unconfined Compressive Strength) With the Index Properties of Soils Stabilised with Stone Dust, Ordinary Portland Cement (OPC) And Portland Slag Cement (PSG) Like LL, PL, PI, OMC, And MDD. Correlation Co-Efficient (R^2) Value of Index Properties with Soaked CBR Is Determined. In This Study Thirty (31) Number of Soil Samples (Having 44<LL<84) Were Collected from Different Parts of Medak District Region (Telangana). Different Laboratory Tests Including Atterberg Limits, Specific Gravity, Gradation Analysis, Soaked CBR, UCS and Compaction Were Performed on These Samples and Various Linear Relationships Were Established Between Index Properties and Soaked CBR As Well as UCS Of the Samples Using Statistical Software (SPSS) And Microsoft Excel. Simple And Multiple Linear Regression Analysis Was Performed and No of Predictive Equations Were Developed for Estimating the Soaked CBR And UCS Value from The Index Properties of Soil with A Maximum R^2 Value Of 0.99.

Keywords: Correlation Coefficient (R^2), Regression Analysis, Soaked CBR Value, Unconfined Compressive Strength

DOI Number: 10.14704/nq.2022.20.6.NQ22744 **NeuroQuantology 2022; 20(6):7434-7447**

1. Introduction.

Soil Is Diverse in Formation and Character Therefore Accurate Prediction of Its Engineering Behaviour Is of Research Interest in Civil Engineering Area. The Engineering Behaviour of Soils Varies from Place to Place and Also with Time. Many Attempts Are Made to Predict CBR Values and UCS From the Index Properties of Stabilized Soils. Hence Determining of Factors That Influence the Soil Strength and Studying Their Relationship with California Bearing Ratio Value and Unconfined Compressive Strength on Representative Sample Maybe Considered as Good Insight of Soil Behaviour

The Unique Nature of Soil Properties as It Appears Naturally Is That Being Divergent Spatially and Seasonally Beyond the Designer's Control. Geotechnical Engineers Usually Attempt to Develop Empirical Equations Specific to A Certain Region and Soil Type. However, These Empirical Equations Are More Reliable for The Type of Soil Where the Correlation Is Origin. Hence, It Is Important to Develop Empirical Equations That Best Fit for The Local Area That We Can Access.

Presently India's Infrastructure Is Growing Rapidly. Large Number of New Urban and Lightly Trafficked Roads Are Being Constructed or Planned. The CBR Or California Bearing Ratio Is the Well-Known, Common and Trustful Test Currently Used in Road Construction. The Test Is Being Used for Many Years and Is Familiar to Organisations Involved in The Interpretation of Results, Consequent Road Design and Construction.

California Bearing Ratio Mainly Comes Under the Use of Civil Engineers Particularly for Those

Working in Pavement Construction to Determine Stiffness Modulus and Shear Strength of Sub-Grade. It Shows Comparison of Strength of Subgrade Material to The Strength of Standard Crushed Rock Referred In %Age Values. This Method Was Basically Developed at California Division of Highways In 1930s To Give an Assessment of The Relative Stability of Fine Crushed Rock Base Material.

The CBR Values Are Used by The Engineers to Design the Thickness of Pavement Layer to Be Laid on The Top of The Sub-Grade. The Lower CBR Value Sub-Grade Will Have More Thickness of Pavement as Compared to The Sub-Grade That Has Higher CBR Value. In This Method the Soil Sample Is Compacted in A Standard Mould and Then a Plunger Is Allowed to Penetrate in To the Soil at A Specified Penetration Rate. Load Vs Penetration Curve Is Plotted from The Result of Penetration and Then Compared with The Bearing Resistance of Standard Crushed Rock.

2.Materials and methods

2.1 Soil

Here Thirty two (32) number of disturbed soil sample were collected from the different parts of Sangareddy district of Telangana, India. Those were tested in VNR VJIET laboratory Bachupally, Hyderabad. The collected sample were Black Cotton soils. All samples Were collected from one meter below the ground by using hand operated sampler.

Commonly un stabilized black cotton soil is not used in any construction purposes because of it was poor in strength so among those samples one of the black cotton soil and remaining red soil is stabilised with stone dust and two types cements i.e.(OPC&PSG).This stabilized data (engineering &index properties of soils) was collected from some of my friends and an attempt was made to develop some predictive Empherical formulas to predict the soaked CBR,UCS of soils with respect to their index properties like LL,PL,PI,OMC,MDD by using statistical software SPSS as well as Microsoft excel.

2.2 Methodology

Primarily, in order to address the intended objectives of the study, basic theories and descriptions of CBR test in general and in relation to soil index property of subgrade soil is reviewed. Subsequently, previous works of different researchers with regard to prediction of CBR,UCS value from basic soil index properties were assessed.

In order to have satisfactory data for utilizing the correlations, laboratory tests were conducted by the researcher on samples collected from different localities of Sangareddy, so as to get records of test results of CBR, UCS values along with the associated soil indicates particularly the grain size analysis, Atterberg limits, moisture-density relationships. Then, discussions on sample collection and summary of laboratory test results were presented. Statistical regression analyses of test results were carried out and correlations were developed and also analysed to fit the test results. Under the discussions of the obtained results the suitability of the developed correlations were examined. Finally, a generalized conclusion and recommendation were made.

2.3 Experimental procedure.

2.3.1 Soaked California bearing ratio test (CBR):

In this study, the soaked CBR test is performed as per [10]. As per mentioned IS code procedure heavily compacted soil sample should immersed (along with weights to produce a surcharge equal to the weight of base material and pavement to the nearest 2.5 kg) in a tank of water allowing free access of water to the top and bottom of the specimen. At the end of soaking period mould taken out of the water and allowed to drain 15 minutes and then penetration test was conducted.

2.3.2 UConfined Compressive Sytrenth (UCS)

The UCS test is performed to determine the shear strength characteristics of the soil according [14]. Generally UCS sample is prepared by taking 5kg of soil passing through 4.75μm sieve in a mould. The sample is taken in a tray and suitable water is added according to OMC of that soil and mixed thoroughly. The sample is compacted by using the hammer and 56 evenly distributed blows are given in five equal layers falling at a height of 56cm. The collar is removed and is trimmed off by using the spatula. The sample is extracted using the sample extractor and the extra portion is removed using the knife. The height and diameter of the sample obtained is 7.5cm and 3.5cm. About 15 of such samples are obtained for each soil. These specimens are properly sealed till the testing. Proper care is taken to avoid any moisture loss between the preparation and the subsequent testing of the specimen. The UCS test is conducted for 3 of the specimen to obtain the strength characteristics of the soil. The average of the 2 closer results has been considered as the UCS strength and the undrained cohesion values (Cu) have been obtained

2.3.3 Standard proctor test:

As per [14] the standard proctor test conducted to determine the Optimum Moisture Content (OMC) and Maximum Dry density (MDD) of the soils. It's values are shown in Table 3.

2.3.4 Specific Gravity

Soil Specific Gravity (G) was determined as per guide lines of IS 2720-part 3 As per [13]. The average value of three samples has been taken as the specific gravity of soil. The specific gravity of fine grained soils are determined by density bottle method and which are reported at 27ºc in 100 ml volume.

2.3.5 Grain Size Analysis

Grain size distribution was done by using wet sieve analysis and hydrometer analysis as per guide lines of IS2720 part 4.

2.3.6 Atterberg Limits:

Liquid limit test:

As per [12] liquid limit test was conducted and it's values are shown in Table 2.

Plastic limit test:

As per [12] plastic limit test was conducted on the soil mixed with distilled water by rolling on a glass plate until it is about 3mm diameter and it's values are shown in Table 2.

Plasticity index (PI):

PI=liquid limit(LL)-plastic limit(PL)

2.3.7 Hydrometer analysis:

As per [11] the oven dried sample has been made through 75µm sieve and 50g of soil was taken for testing procedure.

2.3.8 Regression analysis:

The regression analysis is done based on the results obtained from each soil. The results of thirty soils are utilised to fit a best curve with the help of regression analysis. Here soaked CBR value will be Considered as dependent were as LL, PL, PI, OMC, MDD are independent.

3.0 Results and Discussions

3.1 Basic soil Properties

Table1. Results of sieve analysis

Sample number	Clay (%)	Gravel (%)	Sand (%)	Silt (%)	Soil classification
1	9.5	0.9	6.75	82.85	Fine grained
2	30.5	0.8	25.6	43.1	Fine grained
3	18	3.2	26.7	52.1	Fine grained
4	16.5	0	5.85	77.65	Fine grained
5	18	0.3	5.9	75.8	Fine grained
6	16.5	3.35	17.45	62.7	Fine grained
7	17.5	0.35	5.25	76.9	Fine grained
8	8.5	0.6	6.45	84.45	Fine grained
9	20.3	1.8	25.75	52.15	Fine grained
10	12	0	5.3	82.7	Fine grained
11	29.5	1.6	25.4	43.5	Fine grained
12	17	2.4	11.8	68.8	Fine grained
13	14	0.6	10.65	74.75	Fine grained
14	22	1.2	28.55	48.25	Fine grained
15	11.5	0.25	5.05	83.2	Fine grained
16	15	0.9	17.8	66.3	Fine grained
17	26	0	23.4	50.6	Fine grained
18	16	0.2	7.2	76.6	Fine grained
19	14.5	0.2	7.4	77.9	Fine grained
20	20	5.95	12.9	61.15	Fine grained
21	13.5	0.7	5.15	80.65	Fine grained
22	11.5	0	28.7	59.8	Fine grained
23	24.5	0.2	27	48.3	Fine grained
24	26.5	0.4	23	50.1	Fine grained
25	30.0	0	22.8	47.2	Fine grained
26	9.5	0	29.6	60.9	Fine grained
27	30	4.2	23.3	42.5	Fine grained
28	54	0.1	25.2	20.7	Fine grained
29	34.5	0.8	25.1	39.6	Fine grained
30	23.8	0	24	52.2	Fine grained

Table 2. Results of consistency limits

Sample number	Liquid limit (%)	Plastic limit (%)	Plasticity index (%)	Soil classification
1	72	39.6	32.4	MH
2	62.3	31.0	31.25	CH
3	45.6	24	21.6	MH
4	71.6	41.2	30.4	MH
5	71.4	38.9	32.5	MH
6	81.2	44.7	36.46	MH
7	60	32.6	27.4	MH
8	73.2	41.4	31.8	CI
9	44.9	25.1	19.8	MH
10	73	40.8	32.2	CH
11	53	27.47	25.53	CH
12	71.7	37.91	33.79	MH
13	53.5	30.3	23.2	CI
14	48.1	21.6	26.5	MH
15	54.2	31.1	23.1	MH
16	71.4	40.4	31	MH
17	81.6	43.2	38.4	MH
18	83.4	46.2	37.2	MH
19	79.6	45.1	34.5	MH
20	76.2	40.7	35.5	MH
21	77.2	46.6	30.6	MH
22	55	31.3	23.7	MH
23	48.8	27.2	21.6	CI
24	46.1	26.16	19.94	CH
25	55.7	29.3	26.4	CH
26	49.5	30.7	18.8	MI
27	63.8	31.25	32.55	CH
28	73.2	30.43	42.77	CH
29	50.6	27	23.6	CH
30	49.2	23.15	26.05	CI

Table 3.Results of compaction characteristics:

Sample Number	Optimum Moisture Content (%)	Maximum Dry Density (%)	Laboratary Soaked CBR Value (%)
1	28	1.4	4.82
2	15.5	1.53	4.57
3	14	1.81	4.09
4	29	1.39	4.82
5	28	1.38	4.82
6	29	1.31	5.05
7	15	1.56	4.57
8	27.5	1.38	4.82
9	14	1.79	4.09
10	28	1.37	4.82
11	14.5	1.66	4.33
12	27	1.41	4.82
13	16	1.65	4.33
14	14	1.8	4.09
15	17.5	1.63	4.33
16	26	1.41	4.82
17	27.5	1.31	5.05
18	28.5	1.33	5.29
19	29	1.34	5.05
20	27.5	1.41	4.81
21	28	1.35	5.05
22	14	1.65	4.33
23	14.5	1.65	4.09
24	15	1.78	4.09
25	19	1.64	4.33
26	21	1.6	4.57
27	21.5	1.41	4.82
28	20	1.66	4.33
29	18	1.31	5.05
30	18.5	1.79	4.09

Table 4.Adopted soil data

Property Name	Value	
	BC soil	Red soil
Specific gravity	2.6	2.58
Gravel (%)	0	0
Sand (%)	5	20
Silt (%)	33	45
Clay (%)	62	35
Liquid limit(%)	62	38.2
Plastic limit (%)	37.3	16.2
Plasticity index (%)	24.7	22.4
Classification	CH	CI
Optimum moisture content (%)	19.8	16
Maximum dry density (g/cc)	1.48	1.8
UCS (kg/cm^2)	1.74	2.07
CBR (%)	3.74	4.6

*e***ISSN** 1303-5150

Table 5. LL, PL, PI, OMC, MDD, CBR and UCS Results for stone dust (SD) stabilized BC soil

S.NO	SD	LL	PL	PI	OMC	MDD	CBR	UCS
1	5	44	22.2	21.8	24.7	1.481	3.8	4.4
2	7.5	43	21.4	21.6	26.9	1.486	4.3	4.8
3	10	41	19.04	21.96	26.6	1.495	4.8	5.2
4	12.5	39	18.18	20.82	23.8	1.529	5.7	6
5	15	37	17.64	19.36	21.6	1.546	6.7	6.8

Table 6.LL, PL, PI, OMC, MDD, CBR and UCS Results for stone dust (SD) stabilized Red soil

S.NO	SD%	LL	PL	PI	OMC	MDD	CBR	UCS
1	5	42	18.18	23.82	14.7	1.87	6.7	4.6
2	7.5	40	17.6	22.4	15.3	1.877	8.1	5
3	10	38	16.66	21.34	14.1	1.897	9.6	5.5
4	12.5	36	15.38	20.62	16.4	1.914	11.5	6.2
5	15	32	13.33	18.67	16.5	1.936	12.5	7.1

Table 7. LL, PL, PI, OMC, MDD, CBR and UCS Results for cement (OPC) stabilized BC soil

S.NO	OPC%	LL	PL	PI	OMC	MDD	CBR	UCS
1	3	63.8	40.6	23.2	25.3	1.471	21.19	4.2
2	5	65	42.2	23	26.3	1.459	28.42	6.7
3	7.5	67.7	44.8	22.9	26.4	1.447	33.23	7.3
4	10	70.2	49	21.2	29.9	1.44	39.5	9.2

Table 8. LL, PL, PI, OMC, MDD, CBR and UCS Results for cement (PSC) stabilized BC soil

S.NO	PSC%	LL	PL	PI	OMC	MDD	CBR	UCS
1	3	63.1	38.6	24.5	28.6	1.461	18.3	3.6
2	5	64.5	41	23.5	28.3	1.449	20.7	4.4
3	7.5	65.7	43.4	22.3	26.4	1.436	24.57	5.6
4	10	68.2	46.4	21.8	32.9	1.428	29.87	7.5

Table 9.LL, PL, PI, OMC, MDD, CBR and UCS Results for cement (OPC) stabilized Red soil

S.NO	OPC%	LL	PL	PI	OMC	MDD	CBR	UCS
1	3	44.6	18.8	25.8	15.4	1.779	32.73	5.2
2	5	46.9	23.9	23	15	1.764	35.17	6.7
3	7.5	50.2	28.6	21.6	17.3	1.748	40.46	8.4
4	10	55.4	34.2	21.2	17.9	1.739	42.4	10.2

Table 10 LL, PL, PI, OMC, MDD, CBR and UCS Results for cement (PSC) stabilized Red soil

S.NO	PSC%	LL	PL	PI	OMC	MDD	CBR	UCS
1	3	42.7	17.4	25.3	17.4	1.763	29.39	4.8
2	5	44.6	22.2	22.4	15.9	1.757	31.7	6.2
3	7.5	48	26.6	21.4	16.8	1.734	35.2	8.2
4	10	52.1	33.2	18.9	19	1.726	39.9	9.9

3.2 PRAPOSED EQUATIONS FOR PREDECTING THE SOAKED CBR VALUE, UN CONFINED COMPRESSIVE STRENGTH WITH INDEX PROPERTIES OF DIFFERENT SOILS

Here number of predictive equations were developed to predict the laboratory soaked CBR value with index properties of soil by using statistical software IBM SPSS and Microsoft excel on doing both multiple and linear regression analysis.

proposed equations for predicting the soaked CBR value with index properties of virgin black cotton soils

1).$CBR_{(soaked)}$ = -2.060*MDD+7.744 with an R^2 value of 0.943

2). $CBR_{(soaked)}$ = 0.003*OMC-1.961*MDD+7.521 with an R^2 value of 0.944

3).$CBR_{(soaked)}$=-0.002*OMC-1.865*MDD+0.001*LL+0.005*PL+7.251 with an R^2 value of 0.947

Table 11. Experimental and predicted soaked CBR values of virgin soils.

Sample Number	Laboratory Soaked CBR Value	Soaked CBR Value Obtained from Equation 1	Soaked CBR Value Obtained from Equation 2	Soaked CBR Value Obtained from Equation 3
1	4.82	4.86	4.86	4.85
2	4.57	4.59	4.57	4.58
3	4.09	4.02	4.01	4.01
4	4.82	4.88	4.88	4.88
5	4.82	4.90	4.90	4.89
6	5.05	5.05	5.04	5.05
7	4.57	4.53	4.51	4.53
8	4.82	4.90	4.90	4.90
9	4.09	4.06	4.05	4.06
10	4.82	4.92	4.92	4.92
11	4.33	4.32	4.31	4.32
12	4.82	4.84	4.84	4.83
13	4.33	4.35	4.33	4.35
14	4.09	4.04	4.03	4.02
15	4.33	4.39	4.38	4.39
16	4.82	4.84	4.83	4.84
17	5.05	5.05	5.03	5.05
18	5.29	5.00	5.00	5.03
19	5.05	4.98	4.98	5.00
20	4.81	4.84	4.84	4.85
21	5.05	4.96	4.96	4.99
22	4.33	4.35	4.33	4.36
23	4.09	4.35	4.33	4.33
24	4.09	4.08	4.08	4.08
25	4.33	4.37	4.36	4.36
26	4.57	4.45	4.45	4.43
27	4.82	4.84	4.82	4.80
28	4.33	4.32	4.33	4.34
29	5.05	5.05	5.01	4.96
30	4.09	4.06	4.07	4.04

7439

3.2.1 Comparison graph between experimental and predicted soaked CBR values:

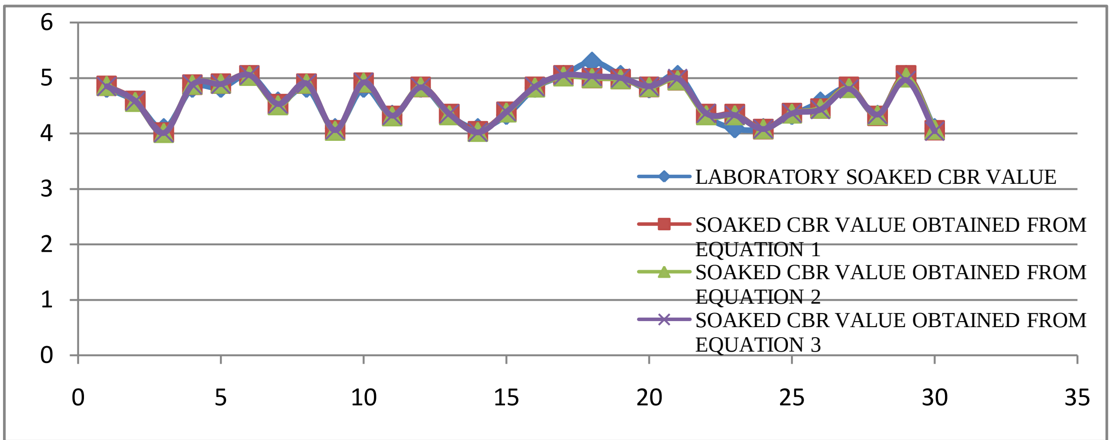

Proposed equations for predicting the soaked CBR and UCS value with index properties of black cotton soil stabilized with stone dust

1).CBR $_{(soaked)}$ =0.288*SD+2.180 with an R^2 value of 0.972

2). CBR $_{(soaked)}$ = -0.358*PL-0.624*PI-4.5*MDD+32.073 with an R^2 value of 0.999

3). UCS =0.240*SD+3.040 with an R^2 value of 0.970

4).UCS = -0.266*PL-0.459*PI+0.612*MDD+19.432 with an R^2 value of 0.98

Table 12. Experimental and predicted soaked CBR and UCS values of black cotton soil stabilized with stone dust

Laboratory Soaked CBR Value	Predected Soaked CBR Value From Equation 1	Predected Soaked CBR Value From Equation 2	Laboratory Tested UCS Value	Predected UCS Value From Equation 3	Predected UCS Value From Equation 4
3.8	3.62	3.86	4.4	4.24	4.43
4.3	4.34	4.25	4.8	4.84	4.73
4.8	5.06	4.83	5.2	5.44	5.20
5.7	5.78	5.69	6	6.04	5.98
6.7	6.50	6.72	6.8	6.64	6.80

3.2.2Comparison graph between experimental and predicted soaked CBR values:

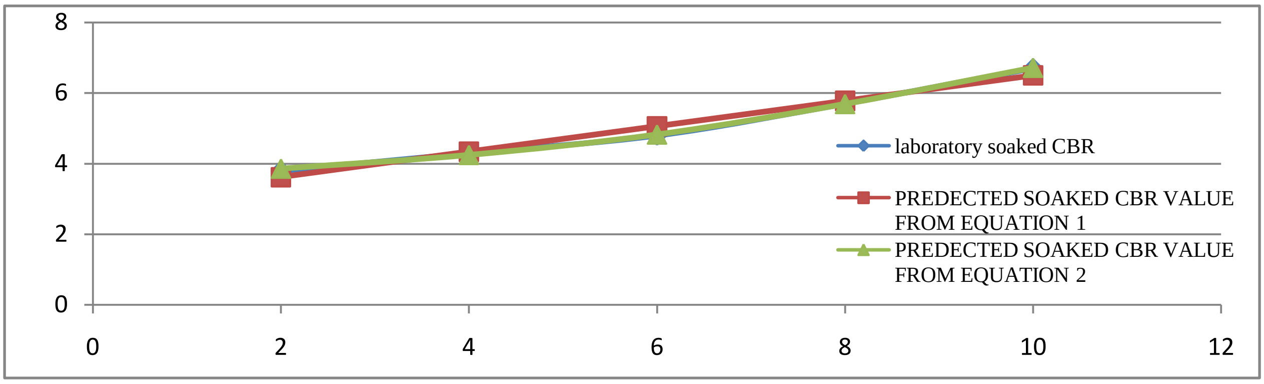

4.2.3 Comparison graph between experimental and predicted UCS values:

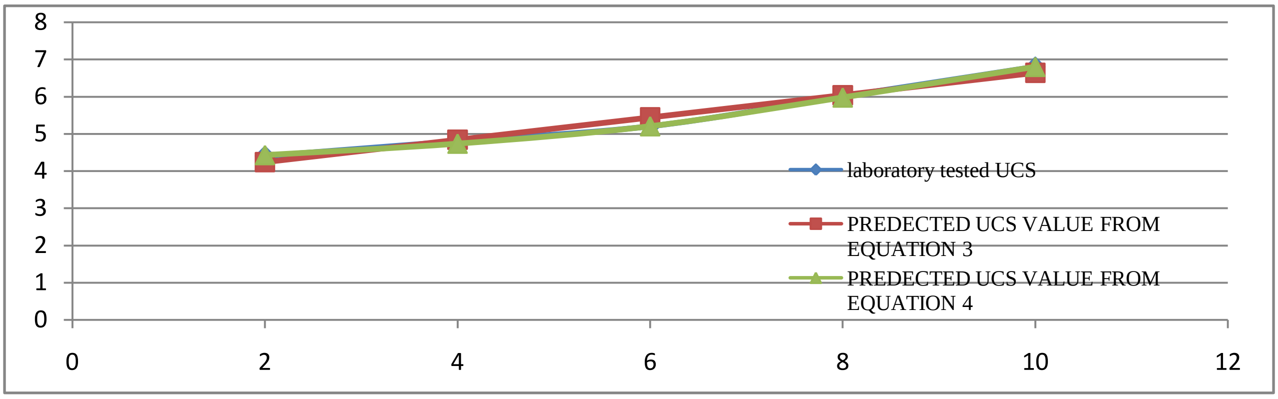

Proposed equations for predicting the soaked CBR and UCS value with index properties of black cotton soil stabilized with stone ordinary Portland cement (opc)

1) CBR $_{(soaked)}$ =2.527*OPC+14.473 with an R^2 value of 0.986
2) CBR $_{(soaked)}$ = 1.240*OMC-0.869*LL-586.077*MDD+907.391 with an R^2 value of 0.99
3) UCS =0.656*OPC+2.665 with an R^2 value of 0.934
4) UCS = -297.717*MDD-1.160*LL-1.598*PI+553.229 with an R^2 value of 0.99

Table 13. Experimental and predicted soaked CBR and UCS values of black cotton soil stabilized with ordinary Portland cement (opc)

Laboratory Soaked CBR Value	Predected Soaked CBR Value From Equation 1	Predected Soaked CBR Value From Equation 2	Laboratory Tested UCS Value	Predected UcCSValue From Equation 3	Predected UCS Value From Equation 4
21.19	22.05	21.20	4.2	4.63	4.21
28.42	27.11	28.43	6.7	5.95	6.71
33.23	33.43	33.24	7.3	7.59	7.31
39.5	39.74	39.51	9.2	9.23	9.21

3.4.4 Comparison graph between experimental and predicted soaked CBR values:

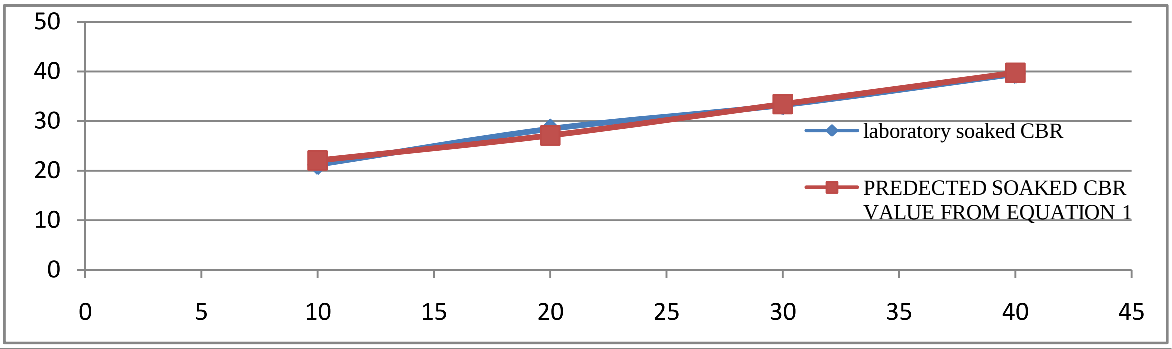

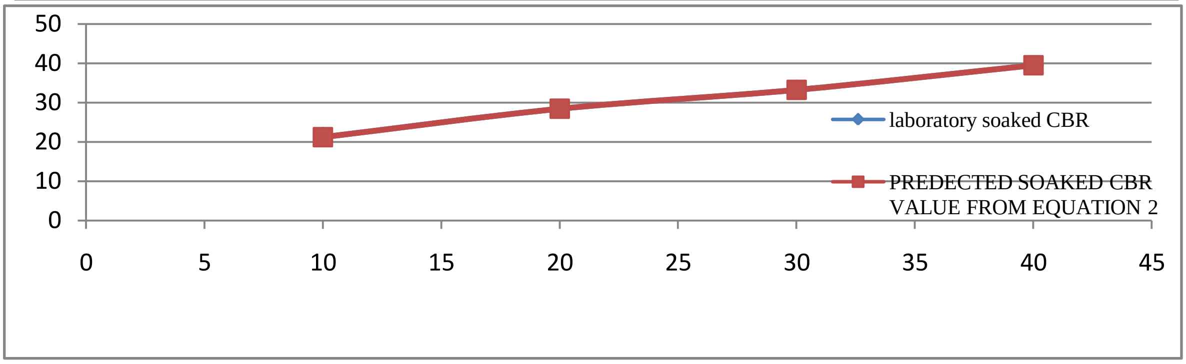

3.4.5 Comparison graph between experimental and predicted UCS values:

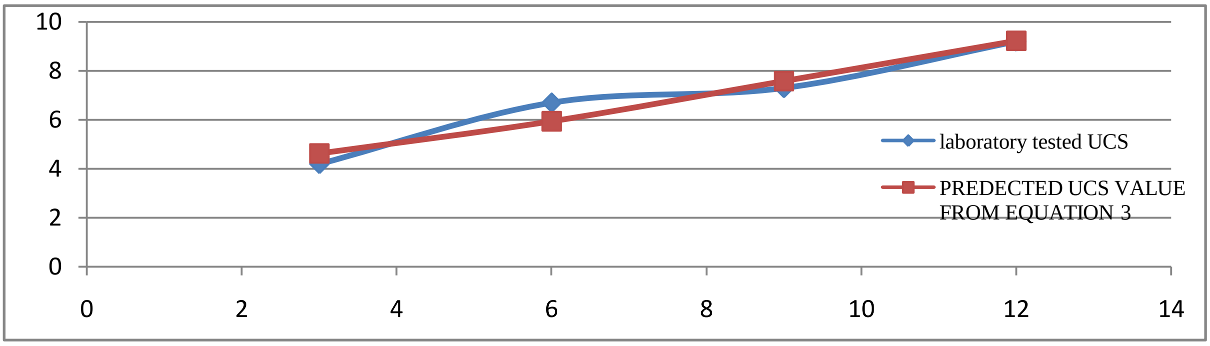

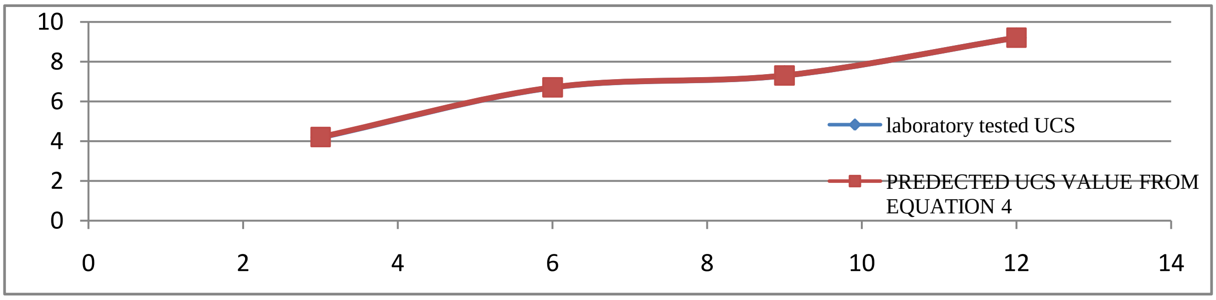

Proposed equations for predicting the soaked CBR and UCS value with index properties of black cotton soil stabilized with Portland slag cement (psc)

1) CBR $_{(soaked)}$ = 1.650*PSC+12.839with an R^2 value of 0.986
2) CBR $_{(soaked)}$ = 1.239*OMC-27.674*PI+2070.225*MDD-2365.185 with an R^2 value of 0.99
3) UCS =0.552*PSC+1.755 with an R^2 value of 0.978
4) UCS = 0.414*OMC-8.448*PI+626.966*MDD-717.270 with an R^2 value of 1.0

Table 14. Experimental and predicted soaked CBR and UCS values of black cotton soil soil stabilized with Portland slag cement (psc)

Laboratory Soaked CBR Value	Predected Soaked CBR Value From Equation 1	Predected Soaked CBR Value From Equation 2	Laboratory Tested UCS Value	Predected UCS Value From Equation 3	Predected UCS Value From Equation 4
18.3	17.79	16.84	3.6	3.41	3.59
20.7	21.09	19.30	4.4	4.52	4.39
24.57	25.21	23.24	5.6	5.90	5.59
29.87	29.34	28.57	7.5	7.28	7.49

3.4.6 Comparison graph between experimental and predicted soaked CBR values:

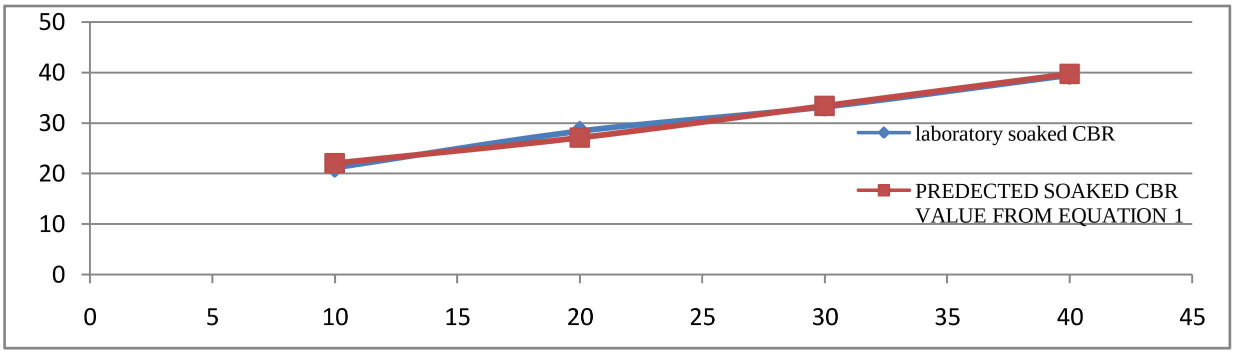

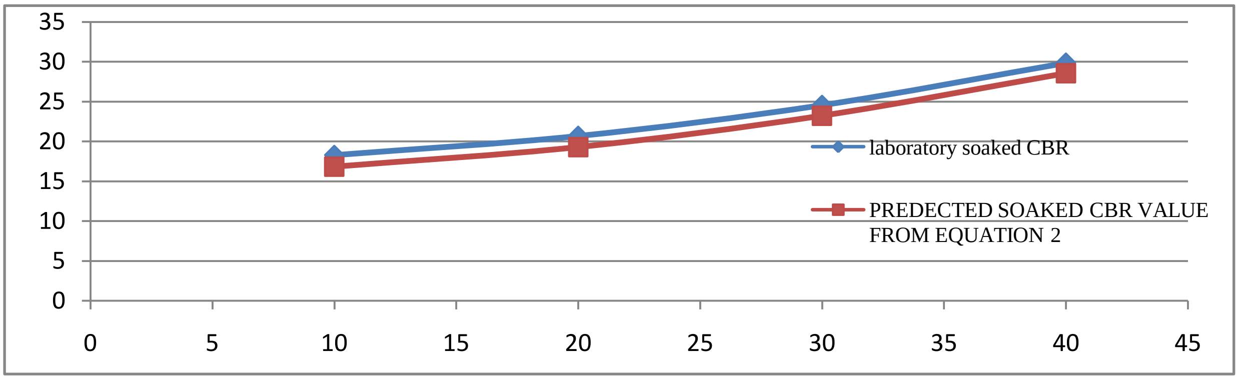

3.4.7 Comparison graph between experimental and predicted UCS values:

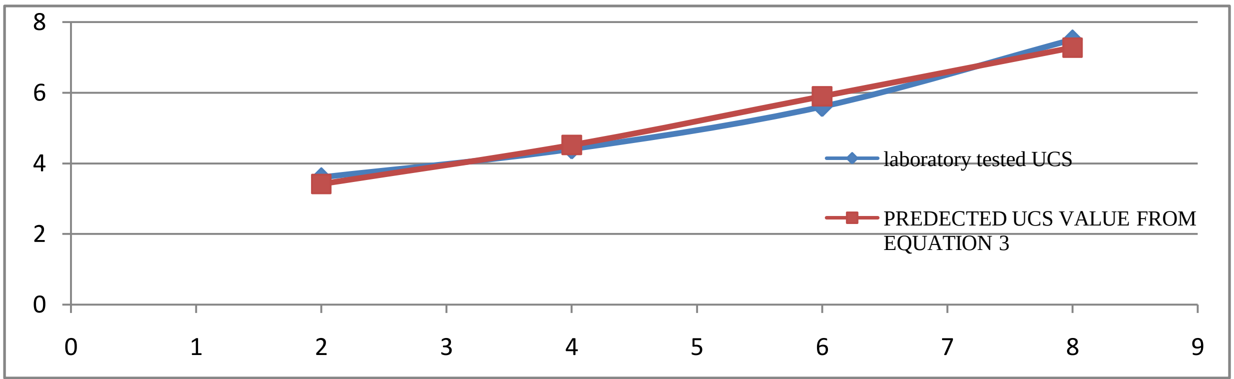

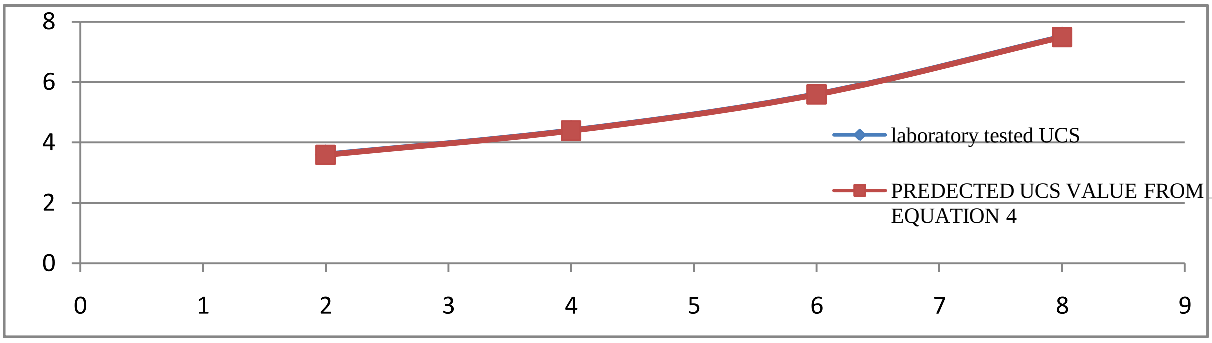

Proposed equations for predicting the soaked CBR and UCS value with index properties of red soil stabilized with stone dust

1) $CBR_{(soaked)} = 0.600*SD+3.680$ with an R^2 value of 0.993
2) $CBR_{(soaked)} = 0.520*OMC-0.804*PI+1.987*PL+156.967*MDD-311.441$ with an R^2 value of 0.999
3) $UCS = 0.248*SD+3.200$ with an R^2 value of 0.974
4) $UCS = 0.065*OMC-0.111*PI-0.168*PL-15.054*MDD-18.786$ with an R^2 value of 0.99

Table 15. Experimental and predicted soaked CBR and UCS values of Red soil stabilized with stone dust

Laboratory Soaked CBR Value	Predected Soaked CBR Value From Equation 1	Predected Soaked CBR Value From Equation 2	Laboratory Tested UCS Value	Predected UCS Value From Equation 3	Predected UCS Value From Equation 4
6.7	6.68	6.70	4.6	4.44	4.61
8.1	8.18	8.10	5	5.06	5.05
9.6	9.68	9.60	5.5	5.68	5.48
11.5	11.18	11.50	6.2	6.30	6.13
12.5	12.68	12.50	7.1	6.92	7.14

3.4.8 Comparison graph between experimental and predicted CBR values:

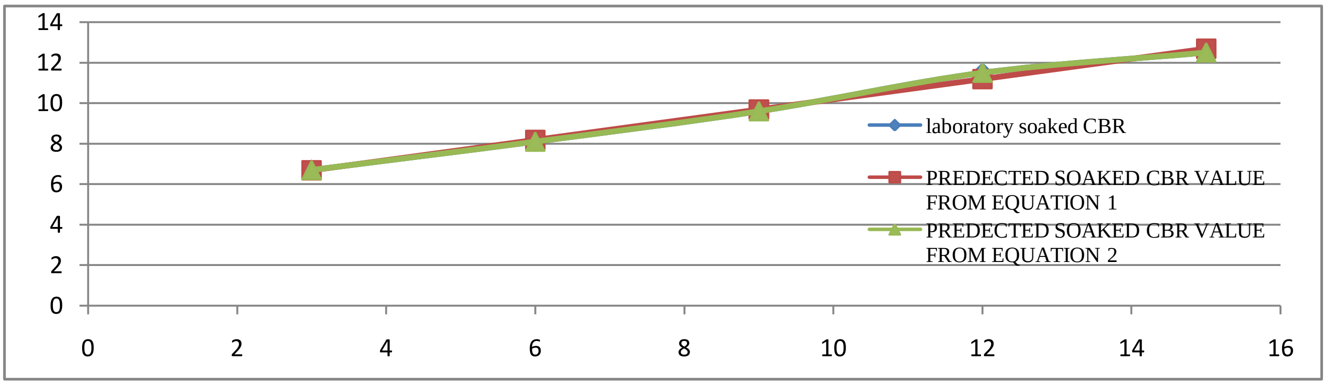

3.4.9 Comparison graph between experimental and predicted UCS values:

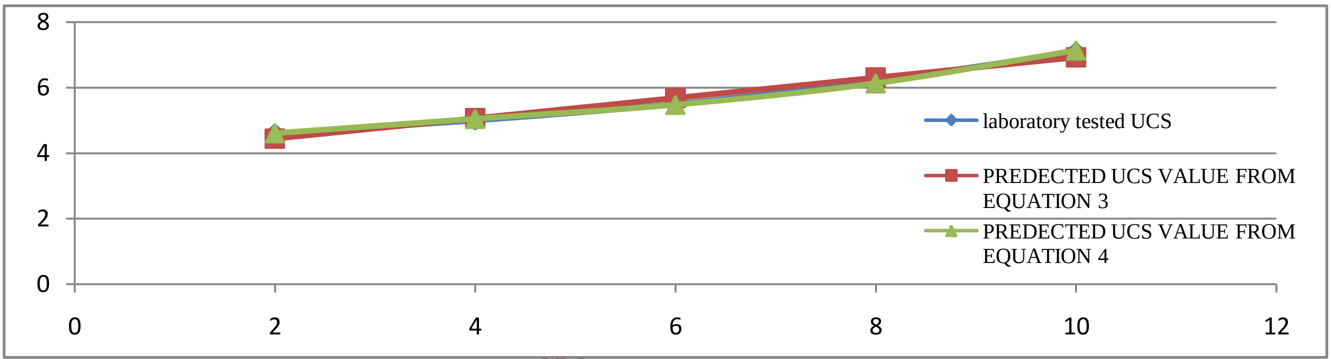

proposed equations for predicting the soaked CBR and UCS value with index properties of red soil stabilized with ordinary Portland cement (opc)

1) $CBR_{(soaked)} = 1.459*OPC+28.389$with an R^2 value of 0.969
2) $CBR_{(soaked)} = 1.524*OMC-0.990*PI+0.121*LL+29.393$with an R^2 value of 1
3) $UCS = 0.710*OPC+3.098$ with an R^2 value of 0.99
4) $UCS = 0.113*OMC-0.297*PI+0.310*LL-2.716$ with an R^2 value of 1

Table 16. Experimental and predicted soaked CBR and UCS values of Red soil stabilized with ordinary Portland cement (opc)

Laboratory Soaked CBR Value	Predected Soaked CBR Value From Equation 1	Predected Soaked CBR Value From Equation 2	Laboratory Tested UCS Value	Predected UCS Value From Equation 3	Predected UCS Value From Equation 4
32.73	32.77	32.72	5.2	5.23	5.19
35.17	35.68	35.16	6.7	6.65	6.69
40.46	39.33	40.45	8.4	8.42	8.39
42.4	42.98	42.39	10.2	10.20	10.18

3.4.10 Comparison graph between experimental and predicted CBR values:

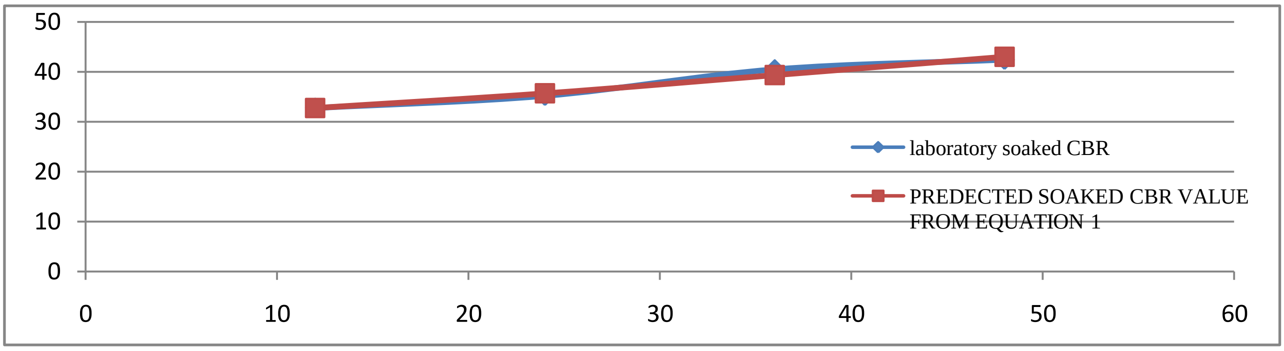

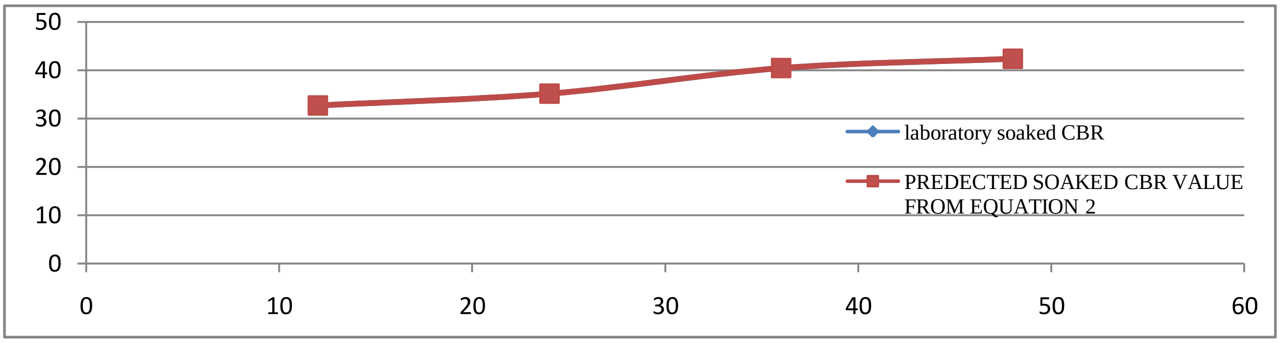

3.4.11 Comparison graph between experimental and predicted UCS values:

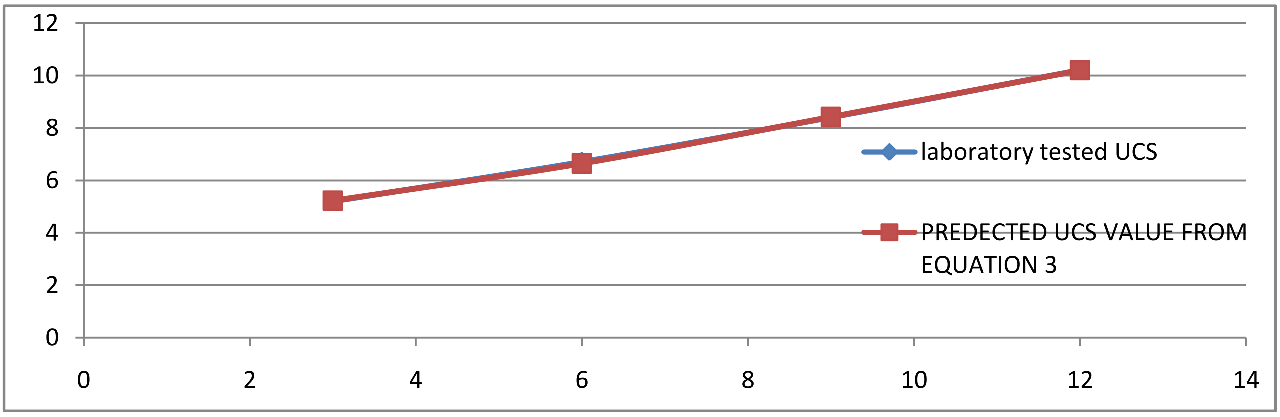

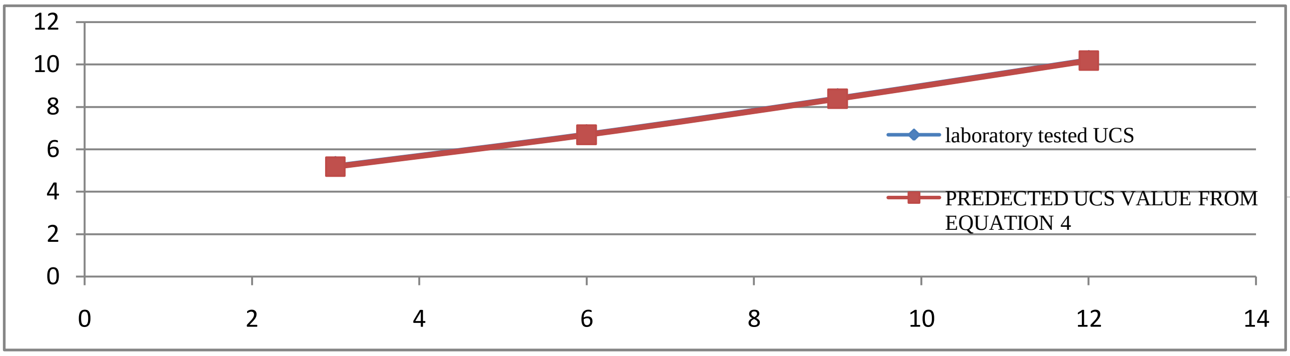

Proposed equations for predicting the soaked CBR and UCS value with index properties of red soil stabilized with Portland slag cement (psc)

1) CBR $_{(soaked)}$ = 1.497*PSC+24.502with an R^2 value of 0.989
2) CBR $_{(soaked)}$ = 0.710*OMC-0.996*PI-81.101*MDD+185.217with an R^2 value of 0.99
3) UCS = 0.736*PSC+2.581with an R^2 value of 0.99
4) UCS =0.087*OMC-0.390*PI-66.579*MDD+130.530 with an R^2 value of 0.99

Table 17. Experimental and predicted soaked CBR and UCS values of red soil stabilized with Portland slag cement (PSC)

Laboratory Soaked CBR Value	Predected Soaked CBR Value From Equation 1	Predected Soaked CBR Value From Equation 2	Laboratory Tested UCS Value	Predected UCS Value From Equation 3	Predected UCS Value From Equation 4
29.39	28.99	29.39	4.8	4.79	4.80
31.7	31.99	31.70	6.2	6.26	6.20
35.2	35.73	35.20	8.2	8.10	8.20
39.9	39.47	39.90	9.9	9.94	9.90

3.4.12 Comparison graph between experimental and predicted CBR values:

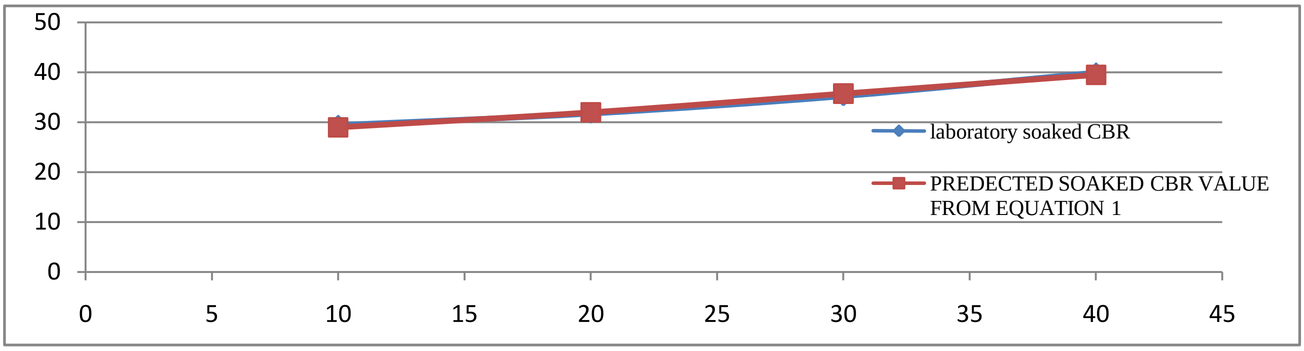

3.4.13 Comparison graph between experimental and predicted CBR values:

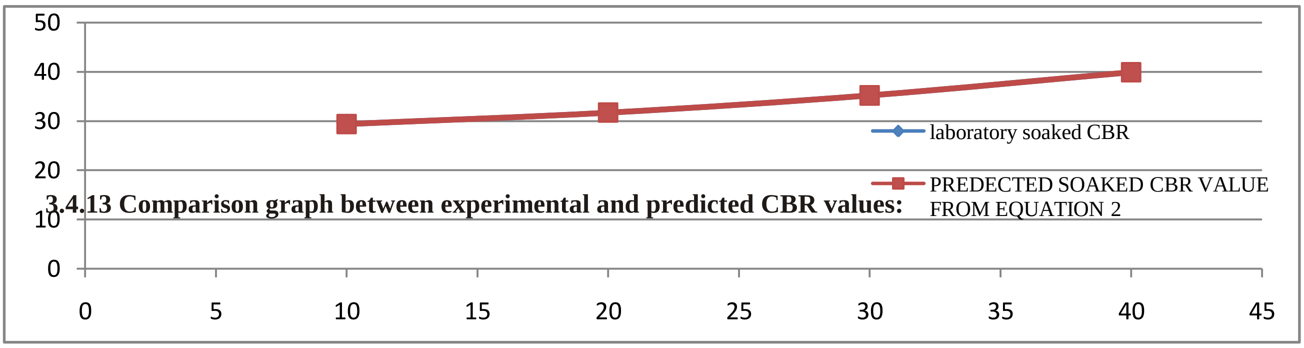

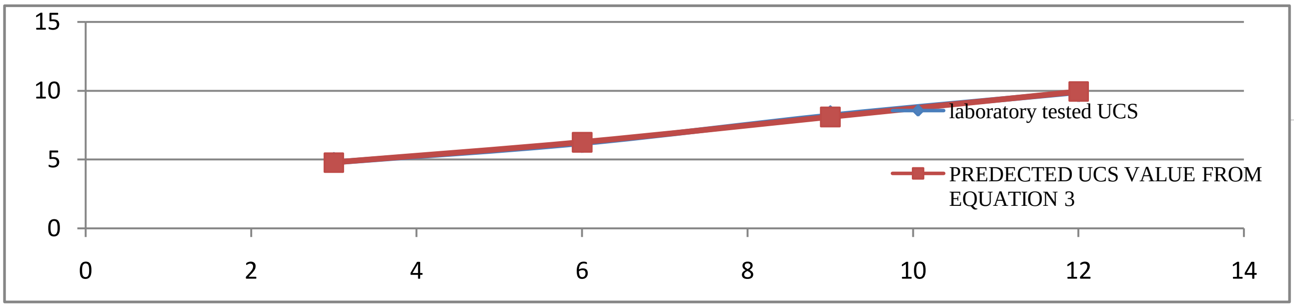

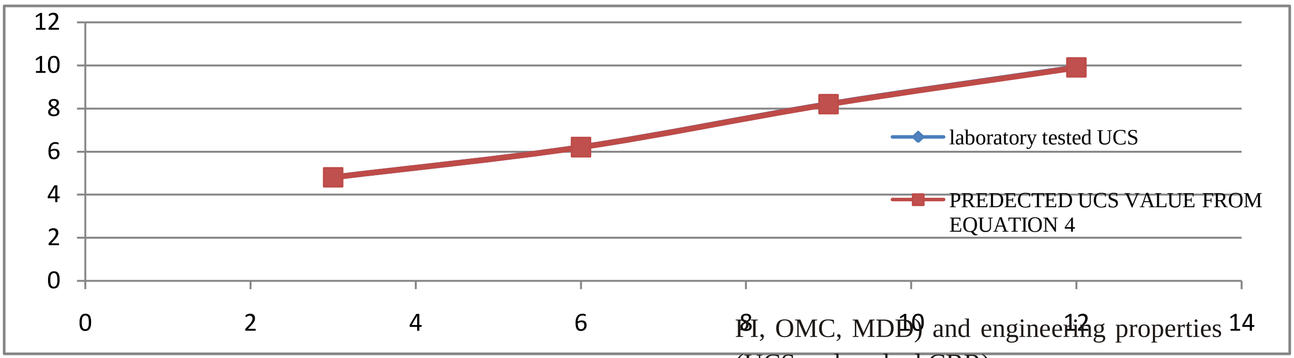

4.0 Conclusion

In this study 31 number of soil samples were tested for soaked CBR, UCS value and equations were developed using IBM SPSS and excel software. From the obtained results, it is concluded that

1) Here two different soils (black cotton soil, red soil) are stabilized with stone dust, ordinary Portland cement (OPC) and Portland slag cement (PSG).
2) For each stabilized material two equations were developed for soaked CBR and UCS
3) All of the simple linear regression analysis (SLRA) was carried out with only % of stabilized materials (%stone dust, %OPC, %PSC).
4) In all regression analysis types (SLRA, MLRA) Index properties (LL, PL, PI, OMC, and MDD) were used as independent variables were as CBR and UCS were dependent variables.
5) In all MLRA equations average R^2 value founded as 0.99.
6) In all SLRA equations average R^2 value founded as 0.98.
7) There is no perfect relation exists between soaked CBR and optimum moisture content as well as UCS and optimum moisture content.
8) All MLRA equations gives the perfect relation between index properties (LL, PL, PI, OMC, MDD) and engineering properties (UCS and soaked CBR).

5.0 FUTURE SCOPE OF THE STUDY

9) The exposure encountered in trying to conduct the current research has revealed areas where further efforts may be proved in the future. Following are some of the recommendations in relation to the subject study:
10) 1. It is recommended to carry out this correlation with a large number of samples including geographical areas in Sangareddy which are not covered by this research.
11) 2. It is also recommended to carry out such a study in other parts of Telangana State especially in regions where Black Cotton soil is abundantly to be found.
12) 3. It is advisable to conduct comparative correlations between soaked and Unsoaked CBR value with soil index properties.
13) 4. It would be of interest to investigate the effect of compaction and moisture content on the value of CBR under varying density and moisture conditions for coarse grained materials

6.0 REFERENCES

*e*ISSN 1303-5150

[1]. Dr.Dilip Kumar Talukdar (2014) "A Study of Correlation between California Bearing Ratio (CBR) Value with Other Properties of Soil" International Journal of Emerging Technology and advanced engineering, Volume 04, Issue01.

[2] Naveen B Shirur, Santosh G Hiremath (2014) "Establishing Relationship between CBR Value and Physical Properties of Soil",ISOR Journal of Mechanical and Civil Engineering (ISOR-JMCE), volume 11, issue05.

[3] Ramasubbarao G.V and Shivakumar G. (2013) "Predicting Soaked CBR Value of Fine Grained Soils Using Index and Compaction Characteristics'' Jordan Journal of Civil Engineering, Volume07.

[4] P.G.Rakaraddi,Vijaygomarsi (2015) " Establishing Relationship Between CBR With Different Soil Properties'', International Journal of Research in Engineering and Technology Volume: 04 Issue: 02.

[5] Mayank Korde and R K Yadav (2015)"Predicting The CBR Value of Different Soils With The Help of Index Properties'', International Journal of engineering Research,Scince and Technology, Volume04,Number03.

[6] Guruprasad Jadhav, Vishwajeet Biradar and Prof. Md KhajaMoniuddin (2016), "Relation between C.B.R Values and Geotechnical Properties of Expansive Soil'', IJSRD - International Journal for Scientific Research & Development Vol. 04, Issue 01

[7] Akshaya Kumar Sabat (2013) **"**Prediction of California Bearing Ratio of a Soil Stabilized with Lime and Quarry Dust Using Artificial Neural Network" EJGE- Vol. 18

[8]. Pradeep Muley and Pradeep Kumar Jain (2013**)** **"** Betterment and Prediction of CBR of stone dust mixed poor soils" Proceedings of Indian Geotechnical Conference December 22-24,2013.

[09] IS 2720-Part 16-1987, "Methods of Test for Soil, Laboratory Determination of CBR, Bureau of Indian Standards", New Delhi, India.

[10] IS 2720-Part 4-1985"Grain Size analysis, Bureau of Indian Standards", New Delhi, India.

[11] IS 2720-part 5-1985, "Determination of Liquid and plastic limit", Bureau of Indian Standards", New Delhi, India.

[12] IS 2720-Part 3-1980, "Determination of specific gravity, Bureau of Indian Standards", NewDelhi, India.

[13] IS 2720-Part 7-1980, "Determination of water content-dry density relation using light compaction", Bureau of Indian Standards, New Delhi, India.

[14]] IS 2720-Part 10-1991Determination of Unconfined Compressive Strength. In this IS code detailed procedure of the calculations along with the apparatus used for performing laboratory unconfined compression test on clayey soil, undisturbed, remoulded or compacted, using controlled rate of strain is given

SILICAFUME BASED GEOPOLYMER CONCRETE-DURABILITY PROPERTIES FOR M60 GRADE

M.Uday Bhaskar
Asst.Professor, Department of Civil Engineering, MallaReddy Engineering College (Autonomus) Maisammaguda, Dhulapally, Secunderabad, Telangana, India 500100.
Miryala Prashanth
Asst.Professor, Department of Civil Engineering, MallaReddy Engineering College (Autonomus) Maisammaguda, Dhulapally, Secunderabad, Telangana, India 500100.
Shantala.T
Asst.Professor, Department of Civil Engineering, Srinivasa Ramanujan Institute of Technology (Autonomus)
,Ananthapuramu Andhara Pradesh, India 515701

Abstract: The present technology which is in use for the manufacturing of ordinary Portland cement concrete is used. In order to activate the geopolymerization process for binding the concrete,the basic material namely silica fume has been used for replacing the ordinary Portland cement completely. A combination of NaOH solution and Na_2SiO_3 is used for activating the silicon content in silica fume.The steps involved in the manufacturing process such as preparation of material, mixing of material, placing of material, compaction of material and curing are given in this paper. In order to enhance the workability of fresh silica fume based geopolymer concrete, the super plasticizer which is naphthalene based is used. It can also be improved by adding extra water.

The M60 grade is used in this paper with different water/binder ratios for case 1, 0.3 for GPC(Geopolymer concrete) and 0.3 for OPC(Ordinary Portland concrete) case 2 , 0.34 for GPC(Geopolymer concrete) and 0.32 for OPC(Ordinary Portland concrete) and the test specimens are prepared and cured in different durability parameters and these specimens are analyzed. The comparision is made for the two cases of the durability properties.

Index Terms – Geopolymer, Silica Fume, Naphthalene, GPC, OPC.

DOI Number: 10.14704/nq.2022.20.5.NQ22541 **NeuroQuantology 2022; 20(6):5327-5337**

1. INTRODUCTION

Concrete, composite construction material which is a mixture of cement, fine aggregate, coarse aggregate and water and a small quantity of air. For over a century the concrete has been using as a leading construction material. It has been estimated that the production of concrete is approximately 2.5 tones i.e.; 1 m^3 per capita. After 2025 the overall world wide usage of natural aggregate will be in the range of 10-13 billion tones. As the concrete can be moulded to any form or shape so it can be used as a desirable building material. Concrete can be used for constructing various structures such as bridges, buildings, dams, barrages, highways etc. The various other parameters such as durability, strength and economy has made the concrete as the most desirable material. Based on the materials which are used in the concrete the concrete can withstand the compression of about 7000 kg/cm^2 or more. The concrete is strong in compression and the tensile strength of concrete is much lower when compared to the compressive strength.

Concrete is the leading construction material throughout the world and is generally used in all types of construction works like high and low raise building and many other infrastructural developmental works. It essentially consists of a mixture of cement, fine aggregate, coarse aggregate, water and admixtures. The major part of aggregate is formed by the materials like sand and gravel. According to the strength parameters and grade of concrete, the mixing of these materials are done in the required proportions

Since the start of the mechanical transformation in 1760 there has been an expansion in the utilization of non-renewable energy source vitality coming about in intensified emanations of GHG's (Greenhouse Gases) (Slanina, 2004). This expanded worldwide dependency on oil, coal and gaseous petrol has brought about the discharge more than 1100 Gt (Giga ton) of CO2 outflows to the atmosphere (IPCC, 2001). The arrival of GHGs adds to anthropogenic prompted a dangerous atmospheric devation with the most critical of these gases being CO2 (Carbon dioxide) (IPCC, 2001). This is because of the sheer amounts that are being transmitted, despite the fact that it doesn't have the most elevated radioactive compelling potential. The cement production releases the large amount of CO2 and forms the major cause for the emissions of green house gases.

Worldwide on an average the amount of CO2 released in to amosphere is of about 5 to 8 percent from the cement industry. The total production of CO2 throughout the world is 42 billion tones in 2014. Out of this there are 3 major contributors namely China producing 12 billion tones (46 %), United States of America producing 6 billion tones (16 %) and India producing 2.6 billion tones (6 %). Cement industry is the major producer of CO2. On an average the cement manufacturing activity contributes to about 6 to 8 % of global anthropogenic CO2 emissions. Cement is only a constituent of concrete and is responsible for 20 to 35 % of the world's GHG's.

Because of concrete magnificent strength, durability properties and its availability, it is used commonly in the construction activity. In reality, the world's most devoured man-made material is concrete and its utilization is increased drastically.

From the above discussions it is been clear that the concrete industry producing vast amount of CO2 around the world and production of concrete is not environmentally friendly, so there is emergency to reduce the usage of cement and this can be achieved by different alternatives

The manufacture of Portland cement clinker involves the calcinations of calcium carbonate according to the reactions:

$3CaCO_3 + SiO_2 \rightarrow Ca_3SiO_5 + 3CO$

$2CaCO_3 + SiO_2 \rightarrow Ca_2SiO_4 + 2CO_2$

In order to scale back additional the GHG emissions related to concrete additional viable different to interchange OPC are being examined with geopolymer materials thought-about to be one such alternative.

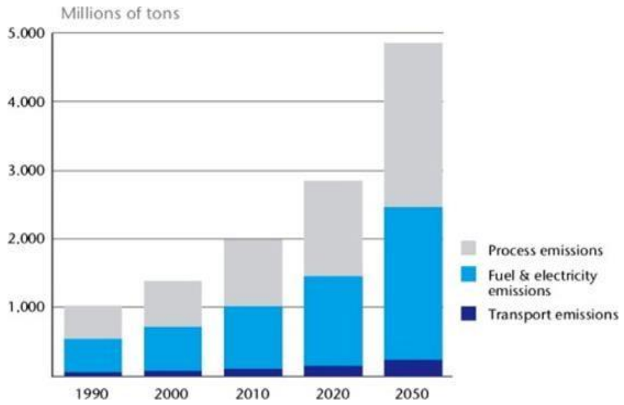

GEOPOLYMER CONCRETE

Due to increase in the awareness in regard to the adverse effects of over utilization of natural resources, most of the advanced environment friendly methods are to be developed for the effective management of the natural resources. Construction activities are one of the most important one for depleting the naturally available resources like cement, sand, gravel, water etc. Due to the increased cost of materials of the concrete, the engineers have focused on the development of alternate ways for reducing the cost of production of the materials of the concrete.

Industrial activities related to the sectors of transportation, steel and energy are responsible for the formation of large amounts blast furnace slag, silica fume, ash, quarry dust and creating a major problem in their disposal.

Davidovitis was the first man to introduce the geopolymer technology in the year 1978. His research depicts that by using the geopolymer technology in the concrete the emission of CO2 can be reduced in to the environment.Geopolymer belong to the family of inorganic polymers. The geopolymer chemical composition is similar to naturally available zeolitic materials, but in the case of micro structure it is amorphous in nature. Any material which is rich in silica content and aluminum can be used for the manufacturing of geopolymer. The combination of NaOH or KOH and Na_2SiO_3 or K_2SiO_3 is the most commonly used alkaline liquid in the geopolymerization technique.

5416

Materials Required For Geopolymer Concrete

Cementitious binder:

In order to produce geopolymer concrete various naturally available materials and industrial by products are used. The most commonly used cementetious binders are silica fume, GGBS, fly ash, metakaolin, rice husk ash etc.

Alkaline activators:

Alkaline activators are the important ingredient of geopolymer mix. The binding property is obtained by igniting the aluminum and silica present in the cementitious binder by undergoing geopolymerization . It mainly uses high pH activators like NaOH and KOH and Na_2SiO_3 or K_2SiO_3

Aggregates:

Aggregates used to produce geopolymer concrete should be chosen and tested as per IS standards.

Super plasticizer:

This is used in concrete to accelerate or decelerate the setting time and also to attain good workability conditions in a concrete

2. LITERATURE REVIEW

A review on geopolymers and geopolymer concrete is presented in this chapter focusing on low amount of calcium fly ash based geopolymer paste and concrete. In order to increase the greenness and durability of the structures , new building materials are found out which can also reduce the cost of construction and also reduces the need of replacing the non obsolescent structures thereby saving the environment . In this regard, geopolymers are best suited material which is having high potential for durability and greenness.

Literature Review On Durability:

Marosszeky M, Munn R,Brungs M andSong X J,, A study on fly ash based geopolymer concrete attacked by sulphuric acid is carried out. They reported that due to sulphuric acid attack there will be corrosion in the geopolymer concrete. This can be controlled by diffusion process.From the SEM analysis it has been observed that there is excellent gel aggregate interface. At the corroded region it is observed that the geopolymer matrix remains similar to the not affected one and for the surrounding aggregates it still functions effectively the binding property.

Sobolev K G,reported that there is an increase in chemical and thermal resistance by adding 50 % of the granulated blast furnace slag by weight in the cement material. It is observed that the permeability is very low and offered a good resistance to freezing and thawing cycles and chemical attack. Even after 140 cycles of freezing and thawing test at -50^{0}C the blast furnace slag destruction has not been observed.

Brito J de , Branco F A and Dos Santos J R, ,identified that when the concrete is subjected to fire attack, there will be a problem in determining the depth of deteriorated concrete and assessment of the concrete structure becomes difficult. So to overcome that a new method called fire behavior test has been developed. By this method the depth of deteriorated concrete is identified by measuring the water absorption and tensile stress failure from the holes drilled in the structure under analysis.

3. METHODOLOGY

MIX DESIGN OF CONCRETE FOR TWO CASES

CASE1

FINAL PROPORTION OF OPC CONCRETE & FINAL PROPORTIONS OF GPC CONCRETE

	Cement	F.A	C.A	Water	Super plasticizer
Ratio	1	1.16	2.45	0.3	0.03

	Silica Fume	F.A	C.A	Water	NaOH	Na_2Sio_3	Super plasticizer
Ratio	1	1.3	3.05	0.09	0.06	0.23	0.015

AMOUNT OF MATERIALS USED IN OPC & GPC COMPOSITION OF SILICA FUME

	OPC (Kg/m³)	GPC (Kg/m³)
Cement	493	_
Silica fume	_	424.62
Fine Aggregate	575	555
Coarse aggregate	1210	1295
NaOH	_	28.31
Na_2SiO_3	_	99.08
Water	133	42.46
Super plasticizer	15	12.73

CASE 2

FINAL PROPORTION OF OPC& GPC CONCRETE

	Cement	F.A	C.A	Water	Super plasticizer
Ratio	1	1.3	2.6	0.32	0.03

	Silica Fume	F.A	C.A	Water	NaOH	Na_2Sio_3	Super plasticizer
Ratio	1	1.36	3.16	0.04	0.1	0.25	0.03

AMOUNT OF MATERIALS USED IN OPC &GPC COMPOSITION OF SILICA FUME

	OPC (Kg/m³)	GPC (Kg/m³)
Cement	463	_
Silica fume	_	409
Fine Aggregate	600	555
Coarse aggregate	1210	1295
NaOH	_	41
Na_2Sio_3	_	103
Water	148	16
Super plasticizer	14	13

4. TEST RESULTS

TESTS ON THE CEMENT:

S.No	Property	Test method	Test Result	Requirements of IS 12269-1987
1	Standard consistency	Vicat Apparatus (IS: 4031 Part - 4)	32%	_
2	Specific gravity	Sp. Gravity bottle (IS:4031 Part - 4)	3.15	_
3	Initial setting time (min)	Vicat Apparatus (IS: 4031 Part - 4)	33	Minimum 30
4	Final setting time (Hours)	Vicat Apparatus (IS: 4031 Part - 4)	8 hrs	Maximum 600
5	Specific Surface Area (m²/Kg)	Blaine's Air permeability (IS:5516-1996)	385	Minimum 225
6	Soundness (mm)	Le-Chatlier's method (IS: 4031 Part – 3)	2	Not more than 10mm
7	Compressive strength (N/mm²)	Compression mould (IS: 4031 Part – 6)	55	53
8	Fineness	Sieve test on sieve no.9 (IS: 4031 Part – 1)	7%	10%

5417

TESTS ON AGGREGATES

S. No	Property	Method	Fine Aggregate	Coarse Aggregate
1	Specific Gravity	Pycnometer IS:2386 Part 3 - 1986	2.6	2.66
2	Bulk Density (Kg/m³)	IS:2386 Part 3 - 1986	1650	1780
3	Fineness Modulus	Sieve Analysis (IS:2386 Part 2 - 1963)	2.76	6.04
4	Absorption (%)	IS:2386 Part 3 - 1986	0.1	0.52
5	Moisture content (%)	IS:2386 Part 3 - 1986	0	0

SILICA FUME AND ITS PROPERTIES

S.No	Property	Test method	Test Result	Requirements of IS 15388: 2003
1	Specific gravity	Sp. Gr bottle (IS:4031 Part - 4)	1.62	_
2	Specific Surface Area (m^2/Kg)	Blaine's Air permeablity (IS:5516-1996)	18000	Minimum 15000
3	Bulk Density (Kg/m³)	IS:2386 Part 3 - 1986	650	_
4	Physical Appearance	_	Powder form	_

DURABILITY TESTS ON CONCRETE :

PERMEABILITY TEST ON CONCRETE

In this test the concrete specimen or mortar of known dimensions is kept in chamber which is specially designed and subject to a known hydrostatic pressure.

CASE 1

	Volume of water collected (ml)	Time (Hrs)	Height of Sample (m)	Area of Sample (cm2)	Pressure Head (m)	Coefficient of permeability (cm/sec)
OPC	9	96	0.1	78.53	100	3.17×10^{-10}
GPC	6	96	0.1	78.53	100	2.8×10^{-10}

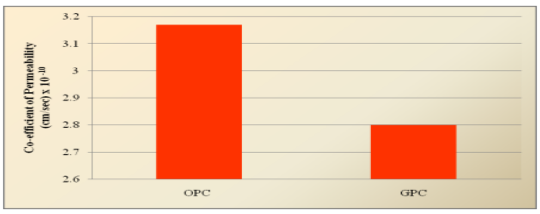

CASE2

	Volume of Water Collected (ml)	Coefficient of Permeability (cm/sec)
OPC	9.5	3.12×10^{-10}
GPC	7	2.63×10^{-10}

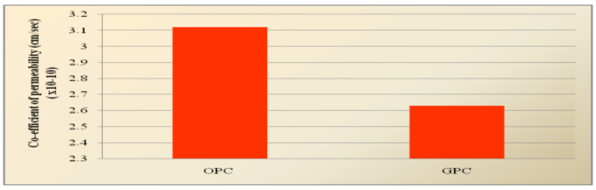

ULTRASONIC PULSE VELOCITY (UPV) TEST

Ultrasonic pulse velocity test is a non destructive test which is conducted according to the IS code 13311:1992. In this test the strength of the material is estimated by measuring the sound speed which is travelling through the materials.

CASE 1

	PULSE VELOCITY (V) (Km/Sec)	
	OPC	GPC
28 Days	4.18	4.25
90 Days	4.79	5.2

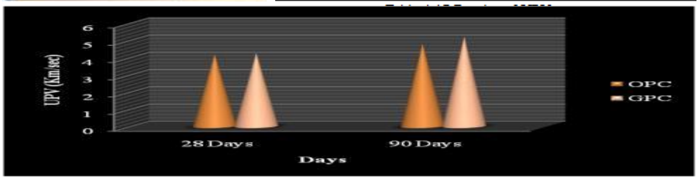

	Pulse Velocity (V) (km/sec)	
	OPC	GPC
28 Days	4.11	4.2
90 Days	4.692	5.036

CASE 2

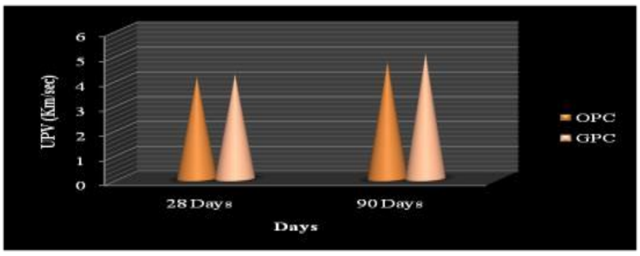

RCPT (RAPID CHLORIDE PENETRATION TEST)

CASE1

	RCPT Value (Columbs)
OPC	1925
GPC	1768

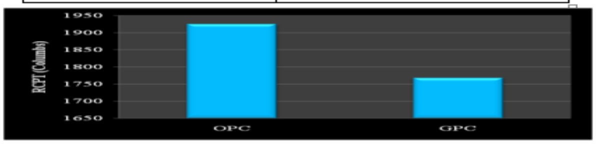

CASE2

	RCPT Value (Columbs)
OPC	1820
GPC	1650

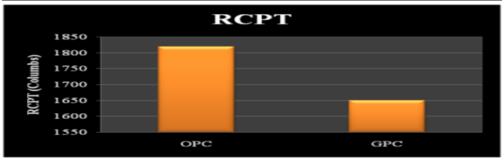

WATER ABSORPTION TEST

As per the code ASTM C 642 this test is conducted on 150mm x 150mm x 150mm concrete cubes for various mix proportions and the water absorption values are calculated.

CASE1

	Water Absorption (%)
OPC	2.78
GPC	2.65

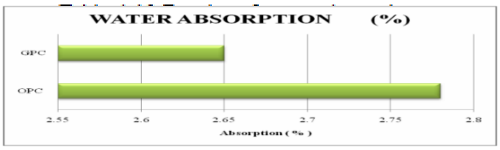

CASE2

	Water Absorption (%)
OPC	2.91
GPC	2.76

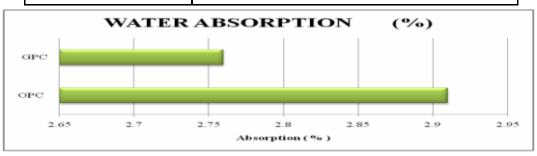

WATER PENETRATION TEST

This test is the method of determination of depth of water penetrated in the concrete hardened surface which is cured for 28 days in water.

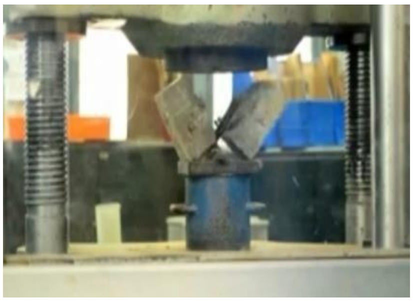

CASE 1

	Water Penetration Depth (mm)
OPC	12.4
GPC	10.9

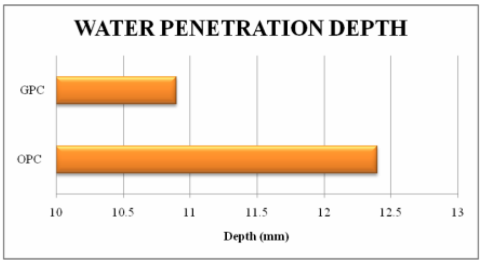

CASE 2

	Water Penetration Depth (mm)
OPC	13.33
GPC	11.00

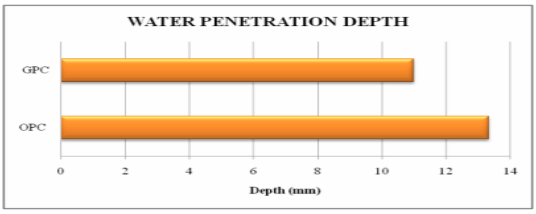

SULPHATE RESISTANCE TEST

Generally sulphates which are present in the ground water and soil come in contact with concrete and causes effect. So in order to study the effect of sulphates on concrete sulphate resistance test is conducted.

SAMPLES CURED IN Na_2SO_4

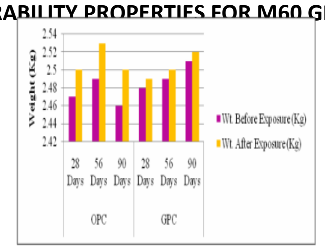

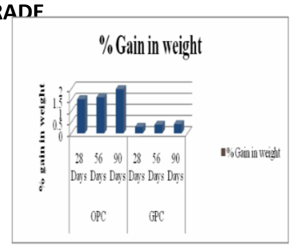

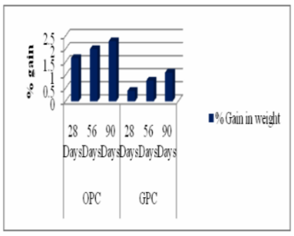

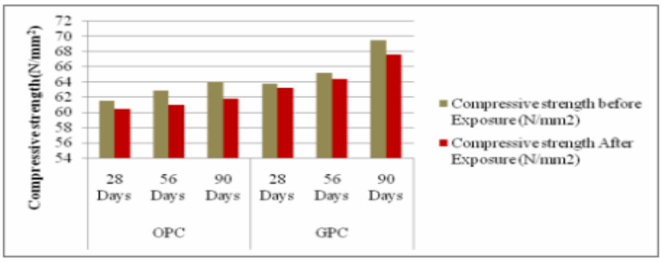

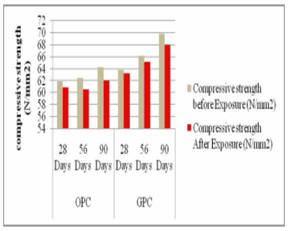

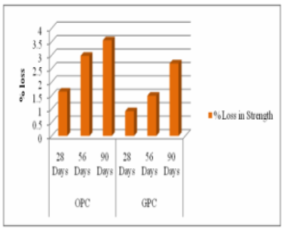

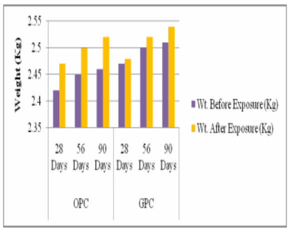

SAMPLES CUREDINMgSO$_4$

CASE1

	OPC			GPC		
	28 Days	56 Days	90 Days	28 Days	56 Days	90 Days
Wt. Before Exposure (Kg)	2.47	2.49	2.46	2.48	2.49	2.51
Wt. After Exposure (Kg)	2.49	2.54	2.53	2.5	2.51	2.55
% Gain in weight	1	2.1	3.2	1	1.3	1.7
Compressive strength before Exposure (N/mm²)	61.5	62.9	64	63.8	65.22	69.5
Compressive strength After Exposure (N/mm²)	60.33	61.2	61.9	63.22	64.2	67.9
% Loss in Strength	1.9	2.7	3.2	0.9	1.56	2.2

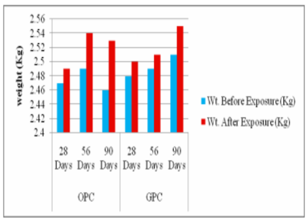

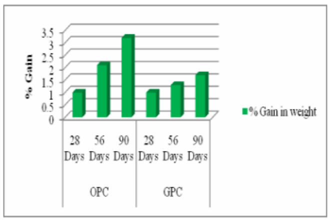

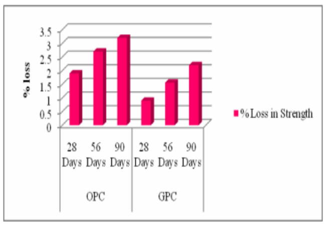

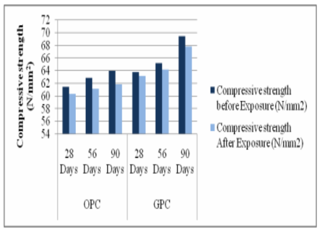

CASE2

CASE2

	OPC			GPC		
	28 Days	56 Days	90 Days	28 Days	56 Days	90 Days
Wt. Before Exposure (Kg)	2.47	2.49	2.46	2.48	2.49	2.51
Wt. After Exposure (Kg)	2.5	2.53	2.5	2.49	2.5	2.52
% Gain in weight	1.54	1.63	2	0.3	0.39	0.42
Compressive strength before Exposure (N/mm²)	61.5	62.9	64	63.8	65.22	69.5
Compressive strength After Exposure (N/mm²)	60.44	61.01	61.8	63.23	64.35	67.65
% Loss in Strength	1.72	3	3.43	0.88	1.33	2.66

	OPC			GPC		
	28 Days	56 Days	90 Days	28 Days	56 Days	90 Days
Wt. Before Exposure (Kg)	2.47	2.49	2.46	2.48	2.49	2.51
Wt. After Exposure (Kg)	2.49	2.54	2.53	2.5	2.51	2.55
% Gain in weight	1	2.1	3.2	1	1.3	1.7
Compressive strength before Exposure (N/mm²)	61.5	62.9	64	63.8	65.22	69.5
Compressive strength After Exposure (N/mm²)	60.33	61.2	61.9	63.22	64.2	67.9
% Loss in Strength	1.9	2.7	3.2	0.9	1.56	2.2

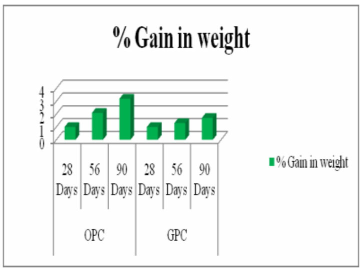

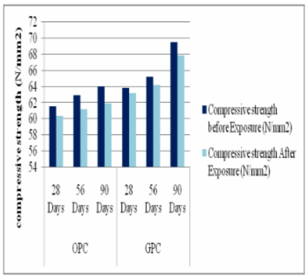

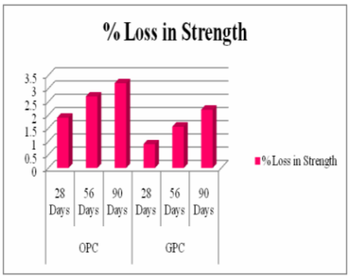

ACID RESITANCE ATTACK

➤ ***SAMPLES CURED IN H_2SO_4***

CASE 1

	OPC			GPC		
	28 Days	56 Days	90 Days	28 Days	56 Days	90 Days
Wt. Before Exposure (Kg)	2.44	2.5	2.54	2.48	2.51	2.55
Wt. After Exposure (Kg)	2.24	2.125	1.85	2.43	2.38	2.295
% Loss in weight	**8**	**15**	**27**	**2**	**5**	**10**
Compressive strength before Exposure (N/mm²)	63.4	64.01	65.9	67.2	69.8	71.6
Compressive strength After Exposure (N/mm²)	60.79	58.88	57.33	64.51	62.9	62.96
% Loss in Strength	**6**	**8**	**13**	**4**	**9**	**12**

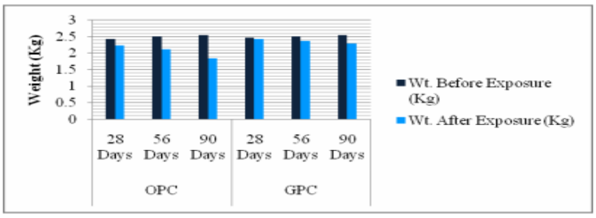

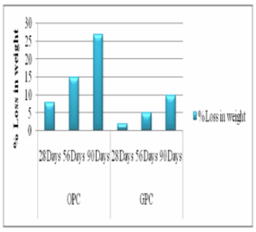

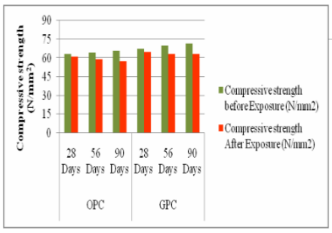

5421

CASE 2

	OPC			GPC		
	28 Days	56 Days	90 Days	28 Days	56 Days	90 Days
Wt. Before Exposure (Kg)	2.48	2.49	2.48	2.5	2.49	2.51
Wt. After Exposure (Kg)	2.3	2.16	1.86	2.45	2.34	2.28
% Loss in weight	7	13	25	2	6	9
Compressive strength before Exposure (N/mm²)	63.1	63.9	65	67	69.2	70.3
Compressive strength After Exposure (N/mm²)	59.3	58.15	56.55	63.65	63.66	62.56
% Loss in Strength	6	9	13	5	8	11

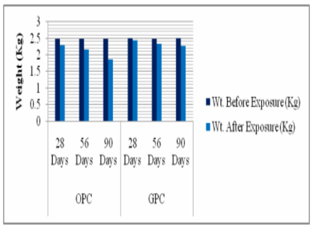

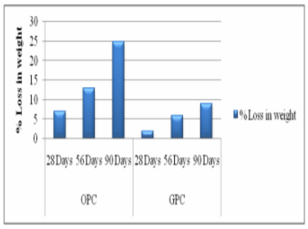

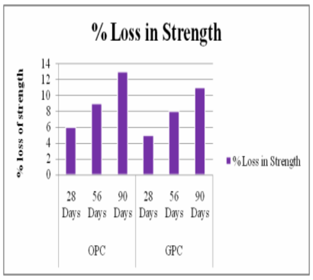

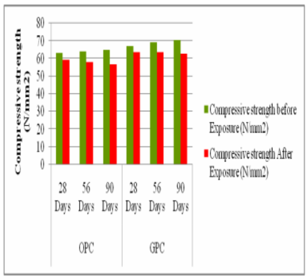

CHLORIDE RESISTANCE ATTACK

The structures which are near to the sea coast are subjected to chloride attack. Due to the penetration of chloride in to the concrete the reinforcement is ubjected to corrosion. So by chloride resistance test the effect of chloride on geopolymer concrete and normal concrete were studied and compared.

➤ ***SAMPLES CURED INNacl***

CASE 1

	OPC			GPC		
	28 Days	56 Days	90 Days	28 Days	56 Days	90 Days
Wt. Before Exposure (Kg)	2.44	2.45	2.47	2.44	2.45	2.46
Wt. After Exposure (Kg)	2.47	2.49	2.53	2.46	2.49	2.52
% Gain in weight	**1**	**1.85**	**2.3**	**0.8**	**1.33**	**2.1**
Compressive strength before Exposure (N/mm²)	61.23	63.8	64.7	62.9	64.22	65.3
Compressive strength After Exposure (N/mm²)	60.55	62.46	62.82	62.3	63.39	64.15
% Loss in Strength	**1.1**	**2.1**	**2.9**	**0.89**	**1.29**	**1.75**

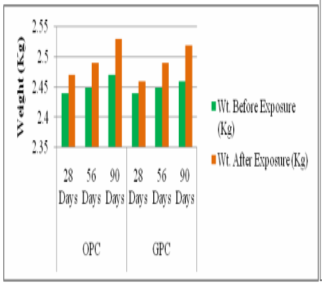

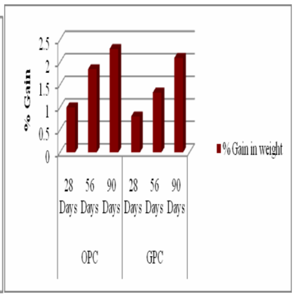

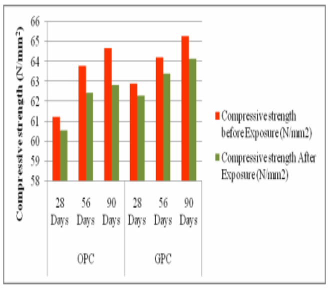

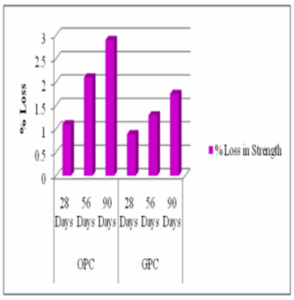

CASE 2

	OPC			GPC		
	28 Days	56 Days	90 Days	28 Days	56 Days	90 Days
Wt. Before Exposure (Kg)	2.46	2.51	2.5	2.49	2.48	2.52
Wt. After Exposure (Kg)	2.48	2.56	2.56	2.51	2.51	2.57
% Gain in weight	1	1.88	2.5	0.9	1.45	2.1
Compressive strength before Exposure (N/mm²)	60.45	62.1	63.9	64.1	68.23	70.1
Compressive strength After Exposure (N/mm²)	59.68	60.87	62.11	63.48	67.24	68.9
% Loss in Strength	1.23	1.98	2.8	0.96	1.44	1.63

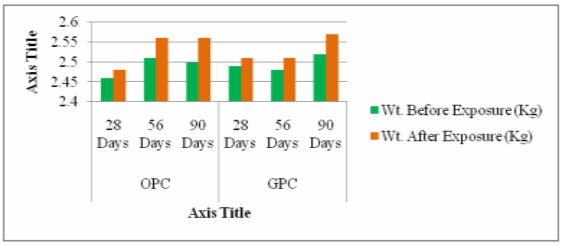

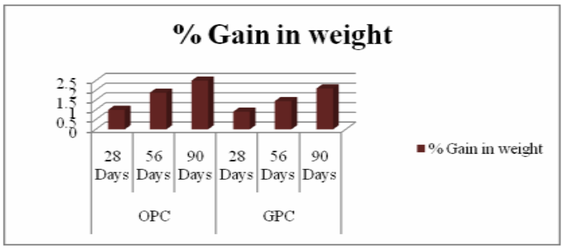

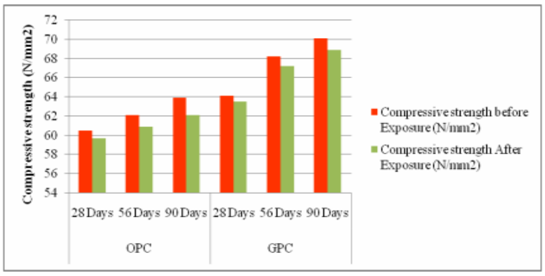

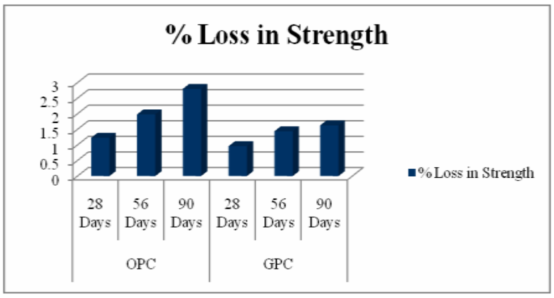

SORPTIVITY

Sorptivity is the rate of absorption of water in to the concrete. This test is based on Darcy's law and was developed by Hall. It is simple and rapid test for determining the tendency of concrete to absorb water by capillary suction.

NeuroQuantology | June 2022 | Volume 20 | Issue 6 | Page 5415-5425 | doi: 10.14704/nq.2022.20.6.NQ22548

CASE 1

TIME (min)	WEIGHT (gm)	GAINED WEIGHT (gm)	CUMILATIVE WEIGHT GAINED (gm)	VOLUME OF WATER (mm3)	SURFACE AREA (mm2)	i=w/(A*Density) (mm)	√ (TIME) (√min)
			(W)	(V)	(A)		
0	776.1	0	0	0	7853.98	0	0
1	777.19	1.09	1.09	1090	7853.98	0.13	1
2	778.21	1.02	2.11	2110	7853.98	0.26	1.41
3	779.41	1.2	3.31	3310	7853.98	0.42	1.73
4	780.38	0.97	4.28	4280	7853.98	0.54	2
5	781.36	0.98	5.26	5260	7853.98	0.67	2.24
9	782.56	1.2	6.46	6460	7853.98	0.82	3
12	783.87	1.31	7.77	7770	7853.98	0.99	3.46
16	785.01	1.14	8.91	8910	7853.98	1.13	4
20	786.23	1.22	10.13	10130	7853.98	1.29	4.47
25	787.52	1.29	11.42	11420	7853.98	1.45	5

Table 4.25 Sorptivity results of OPC

TIME (min)	WEIGHT (gm)	GAINED WEIGHT (gm)	CUMILATIVE WEIGHT GAINED (gm)	VOLUME OF WATER (mm3)	SURFACE AREA (mm2)	i=w/(A*Density) (mm)	√ (TIME) (√min)
			(W)	(V)	(A)		
0	776.29	0	0	0	7853.98	0	0
1	773.82	0.92	0.92	920	7853.98	0.117	1
2	774.76	0.94	1.86	1860	7853.98	0.236	1.41
3	775.85	1.09	2.95	2950	7853.98	0.375	1.73
4	776.83	0.98	3.93	3930	7853.98	0.5	2
5	777.82	0.99	4.92	4920	7853.98	0.626	2.24
9	778.84	1.02	5.94	5940	7853.98	0.756	3
12	779.84	1	6.94	6940	7853.98	0.88	3.46
16	780.84	1	7.94	7940	7853.98	1.01	4
20	781.94	1.1	9.04	9040	7853.98	1.15	4.47
25	783.08	1.14	10.18	10180	7853.98	1.3	5

Table 4.26 Sorptivity results of GPC

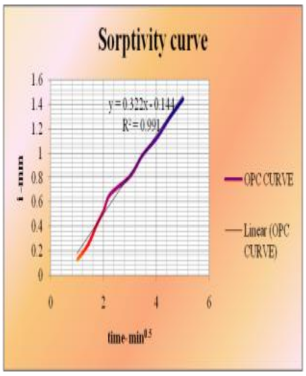

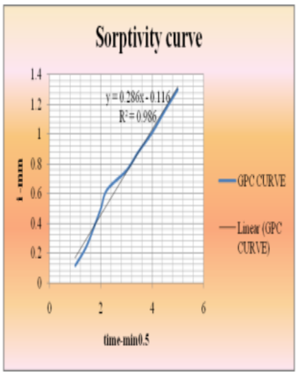

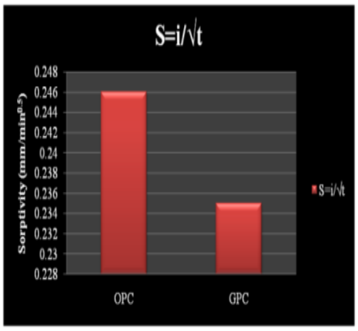

CASE 2

TIME (min)	WEIGHT (gm)	GAINED WEIGHT (gm)	CUMILATIVE WEIGHT GAINED(gm)	VOLUME OF WATER (mm3)	SURFACE AREA (mm2)	i=w/(A*Density) (mm)	√ (TIME) (√min)
			(W)	(V)	(A)		
0	776.1	0	0	0	7853.98	0	0
1	777.19	1.09	1.09	1090	7853.98	0.13	1
2	778.21	1.02	2.11	2110	7853.98	0.26	1.41
3	779.41	1.2	3.31	3310	7853.98	0.42	1.73
4	780.38	0.97	4.28	4280	7853.98	0.54	2
5	781.36	0.98	5.26	5260	7853.98	0.67	2.24
9	782.56	1.2	6.46	6460	7853.98	0.82	3
12	783.87	1.31	7.77	7770	7853.98	0.99	3.46
16	785.01	1.14	8.91	8910	7853.98	1.13	4
20	786.23	1.22	10.13	10130	7853.98	1.29	4.47
25	787.52	1.29	11.42	11420	7853.98	1.45	5

Table 4.25 Sorptivity results of GPC

TIME (min)	WEIGHT (gm)	GAINED WEIGHT (gm)	CUMILATIVE WEIGHT GAINED(gm)	VOLUME OF WATER (mm3)	SURFACE AREA (mm2)	i=w/(A*Density) (mm)	√ (TIME) (√min)
			(W)	(V)	(A)		
0	776.29	0	0	0	7853.98	0	0
1	773.82	0.92	0.92	920	7853.98	0.117	1
2	774.76	0.94	1.86	1860	7853.98	0.236	1.41
3	775.85	1.09	2.95	2950	7853.98	0.375	1.73
4	776.83	0.98	3.93	3930	7853.98	0.5	2
5	777.82	0.99	4.92	4920	7853.98	0.626	2.24
9	778.84	1.02	5.94	5940	7853.98	0.756	3
12	779.84	1	6.94	6940	7853.98	0.88	3.46
16	780.84	1	7.94	7940	7853.98	1.01	4
20	781.94	1.1	9.04	9040	7853.98	1.15	4.47
25	783.08	1.14	10.18	10180	7853.98	1.3	5

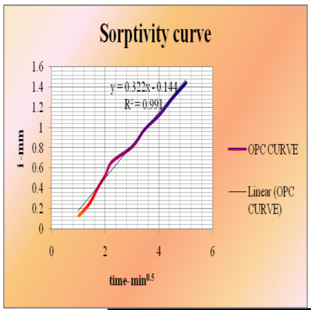

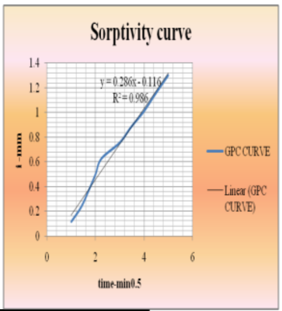

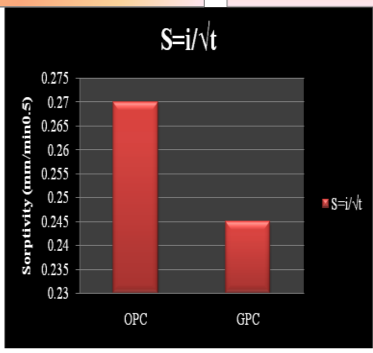

FREEZING THAWING

When the concrete is wet and especially in the presence of deicing chemicals the most destructive factor is freezing and thawing. The deterioration of the concrete is caused mainly because of freezing of water and at the same time expansion in the aggregate particles, paste or both.

CASE1

Environmental testing chamber

Cycles	Weight (Kg)	DENSITY (Kg/m3)	ULTRA PULSE VELOCITY (V) (Km/Sec)	DYNAMIC MODULUS	RELATIVE DYNAMIC MODULUS (R=En/Eo *100)
0	2.59	2590	4.71	51711	100
5	2.585	2585	4.69	51283	99.1
10	2.579	2579	4.66	50404	97.4
15	2.571	2571	4.625	49495.7	95.7
20	2.562	2562	4.6	48790	94.35
25	2.556	2556	4.575	48148	93.11
30	2.541	2541	4.565	47657	92.1
35	2.53	2530	4.555	47243	91.3
40	2.5	2500	4.54	46376	89.68
45	2.496	2496	4.515	45792	88.55
50	2.485	2485	4.51	45505	88

Table 4.27 Results of durability factor of OPC

Cycles	Weight (Kg)	DENSITY (Kg/m3)	ULTRA PULSE VELOCITY (V) (Km/Sec)	DYNAMIC MODULUS	RELATIVE DYNAMIC MODULUS (R=En/Eo *100)
0	2.62	2620	4.95	57776.8	100
5	2.617	2617	4.94	57477	99.4
10	2.61	2610	4.93	57092	98.9
15	2.604	2604	4.915	56614	97.9
20	2.591	2591	4.905	56103	97.1
25	2.58	2580	4.9	55751	96.5
30	2.571	2571	4.885	55217	95.5
35	2.56	2560	4.86	54419	94.1
40	2.55	2550	4.84	53761	93.05
45	2.54	2540	4.82	53109	91.9
50	2.53	2530	4.77	51999	90

Table 4.28 Results of durability factor of GPC

Cycles	0	10	20	30	40	50
COMPRESSIVE STRENGTH N/mm2 (or) Mpa	62.3	62.08	60.09	59.2	58.4	57.9

Table 4.29 Variation of compressive strength across cycles of OPC

Cycles	0	10	20	30	40	50
COMPRESSIVE STRENGTH N/mm2 (or) Mpa	66.9	66.34	65.1	64.03	63.54	61.89

Table 4.30 Variation of compressive strength across cycles of GPC

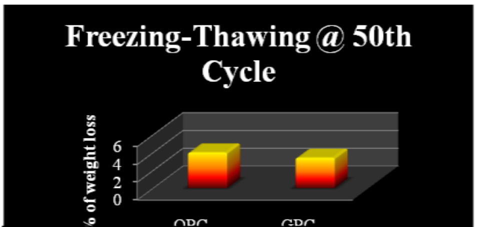

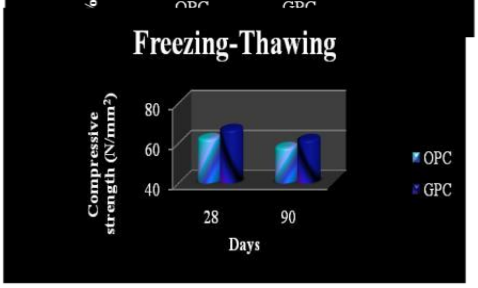

Table 4.29 Variation of compressive strength across cycles of OPC

Cycles	0	10	20	30	40	50
COMPRESSIVE STRENGTH N/mm2 (or) Mpa	62.76	62.08	60.09	59.2	58.4	57.1

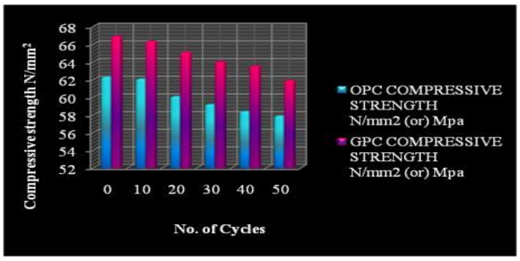

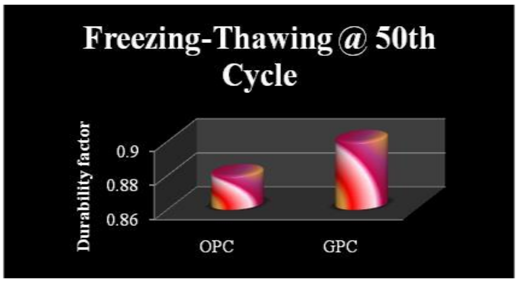

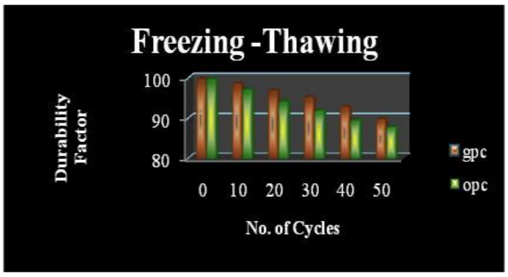

CASE 2

Table 4.27 Results of durability factor of OPC

Cycles	Weight (Kg)	Density (Kg/M3)	Ultra Pulse Velocity (V) (Km/Sec)	Dynamic Modulus	Relative Dynamic Modulus (R=En/Eo *100)
0	2.59	2590	4.71	51711	100
5	2.585	2585	4.69	51283	99.1
10	2.579	2579	4.66	50404	97.4
15	2.571	2571	4.625	49495.7	95.7
20	2.562	2562	4.6	48790	94.35
25	2.556	2556	4.575	48148	93.11
30	2.541	2541	4.565	47657	92.1
35	2.53	2530	4.555	47243	91.3
40	2.5	2500	4.54	46376	89.68
45	2.496	2496	4.515	45792	88.55
50	2.49	2490	4.48	44988	87

Table 4.28 Results of durability factor of GPC

Cycles	Weight (Kg)	Density (Kg/M3)	Ultra Pulse Velocity (V) (Km/Sec)	Dynamic Modulus	Relative Dynamic Modulus (R=En/Eo *100)
0	2.62	2620	4.95	57776.8	100
5	2.617	2617	4.94	57477	99.4
10	2.61	2610	4.93	57092	98.9
15	2.604	2604	4.915	56614	97.9
20	2.591	2591	4.905	56103	97.1
25	2.58	2580	4.9	55751	96.5
30	2.571	2571	4.885	55217	95.5
35	2.56	2560	4.86	54419	94.1
40	2.55	2550	4.84	53761	93.05
45	2.54	2540	4.82	53109	91.9
50	2.53	2530	4.805	52576.8	91

Table 4.30 Variation of compressive strength across cycles of GPC

Cycles	0	10	20	30	40	50
COMPRESSIVE STRENGTH N/mm2 (or) Mpa	67.48	66.34	65.1	64.03	63.54	62.88

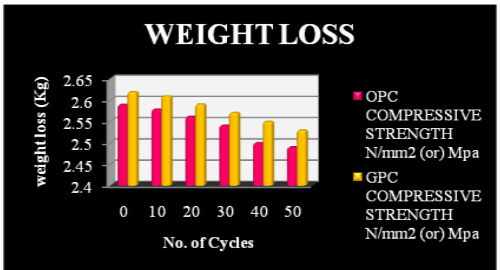

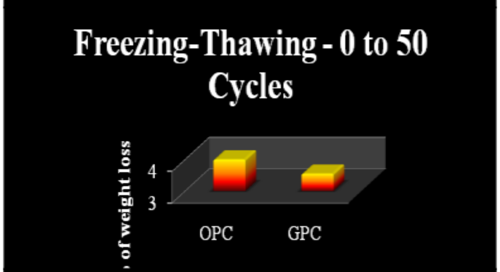

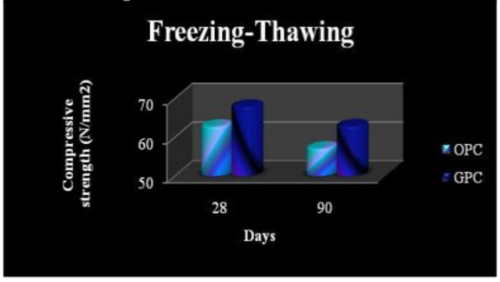

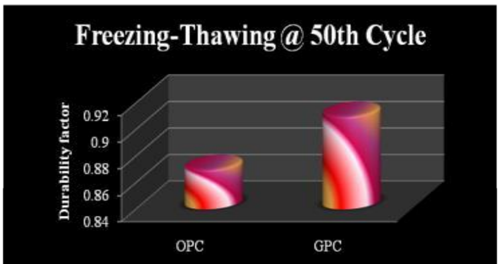

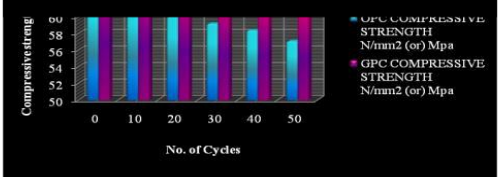

5. CONCLUSIONS

The project achievements are asfollows:

1. The resistance towards the chemical attack on concretehassignificantlyprovenessentialforboththe concrete, where GPC has resisted well in circumstances like sulphate, chloride and acid attacks compared to OPC
2. ThechloridepenetrationinGPCislesscomparatively than OPC, so it can be used in chloride zonearea.
3. The mix of both the concrete are taken special attraction in this, where it is proven in UPV test and tookhugeamountoftimetotraveltherays.Hencewe can conclude the materials are conjoined in the specimens.
4. Atmost care is been taken while testing specimen under freezing – thawing conditions and GPC has evolvedsuccessfulinthatandproventobesuitableinfrozen conditions even by the results

Fromthecumulativeresultswecancometoanconclusionthan replacement of OPC with GPC can be done, which can bring the dual benefit such as preserving the natural resources and reduce the emission of green house gases into theatmosphere.

REFERENCES

1. Song X J, Marosszeky M, Brungs M and Munn R , S. Geopolymer Manufacture and Application - Main problems When Using Concrete Technology. Presented at the Geopolymers 2002 International Conference. Melbourne, Australia: 2002. Siloxo Pty. Ltd.
2. Sobolev K G , Effect of fly ash preliminary calcination on the properties of geopolymer", Journal of Hazardous Materials, Vol. 164, pp. 634-639, 2009.
3. Khaloo A R and Houseinian M R , Chemical Stability of Cementitious Materials Based on Metakaolin. Cement and Concrete Research, Vol. 29: pp. 997-1004, 1999.
4. Ray I and Chattopadhyay R , Use of fly ash in structural concrete: Part 1-Why?"Indian Concrete Journal, Vol. 79, No. 5, pp. 13-22, 2005.
5. Potha Raju M, Shoba M and Rambabu K , Licensed Under Creative Commons Attribution CC BY Geo Polymer Concrete with the Replacement of Granite Aggregate as Fine AggregateInternational Journal of Science and Research (IJSR) ISSN (Online): 2319-7064 Index Copernicus Value (2013): 6.14 Volume 4 Issue 9, September 2015
6. Dos Santos J R, Branco F A and Brito J de , Effect of Alkaline Activator, Water,Superplasticiserand Slag Contents on the Compressive StrengthandWorkability of Slag-Fly Ash BasedGeopolymerMortar Cured under AmbientTemperature World Academy of Science, Engineering and Technology; International Journal of Civil, Environmental, Structural, Construction and Architectural Engineering Vol:10, No:3, 2016

SEISMIC ANALYSIS OF STEEL PLATE SHEAR WALL AND CONCENTRIC BRACED FRAMES

Manasa Shetty
Asst.Professor, Department of Civil Engineering, MallaReddy Engineering College (Autonomous) Maisammaguda, Dhulapally, Secunderabad, Telangana, India 500100.

M.Uday Bhaskar
Asst.Professor, Department of Civil Engineering, MallaReddy Engineering College (Autonomous) Maisammaguda, Dhulapally, Secunderabad, Telangana, India 500100.

Jugal Kishore M
Asst.Professor, Department of Civil Engineering, Kallam Harnadhareddy Institute of Technology (Autonomous), Guntur, Andhra Pradesh, India 522019

Abstract:
Steel Plate Shear Walls (SPSW) were utilized for the seismic retrofitting of various enduring structures at the initial times of advancement. Ductility is the important property of a material that is intended to be employed in the seismic localities. This characteristic of steel enabled its essentiality in the utility of Steel Plate Shear Walls in these areas. The prevalent thesis emphasizes the conduct of a framed building with steel plate shear walls and different types of bracings. This work involves the analysis of a few multi-storied structures with SPSW and bracings by employing the Codal coefficient method conforming to part 1 of Indian Standard 1893. Modeling of SPSW is done using the Strip model in the SAP 2000 (V.14) software which is the famous Finite Element Analysis software. The consequences in a structure due to the involvement of SPSW, different concentric braced frames, contrasting SPSW and X-bracing and the variation of the aspect ratio of SPSW with respect to bending moments, shearing forces, axial loads of beams and columns and story drifts are predominantly discerned in this study. SPSW structure is emerged as ideal among all the concentric braced frames and SPSW.

Keywords: ***Aspect ratio, Codal coefficient method, Concentric braced frames, Steel Plate Shear Walls, Strip model, X-bracing.***
DOI Number: 10.14704/nq.2022.20.6.NQ22780 **NeuroQuantology 2022; 20(6):7827-7834**

1. INTRODUCTION

The structures made by utilizing steel exhibits greater performance to withstand the seismic loads. This performance is mainly attributable to ductility of steel. Due to this property, a forewarning is generated prior to the complete collapse of structure. In case of earthquakes, the loads are highly elevated and in order to successfully oppose these uncommon loads, the buildings must possess adequate stiffness as well as lateral strength. Also, steel members perform poorly with respect to compression due to which these should be concocted with concrete [1]. In order to secure economic and structural gains like minimizing materials usage and speedy buildings, steel and concrete concocted buildings are also utilized [2]. The components that are employed in the buildings to oppose these loads and to show superior conduct in compression are usually shear walls and framed braces [3].

Shear walls are described as the walls similar to the building elements of vertical alignment that are exposed to lateral loadings in their planes. These shear walls include slender steel plates with beams and columns which are termed as SPSW. The mechanism and conduct of shearing resistance of SPSW are symmetrical to vertically aligned plate girders i.e., indirect through diagonal tension. The internal opposing forces in SPSW are diagonal tension forces. Though there are few disadvantages like low flexure stiffness, numerous benefits like steady hysteretic features make the SPSW's utility effective [4]. Un-stiffened, stiffened and concocted concrete and steel are the primary sorts of SPSW. Based on the conduct of steel plates, these are again categorized in to compact and non-compact.

The yielding of the compact SPSWs occurs prior to the initiation of buckling which is comparatively thick in contrast to lean ones. The design of this type is uneconomical and the modeling is done by utilizing a complete shell element as well as isotropic substance. Non-compact SPSWs are of un-stiffened type having lean plates which buckle due to less lateral loads being virtually elastic. To withstand the external shearing forces, the resistance is furnished due to tensile field occurred diagonally. The modeling of these lean

SPSWs is done by employing either shell elements or strip modeling whereas strip modeling is utilized in this study which is more famous than the other.

The middle line of the components in frames which coincides at a joint converges at one point so that a vertical truss pattern is formed in order to withstand lateral loading system are termed as Concentrically Braced Frames (CBF) [5]. These are generally utilized for withstanding wind loads. CBFs produce ductile nature by inelastic actions of the bracings i.e., tensile yield and compressive buckle. Hence, these braces were termed as 'fuses' [6]. Numerous bracing patterns analyzed in the current study are diagonal bracing, X-intersected bracing, K-bracing and X-bracing.

The purpose of this study is to analyze the seismic conduct of SPSWs in which the major goals are:

1. To analyze the conduct of a framed structure in the presence and absence of SPSW.
2. To discern the effect of diverse braced systems on a framed structure.
3. To compare the SPSW and the ideal braced system obtained from above.
4. To deduce the conduct of SPSW in a framed building by changing the aspect ratio.

2. LITERATURE REVIEW

Berman and Michel [7] presented a renewed technique to analyze the SPSWs. This work involves the measuring of infill plate depth through expressions perceived by analyzing strip modeling in the plastic zone.

Alinia and Dastfan [8] studied the consequences that occurred due to beam-columns on the complete conduct of SPSWs. Outcomes discerned that flexure firmness shows null impact whereas torsion rigidity exhibits dominant impact on elastic buckling in shear and extensional firmness lightly shows its impact on the after buckling resistance.

Fariborz and Erfan [9] presented certain formulae to calculate shearing resistance taking into account the consequences of firmness as well as the resistance of the edge components of SPSW in the presence and absence of stiffening elements. This study involves analyzing the non-linear conduct of displacements by imposing a single steady load and the outcomes are contrasted with numerous existing studies.

Topkaya and Kurban [10] conducted an analysis of a particular type of SPSW having steady characteristics along with its height. 3-D linear FEAs have been utilized to derive the preliminary time spans of buildings and these have been contrasted with measures given in design parameters.

Viswanath et al. [11] analyzed seismic resistance of fortified concrete 4-storied structure retrofitted with numerous types of CSB by employing STAAD Pro.

Madhar [12] analyzed tube-shaped CBF by imposing seismic loads using FEM and depicted that structure with CBF fails at middle span plastic hinge. He deduced a fine FEM to assess the hysteretic conduct of CBFs by imposing cyclic loads.

Yipeng et al. [13] perceived the seismic conduct of repaired lean SPSW by using a single bayed 2-storied frame which is imposed with the less cyclic reverse loaded system. In this study, the frame is deteriorated and then repair is done with anchoring method which is again led to deterioration by imposing loads.

Ali [14] analyzed and designed twin shear lapped bolt systems in X-shaped CBF. In this, a hollow CBF is used which is made by the cold method and quasi-static trials are conducted by imposing a cyclic loading system on 6 X-braced samples.

Jia-Chun et al. [15] discerned the conduct of excess load bearing type SPSW by imposing cyclic loading system and produced this SPSW with yielding load which is more than 30lakh N. Here, less yielding type of steel is preferred for shearing web plate in SPSW and firmness deterioration, ductile nature and energy losing features were examined. 7828

Alireza et al. [16] analyzed some seismic load resisted strategies that are newly made and perceived better seismic conduct. In this, the designing strategy and dynamic nonlinearity conduct of frames involving SBS were considered on 3 different storied structures positioned in 3 various types near the beam-bracing coincidence point.

3. STUDY AREA

3.1 Strip modeling

This modeling is processed in two approaches. The approach given by Thorborn involves the strips positioned at consistent angles, normally 45 degrees and Rezaii's approach involves multiple strips positioned at multi-angles with horizontal. This technique fully depends upon the diagonal tensile field response which is produced within no time after the plate buckles. It is suggested by Canadian code, the CAN/CSA-S16-01 [17] for analyzing as well as designing the process of SPSW. While analyzing using this method, steel plates have been swapped with numerous struts in the tensile field. Figures 1 and 2 portray the strip models introduced by Thorborn and Rezaii respectively.

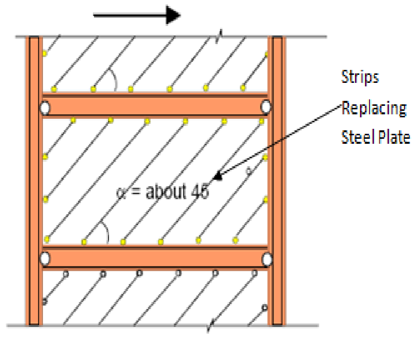

Figure 1. Thorborn's model

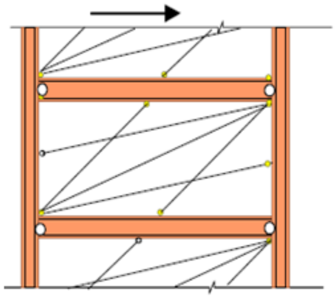

Figure 2. Rezaii's model

3.2 Mechanism of Concentrically braced systems

Imposing load from left to right on a structure with CBF results in tension in left bracing as well as compressive nature is seen in the right bracing as shown in Figure 3. Due to the conduct of CBF, buckling is observed in the right bracing whereas yielding takes place in the right bracing while beam-column is elastically stable. In the former phenomenon, compression resistance goes on reduces as it is generally non-ductile in nature while the latter one is ductile in nature.

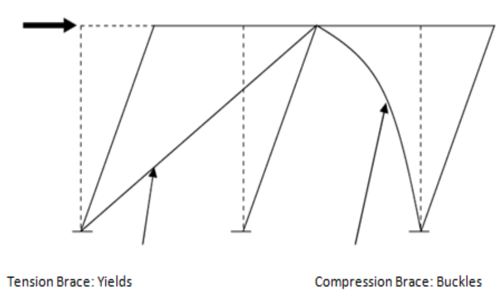

Figure 3. Mechanism of CBF loaded towards the right

Changing the course of loading i.e., right to left, tensile nature is noticed in the bracing in which compression buckling is seen earlier and yielding in tension provides ductile conduct. Meanwhile, compressive nature is noticed in which tensile yielding is seen earlier. Hence, it can be said that when a structure with CBF is exposed to seismic vulnerability, tensile yield and compressive buckle occurs alternatively in the bracings. During this cycle, beam-columns show elastic conduct. This cycle should continue for numerous loadings exhibiting braced edge connections and braced components with no faults and fractures respectively.

3.3 Codal coefficient method

Numerous analyzing methodologies are available to analyze an SPSW structure. As we modeled SPSW by employing strip modeling, the only available option to analyze SPSW structure is by Seismic Coefficient Method (SCM) which is a statically equivalent methodology. SCM follows part 1 of the Indian code 1893 [18] and the steps in the procedure are load considerations, design horizontal seismic coefficient (A_h), fundamental natural period (Ta) and distribution of design force.

4. ANALYSIS

4.1 Structure with SPSW

An analysis is carried out on a G+6 storied structure shown in Figure 4 located in zone 4 having a total height of 2250cm and floor height as 150cm in the presence and absence of SPSW of 6mm thick to estimate its conduct on beams and columns by imposing cyclic loading system.

Initially, the seismic weight of the structure for each floor is estimated and using SCM, calculated force is distributed separately for every story. Bend moments and shearing forces in beams, axial forces in columns and drift varying with the storey are estimated by entering the calculated in the SAP software.

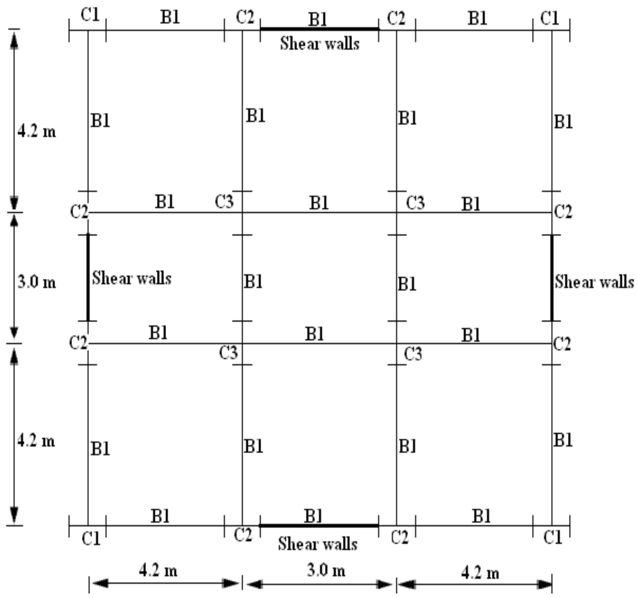

Figure 4. Plan of G+ 6 Storied Structures with SPSW

4.1.1 Bending moment in beams:

The variation of bend moments (BM) of SPSW is presented in Figure 5. Outcomes discern that for a structure with SPSW, BM is high in lower storied beams than those of higher storied ones. It is attributable to the uniform as well as reversed pull brought by vertical elements of the diagonal tensile field of SPSWs located on either side. It is also noticed that BM estimates for middle storied beams are lower than high and low storied ones. This is due to the pull exerted by SPSW which is situated solely on the top side of the ground beam as well as the lower side of the upper beam [20]. Also, the structure having no SPSW shows a very slight variation in BM.

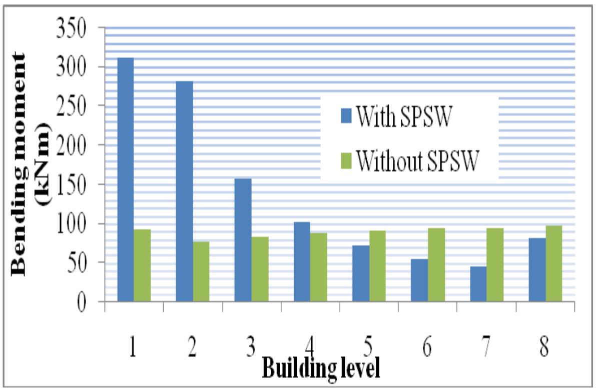

Figure 5. Bending Moment Variation in Beams

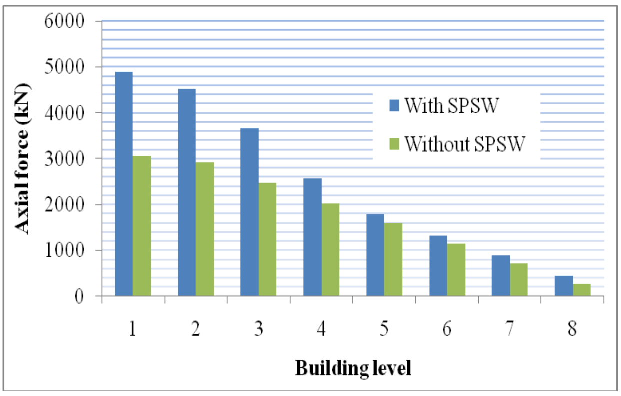

Figure 7. Axial Force Variation on Columns

4.1.2 Shear force in beams:

Taking one beam in each building level into account, analysis is forwarded and the shearing force (SF) estimates of beams are portrayed in Figure 6. SF in beams follows a similar pattern as that of BM in a structure with SPSW. Plinth level beams have shown enormous estimates of SF due to SPSW and thus required to do anchorage effectively for footings [20]. Meanwhile, structure with the absence of SPSW shows inflation pattern initially and then deflates.

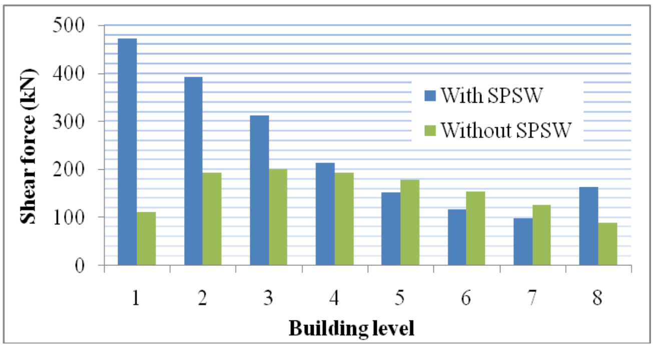

Figure 6. Shear Force Variation in Beams

4.1.3 Axial force in columns:

By taking into account one column in each floor level, axial forces on the columns are estimated in the analysis and the outturns are portrayed in Figure 7. Here, the axial force goes on deflating from lower stories to higher ones in SPSW structure as well as in structure with no SPSW. Moreover, at each level, this force is higher for SPSW structure. This is attributable to the impact of the shear wall [21].

4.1.4 Storey drift:

The story drift measures for all floor levels are mentioned in Figure 8. It is discerned that at ground level, drift value is the same for both SPSW and normal structure. These estimates follow the inflated trend towards higher stories for both structures and are higher for structures without SPSW. Thus, SPSW is beneficial to limit drift in stories [22].

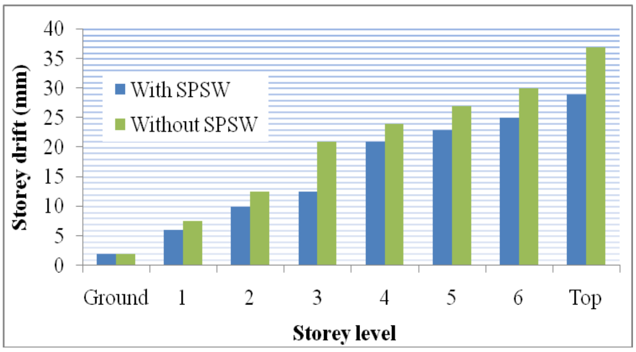

Figure 8. Storey Drift Variation

4.2 Structure with different CBFs

To observe the conduct of different CBFs, analysis is done on a G+4 storied structure of zone 4 having story height as 300cm. Contrasting numerous bracings is done mainly in terms of maximal displacements, axial forces, SF, BM in columns and displacement reduction percent.

4.2.1 Maximum lateral displacement for CBF structure:

Maximal lateral displacement estimates for diverse bracings are portrayed in Figure 9. These estimates are extremely high for a structure having no bracing because these braces use some amount of energy via inelastic distortions using the ductile nature. It is also perceived that these values are minimal for X shaped braced frame and are taken as ideal since these deflated measures manage seismic failure [23]. These displacement measures go on inflating with a rise in the building level.

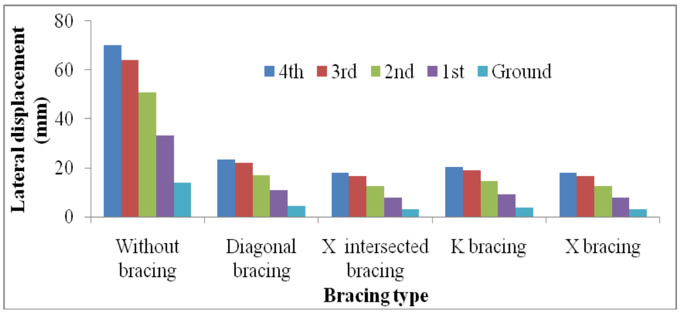

Figure 9. Lateral Displacement Variation for Diverse CBFs

4.2.2 Maximum axial forces in a column for CBF structure:

Figure 10 portrays the maximal column forces for numerous CBFs. Generally, braces inclusion in structures allows columns to handle more axial forces. It is discerned that higher story columns possess higher values. Moreover, X shaped bracing exhibits higher measures compared to all other bracings.

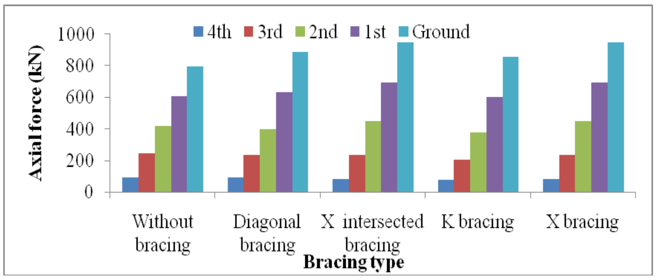

Figure 10. Maximal Axial Force in Columns with Diverse CBFS

4.2.3 Maximum shear force in a column for CBF structure:

Figure 11 portrays the maximal SF estimates for columns of CBF structure. It discerns that structure with the absence of CBF has larger SF than those with CBFs. Among diverse CBFs, X shaped bracing exhibits the least values of SF.

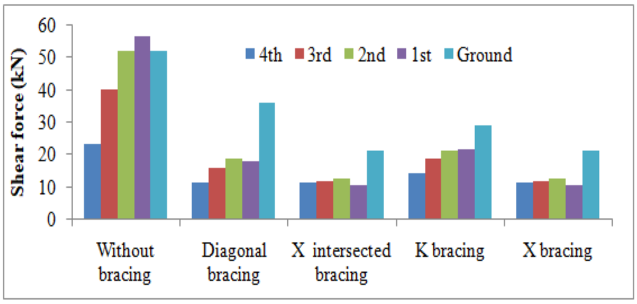

Figure 11. Maximal Shear Force in Column for diverse CBFs

4.2.4 Maximum column moment for CBF structure:

Maximal BM of columns for numerous bracings is portrayed in Figure 12.

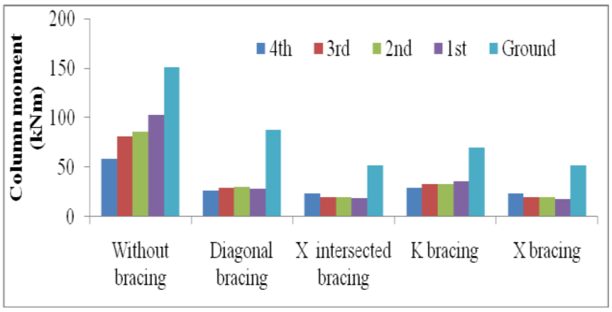

Figure 12. Maximal Column Moment for Diverse CBFs

This follows the same pattern as that of SF for CBF structure. Also, the X-brace type exhibits lower column moments in contrast with all other CBFs.

Contrasting all the bracing types, X shaped bracing exhibits ideal estimates for various parameters mentioned above and is the most preferred CBF in seismic view. Hence, a comparison is made between X-braced and SPSW structures.

5. COMPARISON OF SPSW AND X-BRACED STRUCTURE

For this analysis, the G+9 storied structure of zone 4 is chosen. 3-dimensional view of SPSW of 1.2cm thick and X braced structure is presented in Figure 13(a) and 13(b).

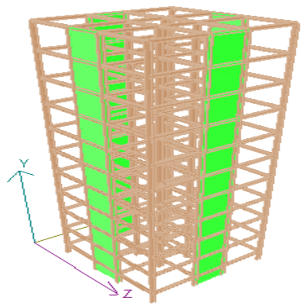

Figure 13 (a). 3D view of the structure with SPSW

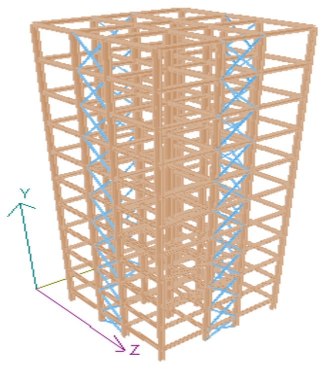

Figure 13 (b). 3D view of the structure with X-bracing

5.1 Beam bending moment and Shear force

BM and SF of beams vary in SPSW and X-braced structures and is portrayed in Figure 14 and 15 respectively. Both the structures follow a similar trend of deflating these estimates. Although SPSW structure portrays lower estimates than X shaped CBF, both the structures exhibit very minute variance in BM and SF that need not be considered when contrasted. This could be attributable to SPSW's diagonal tension which is equivalent to X-bracing's energy dissipation. G represents Ground while R means Roof.

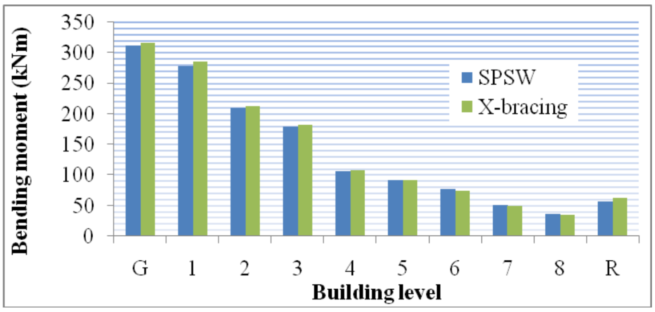

Figure 14. Beam Bending Moments in SPSW and X-Bracing

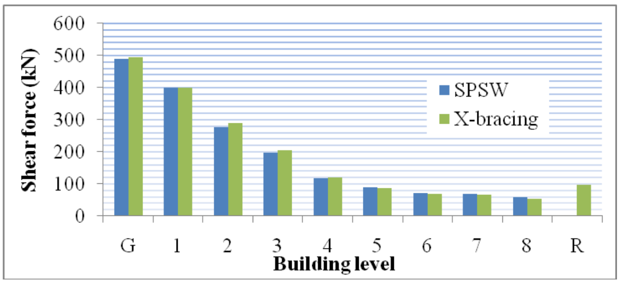

Figure 15. Beam Shear Forces in SPSW and X-Bracing

5.2 Column axial forces

Figure 16 exhibits the axial forces in columns of SPSW and X-braced structure. These force estimates follow the inverse pattern of SF and BM. The minute variance of axial forces is observed between both the structures due to which this variance can be neglected and can be said that both perform equally.

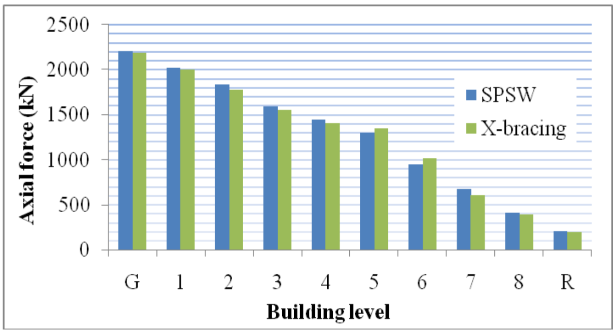

Figure 16. Column Axial Forces in SPSW and X-Bracing

5.3 Storey drift of SPSW and X-brace

Drift estimates of all the building levels of SPSW and X brace are portrayed in Figure 17.

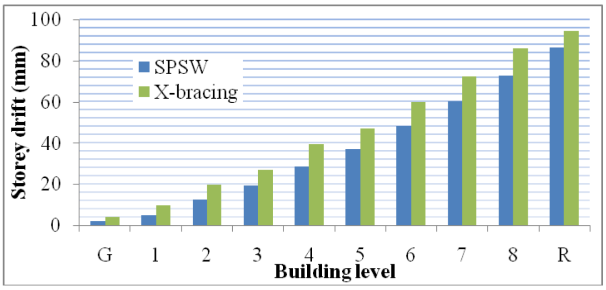

Figure 17. Storey Drift in SPSW and X-Bracing

In this, it is perceived that structure with SPSW has more low drift measures than X braced ones though X brace also procures lower drifts [24]. This means SPSW is more efficient in restricting drift in floor levels.

6. ANALYSIS OF SPSW WITH VARYING ASPECT RATIO

Altering the magnitudes of SPSW influences the conduct of the structure. Aspect ratio means the division value of width with respect to the height of SPSW. In order to analyze in this means, 4 structures having diverse aspect ratios of 0.833,1, 1.33 as well as 1.67 were considered. In this, positioning and a height of 300cm have been maintained the same whereas breadth is altered from 250-500cm with a rise of 50cm. 3-dimensional view of structure analyzing here is portrayed in Figure 18.

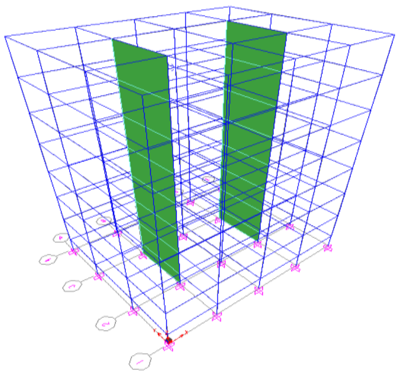

Figure 18. 3D View of SPSW Structure with Varying Aspect Ratio

6.1 Contrasting bending moments and shear forces of beams

The BM and SF estimates of SPSW having diverse aspect ratios are portrayed in Figure 19. It is perceived that both variances of BM and SF are directly proportional to the variance of aspect ratio i.e., deflates with declined aspect ratios and vice versa.

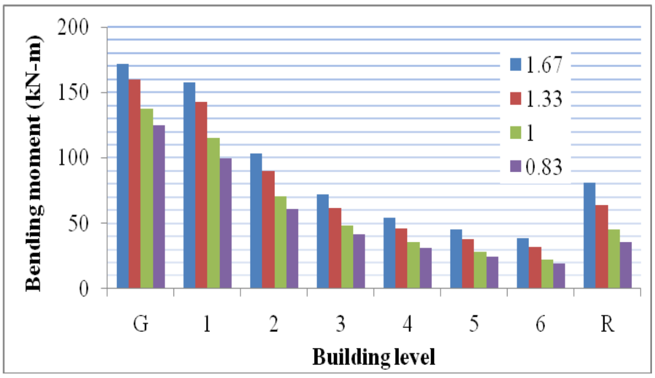

Figure 19. Bending Moment in Variance with Aspect Ratio

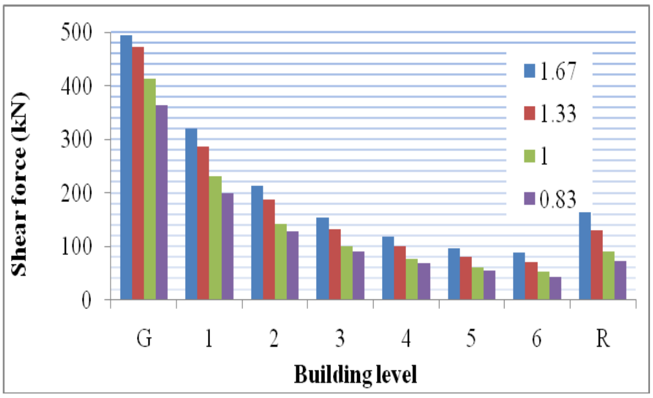

Figure 20. Shear Force in Variance with Aspect Ratio

6.2 Contrasting column forces and moments

Figures 21 and 22 exhibit the column forces and moments for SPSW in variance with aspect ratio. Outturns perceive that both the estimates incline with inflation in the aspect ratios.

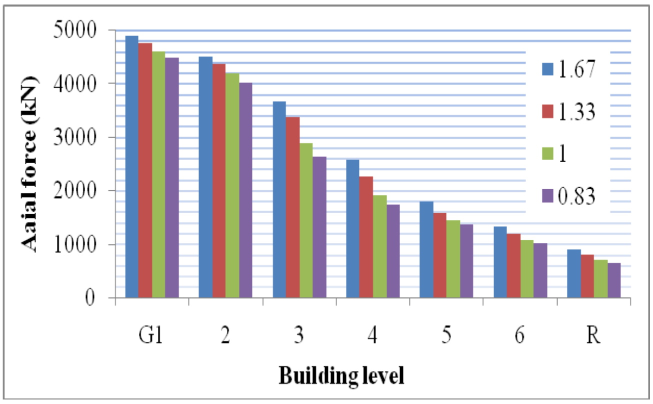

Figure 21. Column Force in Variance with Aspect Ratio

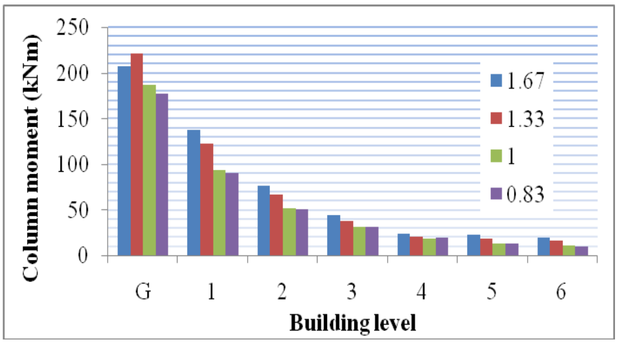

Figure 22. Column Moment in Variance with Aspect Ratio

6.3 Contrasting drift in stories

The estimates of drift in all the floor levels for SPSW structure in variance with aspect ratio is portrayed in Figure 23. From this, it has been perceived that drift is direct to aspect ratio at ground level i.e., rises with inflation in aspect ratio and vice versa. Meanwhile after the bottom level, drift in stories falls down by elevating aspect ratio.

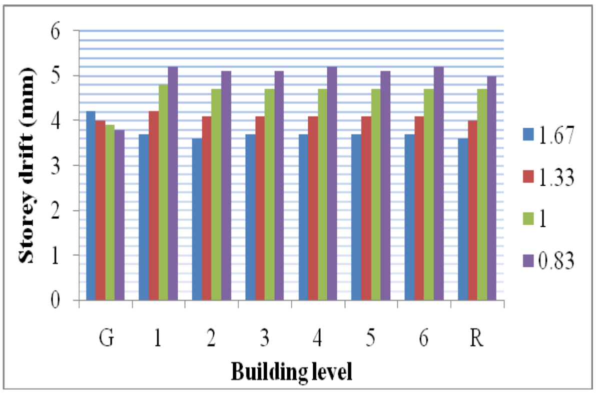

Figure 23. Storey Drift in Variance with Aspect Ratio

7. CONCLUSIONS

On the basis of the above analyses in the prevalent work, the inferences taken out are:

1. Flexure and shear requirements are excess for bottom level floors due to which efficient anchorage is essential whereas bending moment is found least for mid-stories than that of upper as well as lower ones for structures involving SPSWs.
2. Due to the involvement of SPSWs, columns become capable to manage more axial loads in low-level stories.
3. SPSWs resist the drifting of stories and these drift estimates rise with a tallness of structure.
4. Steel braces act against swaying due to which lateral displacements are low. These also minimize shearing and flexural requirements on structural components while the axial loading system acts as a medium for transferring lateral loads.

5. The decrement of displacement in percent for X-brace is excessive in contrast with diverse braced structures. X-brace allows columns to hold increased loads while limits the column moments and shear demands. On account of this, X-brace is evolved as supreme among other concentric braces.
6. SPSW possesses more efficiency than X-brace in terms of story drift whereas both exhibit very minute variance in terms of bending moments, shearing forces and axial forces in the structural components.
7. Increment in the aspect ratio of SPSW inflates the demand of beam bending moments and shearing forces and column forces and moments.
8. The higher aspect ratio of SPSWs turns down the drifting of stories while at the plinth level, this phenomenon is reversed.
9.

REFERENCES

[1] Venkateswar Reddy, K., Jugal Kishore, M., Uday Bhaskar, M. (2019), "Seismic Behavior of Steel-Concrete Composite Structures", International Journal of Engineering and Advanced Technology, vol 9 (2), pp. 4721-4726.
[2] Jugal Kishore, M. (2017), "Analysis of Steel-Concrete Composite Structures", 3rd National Conference on Innovative Research in Civil Engineering (NCIRCE 2K17), TEQIP-II S.C-1.1, January, Malla Reddy Institute of Technology, Hyderabad.
[3] Jialin Liu, Longhe Xu, Zhongxian Li. (2020), "Development and Experimental Validation of a Steel Plate Shear Wall with Self-Centering Energy Dissipation Braces", Thin-Walled Structures, vol. 148, https://doi.org/10.1016/j.tws.2019.106598.
[4] Jin-Guang Yu, Li-Ming Liu, Bo Li, Ji-Ping Hao, Xi Gao, Xiao-Tian Feng, (2019). "Comparative Study of Steel Plate Shear Walls with Different Types of Unbonded Stiffeners", Journal of Constructional Steel Research, vol. 159, pp. 384-396.
[5] Suneel Kumar, M., Senthilkumar, R., Sourabha, L. (2019), "Seismic Performance of Special Concentric Steel Braced Frames", Structures, vol. 20, pp. 166-175.
[6] Federico, G., Giovanni, L., Maurizio, O., Paolo, S. (2019), "Axial Response of Cold-Formed Steel Bracing Members with Holes", Journal of Constructional Steel Research, vol. 161, pp. 70-85.
[7] Berman Jeffrey and Bruneau Michel. (2003), "Plastic Analysis and Design of Steel Plate Shear Walls." Journal of Structural Engineering, ASCE, vol. 129 (11), pp. 1448-1456.
[8] Alinia, M. M., Dastfan, M. (2005), "The Effects of Surrounding Members on Post-Buckling Behavior of Thin Steel Plate Shear Walls (TSPSW)", Z.Y. Shen et al. (Eds)., Fourth International Conference on Advances in Steel Structures (ICASS), Shanghai, China, vol. 2, pp. 1427-1432.
[9] Fariborz Nateghi and Alavi Erfan (2008)," Theoretical Seismic Behaviour of Steel Plate Shear Walls", Proceeding, 14th World Conference on Earthquake Engineering, October, Beijing, China, Proceedings No. 05-05-0120.
[10] Topkaya, C., Kurban, C.O. (2009), "Natural Periods of Steel Plate Shear Wall Systems", Journal of Constructional Steel Research, vol. 65, pp. 542-551.
[11] Viswanath K.G, Prakash K.B., Anant Desai. (2010), "Seismic Analysis of Steel Braced Reinforced Concrete Frames" International Journal of Civil and Structural Engineering, vol. 1 (1), pp. 114-122.
[12] Madhar Haddad. (2010), "Concentric Tubular Steel Braces Subjected to Seismic Loading: Finite Element Modeling", Journal of Constructional Steel Research, vol. 104, pp. 155-166.
[13] Yipeng, D., Jiping, H., Jinguang, Y., Bowen, D., Danlan, L., Liang, Z. (2018), "Seismic Performance of a Repaired Thin Steel Plate Shear Wall Structure", Journal of Constructional Steel Research, vol. 151, pp. 194-203.
[14] Ali Davaran. (2019), "Stability Analysis and Design of Double hear Lap Bolted Connections in Steel X-Bracing Systems", Journal of Constructional Research, vol. 153, pp. 31-41.
[15] Jia-Chun, C., Ji-Dong, X., Zi-Ran, X., Tao, H. (2020), "Cyclic Behavior Study of High Load-Bearing Capacity Steel Plate Shear Wall", Journal of Constructional Research, vol. 172, https://doi.org/10.1016/j.jcsr.2020.106178.
[16] Alireza, T., Majid, G., Reza, V. (2020), "The Investigation into the Effect of Consecutive Earthquake on the Strongback Bracing System", Structures, vol. 24, pp. 477-488.
[17] Canadian Standard Association (CSA). (2001), "Limit States Design of Steel Structures", CAN/CSA-S-16-01, Willowdale, Ontario, Canada
[18] IS 1893. (2002), "Criteria for Earthquake Resistant Design of Structures", Part 1- General Provisions and Buildings (Fifth Revision), Bureau of Indian Standards, New Delhi, India.
[19] IS 800. (2007), "General Construction in Steel- Code of Practice", Bureau of Indian Standards, New Delhi, India.
[20] Londhe R.S. and Chavan. A. P. (2010), "Behavior of Building Frames with Steel Plate Shear Wall". Asian Journal of Civil Engineering, Building and Housing, vol. 11, pp. 95-102.
[21] Jin-guang, Y., Hai-sheng, Y., Xiao-tian, F., Chen, D., Tong-fei, H., Jay, S. (2020), "Behaviour of Steel Plate Sear Walls with Different Types of Partially-Encased H-Section Columns", Journal of Constructional Steel Research, vol. 170, https://doi.org/10.1016/j.jcsr.2020.106123.
[22] Saeid Sabouri-Ghomi, Carlos E. Ventura and Mehdi H. K. Kharrazi. (2005), "Shear Analysis and Design of Ductile Steel Plate Walls", Journal of Structural Engineering, ASCE, vol. 131 (6), pp. 878-889.
[23] Abou-Elfath, H., Mostafa, R., Meshaly, M., Heba, A.F. (2016), "Seismic Performance of Steel Frames Designed Using Different Allowable Story Drift Limits", Alexandria Engineering Journal, http://dx.doi.org/10.1016/j.aej.2016.08.028.
[24] Jui-Liang, L., Meng-Kwee, K., Keh-Chyuan, T. (2019), "Stiffness Configuration of Strongbacks to Mitigate Inter-Story Drift Concentration in Buildings", Engineering Structures, vol. 199, https://doi.org/10.1016/j.engstruct.2019.109615.

eISSN 1303-5150

SEISMIC ANALYSIS OF STEEL PLATE SHEAR WALL AND CONCENTRIC BRACED FRAMES

Manasa Shetty
Asst.Professor, Department of Civil Engineering, MallaReddy Engineering College (Autonomous) Maisammaguda, Dhulapally, Secunderabad, Telangana, India 500100.

M.Uday Bhaskar
Asst.Professor, Department of Civil Engineering, MallaReddy Engineering College (Autonomous) Maisammaguda, Dhulapally, Secunderabad, Telangana, India 500100.

Jugal Kishore M
Asst.Professor, Department of Civil Engineering, Kallam Harnadhareddy Institute of Technology (Autonomous), Guntur, Andhra Pradesh, India 522019

Abstract:
Steel Plate Shear Walls (SPSW) were utilized for the seismic retrofitting of various enduring structures at the initial times of advancement. Ductility is the important property of a material that is intended to be employed in the seismic localities. This characteristic of steel enabled its essentiality in the utility of Steel Plate Shear Walls in these areas. The prevalent thesis emphasizes the conduct of a framed building with steel plate shear walls and different types of bracings. This work involves the analysis of a few multi-storied structures with SPSW and bracings by employing the Codal coefficient method conforming to part 1 of Indian Standard 1893. Modeling of SPSW is done using the Strip model in the SAP 2000 (V.14) software which is the famous Finite Element Analysis software. The consequences in a structure due to the involvement of SPSW, different concentric braced frames, contrasting SPSW and X-bracing and the variation of the aspect ratio of SPSW with respect to bending moments, shearing forces, axial loads of beams and columns and story drifts are predominantly discerned in this study. SPSW structure is emerged as ideal among all the concentric braced frames and SPSW.

Keywords*: Aspect ratio, Codal coefficient method, Concentric braced frames, Steel Plate Shear Walls, Strip model, X-bracing.*
DOI Number: 10.14704/nq.2022.20.6.NQ22780 **NeuroQuantology 2022; 20(6):7827-7834**

1. INTRODUCTION

The structures made by utilizing steel exhibits greater performance to withstand the seismic loads. This performance is mainly attributable to ductility of steel. Due to this property, a forewarning is generated prior to the complete collapse of structure. In case of earthquakes, the loads are highly elevated and in order to successfully oppose these uncommon loads, the buildings must possess adequate stiffness as well as lateral strength. Also, steel members perform poorly with respect to

compression due to which these should be concocted with concrete [1]. In order to secure economic and structural gains like minimizing materials usage and speedy buildings, steel and concrete concocted buildings are also utilized [2]. The components that are employed in the buildings to oppose these loads and to show superior conduct in compression are usually shear walls and framed braces [3].

Shear walls are described as the walls similar to the building elements of vertical alignment that are exposed to lateral loadings in their planes. These shear walls include slender steel plates with beams and columns which are termed as SPSW. The mechanism and conduct of shearing

resistance of SPSW are symmetrical to vertically aligned plate girders i.e., indirect through diagonal tension. The internal opposing forces in SPSW are diagonal tension forces. Though there are few disadvantages like low flexure stiffness, numerous benefits like steady hysteretic features make the SPSW's utility effective [4]. Un-stiffened, stiffened and concocted concrete and steel are the primary sorts of SPSW. Based on the conduct of steel plates, these are again categorized in to compact and non-compact.

The yielding of the compact SPSWs occurs prior to the initiation of buckling which is comparatively thick in contrast to lean ones. The design of this type is uneconomical and the modeling is done by utilizing a complete shell element as well as isotropic substance. Non-compact SPSWs are of un-stiffened type having lean plates which buckle due to less lateral loads being virtually elastic. To withstand the external shearing forces, the resistance is furnished due to tensile field occurred diagonally. The modeling of these lean

SPSWs is done by employing either shell elements or strip modeling whereas strip modeling is utilized in this study which is more famous than the other.

The middle line of the components in frames which coincides at a joint converges at one point so that a vertical truss pattern is formed in order to withstand lateral loading system are termed as Concentrically Braced Frames (CBF) [5]. These are generally utilized for withstanding wind loads. CBFs produce ductile nature by inelastic actions of the bracings i.e., tensile yield and compressive buckle. Hence, these braces were termed as 'fuses' [6]. Numerous bracing patterns analyzed in the current study are diagonal bracing, X-intersected bracing, K-bracing and X-bracing.

The purpose of this study is to analyze the seismic conduct of SPSWs in which the major goals are:

1. To analyze the conduct of a framed structure in the presence and absence of SPSW.
2. To discern the effect of diverse braced systems on a framed structure.
3. To compare the SPSW and the ideal braced system obtained from above.
4. To deduce the conduct of SPSW in a framed building by changing the aspect ratio.

2. LITERATURE REVIEW

Berman and Michel [7] presented a renewed technique to analyze the SPSWs. This work involves the measuring of infill plate depth through expressions perceived by analyzing strip modeling in the plastic zone.

Alinia and Dastfan [8] studied the consequences that occurred due to beam-columns on the complete conduct of SPSWs. Outcomes discerned that flexure firmness shows null impact whereas torsion rigidity exhibits dominant impact on elastic buckling in shear and extensional firmness lightly shows its impact on the after buckling resistance.

Fariborz and Erfan [9] presented certain formulae to calculate shearing resistance taking into account the consequences of firmness as well as the resistance of the edge components of SPSW in the presence and absence of stiffening elements. This study involves analyzing the non-linear conduct of displacements by imposing a single steady load and the outcomes are contrasted with numerous existing studies.

Topkaya and Kurban [10] conducted an analysis of a particular type of SPSW having steady characteristics along with its height. 3-D linear FEAs have been utilized to derive the preliminary time spans of buildings and these have been contrasted with measures given in design parameters.

Viswanath et al. [11] analyzed seismic resistance of fortified concrete 4-storied structure retrofitted with numerous types of CSB by employing STAAD Pro.

Madhar [12] analyzed tube-shaped CBF by imposing seismic loads using FEM and depicted that structure with CBF fails at middle span plastic hinge. He deduced a fine FEM to assess the hysteretic conduct of CBFs by imposing cyclic loads.

Yipeng et al. [13] perceived the seismic conduct of repaired lean SPSW by using a single bayed 2-storied frame which is imposed with the less cyclic reverse loaded system. In this study, the frame is deteriorated and then repair is done with anchoring method which is again led to deterioration by imposing loads.

Ali [14] analyzed and designed twin shear lapped bolt systems in X-shaped CBF. In this, a hollow CBF is used which is made by the cold method and quasi-static trials are conducted by imposing a cyclic loading system on 6 X-braced samples.

Jia-Chun et al. [15] discerned the conduct of excess load bearing type SPSW by imposing cyclic loading system and produced this SPSW with yielding load which is more than 30lakh N. Here, less yielding type of steel is preferred for shearing web plate in SPSW and firmness deterioration, ductile nature and energy losing features were examined.

Alireza et al. [16] analyzed some seismic load resisted strategies that are newly made and perceived better seismic conduct. In this, the designing strategy and dynamic nonlinearity conduct of frames involving SBS were considered on 3 different storied structures positioned in 3 various types near the beam-bracing coincidence point.

3. STUDY AREA

3.1 Strip modeling

This modeling is processed in two approaches. The approach given by Thorborn involves the strips positioned at consistent angles, normally 45 degrees and Rezaii's approach involves multiple strips positioned at multi-angles with horizontal. This technique fully depends upon the diagonal tensile field response which is produced within no time after the plate buckles. It is suggested by Canadian code, the CAN/CSA-S16-01 [17] for analyzing as well as designing the process of SPSW. While analyzing using this method, steel plates have been swapped with numerous struts in the tensile field. Figures 1 and 2 portray the strip models introduced by Thorborn and Rezaii respectively.

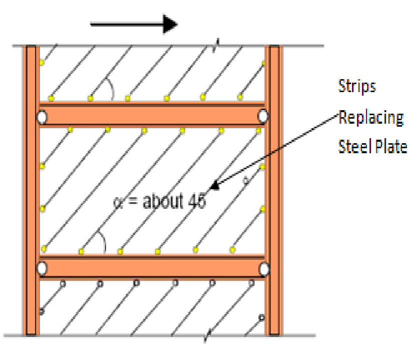

Figure 1. Thorborn's model

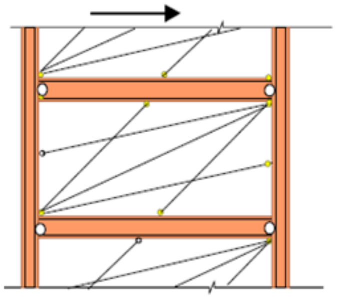

Figure 2. Rezaii's model

3.2 Mechanism of Concentrically braced systems

Imposing load from left to right on a structure with CBF results in tension in left bracing as well as compressive nature is seen in the right bracing as shown in Figure 3. Due to the conduct of CBF, buckling is observed in the right bracing whereas yielding takes place in the right bracing while beam-column is elastically stable. In the former phenomenon, compression resistance goes on reduces as it is generally non-ductile in nature while the latter one is ductile in nature.

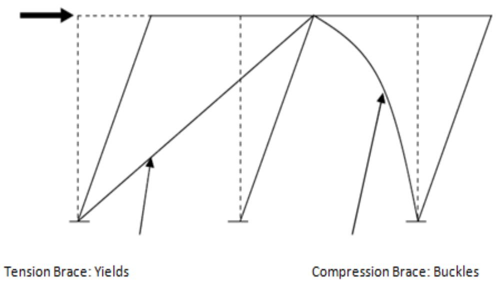

Figure 3. Mechanism of CBF loaded towards the right

Changing the course of loading i.e., right to left, tensile nature is noticed in the bracing in which compression buckling is seen earlier and yielding in tension provides ductile conduct. Meanwhile, compressive nature is noticed in which tensile yielding is seen earlier. Hence, it can be said that when a structure with CBF is exposed to seismic vulnerability, tensile yield and compressive buckle occurs alternatively in the bracings. During this cycle, beam-columns show elastic conduct. This cycle should continue for numerous loadings exhibiting braced edge connections and braced components with no faults and fractures respectively.

3.3 Codal coefficient method

Numerous analyzing methodologies are available to analyze an SPSW structure. As we modeled SPSW by employing strip modeling, the only available option to analyze SPSW structure is by Seismic Coefficient Method (SCM) which is a statically equivalent methodology. SCM follows part 1 of the Indian code 1893 [18] and the steps in the procedure are load considerations, design horizontal seismic coefficient (A_h), fundamental natural period (Ta) and distribution of design force.

4. ANALYSIS

4.1 Structure with SPSW

An analysis is carried out on a G+6 storied structure shown in Figure 4 located in zone 4 having a total height of 2250cm and floor height as 150cm in the presence and absence of SPSW of 6mm thick to estimate its conduct on beams and columns by imposing cyclic loading system.

Initially, the seismic weight of the structure for each floor is estimated and using SCM, calculated force is distributed separately for every story. Bend moments and shearing forces in beams, axial forces in columns and drift varying with the storey are estimated by entering the calculated in the SAP software.

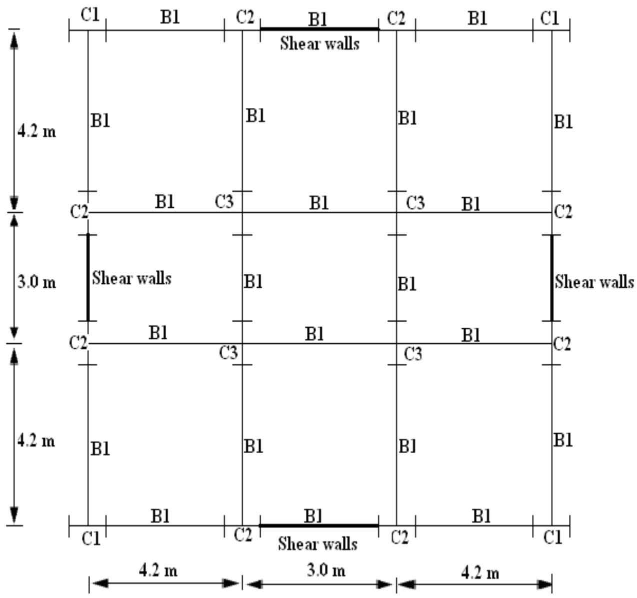

Figure 4. Plan of G+ 6 Storied Structures with SPSW

4.1.1 Bending moment in beams:

The variation of bend moments (BM) of SPSW is presented in Figure 5. Outcomes discern that for a structure with SPSW, BM is high in lower storied beams than those of higher storied ones. It is attributable to the uniform as well as reversed pull brought by vertical elements of the diagonal tensile field of SPSWs located on either side. It is also noticed that BM estimates for middle storied beams are lower than high and low storied ones. This is due to the pull exerted by SPSW which is situated solely on the top side of the ground beam as well as the lower side of the upper beam [20]. Also, the structure having no SPSW shows a very slight variation in BM.

NeuroQuantology | June 2022 | Volume 20 | Issue 6 | Page 7827-7834 | doi: 10.14704/nq.2022.20.6.NQ22780

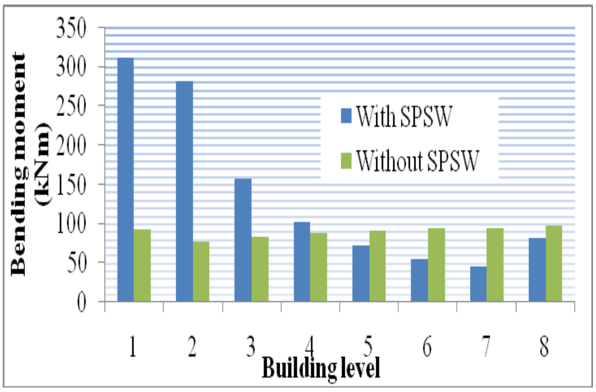

Figure 5. Bending Moment Variation in Beams

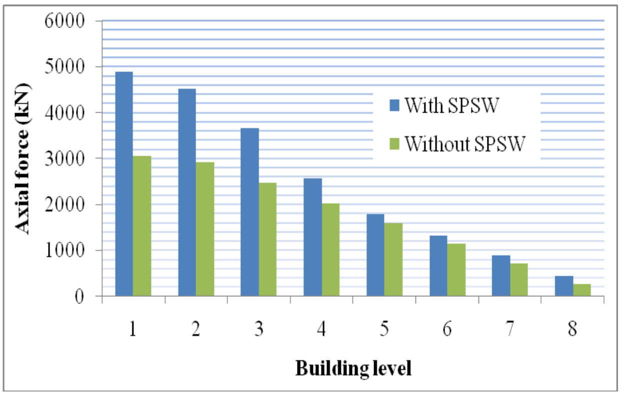

Figure 7. Axial Force Variation on Columns

4.1.2 Shear force in beams:

Taking one beam in each building level into account, analysis is forwarded and the shearing force (SF) estimates of beams are portrayed in Figure 6. SF in beams follows a similar pattern as that of BM in a structure with SPSW. Plinth level beams have shown enormous estimates of SF due to SPSW and thus required to do anchorage effectively for footings [20]. Meanwhile, structure with the absence of SPSW shows inflation pattern initially and then deflates.

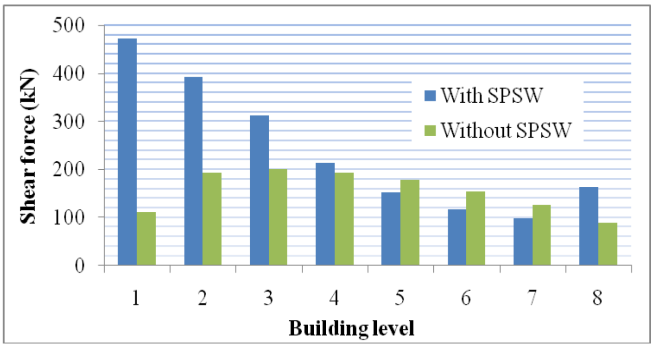

Figure 6. Shear Force Variation in Beams

4.1.3 Axial force in columns:

By taking into account one column in each floor level, axial forces on the columns are estimated in the analysis and the outturns are portrayed in Figure 7. Here, the axial force goes on deflating from lower stories to higher ones in SPSW structure as well as in structure with no SPSW. Moreover, at each level, this force is higher for SPSW structure. This is attributable to the impact of the shear wall [21].

4.1.4 Storey drift:

The story drift measures for all floor levels are mentioned in Figure 8. It is discerned that at ground level, drift value is the same for both SPSW and normal structure. These estimates follow the inflated trend towards higher stories for both structures and are higher for structures without SPSW. Thus, SPSW is beneficial to limit drift in stories [22].

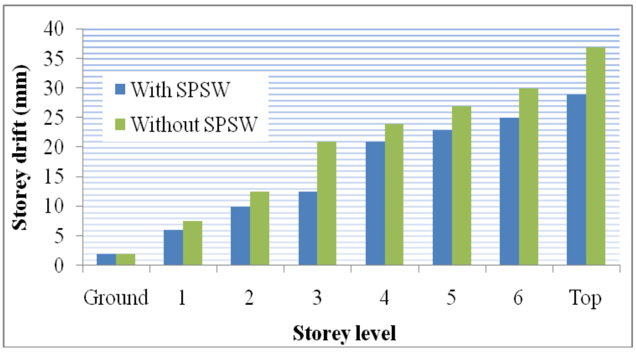

Figure 8. Storey Drift Variation

4.2 Structure with different CBFs

To observe the conduct of different CBFs, analysis is done on a G+4 storied structure of zone 4 having story height as 300cm. Contrasting numerous bracings is done mainly in terms of maximal displacements, axial forces, SF, BM in columns and displacement reduction percent.

4.2.1 Maximum lateral displacement for CBF structure:

Maximal lateral displacement estimates for diverse bracings are portrayed in Figure 9. These estimates are extremely high for a structure having no bracing because these braces use some amount of energy via inelastic distortions using the ductile nature. It is also perceived that these values are minimal for X shaped braced frame and are taken as ideal since these deflated measures manage seismic failure [23]. These displacement measures go on inflating with a rise in the building level.

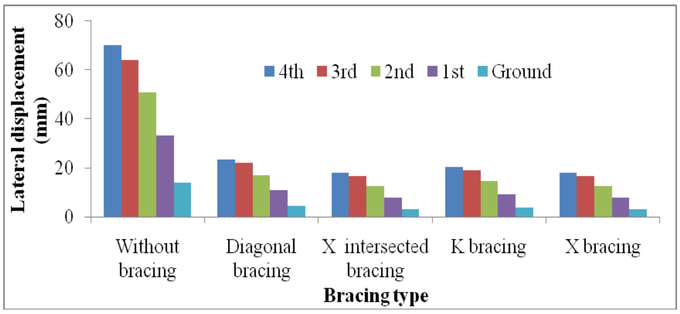

Figure 9. Lateral Displacement Variation for Diverse CBFs

4.2.2 Maximum axial forces in a column for CBF structure:

Figure 10 portrays the maximal column forces for numerous CBFs. Generally, braces inclusion in structures allows columns to handle more axial forces. It is discerned that higher story columns possess higher values. Moreover, X shaped bracing exhibits higher measures compared to all other bracings.

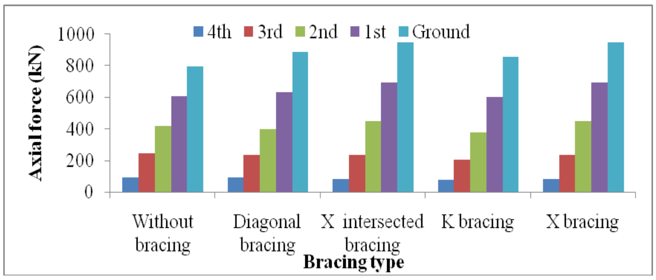

Figure 10. Maximal Axial Force in Columns with Diverse CBFS

4.2.3 Maximum shear force in a column for CBF structure:

Figure 11 portrays the maximal SF estimates for columns of CBF structure. It discerns that structure with the absence of CBF has larger SF than those with CBFs. Among diverse CBFs, X shaped bracing exhibits the least values of SF.

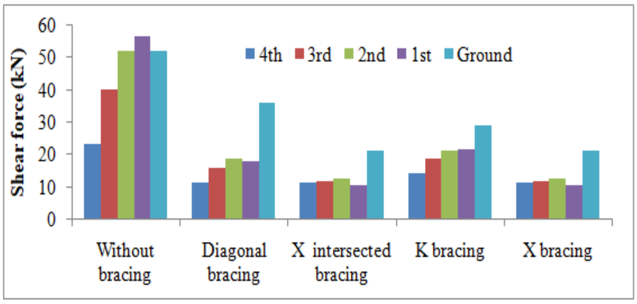

Figure 11. Maximal Shear Force in Column for diverse CBFs

4.2.4 Maximum column moment for CBF structure:

Maximal BM of columns for numerous bracings is portrayed in Figure 12.

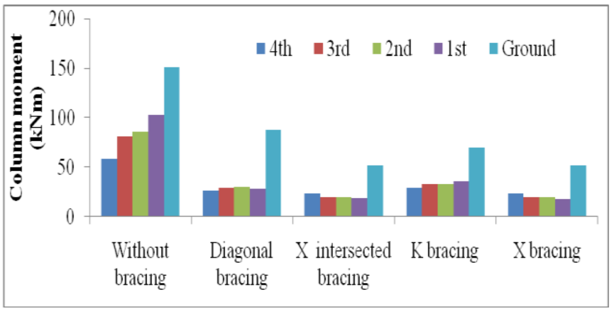

Figure 12. Maximal Column Moment for Diverse CBFs

This follows the same pattern as that of SF for CBF structure. Also, the X-brace type exhibits lower column moments in contrast with all other CBFs.

Contrasting all the bracing types, X shaped bracing exhibits ideal estimates for various parameters mentioned above and is the most preferred CBF in seismic view. Hence, a comparison is made between X-braced and SPSW structures.

5. COMPARISON OF SPSW AND X-BRACED STRUCTURE

For this analysis, the G+9 storied structure of zone 4 is chosen. 3-dimensional view of SPSW of 1.2cm thick and X braced structure is presented in Figure 13(a) and 13(b).

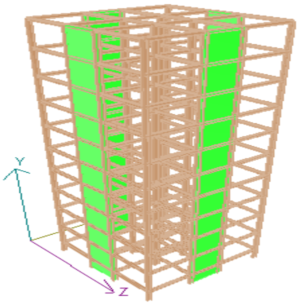

Figure 13 (a). 3D view of the structure with SPSW

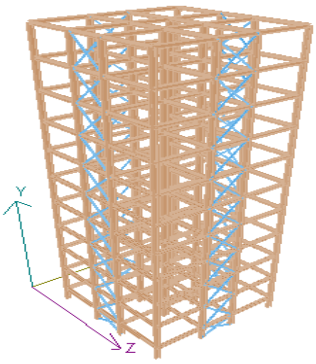

Figure 13 (b). 3D view of the structure with X-bracing

5.1 Beam bending moment and Shear force

BM and SF of beams vary in SPSW and X-braced structures and is portrayed in Figure 14 and 15 respectively. Both the structures follow a similar trend of deflating these estimates. Although SPSW structure portrays lower estimates than X shaped CBF, both the structures exhibit very minute variance in BM and SF that need not be considered when contrasted. This could be attributable to SPSW's diagonal tension which is equivalent to X-bracing's energy dissipation. G represents Ground while R means Roof.

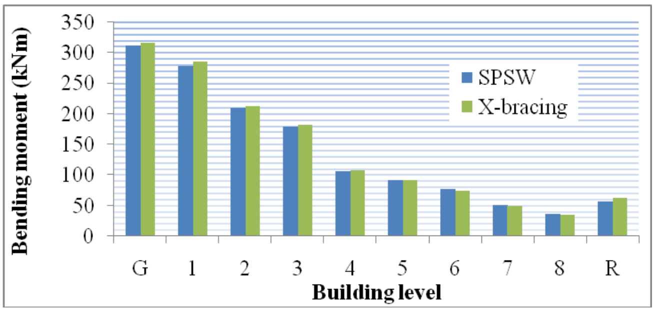

Figure 14. Beam Bending Moments in SPSW and X-Bracing

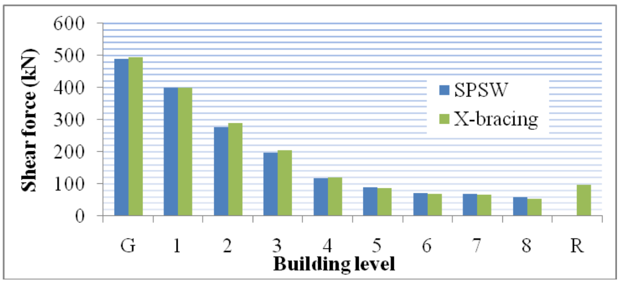

Figure 15. Beam Shear Forces in SPSW and X-Bracing

5.2 Column axial forces

Figure 16 exhibits the axial forces in columns of SPSW and X-braced structure. These force estimates follow the inverse pattern of SF and BM. The minute variance of axial forces is observed between both the structures due to which this variance can be neglected and can be said that both perform equally.

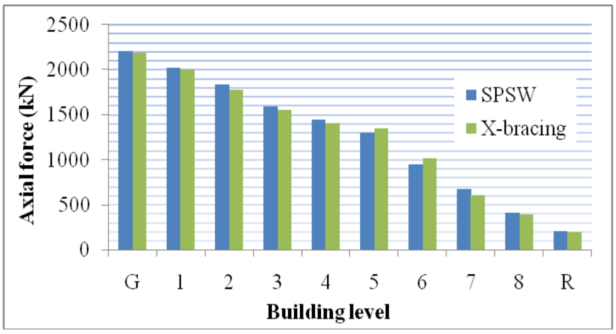

Figure 16. Column Axial Forces in SPSW and X-Bracing

5.3 Storey drift of SPSW and X-brace

Drift estimates of all the building levels of SPSW and X brace are portrayed in Figure 17.

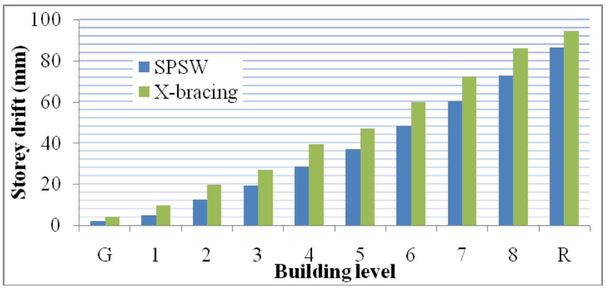

Figure 17. Storey Drift in SPSW and X-Bracing

In this, it is perceived that structure with SPSW has more low drift measures than X braced ones though X brace also procures lower drifts [24]. This means SPSW is more efficient in restricting drift in floor levels.

6. ANALYSIS OF SPSW WITH VARYING ASPECT RATIO

Altering the magnitudes of SPSW influences the conduct of the structure. Aspect ratio means the division value of width with respect to the height of SPSW. In order to analyze in this means, 4 structures having diverse aspect ratios of 0.833,1, 1.33 as well as 1.67 were considered. In this, positioning and a height of 300cm have been maintained the same whereas breadth is altered from 250-500cm with a rise of 50cm. 3-dimensional view of structure analyzing here is portrayed in Figure 18.

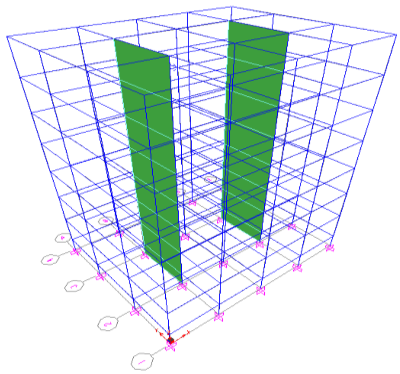

Figure 18. 3D View of SPSW Structure with Varying Aspect Ratio

6.1 Contrasting bending moments and shear forces of beams

The BM and SF estimates of SPSW having diverse aspect ratios are portrayed in Figure 19. It is perceived that both variances of BM and SF are directly proportional to the variance of aspect ratio i.e., deflates with declined aspect ratios and vice versa.

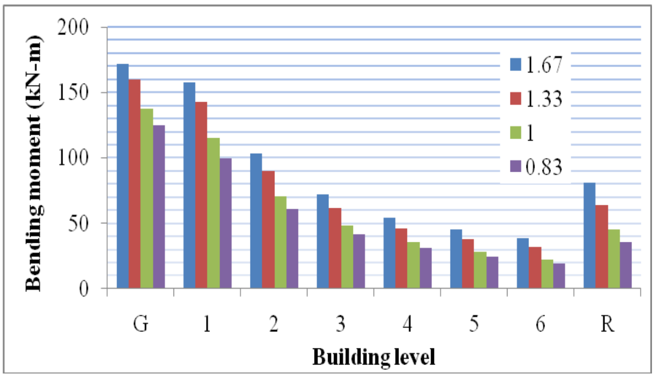

Figure 19. Bending Moment in Variance with Aspect Ratio

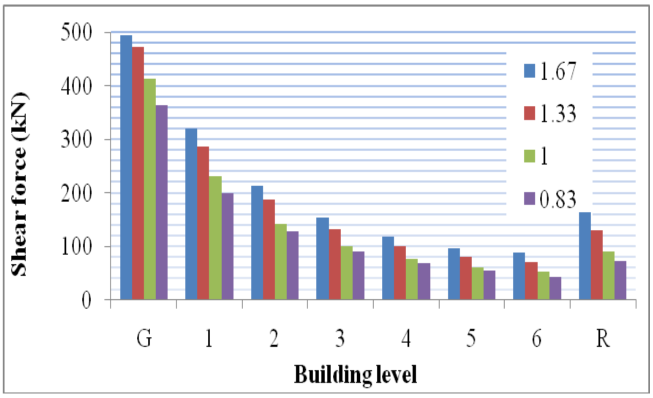

Figure 20. Shear Force in Variance with Aspect Ratio

6.2 Contrasting column forces and moments

Figures 21 and 22 exhibit the column forces and moments for SPSW in variance with aspect ratio. Outturns perceive that both the estimates incline with inflation in the aspect ratios.

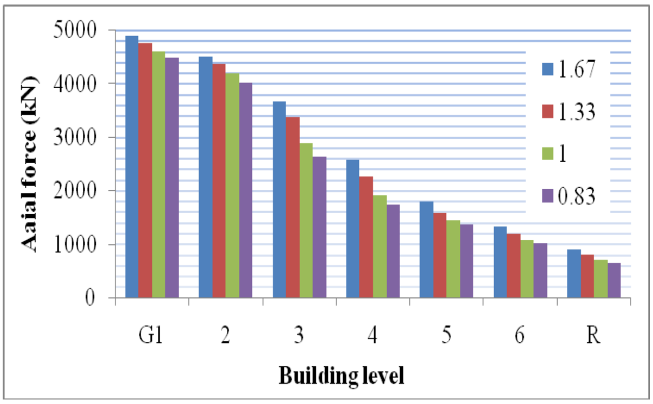

Figure 21. Column Force in Variance with Aspect Ratio

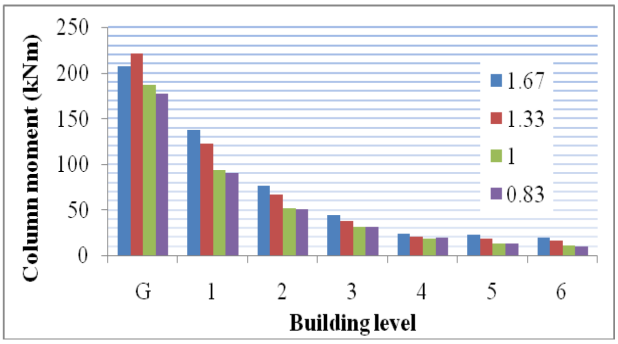

Figure 22. Column Moment in Variance with Aspect Ratio

6.3 Contrasting drift in stories

The estimates of drift in all the floor levels for SPSW structure in variance with aspect ratio is portrayed in Figure 23. From this, it has been perceived that drift is direct to aspect ratio at ground level i.e., rises with inflation in aspect ratio and vice versa. Meanwhile after the bottom level, drift in stories falls down by elevating aspect ratio.

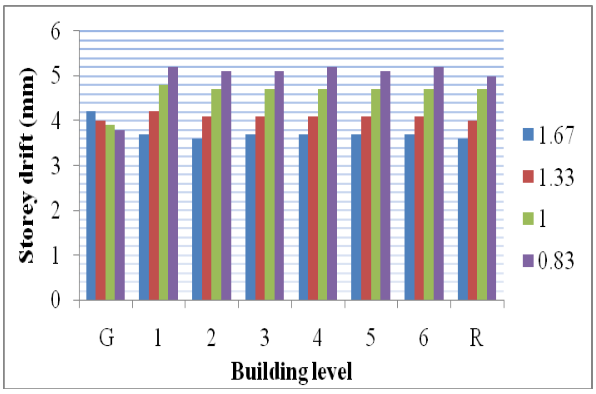

Figure 23. Storey Drift in Variance with Aspect Ratio

7. CONCLUSIONS

On the basis of the above analyses in the prevalent work, the inferences taken out are:

1. Flexure and shear requirements are excess for bottom level floors due to which efficient anchorage is essential whereas bending moment is found least for mid-stories than that of upper as well as lower ones for structures involving SPSWs.
2. Due to the involvement of SPSWs, columns become capable to manage more axial loads in low-level stories.
3. SPSWs resist the drifting of stories and these drift estimates rise with a tallness of structure.
4. Steel braces act against swaying due to which lateral displacements are low. These also minimize shearing and flexural requirements on structural components while the axial loading system acts as a medium for transferring lateral loads.

*e*ISSN 1303-5150

5. The decrement of displacement in percent for X-brace is excessive in contrast with diverse braced structures. X-brace allows columns to hold increased loads while limits the column moments and shear demands. On account of this, X-brace is evolved as supreme among other concentric braces.
6. SPSW possesses more efficiency than X-brace in terms of story drift whereas both exhibit very minute variance in terms of bending moments, shearing forces and axial forces in the structural components.
7. Increment in the aspect ratio of SPSW inflates the demand of beam bending moments and shearing forces and column forces and moments.
8. The higher aspect ratio of SPSWs turns down the drifting of stories while at the plinth level, this phenomenon is reversed.
9.

REFERENCES

[1] Venkateswar Reddy, K., Jugal Kishore, M., Uday Bhaskar, M. (2019), "Seismic Behavior of Steel-Concrete Composite Structures", International Journal of Engineering and Advanced Technology, vol 9 (2), pp. 4721-4726.

[2] Jugal Kishore, M. (2017), "Analysis of Steel-Concrete Composite Structures", 3rd National Conference on Innovative Research in Civil Engineering (NCIRCE 2K17), TEQIP-II S.C-1.1, January, Malla Reddy Institute of Technology, Hyderabad.

[3] Jialin Liu, Longhe Xu, Zhongxian Li. (2020), "Development and Experimental Validation of a Steel Plate Shear Wall with Self-Centering Energy Dissipation Braces", Thin-Walled Structures, vol. 148, https://doi.org/10.1016/j.tws.2019.106598.

[4] Jin-Guang Yu, Li-Ming Liu, Bo Li, Ji-Ping Hao, Xi Gao, Xiao-Tian Feng, (2019). "Comparative Study of Steel Plate Shear Walls with Different Types of Unbonded Stiffeners", Journal of Constructional Steel Research, vol. 159, pp. 384-396.

[5] Suneel Kumar, M., Senthilkumar, R., Sourabha, L. (2019), "Seismic Performance of Special Concentric Steel Braced Frames", Structures, vol. 20, pp. 166-175.

[6] Federico, G., Giovanni, L., Maurizio, O., Paolo, S. (2019), "Axial Response of Cold-Formed Steel Bracing Members with Holes", Journal of Constructional Steel Research, vol. 161, pp. 70-85.

[7] Berman Jeffrey and Bruneau Michel. (2003), "Plastic Analysis and Design of Steel Plate Shear Walls." Journal of Structural Engineering, ASCE, vol. 129 (11), pp. 1448-1456.

[8] Alinia, M. M., Dastfan, M. (2005), "The Effects of Surrounding Members on Post-Buckling Behavior of Thin Steel Plate Shear Walls (TSPSW)", Z.Y. Shen et al. (Eds)., Fourth International Conference on Advances in Steel Structures (ICASS), Shanghai, China, vol. 2, pp. 1427-1432.

[9] Fariborz Nateghi and Alavi Erfan (2008)," Theoretical Seismic Behaviour of Steel Plate Shear Walls", Proceeding, 14th World Conference on Earthquake Engineering, October, Beijing, China, Proceedings No. 05-05-0120.

[10] Topkaya, C., Kurban, C.O. (2009), "Natural Periods of Steel Plate Shear Wall Systems", Journal of Constructional Steel Research, vol. 65, pp. 542-551.

[11] Viswanath K.G, Prakash K.B., Anant Desai. (2010), "Seismic Analysis of Steel Braced Reinforced Concrete Frames" International Journal of Civil and Structural Engineering, vol. 1 (1), pp. 114-122.

[12] Madhar Haddad. (2010), "Concentric Tubular Steel Braces Subjected to Seismic Loading: Finite Element Modeling", Journal of Constructional Steel Research, vol. 104, pp. 155-166.

[13] Yipeng, D., Jiping, H., Jinguang, Y., Bowen, D., Danlan, L., Liang, Z. (2018), "Seismic Performance of a Repaired Thin Steel Plate Shear Wall Structure", Journal of Constructional Steel Research, vol. 151, pp. 194-203.

[14] Ali Davaran. (2019), "Stability Analysis and Design of Double hear Lap Bolted Connections in Steel X-Bracing Systems", Journal of Constructional Research, vol. 153, pp. 31-41.

[15] Jia-Chun, C., Ji-Dong, X., Zi-Ran, X., Tao, H. (2020), "Cyclic Behavior Study of High Load-Bearing Capacity Steel Plate Shear Wall", Journal of Constructional Research, vol. 172, https://doi.org/10.1016/j.jcsr.2020.106178.

[16] Alireza, T., Majid, G., Reza, V. (2020), "The Investigation into the Effect of Consecutive Earthquake on the Strongback Bracing System", Structures, vol. 24, pp. 477-488.

[17] Canadian Standard Association (CSA). (2001), "Limit States Design of Steel Structures", CAN/CSA-S-16-01, Willowdale, Ontario, Canada

[18] IS 1893. (2002), "Criteria for Earthquake Resistant Design of Structures", Part 1- General Provisions and Buildings (Fifth Revision), Bureau of Indian Standards, New Delhi, India.

[19] IS 800. (2007), "General Construction in Steel- Code of Practice", Bureau of Indian Standards, New Delhi, India.

[20] Londhe R.S. and Chavan. A. P. (2010), "Behavior of Building Frames with Steel Plate Shear Wall". Asian Journal of Civil Engineering, Building and Housing, vol. 11, pp. 95-102.

[21] Jin-guang, Y., Hai-sheng, Y., Xiao-tian, F., Chen, D., Tong-fei, H., Jay, S. (2020), "Behaviour of Steel Plate Sear Walls with Different Types of Partially-Encased H-Section Columns", Journal of Constructional Steel Research, vol. 170, https://doi.org/10.1016/j.jcsr.2020.106123.

[22] Saeid Sabouri-Ghomi, Carlos E. Ventura and Mehdi H. K. Kharrazi. (2005), "Shear Analysis and Design of Ductile Steel Plate Walls", Journal of Structural Engineering, ASCE, vol. 131 (6), pp. 878-889.

[23] Abou-Elfath, H., Mostafa, R., Meshaly, M., Heba, A.F. (2016), "Seismic Performance of Steel Frames Designed Using Different Allowable Story Drift Limits", Alexandria Engineering Journal, http://dx.doi.org/10.1016/j.aej.2016.08.028.

[24] Jui-Liang, L., Meng-Kwee, K., Keh-Chyuan, T. (2019), "Stiffness Configuration of Strongbacks to Mitigate Inter-Story Drift Concentration in Buildings", Engineering Structures, vol. 199, https://doi.org/10.1016/j.engstruct.2019.109615.

*e*ISSN 1303-5150

STUDY OF COMPRESSIVE STRENGTH & TENSILE STRENGTH OF CONCRETE BY USING GLASS WASTE & GEOGRIDS

Dr.Venkat Praveen Gannavaram
Professor, Department of Civil Engineering, Sreenidhi Institute of Science and Technology(Autonomous), Ghatkesar, Hyderabad, Telangana-501301
Manasa Shetty
Asst.Professor, Department of Civil Engineering, MallaReddy Engineering College (Autonomous) Maisammaguda, Dhulapally, Secunderabad, Telangana-500100.
L.Kalpana
Asst.Professor, Department of Civil Engineering, Sree Visvesvaraya Institute of Technology and Science, Chowderpally , Devarkadra , Mahabubnagar , Telangana-509204

Abstract:

The main objective of this project work is to have a keen study on the effects of using waste glass pieces as a partial replacement for coarse aggregates. Geo grids are provided as additional to the considered concrete mix, to improve the tensile strengths and stability of soils .Glass is one of the ancient and the most frequently used materials in the world. Glass has a very limited span of life in which it is used. Disposal of waste glass which is derived from various post-consumer beverage bottles is one of the environmental challenges to make it eco friendly. The prior most option for safe environmental and economic disposal of this waste is to recycle them in building materials. So glass waste can be cast-off or reused to avoid environmental problems. Due to the high uplifted material utilization of the construction industry, the utilization of waste glass as a partial replacement for coarse aggregate in structural concrete is particularly striking. Using glass waste in concrete industry is an very interesting possibility for economy on waste disposal sites and conservation of natural resources. Thus the maximum usage of glass waste in concrete production is very much helpful to reach the goal of sustainable construction.

In this experimental work the concrete grade of M40 mix is adopted. According IS: 10262-2008 code guidelines, concrete mix design calculations will be carried M40 mix grade. Various concrete mixes will be prepared by adjusting calculated amount of crushed waste glass at different percentages in the place of coarse aggregate. These mixes were casted by adopting a constant W/C and Aggregate ratio. It is expected to obtain more characteristic strength. The glass wastage used to replace coarse aggregate in the various proportions of 0%, 5%, 10%, 15%, 20%, 25%, 30%, 35%, 40%, 45%, and 50% in place of coarse aggregate. Concrete specimens that were casted are to be tested at 3, 14, and 28 days of proper curing with potable water. The cubes specimens are tested for compressive and tensile stresses by observing compressive strength and tensile strength loads at which the first crack appears.

Based on the test results, the ideal percentage of mix shows the maximum compressive strength.

Key words— Aggregate, Concrete, Glass waste, Geo grids, Mix design.

DOI Number: 10.14704/nq.2022.20.6.NQ22647 **NeuroQuantology 2022; 20(6):6459-6465**

I. INTRODUCTION

1.1 GENERAL

In present day years, there is a colossal pace of studies are research are continued quickly expanding of utilizing waste glass in cement. This intrigue has been bothered by the huge measure of waste glass accessible from void jugs, squander windows glass and compartments. On the off chance that such wastage of glass is utilized in solid generation, at that point it would altogether diminish the transfer of waste glass in to the earth and take care of some of ecological issues. The usage of waste glass as coarse total in cement has been endeavored as of late. With such glass squander use as a development material is among the most earlier decision due to the conceivably diminishing the expense of glass transfer and solid generation. It is normal that conspicuous contrasts happen in the structure between glass cement and unadventurously concrete. This including decreased bond quality between the total and the concrete glue. The interlock shear quality between the coarse total and the bond glue is less with glass squander than with normal total. Also, the friability of glass particles may debilitate the solid.

Glass is a translucent material unreasonable by dissolving a different mix of materials, for example, silica, soft drink cinder, CaCO3 at raised temperatures pursued by cooling some place hardening happen without crystallization. Glass is a material that is broadly utilized in our lives through various fake items, for example, sheet glass, containers, dish sets, and vacuum tubing. Glass is one of the perfect materials for reusing. Using of push off of glass squanders spares parcel of vitality and the expanding responsiveness of glass reusing paces up spotlight on the best possible utilization of waste glass with various structures in different fields. In this trial study, the impact of utilizing locally accessible waste glass as coarse total on the mechanical properties of cement was researched. The examples of cement and mortar that were casted in required sum were tried for compressive quality, parting elasticity, modulus of break and development for different ages and glass extents running from 0% to half. This project brings the results that are having the possibility of using glass waste as a replacement in coarse aggregate that completely forms a new concrete. Coarse aggregate that were partially replaced with (0%,5%, 10%, 20%, 25% ,30%, 35%, 40%, 45%,and 50%) respectively with glass waste. Compressive strength, Tensile strength and Flexural strength were compared with those of concrete specimens made with normal concrete that are made without any replacement of glass waste. The test results resulted in showing an increase in strength for glass waste concrete at a particular percentage of replacement of glass waste. These results clearly indicate that it is possible to manufacture concrete containing glass waste with characteristics similar to those of coarse aggregate. The major aim of environmental authorities is to reduce as far as possible the disposal of glass waste.

1.2 OBJECTIVES

- The effect of adding Glass waste to concrete to improve the characteristic properties of concrete mix.
- The effect of adding Glass waste as an admixture on the durability and the thermal insulation.
- The benefits on addition Glass waste are to minimize the risk of the Environmental Pollution.

1.3 GEO GRID

A geo framework is geo counterfeit material used to strengthen soils and comparable materials. Geo networks are most normally used to strengthen holding dividers, just as sub cases or subsoil underneath streets or structures. Soils pull separated under pressure. Contrasted with soil, geo networks are well-worked in carrying on pressure. This data licenses them to move powers to a bigger zone of soil than would somehow or another be the situation. Geogrids are made from polymer materials, for example, polyester, polyethylene or polypropylene. They potentially will be woven or sewed from yarns, warmth-welded from pieces of material or framed by punching a normal example of gaps in sheets of material, at that point later extended into a lattice.

Geogrid items are for the most part intended for support and, naturally, are indispensably associated with components isolated by in-plane openings. Geogrids appearance resembles a particular class of geosynthetics that are intended for support. These items are described by a generally high elasticity and a consistently dispersed exhibit of enormous gaps (openings between the longitudinal and transverse components). The openings acknowledges to soil particles on either side of the introduced sheet to come into undeviating contact, in this manner expanding the communication between the geogrid and a few soils. Additionally, the openings guarantee vertical waste of a fortified free-depleting soil.

The advancement of techniques for planning generally inflexible polymeric materials by pliable drawing, it might be said "cold working," raised the likelihood that such materials could be utilized in the support of soils for dividers, soak slants, roadway bases and establishment soils. Utilized thusly, the most significant capacity of the subsequent Geogrids is in the territory of fortification. This territory, similarly as with numerous different geosynthetics, is exceptionally dynamic, with various items, materials, arrangements, and so forth. Making up the present Geogrids showcase. The key part of all Geogrids is that the openings between the flanking sets of longitudinal and inclining ribs, called "gaps," are huge enough to take into account soil strike-through from one side of the Geogrids to the next. The ribs of a quantity of Geogrids are often quite stiff compared to the fibers of geotextiles.

1.4 IMPORTANCE OF GEO-GRID

Geogrids primarily improves the basic honesty of soils in roadways, dividers and slants by fortifying and keeping fill materials and conveying burden powers. Geogrids are the best possible answer for architects, designers and temporary workers confronting the difficulties presented by slanting ground and delicate sub grades. Geogrids help soils to with remain at for all intents and purposes any ideal point in evaluation partition applications. In holding divider and angle applications, geogrids can be joined with a wide assorted variety of inverse components to assess the ideal feel for any task. Geogrids cause accessible to keep up for the development availability for streets, expressways, berks, barriers and some other structure application that in advance required the utilization of costly over-exhuming or heaping techniques on powerless sub levels. Geogrids are additionally utilized in substructure fortification applications to decrease total thickness necessities or to broaden roadway execution life.

1.5 TYPES OF GEOGRIDS

1. Expelled Geogrid : Expelled Geogrids are fundamentally level structures in polymer (normally high thickness polyethylene or polypropylene) that are expelled and after that pulled: This might be done oneway way (mono-arranged Geogrids), or in the two principle headings (bi-situated Geogrids). They are utilized in soil and street cobblestone support.

2. Woven Geogrid: Woven Geotextiles are the most grounded textures that are available for disintegration control, adjustment and total division. It additionally Offers an expanded get elasticity, woven geotextiles textures offer a powerful structure that enables them to be effectively executed in practically any area, including the accompanying.

3. Expelled Geogrid: Expelled Geogrids are level structures in polymer (generally high thickness polyethylene or polypropylene) that are expelled and after that pulled: this might be done by one way (mono-situated Geogrids), or in the two fundamental ways (bi-arranged geogrids). They are worn in soil and street clearing fortification.

2. LITERATURE REVIEW

ZainabZ. Ismail and Enas A. AL-, Alaa M. Rashad ,Dr.Haider K. Ammash, Muhammad S. Muhammad, Ali H. Nahhab, S.P. Gautam, VikasSrivastava and V.C. Agarwal, Ahmad Shayan , Roz-Ud-Din Nassar, Parviz Soroushian,Dr.G.Vijayakumar, Ms. H. Vishaliny, Dr. D. Govindarajulu, Shayan and Xu, Shayan and Xu, Binata Debarment. Al, Ghosh S.Ket. al, Musmar.M.Aet. al, Shobana.S et. Al, Subramani.Tet. al.

3. METHODOLOGY

So as to do the investigation on the impact of waste glass as incomplete coarse substitution on the quality of solid, fine total and coarse total, 66 blocks of size 150 mm × 150 mm × 150mm each were casted for various level of wrecked waste and for 0% waste glass for a blend have been thrown in the research center. An exertion has been kept here to coordinate to the quality of 3D shapes through with various level of annihilated glass waste to the particular quality of traditional cement toward the finish of 3, 14 and 28 days of complete relieving under consumable water and to have a thought regarding the ideal level of obliterated waste which doesn't influence the quality of reused concrete extensively. Additionally fine and coarse totals was likewise halfway supplanted by obliterated waste and just solid shapes were thrown and tried following 3, 14 and 28 days for blend extent of 1:1.5:2.3 at a steady w/c of 0.45.

3.1 Cement: In this work, Ordinary Portland cement (OPC) of priya (53 grade) brand was utilized in this project. The physical property of ordinary portlant cement are determined and mentioned the is given in Table 1. The cement satisfies the requirement of IS: 8112-1989. The specific gravity was 2.9 and fineness was 2800 cm2/g

S no	Property	Results
1	Specific gravity	2.9
2	Fineness	4%
3	Standard consistency	29%
4	Initial setting time	30 min
5	Final setting time	600 min

Table 1: Shows the Properties of cement

3.2 Fine aggregate: Fine aggregate are the particle grains of mineral substancederived from the disintegration of rocks under mechanical process. It is distinguished in to required fines from gravel only by the size of grain or constituent part, but is distinct from clays which contain organic minerals.

S no	Property	Results
1	Specific gravity	2.70
2	Particle size	1.18 mm
3	Fineness modulus	2.7

Table 2: Shows the Properties of Fine aggregate

3.3 Glass waste: Waste glass are mostly available locally in various types of factories has been collected and made intoglass waste in to a suitable size in order to add in the concrete. Glass waste is very hard material. Before adding the glass in to tem is the waste is to be prepared to a desired texture and size as that of the coarse aggregate.

Generally, waste product is possibly will be in liquid or in solid waste form. Both of them are vary hazardous to the environment. 6461
Liquid and solid waste types can also be brought together in to one form and can be unrefined, re-usable and recyclable waste.

- Bullet liquid type
- Bullet Solid type
- Bullet Hazardous type
- Bullet Organic type
- Bullet Recyclable type

3.4 MATERIAL PROPERTIES

Physical Properties: Squashed glass (cullet) particles are for the most part fit as a fiddle and may contain some exceptionally level and stretched unpredictable particles. The amount of level and the level of rakishness and the measure of loosened up particles for the most part relies on the level of administration of Littler particles, coming about because of extra measure of squashing to a necessary degree, will bring about the to some degree less precision and decreased measure of level and prolonged particles. Appropriate pounding can practically dispose of extremely sharp edges of the cutted pieces and the relating wellbeing risks is totally connected with instructional manual treatment of the item.

Synthetic Properties: Glass-formers are singular components that can be changed into glass when gent in to contact with oxygen. Silicon dioxide (SiO2), worn as sand, is by a long shot the most general glass-previous. Normal glass contains around 70 percent of SiO2. Soft drink slag (anhydrous sodium carbonate, Na2CO3) goes about as a fluxing specialist in the dissolve. It decreseses the thickness of the curved glass and the dissolving point and that discharges carbon dioxide, and mixes the soften. To accomplish the particular properties Further added substances are additionally brought into glass. For example, either limestone or dolomite is in some cases utilized in lieu of pop cinder. To build the quality of the glass Alumina, lead, and cadmium are utilized and grow protection from synthetic assault. Different iron mixes, chromium mixes, carbon, and sulfur are worn as shading specialists.

Mechanical Properties: trademark mechanical properties for glass are plainly recorded in Table 20-4.(2) is a weak material that breaks from tractable pressure. Rock estimated particles which are more noteworthy than 4.75 mm (No. 4 sifter) size show tolerably poor strength when contrasted with the ordinary total materials. The different properties like inner grating point or shear quality and bearing limit of squashed mixed totals are generally high, its similarity is additionally harsh toward dampness content. Due vitreous, latent character of the material it tends not out of the ordinary great sufficiency properties and grinding.

3.5. Coarse total: Coarse total are the principle key material that is pressed down stone utilized for making concrete. The business rock is quarried, squashed and evaluated. Rock metal of 20 mm size from a neighborhood source was utilized as coarse total. The particular gravity of 2.6 and fineness modulus 6.05 was worn seen from the trial perceptions.

3.6. Water: consumable water which is free from the synthetic substances is utilized for blending and relieving. On expansion of raised level of crushed waste the necessity of water increments for a similar usefulness. In this manner, a steady droop is the one of the principle challenge as it for water necessity however the examples having 0% destroyed waste, w/c of 0.45 has been utilized.

3.7 Concrete: The solid blend configuration is totally conveyed down as per IS: 10262 (1982). The amount of bond in the blend configuration is taken as 380 kg/m3 according to the blend plan estimations which fulfills least necessity of 300 kg/m3 so as to maintain a strategic distance from the balling final result. Great stone total and ordinary waterway sand of zone-III was utilized as coarse total and fine total individually. Most extreme size of coarse total was 12.5 mm. According to IS:383-1970 the sifter investigation was conveyed both the fine and coarse total .Cement might be contorted as a thick mass which is for all intents and purposes counterfeit shake and synthetic compounds that are available in waste may make it waterproof or it tends to be made permeable and profoundly porous for such use as channel beds.

3.8 AFFECTING THE CHOICE OF MIX PROPORTIONS

The various factors affecting the mix design are:

- Compressive Strength
- Workability
- Durability
- Grading and Type Of Aggregate
- Maximum nominal size of aggregate
- Quality Control

3.9 PROPORTIONS

Cement; fine aggregate: coarse aggregate =1:1.5:2.3

Solid blend plans received for whole investigation were attempted as per the system indicated in IS 10262:1967.various blends that were proportioned in this undertaking so as to accomplish a structure compressive quality of 40 MPa following 28 days of relieving. Relating water-concrete proportion was determined as 0.45 and is kept consistent for the whole different blends. A control blend was created containing just common total, and absolutely there are 11 diverse blends were set up at different rates that and all out examples were casted taking all things together and total specimens were casted in all.

s.no	Percentage	Cement	Fine aggregate	Coarse aggregate	Glass waste
1	0%	3	4.5	6.9	0
2	5%	3	4.5	6.55	0.345
3	10%	3	4.5	6.21	0.69
4	15%	3	4.5	5.86	1.03
5	20%	3	4.5	5.52	1.38
6	25%	3	4.5	5.17	1.72
7	30%	3	4.5	4.83	2.07
8	35%	3	4.5	4.88	2.41
9	40%	3	4.5	4.14	2.74
10	45%	3	4.5	3.79	3.104
11	50%	3	4.5	3.45	3.45

Table 3: Shows the Mix proportion calculation

4. RESULTS AND DISCUSSION

4.1 RAW MATERIALS PREPARATION

There are two key sorts of materials in the piece of solid squares. In particular, totals and concretes. The capacity of totals is to outward appearance the primary structure of a brick work square. Various materials can be worn for totals. Sands and destroyed stones are commonplace instances of regular totals. Soot, slag and fly fiery debris are delegate instances of modern waste totals. The capacity of the concrete is to tie the totals together. The method to get ready pink materials is certifiably not a ceaseless procedure. It is done in clusters.

4.2 MIXTURE COMPOSITIONS AND OF GEO GRIDS IN CONCRETE

Expansion of geo frameworks should be possible in an appropriate manner by fallowing various techniques. The expansion ought to have a uniform scattering of the geo matrices so as to anticipate isolation or balling of the GEOGRIDS during blending.

4.3 WORKABILITY

Pristine solid which is demonstrated by the measure of prepared to help inner work required to completely reduced the solid. As battling fit as the expense of work and presence of the completed item Functionality is one of the physical limitations of solid which influence the quality and solidness. When it is effectively set and compacted homogeneous Cement is said to be practicable for example restricted of draining or Isolation. Unworkable solid needs more work or exertion to be compacted set up, likewise honeycombs and pockets may likewise be obvious in completed cement.

4.3.1 Slump Test:

The objective of the test is to quantify the consistency of cement all through the mix."Slump" is essentially a term authored to portray how steady a solid example is. The tests likewise also decide the usefulness of solid, how simple is it to deal with, minimized, and fix concrete without isolation.

4.4 CONCRETE TRANSFERRING AND BLOCK FORMING

The most significant advance in the entire venture where more consideration must be kept is the framing of the solid squares after it is restored under attractive conditions. The solid is moved to a square shaping machine by belt, and later dumped into the square framing mold on beds. At that point the solid is packed and vibrated into specific structures; took from the form yet at the same time on beds and conveyed to be stacked on racks. Presently the item is called square.

4.5 COMPACTION

Compacting of cement is the way toward letting out the captured air from the solid there by diminishing the void in the solid. During the time spent blending and setting of solid air is probably going to get ensnared in the solid. This captured air is expelled from the solid by various path by utilizing appropriate vibrator for example most ordinarily utilized vibrator is table vibrator. Every one of the examples that are casted has under gone the vibration to a reasonable degree so that the test results are to be expected to obtain accurately.

S.No	Replacement of glass waste	Work ability	Slump value	Compressive strength N/mm²	Tensile strength N/mm²
1	0%	GOOD	60 mm	30.75	7.25
2	5%	GOOD	58mm	29.33	7.56
3	10%	GOOD	58 mm	29.04	7.95
4	15%	GOOD	54 mm	27.5	8.35
5	20%	GOOD	60 mm	25.26	8.65
6	25%	GOOD	57mm	26.8	9.35
7	30%	GOOD	64 mm	26.36	10.65
8	35%	GOOD	56 mm	23.9	11.56
9	40%	GOOD	53 mm	25.56	12.65
10	45%	GOOD	60 mm	22.63	14.23
11	50%	GOOD	55mm	20.96	15.26

The various different methods are adopted for compacting the concrete.

- Hand compaction
- Compaction by vibration

The term 'warm of hydration' is applied to the warmth created while the synthetic responses that happens between the bond insect the water that is utilized while blending the solid blends. The warmth makes the solid first make greater and afterward to contract as it cools. because of different synthetic concoctions present in the bond, for example, false compound will prompt the quick setting of the solid and consequently the solid will get early breaks.

4.6 TESTING OF CONCRETE:

Testing of the solid predominantly manages the testing of the solid examples that were casted for at different extents of the substitution and different ages. Each example which was casted at different ages needs to undergo different test like compressive and elasticity by testing on the 3D shape, chamber and bar tests. The example examples which are 28 days old are wanted to get the trademark quality of 40 N/mm2 and measure its solidness by static mean.

Stress is the amount of interior power per unit zone. All materials will fizzle at various degree when subject to various outside activities, for example, burdens or temperature changes. The distortion, for example change in the shape is estimated by the endure a point. Temperature and stickiness are kept up standard for right restoring of squares. Completed squares are tried for the quality, thickness, water entrance, flame resistant, thermo, sound transmission and shrinkage. These examples are tried by pressure testing machine after 3days ,7 days relieving or 28 days restoring. The heap that is applied on the example is noted at the point where the primary break is seen and the example and the equation is applied to figure the particular qualities that are acquired where every example is casted at different level of the fluctuating extent waste and furthermore relieved at different ages.

5. EXPERIMENTAL INVESTIGATIONS

5.1 DETAILS OF SPECIMENS

The 3D shapes examples that are casted for testing of solidarity were of measurements 100 x 100 x 100 mm. The blocks arranged for toughness tests were of size 150 x 150 x 150 mm. No fortifications of any sort were given. Chambers are of distance across 100 mm and stature 200 mm for both regular cement and glass waste cement. Following 24 hours of cast the examples were expelled from the molds. Distinguishing proof imprints were made on the examples. The examples were kept for a relieving time of 3, 14 and 28 days.

Table 4: Shows the Strength of specimen for 3 days

S.No	Replacement of glass waste	Workability	Slump value	Compressive strength N/mm²	Tensile strength N/mm²
1	0%	GOOD	56 mm	38.65	8.25
2	5%	GOOD	58 mm	39.56	8.65
3	10%	GOOD	58 mm	41.88	9.36
4	15%	GOOD	60 mm	41.95	9.65

5	20%	GOOD	60 mm	42.3	10.56
6	25%	GOOD	54 mm	43.96	11.96
7	30%	GOOD	56 mm	44.43	12.36
8	35%	GOOD	52 mm	46.58	12.98
9	40%	GOOD	53 mm	46.9	13.56
10	45%	GOOD	60 mm	36.25	14.36
11	50%	GOOD	56 mm	32.56	15.63

Table 5: Shows the Strength of specimen for 14 days

S.No	Replacement of glass waste	Workability	Slump value	Compressive strength N/mm²	Tensile strength N/mm²
1	0%	GOOD	53 mm	39.65	10.69
2	5%	GOOD	60 mm	42.56	11.56
3	10%	GOOD	56 mm	43.25	12.36
4	15%	GOOD	55 mm	45.68	14.56
5	20%	GOOD	58 mm	42.85	15.89
6	25%	GOOD	60 mm	40.65	16.36
7	30%	GOOD	52 mm	39.25	17.65

Table 6: Shows the Strength of specimen for 28 days

5.2 COMPRESSIVE STRENGTH

In each blend extents 3 examples of different rates of the substitution of the materials, every example is tried under the general testing machine to get the compressive quality. The correlation of compressive quality of regular cement with that of glass waste cement is done after every one of the tests results are out. The solid wherein the coarse totals were halfway supplanted by glass waste demonstrated an expansion in compressive quality. The test outcomes basically demonstrate that there is a hugeness improvement of the compressive quality and are straightforwardly extents to the maturing of relieving. The quality expanded with the quantity of long stretches of restoring. The outcomes demonstrated that there is a 40% expansion in the compressive quality of the solid when contrasted with the ordinary cement at the age of the 3 days restoring .comparatively the test outcomes additionally demonstrated that there is a 90% expansion in the quality at the age of the 14 days.

5.3 SPLIT TENSILE STRENGTH

As shown in Figure 6Samples in every one of concrete were subjected to testing using the compression testing machine. The result of the average strength of cylinders is shown in Table 2 and the comparison of split tensile strength of conventional concrete with that of glass waste concrete is illustrated. The strength increased with the number of days of curing. The maximum tensile strength attained shown in the above table.

5.4 COMPRESSIVE STRENGTH REPRESENTATION BY BAR CHARTS AND LINE CHARTS

5.4.1 3 DAYS OF COMPRESSIVE AND TENSILE STRENGTH REPRENTATION BY BAR CHART GRAPH

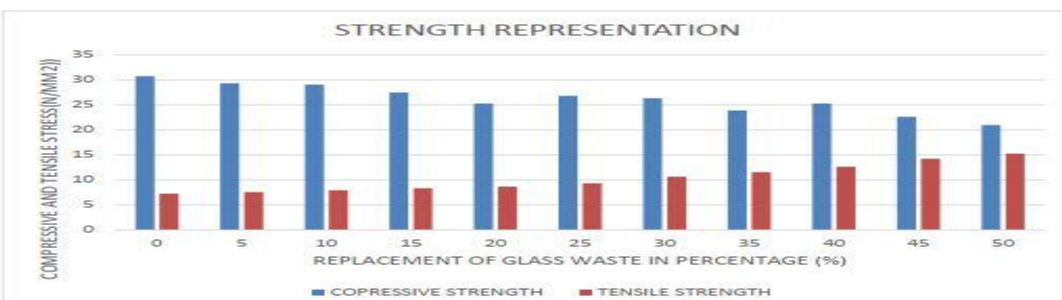

5.4.2 14 DAYS OF COMPRESSIVE AND TENSILE STRENGTH REPRENTATION BY BAR CHART GRAPH

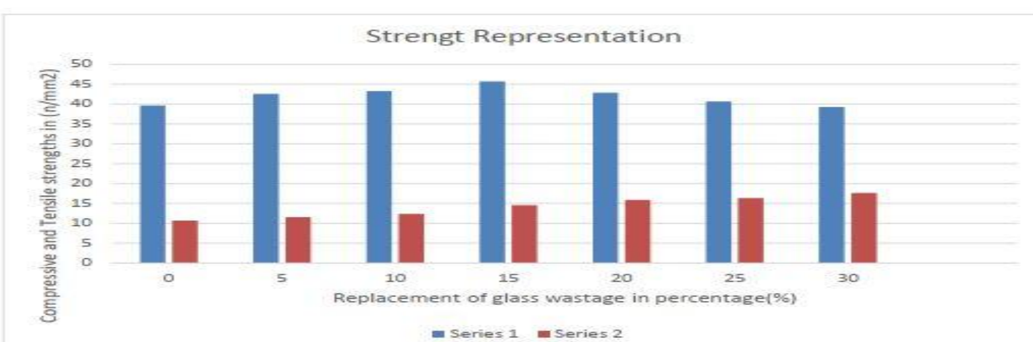

5.4.3 28 DAYS OF COMPRESSIVE AND TENSILE STRENGTH REPRENTATION BY BAR CHART GRAPH

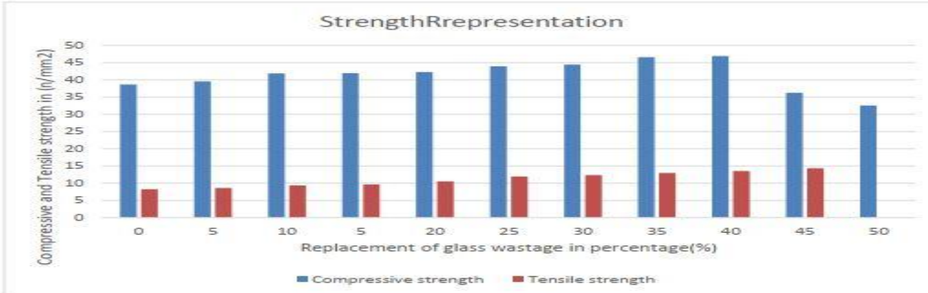

6. CONCLUSION

This trial concentrates to recognize the impacts of actualizing waste glass as a fractional trade for coarse total in auxiliary evaluation concrete. The outcome acquired advantage for the earth, lessening the utilization of crude materials and occupying extra waste from landfill. The fundamental finish of the investigation can be abridged as pursues.

- Compressive quality was begin to increment with the expansion of waste glass to the misunderstanding until the ideal degree of substitution. We have achieved the quality of 40%.
- The ideal rate substitution of coarse glass total was resolved to be 40%.
- Results of the present investigation demonstrate that waste glass total can be agreeably substituted for coarse total at supplanting levels up to 40% with the properties equivalent to the control examples.
- Here we closed utilization of glass waste and geogrids improves the quality upgrade quality when contrast with regular cement.
- By utilizing this glass squander in this venture achieves the compressibility quality by utilizing as halfway substitution on coarse total is an intriguing plausibility on waste transfer and protection of common assets. Consequently usage of glass squander in cement is particularly useful to arrive at the objective of feasible development.

REFERENCES:

[1] Ahmad Shayan, AiminXu "value added utilization of waste glass in concrete India july 2003, Elsevier Journal.
[2] IS: 10262-2009. Recommended guide lines for concrete mix design, New Delhi,ndia : Burea of Indian standard
[3] M.S.Shetty, concrete technology-theory and practice (S.Chand and company Ltd,New Delhi)
[4] Bing , L, Park , R . and Tanaka , H .(2001) "stress strain behavior of a strength concrete confined by ultra high and normal strength transfers reinforcement " ACI Struct.J.,98(3), 395-406
[5] Maryam Poursharifi,Yashar Yasrebi nia, Zahra poursharifi (2012) "Assessment of normal strength concrete and high strength concrete on cage system in earth quake..
[6] Oliveira L.A Pereia de, Gomes J.P. and Castro Santos P.(2010) "Optimization of pozzolanic reaction of ground waste glass incorporated in cement mortars" "Fundacao para Ciencia e Tecnologia" POCI/ECM/55588/2004.
[7] Kumarappan N.(2013) "Partial Replacement Cement in Concrete Using WasteGlass" International Journal of Engineering Researchand Technology (IJERT) Vol.2 Issue 10,ISSN:2278-0181.
[8] Osmani M. and pappu A. (2012) "Utilization of Glass Reinforced Plastic Waste in concrete and cement composition " on sustanaible construction materials.
[9] Shayan Ahmad (2002) "Value-added Utilisation of Waste Glass in Concrete"IABSE Symposium Melbourne.

Materials Today: Proceedings xxx (xxxx) xxx

Contents lists available at ScienceDirect

Materials Today: Proceedings

journal homepage: www.elsevier.com/locate/matpr

Evaluation of strength characteristics and identifying the optimum dosage with the impact of partial replacement of recycled fine and coarse aggregate from construction and demolition waste

C. Vivek Kumar [a,*], M. Palanisamy [b], C. Balakrishna [c], S. Pooja Sri Reddy [c], S. Robert Ravi [d]

[a] Civil Engineering, Gokaraju Rangaraju Institute of Engineering and Technology, Hyderabad, India
[b] Civil Engineering, Balaji Institute of Technology and Sciences, Warangal, India
[c] Civil Engineering, Malla Reddy Engineering College, Hyderabad, India
[d] Civil Engineering, ACE Engineering College , Hyderabad, India

A R T I C L E I N F O

Article history:
Available online xxxx

Keywords:
Recycled coarse aggregate
Recycled fine aggregate
Compressive strength
Split tensile strength
Flexural strength

A B S T R A C T

Natural Sand as fine aggregate (FA) and different sizes and forms of gravel or stones as a coarse aggregate (CA) are used in traditional concrete. Alternative aggregate elements, primarily as a potential application for recycled resources, are gaining in popularity. Although many new types of aggregate substitutes are being studied, along with granulated slag, rice husk ash, or multiple industrial wastes like fiberglass waste products, finely ground plastics, paper, and wood products or wastes, sintered sludge granules, and many others, there is now a lot of work to be done. This study is taken up to utilize the recycled coarse aggregate (Rca) and recycled fine aggregate (Rfa) as a replacement for natural aggregate (NA) in concrete mix and required to find the percentage of Rca and Rfa, as the strength of concrete cannot be achieved by using higher percentage. The purpose of the study is to compare recycled coarse aggregate (Rca) and recycled fine aggregate (Rfa) with natural coarse aggregate (Nca) and sand in terms of specific gravity, water absorption, particle size dissemination. Further, this study will also consider the difference between the performance of Recycled Aggregate Concrete (RAC) for different percentages of recycled coarse aggregate (Rca) and recycled fine aggregate (Rfa) i.e., for 0%, 10%, 15%, 20%, 25%, 30%, 35% replacement. The present study is an investigational study on the behavior of recycled aggregate concrete indicating coarse and fine aggregates for the strength, also identifying the optimum dosage of Rfa, Rca, Nca and Nfa with their performance levels and the relationship between compressive strength (CS), Split Tensile Strength (STS) and Flexural Strength (FS). It has been observed that optimum dosage of Recycled Aggregate proportion has been identified as M1 with Cement + 90% Nfa + 90% Nca + 10% Rfa + 10% Rca + W + 1% SP in CS with 40 N/mm^2 and 20% increase in STS and 16% decrease in FS compared with Conventional Concrete (CC).

1. Introduction

Construction and demolition (CD) waste is the largest source of recycled aggregates. Most of the demolition waste is disposed of by storing it in landfills or using it to redevelop land. However, as the demand for land grows, the areas, power, and breadth of land available to collect waste materials are becoming increasingly restricted. When shipping costs are factored in, the disposal becomes a big issue [1,2]. As a result, it seems that reusing demolition waste is a viable option, with the most suitable and large-scale use being as aggregates of concrete for new buildings. Concrete is the most used building tool in all forms of structural engineering projects around the world [1]. This is largely due to the loss of high-quality primary aggregates and increased environmental

Abbreviations: CD, Construction & Demolotion; Rca, Recycled Coarrse Aggregate; Rfa, Recycled Fine Aggregate; Nca, Natural Coarse Afggregate; Nfa, Natural Fine Aggregate; CS, Compressive strength; STS, Split Tensile Stremgth; FS, Flexural Strength; SEM, Scanning Electron Microscope.

* Corresponding author at: Assistant Professor, Civil Engineering, Gokaraju Rangaraju Institute of Engineering and Technology, Hyderabad, India.

https://doi.org/10.1016/j.matpr.2022.05.265
2214-7853/

Please cite this article as: C. Vivek Kumar, M. Palanisamy, C. Balakrishna et al., Evaluation of strength characteristics and identifying the optimum dosage with the impact of partial replacement of recycled fine and coarse aggregate from construction and demolition waste, Materials Today: Proceedings, https://doi.org/10.1016/j.matpr.2022.05.265

consciousness. As a result, the use of Recycled Concrete Aggregate (RCA) from Construction and Demolition waste (CD waste) in concrete is becoming increasingly widespread [3,4]. Concrete debris, bricks and tiles, sand and dust, wood, plastics, cardboard and paper, and metals are typical components of building and demolition waste. Most of the CD waste is normally made up of concrete debris [1,2,5]. Crushed concrete rubble can be used as a replacement for natural coarse aggregates in concrete or as a sub-base or base coat in pavements after being separated from other CD waste and sieved.

Recycled aggregate is the term for this kind of recycled material [2,6]. Concrete is a long-lasting element characterized by its ability to withstand weathering and chemical attacks while retaining its desired engineering properties [1,2,5,5].

Using RCA in concrete production is also an environmentally sustainable alternative to the continual degradation of resources aggregates, and it may enhance the mechanical characteristics of the cement matrix [3,4]. Because of its porosity, RCA has a reduced unit weight than that of natural aggregates, and as a result, RA can considerably reduce the workability of the concrete [3,4,7]. It has also been claimed that adding RCA enhances HPC's compressive strength which was explained by Bassam et al. [8,9]. Many structures, however, deteriorate1prematurely and severely due to the use of inappropriate materials, bad building practices, inadequate curing, and incorrect mix designs. Many considerations, like a good mix architecture, should be integrated to create a long-lasting structure [10].

Miren Etxeberria et al. [11] discovered that using fly ash increases the endurance of recycled HPC. The substantial water absorption capacity including its ceramics and blended aggregates utilized using finer recycled aggregates resulted in positive internal curing, which reduced shrinkage and improved their applicability over natural aggregate concrete. Md Saifuddin et al, [12] discuss the relevance of Recycled Concrete Aggregate (RAC) physical, structural, and chemical characteristics in the research that was presented to examine the impacts of RCA on strength and durability properties, as well as the workability. Najib N. Gerges et al. [13] discuss during third, half, 2/3, and 100% replacement proportions, coarse aggregates were substituted with Green Bottles coarse aggregates. The substitution of a 1/3 coarse aggregate was seen to be the most effective in maintaining the mix design development characteristics.

Vanchai Sata et al. [14] discussed about geopolymer composites may be made with recycled aggregates from building and demolition waste (CDW), which includes crushed reused concrete, bottom ash, crumbled clay brick, waste tires, and shattered waste glass. As just an alternative to the traditional Portland cement concrete (PCC), recycled aggregates with geopolymers binders can be useful. According to Zhanggen Guo et al. [15], the environmental consequences of RAC blocks are smaller than those of regular concrete blocks. The utilisation of construction and demolition (CD) waste to make concrete building blocks provides numerous advantages and increases the environmental footprint and long-term viability of masonry constructions substantially. Recycled aggregates seemed to be a highly beneficial material that may be used in concrete, but CD waste management is extremely difficult to process and requires considerable machine power. Reuse of CD waste will be a useful approach in the construction industry, in addition to using natural aggregate, which causes natural degradation. The objective of this present study is an investigational study on the behavior of RAC indicating recycled coarse and fine aggregates for the strength, also identifying the optimum dosage of Rfa, Rca, Nca and Nfa with their performance levels and the correlation between compressive strength (CS), Split Tensile Strength (STS) and Flexural Strength (FS).

2. Research significance

For decades, construction engineers all around the world have preferred concrete as a best suitable construction material, which is favored because of its superior performance, longer life expectancy, and cheap maintenance costs. Yearly, smaller structures being demolished to achieve fast urbanization, and newer, larger structures were built in their place. Many forms of conventional mass fills, embankment barrier, foundation or fill for sewage projects, road construction noise barriers, and embankments are examples of uses that do not require any pre-processing. For pavement subbases, most of the unprocessed crushed concrete aggregate is provided as 20 mm and 40 mm RCA fractions. In addition to the natural aggregates (NA), RCA also comprises hydrated cement paste. When compared to identical natural aggregates, such paste lowers the relative density and enhances the porosity.

The larger the porosity of the RCA, the greater the absorption. The act of recycling concrete decreases the quantity of waste that must be disposed of in landfills. Any incorporated metals may be removed and repurposed, and the concrete itself has become aggregate. Furthermore, employing recycled concrete aggregates (RCA) decreases the number of fresh materials required. Concrete recycling contributes to long-term sustainability in a variety of ways. The primary objective of this study was to evaluate the performance of recycled coarse and fine aggregate in concrete of grade of M30, where natural coarse aggregate (Nca) including natural fine aggregate was replaced in various proportions using recycled coarse aggregate (Rca) and recycled fine aggregate (Rfa), such as 10%, 15%, 20%, 25%, and 30%, and to compare the results of control concrete built with natural coarse and fine aggregate to identify the optimum dosage.

3. Materials and methods

3.1. Material characterization

Fine aggregates for Recycled Concrete were procured from various resources and included natural fine aggregate (Nfa) and rocks dust. Concrete blocks, stones, rubble, sediment, and other types of demolition debris were gathered as samples. Following sorting, concrete debris was crushed in a jaw crusher to produce a well-graded recycled coarse aggregate with 10 mm and a maximum size of 4.75 mm in accordance with IS 383: 1970 [10]. The fine fraction passing through a 4.75 mm sieve achieved during the grinding of leftover concrete was utilized to partially replace fine aggregates as recycled fine aggregates (Rfa). The physical characteristics of fine aggregates are being established and are presented in according to IS 2386: 1963 [16].

Figs. 1a and 1b showing scanning electron microscope (SEM) [Fig. 1a], [Fig. 1b] of Nfa and Rfa, correspondingly. All the recycled concrete (RC) mixture arrangements were made with Ordinary Portland cement (OPC) corresponding to Indian standard codes. The chemical and physical characteristics of cement. As natural and recycled aggregate materials like Nfa and Nca for natural aggregates, Rca and Rfa for recycled aggregates respectively are widely available were listed in Table 1 and its particle size distribution of aggregates shown in Fig. 3 and Table 2. Indian standard (IS) codes have been used to identify the properties of natural and recycled aggregates, whereas IS:2386 Part III –1986 [16] is used for identifying the bulk density and specific gravity by Pycnometer method, Fineness modulus is specified as per IS:2386 Part II –1986 [16].

per the studies made by Evangelista et al. [17] for the specific Recycled Fine Aggregate (Rfa) size fractions under investigation were subjected to SEM investigation. The existence of particles

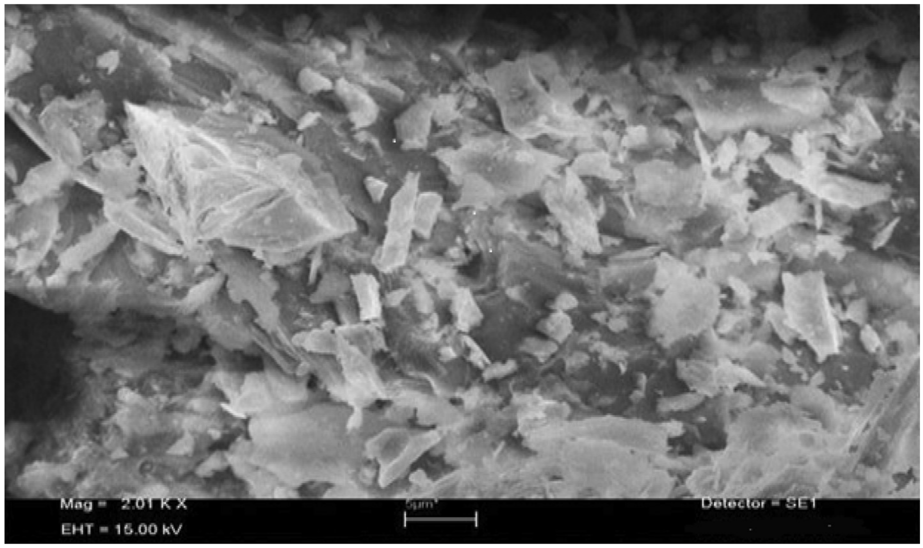

Fig. 1a. SEM of Natural Fine Aggregate (Nfa).

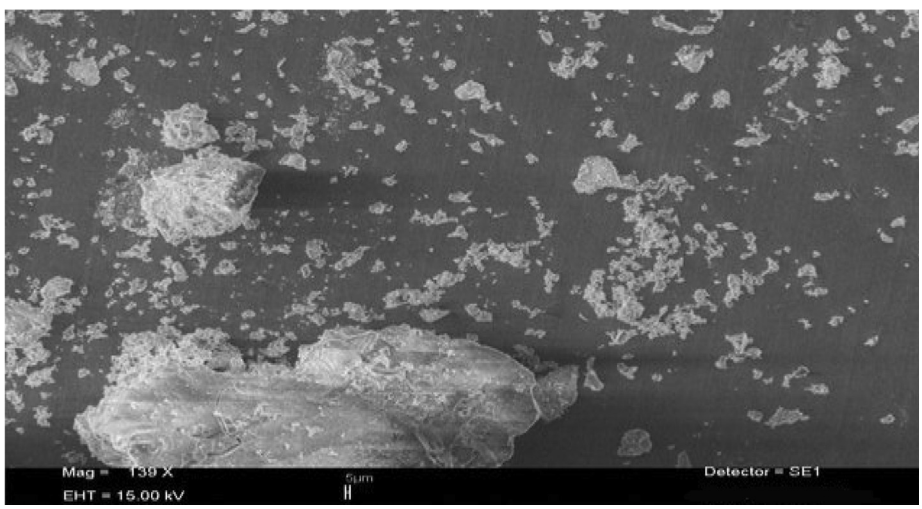

Fig. 1b. SEM of Recycled Fine Aggregate (Rfa).

Table 1
Physical Characteristics Nfa, Nca, Rfa and Rca.

Property	Cement	Property	Nfa	Nca	Rfa	Rca
Specific gravity	3.15	Specific Gravity	2.70	2.536	2.50	2.36
Particle size Distribution	21 µm	Bulk density (Compact)	1711 kg/m^3	1711 kg/m^3	1711 kg/m^3	1812 kg/m^3
Specific area m^2 /kg	330	Bulk density (Loose)	1631 kg/m^3	1631 kg/m^3	1631 kg/m^3	1692 kg/m^3
Colour	Greyish	Fineness Modulus	2.83	3.06	4.50	3.12
PH	11.9	Water Absorption%	2.75	2.83	5.56	5.88

Table 2
Sieve Analysis for Nfa and Rfa.

Type of Aggregate	Aggregate passing (%) w.r.to Sieve Size in mm						
	0.15	0.3	0.6	1.18	2.36	4.75	10
Nfa	0.02	0.08	0.23	0.50	0.83	1.10	1.15
Rfa	0.06	0.15	0.26	0.40	0.66	0.98	1.13

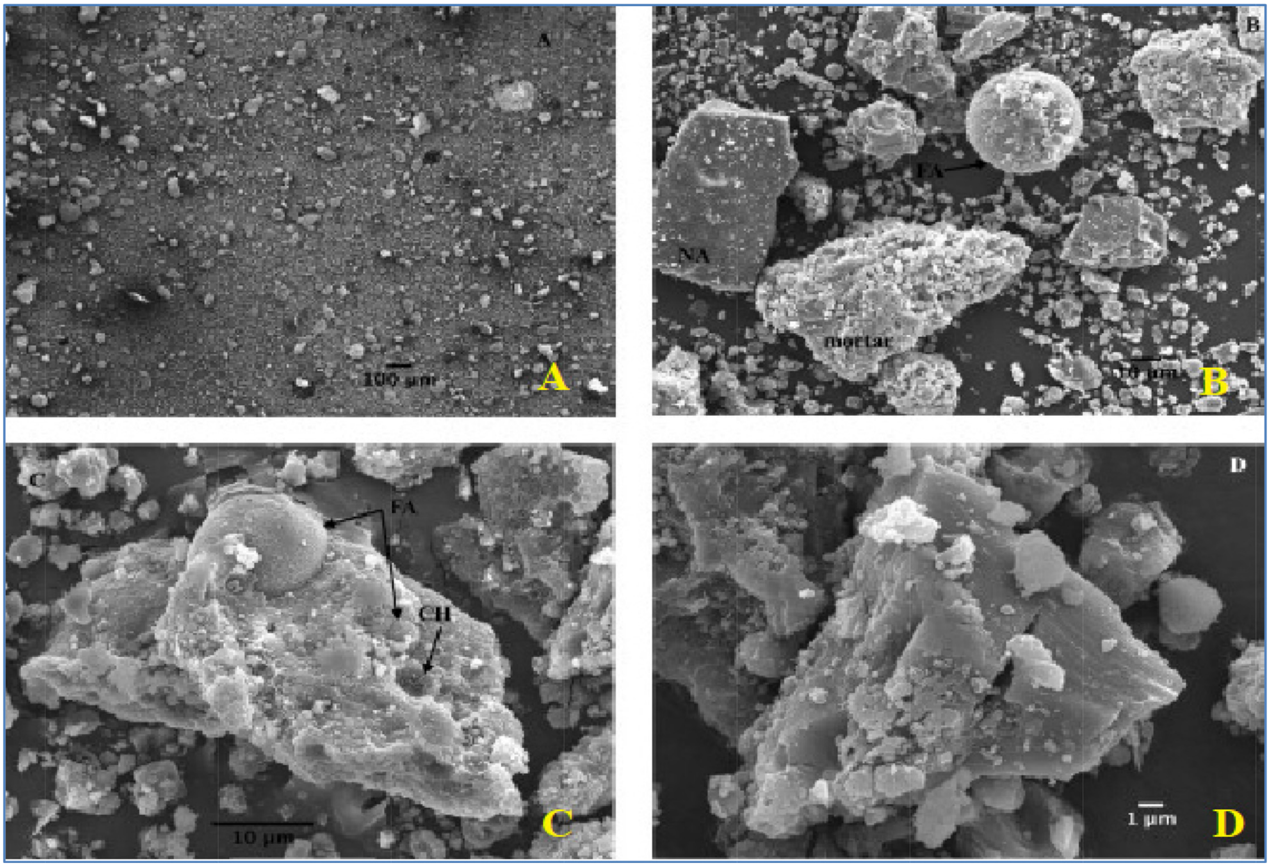

Fig. 2. SEM images of Rfa of the 125 µm size fraction: (A) low magnification image; (B) and (C) detail showing several components present in the aggregates: natural aggregates; (D) Rfa particle with irregular shape and adhered smaller particles.

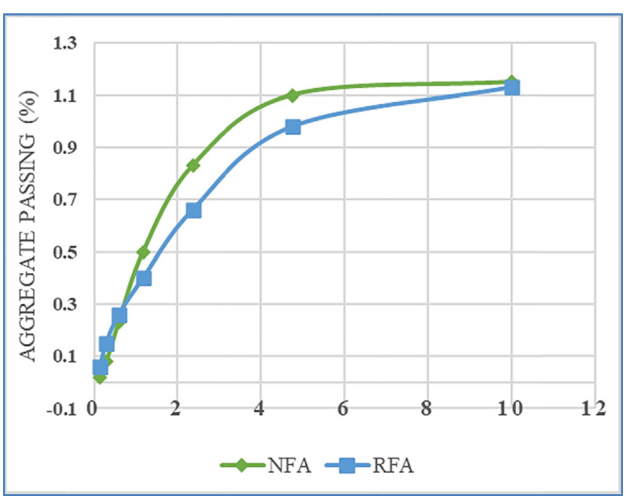

Fig. 3. Graph representing the particle size distribution curve for Nfa and Rfa.

smaller than predicted is confirmed by the 125 µm proportion (Fig. 2), which agrees well with laser diffraction data. The form of the particle is asymmetrical, with just a high roughness and surface area.

Lavado et al., [18] analysed the characteristics of materials made using recycled coarse aggregates (Rca) in the fresh condition. Various RCA crushing rates (primary crushing as well as secondary crushing), water / cement (w/c) ratios (0.35, 0.45, 0.55), and paste volumes (1.25%, 2.5%) were used to make the concrete mixes. Slump cone, flowing table, as well as Vee-Bee Consistometer have all been tested on the experimental concrete mixtures in fresh state. The form and texture for RCA have become more important in blends with decreasing w/c (0.35 and 0.45), which resulted in reduced fluidity as well as consistency. For modest changes in cement paste amount, the mixtures likewise revealed slight dispersion in their fresh-state characteristics. These findings reported before are accurate for RCA mixtures that were only subject-ed to primary crushing, although the variations are more significant.

The purpose of this study is to develop a technique for assessing the phase's liberation both as method for monitoring the efficiency of its extraction process of a fine aggregate generated by secondary crushing of demolition wastes. Based upon the previous literatures, to achieve the characteristic strength and durability test criteria, 100 × 100 mm × 100 mm cubes were decided to cast with each composition. On a concrete vibrating table, sample specimens containing cube mould have been compacted thoroughly. All moulded specimens were completely covered for 24 h before being submerged in the curing tank for such appropriate curing periods. Con-trolled concrete, as well as recycled aggregate concrete (RAC) specimens, were evaluated according to IS 516–1969 [19] after being cured for 3, 7, and 28 days is performed using a Compression testing equipment (CTM) that has a capacity of 200 tonnes for the casted specimen samples. Based on the results from the previous literatures, recycled aggregates can be replaced up to a replacement level of maximum of 30% of the total content of the concrete to be casted.

4. Experimental investigation

For blending, concrete M30 of recycled fine aggregates (Rfa) and recycled coarse aggregates (Rca) integrated concretes manufactured using, mix proportioning had been done using the Indian Code for Mix Design (MD) methodology to determine the best mix. Various trial mixes were seen on a variety of concrete mixes developed with a diversity of feasible combinations, with the goal of progressing mixed concrete blends. In this investigation, six different proportions of concrete mixes were developed, as well as a control mix. The water-cement ratio (w/c) was 0.4 throughout all six permutations, and the control OPC concrete was developed to generate M30 and cube specimens for M30 grade utilizing BIS / ACI techniques by Vivek Kumar et al. [20,21]. The adherent mortar towards the aggregates was also crucial for this. Because recycled aggregates have a greater water absorption capacity, it is best to keep the layer of the aggregate wet and dry before commencing the concrete mixing process.

Ordinary Portland Cement (OPC) is the predominant binder for fresh and hardened properties of Recycled aggregate concrete (RAC). In this study, the OPC 53 grade was employed. Cement was evaluated for physical characteristics in accordance with IS: 4031-1968 [22] as well as found to fulfil various IS 12229-1987 [23] requirements. The maximum amount for active blended elements that could be mixed with cement is 15 percent of the total mass. As mentioned earlier, coarse aggregate, fine aggregate, and cement were utilized to create a design mix with M30 grade concrete to produce Recycled Aggregate Concrete (RAC) with a target compressive strength of 38.25 N/mm^2 or MPa for this study. The materials' weight ratio became 1:1.882:3.271:0.4. (Cement: Fine aggregate: Coarse aggregate: Water).

The maximum cement content is limited to 450 kg per cubic metre of concrete, according to clause 8.2.4.2 of IS 456-2000 [24]. Following trail mixes, improved quantities in kilogram per cubic metre for grade (M30) integrated concrete mixes are achieved without affecting the necessary strength properties. The mix proportioning for M30 grade made as per IS 10,262: 2009 [25] have been stated in Table 3 and amount of recycled aggregate concrete (RAC) with various blending of Rfa, Rca have been quantified in this Table 4.

The various formulations of mixes which is arrived for the Natural Fine and Coarse Aggregate and Recycled fine and coarse aggregate are as follows.

M1: C + 90% Nfa + 90% Nca + 10% Rfa + 10% Rca + W + 1% SP.
M2: C + 80% Nfa + 80% Nca + 20% Rfa + 20% Rca + W + 1% SP.
M3: C + 70% Nfa + 70% Nca + 30% Rfa + 30% Rca + W + 1% SP.
M4: C + 85% Nfa + 85% Nca + 15% Rfa + 15% Rca + W + 1% SP.
M5: C + 75% Nfa + 75% Nca + 25% Rfa + 25% Rca + W + 1% SP.
M6: C + 65% Nfa + 65% Nca + 35% Rfa + 35% Rca + W + 1% SP.

For two reasons, conventional concrete mixes often carry a combination of adding water initially, particle size distribution (PSD), filling effect, and voids all through the solids stable system all have a big impact on the water consumption and workability. Modifying the Superplasticizer (SP) dosage between 100 and 150 mm resulted in the desired slump. Mix proportions for control OPC and recycled aggregate concrete (RAC) mix for grade M30 in Table 4.

The use of recycled aggregate (RA) made from CD wastes to substitute natural aggregate (NA) in concrete is often recognized as a cost-effective measure to resolve both issues at the same time. The characteristics of recycled coarse aggregate (RCA) and their impact on the strength and durability properties of concrete have been the subject of extensive investigation as studied by Biao Lia et al. [26].

Traditional concrete mixtures normally contain a lot of mixing water for two reasons: To begin with, distribution of particle size, particle filling impact, and spaces throughout the solid stable system have a major impact on the water demand as well as workability. The needed slump was achieved by modifying the Superplasticizer (SP) dose from 100 to 150 mm. Mix proportions for control OPC and recycled aggregate concrete (RAC) mixes for grade M30 in Table 3. Slump testing was used to determine the workability of concrete mix. Recycled aggregate concrete (RAC), which is made by partially or completely replacing natural aggregates in the concrete mix with recycled aggregates, has been shown to have significant environmental and economic benefits, such as a reduction in natural resource consumption and waste sent to landfills. As per studies made by Silva et al. [27], RAC on the other hand must be viewed also as secondary material of lower quality than the normal aggregates used during manufacturing, despite its numerous environmental benefits. Compressive strength (CS), as determined by conventional tests to acquire concrete characteristics, is regarded as a key indicator of normal aggregate concrete conditions and may even be utilized to estimate other values [26–28].

Studies made by Sallehan Ismail et al., [29] explained about slump flow is the process of releasing concrete from the slump cone to verify that consistency of fresh concrete satisfies the required standards. Naturally obtained fine aggregate have a rough surface roughness and a higher angularity, which causes more agitation amongst these particles, resulting in a reduction in concrete workability. Because when RA substitution ratio is increased, the cement pastes of FA shall be increased, causing greater friction between both the particles, and lowering the slump throughout the concrete. The workability of fresh concrete as determined by the slump test is shown in Table 4.

As per studies made by Ashraf M Wagih et al., [30], the compressive strength of concrete is often regarded as its most useful mechanical property, as it provides a comprehensive representation of the material's quality and has been associated with other characteristics. RAC mechanical properties have been observed to be reduced by up to 40% in the past. The loss in compressive strength due to a 25% substitution of NCA aggregate was minimal (2–4%). The compressive strength of concrete is repeatedly regarded as its most useful mechanical property, as it provides a comprehensive representation of the material's quality and has been linked to other characteristics. RAC mechanical properties have been observed to be reduced by up to 40% in the past. Biao Lia [26] described that, when the replacement ratio was increased to more exceeding 50%, there was a non-linear decline in compressive strength of 15–23% compared with conventional concrete.

By bridging the hydration products and reducing the pores, the addition of 10% SF in RC considerably decreased the pores and compressed ITZ; the ITZ of this concrete was extremely near to that of ordinary concrete (CC). The RC comprising these two pozzolans had highly porous and uncompressed microstructures because of

Table 3
Mix proportions for M30 grade concrete as per IS 10262:2009[25].

Type	Cement (kg)	Fine aggregate (kg)	Coarse aggregate (kg)	W/C Ratio
CC	362	682.60	1184.4	0.4
Mix ratio	1	1.882	3.271	

Table 4
Quantities for Recycled Aggregate Concrete Mixes for 1 m^3 concrete.

Mix	Cement (kg)	Nfa (kg)	Rfa (kg)	Nca (kg)	Rca (kg)	Water (litres)	SP (litres)
M1	362	682.60	68.26	1184.4	118.44	162.9	1.81
M2	362	546.08	136.52	947.52	236.88	162.9	1.81
M3	362	477.82	204.78	829.08	355.32	162.9	1.81
M4	362	580.21	102.39	1006.40	177.60	162.9	1.81
M5	362	511.95	170.65	888.30	296.10	162.9	1.81
M6	362	443.69	238.91	769.86	414.54	162.9	1.81

Table 5
Compressive, Split Tensile and Flexural strength results of M30 grade at different ages of RAC concrete mixes.

Mix	Compressive Strength (MPa)			Split Tensile Strength (MPa)			Flexural Strength (MPa)		
	7 days	14 days	28 days	7 days	14 days	28 days	7 days	14 days	28 days
Mc	23.50	30.70	37.80	2.66	3.68	4.22	3.35	4.90	6.81
M1	27.65	27.20	40.00	2.48	3.29	3.46	3.30	4.82	6.84
M2	32.93	25.17	37.00	2.50	3.32	3.67	3.42	4.85	6.80
M3	28.44	23.80	34.00	2.55	3.36	3.54	3.86	4.72	6.82
M4	26.59	22.50	32.00	2.35	3.12	3.26	3.73	4.50	6.84
M5	28.44	21.98	31.40	2.21	2.89	3.01	3.59	4.46	5.86
M6	20.56	19.88	28.70	2.48	3.29	3.42	2.85	3.76	5.63

the delayed pozzolanic activity in the FA and the poor reactive capacity as per studies made by Hasan Jalilifar et al., [31]. The impact of Rfa of substantial variations at such a replacement level of 50% on the microstructure and hardened characteristics of concrete had first been researched, through which the plastic viscosity of concrete mix in the fresh state, and the characteristics strength properties at various ages such as 7, 14 and 28 days, were determined by Ashraf M. Wagih et al. [31].

On a Compression Testing Machine (CTM), concrete cube specimens were evaluated to determine their typical strength, as per Indian Standard was attained. As stated in Table 5 and Fig. 4a, compressive strength (CS) was obtained employing concrete cubes (100*100*100 mm) and split tensile strength (STS) was determined using cylinder samples (200*100 mm) stated in Fig. 4b. After dipping in water, the characteristic compressive strength test on 100 mm size cubes is performed according to IS: 516-1959 [19]

Fig. 4a. Compressive Strength of RAC – 10%.

between age of 7, 14 and 28 days.) shown in Fig. 4d for the compression value of RAC. Effect of Splitting and dispersion of Nfa, Nca, Rfa and Rca for RAC – 10% is shown in 4(e). The FS of RAC with a schematic sketch and testing diagram has been shown in Fig. 4c and Fig. 4e, Fig 4f.

4.1. Relation between compressive, split tensile and flexural strength of RAC

The indirect tensile strengths, also termed as flexural strength (FS) as well as splitting tensile strengths, are estimated using regression models in this work by using RCC's compressive strength. The results reveal that the RCC's flexural strength is within the projected ranges for a specified compressive strength using standard concrete formulations. The relationships between different mechanical characteristics were developed using experimental results from compression and tensile testing. This image may be used to create a regression equation employing linear regression analysis.

As indicated in Fig. 5a), the Central Road Research Institute (CRRI) in Delhi performed a comprehensive investigation to determine the relationship between concrete tensile and compressive strength for the construction of concrete pavements. Fig. 5b shows the relationship between CS, STS and FS resulting the greater the compressive strength (CS), the greater the tensile strength (STS), however, the rate of tensile strength development is decreasing. Concrete's tensile strength is much more vulnerable to poor curing than its compressive strength (CS). The relationship is expressed in the form of the modulus of rupture, a more direct measurement of flexural strength that may be calculated by multiplying the compressive strength by 2.3. The compressive and tensile strength relationship is also influenced by the type of coarse aggregate used in the concrete. If all the other factors remain constant and equal, rounded aggregate concrete can have lower tensile strength than crushed aggregate concrete [5,27,29,30].Relation between Compressive, Split Tensile and Flexural Strength of RAC.

The indirect tensile strengths, also termed as flexural strength (FS) as well as splitting tensile strengths, are estimated using regression models in this work by using RCC's compressive strength. The results reveal that the RCC's flexural strength is within the projected ranges for a specified compressive strength using standard concrete formulations. The relationships between

Fig. 4b. Compressive Strength of RAC – 35%.

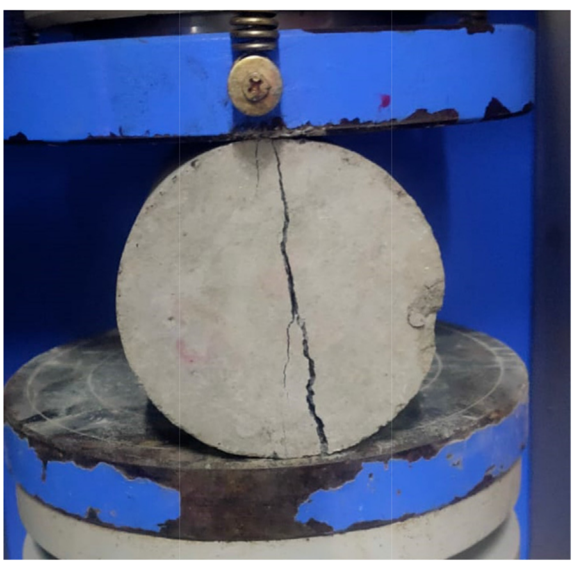

Fig. 4c. Split Tensile Strength of RAC – 10%.

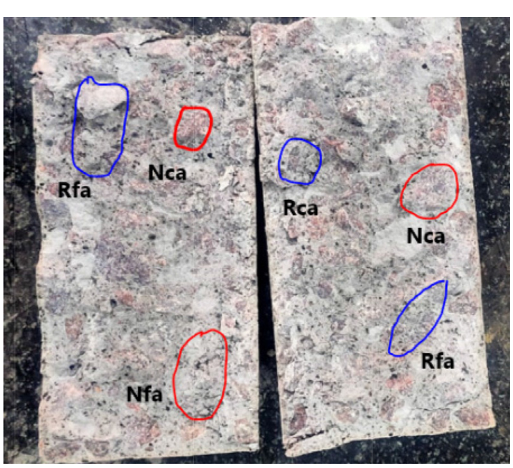

Fig. 4d. Effect of Splitting and dispersion of Nfa, Nca, Rfa and Rca for RAC – 10%.

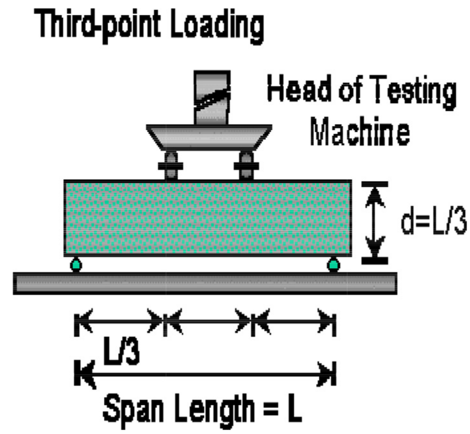

Fig. 4e. Experimental Setup for Flexural Strength (2 Point Loading).

Fig. 4f. Effect of loading for Flexural Strength with 2 Point Loading.

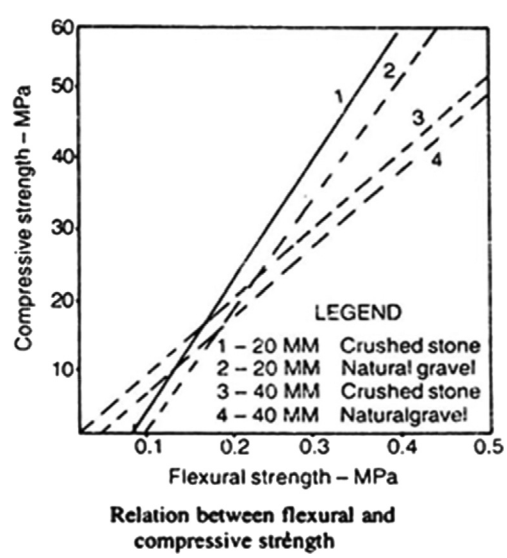

Fig. 5a. Relationship for CS and STS as per CRRI.

different mechanical characteristics were developed using experimental results from compression and tensile testing. This image may be used to create a regression equation employing linear regression analysis.

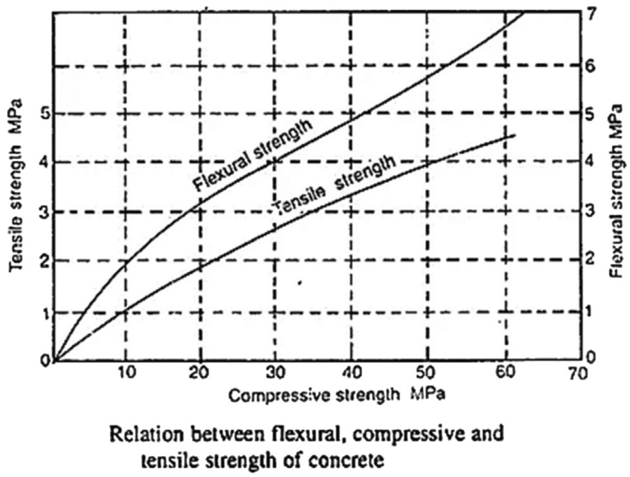

Fig. 5b. Relationship for CS, FS and STS as per IS 456: 2000.

As indicated in Fig. 5a., the Central Road Research Institute (CRRI) in Delhi performed a comprehensive investigation to determine the relationship between concrete tensile and compressive strength for the construction of concrete pavements. Fig. 5b shows the relationship between CS, STS and FS resulting the greater the compressive strength (CS), the greater the tensile strength (STS), however the rate of tensile strength development is decreasing. Concrete's tensile strength is much more vulnerable to poor curing than in its compressive strength (CS). The relationship is expressed in the form of the modulus of rupture, a more direct measurement of flexural strength that may be calculated by multiplying the compressive strength by 2.3. The compressive and tensile strength relationship is also influenced by the type of coarse aggregate used in the concrete shown in Fig. 6. If all the other factors remain constant and equal, rounded aggregate concrete can have lower tensile strength than crushed aggregate concrete [20].

4.2. Relation between CS and STS

$$\boldsymbol{F_{st}} = \boldsymbol{k} * (\boldsymbol{F_c})^{\boldsymbol{n}} \quad \text{(A)}$$

where, F_{st} – Split tensile strength, F_c – Compressive strength of concrete, the relation between them stated previously by ACI code 318-19: Building Code Requirements for Structural Concrete [32]. The empirical formula for the relation in listed below as per ACI code.

k may be assumed as 0.56, 0.634.

n may vary from 0.5 to 0.75, say n = 0.5.

$$\boldsymbol{F_{st}} = 0.634 * (\boldsymbol{F_c})^{0.5} \quad (1)$$

$$\boldsymbol{F_{st}} = 0.56 * (\boldsymbol{F_c})^{0.5} \quad (2)$$

4.3. Relation between CS and FS

$$\boldsymbol{F_{fs}} = \boldsymbol{k} * (\boldsymbol{F_c})^{\boldsymbol{n}} \quad \text{(1B)}$$

where, F_{fs} – Flexural strength, Fc – Compressive strength of concrete, the relation between them states previously by ACI CODE-318–19: Building Code Requirements for Structural Concrete[32]. The empirical1formula for the relation in listed below as per ACI code.

k may be assumed as 0.62, 0.94.

n may vary from 0.5 to 0.75, say n = 0.5.

$$\boldsymbol{F_{fs}} = 0.62 * (\boldsymbol{F_c})^{0.5} \quad (3)$$

$$\boldsymbol{F_{fs}} = 0.94 * (\boldsymbol{F_c})^{0.5} \quad (4)$$

5. Result and discussions

5.1. Compressive strength of RAC

Concrete specimens' CS can reveal information about the cementing process, the quality of the concrete matrix, and its relationship to the recycled and natural aggregates. This test is extremely important in the design of structures by making Modifications in specimen, sample size, mould form, and processing circumstances can all alter the findings. Compression strength tests are carried out on conventional concrete and recycled aggregate concrete (RAC) in Compression Testing Machine (CTM), with percentages rising by 5% every five percent from 10% to 35% and corresponding strength parameters have been arrived in Table 4.

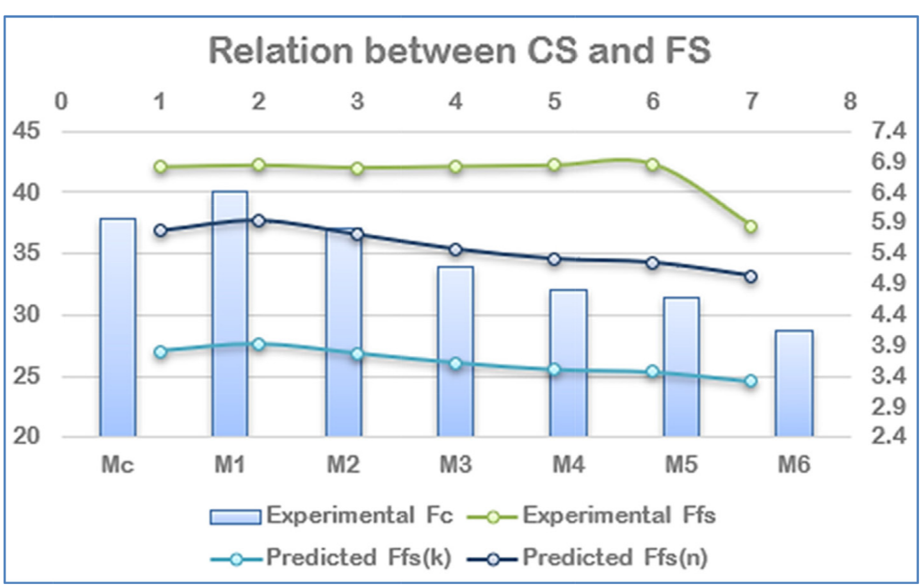

Fig. 6. Correlation between CS and STS (Experimental vs Predicted).

The findings shows that strength of the aggregate diminishes as the fraction of natural aggregate (NA) substituted by recycled coarse aggregate (RCA) rises. At 10% replacement, the compressive strength (CT) is 40 MPa. At 15% replacement, the compressive strength (CT) is 37 MPa in which the strength of the material has declined by 7.5 percent. At 20% replacement, the compressive strength is 34 MPa and the material's compressive strength has been reduced by 15%. At 25% replacements, the compressive strength is 32 MPa and it has been reduced by 20%. At 30% replacement, the compressive strength is 31.4 MPa has dropped by 21.5% as shown in Fig. 7a and values presented in Table 5.

The compressive intensity is 28.7 MPa at a 35% replacement phase has decreased by 28.25%, while comparing to the conventional concrete made with natural aggregate. The recycled aggregate specimen has a higher compressive strength than the building wastes recycled aggregate sample. The optimum percentage of recycled aggregate (Both FA and CA) replacement, on the other hand, is 10% of Recycled aggregate with 90% natural aggregate (M1) having the proportioning of Cement (C) + 90% Nfa + 90% Nca + 10% Rfa + 10% Rca + W + 1% SP.

5.2. Splitting tensile strength of RAC

Recycled Fine aggregates (RFA) comprise not only the source river sand, as well as a significant quantity of cement matrix that exists either as fine particles with a very great absorption capacity and these having the adherent mortars on the base of the river sand grains. The tests were performed using a 1000 KN compressive strength was determined in accordance with IS: 5816-1999 procedures. After 7 and 28 days, cylindrical specimens with a diameter of 150 mm and a height of 300 mm were subjected to split tensile strength testing. Table 5 shows the split tensile strength values for various percentages of partial cement replacement levels of Rfa and Rca at 7,14- and 28-days curing period.

As compared to the recycled aggregate concrete (RAC) with the mix proportion M2 (C + 80% Nfa + 80% Nca + 20% Rfa + 20% Rca + W + 1% SP) producing higher strength in the mix, whereas from M3 to M6 it was lowering the compressive strength with respect to the proportioning of Rfa and Rca displayed in Fig. 7b. Meanwhile the proportioning of the partial replacement of fine and coarse aggregate has the strength deviation as compared to conventional or traditional concrete. The following graph shows that splitting tensile strength value can be improved with the addition of superplasticizers and hence due to the impact of the reduction in strength in RAC, the splitting tensile strength can be improved by using mineral admixtures to enhance the durability of the RAC. But at the same time, RAC cannot be suggested for the highly durable structures.

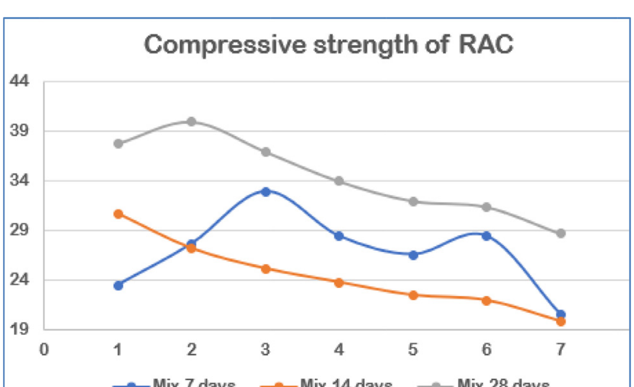

Fig. 7a. Results showing CS for M30 RAC mixes.

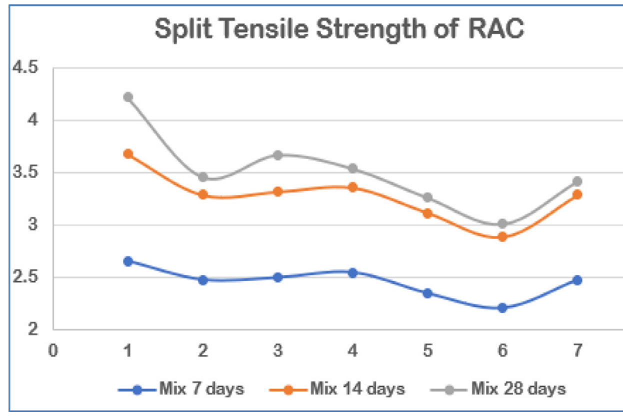

Fig. 7b. Results showing STS for M30 RAC mixes.

5.3. Flexural strength of RAC

Recycled aggregate has a minimal effect on flexural strength with several findings suggests that flexural strength reductions in RAC is restricted to 10%. Many have already stated that the flexural behaviour of RAC is remarkably comparable to that of natural aggregate concrete (NAC). The shape and size of the specimens have an impact on its strength although a large specimen with a greater number of crucial cracks has a higher chance of causing failure. Since a huge pore or a more ductile substance may prevent the propagation of a crack in concrete, the energy released at the starting of cracking may not even be adequate to sustain the propagation of the crack.

The flexural strength is shown in the given figure, and the results demonstrate that as the percent replacement of RA rises, the strength obtained decreases. With NAC, the 7 days flexural strength is 3.42 N/mm^2 and 3.26 N/mm^2 for water cement ratio as 0.40 were showing FS for M30 RAC mixes in Fig. 7c.

5.4. Relationship between compressive, splitting tensile and flexural strength of concrete

According to the experimental results, the ratio of split tensile to compressive strengths for NAC and RAC tends to decrease when compressive strength (CS) increases, and the theoretical study revealed that a similar theoretical equation could have been used for both concrete types since these results are completely indistinguishable. The intensity of concrete strength has an impact on the ratio of split tensile strength to compressive strength in both the concrete forms. With increased compressive strength (CS), the ratio decreases as per studies made by Mutiu A.Akinpelu [33].

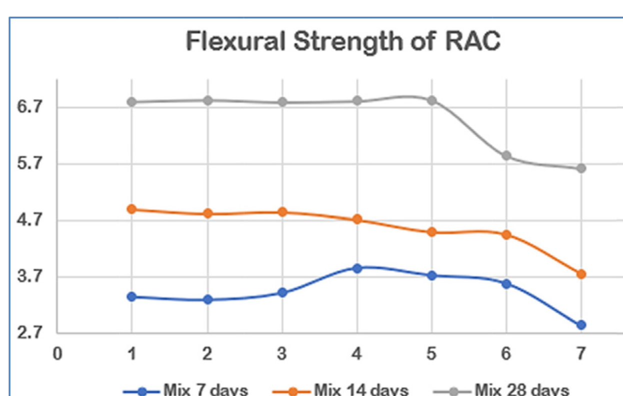

Fig. 7c. Results showing FS for M30 RAC mixes.

Due to the increased absorption and porosity, the use of recycled aggregate resulted in a loss in all mechanical behaviour, as well as influencing the fresh state characteristics and concrete durability parameters.

6. Conclusions

M30 grade concrete have been made for this study with cubes, cylinders and prisms were casted with various mixtures, including all the blended mixes from Mc, M1 to M6 of M30 concrete. Concrete's physical and mechanical properties that contribute to its strength and durability. In general, the condition of recycled aggregate is determined by the loading and exposure conditions of the structures that have been demolished. The following observations are found after the results were received.

- Based on the mechanical properties and workability studies made with Rfa and Rca, the optimum percentage of RAC is 30%. While compared to conventional concrete, the workability of RAC dropped marginally. It is hard to separate foreign particles on an aggregate surface if the fine aggregate is smaller than 5 mm. As a result, the application of existing technologies to improve density and absorption rate has a limit, so that it is too difficult to separate from the concrete structure which needs technology for separation of both FA and CA from the original.
- The compressive (characteristic) strength of RAC mixes with Rfa and Rca with that require the inclusion of a superplasticizer to make this concrete workable, which is comparatively effective when compared to the other mixes that of RAC blended without Recycled FA and CA at 7, 14 and 28 days of curing as shown in Table 4. This demonstrates that using Rfa and Rca will not support the concrete strength alone, so sometimes addition of the supplementary cementitious material (SCM) causes a compressive strength increase.
- The RAC blends having a higher compressive strength as M1 (C + 90% Nfa + 90% Nca + 10% Rfa + 10% Rca + W + 1% SP) of the 28 days curing with compressive strength as 40 MPa as specified in Table 4 and Fig. 7a, which shows that using recycled fine and coarse aggregate (Rfa and Rca) as a partial substitute for natural fine and coarse aggregate (Nfa and Nca) results in greater strength in M1 and it was slowly decreasing from M2 to M7. Between 7 and 28 days, the compressive strength of concrete blends with increased proportion from 15% to 35% of Rfa and Rca indicating the strength may affect using higher use of recycled aggregate impacting the durability of the structure.
- The split tensile strength of the RAC is declining from 20% replacement onwards and more for the conventional concrete 3.68 N/mm^2 and for recycled aggregate concrete 2.89 N/mm^2. At 28 days, Mix M1 had the highest split tensile strength, while Mix M6 had the lowest split tensile strength, indicating that strength may be reduced due to the addition of Rfa and Rca, which affect the strength reduction that might be related to aggregate distribution and particle size.
- The Flexural strength of the RAC is decreasing from 15% replacement and more for conventional concrete 6.81 N/mm^2 and for recycled aggregate concrete 5.86 N/mm^2, while testing the prism specimens. This can be due to the increased mechanical interlocking as just a result of a stronger bond among both recycled fine and coarse aggregate (Rfa and Rca) with hydrated cement paste.
- When samples were acquired and analyzed, the recycled aggregate's physical and mechanical properties showed relatively acceptable range in characteristics strength. Limitations in grading of Rfa and Rca requirements, such as high absorption and aggregate strength, could have been overcome during the proportioning phase, as well as by attaining high packing density. Compressive, split tensile and flexural strength were all comparable in concrete made with various combinations of coarse and fine aggregate without any changes in particle size distribution.
- Adding SCMs to recycled aggregate concrete (RAC) can enhance compressive strength by 16% when compared to a controlled concrete mix and distributing SCM's within a water-superplasticizer solution can maximize compressive strength by 12%. Hence the further studies can made by incorporating with SCM addition with respect to the improvising the strength and durability parameters. Recycled concrete can be made with recycled coarse and fine aggregates (Rca and Rfa) with particle size distribution and grading, also testing for the reliability of FA and CA by standard testing methods.
- The key element in the long-term use and implementation of recycled aggregate concrete (RAC) in the construction sector is the quality and affordability of recycled aggregate (RA). In the current study, recycled aggregate came from a recycling plant that was built with the objective of decreasing construction and demolition waste produced by the building industry and providing an efficient alternative for the reuse of RA. RAC can be utilized as a building material to save resources by reducing cost of construction. In comparison to natural aggregate (NA), RAC has intrinsic drawbacks such as poorer compressive strength, durability, water absorption, and a lower aggregate-cement interfacial transition zone.

Declaration of Competing Interest

The authors declare that they have no known competing financial interests or personal relationships that could have appeared to influence the work reported in this paper.

References

[1] N.D. Oikonomou, Recycled concrete aggregates, Cem. Concr. Compos. 27 (2) (2005) 315–318, https://doi.org/10.1016/j.cemconcomp.2004.02.020.
[2] K. McNeil, T.-K. Kang, Recycled Concrete Aggregates: A Review, Int. J. Concr. Struct. Mater. 7 (1) (2013) 61–69, https://doi.org/10.1007/s40069-013-0032-5.
[3] G. Fathifazl, A. Abbas, A.G. Razaqpur, O.B. Isgor, B. Fournier, S. Foo, New Mixture Proportioning Method for Concrete Made with Coarse Recycled Concrete Aggregate, J. Mater. Civ. Eng. 21 (10) (2009) 601–611, https://doi.org/10.1061/(ASCE)0899-1561(2009)21:10(601).
[4] A.T.W. Yu, C.S. Poon, A. Wong, R. Yip, L. Jaillon, Impact of Construction Waste Disposal Charging Scheme on work practices at construction sites in Hong Kong, Waste Manag. 33 (1) (2013) 138–146, https://doi.org/10.1016/j.wasman.2012.09.023.
[5] S. Yehia, K. Helal, A. Abusharkh, A. Zaher, H. Istaitiyeh, Strength and Durability Evaluation of Recycled Aggregate Concrete, Int. J. Concr. Struct. Mater. 9 (2) (2015) 219–239, https://doi.org/10.1007/s40069-015-0100-0.
[6] S. Marinković, V. Carević, Comparative studies of the life cycle analysis between conventional and recycled aggregate concrete, in: New Trends Eco-Efficient Recycl. Concr.,, Elsevier, 2019, pp. 257–291, https://doi.org/10.1016/B978-0-08-102480-5.00010-5.
[7] G. Fathifazl, A. Ghani Razaqpur, O. Burkan Isgor, A. Abbas, B. Fournier, S. Foo, Creep and drying shrinkage characteristics of concrete produced with coarse recycled concrete aggregate, Cem. Concr. Compos. 33 (10) (2011) 1026–1037, https://doi.org/10.1016/j.cemconcomp.2011.08.004.
[8] N.A. Brake, S. Oruji, L. Haselbach, Increasing Compressive Strength of Recycled Aggregate Concrete Using High Fineness Bottom Ash Blended Cement, in: Int. Conf. Transp. Dev. 2018, American Society of Civil Engineers, Reston, VA, 2018, pp. 401–410, https://doi.org/10.1061/9780784481554.041.
[9] B.A. Tayeh, D.M.A. Saffar, R. Alyousef, The Utilization of Recycled Aggregate in High Performance Concrete: A Review, J. Mater. Res. Technol. 9 (4) (2020) 8469–8481, https://doi.org/10.1016/j.jmrt.2020.05.126.
[10] K.Y. Ann, H.Y. Moon, Y.B. Kim, J. Ryou, Durability of recycled aggregate concrete using pozzolanic materials, Waste Manag. 28 (6) (2008) 993–999, https://doi.org/10.1016/j.wasman.2007.03.003.
[11] F. Pacheco-Torgal, Y. Ding, S. Miraldo, Z. Abdollahnejad, J.A. Labrincha, The suitability of concrete using recycled aggregates (RAs) for high-performance

concrete (HPC), in: Handb. Recycl. Concr. Demolition Waste, Elsevier, 2013, pp. 424–438, https://doi.org/10.1533/9780857096906.3.424.
[12] M. Safiuddin, U.J. Alengaram, M.M. Rahman, M.A. Salam, M.Z. Jumaat, Use of recycled concrete aggregate in Concrete: A review, J. Civ. Eng. Manag. 19 (2013) 796–810, https://doi.org/10.3846/13923730.2013.799093.
[13] N.N. Gerges, C.A. Issa, S.A. Fawaz, J. Jabbour, J. Jreige, A. Yacoub, Recycled Glass Concrete: Coarse and Fine Aggregates, Eur. J. Eng. Technol. Res. 3 (2018) 1–9, https://doi.org/10.24018/ejeng.2018.3.1.533.
[14] V. Sata, P. Chindaprasirt, Use of construction and demolition waste (CDW) for alkali-activated or geopolymer concrete, in: Adv. Constr. Demolition Waste Recycl., Elsevier, 2020, pp. 385–403, https://doi.org/10.1016/B978-0-12-819055-5.00019-X.
[15] Z. Guo, X. Kong, J. Zhang, Y. Sun, A. Tu, T. Jiang, Life-cycle assessment of concrete building blocks incorporating recycled concrete aggregates—A case study in China, in: Adv. Constr. Demolition Waste Recycl., Elsevier, 2020, pp. 515–535, https://doi.org/10.1016/B978-0-12-819055-5.00025-5.
[16] IS:2386-1963, Methods of Test for Aggregates for Concrete, Bur. Indian Stand. (1963) 1–14.
[17] R.A. Robayo-Salazar, W. Valencia-Saavedra, R.M. de Gutiérrez, Construction and demolition waste (Cdw) recycling—as both binder and aggregates—in alkali-activated materials: A novel re-use concept, Sustain. 12 (2020) 1–18, https://doi.org/10.3390/su12145775.
[18] J. Lavado, J.A. Bogas, J. de Brito, A. Hawreen, Fresh properties of recycled aggregate concrete, Constr. Build. Mater. 233 (2020) 117322.
[19] IS 516, Method of Tests for Strength of Concrete, Bur. Indian Stand. (1959) 1–30.
[20] C.V. Kumar, MD.A. Parvez, T. Srinivas, S. Tummala, S. Kosaraju, P. Bobba, S. Singh, Strength Behaviour of Blended Self Cured Concrete made with Cement by partial replacement of Supplementary Cementitious Materials (SCM's), E3S Web Conf. 184 (2020) 01100, https://doi.org/10.1051/e3sconf/202018401100.
[21] C.V. Kumar, P. Manisha, P. Sadula, S. Tummala, S. Kosaraju, P. Bobba, S. Singh, Behavior of Monotonic Loading for Glass Fibre based High Performance Concrete in External Beam-Column Joint using ANSYS, Analysis, E3S Web Conf. 184 (2020) 01088, https://doi.org/10.1051/e3sconf/202018401088.
[22] Is 4031–3,, (Reaffirmed 2005), Methods of Physical Tests for Hydraulic Cement, Part 3: Determination of Soundness [CED 2: Civil Engineering], Bur. Indian Stand. New Delhi. 2005 (1988) 1–10.
[23] IS 12269, IS (Indian Standard). 2013. Ordinary Portland Cement, 53 Grade — Specification. IS 12269-13, Bur. Indian Stand. 6 (1992) 141-142+144.
[24] Is,, 456, Plain Concrete and Reinforced, Bur, Indian Stand. Dehli. (2000) 1–114.
[25] IS:10262 - 2009, Guidelines for concrete mix design proportioning, Bur. Indian Stand. New Delhi. (2009) 1–14.
[26] B. Li, S. Hou, Z. Duan, L. Li, W. Guo, Rheological behavior and compressive strength of concrete made with recycled fine aggregate of different size range, Constr. Build. Mater. 268 (2021) 121172, https://doi.org/10.1016/j.conbuildmat.2020.121172.
[27] F.A.N. Silva, J.M.P.Q. Delgado, A.C. Azevedo, A.G.B. Lima, C.S. Vieira, Preliminary Analysis of the Use of Construction Waste to Replace Conventional Aggregates in Concrete, Buildings. 11 (2021) 81, https://doi.org/10.3390/buildings11030081.
[28] L. Evangelista, M. Guedes, J. de Brito, A.C. Ferro, M.F. Pereira, Physical, chemical and mineralogical properties of fine recycled aggregates made from concrete waste, Constr. Build. Mater. 86 (2015) 178–188, https://doi.org/10.1016/j.conbuildmat.2015.03.112.
[29] S. Ismail, M.A.A. Hamid, Z. Yaacob, Influence of fine recycled concrete aggregates on the mechanical properties of high-strength mortars, in (2018:), https://doi.org/10.1063/1.5055461 020059.
[30] A.M. Wagih, H.Z. El-Karmoty, M. Ebid, S.H. Okba, Recycled construction and demolition concrete waste as aggregate for structural concrete, HBRC J. 9 (3) (2013) 193–200, https://doi.org/10.1016/j.hbrcj.2013.08.007.
[31] H. Jalilifar, F. Sajedi, Micro-structural analysis of recycled concretes made with recycled coarse concrete aggregates, Constr. Build. Mater. 267 (2021) 121041, https://doi.org/10.1016/j.conbuildmat.2020.121041.
[32] 318-99/318R-99: Building Code Requirements for Structural Concrete & Commentary, Tech. Doc. (n.d.).
[33] M.A. Akinpelu, S.O. Odeyemi, O.S. Olafusi, F.Z. Muhammed, Evaluation of splitting tensile and compressive strength relationship of self-compacting concrete, J. King Saud Univ. - Eng. Sci. 31 (1) (2019) 19–25, https://doi.org/10.1016/j.jksues.2017.01.002.

PAPER • OPEN ACCESS

Comparative Analysis & Design of RCC & Steel Preheater Tower Structure by Using STAAD. Pro

To cite this article: B. Vamsi Krishna *et al* 2023 *IOP Conf. Ser.: Earth Environ. Sci.* **1130** 012025

IOP Conf. Series: Earth and Environmental Science 1130 (2023) 012025 doi:10.1088/1755-1315/1130/1/012025

Comparative Analysis & Design of RCC & Steel Preheater Tower Structure by Using STAAD. Pro

B. Vamsi Krishna[1], P. Sudheer Kumar[2], Kurma Chandana[3], Shyamala Bhoomesh[4], P. Venu Gopal[5]

[1]Department of Civil Engineering, Malla Reddy Engineering College, Secunderabad-500100, India

[2]Department of Civil Engineering, Balaji Institute of Technology and Science (Autonomous), Warangal-506330, India

[3]Department of Civil Engineering, Balaji Institute of Technology and Science (Autonomous), Warangal-506330, India

[4]Department of Civil Engineering, Malla Reddy Engineering College, Secunderabad-500100, India

[5]PG-Research Scholar, Structural Engineering, Malla Reddy Engineering College, Secunderabad-500100, India

Abstract: A liquid material after water concrete is the most consuming material in the world, concrete is the most important construction material used extensively to construct buildings, dams, roads, etc. As we know that concrete is a composite material with cement, coarse & fine aggregates bonding together with water that gives hardness with time. As per the 2018 year statistics, India is the second largest producer of cement in the world with 460 million tonnes per year which is over 8% of the global installed capacity. Cement is the most important material in concrete, In India, at present, there are 120 major cement plants and nearly 300 mini cement plants are manufacturing the cement. In Cement plants 'Preheater tower' is used, these preheater tower consists of several cyclones, these raw materials are fed at the top of the preheater tower through cyclones it travels to the bottom of the preheater tower, each cyclone in the preheater serves as a heat exchanger and a separate. In this project, a comparative analysis & design will be done between both the RCC structure & Steel structure Preheater tower as per Indian design standards by using Staad Pro software. In this design process, the loads which are affecting the structure will be taken and designed. And also the pros & cons will be discussed between the RCC & Steel structure Preheater tower. Here the height of the RCC and steel Preheater tower taking as 110 meters. It is observed that Maximum displacements at a height of 110 mts in RCC preheater tower are 130.59 mm and Steel preheater tower is 102.238 mm. The Maximum Moment at critical load combination is more in RCC preheater tower (i.e 205.6 kN.m) than Steel preheater tower (i.e 190.1 kN.m).The Maximum shear at critical load combination is more in Steel preheater tower 62.0 kN is more than RCC preheater tower 28.7 kN.
Keywords: Preheater, Cement Tower, STAAD.Pro, RCC, Steel Structure

1. Introduction

Preheaters are utilized in modern dry oven concrete creation plants to warm the crude blend and drive off carbon dioxide and water before it is taken care of into the furnace. Preheater Building is one of the most indispensable pieces of a concrete plant where the crude dinner is preheated utilizing outlet hot gases of the oven. A 5-stage single-string in-line calciner framework is utilized for this reason. Each phase of the Preheater comprises of manufactured tornadoes and associating gas riser pipes. A logical model of a summed up four-stage suspension tornado preheater framework is introduced. This model was utilized to concentrate because of waste preheater gas and residue sidestep frameworks on preheater execution and productivity. As the detour size (rate) was fluctuated, the intensity content of the detour gas was determined for various steady calcination degrees. These outcomes show that the calcination degree is contrarily relative to the intensity content of waste preheater sidestep gases. While expanding of sidestep opening at steady how much residue oven gas will cause a reduction in the waste intensity content of furnace gases [1].

Cyclone preheater, otherwise called suspension preheater, is the principal concrete technology normally utilized in the new dry cycle concrete creation line. It is the fundamental gas-strong response unit of the concrete crude feast pre-deterioration framework, which takes full advantage of the great temperature fumes gas released from the oven tail and the high-temperature vent gas produced by the burning at the lower part of the decay heater to warm unrefined components in a suspended manner. It replaces the material preheating cycle and halfway calcium carbonate disintegration process in the oven, making the unrefined substance powder completely in touch with the hot air displayed in Figure 1. The quick intensity move speed and high effectiveness of the twister preheater are gainful to work on the warm productivity and clinker result of the calcining framework. In the meantime, it has less moving parts, less helper gear, straightforward support, little space occupation, and its presence abbreviates the length of the concrete rotating oven, the speculation cost is by and large low [2].

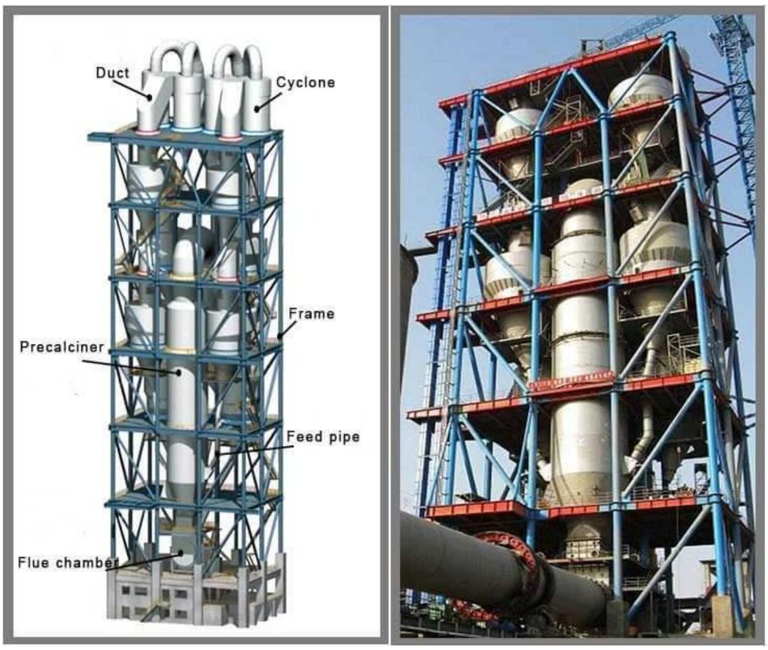

Figure 1: Preheater Tower in Cement Plant

Preheating framework is outfitted with a programmed control framework that can send important information to the PLC control stage. Furthermore, it can likewise understand a solitary guide control toward make the creation interaction more helpful. The preprocessing segment is viewed as the core of the concrete business on the grounds that the real arrangement of concrete clinker happens in the pivotal part (oven) of the handling area. It comprises of the accompanying activities: preheating the unrefined substances; pre calcination, consuming inside the oven; and clinker cooling. The concrete plant and any remaining gear sizes are resolved in view of the handling segment. Run of the mill of concrete plants, the handling unit is nuclear power serious and represents around (90%) of the nuclear power utilized in the concrete creation process displayed in figure 2. With late mechanical advances, most of the fuel is consumed in the calciner to such an extent that the natural substance is completely calcined when it arrives at the rotating oven gulf. This has brought about much lower energy utilization per ton of clinker created [3,4].

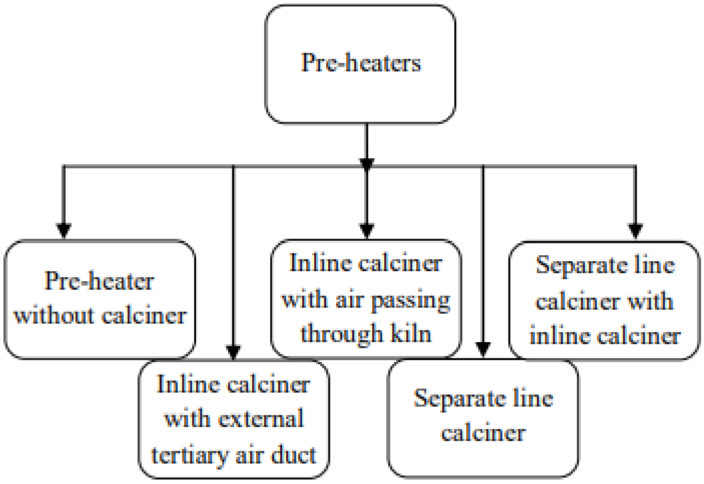

Figure 2: Pre-heaters classification with different pre calciners designs

2. Literature Review

In dry cycle furnaces in ongoing works, the mixed unrefined substance passes the pre-radiator pinnacle to enter the oven. The crude dinner becomes hot before it goes into the furnace in view of utilizing of hot gases from the oven and potentially the cooled clinker at the exit of the cooler to warm the crude feast. The crude dinner is taken care of to the pre-warmer at the highest point of the pinnacle and passes in it by means of the series of twisters. Furnace hot gas and, regularly, the hot air from the cooling framework are blown by means of the series of tornadoes effectively; the crude feast gets the intensity from the hot gases.

Mujumdar et al. [5] grown at first separate models for the preprocessing units (preheater, calciner, revolving furnace, and cooler) and afterward coupled these models together to construct a coordinated test system in the concrete business. The cutting edge clinker creation frameworks involve a rotating furnace, a suspension preheater, and a calcinator. One arrangement that works on the warm productivity of the consuming system is the advancement of the typhoon heat exchanger (suspension preheater). Its proficiency of residue detachment and use of intensity significantly relies upon the applied typhoons and the quantity of their stages, and it likewise influences the warm effectiveness of the furnace. Renovation of existing intensity exchangers involves tremendous monetary misfortune because of the need to stop the activity of the furnace for long free time and high venture costs. Thusly elective and easier arrangements are looked to empower the activity of the intensity exchanger with the base margin times of the oven. **Kozołub et al. [6].**

Pre-heater furnaces arrangement of four-stage typhoon separators is applied to the extraction of huge particles for control defilement of air as well with respect to smooth course of innovative cycles. Application to unforgiving circumstances incorporates such cycles as partition of coal dust downstream coal crushes at power plants or lack of hydration of materials at drying frameworks. They can be likewise utilized as gas reactors or intensity exchangers.

McGlinchey et al. [7] showed the connection of both, the noticed temperature and examples of calcination to the cycles of intensity move which control the oven execution and give techniques for practical estimation to furnace plan. Hypothetical Examination There are many variables influencing heat balance in pre-radiator, for example, sidestep opening, calcination degree in pyroclon framework, the dampness content in crude feast, and measure of overabundance air which restricts the quantity of gases created in this framework. The mass equilibrium of each stage (crude feast and gases) is impacted by the responses occurring in every tornado. In every twister, how much crude feast doesn't approach how much crude dinner outlet, and the contrast between the two amounts results to be the distinction in gas sum between the two positions (gulf and outlet). The mass and intensity adjusts are depicted numerically by framework conditions relying on many elements.

3. Objective and scope of Current Study

The main objective of the project is

The methodology carried out to create the model, calculation of the loads, analysis and design procedures, all the load calculations and the load's aspects are taken by the Indian standard code procedures for industrial structures, each segment of modeling, loading, and, analysis is represented step by step In the rest of this chapter the following are the different aspects of methodology which are been covered

The structural model details of preheater towers for both the RCC and Steel model are listed, which include the cross-sectional data of beams, columns, slab thickness plan, and elevation data of the model shear wall placement for the RCC model and Steel bracing placement for the Steel structure, the different materials used for this modeling and the step by step development of the model using the Staad pro software is represented.

4. Methodology

Discussing the different methodology carried out to create the model, calculation of the loads, analysis and design procedures, all the load calculations and the load's aspects are taken following the Indian standard code procedures for industrial structures, each segment of modeling, loading and, analysis is represented step by step in the rest of this chapter the following are the different aspects of methodology which are been covered show in flowchart figure 3:

- Model development
- Loadings
- Load combinations
- Analysis Procedure
- Design procedure

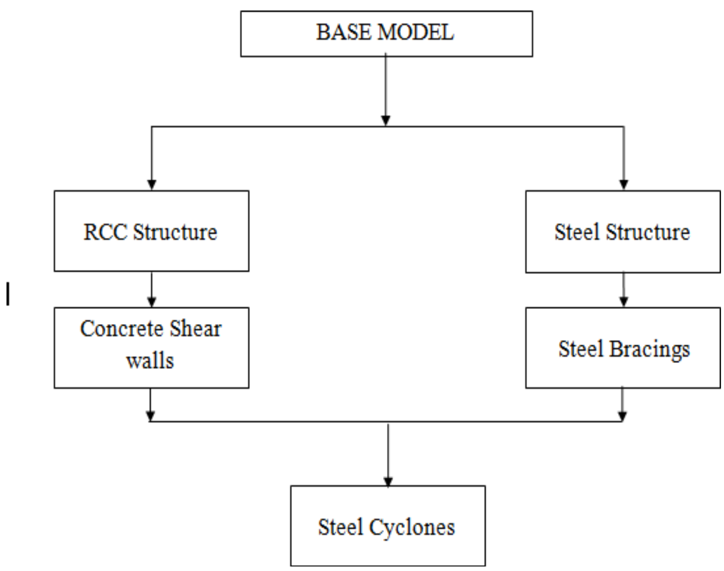

Figure 3: Model development

4.1 Loadings

Both the structures are loaded with the same type of loads and load intensities except for the dead loads of the structure as they are taken based on the materials which are used in the structural elements the following are the different loads that are applied to the structure

1. Dead Load
2. Live Load
3. Equipment Load
4. Temperature Load
5. Wind Load

4.2 Equipment load

The equipment load is considered from the dead load of the cyclones as they are directly connected to the slab elements there is no need to impose the equipment load again on the structure, the dead load of the cyclone itself is considered as the equipment load on the structure.

4.3 Temperature load

A difference of 1000°C is considered for the temperature load; this load is assigned as the change in temperature for the plates of cyclones

4.4 Load combinations

For the design of concrete sections and steel sections, the load combinations are required as they provide the maximum load carrying a capacity load that the structure should withstand when it is designed for the maximum capacity load combination results are taken from the load combinations and to those loads the concrete design is done, all these loads are taken following the IS 875, and IS 456 the following are the load combinations which are taken for both the RCC and Steel model are shown in Table 1 and the structural model load was represented in figure 4

Table 1: Load Combinations

Load Combination	Factor and loads
Combo1	1.50(DL+LL)
Combo2	1.20(DL+LL+WL)
Combo3	1.20(DL+LL-WL)
Combo4	1.2(DL+LL)
Combo5	1.5(DL+LL+WL)
Combo6	1.5(DL+LL-WL)
Combo7	0.9(DL+LL)

The above table represents all the load combinations that are used for the structure

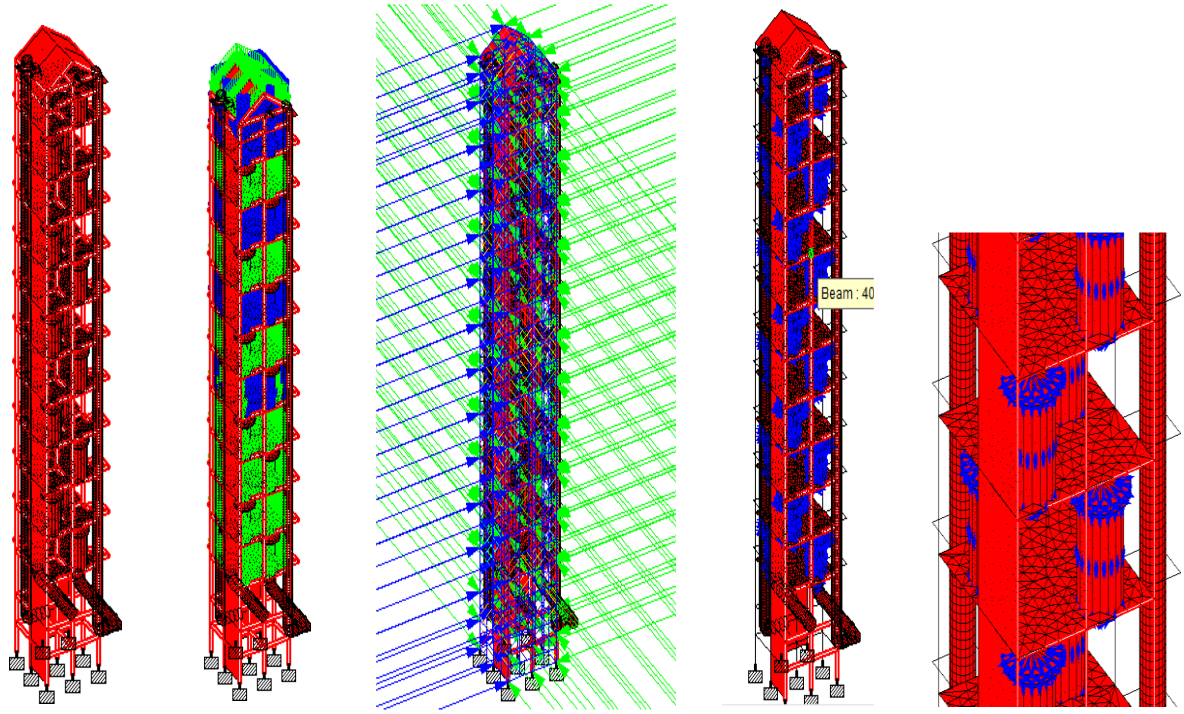

Figure .4 a.) Self-weight of structure (dead load) b.) Floor loads (live loads) c.) Wind load d.) Temperature loads complete structure view e.) Temperature loads cyclones

4.5 Analysis Procedure

For the analysis of the model in this study equivalent, lateral load method confining to the IS 1893-2016 was employed using the Staad Pro software to generate all the different results of bending moments, shear forces, displacements, and resultants. The detailed step-by-step procedure for the analysis is described in the Analysis and Design chapter.

5. Modeling

The structural model details of preheater towers for both the RCC and Steel model are listed, which include the cross-sectional data of beams, columns, slab thickness plan, and elevation data of the model shear wall placement for the RCC model and Steel bracing placement for the Steel structure, the different materials used for this modeling and the step by step development of the model using the Staad pro software is represented.

Table 2: RCC model element Specification

Element	Location	Material	Grade	Dimensions/ Thickness (mm)	Diameter mm
Primary beams	All the main beams in the structure	Concrete	M40	550x600	-
Secondary beams	Support beams for the side tubes	Concrete	M40	230x300	-
Columns	All the main columns	Concrete	M40	1200x1200	-
Slab plates	All the floor slabs and roof slab	Concrete	M40	200	-
Shear wall plate	In both the direction	Concrete	M40	500	-
Cyclone plates	Bottom hopper, cylinder, top cap	Steel	Fu500	125	3600
Duct plates	All the cyclone connecting tubes, inlets, and outlets	Steel	Fu500	100	2000

Table 3: Steel model element Specification

Element	Location	Material	Grade	Specifications/ Thickness (mm)	Diameter mm
Primary beams	All the main beams in the structure	Steel	M40	I125016B55040	-
Secondary beams	Support beams for the side tubes	Steel	M40	ISA200X200X25	-
Columns	All the main columns	Steel	M40	I160016C55040	-
Bracing	Along the outer edge of each floor	Steel	M40	ISMC400	-
Slab plates	All the floor slabs and roof slab	Steel	M40	200	-
Cyclone plates	Bottom hopper, cylinder, top cap	Steel	Fu400	125	3600
Duct plates	All the cyclone connecting tubes, inlets, and outlets	Steel	Fu400	100	2000

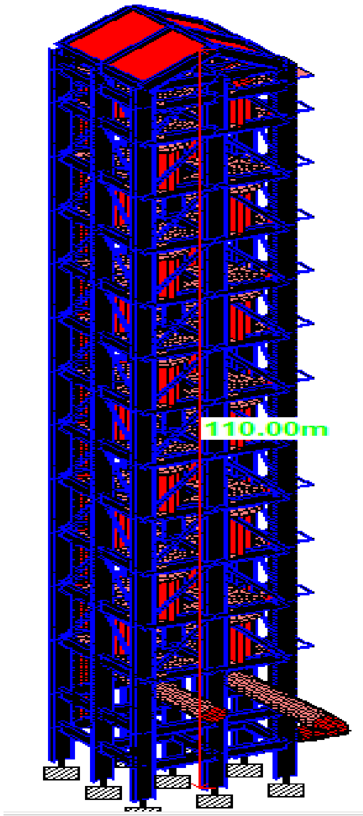

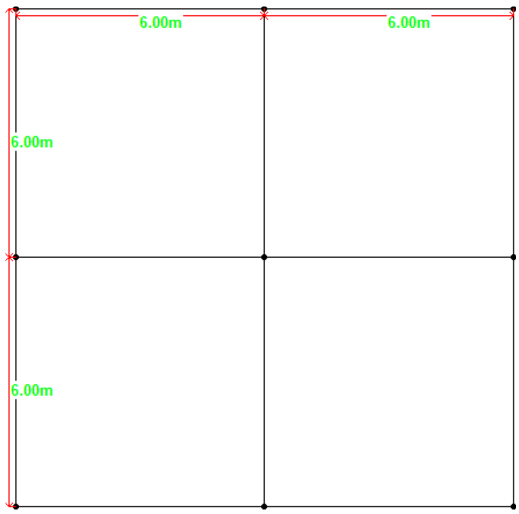

Figure 5: a.) 3D view representing the height of the tower b.) Plan view

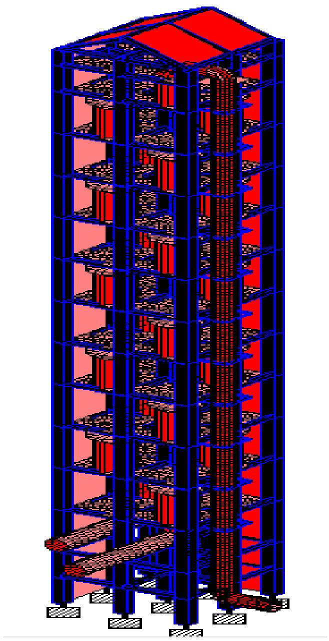

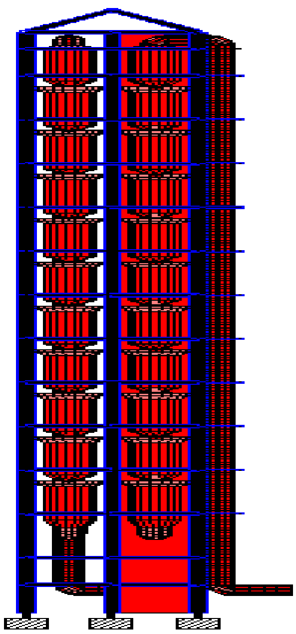

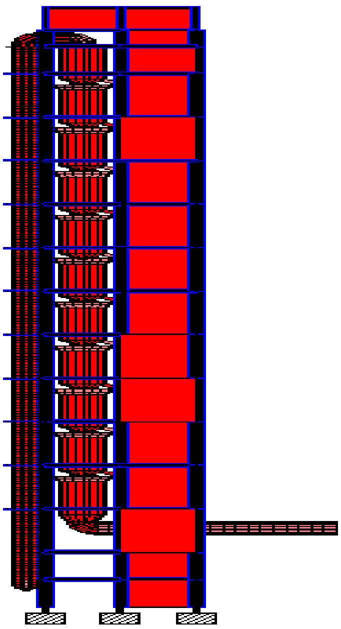

Figure 6: a.) RCC model 3D view b.) RCC model Front view c.) RCC model side view

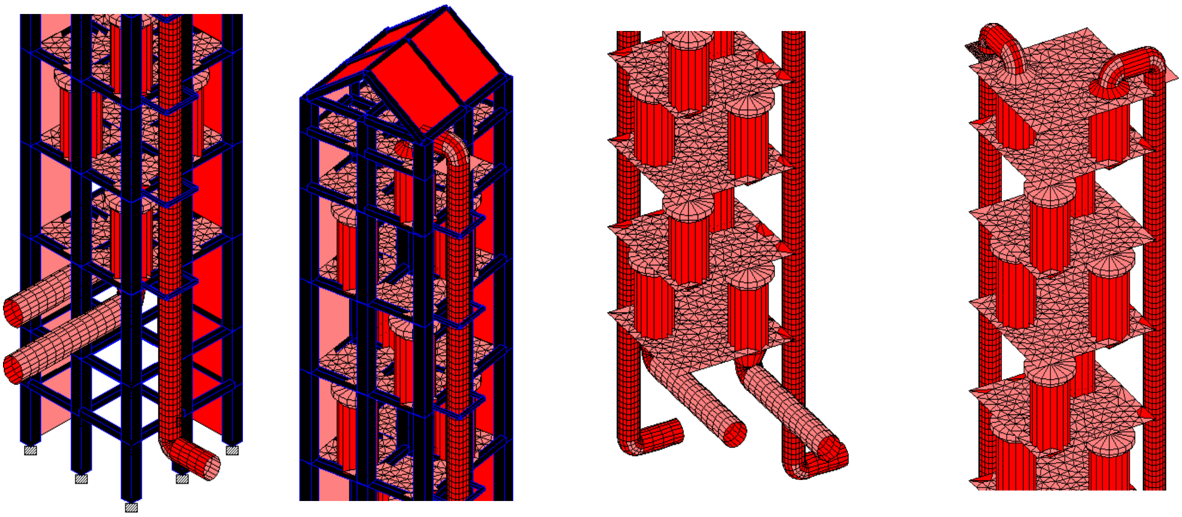

Figure 7: a.) RCC model bottomRCC model top b.) Cyclones view bottom c.) Cyclones View Top

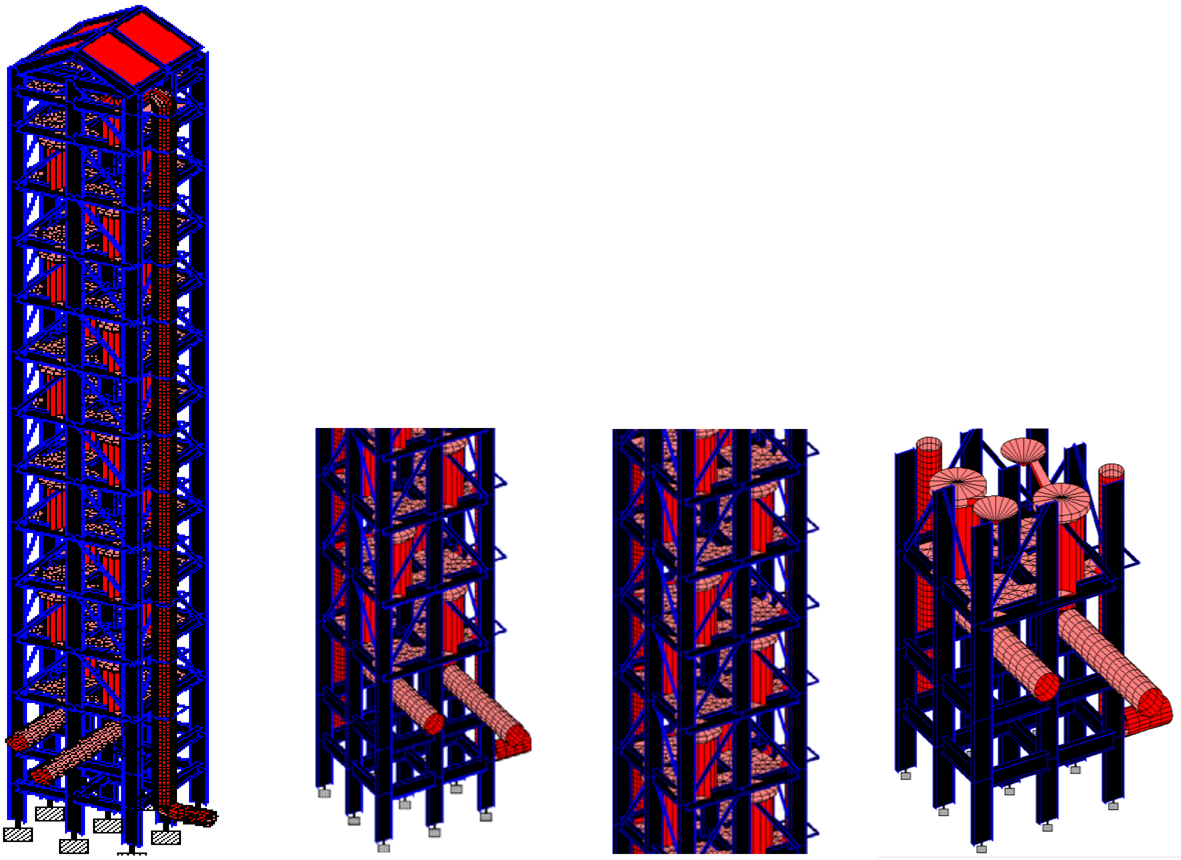

Figure 8: a.) Steel model 3D view, b.) Steel model bottom view, c.) Steel model mid section view, d.) Steel model Cyclones bottom view

6. Results and Discussions

The results of both the RCC and steel models obtained from the lateral load analysis for the given load conditions include the displacements of the structure at different heights, moments, and shear generated on each floor along the height of the structure temperature stresses in cyclones and concrete design of beams and columns

6.1 Displacements

The following table 4 are the maximum displacements that are obtained from both RCC and steel models at different heights for a critical load combination

Table 4: Displacements

Height (m)	Maximum displacements	
	RCC structure (mm)	Steel structure (mm)
110	130.591	102.238
108	126.974	98.504
98	118.890	88.027
90	108.87	81.179
82	98.762	86.07
74	88.57	78.44
66	78.22	71.49
58	67.76	50.690
50	57.09	57.72
42	46.33	36.673
34	35.45	44.95
26	24.75	38.810
18	14.64	33.104
10	5.959	8.302

The following figure .9 plots the differences between displacements at different heights in both the models

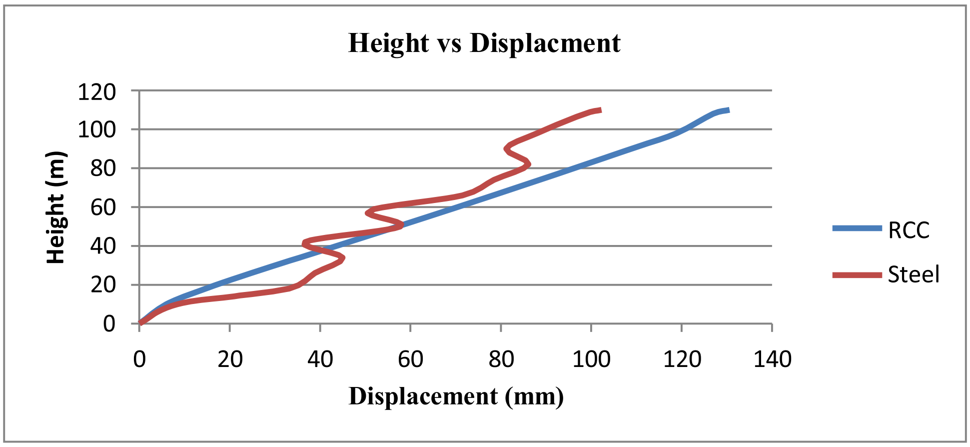

Figure 9: Displacements plot

6.2 Moments

The following are the maximum moments generated in the central column for critical load combinations shown in table 5

Table 5: Maximum Moments critical load combination

level	Maximum Moments	
	RCC structure (kN.m)	**Steel structure (kN.m)**
L2	205.650	190.104
L3	222.364	36.107
L4	212.281	34.02
L5	189.98	36.630
L6	162.356	28.95
L7	133.58	22.86
L8	163.475	18.58
L9	72.280	13.636
L10	37.130	7.96
L11	4.515	6.478
L12	5.3957	9.389

Note: level 2 starts from the floor where cyclones start

6.3 Shear forces

The following are the maximum shear forces generated in the central column for critical load combinations are shown in table 6

Table 6: Maximum Shear forces critical load combination

level	Maximum shear forces	
	RCC structure (kN)	**Steel structure (kN)**
L2	28.70	62.0
L3	21.86	41.66
L4	9.918	38.94
L5	5.981	36.86
L6	7.121	32.53
L7	11.863	23.16
L8	26.05	22.05
L9	32.512	15.15
L10	45.815	6.14
L11	64.872	5.831
L12	6.776	15.304

Note: level 2 starts from the floor where cyclones start

6.4 Temperature stresses

Due to the temperature loads given to the cyclones, this cyclone will undergo a larger amount of temperature stresses in this analysis the maximum temperature stress observed in the cyclones are Temperature stress = 2544 N/mm^2 shown in figure 10.

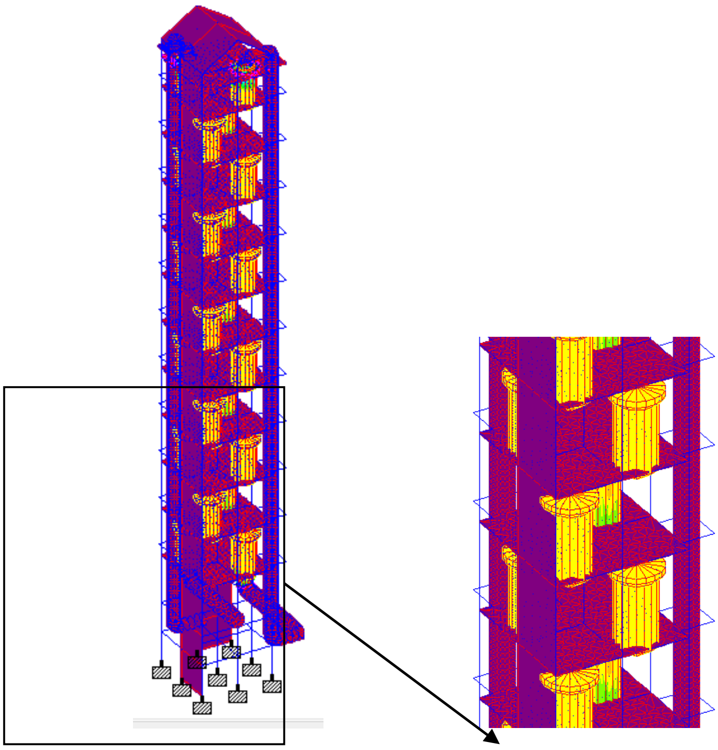

A. B.

Figure 10: a.) Temperature stresses b.) Section view

6.5 Concrete Design

After analyzing the structure for different load cases and load combinations the critical load combination is taken by default and the concrete design is being done to that load combination the following are the outputs from the concrete design for critical elements which has the highest moment and shear forces shown in table 7

Table 7: Concrete design outputs

Element	Dimensions (mm)	Concrete grade	Rebar grade	Area of steel required (mm2)	Reinforcement provided
Primary beam	550 x 600	M40	Fe550	1420	#28@18Ø

Secondary beam	230 x 300	M40	Fe550	120	#6@10Ø
Column	1200 x 1200	M40	Fe550	2939	#40@20Ø

7. Conclusions:

The following conclusions have been drawn from the comparative assessment of the RCC & Steel PreheaterTower structure: -

- Increasing of bypass opening value plays a major role in the calcination process because its high proportion up to about (89- 97%) takes place in the pre-heating system in the dry process for cement production.
- Increasing of calcination degree with a constancy of bypass opening value will lead to an increase in the heat content of gases, whereas at the stability of calcinations degree, decreasing of bypass opening value will increase gases' heat content.
- The series of cyclones' temperature increasing will slightly increase about 1% of the heat content of gases and 0.9 % of the dust heat content.
- It is observed that Maximum displacements at a height of 110 mts in RCC preheater tower are 130.59 mm and Steel preheater tower is 102.238 mm.
- The Maximum Moment at critical load combination is more in RCC preheater tower (i.e 205.6 kN.m) than Steel preheater tower (i.e 190.1 kN.m).
- The Maximum shear at critical load combination is more in Steel preheater tower 62.0 kN is more than RCC preheater tower 28.7 kN.

References:

1. Kabir, G., et al. “Energy Audit and Conservation Opportunities for Pyroprocessing Unit of a Typical Dry Process Cement Plant.” *Energy*, vol. 35, no. 3, Mar. 2010, pp. 1237–1243, 10.1016/j.energy.2009.11.003. Accessed 26 Mar. 2021.
2. Kolip, Ahmet. “MATHEMATICAL MODELLING of CLINKER PRODUCTION with SERIAL FLOW PREHEATER CYCLONES and PRECALCINER.” *Stavební Obzor - Civil Engineering Journal*, vol. 28, no. 3, 2019, pp. 357–371, 10.14311/cej.2019.03.0029. Accessed 7 Sept. 2021.
3. Madlool, N. A., et al. “Investigation of Waste Heat Recovery in Cement Industry: A Case Study.” *International Journal of Engineering and Technology*, vol. 4, no. 5, 2012, pp. 665–667, 10.7763/ijet.2012.v4.457. Accessed 20 Sept. 2019.
4. McGlinchey, Don, and Álvaro Ramírez-Gómez. “International Conference for Conveying and Handling of Particulate Solids (CHoPS2015).” *Particulate Science and Technology*, vol. 34, no. 4, 15 June 2016, pp. 423–423, 10.1080/02726351.2016.1190902. Accessed 28 Dec. 2019.
5. Mujumdar . “Identifying Energy Saving Opportunities in a Process Plant through Preliminary Energy Audit.” *Jurnal Teknologi*, vol. 38, no. 1, 1 June 2013, 10.11113/jt.v38.481.
6. Kozołub “Energy Saving Opportunities in Jordanian Pharmaceutical Industries.” *Perspectives of Innovations, Economics and Business*, 3 Apr. 2012, pp. 35–50, 10.15208/pieb.2012.04. Accessed 21 Nov. 2019.
7. McGlinchey et al. “Environmental Impact Assessment of Cement Industries Using Mathematical Matrix Method: Case of Ghayen Cement, South Khorasan, Iran.” *Environmental Science and Pollution Research*, vol. 28, no. 18, 8 Jan. 2021, pp. 22348–22358, 10.1007/s11356-020-12012-3

Hindawi
Journal of Nanomaterials
Volume 2022, Article ID 4994658, 7 pages
https://doi.org/10.1155/2022/4994658

Research Article

Effect of Fiber Mixing and Nanoclay on the Mechanical Properties of Biodegradable Natural Fiber-Based Nanocomposites

Razan A. Alshgari,[1] K. Sargunan,[2] C. Selin Ravi Kumar,[3] M. V. Vinayagam,[4] J. Madhusudhanan,[5] S. Sivakumar,[6] Saikh Mohammad Wabaidur,[1] M. A. Islam,[7] and G. Ramasubramanian[8]

[1]*Chemistry Department, College of Science, King Saud University, Riyadh 11451, Saudi Arabia*
[2]*Department of Civil Engineering, Vidya Academy of Science & Technology Technical Campus, Kilimanoor, Kerala 695602, India*
[3]*Department of Civil Engineering, Malla Reddy Engineering College (Autonomous), Hyderabad, Telangana 500100, India*
[4]*Department of Mechanical Engineering, Sree Krishna College of Engineering, Vellore, Tamil Nadu, India*
[5]*Department of Biotechnology, Anand Institute of Higher Technology, Kazhipattur, Tamil Nadu 603103, India*
[6]*Department of Civil Engineering, PSNA College of Engineering and Technology, Dindigul, Tamil Nadu 624622, India*
[7]*Faculty of Biology, University of Manchester, UK*
[8]*Department of Chemistry, Seenu Atoll School, Maldives*

Correspondence should be addressed to G. Ramasubramanian; raman@satollschool.edu.mv

Received 20 May 2022; Revised 17 July 2022; Accepted 30 July 2022; Published 7 September 2022

Academic Editor: Ram Prasad

Combining two types of fibers may aid in improving the fundamental properties of organic fiber-reinforced hybrid polymeric materials. Biomaterials created from raw materials are gaining appeal in the industrial sector due to their high quality, as well as sustainability and environmental considerations. Natural fiber-reinforced hybrid nanocomposites were created in this work using a compression moulding technique with wood particles, hemp fiber, polypropylene, and montmorillonite nanoclay. Following that, the impacts of fiber mixture and vermiculite on mechanical and compostable qualities were studied. Both the coir and the hemp fibers were alkali-treated to minimize their hydrophilic nature before even being employed. Using universal tensile testing equipment, the mechanical characteristics of the prepared composites were investigated and found to be improved following fiber blending and nanoparticle inclusion. The maximum strength was occurred at the combinations like 10 wt. % of wood particle, hemp, nanoclay, and 70% of polypropylene matrix. Scanning electron microscopy showed that nanoclay significantly increased the adherence and interoperability between fiber and the polymer matrices. The good biocompatibility and water absorption capabilities of the nanocomposite were increased by mixing fibers, but nanoparticle additions seemed to have the opposite impact.

1. Introduction

Agricultural leftovers that are plentiful and present difficulties when processed have recently been the topic of investigation due to growing awareness of environmental concerns. Field crop leftovers are frequently generated in billions of tonnes and are cheap; though solitary, a minor percentage of the waste is used as domestic petroleum or nourishment, while the majority is charred in the turf, polluting both the air and the environment. The challenge might be solved by using these leftovers as reinforcement material in polymer composites. It will also increase the value of the agrifood stream restraint. Fabric-based polymer matrix composites have lately been enough to substitute high strength concrete in the building and construction industry. Natural fibers are replacing traditional synthetic materials as reinforcing agents because of their nonpollutant, anticorrosiveness, good mechanical properties, light

Table 1: Natural fibers and their mechanical properties.

Fibers	Density (g/cm^3)	Tensile strength (MPa)	Young's modulus (GPa)	Elongation at break (%)
Abaca	1.5	980	—	—
Banana	1.35	355	33.8	5.3
Coir	1.25	220	6	15-25
Cotton	1.51	400	12	3-10
Flax	1.4	800-1500	60-80	1.2-1.6
Hemp	1.48	550-900	70	1.6
Jute	1.46	400-800	10-30	1.8
Kenaf (bast)	1.2	295	—	2.7-6.9
Pineapple	1.5	170	82	1-3
Ramie	1.5	500	44	2
Sisal	1.33	600-700	38	2-3

Figure 1: Abstraction of cannabis fiber from cannabis shrub.

weight, low price, recyclability, and good biocompatibility, as well as their good ecological effects [1, 2]. The use of renewable resources in polymeric composites may aid in reducing CO_2 emissions from plastic burning. Despite its usefulness, organic fiber-based composite materials have lesser elasticity, tensile strength, durability, and water resistance than artificial fiber-based composite materials. To address these challenges, natural materials might be combined with a tougher inorganic or organic fiber in polymer matrices. This will result in hybrid composites that make better use of the best attributes of the components, resulting in an optimal, superior, and more cost-effective combination [3]. Manufacturers may customize composites using organic fiber-reinforced hybrid polymeric materials at a cheap cost, which is not possible with binary mixtures of one fiber and one filler spread in the matrices [4]. Organic cellulosic fibers are reusable, nonabrasive, have good mechanical qualities, and are ecologically benign, making them desirable in engineering disciplines including automobiles and construction. Wood, jute, ramie, and hemp, out of all natural materials, have the greatest opportunity as hybrid composite reinforcement across the globe [5]. Due to its light weight, specific strength, biodegradability, simple accessibility, recyclability, and low price, wood fiber has achieved tremendous popularity as a filler in polymeric materials. Wood-reinforced polymers of various kinds have previously been developed and marketed [6]. The inclusion of wood fiber increased the elasticity, rigidity, toughness, durability, and flame retardancy of the polymers [7]. Hemp, on the other hand, is the toughest natural fiber since it is derived from the stem of the hemp plant. Cannabis is a millennia plant that is today regarded as one of the most environmentally friendly commercial materials. Herbs were sometimes mistakes to their resemblance to marijuana indica. Hemp could be grown in a wide range of climatic areas on a variety of extremely good, upgrading circumstances with such a wonderful yield even without agrochemicals, attaining elevations of 2-3 meters and a radius of 6-internal diameter. The cannabis seeds are regarded as a poor socioeconomic organic metabolic end due to its high hygroscopicity and tannin content. Processing techniques could result in better cannabis strands with an undigested surface of the fiber and more customization. Cannabis threads implanted in a lignocellulosic or phenolic foundation are produced into various architectural configurations [8, 9]. Cannabis fiber building has previously been extensively researched, resulting in useful, in-depth information being available in cultural canon. Hemp fibers are longer, stronger, and harder than other plant fabrics like silk, and they are also coarser; so, they are used in engineering fields. As a result, composites (airline sector, sporty products, etc.), structural and building materials, geotextiles,

Table 2: Parameters and their constraints of nanocomposites.

Sample No.	Wood particle (wt. %)	Hemp (wt. %)	Nanoclay (wt. %)	Polypropylene matrix (wt. %)
1	30	0	0	70
2	0	30	0	70
3	15	15	0	70
4	15	0	15	70
5	0	15	15	70
6	10	10	10	70

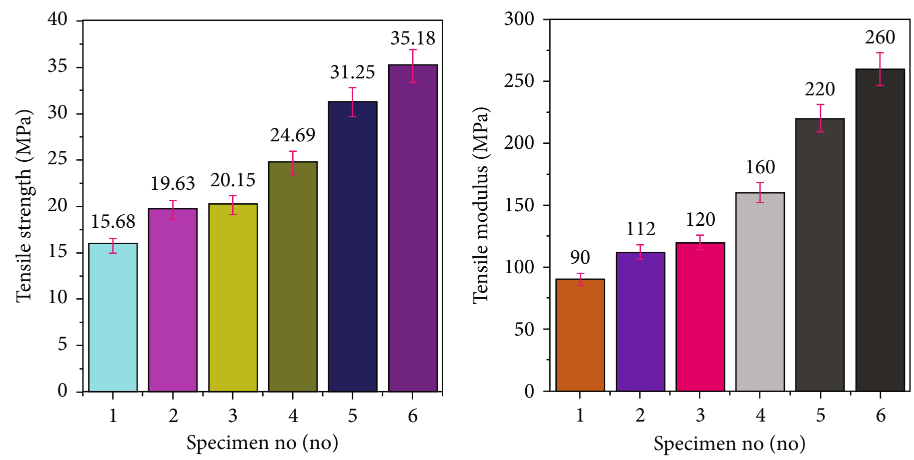

(a) (b)

Figure 2: (a) Tensile strength. (b) Tensile modulus of nanohybrid composite.

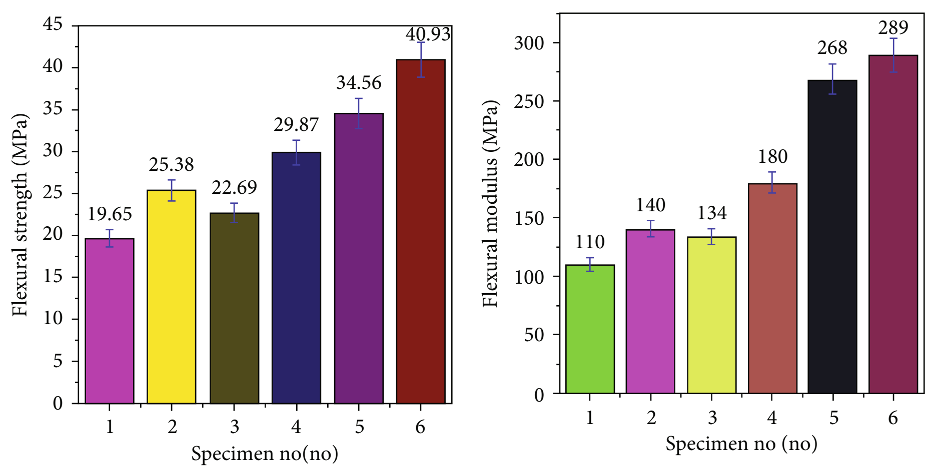

(a) (b)

Figure 3: (a) Flexural strength. (b) Flexural modulus of nanohybrid composite.

and other uses account for nearly a quarter of the marijuana fibers utilized in commercial processes. Throughout their life span, hemp fibers exhibit a variety of forms, thicknesses, topologies, and characteristics. In comparison to other cellulosic fibers, this has a considerable lignin content, moderate cellulose content, and a large microfibril inclination, which results in poorer tension strength and increased elasticity. This chemical structure minimizes the product's reactivity with polymeric radical generated throughout manufacturing, as well as its serviceability [10, 11], and the mechanical possessions of different threads is revealed in Table 1.

Nanocomposites outperform conventional polymers in terms of weight, durability, and simplicity of processing [12]. Nanomaterials are made up of tiny components with the lowest single measurement in the nanometric variety (i.e., less than 100 nm) that permits them to fill a matrix more efficiently. The nanoparticles known as "nano clays" are made up of stacked crystalline silicon dioxide. The nanoclay seems to have a higher surface area and a porous structure, resulting in significant interface contact between the polymers and the nanofiller, enhancing the polymer characteristics dramatically. Because of their exceptional mechanical, visual, electronic, and fire reserve capabilities, nanocomposites supplemented using biological and chemical nanostructures have attracted a lot of interest [13, 14]. Nanocomposites are a new type of nanocrystalline hybridization material made up of biodegradable polymers with one or more inorganic nanoparticles. They constitute the nexus of nanotechnology, materials engineering, and biology [15]. The creation of nanocomposites with improved thermodynamic, physical, and multifunctional qualities has been pursued. Furthermore, biopolymer-based materials made using renewable technologies have demonstrated digestibility and biocompatibility in pharmaceuticals, packaged food, and agricultural applications. Numerous research have been directed on normal fabric-strengthened polymeric materials that have been hybridized with synthetic fiber [16, 17]. On the other hand, natural fiber hybrid nanocomposite and their combination with natural fibers and nanoclay, on the other hand, have received much interest. The primary purpose of this work was to determine how combining fiber types and adding nanoclay to wood/hem/nanoclay hybrid

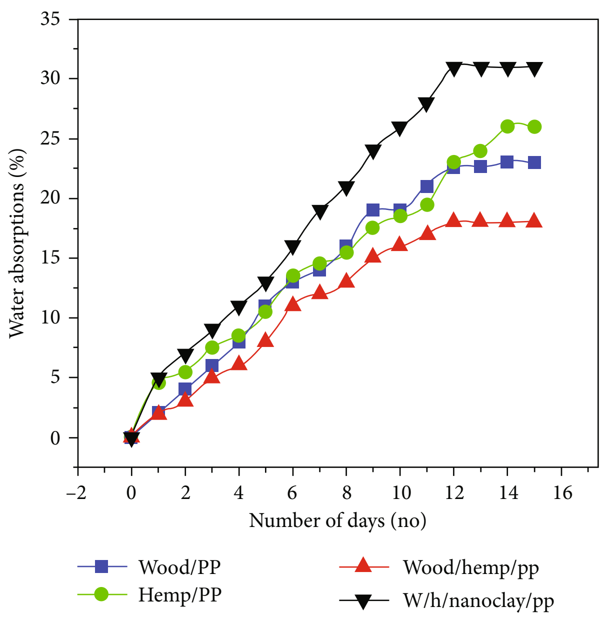

Figure 4: Water absorption behavior of wood/hemp/nanoclay/PP-based hybrid composites.

polypropylene biomaterials influenced their mechanical and biodegradable properties.

2. Resources and Techniques

2.1. Resources. In the composite system, wood fiber, hemp fiber, and nanoclay were employed as reinforcing fillers. Rithu Timber Industry in Madurai, Tamil Nadu, India, processed and gathered wood fiber. A GVR fiber factory in Madurai, Tamilnadu, India, processed and gathered hemp fiber. The nanoclay, sodium hydroxide, and polypropylene (PP) were provided by the Naga chemical company in Chennai, Tamilnadu, India. Figure 1 shows demonstrations of the subtraction procedure of hemp fiber from the hemp plant.

2.2. Alkaline Treatment. Unprocessed cannabis was washed in 2-3% scrubbing chemicals for 30 minutes at 50-60°C and disinfected with plain water before curing in an elevated furnace at around 80°C for 30 minutes, as stated. Washed threads became referred to as "raw threads." The threads are then disinfected via immersing them in a 2 : 1 combination of toluene and methanol for 60 to 78 h at 35°C, followed by a vigorous rinsing in 24 hours. Finally, the fibers were again engrossed in a 5 percent NaOH solvents at ambient conditions for 4 hours.

2.3. Fabrication of Hybrid Composites. Firstly, a stainless-steel mould with a size of $300 \times 300 \times 3$ mm was refined. The matrix material was mixed well with the hardener to create a good matrix system. The compression moulding technique was used to construct the composite from wood/hemp/nanoclay combinations. By hand stirring with a glass rod, varying weight percents of nanoclay powder were disseminated in the produced polypropylene. This matrix mixture was scattered over the mould's layers of fibers. The combinations were warmed to 170°C inside the compression moulding machine for 15 minutes. The composite was chilled in the atmospheric air for numerous proceedings to avoid any contraction that may have occurred throughout the abstraction method. The parameters of the nanocomposites are listed in Table 2. That parameter provides better improvement with mechanical properties which was proved by the various researchers [15–17].

2.4. Testing of Hybrid Composites. For tension behavior, the produced laminate specimens were taken and converted to ASTM D 638-03 analogues and ASTM D-790 for bending behavior [7]. Morphological examinations of cracked laminate material were carried out using SEM. Prior to SEM analysis, the samples were being laved, desiccated, and then chemically covered using tens of nanometers of golden to improve the ionic properties of the mixtures. The models were dehydrated for 1 hour at 70°C in a microwave and then cooled to a consistent weight in the outdoors. Following that, the composite samples were submerged in purified water for 10 days, as per ASTM D570 [18]. Each and every day, the models were detached from the aquatic, cleaned with tissue paper, reweighed and quantified, and then returned to the liquid. The below formula was used to compute the water uptake rates in Equation (1).

$$\text{Moisture absorption} = \left(\frac{W_2 - W_1}{W_1}\right) * 100. \qquad (1)$$

W_2 is the heaviness of the model after immersing, and W_1 is the heaviness of the model before absorption. Each kind of sample was subjected to five experiments, with the average results provided.

3. Result and Discussion

3.1. Tensile Strength. The tension properties and tensile modulus of different nanocomposites are shown in Figures 2(a) and 2(b). As shown in the figure, the tensile strength and tensile modulus of the hemp and polypropylene composite and the wood and polypropylene composite were almost identical. This might be related to the fact that wood and hemp fibers have comparable cellulose content [18]. Owing to its increased hemi cellulose concentration, hemp fiber is much more hydrophilic than wood fiber, while polypropylene is hydrophobic by nature. As a consequence, the hydrophilic hemp/wood and the hydrophobic polypropylene did not adhere properly, leading to a reduction in tensile strength and tensile modulus. When hemp fiber was mixed with wood fiber in PP and nanoclay was added, hybrid composites outperformed wood/PP and hemp/PP composites in terms of tensile strength and modulus. It is thought that composite materials with hemp or wood have higher tensile characteristics than other compositions because of fiber/matrix bonding, resulting in an even and efficient stress distribution across fibers. In addition, once nanoclay was added, the hybrid composites had the highest tensile strength and modulus. The nanoclay improved the mechanical characteristics of the composites by increasing

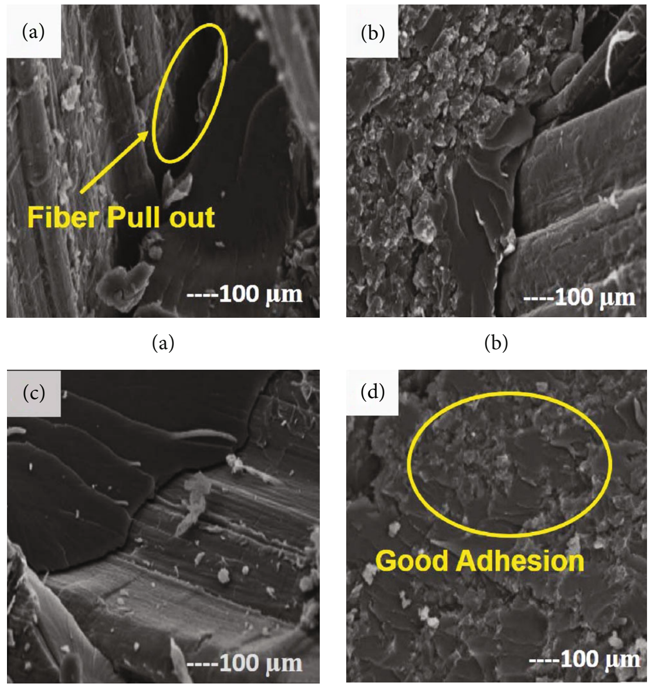

(a) (b) (c) (d)

Figure 5: SEM image of (a) wood/PP, (b) hemp/PP, (c) wood/hemp/PP, and (d) wood/hemp/nanoclay/PP-based hybrid composite.

interfacial contact and adherence between both the fiber and the polymer matrices. A prior study had shown similar findings [19].

3.2. Flexural Strength. Flexural loading seems to be the most popular application rate of the deformation technique, which involves stretching a square sample to fracture or using a multiple point flexural evaluation technique. The maximal strain inside the substance at its yielding point is reflected in the flexural strength, and it is shown in Figures 3(a) and 3(b). It shows wood/PP composites, and the hemp/PP composites revealed the highest flexural strength. This result demonstrates that the adherence of hemp fiber was good compared to wood. Polypropylene composites' three-point bending strength increased with the addition of nanoclay. The addition of nanoclay increased the strength properties of the composite material, with a combination of wood/hemp/nanoclay/PP having the maximum bending strength value. The trends observed in the bending strength of the composite show the high surface area exhibited by the small filler particles, which improves the dispersion between the filler and the matrix and improves the interfacial bond [20, 21]. The SEM image discernibly shows the above trends. Polypropylene has brilliant adhesion to a variety of materials and can be further supported by adding fibers and particles. The outcomes show that hybrid nanoclay and wood/hemp/PP composites provide the finest consequences in both tensile and bending cases compared to other combinations.

3.3. Moisture Absorption Behavior. Figure 4 shows demonstrations of the moisture content levels of dissimilar composite materials. At the beginning, the rate of water updating for all composite materials was high, but this level has become almost consistent and reduced in the end phase. According to the findings, all the composite materials exhibit a high moisture uptake rate with the increased time durations. After the first day, moisture content ranged from 7 to 14%, and it climbed to 17 to 33% for various produced composites. The hybrid nanocomposites produced with nanoclay had the greatest percentage of water fascination of all the composite materials. This could be owing to the hybrid nanocomposite's enhanced hydrophilic character after fiber blending and nanoclay inclusion. In comparison to the other composites, the hemp/PP amalgamated had the maximum aquatic preoccupation standards. This is owing to the enormous number of OH groups found on the interfaces of hemp fibers. In the hemp/PP composites, the quantity of hydroxyl groups and microvoids increased, resulting in a significant increase in moisture fascination. The hybrid combination of wood and hemp, on the other hand, absorbed the least quantity of water. However, the accumulation of hydrophilic fillers to the hybrid nanocomposite occasioned in greater moisture absorption than the hybrid composite [15].

3.4. Fractography Analysis. The morphologies of nanomaterials were examined using SEM. Figure 5 presents the tension fracture boundaries of nanomaterials and hybridized nanofiber. The timber mixture as well as the hemp/PP mixture seemed to have the smoothest interfaces of all manufactured configurations, as illustrated in Figures 5(a) and 5(b), resulting in reduced material characteristics. The aspect of timber nanocomposites was equivalent to that of the timber and hemp/PP hybrids, as can be seen in Figure 5(c). Because the energy spent was low, the intermediate connection between the fibers and resin was not really able to withstand fiber pull-out after collision [22]. The hybrid composite had a more flawless texture than the individual materials, as shown in Figure 5(d). The introduction of nanoclay to the hybrid mixture enhances the material characteristics of the bio-based nanomaterials by increasing interfacial interaction and superficial roughness.

4. Conclusion

The mechanical and water absorption evaluation of many wood, hemp, nanoclay, and polypropylene-based nanocomposites was identified, and the following conclusions were obtained. Wood/hemp/nanoclay/PP hybrid composites outperformed wood/PP, hemp/PP, and wood/hemp/PP composites in terms of tensile and flexural strength. This might clearly demonstrate how effectively the polymer matrix and fibers interact. The nanoclay filler advances hybrid composite mechanical strength by boosting adhesive bonding strength. This is immediately apparent in SEM analysis. The wood/hemp/PP combination absorbs the most water when compared to other combinations. Nanoclay addition, on the other hand, has the opposite effect on these characteristics.

Data Availability

The data used to support the findings of this study are included within the article. Further data or information is available from the corresponding author upon request.

Conflicts of Interest

The authors state that the publishing of this paper does not include any conflicts of interest.

Acknowledgments

The authors appreciate the supports from Seenu Atoll School, Maldives, for the research and preparation of the manuscript. The authors thank the University of Manchester, Vidya Academy of Science & Technology Technical Campus, Malla Reddy Engineering College, PSNA College of Engineering and Technology for providing assistance in this work. This work was funded by the Researchers Supporting Project Number (RSP-2021/265), King Saud University, Riyadh, Saudi Arabia.

References

[1] M. N. M. Layth Mohammed, G. P. Ansari, M. Jawaid, and M. S. Islam, “A review on natural fiber reinforced polymer composite and its applications,” *International Journal of Polymer Science*, vol. 2015, Article ID 243947, 15 pages, 2015.

[2] V. Mohanavel, S. Suresh Kumar, J. Vairamuthu, P. Ganeshan, and B. Nagaraja Ganesh, “Influence of stacking sequence and fiber content on the mechanical properties of natural and synthetic fibers reinforced penta-layered hybrid composites,” *Journal of Natural Fibers*, pp. 1–13, 2021.

[3] A. K. Saravanan, A. Rajendra Prasad, D. Muruganandam, G. Saravanan, S. Vivekanandan, and M. Sudhakar, “Study on natural fiber composites of jute, pine apple and banana compositions percentage of weight basis for thermal resistance and thermal conductivity,” *Materials Today: Proceedings*, vol. 37, no. 2, pp. 147–151, 2021.

[4] D. Logendran, K. Gurusami, M. C. Anand Chakaravarthi, G. Puthilibai, M. Suresh, and M. Sudhakar, “Experimental research on glass fibres / caustic soda treated banana fibers hybrid composite,” *Materials Today: Proceedings*, vol. 33, no. 7, pp. 4408–4411, 2020.

[5] L. Karikalan, M. Chandrasekran, S. Ramasubramanian, and S. Baskar, “Hybridization of composites using natural and synthetic fibers for automotive application,” *International Journal of Scientific Research in Science and Technology*, vol. 3, no. 7, pp. 916–920.

[6] V. Ganesan, V. Shanmugam, B. Kaliyamoorthy et al., “Optimisation of mechanical properties in saw-dust/woven-jute fibre/polyester structural composites under liquid nitrogen environment using response surface methodology,” *Polymers (Basel).*, vol. 13, no. 15, p. 2471, 2021.

[7] M. Boopalan, M. Niranjanaa, and M. J. Umapathy, “Study on the mechanical properties and thermal properties of jute and banana fiber reinforced epoxy hybrid composites,” *Composites. Part B, Engineering*, vol. 51, pp. 54–57, 2013.

[8] G. Velmurugan, K. Babu, L. I. Flavia, C. S. Stephy, and M. Hariharan, “Utilization of grey Taguchi method to optimize the mechanical properties of hemp and coconut shell powder hybrid composites under liquid nitrogen conditions,” *IOP Conf. Ser. Mater. Sci. Eng.*, vol. 923, no. 1, p. 012045, 2020.

[9] G. Velmurugan, T. Shaafi, and M. S. Bhagavathi, “Evaluate the tensile, flexural and impact strength of hemp and flax based hybrid composites under cryogenic environment,” *Mater. Today Proc.*, vol. 50, pp. 1326–1332, 2022.

[10] X. Li, L. G. Tabil, and S. Panigrahi, “Chemical treatments of natural fiber for use in natural fiber-reinforced composites: a review,” *Journal of Polymers and the Environment*, vol. 15, no. 1, pp. 25–33, 2007.

[11] F. Tanasă, M. Zănoagă, C. A. Teacă, M. Nechifor, and A. Shahzad, “Modified hemp fibers intended for fiber-reinforced polymer composites used in structural applications—a review. I. Methods of modification,” *Polymer Composites*, vol. 41, no. 1, pp. 5–31, 2020.

[12] A. Sreenivasulu, S. Rajkumar, S. Sathyanarayana, S. S. Kumar, G. V. Gaurav, and B. D. I. Premkumar, “Impact of nano-filler WC on the fracture strength of epoxy resin,” *Materials Today: Proceedings*, vol. 59, no. 2, pp. 1420–1424, 2022.

[13] N. E. Zafeiropoulos, C. A. Baillie, and J. M. Hodgkinson, “Engineering and characterisation of the interface in flax fibre/polypropylene composite materials. Part II. The effect of surface treatments on the interface,” *Composites. Part A, Applied Science and Manufacturing*, vol. 33, no. 9, pp. 1185–1190, 2002.

[14] M. S. Ravi Theja, P. Ramshankar, M. C. Sashikkumar et al., “Investigation into mechanical properties of EPDM/SBR-nanoclay nanocomposites,” *Materials Today: Proceedings*, vol. 59, pp. 1508–1512, 2022.

[15] N. A. Rahman, A. Hassan, R. Yahya, R. A. Lafia-Araga, and P. R. Hornsby, “Polypropylene/glass fiber/nanoclay hybrid composites: morphological, thermal, dynamic mechanical

and impact behaviors," *Journal of Reinforced Plastics and Composites*, vol. 31, no. 18, pp. 1247–1257, 2012.

[16] K. Majeed, M. Jawaid, A. Hassan et al., "Potential materials for food packaging from nanoclay/natural fibres filled hybrid composites," *Materials and Design*, vol. 46, pp. 391–410, 2013.

[17] E. M. Fernandes, R. A. Pires, J. F. Mano, and R. L. Reis, "Bionanocomposites from lignocellulosic resources: properties, applications and future trends for their use in the biomedical field," *Progress in Polymer Science*, vol. 38, no. 10-11, pp. 1415–1441, 2013.

[18] V. Ganesan and B. Kaliyamoorthy, "Utilization of Taguchi Technique to Enhance the Interlaminar Shear Strength of Wood Dust Filled Woven Jute Fiber Reinforced Polyester Composites in Cryogenic Environment," *Journal of Natural Fibers*, vol. 19, no. 6, pp. 1–12, 2022.

[19] M. Saiful Islam, S. Hamdan, I. Jusoh, M. Rezaur Rahman, and A. S. Ahmed, "The effect of alkali pretreatment on mechanical and morphological properties of tropical wood polymer composites," *Materials and Design*, vol. 33, pp. 419–424, 2012.

[20] G. Velmurugan and K. Babu, "Statistical analysis of mechanical properties of wood dust filled jute fiber based hybrid composites under cryogenic atmosphere using Grey-Taguchi method," *Materials Research express.*, vol. 7, no. 6, 2020.

[21] F. Sarker, P. Potluri, S. Afroj, V. Koncherry, K. S. Novoselov, and N. Karim, "Ultrahigh performance of nanoengineered graphene-based natural jute fiber composites," *ACS Applied Materials & Interfaces*, vol. 11, no. 23, pp. 21166–21176, 2019.

[22] X. Wang, H. Sun, H. Bai, and L. P. Zhang, "Thermal, mechanical, and degradation properties of nanocomposites prepared using lignin-cellulose nanofibers and poly (lactic acid)," *BioResources*, vol. 9, no. 2, pp. 3211–3224, 2014.

Analysis of BIM Use in Green Construction

Veeranki Surya Teja[1], Dr. C. Selin Ravi kumar[2], Dr. J. Prakash Arul Jose[3], Dr. JayantDamodar Supe[4],J. Chandra Mohan[5], Rajat Palya[6]

[1]Assistant Professor, Professor, Andhra Loyola Institute of Engineering and Technology, India

[2]Associate Professor, Department of Civil Engineering, Malla Reddy Engineering College (Autonomous), Hyderabad

[3]Professor, Department of Civil Engineering, Paavai Engineering College Namakkal, Tamilnadu

[4]Associate Professor, Department of Civil Engineering, RCET, Bhilai, Chhattisgarh, India

[5]Assistant Professor, Department of Architecture and Planning, University College of Architecture and Planning, Acharya Nagarjuna University

[6]Research Scholar, Department of Civil Engineering, RKDF University Bhopal, Madhya Pradesh, India

Mail- veeranki.suryateja@gmail.com[1]

Abstract

In this paper, the creators investigate the qualities and necessities of carefully upheld "green" building plan. Very much arranged, coordinated and interdisciplinary computerized plan rehearses assume a crucial part in the iterative cycles of manageable structure plan. Dissimilar to conventional approaches to working, the administration of plan data and cycle combination in green structure configuration includes a more extensive territory and a bigger number of experts using refined ecological demonstrating and examination frameworks. To comprehend the intricacies encompassing data the executives in this unique circumstance, the creators center around issues connecting with: 1) data trade and model administration, and 2) multidisciplinary configuration process coordination. Various parts of maintainable plan displaying procedures are investigated corresponding to innovation prerequisites, data trade, and multi-disciplinary joint effort. At long last, the writing is blended in a calculated guide outlining the key variables recognized by the review. The trouble of green development lies in the successful command over the development cycle through constraint on asset utilization and the executives of development progress. By dissecting the utilization of BIM in development, particularly in green development, from the parts of development process, cost examination, security and timetable administration, this paper means to figure out issues in current green development and proposition relating procedures to advance green development.

DOI Number: 10.14704/nq.2022.20.11.NQ66170 **NeuroQuantology 2022; 20(11): 1764-1771**

Introduction

Natural issues, for example, ecological corruption typically happen in development, yet it is found that the cycles where misuse of asset and ill-advised development seem are where cost can be decreased and climate can be safeguarded subsequent to examining development through a few mechanical strategies. Green structure, with its remarkable idea, is a sort of development directed by the possibility of practical improvement which is not the same as customary structure [1]. It is more sensible as it could reduce down expense at any point as well as decrease squander outflow and effect on the constructed climate. Thusly, high innovations utilized in genuine development should be planned and examined ahead of time. This paper plans to concentrate on the use of BIM in green development.

Recreation by joining elements, for example, materials and energy is much of the time utilized in development to show objects in a natural way [2]. In the hazardous development time of compositional data, the development business actually should get more precise data and guarantee a successful development cycle to decrease energy utilization and natural effect. In this cycle the entire development can be recreated through PC demonstrating and advanced reenactment innovation to unequivocally deal with the genuine interaction and at the same time lead genuine development and computer experience development. Breaking down bad prospects in development can assist with accomplishing a proficient management over the entire cycle and guarantee an organized improvement in genuine development [3].

BIM innovation gives a logical and powerful compositional stage for overseeing and carrying out green development. With reproduction of development interaction and data shared by all staff part, it breaks the shackle of conventional development and really advanced and works on the eventual outcomes of green development [3].

BIM Innovation

BIM innovation is the most broadly involved assistant innovation in development that can reenact the structure cycle to figure out its drawbacks as per development plan. This innovation can likewise assist with finding and work on potential issues in time in order to refresh the development plan and work with development [5].

Meaning of BIM

BIM is a computerized compositional model stage through which individuals can reproduce the structure cycle and offer pertinent data. BIM stage can give sound data to draftsmen, fashioners, specialists, development supervisors and show each development cycle in a 3D model to survey the arrangement and reenact the development interaction. Changes of plan can be made immediately to take out burdens in development and produce more solid results. Fundamentally, BIM can imitate the development interaction as well as store all engineering data to compute preciselythe measure of materials. Moreover, it can lead crash and stress examination in development and save enormous data in design model to deal with the development cycle and every development file.

Attributes of BIM

BIM innovation, a PC demonstrating in which 3D model is shaped to offer a data sharing stage for all parties,can help keep up with, oversee and fix the structure to keep its quality and security [7].

PC demonstrating is applied in the existence cycle to keep significant data of development in a consistent data set where data can be called whenever to dissect the structure in a thorough way and improve precision of planning process. That is the real working course of BIM and what makes BIM unique in relation to different stages [8].

Design model might arrangement different boundaries and update the development at any point cost, cycle, progress and plan continuously so that all gatherings can comprehend the development and act as per the gave data to keep away from potential errors. BIM, a kind of 3D displaying, change the old 2D designs. BIM joins 3D displaying with computer generated reality to progressively mimic the development cycle in congruity with the genuine one. Furthermore, this stage can accumulate all gatherings to really participate and advance development program.

BIM's greatest contrast from other compositional reproduction advancements is areas of strength for its in coordinating data in all segments from offering to support. Pertinent data can be brought progressively to accomplish data based administration and support all gatherings' cooperation, which changes the customary data transmission mode in development. BIM can upgrade efficiency,boost money saving advantage and make starting points for exceptional yields [9]. It tends to be drawn from the above investigation that the center of BIM is the mix of 3D with data based stage. BIM data set can store and move message to arrange development methodology including direction, plan, development and support and to lessen potential dangers in development to guarantee security.

Application of BIM in Green Construction

Green structure innovation is a sort of natural structure mode which consents withthe supportable improvement idea, planning to guarantee an organized advancement among development and climate by decreasing energy consumptionand lessen influence on the fabricated climate [10]. As green development is more perplexing than conventional development, green innovation and BIM ought to be placed into utilization to reenact the green structure plan. Green structure is a youthful sort of design and it needs BIM to flourish.

Mechanical Help for Green Development

Green development practice ought to be stressed in genuine development as it is more mind boggling [11]. In the plan period, convoluted drawings ought to typify development articles and cycle. The 2D model makes a chaotic visual discernment, subsequently causing human carelessness and significant bumble in plan. A basic part in development can include handfuls and even many drawings to show the genuine development process while customary development neglects to do as such. Thusly, BIM can be applied to exhibit the green development and examine potential issues that might happen in various designs to track down the best arrangement and decide a dependable green innovation. This cycle mostly utilizes BIM's perception capability and improves the green plan to facilitate all areas in consistence with green development requests.

Qualities and necessities of Green BIM

The data the executives requests of a multidisciplinary configuration process can't be overseen by a solitary partner association. It requires a scope of configuration, task and IT experts to facilitate and bring together the plan spaces of various structure frameworks. A thorough comprehension of the staggered interconnections between innovations, individuals, project stages, cycles and frameworks is expected to address the (occasionally contending) necessities of Green BIM. Powerful data the executives rehearses should satisfy the needs of the ceaseless age, transmission, distributing, deciphering, putting away and recovering of an extensive variety of building plan information. Green BIM requires thought of the strategy , cycle and innovation based components that support the BIM procedure [12], as well as methodologies for effective data the board that can uphold information move and interpretation in multi-disciplinary ESD coordinated efforts [13].

Data the board

The hidden necessities of data the board in Green BIM undertakings should be visible to connect with four factors: 1) number of members trading data, 2) data guidelines, conventions and organization, 3) idealness of data trade, and 4) jobs and obligations while trading data. In tending to strategy based data the board issues, different arrangements have been proposed including authoritative records, trade conventions, demonstrating principles, and determination of the degree of detail (LoD) in displaying, (for example, those found in BIM the executives plan layouts and structures determining e.g., LoD 100 to LoD 500) [14]. Interoperable record trade diagrams can to some degree help with the specialized troubles encompassing similarity (e.g., .ifc, Gbxml, .dwg, And so forth), which empowers the improvement of a coordinated information rich model. Exact and ideal data is expected to beat the antagonistic impacts of industry fracture during the plan interaction, giving precise and facilitated 3D models for Green BIM. Tzortzopoulos-Fazenda and Cooper [15] characterize plan the executives as a badly organized process and the everyday working limits as being uncertain. Data trade in this way, requires clear cut norms and conventions before beginning of the plan cycle. Following the practicality of plan data for Green BIM ventures and planning this with the abilities and interoperability necessities of ESD advancements is fundamental for understanding corresponding undertaking interdependencies inside the plan group. Figure 2 presents an illustration of the potential data trade and correspondence designs happening during a Green BIM project, recognizing an organization of undertaking interdependencies. Green BIM is reliant upon the utilization of computerized plan advances for the reasons for both item frameworks mix and configuration process coordination - such combination can be better tended to in the event that the components of ESD and GBC are viewed as in equal. This prompts the second subject of this segment: multidisciplinary cooperation - including the between authoritative undertaking conditions and data displaying necessities.

Crash Really take a look at in Development

It is unavoidable to see a few crashes in construction.The coming about underlying harms won't just bring unavoidable misfortune yet in addition amount to the expense, which disregards green structure standard. BIM's reproduction of development can distinguish primary strength and lender of conceivable accident and change development routes in plan to stay away from large accident and increment proficiency.

Streamlining of Pipeline Format

Pipeline format is a significant part in development as it is required in both plan and building process. Pipelines in each part will be appropriately figured out how to guarantee a sensible grouping of development and stay away from modify. Crash check utilized in pipeline format can test lastly coordinate the development cycle in the last arrangement to break down and advance the development unique cycle thoroughly. As a muddled method where authenticity and dauntlessness ought to be exhaustively considered to track down the best arrangement after simplification,pipeline format lessens development cost as well as techniques to assist with finishing development in an early date.

Plan The executives in Green Development

Development plan doesn't just allude to the end so as to complete subsequent work yet in addition a method for decreasing expense. Green development will be a legitimate interaction where asset can be savedthrough successful administration. Other than fruition in time plan, green development stresses successful control which can diminish probability of mishaps and figure out potential issues and arrangements ahead of time. Green development is more confounded than normal development, which expects for use of BIM to mimic the interaction, examine ordinary headway, make game plans and portions lastly deal with the entire cycle. After a complete examination of development, BIM can assist with guaranteeing all development methods to fit in the timetable track down deficiencies in development and diminish misuse of asset and time. On that premise, development can be finished in time plan and decrease dangers of deferral.

Cost Administration in Green Development

Green development centers around limit of asset preservation and a quality development in time plan diminish natural contamination and keep up with biological climate. BIM can be utilized in development to mimic each part including the utilization of materials, make an exact expense financial plan on compensations and potential dangers and contrast different structure process with get the best intend to limit cost while guaranteeing security, progress and quality. Moreover, BIM model can analyze development data in 3D and join factors, for example, cost and time toestimate the expense of the best arrangement and inflate money saving advantages of green development. It is important to make information reproduction through BIM stage to show up at a doable arrangement and establish a strong starting point for genuine development.

Toward a Green BIM the executives system

The writing survey features an absence of investigation into the particular demonstrating prerequisites and related difficulties encompassing reproduction and examination for Green BIM and its arrangement with the somewhat ongoing presentation of GBC processes. Demonstrating interdependencies between building frameworks stay a significant test to the coordination of configuration processes (e.g., water effectiveness investigation requires nitty gritty displaying of various structure frameworks, including MEP administrations, pressure driven hardware). A Green BIM the executives plan that is fit for supporting the movement of ESD all through the plan stages requires further thought of data the board rehearses, for example, the detail of data trade conventions, the LOD in ESD displaying, and programming and interoperability necessities. Therefore plan coordination should zero in on ESD displaying, reproduction and examination with an accentuation on „co-design‟ strategies. In a bid to structure and legitimize the administration and coordination issues of Green BIM, the creators have combined the connected writing in a reasonable system pointed toward fostering a Green BIM the executives technique. Figure 4 depicts the system as a guide that structures the prerequisites of innovation, strategy and cycle the executives for Green BIM. The proposed guide sorts out these prerequisites from the underlying phases of undertaking intending to the last phases of configuration utilizing the AIA‟s (2007) meaning of IPD project stages (Conceptualisation, Rules Configuration, Itemized Plan, and Execution Reports). The between connecting parts depicted in the guide are as per the following.

1) Conceptualisation Stage:

During this stage, a „Green BIM Prerequisites Assessment‟ framework is crucial for project commencement. Client and undertaking goals for GBC and ESD should be distinguished related to the subtleties of carrying out BIM apparatuses and processes, as well as IPD techniques and legally binding plans. Data and demonstrating principles, conventions, alongside particular of the degree of detail (LoD) all through the plan cycle, plan colleagues liable for creating data, and the ESD reenactment and investigation prerequisites ought to be characterized. To characterize these distinguishing the degree and reason for the undertaking before then, at that point: (a) surveying GBC measures determinations, (b) recognizing assets including key entertainers and evaluating BIM abilities for ESD and GBC by planning rules to BIM devices, and (c) evaluating generally speaking venture association capacities to accomplish wanted GBC targets is first essential. When these prerequisites evaluation exercises have been accomplished it is then conceivable to illuminate the improvement regarding IPD strategies and agreements as well as give the premise to a Green **BIM system.**

2) Criteria Plan Stage:

During this stage, it is significant to foster the Green BIM execution technique; this methodology requires: (a) appraisal of the possibility of GBC/ESD and BIM instruments to accomplish designated credits, (b) recognizable proof of an ESD plan movement plan that guides plan members with instructive conditions across displaying, recreation and investigation exercises (e,g., water proficiency, energy productivity, sunshine investigation and material assets), (c) characterize displaying norms and correspondence mediums, (d) refine data trade conventions and survey interoperability prerequisites between structural displaying and ESD group specialists prior to starting the plan interaction, and (e) map proportional ESD task interdependencies between configuration group members comparative with GBC measures. In this way during the Standards Configuration stage, itemized process stages, stage entryways and a cycle the executives network (depicting equal undertaking interdependencies) ought to be created. This will help with planning interdependencies between plan action plan and discipline-explicit BIM innovations with accentuation on ESD strategies and examination instruments. As a feature of this planning system, taking into account the interoperability necessities of every product application is likewise vital. When this methodology has been created IPD authoritative plans can be assessed and refreshed to guarantee that the designated GBC credits can be accomplished cooperatively.

3) Detailed Plan Stage:

The definite plan stage should be upheld by a thorough cycle coordination plan that will characterize a Green BIM plan the board approach. Before starting plan there is a need to set up a plan action plan, in view of cycle the board grid adjusting ESD goals and configuration undertakings with data prerequisites and stage entryways of the GBC cycle. To deliver and execute such an arrangement it is important to: (a) update stage entryways for the nitty gritty plan process (b) map stages entryways to and update the plan action and demonstrating plans as well as data conventions, (c) foster an ESD and GBC process coordination map, (d) characterize the executives jobs and obligations, (d) screen and assess assets, plans and conventions. These parts of a Green BIM coordination plan can then be utilized to illuminate and refresh the general strategy and plan the board framework in an iterative manner.

Conclusion

This paper examines the use of BIM and existing issues in green development with the expectation that BIM, with its recreation capability, can take care of these issues by working on quality and security and decreasing the development period and cost. Green structure is more complicated than different structures and not full adequately grown, hence it ought to zero in additional on reasonableness and necessities BIM as its mechanical help in doing impact check, enhancing the pipeline format and overseeing green development progress and cost. By making full play of BIM, strong groundwork can be laid for green development to decrease a wide range of dangers and guarantee a compelling development process. The writing uncovers various basic components of Green BIM enveloping mechanical, interaction and strategy based ascribes. Studies encompassing late improvements in advanced demonstrating and examination advances show how they aid informed direction and meeting GBC systems. Further, a scope of studies recording model structure projects give proof of Green BIM executions and the difficulties confronted and accomplishments made. Various industry-driven BIM the board conventions are additionally announced in the writing. Specialists reason that it is important to perceive the meaning of plan the executives philosophies and the significance of supporting manageable structure configuration by tending to the critical necessities of data demonstrating and trade in multidisciplinary plan conditions.

References

1. Abanda F H, Byers L (2016) An investigation of the impact of building orientation on energy consumption in a domestic building using emerging BIM (Building Information Modelling). Energy, No. 97, PP. 517-527.
2. Akinade O O, Oyedele L O, Munir K (2016) Evaluation criteria for construction waste management tools: towards a holistic BIM framework. International Journal of Sustainable Building Technology & Urban Development, Vol. 7, No. 1, PP. 1-19.
3. Araszkiewicz K (2016) Green BIM Concept – Scandinavian Inspirations. Archives of Civil Engineering, Vol. 62, No. 1, PP. 99-110.
4. Chen P H, Nguyen T C (2016) Integrating BIM and Web Map Service (WMS) for Green Building Certification ☆. Procedia Engineering, No. 164, PP. 503-509.
5. Choi J, Ryu H G (2015) Application and Effects Analysis of BIM(Building Information Modeling) for Construction Management of a Construction Field. Rev.bras.ciênc.solo,Vol. 15, No. 1, PP. 115- 121.
6. Ilhan B, Yaman H (2016) Green building assessment tool (GBAT) for integrated BIM-based design decisions. Automation in Construction, No. 70, PP. 26-37.
7. Jin-Fang, Li-Shih (2016) Application of BIM (Building Information Modeling) and GIS (Geographic Information System) to Railway Maintenance Works in Taiwan. Journal of Traffic & Transportation Engineering, Vol. 4, No. 1, PP. 18-22.
8. Lee S, Tae S, Roh S (2015) Green Template for Life Cycle Assessment of Buildings Based on Building Information Modeling: Focus on Embodied Environmental Impact. Sustainability, Vol. 7, No. 12, PP. 16498-16512.
9. Pavlovskis M, Antuchevičienė J, Migilinskas D (2016) Conversion of Industrial Buildings and Areas in Terms of Sustainable Development by Using BIM Technology: Analysis and Further Developments. Clinicalence, Vol. 7, No. 5, PP. 505-513.
10. Umar U A, Shafiq N, Malakahmad A (2016) Application of Structural Building Information Modeling (S-BIM) for Sustainable Buildings Design and Waste Reduction: A Review. International Journal of Applied Engineering Research, Vol. 11, No. 2, PP. 1523-1532.
11. Yang Y H, Ren B B (2015) BIM Based Green Building Management Development in the U.S.. Applied Mechanics & Materials, PP. 744-746, 1597-1600.
12. Zhu S, Tu Y (2015) Design Study on Green Sports Building Based on BIM. Open Cybernetics &Systemics Journal, Vol. 9,. No. 1, PP. 2479-2483
13. Jupp, J. and S. Gandhi, Clarifying the role of Building Information Modelling in Green Building Certification, in 37th Annual Conference of Australasian University Building Educators Association (AUBEA)2012: University of New South Wales, Sydney, Australia.

14. den Otter, A. and S. Emmitt, Design team communication and design task complexity: The preference for dialogues. Architectural Engineering and Design Management, 2008. 4(2): p. 121-129.
15. NATSPEC. NATSPEC Construction Information – NATSPEC National BIM guide v.10. 2011.
16. Tzortzopoulos-Fazenda, P. and R. Cooper, Design management from a contractor's perspective: The need for clarity. Architectural Engineering and Design Management,, 2007. 3(1): p. 17-28.

Non-Linear Analysis of Reinforced Concrete Column using Ansys

Dr J Rex[1], Wilfred Rohit Peters[2]
[1] Assosiate Professor, Department of Civil Engineering, Malla Reddy Engineering College (Autonomous), Hyderabad, Telangana, India
[2] Student, Department of Civil Engineering, Malla Reddy Engineering College (Autonomous), Hyderabad, Telangana, India

Abstract

Numerous techniques have been used to evaluate behaviour then occurrence of typical failures of reinforced concrete structures, such as flexural, shear, torsion, buckling, etc. The behaviour of reinforced concrete is usually investigated through large-scale experimental experiments. The complicated behaviour of reinforced concrete members may now be modelled using finite element modelling thanks to the development of powerful numerical analytical tools like the finite element method (FEM). Used in this work are models of reinforced concrete columns that have been loaded axially, symmetrically, and eccentrically. With the help of the FEM programme ANSYS, reinforced concrete columns are analysed using nonlinear finite element analysis up to failure. Simulations about reinforced concrete supports that are imperiled to axially symmetric filling take into account how frequently they are used in laboratories.

Index Terms Flexural, Torsion, Shear, Buckling, Nonlinear Finite Element Analysis, ANSYS

DOI Number: 10.48047/NQ.2022.20.16.NQ880585 **NeuroQuantology 2022; 20(16): 5756-5764**

INTRODUCTION

It is common practise to conduct experimental analysis to investigate the strength of concrete under different loading conditions and for individual component members. This approach reveals the structure's actual behaviour. However, it is costly and time intensive. These structural elements are also examined using finite element theory. In order to evaluate structures, a technique known as finite element analysis (FEA) is performed. This technique accurately predicts how a component will react to different structural loads. Due to its speed and cost-effectiveness, FEA has traditionally been chosen as the method of choice for studying concrete behaviour. The complex behaviour of reinforced concrete columns can now be modelled using finite element modelling thanks to growth about cultured arithmetical investigation gears similar FEM.

Objectives:

This initiative aims to accomplish three primary things:

- To lessen the quantity of input data necessary for large-scale structural analysis.
- To minimise the procedures required for structure analysis.
- To create a reliable MATLAB tool that can analyse a big arrangement utilizing the aforementioned techniques.

NeuroQuantology |December 2022 | Volume 20 | Issue 16 |Page 5756-5764| doi:10.48047/NQ.2022.20.16.NQ880585

MODELLING AND MATERIAL PROPERTIES

2.1 FINITE ELEMENT MODELLING

2.1.1 Element Types

Concrete: Concrete be modelled using Solid65 element. Eight knobs make up the nodes of this element, and each node has three degrees of freedom, allowing for translations in the nodal x, y, and z directions. This substance has the ability to deform plastically, fracture in 3 orthogonal instructions, plus crush. A diagram about component is exposed in Fig.

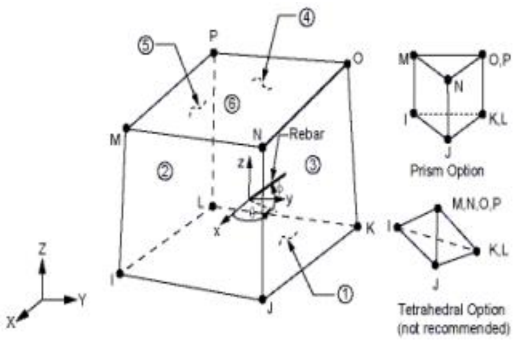

Solid 65 element

Steel Reinforcement: Steel reinforcement is modelled using a Link180 element. This element has two nodes with three degrees of freedom each, which allow for translations in the nodal x, y, and z dimensions. It is a 3D spar element. This substance can also distort plastically. This component is depicted in Figure 2.

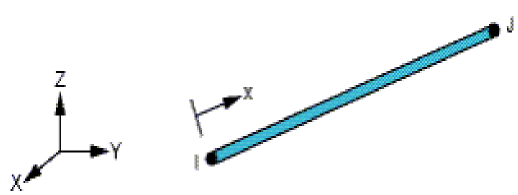

Link 180 element

Steel Plates and Supports: A modelling element called Solid185 is used to represent steel plates and supports. Eight nodes that have 3 degrees about freedom for conversions in the nodal x, y, and z instructions make up component's definition. Allure element has the ability to be plastic, hyper elastic, stress stiffen, creep, have a huge refraction, have a unlimited strain. Solid185 comes now 2 different shapes:

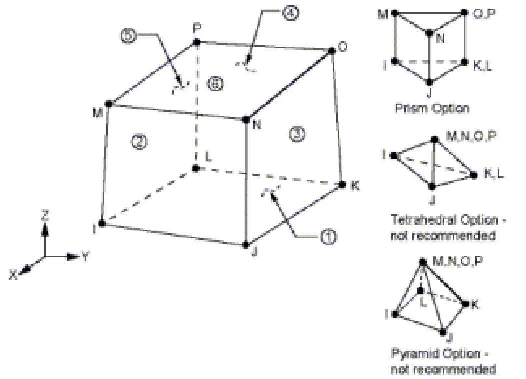

Solid185 Element (Homogeneous Structural Solid) in ANSYS

2.2 Finite Element Modelling of Steel Reinforcement

FEM aimed at protected concrete can simulate steel reinforcement using one of three methods: discrete, embedded, or smeared modelling. The reinforcement is modelled in the work provided the research using a separate modelling method. The bar or beam elements used for reinforcement in the discrete model (Fig) are attached to concrete mesh nodes using bar or beam elements. Because of this, concrete with support net segment the same nodes, and the concrete takes up similar space as support does.

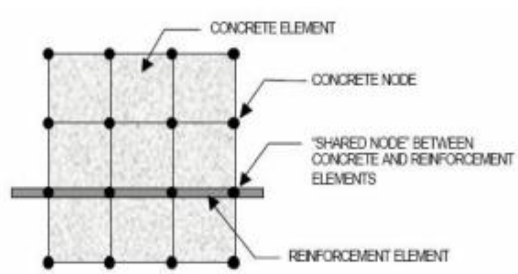

Discrete Models for Reinforcement

eISSN 1303-5150

2.3 Material Properties

Concrete: Concrete has a stress-strain relationship that is both extremely nonlinear and ductile and is a quasi-brittle material. the slow development of microcracks under loading, which is responsible for the nonlinear behaviour. Concrete's tensile strength is normally between 8 and 15 percent of its compressive strength. A typical stress-strain curvature amid normal weight concrete is shown trendy Figure. Concrete's stress-strain bend in compression is linearly elastic up to around 30% of its extreme compressive strength. Outside here opinion, pressure gradually rises until it reaches the highest compressive strength.

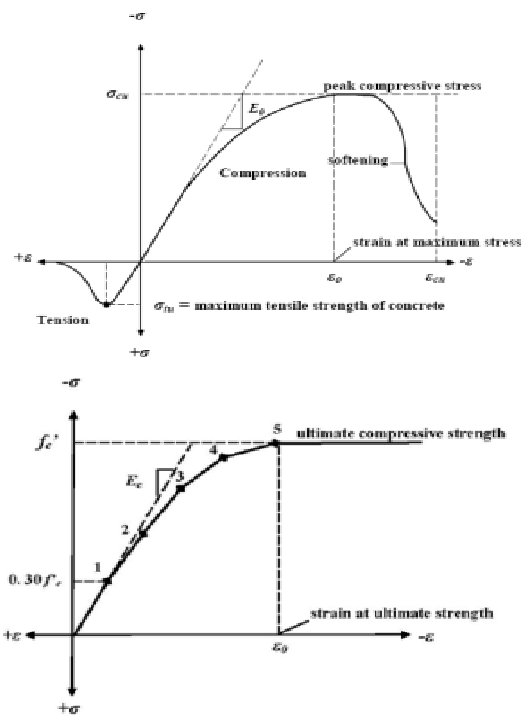

Typical uniaxial compressive and tensile stress-strain curve for concrete

The perfect be able to forecast material failure in concrete (Fig). Failure modes related to both crushing and cracking are taken into account. To specify a disappointment external aimed at the concrete, the 2 input power parameters—ultimate uniaxial tensile and compressive strengths—are required. As a result, a threshold pro material disappointment brought on by a multiaxial stress national can stand resolute.

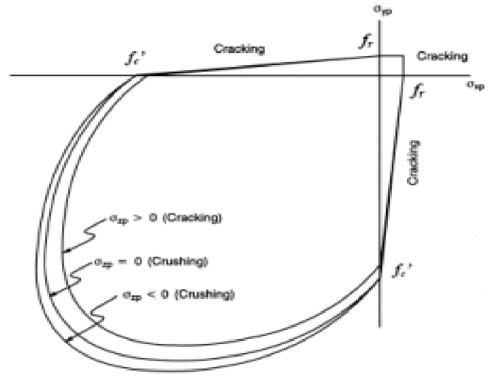

Failure Surface for concrete

Steel Reinforcement: It is believed that the mechanical behaviour of steel reinforcement bars will be elastic bilinear under monotonic tension. A linear elastic phase is first present in the steel bar, charted via a yield phase, strain hardening, and finally a stress decline till break happens. According to Fig., steel bar behaviour under compression and tension loads is same. The yield strength, tangent modulus, and modulus of elasticity are the three most important inputs for steel solid model. Here solidity of the FE perfect of the beam, work-hardening component is introduced here to the steel characteristics.

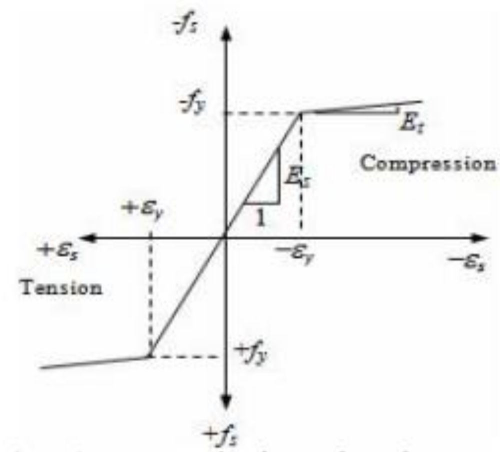

Strain curve for the steel reinforcement

METHODOLOGY AND MATERIAL INVESTIGATION

3.1 Methodology of the Study

Based on the experimental data that is currently available, essential behaviour of protected concrete columns reinforced by carbon fibre reinforced polymers be modelled in the current study. Four series were created from the analysis of 37 column specimens using FEM. Here confirmation revision be conducted to ensure that the theoretic consequences obtained through experimental testing are valid. Following this, a parametric study was conducted to look into impact about maximum significant limitation scheduled the behaviour of RC supports reinforced by CFRP mixtures.

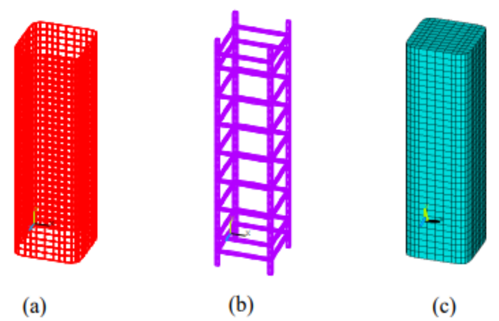

(a) Finite element model column (b) steel elements (c) Mesh of CFRP.

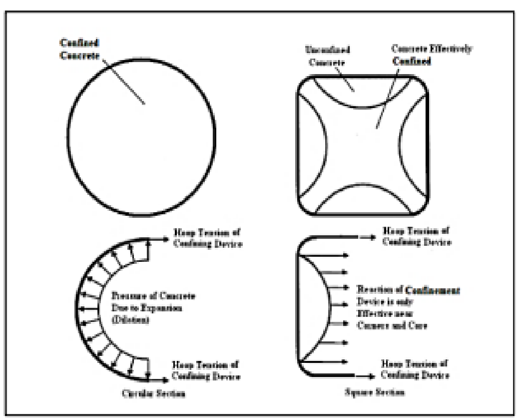

3.2 Material Investigation

Composites are made of two materials combined together, with one of the materials, the reinforcing phase, being embedded in the matrix phase and taking the form of fibers, sheets, or particles. Metal, ceramic, or polymer are all acceptable choices for the matrix and reinforcing materials. Because the overall qualities of composites are better than those of the separate components, they are utilised. For instance, composites made of a polymer and a ceramic material have a higher modulus than the polymer alone yet are less brittle than ceramics. High strength-to-weight ratio (low density, high tensile strength), high creep resistance, high tensile strength at high temperatures, and high toughness are only a few of the factors that influence the choice of composites for certain applications.

3.4 Mechanism of Concrete Column by Confinement

When FRP jackets or any other confining device (steel plates, transverse reinforcing steel, etc.) is fitted to the concrete column, the concrete is not contained since no initial stresses are introduced in the confining device at low levels of stresses in the concrete. According to tests, a concrete column's circular section provides substantially more effective confinement than its square or rectangular counterpart. Figure 1 explains the explanation of this difference in efficacy by demonstrating how a circular section will put quarantine expedient here girdle under pressure with force to continuously apply restricting gravity everywhere boundary, subsequent here total imprisonment. Contrarily forces confinement mechanism to apply the confining response solitary close to the section's angles with in its centre while leaving the sides unconstrained, resulting in the provision of only incomplete detention aimed at pillar.

The influence of confinement on circular and square sections. (Chaallal et.al.,)

3.8 About Ansys

Since the tested parts have thin walls and are perforated along their whole length, finite element analysis is mostly employed to validate them because of how complex their behaviour is under axial stresses. The shell elements found in the ANSYS [1] software offer a useful way to validate the experimental findings. An engineering simulation programme is called ANSYS (computer aided engineering, or CAE). In 1996, ANSYS became a publicly traded company on the NASDAQ. ANSYS received the highest score possible on Investor's Business Daily's Smart Select Composite Ratings in late 2011, making it one of only six technology companies in the world.

- **About ANSYS**

Numerous other publications have also acknowledged ANSYS as a top performance. In order to continuously improve the software, the company dedicates 15% of its annual revenues to research. When it comes to engineering simulation, ANSYS offers a wide variety of solution sets that give users access to almost every area that is needed for the design process. Software from ANSYS is used by businesses across numerous productions. Before becoming an actual entity, implements subject a virtual product to extensive analysis (Here being driven hooked on a brick partition before successively for some years on an asphalt way).

3.9 ANSYS Products

Simulation Technology: Fluid dynamics, explicit dynamics, electromagnetism, structural mechanics, and multiphysics

Workflow Technology: High-Performance Computing, Geometry Interfaces, Simulation Process, and Data Management are some of the technologies used by ANSYS Workbench. The incorporation of computer-based engineering simulation early in the development process, which enables engineers to revise and test ideas at a stage where the cost of making modifications is modest, is now widely acknowledged as a fundamental strategy for success in virtually every industry. The most difficult design problems are solved by ANSYS by using quick, exact, with trustworthy model. With the help of our technology, businesses can confidently forecast how well their products will perform in the real world. They rely on our software to support maintaining the quality of the products and fostering corporate success through innovation. Every product makes a commitment to meet and exceed expectations. By using ANSYS software to simulate frequently and early, our customers can develop their own products more quickly, more efficiently, and with greater innovation.

NeuroQuantology |December 2022 | Volume 20 | Issue 16 |Page 5756-5764| doi:10.48047/NQ.2022.20.16.NQ880585

ANSYS

3.10 ANALYSIS OF RC COLOUMN USING ANSYS

3.10.1 Modeling and Meshing

To model Column, volumes are made. Rectangular mesh is employed to achieve satisfactory results from the Solid65 element. The modelling process uses the nodes produced by the concrete volume's mesh to build the individual reinforcing components. Here "merge items" command combines several things bes located in similar place. They will subsequently be combined into a single entity. In order to limit ideal with obtain a singular resolution, movement limit conditions are required. Applying boundary constraints supports and loadings will guarantee that the model behaves in the same way as the experimental Column. The support has been designed with a hinge and roller in mind. All nodal lines receive the same amount of force.

DESIGN AND DETAILS OF THE RC FRAME

Vertical deflection in columns

As seen in Fig., the free end of the axial column experiences greater vertical deflection when a load is placed there.

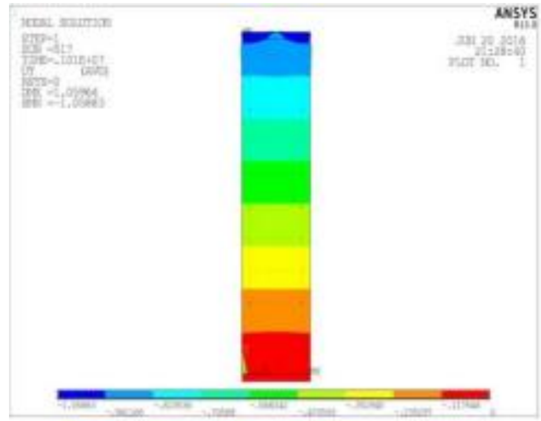

Axial column

As eccentricity rises, the maximum value shifts in favour of the eccentricity and also rises due to the bending effect.

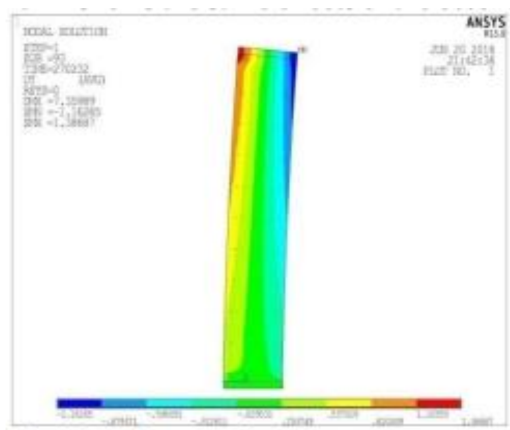

Column with 50mm eccentricity

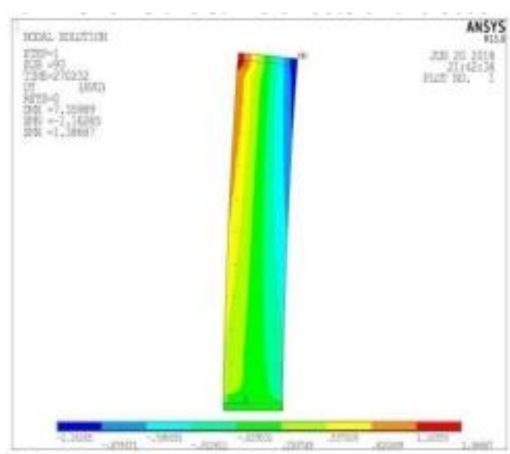

Column with 100mm eccentricity

Horizontal Deflection in Columns

Axial force on a column results in relatively little horizontal displacement, which is caused by concrete deformation from shear failure at the top and great bottom interaction surfaces.

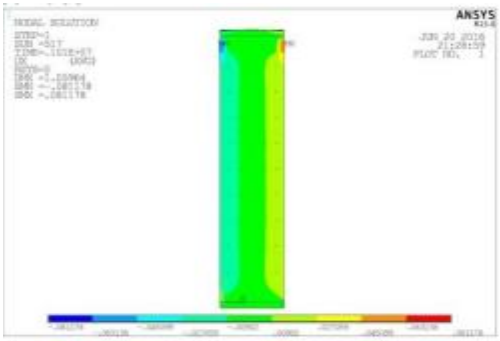

Axial column

The horizontal deflection rises with increasing eccentricity, as depicted in Fig. On the eccentricity's opposing side, tension rises.

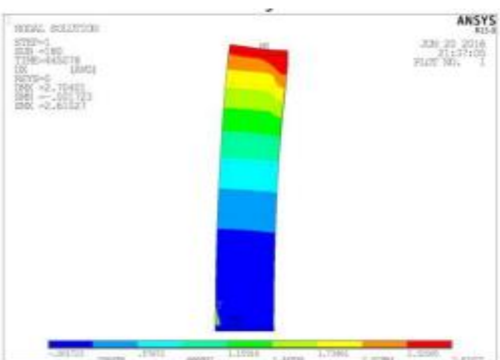

Column with 50mm eccentricity

Additionally, Figure 1 demonstrates that tall columns have higher horizontal refraction than short columns for a given eccentricity. This is because the long column began to buckle due to the slenderness effect, which caused a substantial horizontal deflection before disappointment.

Column with 100mm eccentricity

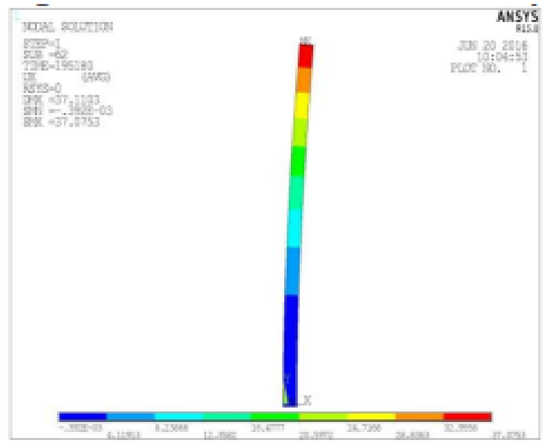

Long column with 50mm eccentricity

RESULTS

5.1 Ultimate load vs Axial Strain

Experimental and numerical results of ultimate load and axial strain

Column	Ultimate load [KN]	Axial Strain
C1	0.93	0.97
C2	0.96	0.95
C3	0.92	1.03
C4	0.98	0.98
C5	0.95	0.98
C6	0.97	1.07

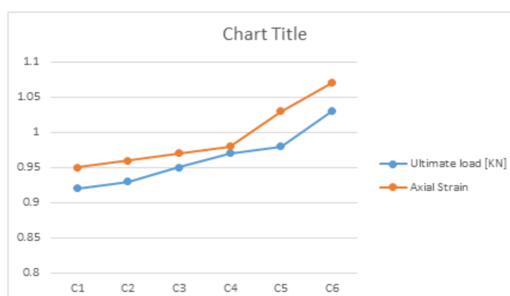

Experimental and numerical results of ultimate load and axial strain

5.2 Ultimate load vs Axial Displacement

Experimental and numerical results of ultimate load and axial Displacement

Column	Ultimate load [KN]	Axial Displacement
C1	0.92	0.99
C2	0.94	1.01
C3	0.96	1.03
C4	0.98	1.05
C5	1.01	1.06
C6	1.05	1.10

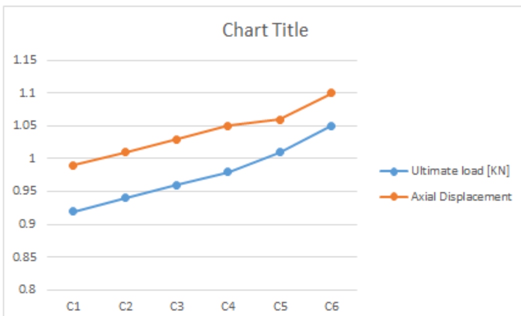

Experimental and numerical results of ultimate load and axial Displacement

5.3 Axial Stress Curves vs Axial Strain Curves

Experimental and numerical results of Axial stress-axial strain curves

Column	Axial Stress Curve[KN]	Axial Strain Curves
C1	0.89	0.91
C2	0.92	0.94
C3	0.95	0.96
C4	0.98	0.98
C5	1.01	1.06
C6	1.05	1.03

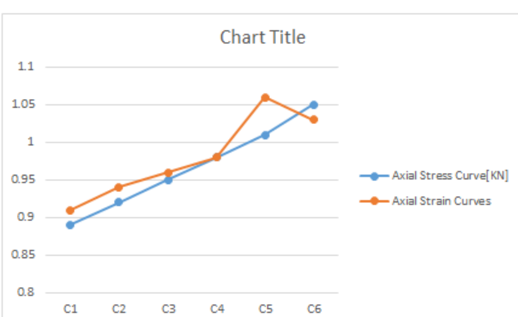

Experimental and numerical results of Axial stress-axial strain curves

CONCLUSIONS

The object about revision existed to explore whether nonlinear finite element investigation of reinforced concrete columns could be carried out using the ANSYS Package software. Thanks to accurate FEA modelling, Here disappointment processes about axial with unusual reinforced concrete supports be clearly identified and closely match predictions. here nonlinear mutual axial with flexible reaction of these schemes up to disappointment have been precisely represented by finite element models of reinforced concrete supports built in ANSYS 15 utilizing the specific concrete components. Future applications about finite element analysis pro non-linear investigation about RC supports will benefit from a fuller understanding of the analysis process employed in this paper, which was developed by previous researchers, and various output plots created by FEA. It has been originate the effects be extra subtle to elements like mesh size, material quality, load increases, etc. founded on ANSYS investigates performed on RC supports.

REFERENCE

[1] Antonio F. Barbosa and Gabriel O. Ribeiro, "Analysis of Reinforced Concrete Structures Using Ansys Nonlinear Concrete Model", Computational Mechanics, New Trends and Applications, Barcelona, Spain (1998).

[2] L. Dahmani, A. Khennane, and S.Kaci, "Crack Identification in Rein-forced Concrete Beams using ANSYS Software," Strength of Materials, Vol. 42, No. 2, pp. 232–240, 2010.

[3] A.J. Wolanski, "Flexural Behavior of reinforced and Prestressed Concrete Beams Using Finite Element Analysis", Master of Science The-sis, Marquette University, Wisconsin, 2004.

[4] D. Kachlakev, T. Miller, S. Yim, "Finite Element Modeling of Rein-forced Concrete Structures Strengthened with FRP Laminates", Final Report SPR 316, Oregon Department of Transportation, 2001.

[5] M.Y.H. Bangash, "Concrete and Concrete Structures: Numerical Modeling and Applications", Elsevier Science Publishers Ltd., London, England. 1989.

[6] J.G. MacGregor, "Reinforced Concrete Mechanics and Design", Prentice-Hall, Inc., Englewood Cliffs, NJ., 1992.

[7] K.J. Willam, and E. P. Warnke, "Constitutive Model for Triaxial Behavior of Concrete," Seminar on Concrete Structures Subjected to Triaxial Stresses, International Association of Bridge and Structural Engineering Conference, Bergamo, Italy, 174. (1974)

Evaluation of strength and durability assessment for the impact of Rice Husk ash and Metakaolin at High Performance Concrete mixes

Article *in* Materials Today: Proceedings · June 2021

DOI: 10.1016/j.matpr.2021.05.449

A.N. Swaminathen
Adi Shankara Institute of Engineering Technology

Vivek Kumar Chandra Kumar
Gokaraju Rangaraju Institute of Engineering & Technology

Materials Today: Proceedings xxx (xxxx) xxx

Contents lists available at ScienceDirect

Materials Today: Proceedings

journal homepage: www.elsevier.com/locate/matpr

Evaluation of strength and durability assessment for the impact of Rice Husk ash and Metakaolin at High Performance Concrete mixes

A.N. Swaminathen [a], C. Vivek Kumar [b,*], S. Robert Ravi [c], Sohang Debnath [d]

[a] Civil Engineering, Sree Dattha Institute of Engineering and Science, Hyderabad, Telangana
[b] Civil Engineering, Gokaraju Rangaraju Institute of Engineering and Technolgy, Hyderabad, Telangana
[c] Civil Engineering, ACE Engineering College, Hyderabad, Telangana
[d] Civil Engineering, Malla Reddy Engineering College, Hyderabad, Telangana

ARTICLE INFO

Article history:
Received 31 March 2021
Received in revised form 19 May 2021
Accepted 21 May 2021
Available online xxxx

Keywords:
Metakaolin
Rice Husk ash
Water absorption
Permeability
Rapid Chlorine Penetration Test

ABSTRACT

Traditional concrete used within the manufacture of High-Performance Concrete (HPC) does not provide the essential consistency. To attain the expected workability, structural reliability, high strength, but durability under adverse environmental conditions, generally available concrete materials must be perfectly shaped to a significant level. available Metakaolin (MK) and Rice husk ash (RHA) acquired were used to replace cement by 0%, 5%mk + 10%rha, 7.5%mk + 10%rha, 10%mk + 10%rha, 5%mk + 12.5%rha, 7.5% mk + 12.5%rha, 10%mk + 12.5%rha, 5%mk + 15%rha, 7.5%mk + 15%rha and 10%mk + 15%rha of its weight in different proportioning. Integration of MK and RHA into concrete increases water requirements, when compared with the control ordinary Portland cement (OPC) blend, integration of MK and RHA greatly improves durability properties; thus, by use of MK and RHA will decrease cement consumption while improving the durability characteristics of concrete such as percentage of water absorption, sorpitivity test, effective porosity, permeability, resistance to acid and rapid chloride penetration tests. Hence, this research paper concludes with strength characteristics and durability parameters for MK and RHA based High Performance Concrete (HPC) mixes.

Selection and peer-review under responsibility of the scientific committee of the International Conference on Futuristic Research in Engineering Smart Materials.

1. Introduction

Concrete is a versatile material, despite of the serious contradictions, concrete remains the most used material in the world for construction of large-scale buildings. Lately, much consideration has been devoted to improving concrete's resilience, especially in adverse environmental conditions. Even during past three decades, it has become apparent that, in addition to hardness, workability also durability are critical requirements for improving concrete. For instance, in nuclear structures subjected to elevated temperatures, the concrete must be strong enough to withstand thermal cracks, and prestressed concrete bridges will not only be strong and have minimal shrinkage and creep. For such a reason, the development of HPC with a design life of more than 100 years, anywhere between 50 years, was prioritized, as well as achieving acceptable performance in a variety of harsh environments. The designer must find an appropriate substance to develop the concrete's durability properties to meet the above requirements.

When structural buildings are completed, these can have flaws such as cracks, spalling of concrete, reinforcement exposure, abnormal deflections, or even other indicators of distress. As building structures are exposed to hostile environments, their stability is a major concern. Structures can degrade due to physical/chemical or mechanical activity, and the components of the cementitious material are particularly vulnerable to exploitation by sulphate ions or chloride ions in aggressive environments such as marine environment. In certain cases, corrosion of steel reinforcement will lead to concrete spalling and degradation of structure quality. Prevent corrosion of structures by using Rice Husk Ash (RHA) and Metakaolin (MK) blends in High Performance Concrete (HPC) along with the structures constructed in marine environments must meet reliability requirements. Traditional concrete mixture is incapable of achieving long-term durability. As a result, HPC must meet the fundamental criteria of longevity. Traditional concrete mixture is incapable of achieving long-term durability.

* Corresponding author.

https://doi.org/10.1016/j.matpr.2021.05.449
2214-7853/
Selection and peer-review under responsibility of the scientific committee of the International Conference on Futuristic Research in Engineering Smart Materials.

Sivakumar et al. [1] have been evaluated the physical and chemical properties of fly ash, rice husk ash, and egg shell powder were investigated. Among the restraints considered were compressive and splitting tensile strength, flexure intensity, permeability, sorpitivity, total charge passed obtained from a rapid chloride permeability test (RCPT), and intensity of chloride ion diffusion. Wild et al. [2] in his study, contributed the construction industry's long-term sustainability, investigates the feasibility of using natural materials like metakaolin in place of Portland cement in the production of High-Performance Concretes (HPC). Thiedeitz [3] investigated the optimal combustion techniques, numerous studies on the best combustion technique have been written. Even most of the work was done in a laboratory environment. The difference in performance of RHA produced in a conservative environment against experimental conditions is useful for assessing and improving RHA production in the future. Luc Courard et al. [4] examined the effectiveness of inclusion and replacement percentages of Metakaolin, comparisons to ordinary Portland cement (OPC) are made.

According to Coleman and Page et al. [5], cement paste incorporated with 10% to 20% MK has better performance than plain Portland cement paste which bind chloride ions added by mixing of water, thus lowering the CI concentrations throughout the pore solution. Schneider [6] evaluation of initiatives and cutting-edge technologies that can significantly reduce the cement industry's CO_2 footprint, which becomes the reduction of emissions and save energy. As a result, HPC must meet the fundamental criteria of longevity. Densification and stabilization of the transition region will boost the characteristics of concrete, reducing the likelihood of micro cracking and in-homogeneity under duty load and increasing the coefficient of permeability as a result.

MK and RHA integration are considered a legitimate way to improve concrete longevity in addition to weight. It can be achieved mainly throughout the interfacial transition zone (ITZ), which has a higher porosity and higher water cement ratio than that of the bulk paste, as well as a different chemical and mineralogical structure as studied by Poon et al. [7]. It is claimed that the MK affects the composition and micro - structural of the ITZ, reducing ion transport and enhancing concrete resilience. It was found that Mehta et al. [8] that incorporating RHA into composites could result in substantial pore refinement throughout the matrix and interfacial region, lowering water permeability.

1.1. Research significance

The massive water adsorption capability, extremely high surface area, and micro spaces and indistinct particles in concrete mixtures cause segregation and bleeding. It is due to the beneficial impact of MK and RHA particles. The removal of bleeding of water results in a greater evolution zone among solid material and cement paste, resulting in a much more non – permeable and stable concrete stated by Aziz et al. [11]. The integration of pozzolanic compounds as a partial substitute for ordinary Portland cement binder in concrete or mortar is also an efficient way of enhancing the fresh state and hardened state properties. This is because the calcium hydroxide Ca $(OH)_2$ formed by cement hydration reacts with pozzolanic materials substances such as RHA, MK, Fly ash, and Silica Fume, leading to the formation of supplementary calcium silicate hydrate (C-S-H) gel, that inhibits present pores and changes pore structure component. The formulation of this gel will help concrete last longer for its durability. This paper mainly focuses on the characteristics required to produce durable concrete materials, as well as mixture proportions and recommendations for building structures which will last more than 100 years. Finally, as per previous literatures, it have been concluded that, available Metakaolin (MK) and Rice husk ash (RHA) acquired were replaced with cement by 0%, 5%mk + 10%rha, 7.5%mk + 10%rha, 10% mk + 10%rha, 5%mk + 12.5%rha, 7.5%mk + 12.5%rha, 10% mk + 12.5%rha, 5%mk + 15%rha, 7.5%mk + 15%rha and 10% mk + 15%rha of its weight, and also strength and durability parameters like percentage of water absorption, permeability and rapid chloride penetration (RCPT) tests have been taken for this study.

2. Investigation of RHA and MK based HPC

2.1. Materials and characterization

All the concrete combinations were made with Ordinary Portland cement (OPC) corresponding to ASTM C. The chemical and physical characteristics of cement. As pozzolanic material substance like MK and RHA are widely available were listed in Table 1.

The RHA were obtained through calcination of metakaolin at temperature variation in between 700 and 900 degrees Celsius for a few minutes (Min-Hong Zhang et al., 1996). Metakaolin is a by-product of super fine pozzolana, which is developed by calcining metakaolin at high temperature in between 700 and 900 degrees Celsius and is primarily composed of alumina and silica stated by J.M. Khatib et al. [2]. Fig. 1 displays Metakaolin and Rice Husk Ash using a digital imaging microscopic tool for scanning electron microscope (SEM). These particles formation of the RHA is spherical, asymmetrical, and consistent, while the soft masses of the Metakaolin are observed, indicating amorphicity of the samples.

High temperatures impact concrete's characteristic compressive strength, modulus of elasticity, mass density, and appearance of surface, according to Savva et al., [19] and according to studies of Aydin [20] cement replacement by pozzolanic materials was the method to enhance fire resistance of the concrete. RHA is a highly reactive pozzolanic substance because of this property, making it suitable for use in lime-pozzolanic blends and as a cement substitute. The reaction of Rice Husk Ash throughout the presence of lime is attributed to a combination between two aspects: non-crystalline siliceous content and with specific surface area. Mohseni et al. [28] examine the impact of using metakaolin and rice husk ash as partial replacement materials for cement and polypropylene as just an addition upon on moisture content characteristics and mechanical properties of concrete in an experimental study.

By dissipating in cement pastes, Portland cement provide a huge proportion of nucleation cites only for precipitation of heat of hydration in materials which have been identified in Scanning Electron micrograph for MK and RHA as mentioned in Fig. 1(a) for MK and Fig. 1(b) for RHA. As just a consequence of every pozzolanic activity between the nebulous silica of its mineral incorporation, even with the CH, this process provides the most homogeneous and denser paste in terms of the available of finer pores [10]. Absolute density and fineness of binders, initial setting time, chemical and mineralogical structure of hydrated additives, flexural and compressive forces, and moisture content of mortars were all measured after 7, 28, and 56 days. By using Energy Dispersive X-Ray Analysis (EDAX) analysis Micrographs of hardened binder blends with MK as in Fig. 2(a) and RHA in Fig. 2(b) particles have taken after 56 days enabled researchers to assess the solidification of various matrixes as well as the formation of pores as studied by Ndigui Billong [26].

The materials of concrete were mixed thoroughly as per ASTM C192 in a drum mixer for about 10 min. Cubes with 150 × 150 mm × 150 mm were casted for each mix to obtain the characteristics strength and durability test parameters. Sample specimens with cube mould were well compacted on a concrete vibrating table. All the casted specimens were perfectly covered

Table 1
Physical and Chemical Characteristics OPC, MK and RHA.

	Properties	Ordinary Portland Cement	Metakaolin	Rice Husk Ash
Physical	Specific gravity	3.12	2.60	2.22
	Particle size Distribution	20 μm	2.5 μm	7 μm
	Specific area m^2/kg	325	13,000	11,250
	Colour	Grey	Off-white	Grey
	PH	12	5.5	8
Chemical composition	Silica	21.54	52	85
	Aluminum oxide	4.68	46	0.5
	Iron oxide	2.46	0.6	0.26
	Titanium dioxide	–	0.65	0.01
	Calcium oxide	62.58	0.09	1.45
	Magnesium oxide	1.08	0.03	0.6
	Sodium oxide	0.24	0.1	1.8
	Potassium oxide	0.87	0.03	3.21
	Loss on Ignition	2.58	1	4% maximum

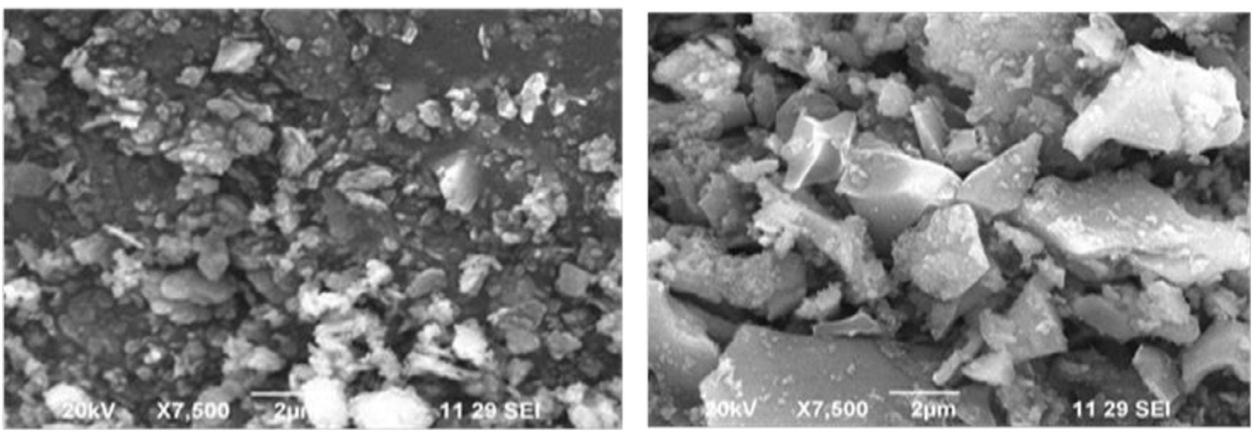

Fig. 1. (a) Scanning Electron micrographs of MK; (b) Scanning Electron micrographs of RHA.

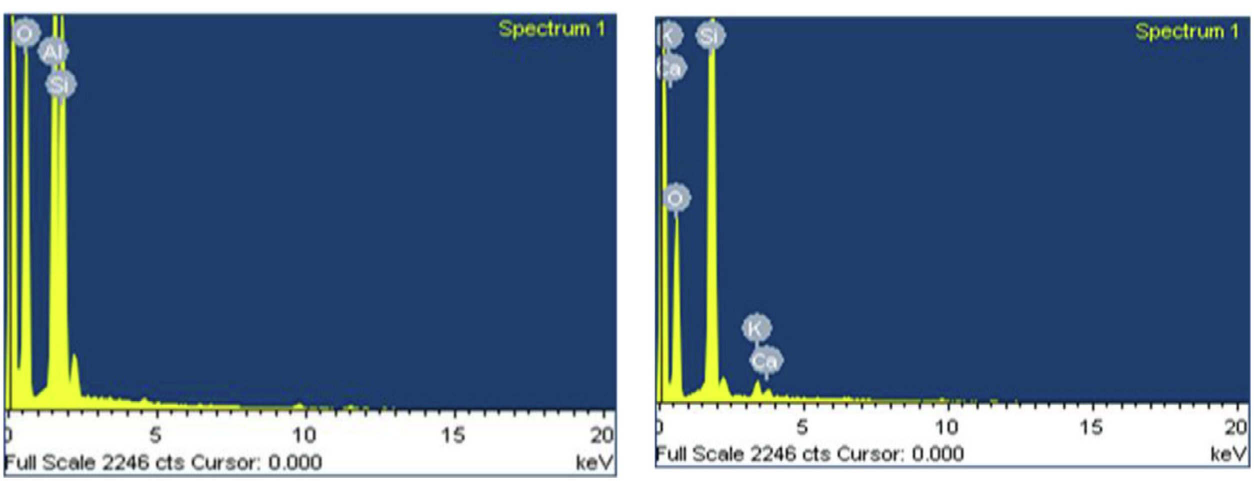

Fig. 2. (a) EDAX of 100% MK particles; (b) EDAX of 100% RHA particles.

for 24 h; the samples were submersed in curing tank for required curing period.

3. Experimental investigation

Nine different proportions of concrete blends, along with a control mix, was designed in this study. Across all nine combinations, the water cement ratio (w/c) were 0.31, and also the control OPC concrete were designed to produce M60 and HPC cubes for M60 grade by using BIS / ACI approaches by Perumal et al., based upon this, the cement content of 560 kg/m3, 476 kg/m^3, 462 kg/m^3, 448 kg/m^3, 462 kg/m^3, 448 kg/m^3, 434 kg/m^3, 448 kg/m^3 and 420 kg/m^3 were adopted for each of the grades.

Mareike Thiedeitz et al. [3] found that raising the RHA content concluded in very low workability, so Superplasticizer (SP) has been used to enhance the fluidity of the blends. The specific gravity test was performed in compliance to ASTM C127 [12] guidelines.

This level is smaller than OPC's level of 3.15, suggesting that RHA is less dense than OPC. Consequently, as per ASTM C127 [12] specifications for coarse and fine aggregates, the specific gravity of siliceous river sand was found to be 2.65, which varies within in the specific gravity with the scale of 2.5–2.9.

As mentioned, coarse aggregate, fine aggregate, and binder were used to build a mix design for M60 grade concrete for making the high-performance concrete with their target strength = 96 MP a) for this analysis. The weight ratio of the materials became 1:1.53:2.2:0.31. (Cement: Fine aggregate: Coarse aggregate: Water) as proportioned in Table Traditional concrete mixtures normally contain a lot of mixing water for two reasons: To begin with, distribution of particle size, particle filling impact, and spaces throughout the solid stable system have a major impact on the water demand as well as workability. The results of slump in and Table 4 and Fig. 4a was achieved by modifying the SP dose from 100 to 150 mm. Mix proportions for control OPC and different Metakaolin and Rice Husk Ash concrete mixes for grade M60 in Table 3.

Concrete specimens were examined on a Compression Testing Machine (CTM) in attempt to decide their characteristic strength, and the ASTM C192 Standard was fulfilled. Compressive strength as mentioned in Fig. 3a was determined using concrete cubes (150*150*150 mm) and indirect tensile strength as shown in Fig. 3b was determined using cylinder samples (200*100 mm) as shown in Table 4 and Fig. 4b. After immersion in water, the characteristic strength test on 150 mm size cubes is performed according to BIS: 516-1959 between age of 7, 14, 28, and 56 days. The experimental testing been conducted for the durability characteristics was saturated water absorption, Rapid Chloride Penetration Test in Fig. 3c (RCPT) and permeability. Saturated water absorption (SWA) measurements have been performed on a 100 mm concrete cube only on ages of 28 and after 90 curing days accordance with ASTM C 642[15].

Before drying, the specimen is weighed and a dried in an oven about 105℃. The drying processes were performed until the distinction among two consecutive experiments on a 24-hour period was nearly identical. After cooling to atmospheric conditions, the dried samples were submerged in water. The water absorption was determined by,

$$\textit{Percentage water absorption} = W_S - W_d/W_d \times 100$$

where, W_s = Mass of specimen at completely saturated form and W_d = Mass of oven dried sample

To determine the electrical conductance of M60 grade HPC mix after 28 days of curing, an RCPT test were performed according to ASTM C 1202 [14]. The specimens used for this experiment was 102 mm × 51 mm cylindrical specimens, and the RCPT testing setup consisted of two reservoirs, also with specimen sample held between the reservoirs using an bonding agent made with epoxy to allow the experiment set up as leakage proof. The first reservoir contained with 0.3 N with NaOH solutions, while the second stored with 3 percent sodium chloride solution. Electrodes were used to apply a 60-volt direct current through the specimen. According to ASTM C 1202 [14], the overall charge transmitted for the period was assessed in coulombs.

$$Q = 900(I_0 + 2I_{30} + 2I_{60} + \dots\dots\dots\dots + 2I_{330} + 2I_{360})$$

Where, Q - charge which passed in coulombs and

I_0 - current instantly when voltage is employed.

At the ages of 28 and also 90 days, water permeability tests were completed on 150 × 150 mm size cubes as per DIN 1048 part V section 3.6 (German standard). The formulae were used to calculate permeability, as followed by;

$$K = Q/AT\,(H/L)$$

K - Coefficient of permeability in cm/sec,

Q - Amount of water in millilitres penetrative over the entire period of examination after the steady state have been attained.

A - Specimen area in cm^2,

T - Time taken in seconds around which Q is evaluated.

H/L - Proportion of pressure head to thickness of specimen.

4. Result and discussions

4.1. Workability of concrete

The degrees of workability of concrete mixes are observed from Slump shown in table 4. The percentage of metakaolin (MK) and rice husk ash (RHA) are incremented, because of the high surface area of MK and RHA. The slump value is gradually diminished with the increments of the replacement level of RHA + MK. This condition is caused by the high reactivity and higher surface area of RHA and MK when contrasted with OPC. The same phenomenon is accounted by Kannan [26]. 'Silica fume and metakaolin generally requires addition of superplasticizer so that concrete could gain its desired workability. The utilization of MK diminished the workability and to get the required slump, High range water reducing admixtures (HRWRA) is essential. HRWRA brought about deflocculation of MK particles and thus a well dispersion of MK particles is accomplished. Hence, it is presumed that the utilization of HRWRA is extremely fundamental in concrete containing fine particles like MK to accomplish well dispersion and better outcomes. This is also expressed by Paiva, H et al. [27].

4.2. Cube compressive strength

It is observed that the compressive strengths at the age of 7 days for HPC trial mixes containing 0, 5 + 10, 7.5 + 10, 10 + 10, 5 + 12.5, 7.5 + 12.5, 10 + 12.5, 5 + 15, 7.5 + 15 and 10 + 15 percent replacements are 40.98, 45.54, 47.65, 46.58, 49.44, 56.44, 51.28, 54.37, 53.79 and 44.34 MPa respectively. The compressive strengths of the HPC trial mixes Mc to M9 at the age of 28 days are 60.20, 55.58, 59.10, 59.91, 69.88, 71.42, 66.50, 63.16, 62.16 and 61.16 MPa respectively. In addition, at the age of 56 days are 64.90, 60.76, 63.71, 68.99, 75.81, 78.86, 76.33, 73.44, 68.84 and 65.36 MPa respectively.

The cube compressive strength at the age of 28 days are gradually developing from 55.58 MPa to 71.42 MPa for the cement replacement level values of 5%Mk + 10%RHA to 7.5%MK to 12.5% RHA (M1 to M5) and lessening to 66.50 MPa to 61.16Mpa for 10%MK + 12.5%RHA to 10%MK + 15%RHA cement replacement level values. From the Table 5, it is noted that in all the ages, the cube compressive strength is increasing for mixes M1 to M5 and diminishing for mixes M6 to M9. Therefore, from the test outcomes, it is presumed that the maximum compressive strength is acquired for

Table 2
Mix proportions for M60 grade concrete as per ASTM C.

Mix	W/C	Cement kg/m³	Fine Aggregate kg/m³	Coarse Aggregate kg/m³	Water lit/m³	SP dosage in %
M60	0.31	500	765.38	1100	155	4.92
Final Mix proportion arrived for M60 grade				***1 : 1.53 : 2.2***		

Table 3
Mix proportions for control and various MK/RHA concrete mixes.

Mix	W/C	% replacement		Mass of cement kg/m^3	Weight of MK kg/m^3	Weight of RHA kg/m^3	Weight of fine aggregate kg/m^3	Weight of coarse aggregate kg/m^3	Water lit/m^3	SP dosage in %
		MK	RHA							
Mc	0.31	0	0	560	0	0	639.39	1100	152.06	2.5
M1	0.31	5	10	476	28	56	616.65	1100	152.06	2.6
M2	0.31	7.5	10	462	42	56	614.41	1100	152.06	2.7
M3	0.31	10	10	448	56	56	612.17	1100	152.06	2.8
M4	0.31	5	12.5	462	28	70	612.08	1100	152.06	2.7
M5	0.31	7.5	12.5	448	42	70	609.84	1100	152.06	2.8
M6	0.31	10	12.5	434	56	70	607.60	1100	152.06	2.9
M7	0.31	5	15	448	28	84	607.51	1100	152.06	2.8
M8	0.31	7.5	15	434	37.5	84	619.13	1100	152.06	2.9
M9	0.31	10	15	420	50	84	618.27	1100	152.06	3.0

(a) Compression Testing of Cubes (b) Permeability test (c) Rapid Chlorine Penetration test

Fig. 3. (a) Compression Testing of Cubes. (b) Permeability test. (c) Rapid Chlorine Penetration test.

Table 4
Workability for control and various MK/RHA concrete mixes.

Mix	% replacement		Slump Value in mm
	MK	RHA	
Mc	0	0	560
M1	5	10	476
M2	7.5	10	462
M3	10	10	448
M4	5	12.5	462
M5	7.5	12.5	448
M6	10	12.5	434
M7	5	15	448
M8	7.5	15	434
M9	10	15	420

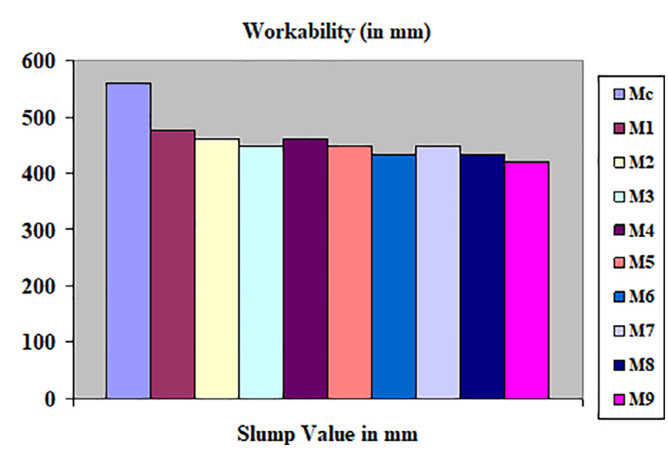

Fig. 4a. Slump results of M60 grade MK/RHA HPC mixes.

blended admixtures of 7.5% MK and 12.5% RHA by partial replacement by weight of cement. Moreover, as the MK and RHA content in HPC mixes increases from zero percent, the cube compressive strength gradually increases up to 7.5%MK and 12.5%RHA content and beyond this level it gradually diminishes. This is because the increase in compressive strength is due to pozzolanic reaction and filler effect of MK and RHA.

Kannan [26] pronounced the cube compressive strength of 55.67 MPa at the age of 28 days with w/b ratio of 0.55 and with 30% (15 + 15%) of RHA + MK combined ternary blended self-compacting concrete. Nguyen et al. [28] demonstrated blend of cement with 10% RHA and 10% SF gave preferable compressive strength than the control sample without RHA and SF. Saraswathy et al. [29] recommended that the blend of cement with 25% RHA gave preferred compressive strength than the control sample without RHA. Justice et al. [30] declared a comparative study by replacing 8% by weight of cement with metakaolin and silica fume proved to be beneficial which gave higher compressive strength.

4.3. Permeability

The coefficient of permeability values is observed to be negligible for HPC mixes and the outcomes are appeared in Table 6. The impact of MK and RHA and variation of permeability at the age of 28 days and 56 days with various percentages of MK and RHA are plotted in the Fig. 5c. The expansion of MK and RHA with con-

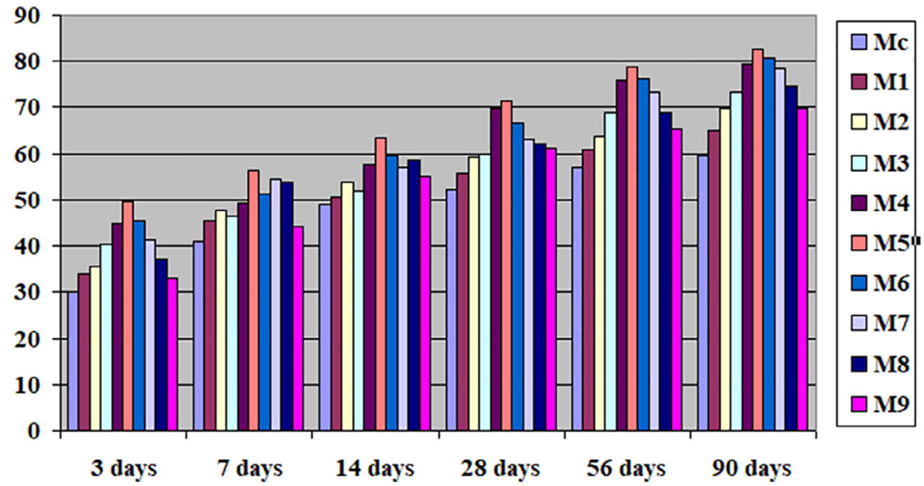

Fig. 4b. Results showing Compressive Strength for M60 RHA & MK mixes.

Table 5
Compressive strength results of M60 grade mixes at different ages MK/RHA concrete mixes

Mix	% replacement		Average cube compressive strength in N/mm^2					
	MK	RHA	3 days	7 days	14 days	28 days	56 days	90 days
Mc	0	0	30.23	40.98	48.87	52.31	57.10	59.50
M1	5	10	34.09	45.54	50.71	55.58	60.76	65.10
M2	7.5	10	35.69	47.65	53.89	59.10	63.71	69.80
M3	10	10	40.23	46.58	52.00	59.91	68.99	73.25
M4	5	12.5	44.91	49.44	57.59	69.88	75.81	79.34
M5	7.5	12.5	49.59	56.44	63.44	71.42	78.86	82.56
M6	10	12.5	45.46	51.28	59.42	66.50	76.33	80.61
M7	5	15	41.33	54.37	56.87	63.16	73.44	78.62
M8	7.5	15	37.20	53.79	58.56	62.16	68.84	74.76
M9	10	15	33.07	44.34	55.23	61.12	65.36	69.76

Table 6
Split Tensile strength and Permeability results of M60 grade MK/RHA concrete mixes

Mix	% replacement		Split tensile strength at 28 days (N/mm^2)	Permeability coefficient 10^{-7} cm/sec		Charge passed as per ASTM equivalent (coulombs)	Remarks
	MK	RHA		28 days	56 days		
Mc	0	0	4.32	7.24	6.84	937	Very low
M1	5	10	4.82	6.88	6.48	722	Very low
M2	7.5	10	5.07	6.58	6.20	632	Very low
M3	10	10	5.42	6.18	5.80	595	Very low
M4	5	12.5	5.77	5.74	5.36	487	Very low
M5	7.5	12.5	6.30	5.26	4.88	438	Very low
M6	10	12.5	5.82	5.66	5.28	426	Very low
M7	5	15	5.47	6.06	5.68	385	Very low
M8	7.5	15	5.32	6.42	6.04	308	Very low
M9	10	15	5.17	6.64	6.22	272	Very low

crete provides better interlocking between the aggregate and cement paste [8]. The permeability value continues diminishing for the HPC mixes from M1 to M5 and increasing trend from M6 to M9. The permeability of the concrete diminishes, because of extreme fineness. From the outcome it is presumed that the utilization of MK and RHA brought about practically impermeable concrete.

Speare et al. and Kartini et al. clarified that the incidence of control concrete was around 3 and 7 times more porous than RHA20 and RHA30 concretes, likewise they expressed the fact that the incidence of RHA led to the diminished coefficient of permeability. Malathy and Subramanian [31] acquired coefficient of permeability of the order of 6.5×10^{-7} to 7.6×10^{-7} cm/sec for concrete mixes containing 5 to 15 percent of cement replacement by silica fume. These observations demonstrate that the HPC mixes developed in the present investigations is considered to have indicated very good performance from the consideration of permeability.

5. Conclusions

5.1. Fresh and mechanical properties of HPC blends

The workability of concrete is observed from slump, compaction factor and Vee-Bee degree, which diminishes as the percentage of MK and RHA in concrete increments as shown in

Fig. 4a. This is not just because of the fact; it is the percentage of MK and RHA increment the water accessible in the system diminishes, thus affecting the workability but also due to the presence of high pozzolanic reactive nature of MK and RHA, which liberates calcium hydroxide.

5.2. Compressive strength of HPC specimens

M60 grade concrete was constructed for this study with a total of 75 cubes, 25 cylinders and 30 prisms were casted with various mixtures, including all the blended mixes from Mc, M1 to M9 of M60 concrete. The following observations are found after the results were received. Metakaolin and Rice Husk Ash are both very fine materials that require the inclusion of a superplasticizer to make HPC workable.

The compressive (characteristic) strength of HPC mixes with Metakaolin and Rice husk ash is higher than that of HPC blended without MK and RHA at 3, 7, 14, 28, 56, and 90 days of curing as shown in Table 2. This demonstrates that using MK and RHA as supplementary cementitious material (SCM) causes a compressive strength increase. Since MK and RHA are pozzolanic materials, the compressive strength of blended HPC concrete progresses as both the proportion of MK and RHA increases from 7.5 to 12.5 percent as demonstrated in Fig. 4b. Also, at age of 28 days, a cement replacement ratio of 7.5 + 12.5 percent for MK and RHA in concrete blends was the optimum level for achieving M60 grade from HPC blends.

5.3. Permeability

For HPC blends, the coefficient of permeability values is found to be negligible, and the results are shown in Table 5. The effect of MK and RHA on permeability and variance of permeability at 28 and 56 days for different percentages with MK and RHA are described in Fig. 5 (Fig. 5a and Fig. 5b). MK and RHA expand with concrete, resulting in strong interlocking among aggregate and cement paste. From M1 to M5, the permeability of the HPC blends decreases, as well as from M6 to M9, this increase. Because of its excessive fineness, the concrete's permeability decreases. It is believed that use of the MK and RHA resulted in practically non - permeable concrete derived from the findings shown in Fig. 5c.

Fig 5a. Fractured Specimen of HPC of M60 graded mix.

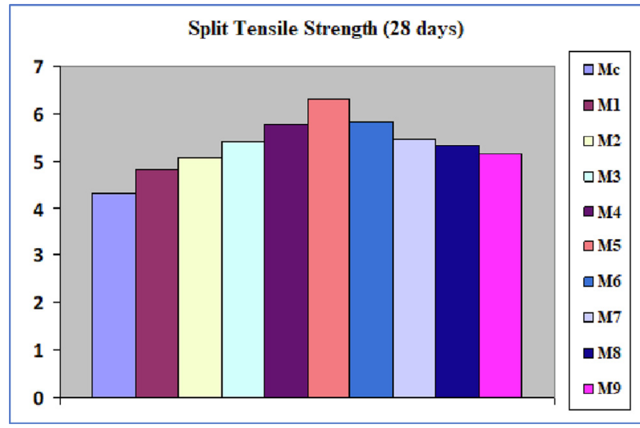

Fig. 5b. Split Tensile strength for 28 days (N/mm^2) results of M60 grade MK/RHA HPC mixes.

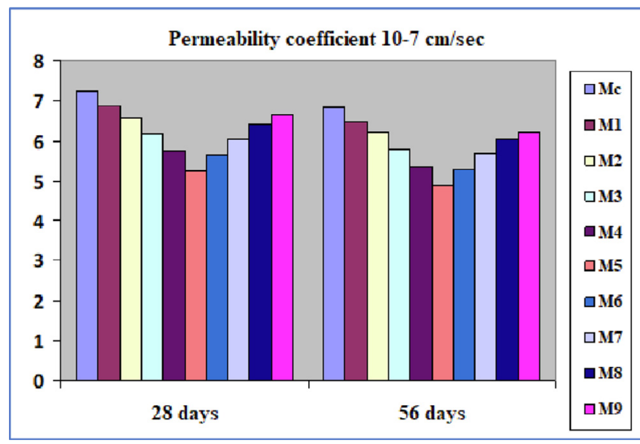

Fig. 5c. Permeability results for 28 and 56 days of M60 grade MK/RHA HPC mixes.

5.4. Rapid chloride Penetration

During the Rapid Chloride Penetration test as denoted in Fig. 5d, as compared to conventional concrete mixes, that MK and RHA concrete mixes had extremely low chloride ion penetrability. According to ASTM C 1202 [14], concrete mixtures of MK and

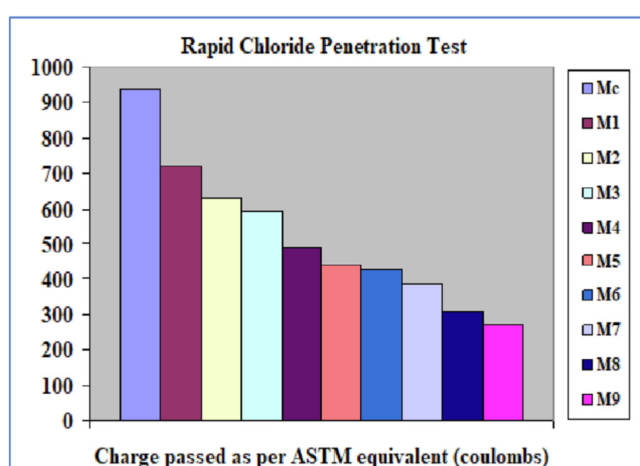

Fig. 5d. RCPT [14] results for MK/RHA HPC mixes.

RHA replacing 7.5 + 12.5% including its cement fit into the category with negligible chloride ion penetrability [16]. As a result, the higher the MK and RHA replacement rate, the greater the binding capability and the relatively lower the chloride ion penetrability of diffusivity. It has been illustrated that adding MK and RHA to concrete mixes as supplementary cementitious materials (SCM's) improves the concrete's durability but also non-corrosion properties, which is extremely effective during marine environmental conditions.

Declaration of Competing Interest

The authors declare that they have no known competing financial interests or personal relationships that could have appeared to influence the work reported in this paper.

References

[1] M. Sivakumar, N. Mahendran, Strength and permeability properties of concrete using fly ash, Rice husk ash and eggshell powder, J. Theor. Appl. Inform. Technol. 66 (2014) 489–499.
[2] S. Wild, J.M. Khatib, A. Jones, Relative strength, Pozzolanic activity and cement hydration in super plasticized Metakaolin concrete, Cem. Concr. Res. 26 (1996) 1537–1544.
[3] M. Thiedeitz, W. Schmidt, M. Härder, T. Kränke, Performance of Rice husk ash as supplementary cementitious material after production in the field and in the lab, Materials 13 (2020) 4319, https://doi.org/10.3390/ma13194319.
[4] L. Courard, A.D.M. Schouterden, F. Ferauche, X. Willium, R. Degeimber, Durability of mortars modified with metakaolin, Cem. Concr. Res. 33 (9) (2003) 1473–1479.
[5] M.F. Rojas, J. Cabrea, The effect of temperature on the hydration phase of metakaolin – lime-water system, Cem. Concr. Res. 32 (2002) 13–16.
[6] V. Antonovich, S. Goberis, The effect of different admixtures on the properties of refractory concrete with Portland cement, J. Mater. Sci. 9 (2003) 379–382.
[7] C.S. Poon, Z.H. Shui, L. Lam, Effect of microstructure of ITZ on compressive strength of concrete prepared with recycled aggregates, Constr. Build. Mater. 18 (6) (2004) 461–468.
[8] V Srinivasa Reddy, R Nirmala "Development of quaternary blended high performance concrete made with high reactivity metakaolin", International Journal of Engineering & Technology, ISSN: 2227-524X, indexed, 7 (2.1) (2018) pp. 79-83.
[10] Koniki Srikanth, P.D. Ravi, A study on mechanical properties and stressstrain response of high strength concrete reinforced with polypropylene–polyester hybrid fibres, Cement, Wapno, Beton 1 (2018) 67–77.
[11] A.N. Givi, S.A. Rashid, F.N.A. Aziz, M.A.M. Salleh, Contribution of rice husk ash to the properties of mortar and concrete: a review, Am. J. Sci. 6 (3) (2010) 157–165.
[12] ASTM C127, America Standard of Testing Materials International, West Conshohocken. Standard test method for specific gravity and absorption of coarse aggregate, (2015).
[14] V. Srinivasa Reddy, R. Nirmala, Development of quaternary blended high performance concrete made with high reactivity metakaolin, Int. J. Eng. Technol. 7 (2.1) (2018) 79–83, https://doi.org/10.14419/ijet.v7i2.1.11048, ISSN: 2227-524X.
[15] ASTM C 1202, Electrical Indication of Concrete's Ability to Resist Chloride Ion Penetration, Vol. 4.02, Annual Book of American Society for Testing Materials, Philadelphia, 2000.
[16] Srinivas T and R. N. Koushik , "Sulphate attack Resistance of Geo-polymer Concrete made with Partial Replacement of Coarse Aggregate by Recycled Coarse Aggregate" International Journal of Innovative Technology and Exploring Engineering , ISSN: 2278-3075, 8(12), DOI:10.35940/ijitee.L2509.1081219, (2019) pp. 112-117.
[19] M.H. Zhang, M.V. Malhotra, High-performance concrete incorporating rice husk ash as a supplementary cementing material, ACI Mater. J. 93 (6) (1996) 629–636.
[20] A. Savva, P. Manita, K.K. Sideris, Influence of elevated temperatures on the mechanical properties of blended cement concretes prepared with limestone and siliceous aggregates, Cement Concr Res. 27 (2005) 239–248.
[26] V. Kannan, Relationship between ultrasonic pulse velocity and compressive strength of self compacting concrete incorporating rice husk ash and Metakaolin 2 (2015) 66–71
[27] H. Paiva, A. Velosa, P. Cachim, V.M. Ferreira, Effect of Metakaolin dispersion on the fresh and hardened state properties of concrete, Cem. Concr. Res. 42 (4) (2012) 607–612.
[28] N. Van Tuan, G. Ye, K. Van Breugel, A.L.A. Fraaij Bui, D. Dai, The study of using Rice husk ash to produce ultra-high performance concrete, Constr. Build. Mater. 25 (4) (2010) 2030–2035.
[29] V. Saraswathy, H.W. Song, Corrosion performance of Rice Husk Ash blended concrete, Constr. Build. Mater. 21 (8) (2007) 1779–1784.
[30] J.M. Justice, L. Kennison, B. Mohr, S. Beckwith, L. McCormick, B. Wiggins, Z. Zhang, K. Kurtis, in: Comparison of two Metakaolins and a Silica Fume used as Supplementary Cementitious Materials, SP-228, ACI, Farmington Hills, 2005, pp. 217–228.
[31] R. Malathy, K. Subramanian, Role of mineral admixtures on the corrosion behavior of reinforcement in High Performance Concrete, in: proceedings of the National seminar on Futuristic in Concrete and Construction Engineering, SRMEC, Chennai, 2003, vol. 2, pp. 5.17–5.24.

Further reading

[9] H.B. Mahmud, E. Majuar, M.F.M. Zain, N.B.A.A. Ham id, Mechanical properties and durability of high strength concrete containing Rice husk ash, J. Adv. Concr. Technol. 79 (1) (2009) 21–30.
[13] ASTM C136. ASTM International, West Conshohocken: Standard Test Method for Sieve Analysis of Fine and Coarse Aggregates (2014).
[17] ASTM C642, America Standard of Testing Materials International, West Conshohocken: Standard test method for density, absorption, and voids in hardened concrete, 2013.
[18] O. Arioz, Effect of elevated temperature on properties of concrete, Fire Saf. J. 42 (2007) 516–522.
[21] S. Aydin, H. Yazici, B. Baradan, High temperature resistance of normal strength and autoclaved high strength mortars incorporated polypropylene and steel fibers, Constr Build. Mater. 22 (2008) 504–512.
[22] N.P. Hasparyk, P.J. Monteiro, H. Carasek, Effect of silica fume and rice husk ash on alkali-silica reaction, Materials J. 97 (4) (2000) 486–492.
[23] K. Sakr, Effects of silica fume and rice husk ash on the properties of heavy weight concrete, J. Mater. Civ. Eng. 18 (3) (2006) 367–376.
[24] V. Goud, N. Soni, G. Varma, K. Kushwah, S. Chaurasia, V. Sharma, Partial replacement of cement with fly ash in concrete and its effect, IOSR J. Eng. 6 (10) (2016) 69–75.
[25] Z. Li, J. Peng, B. Ma, Investigation of chloride diffusion for high-performance concrete containing fly ash, microsilica and chemical admixtures, ACI Mater. J. 96 (3) (1999) 391–396.

Flexural behaviour of hybrid fibre reinforced concrete beams made with various packing factors and fine to total aggregate ratio

V Siva Prasad Raju[1*], *Gorla* Jayasri[2], *Srinivasa Reddy* V[3] and *A* Naga Sai Baba[4]

[1]Assistant Professor of Civil Engineering, GRIET, Hyderabad, India. [1]
[2]M. Tech (Structural Engineering), Department of Civil Engineering, GRIET, Hyderabad, India.
[3]Professor of Civil Engineering, GRIET, Hyderabad, India.
[4]Assistant Professor of Civil Engineering, MREC, Hyderabad, India.

Abstract. The objective of this study is to investigate the flexural behavior of M30 grade PSCC, GFRSCC, SFRSCC and HFRSCC beams made with PF=1.12 and s/a=0.53 and PF=1.14 and s/a=0.57 to understand the effect of copper slag as partial replacement of fine aggregate on its deflection characteristics and cracking behaviour. The yield and ultimate load taken by HFRSCC beams made with optimum PF and s/a ratios are higher than the conventional RCC beam elements. The deflections at centre at failure in HFRSCC beams made with optimum PF and s/a ratios were more than that of conventional beams. This shows improvement in ductility of HFRSCC beams. First crack formation was delayed in M30 grade HFRSCC beams due to dense micro structure with low pore fraction and reduced pore size due to which fatigue strength is increased which in turn increases the time taken for first crack occurrence and thereby increasing the load carrying capacity. The deflection at the mid span decreased in HFRSCC beams which shows that the flexural stiffness of the elements increases thereby reducing the structural member's deformability, increasing strength and hence controlling deflection.

1 Introduction

Self-Compacting concrete, originally developed in Japan has given answers to many mechanical and durability problems and enhanced the strength and durability characteristics of concrete. Introduction of fibers in SCC has further improved its characteristics like crack, resistance, plasticity, impact resistance, durability etc., The Studies on Stress-Strain behavior of concrete are essential in determining the parameters like energy absorption, toughness, plasticity index and they are very useful in design of structures using such concretes. Further modeling the stress-strain behavior helps in predicating their behavior. As only scant work is reported on the mathematical modeling of the stress strain behavior SCC and f FRSCC, an attempt is made to make M30 grade SCC, FRSCC, developed two mathematical models for stress-strain behavior after going thoroughly through different models for stress- strain behavior developed for vibrated concrete. The two models were compared for their suitability for SCC and FRSCC.

2 Methodology

The goal of this research is to look at the flexural behaviour of M30 grade PSCC, GFRSCC, SFRSCC, and HFRSCC beams with PF=1.12 and s/a=0.53 and PF=1.14 and s/a=0.57 to see how copper slag as a partial substitute for fine aggregate affects deflection and cracking behaviour. According to IS: 9399 – 1979, the beams are evaluated under symmetrical two-point flexural stress.

According to Nan Su's recommended criteria for SCC, the ideal packing factor and fine to total aggregate ratio are shown in Table 1. Different combinations of packing factors (PF) (ranging from 1.12 to 1.18) and fine to total aggregate ratios (s/a) (ranging from 0.50 to 0.57) were tested, and it was discovered that the PF & s/a combinations of 1.12 & 0.53 and 1.14 & 0.57 were the most effective, resulting in the highest

* Corresponding author: sprajuv@gmail.com

compressive strengths, which can be attributed to high particle packing densities in SCC mixes.

Table 1. Optimum PF and s/a ratio combinations for M30 grade PSCC mixes

Mix Type	PF	s/a ratio	Compressive Strength (MPa) at 28 days
M30PSCC1	1.12	0.53	40.35
M30PSCC2	1.14	0.57	41.03

Table 2. Dosage of percentage of glass fibre for M30 grade SCC mixes made with optimum combinations of PF and s/a ratios

Type	Percentage of Glass fibre by volume of Concrete	Glass fibre (kg/m^3)	Compressive Strength (MPa)
M30GFRSCC PF=1.12 and s/a=0.53	0.05	1.33	44.16
M30GFRSCC PF=1.14 and s/a=0.57	0.05	1.33	45.05

Table 3. Dosage of percentage of steel fibre for M30 grade SCC mixes made with optimum combinations of PF and s/a ratios

Type	Percentage of Glass fibre by volume of Concrete	Glass fibre (kg/m^3)	Compressive Strength (MPa)
M30GFRSCC PF=1.12 and s/a=0.53	1.0	78.50	43.40
M30GFRSCC PF=1.14 and s/a=0.57	1.0	78.50	44.27

Table 4. Fresh properties for M30 PSCC, SFRSCC, GFRSCC and HFRSCC mixes

	Optimum PFs and s/a ratios	Fly Ash %	Paste volume	Fresh properties					
				Slump (650-800 mm)	J-Ring (0-	V-Funnel	V-T5 (6-15	U-Box (0-30	L-Box (0.8-
M30PSCC	PF=1.12 and s/a=0.53	40.47	28.67	752	5	7	9	21	0.93
M30SFRSCC		40.47	28.67	670	9	10.24	12.27	29	0.82
M30GFRSCC		40.47	28.67	714	7	9.41	10.93	26	0.90
M30HFRSCC		40.47	28.67	708	8	9.81	11.44	28	0.87
M30PSCC	PF=1.14 and s/a=0.57	38.33	27.59	752	7	8	12	21	0.92
M30SFRSCC		38.33	27.59	682	11	9.30	13.81	29	0.83
M30GFRSCC		38.33	27.59	742	9	8.73	11.68	24	0.88
M30HFRSCC		38.33	27.59	727	10	8.90	12.55	28	0.86

Addition of fibre reduces workability in SCC mixes. Workability is reduced drastically in SFRSCC when compared to GFRSCC. In HFRSCC mixes, due to addition of steel and glass fibres workability is affected which can be improved using fly ash and super plasticizers

Table 5. Beam types and designations

Designation of beam	Mix type
Beam 1	M30PSCC PF=1.12 and s/a=0.53
Beam 2	M30SFRSCC PF=1.12 and s/a=0.53
Beam 3	M30GFRSCC PF=1.12 and s/a=0.53
Beam 4	M30HFRSCC PF=1.12 and s/a=0.53
Beam 5	M30PSCC PF=1.14 and s/a=0.57
Beam 6	M30SFRSCC PF=1.14 and s/a=0.57
Beam 7	M30GFRSCC PF=1.14 and s/a=0.57
Beam 8	M30HFRSCC PF=1.14 and s/a=0.57
Under reinforced M30 beams of size 1200 mm x 100 mm x 150 mm Grade of Steel -Fe 415 Tensile Reinforcement -2 No - 10mmφ Tor steel bars Nominal Compression Reinforcement -2 No - 10mm φ MS bars Shear Reinforcement -2 legged - 8mm φ @200mm c/c	

Experimental research revealed that 0.05 percent glass fibre by volume of concrete and 1.0 percent steel fibre by volume of concrete are the best doses of glass and steel fibres to utilise in M30 SCC mixtures. 0.05 percent glass fibre and 1.0 percent steel fibre by volume of concrete are utilised in hybrid fibre reinforced SCC mixtures.

3 Load – deflection relations

The goal of this research is to look at the flexural behaviour of M30 grade PSCC, GFRSCC, SFRSCC, and HFRSCC beams with PF=1.12 and s/a=0.53 and PF=1.14 and s/a=0.57 to see how copper slag as a partial substitute for fine aggregate affects deflection and cracking behaviour.

Table 6. Load deflections of M30 grade PSCC, GFRSCC, SFRSCC and HFRSCC beams made with PF=1.12 and s/a=0.53

Beam 1		Beam 2		Beam 3		Beam 4	
Load (kN)	Deflection (mm)	Load (kN)	Deflection (mm)	Load (kN)	Deflection (mm)	Load (kN)	Deflection (mm)
5	0.22	5	0.18	5	0.16	5	0.15
10	0.52	10	0.37	10	0.35	10	0.34
15	0.78	15	0.69	15	0.62	15	0.58
20	1.26	20	1.01	20	0.99	20	0.97
25	1.68	25	1.50	25	1.43	25	1.35
30	2.16	30	2.06	30	1.94	30	1.81
35	2.67	35	2.50	35	2.22	35	2.07
40	3.19	40	2.86	40	2.69	40	2.49
45	3.78	45	3.60	45	3.47	45	2.98
50	4.62	50	4.39	50	3.75	50	3.65
54	6.81	55	5.76	55	4.93	55	4.39
		60	5.93	60	5.28	60	5.10
		61	7.95	65	6.53	65	6.40
				68	10.27	70	6.57
						74	11

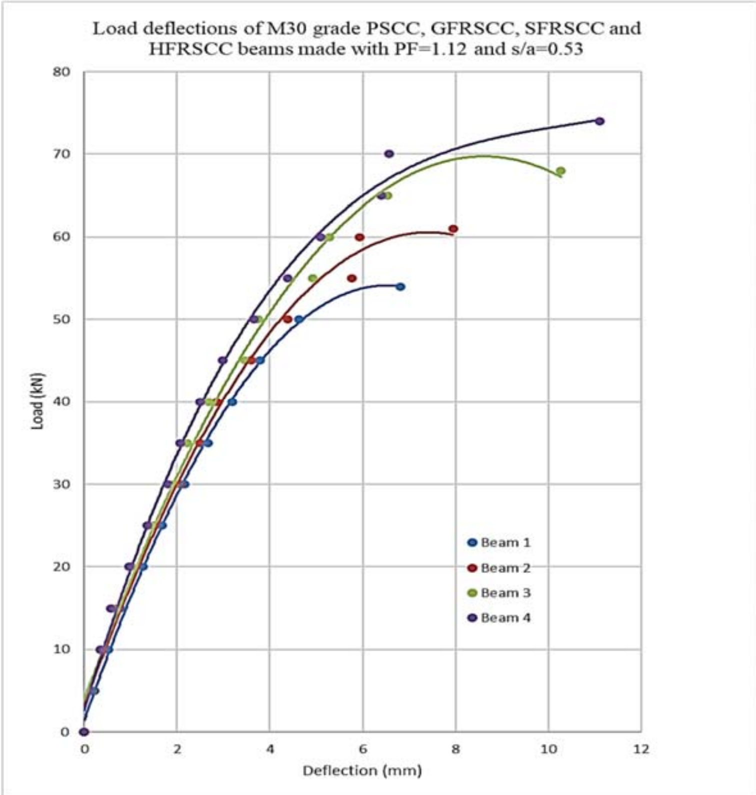

Fig.1. Load deflections curves of M30 grade PSCC, GFRSCC, SFRSCC and HFRSCC beams made with PF=1.12 and s/a=0.53

Table 7. Load deflections of M30 grade PSCC, GFRSCC, SFRSCC and HFRSCC beams made with PF=1.14 and s/a=0.57

Beam 5		Beam 6		Beam 7		Beam 8	
Load (kN)	Deflection (mm)	Load (kN)	Deflection (mm)	Load (kN)	Deflection (mm)	Load (kN)	Deflection (mm)
5	0.21	5	0.17	5	0.15	5	0.14
10	0.49	10	0.35	10	0.33	10	0.32
15	0.74	15	0.66	15	0.59	15	0.55
20	1.20	20	0.96	20	0.94	20	0.92
25	1.60	25	1.43	25	1.36	25	1.28
30	2.05	30	1.96	30	1.84	30	1.72
35	2.54	35	2.38	35	2.11	35	1.97
40	3.03	40	2.72	40	2.56	40	2.37
45	3.59	45	3.42	45	3.30	45	2.83
50	4.39	50	4.17	50	3.56	50	3.47
55	6.47	55	5.47	55	4.68	55	4.17
57	6.93	60	5.63	60	5.02	60	4.85
		65	7.55	65	6.20	65	6.08
		66	8.24	70	9.76	70	6.24
				73	10.89	75	10.55
						78	11.46

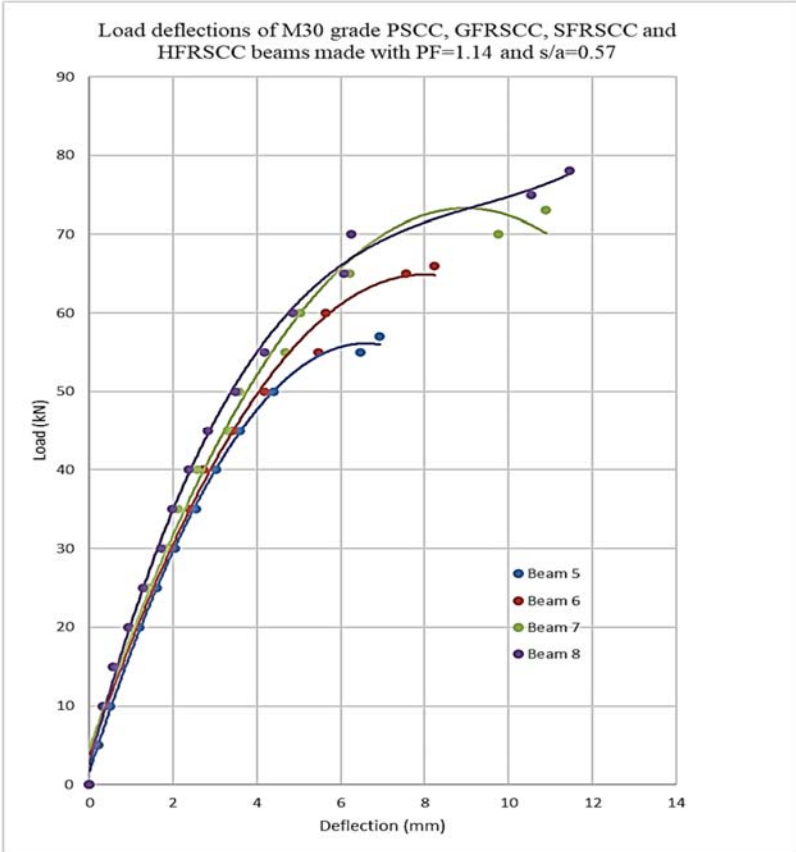

Fig.2. Load deflections curves of M30 grade PSCC, GFRSCC, SFRSCC and HFRSCC beams made with PF=1.14 and s/a=0.57

Table 8. Flexural Characteristics of M30 grade PSCC, GFRSCC, SFRSCC and HFRSCC beams made with various PF and s/a ratios

Beam Designation	M30 Grade Reference Concrete			
	Load at first crack occurrence (kN)	Load at Failure (kN)	Mid-deflection (mm)	Width of crack at failure (mm)
Beam 1	24	55	6.81	0.98
Beam 2	32	62	7.95	0.90
Beam 3	37	69	10.27	0.80
Beam 4	44	75	11.10	0.80
Beam 5	32	58	6.93	0.98
Beam 6	33	67	8.94	0.90
Beam 7	39	74	10.89	0.79
Beam 8	48	79	11.46	0.75

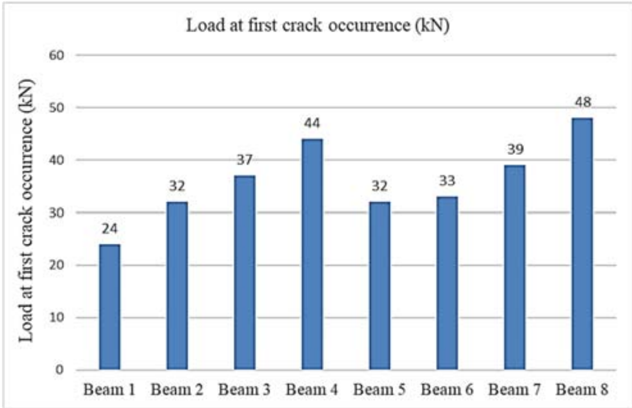

Fig.3. Load at first crack of M30 grade PSCC, GFRSCC, SFRSCC and HFRSCC beams made with various PF and s/a ratios

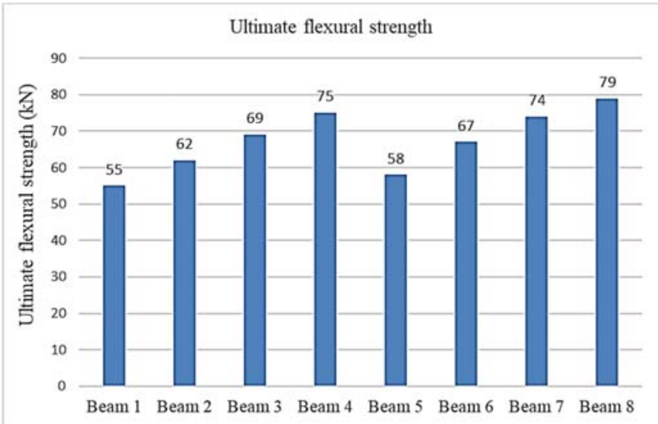

Fig.4. Ultimate flexural strength of M30 grade PSCC, GFRSCC, SFRSCC and HFRSCC beams made with various PF and s/a ratios

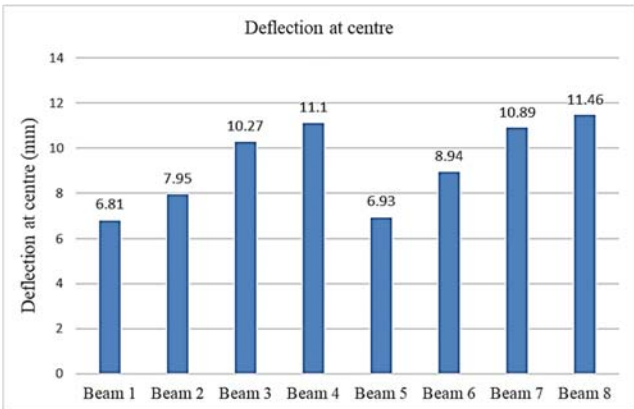

Fig.5. Deflection at centre of M30 grade PSCC, GFRSCC, SFRSCC and HFRSCC beams made with various PF and s/a ratios

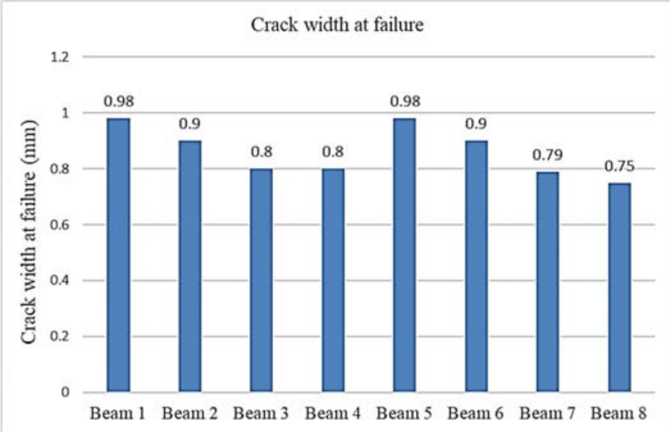

Fig.6. Crack width at failure of M30 grade PSCC, GFRSCC, SFRSCC and HFRSCC beams made with various PF and s/a ratios

4 Conclusions

Flexural parameters such as load at first crack, ultimate flexural strength, deflection at the centre, and crack width at failure are assessed using load–deflection plots. From these obtained results the following observations are made:

1. The yield and ultimate load taken by HFRSCC beams made with optimum PF and s/a ratios are higher than the conventional RCC beam elements.
2. The deflections at centre at failure in HFRSCC beams made with optimum PF and s/a ratios were more than that of conventional beams. This shows improvement in ductility of HFRSCC beams
3. In HFRSCC beams, using hybrid fibres enhances the load at first crack, ultimate flexural strength, and deflection at the centre of failure, while also reducing crack width.
4. The occurrence of the first crack was delayed in M30 grade HFRSCC beams due to a dense microstructure with low pore fraction and reduced pore size, resulting in increased fatigue strength, which in turn increases the time taken for the occurrence of the first crack and thus increases the load carrying capacity.
5. The mid-span deflection of HFRSCC beams reduced, indicating that the components' flexural stiffness increased, lowering the structural member's deformability, improving strength, and therefore regulating deflection.

References

1. Srinivas. T, Abhignya. G and Ramana Rao. N.V, A Review on Geopolymer RCC Beams made with Recycled Coarse Aggregate, E3S Web of Conferences, ICMED, 10-12 July 2020, India (2020).
2. T. Srinivas, S. V. Srinidhi and N.V. Ramana Rao, A Review on Flexural Behavior of RCC Beams Made with Geopolymer Concrete, E3S Web of Conferences, ICMED, 10-12 July 2020, India (2020).
3. T. Srinivas , P. Bhavana, and N. V. Ramana Rao, Effect of Manufactured Sand on Flexural Behavior of Geopolymer RCC Beams: A review, E3S Web of Conferences, ICMED, 10-12 July 2020, India (2020).
4. Srinivas Rao J, S K Tummala, Kuthuri N R, Indonesia Journal of Electrical Engg. & Computer Science, **21** (723), 2020
5. T. Srinivas and N.V.Ramana Rao, IJCIET, Volume **10**, 510 (2019).
6. K. Sai Gopi, Dr. T. Srinivas and S. P. Raju V, E3S Web of Conferences ICMED 184, 01084GRIET, 28-29 February, https://doi.org/10.1051/e3sconf/202018401108 4(2020)
7. Jagannadha Kumar, M.V., Jagannadha Rao, K., Dean Kumar, B., Srinivasa Reddy, V., Int. J. of Civil Eng. and Tech., 9(7), pp. 1133-1141 (2018)
8. Ganta, J.K., Seshagiri Rao, M.V., Mousavi, S.S., Srinivasa Reddy, V., Bhojaraju, C., Structures 28, pp. 956-972 (2020)
9. M. Kavitha, P. B. Bobba and D. Prasad, *2016 IEEE 7th Power India International Conference (PIICON)*, 2016, pp. 1-6
10. Naidu, K.S.S.T., Rao, M.V.S., Reddy, V.S., Int. J. of Innov. Tech. and Explor. Eng.g (IJITEE), 8(9 Special Issue 2), pp. 641-642 (2019)

11. Chandana Priya, C., Seshagiri Rao, M.V., Srinivasa Reddy, V., Int. J. of Civil Eng. and Tech., 9(11), pp. 2218-2225 (2018)
12. K. Satyanarayana, A. V. Gopal, and P.B. Babu, *Proceedings of the Institution of Mechanical Engineers, Part C: Journal of Mechanical Engineering Science*, ***228*(1)**, 152 (2014)
13. Satya Sai Trimurty Naidu, K., Seshagiri Rao, M.V., Srinivasa Reddy, V., Int. J. of Civil Eng. and Tech., 9(11), pp. 2383-2393 (2018)
14. Supriya, Y., Srinivasa Reddy, V., Seshagiri Rao, M.V., Shrihari, S., Int. J. of Rec. Tech. and Engi., 8(3), pp. 5381-5385 (2019)
15. Kotkunde, N., Krishna, G., Shenoy, S.K., Gupta, A.K., Singh, S.K. International Journal of Material Forming, 10 (2), pp. 255-266 (2017)
16. Govardhan, D., Kumar, A.C.S., Murti, K.G.K., Madhusudhan Reddy, G. Materials and Design, 36, pp. 206-214. (2012)
17. Kumar, P., Singhal, A., Mehta, S., Mittal, A. Journal of Real-Time Image Processing, 11 (1), pp. 93-109. (2016)
18. Raghunadha Reddy, T., Vishnu Vardhan, B., Vijayapal Reddy, P. International Journal of Applied Engineering Research, 11 (5), pp. 3092-3102 (2016)
19. Prashant Singh B.T., Babu Bobba Phaneendra and K. Suresh , E3S Web Conf., 87 (2019) 01010
20. Hussaini, S.M., Krishna, G., Gupta, A.K., Singh, S.K. Journal of Manufacturing Processes, 18, pp. 151-158 (2015)

International Journal of Electrical and Computer Engineering (IJECE)
Vol. 12, No. 4, August 2022, pp. 3375~3387
ISSN: 2088-8708, DOI: 10.11591/ijece.v12i4.pp3375-3387

A novel efficient adaptive-neuro fuzzy interfaced system control based smart grid to enhance power quality

Dharamalla Chandra Sekhar[1,2], Pokanati Veera Venkata Rama Rao[3], Rachamadugu Kiranmayi[1]
[1]Department of Electrical and Electronics Engineering, Jawaharlal Nehru Technological University Anantapur, Ananthapuramu, India
[2]Department of Electrical and Electronics Engineering, Malla Reddy Engineering College (A), Maisammaguda, India
[3]Department of Electrical and Electronics Engineering, Maturi Venkata Subba Rao Engineering College, Hyderabad, India

Article Info

Article history:

Received May 13, 2020
Revised Mar 13, 2022
Accepted Mar 26, 2022

Keywords:

Adaptive-neuro fuzzy interfaced system controller
MATLAB/Simulink
Maximum power point tracking
Power quality
PV-wind-grid integration
Smart grid

ABSTRACT

A novel adaptive-neuro fuzzy interfaced system (ANFIS) control algorithm-based smart grid to solve power quality issues is investigated in this paper. To improve the steady-state and transient response of the solar-wind and grid integrated system proposed ANFIS controller works very well. Fuzzy maximum power point tracking (MPPT) algorithm-based DC-DC converters are utilized to extract maximum power from solar. A permanent magnet synchronous generator (PMSG) is employed to get maximum power from wind. To maximize both power generations, back-to-back voltage source converters (VSC) are operated with an intelligent ANFIS controller. Optimal power converters are adopted this proposed methodology and improved the overall performance of the system to an acceptable limit. The simulation results are obtained for a different mode of smart grid and non-linear fault conditions and the proven proposed control algorithm works well.

Corresponding Author:

Dharamalla Chandra Sekhar
Department of Electrical and Electronics Engineering, Jawaharlal Nehru Technological University Ananthapur
Ananthapuramu, Andhra Pradesh, India
Email: daram.sekhar@gmail.com

1. INTRODUCTION

In recent years the usage of renewable energy sources (RES) is popular over traditional fossil fuel-based energy sources like hydro and thermal. RES sources are free from air pollutants (eco-friendly), with more reliability and optimum cost. Extract maximum power from solar different MPPT algorithms are proposed in the literature such as perturb and observe [1], incremental conductance (IC), fuzzy intelligent Maximum power point tracking (MPPT) [2]. In this paper to get maximum power from photovoltaic (PV), the fuzzy MPPT technique is adopted. Maximum power extracted from the wind with tip-speed ratio control, lower relationship-based, perturbation and observation (P&O), hybrid control [3] and intelligent control strategies [4], [5] based techniques like neural, fuzzy, and adaptive-neuro fuzzy interfaced system (ANFIS). Stand-alone integrated hybrid power sources [6], [7] are modeled and controlled well to satisfy the load demand [8]–[10]. It is further extended to dynamic energy management between the RES sources is proposed with conventional control techniques.

After doing a literature review, it was discovered that ANFIS is a popular controller due to its simplicity. As previously stated, it is frequently employed in power system applications. The filter parameter is the most difficult aspect of the ANFIS design. In real-time practice, this filter parameter is tuned based on the user's requirements. We know that the advanced control state feedback control strategy is more versatile, allowing for optimal design [11]–[14].

A blend of neural and fuzzy rationale procedures offers to take care of issues and challenges in the plan fuzzy have been executed by [15]. The new methodology in the design of the neural organization is known as a recurrent neural network (RNN) which is an improvement over the current controllers and actualized in [16]. The yield of a dynamic framework is a component of a past yield or previous information or both, thusly recognizable proof and control of dynamic framework are an inborn errand contrasted with static framework [16]–[21]. The feed forward neural fuzzy organizations have a significant downside so their application is restricted to static planning issues [22]–[27]. In this way, to recognize dynamic frameworks, repetitive neuro fuzzy organizations ought to be utilized. A Takagi–Sugeno–Kang (TSK)-type intermittent fuzzy organization is intended for dynamic frameworks.

In light of audit, it is presumed that the motions in the dynamic power frameworks can be damped by the versatile fuzzy controller [28]. The exploration work is done to check the presentation of FACTS gadgets for upgrading framework execution. The ANFIS controller is proposed for power stabilizer. The proportional integral derivative (PID), as ANFIS controller boundaries are prepared by particle swarm optimization (PSO) in [29], [30]. The ANFIS can be made as self-learning controller utilizing iterative learning strategy clarified. Developmental calculations are equal and worldwide pursuit methods. Since they all the while assess numerous focuses in the inquiry space, they are bound to unite toward the worldwide arrangement clarified.

The next sections of this article are composed as system configuration PV wind integrated grid in section 2. Proposed ANFIS control scheme in section 3. MATLAB environmental based simulation results are presented in section 4 and concluded in section 5.

2. SYSTEM CONFIGURATION

The model of grid integrated solar-wind smart grid system depicts in Figure 1. Smart grid systems include several critical qualities, including performance optimization, system dependability, and operational efficiency. A unique model of a smart grid-connected PV/WT hybrid system is created in this paper. Photovoltaic array, wind turbine, asynchronous (induction) generator, controller, and converters are all part of the system. The model is created with the help of the MATLAB/Simulink software suite. Based on the development of a MPPT, the P&O technique is utilized to maximize the generated power. The proposed model's dynamic behavior is investigated under various operating situations.

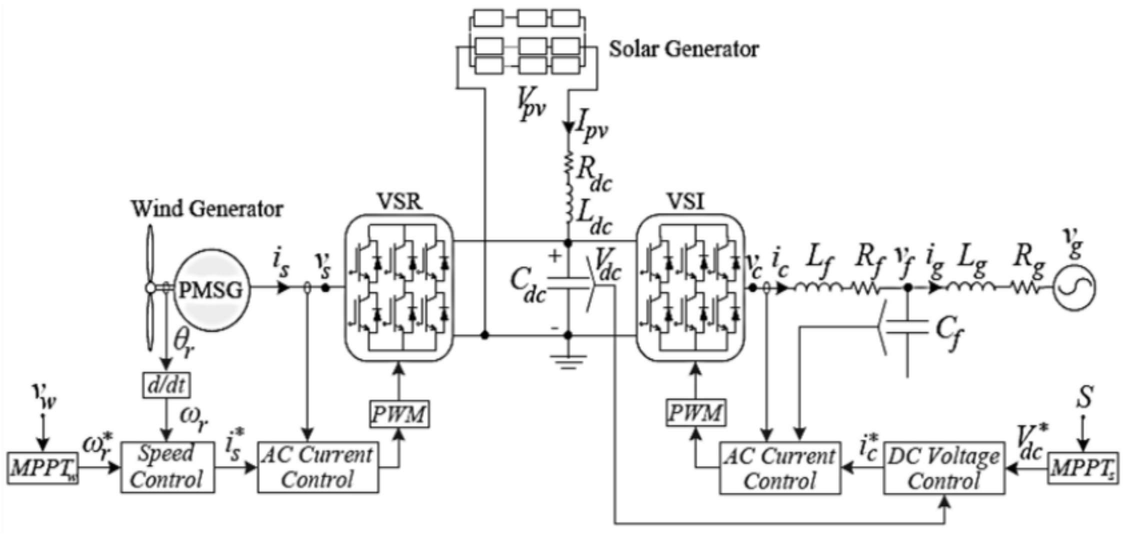

Figure 1. Model of proposed PV-wind integrated grid

2.1. Design of PV cell

A current source in shunt with a diode and two resistors linked anti parallel to each other describe the architecture of a solar cell in general. The power production of solar cells is controlled by these resistors as shown in Figure 2. Both the n-type and p-type sides of the solar cell have ohmic metal-semiconductor connections, and the electrodes are coupled to an external load. Electrons produced on the n-type side, or p-type electrons "caught" by the junction and swept onto the n-type side, may flow through the wire, power the load, and continue through the wire until they reach the p-type semiconductor-metal contact. They recombine with a whole formed on the p-type side of the solar cell as an electron-hole pair, or a hole swept across the junction from the n-type side after being created there. The voltage measured is equal to the difference between the quasi-Fermi levels of the majority carriers (electrons in the n-type section and holes in the p-type portion) at the two terminals.

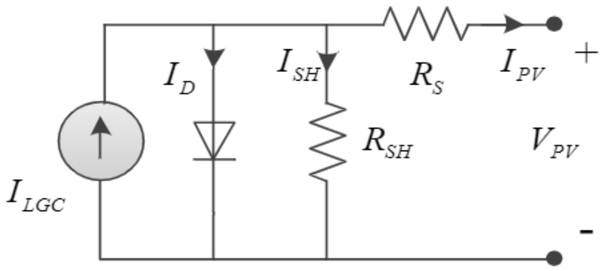

Figure 2. Representation diagram of PV cell

To obtain the required output voltage and current from a PV panel, n number of PV panels is connected in series-parallel configurations, and the voltage and current are stated mathematically;

$$\text{Vseries} = \sum_{j=1}^{n} V_j = \text{V1} + \text{V2} + \cdots \ldots \ldots \ldots + \text{Vn} \tag{1}$$

$$V_{seriesoc} = \sum_{j=1}^{n} V_j = V_{oc1} + V_{oc2} + \cdots \ldots \ldots . + V_{ocn} \text{ for I} = 0 \tag{2}$$

$$I_{parallel} = \sum_{j=1}^{n} I_j = I_1 + I_2 + \ldots\ldots\ldots + I_n \tag{3}$$

$$V_{parallel} = V_1 = V_2 = \ldots\ldots. = V_n \tag{4}$$

By default, bypass diodes are used in solar panels to reduce overvoltage in the system. However, it raises the expense of the system.

2.2. DC-DC converters

In general, regulating, switching series voltage-source converter (VSC) converters by duty ratio expose for optimal performance, switches with some delay cause stress on the switches as well as the converters' life time in DC-DC converters, and PV panels produce less power. To get the maximum power output of the PV module, a fuzzy MPPT algorithm is now used to manage the switching pattern. DC-DC converters with fuzzy logic give the PS network's dynamic performance and overall efficiency are improved by this fuzzy logic controller (FLC) based direct current (DC) converter, which supplies less oscillating voltage to the series VSCs.

2.3. Design of permanent magnetic synchronous based wind energy

Because the permanent magnetic synchronous generator (PMSG) is a brushless DC machine, it has a simple and durable design. When compared to the doubly fed induction generator (DFIG) generator, it is less expensive. By adjusting terminal voltages of the PMSG's rotor circuit, it regulates the actual, reactive power of the wind energy conversion system (WECS) system. As a result, it regulates power factor of the entire WECS. PMSG is used to accomplish desired speed management without the need of slip rings. Mathematically PMSG represents in dq0 axis:

$$\text{Vgq} = (\text{Rg} + \text{p.Lq}).\text{iq} + \text{We.Ld id} \tag{5}$$

$$\text{Vgd} = (\text{Rg} + \text{p Ld}).\text{id} - \text{We Lqiq} \tag{6}$$

where Vgd and Vgq represents the stator voltages in direct and quadrature axis.

$$Te = \frac{3}{2} Pn[\varphi + iq - (Ld - Lq)id\ iq] \tag{7}$$

If id=0, the electromagnetic torque is expressed as in (8).

$$Te = \frac{3}{2}\, Pn\psi f iq \tag{8}$$

The dynamic equation of wind turbine is described by (9).

$$J\frac{dwm}{dt} = Te - Tm - F\,Wm \tag{9}$$

3. CONTROL SCHEME

The implementation of FLC based voltage source inverters (VSI) is comparable to the FLC MPPT method. This mistake is treated as a collection of fuzzily defined rules. By selecting rules, membership function, and de-fuzzification as shown in Figure 3. These fuzzy sets provide proportional integral (PI) control settings. Table 1 and Figure 4. Membership function for Figure 4(a) error, Figure 4(b) change in error, and Figure 4(c) output lists the set of fuzzy rules. The fuzzy logic reasoning differs from traditional multi-valve legitimate frame works in both concept and substance, such as negative big (NB), negative small (NS), zero (Z), positive big (PB), and positive small (PS). The actual value of voltage across (V_{dcact}) point of Coupling is contrast with reference DC voltage (Vdc) that error is optimized with fuzzification then error is rectified send to the system after de-fuzzification.

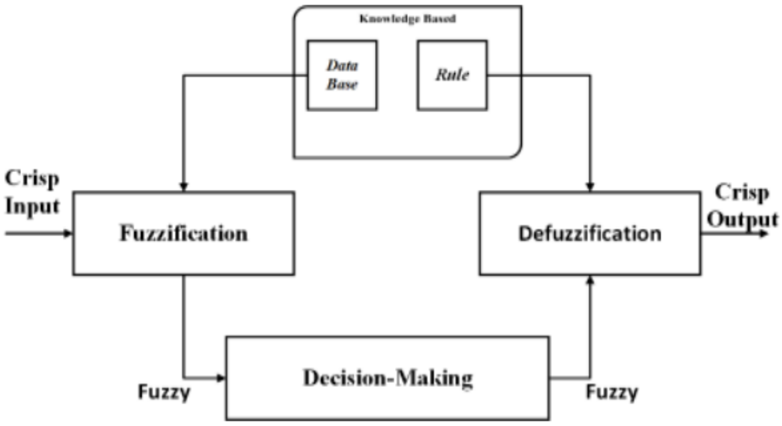

Figure 3. Fuzzy inference system

Table 1. Fuzzy rule set

		Error (E)						
		NB	NM	NS	Z	PS	PM	PB
Change in Error (ΔE)	NB	NB	NB	NB	NS	NS	NS	Z
	NS	NB	NM	NS	NS	Z	PS	PS
	Z	NS	NM	NS	Z	PS	PM	PM
	PS	NS	NS	Z	PS	PM	PB	PB
	PB	Z	NB	PS	PS	PB	PS	PB

3.1. ANFIS based VSI controller design

The control method for operating VSC using an ANN and fuzzy based PV system is presented in Figure 5(a). These approaches give various tuning heuristics and thumb rules for PI controllers for VSC soft switching. The simplification of higher order transfer functions into lower order estimates is common in several of these techniques. Guarantee that the tuning given by these methodologies will result in adequate presentation for all systems, as with any intelligent-based strategy. Five layers are considered in the creation of this ANN human brain network. Layer 1 has 25 neurons, layers 2-4 have 16 neurons, and the 5th layer has 2 neurons, as illustrated in Figure 5(b). The allowable total of squares for a system is expected to be 10-8, and it will converge to a suitable output after around 300 iterations. After the iterations are completed, the output answer is sent to fuzzy to reduce the error. In comparison to other traditional approaches, this ANN with fuzzy will deliver optimal PI parameters and superior outcomes.

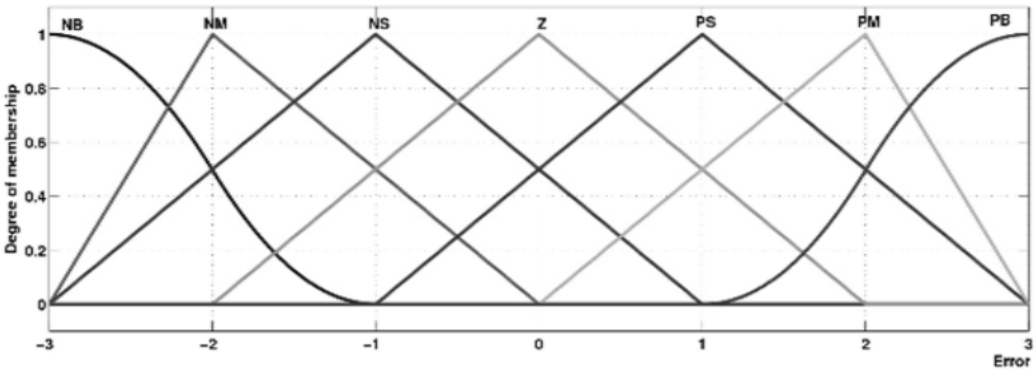

(a)

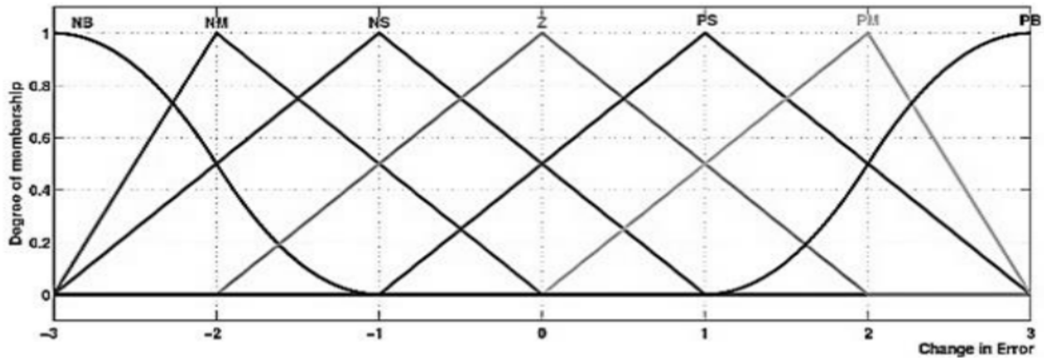

(b)

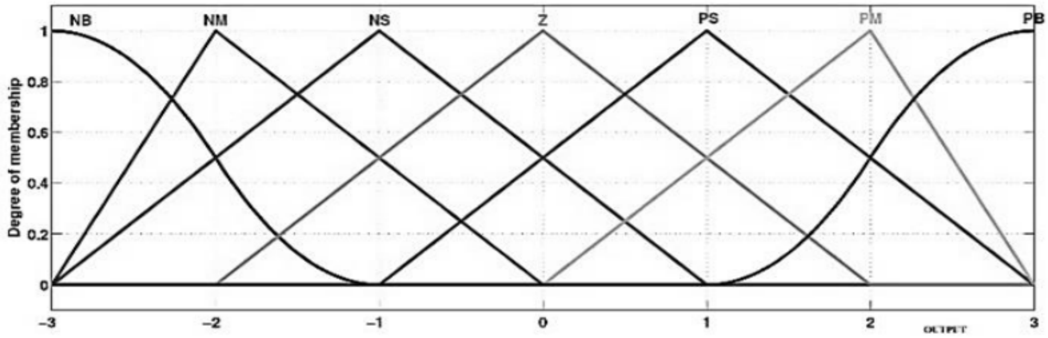

(c)

Figure 4. Membership function for (a) error, (b) change in error, and (c) output

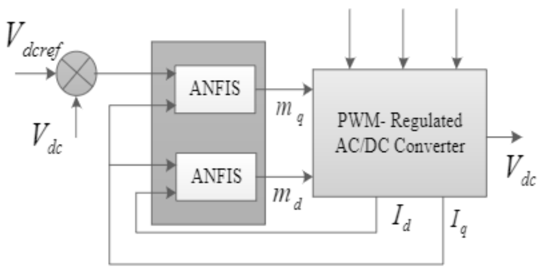

(a)

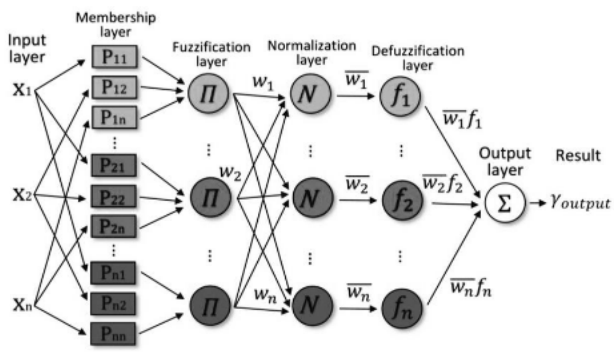

(b)

Figure 5. ANFIS based VSI controller design (a) structure of ANFIS based VSC and (b) process layer of ANFIS

4. SIMULATION RESULT

The variation of DC link voltage (step response) is momentarily considered at point t=1 sec as shown in Figure 6. The variation of PV-wind power production based on its availability considered as shown in Figure 7. In PV cell irradiance considered as 1 kw/ms up to t=0.3, momentarily it is changed to 0.9 $kW/m\%$, the time between 0.3 s to 0.5 s. At t=0.5 s to 0.6 s irradiance is 0.4 $kW/m\%$ decreases, and between t=0.6 s to t=0.8 s irradiance considered as 0.6 $kW/m\%$. Similar variation of wind power generation is considered as 0.82 m/s to t=2 ms. After wind is increased to 1.1 m/s in time between t=2 s to 4 sec. Further wind decreased to 0.7 m/s time between t=4 s to t=6 s and wind increases to drastically up to 1.2 m/s from time between t=6 s to t=8 s.

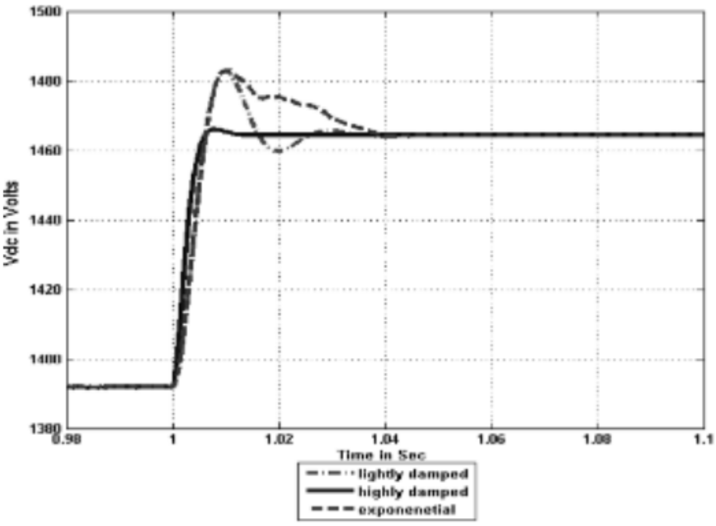

Figure 6. Step variation of DC link voltage

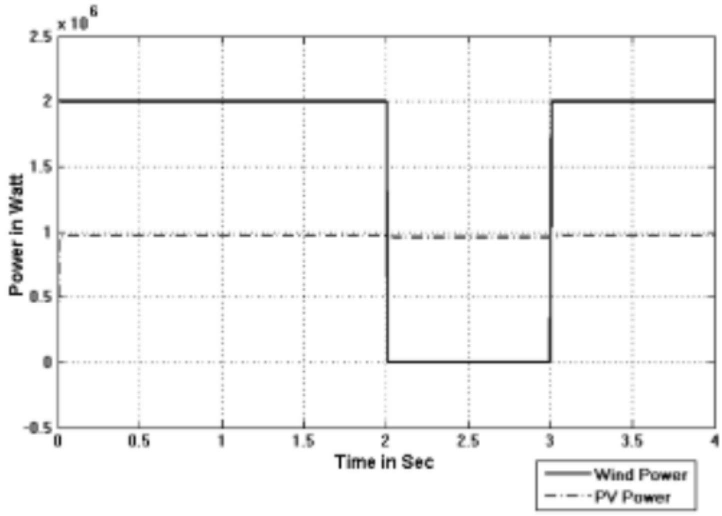

Figure 7. Variation of solar-wind power generation

4.1. ANFIS based VSI controller design

The performance of the smart grid with both PV-wind power generation is shown in Figures 8(a) to 8(g) those are PMSG speed, voltage at DC link capacitor, wind power, solar power, grid current, voltage across CPI, VSR modulation respectively. From the Figures 8(b) and 8(f) it is clear that fixed voltages are produced with even variable PV-wind power generation. Effective power management done between grid-PV-wind (smart grid) with employing ANFIS operated VSC converters.

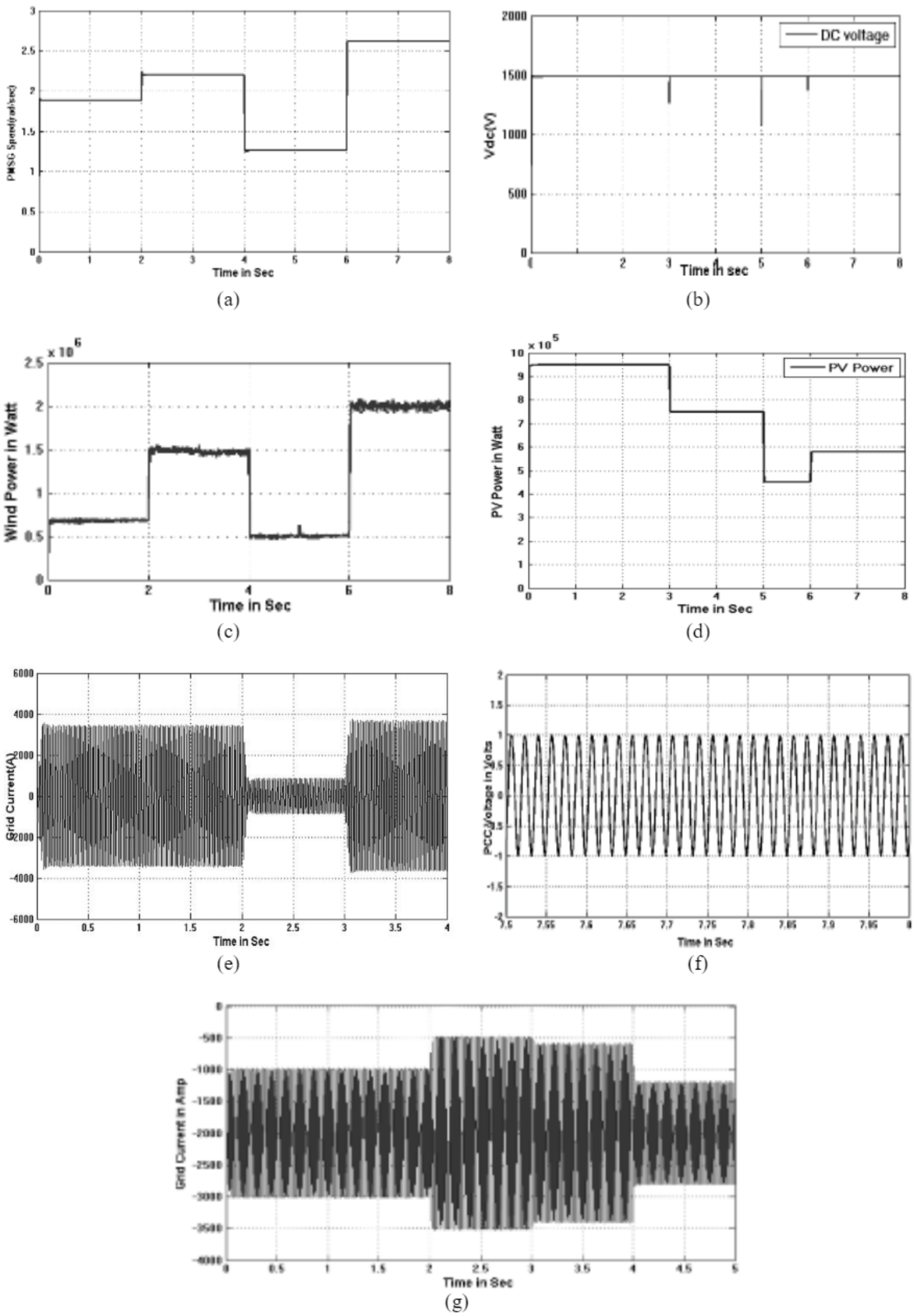

Figure 8. Performance of the smart grid with both PV-wind power generation (a) PMSG speed (rad/sec), (b) DC link voltage, (c) wind power (W), (d) solar power (W), (e) grid current, (f) voltage at CPI, and (g) VSR modulation

4.2. Performance of the system only with wind power generation

The energy management of the smart-grid only with wind is described in this session. In this low or zero irradiance (during night) appearances power establishment done by solar is minimum. In this situation wind energy is only prime responsible to reach the load demand. The output simulation results are illustrated in Figures 9(a) to 9(c). Those are wind speed, wind power and grid current respectively.

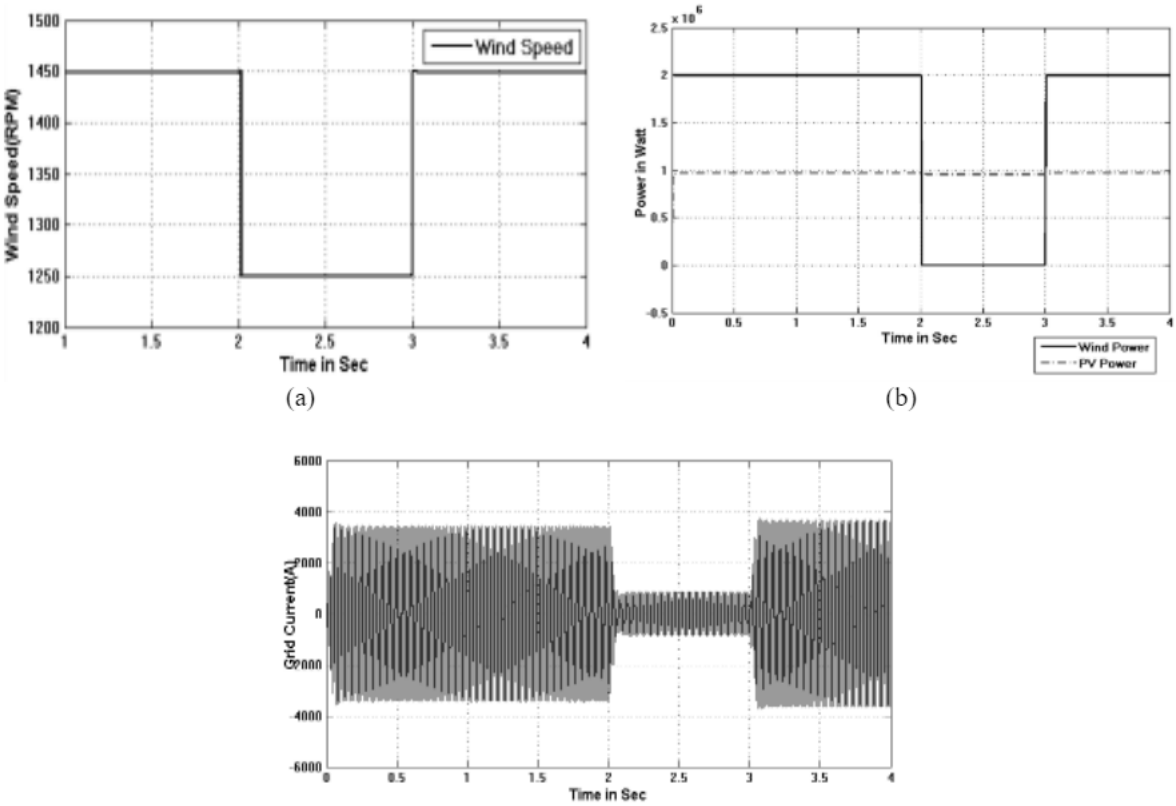

(a) (b)

(c)

Figure 9. Simulation results of the system only with wind power generation (a) wind speed, (b) wind power, and (c) grid current

4.3. Performance of the system only with solar power generation

The performance of the smart grid with solar power and low wind power generation is considered in this condition. The performance of the output simulation results is mentioned in Figure 10. Figures 10(a) to 10(c) show the PMSG speed, solar power, and grid current.

4.4. Performance of the system with symmetrical fault

A symmetrical L-L-L-G (3ph fault) is created for solar power network (1 pu) and wind power (0.5 pu) at t=4 secs. The obtained performance simulation results are shown in Figures 11(a) to 11(c) those are DC link voltage with protection, grid current, and DC link voltage without protection respectively. From Figure 12 comparison of DC link voltage with protection controller and without controller it clear that with using proposed technique the oscillations occurred in grid current is less. It is mitigated within the first four cycles. Total harmonic distortion (THD) of grid current and grid voltage of conventional controller and proposed controller is shown in Figure 13. Comparison THD for grid current with Figure 13(a) conventional controller and Figure 13(b) proposed controller and shown in Figure 14. Comparison THD for grid voltage with Figure 14(a) conventional controller Figure 14(b) proposed controller respectively.

The results show that the THD values of grid current is 19.72% and grid voltage THD is 44.05% with ANFIS controller. This controller is also able to effectively compensate all the parameter. Hence ANFIS controller is most effective of PI controllers developed. Comparison of THD with PI and ANFIS controllers is shown in Table 2.

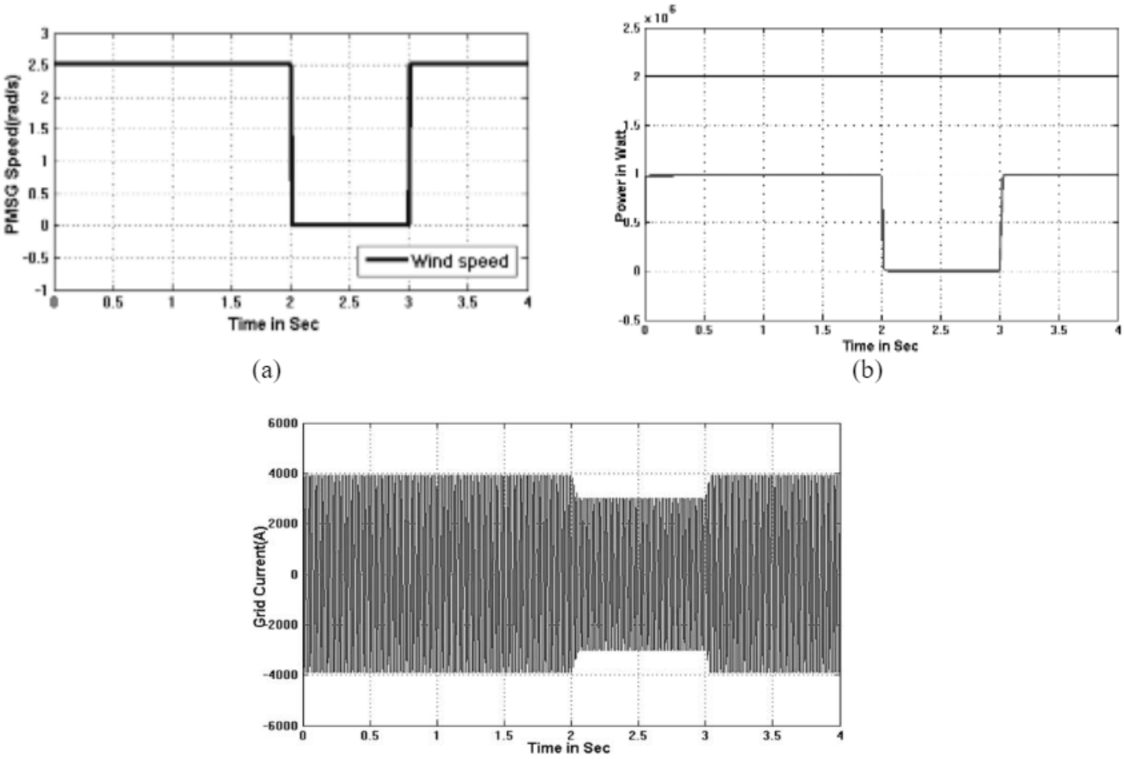

(c)

Figure 10. Simulation result of wind speed, solar power and grid current (a) wind speed, (b) solar power, and (c) grid current

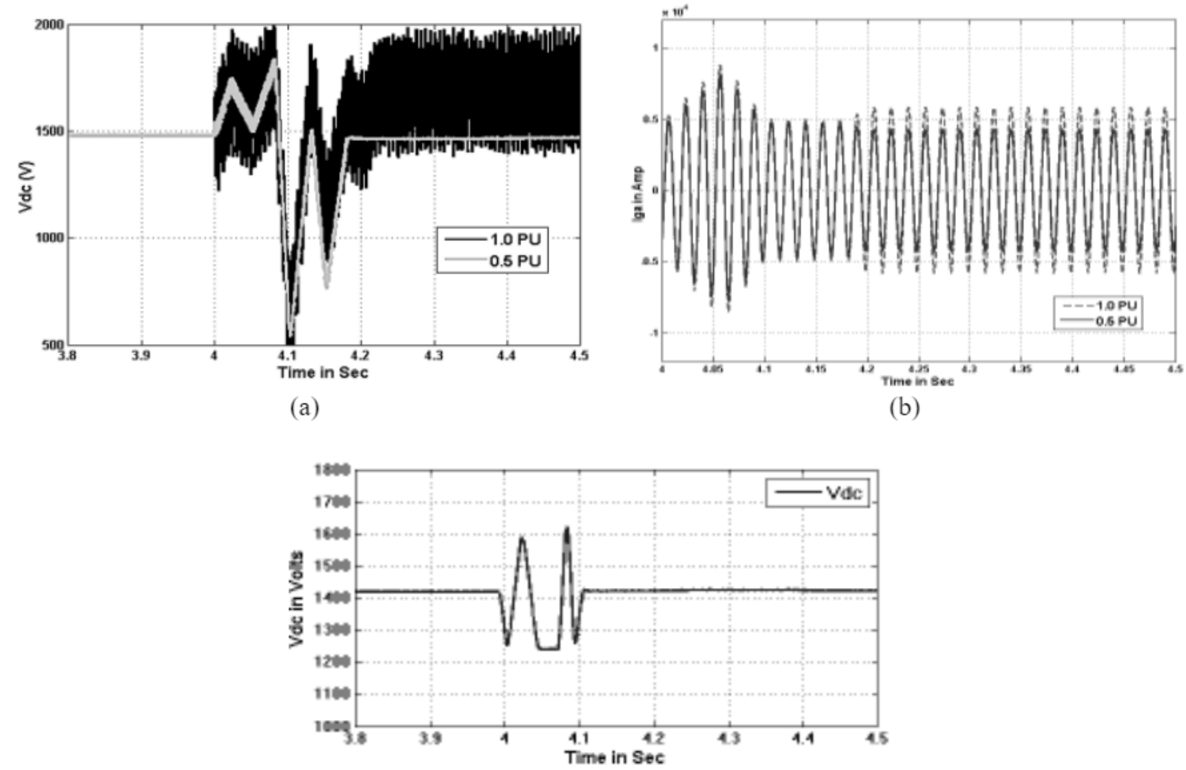

(c)

Figure 11. Simulation results of the system with symmetrical fault (a) DC link voltage with fault and ANFIS controller, (b) grid current with protection, and (c) DC link voltage without protection

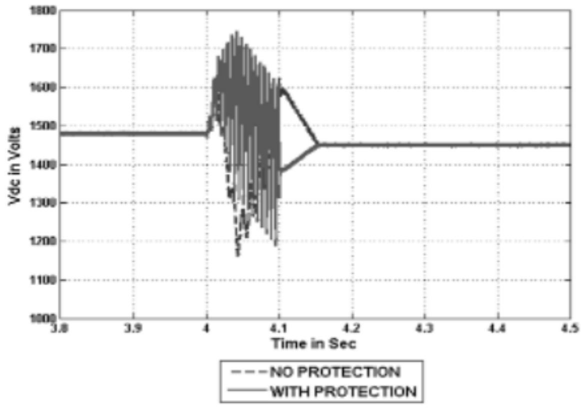

Figure 12. DC link voltage with and without protection

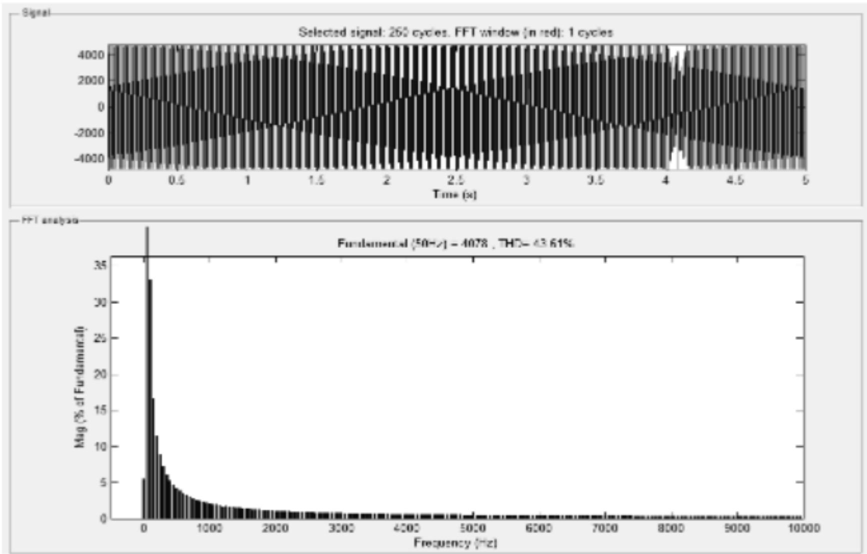

(a)

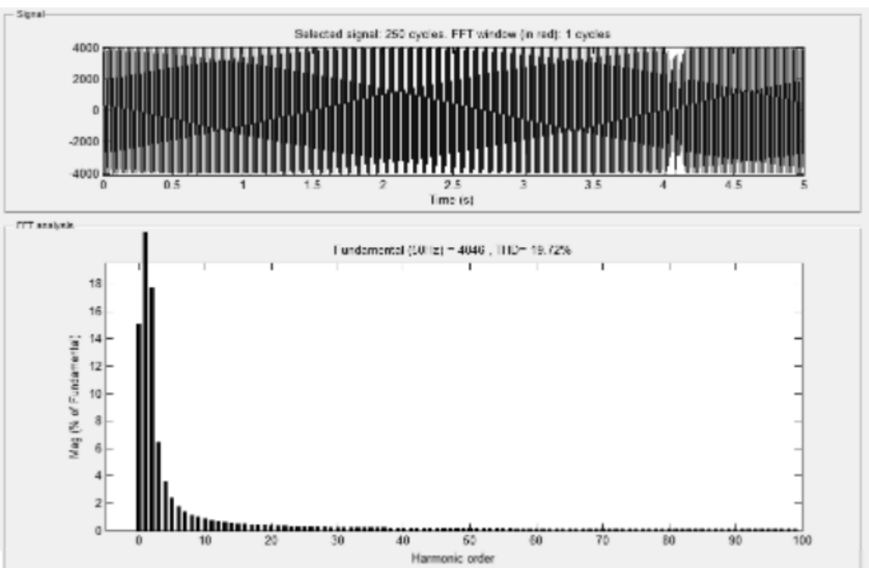

(b)

Figure 13. Comparison THD for grid current with (a) conventional controller and (b) proposed controller

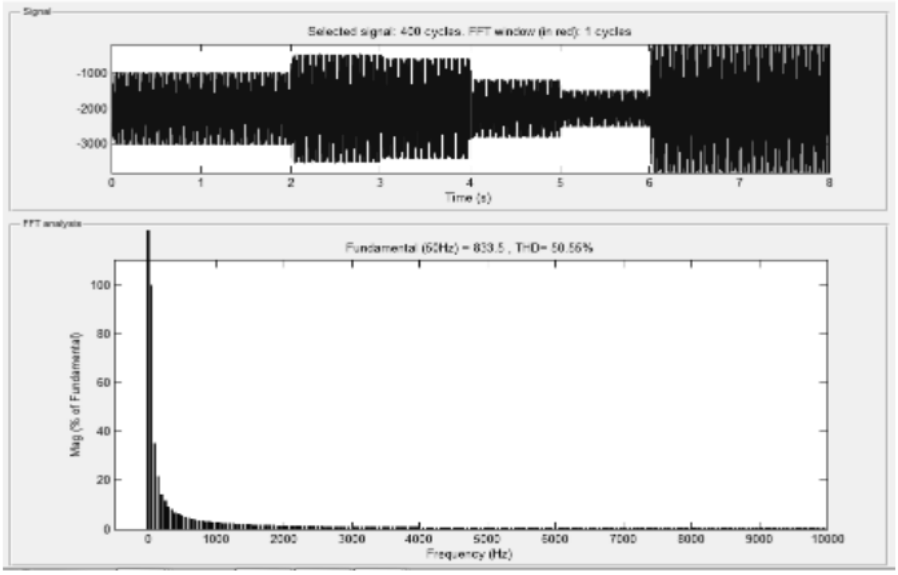

(a)

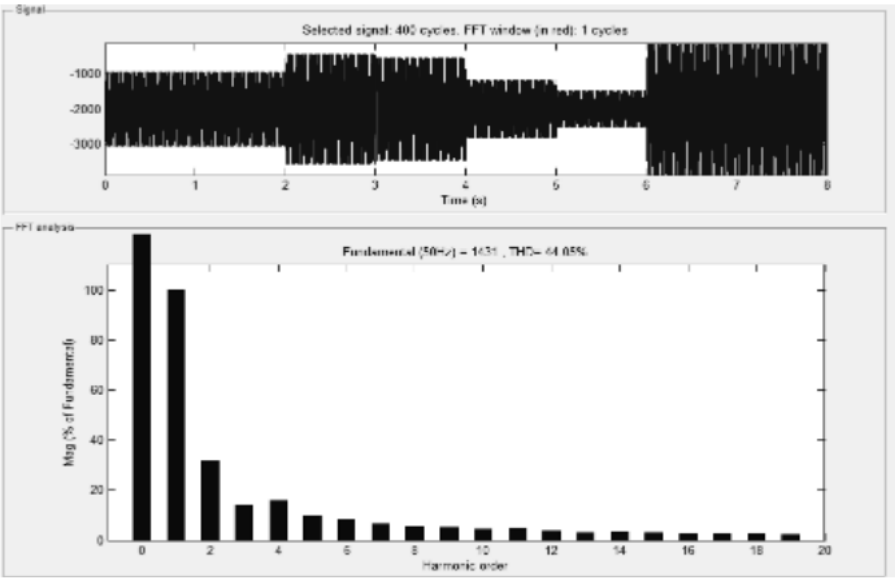

(b)

Figure 14. Comparison THD for grid voltage with (a) conventional controller and (b) proposed controller

Table 2. Comparison table for THD

S. No	Parameters	Conventional Controller (PI)	Proposed Controller (ANFIS)
01	Grid Current	43.61%	19.72%
02	Grid Voltage	50.55%	44.05%

5. CONCLUSION

This research investigates an efficient ANFIS control based smart grid to improve power quality. Obtained simulation results for performance system only with solar power and low wind energy, with wind energy and low solar power and both solar-wind powers are presented. From the simulations it is clear that the current's harmonic content is reduced by 43.61% to 19.72% and voltage harmonics is reduced 55.55% to 44.05% in ANFIS in contrast to conventional PI controller. In addition, it is observed that it has improved dynamic performance compared to the conventional control-based techniques like PI controllers, individual loop control techniques. The proposed ANFIS control-based approach reduces network failure tolerance and improves power quality.

REFERENCES

[1] S. Salman, X. AI, and Z. WU, "Design of a P-&-O algorithm based MPPT charge controller for a stand-alone 200W PV system," *Protection and Control of Modern Power Systems*, vol. 3, no. 1, p. 25, Dec. 2018, doi: 10.1186/s41601-018-0099-8.

[2] D. Haji and N. Genc, "Fuzzy and P&O based MPPT controllers under different conditions," in *2018 7th International Conference on Renewable Energy Research and Applications (ICRERA)*, Oct. 2018, pp. 649–655, doi: 10.1109/ICRERA.2018.8566943.

[3] B. Bhandari, S. R. Poudel, K.-T. Lee, and S.-H. Ahn, "Mathematical modeling of hybrid renewable energy system: A review on small hydro-solar-wind power generation," *International Journal of Precision Engineering and Manufacturing-Green Technology*, vol. 1, no. 2, pp. 157–173, Apr. 2014, doi: 10.1007/s40684-014-0021-4.

[4] M. G. Simoes, B. K. Bose, and R. J. Spiegel, "Fuzzy logic based intelligent control of a variable speed cage machine wind generation system," in *Proceedings of PESC '95-Power Electronics Specialist Conference*, 1995, vol. 1, pp. 389–395, doi: 10.1109/PESC.1995.474840.

[5] R. Chedid, F. Mrad, and M. Basma, "Intelligent control of a class of wind energy conversion systems," *IEEE Transactions on Energy Conversion*, vol. 14, no. 4, pp. 1597–1604, 1999, doi: 10.1109/60.815111.

[6] T. Hirose and H. Matsuo, "Standalone hybrid wind-solar power generation system applying dump power control without dump load," *IEEE Transactions on Industrial Electronics*, vol. 59, no. 2, pp. 988–997, Feb. 2012, doi: 10.1109/TIE.2011.2159692.

[7] K. Kant, C. Jain, and B. Singh, "A hybrid diesel-wind -PV-based energy generation system with brushless generators," *IEEE Transactions on Industrial Informatics*, vol. 13, no. 4, pp. 1714–1722, Aug. 2017, doi: 10.1109/TII.2017.2677462.

[8] K. Sharma and D. K. Palwalia, "Robust controller design for DC-DC converters using fuzzy logic," in *2017 4th International Conference on Signal Processing, Computing and Control (ISPCC)*, Sep. 2017, pp. 477–481, doi: 10.1109/ISPCC.2017.8269726.

[9] P. K. Ray, S. R. Das, and A. Mohanty, "Fuzzy-controller-designed-PV-based custom power device for power quality enhancement," *IEEE Transactions on Energy Conversion*, vol. 34, no. 1, pp. 405–414, Mar. 2019, doi: 10.1109/TEC.2018.2880593.

[10] M. Bollen, J. Zhong, F. Zavoda, J. Meyer, A. McEachern, and F. Córcoles López, "Power quality aspects of smart grids," *Renewable Energy and Power Quality Journal*, vol. 1, no. 08, pp. 1061–1066, Apr. 2010, doi: 10.24084/repqj08.583.

[11] S. Gheorghe, G. Gheorghe, N. Golovanov, and C. Stanescu, "Results of power quality monitoring in Romanian transmission and distribution system operators," in *2016 International Conference on Applied and Theoretical Electricity (ICATE)*, Oct. 2016, pp. 1–6, doi: 10.1109/ICATE.2016.7754628.

[12] M. E. Ralph, "Control of the variable speed generator on the Sandia 34-m vertical axis wind turbine," *presented at the Windpower '89 Conf.* San Francisco, CA, 1989.

[13] T. A. Lipo, "Variable speed generator technology options for wind turbine generators," *NASA Workshop, Cleveland,*. 1984.

[14] C. Nayar and J. H. Bundell, "Output power controller for a wind-driven induction generator," *IEEE Transactions on Aerospace and Electronic Systems*, vol. AES-23, no. 3, pp. 388–401, May 1987, doi: 10.1109/TAES.1987.310837.

[15] P. J. Werbos, "From ADP to the brain: Foundations, roadmap, challenges and research priorities," in *Proceedings of the International Joint Conference on Neural Networks*, Jul. 2014, pp. 107–111, doi: 10.1109/IJCNN.2014.6889359.

[16] P. G. Casielles, J. G. Aleixandre, J. Sanz, and J. Pascual, "Design, installation and performance analysis of a control system for a wind turbine driven self-excited induction generator," in *Proceedings ICEM '90*, 1990, pp. 988–993.

[17] D. A. Torrey, "Variable-reluctance generators in wind-energy systems," in *Proceedings of IEEE Power Electronics Specialist Conference-PESC '93*, 1993, pp. 561–567, doi: 10.1109/PESC.1993.471982.

[18] C. Brune, R. Spe, and A. K. Wallace, "Experimental evaluation of a variable-speed, doubly-fed wind-power generation system," in *Conference Record of the 1993 IEEE Industry Applications Conference Twenty-Eighth IAS Annual Meeting*, 1994, pp. 480–487, doi: 10.1109/IAS.1993.298967.

[19] D. M. F. G. Roger, "IEEE recommended practice and requirements for harmonic control in electric power systems," *IEEE Std 519-1992 (Revision of IEEE Std 519-1992)*, pp. 1–20, 2014, doi: 10.1109/IEEESTD.2014.6826459.

[20] G. C. D. Sousa, B. K. Bose, and J. G. Cleland, "Fuzzy logic based on-line efficiency optimization control of an indirect vector-controlled induction motor drive," *IEEE Transactions on Industrial Electronics*, vol. 42, no. 2, pp. 192–198, Apr. 1995, doi: 10.1109/41.370386.

[21] G. C. D. Sousa and B. K. Bose, "A fuzzy set theory based control of a phase-controlled converter DC machine drive," *IEEE Transactions on Industry Applications*, vol. 30, no. 1, pp. 34–44, 1994, doi: 10.1109/28.273619.

[22] D. Krishna, M. Sasikala, and V. Ganesh, "Adaptive FLC-based UPQC in distribution power systems for power quality problems," *International Journal of Ambient Energy*, pp. 1–11, Feb. 2020, doi: 10.1080/01430750.2020.1722232.

[23] P. E. Bett and H. E. Thornton, "The climatological relationships between wind and solar energy supply in Britain," *Renewable Energy*, vol. 87, pp. 96–110, Mar. 2016, doi: 10.1016/j.renene.2015.10.006.

[24] D. Krishna, M. Sasikala, and V. Ganesh, "Mathematical modeling and simulation of UPQC in distributed power systems," in *2017 IEEE International Conference on Electrical, Instrumentation and Communication Engineering (ICEICE)*, Apr. 2017, pp. 1–5, doi: 10.1109/ICEICE.2017.8191886.

[25] D. Krishna, M. Sasikala, and V. Ganesh, "Fuzzy based upqc in a distributed power system for enhancement of power quality," *International Journal of Pure and Applied Mathematics*, vol. 118, no. 14, pp. 689–698, 2018.

[26] S. Ravi and K. Dhee, "Improvement of dynamic performance of induction motor drives by using flc based MPFC," *International Journal of Innovative Technology and Exploring Engineering (IJITEE)*, vol. 8, no. 2S, pp. 240–245, 2018.

[27] D. C. Sekhar, P. V. V. R. Rao, and V. Ganesh, "Weight feedback adaptive multi objective cooperative scheduling in smart grid application," *International Journal of Recent Technology and Engineering (IJRTE)*, vol. 8, no. 2, pp. 607–611, 2019.

[28] C. R. Reddy and K. H. Reddy, "Islanding detection techniques for grid integrated DG: a review," *nternational Journal of Renewable Energy Research (IJRER)*, vol. 9, no. 2, pp. 960–977, 2019.

[29] R. Thumu, K. Harinadha Reddy, and C. Rami Reddy, "Unified power flow controller in grid-connected hybrid renewable energy system for power flow control using an elitist control strategy," *Transactions of the Institute of Measurement and Control*, vol. 43, no. 1, pp. 228–247, Jan. 2021, doi: 10.1177/0142331220957890.

[30] B. S. Goud, B. L. Rao, and C. R. Reddy, "An intelligent technique for optimal power quality reinforcement in a grid-connected HRES system: EVORFA technique," *International Journal of Numerical Modelling: Electronic Networks, Devices and Fields*, vol. 34, no. 2, Mar. 2021, doi: 10.1002/jnm.2833.

BIOGRAPHIES OF AUTHORS

Dharamalla Chandra Sekhar received the B. Tech Degree in Electrical and Electronics Engineering from Jawaharlal Nehru Technological University Hyderabad, India and the M. Tech in Power Electronics from Jawaharlal Nehru Technological University Hyderabad, India. Currently, He is Research Scholar in Jawaharlal Nehru Technological University Anantapur, India and also, He is an Assistant Professor at the Department of Electrical and Electronics Engineering, Malla Reddy Engineering College (Autonomous), Secunderabad, Telangana, India. His research interests include renewable energy, power quality, power electronics and drives, smart grid, load flow control, particle swarm optimization, power distribution protection, neural networks, fuzzy systems and artificial intelligence applied to power system and power electronics. He can be contacted at e-mail: daram.sekhar@gmail.com.

Pokanati Veera Venkata Rama Rao received the B. Tech Degree in Electrical and Electronics Engineering from Jawaharlal Nehru Technological University Hyderabad, India. M.Tech Degree from Jawaharlal Nehru Technological University Hyderabad, India and Ph.D. Degree in Jawaharlal Nehru Technological University Hyderabad, India. Currently, he is Professor in the Department of Electrical and Electronics Engineering at Maturi Venkata Subba Rao Engineering College (Autonomous), Hyderabad, India. He has authored or coauthored more than 40 refereed journals and 60 conference papers. He received five project grants from external funded organizations. His research interests include the applications of artificial intelligence in electrical power systems, evolutionary and heuristic optimization techniques to power system planning, operation, and control, micro grid, smart grid and electrical vehicles. He can be contacted at e-mail: pvvmadhuram@gmail.com.

Rachamadugu Kiranmayi received the B.Tech. Degree in Electrical and Electronics Engineering from Jawaharlal Nehru Technological University Hyderabad, India. M. Tech. Degree in Electrical Power Systems from Jawaharlal Nehru Technological University Hyderabad, India and Ph.D. Degree in Electrical Engineering from Jawaharlal Nehru Technological University Anantapur, Andhra Pradesh, India. She is currently Professor in the Department of Electrical and Electronics Engineering and the Director, Foreign Affairs and Alumni Matters at Jawaharlal Nehru Technological University Anantapur, Andhra Pradesh, India. She has authored or coauthored more than 50 refereed journals and conference papers. Her research interests include renewable energy sources, micro gird, load flow studies, smart grid, and applications of artificial intelligence. She can be contacted at e-mail: kiranmayi0109@gmail.com.

Journal of Engineering Education Transformations,
Volume No 35, January 2022, Special issue, eISSN 2394-1707

Mitigating the Challenges of Online Learning and Conduct of Examinations - From Faculty Perspective to Student Satisfaction

Shankaranand Jha[1], Santosh Kumar Choudhary[2] and Ritesh Kumar[3]
[1]Department of ECE, Malla Reddy Engineering College, Secunderabad- 500100, India
[2]Department of ECE, VNR Vignana Jyothi Institute of Engineering and Technology, Hyderabad-500090, India
[3]Department of EEE, SR University, Warangal-506371, India

***Abstract*—** This paper aims to explore the effects of imposition of online classes, teaching practices and conduct of examinations on students and faculty alike. The methodologies presented here are the actual practices followed by the faculties while delivering online classes, remote content preparation and distribution, exam guidelines and its implementation during the exams. This paper also explores the exam experience and overall satisfaction from student perspective. Survey was conducted among students in an anonymous way without collecting their identity to gauge their opinion on the way the online classes and exams were conducted. The sample of the study consisted of nearly 142 undergraduate students studying across three engineering colleges. This study finds interesting and mixed conclusions from students. We discuss in brief the challenges faced and how it was overcome by the faculty members and students alike, especially while conducting online examination. Some suggestions have also been made to improve upon not only the online teaching learning processes but also when the pandemic situation normalizes and physical classes would again become the norm.

***Keywords*—** Online classes; online teaching; active learning; COVID-19; student survey; student perception.

***JEET Category*—Research.**

I. INTRODUCTION

THERE was a time when online teaching and learning were seen as a futuristic concept and practiced more as a technological demonstration to fulfill certain institutional obligations. The common areas where it was being widely used were limited to content delivery for faculty development programs and for self-learning in a specialized domain.

Barring Coursera and edX platforms, the scale of online teaching was minuscule. But with unprecedented pandemic induced lockdown, things got drastically changed and have led to the practical implementation of online teaching methods at an extraordinary large scale (Naylor & Nyanjom, 2020; Babinčáková & Bernard, 2020; Pratama & Surahman, 2020; Kavitha & Anitha, 2021). In this context there is a need to understand how teachers and students are responding to the unique transformation at their respective levels.

The strategy for a successful online class lies more in the method of delivery rather than the content itself (Palloff & Pratt, 2013). Active-cooperative learning techniques like flipped classroom and think-pair-share have been discussed in (Jha, 2020) where the importance of a trained faculty has been emphasized. Critical elements like proper course design, activities involving students and the necessary support elements related to online teaching and learning processes have been discussed in (Oliver, 1999). A survey was conducted among teachers in (Saripudin et al., 2020) wherein the familiarities of online teaching tools were examined. In that study, while majority of them agreed that the tools were easy to operate; authors concluded that sufficient preparations by the teachers for conducting online classes were much needed. In literature, various methodologies have been suggested related to active learning techniques in online classes. Learning coefficient has been used to measure the effectiveness of interactive sessions in (Kolhekar et al., 2021). Ultimately, it is the students for whom all these teaching strategies are devised and implemented. So it becomes very indispensable to get the feedback from students. Satisfaction levels of students regarding online classes were found to be moderate in (Simsek et al., 2021). Students' mental health, emotional behavior and previous learning experiences in offline classes greatly influenced the opinion towards online classes (Baltà-Salvador et al., 2021; Platt et al., 2014). Challenges faced by students while preparing and appearing for exams have been discussed in (Simsek et al., 2021; Baltà-Salvador et al., 2021). The psychological aspects of online learning have been discussed in (Gaikwad & Kulkarni, 2021).

Fig. 1. Sample screenshot of Zoom application while students were taking mid-semester exam.

This paper investigates the strategies adopted by the faculty members to conduct interactive online classes and examinations. The overall perception of students is also discussed. Students' reactions have been shown in the result section of this paper which was collected through Google forms in an anonymous way. Based on the observations of faculty members and students' feedbacks, some recommendations have been made in the conclusion section of this paper to further enhance the teaching learning experiences in current scenario and beyond.

II. METHODOLOGY

In a sense, concept of distance learning has been truly adopted in the present scenario with the migration to online platforms. Higher education had the potential to go online earlier also but it lagged the momentum required due to the hesitance that it will not be effective. Due to the pandemic situation arising out of Covid-19, there was no option other than overcoming the reluctance to use the technology extensively. This transformation has not been so smooth. It all started with a simple step like sharing the soft copy of the course presentation with students, which otherwise would have been presented to them in a regular class. This was followed by the conduct of live online classes using Zoom application. Initially there were many problems, for example, making students aware of the software, ensuring that they remain present throughout the lecture hour, etc. With the use of technology, there is more openness in the content delivery also. These contents can be accessed in real time by the Quality Assessment team of the institute. Those materials can be shared to the concerned students anytime with minimal costs involved.

For an online activity to succeed, it is very important that the students remain engaged throughout the duration of that activity (Williams et al., 2018). To achieve this, questions were asked in the middle of the sessions and students were supposed to answer either orally or using chat box.

Apart from flipped classroom technique (Bishop & Verleger, 2013) wherein students were asked to come prepared after going through certain videos, they were also engaged in real time. Students were pre notified and made to get acquainted through the online applications so that they don't feel any technical problems during live classes. For learning management system, Canvas was used to deliver write ups and assignments. The recorded lectures were also made available for the benefit of especially those who missed out live classes due to any reason.

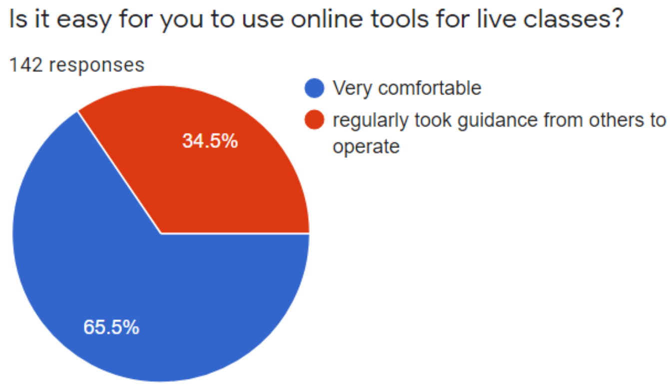

Fig. 2. (color online) Students' response for ease of using online tools for live classes.

As per extant government directions to contain pandemic situation, the mid-term examinations were also conducted online facilitated by visual monitoring of students through online Zoom application. Students were assigned to different rooms within the Zoom application window for proper monitoring by an individual faculty assigned to a particular room. Clear instructions and rubrics were given for the online exams. They were asked to position themselves and arrange the accessories in such a way that they are visible online during exams as can be seen from the figure 1.

For collecting students' views and to gauge their perceptions regarding online classes, a Google form containing questionnaires were circulated among them. To keep the feedback process free of any external influence, students' identification data were not collected. This form was circulated among 190 engineering students studying in undergraduate courses in three different engineering colleges out of which 142 responded. The students belonged to a mix of 2nd, 3rd and final year courses. Some of the feedback questions that were asked are: "Is it easy for you to use online tools for live classes, Were you satisfied with the way of explanation in online classes, Did you feel involved in class, Your overall satisfaction with this online class, Which mode will you prefer in the upcoming semester, etc.

There were many challenges in conducting online classes and exams. The most prominent was the slow internet speed faced by the students. Since students were at different geographical locations, connectivity was the main issue. Although all students possessed smartphones, many of them were not apt enough for long hour studies due to the lack of suitable screen sizes. In some cases absence of personal computer facilities was also a concern. To ensure minimal effects on students on account of lack of proper facilities, self-explanatory hand-outs were provided to them.

For faculty, taking up numerical topics in online mode posed a significant challenge. While in normal blackboard environment, teacher has the flexibility to interact with students and steer them to the desired outcomes, there is no such level of flexibility in online mode. This was overcome to a certain extent by randomly asking students (pointedly by their roll numbers) to spell out the next steps in that particular problem solving process. This also ensured active participation from them. Also, there were instances where students just logged in to the online classes for attendance but moved away from the system while classes were in progress. To minimize such instances, questions were asked through chat box directed at a particular student.

III. Result

Before the start of online activities and exams, it was ascertained that all students have suitable resources and their technical queries were answered to their satisfaction. Students were also contacted privately to know their problems. For their enthusiasm, many of them were acknowledged for their promptness during online activities.

Figure 2-6 shows the student survey data extracted from the Google form. Figure 2 shows the response of students related to how convenient they were at using the online tools for the live classes. Before start of the online class, students were made aware of the features of online tools to be used during the semester. Some of them had to take regular guidance from others to be comfortable with the system. Figure 3 gives insight into the extent to which internet connectivity was an issue with the students. While signal problem is the dominant one, some did have economic concern. Figure 4 shows the student response related to chat box query by the faculty. Student involvement in class is very important for improvement of critical thinking and skill enhancement. Figure 5 shows the students' response when asked about their involvement in class. Through student engagement, course outcomes can be easily attained. Getting students to concentrate and participate in the online activities is a challenging task. Some of the techniques employed to mitigate this challenge were: students were encouraged to ask doubt, some of the presentation slides were made dynamic, and anecdotes were given while explaining certain concepts.

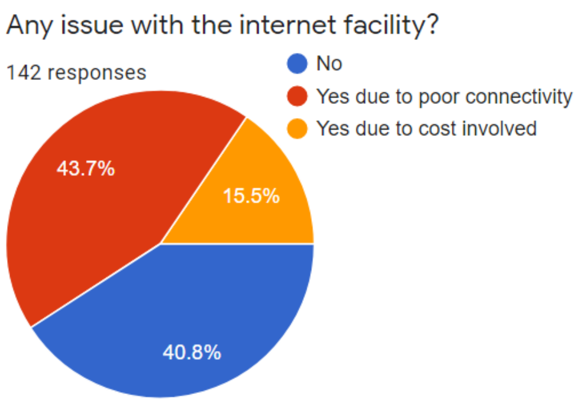

Fig. 3. (color online) Students' feedback highlighting internet issues during live online classes. Although internet facility is within the reach of every student, its speed remains a matter of concern for attending live classes.

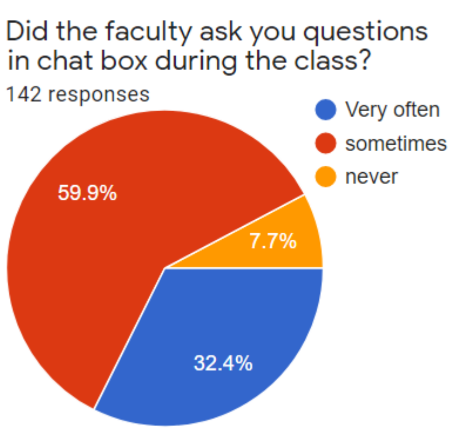

Fig. 4. (color online) Students' response that highlights the use of chat box as an interactive measure for student engagement.

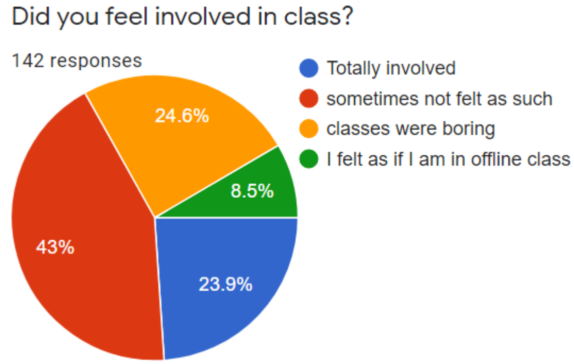

Fig. 5. (color online) Students' response when asked about their involvement in online classes. It included active participation in activities as and when initiated by the faculty. Getting students immersed in online classes is a challenging task especially when there are at least four back to back live classes of an hour each totaling four continuous hours.

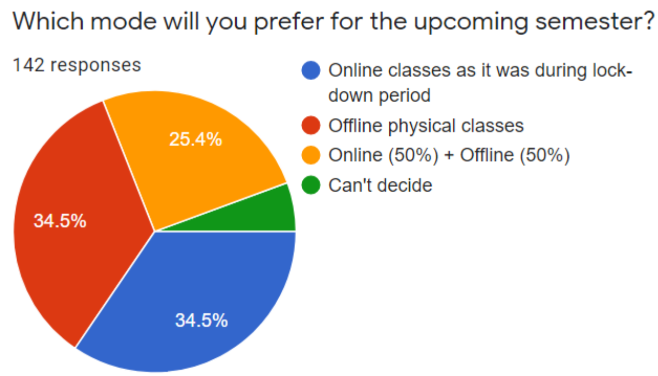

Fig. 6. (color online) Students' response when asked about their preference for mode of conduct of classes for the upcoming semester. Inclination towards some form of online component has been preferred by 34.5% + 25.4% = 59.9% students while 34.5% were in favour of offline physical classes.

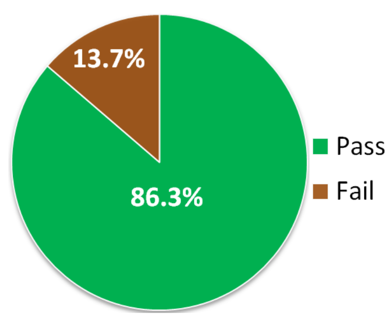

Fig. 7. (color online) Students' performance in terms of results. Out of a total of 190 students, 164 (86.3%) of them passed in the subjects the authors taught in online mode.

TABLE I
SOME OF THE STUDENTS' DESCRIPTIVE FEEDBACK FOR ONLINE CLASSES IN THEIR OWN WORDS

Advantages of online classes	**Disadvantages of online classes**
We can explore more in our leisure time that means after completion of online classes, we can study further in internet. If offline classes are conducted, we feel tired after completion of college daily.	Cost of internet, health issues. Increasing eyesight problems with frequent headaches, Laziness increased.
Travelling expenses were reduced.	You can't pay attention. Direct interaction is better than indirect interaction.
In present pandemic situation all the students and faculty are safe because of these online classes.	Main problem is sometimes if the server is down and there is no net so we can't listen to class and also at home we can't keep interest in listening to class.
We can listen to the class from anywhere.	Lack of interest and understanding. Missing Practical study.
Self-Paced Learning.	I missed the way of explanation which I used to love in offline classes.

Figure 6 shows the preference of students for the mode of class which they wish for the upcoming semester. It is interesting to see that the percentage in favour of offline physical classes and online classes are same. But when we take a closer look at the survey result, the preference of online class is more once the overall percentage is calculated by adding the online components 34.5% + 25.4% = 59.9%. The logic for online preference can be further deciphered by looking at Table 1 where feedback related to advantages and disadvantages of online classes in students' own words have been summarized. The impact on students' performance in terms of examination results is indicated in figure 7. While regular classes and mid-semester examinations were conducted online, the end-semester examinations were conducted in offline pen & paper mode. This result analysis on students' performance takes into account mid as well as end semester exams both. With a pass percentage of 86.3%, it may be recognized that the challenges of online teaching & learning processes can be overcome with suitable and consistent efforts, some of which have been discussed earlier in this paper.

IV. CONCLUSION

In conclusion it can be inferred that though students faced certain problems in online classes, majority are in favour of retaining some online component for the conduct of classes. From student feedback it is observed that the preference for online classes are mainly due to the prevailing pandemic situation and it's time-saving also as commuting time to college is saved and that can be utilized for other skill development activities. Also, students can watch the recorded lectures. At the same time they also rued the online classes as there is little scope of peer interaction, continuous use of devices lead to health concerns like eyesight problem etc. From faculty perspective it has been a challenging exercise to provide students a sense of offline experience in online mode. It takes a lot of efforts to conduct online classes effectively. Through proper planning and student engagement initiatives, online activities can be smoothly conducted and thereby course outcomes can be realized.

REFERENCES

Babinčáková, M., & Bernard, P. (2020). Online experimentation during COVID-19 secondary school closures: Teaching methods and student perceptions. *Journal of chemical education, 97*(9), 3295-3300.

Baltà-Salvador, R., Olmedo-Torre, N., Peña, M., & Renta-Davids, A. I. (2021). Academic and emotional effects of online learning during the COVID-19 pandemic on engineering students. *Education and Information Technologies*, 1-28.

Bishop, J., & Verleger, M. A. (2013, June). The flipped classroom: A survey of the research. In 2013 *ASEE Annual Conference & Exposition* (pp. 23-1200).

Gaikwad, H. V., & Kulkarni, S. S. (2021). Unmasking Students' Learning Experiences during Coronavirus Pandemic. *Journal of Engineering Education Transformations, 34*, 219-225.

Jha, S. (2020). A Case Study of Implementation of Active-Cooperative Learning Approaches Introduced through a Faculty Development Programme and their Effects on the Pass Percentage of Undergraduate Engineering Students. *Journal of Engineering Education Transformations, 34*(1), 7-11.

Kavitha, D., & Anitha, D. (2021). Measuring the effectiveness of Individual assessment methods in Collaborative/Cooperative activity in online teaching. *Journal of Engineering Education Transformations, 34*, 637-641.

Kolhekar, M., Shah, M., & Jadjav, A. (2021). Engaging Students Actively for Effective Teaching-Learning. *Journal of Engineering Education Transformations, 34*, 407-416.

Naylor, D., & Nyanjom, J. (2020). Educators' emotions involved in the transition to online teaching in higher education. *Higher Education Research & Development*, 1-15.

Oliver, R. (1999). Exploring strategies for online teaching and learning. *Distance Education, 20*(2), 240-254.

Palloff, R. M., & Pratt, K. (2013). Lessons from the virtual classroom: The realities of online teaching. John Wiley & Sons.

Platt, C. A., Amber, N. W., & Yu, N. (2014). Virtually the same?: Student perceptions of the equivalence of online classes to face-to-face classes. *Journal of Online Learning and Teaching, 10*(3), 489.

Pratama, U. N., & Surahman, E. (2020, October). Investigating Student Responses of Online Learning during the Covid-19 Pandemic in Performing Art Education. In *2020 6th International Conference on Education and Technology* (ICET) (pp. 64-69). IEEE.

Saripudin, S., Sumarto, S., Juanda, E. A., Abdullah, A. G., & Ana, A. (2020). Vocational School Teachers' Perceptions of E-Learning during COVID-19. *Journal of Engineering Education Transformations, 34*, 7-13.

Simsek, I., Kucuk, S., Biber, S. K., & Can, T. (2021). Online Learning Satisfaction in Higher Education Amidst the Covid-19 Pandemic. *Asian Journal of Distance Education, 16*(1), 247-261.

Williams, K. M., Stafford, R. E., Corliss, S. B., & Reilly, E. D. (2018). Examining student characteristics, goals, and engagement in Massive Open Online Courses. *Computers & Education, 126*, 433-442.

SSRG International Journal of Electrical and Electronics Engineering
ISSN: 2348 – 8379 / https://doi.org/10.14445/23488379/IJEEE-V9I9P104

Volume 9 Issue 9, 32-37, September 2022

Original Article

Deep Learning-Based Image Processing Approach for Irradiance Estimation in MPPT Control of Photovoltaic Applications

J. Shirisha[1], C. P. Thamil Selvi[2], S. Saru Priya[2*], V. Saravanan[2*], B. Sakthivel[3*], R. Surendiran[3#]

[1]*Department of ECE, Malla Reddy Engineering College, Hyderabad.*
[2]*Department of CSE, PPG Institute of Technology, Coimbatore.*
[2*]*Department of ECE, Velammal Engineering College, Chennai.*
[3*]*Department of ECE, Pandian Saraswathi Yadav Engineering College, Sivagangai.*
[3#] *School of Information Science, Annai College of Arts and Science, Kumbakonam, ORCID:0000-0003-1596-7874.*

[3#]*Corresponding Author : surendiranmca@gmail.com*

Received: 19 July 2022 Revised: 09 September 2022 Accepted: 17 September 2022 Published: 30 September 2022

Abstract *- Renewable energy contributes significantly to power generation to tackle the energy demand. Renewable energy is obtained from solar, wind, hydroelectric, etc. Among these, solar energy is considered the best suitable energy in terms of cleanliness and directly converts sunlight into electrical power by solar photovoltaic (PV) module. Solar panels' randomly changing power output due to irradiance is the biggest problem with solar panels. The concept of maximum power point tracking (MPPT) techniques is introduced to tackle this non-linear behavior of PV and optimize the PV system's efficiency. Various MPPT techniques have been proposed based on conventional and intelligent methods. In this work, a novel image processing-based MPPT technique is introduced to increase the efficiency of PV. The irradiance level is accurately classified using the self-learned EfficientNetB0 deep learning model. The parameters of the EfficientNetB0 model are adjusted using Tuna Swarm Optimization. Results show that the tracking efficiency is higher than other intelligent MPPT techniques. Also, the classification accuracy of the proposed learning model is superior to conventional models.*

Keywords *- MPPT, PV and EfficientNetB0.*

1. Introduction

PV systems are cost-effective renewable energy sources used to reduce global warming and reduce the necessity of fossil fuels. The effectiveness of PV is a good alternative to avoid environmental pollution and reduce CO2 emissions. The efficiency of a PV system is greatly affected by the seasonal climate conditions and the non-linear behavior of solar irradiance. The concept of MPPT is used to overcome these issues and improve the PV system's efficiency under partial shading conditions.

The general block of PV-based power generation is shown in Fig 1. The solar-based power system consists of a PV array, DC-DC converter and MPPT controller. The major function of the MPPT controller is to generate a duty cycle for the DC-DC converter by measuring PV output voltage and current. The maximum power is achieved by the suitable adjustment of duty cycles, which control the charging and discharging of the inductor and capacitors in the converter.

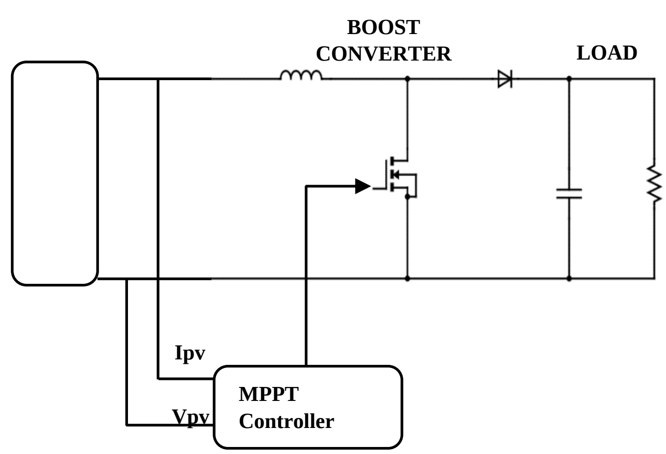

Fig. 1 The elements of solar power generation.

Generally, the MPPT techniques are classified into two categories: non-uniform irradiance and uniform radiance. The well-known non-uniform irradiance MPPT technique is Perturb and Observe (P&O) Method, Incremental Conductance (INC) Method, Hill Climbing (HC) Method and Current Sweep (CS) Method etc. the uniform irradiance MPPT technique uses artificial intelligence to achieve maximum power. The well-known uniform irradiance MPPT technique are neural network MPPT, Perturb and Observe with Genetic Algorithm, hybrid grey wolf optimization with a fuzzy logic controller, an artificial neural network with particle swarm optimization etc. However, these techniques are suffered from implementation costs and less tracking efficiency. Recently, the image processing-based solution has given promising results in automation, recognition, classification, etc. Deep learning (DL) based image processing techniques are a good candidate for automation. In this work, the DL model-based irradiance estimation is proposed for PV-MPPT to overcome the drawbacks of conventional MPPT techniques. The self-learned EfficientNetB0 deep learning model classifies the image captured from the camera. Then, the duty cycle is adjusted based on the irradiance level to achieve an MPPT.

The main objective of the proposed work is as follows:

- To propose a deep learning model-based irradiance estimation
- To increase a tracking speed
- To avoid communication between converters

This paper is structured in this fashion: In 2, the existing works related to MPPT are discussed. 3 describes the proposed deep learning-based MPPT. 4 presents the results & discussion part. 5 concludes the work.

2. Related work

Many researchers have applied MPPT methods to achieve optimal efficiency with low overhead and cost. Several MPPT methods are based on soft computing Approaches, such as fuzzy, neural networks etc. Lin et al. 2020 proposed a Group Searching Optimizer-based P&O to achieve maximum power. The fitness function for optimization is derived from voltage and current. Then, an optimizer is used to solve the fitness function. The proposed MPPT can decrease the steady state oscillations and improve the convergence speed.

Mohammed Salah Bouakkaz et al. developed a fuzzy integrated MPPT controller to handle sudden changes in climatic conditions. Fuzzification and de-fuzzification are applied in voltage and current parameters to adjust the duty cycles. A system's efficiency varies based on the type of membership used.

The multi-layered feed-forward network-based MPPT is proposed by Farhat, S.; et al. 2013 for maximizing efficiency. The neuron weight of each layer is adjusted to increase the tracking efficiency. The activation function of the sigmoid is integrated to propagate the importance of the data to the next layers. The complexity of the model increases when the number of layers increases. Padmanaban et al. 2019 developed a hybrid fuzzy and particle swarm optimization-based controller for MPPT. To avoid a local minima problem in swarm optimization, the fuzzy logic is combined to set an initial population of the particles.

Several MPPT methods are based on image processing techniques, such as machine learning, deep learning, etc. Ye, Beijing et al. 2017 analyzed the behaviour of PV modules with shadow images. The local thresholding algorithm is used for image segmentation and shadow identification. The forecasting accuracy is considerably increased with the addition of image processing techniques to the PV system.

To avoid periodic curve scanning of conventional MPPT methods, the image-based irradiance estimation is proposed by Mahmoud et al. 2016. The response function of cameras is estimated by pixel processing, and irradiance level is predicted for duty cycle adjustments. Matlab implantation results show that the proposed approach increases 8% of efficiency when compared to existing methods. Hu proposes the concept of thermal imaging-based fault detection and irradiance prediction, Yihua et al. 2019. the faulty and healthy PV cells were identified and separated using thermal imaging. Also, the maximum power point is achieved through image-based temperature prediction.

Alsmad et al. 2020 proposed a new optical imaging-based MPPT for PV systems. The non-linear mapping of image pixels is utilized to control the DC-DC converter. Results show that the proposed method can extract the maximum power under partial shading conditions without any measurements.

3. Proposed image processing based MPPT

The block diagram of the proposed MPPT is shown in Figure 1. The image captured from the camera is used for irradiance estimation. The parameter-tuned DL model of EfficientNetB0 is applied for classification. The network model parameters are adjusted by tuna optimization to the error function.

3.1. Tuna Hunting Optimization (THO)

An optimization algorithm is used to solve complex and non-linear problems with decision-making. The real-world problems are framed as a fitness function and can be solved by identifying the best solution. Tuna optimization is a metaheuristic optimization developed to find the best solution in a search space inspired by hunting behavior. Tuna is a carnivorous marine fish with unique hunting behavior to catch prey. It follows two strategies to hunt the prey: Spiral Foraging and Parabolic Foraging. This Foraging behaviour is mathematically modelled to solve the problems. The steps of THO are as follows:

3.1.1. Initialization

The population are randomly generated as follows:

$$P_i^{int} = r(ul - ll) + ll, i = 1,2.\ldots. N \tag{1}$$

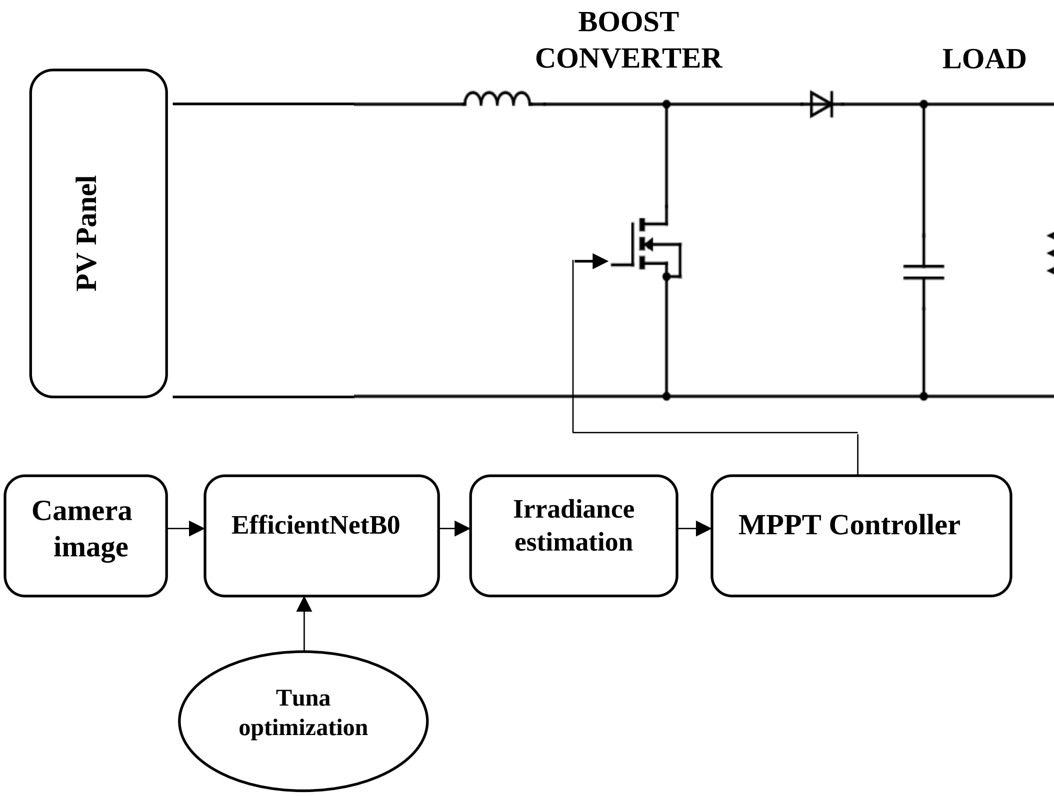

Fig. 2 Block diagram of proposed MPPT technique

Where P^{oint} is the position of an individual. ul and ll denote the upper and lower limit for solution search

3.1.2. Spiral Foraging

The group of tuna forms a tight spiral around the prey. This stage is considered an exploration stage of THO. The spiral foraging can be mathematically formulated as follows:

$$P_i^{t+1} = \begin{cases} c1.\,(P_{best}^t + c2.\,|P_{best}^t - P_i^t| + c3.\,P_i^t), & i = 1; \\ c1.\,(P_{best}^t + c2.\,|P_{best}^t - P_i^t| + c3.\,P_{i-1}^t), & i = 2,3\ldots N \end{cases} \quad (2)$$

Where P_{best}^t is the best position to hunt prey, c1, c2, and c3 are coefficients used to control the movement and to avoid local minima problems.

3.1.3. Parabolic Foraging

In these stages, the tunas create parabolic regarding the target. This step is used to improve the global exploitation property of tuna optimization. The formation of parabolic mathematically modelled as follows:

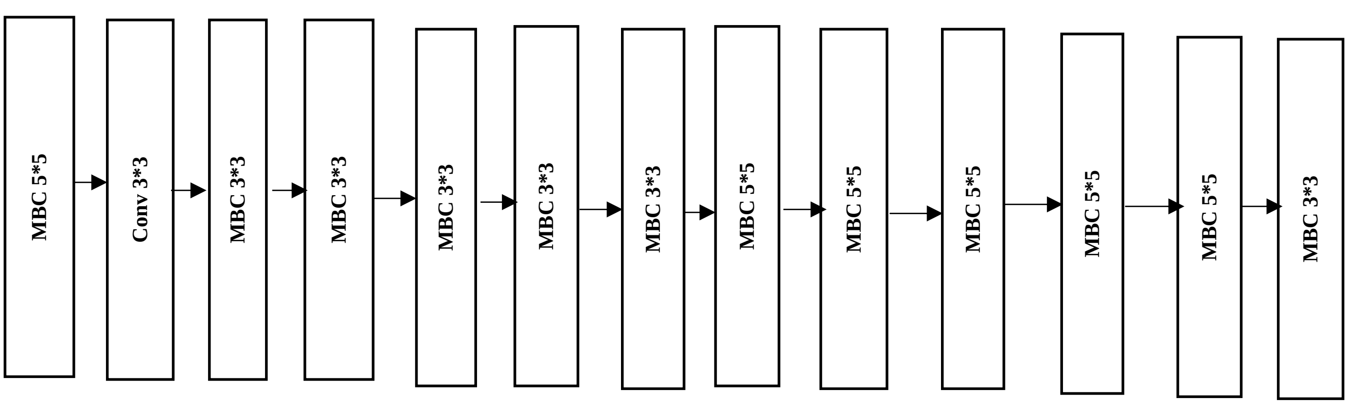

Fig. 3 Architecture of EfficientNetB0

$$P_i^{t+1} = \begin{cases} P_{best}^t + r1.(P_{best}^t - P_i^t) + r2 * s^2 * (P_{best}^t - P_i^t), \\ r2 * s^2 * P_i^t), \end{cases} \quad (3)$$

$$s = (1 - \frac{t}{t_{max}})^{\frac{t}{t_{max}}} \quad (4)$$

Where r1 is the random number that varies between zero to one, and r2 is the random number that varies between 1 to -1.

3.2. EfficientNetB0

EfficientNetB0 is a type of CNN that follows a uniform scaling method to improve image classification performance. Unlike other models that use compound coefficients to scale the whole dimension of length and width uniformly. In addition, it extracts features from the image using multiple convolutional (MC) layers and the mobile inverted bottleneck Conv (MIBC). Increasing the parameters in the model will achieve higher accuracy levels, as shown in Figure 3. The parameters of the EfficientNetB0 model are tuned using tuna optimization

3.2.1. Hyperparameter Tuning in EfficientNetB0

The accuracy of the classification model depends on the values of the hyperparameter. EfficientNetB0 consists of two types of hyperparameters: network structure-based hyperparameters and learning parameter-based hyperparameters. This work learning parameter of epochs, learning rate and batch size is adjusted based on tuna optimization. The proper parameters are recognized through the use of a tuna swarm for achieving higher accuracy.

- Initialize EfficientNetB0 parameters.
- Initialize Tuna optimization parameters.
- Set P_i^{int}, ul , ll ,c1 ,c2 and c3 parameters of optimization .
- Use the initial population to produce the EfficientNetB0 model.
- Calculate the error rate for the fitness function.
- Get the best solution having the least fitness in the population.
- Go to the last step of returning the best parameter when the criteria are satisfied; increment the number of iterations.
- Increment the number of iterations and update the population, go to create a model creating step again
- Return the best values parameter.

4. Experimental Results

The proposed classification model and MPPT technique are implemented using MATLAB. The panel and converter design parameters for simulation are given in table 1 & table 2. The proposed technique is compared against other conventional and intelligent techniques to evaluate performance.

Table 1. Parameters of PV system

MODEL -SunPower SPR-315E-WHT-D	
Maximum power(W)	500
Open circuit voltage(Voc)	13
Short circuit current (Isc)	5.8
The voltage at the maximum PowerPoint	12
Current, at the maximum PowerPoint	5.57
Temperature coefficient of Voc	-0.3131

Table 3. Efficiency analysis of proposed MPPT

Methods	Average power(W)	Voltage at MPP(V)	Current at MPP(A)	Tracking time (s)	Tracking efficiency (%)
P&O	222.5	89	2.5	0.76	58.9
Fuzzy	259.656	139.6	1.86	4.1	95.62
Swarm based optimizer	271.2	142.8	1.9	2.9	97.18
Proposed	279.3	147	1.9	0.81	98.67

Table 2. Parameters of the boost converter

Parameter	Values
Inductor (L)	960 mH
Capacitor (C)	960 µF
R	100 ohms

The performance of average time, tracking time and tracing efficiency is given in table 3. The results observed that the P&O-based approach traces a maximum power of 222.5 W with a tracking time of 0.76s. The Fuzzy based MPPT traces maximum power of 259.656 W with a tracking time of 4.1s. The Swarm-based MPPT traces maximum power of 271.2W with a tracking time of 2.9s. The proposed MPPT traces maximum power of 279.3W with a tracking time of 0.81s. The tracking efficiency performance of the proposed model is graphically shown in Figure.

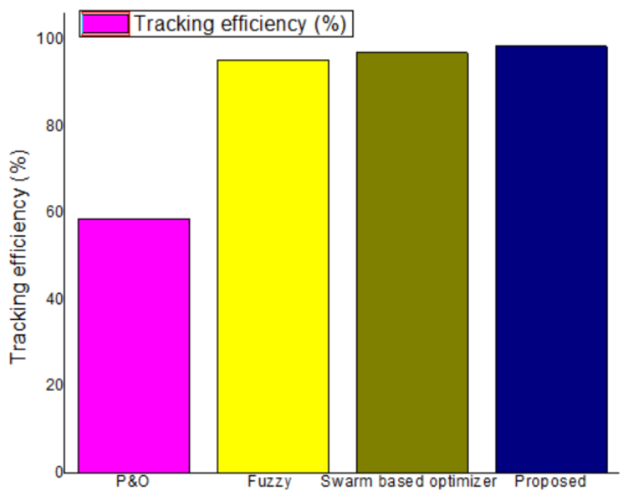

Fig. 4 Analysis of Tracking efficiency (%)

The proposed parameter-tuned EfficientNetB0 model is compared with other classifiers in terms of Accuracy (ACC), Specificity(SPC), Recall (REC) and Precision rate (PRE) as follows :

$$ACC = \frac{TP+TN}{(TP + TN+FP + FN')} \tag{5}$$

$$SPC = \frac{TN}{(TN + FP')} \tag{6}$$

$$REC = \frac{TP}{(TP + FN')} \tag{7}$$

$$PRE = \frac{TP}{(TP + FP')} \tag{8}$$

Where FP is the false positive, FN is the false negative; TP is the true positive, and TN is the true negative of the samples.

Table 4 observed that the proposed Optimized EfficientNetB0 model performs better in terms of all the parameters. The result attained in all iterations for ACC, PRE, REC, and SPE are 97.86 %, 96.89%, 97.4 % and 96.67 %, respectively. The performance of the proposed model is graphically shown in Fig. 5.

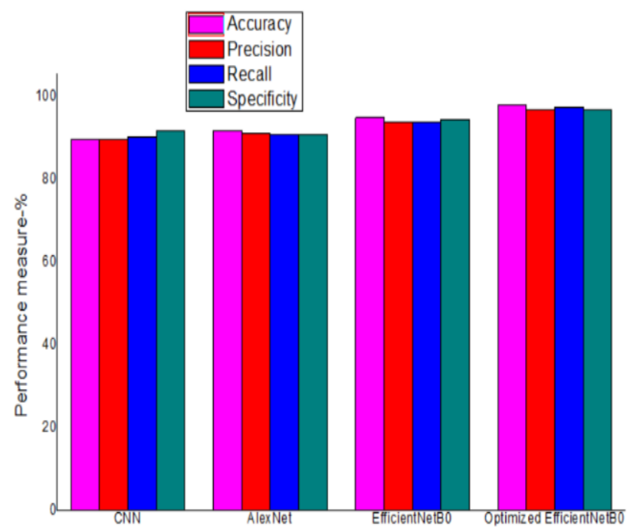

Fig. 5 Analysis of accuracy, precision, recall and specificity

Table 4. Classification performance of proposed and existing models.

Method	Accuracy	Precision	Recall	Specificity
CNN	89.62	89.5	90.2	91.6
AlexNet	91.8	91.2	90.8	90.95
EfficientNetB0	94.86	93.92	93.8	94.5
Optimized EfficientNetB0	97.86	96.89	97.4	96.67

5. Conclusion

To improve the conventional MPPT techniques, an optimized deep learning model-based irradiance estimation is proposed. The DL model of EfficientNetB0 is combined with tuna optimization for better prediction results. The proposed model's classification results prove the model's better suitability for irradiance estimation. Further, the image-based approach shows better results regarding power efficiency, tracking time, etc.

References

[1] Lin, Biyuan; Wang, Lei; Wu, Q. H, “Maximum Power Point Scanning for PV Systems Under Various Partial Shading Conditions,” *IEEE Transactions on Sustainable Energy*, pp.1–1, 2020.

[2] A. Bindhu, Dr. K. K. Thanammal, "Analytical Study on Digital Image Processing Applications," *SSRG International Journal of Computer Science and Engineering*, vol. 7, no. 6, pp. 4-7, 2020. Crossref, https://doi.org/10.14445/23488387/IJCSE-V7I6P102.

[3] Mohammed Salah Bouakkaz;Ahcen Boukadoum;Omar Boudebbouz;Issam Attoui;Nadir Boutasseta;Ahmed Bouraiou; , “Fuzzy logic-based Adaptive Step Hill Climbing MPPT Algorithm for PV Energy Generation Systems,” *2020 International Conference on Computing and Information Technology (ICCIT-1441),* 2020.

[4] Ho Soonmin, Masoud Taghavi, "Solar Energy Development: Study Cases in Iran and Malaysia," *International Journal of Engineering Trends and Technology*, vol. 70, no. 8, pp. 408-422, 2022. Crossref, https://doi.org/10.14445/22315381/IJETT-V70I8P242.

[5] Farhat, S.; Alaoui, R.; Kahaji, A.; Bouhouch, L, “Estimating the photovoltaic MPPT by artificial neural network,” [IEEE 2013 International Renewable and Sustainable Energy Conference (IRSEC) - Ouarzazate (2013.3.7-2013.3.9)], *International Renewable and Sustainable Energy Conference (IRSEC)*, pp.49–53, 2013.

[6] Dr. V. Baby Deepa, R. Malathi *"A Review of Image Processing In Different Techniques,"* International Journal of Computer and Organization Trends , vol.10, no.5, pp.12-15, 2020. Crossref, https://doi.org/10.14445/22492593/IJCOT-V10I5P302.

[7] Padmanaban, Sanjeevikumar; Priyadarshi, Neeraj; Bhaskar, Mahajan Sagar; Holm-Nielsen, Jens Bo; Ramachandaramurthy, Vigna K.; Hossain, Eklas , “A Hybrid ANFIS-ABC Based MPPT Controller for PV System with Anti-Islanding Grid Protection: Experimental Realization,” *IEEE Access*, pp.1–1, 2019. doi:10.1109/ACCESS.2019.2931547

[8] Zakarya Benizza, Ahmed Mouhsen, Ezzitouni Jarmouni , "ANNs Based Unit for Power Control in a Micro Data Center," *International Journal of Engineering Trends and Technology* , vol.69, no.5, pp.6-10, 2021. Crossref, https://doi.org/10.14445/22315381/IJETT-V69I5P202.

[9] Ye, Beijia; Qi, Jun; Li, Yuanchao; Xie, Luyao; Yang, Fan, “Research on PV array output characteristics based on shadow image recognition, “ [IEEE 2017 IEEE Conference on Energy Internet and Energy System Integration (EI2) - Beijing, China (2017.11.26-2017.11.28)] , *IEEE Conference on Energy Internet and Energy System Integration (EI2)* , pp.1–6, 2017.

[10] Manasa M, Dr. Sidheshwar Prasad, "Hybrid Model of Photovoltaic Power Plant for Electric Vehicle Charging System,” *International Journal of Computer & organization Trends (IJCOT),* vol.4, no.3, pp.90-95, 2014. Crossref, https://doi.org/10.14445/22492593/IJCOT-V9P306. ISSN:2249-2593.

[11] Mahmoud, Yousef; El-Saadany, Ehab , “A Novel MPPT Technique based on an Image of PV Modules,” *IEEE Transactions on Energy Conversion*, pp.1–1, 2016.

[12] Hu, Yihua; Cao, Wenping; Wu, Jiande; Ji, Bing; Holliday, Derrick, “Thermography-Based Virtual MPPT Scheme for Improving PV Energy Efficiency Under Partial Shading Conditions,” *IEEE Transactions on Power Electronics*, vol.29, no.11, pp. 5667–5672, 2014.

[13] John Nweke, Arthur Ekwue, Emenike Ejiogu , "Economic Feasibility of Integrating Solar Photovoltaic Distributed Generation With Nigerian Power System," *International Journal of Recent Engineering Science*, vol.7, no.3, pp.61-71, 2020. Crossref, https://doi.org/10.14445/23497157/IJRES-V7I3P113.

[14] Alsmadi, Mohammad; Mahmoud, Yousef, “ Image-Based Differential Power Processing for Photovoltaic Microinverter,” *IEEE Transactions on Energy Conversion*, pp.1–1, 2020.

[15] N. E. Zakzouk, M. A. Elsaharty, A. K. Abdelsalam, A. A. Helal, and B. W. Williams, "Improved performance low-cost incremental conductance PV MPPT technique," *IET Renewable Power Generation*, vol. 10, no. 4, pp. 561–574, 2016.

[16] Niharika Agrawal, and Mamatha Gowda. "Power Flow Enhancement by TCSC using Two Different Types of Pulse Generators" *International Journal of Recent Engineering Science* , vol. 9, no. 1, pp. 31-38, 2022. Crossref, https://doi.org/10.14445/23497157/IJRES-V9I1P105.

[17] D. C. Huynh and M. W. Dunnigan, "Development and Comparison of an Improved Incremental Conductance Algorithm for Tracking the MPP of a Solar PV Panel," *IEEE Transactions on Sustainable Energy*, vol. 7, no. 4, pp. 1421–1429, 2016.

[18] K.Kiruthiga, A.Dyaneswaran, B.Kavitha, Dr.R.Prakash ." A Grid Connected Hybrid Fuel Cell-PO Based MPPT for Partially Shaded Solar PV System,” *International Journal of P2P Network Trends and Technology (IJPTT)*, vol.4, no.2, pp.42-46, 2014. ISSN:2249-2615,

[19] 11 M. A. Elgendy, D. J. Atkinson, and B. Zahawi, "Experimental Investigation of the Incremental Conductance Maximum Power Point Tracking Algorithm at High Perturbation Rates," *IET Renewable Power Generation*, vol. 10, no. 2, pp. 133–139, 2016.

[20] T. Esram and P. L. Chapman, "Comparison of Photovoltaic Array Maximum Power Point Tracking Techniques," *IEEE Trans. Energy Convers.*, vol. 22, no. 2, pp. 439–449, 2007.

Measurement: Sensors 24 (2022) 100473

Contents lists available at ScienceDirect

Measurement: Sensors

journal homepage: www.sciencedirect.com/journal/measurement-sensors

Challenges in internet of things towards the security using deep learning techniques

K.C. Ravikumar [a,*], Pandi Chiranjeevi [b], N. Manikanda Devarajan [c], Chamandeep Kaur [d], Ahmed I. Taloba [e,f]

[a] Department of Computer Science Engineering, Sridevi Women's Engineering College, India
[b] Ace Engineering College, Ghatkesar, Hyderabad, India
[c] Department of Electronics and Communication Engineering, Malla Reddy Engineering College, Medchal - Malkajgiri District, Telangana, 500100, India
[d] Computer Science Department, Jazan University, Jizan, Saudi Arabia
[e] Department of Computer Science, College of Science and Arts in Qurayyat, Jouf University, Saudi Arabia
[f] Information System Department, Faculty of Computers and Information, Assiut University, Assiut, Egypt

ARTICLE INFO

Keywords:
Internet of things
Security
Challenges
Deep learning
Vulnerabilities

ABSTRACT

Securing IoT devices and delivering end-to-end security in an IoT ecosystem presents a variety of issues. Regardless of the way that security concerns are not new with regards to data innovation, the qualities of numerous IoT arrangements give new and special security issues. It's anything but a main concern to resolve these issues and guarantee the security of IoT items and administrations. Clients should have certainty that IoT gadgets and related information administrations are secure, especially as this innovation develops more unavoidable and coordinated into our day by day lives. The goal of this article is to provide an overview of the Internet of Things and to go through all of the known security concerns that the Internet of Things faces today. All of the findings are based on publicly available documentation for essential Internet of Things components. Threats to IoT security, both inherent and newly developed, are discussed, as well as numerous potentials. The attack surfaces of the IoT system are examined, as well as the potential hazards associated with each surface. We then, at that point go over the benefits, weaknesses, and qualities of every Deep Learning approach for IoT security. We talk about the advantages and disadvantages of applying Deep Learning to IoT security. Future exploration headings could be founded on these chances and difficulties.

1. Introduction

The Internet of Things (IoT) is an organization comprised of interconnected gadgets. These gadgets are equipped for detecting their current circumstance and sharing and handling information that can be made accessible to an assortment of utilizations. Despite the fact that it is as yet in its beginning phases, the Internet of Things can possibly introduce another time of figuring. It's difficult to foresee what the Internet of Things' innovation will mean for our day by day lives and ways of life. The Internet of Things (IoT) was immediately made and received in an assortment of fields, including industry, farming, and the military [1]. Since the Internet of Things is so generally utilized and innovatively assorted, new gadgets are constantly being coordinated into it, either as IoT terminals or as IoT branches [2]. As an open Internet-based climate, IoT gadgets face a wide scope of safety dangers, as they are continually assaulted and annihilated by the rest of the world [3]. Therefore, there is a need to build security issue identification in IoT. The Internet of Things (IoT), a new creation in data and correspondences innovation, has dominated customary detecting of general conditions. IoT innovations have made it simpler to make arrangements that work on individuals' personal satisfaction. The Internet of Things (IoT) is one of the quickest developing registering advances, with an expected 50 billion gadgets by 2020 (see Figs. 1–4).

By leveraging fundamental IoT technologies such as communication technologies, pervasive and ubiquitous computing, embedded devices, Internet protocols, sensor networks, and AI-based applications, IoT devices can become smart objects. Calculation and communication are extended to additional IoT devices with differing specifications due to

* Corresponding author.
E-mail addresses: kcravikumar1971@gmail.com (K.C. Ravikumar), chiruanurag@gmail.com (P. Chiranjeevi), nmdeva@gmail.com (N. Manikanda Devarajan), kaur.chaman83@gmail.com (C. Kaur), aitaloba@ju.edu.sa (A.I. Taloba).

https://doi.org/10.1016/j.measen.2022.100473
Received 27 June 2022; Received in revised form 15 September 2022; Accepted 16 September 2022
Available online 29 September 2022

the widespread interconnection of physically scattered IoT devices [4]. These devices have a variety of sensors that allow them to collect data in real time from faraway physical devices. The Internet of Things (IoT), for example, has significantly advanced the traditional detection of surrounding situations. IoT technologies have the ability to collect, quantify, and comprehend the surrounding environments, allowing for modernizations that improve quality of life [6]. This circumstance simplifies new forms of communication between things and humans, allowing smart cities to be implemented [2]. The Internet of Things (IoT) is one of the most rapidly growing sectors in IT history, with an estimated 50 billion devices in use by 2020. On the one hand, IoT technologies are critical for developing real-world intelligent applications like smart healthcare, smart homes, and smart cities. Furthermore, the cross-cutting and large-scale nature of IoT systems, as well as the many components engaged in their deployment, has posed additional security challenges.

IoTs are intricate and contain a variety of integrative configurations. As a result, sustaining the IoT system's safety requirement on a large-scale attack surface is difficult. To meet the security requirements, solutions must take a holistic approach.IoT devices, on the other hand, are generally used in an unsupervised setting. As a result, a trespasser will be able to physically gain access to these devices. IoT devices are frequently connected to wireless networks, allowing an intruder to listen in on a communication channel and gain access to private information. Due to their limited computing and power resources, IoT devices are unable to handle elaborate safety frameworks [5].Because the IoT system is complex, it is due not only to limited compute, communication, and power resources, but also to trustworthy interaction with a physical domain, particularly the behaviour of a physical environment in unpredictable and unanticipated modes. It's also a part of a cyber-physical system; IoT systems must continually adapt and survive in their own right.IoTs are intricate and contain a variety of integrative configurations. As a result, sustaining the IoT system's safety requirement on a large-scale attack surface is difficult. To meet the security requirements, solutions must take a holistic approach.Furthermore, the IoT environment introduces new attack surfaces. The IoT's intertwined and networked ecosystems create these attack surfaces. As a result, security in IoT systems is at a higher risk than in other IT systems, and

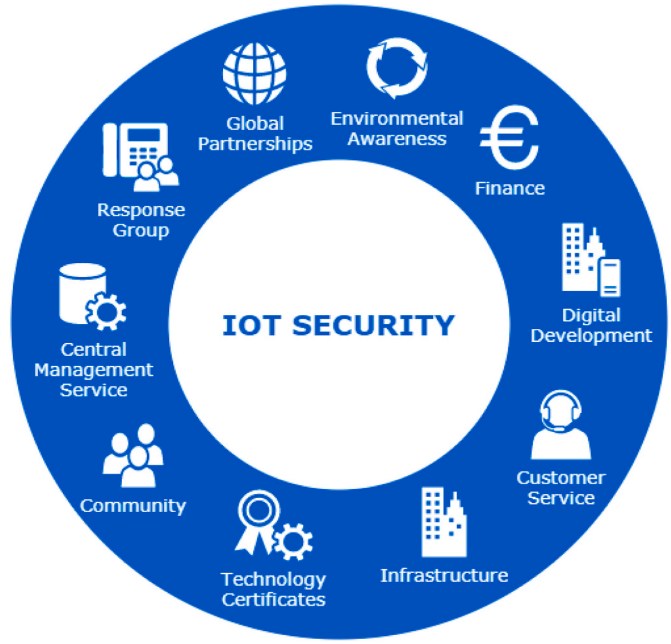

Fig. 2. IoT security.

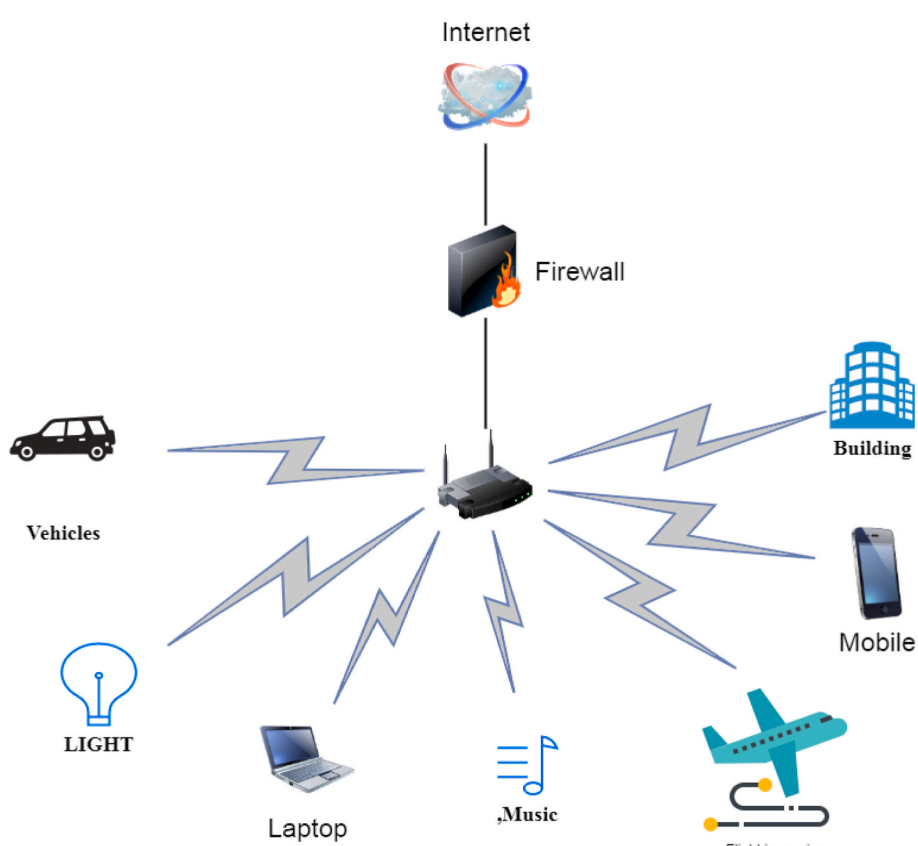

Fig. 1. Internet of things.

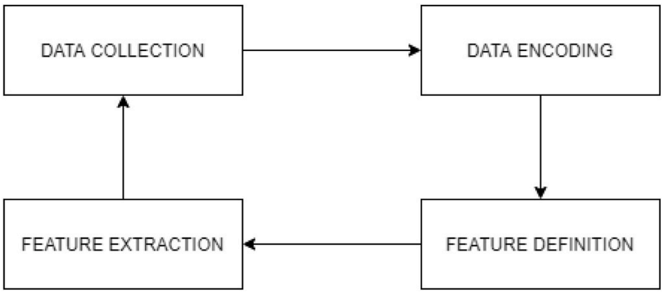

Fig. 3. Block diagram.

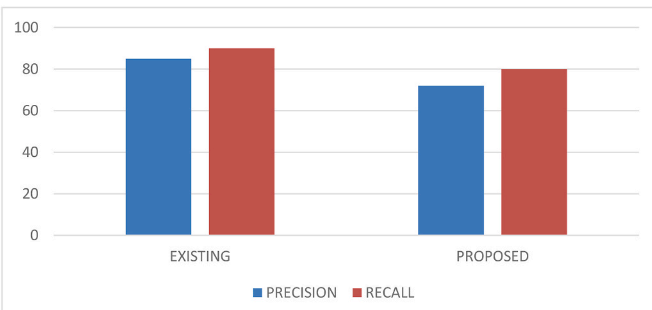

Fig. 4. Comparisons between existing & Proposed method.

typical solutions may be inadequate [7].Security gateways, firewalls, code signatures, and encryption technology are among the existing security technologies, but they are all passive safety defence measures that cannot perform active detection and reaction. By recording data attributes and evaluating attack behaviour, IoT security detection determines whether the IoT is in a dangerous environment.Rapid action may be performed in the event of an attack to intercept attack information and prevent loss [8]. This method allows for active IoT security detection as well as passive defence.Traditional security detection systems, on the other hand, can't provide adequate security protection for IoT since it has limited computational capability and connects a huge number of external devices [9].As a result, safety detection systems tailored to the Internet of Things must be developed. Smart sensing technology [16] is quickly evolving, and deep learning algorithms may now be used in the context of sophisticated IoT attack types and large amounts of data. The computing capacity of computers has been substantially boosted because to deep learning. The deep learning algorithm, in comparison to the machine learning method, can handle big, complex datasets.The deep learning algorithm, as opposed to the machine learning algorithm, can handle huge, high-dimensional data samples.However, the existing deep learning technique has low precision and robustness, and its success is dependent on the data samples' features [10]. As a result, in order to effectively support IoT, deep learning algorithms must be upgraded.

2. Related works

The Internet of Things (IoT) connects billions of smart gadgets so that they can communicate with one another without the need for human intervention. The author [11] discusses how IoT technology has advanced quickly and is now widely employed in a variety of industries, including industry, agriculture, and the military.Because the Internet of Things is so widely used and technologically diverse, new devices are continuously being integrated into it, either as IoT terminals or as IoT branches [2]. Security gateways, firewalls, code signatures, and encryption technology are among the existing security technologies, but they are all passive safety defence measures that cannot perform active detection.

Badri Narayanan and colleagues [12] presented a convolutional neural network structure including an encoder network, a decoder network, and a pixel classification layer that can transfer the low-resolution encoder feature map to the full-input resolution feature map for pixel classification.Several academics have looked at IoT security in order to create a practical guide on existing IoT security issues as well as a roadmap for future work. Most existing IoT security surveys, on the other hand, haven't directly addressed ML/DL applications in terms of IoT security.

In [4], the author concentrated on legal issues and regulatory approaches in order to establish if IoT frameworks fit confidentiality and security criteria. In the context of the dispersed IoT, Novel, Zhou, and Lopez [3] examined security and secrecy.They also noted a number of issues that must be solved, as well as the security and confidentiality advantages of the dispersed IoT method. The growth of vulnerabilities and dangers in IoT systems, such as ransom ware attacks and security issues, was examined in a paper published in Ref. [2].

Xiao et al. looked explored machine learning methods for protecting data privacy and security in the setting of the Internet of Things. Their research also identified three obstacles to ML implementation in IoT systems in the future.

Chun-Cheng Lin et al. (2021) outline energy sharing in local areas as part of the Internet of Energy, with energy swapping to increase the use of sustainable electricity and reduce grid energy waste. To answer these issues, a hybrid algorithm is applied, which provides a defined technique to ensure the possibility of a result. The simulation was done performed on issues with complexity ranging from 5 to 20.The simulations were conducted on challenges involving complexes of 5–150 dwellings. The results showed that the technology outperformed the previous method, although there was a balance in the energy use of the complex's homes.

A.T.D Pereraetal (2020) proposed a theoretical game method to evaluate the distributed energy frameworks for the implementation of energy. A optimization algorithm optimises the individual energy hub and its interconnection. Network integration can be significantly improved and the cost of generating energy can be reduced. The current study also fails to account for the variation in performance due to concerns that arise throughout the optimization process.

Y.Liuetal(2020) explains an optimal planning technique based on interval optimization for energy grid areas. The planning strategy for the Energy Internet Zone was proposed based on optimizing the intervals. PV systems are a high-risk asset in HEI planning; they are preferred by DMs with a low level of optimism and avoided by others.

Hossein Shahinzadehetal(2019) discussed about the use of Internet of Energy which is a type of internet of things (IoT) application in smart power systems, has emerged as a result of the integration of ICT with the present trend of technical progress in the energy sector. The use of internet-based technologies in power systems has numerous benefits for power systems in various sectors, and it paves the way for a bright future for the energy sector's development.

Y. R. Kafleetal(2018) analyse what's more, contrast present-day web and energy organizations and administrations, distinguishing key functionalities and the primary specialized difficulties to be looked in changing the power dissemination framework to an adaptable yet dependable and hearty stage for the trading of electrical energy. The Internet will be used to monitor and exploit scattered energy resources in the future power grid, but it will also resemble the Internet.

3. Methodology

3.1. Iot security threats

IoT interfaces the Internet to the actual world to make astute communications between the actual world and its environmental factors. IoT gadgets are regularly utilized in a scope of settings to accomplish different objectives. Their working, then again, should meet a general security need in both digital and actual states. IoT frameworks are confounded and include an assortment of gadgets. Thus, while making powerful IoT security strategies, the upkeep of the security need with the huge scope assault surface of the accompanying significant security properties ought to be thought of.

Confidentiality: For IoT frameworks, classification is a basic security component. IoT gadgets can store and communicate delicate information that ought not be imparted to unapproved people. The IoT framework is a test since it is clinical (patient-explicit) and individual. To accomplish the ideal degree of wellbeing, the arrangement should adopt a comprehensive strategy.

Integrity: Data from IoT devices is typically transmitted over wireless connection and can only be modified by authorised parties. To establish an effective control system for detecting changes while communicating over an unprotected wireless network, integrity characteristics are required.

Authentication: Prior to some other activity, the personality of elements should be altogether settled. Notwithstanding, the idea of IoT frameworks implies that verification needs fluctuate starting with one gadget then onto the next. In an IoT framework, for instance, where a help should give powerful security as opposed to high adaptability, confirmation ought to be strong.

Authorization: Approval alludes to the way toward conceding clients admittance to an IoT framework, like an actual sensor. Machines, people, and administrations would all be able to be clients. Information procured by sensors, for example, ought to just be conveyed to and gotten to by approved clients.

Availability: The administrations given by IoT frameworks should be open to approved gatherings consistently. The accomplishment of IoT organization relies upon accessibility. Various dangers, like DoS or dynamic impedance, may, notwithstanding, render IoT frameworks and gadgets unusable. Accordingly, guaranteeing the proceeded with accessibility of IoT administrations to clients is a significant part of IoT security.

4. Deep learning in iot

As a result of its remarkable nature of issue goal, learning calculations have been generally utilized in various genuine world applications. These calculations are responsible for robotizing the production of machines during the trial. Learning calculations have as of late been broadly utilized by and by. The formation of new calculations, just as the accessibility of huge information and the ascent of minimal expense registering methods, has all supported the current advancement of learning calculations.

Most IoT applications depend on a canny learning strategy to perceive and comprehend their environmental factors. Many AI strategies have recently been proposed to give information to IoT gadgets. Notwithstanding, with the ascent in prevalence of profound neural organizations and profound learning as of late, the utilization of profound neural organizations in the IoT business has gotten more attention.The top three specialized patterns reported at the Gartner Symposium/ITxpo are profound learning and the Internet of Things. Customary AI calculations have neglected to deal with the scientific necessities of IoT frameworks, which produce information at such a fast rate and volume that man-made consciousness calculations with present day information insightful capacities are required.

4.1. Deep learning methods for IoT security

DL applications to IoT frameworks have as of late been a basic examination theme. When contrasted with customary ML, the main benefit of DL is its better in huge informational indexes. Since numerous IoT frameworks create a great deal of information, DL approaches are a solid match for them. Besides, the DL can recover muddled portrayals from information consequently. Profound associations of the IoT climate might be conceivable with DL draws near. Profound Binding is a uniform convention that empowers IoT-based gadgets and applications to speak with each other without the requirement for human contribution. IoT devices in a shrewd house, for instance, can interface naturally to make a genuinely brilliant home. Since they may catch various leveled portrayals inside the profound engineering, DL approaches are now and again known as progressive learning techniques.

The theory of functioning of DL is based on the signal processing systems of the human brain and neurons.

4.2. Convolution neural networks

CNNs were made to limit the quantity of information boundaries in a standard fake neural organization (ANN). Three methodologies are utilized to diminish information boundaries: scanty connection, boundary sharing, and equivalent portrayal [11]. Diminished layer associations further develop adaptability and increment the intricacy of a CNN's driving time. Convolution and bunching layers shift back and forth among convolution and grouping layers in a CNN. Convolution layers utilize a few equivalent measured channels (centers) to tangle information boundaries. The pooling layers take care of their work. Most extreme or normal pooling to diminish the size of succeeding layers through down inspecting. Normal pooling midpoints the upsides of each group in the past layer, though max pooling isolates the contribution to non-covering bunches and chooses the greatest incentive for each group in the past layer. The actuation unit, which applies a non-straight enactment work on every part of the usefulness space, is another vital layer of a CNN. The amended straight unit (ReLU) initiation work is utilized as the nonlinear enactment work, which includes hubs with the actuation work.

4.3. Feature learning process

Information extraction is generally characterized as the social affair, pre-treatment, and extraction of information. For the motivations behind our exploration, we'll separate it into four stages: information gathering, information encoding, characterizing usefulness, and removing usefulness. In light of existing attributes gathered from IoT security conduct information bases, security highlights are named static highlights, dynamic highlights, and causal highlights.

Crude information, for example, RF signals, gadget boundaries, warm temperature, and crude organization parcels are gained during the information assortment stage. Crude information can be very huge, contain an assortment of information organizes, and contain an immense number of irrelevant passages, accordingly sort out some way to deal with it. Singular pixels inside a specific picture or individual bundles inside an organization traffic stream are instances of fundamental components of interest that are available inside the information [13,14]. Information encoding is the demonstration of characterizing the fundamental component of interest that is contained inside the info. Each segment is addressed as xi for this situation.

When characterizing attributes [15], the information is coordinated in a way that takes into consideration a steady investigation of the information object. As a rule, input things are coordinated as a conveyance, a grouping, a network, or, all the more as of late, a tensor in profound learning. The crude sources of info can be transformed into an arrangement that can be used as contribution for a profound learning model after the information has been encoded. The way toward characterizing characteristics is addressed as D, while the information subsequent to characterizing qualities is addressed as.

$$X = D\,(x_1, x_2, \ldots, x_k), \tag{1}$$

where D is the technique for organizing the fundamental component into foreordained successions. The highlights are gotten from the data sources, contingent upon the meaning of the attributes. To create highlights from coordinated information things, strategies like measurable techniques, series investigation, recurrence examination, and AI are used. The component separate is characterized as follows.

$$V = F(X) = F(D(x_1, x_2, \ldots, x_k)), \tag{2}$$

The letter F stands for function extraction methods. Normally, function vectors with fixed length V = are the output of function extraction (v1, v2,…, vm).In this paper, we offer a two-step data preprocessing phase: (1) a data encoding process for extracting relevant features from mixed raw inputs, and (2) a feature defining procedure for giving our data structure.

4.4. Deep learning for device feature extraction

IoT organizations can incorporate an immense number of connected gadgets, making it hard to distinguish a particular gadget inside an organization. We'll see how to recognize a particular IoT gadget utilizing usefulness extraction strategies.

Profound learning's capacity to naturally take in important highlights from crude sources of info, like auto encoders, is one of its most huge properties. Inside and out learning approaches for gadget extraction can be classified dependent on the crude information they use for gadget ID. Sensor commotion, radio recurrence attributes, and energy utilization may all mirror the gadget's exceptional nature. Undeniable level highlights might be recuperated utilizing profound learning, and surprisingly very minuscule varieties across gadgets can be distinguished. This is the circumstance with camera distinguishing proof, when crude photographs from the camera can be gathered. We start by characterizing the crude picture assortment since I can extricate the commotion design from photos that are viewed as novel to a gadget. Coming up next are a few instances of normal commotion profiles:

$$N = I - F(I), \tag{3}$$

where I is the first picture including the first commotion and F(i) is the demonstrated form of I. Measurable methodologies consider lingering commotion as a two-dimensional dissemination and concentrate highlights like mean, max, lopsidedness, and kurtosis to extricate signal clamor designs from an image. Clamor signs can be dealt with as a two-dimensional sign utilizing a recurrence portrayal, and afterward techniques like wavelet change or Fourier change can be utilized to decide the recurrence of commotion level. Dissimilar to the methodologies portrayed above, profound learning calculations, for example, those depicted in Ref. [10] input the sign clamor grid straight into the CNN, which attempts to remove highlights from commotion consequently with least human collaboration.

They gain proficiency with the sign clamor model with the sign commotion extraction stage utilizing profound learning. The creators extricate K non covering patches Pk, k [1, K] with a size of 64,64 pixels for each shading picture I and its camera model L. They eliminate all locales where the normal pixel esteem is close to a large portion of the picture's dynamic reach to try not to choose uninformative districts of the picture (e.g., dull and immersed pixels). The image of the clamor work is removed from the spaces utilizing the CNN. Then, at that point, to distinguish the contrasts between unmistakable camera models, a bunch of (N 1)/2 direct parallel SVMs is prepared.

RF fingerprinting was studied in a similar way. Signals from several devices are collected in RF (IQ). They see the Zigbee device's base band as a complicated time series that looks like this:

$$r(t) = s_1(t) + n_1(t), \tag{4}$$

The commotion is addressed by n(t). Noteworthy stage and quadrature (I and Q) information from six ZigBee gadgets creating 0, 1, 5, 10, and 15 dBm were utilized as preparing information. They investigate with various window widths addressing the quantity of I and Q input arrangements in profound learning models, like 16, 32, 64, 128, and 256. At long last, they think about the presentation of a few profound learning models in the arrangement of Zigbee peripherals.

A thermal map of the devices can be used to create a standard device model in terms of energy usage. This could lead to the detection of a malicious hardware update. The authors grouped the bullets into numerous equal-sized grids in their study. The running chip is then fed with a randomly generated "excitation vector." Finally, they take temperature readings in equilibrium for each grid.Data from devices must first be collected in order to construct a device reconnaissance pattern. Second, the data must be translated into characteristics that can be fed into a deep learning model as inputs.Matrix, sequence, or statistical contributions are common to the in-depth learning framework. Then, using deep learning, a typical device pattern can be created.

Customary AI approaches depend on human work to separate highlights, which is hard proportional when managing IoT gadgets. Moreover, physically organized capacities might be designated or changed by an aggressor. Delegate highlights could be resolved consequently utilizing profound learning methods like autoencoders, which could be utilized for finger impression gadgets.

4.5. Network behaviour modelling with deep learning

Packets, streams, and talks among communication entities are the core aspects that are frequently considered when modelling network behaviour. Data concerning network traffic, unlike other types of data, is heterogeneous.The timestamp, connection ID, and data description are the three pieces of a basic network traffic entry. As a result, p = time, header, content > might be used to represent a packet. A sequence of packets running between communication nodes can be formally characterised as network behaviour:

$$X = (p_1, p_2, \ldots, p_m), \tag{5}$$

where the packages are sorted by timestamps.

It can be challenging to extract features directly from a package sequence due to the diverse nature of a network capture. To inform the feature representation, statistical characteristics are often generated over a short time frame. Email time, packet length, number of packets, transmitted bytes, and received bytes are all functions that can be retrieved. This data could indicate network behaviour characteristics including communication frequency, traffic volume, and connectivity. Furthermore, these characteristics may indicate the buffer size and compute capacity of a device, as well as the services it offers. The following is a description of the procedure:

$$S = S(X) = S(w_1, w_2, \ldots, w_k), \tag{6}$$

where the series of bundles that fall into the ith time window can be portrayed. Time, association, and content are ordinarily utilized by scholastics to separate uncorrelated measurable factors. In network conduct demonstrating, profound learning fills two needs: (1)automatic extraction of significant level organization traffic qualities, and (2) programmed distinguishing proof of applicable highlights across a few measurements. Profound learning-based conduct displaying can be described as,

$$V = H(S) = H(w_1, w_2, \ldots, w_k), \tag{7}$$

The black box is a non-straight capacity utilized in profound learning, and H represents it. From that point forward, you can make a fixed length conduct vector to address network security. The black box is a non-direct capacity utilized in profound learning, and H represents it. From that point onward, you can make a fixed length conduct vector to address network security. They utilize Interarrival Time (API) as usefulness to assemble an API outline, like the work in. The diagrams are then changed to photographs, and all pictures are resized to 160 by 160 pixels prior to being taken care of into a neural organization to identify gadget personal conduct standards. Bundle groupings are considered via looks for gadget network traffic. They began by partitioning the traffic into sub-currents with a period time frame. Data identified with parcel tally, bundle length insights, and convention related highlights are recovered for each sub-stream. The undeniable level properties of the whole stream are then removed utilizing a CNN course model. To get ordinary profiles from IoT gadgets, both utilize auto-encoders. Gather bundle size, parcel tally, parcel jitter, and bundle size from the progression of bundles, and afterward use the auto encoder to revamp the first contribution to request to find gadgets that act strangely.

5. Results and discussion

To verify the Deep Learning framework, we require a set of performance metrics and a set of benchmark data to evaluate the performance of DL-based approaches.

5.1. Evaluation measure

Perhaps the most generally utilized measurements in Machine Learning is exactness. The measure of genuine positive expectations isolated by the all out number of positive gauges is known as accuracy (regardless of whether valid or bogus). The quantity of fake alerts in an interruption location framework is addressed by tp.

$$\text{Precision} = \frac{t_p}{(t_p + f_p)} \tag{8}$$

where tp indicates the quantity of precise cases named positive and fp means the quantity of erroneous cases named positive.

Review is another incessant exhibition metric (additionally called affectability). The quantity of genuine positive expectations for all sure circumstances is characterized as the update. A review can be depicted as follows:

$$\textbf{Recall} = \frac{\textbf{tn}}{(\textbf{tp} + \textbf{fp})} \tag{9}$$

where tn is the quantity of positive cases that have been misclassified as regrettable (bogus negatives). In an interruption discovery framework, fn is the quantity of assaults that go undetected. Precision and review regularly have a to and fro association, with one improving to the detriment of the other.

6. Challanges

Efficiency: IoT gadget asset limits keep on being a generous obstruction to profound learning model arrangement. In the organization of profound learning in genuine IoT frameworks, memory effectiveness and time proficiency would be two significant concerns. Albeit profound learning models can be prepared disconnected, conveying them is as yet a test. The high number of nonlinear and layered neurons used in the profound learning design gives a profound learning model its force.Deep learning models make decisions based on raw input that passes through overlaid neurons. In resource-constrained applications, reducing the amount of storage and computing required for deep learning model execution is a constant issue.Diverse new designs outperform cutting-edge performance thanks to the advent of deep learning technologies. However, many of these were not created specifically for the IoT framework. The ability to fully adapt these algorithms to an IoT context will undoubtedly aid in improving the results of recent studies.

Adaptive: Deep learning must be adaptive in the same manner that the IoT ecosystem's devices and apps change on a daily basis. Zero-day attacks are bound to occur in a genuine network. The IoT system is then updated with new functionalities. Moreover, as extra gadgets join the organization, the appropriation of organization traffic or sign recurrence is probably going to move. A static model will battle to adjust to evolving conditions, maybe prompting an expansion in bogus positives and negatives. The interest of the end client is another variable that is continually evolving. Profound learning applications in the IoT face new obstacles because of these changes.

Heterogeneous Data IoT gadgets produce a lot of information of different sorts and sizes, for example, information from signal recurrence and organization traffic, which, while coming from a similar gadget, will be in various structures. Indeed, even information of a similar sort, like the quantity of bundles and bytes, can have various scales. They're completely identified with network usefulness, yet they're scaled in an unexpected way. It's an endless trouble to sort out some way to manage these unique informational collections.

7. Conclusion

The various innovations, going from actual gadgets and remote transmission to versatile and cloud models, should be gotten and combined with different advancements, the necessities for ensuring IoT gadgets have gotten mind boggling. Profound Learning's development has worked with the making of various solid logical methodologies that might be utilized to further develop IoT security. Profound learning has a ton of potential in the IoT system, as we've found in this post. This examination centers around the utilization of profound learning innovation to the investigation of gadget security with regards to the Internet of Things. The exhibition of profound learning gadgets specifically was completely investigated. At last, we discussed the issues of web of things security.

CRediT authorship contribution statement

K.C. Ravikumar: Conceptualization, Methodology. **Pandi Chiranjeevi:** Data Collection related to IoT Challenges. **N. Manikanda Devarajan:** system Concepts drafting. **Chamandeep Kaur:** Implementation and validation. **Ahmed I. Taloba:** Additional Validation.

Declaration of competing interest

The authors declare that they have no known competing financial interests or personal relationships that could have appeared to influence the work reported in this paper.

Data availability

No data was used for the research described in the article.

References

[1] R.H. Weber, Internet of things–new security and privacychallenges, Comput. Law Secur. Rep. 26 (1) (2010) 23–30.
[2] R. Roman, J. Zhou, J. Lopez, On the features andchallenges of security and privacy in distributed internet ofthings, Comput. Network. 57 (10) (2013) 2266–2279.
[3] I. Yaqoob, et al., The rise of ransomware and emergingsecurity challenges in the Internet of Things, Comput. Network. 129 (2017) 444–458.
[4] L. Xiao, X. Wan, X. Lu, Y. Zhang, D. Wu, IoT SecurityTechniques Based on Machine Learning, 2018 arXiv preprintarXiv:1801.06275.
[5] A.L. Buczak, E. Guven, A survey of data mining andmachine learning methods for cyber security intrusiondetection, IEEE Communications Surveys & Tutorials 18 (2) (2016) 1153–1176.
[6] P. Mishra, V. Varadharajan, U. Tupakula, E.S. Pilli, ADetailed Investigation and Analysis of Using MachineLearning Techniques for Intrusion Detection, IEEECommunications Surveys & Tutorials, 2018.
[7] A. Al-Fuqaha, M. Guizani, M. Mohammadi, M. Aledhari, M. Ayyash, Internet of things: a survey on enablingtechnologies, protocols, and applications, IEEECommunications Surveys & Tutorials 17 (4) (2015) 2347–2376.
[8] A. Whitmore, A. Agarwal, L. Da Xu, The Internet ofThings—a survey of topics and trends, Inf. Syst. Front 17 (2) (2015) 261–274.
[9] Z. Yang, Y. Yue, Y. Yang, Y. Peng, X. Wang, W. Liu, Study and application on the architecture and keytechnologies for IOT, in: Multimedia Technology (ICMT),2011 International Conference on, IEEE, 2011, pp. 747–751.
[10] M. Wu, T.-J. Lu, F.-Y. Ling, J. Sun, H.-Y. Du, Research on the architecture of Internet of things, in: Advanced Computer Theory and Engineering (ICACTE),2010 3rd International Conference on, vol. 5, IEEE, 2010. V5-484-V5-487.

[11] C. Perera, A. Zaslavsky, P. Christen, and D.Georgakopoulos, "Context aware computing for the internetof things: a survey," IEEE communications surveys &tutorials, vol. 16, no. 1, pp. 414-454.

[12] P. Sethi, S.R. Sarangi, Internet of things: architectures,protocols, and applications, Journal of Electrical andComputer Engineering 2017 (2017).

[13] D. Zeng, S. Guo, Z. Cheng, The web of things: Asurvey, JCM 6 (6) (2011) 424–438.

[14] M.A. Razzaque, M. Milojevic-Jevric, A. Palade, S. Clarke, Middleware for internet of things: a survey, IEEE Internet Things J. 3 (1) (2016) 70–95.

[15] S. Neely, S. Dobson, P. Nixon, Adaptive middlewarefor autonomic systems, in: Annales des télécommunications, vol. 61, Springer, 2006, pp. 1099–1118, 9-10.

[16] Ramachandran Veerachamy, Ramalakshmi Ramar, S. Balaji, L. Sharmila, Autonomous application controls on smart irrigation, Comput. Electr. Eng. 100 (2022) 1–9.

Emerging challenges in IoT, Blockchain and Data Mining for effective treatment of Covid and flu diseases through Telemedicine process

Kireet Muppavaram[1*], Kiran Kumar Mamidi[2], Manyam Thaile [3], Bhaskar .T[4]

[1] Department of CSE, GITAM School of Technology, GITAM University(DU),Hyderabad, India.
[2] Department of AIML, Gokaraju Rangaraju Institute of Engineering and Technology,Hyderabad, India.
[3] Department of CSE, Malla Reddy Engineering College, Secunderabad, India.
[4] Department of CSE, CMR College of Engineering and Technology, India

Corresponding Author Email: kmuppava@gitam.edu

Abstract—
In this present era of 21st Century due to the dangerous infected disease Covid-19 all over the world telemedicine has played a major role in many parts of the world for remote monitoring of the covid-19 patients. Still there are many gaps in online remote monitoring in telemedicine process and as a result effective monitoring of the patients is not possible in many areas in the world. The detection of patients from remote place is considered as need of the day. This study presents the new challenges in the area of telemedicine or e-healthcare system. In this study we carefully analysed the present telemedicine process and we found that effective application of IoT, blockchain technologies and data mining can enhance the telemedicine process. This paper presents the new challenges in IoT, blockchain technologies and data mining where the researchers can work to fill the gaps in telemedicine process.
.

Index Terms— Telemedicine, e-healthcare, IoT, blockchain ,data mining, remote monitoring, covid-19

DOI Number: 10.14704/nq.2022.20.11.NQ66158 **NeuroQuantology 2022; 20(11): 1652-1657**

1 INTRODUCTION

ONE of the major challenges in this century is to provide quality of health services to people all over the world. The World Health Organization (WHO) has expressed the vision of health for all strategy in this 21st century. The population all over the globe is vastly expanding and the number of physical checkups for the mankind are not at all the solution to reach the motto of "Health for all". From more than 30 years of research in the area of providing the quality of health services researchers came up with a solution of Telemedicine which is accepted globally. Telemedicine is a process of using electronic information and communication technology to diagnose the patients who are at distance places. The health analysts after observing this Covid situation all over the world confirmed that telemedicine plays a major role in near future to diagnose the patients from remote place all over the world.

Telemedicine is medicine offered to the people who are at a distance. The World Health Organization (WHO) defines the

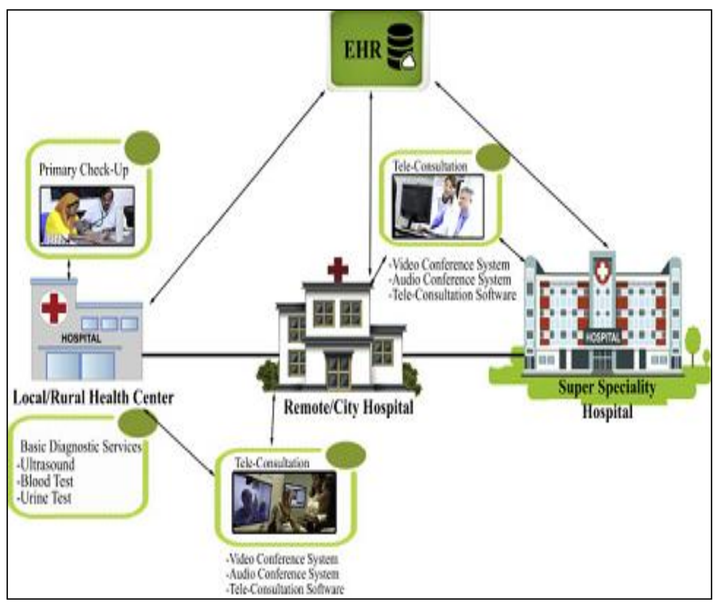

Figure 1 Effective Telemedicine Process

telemedicine as the "delivery of health care services" when the distance is the major factor for the patient. Telemedicine includes the usage of Information communication technology (ICT) devices for the remote monitoring of the patient. The remote monitoring includes several diagnoses through online by using video consultations, e-mail consultation,

smartphones, wireless tools etc. There are several treatments that can be done using Telemedicine like diagnosis of injuries, head ache, back pain enquiries about health issues, post treatment checkups.

The success of telemedicine in the last thirty years is dependent on the technologies that were used in implementing the system between the people and analysts or doctors. The history of telemedicine says that the concept of telemedicine initially started using telephones by tele-consultations. Slowly the way of consultations has been

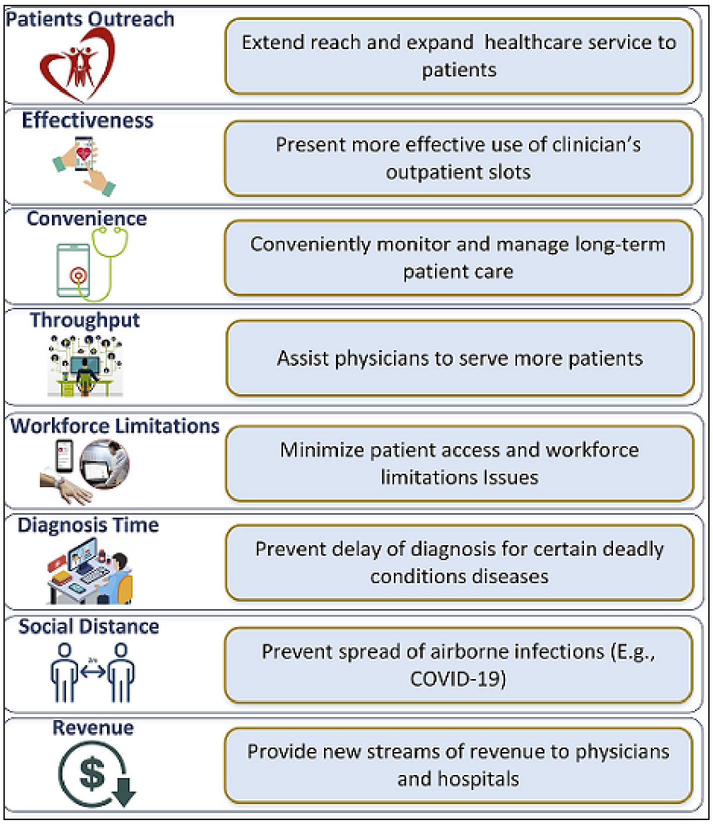

Figure 2 : Adavantages of Telemedcine services

enhanced by using ICT devices. The Information Technology has played a big role in expanding and implementing the easiest way of providing healthcare to the people.

During this Covid period all over the world telemedicine is playing a major role in providing the health services to the people. There were number of computational applications which were used in expanding the telemedicine services. In this Internet era, Internet of things(IoT), Blockchain Technologies and Data mining applications are playing a major role in diagnosing the several diseases by

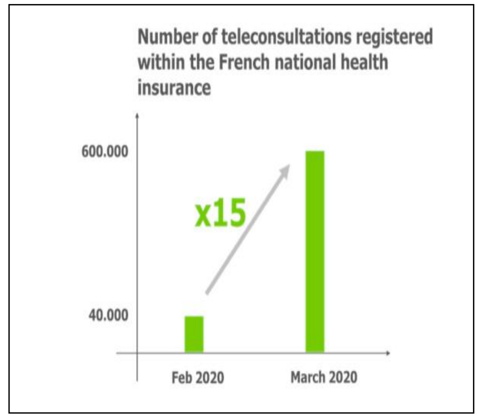

Figure3: Tele-consultations in 2020

providing the major reports to the analysts.In this paper we analysed the role played by these mentioned three technologies and presented their role in expanding the telemedicine services.

2 Related work

Castro, D et all [1] worked on IoT solutions applied to Healthcare. This paper talks about the solutions provided by IoT to the health care industry. The scenario in the below figure shows that how IoT wearables are used on the patient body and how they were transmitted to the analysts or doctors at remote place.

G. Subramanian and A. Sreekantan Thampy [2] worked on implementation of blockchain in providing healthcare s diabetics patients in pandemic situations. This worked focused on designing and implementation of the blockchain consortium. This can help in providing telemedicine to the patients with diabetics in pandemic situations.

.A. A. Mazlan et al [3] worked on usage of blockchain technology in healthcare. This paper shows that traditional way of exchanging the Electronic health records in the process of remote monitoring in telemedicine have limitations in the form of attackpoints. This paper also shows that how blockchain is used in addressing the limitations of exchange of Electronic health records(EHR) in the process of e-healthcare or telemedicine.

T.T. Kuo et al [4] worked on adapting the blockchain technology for the privacy preserving machine learning. They built a model which does not reveal any kind of patients information during the health information exchange in remote monitoring. This model also discusses about the issues in applying blockchain technology for privacy preserving machine learning.

A. Yassine,et al [5] worked on extracting the patterns of human activities from smart home big data. They proposed human activity pattern mining model based on the variations in smart homes. They used the association algorithms of FP-growth for recognizing the patterns and applied clustering algorithms.

B. Alkouz, et al [6] worked on predicting the spread of flu using the twitter data. They considered the physical data from the hospitals and reporting data from the reports of twitter. Based on the data from the twitter they classified the reported data and non reported data. They developed a model which uses the no of Influenza related visits to hospitals which can predict the spread of the flu in future.

Muhammad Mahtab Alam et all [8] worked on role of communication technology in IoT helathcare. This paper shows how IoT devices are used in diagnosing the infectious diseases, cordiovascular diseases, Musculoskeletal disorders (MSDs), Neuromuscular disorders. The devices like LOC(Lab-on-chip) device which uses Point of Care Testing (POCT) for detecting the infectious diseases play a major role in detecting the skin diseases, spreading diseases. These type of IoT devices are much helpful in detecting the diseases like covid which is a need of the day.

X. Xiang et al [9] worked on authentication factors of E-health systems. This work focused on designing and implementation of authentication to health care systems and resolved the problems related to the privacy concerns on patients health records. This method is light weight computation method in order to verify the identity.

Wong Kok Seng et al[10] worked on collaborative support for medical datamining in telemedicine. This worked focused on how data mining techniques are used to extract the confidential information of patient health record. The main work focused on when two different hospitals required collaborative operations. This method clearly specifies how the patient data can be extracted when the patients full record passes to different levels.

The existing methods using IoT, blockchain and data mining techniques gave directions in providing solutions to the telemedicine process. Though existing solutions are providing the solutions to the problems that come in telemedicine process, there are many challenges in protecting the privacy issues, patients data by using these technologies. To provide the effective telemedicine process there are different challenges in Blockchain, IoT and data mining. In this paper we carefully investigated the challenges which are required to provide the solutions to the effective telemedicine process.

3. New Challenges In Applying IoT, Blockchain And Data Mining To Enhance Telemedicine/ E-Healthcare

3.1 Challenges in applying IoT to E-healthcare

3.1.1Confidentiality of EHR records

In 2020, during this covid attack all over the world telemedicine has become a major platform for diagnosing many patients all over the world. The diseases like covid, flu which spreads easily need a time-to-time analysis of the patients which is not possible by treating the patients physically everytime. The previous IoT or smart devices helped in knowing the spread of the disease across various locations. The biggest challenge through this IoT devices is providing confidentiality to the patients data. Most of the EHR records, patients information is exchanged using wireless communication which may have a chance of eavesdropping. There are no relevant and safer solutions where the confidentiality of patients record is preserved.

3.1.2 Enhanced report generation

Another issue through IoT devices is not having proper extraction of patients information. The existing wearable devices are much concentrated towards heart rate, BP etc and then the information is sent through online or application services. In this particular area there are different challenges where more enhanced way of patients reports are to be generated. In order to get efficient results 'accupoint detector' is to be embedded into IoT devices.

3.1.3 Device Provisioning

The device provisioning is the process of configuring each and every device which is involved in the process of patients information exchange. The device might be a sensor, mobile devices, tags, desktop computer, laptop, smart watches or any other hand held devices. The biggest challenge here is to configure the devices involved in patients information exchange. This provisioning of IoT devices used in the process of telemedicine involves allocation of Device ID, patients ID ,storage etc. In order to ensure the security to electronic heath records of the patients device provisioning all over the network is the need of the day.

3.1.4 Device management

The device management for patients information exchange between different analysts is one more challenge in IoT in telemedicine. Considering the scenario where a patients whose record is maintained by one of the hospital and due to need in more expert treatment analysis patient wants to change his hospital. In that scenario if the device management is done by third trusted third party patient can directly exchange his Device ID, patients ID to the other hospital, by which patients condition can be completely known to new hospital doctors. Most of the existing IoT device management is done by hospitals which may not allow the patient to exchange his information to other hospital due to their competative problems. The challenge here if the device management is done by trusted third party it resolves most of the problems.

3.2 Challenges in applying blockchain technology in Telemedicine or e-healthcare sector

The blockchain technology is slowly applied to many domains and it has become a huge buzzword in many applications all over the world. The applications from banking sector to the supply chain logistics and it is ready for the disruption. The blockchain revolution in this digital transformation has a greater impact in the healthcare industry applications of telemedicine. There are many opportunities in the area of telemedicine where blockchain has expanded its services in maintenance of medical records to the pharmaceutical supply chains to smart contracts for the payment distribution. We carefully investigated and found that there are three different ways where the blockchain can enhance the telemedicine process

3.2.1. Protected Health records

In telemedicine process the EHR records are the major area, the maintenance of electronic health records securely is one of the difficult tasks in healthcare system. The patients electronic health record size increases by the number of visits to the doctor. The reason for growth of records is every doctor in every hospital has different way of health record storage and as a result it is not easy for healthcare providers to obtain them. For example if the patient needs to check up for covid or any flu checkup initially every doctor asks few previous history of the patient to get to know about the patients condition. There will be different problems faced by the common man in his lifetime he may visit an orthopedician, opthmologist, etc different specialists in different times, every time the patient visits a new specialist he needs to submit the previous history to the new specialist. There should be a common health information exchange system in order to solve this problem where the doctors can share the preivous history of the patient to analyse the patient's condition in much more efficient way. There are only few companies which came up to solve this problem but it is still a challenge for blockchain reasearchers. The primary objective is to provide the patient an authority over his complete medical history and to provide the one stop access to the patients and as well as doctors. Blockchain by enabling the data security provides more efficient required access to the patients as well as doctors or analysts.

3.2.2. Medicinal product quality-authentication

The pharmaceutical industry has high standards in terms of medical products maintainance, product security and safety. Still there are many gaps in this area due to the miss-communication between healthcare professionals. There are different medical products which needs product quality authentication. There are different companies working on the authenticity of the product, the biggest challenge in this area is to prove the quality of the specific medicinal products whether they have been maintained in the mentioned environment conditions or not. For example some medicinal products specifically needs to be kept in low temperatures to maintain their medicinal power, proving this medicinal products kept in mentioned temperature conditions which proves quality of the medicinal product is the biggest challenge.in blockchain in healthcare.

Figure 3 :Blockchain in E-healthcare or Telemedicine

3.3.3 Genomic Blockchain Network

In the Healthcare industry the blockchain platforms are built by different companies like Nebula Genomics , EncrypGen by which the people can share their genomic data efficiently in a secure way. The analysts say that there are different opportunities in personal genome sequencing which will create an areaa of expanding data market in worth of millions of dollars . In this particular area the main challenges are to protect from the MITM(man-in-the middle attacks), solve the security related issues and ensuring or proving the source of the data from its end user. One of the biggest challenge here is to improve the genomic data protection and ensure the buyers can acquire protected genomic data and also should address the mining duplications issues in genomic big data.

3.3.4 Security vulnerabilities of smart contracts

The medical history of the patient reports can be disrupted, tampered by the suspected bugs and vulnerabilities in the smart contracts. For example considering an attack like reentrancy Vulnerability attack[ ] can be occurred if the smart contract has privileges to collude with the other smart contract which can later have chances of modifying the patients health record. The reentrancy vulenerability attacks are one of the primary attacks where they can extract the funds of the authorized users from their wallets. There are many solutions and methods proposed by the scientists and researchers, but still there are inadequate to detect the reentrancy vulnerability attacks. It is therefore important to take precautionary and preventive measures in order to test the smart contracts for protecting patient health records.

3.3 Challenges in Data Mining in Telemedicine or Healthcare

Data mining is one of the effective areas which played a major role in building the telemedicine system. Data mining is used in prediction of medical industry needs which helped in decreasing the cost and effective diagnosis for patients by using the pattern generation. There are different challenges in the area of data mining for the effective building of telemedicine system which are as follows

eISSN 1303-5150

3.3.1 Report generations in flu diseases

The treatments in telemedicine involves effective report generation of patients. The existing devices have solutions to heart-attacks and BP checkups by using data mining predictions but there are no proper prediction systems for flu diseases. The flu diseases like covid, influenza etc requires the report generation on daily basis through out the cycle of detection i.e covid requires the analysis and generation of patients reports for 14-15 days by which the doctors or physicians can check the condition of patient online.

3.3.2 Fraud detection

The online frauds have been increased these days. Telemedicine is also one of the area where many fraudsters have targeted. There is no proper sytem which predicts these fraud detections. The online doctors profiles need to be analysed and produced in online which predicts the actual doctors identity. There is a research challenge in this area by using data mining to predict the identity and associate the doctor to the patients online requirement.

3.3.3 Symptoms- Treatment- Association

There are certain new diseases where the actual symptoms of the disease are unknown. Considering Covid as one of the disease where this disease does not have a common pattern, in general the treatments or diagnosis can be given to the patients based on the symptoms and spread of the disease. In case of covid the pattern is still in research. To analyse the new diseases there are new challenges in the area of data mining in healthcare whether any graph mining techniques can be used to associate the common symptoms of the disease.

The analysis of role of IoT, blockchain and data mining in the area of telemedicine made us to get the challenges for future researches. In order to address some of the challenges in telemedicine we further analysed different reports and found that there is a peculiar need in the area of patients treatment matching with previous history. We developed an algorithm where patients health history is stored and compared with previous treatments in order to give effective diagnosis to the patient

5 Conclusion

The World health organization says that health services should be provided for all in an easier and effective way. The present covid-19 situation all over the world made the analysts to use the telemedicine system in more effective way. The telemedicine has become need of the day to provide healthcare and to reach the diagnosis for the infective diseases all the people over the world In this study we carefully analysed the roles played by IoT, blockchain technology and data mining to enhance the telemedicine process. We presented the new challenges where the reasearchers can concentrate in applying IoT, blockchain technology and data mining to enhance the telemedicine system to reach the healthcare services to many people.

References

[1] Castro, D., Coral, W., Cabra, J., Colorado, J., Méndez, D. and Trujillo, L., Survey on IoT solutions applied to Healthcare DYNA, 84(203), pp. 192-200, December,2017 , ISSN 0012-7353 1656
DOI: http://dx.doi.org/10.15446/dyna.v84n203.

[2] G. Subramanian and A. Sreekantan Thampy, "Implementation of Blockchain Consortium to Prioritize Diabetes Patients’ Healthcare in Pandemic Situations," in *IEEE Access*, vol. 9, pp. 162459-162475, 2021, doi: 10.1109/ACCESS.2021.3132302

[3] A. A. Mazlan, S. Mohd Daud, S. Mohd Sam, H. Abas, S. Z. Abdul Rasid and M. F. Yusof, "Scalability Challenges in Healthcare Blockchain System—A Systematic Review," in *IEEE Access*, vol. 8, pp. 23663-23673, 2020, doi: 10.1109/ACCESS.2020.2969230

[4] T.T. Kuo and L. Ohno-Machado, “ModelChain: Decentralized Privacy-Preserving Healthcare Predictive Modeling Framework on Private Blockchain Networks,” arXiv:1802.01746 [cs], Feb. 2018

[5] A. Yassine, S. Singh and A. Alamri, "Mining Human Activity Patterns From Smart Home Big Data for Health Care Applications," in IEEE Access, vol. 5, pp. 13131-13141, 2017, doi: 10.1109/ACCESS.2017.2719921

[6] B. Alkouz, Z. A. Aghbari and J. H. Abawajy, "Tweetluenza: Predicting flu trends from twitter data," in Big Data Mining and Analytics, vol. 2, no. 4, pp. 273-287, Dec. 2019, doi: 10.26599/BDMA.2019.9020012

[7] H. Goto, Y. Hasegawa, and M. Tanaka, “Efficient Scheduling Focusing on the Duality of MPL Representation,” *Proc. IEEE Symp. Computational Intelligence in Scheduling (SCIS '07)*, pp. 57-64, Apr. 2007, doi:10.1109/SCIS.2007.367670. (Conference proceedings)

[8] M. M. Alam, H. Malik, M. I. Khan, T. Pardy, A. Kuusik and Y. Le Moullec, "A Survey on the Roles of Communication Technologies in IoT-Based Personalized Healthcare Applications," in IEEE Access, vol. 6, pp. 36611-36631, 2018, doi: 10.1109/ACCESS.2018.2853148.

[9] X. Xiang, M. Wang and W. Fan, "A Permissioned Blockchain-Based Identity Management and User Authentication Scheme for E-Health Systems," in *IEEE Access*, vol. 8, pp. 171771-171783, 2020, doi: 10.1109/ACCESS.2020.3022429

[10] Wong Kok Seng, R. Bin Besar and F. S. Abas, "Collaborative Support for Medical Data Mining in Telemedicine," *2006 2nd International Conference on Information & Communication Technologies*, 2006, pp. 1894-1899, doi: 10.1109/ICTTA.2006.1684678.

[11] J. Williams, “Narrow-Band Analyzer,” PhD dissertation, Dept. of Electrical Eng., Harvard Univ., Cambridge, Mass., 1993. (Thesis or dissertation)

[12] E.E. Reber, R.L. Michell, and C.J. Carter, “Oxygen Absorption in the Earth’s Atmosphere,” Technical Report TR-0200 (420-46)-3, Aerospace Corp., Los Angeles, Calif., Nov. 1988. (Technical report with report number)

[13] L. Hubert and P. Arabie, “Comparing Partitions,” *J. Classification,* vol. 2, no. 4, pp. 193-218, Apr. 1985. (Journal or magazine citation)

[14] R.J. Vidmar, "On the Use of Atmospheric Plasmas as Electromagnetic Reflectors," *IEEE Trans. Plasma Science*, vol. 21, no. 3, pp. 876-880, available at http://www.halcyon.com/pub/journals/21ps03-vidmar, Aug. 1992. (URL for Transaction, journal, or magzine)

[15] J.M.P. Martinez, R.B. Llavori, M.J.A. Cabo, and T.B. Pedersen, "Integrating Data Warehouses with Web Data: A Survey," *IEEE Trans. Knowledge and Data Eng.*, preprint, 21 Dec. 2007, doi:10.1109/TKDE.2007.190746.(PrePrint)

Detection of Cyber Hacking Breaches using Machine Learning Algorithm

Dr. A. Rama Swamy Reddy[1], Talasila Alekhya[2]

[1] Professor, Department of CSE ,**Malla Reddy Engineering College**, Hyderabad, Telangana, India.

[2,]PG Scholars, Department of CSE,**Malla Reddy Engineering College**, Hyderabad, Telangana, India

ABSTRACT:

Analyzing the data gathered from cyber events is crucial if we are to understand the present state of the threat environment. There are still a lot of unanswered questions in this field of study. Based on malware attacks that occurred between 2005 and 2017, we did a statistical analysis of the data. Contrary to popular belief, we discover that hacking violation case inter-arrival durations and violation dimensions must be created by stochastic processes, not circulatory systems, as previously thought. This is because of autocorrelations. As a next step, we present stochastic process models for inter-arrival times and violation dimensions. These designs can also forecast the intervals between arrivals and the sizes of violations. For a better understanding of how hacking incidents are progressing, we do both qualitative and quantitative trend assessments on the data set. A current understanding of cyber security shows an increase in the frequency and severity of cyber attacks without an increase in their size.

Keywords: Cyber Hacking Breaches,Machine Learning, Attacks,Classifications.

DOI Number: 10.14704/nq.2022.20.10.NQ551478 **NeuroQuantology 2022; 20(10):1654-1665**

1. INTRODUCTION.

Is the number of cyber attack-related data breaches increasing, decreasing, or staying the same? As a starting point, researchers considered these issues. We can get an accurate picture of the present condition of cyber dangers if the response to this question is founded on fundamental principles. This problem has not been addressed in previous studies. Accidental violations (i.e. events caused by lost, thrown-away, or taken gadgets) and malicious breaches were included in the dataset reviewed in [9], despite the fact that the dataset examined in [7] only included instances that occurred between 2000 and 2008. (Which are caused by cyber attacks)? Since human error is more likely than a cyber attack to be the cause of a negligent breach, we're not included it in our present research. This study will focus on the hacking sub-category, which includes malware, insider, credit card scams, and unidentifiable, while keeping in mind that the other three sub-categories are fascinating on their own and must be examined independently.

1.1 THE SYSTEM THAT IS NOW IN USE.

Cyber-attacks are increasing, diminishing, or stabilizing as the source of data breaches, as many previously unsolved questions have shown during this inquiry. The current condition of cyber risks can be better understood if a clever solution to this problem is found. There hasn't been any past investigation into this topic. When it comes to data, however, [7] only covers the period from 2000 to 2008, whereas [9] includes two sorts of occurrences: negligent breaches (i.e., incidents caused by lost, discarded, or stolen tools) and harmful breaches (i.e., incidents caused by cyber-attacks). Our research doesn't include careless infractions because human mistake is more common than cyber attacks. These include hacking (including malware), insider, and payment card fraudulence as well as unknown. There are three subcategories in this research study, however only the hacking sub-category will be examined in depth. Researchers have only lately begun modeling data breach occurrences. Individuality losses were also examined by Mallart and Cornett from 2000 to 2008. Breaches increased considerably between 2000 and 2006, but after that, they stayed stable. More than 2,253 breaches were studied over the course of several years by Edwards and his colleagues (2005 to 2015). They found that data breaches have not gotten bigger or more frequent over time. Wheatley et al. conducted a study that analyzed a dataset including information on breaches that occurred between 2000 and 2015. In contrast to the frequency of large-scale breaches at US organizations (i.e., those that compromise more than 50,000 documents), the frequency of breaches at non-US companies reveals a growing trend.

1.2 SYSTEM LAYOUT.

This research makes the following three contributions. We show that stochastic processes, rather than circulations, should be used to model hacker breach event interracial times (which indicate occurrence regularity). ARMA refers for "Autoregressive and also Moving Ordinary," while GARCH stands for "Generalized Autoregressive Conditional Heteroskedasticity." ARMA-GARCH can effectively define the evolution of the inter-arrival periods of hacking violations. It is possible to properly predict arrival times and violation dimensions using stochastic procedure models. Stochastic processes, rather than distributions, should be employed to simulate various aspects of cyber risk, as this article shows. That's what we believe. Copulas can be utilized to explain the correlation between case arrival times and breach sizes identified in our study. In order to accurately anticipate inter-arrival periods and violation magnitude, it is necessary to take dependence into account. According to our knowledge, this is the first study to establish that this reliance exists and its implications. Using both qualitative and quantitative data, we identify trends and patterns in cyber hacking breaches. The frequency of hacking breaches is increasing, but the scale of the breaches implies that private hacking violations will not get significantly worse in terms of damages... Various studies that can provide in-depth insights into other threat mitigation strategies may benefit from this study's findings. A grasp of the hazards of data breaches is beneficial to insurance companies, government organizations, and other regulatory entities.

2. SYSTEM ANALYSIS AND DESIGN

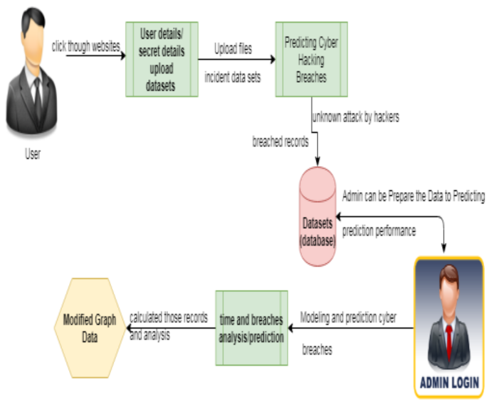

Fig :Architecture

The life cycle of a software application is defined as the time it takes to design, test, and then implement the software.

During the first round of research, we refine the design.
Initiation of the Application Process

For software applications, there is an initial evaluation and a comprehensive evaluation. The Expert performs a preliminary analysis to determine what is needed and whether there are any cost advantages to be had. Research studies that include all of the relevant variables aid in the development and expansion of the programmed.

It's called the Criterion System (SRS).

Software Application Requirement Specification is a document that completely describes what the recommended should do, but does not specify exactly how the software application programmed accomplishes this task. "

The Requirement for Performance...

1) High throughput and a fast procedure time are required.
2) The outcome should be both quick and exact.

Top Qualities of a Great Software Application.

This application is very easy to maintain because it is directly linked to the data source.

If you've ever had trouble finding a new app due to the fact that there are simply way too many options, this collection is for you.

For future enhancements, this programmed is quite flexible.

Requirements in terms of the available technology.

Demands placed on the software.

In the software application's

The second step in the life cycle of a computer system is its style, which is the fundamental layout. The system's capabilities are still being established and tested. The first step is to generate a list of programmed requirements. This document outlines the information inputs, circulation, and outcomes generation processes.

There is a shift from individual-oriented data to system data throughout the layout phase. Physical procedures, equipment, and computer programmers are all given responsibilities at the layout phase. In the initial stages of research, flow diagrams are generated and then dissolved until all system facets appear to be working properly

Data organization, software development (such as formulas), and partnerships between various components of a system are all part of design as a multi-step process. The formation of a style is a multifaceted process that includes both logical and physical components. Using reviews, linkages are made between the current system and the needs that have been gathered. The physical plan specifies the software and hardware required to meet the needs of the local layout.

Modularization has taken place at this point in time. The quality of each component's preparation is critical to the overall success of the integrated system. Step-by-step alterations in a work are the norm when it comes to altering it. Such an ingredient must be administered throughout the interphone as well. The design approach is constantly evolving as new techniques, improved evaluation, and also a greater understanding of software application design are developed.

A wide variety of software format approaches exist, each with its own set of design quality standards. – Software programmed style have three technological tasks: design, coding, and testing.

As the software's requirements vary, so does its integrity. The format system transforms the academic solution of the expediency study into a real-world reality.

The ability to put things together in a variety of ways.

Representations for the Object-Oriented Modeling Language.

The acronym for the Unified Modeling Language (UML) is UML. Rational Software Application Corporation, James Rumbaing, and Invar Jacobson were all involved in the development of this object-oriented symbols system. This group of eminent computer experts designed a complex technology mix. To model object-oriented software, the Things Management Group (OMG) has established UML as a necessity.

They are classified into three categories:

Planned routines for the average person. This is a visual representation of the way systems and processes behave in the real world. Also included are representations of the user's job, status devices and use contexts.

Illustrations illustrating the exchange of information. The relationships between objects are the focus of this type of habit arrangement. This area includes interactive, series, and temporal representations.

Structure diagrams, if you will. A non-time-bound visual representation of a set of requirements. Classes, composite structures, and product layouts are all covered in this group.

There are many different types of UML diagrams.

UML defines nine different types of diagrams, including classes (plans), products, use cases, series, partnerships, and state charts.

Class diagrams and floor plans.

Improved representations like UML constitute the bulk of object-oriented methods. A system's rigid structure is described by them.

Illustrations of the Plan of Action.

Package representations are occasionally used by programmers as an alternative to portrayals. In order to avoid the need for plans that are not compatible with one another, package diagrams organize system components into relevant categories

Item Diagrams.

The fixed structure of the system is depicted in object diagrams (or flowcharts). Verifying the accuracy of course representations can be done by using these tools.

It's a smart idea to make use of Situation Diagrams.

The usage of stars and arrowheads in situation diagrams and examples can be utilized to design system performance.

Inter-class communication should be envisioned as a stream of messages moving back and forth in time.

Partnership diagrams.

As a collection of messages, interactions between items are depicted. Collaboration diagrams represent both the system's structure and its dynamic behaviour.

State graphs and their layouts.

Statecharts are visual representations of a system's dynamic reaction to external stimuli. You can use state chart diagrams to model entities that change their state based on information.

Job flowcharts

Job depictions explain system characteristics by illustrating how control is passed from one activity to the next. A task is a system class procedure that results in a change to the state of the system. Task diagrams are frequently used in the design of refinement and also company procedures, as well as internal procedures.

Organization of an object's various components.

Component layouts describe the physical arrangement of software components such as resource code, run-time (binary) code, and executables.

Plans for carrying out the action.

Release formats depict the system's physical resources, such as its nodes, components, and links.

3 .Problem Statement

we make the following three contributions. First, we show that both the hacking breach incident interarrival times (reflecting incident frequency) and breach sizes should be modeled by stochastic processes, rather than by distributions. We find that a particular point process can adequately describe the evolution of the hacking breach incidents inter-arrival times and that a particular ARMA-GARCH model can adequately describe the evolution of the hacking breach sizes, where ARMA is acronym for “AutoRegressive and Moving Average” and GARCH is acronym for “Generalized AutoRegressive Conditional Heteroskedasticity.”We show that these stochastic process models can predict the inter-arrival times and the breach sizes. To the best of our knowledge, this is the first paper showing that stochastic processes, rather than distributions, should be used to model these cyber threat factors. Second, we discover a positive dependence between the incidents inter-arrival times and the breach sizes, and show that this dependence can be adequately described by a particular copula. We also show that when predicting inter-arrival times and breach sizes, it is necessary to consider the dependence; otherwise, the prediction results are not accurate. To the best of our knowledge, this is the first work showing the existence of this dependence and the consequence of ignoring it. Third, we conduct both qualitative and quantitative trend analyses of the cyber hacking breach incidents. We find that the situation is indeed getting worse in terms of the incidents inter-arrival time because hacking breach incidents become more and more frequent, but the situation is stabilizing in terms of the incident breach size, indicating that the damage of individual hacking breach incidents will not get much worse. We hope the present study will inspire more investigations, which can offer deep insights into alternate risk mitigation approaches. Such insights are useful to insurance companies, government agencies, and regulators because they need to deeply understand the nature of data breach risks.

4 .ALGORITHM:

SUPPORT VECTOR MACHINE

“Support Vector Machine” (SVM) is a supervised machine learning algorithm which can be used for both classification and regression challenges. However, it is mostly used in classification problems. In this algorithm, we plot each data item as a point in n-dimensional space (where n is number of features you have) with the value of each feature being the value of a particular coordinate. Then, we perform classification by finding the hyper-plane that differentiate the two classes very well (look at the below snapshot).Support Vectors are simply the co-ordinates of individual observation. Support Vector Machine is a frontier which best segregates the two classes (hyper-plane/ line).More formally, a support vector machine constructs a hyper plane or set of hyper planes in a high- or infinite-dimensional space, which can be used for classification, regression, or other tasks like outliers detection. Intuitively, a good separation is achieved by the hyper plane that has the largest distance to the nearest training-data point of any class (so-called functional margin), since in general the larger the margin the lower the generalization error of the classifier.Whereas the original problem may be stated in a finite dimensional space, it often happens that the sets to discriminate are not linearly separable in that space. For this reason, it was proposed that the original finite-dimensional space be mapped into a much higher-dimensional space, presumably making the separation easier in that space.

5. MODULES:

ADMIN.

In this module, the administrator will be able to predict malware in this application. There is a visual examination of the user projections and assessments after a client logs in.

This module provides the client with all of the information they need, including details, evaluation, malware data, enamelware data, branched evaluation, and aesthetic analysis.

UPLOAD DATA

The data resource to database can be uploaded by both administrator and authorized user. The data can be uploaded with key in order to maintain the secrecy of the data that is not released without knowledge of user. The users are authorized based on their details that are shared to admin and admin can authorize each user. Only Authorized users are allowed to access the system and upload or request for files.

ACCESS DETAILS

The access of data from the database can be given by administrators. Uploaded data are managed by admin and admin is the only person to provide the rights to process the accessing details and approve or unapproved users based on their details.

DATA ANALYSIS

Data analyses are done with the help of graph. The collected data are applied to graph in order to get the best analysis and prediction of dataset and given data policies. The dataset can be analyzed through this pictorial representation in order to better understand of the data details.

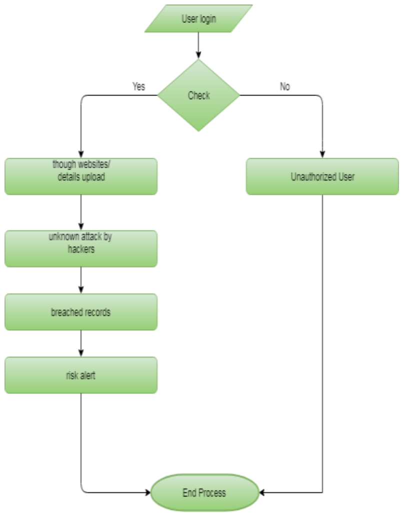

Fig: Flow Chart

6 .METHODOLOGY

Specifying, designing, and coding are the three stages of the software development process that are thoroughly evaluated during software screenings. A closer look reveals an intriguing anomaly in the software's source code. Getting the software from a conceptual design to a working prototype was a primary objective early on in development.

During the screening phase, the generated system is tested on a variety of data sets. System screening relies heavily on how test results are shown. When testing this system, the results of the tests were used to determine how well it performed. Test data was used to identify and correct systemic errors. Tests were required before the planned system could be put into operation.... A variety of techniques are used in testing, including:

The system must be fixed if it isn't working properly.

Interoperability evaluations

Individual System Acceptance Testing Validation

The early stages of device testing

In software development, testing is concentrated on the module because it is the smallest system. A series of tests has been written here by the programmer in preparation for the system's eventual integration into a larger system. Coders carried out a preliminary check. In order to make certain that each module is on track to accomplish its objectives, we perform a thorough evaluation on each individual one. Using a multi-pronged approach, we make certain that none of the types are infected. The following is a list of the test cases that were run.

Users will be prompted to input a value if the use rid and password fields are left blank in the login form.

Participants will see an error notice if they attempt to log in using an invalid use rid or password. "The login credentials you entered are incorrect. Do it again if the first attempt fails "There are so many questions that I have no idea where to begin...

Every field on the book's entry page and the new student/teacher screen requires a value to be input. Error notifications could instead be sent through customer care.

A member id, book number, concern day, and return date are necessary for publishing transactions. If the fields are left blank, the user will see the error message "Fields need not to be blank."

Verification/Checkingof Combinations

Creating a program's structure and testing for faults in the user interface are both referred to as "integration screening." As a result of extensive testing, all components of a predetermined programmed structure will be included. This action is the culmination of everything that has come before it. The entire programmed has been put through its paces. Users may find the interfaces difficult to navigate. There are bound to be a slew of errors in this situation.

There are two ways to perform a combination screening:

Assimilation in the reverse direction
A bottom-up approach to integration

In order to build a more sophisticated system, the first step is to downgrade huge modules to smaller ones. As opposed to this, overhead assimilation utilizes a mechanism in which smaller bits are mixed with larger ones. Here's an example of a combo that's been turned upside down. It was tough to adapt because there were so many variables. In spite of this, each error was fixed and then passed on to the next phase of testing.

It has been thoroughly tested to ensure that the system's user may easily switch between different screens...

The database and forms have been thoroughly tested to guarantee that they work together seamlessly. The user will be notified if there is a problem with the gadget.

End-user acceptance testing (AET) (UAT)

A system must have the support of its users before it can be considered a success. With the person who would be using it on a regular basis, the system was thoroughly tested to ensure that it would meet the needs of its target audience. This is the case as a result of the following factors:

It is possible to define a system as a set of separate instructions...

In order to move forward, the application system's technical requirements must be specified in great detail before any work can begin. End-user supervisors from several departments were consulted before finalizing the system specifications.

Users' requirements are taken into account during the development of the product. The current situation and the intended outcome of putting in place the new information system

Based on the issue at hand, and how thoroughly an inquiry is conducted, a system's performance is determined. Determining a client's needs, rather than their desires, through in-depth analysis An organized system lays out exactly how and when each task or activity should be accomplished and who is responsible for it.

were put through its paces.

System screening is the process of verifying that all of the software/system components match the requirements given in the software specification (SRS).

After the system has gone through integration testing, a last round of testing is conducted. Non-functional requirements should also be tested as part of a system's development. Methods of system screening differ greatly from one enterprise to the next.

The software and hardware requirements for this project have been met and tested. Specifications for the hardware and software were strictly adhered to.

7 .RESULT

Home page

Login

User Home page

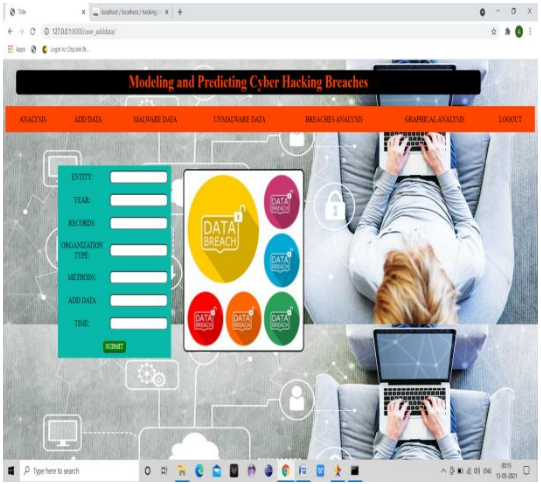

Analysis

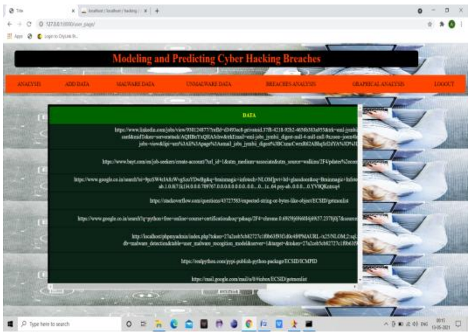

Malware Data

eISSN 1303-5150

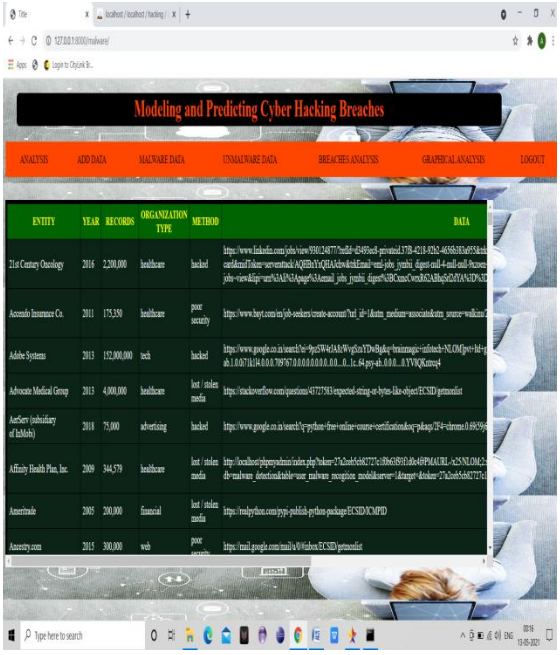

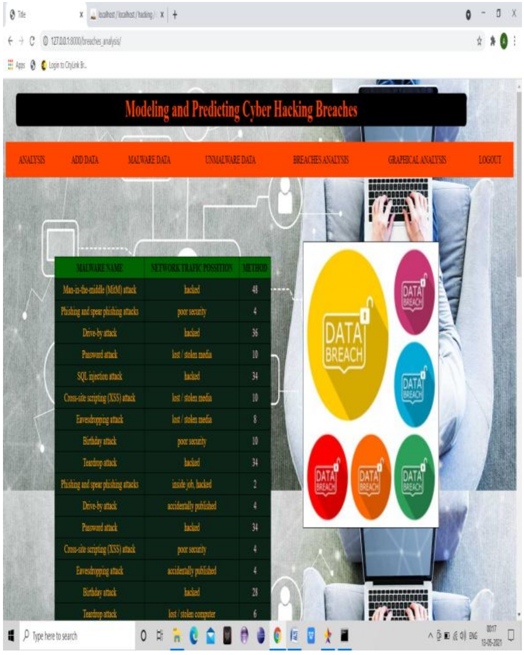

Unaware Data

Graphical Analysis

1662

Breaches Analysis

Bar chart

NeuroQuantology | August 2022 | Volume 20 | Issue 10 | Page 1654-1665 | doi: 10.14704/nq.2022.20.10.NQ55148

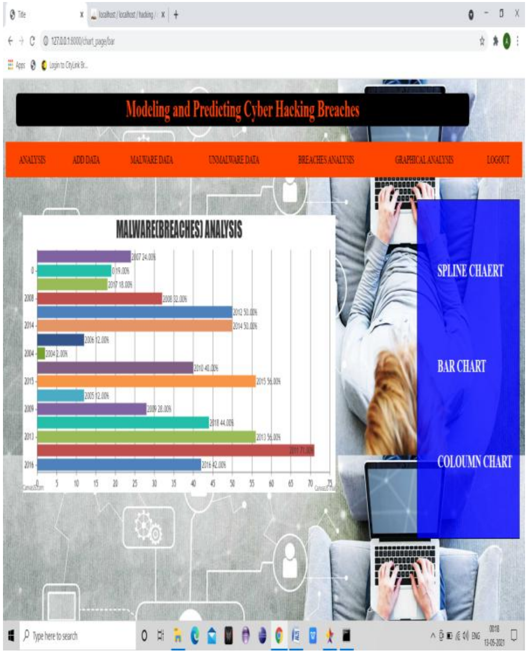

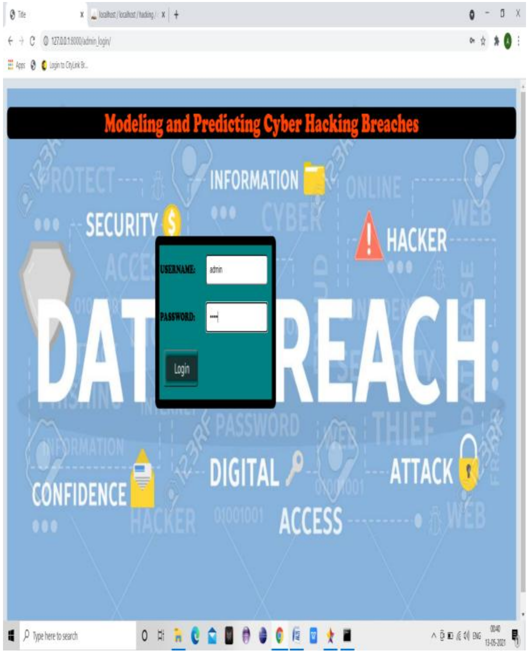

Column chart

User details Analysis

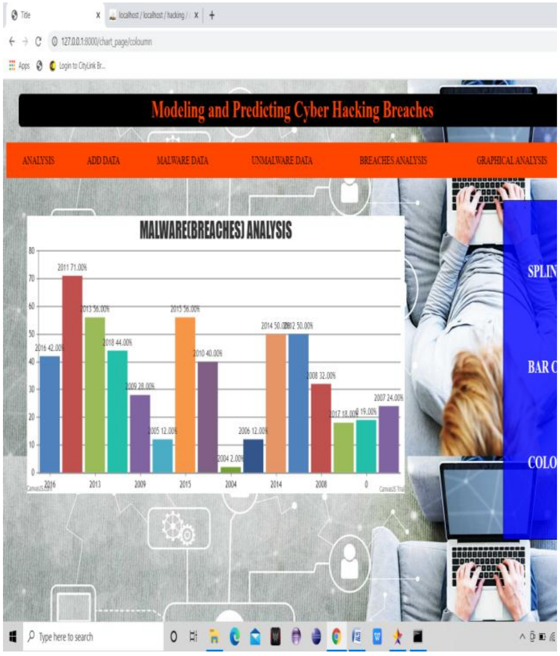

Admin Analysis

Admin Login

eISSN 1303-5150

www.neuroquantology.com

4.5 Test Cases

Test case for Login form:

FUNCTION:	LOGIN
EXPECTED RESULTS:	Should Validate the user and check his existence in database
ACTUAL RESULTS:	Validate the user and checking the user against the database
LOW PRIORITY	No
HIGH PRIORITY	Yes

Test case for User Registration form:

FUNCTION:	USER REGISTRATION
EXPECTED RESULTS:	Should check if all the fields are filled by the user and saving the user to database.
ACTUAL RESULTS:	Checking whether all the fields are field by user or not through validations and saving user.
LOW PRIORITY	No
HIGH PRIORITY	Yes

8 .CONCLUSION AND FUTUREWORK

CONCLUSION

Stochastic processes rather than distributions should be used to represent this hacking dataset's arrival time and attack volume, according to the analysis. In this work, the statistical designs used to arrive at a sufficient degree of suitability and forecast precision have been demonstrated. As a rule of thumb, we suggest utilizing a copula-based approach to foresee the combined likelihood that an event with a particular magnitude of breach dimension would occur in the future. To put it another way, this paper's methods are superior to those in the literature since they take into consideration both temporal linkages and the reliance between event inter-arrival durations and violation sizes. We used both qualitative and quantitative methods to glean extra information. Cyber hacking incidents are becoming more frequent, but the amount of harm they wreak isn't, according to our research, growing. Using this paper's methods, you may analyze similar datasets.

Future Scope:

There are still many unanswered questions. Examples of this can be found in the research of predicting extremely large numbers and handling missing data, for example (i.e., violation cases that are not reported). It's also a good idea to figure out the exact time of the breach events. A further investigation is needed to establish the probability of a security breach taking place (i.e., the upper bound of prediction precision).

9 .REFERENCES

[1] P. R. Clearinghouse. Privacy RightsClearinghouse's Chronology of Data Breaches.

Accessed: Nov 2017. [Online]. Available:https://www.privacyrights.org/data-breaches

[2] ITR Center. Data Breaches Increase 40 Percent in 2016, Finds New Report From Identity Theft Resource Center and CyberScout Accessed: Nov 2017. [Online]. Available: http://www.idtheftcenter.org/2016databreaches.html

[3] C. R. Center. Cybersecurity Incidents. Accessed: Nov 2017 [Online].Available:https://www.opm.gov/cybersecurity/cybersecurity-incidents

[4]IBM Security. Accessed: Nov 2017 [Online] Available: https://www.ibm.com/security/data-breach/index.html

[5] NetDiligence. The 2016 Cyber Claims Study. Accessed: Nov 2017. [Online]. Available: https://netdiligence.com/wp-content/uploads/2016/10/P02_NetDiligence 2016-Cyber-Claims-Study-ONLINE.pdf

[6] M. Eling and W. Schnell, "What do we know about cyber risk and cyber risk insurance?" J. Risk Finance, vol. 17, no. 5, pp. 474-491, 2016.

[7] T.Maillart and D. Sornette, "Heavy-tailed distribution of cyber-risks"Eur Phys L B. vol 75, no. 3, pp. 357-364 2010

[8] R B. Security. Datalossdb. Accessed: Nov 2017 [Online]. Available:https://blog.datalossdb.org

[9] B. Edwards, S. Hofmeyr, and S. Forrest, "Hype and heavy tails: A closer look at data breaches," J. Cybersecur,, vol. 2, no. 1, pp. 3-14, 2016.

[10] S. Wheatley, T. Maillart, and D. Sornette, "The extreme risk of personal data breaches and the erosion of privacy," Eur. Phys. J. B, vol. 89, no. 1, p. 7, 2016.

[11] P. Embrechts, C. Klüppelberg, and T. Mikosch, Modelling Extremal Events: For 5 Insurance and Finance, vol. 33. Berlin, Germany: Springer-Verlag, 2013.

[12] R. Böhme and G. Kataria Model and measures for correlation in cyber: insurance in Pros Workshop Econ, Inf. Secur. (WEIS), 2006, pp. 1-26. [13] H Herath and T. Herath. "Copula-based actuarial model for pricing cyber-insurance policies," Insurance Markets Companies: Anal. Actuarial Comput, vol. 2, no. 1, pp. 7 20, 2011.

[14] A. Mukhopadhyay. S. Chatterjee, D. Saha, A. Mahanti, and S. K. Sadhukhan, "Cyber-risk decision models: To insure it or not?" Decision Support Syst., vol. 56, pp.11-26, Dec. 2013.

[15] M. Xu and L Hua (2017). CybersecurityInsurance: Modeling and Pricing.

[Online].Available:https://www.soa.org/research reports2017/cybersecurity-insurance

[16] M. Xu, L. Hus, and S. Xu. "A vine copula model for predicting the effectiveness of cyber defense early-warning." Technometrics, vol. 59, no. 4, pp. 508-520, 2017.

[17] C. Peng, M. Xu, S. Xu, and T. Hu. "Modeling multivariate cybersecurity risks," J.Appl. Stat., pp. 1-23, 2018.

[18] M. Eling and N. Loperfido. "Data breaches: Goodness of fit, pricing, and risk measurement." Insurance, Math Econ., vol. 75, pp. 126-136, Jul. 2017.

[19] KK Bagchi and G. Udo. "An analysis of the growth of computer and Internet security breaches, Commun Assoc. Inf. Syst., vol. 12, no. 1, p. 46, 2003.

[20] E Condon, A He and M. Cukier, "Analysis of computer security incident data using time series models," in Proc. 19th Int. Symp. Softw Rel. Eng. (ISSRE), Nov. 2008, PP. 77-86

IJCRT.ORG ISSN : 2320-2882

INTERNATIONAL JOURNAL OF CREATIVE RESEARCH THOUGHTS (IJCRT)

An International Open Access, Peer-reviewed, Refereed Journal

BIG DATA PROCESSING USING MINING ALGORITHAM IN DATA SETS FOR DATA BASE SYSTEMS

Ms Akanksha Akulwar [1]
Assistant Professor

Mr. P.V. Ramana Murthy [2]
Associate Professor

Dr. P. Srinivas[3]
Professor

[1,2,3] Department of Computer Science and Engineering
Mala Reddy Engineering College (Autonomous)
Maisammaguda, Dist. Medchal, Secundrabad /500100, Telangana State, India

***Abstract*—** The fundamental challenge for a lot of big data programs must be to search data volumes and take functional understanding for other hobbies. Focused by real-world programs controlling of massive Data were revealed to acquire demanding yet very compelling job. We make as read the efficient theorem that differentiates highlights of big data rising, and signifies big human sources representation, in the thought of data mining. Suggested theorem recommends that important highlights of big data are large by heterogeneous and varied data sources self-directed with distributed additionally to decentralized control, and sophisticated, developing in data associations featuring think that big data necessitate a sizable intelligence to boost data for finest values. We submit big human sources depiction, in the thought of data mining which data-driven structure involves demand determined selection of information sources, mining additionally to analysis, modeling of user interest, and contemplation on security.

***Keywords*—** Big Data, Heterogeneous, Big data processing, Data Mining, Decentralized, Data Sources, Modeling, Security and Statistics.

I. INTRODUCTION

In a number of domains, big data are quickly growing coupled with growth of big data services where choice of facts are ongoing to develop very that's before capacity of generally used tools for controlling inside the reasonable time period. In a number of conditions, types of understanding extraction must be especially ingenious since storage inside the entire observed particulars are practically infeasible. Exceptional volumes of understanding need a effective data analysis to attain fast response for giant data. Big data appears by large data volume, various and self-directed sources by distributed furthermore to decentralized control, and search within the complicated and developing relations between data. These traits ensure it's severe challenge to discover from helpful understanding from big data. Our work provides an efficient theorem that differentiates popular features of big data rising, and signifies big human sources representation, in the idea of data mining. The recommended data-driven structure involves demand determined choice of information sources, mining furthermore to analysis, modelling of user interest, and contemplation on security. When the thought of big data concerns regarding data volumes, our theorem recommends that important popular features of big data are large by heterogeneous and varied data sources self-directed with distributed furthermore to decentralized control, and complicated, developing in data associations [1]. These traits believe that big data necessitate a big intelligence to improve data for finest values.

II. METHODOLOGY

Various information collectors desire their own methods for data recording, to guide to numerous data illustrations. The heterogeneous quality describes various representations for similar individual, as well as other features reference features concerned for representation of all the single observation. Autonomous reasons for data by distributed in addition to decentralized controls are most significant feature regarding services of massive data. Being autonomous, way of getting generates in addition to gather data missing of concerning connected obtaining a centralized control. The big data volumes apply prone to attacks when the complete system must depend on centralized control unit [2]. When big data volume increases, thus perform difficulty and relations beneath the data. Inside a energetic world, features which are useful for representation of individuals symbolizes our connections might evolve regarding additional conditions. This type of issue is becoming realism for programs of massive data, where secret's to acquire complex data relations, in addition to evolving changes to discover practical designs from collections of massive data. Our work bakes a dependable theorem that differentiates popular features of big data rising, and signifies big human sources representation, in the idea of data mining. It recommends that important popular features of big data are large by heterogeneous and varied data sources, self-directed with distributed in addition to decentralized control, and complex, developing in data associations. Processing of massive data depends on parallel programming models in addition to provision of cloud platform of massive data services for community purpose. For programs that concern big data and outstanding data volumes, it's frequently that data are distributed at various locations, denoting that clients ignore possess data storage. For implementation of mining programs of massive data acquiring a effective method of data access is important, created for clients who employ a third party to teach their information. For modifying to multisource, huge, active big data, researchers enhanced the standard techniques of understanding mining often [3]. Huge, heterogeneous in addition to synchronized popular features of multisource information offer critical versions among single-source understanding discovery in addition to mining of multisource data.

III. FRAME WORK FOR BIG DATA PROCESSING SYSTEM USING MINING ALGORITHM

For database system of intelligent learning for controlling of massive data, important secret's to enhance towards an very huge data volume and offer remedies for features featured obtaining a HACE theorem. This method recommends that important popular features of big data are large by heterogeneous and varied data sources self-directed with distributed in addition to decentralized control, and complex, developing in data associations. Hence these traits submit that big data necessitate a large intelligence to enhance data for finest values. Presenting processing structure of massive data was proven in fig1 the includes three groups for instance data getting the opportunity to view in addition to computing denoting group-I, data privacy in addition to domain understanding denoting of group-II additionally to computations of massive data mining denoting group-III [4]. Our work signifies big human sources representation; in the idea of data mining which data-driven structure involves demand determined choice of information sources, mining in addition to analysis, modeling of user interest, and contemplation on security. Offering of massive data depends on parallel programming models in addition to provision of cloud platform of massive data services for community purpose. Challenges at group-I spotlight on techniques of understanding getting the opportunity to view. While big details are stored up at various locations and understanding volumes might continuously develop, a reliable platform should consider important data storage for computing. Challenges made at group-II focus on semantics in addition to domain understanding for a lot of programs of massive data which information makes advantages towards mining procedure to find yourself in big data in addition to mining computations. Group-III mainly focuses on formula designs in managing of injuries that's elevated by volumes of massive data, allocation of distributed data, and by means of complicated and active data features. Outstanding volumes of understanding need a effective data analysis to attain fast response for giant data. In representative systems of understanding mining, mining process necessitate intensive computing models for analysing of understanding. Hence computing platform is needed to contain competent use of two resource types and they are data additionally to computing processors [5]. For mining of understanding, as data level is secluded from ability that single pc holds, a distinctive structure of massive human sources is determined by cluster computers having a high-performance computing proposal, having a data mining task that's organization by controlling of countless parallel programming tools [5]. Semantics in addition to application understanding reference several features in big data connected with rules, user understanding, in addition to domain data. Two most critical issues for this group comprise talking about of understanding and privacy domain in addition to application information [6]. While programs of massive data are featured by autonomous sources in addition to decentralized controls, mixing of distributed data sources towards centralized site for mining is unaffordable because of prospective transmission cost in addition to privacy issues a Big Data Processing System (BDPS).

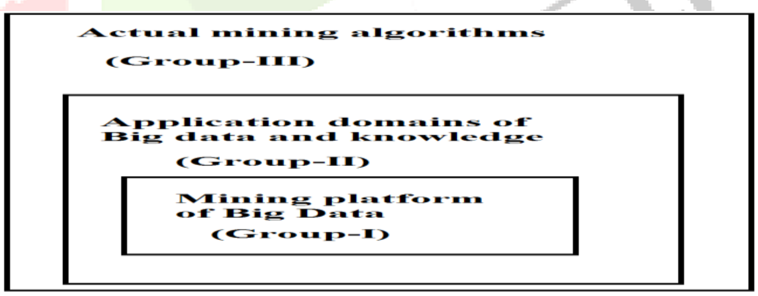

Figure 1: A Framework for Big Data Processing System (BDPS)

IV. CONCLUSIONS

Important highlights of big data are plenty of volume of data that's symbolized by heterogeneous additionally to numerous dimensionalities. Due to multisource, huge, heterogeneous, additionally to active highlights of application data that's concerned in distributed setting, among most important highlights of big details is to complete computing on peta byte by difficult computing procedure. For programs regarding big data and outstanding data volumes, it's frequently that data are distributed at various locations, denoting that clients ignore possess data storage. Our work comprises a ingenious theorem that differentiates highlights of big data rising, and signifies big human sources representation, in the thought of data mining. This model recommends that important highlights of big data are large by heterogeneous and varied data sources self-directed with distributed additionally to decentralized control, and sophisticated, developing in data associations. These traits are convinced that big data necessitate a sizable intelligence to boost data for finest values. We introduce sizable human sources representation, in the thought of data mining which model involves demand determined selection of information sources, mining additionally to analysis, modelling of user interest, and contemplation on security. In distinctive systems of understanding mining, mining procedure necessitate intensive computing models for analyzing of understanding.

REFERENCES

[1] Y.-C. Chen,W.-C.Peng, and S.-Y. Lee, "Efficient Algorithms for Influence Maximization in Social Networks," Knowledge and Information Systems, vol. 33, no. 3, pp. 577-601, Dec. 2012.

[2] A. Labrinidis and H. Jagadish, "Challenges and Opportunities with Big Data," Proc. VLDB Endowment, vol. 5, no. 12, 2032-2033, 2012.

[3] Y. Lindell and B. Pinkas, "Privacy Preserving Data Mining," J. Cryptology, vol. 15, no. 3, pp. 177-206, 2002.

[4] W. Liu and T. Wang, "Online Active Multi-Field Learning for Efficient Email SpamFiltering," Knowledge and Information Systems, vol. 33, no. 1, pp. 117-136, Oct. 2012.

[5] E.Y. Chang, H. Bai, and K. Zhu, "Parallel Algorithms for Mining Large-Scale Rich-Media Data," Proc. 17th ACM Int'l Conf. Multimedia, (MM '09,) pp. 917-918, 2009.

[6] R. Chen, K. Sivakumar, and H. Kargupta, "Collective Mining of Bayesian Networks from Distributed Heterogeneous Data," Knowledge and Information Systems, vol. 6, no. 2, pp. 164-187, 2004.

STRESS DETECTION IN IT PROFESSIONAL BY MACHINE LEARNING

ABDUL GAFFAR KHAN[1], DR. D. KRISHNA MADHURI[2]
[1]PG SCHOLAR, [2]ASSOCIATE PROFESSOR
MALLA REDDY ENGINEERING COLLEGE, HYDERABAD, TELANGANA.

Abstract:-

Stress levels amongst the Indian employees have increased due to a variety of factors and are a matter of great concern for the organizations. This study is based on Indian working professionals and real data has been collected by using non-probability convenience sampling. A questionnaire was drafted based on eighteen factors affecting the mental health of professionals. This study addresses two dimensions, first is to identify the important influential features that trigger stress in the lives of working professionals, and the second is to predict the stress levels. Various supervised machine learning algorithms have been experimented with and of all these algorithms, the Support Vector Machine Regressed model showed the best performance. The main contribution of the paper lies in the identification and ranking of ten important stress triggering features that can guide organizations to develop policies to take care of their employees. The other deliverable is the development of a GUI-based stress prediction software based on Machine learning techniques. As the globalization, is expanding individuals twist towards the cutting-edge life Stress issue turns into a significant issue among in experts and understudies life. The term pressure is causing different mental issue face to face. Understudies of various courses and distinctive expert college are expanding ambushed with this pressure. The points of this examination are to research natural, social, mental and scholarly postgraduate and doctoral understudies. The quantities of tests of this investigation are 220 undergrad and postgraduate understudies. The information of my examination was gathered independent from anyone else – planned poll and by PSS Scale and the overview has organized inquiries which were gathered through google dox. There are many pressure expectation calculations has been proposed like SVM, KNN, RANDOM FOREST, NAVIE BAYES, LOGISTIC REGRESSION, DECISION TREE. Different machine learning methods are utilized that related in this field. Too, it talks about the application territories and difficulties for stress forecast with knowledge into the past research work.

Keywords: Stress, Prediction, classification, Machine learning, Questionnaires survey, weka tool.
DOI Number:10.14704/nq.2022.20.8.NQ44559 **NeuroQuantology 2022; 20(8): 5268-5282**

5268

I. INTRODUCTION

Modern society is witnessing a continuous deterioration in the occupational health of working professionals in India. According to the latest reports for the year 2020, by ADP Research Institute, 70 percent of the Indian workforce is suffering from stress at their workplace which is a matter of grave concern. Survey reports by 1to1help, an Employee Assistance Program provider in India have found that there has been a large increase in the number of employees who are highly depressed or are vulnerable to suicides due to an increase in stress in their lives. Another surveyor, Optum affiliated with Nasscom, observed that almost half of the Indian employees suffered from some type of stress or mental health issue. They surveyed eight lacs employees in seventy major organizations, each with a minimum staff of four thousand and five hundred. The results were alarming and stated that the ratio of employees at high risk of taking their lives due to stress had increased from 4% to 8% in two years. They also found that family, money, and job were the most common stressors amongst the employees.

Parenting, pregnancy, change, care giving, and social isolation were some more factors that led to stress. Some employees also fear for their job security in the restructuring of the organization even though they are better paid. It is specifically true for managers who are in a middle-level position and have the responsibility of kids as well as loans. Employees are also found to be struggling with stress in their personal lives due to broken relationships or marriages. Newer factors like social media also contribute to the intense peer pressure that expects people to have a certain lifestyle or be a certain image to qualify as successful. This undue and unmanaged stress leads to mental health issues *viz.* anxiety and depression, and damage to physical health by causing frequent headaches, elevated blood pressure, chest pain, upset stomach, and problems sleeping.

Stress is an issue which is expanding step by step which additionally influences the individual physical and mental wellbeing. [1] As the individual are moving toward the path for accomplishing development in their own and calling which is the significant reason for worry in the present life. Nowadays as the challenge is expanding in each field, the anxieties become the serious issue which influences the person's wellbeing which additionally causes genuine medical problems [2]. The expression "Stress" signifies when there is an issue which cause inconvenience to the individual and give them any sort of mental issue. On the off chance that the pressure is antagonistic and influences the individual wellbeing is called misery and this additionally lead to the different mental issue or confusion. It sways on our body opposition which may cause may difficult issues which we are uninformed of and these sort of issue prompts serve physical medical problems like, coronary failure, mind related issue, rest issue [3]. Stress is basic in our day by day schedule life, which is pressure yet the vast majority of the pressure is trouble. Stress come when humans fail to wellbeing himself in the environment with high challenge. Mostly stress occurs when people tried to act against their emotion or mental condition [4].

Human body controls its inside condition by different physiological procedures, and keeps up at a specific condition of balance called as homeostasis. "Hans Selye was the dad of stress specialists and have given numerous speculations on worry in look into. His view in 1956 was the "Stress is an inclination of enthusiastic or physical pressure." Selye accepted that the biochemical impacts of pressure would be experienced independent of whether the circumstance was certain or negative. In 2010, Hornby is characterized worry as "weight or stress achieved by issues for an amazing duration. As per lazarus and Folkman in 1894, Stress emerges when an individual neglect to adapt to the extrenal condition or encompassing because of unexpected situation of exceptional requests on him/her. It rises when an individual has selected prerequisite (Fairbrother and caution, 2013) which consistently doesn't organize with his capacity. In this time, understudies square measure casualties of economic process and its difficulties., family troubles, love disappointments (Blain and McArthur, 1961), negative economic, everyday problems (Carr and Umberson, 2013), and scholastic weight on the understudies square measure purpose of pressure currently a days in light-weight of the burden. apart from this displaying style, approach of mastering and affiliation among understudies and professional person within the study passageway square measure a component of distinct factors that deliver regarding strain, throughout tests, When understudies neglects to urge nice stamps in assessment, they get American state persuaded that builds the suicidal inclination among them. consistent with United Nations agency reports in 2014, suicide worth is high amongst understudies because of the very fact of studious weight. In India ,857 understudies students complete it all because of the scholastic check pressure or weight, (Desai, 2006). The National Crime Records Bureau a pair of,471 understudies have distributed suicide(2013) because of the very fact of assessment disappointment in India. to boot the days of India's Survey (September ten, 2014) has expressed that Martinmas of the understudies and seven.8 % school understudies have endeavored suicide and out of every 3 suicide, there's one early life United Nations agency incorporates a location with the age gathering of 14–28 years. All things considered, "the subject of stress is bewildered and complex [13]. Stress can be defined by different aspects known as stressors including, social stress, environment, physiological, thoughts, emotional, anxiety.

II. SOURCES OF STRESS

We can experience stress from four basic sources:

A. The Environment

The external source of stress can occur by the environment in which the individual is unable to adjust with the external or internal stimulus which results in the cause of stress. Examples of environmental or external stressors include weather - cold or hot, disturbance, crowding, pollution, traffic, unsafe environment and increase level of crime.

B. Social Stress

The outside wellspring of stress can happen by the earth wherein the individual can't modify with the outer or inward improvement which bring about the reason for pressure. Instances of natural or outside stressors incorporate climate – cold or hot, unsettling influence, swarming, contamination, traffic, hazardous condition and increment level of wrongdoing.

C. Physiological

Everybody can encounter various Stressors throughout their life, on account of the distinctive social job we play in our public activity. Each individual assumes an alternate social job in their everyday life so as to live in a general public, for example, parent, life partner, guardian and representative. A few instances of social stressors incorporate cut-off times, money related issues, work uncertainty, introduction, contradictions, interest for your time and consideration, loss of cherished one, separate, coworking. This pressure happens when an individual can't assume a social job and not ready to rival the various individuals from the general public.

D. Thoughts

Each individual is unique and each individual see a similar circumstance in an alternate sense or way. Some individual translates and sees circumstance as upsetting, troublesome, and agonizing and some individual see the conditions as a lovely and attempt to unravel that circumstance smoothly and quietly. Some circumstance in life is pressure inciting, however it is our considerations that decide if they are issue for us and open door for us.

III. MACHINE LEARNINGTECHNIQUES

Machine learning has huge application in every area and it is growing rapidly because of its effective [4] approaches in prediction and classification. The dataset used in this approach. Basically, machine learning are two types supervised and Unsupervised.[1] Now we are discussing some techniques of machine learning are -:

A. Naïve Baye's

Naive Baye's classifier belongs to the formula of probabilistic classifier [1]. It is based on the Baye's Theorem. Despite its naive design and simplicity i.e. t can be applied to very complex problems. This classifier is based on the assumption that feature is independent of any other feature. Naive Baye's classifier uses maximum label time.

B. Logistic Regression

Logistic Regression is a type of technique used in machine learning. Logistic regression is widely used for the statistical model. Logistical regression is also known as statistical learning technique in supervised machine learning method dedicated to 'classification' task.

C. Multilayer Perceptron

Multilayer perceptron (MLP) is a class of feed forward neural system. It comprise of three layers. They are related with different loads. The Input layer ,Hidden Layer and the Output Layer [4].

D. Baye's Net Baye's

Net utilizes the strategy that can actuate a Bayesian system B, that encodes a circulation PB(A1,...,An, C), from a given preparing set. We would then be able to utilize the subsequent display so given a lot of characteristics a1,...,an, the classifier dependent on B restores the name c that boosts the back likelihood PB(c|a1,...,an).

IV. LITERATURE REVIEW

In past, many descriptive and inferential approaches have been applied by researchers all over the world to understand the stress-causing factors from various dimensions. These factors *viz.* workplace environment, workload, job security, relationship with family members, have been studied by researchers with a statistical approach or data mining approach. Many such papers have been critically studied and analyzed to derive a systematic methodology for the prediction of stress based on minimum features. These papers are based on data of employees of different organizations like sugar mills, agricultural institutes, banks, and educational institutes, all sectors being from various countries like India, Malaysia, Vietnam, and China. Most of the authors have applied a statistical approach in their studies for finding a correlation between various stress-causing factors and regression analysis for understanding cause-effect relationships. Many of them have checked the reliability of their questionnaire by using Cranach's alpha coefficient for each stress-causing factor. A summary of different papers has been presented that built the basis of selection of influential factors and finally minimizing the set of features so that a machine learning algorithm can make a prediction even before the actual serious impact of stress creeps in.

Prasad et al. (2015) have tried to find out the causes of stress in the employees of the International Agricultural Research Institute, Hyderabad, and its effects on their performances. They also wanted to find out the proficiency of the management techniques used at the workplace to reduce stress and evaluate how workplace stress affects them physiologically. The authors collected the information of 200 employees via a structured questionnaire and checked its authenticity with the help of Cronbach's alpha coefficient for each variable. In this paper, the performances of the employees were checked based on absenteeism, poor work relations, reduced productivity, low self-esteem, and feeling of boredom at the place of work. They found that stress existed on a medium level amongst the employees and it negatively affected their performance. The authors used Regression analysis to find the cause-and-effect relationship between the factors and the performances of the employees. Karl Pearson's correlation coefficient was also calculated to find the relation between the various stress-causing factors and the performance.

With a focus on stress-causing factors that fall under just one category, Pattnaik and Mishra(2016) looked into organizational factors as a reason for bringing in stress. They tried to find out people's thoughts towards the relation between stress and competition in the workplace. The data of 72 employees were collected via a structured questionnaire, and telephonic, personal, and online interviews. The data were interpreted with the help of categorizing of data, tables, and pie charts and it was found that the employees do experience stress which has both negative and, in some cases, even positive effects. The two prime factors were excessive workload and organizational conflicts. The men felt frustrated and also felt a lack of concentration when stressed whereas the women felt frustrated and exhausted when stressed and both experienced lifestyle imbalance. Both female and male employees also faced physiological effects. The employees believed that stress is more in a highly paid job and they also felt that the facilities to manage stress at the workplace is not enough. It was observed that the female employees were more vocal in comparison to men in terms of sharing the problems related to stress.

A similar study has been conducted by Saravanan and Muthu Lakshmi (2019) to calculate the stress level of the employees of a Nationalized Bank in Trichy city. The sample size of the employees was 100 and a structured questionnaire was utilized to collect the data. The questionnaire was built with the help of a statistical package of Social Sciences. The answers of the questionnaire lay on a Likert scale of 1 (Strongly disagree) to 5 (Strongly disagree) for stress management. The data was then studied with the help of graphs and statistics and it was found that major stressors were interpersonal conflict and work pressure. They also concluded that more than fifty percent of employees can manage stress. They recommended that stress can be managed by meditation, yoga, exercise, different types of therapy, networking, and hobbies. Next, the teaching staff of an educational institute was studied by Rawal & Mhatre, 2018, to identify the factors that cause stress. The authors investigated the impact of stress on their productivity and performance and suggested recommendations to tackle stress. They conducted their study with the help of a questionnaire formed with help of primary and secondary data. It was found that the professors faced work-related stress along with family-related stress. They often had an overload of work and would neglect their homes to meet deadlines at the organization. But they feel that the measures taken by the organization to help manage stress do work well and they can comfortably manage a social life. This study too focussed on a general approach towards reducing stress.

Another study was done on a sample size of 100 participants that focussed on three major features *viz.* workload, job security, and shift duty concerning the performance of the employees (Vijayan, 2017). The authors studied the relation of the stressors and their impact on performance at the place of work by applying different statistical methods *viz.* T-test, Chi-square, correlation, and regression. It was found that the mentioned three features are positively correlated and have a huge impact on employees' performance. Of these features, the workload was found to be impacting the most on the performance of the employees.

Kuong and Yen (2016) conducted a study in Vietnam by collecting data from a sample size of 378 employees, using a structured questionnaire with a Likert scale of 1 to 5. They utilized SPSS software for exploratory factor analysis to enhance the dependability and authenticity of the measured variables and to find the relation between them. It was done with the help of Kaiser-Meyer-Olkin (KMO) and Bartlett's test of sphericity. They also made use of Varimax Rotation for independent and dependent variables. Path analysis and multiple regression were used to find the relation between the dependent and independent variables. The study was mainly done on five major features *viz.* work overload, role ambiguity and role conflict, working relationship, career development, working environment, and their effect on the job stress and job performance was analyzed. They found that these factors affect job performance through job stress directly and indirectly. They concluded that the working environment was the major factor that affected job stress, followed by working relationships and career development whereas working relationships came out to be the major factor that affected job performance followed by working environment, job stress, and career development. These three features were related to job stress positively. They also found that work satisfaction played a big role in stress levels and performance. The authors were able to rank the stressors but could not do any prediction of stress levels.

In yet another work, the authors (Murali et al., 2017) aimed to find the effects of mainly four factors viz. workload, the pressure of time, lack of motivation, and role ambiguity on the performance of employees. The study was done on employees of a Malaysian organization and the sample size used was 136 respondents who were between the age of 20 to 60years and had 30years of experience in the field. Data was collected through questionnaires with a Likert scale of 1-5 whose normality was checked with the help of Kurtosis and Skewness and reliability was checked with the help of Cronbach Alpha. Descriptive analysis, correlation analysis, and regression analysis were applied to interpret the data. They found that the major factors that affected the performance of the employees were time pressure and role ambiguity. They also found that less support from the organization adds to the job stress and job dissatisfaction. There are little different findings by Sahoo, 2016 based on Health and safety executive model, and the main contributors for stress have been identified as job content, workload, and workplace, working hours, participation at the place of work, authority, career development, pay and position in the organization, interpersonal relationships, organizational culture, work-home interface. The effect of stress has been analyzed from two dimensions *viz*. on individuals and organizations. The effects of work stress on individuals were physical, emotional, intellectual, behavioral. Effects on the organization came out to be high staff turnover and recruitment costs, high absenteeism and presenteeism levels, reduced productivity levels, increased health and safety issues, litigation, reputational damage, increased training costs. The author has also listed the resources that could help manage, reduce and prevent stress to help the employees.

An interesting and unique study has been performed by Lawanont and Inoue (2018) that made use of multiple sensors, Raspberry Pi, and Arduino to collect data. Three force sensors were used to study the working behavior, the first sensor in the cushion of the seat, the second in the table mat, the third in the mouse pad. The amount of pressure applied can be related to the stress levels of a person. Temperature and humidity sensors, ambient light sensors, etc were used to collect data about the working environment. The Arduino board was connected to all sensors and the pre-processing of the data was done via the Raspberry pi. A 10-question survey known as PSS (perceived stress scale) was used to calculate the stress levels of a person for a month. This study was performed on 7 participants. Unsupervised learning was utilized on the data frame to form clusters to find the relation between the level of stress and the working behavior of each feature. They made use of k-means clustering and hierarchical algorithm for the clustering of data. These clusters were then used to analyze and interpret the data. In both the algorithms, the environmental features were alike between the two clusters. The characteristics of the clusters also indicated information about working behavior that was related to PSS score such as, where working behaviors in cluster A (higher stress) were probable to have fewer changes in active working whereas cluster B represents more active working. Most of the cluster's members showed that it was also related to the lower PSS score. Results showed cluster B consisted of the working behavior that led to the lower stress level. With this approach too, the prediction model could not be developed.

A study by Reddy et al. (2018), is based on the survey conducted by OSMI (Open Sourcing Mental Illness) during the year 2017. It consisted of 750 responses from the employees. The dataset at first contained 68 features from both personal and work life. The authors used many machine learning techniques like Logistic Regression, KNN Classifier, Decision Trees, Random Forest Classifier, Boosting, and Bagging. To evaluate the models, they used Classification Accuracy, False Positive Rate, Precision, AUC (Area under Curve) Score, Cross-validation AUC. They found that boosting achieved the highest accuracy of 75.13, thus performing better than other models when accuracy, false-positive rate, and precision are taken into account. Whereas with cross-validation AUC, Random forest classifier achieved the higher score. They also found that women were more mentally stressed than men and the employees at a tech organization had a higher risk of developing stress and mental illness. To achieve a better performance response, an ensemble of the basic machine learning algorithms has been experimented with by Odusami et al. (2021). The authors developed a hybrid machine learning model, K_LoRD, that is based on four different algorithms *viz*. K Nearest Neighbor, Logistic Regression, Random Forest and Decision Tree. This hybrid model outperformed the ordinary individual models in terms of Accuracy and Receiver Operating Curve for the prediction of customer churn in the Telecommunication industry.

Fei and Bing (2012) performed an interesting study that applied exploratory factor analysis and further authenticated the results by performing confirmatory factor analysis. The findings relate the dynamic development of the working state of the workers with their psychological contract content with the organization. The authors analyzed two groups of participants where the first group had 169 participants from Beijing, Tianjin, and Langfang, and the second group had 219 participants from Beijing, Tianjin, Qingdao, and Shanghai. They conducted this study based on their background, work stress calculations consisting of eight features, and psychological contract calculations which comprises of nineteen features. To analyze the data, the authors made use of regression analysis and found that at various levels of educational background there are various and diverse effects of transactional contracts for workers on work stress. Like for example, people tend to go for rewards equivalent to how much effort their job expects from them. In the model of this study, three angles of the scalene triangle are the dimensions of psychological contract notable by the worker. A point inside the scalene triangle is the work stress that is in line with the policies to manage the psychological contract, which forms the best balance of work stress fitting in with the psychological contract structure. In particular, as the dynamic development of the working state of the workers, their psychological contract content also changes, which in turn affects their perception of investment symbols given by the organization.

Burman and Goswami (2018) have reviewed the work of various authors that focussed on stress at the workplace and categorized them based on certain factors. The authors divided all sources and literature into four categories as journals, author profile, research methodology, and type of industries/research. They discovered that after reviewing the conceptual and descriptive research material on work stress, they could draw the basics and understanding of it. The study also found that there were a greater number of empirical studies than exploratory and longitudinal studies and that the bulk of the articles were not by professionals but rather by academicians. The top three contributors to these research papers and materials were from the US, UK, and India in that order. They also discovered that even though India has contributed to this research, based on both practical and conceptual knowledge related to stress, and its effects but the scientific findings have not been put to much use to deal with the actual problem. Adequate management techniques and tools are not being used to reduce stress levels; they are still only on paper. The research material also shows that stress from a workplace affects their performance and productivity at the organization as well as their physical and psychological well-being. Work stress can also lead to various diseases like coronary heart disease, blood pressure, depression, anxiety, nervousness, etc.

A study chose a sample size of 130 participants from various private institutes in Hyderabad, India by Stratified Random Sampling (Rahoo et al., 2017). The objective of the study was to find out the causes of work stress amongst the faculty members and how satisfied the members were in a private institute. They discovered that several stressors were disturbing the teachers. Demands at work, work relationships, role, position, pace and intensity of change in the workplace, and lack of support were found to be a major stressors. It was found that Age, Gender, and Marital status directly affect stress due to major differences found in the analysis of each factor and its relationship with stress. After combining the results of analyzing all the factors including the main cause of tension between the participants, poor peer relations, lack of rest, long working hours, harassment by the staff, lack of communication, lack of wage employment, and limited training, were major stressors and it was also witnessed that workplace stress plays a major role in the stress in an individual's lives. Stress and job burnout outgrow when there is role erosion, role overload, resource inadequacy, role isolation, and role ambiguity at the workplace. Here the focus was related to roles played by employees in various spheres of their jobs.

A case study in China had a sample size of 240 respondents, their data was collected via a questionnaire consisting of twenty-four questions (Meng & Wang, 2018). The prime statistical methods ANOVA and multifactor line regression were used for the analysis of the work stress of the university faculty. It was observed that the levels of stress of university faculty are significantly affected by professional status, age, and period of teaching. Along with them, administrative affairs, structural constraints, and personal characteristics play a major role in the work stress of the faculty members. This empirical study discovered that the mechanism used for evaluation which is based on quantitative performance indicators has significantly increased the occupation-related stress on the teachers.

Another research by Bhui, et al. (2016), aimed to recognize the stressors at the workplace and also the personal, individual, and organizational management programs or techniques that employees use to reduce their stress in public organizations, private organizations, and NGOs. Their sample size was 51 participants from various organizations. Qualitative interviews were conducted to collect the data from the participants. Results showed that unfavorable working environments and management practices were major and common stressors in the workplace. Along with those factors, unrealistic requests of work, lack of support, bad or unfair treatment, low decision-making freedom, lack of appreciation, effort–recognition imbalance, conflicting roles, lack of transparency, and poor communication within the organization were some more factors that led to increase in the stress levels of the employees. They found that organizational programs were found to be very helpful in reducing stress levels if there was an improvement in the management styles, which included physical exercise, breaks in between, and making sure that there is enough time for planning work tasks. Also, to prevent and reduce stress, personal interventions were very significant.

Shapiro et al. (2005) have gone a step ahead by suggesting a stress management program, for health care professionals that would decrease the level of stress and improve their quality of life. Frank et al. (2015) also studied the effectiveness of a similar type of mindfulness-based stress reduction (MBSR) program on educators. They observed the improvement in the quality of sleep of the respondents. These authors also could not provide any insight into understanding and predicting stress in advance.

One similar study by Rawat and Sultana (2021) demonstrates the application of Machine Learning algorithms for advanced resource planning in Hospital Emergency Departments. The authors have developed their model called light gradient boosted machines (LGBM) and found that its accuracy and time taken for prediction is better than other ordinary ML models like decision tree and GBM.

After reviewing all these research work by various authors globally, it was observed that none of the studies was offering a complete solution from the identification of stress-causing factors to the selection of a minimal subset of important stressors to the prediction of stress. Hence, the following three research gaps were observed:

1. It was found that none of the studies is based on all factors that surround the lives of working professional's *viz*. Organization Specific, Personal Factors, Work Environment Specific and Job Profile Specific

2. It was also observed that none of the studies focuses on the identification of the most influential stress-causing factors in a ranked manner.

3. Also, none of the studies is able to predict the stress level of the respondent.

This paper fills these gaps with the help of machine learning algorithms for ranking stress-causing factors and comparing and then applying the most accurate algorithm for the prediction of stress. Machine learning algorithms can provide a reasonably good accuracy of prediction with the number of records that are equal to more than ten times that of the number of features or questions.

V. IMPLEMENTATION

In this paper, we are using different types of Machine Learning technique to predict the stress level of the students. In the questionnaires test, we understand the student's different types circumstances and situations. This proposed model includes PSS dataset collection, pre-processing, feature extraction shows the comparison on the basis of their performance parameters

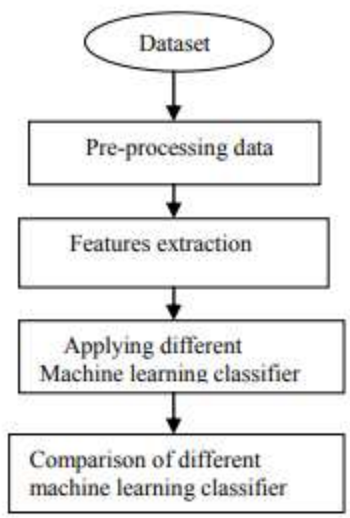

Fig-1(overall methodology)

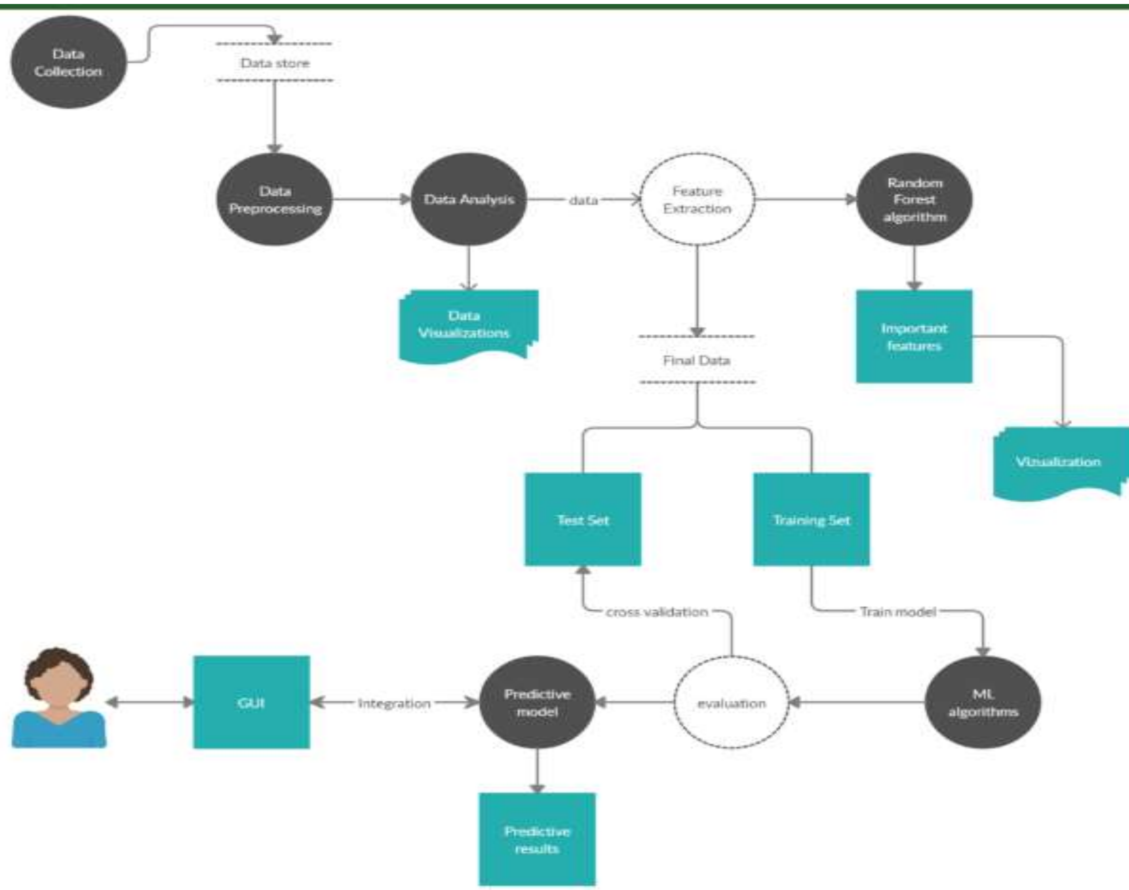

Fig 2. System Framework for the Stress Prediction model

Data Pre-Processing

The collected data had some missing fields and some outliers; hence data cleaning was done. Finally, the dataset was reduced to 197 entries. Demographic fields from the dataset were also eliminated before the application of the machine learning algorithm.

Depending on the answers to 18 questions, each answer was given a numeric value from 1 to 5 depending on whether the answer on the Likert scale reduces or increases the stress levels. For example, if the respondent says that he/she “Always” gets “Support from family”, then the transformed value for Always is 1 (Low stress) and if he says he “Never” gets “Support from family”, then the transformed value for “Never” is 5 (High stress). Corresponding to answers to all 18 questions, a score was calculated and it was transformed to Low stress (<1.33), medium stress (1.34 to 2.66), or a high stress (>2.66).

Exploratory Data Analysis

To get deep insight into collected data in terms of sample characteristics, observing the patterns, identifying outliers, various bar charts and heat maps were generated by using popular plotting libraries of Python as given below:

Matplotlib: Low level, provides lots of freedom.

Pandas Visualization: Easy to use interface, built on Matplotlib.

Seaborn: High-level interface, great default styles.

Bar chart for observing stress levels among participated males and females showed that the majority of both genders experienced medium-level stress. It was noticed that 56.8% of males and

48.61% of females fall in the category of medium-level stress. This is shown in Figure 2 and the corresponding data is shown in Table 1

Table 1 Categorization of males and females according to the level of stress

Stress Level	Gender	
	Male	Female
High	19(14.4%)	17(22.22%)
Medium	74(56.8%)	37(48.61%)
Low	38(28.8%)	23(29.17%)

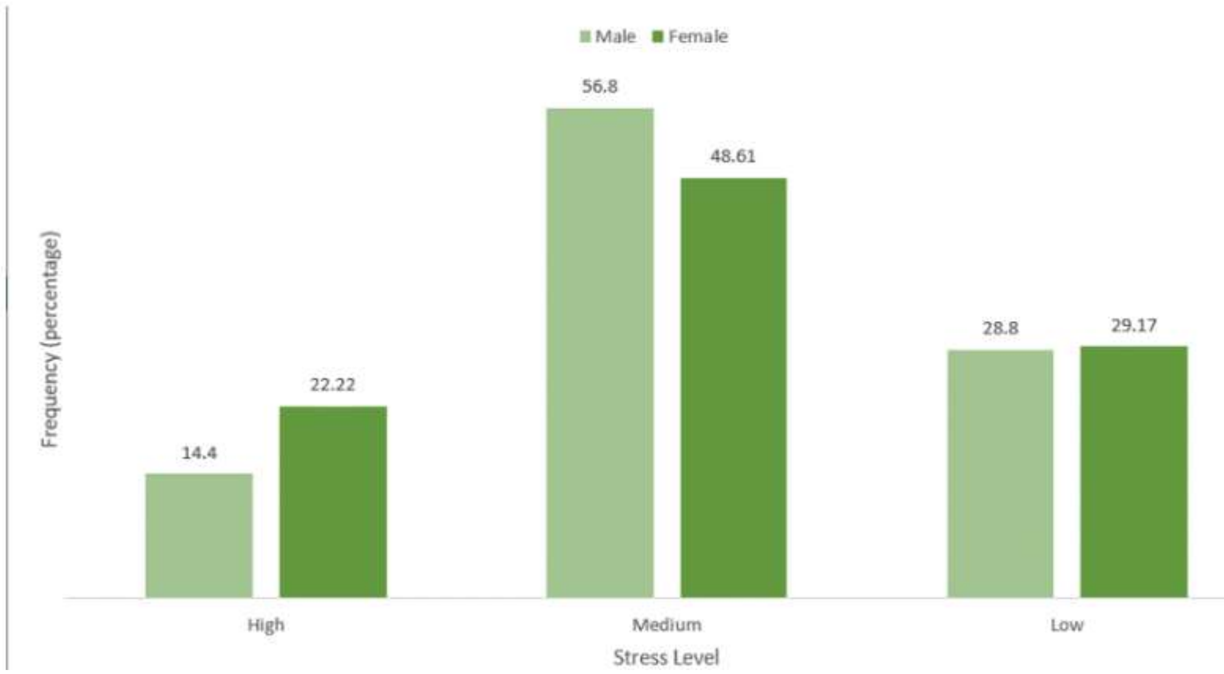

Fig 3. Percentage of male and female under three different categories of stress

5278

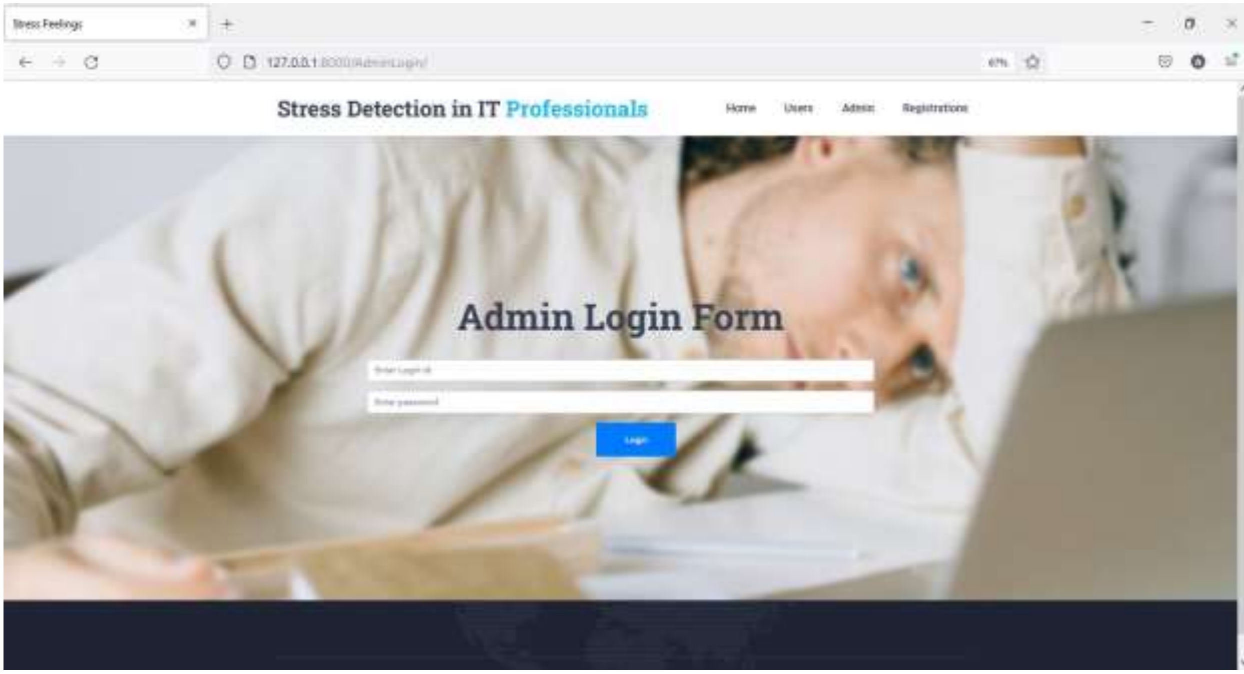

Fig 4 output 1 indicates admin login form

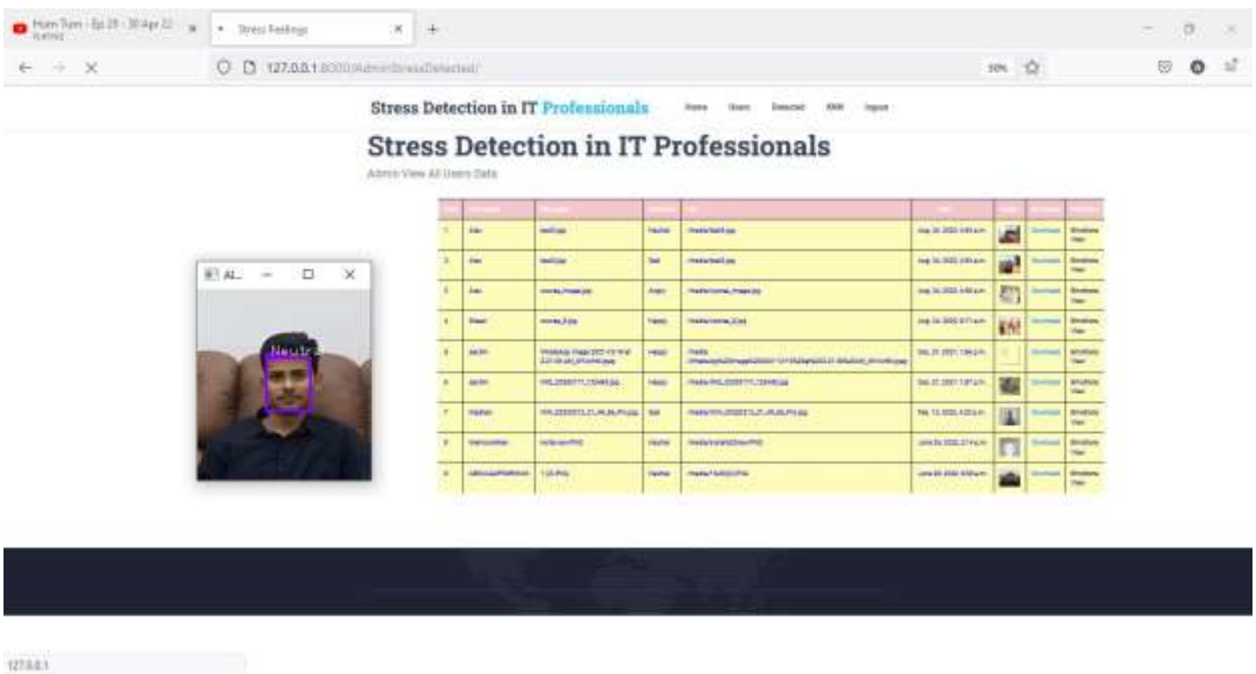

Fig 5 output 1 indicates admin details

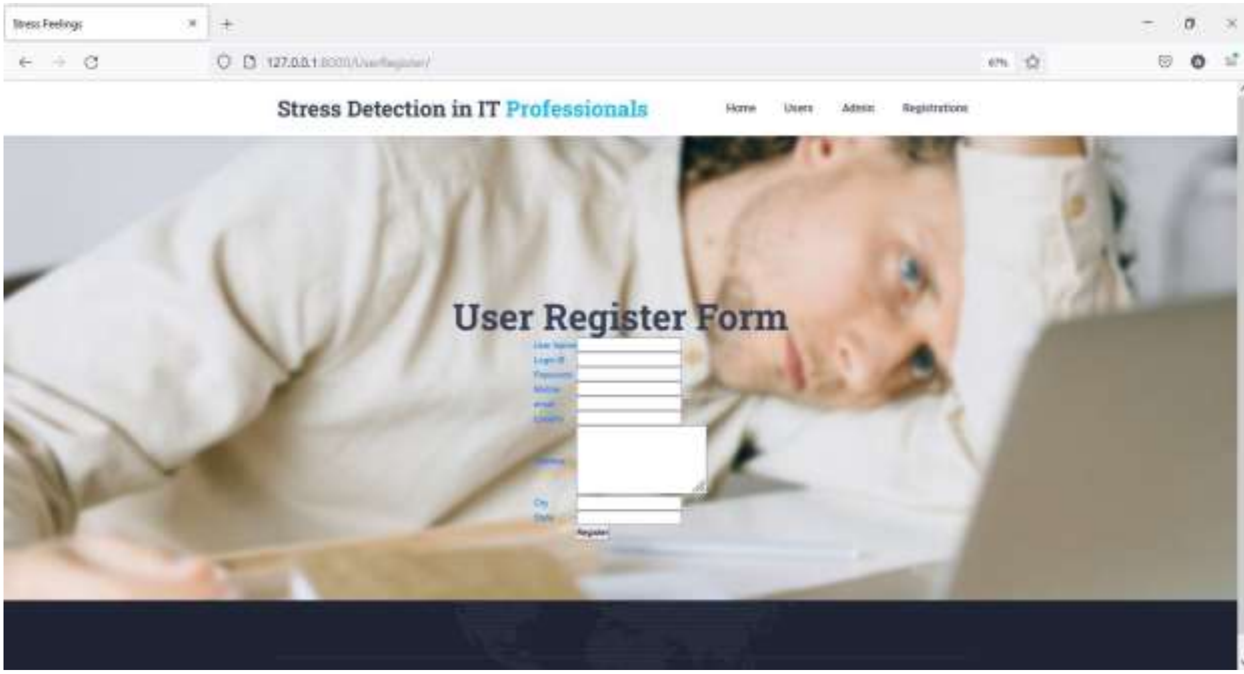

Fig 6 User registration form

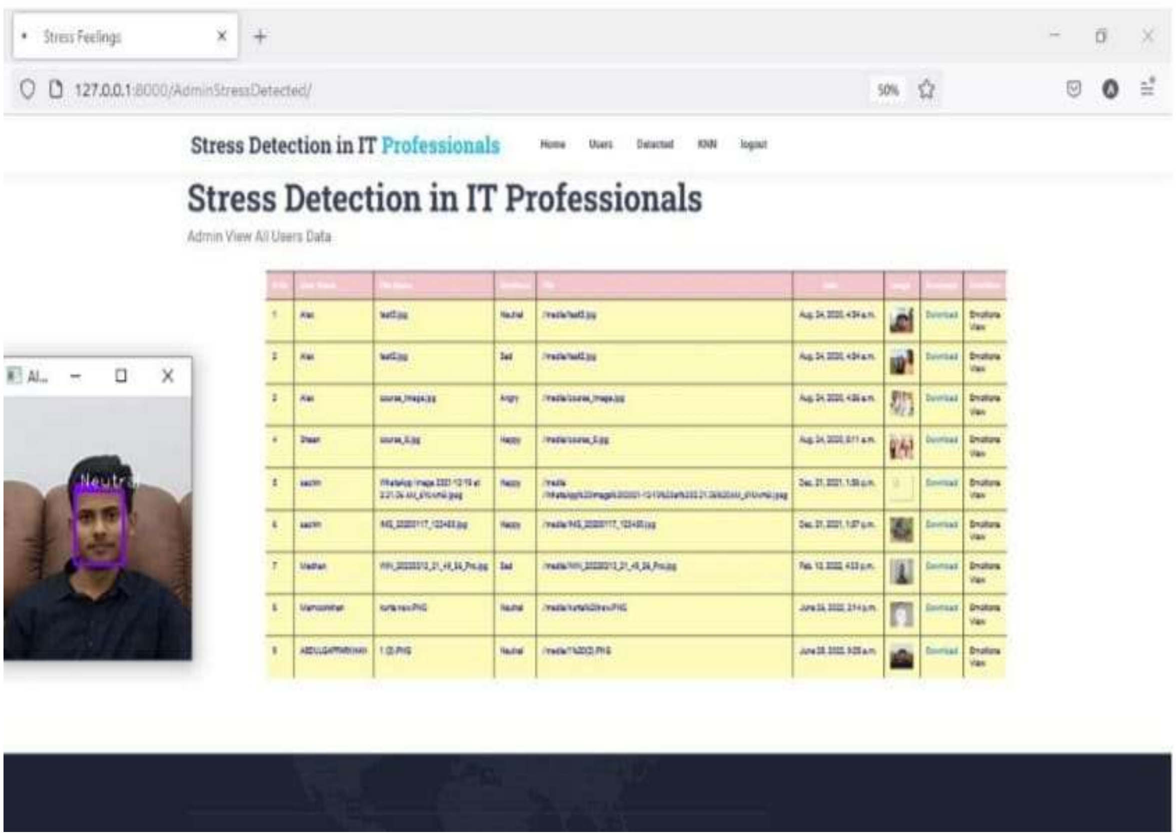

Fig 7 indicates user's activation list

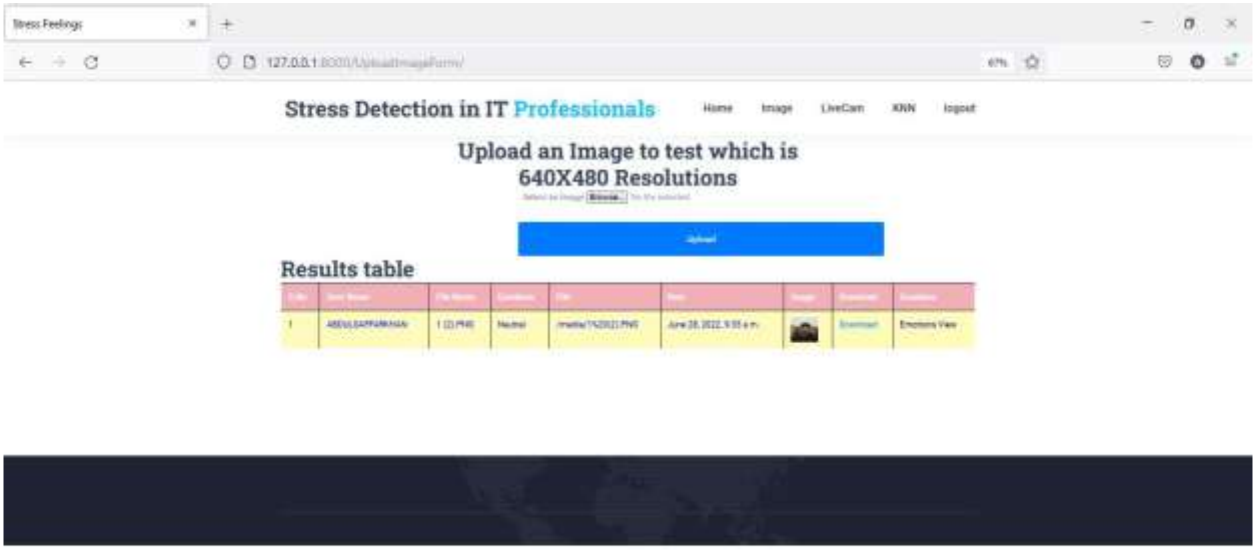

Fig 8 indicates users image uploading

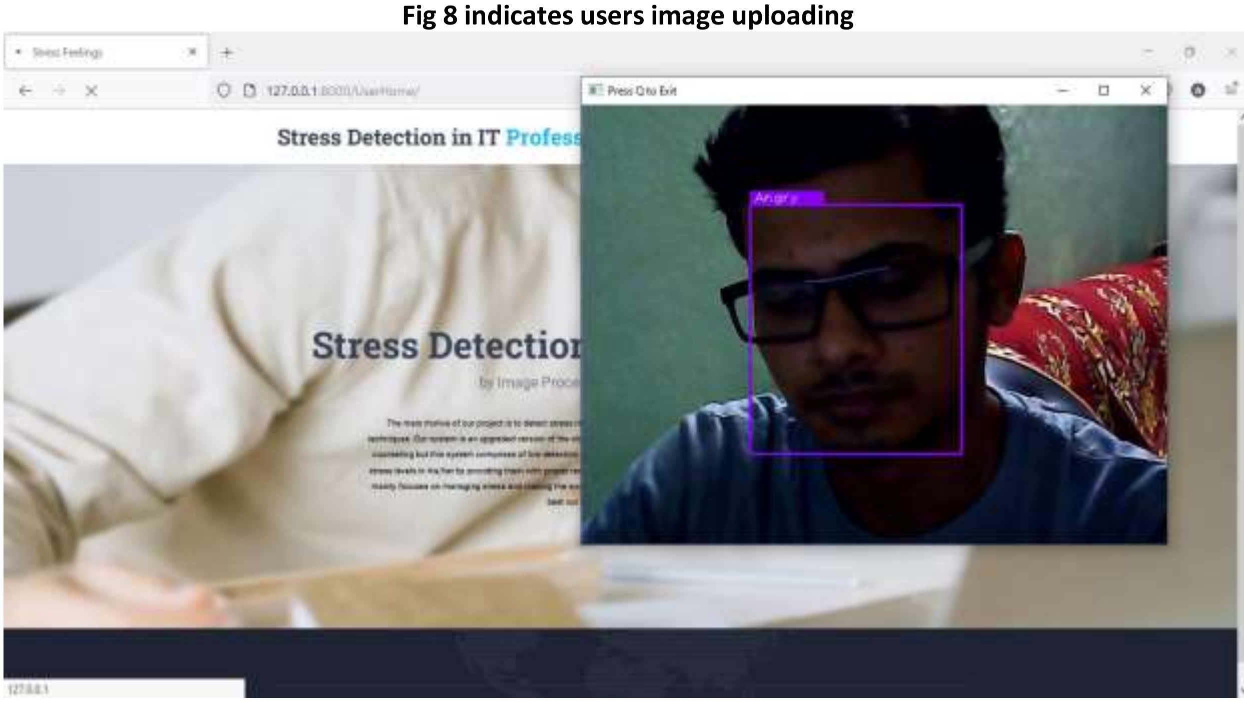

Fig 9 indicates users live activation

VI. CONCLUSION

Psychological stress is injures to health. In existing system stress is identified in face to face interview, communication or any other activities. Where two or more people are analyzed by another. In this proposed a system framework for detecting users‟ psychological stress states by using users‟ weekly social media data, leveraging tweets‟ content as well as users‟ social interactions. Here uses a words dictionary rating from -5 to +5 each word. To Classify and predict the data applied the SVM and NB algorithm. To improve result accuracy implemented the Word Sense Disambiguation by using n gram and Skip-gram model. Support Vector Machine with WSD and N gram gives

65% precision and 67% recall. This implemented system will be helpful to detect Stress by using their daily conversations on social media data, without knowing to the user and categories the user as stressed or relaxed. In future work, smiley, like and dislike symbols can be considered for categorization of collected data, as it has major contribution to expresses feelings.

References

1. Reshmi Gopalakrishna Pillai, Mike Thelwall, Constantin Orasan, “Detection of Stress and Relaxation Magnitudes for Tweets”, International World Wide Web Conference Committee ACM, 2018.

2. Huijie Lin, Jia Jia, JiezhonQiu, “ Detecting stress based on social interactions in social networks”, IEEE Transactions on Knowledge and Data Engineering, 2017.

3. Mike Thelwall TensiStrength, “Stress and relaxation magnitude detection for social media texts”, Information Processing & Management Science direct, 2017.

4. Jiawei Han, Michelin Kamber, Morgan Kaufman “Data Mining Concepts and Techniques”,2nd Edition, Elsevier, 2003.

5. Munmun De Choudhury, Michael Gamon, Scott Counts, Eric Horvitz, “Predicting Depression via Social Media”, Seventh International AAAI Conference on Weblogs and Social Media, 2013. 6. Thelwall Mike, Kevan Buckley, Paltoglou, “Sentiment strength detection for the social Web”, Journal of the American Society for Information Science and Technology, 2013

7. Thelwall M., Buckley, Paltoglou, Cai, Kappas, “Sentiment strength detection in short informal text”. Journal of the American Society for Information Science and Technology, 2010.

8. Dr. G V Garje, Apoorva Inamdar, Harsha Mahajan, “Stress Detection And Sentiment Prediction: A Survey”, International Journal of Engineering Applied Sciences and Technology, 2016.

9. Alok Ranjan Pall, DigantaSaha, “Word Sense Disambiguation: A Survey", IJCTCM Vol.5 No.3, July 2015.

10. Xinxiong Chen, Zhiyuan Liu, Maosong Sun, “A Unified Model for Word Sense Representation and Disambiguation”, Association for Computational Linguistics, 2014

A LIGHT WEIGHT CONVOLUTION NURAL NETWORK FOR REALTIME FACIAL EXPRESSION DETECTION

Dr. B. Hari Krishna[1], Nandhaihgari Rohith[2]

[1] Professor, Department of CSE ,**Malla Reddy Engineering College**, Hyderabad, Telangana, India.

[2,]PG Scholars, Department of CSE,**Malla Reddy Engineering College**, Hyderabad, Telangana, India

ABSTRACT

This task shows the utilization of component extraction of looks with mix of brain network for the acknowledgment of various facial feelings (cheerful, miserable, irate, dread, astounded, nonpartisan etc..). People are fit for creating huge number of facial activities during correspondence that shift in intricacy, power, and significance. In this task by utilizing a current fer2013 information we have accomplished 75% exact outcomes and it is simple and least complex way than Emotion acknowledgment utilizing mind action framework. Purposed framework relies on human face as we probably are aware face likewise mirrors the human mind exercises or feelings. In this undertaking, Convolutional brain network has been utilized for improved results, which is amazing with regards to highlight acknowledgment from a picture and we have Haar-Cascade to identify the locale of picture which contains the face so the model just needs to work with the face area.

The coming of computerized reasoning innovation has diminished the hole of human and machine. Computerized reasoning prepares man to make more close to consummate humanoids. Look is a significant instrument to impart one's feelings non verbally. This paper presents a new procedure of profound brain networks for grouping looks in a viable way. Broad consideration look acknowledgment (FER) has gotten as of late as looks are considered as the quickest correspondence vehicle of a data. Look acknowledgment gives a superior comprehension towards an individual's considerations or perspectives and dissecting them with the presently moving profound learning strategies supports the precision rate definitely contrasted with the conventional best in class frameworks. This undertaking gives a concise about different application fields of FER and openly accessible datasets utilized in FER and surveys the most recent exploration in the field of FER utilizing Random Forest Algorithm, Convolutional Neural Network (CNN) and profound learning. In conclusion, it closes the effective strategy among them.

Keywords: CNN,FER,face detection,Haar-Cascade.

DOI Number: 10.14704/nq.2022.20.10.NQ55147 **NeuroQuantology 2022; 20(10):1647-1653**

INTRODUCTION

FACIAL articulation is one of the most impressive, regular and widespread signs for individuals to convey their close to home states and aims [1], [2]. Various examinations have been led on programmed look examination due to its down to earth significance in friendly mechanical technology, clinical treatment, driver weariness reconnaissance, and numerous other human-PC cooperation frameworks. In the field of PC vision and AI, different look acknowledgment (FER) frameworks have been investigated to encode appearance data from facial portrayals. As soon as the 20th 100 years, Ekman and Friesen [3] characterized six fundamental feelings in light of cross-culture study [4], which demonstrated that people see specific essential feelings similarly paying little mind to culture. These

prototypical looks are outrage, disdain, dread, satisfaction, trouble,
and shock. Disdain was hence added as one of the essential feelings [5]. As of late, high level examination on neuroscience and brain science contended that the model of six essential feelings are culture-explicit and not widespread [6].

Albeit the influence model in light of fundamental feelings is restricted in the capacity to address the intricacy and nuance of our day to day emotional showcases [7], [8], [9], and other feeling portrayal models, for example, the Facial Action Coding System (FACS) [10] and the persistent model utilizing influence aspects [11], are considered to address a more extensive scope of feelings, the all out model that depicts feelings as far as discrete essential feelings is as yet the most well known viewpoint for FER, because of its spearheading examinations alongside the immediate and natural meaning of looks. Furthermore, in this review, we will restrict our conversation on FER in light of the all out model.

FER frameworks can be separated into two primary classifications as indicated by the element portrayals: static picture FER and dynamic grouping FER. In static-based strategies [12], [13], [14], the element portrayal is encoded with just spatial data from the ongoing single picture, though unique based techniques [15], [16], [17] consider the worldly connection among adjoining outlines in the info look succession. In view of these two visionbased techniques, different modalities, like sound and physiological channels, have additionally been utilized in multimodal frameworks [18] to help the acknowledgment of articulation.

Most of the conventional techniques have utilized high quality elements or shallow learning (e.g., neighborhood double examples (LBP) [12], LBP on three symmetrical planes (LBP-TOP) [15], non-negative lattice factorization (NMF) [19] and meager learning [20]) for FER. In any case, starting around 2013, feeling acknowledgment rivalries, for example, FER2013 [21] and Emotion Recognition in the Wild (EmotiW) [22], [23], [24] have gathered moderately adequate preparation information from testing genuine situations, which verifiably advance the progress of FER from lab-controlled to in-the-wild settings. In the in the mean time, because of the decisively expanded chip handling capacities (e.g., GPU units) and very much planned network design, concentrates on in different fields have started to move to profound learning strategies, which have accomplished the cutting edge acknowledgment exactness and surpassed past outcomes overwhelmingly (e.g., [25], [26], [27], [28]). Similarly, given with more successful preparation information of look, profound learning strategies have progressively been executed to deal with the difficult elements for feeling acknowledgment in nature. Figure 1 delineates this development on FER in the part of calculations and datasets.

Thorough studies on programmed articulation examination have been distributed as of late [7], [8], [29], [30]. These reviews have laid out a bunch of standard algorithmic pipelines for FER. Be that as it may, they center around conventional strategies, and profound learning has seldom been inspected. As of late, FER in view of profound learning has been studied in [31], which is a concise survey without presentations on FER datasets and specialized subtleties on profound FER. Subsequently, in this paper, we make an efficient examination on profound learning for FER errands in view of both static pictures and recordings (picture groupings). We mean to give a newbie to this recorded an outline of the orderly structure and prime abilities for profoundNotwithstanding the strong component learning capacity of profound learning, issues remain when applied to FER. To begin with, profound brain networks require a lot of preparing information to stay away from overfitting. Nonetheless, the current look data sets are not adequate to prepare the notable brain network with profound design that accomplished the most encouraging outcomes in object acknowledgment errands. Furthermore, high between subject varieties exist because of various individual credits, for example, age, orientation, ethnic foundations and level of expressiveness[32].Notwithstandig subject personality predisposition, varieties in posture, enlightenment and impediments are normal in unconstrained look situations. These variables are nonlinearly combined with looks and subsequently reinforce the prerequisite of profound organizations to address the enormous intra-class fluctuation and to learn powerful articulation explicit portrayals

LITERATURE SURVEY

As there is no staff accessible in automated eateries, it is challenging for the café the executives to gauge how the idea and the food is capable by the clients. Existing rating frameworks, like Google and Trip Advisor, just to some extent tackle this issue, as they just cover a piece of the client's viewpoints. These rating frameworks are just utilized by a subset of the clients who rate the eatery on free evaluating stages on their own drive. This applies for the most part to clients who experience their visit as exceptionally certain or negative.

[1] Different sorts of moderate advances contain did for Automatic FER frameworks. To produce a component vector for preparing, relationship among facial contraption is utilized for mathematical qualities found lying on spot and perspective of 52 level of facial marker spots. Here essential perspective and Euclidean distance is determined including each couple of milestones inside a structure and afterward distance alongside point values be deducted as of the matching space in addition to point upsides of essential casing in record string. Two classifiers strategies are utilized here: multi class AdaBoost in the organization of dynamic time traveling and SVM on the helped highlight vectors.

[2] Diverse face spreads contain different styles of detail so look highlights are routinely mined on or after all inclusive face region. Cheerful et al. utilized a methodology of Local Binary Pattern (LBP) histogram with different piece ranges starting around a general veneer district as a trademark vector in addition to after that ordered different look through Principal Component Analysis (PCA). However this strategy is applied in immediate climate, its accuracy is ruined as of not ready to reflect nearby contrasts of facial areas to trademark vector.

[3]Diverse face areas contain complete opposites forces of importance. For example, contrast with temple in addition to cheek, eyes notwithstanding mouth contains extra data. Ghimire et al. separated entire face district snared on

eISSN 1303-5150

area exact neighborhood territories to remove appearance highlights and utilizing a gradual pursuit strategy, significant nearby locales were distinguished which gives improvement in acknowledgment precision and decrease in include aspects. Numerous scientists have recognized different element extraction techniques and classifiers for customary methodologies. For look acknowledgment notable techniques for trademark mining like Histogram of Oriented Gradients (HOG), Local Binary Pattern (LBP), distance alongside point connection flanked by facial tourist spots in addition to classifiers for example Support Vector Machine (SVM), AdaBoost, Random Forest are utilized established on mined qualities. Advantages of moderate methodologies are that they oblige mediocre registering control with recognition contrasted with Deep learning based techniques. Consequently these methods are peaceful human utilized continuously associations since of their lower computational trouble alongside higher exactness [4].In existing calculation we are use in Haar-adaBoost characterization calculation, in this grouping precision is less.

SYSTEM ANALYSIS

INPUT AND OUTPUT DESIGN

INPUT DESIGN

The info configuration is the connection between the data framework and the client. It contains the creating detail and methods for information planning and those means are important to place exchange information in to a usable structure for handling can be accomplished by reviewing the PC to peruse information from a composed or printed record or it can happen by having individuals entering the information straightforwardly into the framework. The plan of information centers around controlling how much info required, controlling the blunders, staying away from delay, trying not to additional means and keep the interaction straightforward. The information is planned in such a manner so it furnishes security and usability with holding the protection. Input Design thought about the accompanying things:

What information ought to be given as information?

How the information ought to be organized or coded?

The discourse to direct the working staff in giving information.

Techniques for getting ready info approvals and moves toward follow when mistake happen.

OBJECTIVES

1.Input Design is the most common way of changing over a client situated depiction of the contribution to a PC based framework. This plan is essential to stay away from mistakes in the information input cycle and show the right course to the administration for getting right data from the electronic situation.

2. It is accomplished by making easy to understand evaluates for the information section to deal with huge volume of information. The objective of planning input is to make information section simpler and to be liberated from blunders. The information passage screen is planned so that every one of the information controls can be performed. It additionally gives record seeing offices.

3.When the information is placed it will check for its legitimacy. Information can be placed with the assistance of screens. Fitting messages are given as when required so the client won't be in maize of

eISSN 1303-5150

moment. In this way the goal of info configuration is to make an information format that is not difficult to follow

OUTPUT DESIGN

A quality result is one, which meets the necessities of the end client and presents the data obviously. In any framework consequences of handling are conveyed to the clients and to other framework through yields. In yield plan it is resolved the way in which the data is to be dislodged for guaranteed need and furthermore the printed version yield. It is the most significant and direct source data to the client. Effective and insightful result configuration works on the framework's relationship to help client direction.

1. Planning PC result ought to continue in a coordinated, thoroughly examined way; the right result should be created while guaranteeing that each result component is planned so that individuals will find the framework can utilize effectively and successfully. At the point when investigation plan PC yield, they ought to Identify the particular necessary result to meet the necessities.

2.Select strategies for introducing data.

3.Create archive, report, or different configurations that contain data created by the framework.

The result type of a data framework ought to achieve at least one of the accompanying goals.Pass data about on past exercises, current status or projections of theFuture.

Signal significant occasions, open doors, issues, or alerts.

 Trigger an activity.

Affirm an activity.

EXISTING SYSTEM:

As there is no staff accessible in automated cafés, it is challenging for the eatery the board to gauge how the idea and the food is capable by the clients. Existing rating frameworks, like Google and TripAdvisor, just to some degree tackle this issue, as they just cover a piece of the client's perspectives. These rating frameworks are just utilized by a subset of the clients who rate the eatery on free evaluating stages on their own drive. This applies basically to clients who experience their visit as exceptionally sure or negative.

PROPOSED SYSTEM:

To tackle the above issue, all clients should be propelled to give a rating. This paper presents a methodology for an eatery rating framework that asks each client for a rating after their visit to build the quantity of evaluations however much as could reasonably be expected. This framework can be utilized automated eateries; the scoring framework depends on look identification utilizing pretrained convolutional brain organization (CNN) models. It permits the client to rate the food by taking or catching an image of his face that mirrors the relating sentiments. Contrasted with text-based rating framework, there is considerably less data and no singular experience reports gathered. Notwithstanding, this straightforward quick and energetic rating framework ought to give a more extensive scope of feelings about the encounters of the clients with the café idea.

BENEFITS :- Security

Further developing memory use through parallelization

SCOPE

Last however not the least, human expressive ways of behaving in reasonable applications include encoding according to alternate points of view, and the look is just a single methodology. Albeit unadulterated demeanor acknowledgment in light of noticeable face pictures can accomplish promising outcomes, consolidating with different models into a significant level system can give correlative data and further upgrade the vigor. For instance, members in the EmotiW difficulties and Audio Video Emotion Challenges (AVEC) [252], [253] considered the sound model to be the second most significant component and utilized different combination methods formultimodalinfluence acknowledgment. Moreover, the combination of different modalities, for example, infrared pictures, profundity data from 3D face models and physiological information, is turning into a promising exploration heading because of the enormous complementarity for looks.

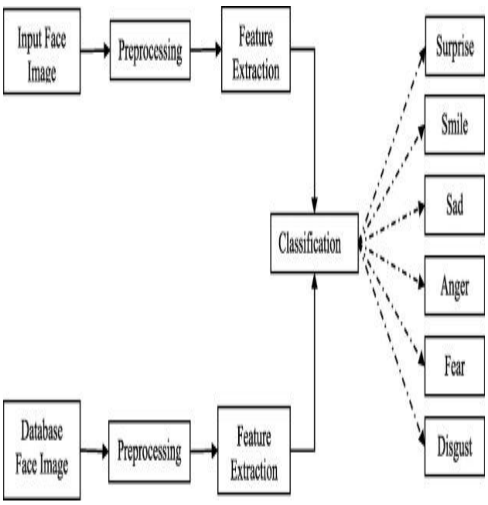

Architecture

CNN Model:

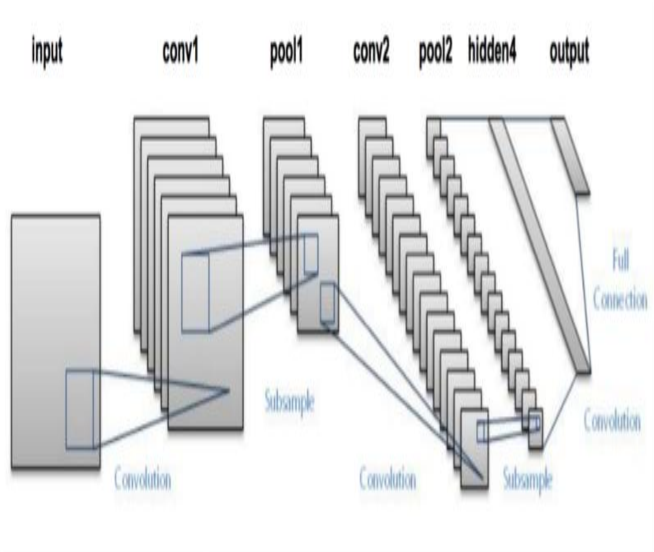

Fig: CNN

How a human figures out how to perceive objects, we have to demonstrate a calculation on a huge number of pictures before it is have the capacity to sum up the information and make expectations for pictures it has never observed. PCs 'see' uniquely in contrast to we do. Their reality comprises of just numbers. Each picture can be spoken to as 2- dimensional varieties of numbers, known as pixels. 1652

Any of the case have thing that they see pictures in an unexpected way, doesn't mean we can't prepare them to perceive designs, as we do. Its need to be consider what a picture is in an unexpected way.

we utilize a particular kind of Artificial Neural Network, a Convolutional Neural Network (CNN). The name comes from it’s the most important tasks in the system called convolution.

RESULTS

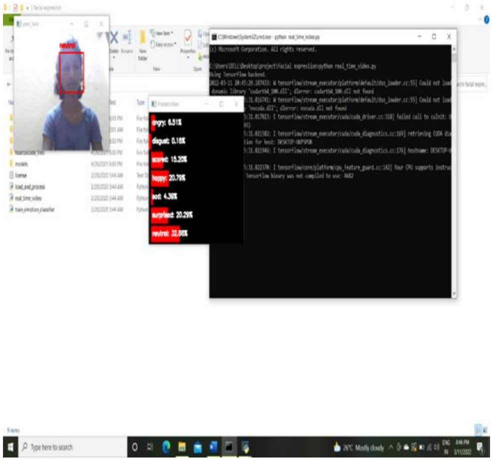

Fig : Results

The present project is aimed at classification of phishing websites based on the features.

For that we have taken the phishing dataset which collected from uci machine learning repository and we built our model with three different classifiers like SVC, Naïve Bayes, ELM and we got good accuracy scores.

There is a scope to enhance it further. if we can have more data our project will be much more effective and we can get very good results.

For this we need API integrations go get the data of different websites.

CONCLUSION

Information predispositionand conflicting explanationsare exceptionally normalamong various look datasets because of changed gathering conditions and the abstraction of commenting on.Scientists regularly assess their calculations inside a particular dataset and can accomplish good execution. Notwithstanding, early cross-data set tests have shown that errors between data sets exist because of the different assortment conditions and development pointers [12]; thus, calculations assessed through intra-data set conventions need generalizability on concealed test information, and the exhibition in cross-dataset settings is significantly decayed. Profound space adaption and information refining are choices to address this inclination [226], [251]. Moreover, due to the conflicting articulation comments, FER execution can't continue improving while developing the preparation information by straightforwardly combining different datasets [167]. One more typical issue in look is class irregularity, which is a consequence of the reasonable items of information securing: evoking and it is not difficult to clarify a grin,

REFERENCES

[1] C. Darwin and P. Prodger, The expression of the emotions in man and animals. Oxford University Press, USA, 1998.

[2] Y.-I. Tian, T. Kanade, and J. F. Cohn, “Recognizing action units for facial expression analysis,” IEEE Transactions on pattern analysis and machine intelligence, vol. 23, no. 2, pp. 97–115, 2001.

[3] P. Ekman and W. V. Friesen, “Constants across cultures in the face and emotion.” Journal of personality and social psychology, vol. 17, no. 2, pp. 124–129, 1971.

[4] P. Ekman, “Strong evidence for universals in facial expressions: a reply to russell’s mistaken critique,” Psychological bulletin, vol. 115, no. 2, pp. 268–287, 1994.

[5] D. Matsumoto, “More evidence for the universality of acontempt expression,” Motivation and Emotion, vol. 16, no. 4, pp. 363–368, 1992.

[6] R. E. Jack, O. G.Garrod, H. Yu, R. Caldara, and P. G. Schyns,“Facial expressions of emotion are notculturallyuniversal,”Proceedings of the National Academy of Sciences, vol. 109, no. 19, pp. 7241–7244, 2012

Access provided by: **Malla Reddy Engineering College** Sign Out

Plant Disease Prediction using Transfer Learning Techniques

Publisher: IEEE Cite This PDF

A. Lakshmanarao ; N. Supriya ; A. Arulmurugan **All Authors**

Abstract: Plant diseases are a significant hazard to feed a growing population, but due to a lack of infrastructure in many regions of the world, timely detection is challenging. F... **View more**

Metadata

Abstract:

Plant diseases are a significant hazard to feed a growing population, but due to a lack of infrastructure in many regions of the world, timely detection is challenging. Finding and detecting plant illness is essential in agricultural production. It takes a great deal of time and effort to find the disease. Agricultural sector can also reap the benefits of machine learning and deep learning. There has been a recent rise in the use of ML & DL techniques in plant disease identification. In this paper, we applied transfer learning technique for plant disease prediction. We used a 'plantvillage' dataset collected from Kaggle. Images of fifteen different types of plant leaves (Tomato, Potato, Pepper bell), from three distinct plants are included in this collection. We split the original dataset into three parts for three different plants and applied three transfer learning techniques VGG16, RESNET50, Inception and achieved accuracy of 98.7%, 98.6%, 99% respectively. The results of experiments shown that our proposed model achieved good accuracy when compared to traditional models.

Published in: 2022 Second International Conference on Advances in Electrical, Computing, Communication and Sustainable Technologies (ICAECT)

Date of Conference: 21-22 April 2022

INSPEC Accession Number: 21845461

Date Added to IEEE *Xplore*: 01 July 2022

DOI: 10.1109/ICAECT54875.2022.9807956

ISBN Information:

Publisher: IEEE

Conference Location: Bhilai, India

Contents

I. Introduction

The primary energy source for the human body is plants. A wide range of plant diseases can easily impact farming-based products. Farmers suffer ecological, social, and economic losses as a result of these diseases. The entire economy will be harmed if agricultural products decline. There are a variety of plant diseases on the earth. A decrease in the quality of agricultural products and a large decrease in returns could be caused by these illnesses, which could also jeopardize food safety. Preventative measures begin with early discovery and diagnosis of plant diseases. Agricultural technicians are typically the ones that identify and diagnose plant diseases in the field. Farmers face ever-increasing hurdles every day as population grows. Farming relies heavily on the availability of land and water. To handle these issues in real time, modern agriculture employs a wide range of technological advances. This paper describes a method for detecting and classifying leaf diseases. We used a Kaggle plantvillage dataset for out experiments. Some of the plant leaf images from the dataset are shown in Fig-1, Fig-2.

Authors

Figures

References

Keywords

Metrics

IJCRT.ORG ISSN : 2320-2882

INTERNATIONAL JOURNAL OF CREATIVE RESEARCH THOUGHTS (IJCRT)

An International Open Access, Peer-reviewed, Refereed Journal

BIG DATA PROCESSING USING MINING ALGORITHAM IN DATA SETS FOR DATA BASE SYSTEMS

Ms Akanksha Akulwar [1]
Assistant Professor

Mr. P.V. Ramana Murthy [2]
Associate Professor

Dr. P. Srinivas[3]
Professor

[1,2,3] Department of Computer Science and Engineering
Mala Reddy Engineering College (Autonomous)
Maisammaguda, Dist. Medchal, Secundrabad /500100, Telangana State, India

Abstract**—** The fundamental challenge for a lot of big data programs must be to search data volumes and take functional understanding for other hobbies. Focused by real-world programs controlling of massive Data were revealed to acquire demanding yet very compelling job. We make as read the efficient theorem that differentiates highlights of big data rising, and signifies big human sources representation, in the thought of data mining. Suggested theorem recommends that important highlights of big data are large by heterogeneous and varied data sources self-directed with distributed additionally to decentralized control, and sophisticated, developing in data associations featuring think that big data necessitate a sizable intelligence to boost data for finest values. We submit big human sources depiction, in the thought of data mining which data-driven structure involves demand determined selection of information sources, mining additionally to analysis, modeling of user interest, and contemplation on security.

Keywords**—** Big Data, Heterogeneous, Big data processing, Data Mining, Decentralized, Data Sources, Modeling, Security and Statistics.

I. INTRODUCTION

In a number of domains, big data are quickly growing coupled with growth of big data services where choice of facts are ongoing to develop very that's before capacity of generally used tools for controlling inside the reasonable time period. In a number of conditions, types of understanding extraction must be especially ingenious since storage inside the entire observed particulars are practically infeasible. Exceptional volumes of understanding need a effective data analysis to attain fast response for giant data. Big data appears by large data volume, various and self-directed sources by distributed furthermore to decentralized control, and search within the complicated and developing relations between data. These traits ensure it's severe challenge to discover from helpful understanding from big data. Our work provides an efficient theorem that differentiates popular features of big data rising, and signifies big human sources representation, in the idea of data mining. The recommended data-driven structure involves demand determined choice of information sources, mining furthermore to analysis, modelling of user interest, and contemplation on security. When the thought of big data concerns regarding data volumes, our theorem recommends that important popular features of big data are large by heterogeneous and varied data sources self-directed with distributed furthermore to decentralized control, and complicated, developing in data associations [1]. These traits believe that big data necessitate a big intelligence to improve data for finest values.

II. METHODOLOGY

Various information collectors desire their own methods for data recording, to guide to numerous data illustrations. The heterogeneous quality describes various representations for similar individual, as well as other features reference features concerned for representation of all the single observation. Autonomous reasons for data by distributed in addition to decentralized controls are most significant feature regarding services of massive data. Being autonomous, way of getting generates in addition to gather data missing of concerning connected obtaining a centralized control. The big data volumes apply prone to attacks when the complete system must depend on centralized control unit [2]. When big data volume increases, thus perform difficulty and relations beneath the data. Inside a energetic world, features which are useful for representation of individuals symbolizes our connections might evolve regarding additional conditions. This type of issue is becoming realism for programs of massive data, where secret's to acquire complex data relations, in addition to evolving changes to discover practical designs from collections of massive data. Our work bakes a dependable theorem that differentiates popular features of big data rising, and signifies big human sources representation, in the idea of data mining. It recommends that important popular features of big data are large by heterogeneous and varied data sources, self-directed with distributed in addition to decentralized control, and complex, developing in data associations. Processing of massive data depends on parallel programming models in addition to provision of cloud platform of massive data services for community purpose. For programs that concern big data and outstanding data volumes, it's frequently that data are distributed at various locations, denoting that clients ignore possess data storage. For implementation of mining programs of massive data acquiring a effective method of data access is important, created for clients who employ a third party to teach their information. For modifying to multisource, huge, active big data, researchers enhanced the standard techniques of understanding mining often [3]. Huge, heterogeneous in addition to synchronized popular features of multisource information offer critical versions among single-source understanding discovery in addition to mining of multisource data.

III. FRAME WORK FOR BIG DATA PROCESSING SYSTEM USING MINING ALGORITHM

For database system of intelligent learning for controlling of massive data, important secret's to enhance towards an very huge data volume and offer remedies for features featured obtaining a HACE theorem. This method recommends that important popular features of big data are large by heterogeneous and varied data sources self-directed with distributed in addition to decentralized control, and complex, developing in data associations. Hence these traits submit that big data necessitate a large intelligence to enhance data for finest values. Presenting processing structure of massive data was proven in fig1 the includes three groups for instance data getting the opportunity to view in addition to computing denoting group-I, data privacy in addition to domain understanding denoting of group-II additionally to computations of massive data mining denoting group-III [4]. Our work signifies big human sources representation; in the idea of data mining which data-driven structure involves demand determined choice of information sources, mining in addition to analysis, modeling of user interest, and contemplation on security. Offering of massive data depends on parallel programming models in addition to provision of cloud platform of massive data services for community purpose. Challenges at group-I spotlight on techniques of understanding getting the opportunity to view. While big details are stored up at various locations and understanding volumes might continuously develop, a reliable platform should consider important data storage for computing. Challenges made at group-II focus on semantics in addition to domain understanding for a lot of programs of massive data which information makes advantages towards mining procedure to find yourself in big data in addition to mining computations. Group-III mainly focuses on formula designs in managing of injuries that's elevated by volumes of massive data, allocation of distributed data, and by means of complicated and active data features. Outstanding volumes of understanding need a effective data analysis to attain fast response for giant data. In representative systems of understanding mining, mining process necessitate intensive computing models for analysing of understanding. Hence computing platform is needed to contain competent use of two resource types and they are data additionally to computing processors [5]. For mining of understanding, as data level is secluded from ability that single pc holds, a distinctive structure of massive human sources is determined by cluster computers having a high-performance computing proposal, having a data mining task that's organization by controlling of countless parallel programming tools [5]. Semantics in addition to application understanding reference several features in big data connected with rules, user understanding, in addition to domain data. Two most critical issues for this group comprise talking about of understanding and privacy domain in addition to application information [6]. While programs of massive data are featured by autonomous sources in addition to decentralized controls, mixing of distributed data sources towards centralized site for mining is unaffordable because of prospective transmission cost in addition to privacy issues a Big Data Processing System (BDPS).

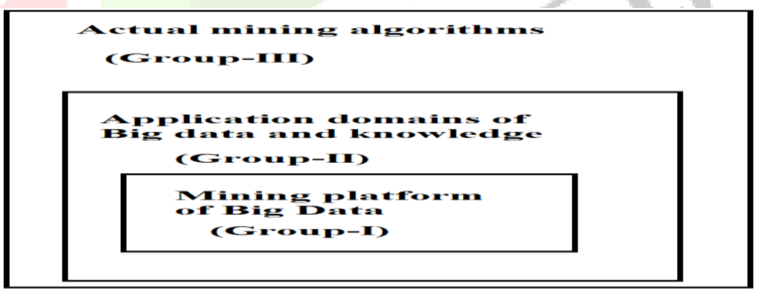

Figure 1: A Framework for Big Data Processing System (BDPS)

IV. CONCLUSIONS

Important highlights of big data are plenty of volume of data that's symbolized by heterogeneous additionally to numerous dimensionalities. Due to multisource, huge, heterogeneous, additionally to active highlights of application data that's concerned in distributed setting, among most important highlights of big details is to complete computing on peta byte by difficult computing procedure. For programs regarding big data and outstanding data volumes, it's frequently that data are distributed at various locations, denoting that clients ignore possess data storage. Our work comprises a ingenious theorem that differentiates highlights of big data rising, and signifies big human sources representation, in the thought of data mining. This model recommends that important highlights of big data are large by heterogeneous and varied data sources self-directed with distributed additionally to decentralized control, and sophisticated, developing in data associations. These traits are convinced that big data necessitate a sizable intelligence to boost data for finest values. We introduce sizable human sources representation, in the thought of data mining which model involves demand determined selection of information sources, mining additionally to analysis, modelling of user interest, and contemplation on security. In distinctive systems of understanding mining, mining procedure necessitate intensive computing models for analyzing of understanding.

REFERENCES

[1] Y.-C. Chen,W.-C.Peng, and S.-Y. Lee, "Efficient Algorithms for Influence Maximization in Social Networks," Knowledge and Information Systems, vol. 33, no. 3, pp. 577-601, Dec. 2012.

[2] A. Labrinidis and H. Jagadish, "Challenges and Opportunities with Big Data," Proc. VLDB Endowment, vol. 5, no. 12, 2032-2033, 2012.

[3] Y. Lindell and B. Pinkas, "Privacy Preserving Data Mining," J. Cryptology, vol. 15, no. 3, pp. 177-206, 2002.

[4] W. Liu and T. Wang, "Online Active Multi-Field Learning for Efficient Email SpamFiltering," Knowledge and Information Systems, vol. 33, no. 1, pp. 117-136, Oct. 2012.

[5] E.Y. Chang, H. Bai, and K. Zhu, "Parallel Algorithms for Mining Large-Scale Rich-Media Data," Proc. 17th ACM Int'l Conf. Multimedia, (MM '09,) pp. 917-918, 2009.

[6] R. Chen, K. Sivakumar, and H. Kargupta, "Collective Mining of Bayesian Networks from Distributed Heterogeneous Data," Knowledge and Information Systems, vol. 6, no. 2, pp. 164-187, 2004.

Published: 16 May 2022

Analysis of influencing features with spectral feature extraction and multi-class classification using de… network for speech recogni…

Dinesh Kumar Anguraj, J. Anitha, S. John … L. Ramesh, Seetha Rama Krishna & D. My…

J. Anitha

Department of CSE, Malla Reddy Engineering College (A), Dhulapally, Secunderabad, Telangana, India

International Journal of Speech Technolog… (2022)

Abstract

There is a drastic need for extracting information from non-linguistic features of the audio sources. It leads to the eminent rise of speech technology over the past few decades. It is termed computational para-linguistics. This research concentrates on extracting and providing a robust feature that examines the characteristics of speech data. The factors are analysed in a spectral way which stimulates the auditory elements. The speech enhancement technological process is being initiated with pre-processing, feature extraction, and classification. Initially, the input data conversion is done with ADC of 16 kHz sampling frequency. The spectral features are extracted with minimal Mean Square Error to enhance the re-construction ability and eliminate the redundancy characteristics. Finally, the deep neural network is adopted for multi-class classification. The simulation is performed in MATLAB 2020a environment, and the empirical outcomes are evaluated with existing approaches. Here, metrics like Mean Square Error, accuracy, Signal-to-Noise ratio (SNR) and features retained are computed efficiently. The anticipated model shows a trade-off in contrast to prevailing approaches. The outcomes demonstrate a better recognition rate and offer significant characteristics in selecting the most influencing features.

References

Deng, J., Xu, X., Zhang, Z., Frühholz, S., & Schuller, B. (2016). Exploitation of phase-based features for whispered speech emotion recognition. *IEEE Access, 4*, 4299–4309.

El-Maghraby, E. E., Gody, A., & Farouk, M. (2020). Noise-robust speech recognition system based on multimodal audio-visual approach using different deep learning classification techniques. *Egyptian Journal of English Language, 7*(1), 27–42.

Fan, Y., Jiang, Q.-Y., Yu, Y.-Q., & Li, W.-J. (2019). Deep hashing for speaker identification and retrieval. In *Proceedings of Interspeech* Graz, pp. 2908–2912.

He, N., & Zhao, H. (2017). A retrieval algorithm of encrypted speech based on syllable-level perceptual hashing". *Computer Science and Information Systems, 14*(3), 703–718.

Ioffe, S., & Szegedy, C. (2015). Batch normalisation: Accelerating deep network training by reducing internal covariate shift. In *The Proceedings of Machine Learning Research*., pp. 1–9.

Khonglah, B.K. & Prasanna, S. R. M. (2016). Low frequency region of vocal tract information for speech/music classification. In *Proceedings of IEEE Region 10 Conference*, pp. 2593–2597.

Kim, B. & Pardo, B.A. (2019). Improving content-based audio retrieval by vocal imitation feedback.' In *Proceedings of the IEEE International Conference on Acoustics Speech Signal Process. (ICASSP)*, Brighton, pp. 4100–4104.

Kruspe, A., Zapf, D., & Lukashevich, H. (2017) Automatic speech/music discrimination for broadcast signals. In Proceeding of INFORMATIK *Gesellschaft für Informatik*, Bonn, pp. 151–162.

Li, L. W., Fu, T., & Hu, W. (2019). Piecewise supervised deep hashing for image retrieval. *Multimedia Tools and Applications, 78*(17), 24431–24451.

Li, Y., Kong, X., & Fu, H. (2019). Exploring geometric information in CNN for image retrieval". *Multimedia Tools and Applications, 78*(21), 30585–30598.

Li, Y., Tao, J., Chao, L., Bao, W., & Liu, Y. (2017). CHEAVD: A Chinese natural emotional audio_visual database. *Journal of Ambient Intelligence and Humanized Computing, 8*(6), 913–924.

Liu, Z. T., Xie, Q., Wu, M., Cao, W.-H., Mei, Y., & Mao, J.-W. (2018). Speech emotion recognition based on an improved brain emotion learning model. *Neurocomputing, 309*, 145–156.

Mao, Q., Dong, M., Huang, Z., & Zhan, Y. (2014). Learning salient features for speech emotion recognition using convolutional neural networks. *IEEE Transactions on Multimedia, 16*(8), 2203–2213.

Masoumeh, S., & Mohammad, M. B. (2014). A review on speech-music discrimination methods. *International Journal of Computer Science and Network Solutions, 2*, 67–78.

Mirsamadi, S, E. Barsoum, & C. Zhang, (2017). Automatic speech emotion recognition using recurrent neural networks with local attention. In *Proceedings of the IEEE International Conference on Acoustics, (ICASSP)*, pp. 2227–2231.

Papakostas, M., & Giannakopoulos, T. (2018). Speech-music discrimination using deep visual feature extractors. *Expert Systems with Applications, 114*, 334–344.

Rahmani, A.M. & F. Razzazi. (2019). An LSTM auto-encoder for single-channel speaker attention system. In *Proceeding of the 9th International*

Conference Computer Knowledge. Engineering (ICCKE), Mashhad, pp. 110–115.

Song, P., Zheng, W., Ou, S., Zhang, X., Jin, Y., Liu, J., & Yu, Y. (2016). Crosscorpus speech emotion recognition based on transfer non-negative matrix factorisation. *Speech Communication, 83*, 34–41.

Srinivas, D., Roy, D., & Mohan, C.K. (2014). Learning sparse dictionaries for music and speech classification. In *Proceeding of the 19th International Conference on Signal Processing,* pp. 673–675.

Sun, W., Zou, B., Fu, S., Chen, J., & Wang, F. (2019). Speech emotion recognition based on DNN-decision tree SVM model. *Speech Communication, 115*, 29–37.

Swain, M., Routray, A., & Kabisatpathy, P. (2018). Databases, features and classi_ers for speech emotion recognition: A review. *International Journal of Speech Technology, 21*(1), 93–120.

Wang, Z.Q. & Tashev, I. (2017) Learning utterance-level representations for speech emotion and age/gender recognition using deep neural networks. In *Proceedings of the IEEE International Conference on Acoustics, (ICASSP)*, pp. 5150–5154.

Wen, G., Li, H., Huang, J., Li, D. & Xun, E (2017). Random deep belief networks for recognising emotions from speech signals. *Computational Intelligence and Neuroscience*

Xu, Y., Kong, Q., Wang, W. & Plumbley, M.D. (2018). Large-scale weakly supervised audio classification using gated convolutional neural network. In *Proceedings of the IEEE International Conference on Acoustics, Speech Signal Process. (ICASSP)*, Calgary, pp. 121–125.

Yu, J., Markov, K., & Matsui, T. (2019). Articulatory and spectrum information fusion based on deep recurrent neural networks. *IEEE/ACM Transactions on Audio, Speech, and Language Processing, 27*(4), 742–752.

Zhang, Z. (2016). Mechanics of human voice production and control". *Journal of the Acoustical Society of America, 140*(4), 2614–2635.

Zhang, H., Li, Y., Hu, Y., & Zhao, X. (2020). An encrypted speech retrieval method based on deep perceptual hashing and CNN-BiLSTM. *IEEE Access, 8*, 148556–148569.

Zhang, Z., Pi, Z., & Liu, B. (2015). Troika: A general framework for heart rate monitoring using wrist-type photoplethysmographic signals during intensive physical exercise. *IEEE Transactions on Biomedical Engineering, 62*(2), 522–531.

Zhang, N. & Lin, J. (2018). An efficient content based music retrieval algorithm. In *Proceedings of the 5th International Conference on Vehicle Technology and Intelligent Transport Big Data Smart City (ICITBS)*, Xiamen, pp. 617–620.

Author information

Authors and Affiliations

Computer Science and Engineering, Koneru Lakshmaiah Education Foundation, Vaddeswaram, Guntur, Andhra Pradesh, India

Dinesh Kumar Anguraj

Department of CSE, Malla Reddy Engineering College (A), Dhulapally, Secunderabad, Telangana, India

J. Anitha

Computer Science and Engineering, Saveetha Institute of Medical and Technical Sciences (SIMATS), Chennai, Tamil Nadu, India

S. John Justin Thangaraj

Dr MGR Educational and Research Institute, Maduravoyal, Chennai, Tamil Nadu, India

L. Ramesh

CreovSys Solutions India Private Limited, Tiruppur, Tamil Nadu, India

Seetha Rama Krishna & D. Mythrayee

Corresponding author

Correspondence to D. Mythrayee.

Additional information

Publisher's Note

Springer Nature remains neutral with regard to jurisdictional claims in published maps and institutional affiliations.

Rights and permissions

About this article

Cite this article

Anguraj, D.K., Anitha, J., Thangaraj, S.J.J. *et al.* Analysis of influencing features with spectral feature extraction and multi-class classification using deep neural network for speech recognition system. *Int J Speech Technol* **25**, 907–920 (2022). https://doi.org/10.1007/s10772-022-09974-9

Received	Accepted	Published
03 March 2021	10 April 2022	16 May 2022

Issue Date

December 2022

DOI

https://doi.org/10.1007/s10772-022-09974-9

Keywords

Speech **Non-linguistic features**

Spectral features Deep neural networks

Mean square error

IoT based application designing of Deep Fake Test for Face animation

Kotari Sridevi
Department of CSE, Muffakham Jah College of Engg & Tech, Hyderabad, Telangana-500034, India

Kanaprthi Suresh Kumar
Department of CSE – Data Science, Malla Reddy University, Hyderabad, Telangana-500100, India

D Sameera
Department of CSE, B V Raju Institute of Technology, Hyderabad, Telangana-502313, India

Yugandhar Garapati
Department of CSE, GITAM Deemed to be University, Hyderabad, Telangana-500090, India

D Krishnamadhuri
Department of CSE, Mallareddy Engineering College, Hyderabad, Telangana-500100, India

Srikanth Bethu*
Department of CSE – AIML & IOT, VNRVJIET, Hyderabad, Telangana-500090, IndiaResearch Scholar, Department of CSE, National Institute of Technology, Warangal, Telangana-506004, India

ABSTRACT

Development of Deep Learning models of Internet of Things (IoT) enclosures with limited resources are difficult because Both Quality of Results are difficult to achieve - QoR as follows two models, DNN Model, and Inference Accuracy and Quality of Services such as power consumption, throughput, and latency. Currently, the development of DNN models is often separated from deploying them to IoT devices, which leads to the most effective solution. If there are many records that represent objects of substantially the same class (face, human body, etc.), you can apply frames to each object of this class. To achieve this, use an independent representation to distinguish between appearance and progress data. Deep fake detection is achieved by using a novel, lightweight Deep Learning method on the IoT platform that is memory-efficient and lightweight. It is carried out in two different stages. The first phase of the deep fake test aims to implement a method of extracting images from a video and using them in conjunction with a Deep Neural Network to implement a test for face animation. It has been reported that the impact of the background elimination has been reported before the background subtraction. Here the Trans GAN model is used for the image classification. In the second phase, the work can be recorded and executed by the IOT device that can record live video streams and then detect activity involved in live video. An activity detection prototype based on IoT devices with small processing power is presented. This prototype provides improvements to the system, extending its application in various ways to improve portability, networking, and other equipment capabilities. The proposed architecture will be evaluated against four highly competitive object detection benchmarking tasks CIFAR10, CIFAR100, SVHN, and ImageNet.

CCS CONCEPTS

• **Computing Methodologies**; • **Modelling and Simulation**; • **Model Development and Analysis**; • **Model verification and Validation**;

KEYWORDS

Deep Fake, Face animation, Object detection, GAN

ACM Reference Format:
Kotari Sridevi, Kanaprthi Suresh Kumar, D Sameera, Yugandhar Garapati, D Krishnamadhuri, and Srikanth Bethu. 2022. IoT based application designing of Deep Fake Test for Face animation. In *2022 6th International Conference on Cloud and Big Data Computing (ICCBDC 2022), August 18–20, 2022, Birmingham, United Kingdom.* ACM, New York, NY, USA, 7 pages. https://doi.org/10.1145/3555962.3555967

1 INTRODUCTION

Face animation [1] is a difficult problem that continues to challenge researchers who want to recreate the nuances that make up a human face. The face has many parts that need to be accurately simulated to create a compelling face approximation. Features such as facial expressions, wrinkles, and skin texture are easy clues when comparing a real face to an animated face. Expressions need to be formed naturally, as humans do not completely transition between different emotional states. Creating the wrinkles that show emotional strength in the right areas to suit character's mood. The skin needs to be properly connected to different parts of the environment. Humans are very good at identifying these factors that make the face look unnatural, and there are many theories as to why humans are so good at this task. One theory is that it has evolved this ability to identify healthy individuals for reproduction. Another theory is that replicas of humanoids remind us of death and thus provoke eerie emotions due to our fear of death. Regardless of which theory is true, humans are good at identifying faces and have developed

*Srikanth Bethu is a Research Scholar in the Department of Computer Science and Engineering in National Institute of Technology, Warangal, Telangana - 506004, India. Working as Assistant Professor in the Department of CSE-AIML&IOT in VNR VJIET College, Hyderabad, India.

ICCBDC 2022, August 18–20, 2022, Birmingham, United Kingdom

ACM ISBN 978-1-4503-9657-8/22/08…$15.00
https://doi.org/10.1145/3555962.3555967

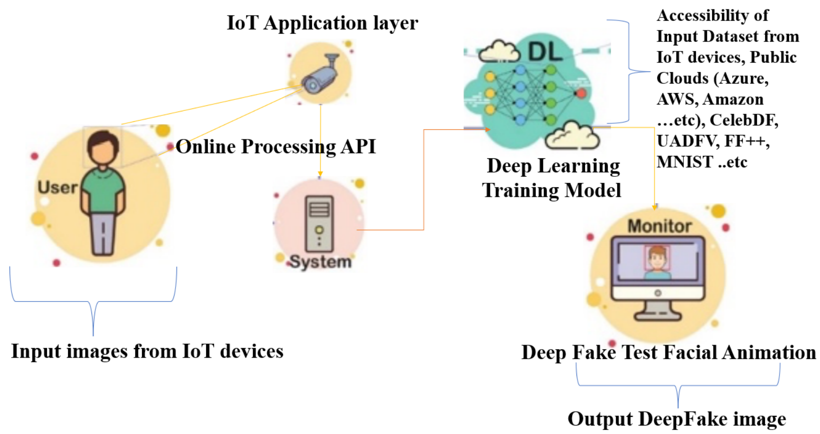

Figure 1: Overview of the IoT based Deep Fake Test

eerie emotions about human-like faces. This phenomenon, known as the uncanny valley, is an important factor in determining the quality of facial animation. Facial animation is difficult because it needs to convey human emotions in approximation without disturbing people trained to find defects. Due to the complexity of the human face and the powerful ability of humans to detect defects in facial approximation, there are many face animation methods that seek to create attractive faces that meet the needs of different applications. Realistic facial animation is not needed in animated films, but it is needed to prevent the aging of actors acting with other real actors. There are so many approaches to face animation that it can be difficult for artists and developers to choose the best approach for their needs.

With the quick development of the Internet of Things (IoT) [2], society has entered every other period. The IoT enjoys several unmistakable benefits, like protection, ongoing, computerization, embeddedness, interoperability, and interconnection. With regards to the Internet of Things and 5G, the rate of the company is constantly improving, which incorporates lodging to individuals, but similarly works with statistics misrepresentation. Simultaneously, profound gaining knowledge of is blasting as every other innovation. Some distance accomplishing use of profound gaining knowledge of innovation has obtained superb improvement distinctive fields, but similarly made useful criminal situations for responsible parties. For instance, the deep fake method, which has prompted horrible effect on the overall public as of late, can't simply produce sensible phony pictures, recordings, and sound substance, but similarly manufacture evidence for digital wrongdoing. The maltreatment of this approach has truly undermined the company statistics and statistics protection of the 2 human beings and the overall public. Thusly, the exam of deep fake identity innovation is of terrific significance to assure the realness of video, picture, and sound communicated with inside the company.

The above Fig 1. Shows the overview of IoT based Deep Fake Test [3] process. In the first stage, an approach for implementing a deep fake test for face animation has been proposed by the background subtraction of images from the video, followed by a Deep Neural Network [4]. It has been reported that the impact of the background elimination has been reported before the background subtraction. Here the DenseNet [5] model is used for the image classification and feature extraction. In the second stage, the work can be recorded and executed by the IOT device that can record live video streams and then detect activity involved in live video. Finally, the result will be displayed on system monitor with real image at one window and fake animation image at another window.

2 RELATED WORK

This looks at offers an inner and out audit of superior manipulate processes carried out to facial substance due to the large quantity of attainable risky applications, e.g., the age of phony information that could provide falsehood in political selections and protection dangers. We see 4 types of controls: i) entire face blend, ii) person trade, iii) trait manipulate, and iv) demeanour trade. These 4 precept types of face manipulate [6] are grounded through the exam neighbourhood area, getting maximum attention over the maximum latest couple of years. Moreover, we moreover audit on this assessment some different trying out and volatile face manipulate strategies that aren't so well-known but like face transforming. The existed datasets aren't ok to foster reliable region techniques. While the cutting-edge live finder can't protect such recordings because the assault.

Several datasets have been created to study Deep Fake [6] location strategies. UADFV and CelebDF collect YouTube footage to create face-wapping footage, and DFDC captures 48,190 footage featuring paid entertainers to create large commercial datasets of over 104,500 footages.

Much of this set of work involves identifying changes in facial features that are barriers to existing deep fake datasets. Deep Fake's facial movements were sent to mobile phones, creating many false recordings and broadcasts on the Internet. Therefore, these fake records challenge the security of many advanced systems in our day-to-day operations. For example, facial recognition systems rely heavily on live detection to ensure that a customer is a real person by expecting the customer to perform a series of explicit activities in the recording. The below Table 1. Shows the summary report of Deep Fake Detection methods.

Table 1: Summary report of Deep Fake detection methods

Methodology used	Techniques and Classifiers used	Key elements and features	Streaming type	Names of datasets used
Eye blinking,Eye aspect ratio	Long Term Recurrent Convolutional Network (LRCN)	LRCN used for Eye blinking detection with the temporal patterns	Videos and images	50 interview videos and their related deep fakes
Spatial temporal features	Recurrent Convolutional Network (RCN)	CNN DenseNet	Videos and images	Face Forensics++ datasets
Infra-frame and temporal inconsistencies	Convolutional Neural Networks and LSTM	Frame level features and sequence descriptors	Videos and images	Videos collected from different websites
Face warping artifacts	VGG-16, ResNet 50, 101, 152	CNN used for artifacts detection using resolution of the warped face	Videos and images	UADFV, Deep Fake TIMIT
MesoNet	CNN	Meso-4, meso inspection-4	Videos and images	Online videos, Face Forensics Face2Face approach
Eye, teach and Facial texture	Logistic Regression and NN	Used for classification	Videos and images	Youtube videos
PRNU analysis	PRNU	Pattern analysis using sensors of digital camera	Videos and images	Deep Face lab videos
Attribution based confidence	ResNet50 mode, VGG Face2	Detects deep fakes without training	Videos and images	Vid TIMIT, COHFACE
Deep Network Processing	DCGAN, WGAN, PGGAN	Generalization by GAN images. Deep Networks are used for identification of real and fake images.	Videos and images	Celeb-A HQ

2.1 Deep Fake and Live detection

The live indicator primarily protects against 'Replay Attacks', which are attacks at the psychical level. A 3D printed cover could be fabricated by aggressors, or they could print out a paper model of the victim's face and wear it. To safeguard against such assaults, numerous location techniques have been proposed. A few methodologies attempt to identify the distinctions between genuine countenances and falsification faces. De et.al., gauge the invariant of facial focuses for recognition. Komulainen genuinely think identifying faces' dynamic muscle change can recognize the ridiculing. Wang et al., distinguish the blood stream change under the skin to isolate facial cover and genuine face [7]. They as a rule expect clients to do some activity, like squinting or yawing, to work on the presentation. Most of the datasets are created using character transaction calculations, but some work for facial vividness, few of existing datasets are CelebDF, DFDC, FF ++.

2.2 Challenges

A fair dataset containing facial movements is FF ++. Considering that this dataset is quite small, it is hard to cover deep fake information. The face vibrancy of deep fake datasets needs to be well sorted and smarter to cover motion [8] classification for future downstream projects than the simple causality spoken in FF ++. Insists. For example, vitality indicators regularly request explicit facial activity [9] object or appearance as information. As a result, it unites us and proposes a vast range and activity datasets of obvious facial vibrancy. Table 2 below shows important data for existing datasets and accuracy.

Table 2: Information of existing datasets and their possibilities

Dataset type	Real images	Fake images	Types of generation	Action specific	Accuracy
UADFV	48	48	Face swapping	No	85.9%
Celeb-DF	595	5640	Face swapping	No	87.1%
DFDC	48200	104550	Face swapping	No	89.9%
FF++	1001	4001	Animation and Swap	No	90.1%
ForgeryNet	91632	121620	Animation and Swap	No	90.2%
Deep Fake MNIST	1001	1001	Image animation type	Yes	92.2%

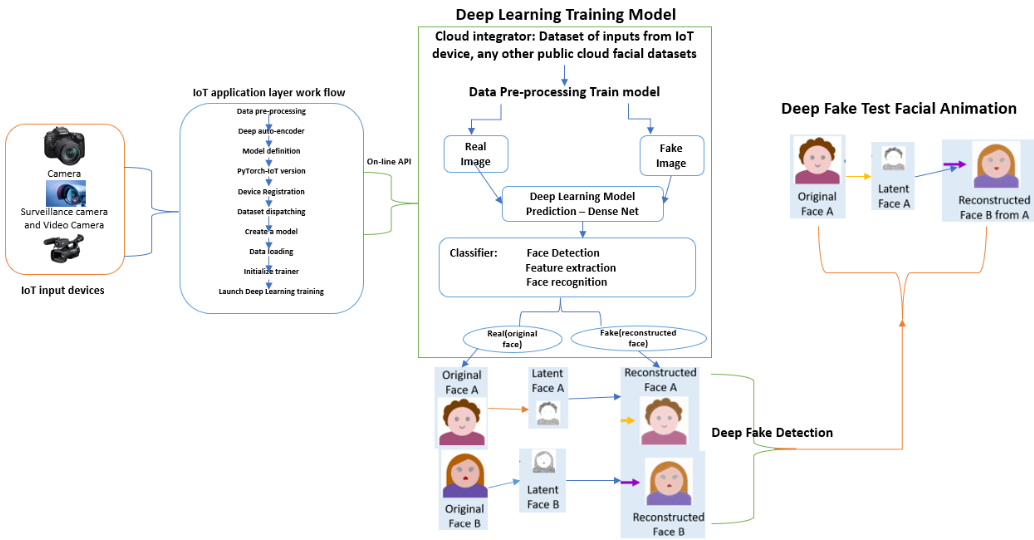

Figure 2: Proposed approach for IoT based Deep Fake Test

3 METHODOLOGY

The proposed approach includes the IoT based application for image animations primary motion model in live recording. The above Fig 2. Shows the proposed approach of IoT Deep Fake Test [10]. For better results, using the VoxCeleb dataset, Mode dataset, MGIF dataset, Taiichi and Nemo datasets. This strategy is also relevant for datasets such as ADFES, UADFV, DFDC, FF ++, and Deep Fake MNIST +. To improve the visual quality of the approach is to 1) crop the real image to a square, 2) make sure the icon's face isn't too close or too far, and 3) use a uniform base image. This is also applicable to images under low lighting. The work is done in two stages. First phase proposes a method for implementing activity verification using 3D CNN in conjunction with basic image extraction methods [11]. We investigate the effects of background subtraction before applying 3D-CNN. The second phase is to extend the work further and run it on the Raspberry Pi [12]. This allows you to record a large amount of video and then recognize the actions associated with the video. In this sense, proof of action is provided using a small IoT based gadget that can update the framework and extend its application in different structures.

3.1 Generative Adversarial Network - GAN

TransGAN, a pure transformer-based GAN architecture based on this paper, provides a coherent set of efforts and innovations to address those challenges. We also develop a unique training recipe based on the innovative TransGAN architecture that also addresses the stability issue brought by both GAN and Transformer, which stabilizes both their optimization and generalization. The goal is to demonstrate the need for data augmentation, layer normalization, and relative position-coding as a replacement for absolute token locations. Using only a transformer and no convolution, we built the first GAN [13]. TransGAN is equipped with a new grid self-attention mechanism and a memory-friendly generator and a multi-scale discriminator.

3.2 IoT based Deep Fake

The proposed architecture developed a IoT based Deep learning Deep Fake cloud deployable system, for real time object detection [14] Internet of Things and liveliness. This framework uses IoT Application Layer and adapts to user Deep Learning Training model where the results are generated. The important elements of this model are described below as follows to make the Deep Fake creation. The whole process is programmed by using Aurdino/

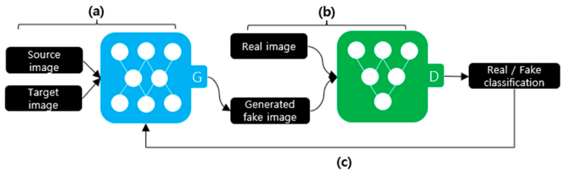

Figure 3: Deep Fake creation process from IoT input device sensors

Raspberry pi, it is acting as interface between the IoT system and Deep Learning system. The whole process is designed [14]res as on-line process

1. IoT input devices [14] – Camera, Surveillance Camera, Video camera can be used for taking live images, also used to record the video to create image datasets.
2. IoT Application Layer – The captured images from the IoT input devices are stored in the cloud system and accessed for the dataset creation. Here the interface is created with IoT cloud system where Data pre-processing is done.

Later the Device registration is created with On-Line API between Deep Learning training network model to dispatch the dataset into created model. The data is loaded by the model trainer to launch the Deep Learning Training process.

1. Deep Learning Training Model – The procedure is divided into a pre-treatment process and a classification process. The pre-processing process extracts the face image from the frame image, extracts the features of computer vision [15], and then extracts the differences between the frames. The classification process uses DNN [16] to detect deep fake by getting the variance of the specified number of frames from the pre-processed data.

3.3 Live Detection and Deep Fake

In contrast, the latest live detector defended primarily against replay attacks, which were attacks of a psychic nature. Using a 3D printer, attackers could create a 3D mask of a victim. And they could print out the victim's face on paper and wear it. A wide range of detection methods has been developed to stop such attacks. There are some methods that attempt to differentiate between real and fake faces [16]. The results of our experiments demonstrate that it is possible to spoof IOT live detectors in the market with facial animation data with specific actions. Recent proposals have surfaced for several Deep Fake datasets that can be used to generate realistic results to spoof people in response to the rising concerns regarding Deep Fake [16] techniques. The data is, however, generated by using identity swapping algorithms, and the facial animation dataset is only one of several.

Fig. 4 demonstrates our proposed pipeline for generating and collecting a Deep Fake Deep Learning and customized IoT dataset. To create the source identity images, we first collect videos from the VoxCeleb1 website and extract the frames from those videos. Following that, we filmed a series of driving videos with ten volunteer actions. For VoxCeleb1 videos, which have a 256x256 resolution and are face-cropped.

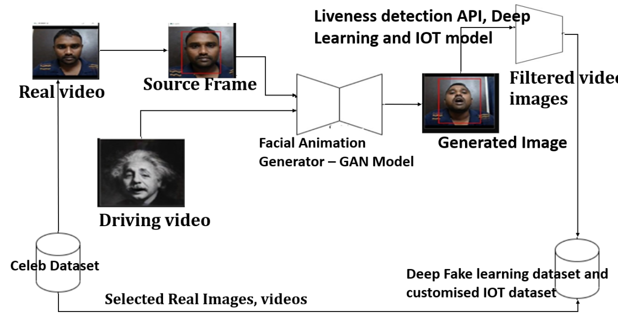

Figure 4: Workflow of Deep Fake creation and detection

4 IMPLEMENTATION

All trained models are then tested on a different subset of the dataset (not the subset used for training). The collected testing data is then used to calculate the accuracy of the models which is used for evaluating the models. The data collected from training and testing the models refers to measurements such as whether the time of training the models on the IoT is reasonable, if merging the model from multiple sources is a good way to train a model at scale and if the results will be affected by the conversion and/or aggregation process.

An IoT based cloud incorporation framework engineering for object location which can oversee input pictures to give results in close to continuous is displayed in Fig 2. It coordinates different equipment and programming parts and permits organized correspondence.

The framework has the accompanying equipment parts:

1. Input Sensors: These incorporate cameras and camcorders that might be joined with the door gadget.
2. Entryway: Different kinds of door gadgets exist which incorporate cell phones, PCs, and tablets.
3. IoT Application Layer: The layer compartments present in private cloud or public cloud play out the calculation task and involve the profound learning models for object location. The cloud hubs might include Single Board Computers (SBCs) like Raspberry Pis. The assignment shipped off the application layer is sent to the Deep learning model compartments.

The proposed software modules of the framework are:

a) Texture Services: They are responsible for carrying out the basic functions of a foundation.
b) Entry/Gateway Interface: It shows the location of the framework prepared gadget at the passage device via the Graphical User Interface (GUI) [17].
c) Deep Learning Module: This module plays out the calculation task and changing info picture over to coming about sectioned and arranged yield picture.

Object discovery calculation in view of DenseNet [18] object identification [18] to accomplish a specific level of exactness while decreasing the boundaries of the model. Involving less boundaries is a huge improvement effectiveness.

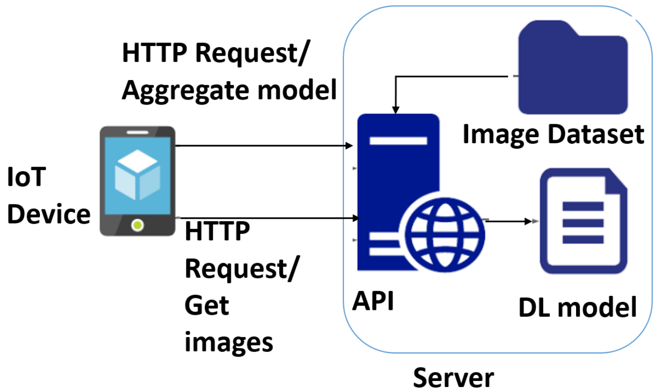

Figure 5: Application online API model

a) Network Topology: To significantly enhance the cloud capabilities of the DL prepared model [19], we have also installed a Virtual Private Network (VPN) which enables us to setup virtual machines in a Cloud Data Center (CDC) and other cloud assets.
b) On-Line API: This interface is built specifically for android gadgets that are used outside. It is the Internet-of-Thing's administration that handles the correspondence of the information picture transmitted by the camera. This assistance sends images to be calculated via HTTP – POST.

5 RESULTS AND DISCUSSION

For challenging samples, we utilize two public live detection APIs. Among them is Tianyan Data. Tianyan Data's API can detect live through an action, such as blinking, yawning, nodding, and opening one's mouth. A specific action must be performed by the input face video while passing the spoofing test to pass detection. The second calculation is based on Baidu's [20] algorithm. With their detector, you can detect live no matter what actions are taken. According to both companies, their spoofing detectors can detect 99% of all malicious activity.

The animation videos which detail all actions are passed on to the APIs to distinguish the samples which are difficult for the live detector to detect. In addition to the 10 specific actions, the Deep fake MNIST+ dataset also includes 10,000 real face videos culled from VoxCeleb1. Several thousand videos are included in each action, and all of them can spoof the APIs. Our video filters use the TianyanData API [21] as well as the Baidu API [22] to filter videos showing blinking, laughing, yawning, and opening mouths.

Two APIs who filter videos of these actions might be the reason for the lower average spoofing rates of blinking, yawning, nodding, and opening mouth actions than others. Furthermore, Tianyan-Data's API requires additional action detections, which reduce the chances of an attack. While yawning and nodding require large angles of head movement, spoofing success rates for these actions are lower than those that do not. There could be a reasonable explanation, such as a single image of the frontal face does not contain enough detail to encompass all the information about the head, such as profile images, resulting in a lower head movement quality. A 71% spoofing rate has been recorded for simile videos. There might be difficulty detecting the spoofing details because the smile action does not cause a significant head movement. Videos with yaw are more likely to be detected, but they have only a 23% success rate. The results are given below in Fig 6 and Fig 7

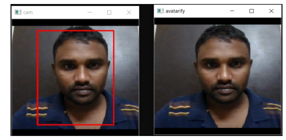

Figure 6: Successfully running the application with the detection of system camera – real image. Data set is accessed and running on the background. Successfully running the Deep Fake application, testing real image and fake image.

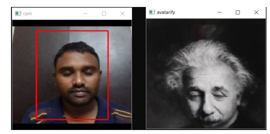

Figure 7: Deep fake image action – left side head rotation, opening mouth, facial expression, showing teeth, closing eyes

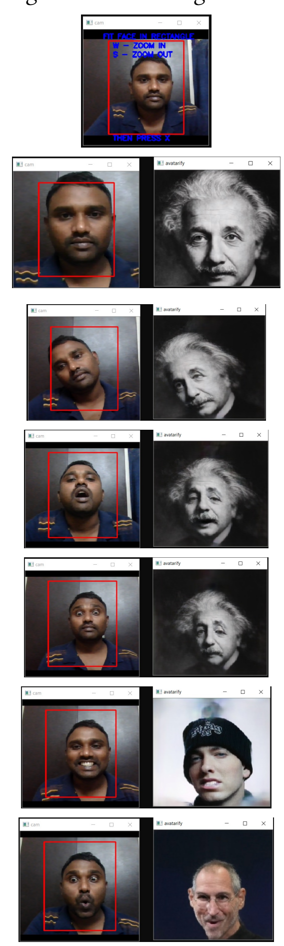

Table 3: Information of existing datasets and their accuracy result comparisons

	Real#	Fake	Types of generation	Action specific	Accuracy
UADFV	48	48	Face swapping	No	85.5%
Celeb-DF	595	5640	Face swapping	No	87.6%
DFDC	48200	104550	Face swapping	No	88%
FF++	1001	4001	Animation and Swap	No	89%
ForgeryNet	91632	121620	Animation and Swap	No	89.5%
Deep Fake MNIST	1001	1001	Image animation type	Yes	90.5%
FFHQ,LSUN,MGIF,VoxCeleb, Taichi, Nemo	50000	50000	Image animation type	Yes	90%
Customized-IoT-based Dataset	100000	100000	Image animation type	Yes	96.5%

The accuracy rates all the executed datasets and Customized IoT based datasets shown in Table 3. It is observed that Customized IoT based dataset gets the more accuracy than the other datasets, as it is having the live detection.

6 CONCLUSION

Using an IoT-Deep Learning algorithm based on the variance of a certain number of frames, we present a method of detecting deep fake videos through the extraction of the rate at which computer vision features change between frames. To solve the problem of avoiding detection methods due to changes in various metrics, the problem of avoiding detection methods wasn't solved as existed in existing deep fake detection methods. The proposed model will be deployed and tested using IoT On-Line API platform service.

A simple GAN with pure transformers is being built for the first time in this study. Our architectures and methods have been carefully designed to ensure the best training results. So, by combining TransGAN's performance across multiple datasets, and scaling it up to higher-resolution generative tasks, we have achieved state-of-the-art performance on various datasets. However, even though TransGAN provides an encouraging starting point, more can be explored, such as moving towards extremely high-resolution generation tasks (e.g., 1024x1024), which would be our next direction.

REFERENCES

[1] Thanh Thi Nguyen, Cuong M. Nguyen, Dung Tien Nguyen, Duc Thanh Nguyen, Saeid Nahavandi, Fellow, IEEE "Deep Learning for Deepfakes Creation and Detection: A Survey".

[2] Xiaofan Zhang, Cong Hao, Yuhong Li, Yao Chen, Jinjun Xiong, Wen-mei Hwu, Deming Chen "A Bi-Directional Co-Design Approach to Enable Deep Learning on IoT Devices".

[3] Ashwin Geet D'Sa and Dr. BG Prasad "An IoT Based Framework For Activity Recognition Using Deep Learning Technique" .

[4] Shreshth Tuli, Nipam Basumatary and Rajkumar Buyya "EdgeLens: Deep Learning based Object Detection in Integrated IoT, Fog and Cloud Computing Environments".

[5] Gautam Raj Mode, Prasad Calyam, Khaza Anuarul Hoque "False Data Injection Attacks in Internet of Things and Deep Learning enabled Predictive Analytics".

[6] Ruben Tolosana, Ruben Vera-Rodriguez, Julian Fierrez, Aythami Morales and Javier Ortega-Garcia "DeepFakes and Beyond: A Survey of Face Manipulation and Fake Detection".

[7] Dogucan Yaman, Fevziye Irem Eyiokur, Hazım Kemal Ekene "EAR2FACE: DEEP BIOMETRIC MODALITY MAPPING".

[8] Aliaksandr Siarohin, Oliver J. Woodford, Jian Ren, Menglei Chai and Sergey Tulyakov "Motion Representations for Articulated Animation".

[9] Quanyu Liao, Yuezun Li, Xin Wang, Bin Kong, Bin Zhu, Siwei Lyu, Youbing Yin, Qi Song, Xi Wu "IMPERCEPTIBLE ADVERSARIAL EXAMPLES FOR FAKE IMAGE DETECTION".

[10] Tuo Zhang, Chaoyang He, Tianhao Ma, Lei Gao, Mark Ma, Salman Avestimeh "FEDERATED LEARNING FOR INTERNET OF THINGS: A FEDERATED LEARNING FRAMEWORK FOR ON-DEVICE ANOMALY DATA DETECTION".

[11] Wadii Boulila, Ayyub Alzahem, Aseel Almoudi "A Deep Learning-based Approach for Real-time Facemask Detection".

[12] Adil Shaik, Uma Vidyadhari Chetlur "Design and implementation of an AI-based Face Recognition model in Docker Container on IoT Platform".

[13] Chaoning Zhang, Philipp Benz, Dawit Mureja Argaw, Seokju Lee, "ResNet or DenseNet? Introducing Dense Shortcuts to ResNet".

[14] Jiajun Huang, Xueyu Wang, Bo Du, Pei Du, Chang Xu "DeepFake MNIST+: A DeepFake Facial Animation Dataset".

[15] Niuniu Zhang, Pan Xu and Zengren Song "Deepfake Detection Method Based on Cross-Domain Fusion".

[16] Alakananda Mitra, Saraju P. Mohanty, Peter Corcoran "EasyDeep: An IoT Friendly Robust Detection Method for GAN Generated Deepfake Images in Social Media".

[17] Mihui Kim, Gihun Lee "Deepfake Detection Using the Rate of Change between Frames Based on Computer Vision".

[18] DFaker. Available at https://github.com/dfaker/df

[19] FakeApp 2.2.0. Available at https://www.malavida.com/en/soft/fakeapp/

[20] DeepFaceLab. Available at https://github.com/iperov/DeepFaceLab

[21] Faceswap-GAN. Available at https://github.com/shaoanlu/faceswapGAN

[22] FaceNet. Available at https://github.com/davidsandberg/facenet.

IoT and Cloud based Face detection application design for Surveillance systems using Deep Learning

Gouri R Patil
Department of IT, Muffakham Jah College of Engg & Tech, Hyderabad, Telangana-500034, India

Srikanth BETHU*
Department of CSE – AIML & IOT, VNRVJIET, Hyderabad, Telangana-500090, IndiaResearch Scholar, Department of CSE, National Institute of Technology, Warangal, Telangana -506004, India

Y.V.K. Durga Bhavani
Department of IT, Vijaya Institute of Technology for Women, Vijayawada, AP-521108, India

B Hari Krishna
Department of CSE, Mallareddy Engineering College, Hyderabad, Telangana-500100, India

Adluri Vijaya Lakshmi
Department of CSE, B V Raju Institute of Technology, Hyderabad, Telangana-502313, India

B Sankarababu
Department of Computer Science and Engineering, GRIET, Hyderabad, Telangana-500090, India

ABSTRACT

Semantic Index, Human Action Detection, and Event Detection are video surveillance packages that assist automate surveillance tasks. Video surveillance structures have entered the generation of virtual surveillance structures in which virtual video is used to traverse the course of different virtual facts. Advances in storage, telecommunications, and facts compression have enabled the increase of more than one technology in virtual surveillance structures. Using more than one video surveillance fashion in risky conditions extends the competencies of rule implementation organizations. In addition, video surveillance enables the form of a motion to carry out in one-of-a-kind conditions. In addition, spotting a particular man or woman in a video is essential for added security, multimedia, and multimedia packages, including offline, seek, and online monitoring of involved humans within the video. The proposed IoT- Cloud based Face detection application is designed to find a person from a huge size dataset and that can generate more accurate results. This application uses Deep Learning methods to find exactness when classifying the images. IoT here is used for liveness detection by comparing all the images present in cloud systems. For results comparison, we used Haar Cascade and DenseNet architectures.

CCS CONCEPTS

• **Computing Methodologies**; • **Modelling and Simulation**; • **Model Development and Analysis**; • **Model verification and Validation**;

*Srikanth Bethu is a Research Scholar in the Department of Computer Science and Engineering at National Institute of Technology, Warangal, Telangana, India. Working as Assistant Professor in the Department of CSE-AIML & IOT in VNRVJIET college, Hyderabad, Telangana, India.

ICCBDC 2022, August 18–20, 2022, Birmingham, United Kingdom

ACM ISBN 978-1-4503-9657-8/22/08…$15.00
https://doi.org/10.1145/3555962.3555971

KEYWORDS

IoT, Surveillance system, Face detection, Person identification

ACM Reference Format:
Gouri R Patil, Srikanth BETHU, Y.V.K. Durga Bhavani, B Hari Krishna, Adluri Vijaya Lakshmi, and B Sankarababu. 2022. IoT and Cloud based Face detection application design for Surveillance systems using Deep Learning. In *2022 6th International Conference on Cloud and Big Data Computing (ICCBDC 2022), August 18–20, 2022, Birmingham, United Kingdom.* ACM, New York, NY, USA, 7 pages. https://doi.org/10.1145/3555962.3555971

1 INTRODUCTION

Face recognition systems have many implementations and applications in various fields and industries such as the Online Face recognition Payment system which can be used for contactless payments for Online shopping and Business. We can reduce the card system and introduce a contactless payment system by integrating facial recognition in shopping malls for ease for customers so, they wouldn't even need to carry cards. Access and Security: In addition to payment confirmation, facial popularity can be linked to physical devices and objects. Instead of using a password, you can access your customer's mobile phone or other electronic devices through the owner's facial features [1]. Innovative face shields should benefit organizations or institutions that want to process sensitive records and tightly control who enters the facility. The use of criminal identification facial recognition to keep unauthorized people away from the facility, it will help them to be firmly planted in the facility.

Object detection and monitoring are widespread in ultra-modern virtual societies, and IoT-enabled devices such as cameras are ubiquitous. Autonomous video surveillance analyses object detection, segmentation, and categorical video sequences for various applications. Therefore, object recognition is essential in the vibrant realm of imaginative and optimistic computer research. In recent years, considerable creative, positive, and profound advances in computer processing have made such object recognition software programs much faster and more accurate, and accurate.

In reaction to the ones increasing the number of state of art and suitable manipulated content material, sizeable efforts are being accomplished through the studies network to layout advanced techniques for face manipulation detection. Traditional faux detection techniques in media forensics [2] were generally primarily based on digital digicam fingerprints (the evaluation of the intrinsic fingerprints delivered through the digital digicam device, each hardware, and software program, together with the optical lens, color clear out array, and interpolation, and compression [3], amongst others) and out digital digicam fingerprints (the evaluation of the outside fingerprints delivered through enhancing software program, together with copy paste or copy pass one-of-a-kind factors of the image, lessen the body fee in a video [4], etc).

1.1 Face manipulation and detection

Facial [5] manipulations can be labeled into four critical corporations regarding the manipulation volume. Entire Face Synthesis - this manipulation [6] creates whole non-existent face images, generally thru powerful GAN, e.g., thru the modern StyleGAN technique. Identity Swap - this manipulation consists of converting one man or woman's face in a video with a few different man or woman's faces. Attribute Manipulation- this manipulation, known as face editing or face retouching, consists of modifying some attributes of the face, including the shadeation of the hair or the skin, the gender, the age, inclusive of glasses, etc. One example of this form of manipulation [6] is the well-known FaceApp molecular application. Expression Swap- this manipulation, known as face reenactment, consists of modifying the man or woman's facial capabilities. In this we reputation on the most well-known techniques, Face2Face and Neural Textures [7], which replaces the facial capabilities of one man or woman in a video with the facial capabilities of a few different man or woman.

1.2 Need of IoT and Cloud systems

Along with the quicker Internet velocity and different endpoints delivered using the 5G, billions of IoT gadgets online might be deployed. However, for the records anomaly detection task, the centralized over the cloud technique will not shape this fashion because of records privateness and extraordinarily excessive communication/garage overhead centralizing records from several IoT gadgets. As such, researchers try to deal with those demanding situations using Deep learning, a trending paradigm that could educate a worldwide or customized version without centralizing records from side gadgets. IoT [8] and IoT Defender appoint Deep Learning for intrusion detection in IoT gadgets by using collaboratively schooling remoted datasets for a worldwide or maybe customized version. Beyond detecting the ordinary records, it even considers an opposed setup wherein numerous malicious individuals poison the federated version.

2 RELATED WORK

Athira Nambiar, Alexandre Bernardino, Jacinto C. Nascimento, "Wholeness-Based Person Reidentification: A Survey," This article outlines the artistic work done in gait assessments for cognitive recognition over the last decade and reviews key steps, datasets, and assessment methods. People's way of walking has a strong relationship with their individuality. Some studies have shown that accurate estimates of observed development plans are available so that two humans and machines can see humans in resources that take advantage of their progress. For surveillance applications, walks are just as fascinating. This is because it does not require the active participation of customers and is difficult to counterfeit. In any case, acquiring an excellent level of a human [9] developmental structure under free circumstances (e.g., individual recognition of positive demands) was ultimately an attempt. Existing advances (camcorders) enjoy the evil effects of context, sunlight, clothing, more items, and multiple assortment changes within a personal look. New 3D sensors open up new possibilities in this area, but at the same time, many research agendas remain unresolved.

Yun Yang and Dapeng Tao, "Reidentification of People-Based on Ensemble Learning Using a Pair of Functional Presentations." In this article, manufacturers introduce a new character reidentification tool with excellent highlighting that conveys a weighted employer's reading. In their technique, they received the RSKISS metric during the adjustment procedure. It retains its strength in dealing with an inadequate set of equipment. First, the RSKISS metric is observed for the four specified highlight areas of the guidance set. At this point, many cells are evaluated, and the importance of the various highlights displayed along with the resources that take advantage of their uniqueness is determined. Ultimately, graduation attempts are achieved by the opportunity to become a member of multiple adjustments obtained from an exceptionally comprehensive presentation through a weighted employer chart. As a non-unique structure, the weighted employer module with extensive usage resources makes it easy to integrate problems. Tests show that our technique is aggressive when probing with some of the best approaches and provides promising character reidentification techniques along One's Traces.

Luca Bondi et al. suggested using the movement CNN [10] to avoid the problem of overfitting the CNN and to increase the movement's popularity. The input data is transcended into separate streams (Spatial and Temporal). RGB video frames were created as input for spatial movement. The stack optical drift received using the TLV1 approach is used as an input for temporal motion. A learning fee of 0.00001 is used for the first 10,000 iterations, followed by a procedure of 0.000001. Stochastic gradient descent is used to build the model. The stream from the CNN [10] is treated as a feature extractor, and the remaining max-pooling layer is used as a vector of functions. Two fusion techniques are used to fuse functions. One is to Use a linear weight fusion approach to characterize the pixels of the spatial and temporal characterization map, where the weights represent importance. Second is Chain fusion transforms all actual ability combinations into a single vector. The national aggregate descriptor (VLAD) and time pyramid pooling (TPP) vectors are used to collect video diploma skills. Classes are mainly achieved based on SVM. The Caffee Toolbox is used to implement CNN [15]. The UCF101 dataset using the linear weighted fusion technique reported 90.5% accuracy, and the HMDB51 dataset using the linear weighted fusion technique reported 63.4% accuracy.

From this, we can conclude that no sincere approach to hobby popularity can be used. However, each step prioritized some algorithms [11] that could be used to detect hobbies. Some necessary steps include how to approach feature extraction and subsequent feature representation. Then use the class of features represented to categorize the activity. In addition, we can see that most IoT-based [12] absolute hobby popularity uses sensor-based absolute hobby popularity, that uses a method of recording video using a static virtual camera and then processing the video using a portable, pocket-sized computer like Raspberry Pi.

3 METHODOLOGY

To develop and deploy the proposed system, we used a facial recognition platform to harness the computing power of IoT and cloud resources. It is a platform for developing and deploying applications in cloud infrastructure. It provides a runtime environment and API that enables the development of .NET applications that leverage public or private cloud computing capabilities. The public cloud may contain virtual machines (VM) provided by cloud service providers such as Azure and Amazon Web Services. The private cloud can contain corporate cloud VMs on the local area network (LAN). The core components of the framework are designed and implemented in a service-oriented way. It provides dynamic provisioning and the ability to dynamically acquire resources and integrate them with existing frameworks and software solutions. Dynamic provisioning is provided in the framework using two primary services: resource provisioning and scheduler service. Overall, as shown in Fig 1.

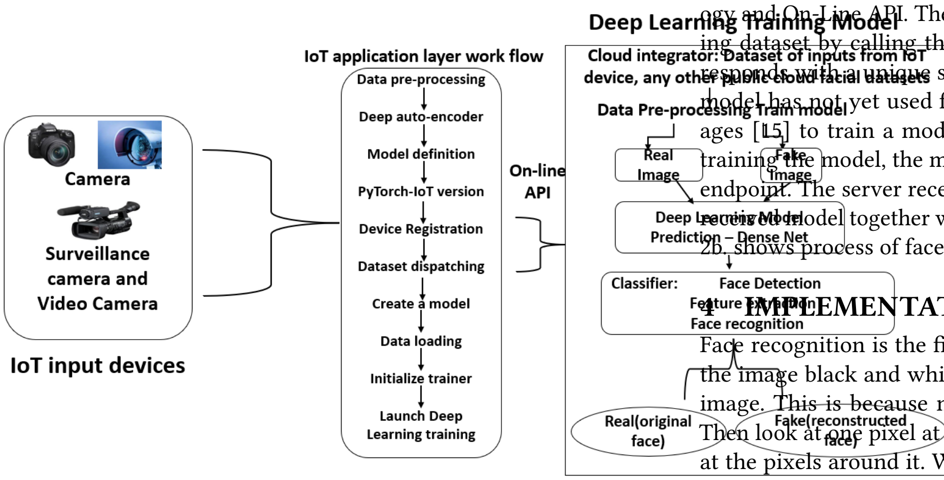

Figure 1: IoT-Cloud Deep Learning Training model for face detection

The procedure is divided into a pre-treatment process and a classification process. The pre-processing process extracts the face image [13] from the frame image [13], extracts the features of computer vision, and then extracts the differences between the frames. The classification process uses DNN to detect face by getting the variance of the specified number of frames from the pre-processed data. It relates to IoT system framework by On-Line API. From Cloud system the data is integrated to create dataset and datasets from any other cloud networks. The data is pre-processed by the Deep Neural Networks and the prediction of the model is trained by the DenseNet.

Face detection [13] is done by the DenseNet by using the image features. The model classifier checks the features of all the images from the trained model datasets. Feature extraction and feature selection done by the Convolutional networks [14] to differentiate the real and fake images. It also creates the latent images of real and fake images. The Face detection is done by creating the latent images and these images are used to make the test. The outcome of test is designed with reconstructed image, that is original image with face animation or without. For object detection [15] we use both Haar Cascade and OpenCV DNN along with DenseNet for classification. Fig 1 shows the Dense net connection along with input and output process.

3.1 Workflow of the training model

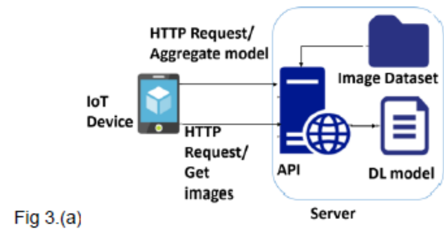

The above Fig 2a. shows the workflow of training model, and it contains Texture Services, Establishment Services, Entry/Gateway Interface, Deep Learning Module, Object detection, Network Topology and On-Line API. The IoT device requests a subset of the training dataset by calling the /GetImages API-endpoint. The server responds with a unique subset of the dataset which the ensemble model has not yet used for training. The IoT device uses the images [15] to train a model locally. Once the device has finished training the model, the model is sent to the Aggregate Model API-endpoint. The server receives the trained model and combines the received model together with the current Deep Learning model. Fig 2b. shows process of face detection.

4 IMPLEMENTATION

Face recognition is the first step in this process [16]. First, make the image black and white to detect a human [16][17] face in an image. This is because no color data is needed to find the face. Then look at one pixel at a time in the image. For each pixel, looks at the pixels around it. When a frame of video is supplied to the system, the system must first determine the faces and the number of faces present in the frame. Next, understand that the system can recognize the identified face, and even if the face is rotating in different directions, it must recognize it as a human face. Face detection is the first important step in face detection and is used to detect faces in images. This is the area of object detection [18] and can be used in a wide range of areas such as security, biometrics, enforcement, rerouting, and personal protection. It is common to find real-time [18] traces of police jobs, people, and things. It is commonly used in cameras to detect multiple phenomena within a frame.

Haar cascade is implemented using OpenCV was, whereas DenseNet is implemented using PyTorch. OpenCV (Open-Source Computer Vision) is one of the largest open-source libraries for operating computer vision, machine learning, image processing [18], and many more. OpenCV is portable because it supports a wide range of programming languages such as C++, Java, etc. It is used for processing images and videos to identify faces and objects and also for the handwriting of a human. When OpenCV

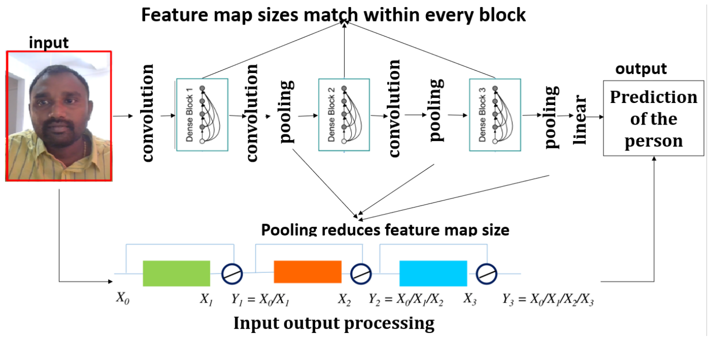

Figure 1: DenseNet model to use for IoT-Cloud Deep Learning Training model for face detection

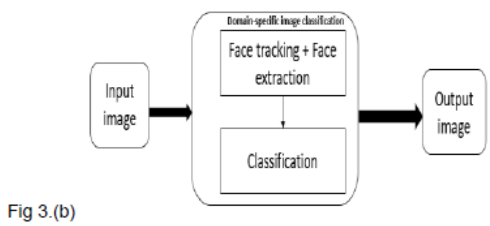

Figure 2: (a) Workflow of Training model and (b) Extraction of output image process face detection

is integrated with another library, like NumPy, which is a highly optimized library for Mathematical operations, the number of advantages increases in your Arsenal, i.e., any operations one can do in NumPy by combining with OpenCV. Face recognition is a library with many modules for dealing with faces in images. It helps in locating the facial features [19] known as facial node points. Install the newest Python3 in your operating system. Check if pip3 and python3 are properly installed or not. Upgrade your pip to avoid errors throughout installation. Enter the subsequent command to put in Face Recognition exploitation pip3.

4.1 Haar Cascade model

There are three types of feature extractors. They are edge features, line features, Four- rectangle features. Haarcascade_frontalface_default.xml is one of the essential classifiers [19] of haar cascade classifier, which is used for face detection [19] and face recognition purpose the working model of the function is to extract the frontal face features of the person such as eyes, nose, lips, and chin at a time and capture the face image for different purpose such as face id unlock, face registration, etc.

In the face recognition system, there are two modes of operation. One is for Verification / Authentication of the face images other one is for Identification purposes. LBPH algorithm [19] is the mixture of the Local Binary Patterns (LBP) and Histograms of Oriented Gradients (HOG) descriptor. There are four valuable parameters in the LBPH algorithm. Radius- It is used for building circular local binary patterns, Neighbors- These are several sample points for building the circular local binary pattern, Grid X- These are the number of cells in the horizontal direction, and Grid Y- These are the number of cells in the vertical direction.

First, the facial image (grayscale) is considered a window of 3x3 pixels. This 3x3 matrix is converted into a Threshold value based on the intensity of pixels. Based on the central value (threshold), we set a Binary Pattern based on the threshold value (Higher or equal threshold = 1, Lower threshold hold = 0). To calculate the distance between two histograms, the formula for calculating confidence using Euclidean distance is given as eq 1.

$$D = \sqrt{\sum_{i=1}^{n} (hist1 - hist2)^2}$$

4.2 DenseNet model

Dense Convolutional Network (DenseNet) connects every layer to all different layers in a feedforward manner. Whereas conventional L-layer convolutional networks [11] have L connections, one among every layer and the layers that comply with it, our community has L(L1) / 2 direct connections. For every layer, the characteristic maps of all preceding layers are used as entering, and people characteristic maps are used to enter all text layers. DenseNet has numerous appealing advantages. It mitigates the vanishing gradient problem, complements characteristic propagation, enables characteristic reuse, and drastically reduces the range of parameters. All pre-educated fashions count on an addition normalized enter photograph. H. A mini-batch of three-channel RGB photos withinside the layout (three x H x W). Here, H and W have to be at the most minor 224. The photograph has to be loaded into the variety [0, 1] after which normalized as follows: mean = [0.481, 0.454, 0.416] and std = [0.226, 0.227, 0.228]. Fig 3 shows PyTorch DenseNet implementation process.

4.3 Dataset preparation

If the videos are in a folder with images, resize them to the same size, for example, 256x256, the videos can be in a .gif, .mp4 or .mp4 folder. Rather than having a single folder with all the frames in '.png' format for each video, we recommend making separate folders for each video. Lossless format offers high-performance i/o. Put the training videos in the train and the testing in the test folders in the folder data/dataset name. A configuration file config/dataset_name.yaml

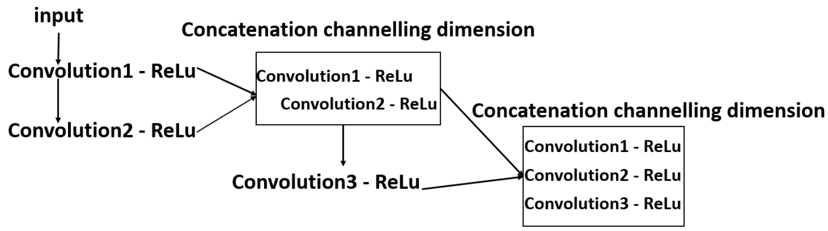

Figure 3: PyTorch DenseNet implementation

Fig 5. (b)

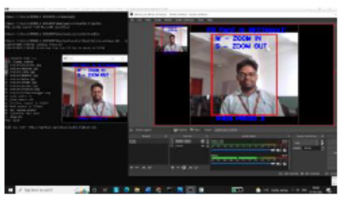

Figure 4: (a). Application running for Capturing image for face detection, (b) face recognized person wearing goggles

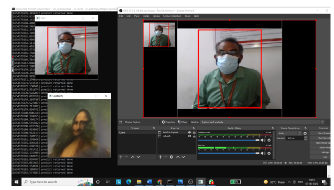

Figure 5: Capturing image in livestreaming and face detection person matching from public cloud dataset, person identification wearing mask and goggles

should be created with dataset_params specifying the root directory. Training parameters should also be adjusted for epochs.

5 RESULTS AND DISCUSSION

To take an input capture a face image from the camera. In particular, you need to capture the face (Phase1) and recognize it while comparing it to the new face (Phase 3) that will be captured in the future. The best and most unusual way to find a face (or another object) is to use a powerful high-density classification object detection method. The rulebook requires many good images (face images) and bad images (faceless images) to teach classifiers and then extracting skills from it.

Data Gathering: After Face detection, multiple Captured face images are stored in a dataset folder with a face id. In phase – I, that is face detection and Gathering in this stage we will run the face detection and data gathering source code which is facedataset.py. The code runs and executes to gives the output screen as shown in the figure Fig 4, so it will ask to enter the user id and press Enter. And then the camera starts to initialize for detecting the face and capturing the face images. As shown in the Fig 4 a new window will pop up for detecting the face and capturing the face images.

Fig 5. (a)

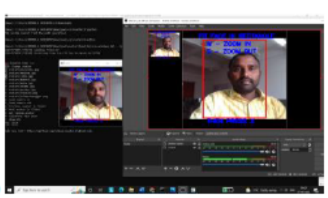

Face data (Grayscale image) with the respective id's will be trained with help of LBPH (Local Binary Pattern Histograms) Face Recognizer, which converts the datasets (face, ids) into "yml" file (store content network connections as a database file. Phase – II: Train the Recognizer / Model using LBPH Algorithm and producing yaml source file. In phase – II, we must consider all the user data from our database with the trainer "PyTorch." This is all done directly with a specific Dense channeling function. The resultant will be a .yml file that contains all the facial node points processed by LBPH (local Binary Patterns and Histograms) algorithm.

When we run the training model file i.e., Facetrain.py, It run and produces the following output as shown in the figure. i.e., Training faces. It will take few seconds. Based on the number of person images captured the model take time to run and produces an output as shown that "faces trained. Exiting Program" with the trainer file which is yml file in "trainer/" directory. Fig 5 shows the application running capturing image into the system using IoT device, the red colored rectangular box indicates the capturing of person face as a object and stored into a database. It also shows the person wearing goggles face capturing from IoT device and stored into system database. Fig 5 shows the capturing multiple face images in live streaming and trying to compare with public cloud datasets. It also shows the person wearing mask capturing the face and trying to match with person in public cloud datasets.

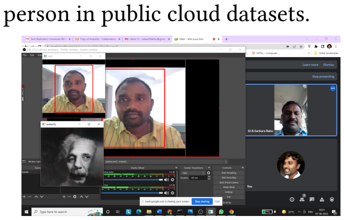

Phase 3 is a testing phase to verify and test the identification process; capture a new face with the camera. If the person has previously captured and trained a face, the cognitive function makes a "prediction" by returning an ID and an index showing how confident the cognitive function is in the match. Finally, faces are detected and recognized by comparing the database for Identification. In Phase – 3, we test for the trained model, this phase is for proper

Table 1: Results Comparison

Model	Dataset	Data type	Action specific	Accuracy
Haar Cascade	UADFV	Face Swapping	No	90.1%
	Celeb-DF	Face Swapping	No	89.8%
	DFDC	Face Swapping	No	90.2%
	FF++	Image animation	No	91%
	UCF101	Image animation	No	90%
DenseNet	FFHQ	Image animation	Yes	95.5%
	VoxCeleb	Image animation	Yes	95.6%
	Taichi	Image animation	Yes	94%
	Nemo	Image animation	Yes	94.5%
	Celeb-DF	Face swapping	No	95%
	FF++	Face swapping	No	95.4%

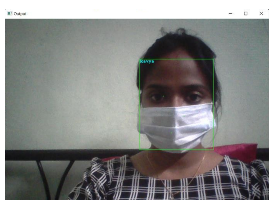

Figure 6: Identification of person in live video displaying with name individually from public cloud dataset with accuracy score, person identification wearing mask and without mask

testing and identification purposes, where we can see the output with the model's name and confidence score, which is the model's accuracy, as shown in the figure. In the figure, the system can recognize the faces of the person based on their facial characteristics. In the outcome, we can see the person's name and their names with the confidence score. The system database is created by using IoT devices during live streaming. When person exposes to IoT devices the system captures face image and stores into system database.

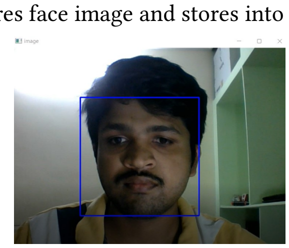

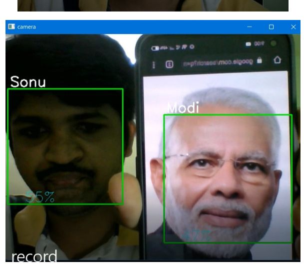

Fig 6 shows the person face is captured when he faces the camera, and his image is store into system database. Now the person identification along with person present in the public datasets is done when they face the system camera. Both system dataset and public cloud datasets are running at a time to identify the persons using their faces. Both the persons are identified with accuracy rate of 95% with their name. The mobile here is taken as a IoT device to display image from cloud datasets while facing the camera. Therefore, the application is expected to recognize the person by comparing the dataset. Which required less time to train the model and has high accuracy in identifying the person. Haar cascades are a classical (non-deep learning) approach that uses hand-engineered features while CNN is a deep learning approach which learns features automatically. Haar cascades are faster at inference, but less accurate while CNNs are slower at inference, but more accurate. Table 1 shows the results comparison for CNN models.

6 CONCLUSION

A reliable, safe, fast, and efficient system has been developed that manually replaces the unreliable system. The system saves time, reduces and reduces administrative work, replaces stationery with electronic devices, and reduces the human resources required for this purpose. The methods and models discussed in Related work can generate only 90% of accuracy whereas models used in this paper are able to generate 95% accuracy. Deep Learning has the capability of producing the up to 100% accuracy when it is integrated with other technologies like IoT and Cloud computing. Here the use of IoT gives the experience of capturing images during live streaming and considered as system database that are used to compare the images with the public cloud datasets at a time to predict the results. The use of DenseNet given the possibility of high-performance results. The idea of designing this application will also help the solving the problem of DeepFake detection of the persons.

REFERENCES

[1] Adjust and Exaggerate Facial Features. Adobe Photoshop, 2016. [Online]. Available: https://helpx.adobe.com/photoshop/how-to/ face-aware-liquify.html.

[2] B. Meden, R. C. Mallı, S. Fabijan, H. K. Ekenel, V. Struc, and P. Peer, "Face Deidentification with Generative Deep Neural Networks," IET Signal Processing, vol. 11, no. 9, pp. 1046–1054, 2017.

[3] Darius Afchar, Vincent Nozick, Junichi Yamagishi, and Isao Echizen. 2018. Mesonet: a compact facial video forgery detection network. In 2018 IEEE International Workshop on Information Forensics and Security (WIFS). IEEE, 1–7.

[4] Eggensperger, K., Lindauer, M., & Hutter, F. (2019). Pitfalls and best practices in algorithm configuration. Journal of Artificial Intelligence Research (JAIR), 64, 861–893.

[5] S. W. Bailey, D. Omens, P. Dilorenzo, and J. F. O'Brien. Fast and deep facial deformations. ACM Transactions on Graphics, 39(4), July 2020.

[6] Chaoning Zhang, ResNet or DenseNet? Introducing Dense Shortcuts to ResNet, WACV 2021, IEEE Explorer.

[7] J. Aggarwal and M. Ryoo, "Human Activity Analysis: A Review," ACM Comput. Surv., vol. 43, no. 3, pp. 16:1–16:43, Apr. 2011. [Online]. Available: http://doi.acm.org/10.1145/1922649.1922653.

[8] Shreshth Tuli, EdgeLens: Deep Learning based Object Detection in Integrated IoT, Fog and Cloud Computing Environments, 2020, IEEE Explorer.

[9] Han, Junwei, Dingwen Zhang, Gong Cheng, Nian Liu, and Dong Xu. "Advanced deep-learning techniques for salient and category-specific object detection: a survey." IEEE Signal Processing Magazine 35, no. 1 (2018): 84-100.

[10] Yeh, C. Y., Chen, H. W., Tsai, S. L., and Wang, S. D. (2020). Disrupting image-translation-based deepfake algorithms with adversarial attacks. In Proceedings of the IEEE Winter Conference on Applications of Computer Vision Workshops (pp. 53-62).

[11] B. Wang, Y. Lei, N. Li, and T. Yan, "Deep separable convolutional network for remaining useful life prediction of machinery," Mechanical Systems and Signal Processing, vol. 134, p. 106330, 2019.

[12] C. Rathgeb, C. I. Satnoianu, N. E. Haryanto, K. Bernardo, and C. Busch, "Differential Detection of Facial Retouching: A MultiBiometric Approach," IEEE Access, vol. 8, pp. 106 373–106 385, 2020

[13] Dzemila Sero, Arslan Zaidi, Jiarui Li, Julie D White, Tomás B González Zarzar, Mary L Marazita, Seth M Weinberg, Paul Suetens, Dirk Vandermeulen, Jennifer K Wagner, *et al.* Facial recognition from DNA using face-to-DNA classifiers. Nature communications, 10(1):2557, 2019.

[14] Shengju Qian, Kwan-Yee Lin, Wayne Wu, Yangxiaokang Liu, Quan Wang, Fumin Shen, Chen Qian, and Ran He. Make a face: Towards arbitrary high fidelity face manipulation. In Proceedings of the IEEE International Conference on Computer Vision, 2019

[15] Sheng-Yu Wang, Oliver Wang, Richard Zhang, Andrew Owens, and Alexei A Efros, "Cnn-generated images are surprisingly easy to spot... for now," in CVPR, 2020.

[16] Khaled Riad, Teng Huang, and Lishan Ke. A dynamic and hierarchical access control for iot in multi-authority cloud storage. Journal of Network and Computer Applications, 160:102633, 04 2020. doi: 10.1016/j.jnca.2020.102633.

[17] A. Smith, "Deepfakes are the most dangerous crime of the future, researchers say." https://www. independent.co.uk/lifestyle/gadgets-and-tech/news/ deepfakes-dangerous-crime-artificial-intelligence-a9655821.html, 2020. [Online; accessed 19-May-2021].

[18] S. Meivel, K.I. Devi, S.U. Maheswari, J.V. Menaka, "Real-time data analysis of face mask detection and social distance measurement using Matlab," Materials Today: Proceedings, 2021.

[19] Luca Bondi, Silvia Lameri, David Guera, Paolo Bestagini, ¨ Edward J. Delp, and Stefano Tubaro. Tampering Detection and Localization through Clustering of Camera-Based CNN Features. In IEEE Computer Vision and Pattern Recognition Workshops, 2017. 3.

Asian Journal of Chemistry; Vol. 34, No. 4 (2022), 1009-1014

ASIAN JOURNAL OF CHEMISTRY

https://doi.org/10.14233/ajchem.2022.23707

Exfoliation of MoS_2-RGO Hybrid 2D Sheets by Supercritical Fluid Process

Murthy Muniyappa[1], Mahesh Shastri[1,2], Manjunath Shetty[3], Vinay Gangaraju[1], Jagadeesh Babu Sriramoju[4], Sindhushree Muralidhar[1], Manikanta P. Narayanaswamy[1], Mudike Ravi[1], Navyarani Marlingaiah[5], Prasanna D. Shivaramu[1], Ananda Kumar C S[1] and Dinesh Rangappa[1,*]

[1]Department of Applied Science (Nanotechnology), PG Centre Bangalore Region, Visvesvaraya Technological University, VIAT, Muddenahalli, Chikkaballapur-562101, India
[2]Department of Electronics & Communication, Nagarjuna College of Engineering & Technology, Devanahalli, Bengaluru-562164, India
[3]Department of Aeronautical and Automobile Engineering, Manipal Institute of Technology, Manipal-576104, India
[4]Department of Physics, Malla Reddy Engineering College, Maisammaguda, Hyderabad-500100, India
[5]Department of Applied Sciences, Dayanand Sagar University, Kumar Swamy Layout, Bengaluru-560111, India

*Corresponding author: E-mail: dineshrangappa@gmail.com; dinesh.rangappa@vtu.ac.in

Received: 3 January 2022; *Accepted*: 19 February 2022; *Published online*: 10 March 2022; AJC-20747

Layered 2D transition metal dichalcogenides (TMD's) have been considered as an important class of materials in the field of energy and environmental applications. Therefore, it is desirable to fabricate 2D hybrid TMD's materials in simple solution processing methods. In this study, MoS_2-RGO hybrid 2D few layered sheets are produced by supercritical fluid process (SCF) by using ethanol as solvent at 250 ºC in a short duration of 0.5 h. Atomic force microscopy (AFM), transmission electron microscope (TEM) and scanning electron microscope (SEM) images confirmed the formation of 2D hybrid few layered sheets. The electrochemical impedance measurement indicates fivefold increase in conductivity of bulk MoS_2. This work presents rapid and one pot exfoliation of MoS_2 and simultaneous reduction of GO that can facilitate the production of 2D hybrid materials.

Keywords: 2D, Transition metal dichalcogenides, RGO, MoS_2, Supercritical fluids.

INTRODUCTION

Metal dichalcogenides are an attractive group of materials, which are being applied in catalysis, hydrogen generation, battery applications, sensors, transistors, solar cells, *etc*. [1-4]. Layered 2D transition metal dichalcogenides (TMD's) have chemical structure in the form of MX_2 where, M denotes transition metal and X denotes chalcogen atom. TMD's consists of layered structures bonded with weak van der Waals forces. However, transition metal and chalcogens are covalently bonded [5-7]. The electronic and optical properties of TMD's mainly depends upon the number of layers and phases [3,8]. Among various TMD's, the MoS_2 is non-toxic, stable and earth abundant material. It offers lot of applications in energy and environmental field such as photocatalysis, electrocatalysis, sensors, electrochemical energy storage and hydrogen generation [5-7,9-11]. Inspite of all these intriguing properties, MoS_2 shows some drawbacks in terms of its electrical and optical properties. Now a days for improving its electrical properties, one of the most trending carbon based 2D material, graphene has been composited with MoS_2 [3,12-16].

The MoS_2 can be synthesized by two approaches namely top down and bottom-up approach. In bottom-up approach, a chemical reaction occurs between salts of Mo and sulfur to form MoS_2 [17-19]. Some of the examples for bottom-up approach are chemical vapour deposition, hydro or solvothermal methods [9,20-22]. In top-down approach bulk materials are chipped in to smaller or thinner sheets by mechanical shearing or micro mechanical cleavage. Ultrasonication and intercalation of Li compounds between the layers of MoS_2 is carried out to separate each layer by suppressing the weak van der Waals forces [23]. Some of the challenges in these methods include high manpower, vacuum or inert atmosphere requirement, low yield, poor quality and time consumption [24-27]. To avoid these drawbacks, one has to look for facile solution based processing for obtaining high quality, large yield in less time consuming techniques.

These aspects require a supercritical fluid process (SCF) process because of its excellent physico-chemical properties. Rangappa *et al.* [28] reported exfoliation of pristine graphite into few layered graphene sheets under SCF process. Recently, Truong *et al.* [29] has studied exfoliation of few layered MoS_2 and MoSe sheets in dimethyl formamide as a supercritical fluid for Mg-ion battery application at 400 ºC for 1 h duration. Thangaswamy & Sathish [30] reported the exfoliation of MoS_2 nano-scrolls in DMF based SCF process for luminescent application. Here, reaction was carried out at temperature 400 ºC for 1 h duration. However, there are no reports on the simultaneous exfoliation and reduction of MoS_2 and GO 2D few layered sheets by SCF at low temperature and short reaction time.

Therefore, it is imperative to concentrate on lower temperature supercritical solvents and short reaction time technique for obtaining hybrid MoS_2-RGO 2D few layered sheets. At supercritical temperature and pressure, solvents exhibit zero surface tension, high wettability, high diffusivity, low viscosity and high solvating power [31]. By inspiring with these fascinating properties, we demonstrate a direct, simple and one step approach for the preparation of hybrid MoS_2-RGO 2D few layered sheets. Electrochemical impedance spectra was carried out to determine the conductivity of the as prepared hybrid MoS_2-RGO 2D few layered sheets.

EXPERIMENTAL

The chemicals *viz.* ethanol, sodium nitrate, graphite powder, potassium permanganate, hydrochloric acid and hydrogen peroxide (100%) were purchased from Merck Chemicals. All the chemicals were used without further purification. Bulk MoS_2 were purchased from SRL Ltd., India and used without any purification.

Crystal structure and phase were identified by using powder X-ray diffractometer (XRD, Rigaku ultima-IV). The range of measurement was from 10º to 70º at 0.02 steps/s using Cu$K\alpha$ as X-ray source. The morphology of the samples were analyzed by using scanning electron microscope (SEM, SU1510) and transmission electron microscopy (JEOL, JEM 2100). The number of layers and surface topography were analyzed using atomic force microscopy (AFM, Park system). An absorbance spectrum was recorded by UV-VIS spectroscope (Perkin-Elmer, Lambda 750). To confirm the layered structure of as synthesized samples, Raman spectroscopy was carried out. Electrochemical impedance spectra were carried out in the range of 0.01-10^6 Hz in OrigaLys electrochemical workstation. All the measurements were made on a standard three-electrode system. The Ag/AgCl was used as a reference electrode, Pt wire was used as counter electrode and FTO coated sample (3 cm × 6 cm) were used as a working electrode with 0.1 M Na_2SO_4 as an electrolyte.

Preparation of graphene oxide (GO): Graphene oxide (GO) was prepared by using modified Hummer's method as reported in the literature [32]. Initially, a mixture of HNO_3 and HCl were taken in a beaker and placed in an ice bath on magnetic stirrer. Graphite powder (1 g) was added in to the above acid mixture followed by addition of 1 g sodium nitrate. After stirring the mixture for 0.5 h, 6 g of $KMnO_4$ was slowly added. It was observed that solution turns into pink colour after stirring vigorously for 1 h. The ice bath was removed and increases the hot plate to 50 ºC. Simultaneously, added 200 mL of deionized water followed by 30% H_2O_2. The formation of light-yellow bubbles confirmed the formation graphene oxide. Then the obtained GO was washed until it reaches to a neutral pH by repeated centrifugation.

Preparation of MoS_2/RGO 2D few layered sheets: In a typical experiment, 40 mg of bulk MoS_2 and 40 mg GO was added to 10 mL ethanol and mixed by magnetic stirrer. After complete dispersion of GO and MoS_2 the mixture was transferred to SCF reactor and placed in tubular furnace at 250 ºC for 0.5 h. Then, obtained black coloured solution was sonicated for 15 min and kept it for 2 min until unexfoliated bulk sheets were settled down. The dispersed black colour solution was washed in deionized water and ethanol to remove any impurities present in the sample. Then samples were dried overnight at 70 ºC. The formation or exfoliation mechanism is shown in **Scheme-I**. At supercritical fluid state, the ethanol displays high diffusivity and excellent wettability, hence it diffuses between the layers of both GO and bulk MoS_2 by overcoming the weak van der Waal's force separate the layers as shown in **Scheme-I**.

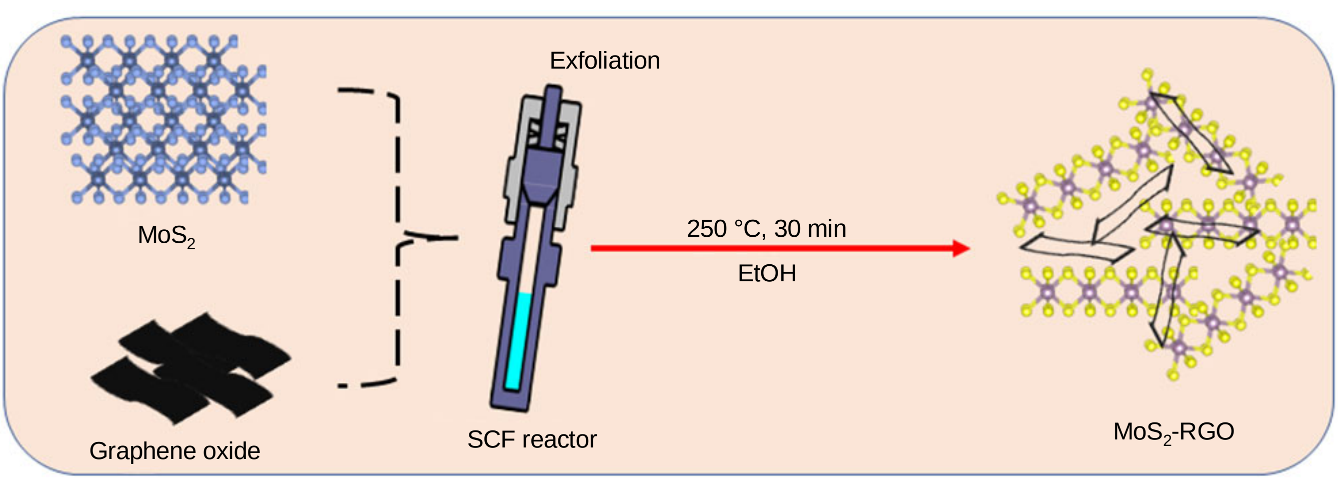

Scheme-I: Schematic of one step simultaneous MoS_2-RGO exfoliation and reduction process leading to hybrid 2D few layered sheets

RESULTS AND DISCUSSION

XRD studies: Formation of graphene oxide (GO) was confirmed by XRD analysis as shown in Fig. 1. The peak at 10.5º indicates successful oxidation of graphite powder into few layered graphene oxide. The crystal structure and phase purity of the obtained MoS_2-RGO hybrid 2D few layered sheets exfoliated by SCF process was confirmed by XRD measurement as shown in Fig. 2. The bulk MoS_2 diffraction were matched to 2H phase MoS_2 with lattice constants a = b = 3.1612 Å and c = 12.2985 Å. The XRD patterns were matching with PDF card no 9007660. The bulk MoS_2 exhibits high intensity peak that corresponds to 2θ values at 14.64º (002), 39.80º (103). Whereas, the SCFs treated MoS_2-RGO shows less intensity peaks (002) at 2θ 14.78º. The reduced intensity confirms the exfoliation of bulk MoS_2 into few layered MoS_2 [30]. The broad peak between 25º to 30º indicates successful reduction of GO into RGO.

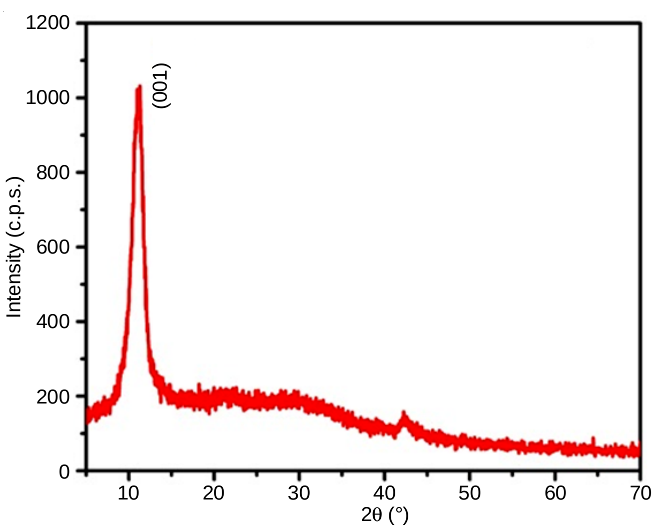

Fig. 1. XRD pattern of GO prepared by modified Hummer's route

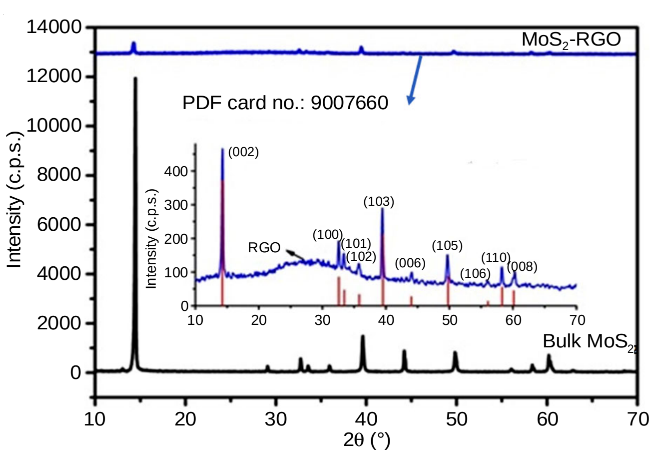

Fig. 2. XRD patterns of bulk MoS_2 and MoS_2-RGO hybrid 2D few layered sheets exfoliated by SCF process

Raman studies: In order to further assure successful exfoliation and formation of MoS_2-RGO few layered sheets, Raman spectroscopy analysis was carried out as shown in Fig. 3. In earlier reports, the vibrations modes E_{2g} (in plane) and A_{1g} (out of plane) for bulk MoS_2 was reported at 383.4 cm^{-1} and 409.1 cm^{-1} [30]. Whereas, after exfoliation the peaks were red shifted from 383.4 cm^{-1} to 381 cm^{-1} indicating successful exfoliation [30]. The decrease in the peak width infers the decreased number of layers. The D and G band peaks at 1353 cm^{-1} and 1593 cm^{-1}, respectively, indicates presence of carbon layers [33]. The ratio of D to G bands is greater than 1 indicates successful reduction of RGO [22]. The D/G ratio for the MoS_2-RGO few layered sheets was found to be 1.17, which indicates the successful reduction of RGO from GO.

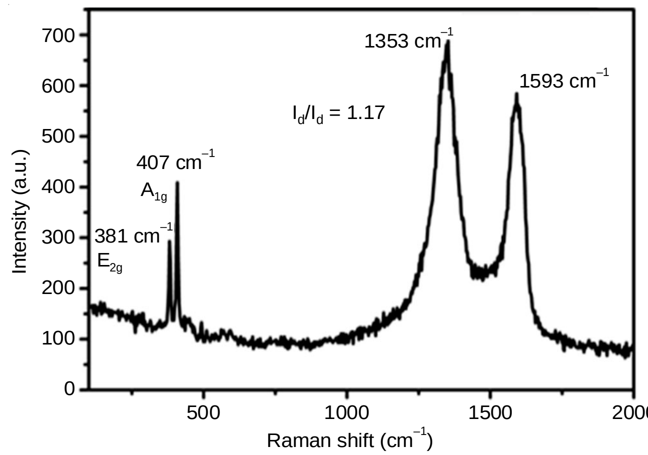

Fig. 3. Raman spectra of MoS_2-RGO hybrid 2D few layered sheets exfoliated by SCF process

SEM studies: Figs. 4a-b show the SEM images of bulk MoS_2 and Figs. 4c-d show exfoliated MoS_2-RGO 2D hybrid sheets. The morp-hology of the bulk MoS_2 powder shows the stacked layers of 5 to 10 µm size. After the SCF ethanol exfoliation, MoS_2 layers were crumbled into few layers of sheets with smaller thickness. The smaller exfoliated MoS_2 sheets were covered by reduced graphene oxide sheets (RGO).

TEM studies: Further, to confirm the exfoliation of bulk MoS_2 into few layered MoS_2 sheets along with reduction of GO to RGO, the TEM analysis has been carried out as shown in Fig. 5. From the TEM images it is very clear that few layers of MoS_2 sheets are present with sizes ranging from 20 to 30 nm. The MoS_2 layers were covered by transparent very thin layers of RGO, which is consistent with SEM analysis. Hence, formation of MoS_2-RGO 2D hybrid sheets under supercritical fluid process is confirmed.

AFM studies: Fig. 6 represents atomic force microscopy images and its corresponding line profile of the produced MoS_2-RGO 2D hybrid sheets. The presence of smaller sized sheets was confirmed in the AFM image. The line profiles of the sheets were found to be 16 nm. Around 20 to 25 single layers of MoS_2-RGO sheets piled to up to form 16 nm height of thesample by considering the thickness of MoS_2 is 0.65 nm and single layer reduced graphene oxide thickness is 0.35 nm. In AFM image, a presence of few bigger sized sheets was observed, which arises due to aggregation or stacking of sheets one above the other during the sample preparation therefore, excluded for line profile measurement.

UV-visible studies: Fig. 7 shows the UV-vis absorbance spectra of MoS_2-RGO 2D nanosheets prepared by SCF process.

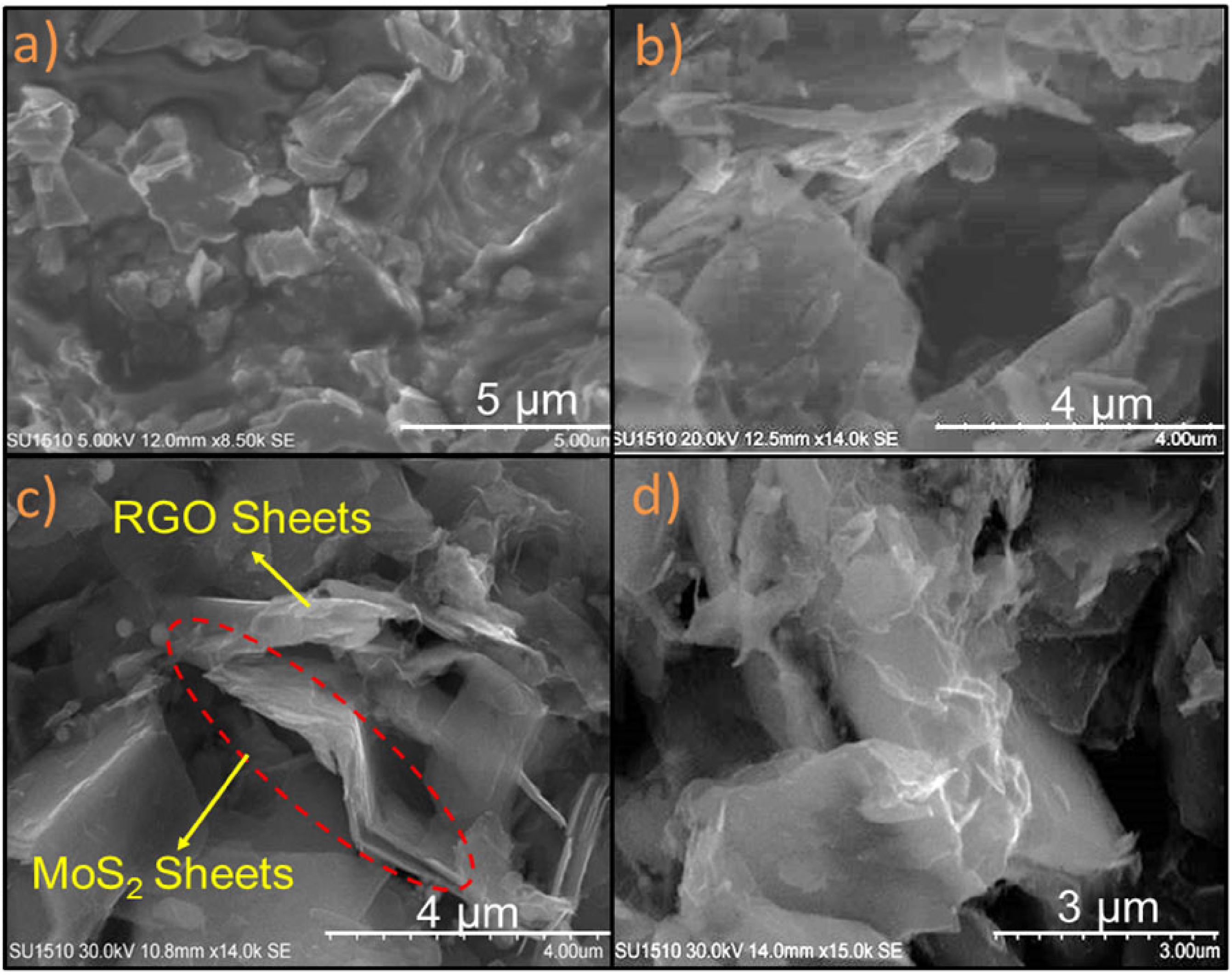

Fig. 4. SEM images of (a-b) bulk MoS_2, (c-d) MoS_2-RGO hybrid 2D few layered sheets exfoliated under SCF process

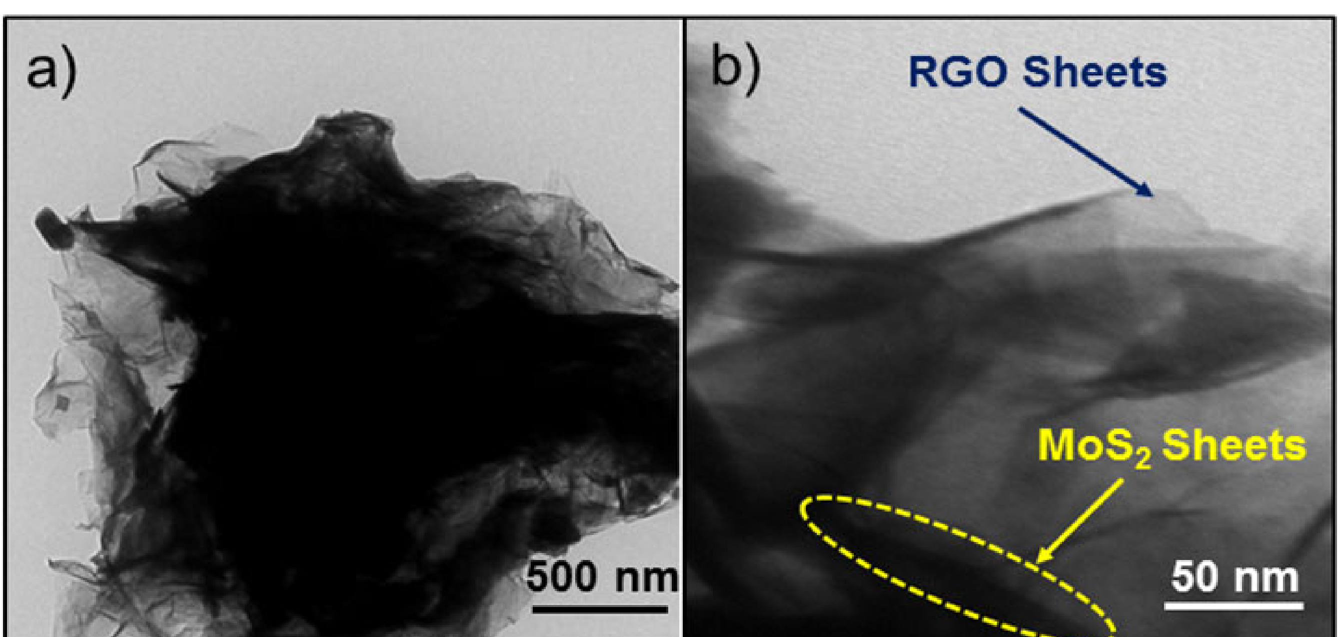

Fig. 5. TEM images of (a-b) MoS_2-RGO hybrid 2D few layered sheets exfoliated under SCF process

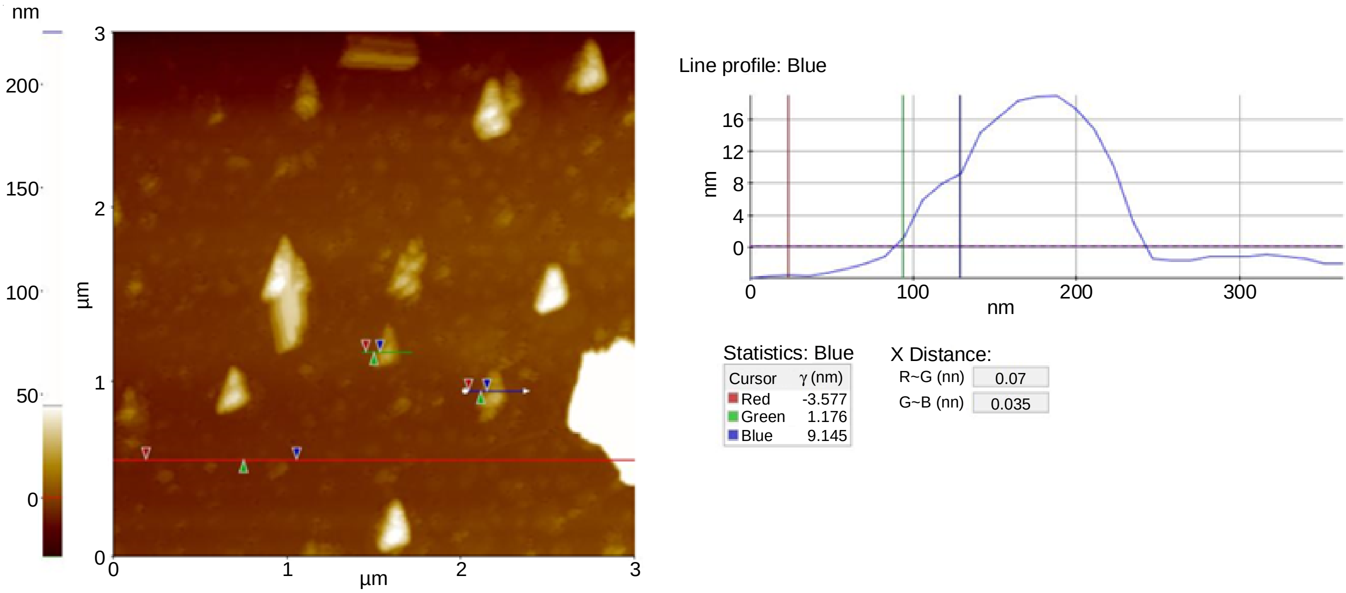

Fig. 6. AFM Image and corresponding line profile of MoS_2-RGO hybrid 2D few layered sheets exfoliation by SCF process

According to previous reports the peak at 328 nm indicates presence of MoS_2 and peak at 280 nm indicates presence of RGO, which confirms the successful reduction of GO into RGO [30,32]. Probably, the two peaks were submerged in to a single peak, which indicates the successful exfoliation of MoS_2-RGO 2D sheets.

Electrochemical studies: Fig. 8 represents electrochemical impedance spectra of bulk MoS_2 and MoS_2-RGO hybrid 2D few layered sheets exfoliated by SCF process. In the impedance plot, the semicircle represents the charge transfer resistance. In the plot of bulk MoS_2, the arc was found to be around 300 ohms, whereas in MoS_2-RGO hybrid 2D few layered sheets it decreased to 65 ohms. Approximately, five folds of charge transfer resistance was decreased after loading with RGO. Therefore, inclusion of RGO in MoS_2-RGO hybrid 2D few layered sheets improves the conductivity of the hybrid 2D sheets, which is useful in the applications where, charge transfer or conductivity plays a crucial role.

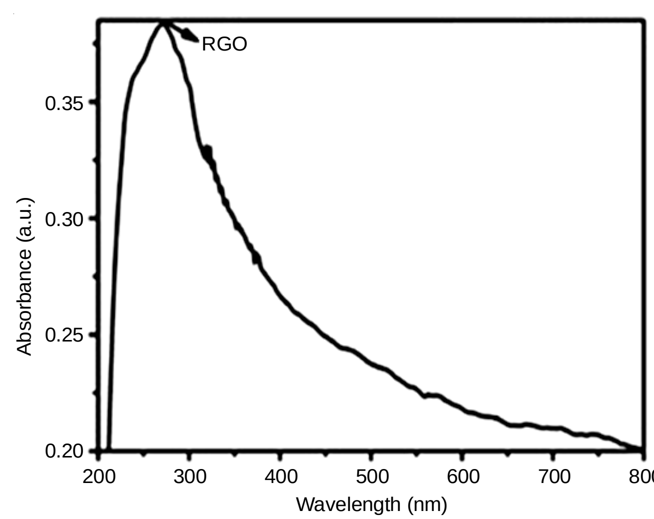

Fig. 7. UV-Vis spectroscopy of MoS_2-RGO hybrid 2D few layered sheets exfoliation by SCF process

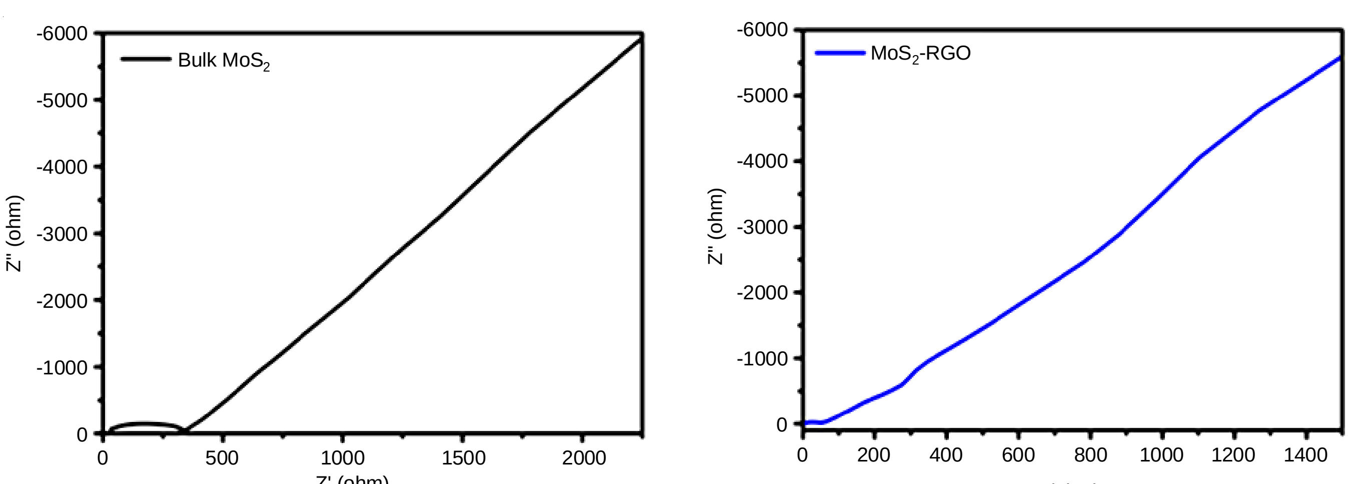

Fig. 8. Impedance spectra of bulk MoS_2 and MoS_2-RGO hybrid 2D few layered sheets exfoliated by SCF process

Conclusion

A direct, simple and one step supercritical fluid process (SCF) process was demonstrated for the preparation of hybrid MoS_2-RGO 2D few layered sheets. This process offers low temperature and short reaction time for simultaneous exfoliation and reduction of hybrid MoS_2-RGO 2D few layered sheets. Formation of few layered MoS_2 and reduction of GO was confirmed XRD, TEM and AFM analysis. The addition of RGO in to MoS_2 increases five folds conductivity of bulk MoS_2 which, opens up scope for many applications in the field of energy and environment.

CONFLICT OF INTEREST

The authors declare that there is no conflict of interests regarding the publication of this article.

REFERENCES

1. M. Chhowalla, H.S. Shin, G. Eda, L.J. Li, K.P. Loh and H. Zhang, *Nat. Chem.*, **5**, 263 (2013); https://doi.org/10.1038/nchem.1589
2. A.K. Geim and I.V. Grigorieva, *Nature*, **499**, 419 (2013); https://doi.org/10.1038/nature12385
3. D. Jariwala, V.K. Sangwan, L.J. Lauhon, T.J. Marks and M.C. Hersam, *ACS Nano*, **8**, 1102 (2014); https://doi.org/10.1021/nn500064s
4. Q.H. Wang, K. Kalantar-Zadeh, A. Kis, J.N. Coleman and M.S. Strano, *Nat. Nanotechnol.*, **7**, 699 (2012); https://doi.org/10.1038/nnano.2012.193
5. H. Li, Z. Yin, Q. He, H. Li, X. Huang, G. Lu, D.W.H. Fam, A.I.Y. Tok, Q. Zhang and H. Zhang, *Small*, **8**, 63 (2012); https://doi.org/10.1002/smll.201101016
6. L. Cao, Y. Yu, S. Huang and W. Yang, Layer-dependent Electrocatalysis of MoS_2 for Hydrogen Evolution Layer-Dependent Electrocatalysis of MoS_2 for Hydrogen Evolution, Department of Materials Science and Engineering, North Carolina State University, Raleigh NC (2014).
7. S. Bertolazzi, J. Brivio and A. Kis, *ACS Nano*, **5**, 9703 (2011); https://doi.org/10.1021/nn203879f
8. K.F. Mak, C. Lee, J. Hone, J. Shan and T.F. Heinz, *Phys. Rev. Lett.*, **105**, 136805 (2010); https://doi.org/10.1103/PhysRevLett.105.136805
9. C. Lee, H. Yan, L.E. Brus, T.F. Heinz, J. Hone and S. Ryu, *ACS Nano*, **4**, 2695 (2010); https://doi.org/10.1021/nn1003937
10. L. Wei, Y. Chen, Y. Lin, H. Wu, R. Yuan and Z. Li, *Appl. Catal. B*, **144**, 521 (2014); https://doi.org/10.1016/j.apcatb.2013.07.064
11. A. Sobczynski, *J. Catal.*, **131**, 156 (1991); https://doi.org/10.1016/0021-9517(91)90332-X
12. H. Wang, H. Feng and J. Li, *Small*, **10**, 2165 (2014); https://doi.org/10.1002/smll.201303711
13. X. Wang, Z. Zhang, Y. Chen, Y. Qu, Y. Lai and J. Li, *J. Alloys Compd.*, **600**, 84 (2014); https://doi.org/10.1016/j.jallcom.2014.02.127
14. H.Y. Chang, S. Yang, J. Lee, L. Tao, W.S. Hwang, D. Jena, N. Lu and D. Akinwande, *ACS Nano*, **7**, 5446 (2013); https://doi.org/10.1021/nn401429w
15. Q. He, Z. Zeng, Z. Yin, H. Li, S. Wu, X. Huang and H. Zhang, *Small*, **8**, 2994 (2012); https://doi.org/10.1002/smll.201201224
16. M. Latorre-Sánchez, I. Esteve-Adell, A. Primo and H. García, *Carbon*, **81**, 587 (2015); https://doi.org/10.1016/j.carbon.2014.09.093
17. W. Zhou, X. Zou, S. Najmaei, Z. Liu, Y. Shi, J. Kong, J. Lou, P.M. Ajayan, B.I. Yakobson and J.-C. Idrobo, *Nano Lett.*, **13**, 2615 (2013); https://doi.org/10.1021/nl4007479
18. A.M. Van Der Zande, P.Y. Huang, D.A. Chenet, T.C. Berkelbach, Y. You, G.H. Lee, T.F. Heinz, D.R. Reichman, D.A. Muller and J.C. Hone, *Nat. Mater.*, **12**, 554 (2013); https://doi.org/10.1038/nmat3633
19. J.D. Tobias, *Anesthesiology*, **96**, 1522 (2002); https://doi.org/10.1097/00000542-200206000-00039
20. H. Li, J. Wu, Z. Yin and H. Zhang, *Acc. Chem. Res.*, **47**, 1067 (2014); https://doi.org/10.1021/ar4002312
21. O. Lopez-Sanchez, D. Lembke, M. Kayci, A. Radenovic and A. Kis, *Nat. Nanotechnol.*, **8**, 497 (2013); https://doi.org/10.1038/nnano.2013.100
22. A. Winchester, S. Ghosh, S. Feng, A.L. Elias, T. Mallouk, M. Terrones and S. Talapatra, *ACS Appl. Mater. Interfaces*, **6**, 2125 (2014); https://doi.org/10.1021/am4051316
23. Z. Zeng, Z. Yin, X. Huang, H. Li, Q. He, G. Lu, F. Boey and H. Zhang, *Angew. Chem. Int. Ed.*, **50**, 11093 (2011); https://doi.org/10.1002/anie.201106004
24. G.S. Bang, K.W. Nam, J.Y. Kim, J. Shin, J.W. Choi and S. Choi, *ACS Appl. Mater. Interfaces*, **6**, 7084 (2014); https://doi.org/10.1021/am4060222
25. J.N. Coleman, M. Lotya, A. O'Neill, S.D. Bergin, P.J. King, U. Khan, K. Young, A. Gaucher, S. De, R.J. Smith, I.V. Shvets, S.K. Arora, G. Stanton, H.-Y. Kim, K. Lee, G.T. Kim, G.S. Duesberg, T. Hallam, J.J. Boland, J.J. Wang, J.F. Donegan, J.C. Grunlan, G. Moriarty, A. Shmeliov, R.J. Nicholls, J.M. Perkins, E.M. Grieveson, K. Theuwissen, D.W. McComb, P.D. Nellist and V. Nicolosi, *Science*, **331**, 568 (2011); https://doi.org/10.1126/science.1194975
26. K.R. Paton, E. Varrla, C. Backes, R.J. Smith, U. Khan, A. O'Neill, C. Boland, M. Lotya, O.M. Istrate, P. King, T. Higgins, S. Barwich, P. May, P. Puczkarski, I. Ahmed, M. Moebius, H. Pettersson, E. Long, J. Coelho, S.E. O'Brien, E.K. McGuire, B.M. Sanchez, G.S. Duesberg, N. McEvoy, T.J. Pennycook, C. Downing, A. Crossley, V. Nicolosi and J.N. Coleman, *Nat. Mater.*, **13**, 624 (2014); https://doi.org/10.1038/nmat3944
27. A. Shmeliov, M. Shannon, P. Wang, J.S. Kim, E. Okunishi, P.D. Nellist, K. Dolui, S. Sanvito and V. Nicolosi, *ACS Nano*, **8**, 3690 (2014); https://doi.org/10.1021/nn5003387
28. D. Rangappa, K. Sone, M. Wang, U.K. Gautam, D. Golberg, H. Itoh, M. Ichihara and I. Honma, *Chem. Eur. J.*, **16**, 6488 (2010); https://doi.org/10.1002/chem.201000199
29. Q.D. Truong, M. Kempaiah Devaraju, Y. Nakayasu, N. Tamura, Y. Sasaki, T. Tomai and I. Honma, *ACS Omega*, **2**, 2360 (2017); https://doi.org/10.1021/acsomega.7b00379
30. P. Thangasamy and M. Sathish, *J. Mater. Chem. C Mater. Opt. Electron. Devices*, **4**, 1165 (2016); https://doi.org/10.1039/C5TC03630E
31. K. Chang and W. Chen, *Chem. Commun.*, **47**, 4252 (2011); https://doi.org/10.1039/c1cc10631g
32. M.N. Rani, M. Murthy, N.S. Shree, S. Ananda, S. Yogesh and R. Dinesh, *Ceram. Int.*, **45**, 25020 (2019); https://doi.org/10.1016/j.ceramint.2019.04.195
33. Y. Zhan, Z. Liu, S. Najmaei, P.M. Ajayan and J. Lou, *Small*, **8**, 966 (2012); https://doi.org/10.1002/smll.201102654

RADIATION, RADIATION ABSORPTION, CHEMICAL REACTION AND HALL EFFECTS ON UNSTEADY FLOW PAST AN ISOTHERMAL VERTICAL PLATE IN A ROTATING FLUID WITH VARIABLE MASS DIFFUSION WITH HEAT SOURCE

D. Chenna Kesavaiah[1], P. Govinda Chowdary[2], G. Rami Reddy[3], Dr. Nookala Venu[4]

[1, 2]Department of Basic Sciences & Humanities, Vignan Institute of Technology and Science, Deshmukhi (V), Pochampally (M), Yadadri-Bhuvanagiri (Dist), TS-508284, India
Email: chennakesavaiah@gmail.com & Email: chowdary.ratp@gmail.com

[3]Department of Mathematics, Malla Reddy Engineering College (Autonomous), Dulapally (V), Kompally (M), Medchal Malkajgiri (Dist), TS-500100, India

[4]Department of Electronics and Communication Engineering,
Balaji Institute of Technology and Science (Autonomous), Narsampet, Warangal, TS -506331, India
Email: venunookala@gmail.com

Abstract

The main objective of this paper is the unsteady MHD free convection heat and mass transfer for a heat generation/absorption with radiation absorption in the presence of a reacting species over an isothermal vertical plate has received little attention. Hence the main objective of this paper is to investigate the effects of thermal radiation, chemical reaction, heat source of an electrically conducting fluid past an isothermal vertical porous plate subjected to variable suction. The mathematical model, derived from the Navier-Strokes equation was reduced to a system of coupled partial differential equation for velocity, temperature and concentration using Boussinesq's approximation. The dimensionless governing equations are tackled using the usual perturbation technique. Also, the effects of velocity, temperature and concentration fields were intercepted for various physical parameters with the help of graphs.

Keywords: Radiation, Chemical reaction, Radiation absorption, Isothermal plate, Heat and Mass transfer

DOI Number: 10.14704/nq.2022.20.11.NQ66077 **NeuroQuantology 2022; 20(11): 800-815**

INTRODUCTION

Convection flows in porous media has gained significant attention in recent years because of their importance in engineering applications such as geothermal systems, solid matrix heat exchangers, thermal insulations, oil extraction and store of nuclear waste materials. These can also be applied to underground coal gasification, ground water hydrology, wall cooled catalytic reactors, energy efficient drying processes and natural convection in earth's crust. In view of the above (Pop and Watanabe, 1994) explained in detailed hall effects on magnetohydrodynamic free convection about a semi infinite vertical flat plate, (Chenna Kesavaiah et. al, 2021) expressed Radiative MHD Walter's Liquid-B flow past a semi-infinite vertical plate in the presence of viscous dissipation with a heat source, (Vajravelu and Hadjinicolaou, 1997) illustrated the convective heat transfer in an electrically conducting fluid at a stretching surface with uniform free stream, (Rami Reddy et. al, 2021): Hall effect on MHD flow of a viscoelastic fluid through porous medium over an infinite vertical porous plate with heat source, (Chenna Kesavaiah and Venkateswarlu, 2020) has been considered chemical reaction and radiation absorption effects on convective flows past a porous vertical wavy channel with travelling thermal waves, (Mallikarjuna Reddy et. al, 2019) studied the radiation and diffusion thermo effects of viscoelastic fluid past a porous surface in the presence of magnetic field and chemical reaction with heat source, (Srinathuni Lavanya and Chenna Kesavaiah, 2017) motivated study on heat transfer to MHD free convection flow of a viscoelastic dusty gas through a porous medium with chemical reaction, (Abel et. al, 2001): Convective heat and mass transfer in a viscoelastic fluid flow through a porous medium over a stretching sheet. (Mallikarjuna Reddy et. al, 2018) observed that the effects of radiation and thermal diffusion on MHD heat transfer flow of a dusty viscoelastic fluid between two moving parallel plates, (Salem and Abd El-Aziz, 2008) the effect of Hall currents and chemical reaction on hydromagnetic flow of a stretching vertical surface with internal heat generation/absorption, (Chenna Kesavaiah and Sudhakaraiah, 2014) studied the effects of heat and mass flux to MHD flow in vertical surface with radiation absorption,

Convective flows with simultaneous heat and mass transfer under the influence of a magnetic field and chemical reaction arise in many transport processes both naturally and artificially in many branches of science and engineering applications. This phenomenon plays an important role in the chemical industry, power and cooling industry for drying, chemical vapour deposition on surfaces, cooling of nuclear reactors and petroleum industries. Natural convection flow occurs frequently in nature. It occurs due to temperature differences, as well as due to concentration differences or the combination of these two, for example in atmospheric flows, there exists differences in water concentration and hence the flow is influenced by such concentration difference. Some of the authors considered (Rajaiah et. al, 2015) has been studied chemical and Soret effect on MHD free convective flow past an accelerated vertical plate in presence of inclined magnetic field through porous medium, (Chamkha and Khaled, 2000) extended the work on similarity solutions for hydromagnetic mixed convection heat and mass transfer for Hiemenz flow through a porous medium, (Chenna Kesavaiah et. al, 2013) viewed the natural convection heat transfer oscillatory flow of an elastico-viscous fluid from vertical plate, (Chenna Kesavaiah and Satyanarayana, 2013) explained on MHD and Diffusion Thermo effects on flow accelerated vertical plate with chemical reaction, (Nield and Bejan, 1999) given detailed information on convection in porous media, (Chenna Kesavaiah et. al, 2013) illustrated the radiation and Thermo - Diffusion effects on mixed convective heat and mass transfer flow of a viscous dissipated fluid over a vertical surface in the presence of chemical reaction with heat source, (Ibrahim et. al, 2008) the study on effect of the chemical reaction and radiation absorption on the unsteady MHD free convection flow past a semi infinite vertical permeable moving plate with heat source and suction, (Karunakar Reddy et. al, 2013) abstracted on MHD heat and mass transfer flow of a viscoelastic fluid past an impulsively started infinite vertical plate with chemical reaction, (Stanford Shateyi and Sandile Motsa, 2011) expressed the detailed information on the effect of unsteady magnetohydrodynamic convective heat and mass transfer past an infinite vertical plate in a porous medium with thermal radiation, heat generation/absorption and chemical reaction, (Ch Kesavaiah et. al, 2013) effectively studied the effects of radiation and free convection currents on unsteady Couette flow between two vertical parallel plates with constant heat flux and heat source through porous medium,

When technological processes take place at higher temperatures thermal radiation heat transfer has become very important and its effects cannot be neglected. The effect of radiation on MHD flow, heat and mass transfer become more important industrially. Many processes in engineering areas occur at high temperature and knowledge of radiation heat transfer becomes a very important for the design of the pertinent equipment. The quality of the final product depends to a great extent on the heat controlling factors, and the knowledge of radiative heat transfer in the system can lead to a desired product with sought qualities. (Rajaiah and Sudhakaraiah, 2015) expressed on unsteady MHD free convection flow past an accelerated vertical plate with chemical reaction and Ohmic heating, (Ch Kesavaiah et. al, 2012) illustrated on the radiation and mass transfer effects on moving vertical plate with variable temperature and viscous dissipation, (Ibrahim et. al, 2008) motivated study on the effect of chemical reaction and radiation absorption on the unsteady MHD free convection flow past a semi infinite vertical permeable moving plate with heat source and suction, (Satyanarayana et. al, 2011): Viscous dissipation and thermal radiation effects on an unsteady MHD convection flow past a semi-infinite vertical permeable moving porous plate, (Mohamed, 2009) has been considered Double-Diffusive convection radiation interaction on unsteady MHD flow over a vertical moving porous plate with heat generation and Soret effects, (Ch Kesavaiah et. al, 2011) expressed the effects of the chemical reaction and radiation absorption on an unsteady MHD convective heat and mass transfer flow past a semi-infinite vertical permeable moving plate embedded in a porous medium with heat source and suction, (Haranth and Sudhakaraiah, 2015) motivated study on viscosity and Soret effects on unsteady hydromagnetic gas flow along an inclined plane, (Chenna Kesavaiah, 2021) has been considered the MHD effect on convective flow of dusty viscous fluid with fraction in a porous medium and heat generation, (Ali, 2007): The effect of lateral mass flux on the natural convection boundary layers induced by a heated vertical plate embedded in a saturated porous medium with internal heat generation, (Cussler, 1988): Diffusion mass transfer in fluid systems, (Das et. al, 1994) illustrated the effects of mass transfer on flow past an impulsively started infinite vertical plate with constant heat flux and chemical reaction, (Anjalidevi and Kandasamy, 1999) the effects of chemical reaction, heat and mass transfer on laminar flow along a semi infinite horizontal plate, (Seddeek, 2007) motivated study on the effects of chemical reaction and variable viscosity on hydromagnetic mixed convection heat and mass transfer for Hiemenz flow through porous media with radiation,

The study of heat generation or absorption in moving fluids is important in problems dealing with chemical reactions and those concerned with dissociating fluids. Heat generation effects may alter the temperature distribution and this in turn can affect the particle deposition rate in nuclear reactors, electronic chips and semi conductor wafers. Although exact modelling of internal heat generation or absorption is quite difficult, some simple mathematical models can be used to express its general behaviour for most physical situations. Heat generation or absorption can be assumed to be constant, space-dependent or temperature-dependent. (Cortell, 2008) observed the effects of viscous dissipation and

radiation on the thermal boundary layer over a nonlinearly stretching sheet,

R C Bataller (2008): Radiation effects for the Blasius and Sakiadis flows with a convective surface boundary condition. *Appl. Math. Comput.,* Vol. 206, pp. 832-840

V Aliakbar, A Alizadeh-Pahlavan and K Sadeghy (2009): The influence of thermal radiation on MHD flow of Maxwellian fluids above stretching sheets, *Commun. Nonlinear Sci. Numer. Simulat., Vol.* 14 (3), pp. 779-794

G S Seth, G K Mahato, S Sarkar and M S Ansari (2012): Effects of Hall current on hydromagnetic natural convection flow of a heat absorbing fluid past an impulsively moving vertical plate with ramped temperature, *Int. J. Appl. Math. Res.,* Vol. 1, pp. 462–486

S Das, B C Sarkar and R N Jana (2013): Hall effect on MHD free convection boundary layer flow past a vertical flat plate, *Meccanica*, Vol. 48, pp. 1387–1398

B C Sarkar, S Das and R N Jana (2013): Hall Effects on Unsteady MHD Free convective flow past an accelerated moving vertical plate with viscous and Joule dissipations, *Int. J. Comp. Appl*., Vol. 70, pp. 19–28

P Muthucumarswamy and L Jyanthi (2014): Hall Effects on MHD Flow past an infinite vertical plate in the presence of rotating fluid of variable temperature and uniform mass diffusion with first order chemical reaction, *International Journal of Applied Engineering Research,* Vol. 9(24), pp. 26259–26271

J C Crepeau and R Clarksean (1997): Similarity solutions of natural convection with internal heat generation, *J. Heat Transfer,* Vol. 119, pp. 183-185

P M Patil and P S Kulkarni (2008): Effects of chemical reaction on free convective flow of a polar fluid through a porous medium in the presence of internal heat generation. *International Journal of Thermal Sciences,* Vol. 47, pp. 1043-1054

M A Salem and M Abd El-Aziz (2008): Effect of Hall currents and chemical reaction on hydromagnetic flow of a stretching vertical surface with internal heat generation/absorption, *Applied Mathematical Modelling, Vol.* 32, pp. 1236-1254

M A Samad and M Mohebujjaman (2009): MHD Heat and mass transfer Free convection flow among a vertical stretching sheet in presence of magnetic field with heat generation. *Research Journal of Applied Science, Engineering and Technology,* Vol. 1(3), pp. 98-106

R Muthucumaraswamy, A Prema and K Muthuracku (2015): Hall Effect on MHD flow past an exponentially accelerated isothermal vertical plate with variable Mass diffusion in the presence of rotating fluid, annals of faculty engineering Hunedoara, *International Journal of Engineering,* Vol. 13(5), pp. 229–236

V D Kumaar, R Muthucumaraswamy and L Manjula (2020): Hall effect unsteady flow past an isothermal vertical plate in a rotating fluid with variable mass diffusion in the presence of chemical reaction of first order, *Advances in Mathematics: Scientific Journal,* Vol. 9 (5), pp. 2749–2759

In spite of all the previous studies, the unsteady MHD free convection heat and mass transfer for a heat generation/absorption with radiation absorption in the presence of a reacting species over an infinite permeable plate has received little attention. Hence the main objective of this paper is to investigate the effects of thermal radiation, chemical reaction, heat source of an electrically conducting fluid past an infinite vertical porous plate subjected to variable suction. The mathematical model, derived from the Navier-Strokes equation was reduced to a system of coupled partial differential equation for velocity, temperature and concentration using Boussinesq's approximation. The dimensionless governing equations are tackled using the usual perturbation technique. Also, the effect of velocity, temperature and concentration fields were intercepted for various physical parameters like Hall parameter, Hartmann number, thermal Grashof number, mass Grashof number, Schmidt number, chemical reaction parameter and rotation parameter.

MATHEMATICAL FORMULATION

An unsteady hydromagnetic flow of fluid past an infinite isothermal vertical plate with varying mass diffusion exists. The fluid and the plate rotate in unison with a uniform angular velocity Ω' about the $z'-$ axis normal to the plate. Initially the fluid is assumed to be at rest and surrounds an infinite vertical plate with temperature T'_∞ and concentration C'_∞. A magnetic field of uniform strength B_0 is transversely applied to the plate. The $x'-$axis is taken along the plate in the vertically upward direction and the $z'-$axis is taken normal to the plate. The physical model of the problem shown in fig. (1). At time $t'>0$, the plate and the fluid are at the same temperature T'_∞ in the stationary condition with concentration level C'_∞ at all the points. At time $t'>0$, the plate is subjected to a uniform velocity $u=u_0$ in its own plane against the gravitational force. The plate temperature and concentration level near the plate are raised uniformly and are maintained constantly thereafter. All the physical properties of the fluid are considered to be constant except the influence of the body force term. Then under the usual Boussinesq's approximation the unsteady flow equations are momentum equation, energy equation, and mass equation respectively.

Equation of Momentum:

$$\frac{\partial u'}{\partial t'}-2\Omega' v=v\frac{\partial^2 u}{\partial z^2}-\frac{1}{\rho}\frac{\partial \rho}{\partial x}+g+\frac{B_0}{\rho}j_y \quad (1)$$

$$\frac{\partial v}{\partial t}-2\,\Omega'\,u=v\,\frac{\partial^2 v}{\partial z^2}-\frac{B_0}{\rho}j_x \qquad (2)$$

Equation of Energy

$$\rho c_p\frac{\partial T'}{\partial t'}=k\frac{\partial^2 T'}{\partial z^2}-\frac{\partial q}{\partial z}-Q_0\left(T'-T'_\infty\right)+Q_l'\left(C'-C'_\infty\right) \qquad (3)$$

Equation of diffusion

$$\frac{\partial C'}{\partial t'}=D\frac{\partial^2 C}{\partial z^2}-Kr'\left(C'-C'_\infty\right) \qquad (4)$$

As, no large velocity gradient here, the viscous term in equation (1) vanishes for small and hence for the outer flow, beside there is no magnetic field along $x-$direction gradient, so this results in,

$$0=D\frac{\partial \rho}{\partial x}-p_\infty g \qquad (5)$$

By eliminating the pressure term from equation (1) and (5), we obtain

$$\frac{\partial u'}{\partial t'}-2\Omega' v=v\frac{\partial^2 u}{\partial z^2}-\frac{1}{\rho}\frac{\partial \rho}{\partial x}+\left(\rho_\infty-\rho\right)g+\frac{B_0}{\rho}j_y \qquad (6)$$

The Boussinesq approximation gives

$$\rho_\infty-\rho=\rho_\infty\beta\left(T'-T'_\infty\right)+\rho_\infty\beta\left(C'-C'_\infty\right) \qquad (7)$$

On using (7) in the equation (6) and noting that ρ_∞ is approximately equal to 1, the momentum equation reduces to

$$\frac{\partial u'}{\partial t'}-2\Omega' v=v\frac{\partial^2 u}{\partial z^2}+\frac{B_0}{\rho}j_y+g\,\beta\left(T'-T'_\infty\right)+g\,\beta^*\left(C'-C'_\infty\right) \qquad (8)$$

The generalized Ohm's law with Hall currents is taken into account and ion – slip and thermo-electric

$$j+\frac{\omega \mathrm{T}_e}{B_0}(j\times B)=\sigma\left[E+q\times B\right] \tag{9}$$

The equation (9) gives

$$j_x - mj_y = \sigma v B_0 \tag{10}$$

$$j_y - mj_x = \sigma u B_0 \tag{11}$$

where $m=\omega_e \mathrm{T}_e$ is Hall parameter;

Solving (10) and (11) for j_x and j_y, we have

$$j_x=\frac{\sigma B_0}{\left(1+m^2\right)}(v-mu) \tag{12}$$

$$j_y=\frac{\sigma B_0}{\left(1+m^2\right)}(u-mv) \tag{13}$$

where B_0 – Imposed magnetic field, m – Hall parameter, ν – Kinematic viscosity, Ω_z – Component of angular viscosity, Ω – Non-dimensional angular velocity, J_z – component of current density j, ρ – Fluid density, σ – Electrical conductivity, t' – Time, μ – Coefficient of viscosity, T – Temperature of the fluid near the plate, T_w – Temperature of the plate, θ – Dimensionless temperature, T_∞ – Temperature of the fluid far away from the plate, C – Dimensionless concentration, κ – Thermal conductivity, β – Volumetric coefficient of thermal expansion, β^* – Volumetric coefficient of expansion with concentration, C' – Species concentration in the fluid, C_w – Wall concentration, C_∞ – Concentration for away from the plate, t – Non-dimensional time (u,v,w) – Components of velocity field F, (U,V,W) – Non dimensional velocity components, (x,y,z) – Cartesian co-ordinates.

On the use of (12) and (13), the momentum equations (8) and (2) become

$$\frac{\partial u'}{\partial t'}=\nu\frac{\partial^2 u}{\partial z^2}+2\Omega' v-\frac{\sigma\mu_e^2 H_0^2}{\rho\left(1+m^2\right)}(u+mv)+g\ \beta\left(T'-T'_\infty\right)+g\ \beta^*\left(C'-C'_\infty\right) \tag{14}$$

$$\frac{\partial v}{\partial t'}=\nu\frac{\partial^2 u}{\partial z^2}+2\Omega v-\frac{\sigma\mu_e^2 H_0^2}{\rho\left(1+m^2\right)}(v-mu) \tag{15}$$

$$\rho c_p\frac{\partial T'}{\partial t'}=k\frac{\partial^2 T'}{\partial z^2}-\frac{\partial q}{\partial z}-Q_0\left(T'-T'_\infty\right)+Q_l'\left(C'-C'_\infty\right) \tag{16}$$

$$\frac{\partial C'}{\partial t'}=D\frac{\partial^2 C'}{\partial z^2}-Kr'\left(C-C'_\infty\right) \tag{17}$$

Due to small Coriolis force, the second term on the right side of the equation (14) and (15) comes into existence.

The boundary conditions are given by:

$$u=0,\quad T=T_\infty^*,\ \ C=C_\infty^*,\ \ \forall\ \ y,t'\le 0$$

$$t'>0:\ \left.\begin{array}{l} u=u_0, T\to T_w, \\ C'=C'_\infty+\left(C'_w-C'_\infty\right)\end{array}\right\}\quad at\quad y=0$$

$$u\to 0, T\to T_\infty, C'\to C'_\infty\quad at\ \ y\to\infty$$

$$\left.\begin{array}{l} u=0,\quad T=T \\ C=C_\infty,\ v=0\end{array}\right\}\ \ \forall\ \ y,t'\le 0 \tag{18}$$

$$\left.\begin{array}{l} u\to u, T\to T_w \\ C'=C'_w v=0\quad at\quad z=0\end{array}\right\}\ \forall\ t'\le 0 \tag{19}$$

The dimensionless quantities are introduced as follows:

$$U=\frac{u}{u_0},\ V=\frac{v}{u_0},\ t=\frac{t'u_0^2}{\nu},\quad Z=\frac{zu_0^2}{\nu^2}$$
$$Gr=\frac{g\beta\nu\left(T_\omega-T_\infty\right)}{u_0^{\ 3}},M^2=\frac{\sigma\mu_e^2H_0^{\ 2}\nu}{2\rho u_0^{\ 2}}$$
$$Gc=\frac{g\beta^*\nu\left(C'_\omega-C'_\infty\right)}{u_0^{\ 3}},\quad \Omega=\Omega\frac{\nu}{u_0^2}\quad (20)$$
$$\Pr=\frac{\mu c_p}{\kappa},\ Kr=\frac{Kr'\nu}{u_0^2},\ Q=\frac{Q_0\nu}{\rho C_p u_0^{\ 2}}$$
$$Q_l=\frac{Q_l'\nu}{\rho C_p u_0^{\ 2}},\qquad R=\frac{16a^*\sigma\nu^2T_\infty^3}{k\,u_0^2}$$

where $Sc-$ Schmidt number, $Gr-$Thermal Grashof number, $Gc-$Mass Grashof number, $\Pr-$Prandtl number, $M-$Hartman number, $Kr-$Chemical reaction parameter, $R-$Radiation parameter, Q_l-Radiation absorption parameter, $Q-$heat source parameter.

Together with the equation (1), (2), (3) and (4), boundary conditions (18), (19), using (20), we have

$$\frac{\partial U}{\partial t}=\frac{\partial^2U}{\partial Z^2}+2V\left(\Omega-\frac{2m^2}{1+m^2}\right)+\frac{2m^2}{1+m^2}U+Gr\ \theta+Gc\ C \quad (21)$$

$$\frac{\partial V}{\partial t}=\frac{\partial^2V}{\partial Z^2}-2U\left(\Omega+\frac{2m^2}{1+m^2}\right)+\frac{2m^2}{1+m^2}V \quad (22)$$

with the boundary conditions

$$\left.\begin{array}{l}U=0,\ \ \theta=0\\ C=0,\ \ v=0\end{array}\right\}\quad \forall\ \ Z,t\le 0$$
$$\left.\begin{array}{l}U\to 1,\ \ \theta\to 1\\ C\to t,\ \ v\to 0\end{array}\right\}\quad \forall\quad t>0 \quad (23)$$
$$\left.\begin{array}{l}U\to 0,\ \ \theta\to 0,\\ C\to 0,\ \ V\to 0\end{array}\right\}\quad \forall\quad t>0 \quad (24)$$

Now equations (21), (22) and the boundary conditions (23), (24) can be combined to give:

$$\frac{\partial F}{\partial t}=\frac{\partial^2F}{\partial Z^2}-F\ a+Gr\ \theta+Gc\ C \quad (25)$$

$$\frac{\partial\theta}{\partial t}=\frac{1}{\Pr}\frac{\partial^2\theta}{\partial Z^2}-\frac{1}{\Pr}\left(R+Q\right)\ \theta-\frac{1}{\Pr}Q_l\ C \quad (26)$$

$$\frac{\partial C}{\partial t}=\frac{1}{Sc}\frac{\partial^2C}{\partial Z^2}-Kr\ C \quad (27)$$

where $F=U+iV$ and

$$a=2\left[\frac{M^2}{\left(1+m^2\right)}+i\left(\Omega-\frac{M^2m}{\left(1+m^2\right)}\right)\right]$$

In this study the value of (rotation parameter) is taken to be $\Omega-\dfrac{M^2m}{\left(1+m^2\right)}$, as a result of this the transverse velocity vanishes

with the boundary conditions

$$\begin{array}{l}F=0,\ \ \theta=0,\ \ C=0\ \ \ \forall\ \ Z,t\le 0\\ F\to 1,\ \ \theta\to 1,\\ C\to t,\ \ at\ Z=0\ \ \ \forall\ \ \ \ t>0\\ F\to 0,\ \ \theta\to 0\\ C\to 0,\ \ \ at\ Z\to\infty\ \ \ \forall\ \ \ \ t>0\end{array} \quad (28)$$

Method of Solution

Equation (25) – (27) are coupled, non – linear partial differential equations and these cannot be solved in closed – form using the initial and boundary conditions (28). However, these equations can be reduced to a set of ordinary differential equations, which can be solved analytically. This can be done by representing the velocity, temperature and concentration of the fluid in the neighborhood of the fluid in the neighborhood of the plate as

$$\begin{array}{l}F\left(z,t\right)=F_0\left(z\right)e^{i\omega t}\\ \theta\left(z,t\right)=\theta_0\left(z\right)e^{i\omega t}\\ C\left(z,t\right)=C_0\left(z\right)e^{i\omega t}\end{array} \quad (29)$$

Substituting (29) in Equation (25) – (27) and equating the harmonic and non – harmonic terms, we obtain

$$F_0''-\beta_3^2F_0=-Gr\,\theta_0-GmC_0 \quad (30)$$

$$\theta_0''-\beta_2^2\theta_0=0 \quad (31)$$

$$C_0'' - \beta_1^2 Sc\, C_0 = 0 \tag{32}$$

The corresponding boundary conditions can be written as

$$\begin{aligned} &F_0 = 1,\ \theta_0 = 1,\ \ C_0 = t, \qquad at\ Z = 0 \\ &F_0 = 0,\ \theta_0 = 0, C_0 = 0, \qquad as\ Z \to \infty \end{aligned} \tag{33}$$

Solving the equations (30) – (32) under the boundary condition (33), we get the solution for fluid velocity; temperature; concentration is expressed below using perturbation method:

$$F_0 = Z_1 e^{-\beta_2 y} + Z_2 e^{-\beta_1 y} + Z_3 e^{-\beta_3 y}$$

$$\theta_0 = B_2 e^{-\beta_2 y}$$

$$C_0 = t\ e^{-\beta_1 y}$$

In view of the above equation (29) becomes

$$F(z,t) = \left\{ Z_1 e^{-\beta_2 y} + Z_2 e^{-\beta_1 y} + Z_3 e^{-\beta_3 y} \right\} e^{i\omega t}$$

$$\theta(z,t) = \left\{ B_2 e^{-\beta_2 y} \right\} e^{i\omega t}$$

$$C(z,t) = \left\{ t\ e^{-\beta_1 y} \right\} e^{i\omega t}$$

Coefficient of Skin-Friction

The coefficient of skin-friction at the vertical porous surface is given by

$$C_f = \left(\frac{\partial F}{\partial Z} \right)_{z=0} = -\left(Z_1 \beta_2 + Z_2 \beta_1 + Z_3 \beta_3 \right)$$

Coefficient of Heat Transfer

The rate of heat transfer in terms of Nusselt number at the vertical porous surface is given by

$$Nu = \left(\frac{\partial T}{\partial Z} \right)_{z=0} = -B_2 \beta_2$$

Sherwood number

$$Sh = \left(\frac{\partial C}{\partial Z} \right)_{Z=0} = t\ \beta_1$$

RESULTS AND DISSCUSSIONS

Final results are shown graphically for various parameters like thermal Grashof number(Gr), rotation parameter(Ω), modified Grashof number(Gc), Prandtl number$(\Pr)$, Schmidt number(Sc), Chemical reaction parameter (Kr), Hartman number (M), Radiation parameter (R), Radiation absorption parameter (Q_l), heat source parameter (Q) on the velocity, temperature and concentration profiles can be analyzed from Fig. (2) – (17). The influence of thermal buoyancy force parameter (Gr) on the axial velocity shows in Fig. (2). As can be seen from this figure, the axial velocity profile increases with increases in the values of the thermal buoyancy. We actually observe that the axial velocity overshoot in the boundary layer region. Buoyancy force acts like a favourable pressure gradient which accelerates the fluid within the boundary layer therefore the solutal buoyancy force parameter (Gc) has the same effect on the velocity as Gr. From this figure we observe that the effect of magnetic field is to decrease the value of velocity profile throughout the boundary layer which results in the thinning of the boundary layer thickness. The influences of the Schmidt number (Sc) on the axial velocity profiles are plotted in Fig. (3) respectively. It is noticed from this figure that, the axial velocity decrease on increasing Sc. The Schmidt number embodies the ratio of the momentum to the mass diffusivity. The Schmidt number therefore quantifies the relative effectiveness of momentum and mass transport by diffusion in the hydrodynamic (velocity) boundary layer. Fig. (4) display the effect of magnetic field parameter or Hartmann number (M) on axial velocity. It is seen from these figures that the axial velocity increases when M increases. That is the axial velocity fluid motion is retarded due to application of transverse magnetic field. This phenomenon clearly agrees with the fact that Lorentz force that appears due to interaction of the magnetic field and fluid axial velocity resists the fluid motion. The influence of the hall parameter (m) on axial velocity profiles is as shown in Figs. (5) respectively. It is observed from these figures that the axial velocity profiles increase with an increase in the hall parameter m. This is because, in general, the Hall currents reduce the resistance offered by the Lorentz force. This means that Hall currents have a tendency to increase the fluid velocity components. Fig. (6) illustrates the influence of rotation parameter (Ω) on the velocity. Physically, the presence of rotation parameter effect has the tendency in resulting in a net reduction in the flow velocity. This behaviour is seen from this figure in which the velocity decreases as Ω increases. Fig. (7) illustrates the behaviour of axial velocity profiles for different values of the chemical reaction parameter (Kr). It is pertinent to mention that $(Kr > 0)$ corresponds to a destructive chemical reaction. It can be seen from the profiles that the axial velocity increases in the degenerating chemical reaction in the boundary layer. This is due to the fact that the increase in the rate of chemical reaction rate leads to thinning of a momentum in a boundary layer in degenerating chemical reaction. It can be seen from the profiles that the cross flow axial velocity reduces in the degenerating chemical reaction. It is evident from Fig. (8) that, the thermal radiation parameter (R) leads to increases in the axial velocity with increasing values of thermal radiation parameter. Thus, the Fig. (8) are in excellent agreement with the laws of Physics. Thus as R increases, the axial velocity increases. Now, from this figure, it may be inferred that radiation has a more significant effect on temperature than on velocity. Thus, the thermal radiation does not have a significant effect on the velocities but produces a comparatively more pronounced effect on the temperature of the mixture. It is noticed form Fig. (9) that the effects of rotation on the axial respectively. It is evident from this figure that, axial velocity increases on increasing in reaction parameter (K). This implies that rotation retards fluid flow in the axial velocity flow direction and accelerates fluid flow in the axial velocity flow direction in the boundary layer region. The hydrodynamic boundary layer decreases as the heat source (Q) effects increase. The effects of on the velocity field are shown in Fig (10). It is clearly seen from this figure that the velocity profiles decrease monotonically with the increase of suction parameter indicating the usual fact that suction stabilizes the boundary layer growth. The effect of increasing the value of the radiation absorption parameter (Q_l) on the velocity is shown in Fig. (11). we observe in this figure that increasing the value of the radiation absorption parameter the axial velocity decreases. The influence of Prandtl number, radiation parameter, heat source parameter and radiation absorption on the temperature distribution is respectively, shown on Figs. (12) - (15).

Fig. (12) Shows the temperature profile for different values of Prandtl number (Pr). It is observed that temperature increases with decrease in values of Prandtl number and also heat transfer is predominant in air when compared to water. Fig. (13) indicates that effect of radiation parameter (R) on the temperature profiles. It is deduced that temperature profiles decrease of the fluid near the plate decrease when radiation parameter are increased. Physically, thermal radiation causes a fall in temperature of the fluid medium and thereby causes a fall in kinetic energy of the fluid particles. This results in a corresponding decrease in fluid velocities. The effect of heat source parameter (Q) on the temperature profile is shown on Fig (14). It is seen from this figure that the effect of heat source parameter (Q) is to decrease temperature in the boundary layer as the radiated heat is absorbed by the fluid which in turn increases the temperature of the fluid very close to the porous boundary layer and its effect diminishes far away from the boundary layer. From Fig. (15) We observe that the effect of radiation absorption is to enhance heat transfer as thermal boundary layer thickness decreases with increase in the radiation absorption parameter. Figs. (l6) and (17) depict the influence of the non-dimensional chemical reaction parameter γ and the Schmidt number(Sc) on concentration profiles, respectively. From Fig. (16). the effect of chemical reaction parameter is very important in the concentration field. Chemical reaction increases the rate of interfacial mass transfer. Reaction reduces the local concentration, thus increases its concentration gradient and its flux. In Fig. (17) We see that the concentration profiles decrease with increasing values of the Schmidt number.

Conclusions:

The following main conclusions can be drawn from the present paper:

- Wall suction stabilizes the velocity, thermal as well as concentration boundary layer growth.
- Boundary layer flow attains minimum velocity values for large Hartmann numbers.
- Buoyancy parameter is to increase the velocity distribution in the momentum boundary layer.
- The presence of heat source effects cause reductions in the fluid temperature which resulted in decreases in the fluid velocity.
- The concentration decreases with increasing the chemical reaction parameter.
- Both the velocity and temperature profiles decrease with increasing values of radiation absorption parameter.
- These results might find wide applications in engineering, such as geothermal system, heat exchangers, and nuclear waste depositors.

APPENDIX

$$\beta_1^2=(i\omega+Kr)Sc,\beta_2^2=(i\omega \Pr+R+Q)$$

$$\beta_3^2=(i\omega+Q),B_1=-\frac{tQ_l}{\beta_1^2-\beta_2^2}$$

$$B_2=(1-B_1),Z_1=-\frac{B_2Gr}{\beta_1^2-\beta_3^2}$$

$$Z_2=-\frac{t\ Gc}{\beta_1^2-\beta_3^2},Z_3=(1-Z_1-Z_2)$$

REFERENCES

Pop, T Watanabe. Hall effects on magnetohydrodynamic free convection about a semi infinite vertical flat plate, Int. J. Eng. Sci., 1994; 32: 1903-1911

Chenna Kesavaiah Damala, Venkateswarlu Bhumarapu, Oluwole Daniel Makinde. Radiative MHD Walter's Liquid-B flow past a semi-infinite vertical plate in the presence of viscous dissipation with a heat source, Engineering Transactions, 2021; 69 (4): 373–401

Vajravelu K and Hadjinicolaou A. Convective heat transfer in an electrically conducting fluid at a stretching surface with uniform free stream, Int. J. Eng. Sci., 1997; 35: 1237-124

Rami Reddy G, Chenna Kesavaiah D, Venkata Ramana Musala and Bkaskara Reddy G. Hall effect on MHD flow of a viscoelastic fluid through porous medium over an infinite vertical porous plate with heat source, Indian

Journal of Natural Sciences, 2021; 12 (68): 34975-34987

Chenna Kesavaiah D and B Venkateswarlu B. Chemical reaction and radiation absorption effects on convective flows past a porous vertical wavy channel with travelling thermal waves, International Journal of Fluid Mechanics Research, 2020; 47 (2):153-169

Mallikarjuna Reddy B, Chenna Kesavaiah D and G V Ramana Reddy G V. Radiation and diffusion thermo effects of viscoelastic fluid past a porous surface in the presence of magnetic field and chemical reaction with heat source, Asian Journal of Applied Sciences, 2019; 7 (5): 597-607

Srinathuni Lavanya and Chenna Kesavaiah D. Heat transfer to MHD free convection flow of a viscoelastic dusty gas through a porous medium with chemical reaction, International Journal of Pure and Applied Researches, 2017; 3 (1): 43- 56

Abel M S, Kan S K and Prasad K V. Convective heat and mass transfer in a viscoelastic fluid flow through a porous medium over a stretching sheet. International Journal of Numerical Methods for Heat and Fluid flow, 2021; 11(8): 779-792

Mallikarjuna Reddy B, Chenna Kesavaiah D and Ramana Reddy G V. Effects of radiation and thermal diffusion on MHD heat transfer flow of a dusty viscoelastic fluid between two moving parallel plates, ARPN Journal of Engineering and Applied Sciences, 2018; 13 (22): 8863-8872

Salem A M and Abd El-Aziz M. Effect of Hall currents and chemical reaction on hydromagnetic flow of a stretching vertical surface with internal heat generation/absorption. Applied Mathematical Modelling, 2008; 32: 1236-1254

Chenna Kesavaiah D and Sudhakaraiah A. Effects of heat and mass flux to MHD flow in vertical surface with radiation absorption, Scholars Journal of Engineering and Technology, 2014; 2 (2): 219-225

Rajaiah M, Sudhakaraih A, Varma, S V K and Venkatalakshmi P. Chemical and Soret effect on MHD free convective flow past an accelerated vertical plate in presence of inclined magnetic field through porous medium. i-manager's Journal on Mathematics, 2015; 4(1): 32-39

Chamkha A J and A R A Khaled A R A. Similarity solutions for hydromagnetic mixed convection heat and mass transfer for Hiemenz flow through a porous medium. Int. J. Numerical Methods for Heat and Fluid Flow, 2000; 10: 94-115

Chenna Kesavaiah D, Satyanarayana P V, A Sudhakaraiah, Venkataramana S (2013): Natural convection heat transfer oscillatory flow of an elastico-viscous fluid from vertical plate, International Journal of Research in Engineering and Technology, 2013; 2 (6): 959-966

Chenna Kesavaiah D, Satyanarayana P V. MHD and Diffusion Thermo effects on flow accelerated vertical plate with chemical reaction, Indian Journal of Applied Research, 2013; 3 (7): 310-314

Nield D A and Bejan. A Convection in Porous Media, 2nd edition. Springer-Verlag, 1999; New York.

Chenna Kesavaiah D, P Satyanarayana P V and Venkataramana S. Radiation and Thermo - Diffusion effects on mixed convective heat and mass transfer flow of a viscous dissipated fluid over a vertical surface in the presence of chemical reaction with heat source, International Journal of Scientific Engineering and Technology, 2013; 2 (2): 56-72

Ibrahim F S, Elaiw A M and A A Bakar A A. Effect of the chemical reaction and radiation absorption on the unsteady MHD free convection flow past a semi infinite vertical permeable moving plate with heat source and suction, Communications in Nonlinear Science and Numerical Simulation, 2008; 13: 1056-1066

Karunakar Reddy S, Chenna Kesavaiah D and Raja Shekar M N. MHD heat and mass transfer flow of a viscoelastic fluid past an impulsively started infinite vertical plate with chemical reaction, International Journal of Innovative Research in Science, Engineering and Technology, 2013; 2 (4): 973- 981

Stanford Shateyi and Sandile Motsa. Unsteady magnetohydrodynamic convective heat and mass transfer past an infinite vertical plate in a porous medium with thermal radiation, heat generation/absorption and chemical reaction, Advanced Topics in Mass Transfer, INTECH Publishers, 2011; 145-162

Ch Kesavaiah Damala, Satyanarayana P V and Sudhakaraiah A. Effects of radiation and free convection currents on unsteady Couette flow between two vertical parallel plates with constant heat flux and heat source through porous medium, International Journal of Engineering Research, 2013; 2 (2): 113-118

Rajaiah and M Sudhakaraiah A. Unsteady MHD free convection flow past an accelerated vertical plate with chemical reaction and Ohmic heating, International Journal of Science and Research, 2015; 4 (2): 1503-1510

Ch Kesavaiah D, Satyanarayana P V, Gireesh Kumar J and S Venkataramana S. Radiation and mass transfer effects on moving vertical plate with variable temperature and viscous dissipation, International Journal of Mathematical Archive, 2012; 3 (8): 3028-3035

Ibrahim F S, A M Elaiw and A A Bakr. Effect of chemical reaction and radiation absorption on the unsteady MHD free convection flow past a semi infinite vertical permeable moving plate with heat source and suction, Commun Nonlinear Sci. Numer. Simulat., 2018; 13: 1056-1066

P V Satyanarayana, D Ch Kesavaiah and S Venkataramana (2011): Viscous dissipation and thermal radiation effects on an unsteady MHD convection flow past a semi-infinite vertical permeable moving porous plate, International Journal of Mathematical Archive, Vol. 2(4), 2011, pp. 476-487

R A Mohamed (2009): Double-Diffusive convection radiation interaction on unsteady MHD flow over a vertical moving porous plate with heat generation and Soret effects, Applied Mathematical Sciences, Vol. 3 (13), pp. 629-651

Ch Kesavaiah D, Satyanarayana P V and Venkataramana S. Effects of the chemical reaction and radiation absorption on an unsteady MHD convective heat and mass transfer flow past a semi-infinite vertical permeable moving plate embedded in a porous medium with heat source and suction, Int. J. of Appl. Math and Mech. 2011; 7 (1): 52-69

Haranth Y and Sudhakaraiah A. Viscosity and Soret effects on unsteady hydromagnetic gas flow along an inclined plane, International Journal of Science and Research, 2015; 4 (2): 2650-2654

Chenna Kesavaiah D, Ramakrishna Goud T, Nookala Venu, Seshagiri Rao Y V. MHD effect on convective flow of dusty viscous fluid with fraction in a porous medium and heat generation, Journal of Mathematical Control Science and Applications, 2021; 7 (2): 393-404

Ali M E. The effect of lateral mass flux on the natural convection boundary layers induced by a heated vertical plate embedded in a saturated porous medium with internal heat generation, Int. J. Thermal Sci., 2007; 46: 157-163

Cussler E L. Diffusion mass transfer in fluid systems, Cambridge University Press, London, 1998

Das U N, Deka R and Soundalgekar V M. Effects of mass transfer on flow past an impulsively started infinite vertical plate with constant heat flux and chemical reaction. J. Forshung Im Ingenieurwesen Engineering Research Bd., 1994; 60: 284-287

S P Anjalidevi and R Kandasamy (1999): Effects of chemical reaction, heat and mass transfer on laminar flow along a semi infinite horizontal plate, Heat and Mass Transfer, Vol. 35, pp. 465-467

Seddeek M A, Darwish A A and Abdelmeguid M S. Effects of chemical reaction and variable viscosity on hydromagnetic mixed convection heat and mass transfer for Hiemenz flow through porous media with radiation, Commun Nonlinear Sci. Numer. Simulat., 2007; 15: 195-213

Cortell R. Effects of viscous dissipation and radiation on the thermal boundary layer over a nonlinearly stretching sheet. Phys Lett A, 2008; 372: 631-636

Bataller R C. Radiation effects for the Blasius and Sakiadis flows with a convective surface boundary condition. Appl. Math. Comput., 2008; 206: 832-840

Aliakbar V, Alizadeh-Pahlavan A and K Sadeghy K. The influence of thermal radiation on MHD flow of Maxwellian fluids above stretching sheets, Commun. Nonlinear Sci. Numer. Simulat., 2019; 14 (3): 779-794

Seth G S, Mahato G K, Sarkar S and Ansari M S. Effects of Hall current on hydromagnetic natural convection flow of a heat absorbing fluid past an impulsively moving vertical plate with ramped temperature, Int. J. Appl. Math. Res., 2012; 1: 462–486

Das S, Sarkar B C and Jana R N. Hall effect on MHD free convection boundary layer flow past a vertical flat plate, Meccanica, 2013; 48: 1387–1398

Sarkar B C, Das S and R N Jana R N. Hall Effects on Unsteady MHD Free convective flow past an accelerated moving vertical plate with viscous and Joule dissipations, Int. J. Comp. Appl., 2013; 70: 19–28

Muthucumarswamy P and L Jyanthi. Hall Effects on MHD Flow past an infinite vertical plate in the presence of rotating fluid of variable temperature and uniform mass diffusion with first order chemical reaction, International Journal of Applied Engineering Research, 2014; 9 (24): 26259–26271

Crepeau J C and Clarksean R. Similarity solutions of natural convection with internal heat generation, J. Heat Transfer, 1997; 119:183-185

Patil P M and Kulkarni P S. Effects of chemical reaction on free convective flow of a polar fluid through a porous medium in the presence of internal heat generation. International Journal of Thermal Sciences, 2008; 47: 1043-1054

Salem M Aand Abd El-Aziz M. Effect of Hall currents and chemical reaction on hydromagnetic flow of a stretching vertical surface with internal heat generation/absorption, Applied Mathematical Modelling, 2008; 32: 1236-1254

Samad M A and Mohebujjaman M. MHD Heat and mass transfer Free convection flow among a vertical stretching sheet in presence of magnetic field with heat generation. Research Journal of Applied Science, Engineering and Technology, 2009; 1 (3): 98-106

Muthucumaraswamy R, Prema A and Muthuracku K. Hall Effect on MHD flow past an exponentially accelerated isothermal vertical plate with variable Mass diffusion in the presence of rotating fluid, annals of faculty engineering Hunedoara, International Journal of Engineering, 2015; 13(5): 229–236

Kumaar V D, Muthucumaraswamy R and Manjula L. Hall effect unsteady flow past an isothermal vertical plate in a rotating fluid with variable mass diffusion in the presence of chemical reaction of first order, Advances in Mathematics: Scientific Journal, 2020; 9 (5): 2749–2759

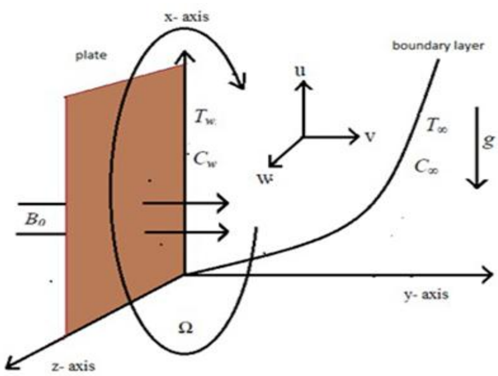

Fig. (1): The geometrical model of the problem

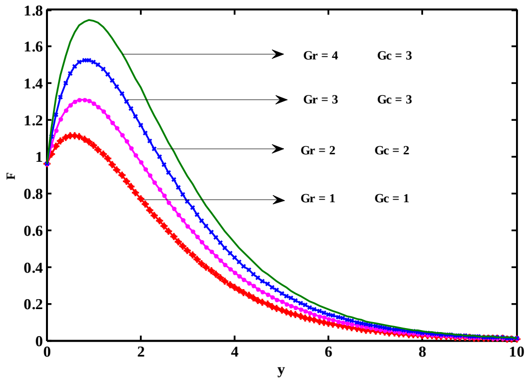

Fig. (2): Axial velocity profiles for different values of Gr, Gc

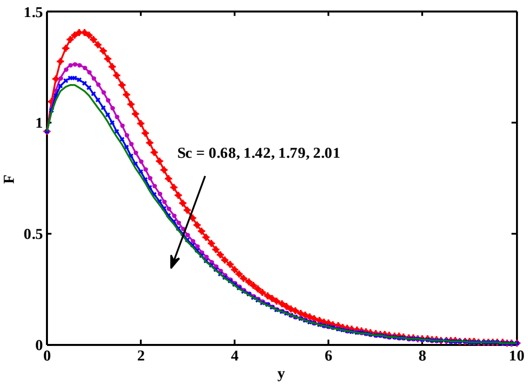

Fig. (3): Axial velocity profiles for different values of Sc

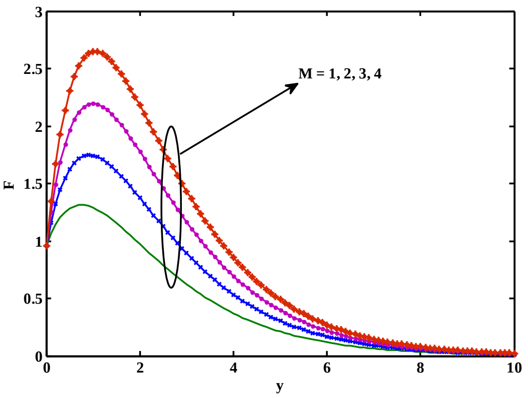

Fig. (4): Axial velocity profiles for M

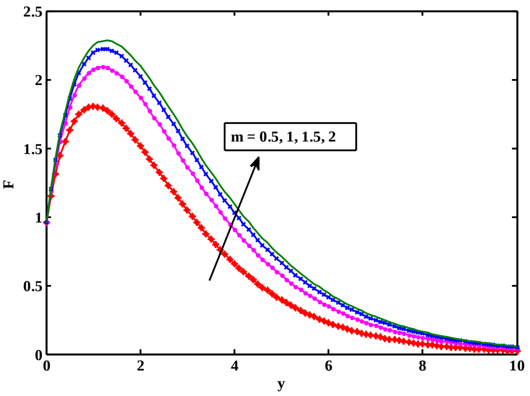

Fig. (5): Axial velocity profiles for m

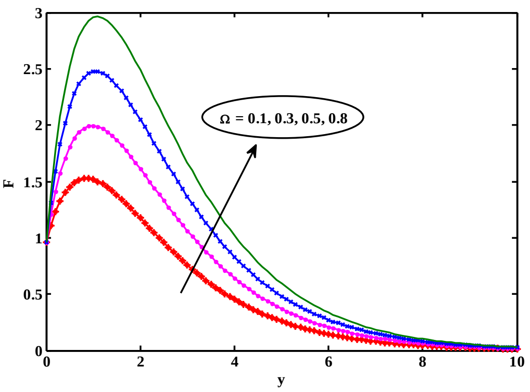

Fig. (6): Axial velocity profiles for Ω

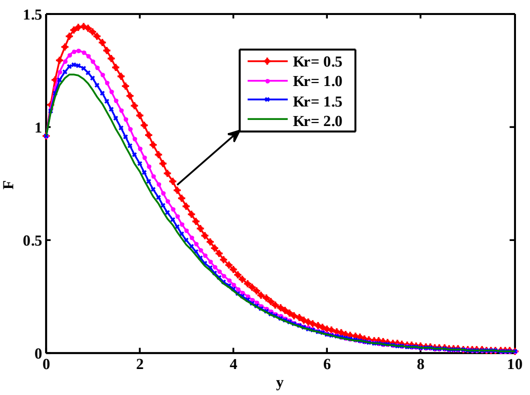

Fig. (7): Axial velocity profiles for Kr

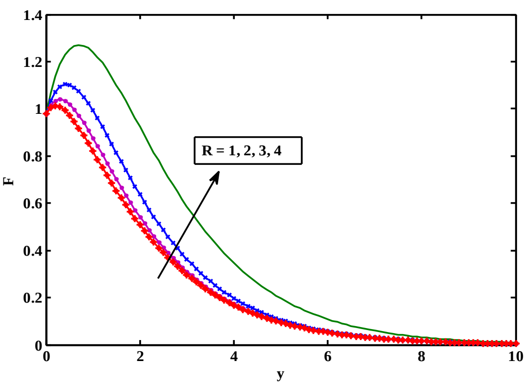

Fig. (8): Axial velocity profiles for R

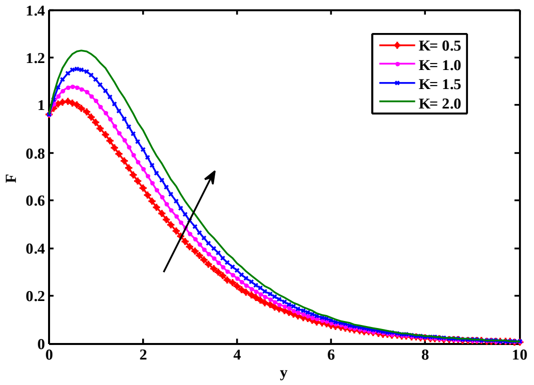

Fig. (9): Axial velocity profiles for K

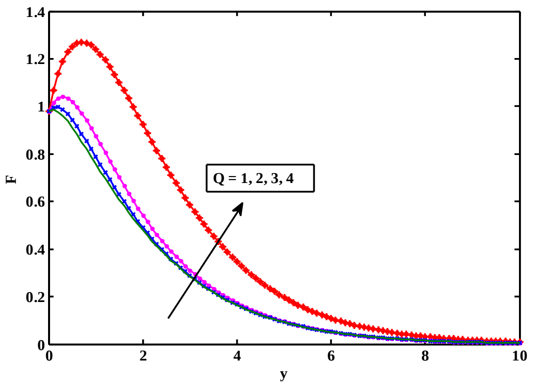

Fig. (10): Axial velocity profiles for Q

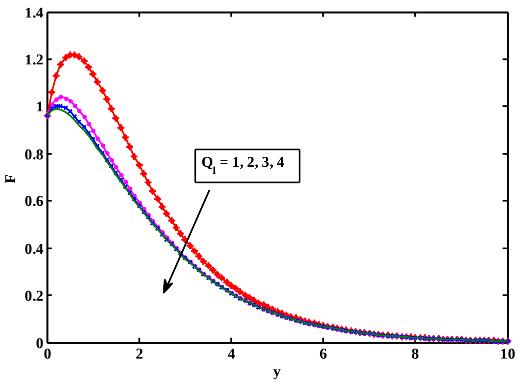

Fig. (11): Axial velocity profiles for Q_l

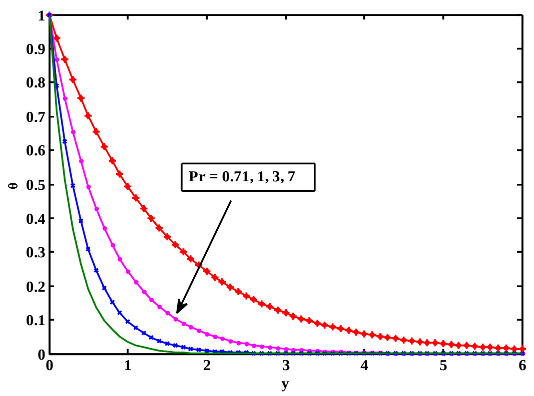

Fig. (12): Temperature profiles for Pr

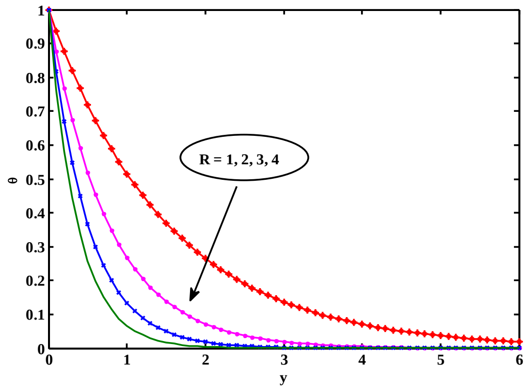

Fig. (13): Temperature profiles R

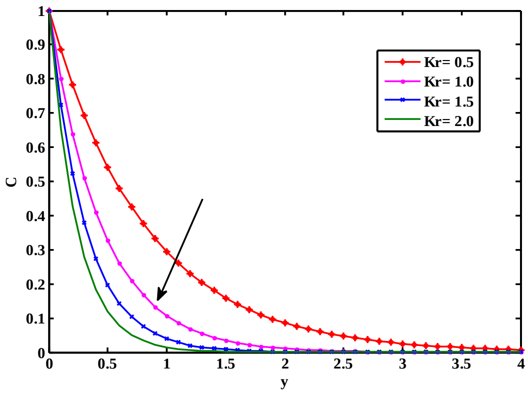

Fig. (16): Concentration profiles for Kr

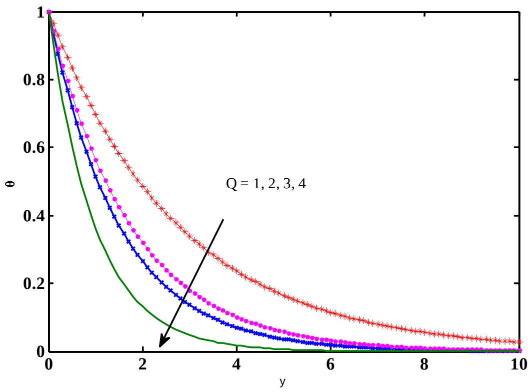

Fig. (14): Temperature profiles for Q

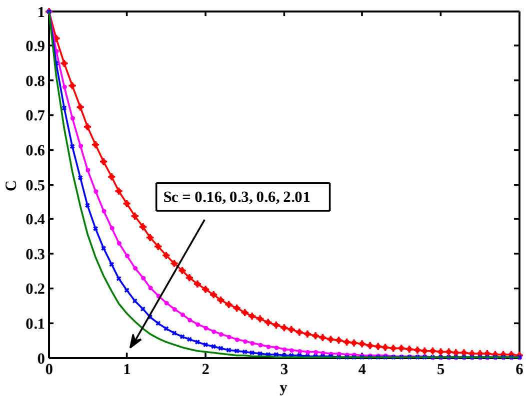

Fig. (17): Concentration profiles for Sc

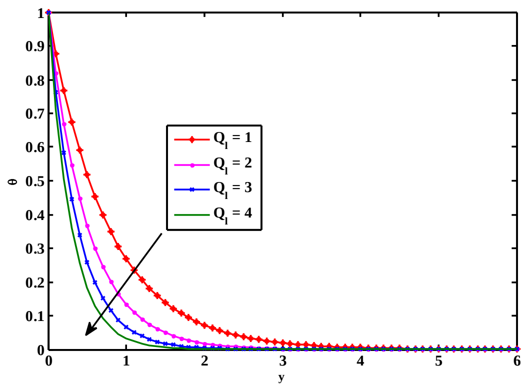

Fig. (15): Temperature profiles for Q_l

DUFOUR AND CHEMICAL REACTION EFFECTS ON TWO DIMENSIONAL INCOMPRESSIBLE FLOW OF A VISCOUS FLUID OVER MOVING VERTICAL SURFACE

Anita Tuljappa[1], V. Nagaraju[2], G. Rami Reddy[3], Dr. Nookala Venu[4]

[1]Department of Mathematics, Vijayanagara Srikrishna Devaraya University, Ballari, Karnataka,Pin-583105, India

Email: anita.birapur@gmail.com

[2]Department of Basic Sciences & Humanities, Vignan Institute of Technology and Science, Deshmukhi (V), Pochampally (M), Yadadri-Bhuvanagiri (Dist), TS-508284, India

Email: vellanki.nagsra@gmail.com

[3]Department of Mathematics, Malla Reddy Engineering College (Autonomous), Dulapally (V), Kompally (M), Medchal Malkajgiri (Dist), TS-500100, India

Email: dr.g.ramireddy76@gmail.com

[4]Department of Electronics and Communication Engineering, Balaji Institute of Technology and Science (Autonomous), Narsampet, Warangal, TS -506331, India

Email: venunookala@gmail.com

ABSTRACT

The extensive variety of issues include reactions kinetics, simulations and optimizations of different models of reactors including basic explorations of the processes of temperature and mass and momentum transfer that taken places with chemical reaction. Based on this criteria, it is discussed the impacts of the Dufour consequences on natural convective heat and mass transfer for the unsteady two dimensional boundary layer flow through a vertical surface. The resultant governing boundary layer equations are nonlinear and coupled form of partial differential equations which are solved analytically using two-term harmonic and non-harmonic function. The effects of different physical parameters on the velocity, temperature and concentration fields as well as skin friction are discussed in detail.

KEYWORDS: MHD, Porous medium, Vertical surface, Chemical reaction

DOI Number: 10.48047/NQ.2022.20.20.NQ109009 **NeuroQuantology2022;20(20): 63-74**

INTRODUCTION

The combined heat and mass transfer with natural convective fluid flow though an inundated permeable medium has most imperative applications in the geothermal and geophysical industrial engineering they are, the extraction of geothermal energy, the migration of wetness in fibrous insulations, underground disposal of nuclear wastes, and the distribution of chemical pollutants in saturated soils. As well, the temperature and mass transport is concurrently distressing each other that would cause the cross diffusion effects. The heat transport reasoned with the concentration gradient is known as Dufour effects. Towards attained most significant concepts of costs and energies, intensification of heat transport played an extremely requisite role. In view of the above (Omowaye et.al. 2015)Considered Dofour and Soret effects on steady MHD convective flow of a fluid in a porous medium with temperature dependent viscosity: Homotopy analysis approach, (Dursunkaya et.al. 1992) observed Diffusion thermo and thermal diffusion effects in transient and steady natural convection form a vertical surface, (Gbadeyan et.al. 2018)Considered Soret and Dufour effects on heat and mass transfer in chemically reacting MHD flow through a wavy channel, (Mabood et.al. 2015) Observed MHD stagnation point flow and transfer impinging on stretching sheet with chemical reaction and transpiration, (Tasawar Hayat et.al. 2018) presented Numerical investigation of MHD flow with Soret and Dufour effect.(Jena et.al. 2018) Chemical reaction effect on MHD viscoelastic fluid flow over vertical stretching sheet with heat source/sink, (Tripathy et.al. 2015)studied chemical reaction effects on MHD free convective surface over a moving vertical plate through porous medium, for more information we refereed Applied Numerical Methods by (Carnahan et.al. 1996), (Rajput et.al. 2011) discussed radiation and chemical reaction effect on free convection MHD flow through a porous medium bounded by vertical surface, (Reddy et. al. 2013) considered chemical reaction and radiation effects on MHD free convection flow through a porous medium bounded by a vertical surface with constant heat and mass flux, (Sudershan Reddy et. al. 2012) studied radiation and chemical reaction effects on free convection MHD flow through a porous medium bounded by vertical surface.

The present developments in the field of science and technology are levitating the demands for exceptional characteristic packed together machines with the better performances, speed and accurate rolling, and extended life span. Therefore, the scholars and scientists congregated to working on the thermal organization of heat transport machines. The curiosity of combined hat and mass transport with natural convection in a fluid saturated porous medium intervenes in countless manufacturing, technical and industrial companies such as hydro-geological, earth sciences, electronically applications getting cold through fans, terrestrial heat power exploitations, petroleum repositories, and invent of steel, underrating and atomic strength factories. An extensive version of the existing in sequence is granted in the modern researchers (Neild and Bejan, 2006) and (Ingham and Pop, 2005). Current years, substantial emphasis committed towards investigate the hydromagnetic flow for heat and mass transport since for claims through physics of the earth, aeronautical studies, and engineering in chemistry. (Makinde, 2010) premeditated the MHD boundary layer flow with heat and mass transport past a moving vertical plate in the occurrence of magnetic field. (Palani and Srikanth, 2009) explored the hydromagnetic flow of an electrically conducting fluid across a semi-infinite vertical plate under the effect of magnetic field. (Duwairi, 2005) observed viscous and Joule-heating outcomes on compelled convective flow from disseminate isothermal surface. The result of viscous dissipation is frequently distinguished by the Eckert number and it is performed an extremely imperative responsibility in geo-scientific flow and in atomic industry has been studied by (Alim et. al, 2007). This is addition performs an essential task in natural convection into a variety of proceedings on huge measures or for bulky heavenly bodies. The results of suction on boundary sheet flow also have superior influence in excess of the industrial functioning and have made extensively deliberated by abundant leading scientists. Multiple creators have explored the results of viscous dissipation and constant suction in distinct plane this embodiment. (Uwanta, 2012) explained the consequences of chemical substance retort and emission for heat and mass transport over a semi-infinite vertical permeable plate with invariable flux and diffusion. (Mansour et. al, 2008) deliberated an impact of chemical reaction and viscous dissipation for hydromagnetic free convection flow. The end product of compound response and heat and mass transfer along a sequence with heat source and absorption or inoculation by (Kandasamy et. al, 2005) A hypothetical study on the control of emission for a steady natural convective heat and mass transport through an isothermal stretching sheet by the occurrence of unvarying magnetic field with viscous dissipation effect has been studied by (Govardan et. al, 2012)

A typical chemical reaction is always dependent on a decent quantity of activation energy no matter it is linear or binary, to start off. The Arrhenius equation is therefore, necessary for a model involving chemical reaction to calculate the amount of this activation energy. This equation describes the variation of temperature within the system due to the chemical reaction phenomena. Several industrial applications are linked with fluid flow analysis based on chemical reaction due to which researchers have adopted this factor frequently in their models.(Hamid and Khan, 2018) has been given impacts of binary chemical reaction with activation energy on unsteady flow of magneto-Williamson nanofluid, (Dhlamini et. al, 2019) experimental study onactivation energy and binary chemical reaction effects in mixed convective nanofluid flow with convective boundary conditions.

In a decades, some of the authors shown their research motivation in a Varity of problems considered and observed the physical behaviours of various parameters introduced and solved given their opinions, some of them, (Ch Kesavaiah et. al, 2013) has been studied the effects of radiation and free convection currents on unsteady Couette flow between two vertical parallel plates with constant heat flux and heat source through porous medium, Srinathuni Lavanya and D Chenna Kesavaiah, 2017) considered heat transfer to MHD free convection flow of a viscoelastic dusty gas through a porous medium with chemical reaction,(Chenna Kesavaiah and Sudhakaraiah, 2014) motivated study on effects of heat and mass flux to MHD flow in vertical surface with radiation absorption, (Chenna Kesavaiah and Satyanarayana, 2013) gave their opinion onMHD and Diffusion Thermo effects on flow accelerated vertical plate with chemical reaction,(ChKesavaiah et. al, 2012) detailed information on radiation absorption, chemical reaction and magnetic field effects on the free convection and mass transfer flow through porous medium with constant suction and constant heat flux, (Karunakar Reddy et. al, 2013) expressed their ideas on MHD heat and mass transfer flow of a viscoelastic fluid past an impulsively started infinite vertical plate with chemical reaction, (Chenna Kesavaiah et. al, 2013) motivated study on natural convection heat transfer oscillatory flow of an elastico-viscous fluid from vertical plate, (ChKesavaiah et. al, 2012) observed that the radiation and mass transfer effects on moving vertical plate with variable temperature and viscous dissipation, (Mallikarjuna Reddy et. al, 2018) shown the effects of radiation and thermal diffusion on MHD heat transfer flow of a dusty viscoelastic fluid between two moving parallel plates, (ChennaKesavaiah et. al, 2013) measured the radiation and Thermo - Diffusion effects on mixed convective heat and mass transfer flow of a viscous dissipated fluid over a vertical surface in the presence of chemical reaction with heat source,(Chenna Kesavaiah and Venkateswarlu, 2020) given out line on chemical reaction and radiation absorption effects on convective flows past a porous vertical wavy channel with travelling thermal waves, (Chenna Kesavaiah et. al, 2018) has been considered MHD free convection heat and mass transfer flow past an accelerated vertical plate through a porous medium with effects of hall current, rotation and Dufour effects, (Chenna Kesavaiah et. al, 2021) expressed the radiative MHD Walter's Liquid-B flow past a semi-infinite vertical plate in the presence of viscous dissipation with a heat source, (Bang ChuolNhial et. al. 2022) motivated study onhall current, rotation and chemical reaction effects on MHD free convection flow past an accelerated vertical plate through a porous medium,(Bang ChuolNhial et. al. 2022) detailed information has been given radiation and mass transfer effects on MHD free convection flow over an inclined plate, (Nagaraju et. al. 2019) observed MHD viscoelastic fluid flow past an infinite vertical plate in the presence of radiation and chemical reaction,(Nagaraju et. al. 2018) studied radiation effects on MHD convective heat and mass transfer flow past a semi-infinite vertical moving porous plate in the presence of chemical reaction.

FORMULATION OF THE PROBLEM

We considered the steady, two-dimensional laminar, incompressible flow of a chemically reacting, viscous fluid on a continuously moving vertical surface in the presence of a uniform magnetic field and Dufour effect, uniform heat and mass flux effects issuing a slot and moving with uniform velocity in a fluid at rest. Let $x-$ axisbe taken along the direction of motion of the surface in the upward direction and $y-$ axis is normal to the surface are shown in figure (1).

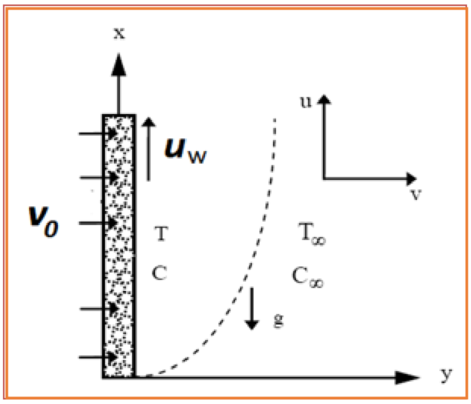

Fig. (1): Geometry of the problem

The temperature and concentration levels near the surface are raised uniformly. The induced magnetic field, viscous dissipation is assumed to be neglected. Now, under the usual Boussinesq's approximation, the flow field is governed by the following equations.

Continuity equation

$$\frac{\partial u}{\partial x}+\frac{\partial v}{\partial y}=0 \tag{1}$$

Momentum equation

$$u\frac{\partial u}{\partial x}+v\frac{\partial u}{\partial y}=\nu\frac{\partial^2 u}{\partial y^2}-\frac{\sigma B_0^2}{\rho}-\frac{\nu}{K_p}u \qquad g\beta\left(T'-T'_\infty\right)+g\beta^*\left(C'-C'_\infty\right) \tag{2}$$

Energy equation

$$\rho C_p\left(u\frac{\partial T'}{\partial x}+v\frac{\partial T'}{\partial y}\right)=k\frac{\partial^2 T'}{\partial y^2}+\frac{D_M K_T}{C_s C_p}\frac{\partial^2 C'}{\partial y^2} \tag{3}$$

Diffusion equation

$$u\frac{\partial C'}{\partial x}+v\frac{\partial C'}{\partial y}=D\frac{\partial^2 C'}{\partial y^2}-Kr'\left(C'-C'_\infty\right) \tag{4}$$

The initial and boundary conditions

$$\left.\begin{array}{l} u=u_w, v=-v_0\, const, <0 \\ \dfrac{\partial T}{\partial y}=-\dfrac{q}{k}, \qquad \dfrac{\partial C}{\partial y}=-\dfrac{j''}{k} \end{array}\right\} \; at \quad y=0 \tag{5}$$

$$u\to 0, T\to T'_\infty, C\to C'_\infty \qquad as \;\; y\to\infty$$

Where u, are velocity components in x and y directions respectively. g is the acceleration due to gravity, β is volumetric coefficient of thermal expansion, β^* is the volumetric coefficient of expansion with concentration, is the temperature of the fluid, C' is the species concentration, T'_w is the wall temperature, C'_w is the concentration at the plate, T'_∞ is the free steam temperature far away from the plate, C'_∞ is the free steam concentration in fluid far away from the plate, ν is the kinematic viscosity, Du is the species diffusion coefficient, Kr is the chemical reaction parameter. The term is assumed to be the amount of heat generated or absorbed per unit volume. Q_0 is a constant, which may take on either positive or negative values. When the wall temperature T'_w exceeds the free steam temperature T'_∞, the source term represents the heat source $Q_0>0$ when and heat sink when $Q_0<0$. The first term and second term on the right hand side of the momentum equation (2) denote the thermal and concentration buoyancy effects respectively.

In order to write the governing equations and the boundary conditions the following non-dimensional quantities are introduced.

$$Y=\frac{yv_o}{\nu},\quad U=\frac{u}{u_w},\quad k=\frac{K_p v_0^2}{\nu^2}$$

$$T=\frac{T'-T'_\infty}{\left(\dfrac{q\nu}{kv_0}\right)},Sc=\frac{\nu}{D},\Pr=\frac{\mu C_p}{k}$$

$$C=\frac{C'-C'_\infty}{\left(\dfrac{j''\nu}{kv_0}\right)},\quad Gr=\frac{\nu g\beta\left(\dfrac{q\nu}{kv_0}\right)}{u_w v_0^2} \quad (6)$$

$$M=\frac{\sigma B_0^2\nu}{\rho},\quad Du=\frac{D_M K_T j''}{c_s c_p \nu q\rho C_p}$$

$$Gc=\frac{\nu g\beta^*\left(\dfrac{j''\nu}{kv_0}\right)}{u_w v_0^2},Kr=\frac{Kr'\nu}{v_0^2}$$

In view of (6) the equations (2) – (4) are reduced to the following non-dimensional form

$$\frac{d^2U}{dY^2}+\frac{dU}{dY}-\left(M+\frac{1}{k}\right)U=-GrT-GrC \quad (7)$$

$$\frac{d^2T}{dY^2}+\Pr\frac{dT}{dY}=-Du\Pr\frac{d^2C}{dY^2} \quad (8)$$

$$\frac{d^2C}{dY^2}+Sc\frac{dC}{dY}-KrSc\,C=0 \quad (9)$$

Corresponding initial and boundary conditions in non-dimensional form are

$$U=1,\frac{\partial T}{\partial Y}=-1,\frac{\partial C}{\partial Y}=-1 \quad at \quad Y=0 \qquad (10)$$
$$U\to 0,T\to 0,C\to 0 \quad as \quad Y\to\infty$$

where Gr is the thermal Grashof number, Gc is the solutal Grashof number, M is the magnetic parameter, k is the permeability parameter, $\Pr$ is the fluid Prandtl number, Du is the Dufour number , Sc is the Schmidt number and Kr is the chemical reaction parameter.

METHOD OF SOLUTION

The study of ordinary differential equations (7), (8) and (9) along with their initial and boundary conditions (10) have been solved by using the method of ordinary linear differential equations with constant coefficients. We get the following analytical solutions for the velocity, temperature and concentration

$$U=\left(L_1+L_3\right)e^{m_2y}+L_2e^{m_4y}+L_4e^{m_6y}$$

$$T=J_1e^{m_2y}+J_2e^{m_4y}$$

$$C=-\frac{1}{m_2}e^{m_2y}$$

Skin friction

$$\tau=\left(\frac{\partial U}{\partial y}\right)_{y=0}=m_2\left(L_1+L_3\right)+m_4L_2+m_6L_4$$

Nusselt number

$$Nu=\left(\frac{\partial T}{\partial y}\right)_{y=0}=m_2J_1+m_4J_2$$

Sherwood number

$$Sh=\left(\frac{\partial C}{\partial y}\right)_{y=0}=-1$$

RESULTS AND DISCUSSION

In order to analyze the results are carried out for various values of thermal Grashof number (Gr), solutal Grashof number (Gc), magnetic parameter (M), permeability parameter (k), Prandtl number $(\Pr)$, Dufour number (Du) , Schmidt number (Sc) and Chemical reaction parameter (Kr) for various values of Gr = 5.0, Kr = 1.0, Sc= 0. 84, Pr= 0.72, Du=1.0, M=1.0, K=1.0, Gc=5.0 Figs. (2 and 3) disclosed the consequence of thermal and solute Grashof number on the fluid velocity. The Grashof number means the qualified outcome of the heat buoyancy force for the viscous hydrodynamic force through the boundary layer, at the same time as the mass Grashof number established the proportion for the concentration buoyancy force to the viscous hydrodynamic force. As accepted the fluid velocity enhances through good quality of the strengthening of thermal and solute buoyancy forces. The resulting velocity delivery increases quickly after that to the porous surface and this decline effortlessly for the gratuitous flow area. The momentous velocity transversely the boundary layer enlarges through an enhancing in Gr and/or Gm. Therefore, boundary layer thickness augments with boost up in Gr and/or Gm. The repeal tendency is observed with ever-mounting in Dufour parameter illustrated in Fig. (4). Dufour parameter narrates a consequence for the thermal gradients provoking noteworthy mass diffusion consequences. A raise in Dofour parameter, enhance the momentum transport through the boundary layer, hence, the velocity enlarges in complete fluid region. For unlike quantities of the permeability parameter K for velocities and is conspired through Fig. (5). Evidently, the growing quantities of K be probable to rising of the velocity on the porous walls and hence development in the momentum boundary layer thickness. Inferior the permeability lesser noteworthy the fluid velocity is respected inside the vertical surface employed by the fluid. The outcome of chemical reaction parameter on velocity is observed in Fig. (6), it is notice that an increasing chemical reaction parameter the velocity increases. Hence, this is found that disparaging chemical reaction make ineffective the resistive Lorentz force in increasing the resultant velocity throughout the fluid region. Fig. (7) explored that, the influence of the magnetic field parameter M for the resultant velocity distribution. The profiles are parabolise character. The velocity transversely the boundary layer trim downs through an amplifying in the Hartmann number M, this participates a principal responsibility to shrink in the layer width caused by Lorentz forces. Fig. (8) Portrayed the resultant velocity within the boundary layer augments with escalating in Prandtl number. Rising the values of Prandtl number trend to reduces the velocity and so pick up the rate of the momentum boundary layer thickness. It is explored by Fig. (9).That for the velocity with the different values of Schmidt number. On increases in Schmidt numberbe predisposed to reduce of the velocity and boost up the momentum boundary layer thickness. The impacts from Prandtl number (Pr), Dufour number (Du)on the temperatures of the fluid surrounded by the vertical channel is shown in Fig. (10) and Fig. (11). It is observed that, a raise in Prandtl number decline the fluid temperature throughout the fluid region shown in fig (10). Identical manners are noticed with growing in Dufour parameter (Du) in fig. (11). The Dufour parameter (Du) connotes the involvement of the attentiveness gradients for the caloric energy discharge during the flow. This is observed as Dufour parameter amplifies and is monotonically raise in temperature distribution.The concentration interpretation with the parameters like, the chemical reaction parameter (Kr) and Schmidt number (Sc) are publicized from Fig. (12) and (13). The concentration accentuate with heighten in chemical reaction parameter during the fluid medium Fig. (12). It is depicted the transient flow pattern for the variation of chemical reaction parameter with time. The concentration at the left plate is high and it gradually decreases towards the right plate. It is perceived that, from fig. (13)Concentration field lessens through widening in Sc during the fluid region. The Schmidt number discriminates the proportion of thickness of viscous to the solute diffusivity. The Schmidt number is defining the virtual efficiency of momentum and mass transfer through dispersions in the velocity and solutal boundary layers. It is found that, an amplifying in the values of Sc induced the absorption of spices and those boundary layer thicknesses to diminish expansively. From figure (14), we observed that the skin friction for various values of chemical reaction parameter versus Grashof number, it is clear that an increasing in chemical reaction parameter, the results also rises in the vertical surface.

CONCLUSIONS

We analysed the effect of diffusion - thermo (Dufour) on MHD free convective heat and mass transfer two-dimensional steady boundary layer flow of a viscous incompressible electrically conducting fluid through a porous medium with variable permeability over a vertical surface in the presence of first order chemical reaction and oscillatory suction. The governing unsteady boundary layer problems are solved numerically.

The main conclusions of this study are as follows:

- Velocity profiles of the fluid increases with increasing values of Grashof number.
- Velocity profiles of the fluid increases with increasing values of modified Grashof number.
- Velocity profiles of the fluid increases with increasing values of Dufour number
- Velocity profiles of the fluid increases with increasing values of porous permeability number.
- Temperature profiles decreases with increases in Dufour number and Prandtl number.
- Concentration profiles decreases with increasing values of Schmidt number and chemical reaction parameter.
- Skin friction increases with increasing values of porous permeability parameter versus Grashof number.

APPENDIX

$$\beta = \left(M + \frac{1}{K}\right),$$

$$m_2 = -\left(\frac{Sc + \sqrt{Sc^2 + 4KrSc}}{2}\right),\ m_4 = -(\Pr),$$

$$m_6 = -\left(\frac{1 + \sqrt{1 + 4\beta}}{2}\right)$$

$$J_1 = \left(\frac{Du \Pr m_2}{m_2^2 + \Pr m_2}\right), J_2 = -\left(\frac{1 + J_1 m_2}{m_2}\right)$$

$$L_1 = -\left(\frac{GrJ_1}{m_2^2 + m_2 - \beta}\right), L_2 = -\left(\frac{GrJ_2}{m_4^2 + m_4 - \beta}\right)$$

$$L_3 = \frac{1}{m_2}\left(\frac{Gc}{m_2^2 + m_2 - \beta}\right), L_4 = (1 - L_1 - L_2 - L_3)$$

REFERENCE

Carnahan B, Luther H A, Wikes J O (1996): Applied Numerical Methods, John Wiely & Sons, New York, USA

Dursunkaya Z, Worek W M (1992): Diffusion thermo and thermal diffusion effects in transient and steady natural convection form a vertical surface, Int. J Heat Mass Transfer, 35: 2060-2065

Gbadeyan J A, Oyekunle T L, Fasogbon P F (2018): Soret and Dufour effects on heat and mass transfer in chemically reacting MHD flow through a wavy channel, Journal of Taibah University for Science, 12 (5),:631-651

Jena S, Mishra S R (2018): Chemical reaction effect on MHD viscoelastic fluid flow over vertical stretching sheet with heat source/sink, Ain Shams Engineering Journal, 9 (4):1205-1213

Mabood F, Khan W, Ismail AI (2015): MHD stagnation point flow and transfer impinging on stretching sheet with chemical reaction and transpiration, Chem. Eng., J., 273:430-437

Moorthy M B K, Senthilvadivu K. (2012): Soret and Dufour effects on natural convection flow past a vertical surface in a porous medium with variable viscosity, Journal of Applied Mathematics

Omowaye A J, Fagbade A I, Ajayi A O. (2015): Dofour and Soret effects on steady MHD convective flow of a fluid in a porous medium with temperature dependent viscosity: Homotopy analysis approach, Journal of the Nigerian Mathematical Society, 34: 343-360

Tasawar Hayat, Tehreem Nasir., Muhammad Ijaz Khan., Ahmed Alsaedi. (2018): Numerical investigation of MHD flow with Soret and Dufour effect, Results in Physics, 8:1017-1022

Tripathy R S, Dash G C, Mishra S R, Baag S. Chemical reaction effects on MHD free convective surface over a moving vertical plate through porous medium, Alexandria Engineering Journal, 2015; 54: 673-679

Rajput U S, Surendra Kumar. Radiation and chemical reaction effect on free convection MHD flow through a porous medium bounded by vertical surface, International Journal of Mathematical Archive, 2011; 2 (12): 2660 – 2669

Reddy T S, Raju M C, Varma S V K. (2013): Chemical reaction and radiation effects on MHD free convection flow through a porous medium bounded by a vertical surface with constant heat and mass flux, Journal of Computation and Applied Research in Mechanical Engineering, 2013; 3 (1): 53-62

Sudershan Reddy G, Ramana Reddy G V, Jayarami Reddy K. Radiation and chemical reaction effects on free convection MHD flow through a porous medium bounded by vertical surface, Advances in Applied Science Research, 2012; 3 (3): 1603-1610

Neild D A and Bejan A. Convection in porous media, Springer, New York, 2006

Inghamand D B and Pop I. Transport Phenomena in porous media, Elsevier, Osford, United Kingdom, 2005

Makinde O D. On MHD heat and mass transfer over a moving vertical plate with a convective surface boundary condition, Candian J. Chem. Engg, 2010; 88 (6): 938-990

Palani G and Srikanth U. MHD flow past a semi-infinite vertical plate with mass transfer, Nonlinear Anal. Model Control, 2009; 14 (3): 345-356

Duwairi H M. Viscous and Joule heating effects on forced convection flow from radiate isothermal porous surfaces, Int. J. Numer. Methods Heat Fluid Flow, 2005; 15 (5): 429-440

Alim M A, Alam M D, Mamun A. Joule heating effect on the coupling of conduction with magneto hydrodynamic free convection flow from a vertical plate, Non-Linear Anal Model Contrl., 2007; 12 (3): 307-316

Uwanta I J. Effects of chemical reaction and radiation heat and mass transfer past a semi-infinite vertical porous plate with constant mass flux and dissipation, Eur. J. Sci. Res., 2012; 87 (2): 190-200

Mansour M A, EI-Anssary, Aly A M. Effect of chemical reaction and viscous dissipation on MHD natural convection flows saturated porous media with suction or injection, Int. J. Appl. Math. Mech., 2008; 4 (2): 60-70

Kandasamy R, Periasamy K, Prabhu K K S. Effects of chemical reaction, heat and mass transfer along a wedge with heat source and concentration in the presence of suction of injection, Int. J. Heat Mass Tran., 2005; 48 (7): 1388-1394

Govardhan K, Kishan N, Balaswamy B. Effect of viscous dissipation and radiation on MHD gas flow and heat and mass transfer over a stretching surface with a uniform free stream, J. Eng. Phys. Thermophys., 2012; 85 (4): 909-916

Hamid A, Khan M. Impacts of binary chemical reaction with activation energy on unsteady flow of magneto-Williamson nanofluid, J. Mol. Liq., 2018; 262: 435-442

Dhlamini M, Kameswaran P K, Sibanda P, Motsa S, Mondal H. Activation energy and binary chemical reaction effects in mixed convective nanofluid flow with convective boundary conditions, J. Comput. Des. Eng., 2019, 6: 149-158

Damala Ch Kesavaiah, P V Satyanarayana and A Sudhakaraiah (2013): Effects of radiation and free convection currents on unsteady Couette flow between two vertical parallel plates with constant heat flux and heat source through porous medium, International Journal of Engineering Research, Vol. 2 (2), pp. 113-118

Srinathuni Lavanya and D Chenna Kesavaiah (2017): Heat transfer to MHD free convection flow of a viscoelastic dusty gas through a porous medium with chemical reaction, International Journal of Pure and Applied Researches, Vol. 3 (1), pp. 43 - 56

D Chenna Kesavaiah and A Sudhakaraiah (2014): Effects of heat and mass flux to MHD flow in vertical surface with radiation absorption, Scholars Journal of Engineering and Technology, 2(2): pp. 219-225

D Chenna Kesavaiah, P V Satyanarayana (2013): MHD and Diffusion Thermo effects on flow accelerated vertical plate with chemical reaction,Indian Journal of Applied Research, Vol. 3 (7), pp. 310-314

DamalaChKesavaiah, P V Satyanarayana and S Venkataramana (2012): Radiation absorption, chemical reaction and magnetic field effects on the free convection and mass transfer flow through porous medium with constant suction and constant heat flux, International Journal of Scientific Engineering and Technology, Vol.1 (6), pp. 274-284,

S Karunakar Reddy, D Chenna Kesavaiah and M N Raja Shekar (2013): MHD heat and mass transfer flow of a viscoelastic fluid past an impulsively started infinite vertical plate with chemical reaction, International Journal of Innovative Research in Science, Engineering and Technology, Vol. 2 (4), pp.973- 981

D Chenna Kesavaiah, P V Satyanarayana, A Sudhakaraiah, S Venkataramana (2013): Natural convection heat transfer oscillatory flow of an elastico-viscous fluid from vertical plate, International Journal of Research in Engineering and Technology, Vol. 2 (6), pp. 959-966

DChKesavaiah, P V Satyanarayana, J Gireesh Kumar and S Venkataramana (2012): Radiation and mass transfer effects on moving vertical plate with variable temperature and viscous Dissipation, International Journal of Mathematical Archive, Vol. 3 (8), pp. 3028-3035

B Mallikarjuna Reddy, D Chenna Kesavaiah and G V Ramana Reddy (2018): Effects of radiation and thermal diffusion on MHD heat transfer flow of a dusty viscoelastic fluid between two moving parallel plates, ARPN Journal of Engineering and Applied Sciences, Vol. 13 (22), pp. 8863-8872

DChennaKesavaiah, P V Satyanarayana and S Venkataramana (2013): Radiation and Thermo - Diffusion effects on mixed convective heat and mass transfer flow of a viscous dissipated fluid over a vertical surface in the presence of chemical reaction with heat source, International Journal of Scientific Engineering and Technology, Vol. 2 (2), pp: 56-72

D Chenna Kesavaiah and B Venkateswarlu (2020): Chemical reaction and radiation absorption effects on convective flows past a porous vertical wavy channel with travelling thermal waves, International Journal of Fluid Mechanics Research, Vol. 47 (2), pp. 153-169

D Chenna Kesavaiah, Ikramuddin Sohail Md , R S Jahagirdar (2018): MHD free convection heat and mass transfer flow past an accelerated vertical plate through a porous medium with effects of hall current, rotation and Dufour effects, Suraj Punj Journal For Multidisciplinary Research, Vol. 8 (11), pp. 46-62

Chenna Kesavaiah Damala, Venkateswarlu Bhumarapu, Oluwole Daniel Makinde (2021): Radiative MHD Walter's Liquid-B flow past a semi-infinite vertical plate in the presence of viscous dissipation with a heat source, Engineering Transactions, Vol. 69(4), pp. 373–401

Bang ChuolNhial, V Nagaraju Vellanki, V Sri HariBabu, G Y Sagar (2022):Hall current, rotation and chemical reaction effects on MHD free convection flow past an accelerated vertical plate through a porous medium, Journal of Positive School Psychology, Vol. 6 (5), pp:707-716

Bang ChuolNhial, V Sri HariBabu, V Nagaraju Vellanki, G Y Sagar (2022):radiation and mass transfer effects on MHD free convection flow over an inclined plate, Journal of Positive School Psychology, Vol 6(5), pp:697-706

V Nagaraju, K Hemalatha and V SrihariBabu. (2019): MHD Viscoelastic Fluid flow Past an Infinite Vertical Plate in the Presence of Radiation and Chemical Reaction, International Journal of Applied Engineering Research, Vol. 14(5), pp: 1062-1069

V Nagaraju, K Hemalatha and V Srihari Babu (2018): Radiation effects on MHD convective heat and mass transfer flow past a semi-infinite vertical moving porous plate in the presence of chemical reaction, International journal of engineering sciences and research technology, 7(8), pp: 146-161

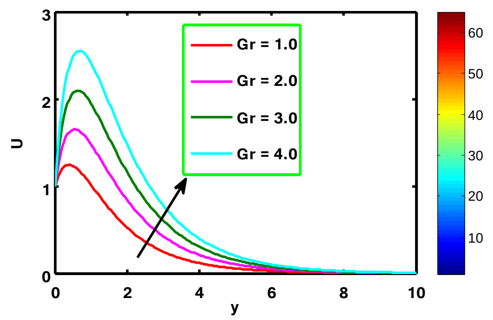

Fig. (2): Velocity Profiles for different values of Gr

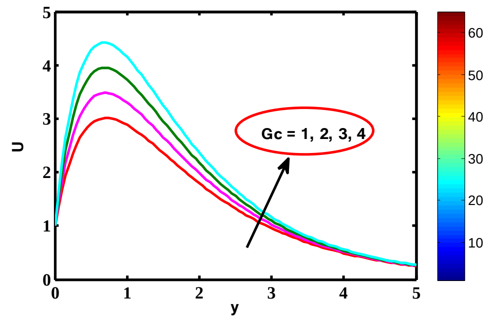

Fig. (3): Velocity Profiles for different values of Gc

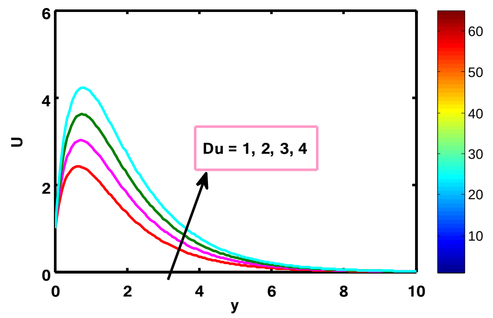

Fig. (4): Velocity Profiles for different values of Du

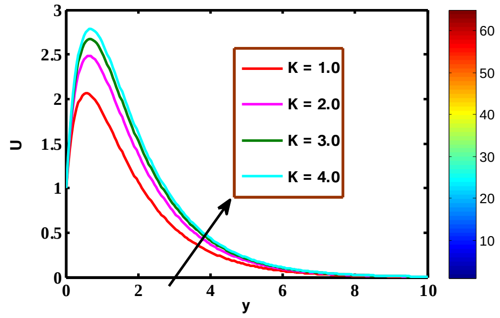

Fig. (5): Velocity Profiles for different values of K

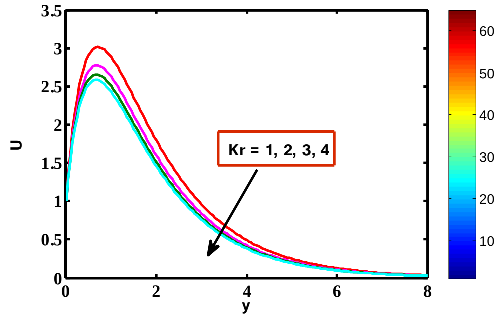

Fig. (6): Velocity Profiles for different values of Kr

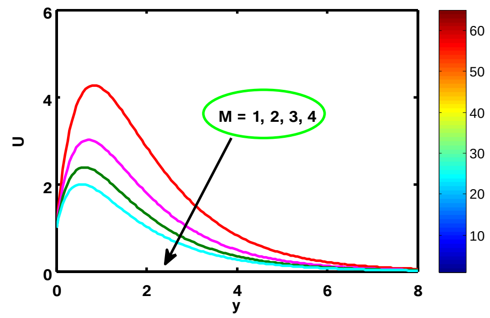

Fig. (7); Velocity profiles for different values of M

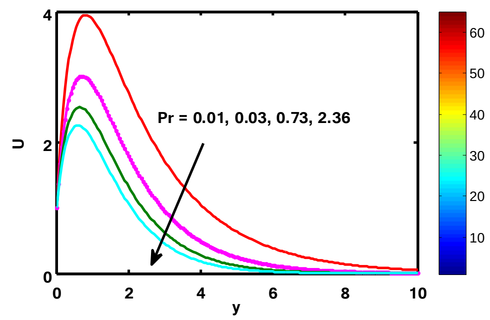

Fig. (8): Velocity Profiles for different values of Pr

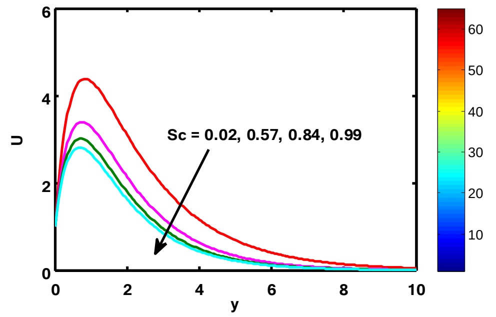

Fig. (9): Velocity Profiles for different values of Sc

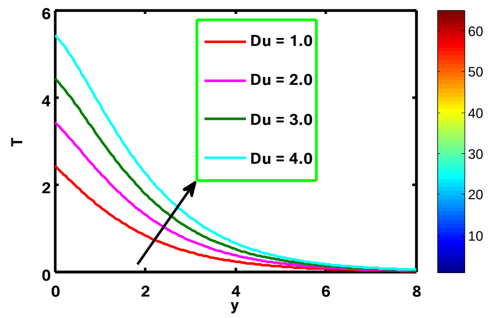

Fig. (10): Temperature profiles for different values of Du

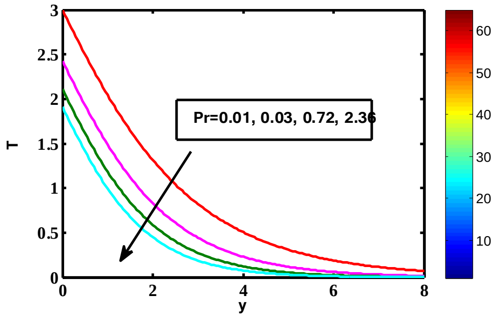

Fig. (11): Temeprature Profiles for different values of Pr

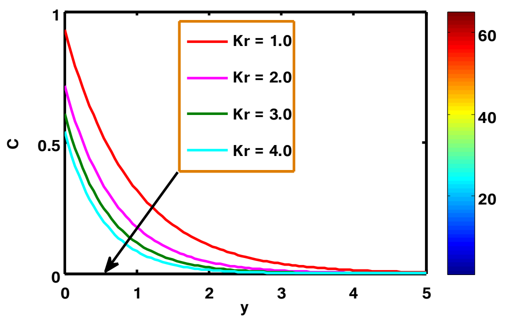

Fig. (12): Concentration profiles for different values of Kr

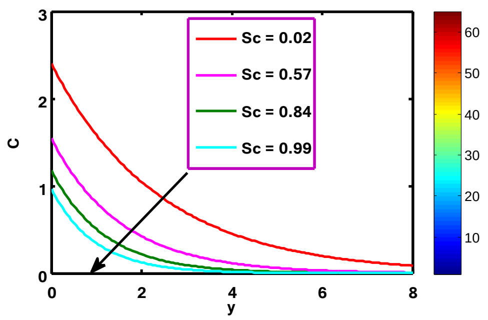

Fig. (13): Concentration profiles for different values of Sc

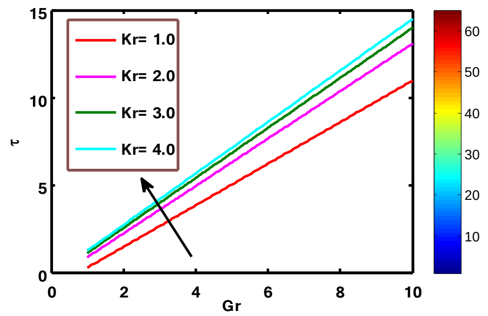

Fig. (14): Skin friction for different values of K versus Gr

RESEARCH ARTICLE

Heat Transfer of A Peristaltic Electro - Osmotic Flow of A Couple Stress Fluid through an Inclined Asymmetric Channel with Effects of Thermal Radiation

K. Venugopal Reddy[1]*, Mantha Srikanth[2] and K. Ramakrishna Reddy[3]

[1]Associate Professor, Department of Mathematics, Malla Reddy Engineering College (Autonomous), Maisammaguda, Hyderabad, Telangana, India.
[2]Assistant Professor, Department of Mathematics, Malla Reddy Engineering College (Autonomous), Maisammaguda, Hyderabad, Telangana, India.
[3]Professor, Department of Mathematics, Malla Reddy Engineering College (Autonomous), Maisammaguda, Hyderabad, Telangana, India.

Received: 02 Sep 2022 Revised: 20 Oct 2022 Accepted: 23 Nov 2022

***Address for Correspondence**
K. Venugopal Reddy
Associate Professor,
Department of Mathematics,
Malla Reddy Engineering College (Autonomous),
Maisammaguda, Hyderabad, Telangana, India.
Email: venugopal.reddy1982@gmail.com

ABSTRACT

The presented article addresses the electro-osmotic peristaltic flow of a couple-stress fluid bounded in an inclined asymmetric micro-channel. The viscous dissipation, Joule heating and chemical reaction effects are employed simultaneously in the flow analysis. Heat and mass transfer have been studied under large wave length and small Reynolds number. The resulting nonlinear systems are solved numerically. The influence of various dominant physical parameters is discussed for velocity, temperature distribution, and the pumping characteristics.

Keywords: Peristaltic flow; Electro-osmotic flow; Couple stress fluid; Magnetic field; Heat transfer; Mass transfer; Inclined asymmetric micro-channel;

INTRODUCTION

Recent investigations in miniaturization and micro-fabrication have taken into assuming a lot of applications extending from organic to refrigerating of microelectronics in [1 - 9]. Many favors such as an important reduction in the utilization of required materials, ability to achieve in-vitro experiments on the continuous motion in a manner

similar to the real situation in a living biological system, being portable and vibration-free are using micro fluidic devices. Electro-osmotic transports with thermal effects of liquids in micro channels are reported in [10]. The heat transfer investigation of electro-osmotic motion in a slowly varying non-symmetric micro-channel is presented in [11]. Stokes developed the couple stress fluid model. When additives are mixed in the fluid then cohesive forces of fluid resists additive factors. This resistance creates a combined force and then a couple stress is generated in the fluid. Such fluid is known as couple stress fluid. This model is regarded as generalization of Newtonian fluid model dealing with body couples and couple stresses in fluid medium. Note that couple stress fluid has an asymmetric stress tensor. Relevant studies in this direction are given in the investigations [12 – 18]. Bio-fluids propel from one place to another place by continuous process of muscle contraction and relaxation. This process is known as peristaltic transport. The peristaltic transport phenomenon is mainly due to the neuromuscular property of any tubular smooth muscle structure. This mechanism is responsible for the transport of biological fluids in several physiological processes such as urine transport from kidney to the bladder, the movement of chyme into the gastrointestinal tract, fluids in the lymphatic vessels, bile from the gallbladder into the duodenum, the embryo transport in non-pregnant uterus, the movement of spermatozoa in the ducts efferent of the male reproductive tract, the movement of the ovum in the fallopian tube and the circulation of blood in small blood vessels are depicted in [19 – 33]. Thus the major focus of this study is to analyze the viscous dissipation, Joule heating effects on MHD electro-osmotic peristaltic flow of couple stress fluid in an inclined asymmetric micro channel. Mathematical formulation of problem is presented. The results are obtained after employing long wavelength and low Reynolds number approximation. The velocity, temperature, concentration, pressure gradient and pressure rise have been proposed for the pertinent parameters of interest.

Mathematical Formulation and analysis

We analyze the electro-osmotic peristaltic flow of an electrically conducting incompressible couple stress fluid and heat transfers through an inclined asymmetric micro-channel with charged walls under the influence of an imposed the magnetic field. The flow is assumed to be asymmetric about x' and the liquid is flowing in the x'-direction. The hydrophobic micro-channel is bounded by slowly varying walls at $y' = h_1(x')$ and $y' = h_2(x')$ respectively, in which the length of the channel (L) is assumed to be much larger than the height, i.e., $L >> (h_1 + h_2)$. Fig. 1 below depicts the schematic diagram of the problem under current study.

Electrical Potential Distribution

The basic theory of electrostatics is related to the local net electric charge density ρ_e in the diffuse layer of EDL and charge density is coupled with the potential distribution ψ' through the Poisson-Boltzmann equation for the symmetric electrolyte is given by

$$\frac{d^2\psi'(y')}{dy'^2} = \frac{2n_0 e z_v}{\varepsilon}\sinh\left(\frac{e z_v \psi'(y')}{k_B T_{av}}\right) \qquad \text{... (3)}$$

where η_o represents the concentration of ions at the bulk, ε is the charge of a proton, z_v is the valence of ions, ε is the permittivity of the medium, k_B is the Boltzmann constant and T_{av} is the boundary conditions for potential function are taken as

$$\psi'(y') = \psi_1' \quad \text{at} \quad y' = h_1'(x'),$$
$$\psi'(y') = \psi_2' \quad \text{at} \quad y' = h_2'(x'), \qquad \text{...(4)}$$

where ψ_1' and ψ_2' are the electric potential at the upper and lower wall respectively. Let us now introduce the following non-dimensional variables,

$$[\psi_O,\psi_1,\psi_2]=\frac{ez_v}{k_B T_{av}}[\psi',\psi_1',\psi_2'],\quad y=\frac{y'}{d_1'}\ \text{ and }\ x=\frac{x'}{L} \qquad (5)$$

The dimensionless form of Eqs. (1) - (2) and the Poisson-Boltzmann equation defined in (3) take in the following form,

$$h_1(x)=\frac{h_1'}{d_1'}=1+a\cos(2\pi x), \qquad (6)$$

$$h_2(x)=\frac{h_2'}{d_1'}=-d-b\cos(2\pi x+\phi), \qquad (7)$$

and

$$\frac{d^2\psi_O}{dy^2}=k^2\sinh(\psi_O), \qquad (8)$$

where $a=\frac{a_1'}{d_1'}$, $b=\frac{a_2'}{d_1'}$, $d=\frac{d_2'}{d_1'}$ and $k=\frac{d_1'}{\lambda}$ is defined as the electro-osmotic parameter, λ_2 is the reciprocal of the EDL thickness and is defined by $\frac{1}{\lambda}=\left(\frac{2n_o e^2 z_v^2}{\varepsilon k_B T_{av}}\right)^{\frac{1}{2}}$. Thus the electro-osmotic parameter is inversely proportional to EDL thickness λ. The dimensionless form of boundary conditions defined in (4) using the dimensionless variables (5) reduce to

$$\psi_o(y)=\psi_1 \quad \text{at} \quad y=h_1(x),$$
$$\psi_o(y)=\psi_2 \quad \text{at} \quad y=h_2(x). \qquad (9)$$

We assumed that the electric potential is much smaller than the thermal potential for which the Debye-Hiickel linearization principle can be approximated as $\sinh(x)\approx x$. On the basis of this assumption, the solution of Poisson-Boltzmann equation (8) takes in the form

$$\frac{d^2\psi_o}{dy^2}=k^2\psi_o\ . \qquad (10)$$

Finally, by employing the boundary conditions (9), the closed form solution of the equation (10) is given as

$$\psi_o(y)=F_1\cosh(ky)+F_2\sinh(ky)\ . \qquad (11)$$

Couple Stress fluid Model

The given set of pertinent field equations governing the flow, in laboratory frame is

$$\frac{\partial U}{\partial X}+\frac{\partial V}{\partial Y}=0 \qquad (12)$$

$$\rho\left(\frac{\partial U}{\partial t}+U\frac{\partial U}{\partial X}+V\frac{\partial U}{\partial Y}\right)=-\frac{\partial P}{\partial X}+\mu\left(\frac{\partial^2 U}{\partial X^2}+\frac{\partial^2 U}{\partial Y^2}\right)-\eta\left(\frac{\partial^4 U}{\partial X^4}+2\frac{\partial^4 U}{\partial X^2\partial Y^2}+\frac{\partial^4 U}{\partial Y^4}\right)-\sigma B_0^2 U-\frac{\mu}{k_o}U+\rho g\beta_T(T-T_0)\sin\alpha+\rho_e E$$

(13)

$$\rho\left(\frac{\partial V}{\partial t}+U\frac{\partial V}{\partial X}+V\frac{\partial V}{\partial Y}\right)=-\frac{\partial P}{\partial Y}+\mu\left(\frac{\partial^2 V}{\partial X^2}+\frac{\partial^2 V}{\partial Y^2}\right)-\eta\left(\frac{\partial^4 V}{\partial X^4}+2\frac{\partial^4 V}{\partial X^2\partial Y^2}+\frac{\partial^4 V}{\partial Y^4}\right)$$
$$-\frac{\mu}{k_o}V+\rho g\beta_T\left(T-T_0\right)\cos\alpha \quad (14)$$

$$\rho c_p\left(\frac{\partial T}{\partial t}+U\frac{\partial T}{\partial X}+V\frac{\partial T}{\partial Y}\right)=k^*\left(\frac{\partial^2 T}{\partial X^2}+\frac{\partial^2 T}{\partial Y^2}\right)+Q_0-\frac{\partial q_r}{\partial Y}+\sigma B_0^2u^2+\sigma E^2 \quad (15)$$

where (U,V) are the velocity components in the laboratory frame, ρ is the density, P is the pressure, μ is the viscosity coefficient , η is the couple stress viscosity parameter, σ is the electric conductivity of the fluid, B_0 is the applied transverse magnetic field, k_0 is the permeability parameter, g is the acceleration due to the gravity, β_T and β_C are the coefficient of thermal and concentration expansions, T is the temperature , α is the inclination angle, c_p is the specific heat at constant pressure, k^* is the thermal conductivity , Q_0 is the dimensional heat absorption coefficient, C is the concentration in the reference to fixed frame system, D is the coefficient of mass diffusivity, K_T is the thermal diffusion ratio, T_m is the mean temperature, k_1 is the chemical reaction parameter and α is the inclination angle. The radiative heat flux in the $X-$direction is considered as negligible compared to $Y-$direction. By using Rosseland approximation for thermal radiation, the radiative heat flux q_r is specified by

$$q_r=-\frac{16\sigma^* T_o^3}{3k^*}\frac{\partial T}{\partial Y} \quad (16)$$

where σ^* and k^* are the Stefan-Boltzmann constant and the mean absorption coefficient respectively.
The coordinates and velocities in the wave frame (x,y) and the laboratory frame (X,Y) in a coordinate system moving with the wave speed c in which the boundary shape is stationary and are related by

$$x=X-ct, y=Y, u=U-c, v=V, p(x,y)=P(X,Y,t), \bar{T}(x,y)=T(X,Y,t) \quad (17)$$

where u,v are the velocity components, p is the pressure, T is the temperature and C is the concentration in the wave frame. Introducing the following non-dimensional quantities

$$\bar{x}=\frac{x}{\lambda},\bar{y}=\frac{y}{d_1},\bar{u}=\frac{u}{c},\bar{v}=\frac{v}{c}, h_1=\frac{H_1}{d_1}, h_2=\frac{H_2}{d_1}, \bar{t}=\frac{ct}{\lambda}, \bar{p}=\frac{d_1^2}{\lambda\mu C}p, \delta=\frac{d_1}{\lambda},$$
$$d=\frac{d_2}{d_1}, a=\frac{a_1}{d_1}, b=\frac{a_2}{d_1}, \mathrm{Re}=\frac{\rho c d_1}{\mu}, M=\sqrt{\frac{\sigma}{\mu}}B_0 d_1, Da=\frac{k_0}{d_1^2}, \gamma=\sqrt{\frac{\mu}{\eta}}d_1,$$
$$Gr=\frac{\rho g d_1^2\beta_T\left(T_1-T_0\right)}{\mu C}, \bar{\psi}=\frac{\psi}{cd_1}, \mathrm{Pr}=\frac{\mu c_p}{k^*}, \theta=\frac{\bar{T}-\bar{T}_0}{\bar{T}_1-\bar{T}_0}, \beta=\frac{Q_0 d_1^2}{k^*\left(\bar{T}_1-\bar{T}_0\right)}, Sc=\frac{\mu}{\rho D},$$
$$\gamma_1=k_1\frac{d_1^2}{\upsilon}, Rd=\frac{16\sigma^* T_o^3}{3k^*\bar{\mu}_o c_f}, C_o=\frac{\left(-\frac{d\bar{p}}{d\bar{X}}\right)d_1^2}{\mu U_{HS}} \quad (18)$$

where δ is the dimensionless wave number, Re is the Reynolds number, M is the Hartmann number, Da is the Darcy number, γ is the couple stress parameter, Gr is the local temperature Grashof number, Pr is the Prandtl number, Rd is the thermal radiation parameter, β is the heat generation parameter, γ_1 is the chemical reaction parameter, Sr is the Soret number and A is the Joule heating parameter. Using the above transformations (17) and (18) and non-dimensional quantities (19), the governing flow field equations (13) - (15), after dropping the bars, we get

The dimensional equations of the couple stress fluid are

$$\frac{\partial^4\psi}{\partial y^4}-\frac{1}{\gamma^2}\frac{\partial^6\psi}{\partial y^6}-\left(M^2+\frac{1}{Da}\right)\frac{\partial^2\psi}{\partial y^2}+\frac{d^3\psi_o}{dy^3}+Gr\frac{\partial\theta}{\partial y}\sin\alpha=0 \tag{19}$$

$$\frac{(1+Rd)}{\mathrm{Pr}}\frac{\partial^2\theta}{\partial y^2}+Ec\left[\left(\frac{\partial^2\psi}{\partial y^2}\right)^2+\frac{1}{\gamma^2}\left(\frac{\partial^3\psi}{\partial y^3}\right)^2\right]+EcM^2\left(\frac{\partial\psi}{\partial y}\right)^2+A=0 \tag{20}$$

with the corresponding boundary conditions are

$$\psi=\frac{F}{2},\ \frac{\partial\psi}{\partial y}+L\frac{\partial^2\psi}{\partial y^2}=-1,\frac{\partial^3\psi}{\partial y^3}=0,\theta=0 \text{ at } y=h_1=1+a\cos(2\pi x) \tag{21}$$

$$\psi=-\frac{F}{2},\ \frac{\partial\psi}{\partial y}-L\frac{\partial^2\psi}{\partial y^2}=-1,\frac{\partial^3\psi}{\partial y^3}=0,\theta=1 \text{ at } y=h_2=-d-b\cos(2\pi x+\phi) \tag{22}$$

where L is the velocity slip parameter and F is the flux in the wave frame and the constants a, b, ϕ and d should satisfy the relation

$$a^2+b^2+2ab\cos\phi\le(1+d)^2. \tag{23}$$

The dimensionless mean flow rate Θ in the fixed frame is related to the non-dimensional mean flow rate F in wave frame by

$$\Theta=F+1+d$$

(24)

and in which

$$F=\int_{h_1}^{h_2}\frac{\partial\psi}{\partial y}dy \tag{25}$$

Numerical Solution

The solution of system of coupled non –linear Eqs. (20) - (22) with corresponding boundary conditions in Eq. (23) – (24) are obtained using NDSolve in Mathematica computational software. This section contains the plots and related analyses for different embedded parameters. This section includes the graphs for velocity, temperature, concentration and pressure gradient.

Velocity distribution

Fig. 2 displays the velocity profile for various values of Hartmann number. The velocity decreases and drops with Hartmann number M. Fig. 3 depicts velocity profiles of different values of parameter for osmosis parameter. Velocity profile is seen to raise as osmosis parameter k enlarges. Fig. 4 depicts that the consequences of the parameter λ_1 on the profile of velocity. It is clear that enhance the strength of λ_1 resulted in enhancing the velocity. Fig. 5 indicate that the velocity rises with increasing Da. Fig. 6 reveals that velocity is seen to decrease with the higher values of couple stress parameter. Fig. 7 shows that velocity diminishes with increasing L.

Temperature distribution

Fig. 8 – 11 depicts the deviations in temperature profiles for various values of parameters A, k, Ec and $\Pr$. Fig. 8 presents the consequences of the parameter A on the profile of temperature. It is clear that enhance the strength of A resulted in increasing the temperature. Fig. 9 shows that temperature rises with enhancing k. Fig. 10 shows that the temperature enhances significantly with a rise in Ec. Fig. 11 shows a very significant effect of $\Pr$ on the temperature profiles. It is clear from this figure that the Brinkman number has a impulse to diminish the temperature in the micro-channel. It may be inferred that the thermal conductivity of the fluid declines by enhancing the ratio of momentum diffusivity to thermal diffusivity.

Pumping characteristics

Figs. 13 - 15 represent the profiles of pressure gradient $\left(\frac{dp}{dx}\right)$ for the effects of Slip parameter (L), Osmosis parameter (k) and the couple stress parameter (γ). The pressure gradient has oscillatory behavior in the whole range of the x-axis. From all figures, it is clear that the pressure gradient diminishes with the higher values of L, k and γ. The pressure rise is a significant physical measure in the peristaltic mechanism. The results are prepared and discussed for different physical parameters of interest through Figs. 16 – 18 and which are plotted for dimensionless pressure rise ΔP_λ versus the dimensionless flow rate Θ to the effects of Hartmann number M, chemical reaction parameter γ_1, heat generation parameter β and couple stress parameter γ. The pumping regions are peristaltic pumping are $(\Theta > 0, \Delta P_\lambda > 0)$, augment pumping $(\Theta < 0, \Delta P_\lambda < 0)$, retrograde pumping $(\Theta < 0, \Delta P_\lambda > 0)$, co pumping $(\Theta > 0, \Delta P_\lambda < 0)$ and free pumping $(\Theta = 0, \Delta P_\lambda = 0)$. Fig. 16 is depicted that the pressure rise ΔP_λ depressing with an enhance in Hartmann number M in the both peristaltic pumping region and free pumping region. Fig. 17 depicts that the quite opposite nature that of for the effect of the heat generation parameter β.The influence of couple stress fluid parameter γ on the pressure rise is decreases and which is elucidated from Fig. 18.

Nusselt number

Figs. (19) – (21) exhibits the influence of incorporated parameters such as Hartmann number M, Osmosis parameter k and Joule heating parameter A respectively on magnitude of Nusselt number. The heat transfer coefficient has oscillatory in nature due to peristaltic motion of walls. The heat transfer rate enhances for M, k and A from Figs. 19 - 21.

Sherwood number

The mass transfer coefficient shows the impact of different parameters of λ_1 and k from Figs. 22 – 23. Fig. 22 depicts the Sherwood number depresses with the impact of λ_1 whereas it observes the mass transfer coefficient enhances as the parameter k rises from Fig. 23.

Trapping Phenomenon

The phenomenon of trapping in flow of fluid is trapping and is presented by drawing streamlines in the Figs. 24 - 27. A bolus is having by splitting of a streamline under important conditions and it is followed along with the wave in the wave frame. This process is called trapping. The bolus of trapping is observed to expand by enhancing M from Figs. 24 – 25. However the size of bolus decreases by the rising effects of λ_1 as shown in Figs. 26 – 27.

Concluding Remarks

We have investigated the peristaltic transport of a heat and mass transfer of couple stress fluid on the combined impacts of electro-osmotically and pressure driven flow in an inclined asymmetric micro channel whose walls are varying sinusoidally with different wave trains. Effects of thermal radiation, chemical reaction and Joule heating have been accounted. The numerical solution for velocity, temperature distribution, concentration distribution and pumping characteristics are presented using small wave length and small Reynolds number. The important findings of present study are summarized as follows

- The Electro – osmotic flow of couple stress fluids in an inclined asymmetric channel is strongly depend on Debye length.
- Velocity diminishes with an enhance of L and γ.
- Temperature rises with an strength of A where as depresses with an enhance of Rd .
- It is observed that pressure gradient has oscillatory behavior.
- Pressure rise decreases with an effect of increasing γ
- The absence of Electro – Osmosis, our results are in good agreement with Gnaneswara Reddy *et al.* [33].

REFERENCES

1. K.P. Tikhomolova, Electro-Osmosis, Ellis Horwood, London, 1993.
2. H. Ginsburg, Analysis of plant root electro-potentials, J. Theor. Biol. 37 (1972) 389 – 412.
3. V. Sansalone, J. Kaiser, S. Naili, T. Lemaire, Interstitial fluid flow within bone canaliculi and electro-chemo-mechanica features of the canalicular milieu, Biomech. Model. Mechanobiol. 12 (2013) 533 – 553.
4. E.A. Marshall, The osmotic flow of an electrolyte through a charged porous membrane, J. Theor. Biol. 66 (1977) 107 – 135.
5. S. Grimnes, Skin impedance and electro-osmosis in the human epidermis, Med. Biol. Eng. Compu. 21 (1983) 739 – 749.
6. T.A. Davis, Electrodialysis, in: M.C. Porter (Ed.), Handbook of Industrial Membrane Technology, Noyes Publications, New Jersey, USA, 1990.
7. V. Orsat, G.S.V. Raghavan, E.R. Norris, Food processing waste dewatering by electro- osmosis, Can. Agric. Eng. 38 (1996) 063 – 067.
8. A. Manz, C.S. Effenhauser, N. Burggraf, D.J. Harrison, K. Seiler, K. Fluri, J. Micromech. Microeng. 4 (1994) 257.
9. G.D. Ngoma, F. Erchiqui, Pressure gradient and electroosmotic effects on two immiscible fluids in a microchannel between two parallel plates, J. Micromech. Microeng. 16 (2005) 83 – 90.
10. T.S. Zhao, Q. Liao, Thermal effects on electro-osmotic pumping of liquids in microchannels, J. Micromech. Microeng. 12 (2002) 962.

11. A. Mondal and G.C. Shit, Heat transfer analysis on electro-osmotic flow in a slowly varying asymmetric micro-channel, European Journal of Mechanics-B/Fluids, 60 (2016) 1 - 35.
12. VK. Stokes, Couple stresses in fluids, Phys Fluids, 9 (1966) 1709 – 15.
13. M. Devakar, V. Iyengar, Stokes problems for an in compressible couple stress fluid, Nonlinear Anal Model Control 2008:181 – 90.
14. JS Duan, X Qui, Stokes second problem of viscoelastic fluids with constitutive equation of distributed-order derivative. Appl. Math. Comput. 331(2018)130 – 9.
15. K. Ramesh, Influence of heat and mass transfer on peristaltic flow of couplestress fluid through porous medium in the presence of i nclined magnetic field in an inclined asymmetric channel. J. Mol. Liq.219 (2016) 256 – 71.
16. A. Alsaedi, N Ali, D.Tripathi, T. Hayat, Peristaltic flow of couple stress fluid through uniform porous medium. Appl Math Mech. 35 (2014) 469 – 80.
17. K. Kaladhar, Natural convection flow of couple stress fluid in a vertical channel with Hall and Joule heating effects. Proc.Eng . 127 (2015) 1071 – 8.
18. T. Hayat, M. Iqbal, H Yasmin, F Alsaadi. Hall effects on peristaltic flow of couple stress fluid in an inclined asymmetric channel. Int. J. Bio mathematics, 7(2014)1450057(34pages).
19. T.W. Latham, Fluid motion in a peristaltic pump, MIT Press, Cambridge Mass, USA.
20. A.H. Shapiro, M.Y. Jaffrin, and S.L. Weinberg (1969), Peristaltic pumping with long wavelengths at low Reynolds numbers, J. Fluid Mech., 37 (1969) 799–825.
21. Mekheimer Kh.S., and Elmaboud Y.A., Peristaltic flow of a couple stress fluid in an annulus application of an endoscope. Physica A., Vol. 387, pp. 2403–2415.
22. O.D., Makinde, and P.Y. Mhone (2006), Hydromagnetic effects on internal flow separation in a diverging channel, Romanian Journal of Physics, Vol. 51, pp. 959-966.
23. 23. Hayat T., Javed M., and Ali N., (2008), MHD peristaltic transport of Jeffrey fluid in a channel with compliant walls and porous space, Transp. Porous Media, Vol. 74, pp. 259–274.
24. Mekheimer Kh.S., and Abd elmaboud Y., (2008), Peristaltic flow of a couple stress fluid in an annulus: application of an endoscope, Physica A, Vol. 38, pp. 2403–2415.
25. Adesanya S.O., and Makinde O.D., (2012), Heat transfer to magneto hydrodynamic non-Newtonian couple stress pulsatile flow between two parallel porous plates, Zeitschrift for Naturforschung , Vol. 67a, pp. 647 – 656.
26. Adesanya S.O., and Makinde O.D., (2015), Irreversibility analysis in a couple stress film flow along an inclined heated plate with adiabatic free surface, Physica A, Vol. 432, pp. 222-229.
27. Gnaneswara Reddy M., and Venugopal Reddy K., (2016), Impact of velocity slip and joule heating on MHD peristaltic flow through a porous medium with chemical reaction, Journal of the Nigerian Mathematical society, Vol. 35, pp. 227 - 244.
28. M. Gnaneswara Reddy, K. Venugopal Reddy, and O.D. Makinde, Hydromagnetic peristaltic motion of a reacting and radiating couple Stress fluid in an inclined asymmetric channel filled with a porous medium, Alexandria Engineering Journal, 55 (2016) 1841–1853.
29. M. Mishra, and A. R. Rao, Peristaltic transport of a Newtonian fluid in an asymmetric channel, Z.Angew, Math. Phys., 53 (2003) 532 - 550.
30. M. Kothandapani, and S. Srinivas, Peristatltic transport of a Jeffrey fluid under the effect of magnetic field in an asymmetric channel, Int. J. Nonlinear Mech.,43 (2008) 915–924.
31. F. M. Abbasi, T. Hayat, B. Ahmad, and B. Chen, (2015), Peristaltic flow with convective mass condition and thermal radiation, J. Cent. South Univ., 22 (2015) 2369–2375.
32. M. Gnaneswara Reddy, K. Venugopal Reddy, and O.D. Makinde, (2016) Hydromagnetic peristaltic motion of a reacting and radiating couple Stress fluid in an inclined asymmetric channel filled with a porous medium, Alexandria Engineering Journal, 55 (2016) 1841 - 1853.
33. M. Gnaneswara Reddy, K. Venugopal Reddy, and O.D. Makinde, Heat transfer on MHD peristaltic rotating flow of a Jeffrey fluid in an asymmetric channel, International Journal of Applied and Computational Mathematics, DOI 10.1007/s40819-016-0293-1 (2016).

34. O.D. Makinde, M. Gnaneswara Reddy, and K. Venugopal Reddy, Effects of thermal radiation on MHD peristaltic Motion of Walters-B Fluid with heat source and Slip conditions, Journal of Applied and Fluid Mechanics, 10(2017)1105-1112.

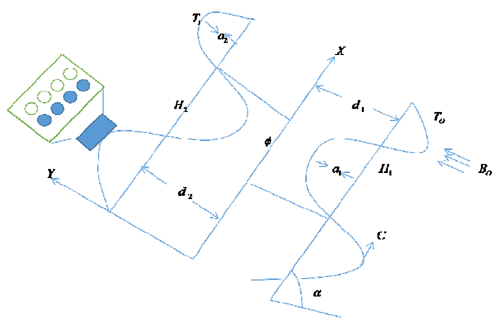

Fig. 1. Physical Model

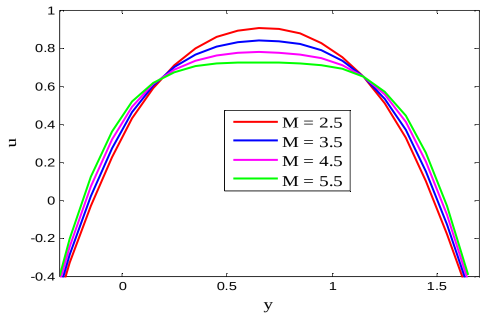

Fig.2. u **for** M

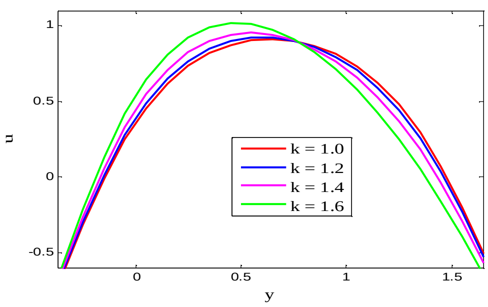

Fig.3. u **for** k

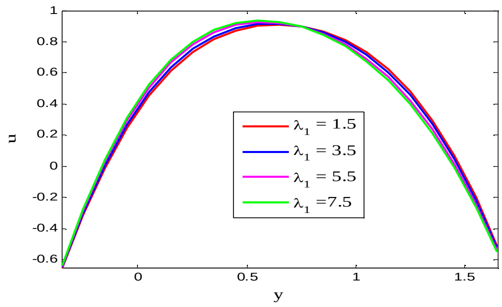

Fig. 4. u **for** λ_1

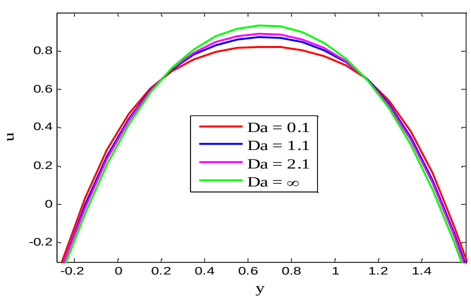

Fig. 5. u **for** Da

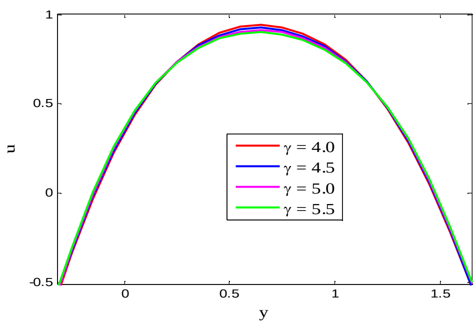

Fig. 6. u **for** γ

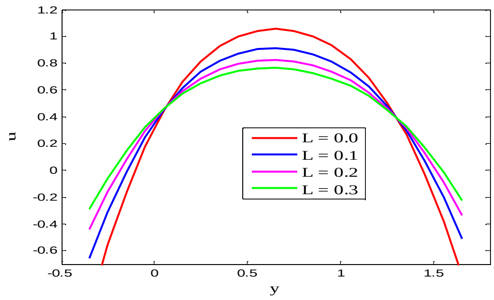

Fig. 7. u **for** L

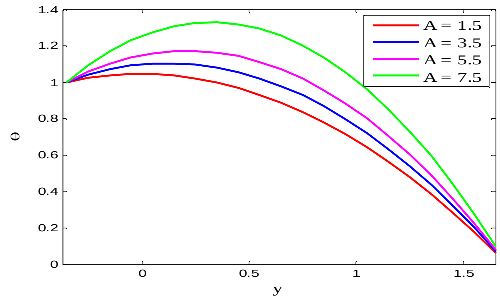

Fig. 8. θ **for** A

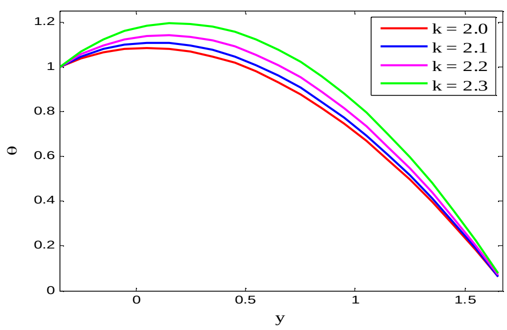

Fig. 9. θ **for** k

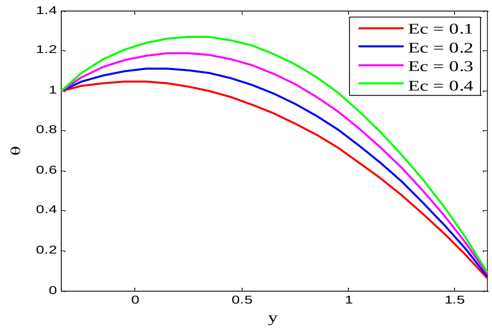

Fig. 10. θ **for** Ec

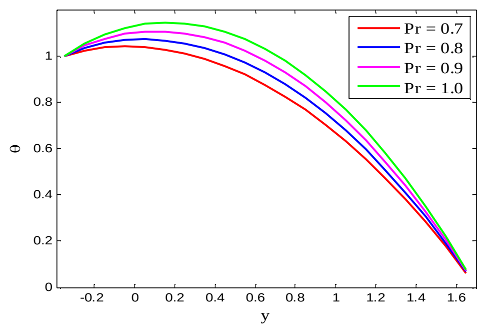

Fig. 11. θ **for** $\Pr$

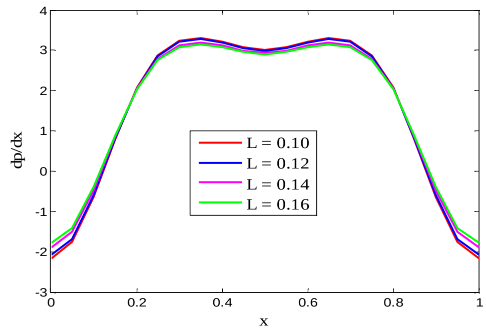

Fig. 12. $\dfrac{dp}{dx}$ **for** L

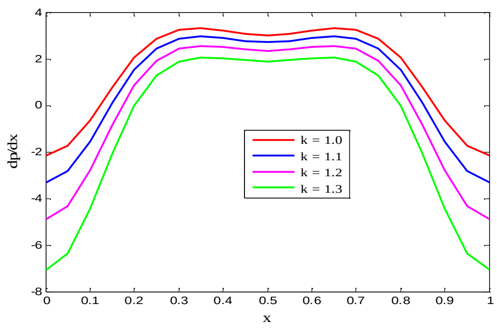

Fig. 13. $\frac{dp}{dx}$ **for** k

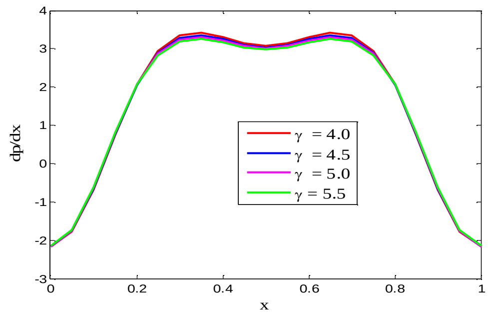

Fig. 14. $\frac{dp}{dx}$ **for** γ

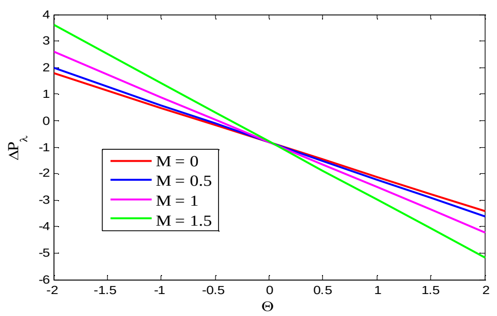

Fig. 15 ΔP_λ **for** M

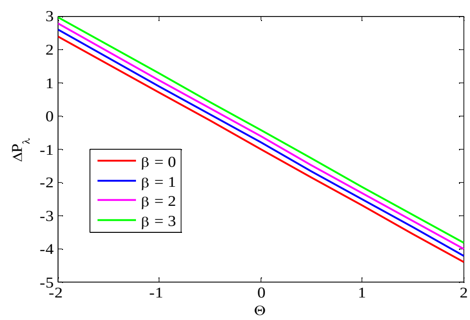

Fig. 16. ΔP_λ **for** β

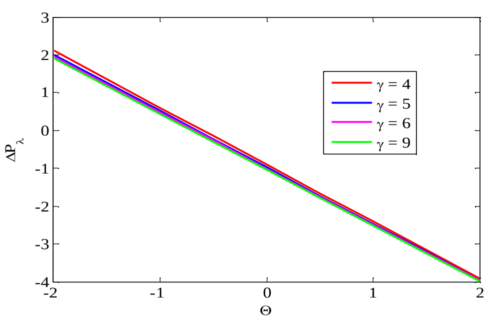

Fig. 17. ΔP_λ **for** γ

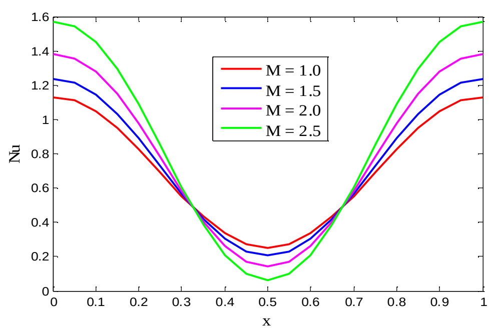

Fig. 18. Nu **for** M

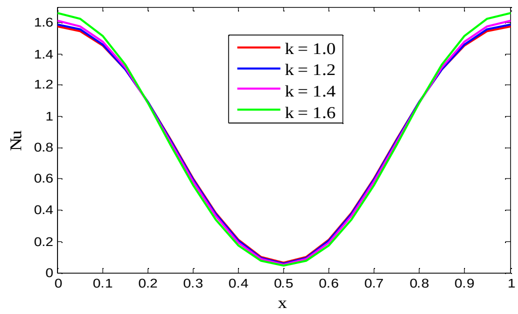

Fig. 19. Nu **for** k

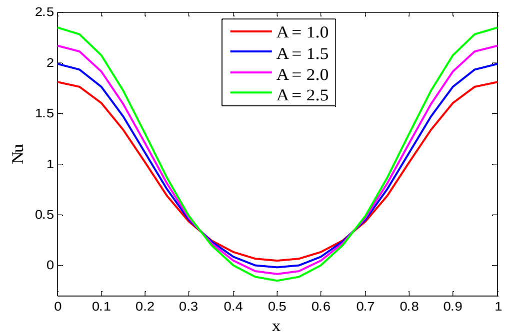

Fig. 20. Nu **for** A

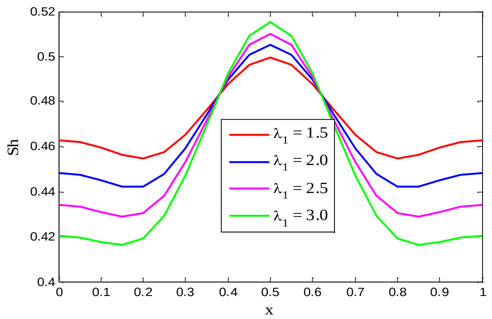

Fig. 21. Sh **for** λ_1

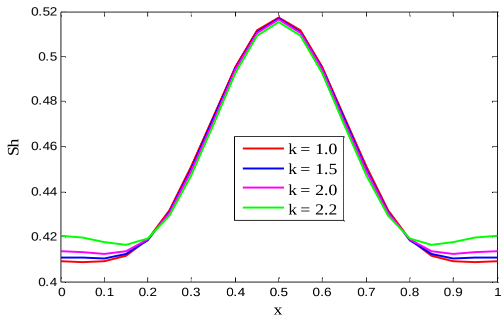

Fig. 22. Sh **for** k

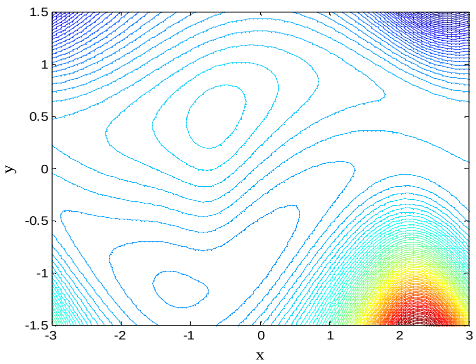

Fig. 23. Effect of M **on stream lines for** $M = 1.5$.

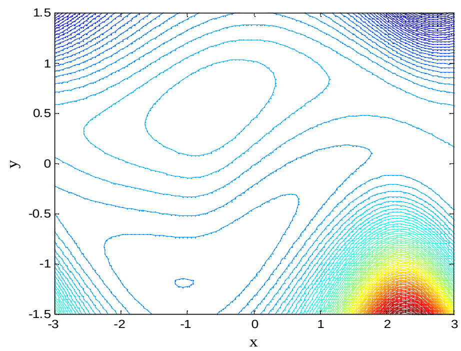

Fig.24. Effect of M **on stream lines for** $M = 1.6$.

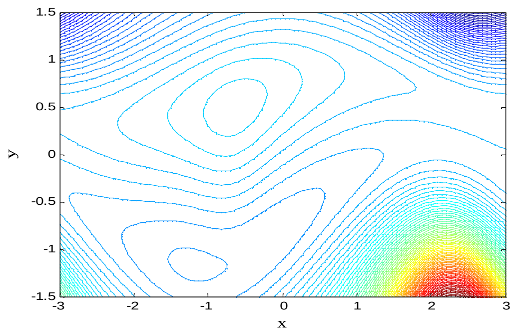	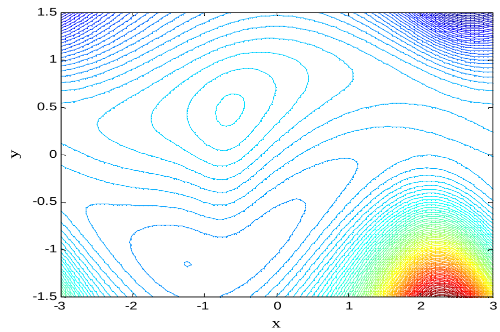
Fig.25. Effect of λ_1 on stream lines for $\lambda_1 = 1.5$.	**Fig.26. Effect of λ_1 on stream lines for $\lambda_1 = 1.6$.**

RESEARCH ARTICLE

Heat Transfer of A Peristaltic Electro - Osmotic Flow of A Couple Stress Fluid through an Inclined Asymmetric Channel with Effects of Thermal Radiation

K. Venugopal Reddy[1]*, Mantha Srikanth[2] and K. Ramakrishna Reddy[3]

[1]Associate Professor, Department of Mathematics, Malla Reddy Engineering College (Autonomous), Maisammaguda, Hyderabad, Telangana, India.
[2]Assistant Professor, Department of Mathematics, Malla Reddy Engineering College (Autonomous), Maisammaguda, Hyderabad, Telangana, India.
[3]Professor, Department of Mathematics, Malla Reddy Engineering College (Autonomous), Maisammaguda, Hyderabad, Telangana, India.

Received: 02 Sep 2022 Revised: 20 Oct 2022 Accepted: 23 Nov 2022

***Address for Correspondence**
K. Venugopal Reddy
Associate Professor,
Department of Mathematics,
Malla Reddy Engineering College (Autonomous),
Maisammaguda, Hyderabad, Telangana, India.
Email: venugopal.reddy1982@gmail.com

ABSTRACT

The presented article addresses the electro-osmotic peristaltic flow of a couple-stress fluid bounded in an inclined asymmetric micro-channel. The viscous dissipation, Joule heating and chemical reaction effects are employed simultaneously in the flow analysis. Heat and mass transfer have been studied under large wave length and small Reynolds number. The resulting nonlinear systems are solved numerically. The influence of various dominant physical parameters is discussed for velocity, temperature distribution, and the pumping characteristics.

Keywords: Peristaltic flow; Electro-osmotic flow; Couple stress fluid; Magnetic field; Heat transfer; Mass transfer; Inclined asymmetric micro-channel;

INTRODUCTION

Recent investigations in miniaturization and micro-fabrication have taken into assuming a lot of applications extending from organic to refrigerating of microelectronics in [1 - 9]. Many favors such as an important reduction in the utilization of required materials, ability to achieve in-vitro experiments on the continuous motion in a manner

similar to the real situation in a living biological system, being portable and vibration-free are using micro fluidic devices. Electro-osmotic transports with thermal effects of liquids in micro channels are reported in [10]. The heat transfer investigation of electro-osmotic motion in a slowly varying non-symmetric micro-channel is presented in [11]. Stokes developed the couple stress fluid model. When additives are mixed in the fluid then cohesive forces of fluid resists additive factors. This resistance creates a combined force and then a couple stress is generated in the fluid. Such fluid is known as couple stress fluid. This model is regarded as generalization of Newtonian fluid model dealing with body couples and couple stresses in fluid medium. Note that couple stress fluid has an asymmetric stress tensor. Relevant studies in this direction are given in the investigations [12 – 18]. Bio-fluids propel from one place to another place by continuous process of muscle contraction and relaxation. This process is known as peristaltic transport. The peristaltic transport phenomenon is mainly due to the neuromuscular property of any tubular smooth muscle structure. This mechanism is responsible for the transport of biological fluids in several physiological processes such as urine transport from kidney to the bladder, the movement of chyme into the gastrointestinal tract, fluids in the lymphatic vessels, bile from the gallbladder into the duodenum, the embryo transport in non-pregnant uterus, the movement of spermatozoa in the ducts efferent of the male reproductive tract, the movement of the ovum in the fallopian tube and the circulation of blood in small blood vessels are depicted in [19 – 33]. Thus the major focus of this study is to analyze the viscous dissipation, Joule heating effects on MHD electro-osmotic peristaltic flow of couple stress fluid in an inclined asymmetric micro channel. Mathematical formulation of problem is presented. The results are obtained after employing long wavelength and low Reynolds number approximation. The velocity, temperature, concentration, pressure gradient and pressure rise have been proposed for the pertinent parameters of interest.

Mathematical Formulation and analysis

We analyze the electro-osmotic peristaltic flow of an electrically conducting incompressible couple stress fluid and heat transfers through an inclined asymmetric micro-channel with charged walls under the influence of an imposed the magnetic field. The flow is assumed to be asymmetric about x' and the liquid is flowing in the x'-direction. The hydrophobic micro-channel is bounded by slowly varying walls at $y' = h_1(x')$ and $y' = h_2(x')$ respectively, in which the length of the channel (L) is assumed to be much larger than the height, i.e., $L >> (h_1 + h_2)$. Fig. 1 below depicts the schematic diagram of the problem under current study.

Electrical Potential Distribution

The basic theory of electrostatics is related to the local net electric charge density ρ_e in the diffuse layer of EDL and charge density is coupled with the potential distribution ψ' through the Poisson-Boltzmann equation for the symmetric electrolyte is given by

$$\frac{d^2\psi'(y')}{dy'^2} = \frac{2n_0 e z_v}{\varepsilon}\sinh\left(\frac{e z_v \psi'(y')}{k_B T_{av}}\right) \qquad \text{... (3)}$$

where η_o represents the concentration of ions at the bulk, ε is the charge of a proton, z_v is the valence of ions, ε is the permittivity of the medium, k_B is the Boltzmann constant and T_{av} is the boundary conditions for potential function are taken as

$$\psi'(y') = \psi_1' \quad \text{at} \quad y' = h_1'(x'),$$
$$\psi'(y') = \psi_2' \quad \text{at} \quad y' = h_2'(x'), \qquad \text{...(4)}$$

where ψ_1' and ψ_2' are the electric potential at the upper and lower wall respectively. Let us now introduce the following non-dimensional variables,

$$[\psi_O,\psi_1,\psi_2]=\frac{ez_v}{k_B T_{av}}[\psi',\psi_1',\psi_2'],\quad y=\frac{y'}{d_1'}\ \text{ and }\ x=\frac{x'}{L} \tag{5}$$

The dimensionless form of Eqs. (1) - (2) and the Poisson-Boltzmann equation defined in (3) take in the following form,

$$h_1(x)=\frac{h_1'}{d_1'}=1+a\cos(2\pi x), \tag{6}$$

$$h_2(x)=\frac{h_2'}{d_1'}=-d-b\cos(2\pi x+\phi), \tag{7}$$

and

$$\frac{d^2\psi_O}{dy^2}=k^2\sinh(\psi_O), \tag{8}$$

where $a=\frac{a_1'}{d_1'}$, $b=\frac{a_2'}{d_1'}$, $d=\frac{d_2'}{d_1'}$ and $k=\frac{d_1'}{\lambda}$ is defined as the electro-osmotic parameter, λ_2 is the reciprocal of the EDL thickness and is defined by $\frac{1}{\lambda}=\left(\frac{2n_o e^2 z_v^2}{\varepsilon k_B T_{av}}\right)^{\frac{1}{2}}$. Thus the electro-osmotic parameter is inversely proportional to EDL thickness λ. The dimensionless form of boundary conditions defined in (4) using the dimensionless variables (5) reduce to

$$\psi_o(y)=\psi_1 \quad \text{at} \quad y=h_1(x),$$

$$\psi_o(y)=\psi_2 \quad \text{at} \quad y=h_2(x). \tag{9}$$

We assumed that the electric potential is much smaller than the thermal potential for which the Debye-Hiickel linearization principle can be approximated as $\sinh(x)\approx x$. On the basis of this assumption, the solution of Poisson-Boltzmann equation (8) takes in the form

$$\frac{d^2\psi_o}{dy^2}=k^2\psi_o\ . \tag{10}$$

Finally, by employing the boundary conditions (9), the closed form solution of the equation (10) is given as

$$\psi_o(y)=F_1\cosh(ky)+F_2\sinh(ky)\ . \tag{11}$$

Couple Stress fluid Model

The given set of pertinent field equations governing the flow, in laboratory frame is

$$\frac{\partial U}{\partial X}+\frac{\partial V}{\partial Y}=0 \tag{12}$$

$$\rho\left(\frac{\partial U}{\partial t}+U\frac{\partial U}{\partial X}+V\frac{\partial U}{\partial Y}\right)=-\frac{\partial P}{\partial X}+\mu\left(\frac{\partial^2 U}{\partial X^2}+\frac{\partial^2 U}{\partial Y^2}\right)-\eta\left(\frac{\partial^4 U}{\partial X^4}+2\frac{\partial^4 U}{\partial X^2\partial Y^2}+\frac{\partial^4 U}{\partial Y^4}\right)-\sigma B_0^2 U-\frac{\mu}{k_o}U+$$
$$\rho g\beta_T(T-T_0)\sin\alpha+\rho_e E \tag{13}$$

$$\rho\left(\frac{\partial V}{\partial t}+U\frac{\partial V}{\partial X}+V\frac{\partial V}{\partial Y}\right)=-\frac{\partial P}{\partial Y}+\mu\left(\frac{\partial^2 V}{\partial X^2}+\frac{\partial^2 V}{\partial Y^2}\right)-\eta\left(\frac{\partial^4 V}{\partial X^4}+2\frac{\partial^4 V}{\partial X^2\partial Y^2}+\frac{\partial^4 V}{\partial Y^4}\right)$$
$$-\frac{\mu}{k_o}V+\rho g\beta_T\left(T-T_0\right)\cos\alpha \tag{14}$$

$$\rho c_p\left(\frac{\partial T}{\partial t}+U\frac{\partial T}{\partial X}+V\frac{\partial T}{\partial Y}\right)=k^*\left(\frac{\partial^2 T}{\partial X^2}+\frac{\partial^2 T}{\partial Y^2}\right)+Q_0-\frac{\partial q_r}{\partial Y}+\sigma B_0^2 u^2+\sigma E^2 \tag{15}$$

where (U,V) are the velocity components in the laboratory frame, ρ is the density, P is the pressure, μ is the viscosity coefficient , η is the couple stress viscosity parameter, σ is the electric conductivity of the fluid, B_0 is the applied transverse magnetic field, k_0 is the permeability parameter, g is the acceleration due to the gravity, β_T and β_C are the coefficient of thermal and concentration expansions, T is the temperature , α is the inclination angle, c_p is the specific heat at constant pressure, k^* is the thermal conductivity , Q_0 is the dimensional heat absorption coefficient, C is the concentration in the reference to fixed frame system, D is the coefficient of mass diffusivity, K_T is the thermal diffusion ratio, T_m is the mean temperature, k_1 is the chemical reaction parameter and α is the inclination angle. The radiative heat flux in the $X-$direction is considered as negligible compared to $Y-$direction. By using Rosseland approximation for thermal radiation, the radiative heat flux q_r is specified by

$$q_r=-\frac{16\sigma^* T_o^3}{3k^*}\frac{\partial T}{\partial Y} \tag{16}$$

where σ^* and k^* are the Stefan-Boltzmann constant and the mean absorption coefficient respectively.
The coordinates and velocities in the wave frame (x,y) and the laboratory frame (X,Y) in a coordinate system moving with the wave speed c in which the boundary shape is stationary and are related by

$$x=X-ct,y=Y,u=U-c,v=V,p(x,y)=P(X,Y,t),\bar{T}(x,y)=T(X,Y,t) \tag{17}$$

where u,v are the velocity components, p is the pressure, T is the temperature and C is the concentration in the wave frame. Introducing the following non-dimensional quantities

$$\bar{x}=\frac{x}{\lambda},\bar{y}=\frac{y}{d_1},\bar{u}=\frac{u}{c},\bar{v}=\frac{v}{c},\ h_1=\frac{H_1}{d_1},\ h_2=\frac{H_2}{d_1},\ \bar{t}=\frac{ct}{\lambda},\ \bar{p}=\frac{d_1^2}{\lambda\mu C}p,\ \delta=\frac{d_1}{\lambda},$$
$$d=\frac{d_2}{d_1},\ a=\frac{a_1}{d_1},b=\frac{a_2}{d_1},\mathrm{Re}=\frac{\rho c d_1}{\mu},M=\sqrt{\frac{\sigma}{\mu}}B_0 d_1,\ Da=\frac{k_0}{d_1^2},\ \gamma=\sqrt{\frac{\mu}{\eta}}d_1,$$
$$Gr=\frac{\rho g d_1^2\beta_T\left(T_1-T_0\right)}{\mu C},\bar{\psi}=\frac{\psi}{cd_1},\Pr=\frac{\mu c_p}{k^*},\ \theta=\frac{\bar{T}-\bar{T}_0}{\bar{T}_1-\bar{T}_0},\ \beta=\frac{Q_0 d_1^2}{k^*\left(\bar{T}_1-\bar{T}_0\right)},\ Sc=\frac{\mu}{\rho D},$$
$$\gamma_1=k_1\frac{d_1^2}{\upsilon},\ Rd=\frac{16\sigma^* T_o^3}{3k^*\bar{\mu}_o c_f},C_o=\frac{\left(-\frac{d\bar{p}}{d\bar{X}}\right)d_1^2}{\mu U_{HS}} \tag{18}$$

where δ is the dimensionless wave number, Re is the Reynolds number, M is the Hartmann number, Da is the Darcy number, γ is the couple stress parameter, Gr is the local temperature Grashof number, Pr is the Prandtl number, Rd is the thermal radiation parameter, β is the heat generation parameter, γ_1 is the chemical reaction parameter, Sr is the Soret number and A is the Joule heating parameter. Using the above transformations (17) and (18) and non-dimensional quantities (19), the governing flow field equations (13) - (15), after dropping the bars, we get

The dimensional equations of the couple stress fluid are

$$\frac{\partial^4\psi}{\partial y^4}-\frac{1}{\gamma^2}\frac{\partial^6\psi}{\partial y^6}-\left(M^2+\frac{1}{Da}\right)\frac{\partial^2\psi}{\partial y^2}+\frac{d^3\psi_o}{dy^3}+Gr\frac{\partial\theta}{\partial y}\sin\alpha=0 \tag{19}$$

$$\frac{(1+Rd)}{\mathrm{Pr}}\frac{\partial^2\theta}{\partial y^2}+Ec\left[\left(\frac{\partial^2\psi}{\partial y^2}\right)^2+\frac{1}{\gamma^2}\left(\frac{\partial^3\psi}{\partial y^3}\right)^2\right]+EcM^2\left(\frac{\partial\psi}{\partial y}\right)^2+A=0 \tag{20}$$

with the corresponding boundary conditions are

$$\psi=\frac{F}{2},\ \frac{\partial\psi}{\partial y}+L\frac{\partial^2\psi}{\partial y^2}=-1,\frac{\partial^3\psi}{\partial y^3}=0,\theta=0 \text{ at } y=h_1=1+a\cos(2\pi x) \tag{21}$$

$$\psi=-\frac{F}{2},\ \frac{\partial\psi}{\partial y}-L\frac{\partial^2\psi}{\partial y^2}=-1,\frac{\partial^3\psi}{\partial y^3}=0,\theta=1 \text{ at } y=h_2=-d-b\cos(2\pi x+\phi) \tag{22}$$

where L is the velocity slip parameter and F is the flux in the wave frame and the constants a, b, ϕ and d should satisfy the relation

$$a^2+b^2+2ab\cos\phi\le(1+d)^2. \tag{23}$$

The dimensionless mean flow rate Θ in the fixed frame is related to the non-dimensional mean flow rate F in wave frame by

$$\Theta=F+1+d$$

(24)

and in which

$$F=\int_{h_1}^{h_2}\frac{\partial\psi}{\partial y}dy \tag{25}$$

Numerical Solution

The solution of system of coupled non –linear Eqs. (20) - (22) with corresponding boundary conditions in Eq. (23) – (24) are obtained using NDSolve in Mathematica computational software. This section contains the plots and related analyses for different embedded parameters. This section includes the graphs for velocity, temperature, concentration and pressure gradient.

Velocity distribution

Fig. 2 displays the velocity profile for various values of Hartmann number. The velocity decreases and drops with Hartmann number M. Fig. 3 depicts velocity profiles of different values of parameter for osmosis parameter. Velocity profile is seen to raise as osmosis parameter k enlarges. Fig. 4 depicts that the consequences of the parameter λ_1 on the profile of velocity. It is clear that enhance the strength of λ_1 resulted in enhancing the velocity. Fig. 5 indicate that the velocity rises with increasing Da. Fig. 6 reveals that velocity is seen to decrease with the higher values of couple stress parameter. Fig. 7 shows that velocity diminishes with increasing L.

Temperature distribution

Fig. 8 – 11 depicts the deviations in temperature profiles for various values of parameters A, k, Ec and $\Pr$. Fig. 8 presents the consequences of the parameter A on the profile of temperature. It is clear that enhance the strength of A resulted in increasing the temperature. Fig. 9 shows that temperature rises with enhancing k. Fig. 10 shows that the temperature enhances significantly with a rise in Ec. Fig. 11 shows a very significant effect of $\Pr$ on the temperature profiles. It is clear from this figure that the Brinkman number has a impulse to diminish the temperature in the micro-channel. It may be inferred that the thermal conductivity of the fluid declines by enhancing the ratio of momentum diffusivity to thermal diffusivity.

Pumping characteristics

Figs. 13 - 15 represent the profiles of pressure gradient $\left(\frac{dp}{dx}\right)$ for the effects of Slip parameter (L), Osmosis parameter (k) and the couple stress parameter (γ). The pressure gradient has oscillatory behavior in the whole range of the x-axis. From all figures, it is clear that the pressure gradient diminishes with the higher values of L, k and γ. The pressure rise is a significant physical measure in the peristaltic mechanism. The results are prepared and discussed for different physical parameters of interest through Figs. 16 – 18 and which are plotted for dimensionless pressure rise ΔP_λ versus the dimensionless flow rate Θ to the effects of Hartmann number M, chemical reaction parameter γ_1, heat generation parameter β and couple stress parameter γ. The pumping regions are peristaltic pumping are $(\Theta > 0, \Delta P_\lambda > 0)$, augment pumping $(\Theta < 0, \Delta P_\lambda < 0)$, retrograde pumping $(\Theta < 0, \Delta P_\lambda > 0)$, co pumping $(\Theta > 0, \Delta P_\lambda < 0)$ and free pumping $(\Theta = 0, \Delta P_\lambda = 0)$. Fig. 16 is depicted that the pressure rise ΔP_λ depressing with an enhance in Hartmann number M in the both peristaltic pumping region and free pumping region. Fig. 17 depicts that the quite opposite nature that of for the effect of the heat generation parameter β .The influence of couple stress fluid parameter γ on the pressure rise is decreases and which is elucidated from Fig. 18.

Nusselt number

Figs. (19) – (21) exhibits the influence of incorporated parameters such as Hartmann number M, Osmosis parameter k and Joule heating parameter A respectively on magnitude of Nusselt number. The heat transfer coefficient has oscillatory in nature due to peristaltic motion of walls. The heat transfer rate enhances for M, k and A from Figs. 19 - 21.

Sherwood number

The mass transfer coefficient shows the impact of different parameters of λ_1 and k from Figs. 22 – 23. Fig. 22 depicts the Sherwood number depresses with the impact of λ_1 whereas it observes the mass transfer coefficient enhances as the parameter k rises from Fig. 23.

Trapping Phenomenon

The phenomenon of trapping in flow of fluid is trapping and is presented by drawing streamlines in the Figs. 24 - 27. A bolus is having by splitting of a streamline under important conditions and it is followed along with the wave in the wave frame. This process is called trapping. The bolus of trapping is observed to expand by enhancing M from Figs. 24 – 25. However the size of bolus decreases by the rising effects of λ_1 as shown in Figs. 26 – 27.

Concluding Remarks

We have investigated the peristaltic transport of a heat and mass transfer of couple stress fluid on the combined impacts of electro-osmotically and pressure driven flow in an inclined asymmetric micro channel whose walls are varying sinusoidally with different wave trains. Effects of thermal radiation, chemical reaction and Joule heating have been accounted. The numerical solution for velocity, temperature distribution, concentration distribution and pumping characteristics are presented using small wave length and small Reynolds number. The important findings of present study are summarized as follows

- The Electro – osmotic flow of couple stress fluids in an inclined asymmetric channel is strongly depend on Debye length.
- Velocity diminishes with an enhance of L and γ.
- Temperature rises with an strength of A where as depresses with an enhance of Rd .
- It is observed that pressure gradient has oscillatory behavior.
- Pressure rise decreases with an effect of increasing γ
- The absence of Electro – Osmosis, our results are in good agreement with Gnaneswara Reddy *et al.* [33].

REFERENCES

1. K.P. Tikhomolova, Electro-Osmosis, Ellis Horwood, London, 1993.
2. H. Ginsburg, Analysis of plant root electro-potentials, J. Theor. Biol. 37 (1972) 389 – 412.
3. V. Sansalone, J. Kaiser, S. Naili, T. Lemaire, Interstitial fluid flow within bone canaliculi and electro-chemo-mechanica features of the canalicular milieu, Biomech. Model. Mechanobiol. 12 (2013) 533 – 553.
4. E.A. Marshall, The osmotic flow of an electrolyte through a charged porous membrane, J. Theor. Biol. 66 (1977) 107 – 135.
5. S. Grimnes, Skin impedance and electro-osmosis in the human epidermis, Med. Biol. Eng. Compu. 21 (1983) 739 – 749.
6. T.A. Davis, Electrodialysis, in: M.C. Porter (Ed.), Handbook of Industrial Membrane Technology, Noyes Publications, New Jersey, USA, 1990.
7. V. Orsat, G.S.V. Raghavan, E.R. Norris, Food processing waste dewatering by electro- osmosis, Can. Agric. Eng. 38 (1996) 063 – 067.
8. A. Manz, C.S. Effenhauser, N. Burggraf, D.J. Harrison, K. Seiler, K. Fluri, J. Micromech. Microeng. 4 (1994) 257.
9. G.D. Ngoma, F. Erchiqui, Pressure gradient and electroosmotic effects on two immiscible fluids in a microchannel between two parallel plates, J. Micromech. Microeng. 16 (2005) 83 – 90.
10. T.S. Zhao, Q. Liao, Thermal effects on electro-osmotic pumping of liquids in microchannels, J. Micromech. Microeng. 12 (2002) 962.

11. A. Mondal and G.C. Shit, Heat transfer analysis on electro-osmotic flow in a slowly varying asymmetric micro-channel, European Journal of Mechanics-B/Fluids, 60 (2016) 1 - 35.
12. VK. Stokes, Couple stresses in fluids, Phys Fluids, 9 (1966) 1709 – 15.
13. M. Devakar, V. Iyengar, Stokes problems for an in compressible couple stress fluid, Nonlinear Anal Model Control 2008:181 – 90.
14. JS Duan, X Qui, Stokes second problem of viscoelastic fluids with constitutive equation of distributed-order derivative. Appl. Math. Comput. 331(2018)130 – 9.
15. K. Ramesh, Influence of heat and mass transfer on peristaltic flow of couplestress fluid through porous medium in the presence of i nclined magnetic field in an inclined asymmetric channel. J. Mol. Liq.219 (2016) 256 – 71.
16. A. Alsaedi, N Ali, D.Tripathi, T. Hayat, Peristaltic flow of couple stress fluid through uniform porous medium. Appl Math Mech. 35 (2014) 469 – 80.
17. K. Kaladhar, Natural convection flow of couple stress fluid in a vertical channel with Hall and Joule heating effects. Proc.Eng . 127 (2015) 1071 – 8.
18. T. Hayat, M. Iqbal, H Yasmin, F Alsaadi. Hall effects on peristaltic flow of couple stress fluid in an inclined asymmetric channel. Int. J. Bio mathematics, 7(2014)1450057(34pages).
19. T.W. Latham, Fluid motion in a peristaltic pump, MIT Press, Cambridge Mass, USA.
20. A.H. Shapiro, M.Y. Jaffrin, and S.L. Weinberg (1969), Peristaltic pumping with long wavelengths at low Reynolds numbers, J. Fluid Mech., 37 (1969) 799–825.
21. Mekheimer Kh.S., and Elmaboud Y.A., Peristaltic flow of a couple stress fluid in an annulus application of an endoscope. Physica A., Vol. 387, pp. 2403–2415.
22. O.D., Makinde, and P.Y. Mhone (2006), Hydromagnetic effects on internal flow separation in a diverging channel, Romanian Journal of Physics, Vol. 51, pp. 959-966.
23. 23. Hayat T., Javed M., and Ali N., (2008), MHD peristaltic transport of Jeffrey fluid in a channel with compliant walls and porous space, Transp. Porous Media, Vol. 74, pp. 259–274.
24. Mekheimer Kh.S., and Abd elmaboud Y., (2008), Peristaltic flow of a couple stress fluid in an annulus: application of an endoscope, Physica A, Vol. 38, pp. 2403–2415.
25. Adesanya S.O., and Makinde O.D., (2012), Heat transfer to magneto hydrodynamic non-Newtonian couple stress pulsatile flow between two parallel porous plates, Zeitschrift for Naturforschung , Vol. 67a, pp. 647 – 656.
26. Adesanya S.O., and Makinde O.D., (2015), Irreversibility analysis in a couple stress film flow along an inclined heated plate with adiabatic free surface, Physica A, Vol. 432, pp. 222-229.
27. Gnaneswara Reddy M., and Venugopal Reddy K., (2016), Impact of velocity slip and joule heating on MHD peristaltic flow through a porous medium with chemical reaction, Journal of the Nigerian Mathematical society, Vol. 35, pp. 227 - 244.
28. M. Gnaneswara Reddy, K. Venugopal Reddy, and O.D. Makinde, Hydromagnetic peristaltic motion of a reacting and radiating couple Stress fluid in an inclined asymmetric channel filled with a porous medium, Alexandria Engineering Journal, 55 (2016) 1841–1853.
29. M. Mishra, and A. R. Rao, Peristaltic transport of a Newtonian fluid in an asymmetric channel, Z.Angew, Math. Phys., 53 (2003) 532 - 550.
30. M. Kothandapani, and S. Srinivas, Peristatltic transport of a Jeffrey fluid under the effect of magnetic field in an asymmetric channel, Int. J. Nonlinear Mech.,43 (2008) 915–924.
31. F. M. Abbasi, T. Hayat, B. Ahmad, and B. Chen, (2015), Peristaltic flow with convective mass condition and thermal radiation, J. Cent. South Univ., 22 (2015) 2369–2375.
32. M. Gnaneswara Reddy, K. Venugopal Reddy, and O.D. Makinde, (2016) Hydromagnetic peristaltic motion of a reacting and radiating couple Stress fluid in an inclined asymmetric channel filled with a porous medium, Alexandria Engineering Journal, 55 (2016) 1841 - 1853.
33. M. Gnaneswara Reddy, K. Venugopal Reddy, and O.D. Makinde, Heat transfer on MHD peristaltic rotating flow of a Jeffrey fluid in an asymmetric channel, International Journal of Applied and Computational Mathematics, DOI 10.1007/s40819-016-0293-1 (2016).

34. O.D. Makinde, M. Gnaneswara Reddy, and K. Venugopal Reddy, Effects of thermal radiation on MHD peristaltic Motion of Walters-B Fluid with heat source and Slip conditions, Journal of Applied and Fluid Mechanics, 10(2017)1105-1112.

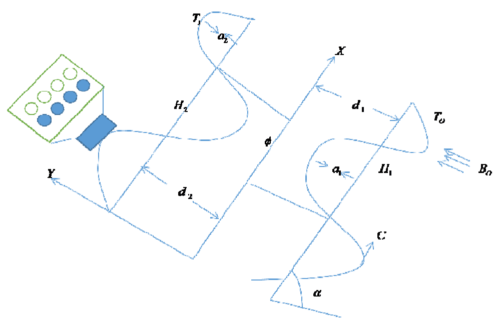

Fig. 1. Physical Model

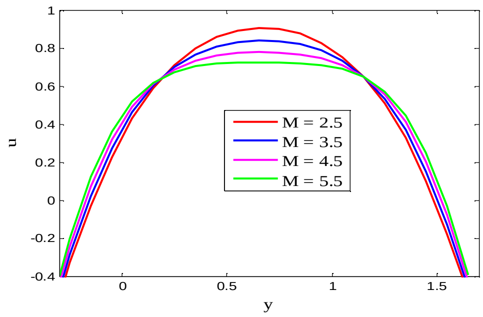

Fig.2. u **for** M

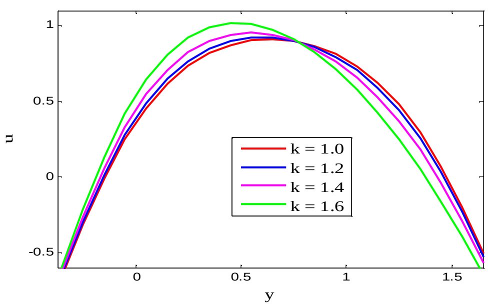

Fig.3. u **for** k

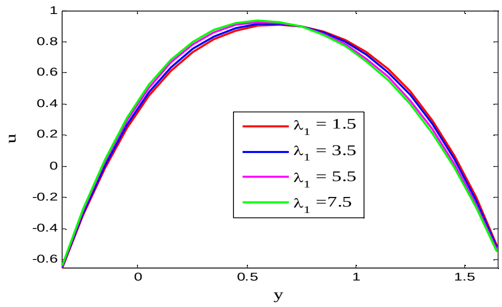

Fig. 4. u **for** λ_1

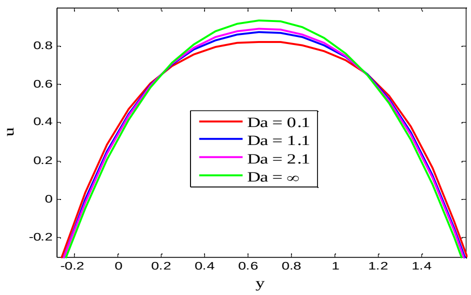

Fig. 5. u **for** Da

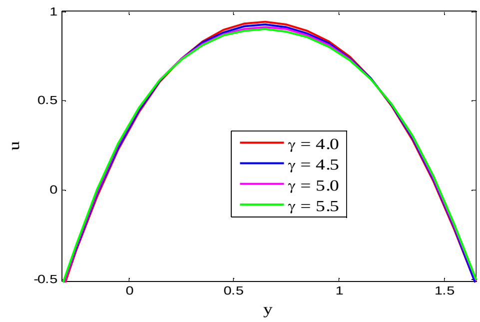

Fig. 6. u **for** γ

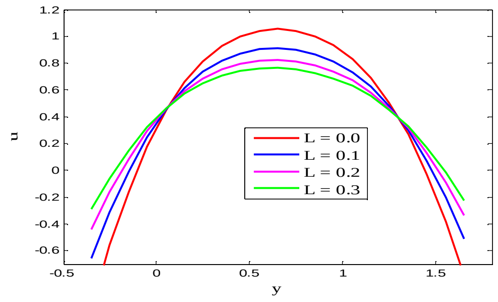

Fig. 7. u **for** L

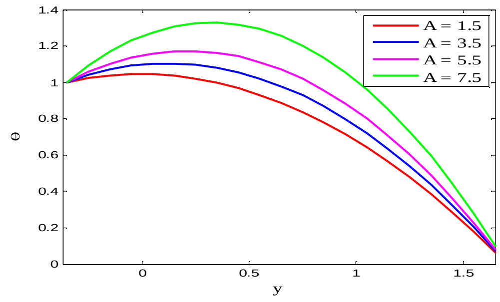

Fig. 8. θ **for** A

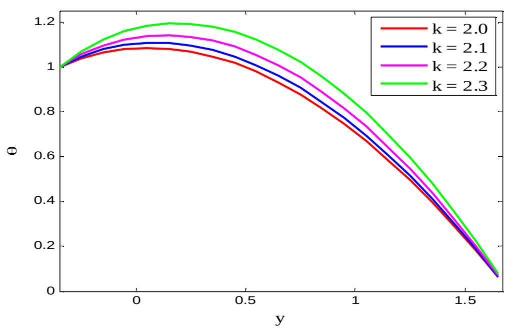

Fig. 9. θ **for** k

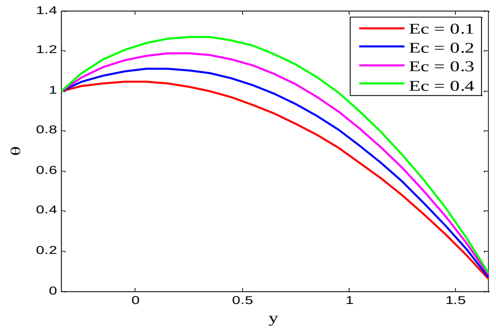

Fig. 10. θ **for** Ec

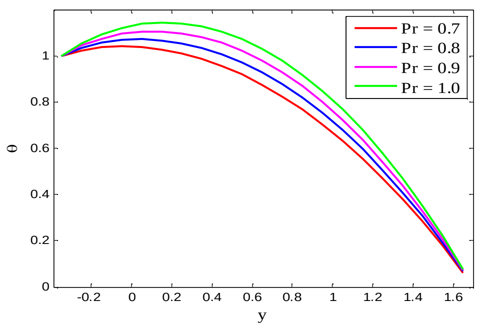

Fig. 11. θ **for** $\Pr$

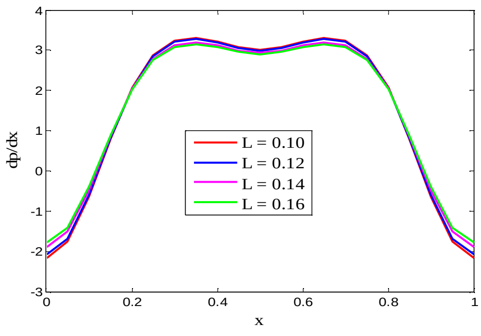

Fig. 12. $\dfrac{dp}{dx}$ **for** L

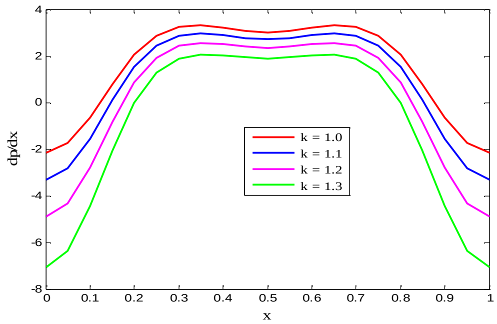

Fig. 13. $\frac{dp}{dx}$ **for** k

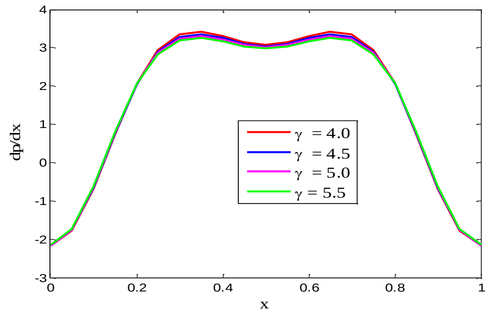

Fig. 14. $\frac{dp}{dx}$ **for** γ

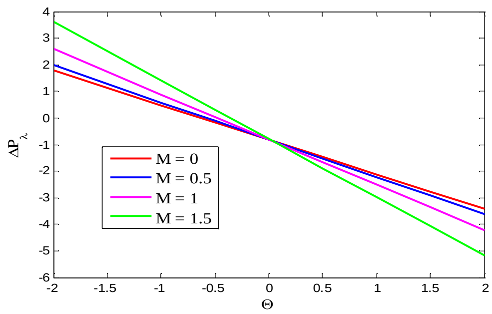

Fig. 15 ΔP_{λ} **for** M

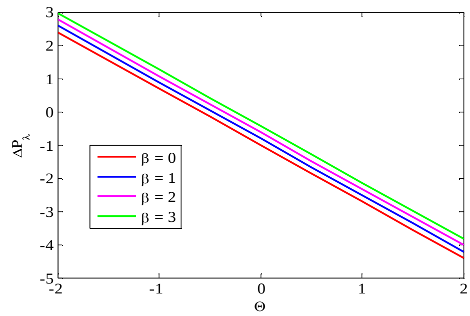

Fig. 16. ΔP_{λ} **for** β

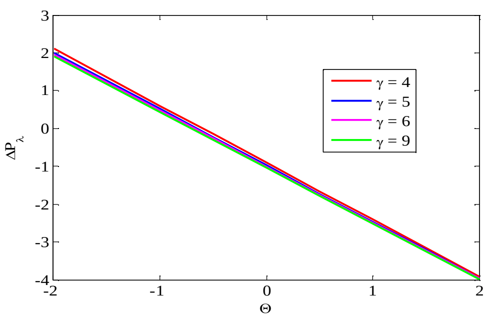

Fig. 17. ΔP_{λ} **for** γ

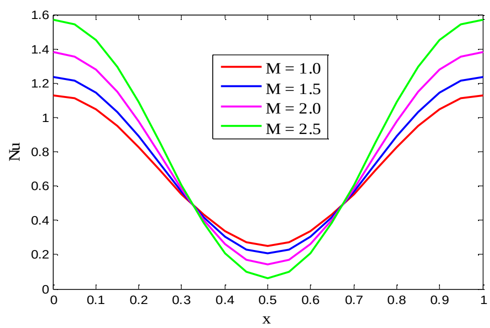

Fig. 18. Nu **for** M

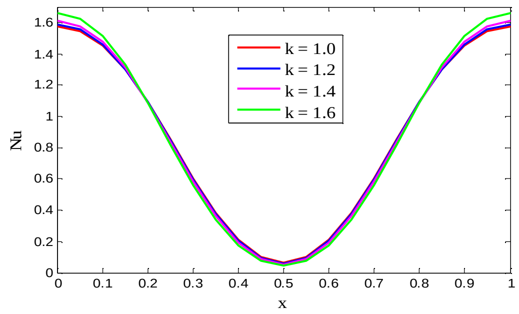

Fig. 19. Nu **for** k

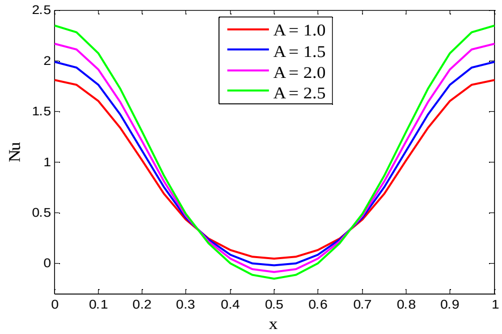

Fig. 20. Nu **for** A

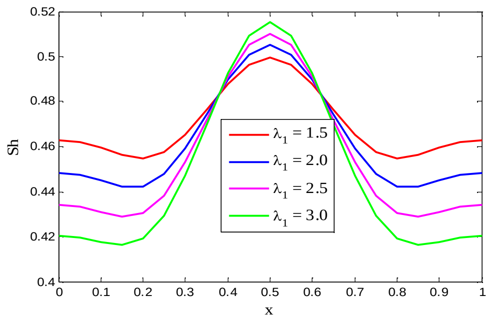

Fig. 21. Sh **for** λ_1

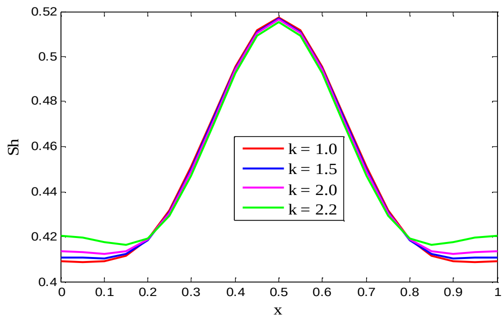

Fig. 22. Sh **for** k

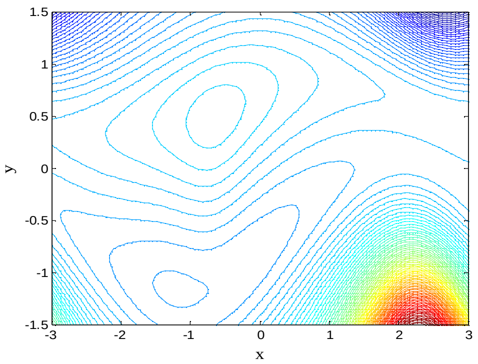

Fig. 23. Effect of M **on stream lines for** $M = 1.5$.

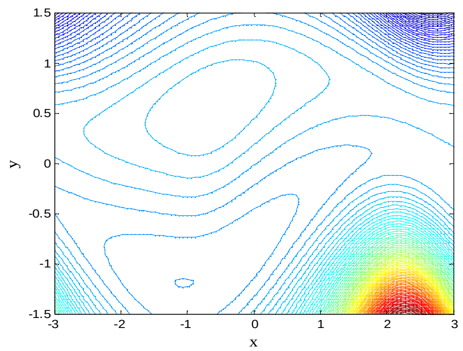

Fig.24. Effect of M **on stream lines for** $M = 1.6$.

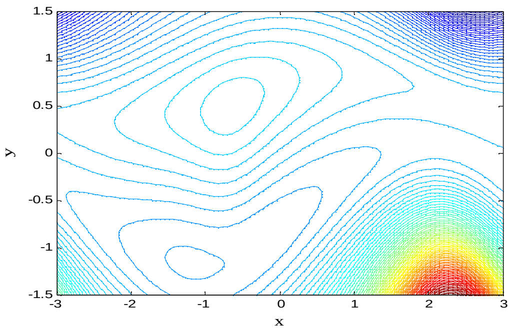

Fig.25. Effect of λ_1 on stream lines for $\lambda_1 = 1.5$.

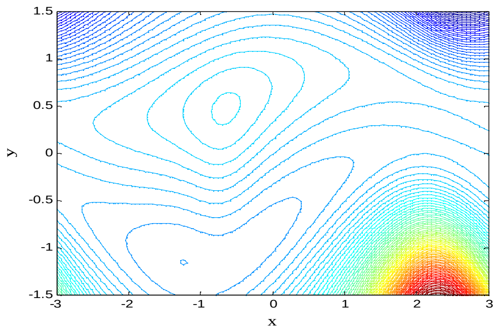

Fig.26. Effect of λ_1 on stream lines for $\lambda_1 = 1.6$.

Indian Journal of Natural Sciences *www.tnsroindia.org.in ©IJONS*

Vol.13 / Issue 75 / December / 2022 *International Bimonthly (Print)* *ISSN: 0976 – 0997*

RESEARCH ARTICLE

Heat Transfer of A Peristaltic Electro - Osmotic Flow of A Couple Stress Fluid through an Inclined Asymmetric Channel with Effects of Thermal Radiation

K. Venugopal Reddy[1]*, Mantha Srikanth[2] and K. Ramakrishna Reddy[3]

[1]Associate Professor, Department of Mathematics, Malla Reddy Engineering College (Autonomous), Maisammaguda, Hyderabad, Telangana, India.
[2]Assistant Professor, Department of Mathematics, Malla Reddy Engineering College (Autonomous), Maisammaguda, Hyderabad, Telangana, India.
[3]Professor, Department of Mathematics, Malla Reddy Engineering College (Autonomous), Maisammaguda, Hyderabad, Telangana, India.

Received: 02 Sep 2022 Revised: 20 Oct 2022 Accepted: 23 Nov 2022

***Address for Correspondence**
K. Venugopal Reddy
Associate Professor,
Department of Mathematics,
Malla Reddy Engineering College (Autonomous),
Maisammaguda, Hyderabad, Telangana, India.
Email: venugopal.reddy1982@gmail.com

ABSTRACT

The presented article addresses the electro-osmotic peristaltic flow of a couple-stress fluid bounded in an inclined asymmetric micro-channel. The viscous dissipation, Joule heating and chemical reaction effects are employed simultaneously in the flow analysis. Heat and mass transfer have been studied under large wave length and small Reynolds number. The resulting nonlinear systems are solved numerically. The influence of various dominant physical parameters is discussed for velocity, temperature distribution, and the pumping characteristics.

Keywords: Peristaltic flow; Electro-osmotic flow; Couple stress fluid; Magnetic field; Heat transfer; Mass transfer; Inclined asymmetric micro-channel;

INTRODUCTION

Recent investigations in miniaturization and micro-fabrication have taken into assuming a lot of applications extending from organic to refrigerating of microelectronics in [1 - 9]. Many favors such as an important reduction in the utilization of required materials, ability to achieve in-vitro experiments on the continuous motion in a manner

similar to the real situation in a living biological system, being portable and vibration-free are using micro fluidic devices. Electro-osmotic transports with thermal effects of liquids in micro channels are reported in [10]. The heat transfer investigation of electro-osmotic motion in a slowly varying non-symmetric micro-channel is presented in [11]. Stokes developed the couple stress fluid model. When additives are mixed in the fluid then cohesive forces of fluid resists additive factors. This resistance creates a combined force and then a couple stress is generated in the fluid. Such fluid is known as couple stress fluid. This model is regarded as generalization of Newtonian fluid model dealing with body couples and couple stresses in fluid medium. Note that couple stress fluid has an asymmetric stress tensor. Relevant studies in this direction are given in the investigations [12 – 18]. Bio-fluids propel from one place to another place by continuous process of muscle contraction and relaxation. This process is known as peristaltic transport. The peristaltic transport phenomenon is mainly due to the neuromuscular property of any tubular smooth muscle structure. This mechanism is responsible for the transport of biological fluids in several physiological processes such as urine transport from kidney to the bladder, the movement of chyme into the gastrointestinal tract, fluids in the lymphatic vessels, bile from the gallbladder into the duodenum, the embryo transport in non-pregnant uterus, the movement of spermatozoa in the ducts efferent of the male reproductive tract, the movement of the ovum in the fallopian tube and the circulation of blood in small blood vessels are depicted in [19 – 33]. Thus the major focus of this study is to analyze the viscous dissipation, Joule heating effects on MHD electro-osmotic peristaltic flow of couple stress fluid in an inclined asymmetric micro channel. Mathematical formulation of problem is presented. The results are obtained after employing long wavelength and low Reynolds number approximation. The velocity, temperature, concentration, pressure gradient and pressure rise have been proposed for the pertinent parameters of interest.

Mathematical Formulation and analysis

We analyze the electro-osmotic peristaltic flow of an electrically conducting incompressible couple stress fluid and heat transfers through an inclined asymmetric micro-channel with charged walls under the influence of an imposed the magnetic field. The flow is assumed to be asymmetric about x' and the liquid is flowing in the x' -direction. The hydrophobic micro-channel is bounded by slowly varying walls at $y' = h_1(x')$ and $y' = h_2(x')$ respectively, in which the length of the channel (L) is assumed to be much larger than the height, i.e., $L >> (h_1 + h_2)$. Fig. 1 below depicts the schematic diagram of the problem under current study.

Electrical Potential Distribution

The basic theory of electrostatics is related to the local net electric charge density ρ_e in the diffuse layer of EDL and charge density is coupled with the potential distribution ψ' through the Poisson-Boltzmann equation for the symmetric electrolyte is given by

$$\frac{d^2\psi'(y')}{dy'^2} = \frac{2n_0 e z_v}{\varepsilon}\sinh\left(\frac{e z_v \psi'(y')}{k_B T_{av}}\right) \quad \dots (3)$$

where η_o represents the concentration of ions at the bulk, ε is the charge of a proton, z_v is the valence of ions, ε is the permittivity of the medium, k_B is the Boltzmann constant and T_{av} is the boundary conditions for potential function are taken as

$$\psi'(y') = \psi_1' \quad \text{at} \quad y' = h_1'(x'),$$
$$\psi'(y') = \psi_2' \quad \text{at} \quad y' = h_2'(x'), \quad \dots (4)$$

where ψ_1' and ψ_2' are the electric potential at the upper and lower wall respectively. Let us now introduce the following non-dimensional variables,

$$\left[\psi_O,\psi_1,\psi_2\right]=\frac{ez_v}{k_BT_{av}}\left[\psi',\psi_1',\psi_2'\right],\quad y=\frac{y'}{d_1'}\ \text{ and }\ x=\frac{x'}{L} \tag{5}$$

The dimensionless form of Eqs. (1) - (2) and the Poisson-Boltzmann equation defined in (3) take in the following form,

$$h_1(x)=\frac{h_1'}{d_1'}=1+a\cos(2\pi x), \tag{6}$$

$$h_2(x)=\frac{h_2'}{d_1'}=-d-b\cos(2\pi x+\phi), \tag{7}$$

and

$$\frac{d^2\psi_O}{dy^2}=k^2\sinh(\psi_O), \tag{8}$$

where $a=\frac{a_1'}{d_1'}$, $b=\frac{a_2'}{d_1'}$, $d=\frac{d_2'}{d_1'}$ and $k=\frac{d_1'}{\lambda}$ is defined as the electro-osmotic parameter, λ_2 is the reciprocal of the EDL thickness and is defined by $\frac{1}{\lambda}=\left(\frac{2n_oe^2z_v^2}{\varepsilon k_BT_{av}}\right)^{\frac{1}{2}}$. Thus the electro-osmotic parameter is inversely proportional to EDL thickness λ. The dimensionless form of boundary conditions defined in (4) using the dimensionless variables (5) reduce to

$$\psi_o(y)=\psi_1 \quad \text{at} \quad y=h_1(x),$$

$$\psi_o(y)=\psi_2 \quad \text{at} \quad y=h_2(x). \tag{9}$$

We assumed that the electric potential is much smaller than the thermal potential for which the Debye-Hiickel linearization principle can be approximated as $\sinh(x)\approx x$. On the basis of this assumption, the solution of Poisson-Boltzmann equation (8) takes in the form

$$\frac{d^2\psi_o}{dy^2}=k^2\psi_o\ . \tag{10}$$

Finally, by employing the boundary conditions (9), the closed form solution of the equation (10) is given as

$$\psi_o(y)=F_1\cosh(ky)+F_2\sinh(ky)\ . \tag{11}$$

Couple Stress fluid Model

The given set of pertinent field equations governing the flow, in laboratory frame is

$$\frac{\partial U}{\partial X}+\frac{\partial V}{\partial Y}=0 \tag{12}$$

$$\rho\left(\frac{\partial U}{\partial t}+U\frac{\partial U}{\partial X}+V\frac{\partial U}{\partial Y}\right)=-\frac{\partial P}{\partial X}+\mu\left(\frac{\partial^2U}{\partial X^2}+\frac{\partial^2U}{\partial Y^2}\right)-\eta\left(\frac{\partial^4U}{\partial X^4}+2\frac{\partial^4U}{\partial X^2\partial Y^2}+\frac{\partial^4U}{\partial Y^4}\right)-\sigma B_0^2U-\frac{\mu}{k_o}U+$$
$$\rho g\beta_T\left(T-T_0\right)\sin\alpha+\rho_eE \tag{13}$$

$$\rho\left(\frac{\partial V}{\partial t}+U\frac{\partial V}{\partial X}+V\frac{\partial V}{\partial Y}\right)=-\frac{\partial P}{\partial Y}+\mu\left(\frac{\partial^2 V}{\partial X^2}+\frac{\partial^2 V}{\partial Y^2}\right)-\eta\left(\frac{\partial^4 V}{\partial X^4}+2\frac{\partial^4 V}{\partial X^2\partial Y^2}+\frac{\partial^4 V}{\partial Y^4}\right)-\frac{\mu}{k_o}V+\rho g\beta_T\left(T-T_0\right)\cos\alpha \quad (14)$$

$$\rho c_p\left(\frac{\partial T}{\partial t}+U\frac{\partial T}{\partial X}+V\frac{\partial T}{\partial Y}\right)=k^*\left(\frac{\partial^2 T}{\partial X^2}+\frac{\partial^2 T}{\partial Y^2}\right)+Q_0-\frac{\partial q_r}{\partial Y}+\sigma B_0^2u^2+\sigma E^2 \quad (15)$$

where (U,V) are the velocity components in the laboratory frame, ρ is the density, P is the pressure, μ is the viscosity coefficient , η is the couple stress viscosity parameter, σ is the electric conductivity of the fluid, B_0 is the applied transverse magnetic field, k_0 is the permeability parameter, g is the acceleration due to the gravity, β_T and β_C are the coefficient of thermal and concentration expansions, T is the temperature , α is the inclination angle, c_p is the specific heat at constant pressure, k^* is the thermal conductivity , Q_0 is the dimensional heat absorption coefficient, C is the concentration in the reference to fixed frame system, D is the coefficient of mass diffusivity, K_T is the thermal diffusion ratio, T_m is the mean temperature, k_1 is the chemical reaction parameter and α is the inclination angle. The radiative heat flux in the $X-$direction is considered as negligible compared to $Y-$direction. By using Rosseland approximation for thermal radiation, the radiative heat flux q_r is specified by

$$q_r=-\frac{16\sigma^* T_o^3}{3k^*}\frac{\partial T}{\partial Y} \quad (16)$$

where σ^* and k^* are the Stefan-Boltzmann constant and the mean absorption coefficient respectively.
The coordinates and velocities in the wave frame (x,y) and the laboratory frame (X,Y) in a coordinate system moving with the wave speed c in which the boundary shape is stationary and are related by

$$x=X-ct, y=Y, u=U-c, v=V, p(x,y)=P(X,Y,t), \bar{T}(x,y)=T(X,Y,t) \quad (17)$$

where u,v are the velocity components, p is the pressure, T is the temperature and C is the concentration in the wave frame. Introducing the following non-dimensional quantities

$$\bar{x}=\frac{x}{\lambda},\bar{y}=\frac{y}{d_1},\bar{u}=\frac{u}{c},\bar{v}=\frac{v}{c},\ h_1=\frac{H_1}{d_1},\ h_2=\frac{H_2}{d_1},\ \bar{t}=\frac{ct}{\lambda},\ \bar{p}=\frac{d_1^2}{\lambda\mu C}p,\ \delta=\frac{d_1}{\lambda},$$

$$d=\frac{d_2}{d_1},\ a=\frac{a_1}{d_1},b=\frac{a_2}{d_1},\mathrm{Re}=\frac{\rho c d_1}{\mu},M=\sqrt{\frac{\sigma}{\mu}}B_0 d_1,\ Da=\frac{k_0}{d_1^2},\ \gamma=\sqrt{\frac{\mu}{\eta}}d_1,$$

$$Gr=\frac{\rho g d_1^2\beta_T\left(T_1-T_0\right)}{\mu C},\bar{\psi}=\frac{\psi}{cd_1},\mathrm{Pr}=\frac{\mu c_p}{k^*},\ \theta=\frac{\bar{T}-\bar{T}_0}{\bar{T}_1-\bar{T}_0},\ \beta=\frac{Q_0 d_1^2}{k^*\left(\bar{T}_1-\bar{T}_0\right)},\ Sc=\frac{\mu}{\rho D},$$

$$\gamma_1=k_1\frac{d_1^2}{\upsilon},\ Rd=\frac{16\sigma^* T_o^3}{3k^*\bar{\mu}_o c_f},C_o=\frac{\left(-\frac{d\bar{p}}{d\bar{X}}\right)d_1^2}{\mu U_{HS}} \quad (18)$$

where δ is the dimensionless wave number, Re is the Reynolds number, M is the Hartmann number, Da is the Darcy number, γ is the couple stress parameter, Gr is the local temperature Grashof number, Pr is the Prandtl number, Rd is the thermal radiation parameter, β is the heat generation parameter, γ_1 is the chemical reaction parameter, Sr is the Soret number and A is the Joule heating parameter. Using the above transformations (17) and (18) and non-dimensional quantities (19), the governing flow field equations (13) - (15), after dropping the bars, we get

The dimensional equations of the couple stress fluid are

$$\frac{\partial^4\psi}{\partial y^4}-\frac{1}{\gamma^2}\frac{\partial^6\psi}{\partial y^6}-\left(M^2+\frac{1}{Da}\right)\frac{\partial^2\psi}{\partial y^2}+\frac{d^3\psi_o}{dy^3}+Gr\frac{\partial\theta}{\partial y}\sin\alpha=0 \tag{19}$$

$$\frac{(1+Rd)}{\mathrm{Pr}}\frac{\partial^2\theta}{\partial y^2}+Ec\left[\left(\frac{\partial^2\psi}{\partial y^2}\right)^2+\frac{1}{\gamma^2}\left(\frac{\partial^3\psi}{\partial y^3}\right)^2\right]+EcM^2\left(\frac{\partial\psi}{\partial y}\right)^2+A=0 \tag{20}$$

with the corresponding boundary conditions are

$$\psi=\frac{F}{2},\ \frac{\partial\psi}{\partial y}+L\frac{\partial^2\psi}{\partial y^2}=-1, \frac{\partial^3\psi}{\partial y^3}=0, \theta=0 \text{ at } y=h_1=1+a\cos(2\pi x) \tag{21}$$

$$\psi=-\frac{F}{2},\ \frac{\partial\psi}{\partial y}-L\frac{\partial^2\psi}{\partial y^2}=-1, \frac{\partial^3\psi}{\partial y^3}=0, \theta=1 \text{ at } y=h_2=-d-b\cos(2\pi x+\phi) \tag{22}$$

where L is the velocity slip parameter and F is the flux in the wave frame and the constants a, b, ϕ and d should satisfy the relation

$$a^2+b^2+2ab\cos\phi\le(1+d)^2. \tag{23}$$

The dimensionless mean flow rate Θ in the fixed frame is related to the non-dimensional mean flow rate F in wave frame by

$$\Theta=F+1+d$$

(24)

and in which

$$F=\int_{h_1}^{h_2}\frac{\partial\psi}{\partial y}dy \tag{25}$$

Numerical Solution

The solution of system of coupled non –linear Eqs. (20) - (22) with corresponding boundary conditions in Eq. (23) – (24) are obtained using NDSolve in Mathematica computational software. This section contains the plots and related analyses for different embedded parameters. This section includes the graphs for velocity, temperature, concentration and pressure gradient.

Velocity distribution

Fig. 2 displays the velocity profile for various values of Hartmann number. The velocity decreases and drops with Hartmann number M. Fig. 3 depicts velocity profiles of different values of parameter for osmosis parameter. Velocity profile is seen to raise as osmosis parameter k enlarges. Fig. 4 depicts that the consequences of the parameter λ_1 on the profile of velocity. It is clear that enhance the strength of λ_1 resulted in enhancing the velocity. Fig. 5 indicate that the velocity rises with increasing Da. Fig. 6 reveals that velocity is seen to decrease with the higher values of couple stress parameter. Fig. 7 shows that velocity diminishes with increasing L.

Temperature distribution

Fig. 8 – 11 depicts the deviations in temperature profiles for various values of parameters A, k, Ec and $\Pr$. Fig. 8 presents the consequences of the parameter A on the profile of temperature. It is clear that enhance the strength of A resulted in increasing the temperature. Fig. 9 shows that temperature rises with enhancing k. Fig. 10 shows that the temperature enhances significantly with a rise in Ec. Fig. 11 shows a very significant effect of $\Pr$ on the temperature profiles. It is clear from this figure that the Brinkman number has a impulse to diminish the temperature in the micro-channel. It may be inferred that the thermal conductivity of the fluid declines by enhancing the ratio of momentum diffusivity to thermal diffusivity.

Pumping characteristics

Figs. 13 - 15 represent the profiles of pressure gradient $\left(\frac{dp}{dx}\right)$ for the effects of Slip parameter (L), Osmosis parameter (k) and the couple stress parameter (γ). The pressure gradient has oscillatory behavior in the whole range of the x-axis. From all figures, it is clear that the pressure gradient diminishes with the higher values of L, k and γ. The pressure rise is a significant physical measure in the peristaltic mechanism. The results are prepared and discussed for different physical parameters of interest through Figs. 16 – 18 and which are plotted for dimensionless pressure rise ΔP_λ versus the dimensionless flow rate Θ to the effects of Hartmann number M, chemical reaction parameter γ_1, heat generation parameter β and couple stress parameter γ. The pumping regions are peristaltic pumping are $(\Theta > 0, \Delta P_\lambda > 0)$, augment pumping $(\Theta < 0, \Delta P_\lambda < 0)$, retrograde pumping $(\Theta < 0, \Delta P_\lambda > 0)$, co pumping $(\Theta > 0, \Delta P_\lambda < 0)$ and free pumping $(\Theta = 0, \Delta P_\lambda = 0)$. Fig. 16 is depicted that the pressure rise ΔP_λ depressing with an enhance in Hartmann number M in the both peristaltic pumping region and free pumping region. Fig. 17 depicts that the quite opposite nature that of for the effect of the heat generation parameter β .The influence of couple stress fluid parameter γ on the pressure rise is decreases and which is elucidated from Fig. 18.

Nusselt number

Figs. (19) – (21) exhibits the influence of incorporated parameters such as Hartmann number M, Osmosis parameter k and Joule heating parameter A respectively on magnitude of Nusselt number. The heat transfer coefficient has oscillatory in nature due to peristaltic motion of walls. The heat transfer rate enhances for M, k and A from Figs. 19 - 21.

Sherwood number

The mass transfer coefficient shows the impact of different parameters of λ_1 and k from Figs. 22 – 23. Fig. 22 depicts the Sherwood number depresses with the impact of λ_1 whereas it observes the mass transfer coefficient enhances as the parameter k rises from Fig. 23.

Trapping Phenomenon

The phenomenon of trapping in flow of fluid is trapping and is presented by drawing streamlines in the Figs. 24 - 27. A bolus is having by splitting of a streamline under important conditions and it is followed along with the wave in the wave frame. This process is called trapping. The bolus of trapping is observed to expand by enhancing M from Figs. 24 – 25. However the size of bolus decreases by the rising effects of λ_1 as shown in Figs. 26 – 27.

Concluding Remarks

We have investigated the peristaltic transport of a heat and mass transfer of couple stress fluid on the combined impacts of electro-osmotically and pressure driven flow in an inclined asymmetric micro channel whose walls are varying sinusoidally with different wave trains. Effects of thermal radiation, chemical reaction and Joule heating have been accounted. The numerical solution for velocity, temperature distribution, concentration distribution and pumping characteristics are presented using small wave length and small Reynolds number. The important findings of present study are summarized as follows

- The Electro – osmotic flow of couple stress fluids in an inclined asymmetric channel is strongly depend on Debye length.
- Velocity diminishes with an enhance of L and γ.
- Temperature rises with an strength of A where as depresses with an enhance of Rd.
- It is observed that pressure gradient has oscillatory behavior.
- Pressure rise decreases with an effect of increasing γ
- The absence of Electro – Osmosis, our results are in good agreement with Gnaneswara Reddy *et al.* [33].

REFERENCES

1. K.P. Tikhomolova, Electro-Osmosis, Ellis Horwood, London, 1993.
2. H. Ginsburg, Analysis of plant root electro-potentials, J. Theor. Biol. 37 (1972) 389 – 412.
3. V. Sansalone, J. Kaiser, S. Naili, T. Lemaire, Interstitial fluid flow within bone canaliculi and electro-chemo-mechanica features of the canalicular milieu, Biomech. Model. Mechanobiol. 12 (2013) 533 – 553.
4. E.A. Marshall, The osmotic flow of an electrolyte through a charged porous membrane, J. Theor. Biol. 66 (1977) 107 – 135.
5. S. Grimnes, Skin impedance and electro-osmosis in the human epidermis, Med. Biol. Eng. Compu. 21 (1983) 739 – 749.
6. T.A. Davis, Electrodialysis, in: M.C. Porter (Ed.), Handbook of Industrial Membrane Technology, Noyes Publications, New Jersey, USA, 1990.
7. V. Orsat, G.S.V. Raghavan, E.R. Norris, Food processing waste dewatering by electro- osmosis, Can. Agric. Eng. 38 (1996) 063 – 067.
8. A. Manz, C.S. Effenhauser, N. Burggraf, D.J. Harrison, K. Seiler, K. Fluri, J. Micromech. Microeng. 4 (1994) 257.
9. G.D. Ngoma, F. Erchiqui, Pressure gradient and electroosmotic effects on two immiscible fluids in a microchannel between two parallel plates, J. Micromech. Microeng. 16 (2005) 83 – 90.
10. T.S. Zhao, Q. Liao, Thermal effects on electro-osmotic pumping of liquids in microchannels, J. Micromech. Microeng. 12 (2002) 962.

11. A. Mondal and G.C. Shit, Heat transfer analysis on electro-osmotic flow in a slowly varying asymmetric micro-channel, European Journal of Mechanics-B/Fluids, 60 (2016) 1 - 35.
12. VK. Stokes, Couple stresses in fluids, Phys Fluids, 9 (1966) 1709 – 15.
13. M. Devakar, V. Iyengar, Stokes problems for an in compressible couple stress fluid, Nonlinear Anal Model Control 2008:181 – 90.
14. JS Duan, X Qui, Stokes second problem of viscoelastic fluids with constitutive equation of distributed-order derivative. Appl. Math. Comput. 331(2018)130 – 9.
15. K. Ramesh, Influence of heat and mass transfer on peristaltic flow of couplestress fluid through porous medium in the presence of i nclined magnetic field in an inclined asymmetric channel. J. Mol. Liq.219 (2016) 256 – 71.
16. A. Alsaedi, N Ali, D.Tripathi, T. Hayat, Peristaltic flow of couple stress fluid through uniform porous medium. Appl Math Mech. 35 (2014) 469 – 80.
17. K. Kaladhar, Natural convection flow of couple stress fluid in a vertical channel with Hall and Joule heating effects. Proc.Eng . 127 (2015) 1071 – 8.
18. T. Hayat, M. Iqbal, H Yasmin, F Alsaadi. Hall effects on peristaltic flow of couple stress fluid in an inclined asymmetric channel. Int. J. Bio mathematics, 7(2014)1450057(34pages).
19. T.W. Latham, Fluid motion in a peristaltic pump, MIT Press, Cambridge Mass, USA.
20. A.H. Shapiro, M.Y. Jaffrin, and S.L. Weinberg (1969), Peristaltic pumping with long wavelengths at low Reynolds numbers, J. Fluid Mech., 37 (1969) 799–825.
21. Mekheimer Kh.S., and Elmaboud Y.A., Peristaltic flow of a couple stress fluid in an annulus application of an endoscope. Physica A., Vol. 387, pp. 2403–2415.
22. O.D., Makinde, and P.Y. Mhone (2006), Hydromagnetic effects on internal flow separation in a diverging channel, Romanian Journal of Physics, Vol. 51, pp. 959-966.
23. 23. Hayat T., Javed M., and Ali N., (2008), MHD peristaltic transport of Jeffrey fluid in a channel with compliant walls and porous space, Transp. Porous Media, Vol. 74, pp. 259–274.
24. Mekheimer Kh.S., and Abd elmaboud Y., (2008), Peristaltic flow of a couple stress fluid in an annulus: application of an endoscope, Physica A, Vol. 38, pp. 2403–2415.
25. Adesanya S.O., and Makinde O.D., (2012), Heat transfer to magneto hydrodynamic non-Newtonian couple stress pulsatile flow between two parallel porous plates, Zeitschrift for Naturforschung , Vol. 67a, pp. 647 – 656.
26. Adesanya S.O., and Makinde O.D., (2015), Irreversibility analysis in a couple stress film flow along an inclined heated plate with adiabatic free surface, Physica A, Vol. 432, pp. 222-229.
27. Gnaneswara Reddy M., and Venugopal Reddy K., (2016), Impact of velocity slip and joule heating on MHD peristaltic flow through a porous medium with chemical reaction, Journal of the Nigerian Mathematical society, Vol. 35, pp. 227 - 244.
28. M. Gnaneswara Reddy, K. Venugopal Reddy, and O.D. Makinde, Hydromagnetic peristaltic motion of a reacting and radiating couple Stress fluid in an inclined asymmetric channel filled with a porous medium, Alexandria Engineering Journal, 55 (2016) 1841–1853.
29. M. Mishra, and A. R. Rao, Peristaltic transport of a Newtonian fluid in an asymmetric channel, Z.Angew, Math. Phys., 53 (2003) 532 - 550.
30. M. Kothandapani, and S. Srinivas, Peristatltic transport of a Jeffrey fluid under the effect of magnetic field in an asymmetric channel, Int. J. Nonlinear Mech.,43 (2008) 915–924.
31. F. M. Abbasi, T. Hayat, B. Ahmad, and B. Chen, (2015), Peristaltic flow with convective mass condition and thermal radiation, J. Cent. South Univ., 22 (2015) 2369–2375.
32. M. Gnaneswara Reddy, K. Venugopal Reddy, and O.D. Makinde, (2016) Hydromagnetic peristaltic motion of a reacting and radiating couple Stress fluid in an inclined asymmetric channel filled with a porous medium, Alexandria Engineering Journal, 55 (2016) 1841 - 1853.
33. M. Gnaneswara Reddy, K. Venugopal Reddy, and O.D. Makinde, Heat transfer on MHD peristaltic rotating flow of a Jeffrey fluid in an asymmetric channel, International Journal of Applied and Computational Mathematics, DOI 10.1007/s40819-016-0293-1 (2016).

34. O.D. Makinde, M. Gnaneswara Reddy, and K. Venugopal Reddy, Effects of thermal radiation on MHD peristaltic Motion of Walters-B Fluid with heat source and Slip conditions, Journal of Applied and Fluid Mechanics, 10(2017)1105-1112.

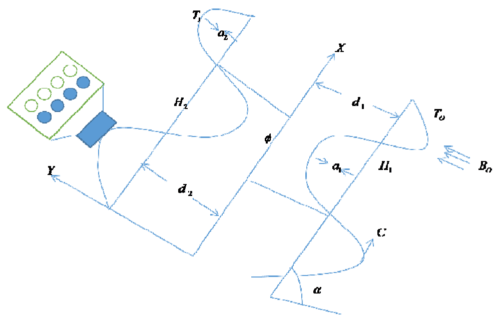

Fig. 1. Physical Model

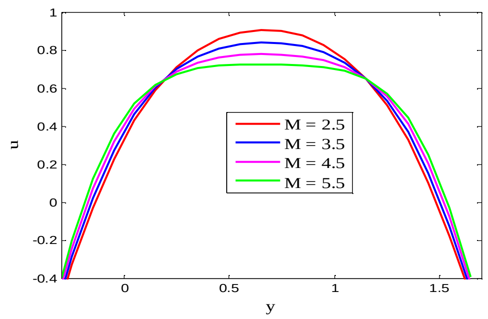

Fig.2. u **for** M

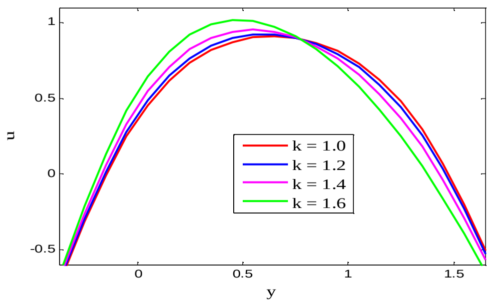

Fig.3. u **for** k

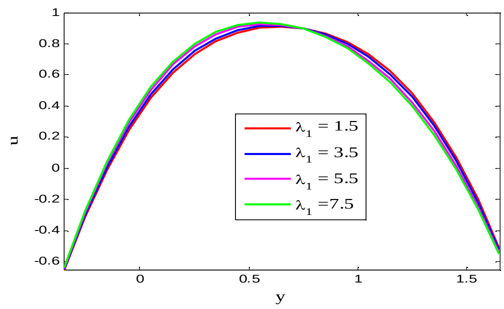

Fig. 4. u **for** λ_1

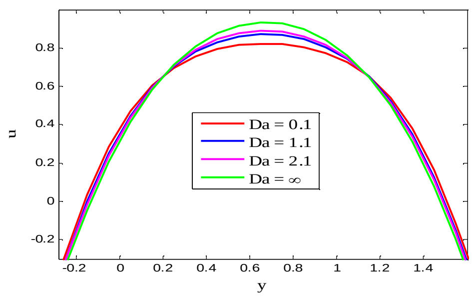

Fig. 5. u **for** Da

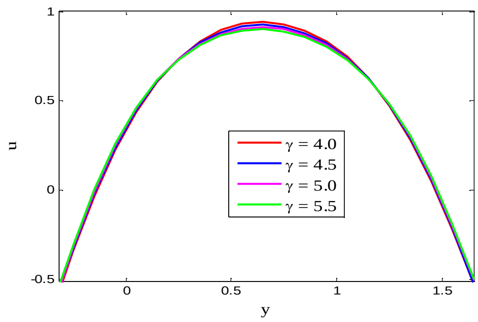

Fig. 6. u **for** γ

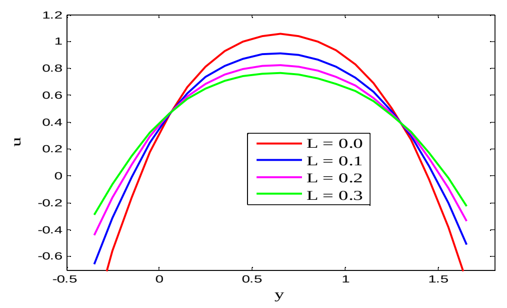

Fig. 7. u **for** L

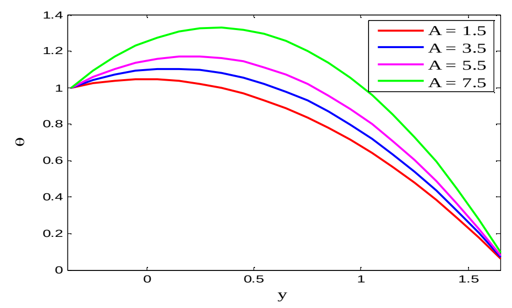

Fig. 8. θ **for** A

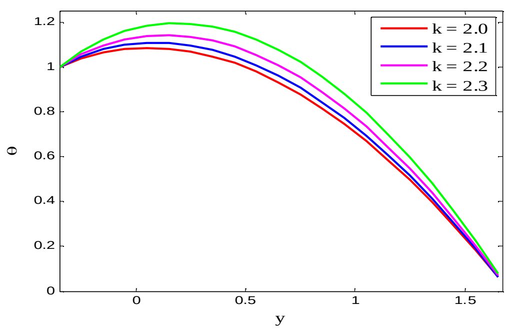

Fig. 9. θ **for** k

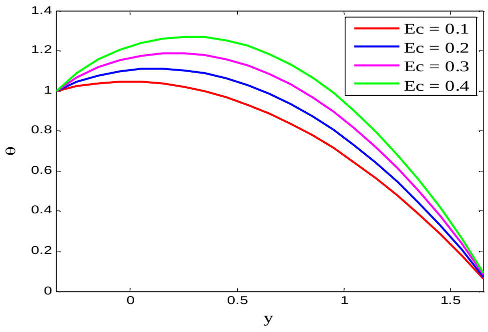

Fig. 10. θ **for** Ec

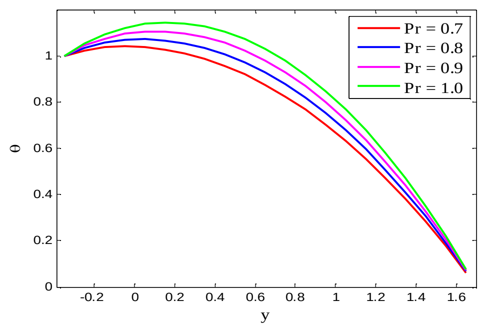

Fig. 11. θ **for** $\Pr$

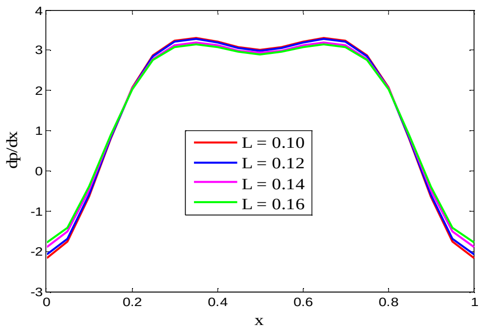

Fig. 12. $\dfrac{dp}{dx}$ **for** L

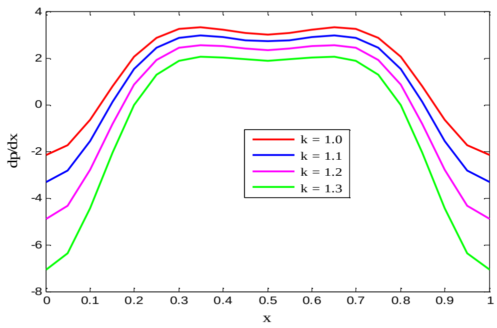

Fig. 13. $\frac{dp}{dx}$ **for** k

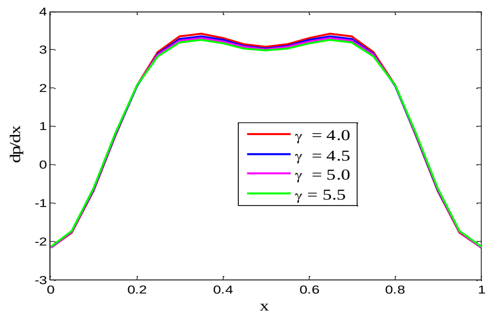

Fig. 14. $\frac{dp}{dx}$ **for** γ

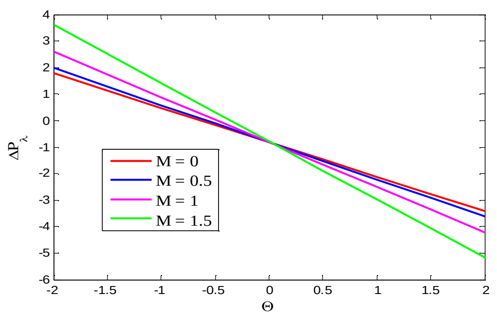

Fig. 15 ΔP_λ **for** M

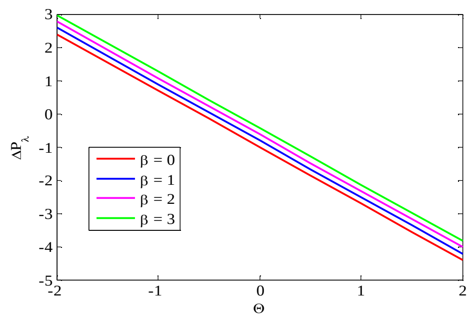

Fig. 16. ΔP_λ **for** β

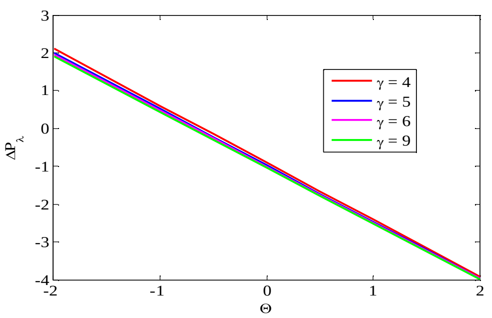

Fig. 17. ΔP_λ **for** γ

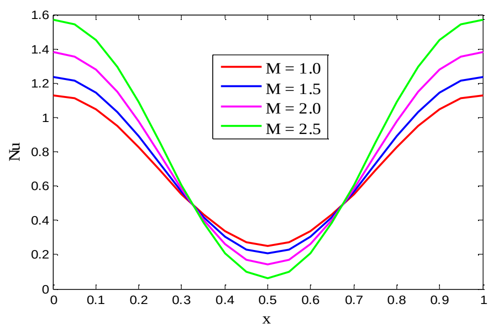

Fig. 18. Nu **for** M

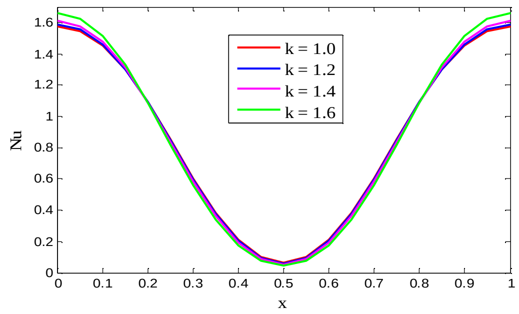

Fig. 19. Nu **for** k

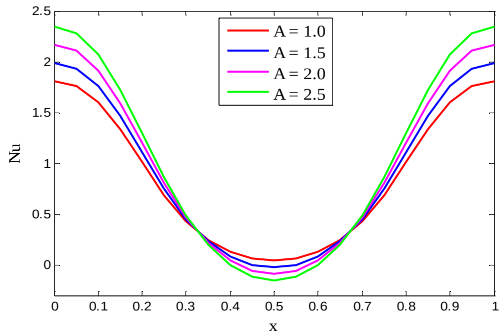

Fig. 20. Nu **for** A

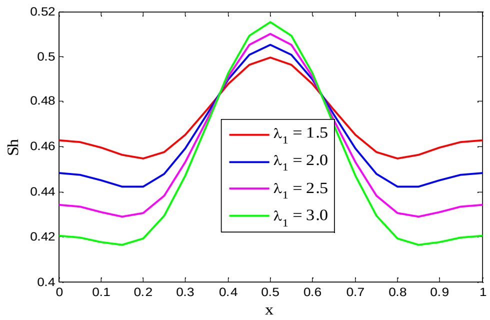

Fig. 21. Sh **for** λ_1

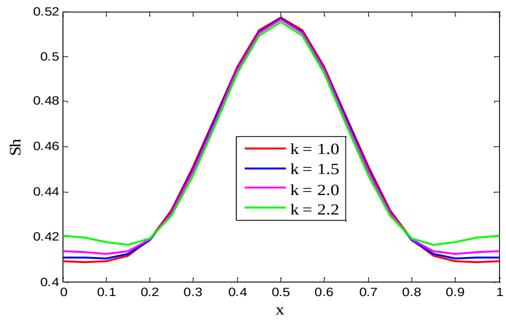

Fig. 22. Sh **for** k

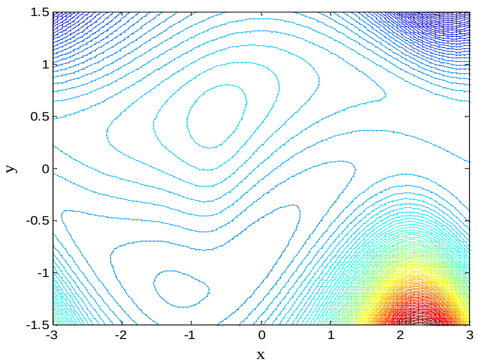

Fig. 23. Effect of M **on stream lines for** $M = 1.5$.

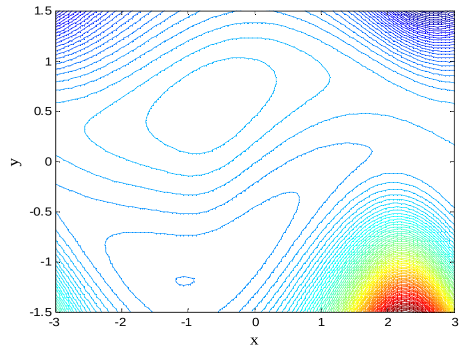

Fig.24. Effect of M **on stream lines for** $M = 1.6$.

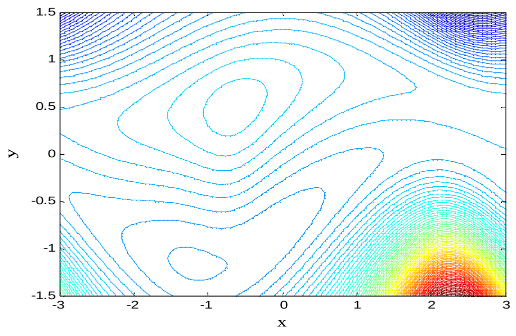	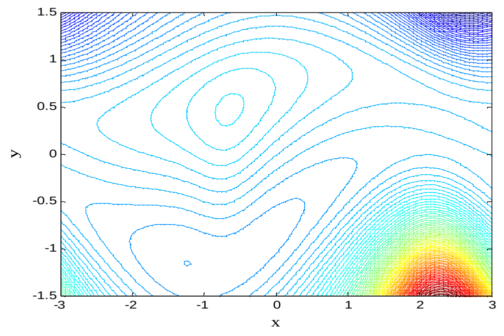
Fig.25. Effect of λ_1 on stream lines for $\lambda_1 = 1.5$.	**Fig.26. Effect of λ_1 on stream lines for $\lambda_1 = 1.6$.**

Journal of Positive School Psychology http://journalppw.com
2022, Vol. 6, No. 5, 1865-1873

AN ANALYTICAL STUDY OF CHEMICAL REACTION EFFECT ON MHD FLOW IN A VERTICAL SURFACE FILLED WITH POROUS MEDIUM

N. Joshna[1] , Y. V. Seshagiri Rao[2] , S. Saroja[3]

[1]*Department of Mathematics, Vignana Bharathi Institute of Technology, Aushapur (V), Ghatkesar (M), Medchal (Dist), TS-501301, India Email: nagendlajoshna@gmail.com*
[2]*Department of Basic Sciences & Humanities, Vignan Institute of Technology and Science, Deshmukhi (V), Pochampally (M), Yadadri-Bhuvanagiri (Dist), T.S-508284, India Email: yangalav@gmail.com*
[3]*Department of Mathematics, Malla Reddy Engineering College (Autonomous), Maisammaguda, Hyderabad-500100, India Email: sandirisaroja@gmail.com*

Abstract

The present paper an analytical study of chemical reaction effect on MHD flow of continuously moving vertical surface filled with a porous medium. The equations governing the flow field are solved by analytical method by using perturbation technique. The velocity, temperature, concentration profiles and skin friction have been evaluated for variation in the different governing parameters through graphs.

Keywords: Chemical reaction, MHD, Vertical surface, Perturbation technique

INTRODUCTION

Chemical reactions are of varying use in industries. Firstly, industries use galvanized products for manufacturing steel which is corrosion resistance. Industries also use electrolysis for manufacturing pure quality of goods and minerals. Industries use chemical reaction for extracting minerals from ores. Chemical reactions are used for reuse of by product if possible for making various compounds that may be useful for the industries, making lubricant which is use for the smooth performance of types of machinery, reuse of by product if possible and it also used for making various compounds that may be useful for the industries, lubricant, which is useful for the smooth performance of types of machinery. In view of the above some of the authors, Tsai and Huang [1] explained heat and mass transfer for Soret and Dufour's effects on Hiemenz flow through porous medium onto a stretching surface, Srinathuni Lavanya and Chenna Kesavaiah [2] observed that heat transfer to MHD free convection flow of a viscoelastic dusty gas through a porous medium with chemical reaction, Jeena et. al. [3] observed that chemical reaction effects on MHD viscoelastic fluid flow over a vertical stretching sheet with heat source/sink, Tripathy et. al. [4] has been studied chemical reaction effect on MHD free convective surface over a moving vertical plane through porous medium, Srinathuni Lavanya and Chenna Kesavaiah [5] considered radiation effects on MHD natural convection heat transfer flow from spirally enhanced wavy channel through a porous medium, Kafoussias and Williams [6] motivated study on thermal diffusion and diffusion thermo effects on mixed free forced convective and mass transfer boundary layer flow with temperature dependent viscosity, Chenna Kesavaiah and Satyanarayana [7] presented radiation absorption and Dufour effects to MHD flow in vertical surface, Sajid and Hayat [8] shows Influence of thermal radiation on the boundary layer flow due to an exponentially stretching sheet, Chenna Kesavaiah and Satyanarayana [9] reveals MHD and Diffusion Thermo effects on flow accelerated vertical plate with chemical reaction, Girish Kumar [10] exhibits chemical reaction effects on MHD flow of continuously moving vertical surface with heat and mass flux through porous medium.

Natural convection in a cavity saturated or partially filled with porous media is still one of the researcher's interests studying because it's a distinguishing tool to augment the heat transfer for some natural and engineering applications also it is used as exquisite isolation for other applications. The motion of fluid due to difference in density resulting from temperature gradients is the main rule of natural convection. The term (natural) comes from the absence of foreign effects such as mixer machine, compressor, pump, etc. The effect of a porous medium in natural convection has received widespread attention, especially in recent time. Bidin and Nazar [11] worked to improve numerical solution of the boundary layer flow over an exponentially stretching sheet with thermal radiation, Ch Kesavaiah et. al. [12] shows that the effects of the chemical reaction and radiation absorption on an unsteady MHD convective heat and mass transfer flow past a semi-infinite vertical permeable moving plate embedded in a porous medium with heat source and suction, Abolbashari et. al. [13] studied entropy analysis for an unsteady MHD flow past a stretching permeable surface in nanofluid, Chauhan et. al. [14] motivated study on radiation effects on natural convection MHD flow in a rotating vertical porous channel partially filled with a porous medium, Srinathuni Lavanya and Chenna Kesavaiah [15] explained on radiation and Soret effects to MHD flow in vertical surface with chemical reaction and heat generation through a porous medium, Khansila and Witayangkurn [16] expressed their views on visualization of natural convection in enclosure filled with porous medium by sinusoidally temperature on the one side, Chaudhary et. al. [17] motivated study on free convection effects on MHD flow past an infinite vertical accelerated plate embedded in porous media with constant heat flux, Chin et. al. [18] observe that effect of variable viscosity on mixed convection boundary layer flow over a vertical surface embedded in a porous medium, Troy et. al. [19] studies on uniqueness of flow of a second order fluid past a stretching sheet, Chenna Kesavaiah and Sudhakaraiah [20] done on effects of heat and mass flux to MHD flow in vertical surface with radiation absorption.

The behaviour of MHD's boundary layer momentum and heat transfer in the presence of an external magnetic field has been a hot issue in a variety of academic domains. Research in the field of nonlinear analysis is equally important from a theoretical standpoint. The use of numerical analysis in partial differential equations (PDEs) is ubiquitous in the study of MHD flow. No analytical solution can be found because of the nonlinearities in the governing equations, and the nonlinear equations are usually solved numerically with appropriate boundary conditions. Many researchers have long used various nonlinear analysis methods to handle nonlinear problems numerically or analytically and have looked at MHD flow and heat transfer on the extended or contracted surface from many theoretical and practical perspectives. Cogly et. al. [21] has been studied a Differential approximation for radiative transfer in a non-gray gas near equilibrium, Samad and Rahman [22] considered thermal Radiation interaction with unsteady MHD flow past a vertical porous plate immersed in a porous medium, Makinde and Mhone [23] expressed heat transfer to MHD oscillatory flow in a channel filled with porous medium, Chenna Kesavaiah and Devika [24] explained on free convection and heat transfer of a Couette flow an infinite porous plate in the presence radiation effect, Anwar Be'g et. al. [25] observe that numerical study of free convection magnetohydrodynamic heat and mass transfer from a stretching surface to a saturated porous medium with Soret and Dufour effects, Chenna Kesavaiah and Venkateswarlu [26] motivated study on chemical reaction and radiation absorption effects on convective flows past a porous vertical wavy channel with travelling thermal waves, Misirlioglu et. al. [27] studied free convection in a wavy cavity filled with a porous medium, Beithou et. al. [28] shows the effect of porosity on the free convection flow of non-Newtonian fluids along vertical plate embedded in a porous media. The same related investigations are studied by various authors from [29] to [40]

The present paper an analytical study of chemical reaction effects on MHD flow of continuously moving vertical surface filled with a porous medium. The velocity, temperature, concentration and skin friction have been evaluated for variation in the different governing parameters.

FORMULATION OF THE PROBLEM

Consider the steady, two - dimensional laminar, incompressible flow of a chemically reacting, viscous fluid on a continuously moving vertical surface in the presence of a uniform magnetic field, uniform heat and mass flux effects issuing a slot and moving with uniform velocity in a fluid at rest. Let $x-axis$ be taken along the direction of motion of the surface in the upward direction and $y-axis$ is normal to the surface. The temperature and concentration levels near the surface are raised uniformly. The induced magnetic field, viscous dissipation is assumed to be neglected. Now, under the usual Boussinesq's approximation, the flow field is governed by the following equations.

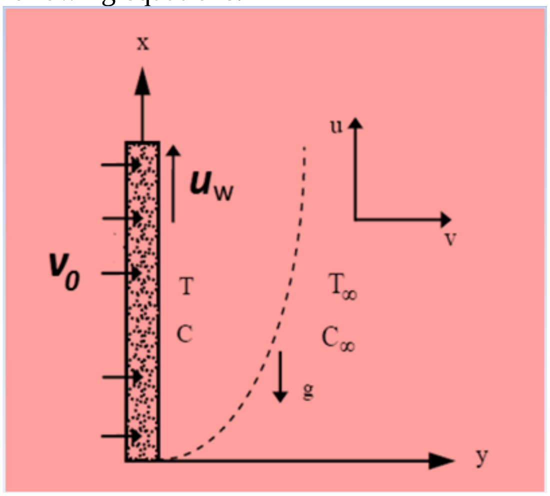

Figure (1): Flow configuration and coordinate system

Continuity equation

$$\frac{\partial u}{\partial x}+\frac{\partial v}{\partial y}=0 \tag{1}$$

Momentum equation

$$u\frac{\partial u}{\partial x}+v\frac{\partial u}{\partial y}=\nu\frac{\partial^2 u}{\partial y^2}-\frac{\sigma B_0^2}{\rho}-\frac{\nu}{K_p}u + g\beta\left(T'-T'_\infty\right)+g\beta^*\left(C'-C'_\infty\right) \tag{2}$$

Energy equation

$$\rho C_p\left(u\frac{\partial T'}{\partial x}+v\frac{\partial T'}{\partial y}\right)=k\frac{\partial^2 T'}{\partial y^2} \tag{3}$$

Diffusion equation

$$u\frac{\partial C'}{\partial x}+v\frac{\partial C'}{\partial y}=D\frac{\partial^2 C'}{\partial y^2}-Kr'\left(C'-C'_\infty\right) \tag{4}$$

The initial and boundary conditions

$$\left.\begin{aligned} &u=u_w, v=-v_0 \text{ constant}, <0,\\ &\frac{\partial T}{\partial y}=-\frac{q}{k},\frac{\partial C}{\partial y}=-\frac{j''}{k}\end{aligned}\right\} at \quad y=0 \tag{5}$$

$$u\to 0, T\to T'_\infty, C\to C'_\infty \qquad as \quad y\to\infty$$

Where u, are velocity components in x and y directions respectively. g is the acceleration due to gravity, β is volumetric coefficient of thermal expansion, β^* is the volumetric coefficient of expansion with concentration, is the temperature of the fluid, C' is the species concentration, T'_w is the wall temperature, C'_w is the concentration at the plate, T'_∞ is the free steam temperature far away from the plate, C'_∞ is the free steam concentration in fluid far away from the plate, ν is the kinematic viscosity, D is the species diffusion coefficient, Kr is the chemical reaction parameter. The term is assumed to be the amount of heat generated or absorbed per unit volume. Q_0 is a constant, which may take on either positive or negative values. When the wall temperature T'_w exceeds the free steam temperature T'_∞, the source term represents the heat source $Q_0>0$ when and heat sink when $Q_0<0$. The first term and second term on the right hand side of the momentum equation (2) denote the thermal and concentration buoyancy effects respectively.

In order to write the governing equations and the boundary conditions the following non-dimensional quantities are introduced.

$$Y=\frac{yv_o}{\nu}, U=\frac{u}{u_w}, \Pr=\frac{\mu C_p}{k}, Sc=\frac{\nu}{D}$$

$$K=\frac{K_p v_0^2}{\nu^2},\ Kr=\frac{Kr'\nu}{v_0^2},\ M=\frac{\sigma B_0^2\nu}{\rho}$$

$$Gr=\frac{\nu g\beta\left(\frac{q\nu}{kv_0}\right)}{u_w v_0^2}, Gc=\frac{\nu g\beta^*\left(\frac{j''\nu}{kv_0}\right)}{u_w v_0^2} \tag{6}$$

$$T=\frac{T'-T'_\infty}{\left(\frac{q\nu}{kv_0}\right)},\qquad C=\frac{C'-C'_\infty}{\left(\frac{j''\nu}{kv_0}\right)}$$

In view of (6) the equations (2) – (4) are reduced to the following non-dimensional form

$$\frac{d^2U}{dY^2}+\frac{dU}{dY}-\left(M+\frac{1}{k}\right)U=-GrT-GrC \tag{7}$$

$$\frac{d^2T}{dY^2}+\Pr\frac{dT}{dY}=0 \tag{8}$$

$$\frac{d^2C}{dY^2}+Sc\frac{dC}{dY}-KrSc\,C=0 \tag{9}$$

The corresponding initial and boundary conditions in non-dimensional form are

$$\begin{aligned} &U=1,\frac{\partial T}{\partial Y}=-1,\frac{\partial C}{\partial Y}=-1 \ at \quad Y=0\\ &U\to 0, T\to 0, C\to 0 \quad as \quad Y\to\infty\end{aligned} \tag{10}$$

The radiative heat flux q_r is given by equation (5) in the spirit of Cogly et.al [9]

$$\frac{\partial q_r}{\partial y} = 4\left(T - T_\infty\right) I \qquad (11)$$

where $I = \int_0^\infty K_{\lambda w} \frac{\partial e_{b\lambda}}{\partial T} d\lambda,\ K_{\lambda w} -$ is the absorption coefficient at the wall and $e_{b\lambda} -$ is Planck's function, I is absorption coefficient

Where Gr is the thermal Grashof number, $\Pr$ is the fluid Prandtl number, Sc is the Schmidt number and Kr is the chemical reaction parameter,

Method of solution

The study of ordinary differential equations (7), (8) and (9) along with their initial and boundary conditions (10) have been solved by using the method of ordinary linear differential equations with constant coefficients. We get the following analytical solutions for the velocity, temperature and concentration

$$U = L_1 e^{m_2 y} + L_2 e^{m_4 y} + L_3 e^{m_6 y}$$

$$T = -\frac{1}{m_2} e^{m_2 y}$$

$$C = -\frac{1}{m_4} e^{m_4 y}$$

Skin friction

$$\tau = \left(\frac{\partial U}{\partial y}\right)_{y=0} = m_2 L_1 + m_4 L_2 e^{m_4 y} + m_6 L_3$$

Nusselt number

$$Nu = \left(\frac{\partial T}{\partial y}\right)_{y=0} = -1$$

Sherwood number

$$Sh = \left(\frac{\partial C}{\partial y}\right)_{y=0} = -1$$

Appendix

$$m_2 = -\Pr; m_4 = -\left(\frac{Sc + \sqrt{Sc^2 + 4KrSc}}{2}\right)$$

$$m_6 = -\left(\frac{1 + \sqrt{1 + 4\beta}}{2}\right), \beta = \left(M + \frac{1}{K}\right)$$

$$L_1 = \frac{1}{m_2}\left(\frac{Gr}{m_2^2 + m_2 - \beta}\right), L_2 = \frac{1}{m_4}\left(\frac{Gr}{m_4^2 + m_4 - \beta}\right)$$

$$L_3 = \left(1 - L_1 - L_2\right)$$

RESULTS AND DISCUSSION

Set of numerical results is shown graphically in figures to illustrate the influence of physical parameters viz., Grashof number, Permeable parameter, Chemical reaction, Magnetic field parameter, Prandtl number and Schmidt number for velocity, temperature, concentration profiles and skin friction on two dimensional incompressible and chemically reacting flow of a viscous fluid on a continuously moving vertical plate in the presence of magnetic field. The thermal Grashof number represents here the effects of free convection currents and receives positive, zero or negative. **Figures (2) - (3)** we observe that an increase in Grashof number and Permeable parameter rise the velocity, but form **figures (4) - (7)** the reverse effects observed in the Chemical reaction parameter, Magnetic parameter, Prandtl number and Schmidt number. It is also observed form the **figure (8)** when increase the Prandtl number lead to decrease in temperature, as well as the concentration profiles shown for the parameters chemical reaction and Schmidt number in **figures (9) - (10)** it shown that the concentration profiles decrease with increasing the above parameters. **Figure (11)** shows that skin friction for magnetic parameter versus Grashof number, it is observed that an increase in magnetic parameter the skin friction decreases.

Conclusion:

An analytical study of chemical reaction effect on MHD flow of continuously moving vertical surface filled with a porous medium. The equations governing the flow field are solved by analytical method by using perturbation technique. Generally our results show that an increase in Grashof number and Permeable parameter raise the velocity.

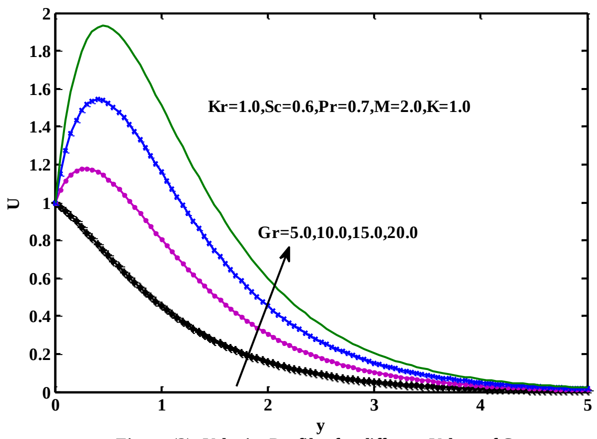

Figure (2): Velocity Profiles for different Values of Gr

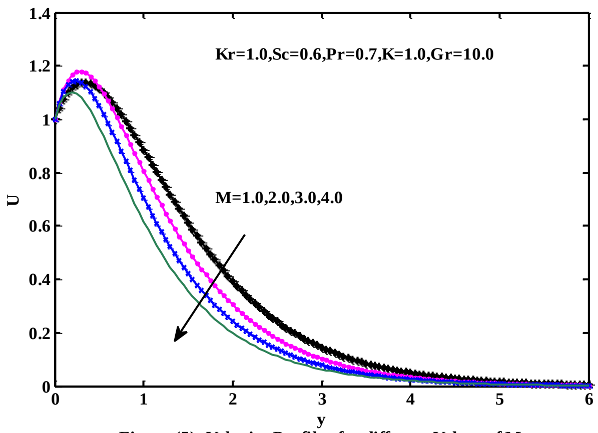

Figure (5): Velocity Profiles for different Values of M

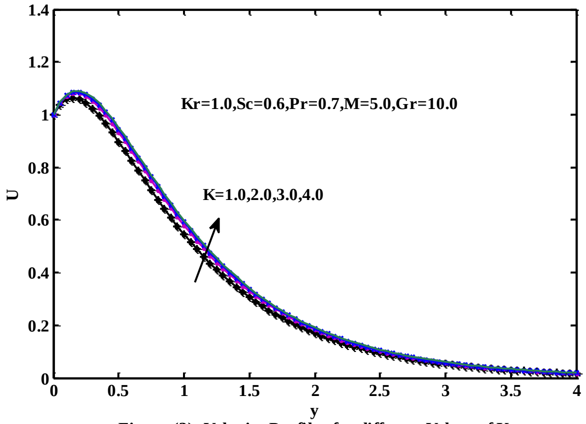

Figure (3): Velocity Profiles for different Values of K

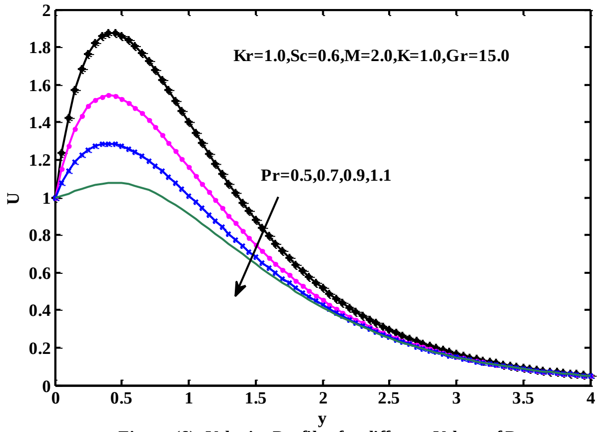

Figure (6): Velocity Profiles for different Values of Pr

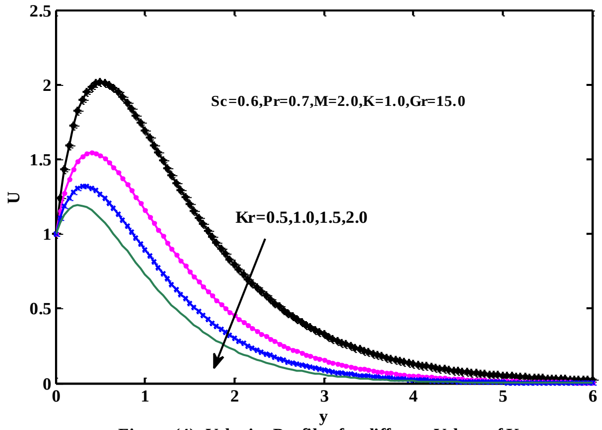

Figure (4): Velocity Profiles for different Values of Kr

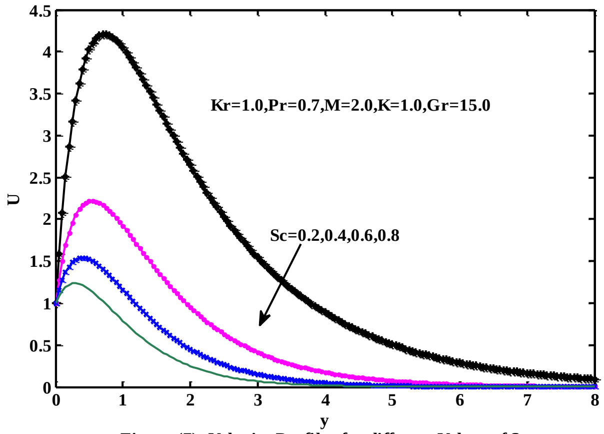

Figure (7): Velocity Profiles for different Values of Sc

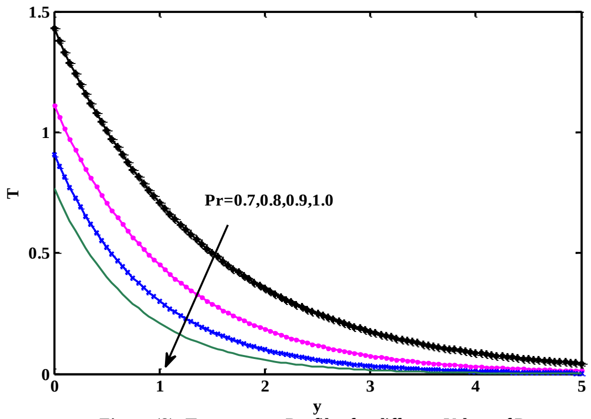

Figure (8): Temperature Profiles for different Values of Pr

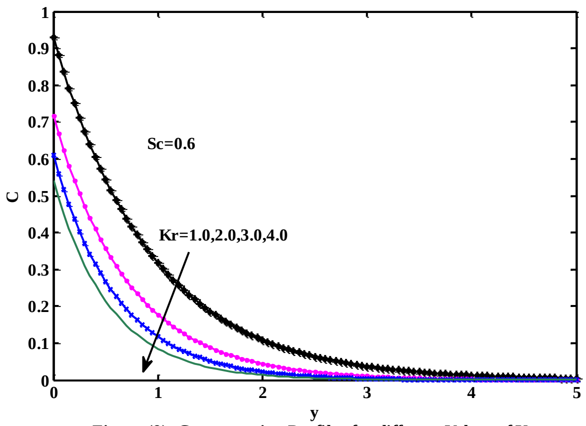

Figure (9): Concentration Profiles for different Values of Kr

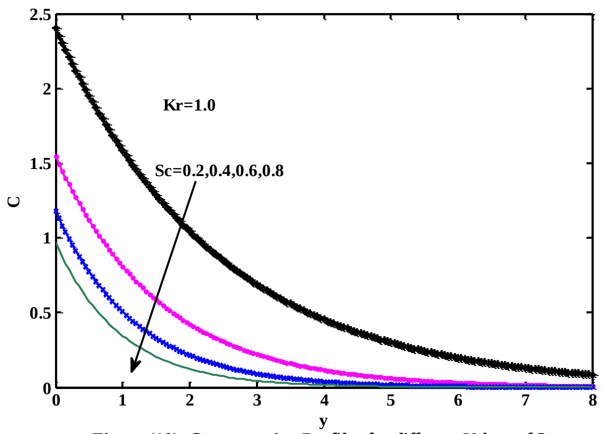

Figure (10): Concentration Profiles for different Values of Sc

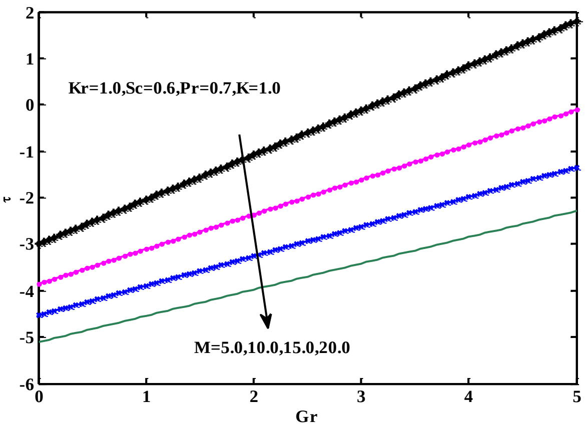

Figure (11): Skin friction for different values of M versus Gr

REFERENCES

[1] R. Tsai, J. S. Huang (2009): Heat and mass transfer for Soret and Dufour's effects on Hiemenz flow through porous medium onto a stretching surface, Int. J. Heat Mass Trasnf. Vol. 52, pp. 2399-2406

[2] Srinathuni Lavanya and D. Chenna Kesavaiah (2017): Heat transfer to MHD free convection flow of a viscoelastic dusty gas through a porous medium with chemical reaction, International Journal of Pure and Applied Researches, Vol. 3 (1), pp. 43 – 56

[3] S. Jeena, G. C. Dash and S. R. Mishra (2018); Chemical reaction effects on MHD viscoelastic fluid flow over a vertical stretching sheet with heat source/sink, Ain Shams Engineering Journal, Vol. 9, pp. 1205-1213

[4] R. S. Tripathy, G.C. Dash, S. R. Mishra and S. Baag (2015): Chemical reaction effect on MHD free convective surface over a moving vertical plane through porous medium, Alex. Eng. J. Vol. 54 (3), pp. 673-679

[5] Srinathuni Lavanya and D. Chenna Kesavaiah (2017): Radiation effects on MHD natural convection heat transfer flow from spirally enhanced wavy channel through a porous medium, International Journal on Future Revolution in Computer Science & Communication Engineering, Vol. 3(10), pp. 130-140

[6] N. G. Kafoussias and E.W. Williams (1995): Thermal diffusion and diffusion thermo

effects on mixed free forced convective and mass transfer boundary layer flow with temperature dependent viscosity, Int. J. Eng. Sci., Vol. 33, 1369-1384

[7] D.Chenna Kesavaiah and P V Satyanarayana (2014): Radiation absorption and Dufour effects to MHD flow in vertical surface, Global Journal of Engineering, Design and Technology, Vol 3(2), pp. 51-57

[8] M. Sajid and T. Hayat (2008): Influence of thermal radiation on the boundary layer flow due to an exponentially stretching sheet, Int. Comm. Heat Mass Trasf. Vol. 35, pp. 347-56

[9] D. Chenna Kesavaiah, P V Satyanarayana (2013): MHD and Diffusion Thermo effects on flow accelerated vertical plate with chemical reaction, Indian Journal of Applied Research, Vol. 3 (7), pp. 310-314

[10] J. Girish Kumar (2013): Chemical reaction effects on MHD flow of continuously moving vertical surface with heat and mass flux through porous medium, International Journal of science, Engineering and Technology Research, Vol. 2 (40), pp. 881-886

[11]B. Bidin and R. Nazar (2009): Numerical solution of the boundary layer flow over an exponentially stretching sheet with thermal radiation, Euro. J. Sci. Res., Vol. 33, pp. 710-717

[12]D. Ch Kesavaiah, P. V. Satyanarayana and S. Venkataramana (2011): Effects of the chemical reaction and radiation absorption on an unsteady MHD convective heat and mass transfer flow past a semi-infinite vertical permeable moving plate embedded in a porous medium with heat source and suction, Int. J. of Appl. Math and Mech. Vol. 7 (1), pp. 52-69

[13] M.H. Abolbashari, N. F. Nazari and M. M. Rashidi (2014): Entropy analysis for an unsteady MHD flow past a stretching permeable surface in nanofluid, Powder Technol., Vol. 267, pp. 256-267

[14] Chauhan, Dileep Singh and Priyanka Rastogi (2010): Radiation effects on natural convection MHD flow in a rotating vertical porous channel partially filled with a porous Medium. Applied Mathematical Science, 4 (13), pp. 648 – 655.

[15] Srinathuni Lavanya, D Chenna Kesavaiah (2014): Radiation and Soret Effects to MHD Flow in Vertical Surface with Chemical reaction and Heat generation through a Porous Medium, International Journal of Computational Engineering Research, Vol, 04, (7), pp. 62-73

[16] P. Khansila and S. Witayangkurn (2012): Visualization of natural convection in enclosure filled with porous medium by sinusoidally temperature on the one side, Applied Mathematical Sciences, Vol. 6 (97), pp. 4801-4812

[17] R. C. Chaudhary, M. C. Goyal and A. Jain (2009): Free convection effects on MHD flow past an infinite vertical accelerated plate embedded in porous media with constant heat flux, Matematicas Ensenanza Universitaria, Vol. 17 (2), pp. 73-82.

[18] K. E. Chin, R. Nazar, N. M. Arifin and I. Pop, (2007): Effect of variable viscosity on mixed convection boundary layer flow over a vertical surface embedded in a porous medium, International Communications in Heat and Mass Transfer, Vol. 34 (4), pp. 464-473

[19] W.C. Troy, E.A. Overman, H.G.B. Ermentrout and J.P. Keener (1987): Uniqueness of flow of a second order fluid past a stretching sheet, Quart. Appl. Math., Vol. 44, pp. 753-5

[20]D. Chenna Kesavaiah and A. Sudhakaraiah (2014): Effects of Heat and Mass Flux to MHD Flow in Vertical Surface with Radiation Absorption, Scholars Journal of Engineering and Technology, 2(2B), pp. 219-225

[21] A. C. Cogly, W. C. Vincentry and S. E. Gille (1968): A Differential approximation for radiative transfer in a non-gray gas near equilibrium, AIAA Journal, 6

[22]M. A. Samad and M. M. Rahman (2006): Thermal Radiation interaction with unsteady MHD flow past a vertical porous plate immersed in a porous medium, J. Naval

Architecture and Marine Eng., Vol. 3, pp. 7 – 14

[23] O.D. Makinde and P.Y. Mhone (2005): Heat transfer to MHD oscillatory flow in a channel filled with porous medium, Rom. Journ. Phys., Vol. 50, Nos. 9–10, pp. 931–938

[24] D. Chenna Kesavaiah and B. Devika (2020): Free convection and heat transfer of a Couette flow an infinite porous plate in the presence radiation effect, Journal of Xi'an University of Architecture & Technology, Vol. XII, (V), pp. 525-543

[25]O. Anwar Be'g, A.Y. Bakier, V.R. Prasad (2009): Numerical study of free convection magnetohydrodynamic heat and mass transfer from a stretching surface to a saturated porous medium with Soret and Dufour effects. Comput. Mater. Sci., Vol. 46, pp. 57-65

[26]D. Chenna Kesavaiah and B. Venkateswarlu (2020): Chemical reaction and radiation absorption effects on convective flows past a porous vertical wavy channel with travelling thermal waves, International Journal of Fluid Mechanics Research, Vol. 47 (2), pp. 153-169

[27]A. Misirlioglu, A. C. Baytas, and I. Pop (2005): Free convection in a wavy cavity filled with a porous medium, International journal of heat and mass transfer, Vol. 48 (9), pp. 1840-1850

[28]N. Beithou, K. Albayrak and A. Abdulmajeed (1998): Effect of porosity on the free convection flow of non-Newtonian fluids along vertical plate embedded in a porous media, Turkish J. of Eng. Envir. Sci. Vol. 22 (3), pp. 203-209.

[29]V Nagaraju, K Hemalatha and V Srihari Babu. (2018): Radiation effects on MHD convective heat and mass transfer flow past a semi-infinite vertical moving porous plate in the presence of chemical reaction, International journal of engineering sciences and research technology, 7(8), pp. 146-161.

[30]V Nagaraju, K Hemalatha and V Srihari Babu. (2019): MHD Viscoelastic Fluid flow Past an Infinite Vertical Plate in the Presence of Radiation and Chemical Reaction, International Journal of Applied Engineering Research, Volume 14(5), pp. 1062-1069.

[31]Omeshwar Reddy V, Neelima A and Thiagarajan S. (2019). "Finite difference solutions of MHD natural convective Rivlin-ericksen fluid flow past a vertically inclined porous plate in presence of thermal diffusion, diffusion thermo, heat and mass transfer effects." International Journal of Applied Engineering Research, 14(3): 703-716.

[32]Nagaraju V, Srihari Babu V and Srilakshmi Ch. (2022). "Numerical investigation of radiation effects on MHD convective heat and mass transfer flow past a semi-infinite vertical moving porous plate in the presence of chemical reaction." International Journal for Research in Applied Science & Engineering Technology, Vol. 10 (1): 1595-1607. https://doi.org/10.22214/ijraset.2022.40105.

[33]V Sri Hari Babu, Nagaraju Vellanki, G Rami Reddy, V. Omeswar Reddy. *(2021):* **"**Radiation and chemical reaction effects on mhd rotating fluid past a moving vertical plate*.***"** Journal of Mathematical Control Science and Applications**,** 7(2*): 301-312.*

[34]Nagaraju Vellanki, Y.V. Seshagiri Rao, G. Rami Reddy, V Sri Hari Babu. (2021): "Radiation effect on unsteady free convection oscillatory couette flow through a porous medium with periodic wall temperature and heat generation." Journal of Mathematical Control Science and Applications, Vol 7(2):269-283.

[35]Omeshwar Reddy V, Y.V. Seshagiri Rao, K. Venugopal Reddy, Shivaleela G *(2021): "*Radiation and mass transfer effects on unsteady hydro magnetic free convection flow through porous medium past a vertical plate with heat flux." Journal of Mathematical Control Science and Applications, *7(2): 285-299.*

[36]Omeshwar reddy V, V.Nagaraju, Y.V. Seshagiri Rao. (2020). "Thermo diffusion, heat and mass transfer analysis of MHD viscoelasticf luid flow towards a vertically inclined plate by perturbation technique."

Journal of Mathematical Control Science and Applications, Vol 6(2):151-164.

[37]Nagaraju V,V Sri Hari Babu, G. Rami Reddy, Lakshmi Appidi. (2021). “A perturbation analysis for effects on chemical reaction and thermal radiation on temperature and concentration on MHD free convection flow past a vertical porous plate in the presence of and heat source parameter.” Journal of Mathematical Control Science and Applications, 7(2):253-267.

[38] Bang Chuol Nhial, V Sri Hari Babu, V. Nagaraju Vellanki, G. Y. Sagar (2022): ‘RADIATION AND MASS TRANSFER EFFECTS ON MHD FREE CONVECTION FLOW OVER AN INCLINED PLATE’, Journal of Positive School Psychology, Vol 6(5), pp.697-706.

[39]Bang Chuol Nhial, V. Nagaraju Vellanki, V Sri Hari Babu, G. Y. Sagar (2022): ‘ HALL CURRENT, ROTATION AND CHEMICAL REACTION EFFECTS ON MHD FREE CONVECTION FLOW PAST AN ACCELERATED VERTICAL PLATE THROUGH A POROUS MEDIUM’, Journal of Positive School Psychology, Vol 6(5),2022, pp.707-716.

[40]Y.Sunita Rani (2019) : ‘Jeffrey Fluid Behaviour on Oscillatory Couette Flow past Two Horizontal Parallel Plates in Presence of MHD and Radiative Heat Transfer‘ in ‘’International Journal of Innovative Technology and Exploring Engineering’’ ISSN: 2278-3075, Volume-8 Issue-11, September 2019.

Journal of Positive School Psychology http://journalppw.com
2022, Vol. 6, No. 4, 10983–10991

Radiation And Chemical Reaction Effects on Unsteady Flow Past an Accelerated Infinite Vertical Plate with Variable Temperature and Uniform Mass Diffusion Through a Porous Medium

Ch. Shashi Kumar[1], P. Govinda Chowdary[2], P. Sarada Devi[3], V. Nagaraju[4]

[1]Department of Mathematics, VNR Vignana Jyothi Institute of Engineering & Technology, Hyderabad, TS-500090, India.

[2,4]Department of Basic Sciences and Humanities, Vignan Institute of Technology and Science, Deshmukhi (V), Pochampally (M), Yadadri-Bhuvanagiri (Dist), T.S-508284, India.
Email: chowdary.ratp@gmail.com

[3]Department of Mathematics, Malla Reddy Engineering College (Autonomous), Maisammaguda, Hyderabad-500100, India, Email: sarada.chakireddy@gmail.com

Abstract

The aim of the present analysis is to study the effect of radiation and chemical reaction unsteady flow of an incompressible viscous fluid past a uniformly accelerated infinite vertical porous plate through the porous medium taking into an account of the presence of the variable temperature, uniform mass diffusion with heat and mass transfer of the dimensionless governing partial differential equations. The velocity, temperature, concentration, skin friction, rate of heat transfer and Sherwood number are shown graphically various parameters involving in the problem.

Keywords: Radiation, Chemical reaction, Vertical plate, Variable temperature, Porous medium

INTRODUCTION

The effect of a chemical reaction depends on whether the reaction is homogenous or heterogeneous. This depends on whether the reaction occurs at an interface or as a single phase volume reaction. In well – mixed systems, if it takes place at an interface, the reaction is heterogeneous; and homogeneous if it takes place in solution. In view of the above some of the authors studied, in view of the above some of the authors are carried out Ch Kesavaiah et. al. [1] explained the effects of the chemical reaction and radiation absorption on an unsteady MHD convective heat and mass transfer flow past a semi-infinite vertical permeable moving plate embedded in a porous medium with heat source and suction, Das et. al. [2] expressed radiation effects on flow past an impulsively started vertical infinite plate, Muthucumaraswamy and Lakshmi [3] shows that first order chemical reaction effects on exponentially accelerated vertical plate with variable mass diffusion in the presence of thermal radiation, Chenna Kesavaiah and Sudhakaraiah [4] implemented the effects of heat and mass flux to MHD flow in vertical surface with radiation absorption, El-Hakiem [5] shows that MHD oscillatory flow on free convection-radiation through a porous medium with constant suction velocity, Karunakar Reddy et. al. [6] exhibited MHD heat and mass transfer flow of a viscoelastic fluid past an impulsively started infinite vertical plate with chemical reaction, Makinde and Mhone [7] demonstrated heat transfer to MHD oscillatory flow in a channel filled with porous medium, Raju [8] reviled MHD chemically reacting viscoelastic fluid past an impulsively started infinite vertical plate with heat and mass transfer effect, Gowri and Selvaraj [9] carried out of fluid performance of unsteady MHD parabolic flow past an accelerated vertical plate in the presence of rotation through Porous medium, Dilip Jose and Selvaraj [10] shows that the convective heat and mass transfer effects of rotation on parabolic flow past an accelerated isothermal vertical plate in the presence of chemical reaction of first order.

However, flow through a porous medium has been of significant interest in recent years particularly among geophysical fluid dynamicity. Examples of natural porous media are beach sand, stand stone, limestone, rye bread, wood, the human lung, bile duct, gall bladder with stones and in small blood vessels. Influence of MHD and radiation effects on oscillatory flow through a porous medium with constant suction velocity has been studied by Chenna Kesavaiah and Satyanarayana [11] has been considered MHD and Diffusion Thermo effects on flow accelerated vertical plate with chemical reaction, Sami Ul Haq et. al. [12] studied general solution for unsteady MHD natural convection flow with arbitrary motion of the infinite vertical plate embedded in porous medium, Srinathuni Lavanya and Chenna Kesavaiah [13] has been considered heat transfer to MHD free convection flow of a viscoelastic dusty gas through a porous medium with chemical reaction, Rajput and Gaurav Kumar [14] carried out the effects of radiation and chemical reaction on MHD flow past a vertical plate with variable temperature and mass diffusion, Adekeye et. al. [15] motivated study on numerical analysis of the effects of selected geometrical parameters and fluid properties on MHD natural convection flow in an inclined elliptic porous enclosure with localized heating, Chenna Kesavaiah et. al. [16] shows that the natural convection heat transfer oscillatory flow of an elastico-viscous fluid from vertical plate, Rout and Pattanayak [17] intended their work through chemical reaction and radiation effect on MHD flow past an exponentially accelerated vertical plate in presence of heat source with variable temperature embedded in a porous medium, Islam and Ahmed [18] expressed the effect of thermal diffusion and chemical reaction on MHD free convective flow past an infinite isothermal vertical plate with heat source.

The study of magneto hydrodynamics with mass and heat transfer in the presence of radiation and diffusion has attracted the attention of a large number of scholars due to diverse applications. In astrophysics and geophysics, it is applied to study the stellar and solar structures, radio propagation through the ionosphere, etc. In engineering we find its applications like in MHD pumps, MHD bearings, etc. Combined heat and mass transfer problems with chemical reaction are of importance in many processes and have, therefore, received a considerable amount of attention in recent years. In processes such as drying, evaporation on the surface of a water, energy transfer in a wet cooling tower and the flow in a desert cooler, heat and mass transfer occur simultaneously. Possible applications of this type of flow can be found in many industries. For example, in the power industry, one of the methods of generating electric energy is directly from a moving conducting fluid. The effects of radiation on MHD flow and heat transfer problem have become more important in industries. At high operating temperature, radiation effect can be quite significant. Many processes in engineering areas occur at high temperature and knowledge of radiation heat transfer becomes very important for the design of the pertinent equipment. Nuclear power plants, gas turbines and the various propulsion devices for aircraft, missiles, satellites and space vehicles are examples of such engineering areas. Such information noted some of the authors by Mallikarjuna Reddy et. al. [19] explained the effects of radiation and thermal diffusion on MHD heat transfer flow of a dusty viscoelastic fluid between two moving parallel plates, Muthucumaraswamy and Radhakrishnan [20] shows that the chemical reaction effects on flow past an accelerated vertical plate with variable temperature and mass diffusion in the presence of magnetic field, Ch Kesavaiah et. al. [21] has been studied radiation and mass transfer effects on moving vertical plate with variable temperature and viscous dissipation, Venkateswarlu and Satya Narayana [22] has been considered chemical reaction and radiation absorption effects on the flow and heat transfer of a nanofluid in a rotating system, Chenna Kesavaiah and Venkateswarlu [23] shows that the chemical reaction and radiation absorption effects on convective flows past a porous vertical wavy channel with travelling thermal waves, Venkateswarlu and Narayana [24] motivated study on variable wall concentration and slip effects on MHD nanofluid flow past a porous vertical flat plate, Chenna Kesavaiah et. al. [25] studied radiative MHD Walter's Liquid-B flow past a semi-infinite vertical Plate in the presence of viscous dissipation with a heat source. Earlier the related work discussed by different authors from [26-40]

The aim of the present analysis is to study the effect of radiation and chemical reaction unsteady flow of an incompressible viscous fluid past a uniformly accelerated infinite vertical porous plate through the porous medium taking into an account of the presence of the variable temperature.

FORMULATION OF THE PROBLEM

The unsteady flow of an incompressible viscous fluid which is initially at rest past an infinite vertical plate with variable temperature through a porous medium is considered. The flow is assumed to be in $x-$direction which takes vertical plate in the upward direction. The $y-$axis is taken to be normal to the plate. Initially the plate and the fluid are in same temperature T' with the same concentration C' level at all points shown in figure (1). At time $t'>0$ the plate accelerated with velocity $u'=\frac{u_0^3 t'}{\nu}$ in its own plane. The plate temperature is raised to T'_w and the level of concentration near the plate is raised to C'_w linearly with the time t.

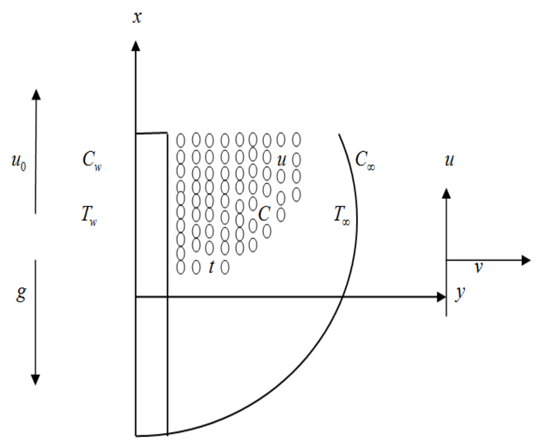

Figure (1): Physical model of the problem

Then by Boussinesq's approximation the unsteady flow is governed by the following equations:

$$\frac{\partial u'}{\partial t'} = g\beta\left(T'-T'_\infty\right)+g\beta^*\left(C'-C'_\infty\right) + \nu\frac{\partial^2 u'}{\partial y'^2}-\frac{\nu}{K'_1}u' \qquad (1)$$

$$\rho c_p\frac{\partial T'}{\partial t'} = \kappa\frac{\partial^2 T'}{\partial y'^2}-\frac{\partial q_r}{\partial y} \qquad (2)$$

$$\frac{\partial C'}{\partial t'} = D\frac{\partial^2 C'}{\partial y'^2}-Kr'\left(C'-C'_\infty\right) \qquad (3)$$

With the following initial and boundary conditions for the fluid flow problem are given below

$$u=0, T'=T'_\infty, C'=C'_\infty \quad \forall \; y \;\&\; t'\le 0$$

$$\left.\begin{aligned} u' &= \frac{u_0^3 t'}{\nu}, \\ T' &= T'_\infty+\left(T'_w-T'_\infty\right)At', \\ C' &= C'_\infty+\left(C'_w-C'_\infty\right)At' \end{aligned}\right\} \text{at } y=0 \;\&\; t'>0 \quad (4$$

$$u\to 0, T'\to T'_\infty, C'\to C'_\infty \quad as \quad y\to\infty$$
)

The following dimensionless variables and parameters of the problem are

$$\left.\begin{aligned} &U=\frac{u'}{u_0},\; t=\frac{t'u_0{}^2}{\nu},\; Y=\frac{y'u_0}{\nu},\; \theta=\frac{T'-T'_\infty}{T'_w-T'_\infty} \\ &C=\frac{C'-C'_\infty}{C'_w-C'_\infty},\; \frac{1}{K}=\frac{k'u_0^2}{\nu^2},\quad F=\frac{4\nu I^*}{\rho C_p u_0^2} \\ &Gr=\frac{g\beta\nu\left(T'_w-T'_\infty\right)}{u_0^3}, Sc=\frac{\nu}{D},\; \Pr=\frac{\mu C_p}{k} \\ &Gm=\frac{\beta' g\nu\left(C'_w-C'_\infty\right)}{u_0^3},\qquad Kr=\frac{Kr'\nu}{u_0^2} \end{aligned}\right\} (5)$$

Then an equations (1) – (3) leads to

$$\frac{\partial U}{\partial t} = Gr\;\theta+Gc\;C+\frac{\partial^2 U}{\partial Y^2}-KU \qquad (6)$$

$$\frac{\partial\theta}{\partial t} = \frac{1}{\Pr}\frac{\partial^2\theta}{\partial Y^2}-F\theta \qquad (7)$$

$$\frac{\partial C}{\partial t} = \frac{1}{Sc}\frac{\partial^2 C}{\partial Y^2}-Kr\,C \qquad (8)$$

The relevant initial and boundary conditions in non- dimensional form are given by

$$\begin{aligned} &U=0,\theta=0,C=0 \quad \forall\; Y\le 0, \&\; t\le 0 \\ &U=t,\theta=t,C=t \quad \text{at} \quad Y=0,\; \&\, t>0 \quad (9) \\ &U\to 0,\; \theta\to 0, C\to 0 \; Y\to\infty \quad t>0 \end{aligned}$$

METHOD OF SOLUTION

Equation (6) - (8) are coupled, non – linear partial differential equations and these cannot be solved in closed – form using the initial and boundary conditions (9). However, these equations can be reduced to a set of ordinary differential equations, which can be solved analytically. This can be done by representing the velocity, temperature and concentration of the fluid in the neighbourhood of the fluid in the neighbourhood of the plate as

$$U(y,t)=U_0(y)+U_1(y)e^{nt}$$
$$\theta(y,t)=\theta_0(y)+\theta_1(y)e^{nt} \qquad (10)$$
$$C(y,t)=C_0(y)+C_1(y)e^{nt}$$

Substitute equation (10) in to the equations (6), (7) and (8) the set of ordinary differential equations are the following form

$$U_0'' - KU_0 = -Gr\,\theta_0 - Gm\,C_0 \qquad (11)$$

$$U_1'' - (K+nt)U_1 = -Gr\,\theta_1 - Gm\,C_1 \qquad (12)$$

$$\theta_0'' - F\,\mathrm{Pr}\,\theta_0 = 0 \qquad (13)$$

$$\theta_1'' - (F+nt)\mathrm{Pr}\,\theta_1 = 0 \qquad (14)$$

$$C_0'' - KrSc\,C_0 = 0 \qquad (15)$$

$$C_1'' - (Kr+nt)Sc\,C_1 = 0 \qquad (16)$$

The exact solution for the fluid velocity $U(y,t)$, fluid temperature $\theta(y,t)$ and species concentration $C(y,t)$ are obtained and expressed from equations from (11) - (16) in the following form:

$$U(y,t)=A_1\,e^{-\sqrt{F\,\mathrm{Pr}}\;y}+A_2\,e^{-\sqrt{KrSc}\;y}+A_3\,e^{-\sqrt{K}\;y}$$
$$\theta(y,t)=t\,e^{-\sqrt{F\,\mathrm{Pr}}\;y}$$
$$C(y,t)=t\,e^{-\sqrt{KrSc}\;y}$$

Skin-friction

$$\left(\frac{\partial U}{\partial y}\right)_{y=0}=-\sqrt{F\,\mathrm{Pr}}A_1-\sqrt{Kr\,Sc}\,A_2-\sqrt{K}A_3$$

Nusselt number

$$\left(\frac{\partial \theta}{\partial y}\right)_{y=0}=-t\sqrt{F\,\mathrm{Pr}}$$

Sherwood number

$$\left(\frac{\partial C}{\partial y}\right)_{y=0}=-t\sqrt{Kr\;Sc}$$

RESULTS AND DISCUSSION

The results are shown graphically for various parameters thermal Grashof number(Gr), modified Grashof number(Gc), Prandtl number(Pr), Schmidt number(Sc), Radiation parameter(F), Permeability parameter(K), Chemical reaction parameter (Kr) and time(t). In this observation the values of the Prandtl number are chosen to represents air $(\mathrm{Pr}=0.71)$ and water $(\mathrm{Pr}=7.0)$; Schmidt number are chosen to represents oxygen $(Sc=0.60)$, Ammonia $(Sc=0.78)$, Carbon Dioxide $(Sc=0.94)$, Ethy benzene $(Sc=2.0)$. The velocity profiles shown from figures (2) – (8); the velocity profiles different values of time$(t=0.2,0.4,0.6,0.8)$ is predicted in figure (2); it is clearly shown that the velocity increases with increasing values of time. The velocity profiles for different values of radiation parameter $(F=1,2,3,4)$ is presented in figure (3), it is observed that the velocity decrease with the increasing values of permeability parameter. For various values of thermal Grashof number and modified Grashof number $(Gr=1,2,3,4;Gc=1,2,3,4)$ are give an exhibition of the velocity profiles in figure (4) and (5), we noticed that the velocity increase with increasing values of thermal Grashof number as well as modified Grashof number. Figures (6) and (7) shown velocity profiles for different values of chemical reaction parameter$(Kr=1,2,3,4)$ and Schmidt number$(Sc=0.60,0.78,0.94,2)$, it is observed that an increasing values of chemical reaction parameter and Schmidt number the velocity decreases. The velocity profiles observed for different values of Prandtl number$(\mathrm{Pr}=0.78,0.9,1,7)$ are shown in figure (8), it is clear that the velocity decreases with increasing values of Prandtl number. The temperature profiles are shown from figures (9) – (11). From figures (9) and figure (10) observed that the temperature profiles for different values of Prandtl number$(\mathrm{Pr}=0.78,0.9,1,7)$ and radiation parameter$(F=1,2,3,4)$, we observed that an increasing Prandtl number and radiation parameters the temperature profiles decreases in both the parameters. Figure (11) displays the temperature profiles for different values of time $(t = 0.2, 0.4, 0.6, 0.8)$ indicates that the temperature profiles increases with increases with time. The concentration profiles are shown from figures (12) – (14). From figures (12) and figure (13) observed that the concentration profiles for different values of chemical reaction parameter $(Kr = 1, 2, 3, 4)$ and Schmidt number $(Sc = 0.60, 0.78, 0.94, 2)$ we observed that an increasing Prandtl number the concentration profiles decreases in both the parameters. Figure (14) displays the concentration profiles for different values of time $(t = 0.2, 0.4, 0.6, 0.8)$ indicates that the concentration profiles increases with increases with time. The skin friction coefficient shown in figure (15) for various values of radiation parameter $(F = 1, 2, 3, 4)$ versus thermal Grashof number (Gr) which is clear that an increasing values of radiation parameter the skin friction coefficient decreases. The rate of heat transfer shown in figure (16) for different values of radiation parameter $(F = 1, 2, 3, 4)$ versus Prandtl number $(\Pr)$, it shows that an increases in Prandtl number the Nusselt number decreases. From figure (18) observed that Sherwood number for different values of Schmidt number $(Sc = 0.60, 0.78, 0.94, 2)$ versus chemical reaction parameter (Kr), we observed that an increasing Schmidt number the Sherwood number decreases.

Conclusions:

We noticed that the

- Velocity increase with increasing values of thermal Grashof number as well as modified Grashof number.
- The velocity profiles for different values of Schmidt number, it is observed that increasing values of Schmidt number the velocity decreases.
- The velocity profiles for different values of chemical reaction parameter and Schmidt number, it is observed that an increasing values of chemical reaction parameter the velocity decreases.

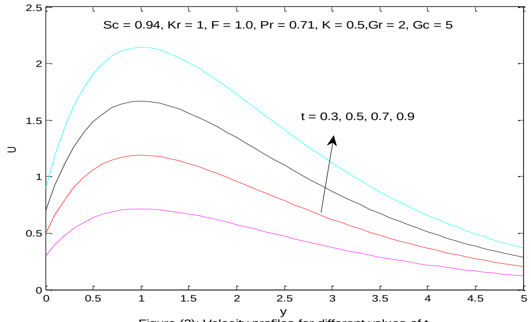

Figure (2): Velocity profiles for different values of t

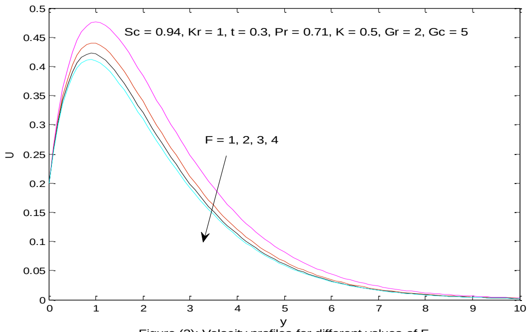

Figure (3): Velocity profiles for different values of F

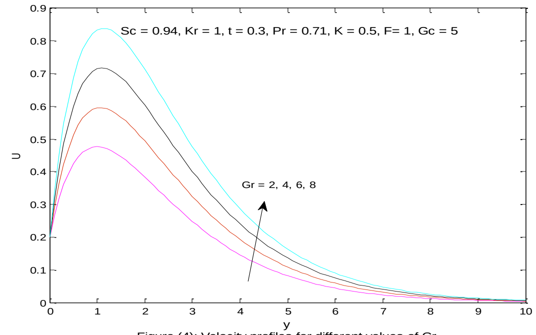

Figure (4): Velocity profiles for different values of Gr

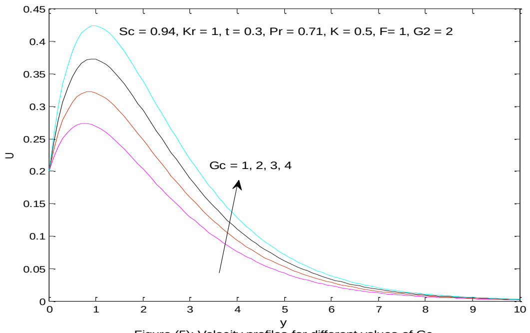

Figure (5): Velocity profiles for different values of Gc

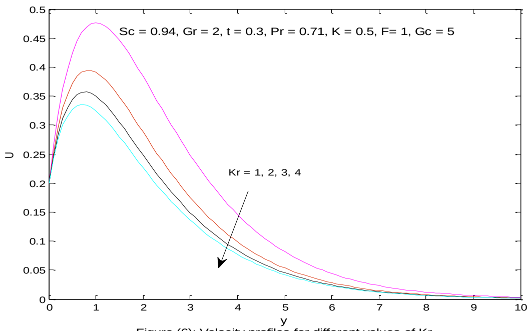

Figure (6): Velocity profiles for different values of Kr

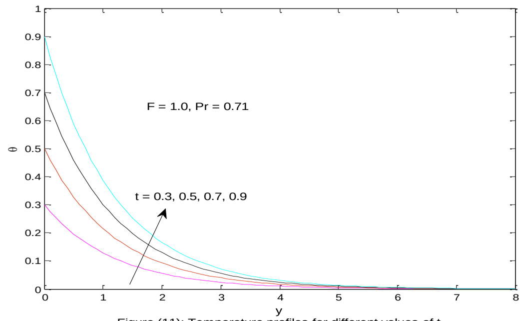

Figure (11): Temperature profiles for different values of t

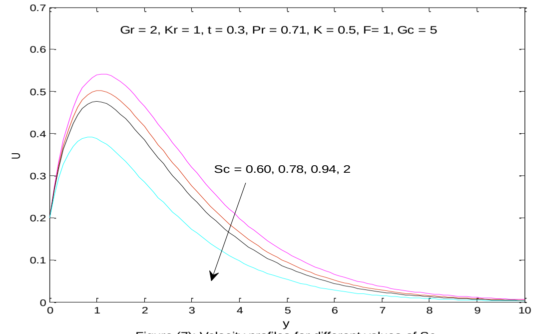

Figure (7): Velocity profiles for different values of Sc

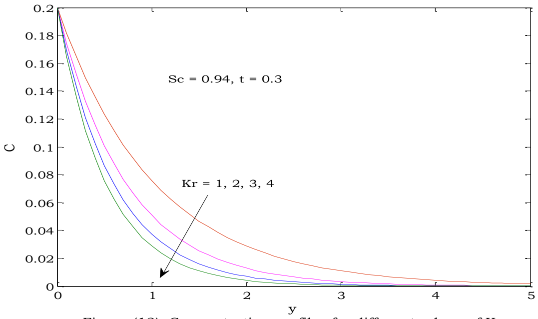

Figure (12): Concentration profiles for different values of Kr

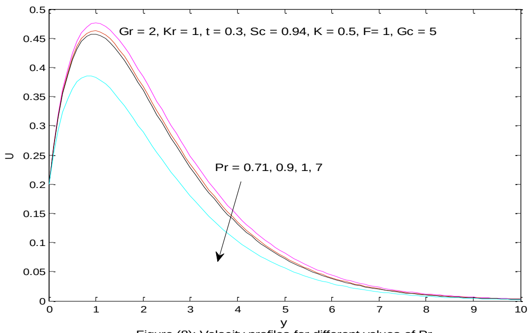

Figure (8): Velocity profiles for different values of Pr

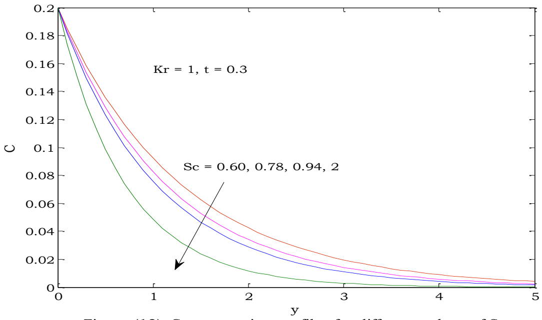

Figure (13): Concentration profiles for different values of Sc

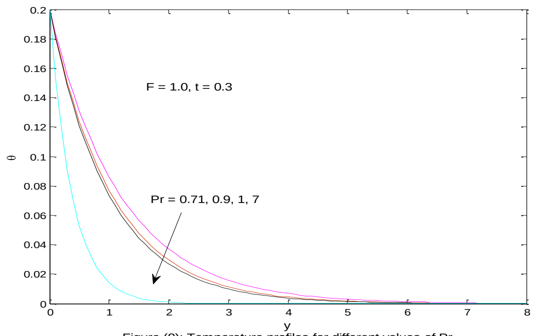

Figure (9): Temperature profiles for different values of Pr

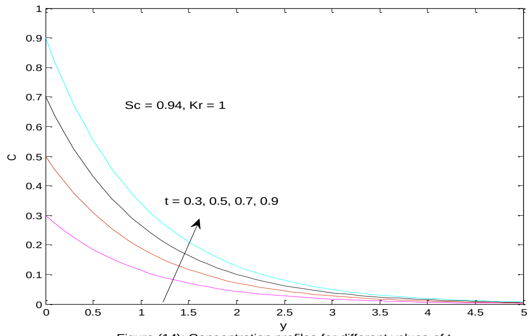

Figure (14): Concentration profiles for different values of t

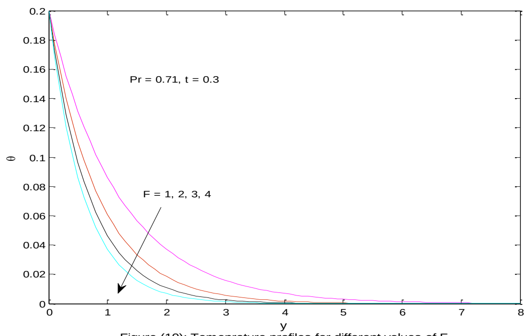

Figure (10): Temeprature profiles for different values of F

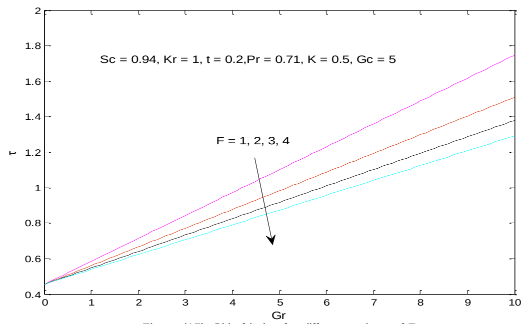

Figure (15): Skin friction for different values of F

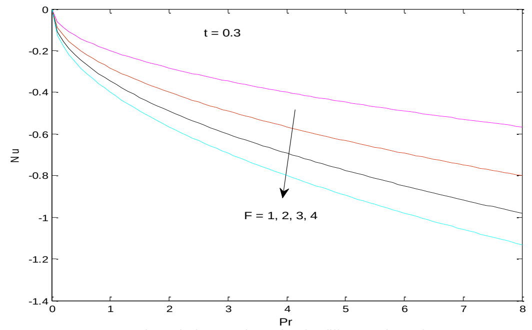

Figure (16): Nusselt number for different values of F

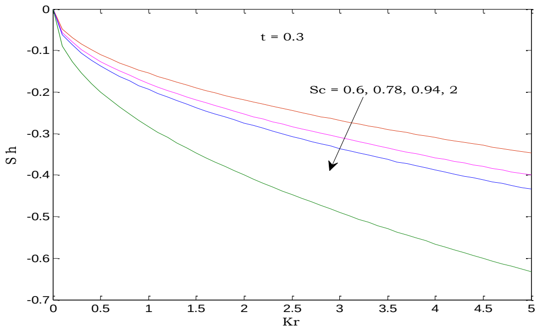

Figure (17): Sherwood number for different values of Sc

APPENDIX

$$A_1 = \frac{Gr\,t}{F\,\Pr - K}, A_2 = \frac{Gc\,t}{KrSc - K}$$

$$A_3 = \left(t - A_1 - A_2\right)$$

REFERENCES

[1] D Ch Kesavaiah, P V Satyanarayana and S Venkataramana (2011): Effects of the chemical reaction and radiation absorption on an unsteady MHD convective heat and mass transfer flow past a semi-infinite vertical permeable moving plate embedded in a porous medium with heat source and suction, *Int. J. of Appl. Math and Mech.* Vol. 7 (1), pp. 52-69

[2] U N Das, R Deka and V M Soundalgekar (1996): Radiation effects on flow past an impulsively started vertical infinite plate, *J, Theo. Mech*, Vol.1, pp. 111-115

[3] R Muthucumaraswamy and C S Lakshmi (2015): First order chemical reaction effects on exponentially accelerated vertical plate with variable mass diffusion in the presence of thermal radiation, *Int. J. Applied Mechanics and Engineering*, Vol. 20 (2), pp. 329-344

[4] D Chenna Kesavaiah and A Sudhakaraiah (2014): Effects of heat and mass flux to MHD flow in vertical surface with radiation absorption, *Scholars Journal of Engineering and Technology*, Vol. 2(2): pp. 219-225

[5] M A El-Hakiem (2000): MHD oscillatory flow on free convection-radiation through a porous medium with constant suction velocity. Journal of Magnetism and Magnet Materials, Vol. 220 (2-3), 271 – 276

[6] S Karunakar Reddy, D Chenna Kesavaiah and M N Raja Shekar (2013): MHD heat and mass transfer flow of a viscoelastic fluid past an impulsively started infinite vertical plate with chemical reaction, *International Journal of Innovative Research in Science, Engineering and Technology*, Vol. 2 (4), pp.973- 981

[7] O.D. Makinde and P. Y. Mhone (2005): Heat transfer to MHD oscillatory flow in a channel filled with porous medium, *Rom. Journal of Physics*, Vol. 50 (9-10), pp. 931 – 938.

[8] D Raju (2017): MHD chemically reacting viscoelastic fluid past an impulsively started infinite vertical plate with heat and mass transfer effect, IJSRR, Vol. 6 (4), pp. 17-28

[9] T. Gowri and A. Selvaraj (2022): Fluid performance of unsteady MHD parabolic flow past an accelerated vertical plate in the presence of rotation through Porous medium, *International Journal of Mechanical Engineering*, Vol. 7 (5), pp. 152-159

[10] S. Dilip Jose and A. Selvaraj (2021): Convective heat and mass transfer effects of rotation on parabolic flow past an accelerated isothermal vertical plate in the presence of chemical reaction of first order, *JP Journal of Heat and Mass Transfer*, Vol. 24 (1), pp. 191-206.

[11]D Chenna Kesavaiah, P V Satyanarayana (2013): MHD and Diffusion Thermo effects on flow accelerated vertical plate with chemical reaction, *Indian Journal of Applied Research*, Vol. 3 (7), pp. 310-314

[12]Sami Ul Haq, Hammad Khaliq, Saeed Ullah Jan, Aisha M. Alqahtani, Iyas Khan and Md. Nur Alam (2022): General solution for unsteady MHD natural convection flow with arbitrary motion of the infinite vertical plate embedded in porous medium, *Journal of Mathematics,* pp. 1-10

[13]Srinathuni Lavanya and D Chenna Kesavaiah (2017): Heat transfer to MHD

free convection flow of a viscoelastic dusty gas through a porous medium with chemical reaction, *International Journal of Pure and Applied Researches,* Vol. 3 (1), pp. 43 – 56

[14] U S Rajput and Gaurav Kumar (2019): Effects of radiation and chemical reaction on MHD flow past a vertical plate with variable temperature and mass diffusion, *Journal of Naval Architecture and Marine Engineering,* Vol. 16, pp. 99-108

[15] T Adekeye, I. Adegun, P. Okekunle, A. K. Hussein, S. Oyedepo, E. Adetiba and O. Fayomi (2017): Numerical analysis of the effects of selected geometrical parameters and fluid properties on MHD natural convection flow in an inclined elliptic porous enclosure with localized heating, *Heat Transfer-Asian Research,* Vol. 46, No.3, pp.261-293

[16] D Chenna Kesavaiah, P V Satyanarayana, A Sudhakaraiah, S Venkataramana (2013): Natural convection heat transfer oscillatory flow of an elastico-viscous fluid from vertical plate, *International Journal of Research in Engineering and Technology, Vol. 2 (6),* pp. 959-966

[17] B R Rout and H B Pattanayak (2013): chemical reaction and radiation effect on MHD flow past an exponentially accelerated vertical plate in presence of heat source with variable temperature embedded in a porous medium, *Annals of the Faculty of Engineering Hunedoara,* Vol. 11 (4), pp. 253-259

[18] S H Islam and N Ahmed (2019): Effect of thermal diffusion and chemical reaction on MHD free convective flow past an infinite isothermal vertical plate with heat source, *Italian Journal of Pure and Applied Mathematics,* Vol. 42, pp. 559–574

[19] B Mallikarjuna Reddy, D Chenna Kesavaiah and G V Ramana Reddy (2018): Effects of radiation and thermal diffusion on MHD heat transfer flow of a dusty viscoelastic fluid between two moving parallel plates, *ARPN Journal of Engineering and Applied Sciences, Vol. 13 (22), pp. 8863-8872*

[20] R. Muthucumaraswamy and M. Radhakrishnan (2012): Chemical reaction effects on flow past an accelerated vertical plate with variable temperature and mass diffusion in the presence of magnetic field, *Journal of Mechanical Engineering and Sciences*, Vol. 3, pp. 251-260

[21] D Ch Kesavaiah, P V Satyanarayana, J Gireesh Kumar and S Venkataramana (2012): Radiation and mass transfer effects on moving vertical plate with variable temperature and viscous Dissipation, *International Journal of Mathematical Archive, Vol. 3 (8)*, pp. 3028-3035

[22]B Venkateswarlu, P V Satya Narayana (2015): Chemical reaction and radiation absorption effects on the flow and heat transfer of a nanofluid in a rotating system, *Applied Nanoscience,* Vol. 5 (3), pp. 351-360

[23]D Chenna Kesavaiah and B Venkateswarlu (2020): Chemical reaction and radiation absorption effects on convective flows past a porous vertical wavy channel with travelling thermal waves, *International Journal of Fluid Mechanics Research*, Vol. 47 (2), pp. 153-169

[24] B Venkateswarlu, P V Narayana (2019): Variable wall concentration and slip effects on MHD nanofluid flow past a porous vertical flat plate, *Journal of Nanofluids*, Vol. 8 (4), pp. 838-844

[25]Chenna Kesavaiah DAMALA, Venkateswarlu BHUMARAPU, Oluwole Daniel MAKINDE (2021): Radiative MHD Walter’s Liquid-B Flow Past a Semi-Infinite Vertical Plate in the Presence of Viscous Dissipation with a Heat Source, *Engineering Transactions*, Vol. 69(4), pp. 373–401

[26]V Nagaraju, K Hemalatha and V Srihari Babu. (2018): Radiation effects on MHD convective heat and mass transfer flow past a semi-infinite vertical moving porous plate in the presence of chemical reaction, *International journal of engineering sciences and research technology*, 7(8), pp. 146-161.

[27]V Nagaraju, K Hemalatha and V Srihari Babu. (2019): MHD Viscoelastic Fluid flow Past an Infinite Vertical Plate in the Presence of Radiation and Chemical Reaction, *International Journal of Applied Engineering Research,* Volume 14(5), pp. 1062-1069.

[28]Omeshwar Reddy V, Neelima A and Thiagarajan S. (2019). “Finite difference solutions of MHD natural convective Rivlin-ericksen fluid flow past a vertically

inclined porous plate in presence of thermal diffusion, diffusion thermo, heat and mass transfer effects." *International Journal of Applied Engineering Research*, 14(3): 703-716.

[29]Nagaraju V, Srihari Babu V and Srilakshmi Ch. (2022). "Numerical investigation of radiation effects on MHD convective heat and mass transfer flow past a semi-infinite vertical moving porous plate in the presence of chemical reaction." *International Journal for Research in Applied Science & Engineering Technology*, Vol. 10 (1): 1595-1607. https://doi.org/10.22214/ijraset.2022.40105.

[30]V Sri Hari Babu, Nagaraju Vellanki, G Rami Reddy, V. Omeswar Reddy. (*2021):* **"**Radiation and chemical reaction effects on mhd rotating fluid past a moving vertical plate**."** *Journal of Mathematical Control Science and Applications***,** 7(2*): 301-312.*

[31]Nagaraju Vellanki, Y.V. Seshagiri Rao, G. Rami Reddy, V Sri Hari Babu. (2021): "Radiation effect on unsteady free convection oscillatory couette flow through a porous medium with periodic wall temperature and heat generation." *Journal of Mathematical Control Science and Applications*, Vol 7(2):269-283.

[32]Omeshwar Reddy V, Y.V. Seshagiri Rao, K. Venugopal Reddy, Shivaleela G *(2021): "*Radiation and mass transfer effects on unsteady hydro magnetic free convection flow through porous medium past a vertical plate with heat flux." *Journal of Mathematical Control Science and Applications, 7(2): 285-299.*

[33]Omeshwar reddy V, V.Nagaraju, Y.V. Seshagiri Rao. (2020). "Thermo diffusion, heat and mass transfer analysis of MHD viscoelasticf luid flow towards a vertically inclined plate by perturbation technique." *Journal of Mathematical Control Science and Applications,* Vol 6(2):151-164.

[34]Nagaraju V,V Sri Hari Babu, G. Rami Reddy, Lakshmi Appidi. (2021). "A perturbation analysis for effects on chemical reaction and thermal radiation on temperature and concentration on MHD free convection flow past a vertical porous plate in the presence of and heat source parameter." Journal of Mathematical Control Science and Applications, 7(2):253-267.

[35] Bang Chuol Nhial, V Sri Hari Babu, V. Nagaraju Vellanki, G. Y. Sagar **(**2022): **'**RADIATION AND MASS TRANSFER EFFECTS ON MHD FREE CONVECTION FLOW OVER AN INCLINED PLATE', *Journal of Positive School Psychology*, Vol 6(5), pp.697-706.

[36]Bang Chuol Nhial, V. Nagaraju Vellanki, V Sri Hari Babu, G. Y. Sagar **(**2022): **'** HALL CURRENT, ROTATION AND CHEMICAL REACTION EFFECTS ON MHD FREE CONVECTION FLOW PAST AN ACCELERATED VERTICAL PLATE THROUGH A POROUS MEDIUM', *Journal of Positive School Psychology*, Vol 6(5),2022, pp.707-716.

[37] V.NAGARAJU, K.HEMALATHA. (2018). "Radiation and Chemical Reaction effects on MHD mixed convective flow of a vertical surface with Ohmic heating and viscous dissipation" *In International journal of mathematical and archive*, vol.9 (2), PP.52-63.

[38] Y. Sunita Rani and V. Kesava Reddy, Variation of Eckert number on hydrodynamic convective fluid flow in the presence of thermal radiation, published in **AIP Conference Proceedings**, Volume No. 2358, Issue: 110012, Page No.110012-1 to 110012- 4, Year: 2021.

[39] Y. Sunita Rani and , Jeffrey Fluid Behaviour on Oscillatory Couette Flow past Two Horizontal Parallel Plates in Presence of MHD and Radiative Heat Transfer, published in ***International Journal of Innovative Technology and Exploring Engineering (IJITEE)***, Volume No. 8, Issue: 11, **ISSN.No.2278-3075** , Page No.3252-3257, Year: 2019.

[40] Y. Sunita Rani and Numerical Research of Hall Current Influence on MHD Convective "Flow in Presence" of Jeffrey Fluid, "Heat and Mass Transfer", published in ***International Journal of Recent Technology and Engineering (IJRTE)***, Volume No. 8, Issue: 3, **ISSN.No.2277-3878** , Page No.7609-7620, Year: 2019.

Bol. Soc. Paran. Mat.
©SPM –ISSN-2175-1188 on line
SPM: www.spm.uem.br/bspm

(3s.) **v. 2022 (40)** : 1–6.
ISSN-0037-8712 in press
doi:10.5269/bspm.42922

Topological Rank of (-1, 1) Metabelian Algebras*

K. Jayalakshmi and K. Hari Babu

abstract: In 1981, Pchelintsev developed the idea for arranging non-nilpotent subvarieties in a given variety by using topological rank for spechtian varieties of algebra as a fixed tool. In this paper we show that for a given topological rank over a field of 2, 3 - torsion free of $(-1, 1)$ metabelian algebra solvable of index 2 that are Lie-nilpotent of step not more than p is equal to P.

Key Words: -1, 1) algebra, Metabelian algebra, Topological rank, Lie-nilpotent algebra, Superalgebra.

Contents

1. Introduction

Belov [5] devoted his study to the construction of infinitely based varieties of associative algebras over an infinite field of arbitrary positive torsions. Il'tyakov [4] proved that a finitely generated alternative PI-algebra over a field of zero torsion a particular, finite dimensional. Then the variety var A, generated by the algebra A, is specht (i.e., each sub-variety is defined by a finite set of identities)

Pchelintsev [10] studied the right alternative metabelian (solvable of index 2) Grassmann algebra of rank 1 and 2. Any identity in a nonnilpotent 2,3-torsion free $(-1, 1)$ metabelian ring of degree greater than or equal to 6 is a consequence of four defining identity of M where M is the metabelian $(-1, 1)$ ring (See [8]).

Platonoa, [12] studied the non-nilpotent subvarieties of the variety of two-step solvable algebras of type (γ, δ) an additive basis of a free metabelian (γ, δ)- algebra and constructed to proved that any identity in a non-nilpotent metabelian (γ, δ) - algebra of degree at least C is a consequence of four defing relations. Badeev [1] provided a chain $\vartheta_1 \subset ... \subset \vartheta_n \subset ... \subset \vartheta$ of varieties of commutative alternative nil-algebras over a field of 3-torsion similarly topological rank of γ_n is linear function on n and topological rank $\vartheta = \mathcal{N}_0$.

In 1985, Isaev [7]shown that non-finitely based varieties of right alternative metabelian algebras can even be produced by limited dimensional algebras. The Specht properties for fixed varieties of right alternative algebras were also learned in [8]-[11]. From 1976, it is familiar [2] that the variety of every right alternative metabelian algebras over an arbitrary field is not Spechtian. So, we can say that the different types of algebra is called spechtian, if it's each subvariety is limited intervals.

The paper is divided into 4 sections. In Section 2, we give some initial results about the free $(-1, 1)$ algebra $F_{(-1,1)^{<p>}}[Z]$ on a finite set Z of produces over F. Section 3, describes to the relations of the free algebras $(-1, 1)^{<p>}$ [Z]. In Section 4, we build a system of linear produces for the space of multilinear polynomials in $F_(-1, 1)^{(<p>)}[Z]$ of enough high degree and obtain the upper bound for topological rank of 2, 3-torsionfree $(-1, 1)^{<p>} \leq P$ by calculating the values of topological ranks of some subvarieties in 2, 3-torsionfree $(-1, 1)^{<p>}$ of special type.

* The project is partially supported by UGC New Delhi Grant No. F.No. 42-17 (2013).
2010 *Mathematics Subject Classification:* 17A30.
Submitted May 24, 2018. Published September 23, 2018

2. Preliminaries

Let F be a field over 2, 3 - torsion free (-1, 1) metabelian algebra defined by the identities

$$(a,b,c)+(a,c,b)=0, \tag{2.1}$$

$$(a,b,c)+(b,c,a)+(c,a,b)=0, \tag{2.2}$$

$$(ab)(ct)=0 \tag{2.3}$$

where $(a,b,c)=(ab)c-a(bc)$ is the associator of the variables a,b,c. By $(-1,1)^{<p>}$ we denote the subvariety of 2,3- torsion free ring $(-1,1)$ distinguished by the identity

$$[[...[z_1,z_2],...,z_p],z_{p+1}]=0 \tag{2.4}$$

of Lie-nilpotentency of step P, where $[a,b]=ab-ba$ is the commutator of a,b. Throughout the paper, F is a 2, 3-torsionfree field; all vector spaces are examined over a field F ; $Z=\{z_1,z_2,...\}$ is a complete set; $\mathfrak{u}=F_{(-1,1)}[Z]$ is a 2, 3-torsionfree $(-1,1)$ algebra on the set Z of produces;L_a and R_a are, consequently, the operators of left and right multiplication by the element a ; the associative algebra, $H_a=R_a-L_a$;$\mathfrak{u}^*$ produced by the right operator R_a and left operator L_a , for $a\in\mathfrak{u}$, transforming $\mathfrak{u}^2$ and by the identical mapping id; Var A is the variety produced by an algebra A.

Recall [2, 10] that $\mathfrak{u}^*$ satisfies the relations

$$R_a^2=0 \tag{2.5}$$

$$[R_aR_b,L_c]=0, \tag{2.6}$$

$$[R_a,L_b]=-L_aL_b. \tag{2.7}$$

We begin by proving the following Lemma.

Lemma 2.1. *The operator R_aR_b lies in the center of $\mathfrak{u}^*$.*

Proof. From relations (2.5) and (2.6) the lemma is proved. □

Lemma 2.2. *The algebra $\mathfrak{u}^*$ makes the relation*

$$3R_aR_b+H_aH_b=2[R_a,H_b]+H_aR_b+H_bR_a. \tag{2.8}$$

Proof. Using equation (2.7), we have $H_aH_b=(R_a-L_a)(R_b-L_b)=R_aR_b-R_aL_b-L_aR_b+L_aL_b=R_aR_b-[R_a,L_b]-L_aR_b-L_bR_a-[R_a,L_b]=R_aR_b-2[R_a,L_b]-L_aR_b-L_bR_a$. From above relation with equations (2.5) and (2.7), we get $3R_aR_b+H_aH_b=4R_aR_b+2[R_a,L_b]-L_aR_b-L_bR_a=2[R_a,L_b]+2[R_a,L_b]+4R_aR_b-2[R_a,L_b]-L_aR_b-L_bR_a=R_aR_b+R_bR_a+2[R_a,H_b]+H_aR_b+H_bR_a=2[R_a,H_b]+H_aR_b+H_bR_a$. □

From now, the notation of both R and H are represented as a usual notation with symbol T. The notation $w=T_a,....,T_b$ indicates, every notation of w could be equivalent to R or H independently. By assuming all notations in some word w are equal to every notation, the usage of operator symbols,

$$T(i_1...i_n)=\begin{cases} R_{a_{i_1}...R_{i_{1_n}}}, & \text{if } T=R,\\ H_{a_{i_1}...H_{i_{1_n}}}, & \text{if } T=H.\end{cases}$$

and $T(\phi)$ =id.

Lemma 2.3. *The algebra $\mathfrak{u}^*$ is extended by the operators $H(i_1,i_2,...,i_n)R(j_1,...,j_m)$.*

Proof. By assuming I be a linear extent of all operators $H(i_1,i_2,...,i_n)R(j_1,...,j_m)$. It suffices to show the inclusions $R(k)I\subseteq I\ and IH(K)\subseteq I$. We note that equation (2.8) yields $R(i)H(j)\in I$. Consequently the inclusion $R(k)I\subseteq I$ can be easily shown by induction on the length of the operator $H(i_1,i_2,...,i_n)$. Simultaneously, Lemma 2.1 implies $IH(K)\subseteq I$.
Assume L be a linear extent in $\mathfrak{u}^*$ of all operators as $L_{x_i}w, w\in\mathfrak{u}^*$. But from equation (2.7), one can show the congruence by generalizing n and representing L as an ideal of $\mathfrak{u}^*$.

$$H(1,...,n)\equiv R(1,...,n)(modL), n\in N. \tag{2.9}$$

□

3. Relations of the free $(-1,1)^{<p>}$-algebra

Let $\mathfrak{u}_p = F_{(-1,1)^{<p>}}[Z]$ be the free 2, 3 - torsion free on the set Z of generators. The following was indicated by Lemma 2.3 .

Lemma 3.1. *The linear extent of all operators of degree $d \geq Pin\mathfrak{u}_p^*$ is extended by the operators $H(i_1,...,i_n)R(j_1,..,j_{d-n}), n < P$. The word "polynomial" defined as homogeneous polynomial of degree greater than or equal to two.*

Definition: Assume $\approx$ be a symmetric relation on the set of polynomials of $\mathfrak{u}$ similarly $f_0 \approx f_1$ if $f_i \approx f_{1-i}R(j_1,...,j_{2k}), i \in \{0,1\}$, and f_{1-i} doesn't depend on the variables $x_{j_1}\dots, xj_{2k}$. With the like symbol $\approx$ we indicate the generated relation on $\mathfrak{u}^* : \xi \approx \eta$ for $\xi,\eta \in \mathfrak{u}^*$ if $(x_ix_j)\ \xi \approx (x_ix_j)\eta$ and ξ,η do not depend on x_i, x_j .

Lemma 3.2. *The algebra $\mathfrak{u}_p$ makes the relation*

$$a^3 \approx 0 \tag{3.1}$$

Proof. By equations (2.5), (2.1) and (2.3), we have $2ba^3 = b(a\circ a^2) = b(a.a^2)+b(a^2.a) = (ba)a^2+b(a^2.a) = b(a^2.a) = ((ba).a)a = (ba).a^2 = 0$.

Therefore, $a^3L = 0$. By applying equations (2.9), for even $n \geq P$, we obtain $a^3 \approx a^3R(1,...,n) = a^3H(1,...,n) = 0$. Hence, We can conclude that nearly every polynomial of algebra $\mathfrak{u}_P$ that is operators of $\mathfrak{u}_p^*$ satisfies some condition $\mathfrak{v}$. For a natural $n, \mathfrak{v}$ sustain for every polynomial of degree more than n. □

Lemma 3.3. *If $f \approx 0$ for $f \in \mathfrak{u}_p$, then almost every operator of $\mathfrak{u}_p^*$ annihilate f.*

Proof. Let $fR(j_1,...,j_{2k}) = 0$, where f doesn't depend on $a_{j_1}...a_{j_{2k}}$. In sight of Lemma 3.1, the degree $d \geq p+2k$ of each operator word $\xi \in \mathfrak{u}_p^*$ can be defined as $\xi = nR(j_1,...,j_{2K}), \eta \in \mathfrak{u}_p^*$. Therefore, using Lemma 2.1, we have $f_\xi = fR(j_1,...,j_{2K})\eta = 0$. □

Lemma 3.4. *Almost all operators of $\mathfrak{u}_p^*$ are skew-symmetric with respect to all their variables.*

Proof. Let $w \in u_p^2$. By equation (2.3) and equation (2.5), the partial linearization (see [9, chap. 1]) of equation (3.1) represented in the form of $(wa)a + (aw)a + a^2w = (aw)a = 0$, whence, $H_aR_a = (R_a-L_a)R_a = -L_aR_a \approx 0$. Hence in aspect of Lemma 3.1, it is used to evaluate $H_aH_a \approx (H_aH_a)R_bR_c = H_a(H_aR_b)R_c \approx -H_aH_bR_aR_c \approx -H_aR_aR_cH_b \approx 0$.
□

Lemma 3.5. *The algebra $\mathfrak{u}_p$ suffices the relation*

$$(ab)T_aT_b \approx 0. \tag{3.2}$$

Proof. Because of Lemma 2.1, 3.4, it suffices to verify that $(ab)R_aR_b \approx 0$. Using equations (2.5), (2.1) and Lemma 3.4, we have $(ab)R_aR_b = -(ab)R_bR_a = -((ab)b)a = -b^2L_aR_a \approx 0$. □

Lemma 3.6. *The algebra $\mathfrak{u}_p^*$ suffices the relations*

$$3R_aR_b - 2[R_a,H_b] + H_aH_b \approx 0, \tag{3.3}$$

$$[R_a,H_bH_c] = 0. \tag{3.4}$$

Proof. Applying Lemma 3.4 in the equation (2.8) we obtain $3R_aR_b - 2[R_a,H_b] + H_aH_b \approx 0$. Now computing this equation towards left and using Jacobi identity we see that $3[R_a,R_bR_c]-2[R_a,[R_b,H_b]]+[R_a,H_bH_c] \approx 0$ that is $[R_a,H_bH_c] \approx 2[R_a,[R_a,H_c]] \approx [R_a,R_b,H_c] - [R_a,[R_a,H_c]] = [H_c,[R_b,R_a]] = 0$.
□

Definition: Assume I be the ideal of $\mathfrak{u}_p^*$. For $\xi, \eta \in \mathfrak{u}_p^*$ we write $\xi \cong \eta (modI)$ if there is $a\theta \in I$ such that $\xi - \eta \approx \theta$. Let $H_n(n < p)$ be the ideal of $\mathfrak{u}_p^*$ generated by all the elements $H(i_1, ..., i_n)$.

Lemma 3.7. *The algebra $\mathfrak{u}_p^*$ suffices the relation*

$$H(1, ..., 2t) \cong 0(mod\mathbb{H}_{2t+1}) \tag{3.5}$$

Proof. We set $\eta = H(1......2t)$. By using equations (3.3) and (3.4), we have $3\eta \approx 3\eta R_a R_b \cong 2\eta R_a H_b \cong 2R_a \eta H_b \cong 0(mod\mathbb{H}_{2t+1})$ □

4. Upper bound for the topological rank of $(-1, 1)^{<P>}$

Definition: An n-allotted variety $(1 \leq n \leq p)$ is a subvariety V of $(-1, 1)^{<p>}$ such that the free V - algebra on the set $X$of generators satisfies the relation

$$\psi(x_1, x_2, ...x_{n+1}) \tag{4.1}$$

where

$$\psi(x_1, x_2...x_{n+1}) = \begin{cases} [[....[x_1, x_2]....x_n], x_{n+1}], & \text{if n is even,} \\ [[....[x_1 x_2, x_3], ...x_n], x_{n+1}], & \text{if n is odd.} \end{cases}$$

Assume A be the free V- algebra on the set Z of produces and v be an n - allotted variety $(n \geq 2)$ and $\mathcal{P}_{d,n}(d \geq 3)$ be the subspace of multilinear polynomials in $\mathcal{A}$ on the variables $z_1, ..., z_d$. We eliminated the indices of variable at the operator symbols and they are arranged in ascending order in order to stop complex formulas while writing down the polynomials of $\mathcal{P}_{d,n}$. For instance, notation $w = (a_2, a_5)H^2R^3$ means the monomial $w = (a_2, a_5)H(1, 3)R(4, 6, 7)$.

Definition: Systematic words are the polynomials of $\mathcal{P}_{d,n}$ of the following types:
1. $(a_1 \circ a_i)H^{2j}R^{d-2j-2}$
2.$[a_1, a_i]H^{2j}R^{d-2j-2}$
3.$[a_2, a_3]H^{2j}R^{d-2j-2}$
4.$[a_1, a_2]H^{2k-1}R^{d-2k-1}$
where $i = 2, 3, ..., d_i; j = 0, 1, ..., t-1; k = 1, 2, ..., n-t-1; t = [\frac{n}{2}]$.

Lemma 4.1. *Approximately every polynomial of $\bigcup_{d=3}^{\infty} \mathcal{P}_{d,n}$is linear combinations of regular words.*

Proof. By Lemma 3.4, there is a degree d of similarly all monomial $(a_1, a_2)T_3, ..., T_d \in \mathcal{P}_{d,n}$ is skew-symmetric w. r. t. $a_3, ..., a_d$. Therefore, in view of relation (3.5) and Lemma 3.1,$\mathcal{P}_{d,n}$ can be spanned by polynomials

$$(x_i \circ x_j)H^kR^{d-k-2}, [x_i, x_j]H^kR^{d-k-2},$$

where $x \circ y = xy + yx, 1 \leq i < j \leq d$, and $k = 0, 1, ..., 2t-1$.

$$(a \circ b)T_c + (b \circ c)T_a + (c \circ a)T_b \approx 0,$$

Linearizing equation (3.1), we obtain

$$[a, b]T_cT_t + [a, b]T_cT_b + [c, b]T_aT_t + [c, t]T_aT_b \approx 0 .$$

By using these relations, it is not difficult to show that $\mathcal{P}_{d,n}$ can be spanned by the polynomials:
1')$(a_i \circ a_j)H^kR^{d-k-2}$,
2')$[a_1, a_i]H^kR^{d-k-2}$,
3') $[a_2, a_3]H^kR^{d-k-2}$,
where $i = 2, 3, ..., d$ and $k = 1, 2, ..., 2t-1$.
Linear extent of all systematic words of type 1) -3) are denoted by w. For even k the polynomials of type 1') -3') lie in w. Let us validate for odd k, prove the polynomials of types 1') -3') can be represented as linear combinations of systematic words.
Because of equation (2.1), we have

$$(a \circ b)H_c = (ac + ba)(R_c - L_c) = (a \circ b)c - c(a \circ b) = (a \circ b)c - (ca)b - (cb)a.$$

Hence, in view of equation (3.4), all polynomials of type 1') lie in w. In addition, using Lemmas 2.1, 3.4, the partial linearization

$$(ab)b + (ba)b + b^2a \approx 0$$

of (3.1), identity (2.1) and relation (3.3), we get

$$\begin{aligned}[a, b]H_b &\approx [a, b]H_cR_cR_u \approx [a, b]R_cR_uH_b = [a, b]R_bR_cH_u \\ &= b^2(2L_a + R_a)R_cH_u = (b^2R_a + b^2L_a)H_cH_u = (b^2R_a + (ab)R_b).\end{aligned}$$

In view of equation (3.4), for odd k the secured relation indicates that the polynomials of types 2'), 3') are skew-symmetric modulo W in respect of every variable. Therefore all polynomials of type 2'), 3') is proportional modulo W to a systematic word of type 4). □

Lemma 4.2. *For all n - allotted variety V ($n \geq 2$) there is a punctured neighbourhood $\bigcup_d^0(V)$ similarly all variety of $\bigcup_d^0(V)$ is (n - 1) - allotted.*

Proof. Because of the restriction 2 torsionfree F, relation (3.1) and Lemma 3.4 implies that for some punctured neighbourhood of V all varieties can be described by a system of identities where every polynomial begins from some enough high degree are multilinear. According to Lemma 4.1, select punctured neighbourhood $\bigcup_d^0(V)$ for all varieties of $m \in \bigcup_d^0(V)$ fulfils an identity $f = 0$, since f is a nontrivial linear combination of regular words of $\mathcal{P}_{d,n}$. Let A be the free $\mathfrak{m}$ − algebra on the set Z of produces. By rewriting the relation (4.1) shortly as $A^2H^{2t} \approx 0$ $n = 2t + 1$ and as $AH^{2t} \approx 0$ if $n = 2t$. Firstly we examine the case $n = 2t + 1$ and we rpove that relation $A^2H^{2t} \approx 0$ and identity $f = 0$ imply $AH^{2t} \approx 0$. From Lemma 4.1, f can be defined as

$$f = \sum_{i=2}^{d}\sum_{j=0}^{t-1}(\alpha_{2j}^{(i)}(a_1 \circ a_i)H^{2j}R^{d-2j-2} + \alpha_{2j+1}^{(i)}[a_1, a_i]H^{2j}R^{d-2j-2})(\mathrm{mod}\ w_{3,4}),$$

where $w_{3,4}$ is the linear extent of systematic words of types 3), 4). By fixing $i \geq 4$ and a minimal index l in case Then by the substituting $a_i := xH^{2t-1}$, for $x \in A$, using the identity $R_a + L_b = 2R_b - H_b$ and relation (3.4), we get $xH^{2t} \approx 0$. Alternatively, writing f as,

$$f \equiv \textstyle\sum_{k=0}^{t-1} g_k + \sum_{k=1}^{t} h_k$$

where

$$g_0 = (\alpha_0[a_1, a_2]a_3 + \beta_0[a_3, a_1]a_2 + \gamma_0[a_2, a_3]a_1)R^{d-3},$$
$$h_t = \xi_t[a_1, a_2]H^{2t-1}R^{d-2k-1},$$

and

$$g_k = (\alpha_k[[a_1, a_2], a_3] + \beta_k[[a_3, a_1]a_2] + \gamma_k[a_2, a_3]a_1)H^{2k-1}R^{d-2k-2},$$
$$h_k = \delta_k(a_1 \circ a_2)H^{2k}R^{d-2k-2} + \varepsilon_k(a_1 \circ a_3)H^{2k-1}R^{d-2k-2} + \zeta_k[a_1, a_2]H^{2k-1}R^{d-2k-1},$$

for $k = 1, ..., t - 1$. If at least one of the coefficient $\alpha_0, \beta_0, \delta_0$ is not zero, then by three consecutive substitutions $a_i = aH^{2t-1}(i = 1, 2, 3)$, we have

$$\begin{cases}(\alpha_0 + \beta_0)aH^{2t} \approx 0, \\ (\alpha_0 + \gamma_0)aH^{2t} \approx 0, \\ (\beta_0 + \gamma_0)aH^{2t} \approx 0.\end{cases}$$

Therefore in view of restriction 2- torsion free F, we get either $aH^{2t} \approx 0$ or $g_0 = 0$. Further, if $\varepsilon_1 \neq 0$, then by the substitution $a_3 := xH^{2t-2}$, we have $xH^{2t} \approx 0$. Alternatively, if at least one of the co-efficient δ_1 or ξ_1 is not zero, by two consecutive substitutions $a_i = xH^{2t-2}(i = 1, 2)$, we obtain

$$\begin{cases}(2\delta_1 + \zeta_1)aH^{2t} \approx 0, \\ (2\delta_1 - \zeta_1)aH^{2t} \approx 0.\end{cases}$$

Thus we have either $aH^{2t} \approx 0$ or $h_1 = 0$ and therefore, f as

$$f = \sum_{k=1}^{t-1} g_k + \sum_{k=2}^{t} h_k$$

Therefore by the same arguments as above, we obtain either $xH^{2t} \approx 0$ or $g_1 = h_2 = ... = g_{t-2} = h_{t-1} = g_{t-1} = 0$ and $f = h_t = \zeta_t[a_1, a_2]H^{2t-1}R^{d-2t-1}$. At this instance, the conclusion of the Lemma indicates $\zeta_t \neq 0$ and, therefore, $AH^{2t} \approx 0$. Let us examine the instance $n = 2t$. We require to show the relation $AH^{2t} \approx 0$ and identity $f = 0$ imply $A^2H^{2t-2} \approx 0$. The systematic word of type 4) with respect to the index $k = t$ vanishes, in contrast the case $n = 2t + 1$. All the other systematic words are equal. Hence by the above alike arguments, decreasing per unit the power $P(t)$ for all substitution $a_i := xH^{p(t)}$ and suppose $x \in A^2$, one can prove that $A^2H^{2t-1} \approx 0$. By (3.5), the obtained relation yields $A^2H^{2t-2} \approx 0$. □

Theorem 4.3. *The topological rank of the variety $(-1, 1)^{<p>}$ is equal to P for all natural P.*

Proof. As mentioned earlier, all 1- assigned variety has the topological rank 1. Thus Lemma 4.2 mean that the topological rank of every n –assigned variety is not greater than n. In particular topological rank $(-1, 1)^{<p>} \leq P$. □

Acknowledgments

This work is partially supported by UGC New Delhi Grant No. F.No. 42-17 (2013).

References

1. Badeev, A.V., the variety N_3N_2 of commutative alternative nil-algebras of index 3 over a field of charcterstic3, Fundam. Prikl. Mat. 8 335-336 Russian(2002).
2. Kuz'min, A.M., On Spechtian Varieties of right alternative algebras, J. Math. Sci., New York 149 1098-1106 1098-1106; translation from Fundam. Prikl. Mat. 12 89-100, (2006).
3. Il'tyakov, A.V., On finite basis of identities of Lie algebra representations, Nova J. Algebra Geom. 1 207-259, (1992).
4. Il'tyakov, A.V., Finiteness of basis of identities of a finitely generated alternative PI-algebra over a field of characteristic zero, Sib. Math. J. 32, 948-961 (1991); translation from Sib. Mat. Zh. 32 61-76,(1991).
5. Belov, A.Ya., Conterexamples to the Specht problem, Sb. Math. 191 329-340, (2000); translation form Mat.sb.191 13-14, (2000).
6. Vais A.Ya., Zel'manov, E.I., Kemer's theorem for finitly generated Jordan algebras, Sov. Math. 33 38-47, (1989); translation from Izv. Vyssh. Uchebn. Zaved. Mat. 6 42-51, (1989).
7. Isaev, I.M., Finite-dimensional right alternative algebras that do not generate finitly based varietities , Algebra Logic 25 86-96, (1986) translation from Algebra Logika 25 136-153, (1986).
8. Jayalakshmi, K., and Hari babu, K., (-1, 1) metabelian rings , Bol. Soc. Paran. Mat. (3s.) v. 35 2 115-125, (2017).
9. Zhavlakov, K.N., Slin'ko, A.M., Shestakov, I.P., and Shirshov, A.I., Rings that are nearly associative, translated from the Russian by Harry F.Smith.(Acedamic press,Inc., New York- London, (1982).
10. Pchelintsev, S.V., On identities of right alternative metabelian grassmann algebras, J. Math. Sci., New York 154 230-248,(2008); translation from Fundam. Prikl. Mat. 13 157-183, (2007).
11. Pchelintsev, S.V., Varieties of algebras that are solvable of index 2, Math. USSR, Sb 43 159-180, (1982); translation from Mat. Sb. 115 (157) 179-203 (1981).
12. Platonova, S.V., Varieties of two- step solvable algebras of type (γ, δ), J. Math. Sci., New York 139 6762-6779, (2006); translation from Fundam. Prikl. Mat. 10 157-180, (2004).
13. Belkin, V.P., Varietities of right alternative algebras, Algebra Logic 15 309-320, (1976); translation from Algebra Logika 15 491-508, (1976).
14. Medvedev, Yu.A., Example of a variety of solvable alternative algebras over a field of characteristic 2 having no finite basis of identities, Algebra Logic 19 191-201, (1980); translation from Algebra Logika 19 300-313, (1980).
15. Medvedev, Yu.A., Finite basis theorem on varieties with a 2- term identity, Algebra Logic 17 458-472, (1978); translation from Algebra Logika 17 705-726, (1978).

K. Jayalakshmi and K. Hari Babu,
Department of Mathematics,
Jawaharlal Nehru Technological University(Autonomous), Anathapuramu. (A.P) ,
India.
E-mail address: kjay.maths@jntua.ac.in, kharis.logic@gmail.com

Numerical Study of Hall Current Effect on MHD Nanofluid with Inclined Plates in the Presence of Brownian motion and Thermophoresis

[1]G. Gangadhar,[2]K. Sharath Babu,[3]V. Srinivasa Kumar

[1]Department of Mathematics, Malla Reddy Engineering College(Autonomous), Secunderabad, Telangana. India. E Mail: gangadharg001@gmail.com

[2]Department of Mathematics, Matrusri Engineering College,Hyderabad, Telangana,India. E Mail: sharathsiddipet@gmail.com

[3]Department of Mathematics,JNTUH College of Engineering, Kukatpally, Hyderabad, Telangana, India. E Mail: vajhasrinu@gmail.com

[*]Corresponding Author: gangadharg001@gmail.com

Article Info

Page Number: 8261 - 8283

Publication Issue:

Vol 71 No. 4 (2022)

Abstract

This research article deals with the impact of Hall current on an electrically conducting nanofluid flow past a continuously stretching surface with heat generation/absorption has been explored. Transverse magnetic field with the assumption of small Reynolds number is implemented vertically. Appropriate similarity transformations are utilized to transform the governing partial differential equations into the non-linear ordinary differential equations. Numerical solutions for the dimensionless velocity, temperature and nanoparticle concentration are computed with the help of the shooting method. The impact of each of the Hall current parameter, Brownian motion parameter, Prandtl number, thermophoresis parameter and magnetic parameter on velocity, concentration and temperature, is discussed through graphs. The skin friction coefficient along the x− and z− directions, the local Nusselt number and the Sherwood number are calculated numerically to look into the inside behavior of the emerging parameters.

Article History

***Article Received**: 25 March 2022*

***Revised**: 30 April 2022*

***Accepted**: 16 December 2022*

***Publication**: 31December 2022*

Keywords: Hall current, MHD, Heat generation, Brownian motion, Thermophoresis

1. Introduction

The use of magnetic field of high intensity to an ionic liquid having less density, the conduction normal to the magnetic field is converted to curling of atomic particles and ions related to magnetic lines of force before occurring the clashing and a current induced perpendicular to both the electric and magnetic fields, is known as Hall effect. This effect is considered with heat or mass transfer analysis under the situation where the effect of the electromagnetic force is strong. Hall current is most prominent on the absolute value and orientation of the current density and thereby on the magnetic force term. Under the effects of Hall currents the convective flow problem with magnetic field is significant in view of engineering uses in electric transformers, transmission lines, refrigeration coils, power generators, MHD accelerators, nanotechnological processing, nuclear energy systems exploiting fluid metals, blood flow control and heating elements. In case of magnetic field of high strength and less density of the gas, the investigation of magnetohydrodynamic flows with Hall current have the best utilizations in the study of Hall accelerators and flight magnetohydrodynamic. Peristaltic flows have vast applications under the effects of applied magnetic field in the magnetohydrodynamic feature of blood, process of dialysis, oxygenation and hypothermia. Exploration of non-Newtonian fluid flows has been the focus of many scientists due to its vast applications in industries and engineering. Important applications are exist in food engineering, petroleum production, power engineering, in polymer solutions and in melt in the plastic processing industries. Hall effect plays an important role when the Hall parameter is high. Hall parameter is the ratio of electron cyclotron frequency to atom-electron collision frequency. So the Hall current effect is high when the electron-atom collision frequency is low [1]. Steady MHD boundary layer flow with free convection over a porous inclined plate was explored by Alam et al. [2] with variable suction and Soret effect in the existence of Hall current. Eldahab [3] studied the free convective MHD flow along with the Hall effects through a stretching sheet. Thamizsudar [4] discussed the impact of Hall current and rotationon the heat and mass transfer of MHD fluid flowing over an exponentially accelerated vertical plate. Ibrahim and Anbessa [5] investigated the mixed convection flow of nanofluid with Hall and ion-slip effects using spectral relaxation method.Raghunath and Mohanaramana [6] studied Hall, Soret, and rotational effects on unsteady MHD rotating flow of a second-grade fluid through a porous medium in the presence of chemical reaction and aligned magnetic field. The chemically reactive second grade via porous saturated space was investigated by Raghunath et al. [7] using a perturbation technique. Veerakrishna et al. [8] have studied Heat and Mass transfer on Free Convective flow of a

Micro-polar fluid through a Porous surface with Inclined Magnetic Field and Hall effects. VeeraKrishna and Chamkha [9] have investigated Hall effects on unsteady MHD flow of second grade fluid through porous medium with ramped wall temperature and ramped surface concentration.

The idea of nanofluid was first introduced by Choi [10] in 1995. The homogeneous mixture of very small particles of size 10−9m and base fluid is called nanofluid. Usually Al, Cu, Ag, T iO_2, $Al2O_3$ etc are used as nanoparticles with base fluids like oil, ethylene glycol, water, etc. While using the nanofluids, the maximum possible thermal properties are targeted to achieve with the least feasible concentration by systematic dispersion and substantial suspension of nanoparticles in the base fluids [11, 12]. These fluids are fit for enhancing the thermophysical properties, for example, thermal diffusivity, convective heat transfer coefficient, viscosity, and thermal conductivity when compared with those of the base liquids like ethylene, tri-ethylene glucose, water or other coolants, polymer solutions and biofluids as expatiated by Choi [13] and Wong and Leon [14]. These fluids possess the distinguished physical and chemical properties and can easily pass through the microchannels and capillaries and don’t block the flow. Fuel cells, hybrid-powered instruments, automotive, food handling industry and refrigeration are few pertinent examples of nanofluids. Buongiorno [15] considered the Brownian diffusion and thermophoresis slip mechanism for the relative velocity of the base fluid and nanoparticles.

Magnetic nanofluids is another imperative subbranch of nanofluids as it has momentous contribution in number of industrial and engineering fields [16]. Hydrodynamic characteristics and heat transfer rate is further manipulated when the magnetic field is applied across the flow of nanofluids. Often aluminum oxide and magnetite are oppressed during the formulation of such fluids. Sheikholeslami et al. [17] investigated the force convection heat transfer of magnetic nanofluids flow in a lid driven semi-annulus enclosure. They used the two phase model for the simulation of nanofluids. They concluded that higher values of Lewis and Hartmann number decrease the rate of heat flux, but it is augmented for the larger values of Reynolds number. Abbasi et al. [18] considered the boundary layer flow of two dimensional Jeffrey nanofluid with hydromagnetic effects over a linearly stretched sheet.

The process of irregular heat generation or absorption has widespread significances in biomedical and many engineering activities such as radial diffusers, the intention of thrust bearing, and crude oil recovery. Polymer processing, space technology, production of glass and heating a room by the open hearth fireplace are some useful industrial and engineering application of radiation. Abel and Nandeppanavar [19] have investigated the impact of variable heat absorption/generation on magnetohydrodynamic flow of non-Newtonian liquid across a stretching surface. It was reported that the local Nusselt number is reduced when the irregular heat source/sink parameters are increased. Sandeep and Sulochana [20], Sandeep [21], Kumar et al. [22], and Ramadevi et al. [23] examined the combined influence of thermal and mass transfer features of non-Newtonian liquids due to stretching of a surface. A numerical treatment was presented with the aid of fourth order Runge-Kutta method (RKF-4). It is also noted that the heat sink/source parameters control the mass and thermal performances. Mahanthesh et al. [24] investigated the heat and mass transfer attributes on MHD viscoelastic fluid flow across a stretching surface with thermophoresis and Brownian motion. The impacts of nonlinear radiation, Brownian motion, and quartic chemical reaction on MHD bioconvective flow of nanofluid over an upper horizontal surface of paraboloid revolution was investigated by Makinde and Animasaun [25], who was reported that the Brownian motion increases concentration bulk fluid while thermophoresis declines it.

Thermophoresis is a process in which the fluid particles move towards a cooler region from the warmer [26]. This movement occurs because molecules from the warmer region having high kinetic energy impinge with the molecules having low energy in the cooler region. The velocity gained by the particles is thermophoresis velocity and the force experienced by the particles is called the thermophoresisforce [27]. Particles deposition due to thermophoresis was measured accurately by Tsai et al. [28]. Applications of thermophoresis can be seen in aerosol technology, radioactive particle expulsion in the nuclear reactor safety simulation, heat exchanger corrosion and deposition of silicon thin film. Layers of glass (SiO_2 and GeO_2) are built up by the deposition of particles on the tube wall with the help of modified chemical vapour deposition process. For very small sized chips, the potential failures increase due to the micro contamination by the particle deposition. The process of thermophoresis can be used to inhibit the deposition of small particles on the electronic chips for the purpose of efficiency. The thermophoresis transport of particles in one-dimensional flow for the thermophoresis velocity was studied first time by Goldsmith and May [29]. A theoretical analysis of thermophoresis of aerosol particles in the laminar flow over a horizontal flat plate was presented by Goren [30].

Motivated by the above studies and applications, the present work examines the effect of Hall Current on MHD heat and mass transfer Nanofluid flow with inclined plates in the presence of Brownian motion and Thermophoresis. The effects of flow regulating parameters on the distributions of flow are presented in tabular and graphical form. This consideration has an important value in engineering and biological research. Analytical and numerical approaches are applied to examine the modeled problem and also compared each other, and good results were obtained.

2. Formulation of the Problem

Here, steady heat andmass transfer ofan incompressible hydromagnetic nanofluid flow along a vertical stretching sheet coinciding with the plane y = 0, has been considered in the presence of the Hall current effects. By keeping theorigin fixed, two opposite and equal forces are assumed to employ along the x-axis so that the sheet stretches linearly in both positive and negative direction (see Figure 1). With the assumption that the Newtonian nanofluid be electrically conducting and heat generating/absorbing, a strong magnetic field has been imposed normal to the direction of flow. Moreover, no electric field has been assumed to apply and the frequency of atom-electron collision has also been considered high for the generation of Hall current effect [31]. Due to the strong magnetic flux density B_0, the Hall current effect is taken into consideration, however the small magnetic Reynolds number is employed and the induced magnetic field is ignored. Hall current effect is strong enough to give rise to a force in the z−direction and a cross flow is induced in the same direction which causes a three dimensional flow. It is further assumed that there are no variations in the flow, heat and mass transfer in the z-direction. This assumption can be achieved by taking the sheet of infinite width. Non-conducting plate is considered so that the generalized Ohm’s law [32] gives J_y=0 in the flow field. Brownian motion and thermophoresis effects are considered using the Buongiorno model [33] for the nanofluid. Further, the effects of viscous dissipation and Joule heating are ignored.

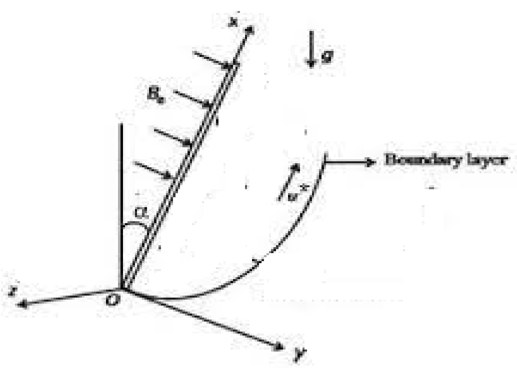

Figure: 1. Physical configuration

By the above mentioned assumptions and Boussinesq approximation, the mathematical form of the problem is

$$\frac{\partial u}{\partial x}+\frac{\partial u}{\partial y}=0 \tag{1}$$

$$u\frac{\partial u}{\partial x}+v\frac{\partial u}{\partial y}=\nu\frac{\partial^2 u}{\partial y^2}-\frac{\sigma B_0^2}{\rho\left(1+m^2\right)}\left(mw+u\right)+ g_C\beta_T(T-T_\infty)\ Cos\alpha+g_C\beta_C(C-C_\infty)\ Cos\alpha \tag{2}$$

$$u\frac{\partial w}{\partial x}+v\frac{\partial w}{\partial y}=\nu\frac{\partial^2 w}{\partial y^2}+\frac{\sigma B_0^2}{\rho\left(1+m^2\right)}\left(mu-w\right) \tag{3}$$

$$u\frac{\partial T}{\partial x}+v\frac{\partial T}{\partial y}=\frac{k}{\rho C_p}\frac{\partial^2 T}{\partial y^2}+\frac{1}{\rho C_p}\left(\frac{ka}{\nu}\right)\left[A^*(T_w-T_\infty)e^{-\eta}+B^*(T-T_\infty)\right] +\tau\left(D_B\frac{\partial C}{\partial y}\frac{\partial T}{\partial y}+\frac{D_T}{T_\infty}\left(\frac{\partial T}{\partial y}\right)^2\right) \tag{4}$$

$$u\frac{\partial C}{\partial x}+v\frac{\partial C}{\partial y}=D_B\frac{\partial^2 C}{\partial y^2}+\frac{D_T}{T_\infty}\frac{\partial^2 T}{\partial y^2} \tag{5}$$

When both A^* and B^* are positive, we have the heat generation case whereas for the negative values of both of them, there is the internal heat absorption.

The corresponding boundary conditions for the governing PDEs are

$$\begin{array}{llllll} u=ax, & v=0, & w=0, & T=T_w, & C=C_w & \text{at } y=0 \\ u\to 0, & v\to 0, & w\to 0, & T\to T_\infty & C\to C_\infty & \text{as } y\to\infty \end{array} \tag{6}$$

The similarity transformation used to transform the PDEs to dimensionless ODEs

$$\eta=\sqrt{\frac{a}{\nu}}y,\ \psi(x,y)=\sqrt{a\nu}x\,f(\eta),\ w=ax\,g(\eta)\ \phi(\eta)=\frac{C-C_\infty}{C_w-C_\infty},\ \theta(\eta)=\frac{T-T_\infty}{T_w-T_\infty}\ \theta=\frac{T}{T_w} \tag{7}$$

Substitute Eq. (7) into Eq. (2), (3), (4), (5) and Eq. (6) yields to obtain the subsequent non dimensional equations

$$f'''+ff''-f'^2+Gr_x\theta Cos\alpha+Gr_c\phi Cos\alpha-\frac{M}{1+m^2}\left(f'+mg\right)=0 \tag{8}$$

$$g''+fg'-f'g+\frac{M}{1+m^2}\left(mf'-g\right)=0 \tag{9}$$

$$\theta'' + \Pr f\theta' + \Pr N_b\left(\theta'\phi' + \frac{N_T}{N_b}\theta'^2\right) + A^* e^{-\eta} + B^*\theta = 0 \tag{10}$$

$$\phi'' + \Pr\ L_e\ f\ \phi' + \frac{N_t}{N_b}\theta'' = 0 \tag{11}$$

The correlated Dimensionless boundary conditions (BCs) are

$$\begin{aligned} &f(0)=0,\quad f'(0)=1,\quad g(0)=0,\quad \theta(0)=0,\quad \phi(0)=1 \qquad at \quad \eta=0 \\ &f'(\eta)\to 0,\quad g(\eta)\to 0,\quad \theta(\eta)\to 0,\quad \phi(\eta)\to 0 \qquad as \quad \eta\to\infty \end{aligned} \tag{12}$$

In the equations that do not include dimensions, the important parameters are defined as

$$M = \frac{\sigma B_0^2}{\rho a},\quad \Pr = \frac{\nu}{\alpha} = \frac{\nu\rho C_p}{k},\quad L_e = \frac{\alpha}{D_B},\quad Gr_x = \frac{g_c\beta_T(T_w - T_\infty)}{a^2 x},$$
$$N_b = \frac{\tau D_B(C_w - C_\infty)}{\nu},\quad N_t = \frac{\tau D_T(T_w - T_\infty)}{\nu},\quad Gr_C = \frac{g_c\beta_C(C_w - C_\infty)}{a^2 x} \tag{13}$$

3. Physical quantities of Interests

The local skin friction coefficient in the direction of x Cf_x, and in the direction of z Cf_z, the local Nusselt number Nu_x, and the local Sherwood number Sh_x are the physical quantities of relevance that influence the flow. These numbers have the following definitions:

$$C\,f_x = \frac{2\tau_{wx}}{\rho(ax)^2},\quad Cf_z = \frac{2\tau_{wz}}{\rho(ax)^2},\quad Nu_x = \frac{xq_w}{k(T_w - T_\infty)},\quad Sh_x = \frac{x\,j_w}{D_B(C_w - C_\infty)} \tag{14}$$

where τwx, τwy, qw and jw are the wall skin friction, wall heat flux and wall mass flux respectively given by

$$\tau_{wx} = \mu\left[\frac{\partial u}{\partial y}\right]_{y=0},\quad \tau_{wz} = \mu\left[\frac{\partial w}{\partial y}\right]_{y=0},\quad q_w = -k\left[\frac{\partial T}{\partial y}\right]_{y=0},\quad j_w = -D_B\left[\frac{\partial C}{\partial y}\right]_{y=0} \tag{15}$$

The coefficient of skin friction, the Nusselt number, and the Sherwood number are all expressed in their non-dimensional versions in terms of the similarity variable as follows:

$$\mathrm{Re}_x^{1/2}\,Cf_x = 2f''(0),\quad \mathrm{Re}_x^{1/2}\,Cf_z = 2g'(0),\quad \mathrm{Re}_x^{1/2}\,Nu_x = -\theta'(0),\quad \mathrm{Re}_x^{1/2}\,Sh_x = -\phi'(0) \tag{16}$$

4. Solution methodology

The system of non-linear ODEs (8-11) subject to the boundary conditions 12 has been solved by the shooting method for various values of the involved parameters. We observed through graphs that for η > 8, there is no significant variation in the behavior of solutions. Therefore, on the basis of such computational experiments, we are pondering [0, 8] as the domain of the problem instead of [0, ∞). We denote f by y_1, g by y_4, θ by y_6 and φ by y_8 for converting the boundary value problem (4.9-4.13) to the following initial value problem consisting of 9 first order differential equations.

$$y_1' = y_2,$$

$$y_2' = y_3,$$

$$y_3' = -y_1 y_3 + y_2^2 - Gr_x y_6 + Gr_c y_8 + \frac{M}{1+m^2}\left(y_2 + m y_4\right),$$

$$y_4' = y_5,$$

$$y_5' = y_2 y_4 - y_1 y_5 - Gr_x y_6 + Gr_c y_8 - \frac{M}{1+m^2}\left(-y_4 + m y_2\right),$$

$$y_6' = y_7,$$

$$y_7' = -\Pr y_1 y_7 - \Pr N_b \left(y_9 y_7 + \frac{N_T}{N_b} y_7^{\ 2} \right) - A^* e^{-\eta} - B^* y_6,$$

$$y_8' = y_9,$$

$$y_6' = -\Pr\, L_e\, y_1\, y_9 - \frac{N_t}{N_b} y_7'$$

5. Results and Discussions

To envision the effect of various physical parameters on tangential velocity $f^i(\eta)$, transverse velocity g(η), nanoparticle concentration φ(η) and temperature θ(η) profiles, Figures 4.2-4.26 are plotted. In all these computations, unless mentioned, otherwise we have considered Nb= 0.3, α=π/3, Nt= 0.7, P r= 0.71, Le = 0.6, M= 0.5, m= 0.2, Grx = 0.5, Gr = 0.5, A^*=0.01, B^*= 0.01

Figures 2 to 5 shows the effect of magnetic parameter M on the tangential velocity f ’(η), transverse velocity g(η), temperature θ(η), and concentration φ(η) profiles, respectively. The velocity profile f’(η) decreases with an increase in the values of M, the same behavior has observed transverse velocity g(η), and temperature θ(η) and concentration φ(η) profiles increase as M increases. As M increases, a drag force, called Lorentz force increases. Since this force opposes the flow of nanofluid, velocity in the flow direction decreases. Moreover, since an electrically conducting nanofluid with the strong magnetic field in the direction orthogonal to the flow are considered, an increase in M increases the force in the z-direction which results in an diminishes in the transverse velocity profile g(η).

In Figures 6-13 the effects of the thermal Grashof Grx and concentration Grashof Grc numbers on the tangential velocity $f''(\eta)$, the transverse velocity $g(\eta)$, temperature and concentration are displayed respectively. As the Grashof number is a ratio of the buoyancy force to the viscous force and it appears due to the natural convection flow, so an increase in the tangential velocity as well as the lateral velocity of the fluid is observed when the thermal and the concentration Grashof numbers are increased as shown in figures 6,7,10,11. It happens because of the fact that higher the Grashof number implies higher the buoyancy force which means higher the movement of the flow. Figures 8 and 9 depict the influence of the solutal Grashof number on the temperature and the concentration profile respectively. An increase in the solutal Grashof number means a decrease in the viscous force which reduces the temperature and the concentration of the fluid. Similarly temperature is reduced when the thermal Grashof number is enhanced and this phenomenon can be observed in Figures 12-13.

Figures 14-17 illustrate the impacts of the Hall parameter m on tangential velocity $f^{i}(\eta)$, transverse velocity $g(\eta)$, nanoparticle concentration $\varphi(\eta)$ and temperature $\theta(\eta)$ profiles, respectively. It is observed that both the velocity $f'(\eta)$ and $g(\eta)$ profiles increase as m increases. But, the temperature and concentration profiles decrease with an increase in m as shown in Figs. 16 and 17. This is because the enclosure of Hall parameter decreases the resistive force caused by the magnetic field due to its effect of reducing the effective conductivity. Hence, the velocity component increases as the Hall parameter increases.

Influence of Brownian motion parameter Nb on the temperature and concentration profiles is studied in Figures 18 and 19. From these figures, we notice that an enhancement in the values of Nb gives rise to the temperature, while it causes a decrease in the nanoparticle concentration profile. Brownian motion is the random motion of nanoparticles suspended in the fluid, caused by the collision of nanoparticles with the fluid particles. An increment in the thermophoretic effect causes an increment in the Brownian motion effect which results in the rise of the temperature due to the increment in the kinetic energy.

Figures 20 and 21 illustrate the effect of thermophoresis parameter Nt on the temperature and the nanoparticles concentration profile. One can observe that temperature and concentration fields increase with an enhancement in Nt. Thermophoresis parameter plays an important role in the heat transfer flow. Thermophoresis force enhances when Nt is increased which tends to move the nanoparticles from the hot region to the cold and as a result the temperature and the boundary layer thickness increase.

Figures 22 and 23 shows the impact of the Lewis number Le on temperature and nanoparticle concentration profiles respectively. It is observed that the temperature increases by increasing Le while concentration decreases with an increase in the Lewis number.

Figures 24-27 illustrate the impacts of the Inclined parameter α on tangential velocity $f^{i}(\eta)$, transverse velocity $g(\eta)$, nanoparticle concentration $\varphi(\eta)$ and temperature $\theta(\eta)$ profiles, respectively. It is observed that both the velocity $f'(\eta)$, $g(\eta)$, temperature and concentration profiles decrease with an increase in α.

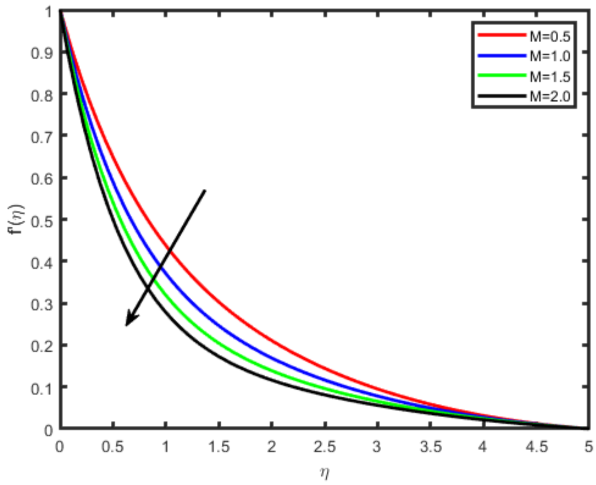

Figure: 2. Effect of M on f΄(n)

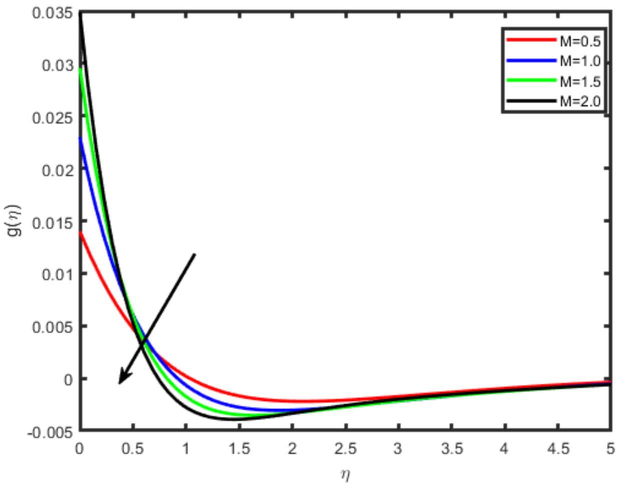

Figure: 3. Effect of M on g(n)

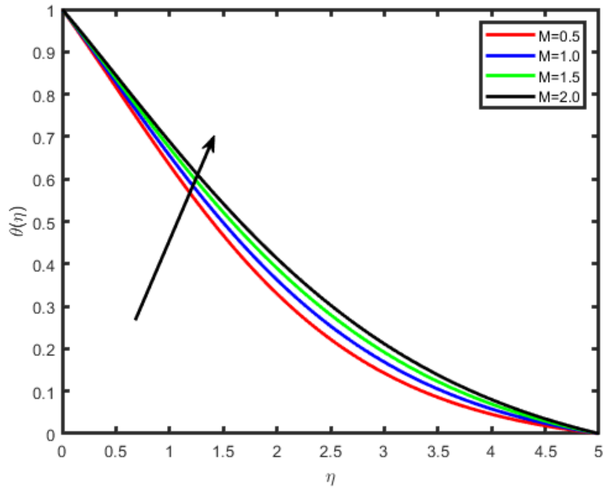

Figure: 4. Effect of M on θ(n)

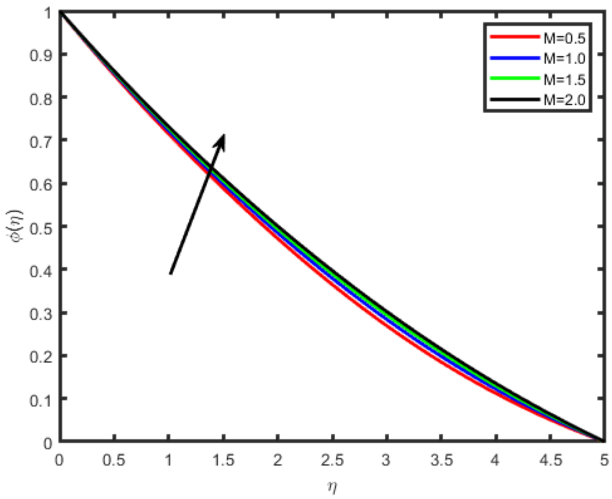

Figure: 5. Effect of M on ϕ (n)

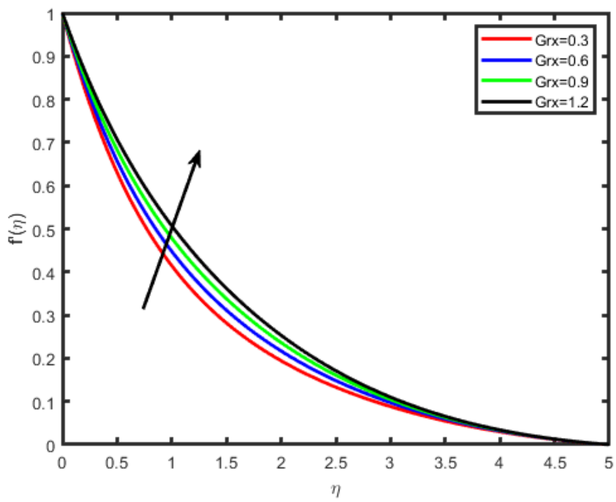

Figure: 6. Effect of Grx on f′(n)

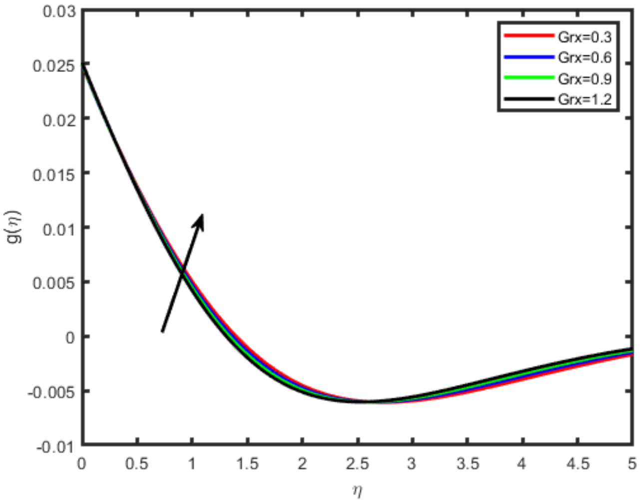

Figure: 7. Effect of Grx on g (n)

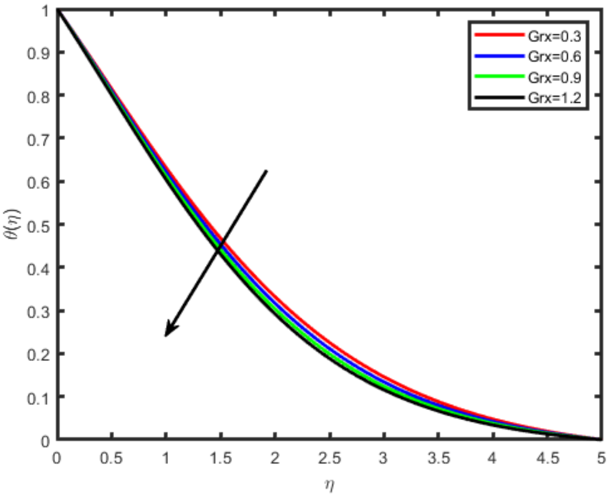

Figure: 8. Effect of Grx on θ (n)

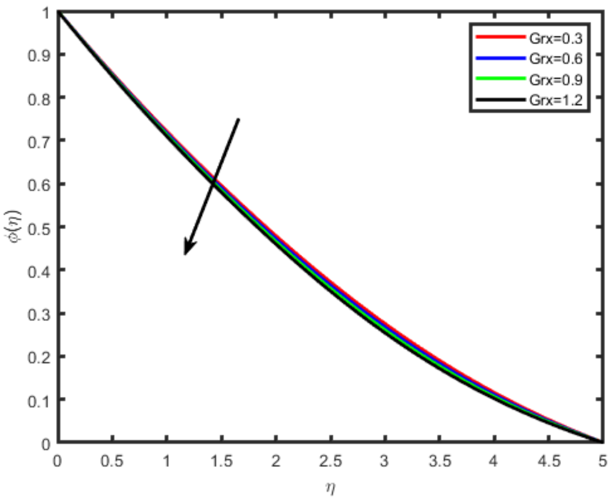

Figure: 9. Effect of Grx on ϕ (n)

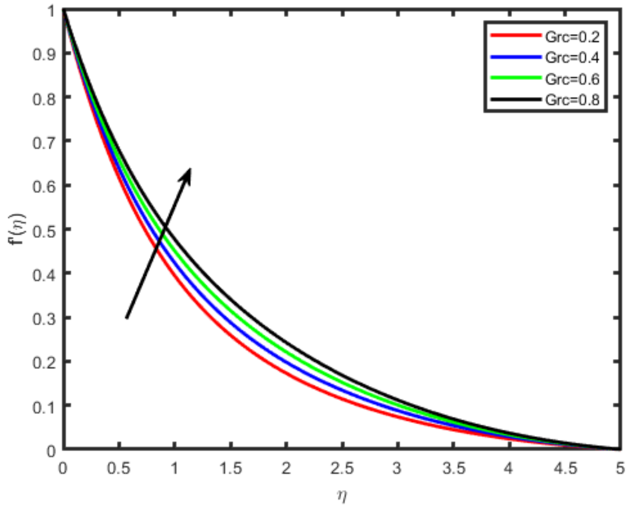

Figure: 10. Effect of Grc on f΄(n)

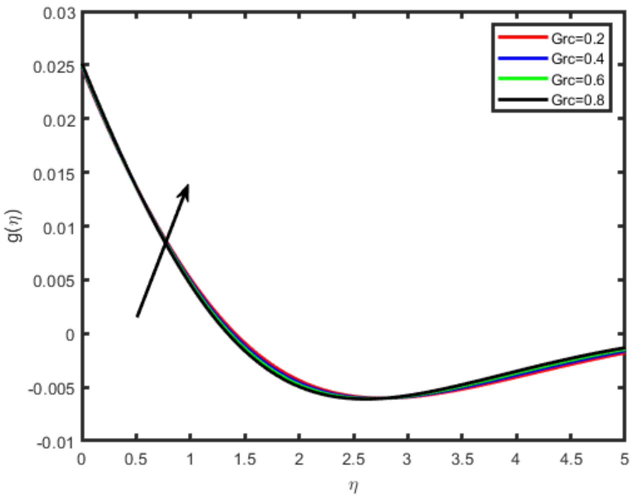

Figure: 11. Effect of Grc on g (n)

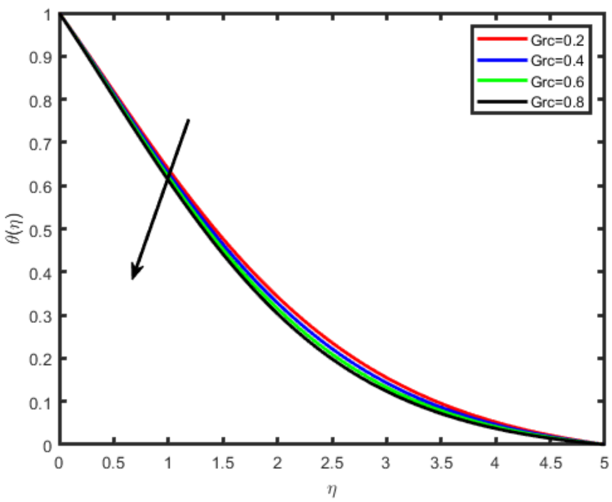

Figure: 12. Effect of Grc on θ (n)

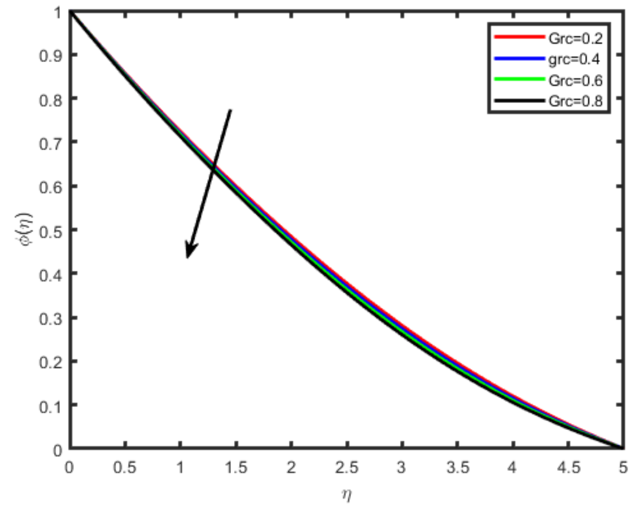

Figure: 13. Effect of Grx on ϕ (n)

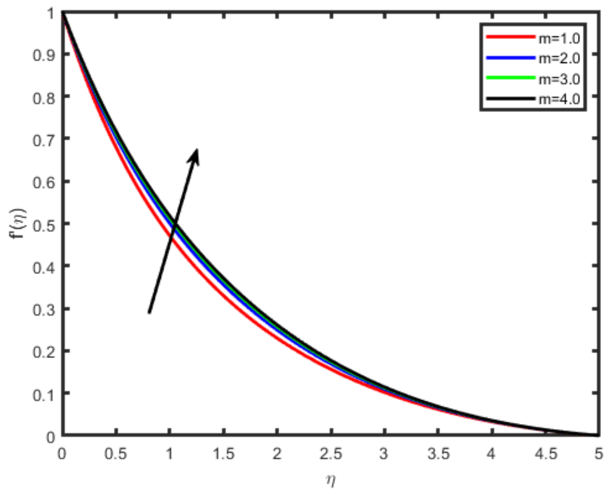

Figure: 14. Effect of m on f'(n)

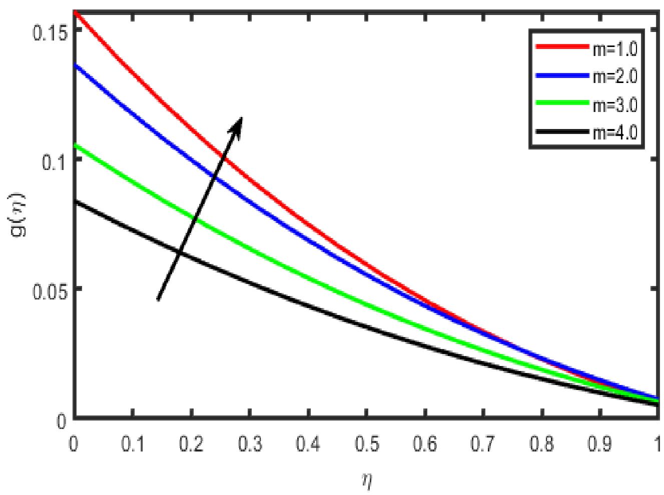

Figure: 15. Effect of m on g(n)

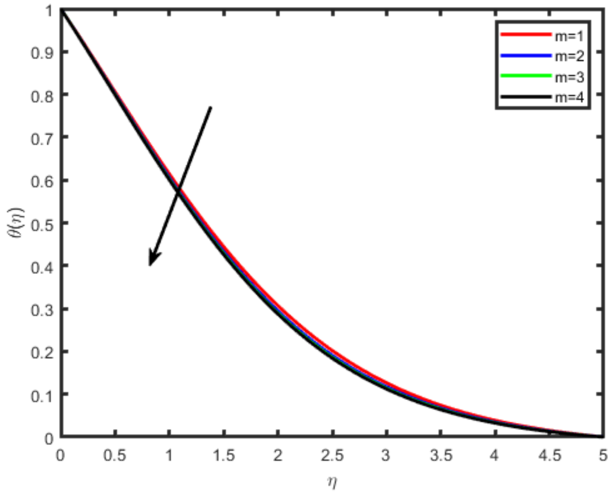

Figure: 16. Effect of m on θ(n)

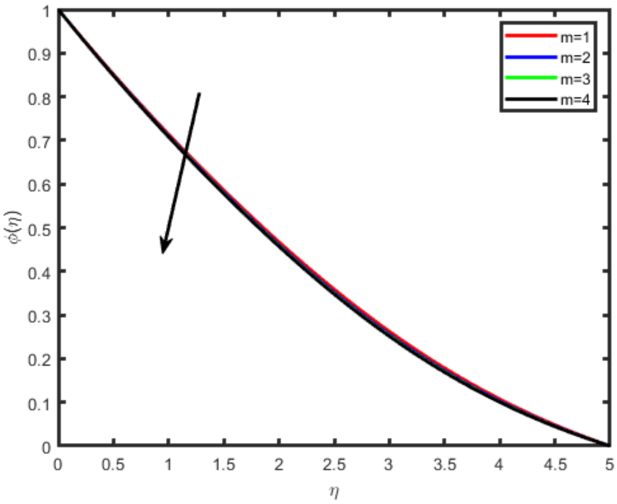

Figure: 17. Effect of m on ϕ(n)

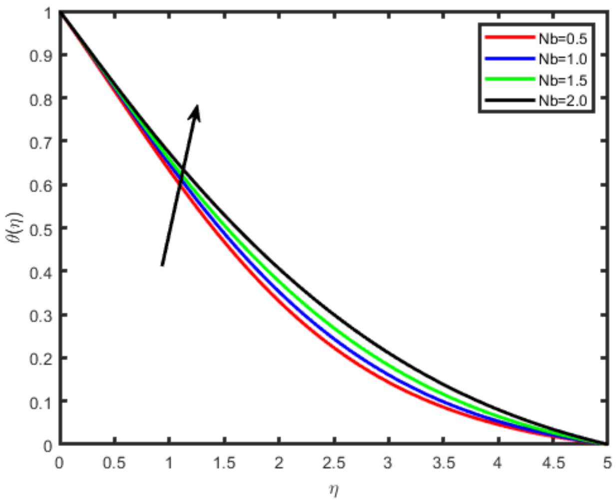

Figure: 18. Effect of Nb on θ(n)

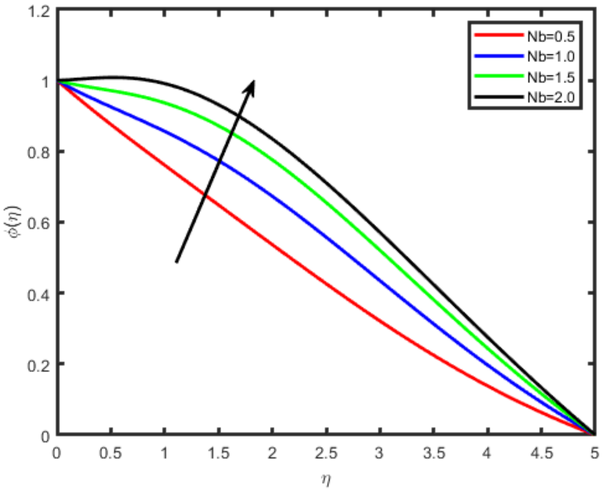

Figure: 19. Effect of Nb on ϕ(n)

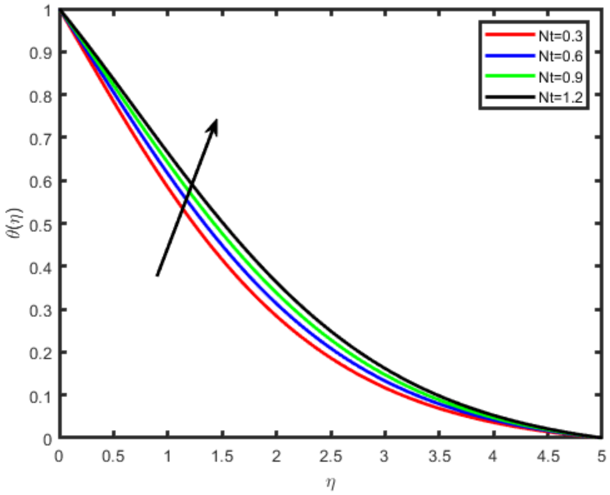

Figure: 20. Effect of Nt on θ(n)

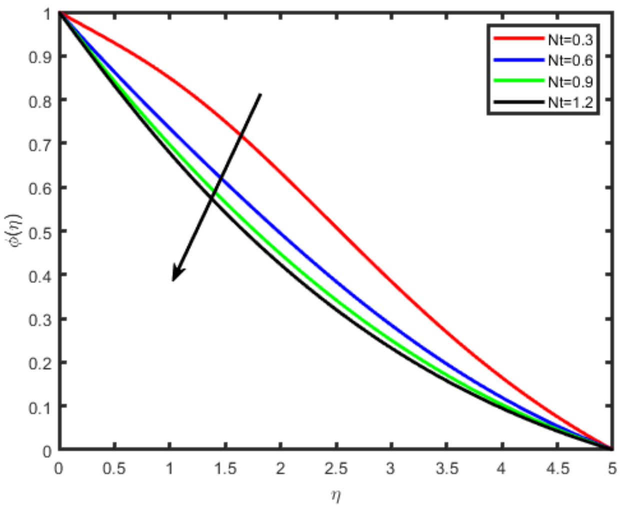

Figure: 21. Effect of Nb on ϕ(n)

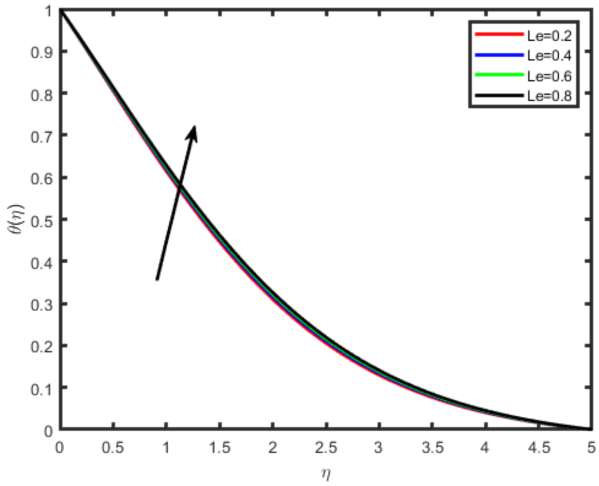

Figure: 22. Effect of Le on θ(n)

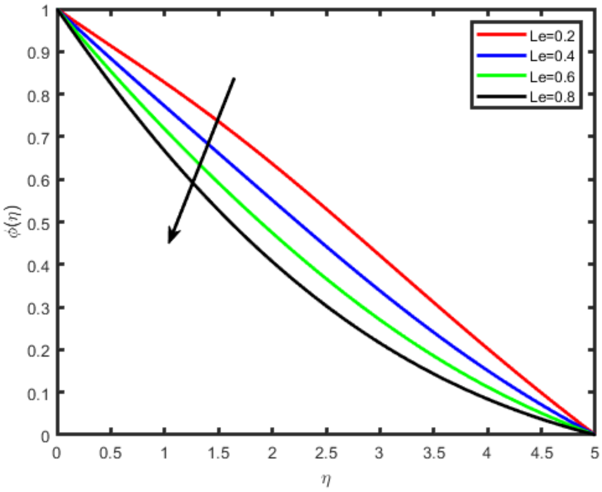

Figure: 23. Effect of Le on ϕ(n)

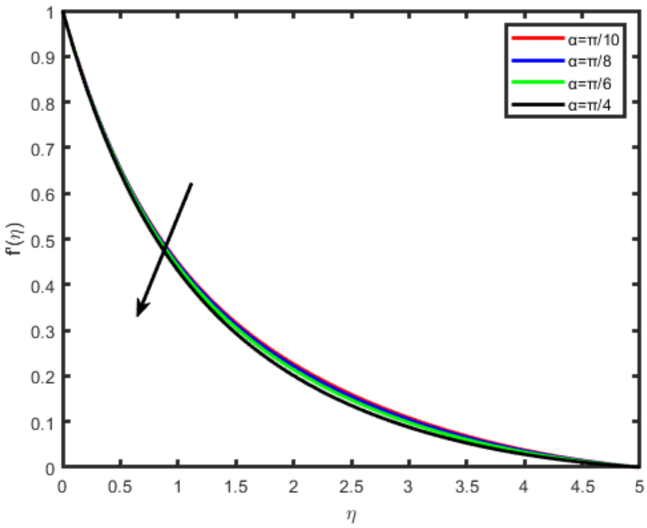

Figure: 24. Effect of α on f́(n)

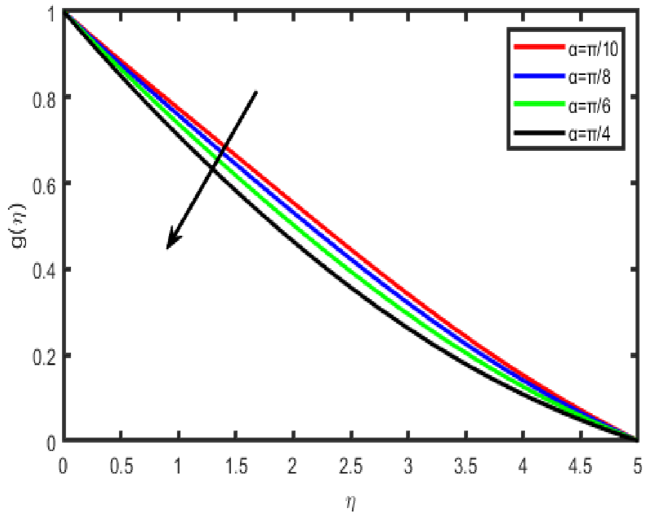

Figure: 25. Effect of α on g(n)

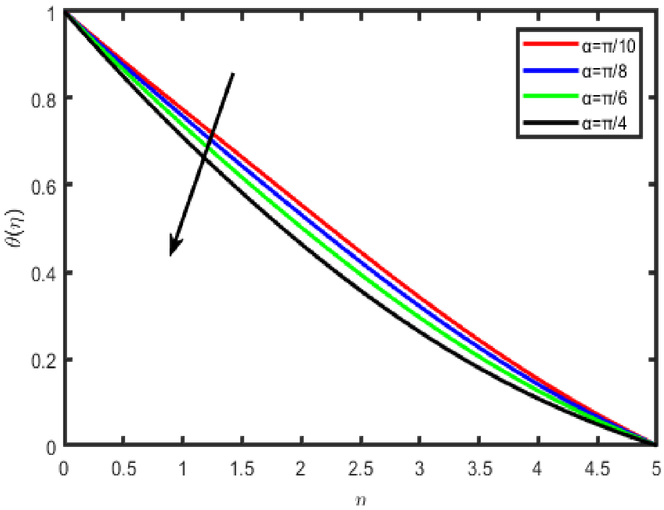

Figure: 26. Effect of α on θ(n)

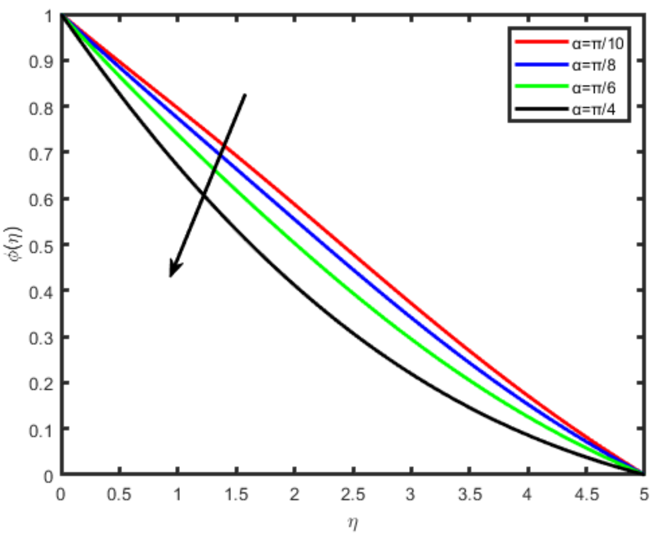

Figure: 27. Effect of α on ϕ(n)

The impact of the various physical parameters on the local Sherwood number, skinfriction coefficient and local Nusselt number, mathematical results are achieved for Nb= 0.3, α=π/3, Nt= 0.7, P r= 0.71, Le = 0.6, M= 0.5, m= 0.2, Grx = 0.5, Gr = 0.5, A^*=0.01, B^*= 0.01, and are enumerated as shown in Table 1. it is viewed that the skin-friction coefficient in x− direction decreases with an increase in the thermal Grashof number Grx, the mass Grashoff number Grc, Hall current parameter m, and Brownian motion parameter Nb, while it increases for the increasing value of magnetic parameter M and Prandtl number Pr, and thermophoresis parameter Nt. A completely opposite behavior is recorded for the coefficient of the skin-friction in the z-direction. Nusselt number increases when the Hall current parameter m, thermal Grashof number, the mass Grashoff number, and Prandtl number, increase whereas it is reduced by increasing the value of Magnetic field parameter M. Sherwood number has increasing behavior for thermal Grashof number Grx, Magnetic field parameter M, Brownian motion parameter Nb and thermophoresis parameter Nt, while it has decreasing behavior for Grashoff number Grc and Prandtl number.

For the authentication of the numerical method used, the results were compared with the previously obtained results Ibrahim and Anbessa [5] for various values of parameters and it indicates an excellent accord as shown in Tables 2.

Table1: Numerical values of $\mathrm{Re}_x^{1/2} Cf_x$, $\mathrm{Re}_x^{1/2} Cf_z$, $\mathrm{Re}_x^{1/2} Nu_x$, $\mathrm{Re}_x^{1/2} Sh_x$

Grx	Grc	m	Nb	M	Pr	Nt	-2f'(0)	-2g'(0)	-θ'(0)	-φ'(0)
0.5							1.2547	0.8521	0.5212	0.9514
1.0							0.9978	0.9125	0.5323	0.9912
1.5							0.7354	0.9542	0.5457	1.0245
	0.3						0.9875	0.8512	0.5032	0.1247
	0.6						0.8475	0.9852	0.5124	0.1108
	0.9						0.7125	1.2521	0.5785	0.9178
		1					1.5214	0.8521	0.3145	0.8852
		2					1.0214	0.9547	0.2978	0.7952
		3					0.8125	0.9985	0.2312	0.9452
			0.2				0.9512	0.9521	0.8452	0.5852
			0.4				0.8152	0.9612	0.8215	0.6124
			0.6				0.7125	0.9852	0.8032	0.6978
				0.5			0.9452	1.0254	0.9875	0.7852

				1.0			1.2454	0.9852	0.9125	0.8952
				1.5			1.4035	0.8512	0.8952	0.9452
					0.68		0.9785	1.0214	0.1254	0.9878
					0.71		0.9120	0.9852	0.1578	0.9452
					0.76		0.8452	0.9032	0.1987	0.9231
						0.3	1.5452	0.9852	0.8542	0.5120
						0.6	1.1254	0.9120	0.8125	0.5921
						0.9	0.8752	0.8962	0.7521	0.6120

Table: 2. Comparison of $-\theta'(0)$ for various values of Pr when Nb= 0.3, Nt= 0.7, P r= 0.71, Le = 0.6, M= 0.5, Grx = 0.5, Gr c= 0.5, A^*=0, B^*= 0, m=0, α=0

Pr	Ibrahim and Anbessa [5]	Present values
0.01	0.019887	0.019852
0.72	0.808635	0.807852
1	1.000000	1.000000
3	1.923687	1.924785
10	3.720676	3.732547

6. Conclusion

The influence of the Hall current on the heat and mass transfer of nanofluid flowing across a linearly stretched sheet is the topic that will be discussed in the present paper. The most significant accomplishments have been broken down into the following categories:

i. The temperature increases as the Brownian motion parameter (Nb) values increase, but the concentration profile of nanoparticles decreases.
ii. The temperature and concentration fields intensify with a rise in the Thermophoresis parameter (Nt).
iii. The temperature and concentration profiles tend to fall when the Prandtl number (Pr) is raised.
iv. The temperature increases by increasing Le while concentration decreases with an increase in the Lewis number

v. The velocity increases with enhance of hall parameter (m), where as the reversal behavior has observed in the case of temperature and Concentration.

References

[1] K. Cramer and S. Pai, Magnetofluid dynamics for engineers and applied physicists, McGraw-Hill, New York, vol. 93, 1973.

[2] M. S. Alam, M. Ali, M. A. Alim, and A. Saha, Steady MHD boundary free convective heat and mass transfer flow over an inclined porous plate with variable suction and Soret effect in presence of Hall current, J. Heat Mass Trans., vol. 49, pp. 155–164, 2014.

[3] E. M. Abo-Eldahab, Hall effects on magnetohydrodynamic free convective flow at a stretching surface with a uniform free stream, Phys. Scr., vol. 63, pp. 29–35, 1999.

[4] M. Thamizsudar and J. Pandurangan, Hall effects and rotation effects on MHD flow past an exponentially accelerated vertical plate with combined heat and mass transfer effects, Int. J. Appl. Mech. Engr., vol. 20, pp. 605– 616, 2015.

[5] W. Ibrahim, T. Anbessa, mixed convection flow of nanofluid with Hall and ion-slip effects using spectral relaxation method, Journal of the Egyptian Mathematical Society, 27(52), pp. 1-21, 2019. https://doi.org/10.1186/s42787-019-0042-9

[6] Raghunath K, Mohanaramana R. Hall, Soret, and rotational effects on unsteady MHD rotating flow of a second-grade fluid through a porous medium in the presence of chemical reaction and aligned magnetic field. International Communications in Heat and Mass Transfer, 137, 2022,106287. https://doi.org/10.1016/j.icheatmasstransfer.2022.106287.

[7] Raghunath K, Mohanaramana R, Nagesh G, Charankumar G, Sami Ullah Khan and Ijaz Khan M. Hall and ion slip radiative flow of chemically reactive second grade through porous saturated space via perturbation approach. Waves in Random and Complex Media, 32. doi: 10.1080/17455030.2022.2108555

[8] M. Veerakrishna, P. V. S. Anand, Ali. J. Chamkha, Heat and Mass transfer on Free Convective flow of a Micro-polar fluid through a Porous surface with Inclined Magnetic Field and Hall effects, Volume 10, Issue 3, 2019, pp. 203-223 DO - 10.1615/SpecialTopicsRevPorousMedia.2018026943

[9] M. VeeraKrishna, Ali J. Chamkha. Hall effects on unsteady MHD flow of second grade fluid through porous medium with ramped wall temperature and ramped surface concentration, Physics of Fluids, 30 (2018): 053101.

[10] S. U. S. Choi, “Enhancing thermal conductivity of fluids with nanoparticles, development and applications of non-Newtonian flows,” ASME J. Heat Trans., pp. 0–8, 1995.

[11] S. M. S. Murshed, K. C. Leong, and C. Yang, “Thermophysical and electrokinetic properties of nanofluids - a critical review,” Appl. Therm. Engr., vol. 28, pp. 2109–2125, 2008.

[12] S. Ozerinc, S. Kakac, and A. Yazicioglu, Enhanced thermal conductivity of nanofluids: a state-of-the-art review, Microfluids Nanofluids, vol. 8, pp. 145–170, 2010.

[13] S. U. S. Choi, Nanofluids: from vision to reality through research, J. Heat Trans., vol. 131, pp. 1–9, 2009.

[14] K. V. Wong and O. Leon, “Applications of nanofluids: current and future,” Adv. Mech. Engr., vol. 2010, pp. 1–10, 2010.

[15] J. Buongiorno, “Convective transport in nanofluids applications of nanofluids: current and future,” ASME J. Heat Trans., vol. 2010, pp. 240–250, 2006.

[16] S. Das, S. Chakraborty, R. N. Jana, and O. D. Makinde, “Entropy analysis of unsteady magneto-nanofluid flow past accelerating stretching sheet with convective boundary condition,” Appl. Math. Mech, vol. 36, pp. 1593–1610, 2015.

[17] M. Sheikholeslami, M. M. Rashidi, and D. D. Ganji, “Numerical investigation of magnetic nanofluid forced convective heat transfer in existence of variable magnetic field using two phase model,” J. Mol. Liq., vol. 212, pp. 117–126, 2015.

[18] F. M. Abbasi, S. A. Shehzad, T. Hayat, A. Alsaedi, and M. A. Obid, “Influence of heat and mass flux conditions in hydromagnetic flow of Jeffrey nanofluid,” AIP Adv., vol. 5, p. 037111, 2015.

[19] Abel, M.S. and Nandeppanavar, M.M., Heat Transfer in MHD Viscoelastic Boundary Layer Flow over a Stretching Sheet with Non-Uniform Heat Source/Sink, Commun. Nonlin. Sci. Numer. Simul., vol. 14, pp. 2120–2131, 2009.

[20] Sandeep, N. and Sulochana, C., Dual Solutions for Unsteady Mixed Convective Flow of MHD Micropolar Fluid over a Stretching/Shrinking Sheet with Non-Uniform Heat Source/Sink, Eng. Sci. Tech., Int. J., vol. 18, pp. 738–745, 2015.

[21] Sandeep, N., Effect of Aligned Magnetic Field on Liquid Thin Film Flow of Magnetic-Nanofluids Embedded with Graphene Nanoparticles, Adv. Powder Tech., vol. 28, no. 3, pp. 865–875, 2017.

[22] Kumar, K.A., Sugunamma, V., and Sandeep, N., Numerical Exploration of MHD Radiative Micropolar Liquid Flow Driven by Stretching Sheet with Primary Slip: A Comparative Study, J. Non-Equilib. Thermodyn., 2018c. DOI: 10.1515/jnet-2018-0069

[23] Ramadevi, B., Sugunamma, V., Kumar, K.A., and Reddy, J.V.R., MHD Flow of Carreau Fluid over a Variable Thickness Melting Surface Subject to Cattaneo-Christov Heat Flux, Multi. Model. Mater. Struct., vol. 15, no. 1, 2019.

[24] Mahanthesh, B., Gireesha, B.J., and Animasaun, I.L., Exploration of Non-Linear Thermal Radiation and Suspended Nanoparticles Effects on Mixed Convection Boundary Layer Flow of Nanoliquids on a Melting Vertical Surface, J. Nanofluids, vol. 7, pp. 833– 843, 2018.

[25] Makinde, O.D. and Animasaun, I.L., Thermophoresis and Brownian Motion Effects on MHD Bioconvection of Nanofluid with Nonlinear Thermal Radiation and Quartic Chemical Reaction past an Upper Horizontal Surface of a Paraboloid of Revolution, J. Mol. Liq., vol. 221, pp. 733–743, 2016.

[26] W. C. Hinds, "Aerosol technology: properties, behavior, and measurement of airborne particles," John Wiley and Sons, New York, 1982.

[27] A. Y. Bakiera and M. A. Mansour, "Combined magnetic field and thermophoresis particle deposition in free convection boundary layer from a vertical flat plate embedded in a porous medium," Int. J. Thermal. Sci., vol. 11, pp. 65–74, 2007.

[28] C. J. Tsai, J. S. Lin, I. Shankar, G. Aggarwal, and D. R. Chen, "Thermophoretic deposition of particles in laminar and turbulent tube flows," Aerosol Sci. Technol., vol. 38, pp. 131–139, 2004.

[29] P. Goldsmith and F. G. May, "Diffusiophoresis and thermophoresis in water vapour systems, in: Aerosol science," C. N. Davies (Ed.), Academic Press, London,, pp. 163–194, 1966.

[30] S. L. Goren, "Thermophoresis of aerosol particles in laminar boundarylayer on flat plate," J. Colloid Interface Sci., vol. 61, pp. 77–85, 1977.

[31] G. W. Sutton and A. Sherman, "Engineering magnetohydrodynamics," McGraw-Hill, New York. USA, 1965.

[32] E. M. Abo-Eldahab and M. A. El-Aziz, "Hall and ion-slip effects on MHD free convective heat generating flow past a semi-infinite vertical flat plate," Phys. Scripta, vol. 61, p. 344, 2000.

[33] J. Buongiorno, "Convective transport in nanofluids applications of nanofluids: current and future," ASME J. Heat Trans., vol. 2010, pp. 240–250, 2006.

micromachines

Article

Recent Development of Heat and Mass Transport in the Presence of Hall, Ion Slip and Thermo Diffusion in Radiative Second Grade Material: Application of Micromachines

V. V. L. Deepthi [1], Maha M. A. Lashin [2], N. Ravi Kumar [3], Kodi Raghunath [4], Farhan Ali [5,*], Mowffaq Oreijah [6], Kamel Guedri [6,7], El Sayed Mohamed Tag-ElDin [8], M. Ijaz Khan [9] and Ahmed M. Galal [10,11]

1 Department of Mathematics, CVR College of Engineering, Hyderabad 500039, India
2 College of Engineering, Princess Nourah Bint Abdulrahman University, Riyadh 84428, Saudi Arabia
3 Department of Mathematics, Malla Reddy Engineering College (Autonomous), Medchal 500100, India
4 Department of Humanities and Sciences, Bheema Institute of Technology and Science, Adoni 518301, India
5 Department of Mathematical Sciences, Federal Urdu University of Arts, Sciences & Technology, Gulshan-e-Iqbal Karachi 75300, Pakistan
6 Mechanical Engineering Department, College of Engineering and Islamic Architecture, Umm Al-Qura University, Makkah 21955, Saudi Arabia
7 Research Unity: Materials, Energy and Renewable Energies, Faculty of Science of Gafsa, University of Gafsa, Gafsa 2100, Tunisia
8 Faculty of Engineering and Technology, Future University in Egypt, New Cairo 11835, Egypt
9 Department of Mechanical Engineering, American Lebanese University, Beirut 1102, Lebanon
10 Mechanical Engineering Department, College of Engineering, Prince Sattam Bin Abdulaziz University, Wadi Addawaser 11991, Saudi Arabia
11 Production Engineering and Mechanical Design Department, Faculty of Engineering, Mansoura University, Mansoura 35516, Egypt
* Correspondence: farhanali.ali15@gmail.com

Citation: Deepthi, V.V.L.; Lashin, M.M.A.; Ravi Kumar, N.; Raghunath, K.; Ali, F.; Oreijah, M.; Guedri, K.; Tag-ElDin, E.S.M.; Khan, M.I.; Galal, A.M. Recent Development of Heat and Mass Transport in the Presence of Hall, Ion Slip and Thermo Diffusion in Radiative Second Grade Material: Application of Micromachines. *Micromachines* **2022**, *13*, 1566. https://doi.org/10.3390/mi13101566

Academic Editor: Kwang-Yong Kim

Received: 18 August 2022
Accepted: 15 September 2022
Published: 21 September 2022

Abstract: This article describes the incompressible two-dimensional heat and mass transfer of an electrically conducting second-grade fluid flow in a porous medium with Hall and ion slip effects, diffusion thermal effects, and radiation absorption effects. It is assumed that the fluid is a gray, absorbing–emitting but non-scattering medium and the Rosseland approximation is used to describe the radiative heat flux in the energy equation. It is assumed that the liquid is opaque and absorbs and emits radiation in a manner that does not result in scattering. It is considered an unsteady laminar MHD convective rotating flow of heat-producing or absorbing second-grade fluid across a semi-infinite vertical moving permeable surface. The profiles of velocity components, temperature distribution, and concentration are studied to apply the regular perturbation technique. These profiles are shown as graphs for various fluid and geometric parameters such as Hall and ion slip parameters, radiation absorption, diffusion thermo, Prandtl number, Schmidt number, and chemical reaction rate. On the other hand, the skin friction coefficient and the Nusselt number are determined by numerical evaluation and provided in tables. These tables are then analysed and debated for various values of the flow parameters that regulate it. It may be deduced that an increase in the parameters of radiation absorption, Hall, and ion slip over the fluid region increases the velocity produced. The resulting momentum continually grows to a very high level, with contributions from the thermal and solutal buoyancy forces. The temperature distribution may be more concentrated by raising both the heat source parameter and the quantity of radiation. When one of the parameters for the chemical reaction is increased, the whole fluid area will experience a fall in concentration. Skin friction may be decreased by manipulating the rotation parameter, but the Hall effect and ion slip effect can worsen it. When the parameter for the chemical reaction increases, there is a concomitant rise in the mass transfer rate.

Keywords: diffusion thermo effect; radiation absorption; porous media; Hall and ion slip effects

1. Introduction

A few decades ago, the majority of academics focused more of their attention on MHD fluid flow difficulties. Still, they overlooked the Hall current and the Ion-slip current in Ohm's law. The flow of MHD heat and mass transfer in the presence of a high magnetic field is essential in solving a wide variety of engineering issues, including those involving astronomy, chemical engineering, and geophysics. There is a good chance that Hall and ion-slip currents play an essential role in the flow of laboratory plasma. As a result, a recent suggestion has been made to investigate the heat and mass transfer of a free-convection MHD flow that goes through an infinite vertical porous plate while considering Hall and ion slip currents. Recent research on magnetohydrodynamic (MHD)-driven flows, on the other hand, is focused on the firm application of a magnetic field since this causes many other complicated phenomena, such as the Hall current, ion slip, Joule heating, and so on (Sutton and Sherman [1]). This application's relevance may be observed in many different engineering processes, such as magnetic fusion systems, energy generators, Hall sensors, and Hall accelerators, as well as in specific astrophysical applications. Abo-Eldahab et al. [2] investigated the combined effects of the hall and ion-slip currents on free convective flow across a semi-infinite vertical plate. Ref. [2] Srinivasacharya and Kaladhar [3] used the homotopy analysis method to investigate the effect of Hall and Ion-slip currents on fully developed electrically conducting fluid flow between vertical parallel plates in the presence of a temperature-dependent heat source. This study was conducted in the presence of a temperature-dependent heat source. After that, Darbhasayanam et al. [4] looked at how Hall and ion slip currents affect the flow of electrically conducting couple stress fluid between two circular cylinders when a temperature-dependent heat source is present. Tani [5] researched the steady motion of an electrically conducting viscous liquid in the presence of Hall current. Motsa and Shateyi [6] performed a numerical analysis on magnetomicropolar fluid flow, heat and mass transfer with suction through porous material to determine the impacts of Hall currents, ion-slip currents, and changing thermal diffusivity on these processes. Attia [7] used an analytical approach to research the flow of a dusty fluid when Hall and ion slip current were present. The flow of a magnetohydrodynamic boundary layer was examined by Ghosh [8] across a stretched sheet while a chemical reaction was taking place. The chemically reactive second grade via porous saturated space was investigated by Raghunath et al. [9] using a perturbation technique. Raghunath et al. [10] have investigated the effects of Soret, Rotation, Hall, and Ion Slip on the unsteady flow of a Jeffrey fluid through a porous medium. At the same time, heat is absorbed, and chemical reactions occur. Sibanda and Makinde [11] have investigated the hydromagnetic steady flow and heat transfer characteristics of an incompressible viscous electrically conducting fluid past a rotating disk in a porous medium with ohmic heating, Hall current and viscous dissipation.

The study of magnetohydrodynamics in the presence of heat and mass transfer, as well as radiation and diffusion, has captured the interest of a sizable number of academics as a result of the wide variety of applications it may be put to use. In the fields of astrophysics and geophysics, it is used to examine the structures of stars and the sun, radio transmission via the ionosphere, and other such phenomena. Its uses may be found in engineering, such as in MHD pumps, MHD bearings, and other places. The process of mass transfer is also quite prevalent in theoretical discussions on the structure of stars, and its effects may be noticeable on the sun's surface. The investigation of the impact of a magnetic field plays a significant role in free convection flow, particularly in the case of liquid metals, electrolytes, and ionized gases. The thermal physics of hydromagnetic issues with mass transport has vast implications in the field of power engineering. Various industrial and environmental activities involve the presence of radiative fluxes. A few examples of this are heating and cooling chambers, energy processes involving the burning of fossil fuels, evaporation from huge open water reservoirs, astrophysical flows, solar power technologies, and the re-entry of space vehicles. Seth and Sarkar [12] investigated the influence of an induced magnetic field on the hydromagnetic natural convection flow of a chemically reacting fluid across a moving vertical plate with ramping wall temperature. The effects of an induced magnetic field on the flow of a free convective channel were studied by Sarveshanand and Singh [13]. Sarma and Pandit [14] investigated the effects of thermal radiation, chemical reactions, and generated magnetic fields on MHD mixed convection flow across a vertical porous plate. Following that, Ojjela et al. [15] investigated the effects that thermophoresis and an induced magnetic field had on a mixed convective Jeffrey fluid contained between two porous plates. Jha and Aina [16] show the interplay of conducting and non-conducting walls on the MHD natural convection flow in a vertical micro-channel with an induced magnetic field. Shaw et al. [17] have studied impact of Entropy Generation and Nonlinear Thermal Radiation on Darcy–Forchheimer Flow of $MnFe_2O_4$-Casson/Water Nanofluid due to a Rotating Disk. Very recently Sharma [18] has studied FHD flow and heat transfer over a porous rotating disk accounting for Coriolis force along with viscous dissipation and thermal radiation. Ram et al. [19] have possessed a Ferrofluid flow over a moving plate in a porous medium is theoretically investigated by solving the boundary layer equations with boundary conditions using Neuringer–Rosensweig model. Mahantesh et al. [20] have studied impacts of a novel exponential space dependent heat source on MHD slip flow of carbon nanoliquids past a stretchable rotating disk. The flow is created due to rotation and stretching of the disk. Vijay and Sharma [21] have studied heat and mass transfer of ferrofluid flow between co-rotating stretchable disks with geothermal viscosity.

The investigation of first-order chemical reactions that include simultaneous heat and mass transfer has attracted many researchers in recent years. It has been the focus of considerable stress in recent times. Evaporation at the surface of a water body and heat and mass transfer all take place concurrently in several different processes, including energy transfer in a wet cooling tower, flow in a desert cooler, and energy transfer in a desert cooler. Some of the uses of this flow may be found in many different sectors, such as the power industry. One of the techniques of producing electrical energy is to directly extract it from moving conducting fluid, which is one of the applications of this flow. Studying heat production or absorption in flowing fluids is vital in issues involving chemical processes that dissociate fluids. These problems may be broken down into two categories: The effects that the creation of heat might cause could potentially change the temperature distribution and, as a result, the pace at which particles are deposited in nuclear reactors, electronic chips, and semiconductors wafers. It is interesting to study the effects of a magnetic field on the temperature distribution and heat transfer when the fluid is not only an electrical conductor but also capable of emitting and absorbing radiation because some fluids are also capable of emitting and absorbing thermal radiation. Because of this, heat transmission through thermal radiation is becoming more significant as we become more concerned with space applications and higher operating temperatures. Recent research conducted by Raghunath and colleagues [22–24] investigated the impact of chemical reactions on different flow geometries. The effects of Soret on the unsteady free convection flow of a viscous incompressible fluid through a porous medium with high porosity bounded by a vertical infinite moving plate have been discussed by Ramachandra et al. [25]. This flow occurs under thermal diffusion, a chemical reaction, and a heat source. Raghunath and Mohanaramana [26] have researched Hall, Soret, and rotational effects on unsteady MHD rotating flow of a second-grade fluid through a porous media in the presence of chemical reaction and aligned magnetic field. Their findings were published not too long ago.

In the fields of geophysics, petrochemical engineering, meteorology, oceanography, and aeronautics, the notion of fluid flow, heat and mass transfer inside a rotating environment plays a very significant part in the applications of these sciences. Applications in geophysics and fluid engineering are where the impetus for scientific study on rotating fluid systems first began. This is where the field has been propelled forward. The effect of rotation significantly impacts the motion of the atmospheres of both planets and the earth. This has implications for several different elements of atmosphere motion. The theory of rotational flow is used for figuring out the fluid's viscosity, constructing centrifugal devices like the turbine, and other similar activities. Ali et al. [27] have studied Saleel, Entropy Generation Analysis of Peristaltic Flow of Nanomaterial in a Rotating Medium through Generalized Complaint Walls of Micro-Channel with Radiation and Heat Flux Effects. Ali et al. [28] have analyzed the slippage phenomenon in hydromagnetic peristaltic rheology with Hall current and viscous dissipation. Awais et al. [29] possessed Convective and peristaltic viscous fluid flow with variable viscosity, J. Engin. Thermophys. Ali et al. [30] investigated Oscillatory Flow in a Porous Channel with Porous Medium and Small Suction. Ali et al. [31] have studied Oscillatory flow of second grade fluid in cylindrical tube. Ilya et al. [32] have possessed Heat source and sink effects on periodic mixed convection flow along the electrically conducting cone inserted in porous medium.

Raghunath et al. [10] conducted research not too long ago in which they studied the effect of Hall and ion-slip currents on the unsteady MHD flows of a viscous, incompressible, and electrically conducting fluid that was occurring between two vertical plates in a rotating system when the lower plate was impulsively started. The work done by Raghunath et al. [10] for the diffusion thermal and Second grade fluid cases will be extended even further with the help of this effort. After obtaining the flow equations in a dimensionless form using the perturbation technique, the flow equations are then analytically solved under the appropriate conditions. The graphical representation and subsequent discussion of the influence of various flow parameters on the fluid velocity, volume flow rate, and surface friction are shown below. The significance of the findings acquired from this research is that they provide the criteria for verifying the accuracy of various numerical or empirical methodologies. In addition, the results that were produced from this study have the potential to be used in the fields of fluid mechanics and heat transport.

2. Formulation of the Problem

We considered the heat and mass transfer of an unsteady two-dimensional MHD convective flow of a viscous laminar heat initiating second-grade liquid over a semi-infinite longitudinal moveable porous layer engrained in consistent permeable material. We adapted to a homogeneous transverse magnetic field. We do this while considering Hall and ion slip consequences. The Cartesian coordinate system is selected so that the x-axis is maintained along the wall in the direction of upward movement, and the z-axis is perpendicular to this orientation. A magnetic field with strength of B_0 and a uniform intensity is moving in a direction that is perpendicular to the flow. In their original, undisturbed states, the fluid and the plate are both rotating in a fixed orientation relative to the perpendicular to the plate at a constant angular velocity. At the surface, the temperature and concentration are subject to random fluctuations; this is true for both the fluid and the plate. The investigational challenge may be seen by looking at the physical model shown in Figure 1.

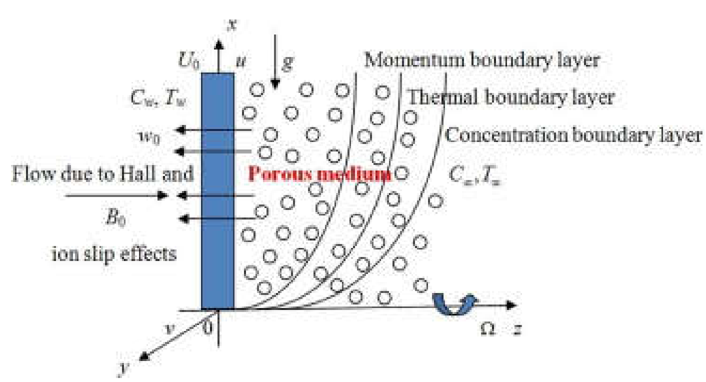

Figure 1. Flow diagram.

The fluid properties are assumed to be constant except that the influence of density variation with temperature has been considered only in the body-force term. The concentration of diffusing species is very small in comparison to other chemical species, the concentration of species far from the wall, C_α s infinitesimally small and hence the Soret and Dufour effects are neglected. The chemical reactions are taking place in the flow and all thermophysical properties are assumed to be constant of the linear momentum equation which is approximated according to the Boussinesq approximation. Due to the semiinfinite plane surface assumption, the flow variables are functions of z and the time t only. The flow governing equations and boundary conditions as followed by Raghunath et al. [10].

$$\frac{\partial u}{\partial x}+\frac{\partial u}{\partial y}=0 \tag{1}$$

$$\frac{\partial u}{\partial t}+w\frac{\partial u}{\partial z}-2\Omega v=-\frac{1}{\rho}\frac{\partial p}{\partial x}+v\frac{\partial^2 u}{\partial z^2}+\frac{\alpha}{\rho}\frac{\partial^3 u}{\partial z^2\partial t}+\frac{B_0 J_y}{\rho}-\frac{v}{k}u+g\beta(T-T_\infty^{**})+g\beta^*(C-C_\infty) \tag{2}$$

$$\frac{\partial v}{\partial t}+w\frac{\partial v}{\partial z}+2\Omega u=-\frac{1}{\rho}\frac{\partial p}{\partial y}+v\frac{\partial^2 v}{\partial z^2}+\frac{\alpha}{\rho}\frac{\partial^3 v}{\partial z^2\partial t}-\frac{B_0 J_x}{\rho}-\frac{v}{k}v \tag{3}$$

$$\frac{\partial T}{\partial t}+w\frac{\partial T}{\partial z}=\frac{k_1}{\rho C_p}\frac{\partial^2 T}{\partial z^2}-\frac{1}{\rho C_p}\frac{\partial q_r}{\partial z}-\frac{Q_0}{\rho C_p}(T-T_\infty)+Q_1(C-C_\infty)+\frac{DK_T}{C_s C_p}\frac{\partial^2 C}{\partial z^2} \tag{4}$$

$$\frac{\partial C}{\partial t}+w\frac{\partial C}{\partial z}=D\frac{\partial^2 C}{\partial z^2}-K_c(C-C_\infty) \tag{5}$$

The proper boundary requirements for the velocity, temperature, and concentration distributions are provided if the assumptions outlined above hold.

$$u=U_0,\quad v=0,\ T=T_w+\varepsilon(T_w-T_\infty)e^{iwt},\ C=C_w+\varepsilon(C_w-C_\infty)e^{iwt}\ \text{ at } z=0 \tag{6}$$

$$u\to U_\infty,\quad v\to 0,\quad T\to T_\infty\qquad C\to C_\infty\qquad \text{as}\quad z\to\infty \tag{7}$$

In light of the fact that the solution to the continuity equation is either a constant or a function of time, we will assume that.

$$w=-w^1{}_0(1+A\varepsilon e^{iwt}) \tag{8}$$

where A is a real positive constant, ε and Aε are small, less than unity, w_0 is the scale of the suction velocity which has a non-zero positive constant.

The Rosseland approximation can be used for the radiative heat flux vector q_r because, for an optically thick fluid, in addition to emission, there is also self-absorption. Since the absorption coefficient is typically wavelength dependent and significant, we can use the Rosseland approximation. Therefore, q_r may be deduced from

$$q_r=\frac{-4\sigma_1}{3k_1}\frac{\partial^2 T^4}{\partial z} \tag{9}$$

where k_1 is the Rosseland mean absorption co-efficient and σ_1 is the Stefan–Boltzmann constant.

We assume that the temperature differences within the flow are sufficiently small so that T^4 can be expressed as a linear function. Using Taylor's series, we expand T^4 to the free stream temperature T and neglect higher order terms. This results in the following approximation:

$$T^4 \approx 4T_\infty^3 T - 3T_\infty^4 \tag{10}$$

As a result, we have

$$\frac{\partial q_r}{\partial z} = \frac{-16\sigma_1 T_\infty^3}{3k_1}\frac{\partial^2 T}{\partial z^2} \tag{11}$$

Equation (4), derived from Equations (10) and (11), may be simplified to

$$\frac{\partial T}{\partial t} + w\frac{\partial T}{\partial z} = \frac{k_1}{\rho C_p}\frac{\partial^2 T}{\partial z^2} - \frac{Q_0}{\rho C_p}(T - T_\infty) + \frac{1}{\rho C_p}\frac{16\sigma_1 T_\infty^3}{3k_1}\frac{\partial^2 T}{\partial z^2} + Q_1(C - C_\infty) + \frac{DK_T}{C_s C_p}\frac{\partial^2 C}{\partial z^2} \tag{12}$$

Because it is presumed that the frequency of electron–atom collisions is very high, it is impossible to ignore Hall and ion slip currents. Therefore, the velocity in the y-direction is caused by Hall currents and ion slip currents. When the magnitude of the magnetic field is exceptionally great, the generalised law of Ohm is adjusted such that it takes into account the Hall effect as well as the ion slip effect (Sutton and Sherman [1]),

$$J = \sigma\left(E + V \times B\right) - \frac{\omega_e \tau_e}{B_0}\left(J \times B\right) + \frac{\omega_e \tau_e \beta_i}{B_0^2}\left(\left(J \times B\right) \times B\right) \tag{13}$$

Further it is assumed that $\beta_e = \omega_e \tau_e \sim O(1)$ and $\beta_i = \omega_i \tau_i \ll 1$, In the Equation (13) the electron pressure gradient, the ion-slip and thermo-electric effects are neglected. We also assume that the electric field $E = 0$ under assumptions reduces to

$$\left(1 + \beta_i \beta_e\right)J_x + \beta_e J_y = \sigma B_0 v \tag{14}$$

$$\left(1 + \beta_i \beta_e\right)J_y + \beta_e J_x = -\sigma B_0 v \tag{15}$$

On solving above Equations (14) and (15), we get

$$J_x = \sigma B_0\left(\alpha_2 u + \alpha_1 v\right) \tag{16}$$

$$J_y = -\sigma B_0\left(\alpha_2 v - \alpha_1 u\right) \tag{17}$$

$$Where\ \alpha_1 = \frac{1 + \beta_e \beta_i}{\left(1 + \beta_e \beta_i\right)^2 + \beta_e^2}, \alpha_2 = \frac{\beta_e}{\left(1 + \beta_e \beta_i\right)^2 + \beta_e^2}$$

when Equations (16) and (17) are introduced into (2) and (3), respectively, the equations that are produced are,

$$\frac{\partial u}{\partial t} + w\frac{\partial u}{\partial z} - 2\Omega v = -\frac{1}{\rho}\frac{\partial p}{\partial x} + v\frac{\partial^2 u}{\partial z^2} + \frac{\alpha}{\rho}\frac{\partial^3 u}{\partial z^2 \partial t} + \frac{\sigma B_0^2\left(\alpha_2 v - \alpha_1 u\right)}{\rho} - \frac{v}{k}u + g\beta(T - T_\infty) + g\beta^*(C - C_\infty) \tag{18}$$

$$\frac{\partial v}{\partial t} + w\frac{\partial v}{\partial z} + 2\Omega u = -\frac{1}{\rho}\frac{\partial p}{\partial y} + v\frac{\partial^2 v}{\partial z^2} + \frac{\alpha}{\rho}\frac{\partial^3 v}{\partial z^2 \partial t} - \frac{\sigma B_0^2\left(\alpha_2 u + \alpha_1 v\right)}{\rho} - \frac{v}{k}v \tag{19}$$

Fusing Equations (2) and (3), let $q = u + iv$ and $\xi = x - iy$, we obtain

$$\frac{\partial q}{\partial t} + w\frac{\partial q}{\partial z} + 2i\Omega q = -\frac{1}{\rho}\frac{\partial p}{\partial \xi} + v\frac{\partial^2 q}{\partial z^2} + \frac{\alpha}{\rho}\frac{\partial^3 q}{\partial z^2 \partial t} + \frac{\sigma B_0^2\left(\alpha_2 v - \alpha_1 u\right)}{\rho} - \frac{v}{k}q + g\beta(T - T_\infty) + g\beta^*(C - C_\infty) \tag{20}$$

Beyond the border layer, Equation (20) provides

$$-\frac{1}{\rho}\frac{\partial p}{\partial \xi}=\frac{dU_{\infty}}{\partial t}+\frac{v}{k}U_{\infty}+\frac{\sigma B_0^2}{\rho}U_{\infty} \tag{21}$$

To standardise the mathematical representation of the physical issue, we will introduce the non-dimensional quantities and parameters listed below.

$$\begin{aligned}
&q^*=\frac{q}{w_0}, w^*=\frac{w}{w_0},\ z^*=\frac{w_0 z}{v},\ U_0^*=\frac{U_0}{w_0}, U_{\infty}^*=\frac{U_{\infty}}{w_0},\ t^*=\frac{t\,w_0^2}{v}, \theta=\frac{T-T_{\infty}}{T_w-T_{\infty}}, \phi=\frac{C-C_{\infty}}{C_w-C_{\infty}},\\
&M^2=\frac{\sigma B_0^2 v}{\rho w_0^2}, \Pr=\frac{v\,\rho C_p}{k_1}=\frac{v}{\alpha}, r=\frac{vg\beta(T_w-T_{\infty})}{w_0^3}, Gm=\frac{vg\beta^*(C_w-C_{\infty})}{w_0^3},\\
&K=\frac{w_0^2 k}{v^2}, Sc=\frac{v}{D}, R=\frac{\Omega v}{w_0^2}, H=\frac{vQ_0}{\rho C_p w_0^2}, S=\frac{w_0^2\,\alpha_1}{\rho v^2},\ K_c=\frac{K_c v}{w_0^2}, F=\frac{16\sigma^* T_{\infty}^3}{3kk_1}\\
&Du=\frac{DK_T}{vC_s C_p}\frac{\left(C_w-C_{\infty}\right)}{(T_w-T_{\infty})}, Q_1=\frac{v\,Q_1(C_w-C_{\infty})}{(T_w-T_{\infty})\,w_0^2}
\end{aligned} \tag{22}$$

By exploiting variables that are not dimensional, the three governing Equations (5), (12), and (20), reduced to

$$\frac{\partial q}{\partial t}-(1+A\varepsilon\,e^{iwt})\frac{\partial q}{\partial z}=\frac{dU_{\infty}}{dt}+\frac{\partial^2 q}{\partial z^2}+S\frac{\partial^3 q}{\partial z^2\partial t}-\lambda\,q+Gr\,\theta+Gm\,\phi \tag{23}$$

$$Where\,\lambda=M^2(\alpha_1+i\alpha_2)+2iR+\frac{1}{K}$$

$$\frac{\partial\theta}{\partial t}-(1+A\varepsilon e^{iwt})\frac{\partial\theta}{\partial z}=-\frac{(1+F)}{\Pr}\frac{\partial^2\theta}{\partial z^2}-H\,\theta+Q_1\phi+D_u\frac{\partial^2\phi}{\partial z^2} \tag{24}$$

$$\frac{\partial\phi}{\partial t}-(1+A\varepsilon e^{iwt})\frac{\partial\phi}{\partial z}=\frac{1}{Sc}\frac{\partial^2\phi}{\partial z^2}-K_c\phi \tag{25}$$

The equations that relate to the boundary conditions are as follows:

$$q=U_0,\quad \theta=1+\varepsilon\,e^{iwt},\ \phi=1+\varepsilon e^{iwt} \qquad \text{at } z=0 \tag{26}$$

$$q=0,\quad \theta=0,\quad \phi=0 \qquad \text{as} \quad z\to\infty \tag{27}$$

3. Solution of the Problem

The expressions (23) and (25) portray a set of partial differential equations that cannot be solved in closed form; nonetheless, if the equations can be reduced to a set of ordinary differential equations in dimensionless form, then the equations can be solved analytically. This can be accomplished by expressing the velocity, temperature, and concentration as,

$$q=q_0\left(z\right)+\varepsilon e^{nt}q_1\left(z\right)+O\left(\varepsilon^2\right) \tag{28}$$

$$\theta=\theta_0\left(z\right)+\varepsilon e^{nt}\theta_1\left(z\right)+O\left(\varepsilon^2\right) \tag{29}$$

$$\phi=\phi_0\left(z\right)+\varepsilon e^{nt}\phi_1\left(z\right)+O\left(\varepsilon^2\right) \tag{30}$$

The following pairs of equations are obtained by substituting the Equations (28)–(30) into the Equations (23)–(25) by equating the harmonic and non-harmonic components, as well as the neglecting and higher order terms of, and by obtaining the following:

$$\frac{\partial^2 q_0}{\partial z^2}+\frac{\partial q_0}{\partial z}-\lambda q_0=-Gr\,\theta_0-Gm\,\phi_0 \tag{31}$$

$$(1+Siw)\frac{\partial^2 q_1}{\partial z^2}+\frac{\partial q_1}{\partial z}-(\lambda+iw)q_1=-Gr\,\theta_1-Gm\,\phi_1-A\frac{\partial q_0}{\partial z} \tag{32}$$

$$\frac{\partial^2\theta_0}{\partial z^2}+\Pr\frac{\partial\theta_0}{\partial z}-(H+F)\Pr\theta_0=-\Pr\left(Q_1\phi_0+D_u\frac{\partial^2\phi_0}{\partial z^2}\right) \tag{33}$$

$$\frac{\partial^2\theta_1}{\partial z^2}+\Pr\frac{\partial\theta_1}{\partial z}-(iw+H+F)\Pr\theta_1=-\Pr\left(A\frac{\partial\theta_0}{\partial z}+Q_1\phi_1+D_u\frac{\partial^2\phi_1}{\partial z^2}\right) \tag{34}$$

$$\frac{\partial^2\phi_0}{\partial z^2}+Sc\frac{\partial\phi}{\partial z}-Sc\,Kc\,\phi_0=0 \tag{35}$$

$$\frac{\partial^2\phi_1}{\partial z^2}+Sc\frac{\partial\phi_1}{\partial z}-(iw+K_c)Sc\,\phi_1=-A\,Sc\frac{\partial\phi_0}{\partial z} \tag{36}$$

The requirements that relate to each border are as follows:

$$q_0=U_0, q_1=0,\ \ \theta_0=1,\ \theta_1=1,\ \phi_0=1,\ \phi_1=1 \qquad \text{at } z=0 \tag{37}$$

$$q_0=0, q_1=0,\ \ \theta_0=0,\ \theta_1=0,\ \phi_0=0,\ \phi_1=0 \qquad \text{as } \ z\to\infty \tag{38}$$

By applying the initial conditions (37) and (38) and then solving Equations (31)–(36), one obtains the following approach:

$$\varphi_0=\exp(-m_1 z) \tag{39}$$

$$\varphi_1=b_1\exp(-m_1 z)+b_2\exp(-m_2 z) \tag{40}$$

$$\theta_0=b_3\exp(-m_1 z)+b_4\exp(-m_3 z) \tag{41}$$

$$\theta_1=b_5\exp(-m_1 z)+b_6\exp(-m_2 z)+b_7\exp(-m_3 z)+b_8\exp(-m_4 z) \tag{42}$$

$$q_0=b_9\exp(-m_1 z)+b_{10}\exp(-m_3 z)+b_{11}\exp(-m_5 z) \tag{43}$$

$$\begin{aligned}q_1=&\,b_{12}\exp(-m_1 z)+b_{13}\exp(-m_2 z)+b_{14}\exp(-m_3 z)+b_{15}\exp(-m_4 z)+\\&b_{16}\exp(-m_5 z)+b_{17}\exp(-m_6 z)\end{aligned} \tag{44}$$

Substituting Equations (39)–(44) into Equations (28)–(30), we acquire the velocity temperature and concentration

$$\begin{aligned}q=&\,b_9\exp(-m_1 z)+b_{10}\exp(-m_3 z)+b_{11}\exp(-m_5 z)+\\&\varepsilon e^{iwt}\begin{pmatrix}b_{12}\exp(-m_1 z)+b_{13}\exp(-m_2 z)+b_{14}\exp(-m_3 z)+\\ b_{15}\exp(-m_4 z)+b_{16}\exp(-m_5 z)+b_{17}\exp(-m_6 z)\end{pmatrix}\end{aligned} \tag{45}$$

$$\begin{aligned}\theta=&\,b_3\exp(-m_1 z)+b_4\exp(-m_3 z)+\varepsilon e^{iwt}(b_5\exp(-m_1 z)+b_6\exp(-m_2 z)\\&+b_7\exp(-m_3 z)+b_8\exp(-m_4 z))\end{aligned} \tag{46}$$

$$\phi = \exp(-m_1 z) + \varepsilon e^{iwt}\,(b_1 \exp(-m_1 z) + b_2 \exp(-m_2 z)) \tag{47}$$

For this particular boundary layer flow, the skin friction co-efficient, the Nusselt number, and the Sherwood number are all crucially significant physical characteristics. The following is a definition and determination of each of these parameters:

3.1. Skin Friction

Very important physical parameter at the boundary is the skin friction which is given in the non-dimensional form and derives as

$$\tau = \left(\frac{\partial q}{\partial z}\right)_{z=0} = -\left(\left(b_9 m_1 + b_{10} m_3 + b_{11} m_5\right) + \varepsilon e^{iwt}\begin{pmatrix} b_{12} m_1 + b_{13} m_2 + \\ b_{14} m_3 + b_{15} m_4 + b_{16} m_5 + b_{17} m_6 \end{pmatrix}\right) \tag{48}$$

3.2. Nusselt Number

Another physical parameter like rate of heat transfer, in the form of Nusselt number, is expressed by

$$Nu = -\left(\frac{\partial \theta}{\partial z}\right)_{z=0} = \left(\left(b_3 m_1 + b_4 m_3\right) + \varepsilon e^{iwt}\,(b_5 m_1 + b_6 m_2 + b_7 m_3 + b_8 m_4)\right) \tag{49}$$

3.3. *Sherwood Number*

The rate of mass transfer in the form of Sherwood number is also derived by

$$Sh = -\left(\frac{\partial \phi}{\partial z}\right)_{z=0} = m_1 + \varepsilon e^{iwt}\,(b_1 m_1 + b_2 m_2) \tag{50}$$

4. Results and Discussion

The present investigation aims to investigate the effects of radiation absorption, Hall, and ion slip on the uncertain free convective flow of an electrically conducting fluid that is viscous and incompressible over an unbounded vertical porous plate. At the same time, a uniform transverse magnetic field is present. A regular perturbation approach is used to find solutions to the governing equations of the flow field when the Eckert number Ec is small. The closed-form solutions for the velocity, temperature, and concentration have been derived analytically. Its behaviour is computationally addressed concerning various flow characteristics such as the Hartmann number (M), the Hall parameter (e), the ion slip parameter (e), the thermal Grashof number (Gr), the mass Grashof number (Gm), the permeability of porous media (K), the radiation absorption criterion (Q_1), the diffusion thermo criterion (Du), the Prandtl number (Pr). For computational intention, we are setting up the values A = 2, Ɛ = 0:001; U_0 = 0.1, while the parameters being M = 2, K = 0.5, R = 1, S = 0.5, Gr = 5, Gm = 3, be = 1, bi = 0.2, Pr = 0.71, H = 1, Sc = 0.22, Kc = 1, Du = 2, Q_1 = 0.5, t = 2 fixed over the range. Figures 2–18 are shown here, with their respective velocities, temperatures, and concentrations represented as distributions. The stresses, Nusselt number, and Sherwood number at the plate are analyzed numerically, explained with governing factors, and summarized in the Tables 1–3. The outcomes of this investigation, as indicated in Table 4, are consistent with the findings of the prior study [10], which Raghunath and his colleagues conducted.

Figures 2 and 3 illustrate the consequences of the thermal buoyancy force, denoted by Gr, and the concentration buoyancy force, characterized by Gm. Increasing the thermal and mass Grashof numbers causes fluid velocity in the principal flow direction inside the boundary layer area. This is the case regardless of whether the Grashof number is increased. This is because an increase in both the thermal and the solutal Grashof number causes a rise in buoyancy effects, and these effects cause more flow in the direction that is already the dominant flow. There is a reverse flow occurring in the direction of the secondary flow. When the temperature and concentration of Grashof numbers are increased, the secondary velocity profiles rise in the boundary layer area further away from the plate. At the same time, they fall closer to the plate. It should also be observed that there is no reversal flow in the secondary flow direction when neither heat nor concentration buoyancy forces are present. This is something that should be taken into consideration. This indicates that the forces associated with buoyancy and the movements of the free stream are to blame for the induction of reverse flow.

We see a decrease in the size of the velocity components u and v, as well as a reduction of the velocity of resultant velocity when the strength of the magnetic field is increased, as shown in Figure 4. Because the effects of a transverse magnetic field on an electrically conducting fluid generate a piezoresistive force (also known as the Lorentz force), which is analogous to the drag force, growing M causes the drag force to raise, which in turn causes the motion of the fluid to slow down as a direct result of the increased drag force. As the passage of time causes the permeability factor (K) to grow, Figure 5 demonstrates that the subsequent velocity component u becomes more concentrated while increasing in height. When K is made higher, the consequent velocity is also pushed higher, increasing the thickness of the momentum boundary layer. A decrease in porosity leads to an increase in fluid speed that is less visible once measured within the flow zone filled by the liquid.

Both Figures 6 and 7 illustrate how the Hall current parameters, denoted by (βe), and the ion-slip parameter, denoted by (βi), affect the fluid velocity. It is clear from looking at Figures 4 and 5 that as the Hall and ion-slip parameters are increased, the fluid velocity in the primary flow direction decreases in the boundary layer region that is close to the plate, but it increases in the boundary layer region that is further away from the plate. This phenomenon can be seen in both of these figures. The fluid velocity in the secondary flow direction increases everywhere in the boundary layer area due to an increase in the hall parameter, except for a narrow region where it disappears. This is because the Hall current is generated as a result of the spiralling of conducting fluid particles around magnetic lines of force, which have the potential to create secondary motion in the flow field. The nature of the ion-slip current on the fluid flow in the secondary flow direction is shown to be the exact opposite of that of the Hall current.

The influence of the diffusion thermo specification can be seen in Figures 8 and 9, which depict the velocity and temperature profiles, respectively. Figure 8 demonstrates the effect of the Dufour number on the primary and secondary velocities, which may be found on this page. It shows that greater values of the Dufour number cause the initial momentum to increase, but it indicates that the behaviour of the second velocity is the exact reverse of what one would expect. This pattern is a direct result of the generation of energy flow, which makes it possible for the rate of motion to pick up speed. Figure 9 makes it clear that an elevation in the values of the Dufour number leads to an accompanying rise in the temperature of the fluid. This is shown by the fact that an increase in the importance of the Dufour number can be seen. The generation of energy flow, which causes a temperature rise, is responsible for this occurrence.

The impact of the radiating absorption characteristic is seen in Figure 10 in both the primary and secondary velocity directions. According to the statistics, the main velocity graphs increase when there is an increase in radiating absorption. Still, the secondary velocity graphs go down when there is a drop in radiating absorptions over the whole liquid region. It was interesting to see how an increase in the radiating absorption characteristics might result in a rise in velocity. Inside the border layers, a description of the effects of the radiation-absorption parameter on the temperatures is depicted. As seen in Figure 11, it has become abundantly clear that the temperature distributions are rising functions of the absorbed radiation. In contrast, the inverse pattern was found when the rotation parameter was used, as shown in Figure 12.

The influence of the radiation factor on the velocity and temperature is shown in Figures 13 and 14. It is clear from looking at Figure 13 shows that a rise in the radiation parameter causes a decrease in the essential velocity, but it has the opposite effect on the secondary velocity. As a consequence of this, the resulting velocity decreases as the value of R increases over the whole of the area that is occupied by the fluid. The influence of the thermal radiation parameter is quite essential when it comes to temperature profiles. It has been discovered that there is a negative correlation between the increase in the radiation parameter and the temperature (Figure 14). As a result of the action of the radiation parameter, it is also possible to observe that the thickness of the thermal boundary layer quickly decreases.

Figure 15 illustrates how the Prandtl number (Pr) influences temperature profiles when certain fluids are present. These fluids include hydrogen (Pr = 0.684), air (Pr = 0.71), carbon dioxide (Pr = 0.72), and water (Pr = 1.0). According to the data in this figure, a rise in the Prandtl number results in a drop in temperature over the whole flow field. This agrees with the theory that the thickness of the thermal boundary layer decreases as the Prandtl number increases. Figure 16 displayed the differences in temperature profiles that resulted from using various values for the heat source specification H. Bringing down the temperature of the flow field, increasing the value of the heat source parameter. This may occur because of the fluid's elastic quality.

Figures 17 and 18 illustrate the chemical reaction parameter Kc's influence and the effect that the Schmidt number has on the concentration distribution. Figure 17 demonstrates an increase in the value of the parameter for the chemical reaction. The concentration profiles were quickly decreased due to Kc. As the number of chemically responsive factors increases, the number of chemical reactions that influence the quantities of solutal particles also increases, which causes the concentration domain to decrease. The end effect of the chemical reaction is a reduction in the breadth of the solute border stratum. In Figure 18, the concentration gradient is shown as having decreased over the whole flow field as the Schmidt number Sc increased. This demonstrates that heavier diffusing species have a higher impact on inhibiting the concentration dispersion of the flow field.

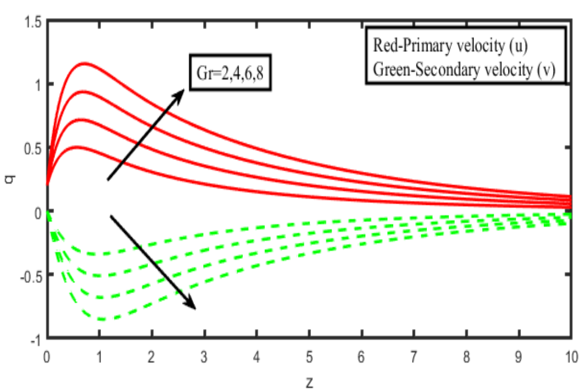

Figure 2. Velocity profiles for u and v for thermal Grashof number (Gr).

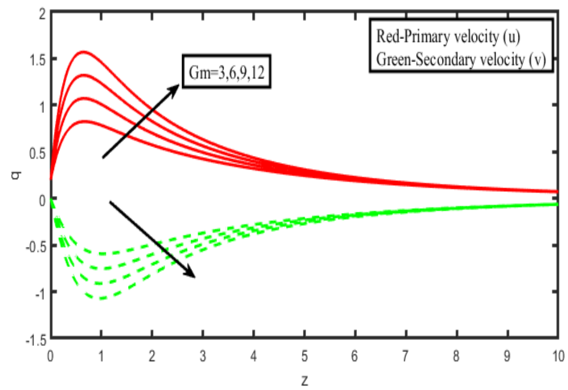

Figure 3. Velocity profiles for u and v for modified Grashof number (Gm).

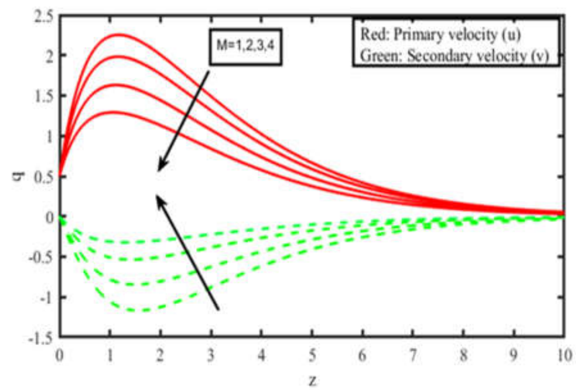

Figure 4. Velocity profiles for u and v for Magnetic field parameter (M).

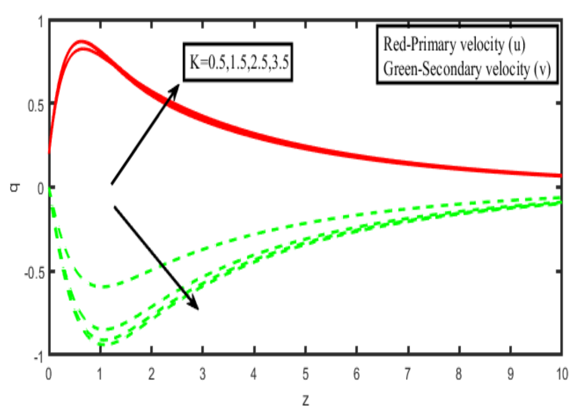

Figure 5. Velocity profiles for u and v for Permeability of porous media (K).

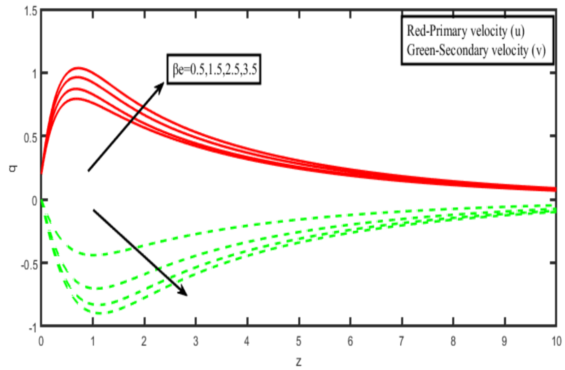

Figure 6. Velocity profiles for u and v for Hall parameter (β_e).

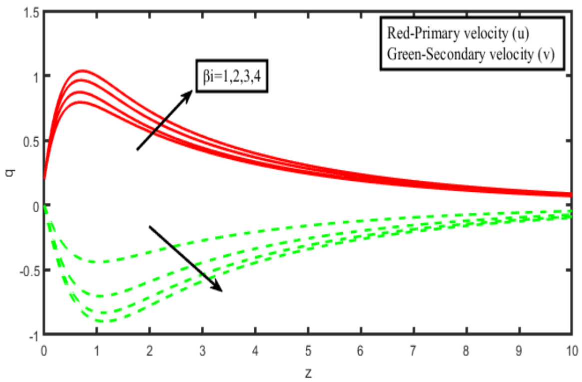

Figure 7. Velocity profiles for u and v for Hall parameter (β_i).

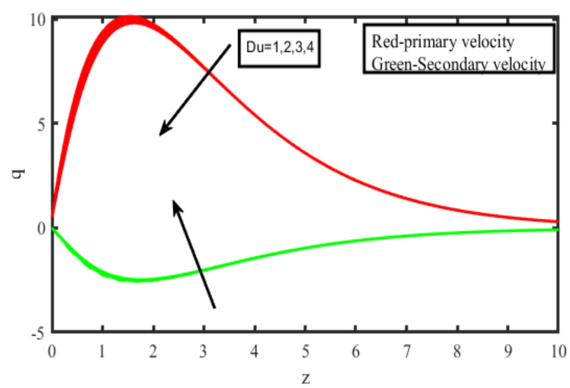

Figure 8. Velocity profiles for u and v for Diffusion thermo specification (D_u).

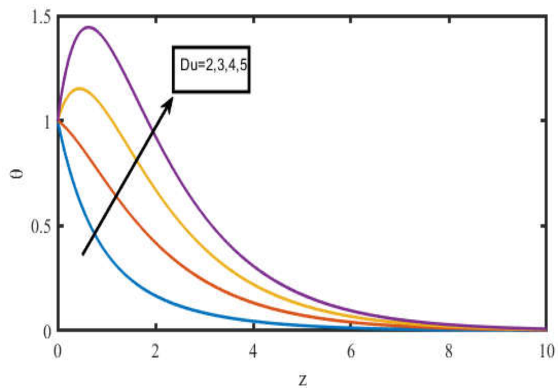

Figure 9. Temperature profiles for Diffusion thermo specification (D_u).

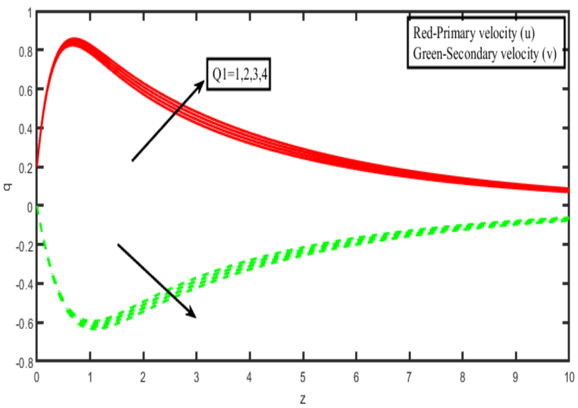

Figure 10. Velocity profiles for u and v for Radiation Absorption (Q_1).

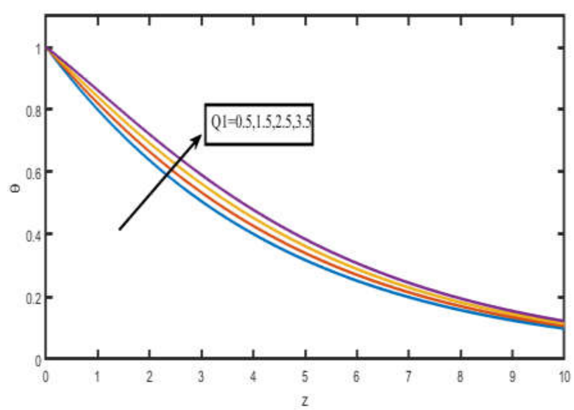

Figure 11. Temperature profiles for Radiation absorption (Q_1).

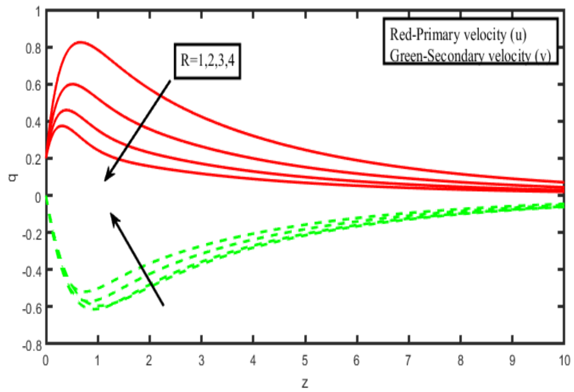

Figure 12. Velocity profiles for u and v for Rotation specification (R).

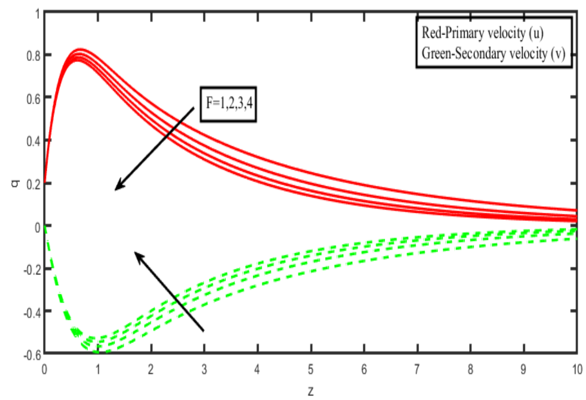

Figure 13. Velocity profiles for u and v for Radiation parameter (F).

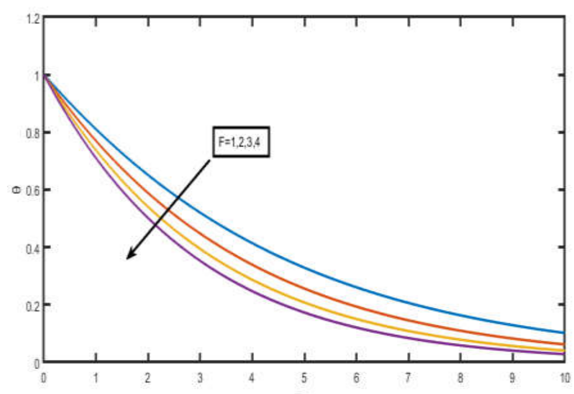

Figure 14. Temperature profiles for Radiation parameter (F).

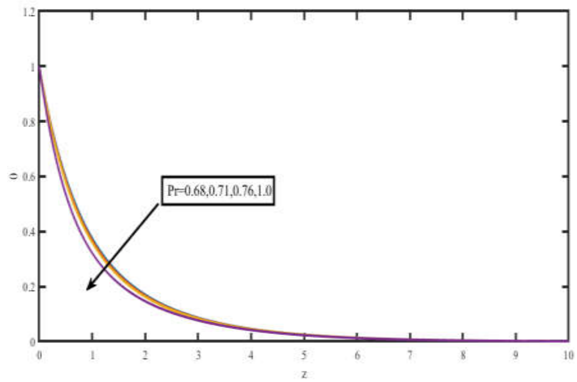

Figure 15. Temperature profiles for Prandtl number (Pr).

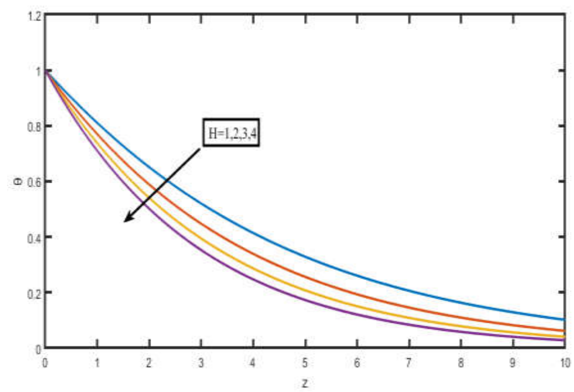

Figure 16. Temperature profiles for Heat absorption Parameter (H).

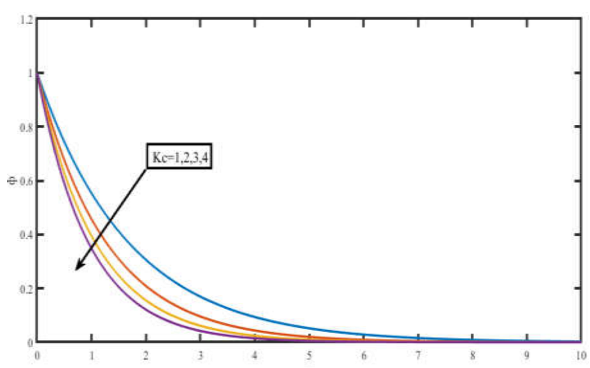

Figure 17. Concentration profiles for Chemical reaction (K_c).

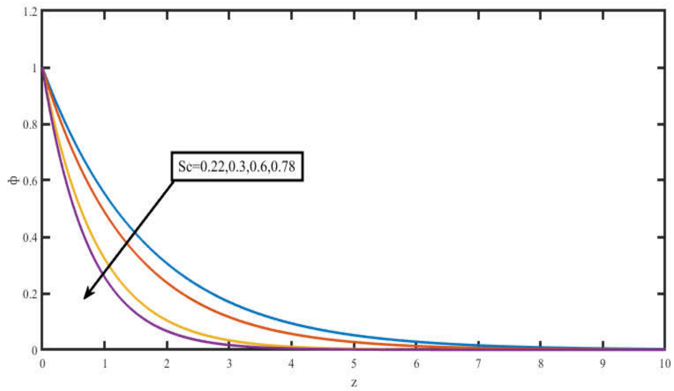

Figure 18. Concentration profiles for Schmidt number (S_c).

The values for the magnitudes of skin friction are summarized in Table 1, which may be found below. An increase in the Hartmann number will be introduced to decrease the amount of skin friction. This application uses second-grade fluid because of its elastic nature, which reduces the frictional drag caused by the liquid. It is explored what happens to similar behavior when the rotation factor, the Prandtl number, the heat source factor, the Schmidt number, the chemical reaction factor, and the amount of time are all enhanced. An increase in the permeability parameter or the second-grade fluid parameter will further improve the expansion of skin friction in intensity on the edge of the surface. The analogous activity is explored for the same when an increase in the thermal Grashof number, mass Grashof number, Hall and ion aspects that affect them are enhanced on the boundary of the surface.

As a consequence, a rise in the Nusselt number also results from an increase in the radiation parameter, the Prandtl number, and the heat source parameters, as shown in Table 2. The radiation absorption parameter and the frequency oscillations of the radiation need to be increased for it to be diminished. According to Table 3, an increase in the Schmidt number, the chemical reaction parameter, the frequency of fluctuations, or non-dimensional time all contribute to strengthening the Sherwood number as time proceeds. In Table 4 expressed as the results of the present study are pretty congruent with the findings of the previous study by Raghunath and colleagues [10]. Recently, investigations regarding nanomaterials are listed in Refs. [33,34].

Table 1. Skin friction.

Gr	Gm	βe	βi	Pr	H	Sc	Kc	R	Du	M	K	S	Q_1	τ
5	3	1	0.2	0.71	1	0.22	1	1	1	2	0.5	0.5	0.5	2.1521
5	3	1	0.2	0.71	1	0.22	1	1	1	3	0.5	0.5	1	2.7852
5	3	1	0.2	0.71	1	0.22	1	1	1	2	1.0	05	1	1.4521
5	3	1	0.2	0.71	1	0.22	1	1	1	2	1.5	0.5	1	3.7852
5	3	1	0.2	0.71	1	0.22	1	1	1	2	0.5	0.5	2	3.5211
5	3	1	0.2	0.71	1	0.22	1	1	1	2	0.5	1.0	3	2.0332
5	3	1	0.2	0.71	1	0.22	1	1	1	2	0.5	1.5	1	2.7852
9	3	1	0.2	0.71	1	0.22	1	1	1	2	0.5	0.5	1	3.7852
12	3	1	0.2	0.71	1	0.22	1	1	1	2	0.5	0.5	1	2.7852
5	6	1	0.2	0.71	1	0.22	1	1	1	2	0.5	0.5	1	5.4621
5	9	1	0.2	0.71	1	0.22	1	1	1	2	0.5	0.5	1	3.3221
5	3	2	0.2	0.71	1	0.22	1	1	1	2	0.5	05	1	3.0214
5	3	3	0.2	0.71	1	0.22	1	1	1	2	0.5	0.5	1	4.7852
5	3	1	0.4	0.71	1	0.22	1	1	1	2	0.5	0.5	1	2.0324
5	3	1	0.6	0.71	1	0.22	1	1	1	2	0.5	0.5	1	3.7852
5	3	1	0.2	5.0	1	0.22	1	1	1	2	0.5	0.5	1	3.0125
5	3	1	0.2	7.0	1	0.22	1	1	1	2	0.5	05	1	2.7852
5	3	1	0.2	0.71	2	0.22	1	1	1	2	0.5	0.5	1	1.3214
5	3	1	0.2	0.71	3	0.22	1	1	1	2	0.5	0.5	1	1.7852
5	3	1	0.2	0.71	1	0.25	1	1	1	2	0.5	0.5	1	2.7852
5	3	1	0.2	0.71	1	0.30	1	1	1	2	0.5	0.5	1	2.1255
5	3	1	0.2	0.71	1	0.22	2	1	1	2	0.5	05	1	2.7852
5	3	1	0.2	0.71	1	0.22	4	1	1	2	0.5	0.5	1	2.1254
5	3	1	0.2	0.71	1	0.22	1	2	1	2	0.5	0.5	1	2.7852
5	3	1	0.2	0.71	1	0.22	1	2	2	2	0.5	0.5	1	2.7852
5	3	1	0.2	0.71	1	0.22	1	2	3	2	0.5	0.5	1	2.6221

Table 2. Nusselt number.

F	Q_1	H	Pr	ω	Du	Nu
2	0.5	1	0.71	π/6	1	1.1251
3	0.5	1	0.71	π/6	1	1.7852
1	1	1	0.71	π/6	1	−0.12541
1	2	1	0.71	π/6	1	−1.65514
1	0.5	2	0.71	π/6	1	1.4521
1	0.5	3	0.71	π/4	1	1.4021
1	0.5	1	5.0	π/3	1	1.2785
1	0.5	1	7.0	π/6	1	1.3210
1	0.5	1	0.71	π/4	1	1.4521
1	0.5	1	0.71	π/3	1	1.0321
1	0.5	1	0.71	π/3	2	1.7520
1	0.5	1	0.71	π/3	3	1.0321

Table 3. Sherwood number.

Sc	Kc	ω	Sh
0.3	1	π/6	0.6521
0.6	1	π/6	0.9852
0.22	2	π/6	0.1201
0.22	3	π/6	0.5200

0.22	1	$\pi/4$	0.4520
0.22	1	$\pi/3$	1.4520

Table 4. Comparison of results for primary velocity (A = 5, n = 0.5, t = 0.5, ϵ = 0.01, U_0 = 0.5, Sc = 0.22, Kc = H = Q_1 = F = 1, Du = 0).

M	K	Gr	Gm	Previous Results Raghunath et al. [10]	Present Values
2	0.5	5	3	0.703484	0.752100
3				0.452455	0.452114
4				0.302545	0.302144
	1.0			0.797822	0.785210
	1.5			0.835478	0.842011
		8		0.934587	0.962214
		12		1.161458	1.122348
			5	0.780458	0.788752
			7	0.851458	0.852147

5. Conclusions

i. By increasing the magnetic field's strength, the rotating speed, or the properties of the second-grade fluid, the velocity produced may be reduced.
ii. Permeability of the porous medium may be enhanced to have the same effect as increases.
iii. The velocity is intended to decrease if the pore size of a porous medium decreases, which is the same behaviour seen in the case of radiation.
iv. An increase in the Hall parameter and the ion slip parameter over the fluid region contribute to the rise in the ultimately produced velocity.
v. The resultant velocity is affected by the thermal and solute buoyancy forces, and it will continue to increase in intensity until it hits a significant threshold.
vi. As the diffusion thermo and radiation absorption parameter, the resulting velocity and temperature.
vii. When both the heat source parameter and radiation increase, the temperature distribution becomes more concentrated. The fluid medium has decreased concentration due to the chemical reaction and the Schmidt number.

Author Contributions: Conceptualization, V.V.L.D. and M.M.A.L.; methodology, N.R.K.; software, N.R.K.; validation, M.I.K., K.R. and F.A.; formal analysis, M.O.; investigation, K.G.; resources, K.G.; data curation, M.I.K.; writing—original draft preparation, V.V.L.D.; writing—review and editing, E.S.M.T.-E.; visualization, A.M.G.; supervision, M.I.K.; project administration, M.M.A.L.; funding acquisition, E.S.M.T.-E. All authors have read and agreed to the published version of the manuscript.

Funding: The authors would like to thank the Deanship of Scientific Research at Umm Al-Qura University for supporting this work by Grant Code: 22UQU4331317DSR85. The authors express their gratitude to Princess Nourah bint Abdulrahman University Researchers Supporting Project (Grant No. PNURSP2022R152), Princess Nourah bint Abdulrahman University, Riyadh, Saudi Arabia.

Data Availability Statement: All the data are clearly available in the manuscript.

Conflicts of Interest: The authors declares no conflict of interest.

Nomenclature

x, y	dimensional co-ordinates (m)
u, v	velocity components along x,y directions (m/s)
A	real positive constant
B_0	applied magnetic field (A/m)
C	non- dimensional fluid concentration (kg/m^3)
C_p	specific heat at a constant pressure (J/kg. K)

C_w	the uniform concentration of the fluid at the plate (kg m^{-3})
C_∞	the concentration of the fluid far away from the plate (kg m^{-3})
D	coefficient of mass diffusivity (m^2/s)
D_M	Chemical molecular diffusivity; m^{-2}·s^{-1}
g	acceleration due to gravity (m s^{-2})
Gr	thermal Grashof number
Gm	mass Grashof number
B	magnetic field vector (A/m)
E	electric field vector (c)
V	velocity vector (m/s)
Q_0	heat source parameter
J	current density vector (A/m^2)
J_x, J_y	current densities along x and y directions
k	permeability of porous medium (m^2)
k_1	thermal conductivity (W/m K)
K	permeability parameter
Kc	chemical reaction parameter (w/mk)
K_l	chemical reaction rate constant
m	Hall parameter
M	Hartmann number
N	constant
Nu	local Nusselt number
P_e	electron pressure (Pascal)
Pr	Prandtl number
q_m	local surface mass flux (kg s^{-1} m^{-2})
q_w	local surface heat flux (W m^{-2})
R	rotation parameter
S	second grade fluid
Sc	Schmidt number
Sh	local Sherwood number
Q_l	radiation absorption parameter
t	time (s)
T_w	the uniform temperature of the fluid at the plate (K)
T_∞	the temperature of the fluid far away from the plate (K)
u_0	plate velocity (m s^{-1})
w	slip velocity (m s^{-1})
w_0	scale of suction velocity
q_r	radiative heat flux
Greek symbols	
β	coefficient of thermal expansion of the fluid
β*	coefficient of mass expansion of the solid
θ	non-dimensional temperature (K)
ϕ	non-dimensional concentration (mol/m^3)
ν	kinematic viscosity (m^2/s)
ρ	fluid density (Kg/m^3)
σ	electrical conductivity (S/m)
Ω	angular velocity (s^{-1})
τ_w	local wall shear stress (pascal)
τ	local skin friction coefficient
τ_e	electron collision time (s)
ω_e	cyclotron frequency (e/mB)
Subscripts and superscripts	
e	electrons
i	ions
w	conditions on the wall
∞	free stream conditions

References

1. Sutton, G.W.; Sherman, A. *Engineering Magnetohydrodynamics*; McGraw-Hill Book Comp: New York, NY, USA, 1965.
2. Abo-Eldahab, E.M.; Aziz, M.A. Hall and ion-slip effects on MHD free convective heat generating flow past a semi-infinite vertical plate flat plate. *Phys. Scr.* **2000**, *61*, 344–348.
3. Srinivasacharya, D.; Kaladhar, K. Mixed convection flow of couple stress fluid between parallel vertical plates with Hall and Ion-slip effects. *Commun. Nonlinear Sci. Numer. Simul.* **2012**, *17*, 2447–2462.
4. Srinivasacharya, D.; Kaladhar, K. Analytical solution of mixed convection flow of couple stress fluid between two circular cylinders with Hall and ion-slip effects. *Turkish J. Eng. Env. Sci*. **2012**, *36*, 226–235.
5. Tani, I. Steady flow of conducting fluids in channels under transverse magnetic fields with consideration of Hall effects. *J. Aerosp. Sci.* **1962**, *29*, 297–305.
6. Motsa, S.S.; Shateyi, S. The Effects of Chemical Reaction, Hall, and Ion-Slip Currents on MHD Micropolar Fluid Flow with Thermal Diffusivity Using a Novel Numerical Technique. *J. Appl. Math.* **2012**, *2012*, 30.
7. Attia, H.A. Transient Hartmann flow with heat transfer considering the Ion-slip. *Phys. Scr.* **2002**, *66*, 470–475.
8. Ghosh, S. Magnetohydrodynamic boundary layer flow over a stretching sheet with chemical reaction. *Int. J. Educ. Sci. Res.* **2015**, *2*, 78–83.
9. Kodi, R.; Ravuri, M.; Gulle, N.; Ganteda, C.; Khan, S.U.; Khan, M.I. Hall and ion slip radiative flow of chemically reactive second grade through porous saturated space via perturbation approach. *Waves Random Complex Media* **2022**, 1–17. https://doi.org/10.1080/17455030.2022.2108555.
10. Raghunath, K.; Ganteda, C.; Lorenzini, G. Effects of Soret, Rotation, Hall, and Ion Slip on Unsteady MHD Flow of a Jeffrey Fluid Through A Porous Medium in The Presence of Heat Absorption and Chemical Reaction. *J. Mech. Eng. Res. Dev.* **2022**, *45*, 80–97.
11. Sibanda, P.; Makinde, O.D. On steady MHD flow and heat transfer past a rotating disk in a porous medium with ohmic heating and viscous dissipation. *Int. J. Numer. Methods Heat Fluid Flow* **2010**, *20*, 269–285. https://doi.org/10.1108/09615531011024039.
12. Seth, G.S.; Sarkar, S. Hydromagnetic natural convection flow with induced magnetic field and nth order chemical reaction of a heat absorbing fluid past an impulsively moving vertical plate with ramped temperature. *Bulg. Chem. Commun.* **2015**, *47*, 66–79.
13. Sarveshanand; Singh, A.K. Magnetohydrodynamic free convection between vertical parallel porous plates in the presence of induced magnetic field. *Springer Plus* **2015**, *4*, 333. https://doi.org/10.1186/s40064-015-1097-1.
14. Sarma, D.; Pandit, K.K. Effects of thermal radiation and chemical reaction on steady MHD mixed convective flow over a vertical porous plate with induced magnetic field. *Int. J. Fluid Mech. Res.* **2015**, *42*, 315–333.
15. Ojjela, O.; Raju, A.; Kambhatla, P.K. Influence of thermophoresis and induced magnetic field on chemically reacting mixed convective flow of Jeffrey fluid between porous parallel plates. *J. Mol. Liq.* **2017**, *232*, 195–206.
16. Jha, B.; Aina, B. Interplay of non-conducting and conducting walls on magnetohydrodynamic(MHD) natural convection flow in vertical micro-channel in the presence of induced magnetic field. *Propuls. Power Res.* **2018**, *7*, 296–307.
17. Shaw, S.; Dogonchi, A.S.; Nayak, M.K.; Makinde, O.D. Makinde, Impact of Entropy Generation and Nonlinear Thermal Radiation on Darcy–Forchheimer Flow of $MnFe_2O_4$-Casson/Water Nanofluid due to a Rotating Disk: Application to Brain Dynamics. *Arab. J. Sci. Eng.* **2020**, *45*, 5471–5490. https://doi.org/10.1007/s13369-020-04453-2.
18. Sharma, K. FHD flow and heat transfer over a porous rotating disk accounting for Coriolis force along with viscous dissipation and thermal radiation. *Heat Transf.* **2022**, *51*, 4377–4392. https://doi.org/10.1002/htj.22504.
19. Ram, P.; Sharma, K.; Bhandari, A. Effect of porosity on revolving Ferrofluid flow with rotating disk. *Int. J. Fluids Eng.* **2010**, *6*, 67–76.
20. Mahanthesh, B.; Gireesha, B.J.; Animasaun, I.L.; Muhammad, T.; Shashikumar, N.S. Shashikumar, MHD flow of SWCNT and MWCNT nanoliquids past a rotating stretchable disk with thermal and exponential space dependent heat source. *Phys. Scr.* **2019**, *94*, 085214. https://doi.org/10.1088/1402-4896/ab18ba.
21. Vijay, N.; Sharma, K. Heat and mass transfer study of ferrofluid flow between co-rotating stretchable disks with geothermal viscosity: HAM analysis. *Chin. J. Phys.* **2022**, *78*, 83–95. https://doi.org/10.1016/j.cjph.2022.05.014.
22. Raghunath, K.; Gulle, N.; Vaddemani, R.R.; Mopuri, O. Unsteady MHD fluid flow past an inclined vertical porous plate in the presence of chemical reaction with aligned magnetic field, radiation, and Soret effects. *Heat Transf.* **2021**, *51*, 2742–2760. https://doi.org/10.1002/htj.22423.
23. Raghunath, K.; Obulesu, M. Unsteady MHD oscillatory Casson fluid flow past an inclined vertical porous plate in the presence of chemical reaction with heat absorption and Soret effects. *Heat Transf.* **2021**, *51*, 733–752. https://doi.org/10.1002/htj.22327.
24. Raghunath, K.; Obulesu, M.; Sujatha, S.; Venkateswaraju, K. Investigation of MHD Casson fluid flow past a vertical porous plate under the influence of thermal diffusion and chemical reaction. *Heat Transf.* **2021**, *51*, 77–394. https://doi.org/10.1002/htj.22311.
25. Vaddemani, R.R.; Kodi, R.; Mopuri, O. Characteristics of MHD Casson fluid past an inclined vertical porous plate. *Mater. Today: Proc.* **2022**, *49*, 2136–2142. https://doi.org/10.1016/j.matpr.2021.08.328.
26. Raghunath, K.; Mohanaramana, R. Hall, Soret, and rotational effects on unsteady MHD rotating flow of a second-grade fluid through a porous medium in the presence of chemical reaction and aligned magnetic field. *Int. Commun. Heat Mass Transf.* **2022**, *137*, 106287. https://doi.org/10.1016/j.icheatmasstransfer.2022.106287.
27. Ali, A.; Sajid, M.; Anjum, H.J.; Awais, M.; Nisar, K.S.; Saleel, C.A. Saleel, Entropy Generation Analysis of Peristaltic Flow of Nanomaterial in a Rotating Medium through Generalized Complaint Walls of Micro-Channel with Radiation and Heat Flux Effects. *Micromachines* **2022**, *13*, 375. https://doi.org/10.3390/mi13030375.

28. Ali, A.; Mumraiz, S.; Anjum, H.J.; Asghar, S.; Awais, M. Slippage phenomenon in hydromagnetic peristaltic rheology with hall current and viscous dissipation. *Int. J. Nonlinear Sci. Numer. Simul.* **2022**, *23*, 635–659. https://doi.org/10.1515/ijnsns-2019-0226.
29. Awais, M.; Bukhari, U.; Ali, A.; Yasmin, H. Convective and peristaltic viscous fluid flow with variable viscosity. *J. Eng. Thermophys.* **2017**, *26*, 69–78. https://doi.org/10.1134/S1810232817010088.
30. Ali, A.; Asghar, S. Oscillatory Flow in a Porous Channel with Porous Medium and Small Suction. *J. Mech.* **2014**, *30*, 153–159. https://doi.org/10.1017/jmech.2014.7.
31. Ali, A.; Asghar, S.; Alsulami, H.H. Oscillatory flow of second grade fluid in cylindrical tube. *Appl. Math. Mech.* **2013**, *34*, 1097–1106. https://doi.org/10.1007/s10483-013-1730-8.
32. Ilya, A.; Ashraf, M.; Ali, A.; Shah, Z.; Kumam, P.; Thounthong, P. Heat source and sink effects on periodic mixed convection flow along the electrically conducting cone inserted in porous medium. *PLoS ONE* **2021**, *16*, e0260845. https://doi.org/10.1371/journal.pone.0260845.
33. Abbasi, A.; Farooq, W.; Tag-ElDin, E.S.M.; Khan, S.U.; Khan, M.I.; Guedri, K.; Elattar, S.; Waqas, M.; Galal, A.M. Heat Transport Exploration for Hybrid Nanoparticle (Cu, Fe_3O_4)-Based Blood Flow via Tapered Complex Wavy Curved Channel with Slip Features. *Micromachines* **2022**, *13*, 1415.
34. Thejas, R.; Naveen, C.S.; Khan, M.I.; Prasanna, G.D.; Reddy, S.; Oreijah, M.; Guedri, K.; Bafakeeh, O.T.; Jameel, M. A review on electrical and gas-sensing properties of reduced graphene oxide-metal oxide nanocomposites. Biomass Conversion and Biorefinery **2022**, 1–11. https://doi.org/10.1007/s13399-022-03258-7.

ISSN: 0974-5823 Vol. 7 (Special Issue 5, April-May 2022)

International Journal of Mechanical Engineering

TESTING OF MULTIVARIATE NONLINEAR REGRESSION HYPOTHESIS USING NONLINEAR LEAST SQUARE (NLS) ESTIMATION

Dr. Kesavulu Poola[1], J. Anil Kumar[2], V. Pavankumari[3], Putta Hemalatha[4], Prof. M. Bhupathi Naidu[5].

[1]Associate professor, CMS - Jain University, Bengaluru.
[2]Assistant professor, S V College of Engineering, Tirupati.
[3]Assistant professor, Malla reddy Engineering College, Hyderabad.
[4]Assistant professor, Institute of Aeronautical Engineering, Hyderabad.
[5]Professor, Department of *Statistics*, S. V. University, Tirupati.

ABSTRACT

The present study paper confers the different models on testing the nonlinear regression hypothesis using nonlinear least squares (NLS) estimator through nonlinear studentized residuals and nonlinear predicted residual. Moreover this research paper mentioned internally nonlinear studentized residuals, externally nonlinear studentized residuals to test the hypothesis of multivariate nonlinear regression models. This research article proposes a new way of parameter estimation using nonlinear least squares method. According to Pesaran, M. Hashem, and Angus s. Deaton. (1978) uses nonlinear least squares asymptotic properties. The key principle of this article is to carter extremely pioneering model of testing nonlinear regression hypothesis using NLS estimator through nonlinear (internally and externally) studentized residuals and predicted NLS Methods.

KEY WORDS: *Nonlinear models, nonlinear least square estimation, Studentized and Predicted residuals*

1. INTRODUCTION

Least squares method and maximum likelihood methods are the quite popular in parameter estimation of linear models. In this approach, the method has to satisfy all pre assumption of normality with mean zero mean and unknown population variance. But in the case of nonlinear models building of construction of inferential facets together with Parameter estimation and hypothesis testing concerning the parameters of the nonlinear regression models are quite difficult. In recent era, researchers focused on the erection of well-organized parameter estimation of the nonlinear regression models. Since three decades these nonlinear models have been studied. The parameter estimation procedures and testing of hypothesis for nonlinear regression models and error assumptions are common analogous to those made for linear regression models. In the present research study some methods of testing multivariate nonlinear hypotheses using nonlinear least square estimation, studentized and predicted residuals for multivariate nonlinear models has been proposed.

2. LEAST SQUARE ESTIMATION OF MULTIVARIATE NONLINEAR REGRESSION MODEL

Suppose, standard multivariate nonlinear regression model.

$$Y_{it} = f_i(X_t, \theta) + e_{it} \qquad i = 1, 2, \ldots M, \qquad t = 1, 2, \ldots n$$

Where $\hat{e}_t = (\hat{e}_{1t}, \hat{e}_{2t}, \ldots \hat{e}_{Mt}) \qquad t = 1, 2, \ldots, n$

Then the multivariate least square estimator minimizes

$$S_n(\theta, \hat{\Sigma}_n) = \frac{1}{n}\sum_{t=1}^{n}\left[Y_t - f(X_t, \theta)\right]' \left(\hat{\Sigma}_n\right)^{-1}\left[Y_t - f(X_t, \theta)\right] \qquad \ldots(2.1)$$

Here we shall tax $\hat{\Sigma}_n$ be any random variable that converges almost surely to Σ and has $\sqrt{n}\left(\hat{\Sigma}_n - \Sigma\right)$ bounded in probability.

i.e., given S>0, there is bound 'b' and sample size N, such that

$$P\left(\sqrt{n}\left|\hat{\sigma}_{\alpha\beta n} - \sigma_{\alpha\beta}\right| < b\right) > 1 - S \qquad \forall n > N$$

Here $\sigma_{\alpha\beta}$ is the typical element Σ.

3. TESTING OF MULTIVARIATE NONLINEAR REGRESSION HYPOTHESIS TESTING USING NLLS ESTIMATOR

The , multivariate nonlinear regression model

$$Y_{it} = f_i\left(X_t, \theta^0\right) + e_{it} \qquad t = 1, 2.,,, n \qquad \text{…(3.1)}$$

Where $f_i\left(X_t, \theta^0\right)$ is a functional form and e_{it} is i.i.d with $N\left(o, \sigma_{In}\right)$

$\therefore$ Test procedure for multivariate nonlinear hypothesis is

$$H_0 : h\left(\theta^0\right) = 0 \;\; \text{.....} \;\; H_1 : h\left(\theta^0\right) \neq 0$$

Here $n\left(\theta^0\right)$ is continuously first-order differential function; Map's ¡ ^{p} and ¡ ^{q} with Jocobian.

$$\therefore H\left(\theta^0\right) = \frac{\partial}{\partial \theta'}\left[h\left(\theta^0\right)\right] \qquad \text{…(3.2)}$$

Here $H\left(\theta^0\right)$ is an order of $q \times p$

In order to estimate $H\left(\theta^0\right)$ at $\theta^0 = \hat{\theta}_n^0$, where $\hat{\theta}_n$ i.e. iterative multivariate NLLS estimator of θ.

Here are two commonly used estimators of Σ and that satisfy the condition under both null and alternative hypothesis.

$$S(\theta, \Sigma) = \sum_{t=1}^{n}\left[Y_t - f\left(X_t, \theta\right)\right]' \sum^{-1}\left[Y_t - f\left(X_t, \theta\right)\right] \qquad \text{…(3.3)}$$

be the sum of square residual, evaluated under the restricted nonlinear least square estimate.

According to the asymptotic F-test, for $H_0 : h(\theta) = 0$, the standard form is

$$F = \frac{\left[S\left(\tilde{\theta}, \hat{\Sigma}\right) - S\left(\hat{\theta}, \hat{\Sigma}\right)\right] / q}{S\left(\hat{\theta}, \hat{\Sigma}\right) / (nM - P)} \sim \chi_q^2 \qquad \text{…(3.4)}$$

Further $S^2 = \dfrac{S\left(\hat{\theta}, \hat{\Sigma}\right)}{nM - P}$ is independently distributed to $\hat{\theta}^0$ as the χ^2 distribution with $(n - p)$ degrees of freedom, Here S^2 is UBE of unknown variance σ^2.

$\therefore$ The nonlinear counterpart to the Wald Test staristic for testing $H_0 : h\left(\theta^0\right) = 0$ is given by

$$W = \frac{\hat{h}'\left(\hat{H}\hat{C}\hat{H}'\right)^{-1}\hat{h}}{qS^2} \sim \left(q, (n - p), \lambda\right) \qquad \text{…(3.5)}$$

Here $\hat{h} = h\left(\hat{\theta}\right)$ and $\hat{H} = H\left(\hat{\theta}\right)$

4. STUDENTIZED RESIDUALS FOR MULTIVARIATE NONLINEAR MODELS

Consider the general multivariate nonlinear regression model

$$Y_{\alpha t} = f_\alpha\left(X_t, \theta_\alpha^0\right) + E_{\alpha t} \qquad \text{…(4.1)}$$

Here θ_α^0 is p-dimensional vector matrix

Suppose $\hat{\theta}$ is the nonlinear least square estimator of θ for large sample, nonlinear least square residual vector.

$$e = \left(Y_i - \hat{Y}_t\right)$$

$$= \left(Y - f\left(\hat{\theta}\right)\right) \qquad \ldots(4.2)$$

Here $\hat{\theta} ;\ \theta + \left(F'F\right)^{-1} F'\varepsilon$ …(4.3)

And $F = F\left(\hat{\theta}\right) = \left[\frac{\partial}{\partial\theta_j} f\left(X_i, \theta\right)\right]_{n\times p}$ …(4.4)

Here $\frac{\partial}{\partial\theta_j} f\left(X_i, \theta\right)$ is the $(i, j)^{th}$ elements of $(n \times p)$ matrix $F(\theta)$ then general relationship between 'e' and 'ε' is

$e ;\ M\varepsilon$

Here $M = \left[I - F\left(F'F\right)^{-1} F'\right]$

or $e ;\ [I - H]\varepsilon$ where $M = \left(H_{ij}\right) = F\left(F'F\right)^{-1} F'$ is a symmetric idempotent matrix (or) HAT matrix

In scalar form

$$e_i ;\ \left[\varepsilon_i - \sum_{j=1}^{n} H_{ij}\varepsilon_j\right], \qquad j = 1, 2, \ldots, n \qquad \ldots(4.5)$$

Here H is HAT Matrix

Trace (H) = Rank (H) = P and $\sum_{i=j}^{n} H_{ij}^2 = H_{ij}$

Here ε follows $N_0\left(0, \sigma^2 I\right)$, so ε following normal distribution with zero mean and variance is $\sigma^2 I$. Here H controls the e.

As we know, variance of each e_i is a function of both σ^2 and $H_{ij}, i = 1, 2, \ldots n.$

The nonlinear least square residuals have a probability distribution that is scalar dependant. So, the nonlinear studentized residuals do not depend on either of these quantities and they have probability distribution and we have both internally nonlinear studentized residuals and externally nonlinear studentized residuals.

a) INTERNALLY NONLINEAR STUDENTIZED RESIDUALS

In nonlinear regression models, internally nonlinear studentized residuals are define by

$$e_i^* = \frac{\hat{e}_i}{\hat{\sigma}\sqrt{1 - h_{ij}}} \sim N(0,1) \qquad i = 1, 2, \ldots n \qquad \ldots(4.6)$$

Here $\hat{\sigma}^2 = \frac{e'e}{n - p}$

$$= \frac{\sum_{i=1}^{n} e_i^2}{n - p} \qquad \ldots(4.7)$$

Here $\left[\frac{e_i^{*^2}}{n - p}\right] \sim \beta$ - distribution with parameters $\frac{1}{2}$ and $(n - p - 1)/2$

It follows, $E\left(e_i^{*'}\right) = 0$ & $Var\left(e_i\right) = 1 \qquad \forall i = 1, 2, \ldots, n$

$$Cov\left(e_i^* e_j^*\right) = \frac{-h_{ij}}{\sqrt{\left(1-h_{ii}\right)\left(1-h_{jj}\right)}} \qquad \forall i \neq j = 1,2,...,n$$

Here h_{ij} add up to the trace of the hat matrix = P. Average 'h' is p/n which should be small, so usually $\sqrt{1-h_{ii}}$.

b) EXTERNALLY NONLINEAR STUDENTIZED RESIDUALS:

The externally nonlinear studentized residuals are define by

$$e_i^{**} = \frac{\hat{\varepsilon}_i / \left(1-h_{ij}\right)}{\sqrt{MSE_{(i)} / \left(1-h_{ij}\right)}} \qquad \text{...(4.8)}$$

$$= \frac{\hat{\varepsilon}_i}{\sqrt{MSE_{(i)}\left(1-h_{ij}\right)}} \qquad \text{...(4.9)}$$

Here $MSE_{(i)}$ is nestimate of σ^2 not baring data point 1.

i.e. $$e_i^{**} = \frac{\varepsilon_i}{\hat{\sigma}_{(i)}\sqrt{\left(1-h_{ij}\right)}} \qquad \forall i = 1,2,...,n \qquad \text{...(4.10)}$$

Based on the Normal distribution $\sigma_{(i)}^2$ and ε_i are

i.e., M.S.E (or) $\hat{\sigma}^2 = \dfrac{\left(n-p-1\right)\sigma_i^2 + \hat{\varepsilon}_i^2 / \left(1-h_{ii}\right)}{n-p}$

(or) $\sigma_{(i)}^2 = \hat{\sigma}^2\left[\dfrac{n-p-e_i^*}{n-p-1}\right]$

So, the relationship between internally and externally nonlinear studentized residuals is given by

$$e_i^{**} = e_i^*\left[\frac{n-p-1}{n-p-e_i^*}\right], \quad i = 1,2,...,n \qquad \text{...(4.11)}$$

5. PREDICTED RESIDUALS FOR MULTIVARIATE NONLINEAR MODELS

Predicted residual sum of squares (PRESS) is also called Leave-one-out (LOO) stochastic, is regularly used in nonlinear regression analysis for cross-validation. In general, In non linear least squares, and studentized residuals fittiing is dependents on all the variables in the data. But in predicted residuals for nonlinear model i.e. i^{th} nonlinear predicted residual is depends on the fit to the data, where i^{th} care is excluded.

Suppose $\hat{\theta}$ is the nonlinear least square estimate of θ based on the full data, and $\hat{\theta}_{(i)}$ be the respective estimate where the i^{th} case is excluded.

Now the i^{th} nonlinear predicted residuals i.e.,

$$e_{(i)} = \left[Y_i - f_i\left(\hat{\theta}_{(i)}\right)\right] \qquad i = 1,2,...,n \qquad \text{...(5.1)}$$

Here $e_{(i)}$ is the prediction error

$\therefore$ the nonlinear PRESS defined by

$$NLPRESS = \sum_{i=1}^{N} e_{(i)}^2 \qquad \text{...(5.2)}$$

So, finally, the relationship between nonlinear predicted residuals and nonlinear studentized residual are given by

(i) $e_i^* = \dfrac{e_{(i)}}{\hat{\sigma}/\sqrt{(1-h_{ij})}}$ …(5.3)

(ii) $e_i^{**} = \dfrac{e_{(i)}}{\hat{\sigma}_{(i)}\sqrt{(1-h_{ij})}}$ … (5.4)

and $e_{(i)} = \dfrac{e_i}{(1-h_{ij})} \quad \forall i = 1, 2, ..., n$ …(5.5)

6. CONCLUSIONS

In the present research study, some inferential methods pertaining to testing of multivariate nonlinear regression models using NLLS estimator, studentized and predicted residuals for multivariate nonlinear models are proposed.

7. REFERENCES

8. Anselin, L., 1984a, Specification tests and model selection for aggregate spatial interaction: An empirical comparison, Journal of Regional Science 24, l-15..
9. Bai, J., A.J. Jakeman, and M. McAleer, 1992, Estimation and discrimination of alternative air pollution models, Ecological Modelling 64, 89-124.
10. Battese, G.E. and B.P. Bonyhady, 1981, Estimation of household expenditure functions: An application of a class of heteroscedastic regression models, Economic Record 57, 80-85.
11. Bera, A. and M. McAleer, 1989, Nested and non-nested procedures for testing linear and log-linear regression models, Sankhya B 51, 212-224.
12. Chai, T. and Draxler, R.R. (2014). Root mean square error (RMSE) or mean absolute error (MAE)? - Arguments against avoiding RMSE in the literature, Geoscientific Model Development, 7, 1247–1250.
13. CoxD R1961 Proceedings of the Fourth Berkeley Symposium on Mathematical Statistics and Probability1 Berkeley University of California Press
14. David Pollard and Peter Radchenko 2006 Journal of Multivariate Analysis 97 548-562
15. Dorugade, A.V., 2014. New ridge parameters for ridge regression. Journal of the Association of Arab Universities for Basic and Applied Sciences, 15, pp.94-99.
16. Dr. Kesavulu Poola , Prof. M. Bhupathi Naidu(2008) . Importance of studentized and press residuals for nonlinear multivariate regression models. Journal of Emerging Technologies and Innovative Research, Volume 5, Issue 7, 353-356
17. Dr. Kesavulu Poola, P Hema Sekhar, and Dr. M Bhupathi Naidu (2020), Combined multiple forecasting model using regression, International Journal of Statistics and Applied Mathematics 2020; 5(6): 147-150
18. Edmond Malinvaud A tribute to his contributions in Econometrics Peter C B PhilipsYale University Frank Nielson 2013 Camel University
19. Engle and Robert F 1983Wald likelihood ratio and Lagrange multipliers tests in Econometrics
20. Jain, S., Chourse, S., Dubey, S., Jain, S., Kamakoty, J., and Jain, D (2016). Regression Analysis – Its Formulation and Execution in Dentistry. Journal of Applied Dental and Medical Science. Vol. 2, No. 1, pp. 199-208.
21. Kesavulu Poola, Vasu K, M Bhupathi Naidu, R Abbaiah and P Balasiddamuni (2016). The effect of multicollinearity in nonlinear regression models in International Journal of Applied Research., 2(12): 506-509.
22. Kloppers, P.H., Kikawa, C.R., and Shatalov, M.Y., (2012). A new method for least squares identification of parameters of the transcendental equations, International Journal of the Physical Sciences, 7, 5218–5223.
23. Kuchibhotla, A.K. and Patra, R.K., 2022. On least squares estimation under heteroscedastic and heavy-tailed errors. The Annals of Statistics, 50(1), pp.277-302.
24. Mahaboob B etal2016 Indian Streams Research Journal 6(4)
25. Mu B, Bai E W, Zheng W X and Zhu Q 2017 Automatic a 77322-335
26. Nagaraj, D., Wu, X., Bresler, G., Jain, P. and Netrapalli, P., 2020. Least Squares Regression with Markovian Data: Fundamental Limits and Algorithms. Advances in Neural Information Processing Systems, 33, pp.16666-16676.
27. Permai, S. D. and Tanty, H. (2018). Linear Regression Model using Bayesian Approach for Energy Performance of Residential Building. Procedia Computer Science. Vol. 135, pp 671-677.
28. Pesaran, M. Hashem, and Angus S. Deaton. "Testing non-nested nonlinear regression models." Econometrica: Journal of the Econometric Society (1978): 677-694.
29. Prabitha, J. and Archana, S. (2015). Application of Regression Analysis in Numeroustimes. International Journal of Science, Enginering and Technology Research. Vol. 4, Issue 4, pp. 1002-1005.
30. Singh, A. S. and Masuku, M. B. (2013). Application of Modeling and Statistical Regression Techniques in Research. Research Journal of Mathematical and Statistical Sciences. Vol. 1, No. 16, pp. 14-20
31. Vuong, Q.H., 1989, Likelihood ratio tests for model selection and non-nested hypotheses, Econometrica 57, 307-333.

32. Wang, S., Qian, L. and Carroll, R.J., 2010. Generalized empirical likelihood methods for analyzing longitudinal data. Biometrika, 97(1), pp.79-93.
33. White, H., 1982, Regularity conditions for Cox's test of non-nested hypotheses, Journal of Econometrics 19, 301-318.
34. Yang, G., Zhang, B. and Zhang, M., 2021. Estimation of Knots in Linear Spline Models. Journal of the American Statistical Association, pp.1-12.
35. Zhang, T., 2009. Some sharp performance bounds for least square regression with l1 regularization. The Annals of Statistics, 37(5A), pp.2109-2144.
36. Zheng, B. and Agresti, A. (2000). Summarizing the predictive power of a generalized linear model, Statist. Med., 19, 1771–1781

Journal of Applied and Natural Science
14(3), 805 - 814 (2022)
ISSN : 0974-9411 (Print), 2231-5209 (Online)
journals.ansfoundation.org

Research Article

Groundwater quality assessment by Water quality index (WQI) and Multivariate statistical analysis (MSA) for coastal zones of Srikakulam district, Andhra Pradesh

A. Ganapathi Rao
Department of Basic Sciences and Humanities (Mathematics), GMRIT, Rajam, Vizianagaram, India
V. Pavan Kumari
Department of Mathematics, Malla Reddy Engineering College, Hyderabad, India
Manoj Kumar Karnena*
Department of Environmental Science, School of Science, GITAM (Deemed to be) University, Visakhapatnam, India

*Corresponding author: Email: manojkumarenviron@gmail.com

Article Info
https://doi.org/10.31018/jans.v14i3.3615
Received: June 12, 2022
Revised: August 2, 2022
Accepted: August 6, 2022

How to Cite
Rao, A. G. *et al.* (2022). Groundwater quality assessment by Water quality index (WQI) and Multivariate statistical analysis (MSA) for coastal zones of Srikakulam district, Andhra Pradesh. *Journal of Applied and Natural Science*, 14(3), 805 - 814. https://doi.org/10.31018/jans.v14i3.3615

Abstract
Groundwater is a vital resource for the drinking water supply to the people in the areas residing in the coastal zones. Rapid industrialization increased the human population, and anthropogenic activities led to groundwater pollution. The water quality should be continuously monitored to analyse the suitability of the water, and it is only possible by the water quality index. In the current study, we attempted to determine the groundwater quality of the Mandal headquarters of the coastal zones of the Srikakulam district, Andhra Pradesh, by using the water quality index (WQi) considering the parameters pH, Electrical conductivity, Total Dissolved Solids, Total Hardness, calcium and magnesium, potassium, and sodium, human health assessment tool, and multivariate statistical analysis. The results found that the WQi of the coastal zones ranged from 49.6 to 361.7, and in the post-monsoon season, the Etcherla Mandal station water was not advisable for drinking. Human health risk assessment showed that children in these sampling stations are more prone to the non-carcinogenic health risks associated with nitrate pollution. Proper reduction measures in the sampling areas must be taken to depreciate nitrate and seepage into the groundwater. Piper plots and correlation matrices showed the anion-cation interaction, and the principal component analyzed and showed the pollution sources. The current study concluded that anthropogenic activities continuously deteriorate groundwater quality, indirect saltwater intrusion was identified, and groundwater treatment is necessary before consumption.

Keywords: Groundwater, Human health, Index, Risk, Water quality

INTRODUCTION

The rapid increase in population and urbanization amplified the demand for groundwater (GW). According to the literature available, it was estimated that 1.5 billion people worldwide rely on groundwater for drinking (Karnena *et al.,* 2022; Li *et al.,* 2021). A developing country like India has a greater need for groundwater as they act as a significant source for drinking. The quality and quantity of the GW are affected at a high rate owing to man-made activities. The GW was affected majorly due to the three main activities. Firstly, due to the overutilization of recalcitrant inorganic fertilizers in the agroindustry. Secondly, they dumped the industrial wastewater directly into the environment and nearest body streams and improper pumping and management of the aquifers (Karnena and Saritha, 2019). In addition, solid waste disposal and single-use product disposal (Vara *et al.,* 2019) in unengineered land is also considered a factor for groundwater contamination as the contaminates or leachate seeps from the soil to the groundwater aquifers (Girija *et al.,* 2007). According to the WHO, 2004 nearly eighty per cent of the diseases caused by the water-born are due to the contamination of the water, which are considered waterborne diseases. Restoration of the groundwater aquifers contaminated with the contaminants is complicated; thus, preventive measures must be followed to prevent pollution. Therefore, there is a need to monitor the groundwater aquifers to avoid contamination regularly. The groundwater quality is deciphered by the physicochemical analysis of the water (Panneerselvam *et al.,* 2020), and it also helps in measuring the health hygiene of the water used for consumption.

The reason for selecting the Mandal headquarters of the district is that these are densely populated, and more people reside near these areas. The collected samples were analyzed according to the Bureau of Indian standards and the Water Quality Index (WQi) performed. The WQi are the arithmetic mean calculation used to determine the water quality in the sampling areas. Horton (1965) was the scientist who invented the analysis, and many researchers (Karnena *et al.,* 2022; Adimalla *et al.,* 2022) adopted and performed these calculations to identify the groundwater quality. Later Karnena and Vara (2019) developed various models for the WQi based on the rating and weightage of the water quality physicochemical parameters obtained by the arithmetical mean. The WQi are dimensionless, and values range from 0 to 200. These have unique digital ratings to help express the water's quality, viz. excellent to unfit for drinking. The WQi is a critical tool for comparing the groundwater quality with the management and helps to select appropriate treatment. This method used the assessment parameters like pH, EC, TDS, TH, calcium and magnesium hardness, potassium, and sodium. The study aimed to calculate the WQi of groundwater of 11 Mandal headquarters of Srikakulam coastal zones of India and evaluate the human health risk assessment (HHR). Even though we have analyzed the nitrates, it was considered for assessing only HHR and comparing the results with statistical analysis.

MATERIALS AND METHODS

Sample collection

A total of eleven samples from coastal zones of Srikakulam district Mandal headquarters were collected

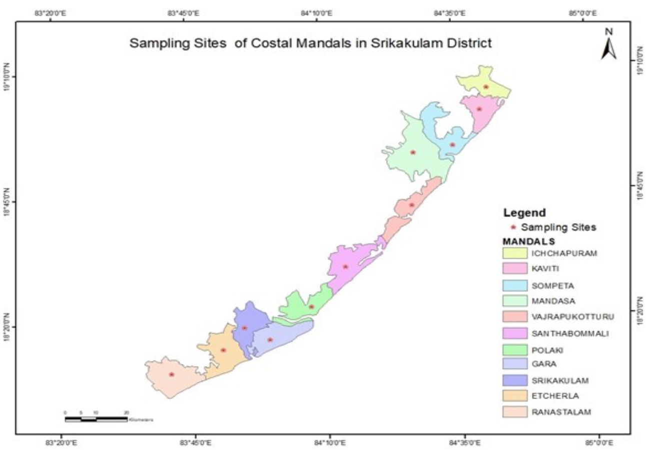

Fig. 1. *Location map of the study area of the Srikakulam district, Andhra Pradesh*

from the bores of varying depths up to 100 m and analyzed the physicochemical parameters for the sample using standard APHA methods in the pre-and post-monsoon of the year 2021 (Fig. 1). All the samples were analyzed at the water and wastewater treatment laboratory of the GITAM (Deemed to be) University.

Physicochemical parameters

The parameters selected for the potable studies were pH, conductivity, total dissolved solids, calcium hardness, magnesium hardness, sulphates, sodium and potassium. The samples were compared with the Bureau of Indian standards to obtain the relationship between parameters.

Water quality index (WQi)

The WQi gives an idea on a scale rating from 0 to 300. In the present study, the WQi is evaluated by the following steps. A weight (w_i) is assigned for each chemical variable conferring to the relative weights obtained from Karnena and Vara, 2019. Further, the relative weight (W_i) was calculated from the following equations (Karnena *et al.,* 2022), and here n represents several samples (*Eq 1 to 4*).

$$W_I = \frac{w_i}{\sum_{i=1}^{n} w_i} \qquad \text{(Eq 1)}$$

The parameters' quality rating (Q_i) is obtained by dividing the concentrations by the relative standards of BIS and multiplying with 100. Cei is the parameter concentration here, and S_i is the potable water standard.

$$Q_i = \frac{Ce_i \times 100}{S_i} \qquad \text{(Eq 2)}$$

The subsequent calculation obtains the Si water standard.

$$SI_i = W_i \times Q_i \qquad \text{(Eq 3)}$$

$$WQI \sum_{i=1}^{n} SI_i \qquad \text{(Eq 4)}$$

The calculated WQi is categorized into excellent (<50), good (50 to 100), poor (100 to 200), very poor (200 to 300) and unfit (>300).

Human health risk assessment (HHR)

HHR helps determine the groundwater quality; further, this method will evaluate the harmful impacts of contamination on newborns, kids, and adults (Adimalla *et al.,* 2019; Chen *et al.,* 2017). The primary sources of adsorption of the contaminants by human bodies are drinking and bathing in groundwater. The current study adopted the HHR assessment by considering drinking pathways as they are significant sources of groundwater entry in the study area. The contamination of nitrate exposure to humans was assumed to be ingested by taking groundwater drinking. The equation below (*Eq 6* and *Eq 7*) was obtained from the USEPA (USEPA, 2004) for analyzing the exposure of dose (Ed) via pathways and for the identification of the non-carcinogenic risk factors (hazardous Quotient) associated with the paths in the particular sampling area (Hq). Adults are represented as A_d, Children described as C_d, and Infants represented as I_f.

$$Di = \frac{\mathrm{Cng} \times \mathrm{Ir} \times \mathrm{De} \times \mathrm{Fe}}{\mathrm{Abw} \times \mathrm{Aet}} \qquad \text{(Eq 5)}$$

$$Hq = \frac{Di}{\mathrm{Fst}} \qquad \text{(Eq 6)}$$

Di- Daily intake, Cng- Concentration of nitrate in groundwater, Ir- Ingestion rate (A_d- 2.5; C_d- 0.3; I_f – 0.78), De- Duration of Exposure (A_d-64; C_d- 12, I_f-<1), Fe- Frequency of Exposure (1 year), Abw- Average body weight (A_d- 57.5; C_d- 18.7; I_f -6.9), Aet- Average time (A_d- 23360; C_d- 4380; I_f -365), Hq- Non-carcinogenic factor quotient, and Fst- Floride standard reference (1.6). All the units are considered as mg/kg/day.

Statistical methods

The piper plots, correlation coefficient matrix, and principal component analysis were analyzed using the Origin software (9.2) to show and distribute the ions in the sampling sites. The piper plots plot the percentage of cations and anions in milliequivalents in the base triangles and help compare the ion accumulations in the sampling sites. This method allows for providing the water quality and origin. Correlation coefficient values of the samples determine the relation matrix and help identify the interrelated parameter analyzed. The principal component analysis evaluates the water quality in the sampling site and further identifies the source of water pollution.

RESULTS AND DISCUSSION

All the Sampling areas analyzed with the physicochemical parameters using the WHO and BIS standards methods are shown in Tables 1 and 2.

pH

pH is the value explicit the groundwater concentrations for determining whether the sampling site's water is alkaline or acidic. The water pH ranges from 7.2 to 8.9 (Fig. 2) in both pre-monsoon and post-monsoon, indicating that the groundwater is slightly alkaline. The limits of the pH given by the BIS range from 6.5 to 8.5; the sampling sites in the pre-monsoon Polaki and Vajrapukothuru and the post-monsoon Etcherla and Gara exceeded the standard limits. In general, the pH alone doesn't directly affect the health of living beings (WHO, 2004).

Electrical conductivity (EC)

The EC of the water is essential for determining the water quality as the increase in these concentrations might lead to the rise in the saltiness and solids in the groundwater. The EC ranges from 520 to 4100 µS/cm (Fig. 3). EC does not have any particular standards for reference; Higher variation of the EC in the sampling areas might be attributed to agricultural and other anthropogenic activities (Subba Rao *et al.,* 2017).

Total dissolved solids (TDs)

TDs mainly consist of inorganic salts, which exist in dissolved forms in groundwater (Edition, 2011). The TDs ranged from 384 to 2624 mg/L in both seasons (Fig. 4). According to the WHO (2004) and BIS (2012), the permissible limit for the TDs is 600 mg/L. The TDs greater than 10^3 mg/L are unacceptable for drinking purposes and require treatment before consumption (Karnena *et al.,* 2022). The sampling sites in the post-monsoon, i.e., Etcherla (710 mg/L), Gara (1400 mg/L) and Polaki (1950 mg/L), exceeded the limit, and Polaki (1770 mg/L) and Kaviti (350 mg/L) exceeded the permissible limits in the pre-monsoon. This might be due to the dissolution of the natural resources during the seasons and anthropogenic agricultural activities (Karnena *et al.,* 2022; Edition, 2011) in the study area.

Total hardness (TH)

The hardness of the water is caused by the dissolution of the polyvalent metal ions, calcium and magnesium ions. TH concentration ranges from 100 to 1200 mg/L (Fig. 5). The prescribed limit for the TH is 300 mg/L suggested by WHO. The sampling areas in the post-monsoon exceeded the limits except for Polaki (410 mg/L), Sompeta (265 mg/L) and Ichchapuram (260 mg/L). In the pre-monsoon, the Gara (500 mg/L) and Polaki (300 mg/L) slightly exceeded the standard limits. Exceeding the permissible might cause the water very hard and unfit for drinking. The areas reported in this section need proper softening treatment before consumption. The hardness of the water might be due to the geographical locations or dissolution of the minerals in pre-monsoon seasons due to perceptions (Adimalla and Qian, 2019).

Cations

Sodium

Sodium is the most reactive metal and is freely available in nature. The excess sodium than the prescribed level by WHO and BIS, i.e., 200 mg/L in the groundwater, might increase the blood pressure, and further tox-

Table 1. Pre-monsoon physicochemical analysis data

Sampling Sites	p H	EC	TDS	Cl	NO_3	SO_4	Na	K	Ca	Mg	TH
Etcherla	8.03	710	454.4	120	3.28	74	60.86	1.52	56	29.17	260
Gara	8.2	1400	896	240	0.65	57	162.49	3.2	84	34	350
Ichchapuram	8.58	1340	857.6	250	25.24	84	228.2	17.5	48	34.03	260
Kaviti	8.19	2600	1664	574.4	2.04	138.7	334	219	72	30.4	304.5
Mandasa	8.5	600	384	81.55	10.21	13.44	67.9	0.78	44	9.73	150
Polaki	8.62	1950	1248	340	6.87	121	257.8	5.2	91	46	410
Ranastalam	8.33	630	403.2	90	12.91	31	116.96	1.36	40	100	100
Santhabommali	7.83	770	492.8	50	2.71	126	93.02	1.12	40	24.31	200
Sompeta	8.52	1000	640	148.93	1.27	39.98	101	8.21	64	25.5	265
Srikakulam	7.2	1320	844.8	230	2	98	220.9	17	48	29.17	240
Vajrapukothuru	8.67	1290	825.6	237.5	7.07	34.99	162	10.5	82	19.5	285

Table 2. Post-monsoon physicochemical analysis data

Sampling Sites	p H	EC	TDS	Cl	NO_3	SO_4	Na	K	Ca	Mg	TH
Etcherla	8.6	4100	2624	939.97	14.71	64	580.46	157	40	121.6	1200
Gara	8.7	2120	1356.8	419.98	5.12	69	328.16	82.16	20	48.64	500
Ichchapuram	7.4	520	332.8	110	43.6	14	56.14	18.03	32	7.29	220
Kaviti	7.7	350	224	60	12.3	12	22.16	2.3	36	7.29	360
Mandasa	7.9	1040	665.6	250	13.35	7	102.36	3.61	40	48.64	600
Polaki	8.34	1770	1132.8	159.99	2.15	44	290.38	56.8	20	24.32	300
Ranastalam	8.1	970	620.8	140	12.91	28	88.44	24.04	48	34.04	560
Santhabommali	7.9	660	422.4	110	47.24	21	54.26	8.42	40	19.45	520
Sompeta	7.8	810	518.4	190	21.47	15	54.24	51.18	52	24.32	300
Srikakulam	7.4	1140	729.6	199.99	7.79	33	74.16	20.17	56	58.36	760
Vajrapukothuru	7.8	600	384	90	19.56	11	49.19	17.47	36	19.45	340

aemia can be observed in women with pregnancy. The sodium concentrations in the pre-monsoon seasons in Ichchapuram, Kaviti (334 mg/L), Polaki (257.8 mg/L) and Srikakulam (220.9 mg/L) crossed WHO's standards; the post-monsoon season in Etcherla (580.6 mg/L), Gara (328.16 mg/L), and Polaki (290.38 mg/L) showed high concentrations of sodium. The attention of sodium in the water range from 22.16 to 580.46 mg/L (Fig. 6) and excess concentration might be attributed to saltwater intrusions as these are nearer to the sea (Basack *et al.,* 2022).

Potassium

Even though the potassium ions are vital for human health, excess concentrations in the groundwater might harm human health, resulting in hyperkalemia, kidney disease, and dietary problems (Karnena and Vara, 2019). The potassium in the sampling sites ranged from 0.78-157 mg/L (Fig. 6). The allowable limit of this cation is ten mg/L. The potassium concentration in the post-monsoon of Kaviti (2.3 mg/L), Mandasa (3.61 mg/L), and Santhabommali (8.42 mg/L) is within the standard limit and other mandals crossed the permissible limits. In contrast, Ichchapuram (17.5 mg/L), Kaviti (219 mg/L), and Vajrapukothuru (10.5 mg/L) crossed the allowable limits in the pre-monsoon. The increase in potassium concentrations is due to the seepage of the agricultural runoff consisting of potassium fertilizers (Pericherla *et al.,* 2020).

Anions

Chlorides

The excess chloride concentration in the groundwater has laxative effects and a salty taste. Thus, chloride is considered an essential parameter for measuring water pollution. Further, the excess chloride in the groundwater is due to the dumping of domestic waste and other anthropogenic activities (Subba Rao *et al.,* 2017). The chloride ranged from 50 to 939.7 mg/L in the sampling sites (Fig. 7). The permissible limit for the chlorides in the groundwater ranged from 200-to 600 mg/L. The excess concentrations of chlorides in the ground might be attributed to the saltwater intrusion in Etcherla, Polaki and Kaviti areas (Basack *et al.,* 2022).

Sulphate

The oxygenated water generally consists of sulphates as they consist of sulfur. Higher levels of sulfur in the water might affect the taste of the water and cause dehydration. The allowable limit of this ion is 400 mg/L, and significant sources of sulphate in the groundwater are due to agricultural runoff (Pericherla *et al.,* 2020). The sulphate concentrations in the water ranged from 7 to 138 mg/L, and all the samples were within the limit (Fig. 7).

Nitrates

Nitrates are considered one of the significant pollutants for water aquifers in and around the agri-land (Zhang *et al.,* 2018). The availability of nitrogenous substances in the geological system is less. These substances in the aquifers are due to the anthropogenic agricultural fertilizers, seepage of the septic tank and runoff. Nitrates in the water of sampling sites ranged from 0.65 to 47.24 mg/L (Fig. 7). The permissible limit in the drinking water suggested by the WHO and BIS is 50 mg/L. Further from the study, all the water samples were within the standards.

Water quality index (WQi)

This index helps evaluate the groundwater quality to identify whether it is suitable for drinking. The quality of the water was classified into excellent (50 and less), good (50-100), poor (100-200), very poor (200-300) and unfit (>300). The current study results ranged: In the post-monsoon season, the Etcherla mandal station (361.7) water form revealed that the water is not advisable for drinking (Fig. 8). In contrast, in the pre-monsoon season, the kaviti mandal station (282.98) water showed poor drinking quality (Tables 3 and 4). The change in the quality of the water standards is attributed to the anthropogenic agricultural and manmade activities in particular areas (Karnena *et al.,* 2022)

Human health risk assessment (HHR)

The HHR was conducted to identify the non-carcinogenic factor in this location; this parameter might vary from seasonal, geographical, and anthropogenic activities. The HHR in the sampling areas ranged from 0.01 to 4.4. As previously stated in the methodology, the Hazardous Quotient (Hq) should not exceed one. The HHR was conducted and adopted using the methods given by the USEPA. Tables 3 and 4 show the quotients and risks associated with nitrates. The values of Hq in infants, children and adults in post-monsoon ranged from 0.03 to 0.6, 0.2 to 4.3, and 0.09 to 1.3;

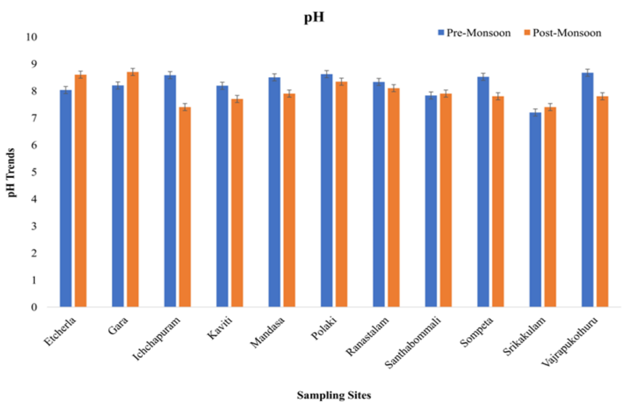

Fig. 2. *Trends of pH in the sampling sites of the district.*

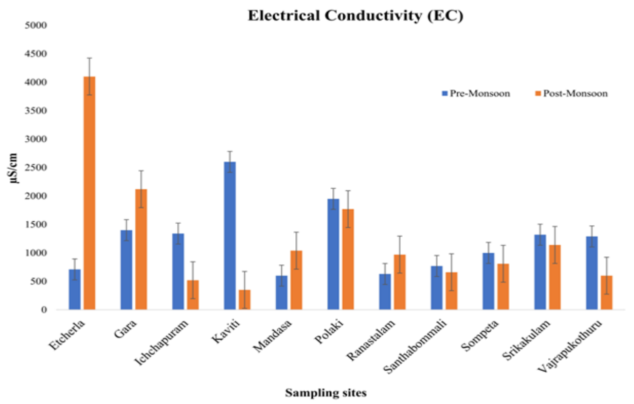

Fig. 3. *Electrical conductivity of the sampling sites of the district.*

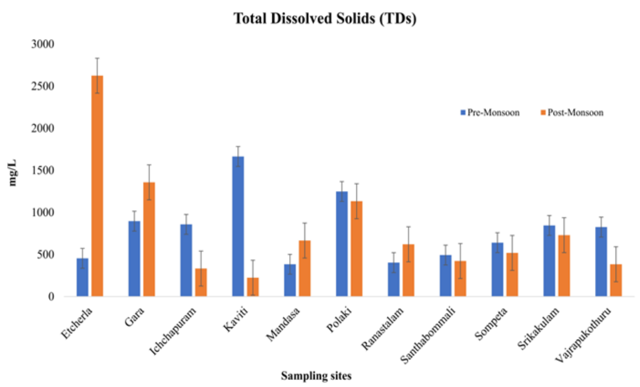

Fig. 4. *TDs in the sampling sites of the district*

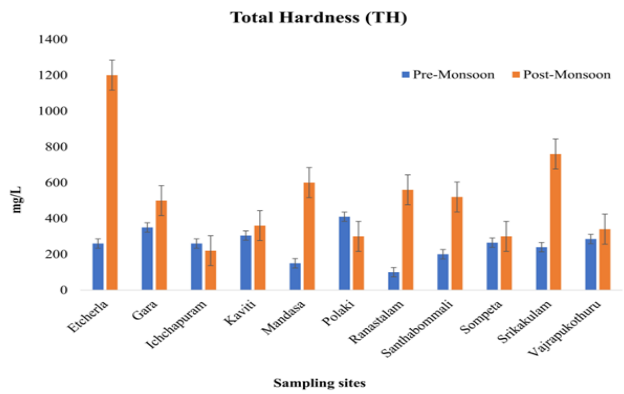

Fig. 5. *TH of the Sampling sites of the district*

whereas in pre-monsoon is 0.01 to 0.4, 0.06 to 1.3, and 0.02 to 1. In the pre-monsoon, adults in Ichchapuram and children in Ichchapuram and Ranastalam are highly prone to the risk of nitrate pollution.

In contrast, in the post-monsoon, the adults in Santhabommali and Ichchapuram, except children in Gara, Polaki, and Srikakulam and infants in all the stations, are prone to the risk of nitrate pollution. Nitrates are considered one of the most contamination sources for drinking water worldwide. The nitrate leaching into the groundwater is due to the agricultural soils (Jalali, 2011; Bawoke and Anteneh, 2020). In their studies, Chen et al. (2016) stated that the higher availability of nitrates in the water is due to the extensive use of fertilizers and irrigation. Elevated concentrations are harmful to the health of living beings. Continuous ingestion and accumulation of the nitrates might cause potential harm to humans by causing methemoglobinemia, thyroids and cancers. The current study revealed that children are more prone to this pollution than adults, and minimizing steps for preventing groundwater contamination have to be adopted in the recent sampling.

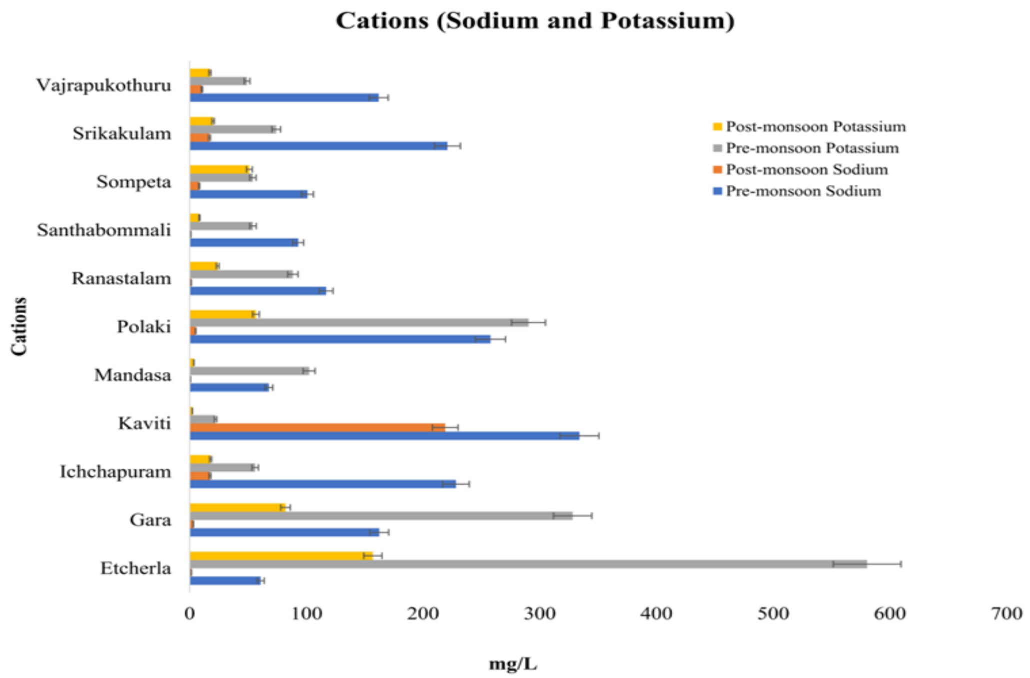

Fig. 6. *Cations in the sampling sites of the district*

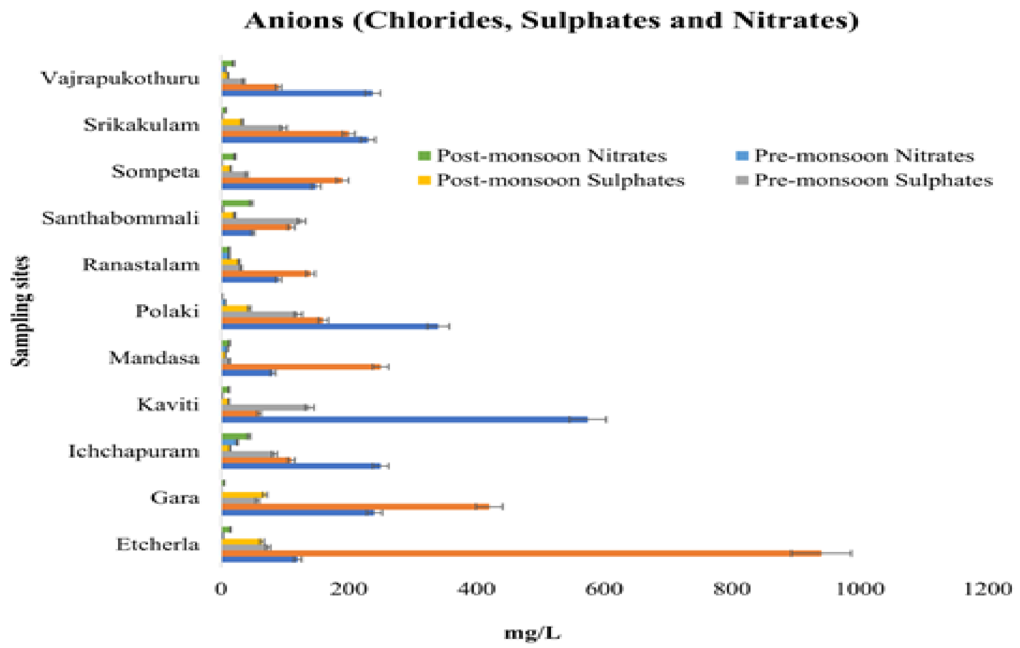

Fig. 7. *Anions in the sampling sites of the district*

Table 3. HHR and WQI of Sampling areas in pre-monsoon

Sampling Sites	HHR (Adult)	HHR (Children)	HHR (Infant)	WQI	Water Quality
Etcherla	0.14261	0.333704	0.05262	64.43	Good
Gara	0.02826	0.06613	0.01043	100.42	Good
Ichchapuram	1.09739	2.567896	0.40492	110.74	Poor
Kaviti	0.0887	0.207548	0.03273	282.98	Poor
Mandasa	0.44391	1.038757	0.1638	49.66	Excellent
Polaki	0.2987	0.698948	0.11021	139.26	Poor
Ranastalam	0.5613	1.313452	0.20711	78.02	Good
Santhabommali	0.11783	0.275713	0.04348	59.99	Good
Sompeta	0.05522	0.129209	0.02037	80.67	Good
Srikakulam	0.08696	0.203478	0.03209	94	Good
Vajrapukothuru	0.30739	0.719296	0.11342	98.79	Good

Table 4. HHR and WQI of Sampling areas in post-monsoon

Sampling Sites	HHR (Adult)	HHR (Children)	HHR (Infant)	WQI	Water Quality
Etcherla	0.63957	1.496583	0.2359893	361.7	Unfit
Gara	0.22261	0.520904	0.082139	188.69	Poor
Ichchapuram	1.89565	4.435826	0.6994652	48.37	Excellent
Kaviti	0.53478	1.251391	0.1973262	38.19	Excellent
Mandasa	0.58043	1.358217	0.2141711	90.33	Good
Polaki	0.09348	0.218739	0.034492	130.8	Poor
Ranastalam	0.5613	1.313452	0.2071123	92.54	Good
Santhabommali	2.05391	4.806157	0.757861	64.4	Good
Sompeta	0.93348	2.184339	0.3444385	91.99	Good
Srikakulam	0.3387	0.792548	0.1249733	104.04	Poor
Vajrapukothuru	0.85043	1.990017	0.3137968	59.42	Good

Statistical analysis

Piper plots

These plots helped to identify water composition and the type of water in the sampling areas. The cations/anions and mixed concentrations can be determined in the water, depending on the geographical locations. More than 70 per cent of the samples in the sampling areas reported diverse concentrations of the ions observed in the piper triangles (Fig. 9). The pre-monsoon mixed composition is found that Ca-Mg-CO_3-HCO_3, SO_4-Cl, and Na-K-Ca. In contrast, in post-monsoon, the compositions are Cl- CO_3-HCO_3, Na-K- CO_3-HCO_3, and Na-K-Mg. The concentrations of the alkali metals are found to be within limits compared to the alkaline earth metals, which results in temporary hardness.

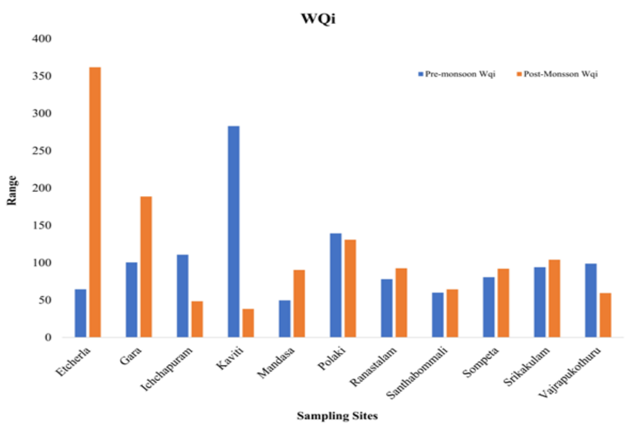

Fig. 8. *WQi of the sampling sites of the district*

Principal component analysis (PCA)

The PCA of the cations and anions of the groundwater is used to determine the relationships and identify how these ions control the overall quality of the groundwater. This analysis separates the chemical variable quantities into clusters. The PCA I is dominated by all the chemical variables in the pre-monsoon, which is observed in Fig. 10. Further from the Fig., salinity and alkalinity are the controlled factors. In contrast, the post -monsoon PCA I was influenced by Mg, sodium and potassium influenced PCA II, and Chlorides and Calcium influenced PCA III. This influence is considered a lithological or non-lithological factor of the pollution in the sampling areas.

Correlation coefficient (CC)

The CC values range from -1 to +1; zero indicates no relationship between the parameters. A strong correlation can be obtained by the positive (r) values and vice versa. The Table 5 and 6 show the importance of the

Table 5. CC of the Sampling sites in the pre-monsoon

	p H	Conductivity	TDS	Chlorides	Nitrates	Sulphates	Sodium	Potassium	Calcium	Magnesium	Total hardness
p H	1										
Conductivity	0.068820231	1									
TDS	0.068820231	1	1								
Chlorides	0.088979929	0.9811515	0.981151	1							
Nitrates	0.446712973	-0.150862	-0.15086	-0.10322	1						
Sulphates	-0.394962174	0.6442542	0.644254	0.560856	-0.20371	1					
Sodium	-0.018693979	**0.9402944**	**0.940294**	**0.925771**	0.079088	0.638611	1				
Potassium	-0.054436668	**0.7673765**	**0.767377**	**0.830241**	-0.18069	0.512991	0.692311	1			
Calcium	0.393984727	0.64494	0.64494	0.598309	-0.33749	0.15048	0.455482	0.199664	1		
Magnesium	0.056236021	-0.090742	-0.09074	-0.07384	0.269734	-0.08016	0.059411	-0.07806	-0.15659	1	
Total hardness	0.174727275	0.7108372	0.710837	0.633186	-0.28347	0.465609	0.56113	0.203601	**0.882133**	-0.29291	1

Table 6. CC of the sampling sites in the post-monsoon

	p H	Conductivity	TDS	Chlorides	Nitrates	Sulphates	Sodium	Potassium	Calcium	Magnesium	Total hardness
p H	1										
Conductivity	0.7621733	1									
TDS	0.7621733	1	1								
Chlorides	0.6597786	0.95852967	0.95853	1							
Nitrates	-0.4394402	-0.3732593	-0.37326	-0.24496	1						
Sulphates	**0.8042876**	0.8432657	0.843266	0.732121	-0.44391	1					
Sodium	**0.8242398**	**0.98207646**	**0.982076**	**0.912009**	-0.37793	0.870372	1				
Potassium	0.7482351	0.95021585	0.950216	0.921193	-0.2981	0.829229	0.943065	1			
Calcium	-0.5191452	-0.1973934	-0.19739	-0.05621	0.135531	-0.38451	-0.37361	-0.20195	1		
Magnesium	0.5328533	**0.90293392**	**0.902934**	0.936839	-0.34925	0.663193	0.812277	0.796824	0.16693687	1	
Total hardness	0.3965663	0.77891882	0.778919	0.83466	-0.22932	0.540434	0.66629	0.631492	0.31174279	0.946889154	1

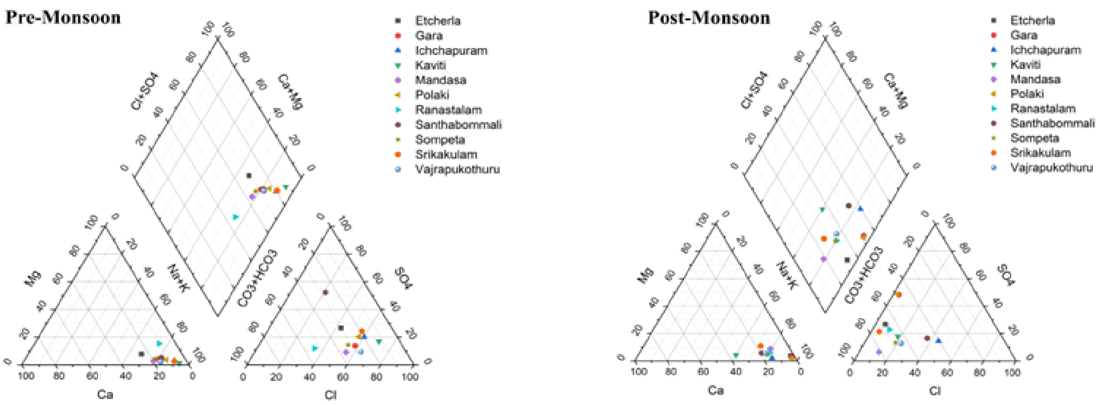

Fig. 9. *Piper plots of the sampling sites of the district.*

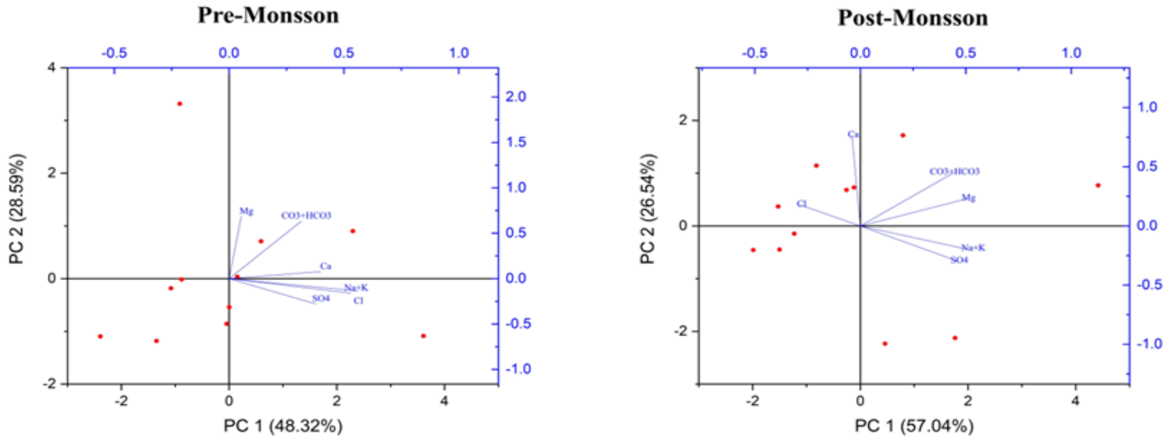

Fig. 10. *PCA of the sampling areas of the district*

CC. In the pre-monsoon, strong CC was observed with Na to Conductivity (0.94), TDS to Na (0.94), Cl to Na (0.92) and Ca to Hardness (0.83). In contrast, in post-monsoon, pH to Na and Sulphates (0.8), Sodium to Conductivity (0.98), TDS and Chlorides (0.98) showed a strong correlation and indicated that chemical parameters are interrelated.

Conclusion

The current article evaluated and highlighted the quality of the drinking water by WQi and further identified the non-carcinogenic risk factor associated with nitrate pollution using the Human Health Assessment (HHA) tool developed by the USEPA. In addition, the overall sampling station quality of the water ranged from slightly alkaline and less complicated water. The WQi of the sampling stations ranges from 49.6 to 361.7, indicating poor water quality in sampling sites Etecherla and Kaviti; According to the HHA, the children residing in these areas are more prone to nitrate pollution, which might be attributed to the excessive use of nitrate fertilizers for agriculture. The statistical data showed that the significant chemical variables identified the essential ions and their interactions responsible for the pollution. Further treatment is necessary to consume this groundwater in a few sampling areas to avoid health-related issues. Continuous evaluation of the groundwater quality by WQi every year seasonally wise is essential in these coastal zones as small indirect traces of the salt water intrusions are observed. The farmers in these areas need to be educated by the government and NGOs to minimize the usage of recalcitrant chemicals and unsustainable agricultural activities polluting the groundwater.

Conflict of interest

The authors declare that they have no conflict of interest.

REFERENCES

1. Adimalla, N. & Qian, H. (2019). Groundwater quality evaluation using water quality index (WQI) for drinking purposes and human health risk (HHR) assessment in an agricultural region of Nanganur, south India. *Ecotoxicol. Environ. Saf.* 176, 153-161 https://doi.org/10.1016/j.ecoenv.2019.03.066
2. Adimalla, N., Manne, R., Zhang, Y., Xu, P., & Qian, H.

(2022). Evaluation of groundwater quality and its suitability for drinking purposes in the semi-arid region of Southern India: An application of GIS. *Geocarto International,* 1-12 https://doi.org/10.1080/10106049.2022.2040603
3. Basack, S., Loganathan, M. K., Goswami, G., & Khabbaz, H. (2022). Saltwater intrusion into coastal aquifers and associated risk management: Critical review and research directives. *J. Coast. Res*, 38, 654-672. https://doi.org/10.2112/JCOASTRES-D-21-00116.1
4. Bawoke, G. T., & Anteneh, Z. L. (2020). Spatial assessment and appraisal of groundwater suitability for drinking consumption in Andasa watershed using water quality index (WQI) and GIS techniques: Blue Nile Basin, Northwestern Ethiopia. *Cogent Eng*, 7, 1748950. https://doi.org/10.1080/23311916.2020.1748950
5. BIS, I. (2012). 10500 Indian standard drinking water–specification, second revision. Bureau of Indian Standards, New Delhi
6. Chen, J., Wu, H., & Qian, H. (2016). Groundwater nitrate contamination and associated health risk for the rural communities in an agricultural area of Ningxia, northwest China. *Expos. Health*, 8, 349-359. https://doi.org/10.1007/s12403-016-0208-8
7. Chen, J., Wu, H., Qian, H., & Gao, Y. (2017). Assessing nitrate and fluoride contaminants in drinking water and their health risk of rural residents living in a semiarid region of Northwest *China. Expos*, Health, 9, 183-195. https://doi.org/10.1007/s12403-016-0231-9
8. Edition, F. (2011). Guidelines for drinking-water quality. WHO chronicle, 38, 104-108.
9. Girija, T. R., Mahanta, C., & Chandramouli, V. (2007). Water quality assessment of an untreated effluent impacted urban stream: the Bharalu tributary of the Brahmaputra River, India. *Environ. Monit. Assess,* 130, 221-236. https://doi.org/10.1007/s10661-006-9391-6
10. Horton, R. K. (1965). An index number system for rating water quality. J Water Pollut Control Fed. 37, 300-306.
11. Jalali, M. (2011). Nitrate pollution of groundwater in Toyserkan, western Iran. *Environ. Earth Sci,* 62, 907-913.
12. Karnena, M. K., & Saritha, V. (2019). Evaluation of Spatial Variability in Ground Water Quality using Remote Sensing. International Journal of Recent Technology and Engineering, 8(2), 4269-4278.
13. Karnena, M. K., Konni, M., Dwarapureddi, B. K., Satyanarayana, Y., & Saritha, V. (2022). GIS-based approach qualitative features of sub-surface water from coastal district in Andhra Pradesh. *Appl. Water Sci*, 12(3), 1-15. https://doi.org/10.1007/s13201-021-01506-1
14. Li, P., Karunanidhi, D., Subramani, T., & Srinivasamoorthy, K. (2021). Sources and consequences of groundwater contamination. Arch. *Environ. Contam. Toxicol*, 80(1), 1-10. https://doi.org/10.1007/s00244-020-00805-z
15. Panneerselvam, B., Karuppannan, S., & Muniraj, K. (2020). Evaluation of drinking and irrigation suitability of groundwater with special emphasizing the health risk posed by nitrate contamination using nitrate pollution index (NPI) and human health risk assessment (HHRA). Human and Ecological Risk Assessment: An International Journal, 27, 1324-1348. https://doi.org/10.1080/10807039.2020.1833300
16. Pericherla, S., Karnena, M. K., & Vara, S. (2020). A review on impacts of agricultural runoff on freshwater resources. *Int. J. Em. Tech*, 11, 829-833.
17. Subba Rao, N., Marghade, D., Dinakar, A., Chandana, I., Sunitha, B., Ravindra, B., & Balaji, T. (2017). Geochemical characteristics and controlling factors of chemical composition of groundwater in a part of Guntur district, Andhra Pradesh, India. *Environ. Earth Sc,*. 76, 1-22. https://doi.org/10.1007/s12665-017-7093-8
18. USEPA, 2004. Risk Assessment Guidance for Superfund Volume I: Human Health Evaluation Manual (Part E). http://www.epa.gov/oswer/riskassessment/ragse/pdf/ introduction.pdf.
19. Vara, S., Karnena, M. K., Dwarapureddi, B. K., & Chintalapudi, B. (2019). Will Single Use Products Lead to Sustainability?. International Journal of Social Ecology and Sustainable Development (IJSESD), 10(2), 37-52. DOI: 10.4018/IJSESD.2019040104
20. World Health Organization, WHO., & World Health Organisation Staff. (2004). Guidelines for drinking-water quality (Vol. 1). World Health Organization.
21. Zhang, Y., Wu, J., & Xu, B. (2018). Human health risk assessment of groundwater nitrogen pollution in Jinghui canal irrigation area of the loess region, northwest China. *Environ. Earth Sci*. 77, 1-12. https://doi.org/10.1007/s12665-018-7456-9

Journal of Mathematical Problems, Equations and Statistics

E-ISSN: 2709-9407
P-ISSN: 2709-9393
JMPES 2022; 3(2): 130-133

www.mathematicaljournal.com
Received: 03-05-2022
Accepted: 07-06-2022

Dr. Kesavulu Poola
Associate Professor, CMS - Jain University, Bengaluru, Karnataka, India

V Pavankumari
Assistant Professor, Malla Reddy Engineering College, Hyderabad, Telangana, India

J Anil Kumar
Assistant Professor, S V College of Engineering, Tirupati, Andhra Pradesh, India

M Bhupathi Naidu
Professor, Department of Statistics, S. V. University, Tirupati, Andhra Pradesh, India

Corresponding Author:
Dr. Kesavulu Poola
Associate Professor, CMS - Jain University, Bengaluru, Karnataka, India

Model specification test against non-nested univariate and multivariate nonlinear regression models

Dr. Kesavulu Poola, V Pavankumari, J Anil Kumar and M Bhupathi Naidu

Abstract
In an econometric model, Non-nested hypothesis tests give the best path to test the specification of univariate and multivariate Regression models. The model introduced by Cox for evaluate different set of hypotheses was used to the alternative between two non-nested linear regression models. This paper examines the current literature on non-nested univariate and multivariate hypothesis testing in the context of nonlinear regression and related models. The paper also covered testing the hypothesis for non-nested univariate and multivariate nonlinear regression models. The principal part of the article derives the results and explains that they are identifiable as generalizations of the univariate-equation case. It is also revealed that the computation of the test statistic involves very little calculation beyond that necessary to estimate the models.

Keywords: Non-nested, univariate, multivariate, nonlinear regression

1. Introduction

Applied econometrician had the experience of assessing a relapse model which appeared, from the outset, to be exceptionally acceptable, however which accordingly ended up, on nearer examination, to be bogus and deluding. The idea of economic data makes this inescapable. In recent era researchers are facing lot problems to find the best model to fit the linear and nonlinear regression models. In addition, especially when the research is at the beginning stages, the researcher may not know whether the existing models could possibly be true or not. The first step is to set the test the specification of each of the available models. Tests for multicollinearity, Consistency of parameter, heteroskedasticity, etc., obviously may be plays vita role in this perspective.

In economic models, non-nested hypothesis provides a path to test the one or more non nested alternative. In the year (1962, 1963) Cox discussed briefly about non-nested models. In the regression analysis parameter, stability, multicolinearilty, serial correlation, heteroscedasticity etc are playing major role. But there are many tests cannot utilize the data that the model being tested is only one of the few model to make sense of similar sort of information. In much case, on the off chance that H_0 is true, and then it follows any non-nested test, say H_1 must be false. Such test commonly named as "Non-nested hypothesis" test.

In an econometric model, if $H_{0,}$ tested with H_1, then H_1 can be condensed to H_0 based on the few multiple constraints on its parameters. Similarly I production functions, Cobb-Douglas production function is nested with in C.E.S production function, because, the elasticity of substitution is unity. Based on this we will consider H_0 and H_1 may be non-nested, if H_0 is not nested with H_0.

Test for model specification (or)te sting of no nested hypothesis are the models for correlation (or) omitted variables. We have sufficient literature is also available on model specification tests. Anselin L (1984) [25], Bera, A. and M. McAleer (1989) [3], Sawa (1978) [23], Sawyer (1980) [24] are contributed their effort on non-nested hypothesis test.

2. Cox test

The hypothetical writing on non-nested testing was basically initiated by Cox (1961, 1962). The principal benefit of the Cox test is, it made sense of overall and simple in nature. The fundamental course of action of this test is that one might test the legitimacy of an null hypothesis (H_0) about how a group of data was created by looking at the noticed proportion of the values of the likelihood functions for H0 and for some non-nested alternative hypothesis, H1, with an estimate of the expected value of this likelihood ratio if H0 were true.

If H1 fits either better or worse than it should if H0 were true, then H0 must be false.
Consider the Cox test statistic

$$T_0 = L(\hat{\theta}_0) - L(\hat{\theta}_1) - T\left(P\lim_{n\to\infty} o \frac{1}{T}\left(L(\hat{\theta}_0) - L(\hat{\theta}_1)\right)\right)_{\theta=\theta_0} \quad (2.1)$$

Here θ_0 and θ_1 vector parameters under the null and alternative hypothesis respectively. T is the no. of observations. $L(\hat{\theta}_i) \ \forall i = 0,1$ is the likelihood function and T_0 is asymptotically normally distributed, with mean zero.
The major problem in Cox test is, to evaluate the third term in (2.1). In (1973) Amemiya tested unconventional specifications of the distribution error term in regression models. Consequently Persaran and Deaton (1978) [15] expanded the Persaran derivation to the case of nonlinear univariate and nonlinear multivariate models.

3. Non-nested univariate nonlinear regression model

Consider univariate nonlinear regression model

$$H_0 : Y = f(\beta) + \varepsilon_0$$

Where

$$\varepsilon_0 \sim N(0, \sigma^2 I) \quad (3.1)$$

Here Y is dependent variable vector, $f(\theta)$ is function of vector

$$H_1 : Y = g(\gamma) + \varepsilon_1$$

Where

$$\varepsilon_1 \sim N(0, \sigma^2 I) \quad (3.2)$$

The model H_0 and H_1 are assumed to be non-nested, then

$$TP\lim_{n\to\infty} o \frac{1}{T} L(\hat{\theta}_0) \quad (3.3)$$

Evaluated at $\hat{\theta}_0$ is simply $L(\hat{\theta}_0)$ then (3.1) becomes

$$T_0 = -L(\hat{\theta}_1) + T\left[P\lim_{n\to\infty} o \frac{1}{T} L(\hat{\theta}_1)\right]\theta_0 = \hat{\theta}_0 \quad (3.4)$$

The concentrated log likelihood function for H_1 is

$$L(\hat{\theta}_1) = -\frac{T}{2}\log \hat{\sigma}_1^2 \quad (3.5)$$

$$\hat{\sigma}_1^2 = \frac{1}{T}(Y - \hat{g})^T (y - \hat{g}) \quad (3.6)$$

Here

Here $\hat{g}$ denotes $g(\hat{\gamma})$, i.e., the estimated values of H_1 computed at maximum likelihood estimates $\hat{r}$.
As we know, $L(\hat{\theta}_1)$ depends only on $\hat{\sigma}_1^2$, then we have to find the Plim of $\hat{\sigma}_1^2$ under H_0, in order to calculate the second term in (3.4).

$$\tilde{\sigma}_1^2 \equiv \frac{1}{T}(Y - \tilde{g})^T (Y - \tilde{g}) \quad (3.7)$$

$$= \frac{1}{T}(Y - f + f - \tilde{g})^T (Y - f + f - \tilde{g}) \quad (3.8)$$

$$= \frac{1}{T}(Y-f)^T (Y-f) + (f-\tilde{g})^T (f-\tilde{g}) + 2(Y-f)^T (f-\tilde{g}) \quad (3.9)$$

Here f is the function of $f(\theta)$. Here $(Y - f)$ a vector follow normal distribution with mean zero and variance σ_0^2 then the estimate $P\lim \hat{\sigma}_1^2$ is

$$\tilde{\sigma}_{10} = \hat{\sigma}_0^2 + \frac{1}{T}(\hat{f} - \tilde{g})^T (\hat{f} - \tilde{g}) \quad (3.10)$$

Based on the (3.4) (3.5) and (3.10), the numerator for Cox test

$$T_0 = \frac{T}{2}\log\frac{\hat{\sigma}_1^2}{\tilde{\sigma}_{10}^2} \quad (3.11)$$

Since nonlinear regression

$$\hat{f} = g(\gamma) + e \quad (3.12)$$

An estimative variance of 'To

$$\hat{V}(To) = \frac{\hat{\sigma}_0^2}{\tilde{\sigma}_{10}^4}(\hat{f} - \tilde{g})^T \left[I - \hat{F}(\hat{F}^T\hat{F})^{-1}\hat{F}^T\right](\hat{f} - \tilde{g}) \quad (3.13)$$

Where 'F' is the Marix derivatives of $f(\theta)$ w.r. to θ
∴ According to the Pesaran, M. H. and Deaton, A. S. (1978), Cox test statistic for nonlinear regression model is

$$N_o = \frac{T_o}{\sqrt{\hat{V}_o(T_o)}} \quad (3.14)$$

The above N_o provides a test of H_o and it explains about the validity of 'H_1'. If N_o is less than zero, it is explaining that, H is rejected under the directions away from 'H_1' and N_o is greater than zero then H_o is rejected in the favour of H_1

4. Non-nested multivariate nonlinear regression model

Cox test and a number of methods of the t-test may be applied in many cases of multivariate nonlinear regression models. So

according to that,
The null hypothesis is

$$H_0 : Y_{ti} = f_{t1}(\theta) + e_{ti}^0$$

Where

$$e_{ti}^0 \sim N(0, \Omega_0) \tag{4.1}$$

The Alternative Hypothesis is

$$H_1 : Y_{ti} = g_{ti}(-r) + e_{ti}^1$$

Where

$$e_{ti}^1 \sim N(0, \Omega_1) \tag{4.2}$$

Here 'i' tends to m equations and t tends to 'T' observation and Ω_j is the mxn covariance matrix for the error terms corresponding to the hypothesis. H_j.
The numerator for the test statistic is

$$T_o = T/2 \log \left| \frac{\hat{\Omega}_1}{\tilde{\Omega}_{10}} \right| \tag{4.3}$$

Where $\hat{\Omega}_1$ is maximum likelihood estimate of Ω_1 and $\tilde{\Omega}_{10}$ is analogously to $\tilde{\sigma}_{10}$.
There are several multivariate cases of t-test are available in the literature. The easiest artificial compound model analogous to the uni-variable model is

$$Y = (1-\alpha) f(\theta) + \alpha\, \hat{g} + e$$

i.e., H_0: $$Yti = (1-\alpha) fti(\theta) + \alpha \hat{g}_{ti} + eti \tag{4.4}$$

Under H_0, Yt is the Covariance Matrix Ω_0. Linearizing around the point $\alpha = 0, \theta = \hat{\theta}$ yields the Multivariable linear regression

$$Y_{ti} - \hat{f}_{ti} = \hat{F}_{ti}^T b + \alpha\left(\hat{g}_{ti} - \hat{f}_{ti}\right) + eti \tag{4.5}$$

$$Y_{ti} - \hat{f}_{ti} = \hat{F}_{ti}^T b + \alpha \hat{h}_{ti} + eti \tag{4.6}$$

When h_{ti} is an element matrix of the Txm.

$$\therefore \hat{h} \equiv \left(\hat{g} - \hat{f}\right) \hat{\Omega}_1^{-1} \hat{\Omega}_0 \tag{4.7}$$

Here $\hat{g}$ and $\hat{f}$ are the Txm matrices with the elements of $\hat{g}_{ti}$ and $\hat{f}_{ti}$ respectively.

5. Conclusion

This paper intended at contributing to the literature existing form of testing nonnested multivariate nonlinear regression models. Non-nested univariate and multivariate models take place regularly in practice and researchers are using a wide variety of methods to test such models against one or more alternatives. This paper has explained the significance of testing of non-nested univariate and multivariate models, especially in the context of linear, and nonlinear regression models.

6. References

1. Balestra P. On the efficiency of ordinary least-squares in regression models. Journal of the American Statistical Association. 1970;65(331):1330-1337.
2. Batese GE, Bonyhady BP. Estimation of household expenditure functions: An application of a class of heteroscedastic regression models, Economic Record. 1981;57:80-85.
3. Bera A, McAleer M. Nested and non-nested procedures for testing linear and log-linear regression models, Sankhya B. 1989;51:212-224.
4. Chai T, Draxler RR. Root mean square error (RMSE) or mean absolute error (MAE)? - Arguments against avoiding RMSE in the literature, Geoscientific Model Development. 2014;7:1247-1250.
5. Cliff KR, Billy KM. Estimation of the Parameters of Linear Regression System using the Simple Averaging Method. Global Journal of Pure and Applied Mathematics. 2017;13(11):7749-7758.
6. Dorugade AV. New ridge parameters for ridge regression. Journal of the Association of Arab Universities for Basic and Applied Sciences. 2014;15:94-99.
7. Dr. Kesavulu Poola, Prof. M. Bhupathi Naidu. Importance of studentized and press residuals for nonlinear multivariate regression models. Journal of Emerging Technologies and Innovative Research. 2008;5(7):353-356
8. Dr. Kesavulu Poola P, Hema Sekhar, Dr. M Bhupathi Naidu. Combined multiple forecasting model using regression, International Journal of Statistics and Applied Mathematics. 2020;5(6):147-150.
9. Kesavulu Poola, Vasu K, Bhupathi Naidu M, Abbaiah R, Balasiddamuni P. The effect of multicollinearity in nonlinear regression models in International Journal of Applied Research. 2016;2(12):506-509.
10. Kikawa CR, Kloppers PH. Multiple linear regression with constrained coefficients: application of the Lagrange multiplier. South African Statistical Journal. 2016;50(2):303-312.
11. Kloppers PH, Kikawa CR, Shatalov MY. A new method for least squares identification of parameters of the transcendental equations, International Journal of the Physical Sciences. 2012;7:5218-5223.
12. Kuchibhotla AK, Patra RK. On least squares estimation under heteroscedastic and heavy-tailed errors. The Annals of Statistics. 2022;50(1):277-302.
13. Nagaraj D, Wu X, Bresler G, Jain P, Netrapalli P. Least Squares Regression with Markovian Data: Fundamental Limits and Algorithms. Advances in Neural Information Processing Systems. 2020;33:16666-16676.
14. Permai SD, Tanty H. Linear Regression Model using Bayesian Approach for Energy Performance of Residential Building. Procedia Computer Science.

2018;135:671-677.
15. Pesaran MH, Deaton AS. Testing non–nested regression models, Econometrica. 1978;46:677-694.
16. Prabitha J, Archana S. Application of Regression Analysis in Numeroustimes. International Journal of Science, Enginering and Technology Research. 2015;4(4):1002-1005.
17. Vuong QH. Likelihood ratio tests for model selection and non-nested hypotheses, Econometrica. 1989;57:307-333.
18. Wang S, Qian L, Carroll RJ. Generalized empirical likelihood methods for analyzing longitudinal data. Biometrika. 2010;97(1):79-93.
19. White H. Regularity conditions for Cox's test of non-nested hypotheses, Journal of Econometrics. 1982;19:301-318.
20. Yang G, Zhang B, Zhang M. Estimation of Knots in Linear Spline Models. Journal of the American Statistical Association; c2021. p. 1-12.
21. Zhang T. Some sharp performance bounds for least square regression with l1 regularization. The Annals of Statistics. 2009;37(5A):2109-2144.
22. Zheng B, Agresti A. Summarizing the predictive power of a generalized linear model, Statist. Med. 2000;19:1771-1781.
23. Sawa T. Information criteria for discriminating among alternative regression models. Econometrica: Journal of the Econometric Society. 1978 Nov 1:1273-91.
24. Sawyer TK, Sanfilippo PJ, Hruby VJ, Engel MH, Heward CB, Burnett JB, *et al*. 4-Norleucine, 7-D-phenylalanine-alpha-melanocyte-stimulating hormone: a highly potent alpha-melanotropin with ultralong biological activity. Proceedings of the National Academy of Sciences. 1980 Oct;77(10):5754-8.
25. Anselin L. Specification tests on the structure of interaction in spatial econometric models. InPapers of the Regional Science Association. Springer-Verlag. 1984 Dec;54(1):165-182.

MAGNETIC FIELD AND CHEMICAL REACTION EFFECTS ON UNSTEADY FLOW PAST A STIMULATE ISOTHERMAL INFINITE VERTICAL PLATE

Ch. Achi Reddy[1],V. Nagaraju[2], Y. V. Seshagiri Rao[3], Dr. Nookala Venu[4]

[1]Department of Humanities & Sciences, MLR Institute of Technology, Dundigal, Hyderabad, T.S - 500043, India
Email: achireddy.ch@gmail.com

[2]Department of Mathematics, Malla Reddy Engineering College (Autonomous), Dulapally (V), Kompally (M), Medchal Malkajgiri (Dist), T.S-500100, India
Email:nagarajuvuppala@gmail.com

[3]Department of Basic Sciences & Humanities, Vignan Institute of Technology and Science, Deshmukhi (V), Pochampally (M), Yadadri-Bhuvanagiri (Dist), T.S-508284, India
Email: yangalav@gmail.com

[4]Department of Electronics and Communication Engineering, Balaji Institute of Technology and Science (Autonomous), Narsampet, Warangal, TS -506331, India
Email: venunookala@gmail.com

Abstract
An exact analysis ofradiation and magnetic field effects on unsteady flow past an accelerated isothermal infinite vertical platein the presence of chemical reaction and heat source. It is assumed that the effect of viscous dissipation in the energy equation and there is a first order chemical reaction between the diffusing species and the fluid cannot negligible. The fluid considered here is a gray, absorbing emitting radiation but a non-scattering medium.The dimensionless governing equations are solved using perturbation technique. The velocity, temperature and concentration profiles are discussed through graphically for different physical parameters.

Keywords: Magnetic field, Infinite vertical plate, Radiation, Radiation absorption, Chemical reaction,
DOI Number: 10.48047/NQ.2022.20.16.NQ880546 **Neuroquantology 2022; 20(16): 5360-5373**

INTRODUCTION
Meanwhile, it is well known that for a simultaneous occurrence of heat and mass transfer in a moving fluid, the relationships between the driven potential and the corresponding fluxes are of important. Also it is noticed that the energy flux (rate of energy transfer per unit area) and mass flux (rate of

mass flow per unit area) can be generated by temperature gradients as well as composition gradients. The energy caused or generated by composition gradients is known as Dufour or diffusion-thermo effect and is considered useful in isotope separation. The mass flux created or generated by temperature gradients is known as Soret or thermal-diffusion effect which is considered useful in mixture of gases with very light molecular weight (hydrogen–helium) and medium molecular weight (nitrogen–air). In view of the above some of the authors studies, (Chenna Kesavaiah et al, 2021) point out on radiative MHD Walter's Liquid-B flow past a semi-infinite vertical plate in the presence of viscous dissipation with a heat source, ((Rajaiah and Sudhakaraiah, 2015) action is an idea an unsteady MHD free convection flow past an accelerated vertical plate with chemical reaction and Ohmic heating, (Rami Reddy et al, 2021) communicated on Hall effect on MHD flow of a viscoelastic fluid through porous medium over an infinite vertical porous plate with heat source, (Chenna Kesavaiah Venkateswarlu, 2020) carried out the research work on chemical reaction and radiation absorption effects on convective flows past a porous vertical wavy channel with travelling thermal waves, (Mallikarjuna Reddy et al, 2019) expressed the radiation and diffusion thermo effects of viscoelastic fluid past a porous surface in the presence of magnetic field and chemical reaction with heat source,(Haranth and Sudhakaraiah, 2015) has been studied the viscosity and Soret effects on unsteady hydromagnetic gas flow along an inclined plane, (Srinathuni Lavanya and Chenna Kesavaiah, 2017) explained on heat transfer to MHD free convection flow of a viscoelastic dusty gas through a porous medium with chemical reaction, (Mallikarjuna Reddy et al, 2018) has motivated study on effects of radiation and thermal diffusion on MHD heat transfer flow of a dusty viscoelastic fluid between two moving parallel plates.

The Soret effect, for instance, has been utilized for isotope separation, and in mixtures between gases with very light molecular weight (H_2, He). For medium molecular weight (N_2, air), the Dufour effect was found to be of a considerable magnitude such that it cannot be neglected. For the temperature interval employed by Soret the ratio of concentration in the cold end to that in the warm end should therefore be 1. 250. This ratio proved to be approximately correct for cupric sulphate; for potassium, sodium and lithium chlorides, however, the average observed ration were, respectively, 1.069, 1.054, and 1.006. The supposition that these solutions might not have a higher rate of diffusion than copper sulphate. When heat and mass transfer occurs simultaneously between the fluxes, the driving potential is of more intricate nature, as energy flux can be generated not only by temperature gradients but by composition gradients as well. The energy flux caused by a composition gradient is called the Dufour or diffusion-thermo effect. Temperature gradients can also create mass fluxes, and this is the Soret or thermal-diffusion effect. Generally, the thermal-diffusion and the diffusion-thermo effects are of smaller-order magnitude than the effects prescribed by Fourier's or Fick's laws and are often neglected in heat and mass transfer processes. There are, however, exceptions. The Soret effect, for instance, has been utilized for isotope separation, and in mixtures between gases with very light molecular weight (H_2, He). For medium molecular weight (N_2, air), the Dufour effect was found to be of a considerable magnitude such that it cannot be neglected, (Chenna Kesavaiah and Sudhakaraiah, 2014) has been considered the effects of heat and mass flux to MHD flow in vertical surface with radiation absorption, (Yeddala et al, 2016) revealed that the finite difference solution for an MHD free convective rotating flow past an accelerated vertical plate,(Chenna Kesavaiah et al, 2013) shows that the natural convection heat transfer oscillatory flow of an elastico-viscous fluid from vertical plate, (Chenna Kesavaiah and Satyanarayana, 2013) has been studied MHD and Diffusion Thermo effects on flow accelerated vertical plate with chemical reaction,(Rajaiah et al, 2015) explained on chemical and Soret effect on MHD free convective flow past an accelerated Vertical plate in presence of inclined magnetic field through porous medium.

When heat and mass transfer occurs simultaneously between the fluxes, the driving potential is of more intricate nature, as energy flux can be generated not only by temperature gradients but by composition gradients as well. The energy flux caused by a composition gradient is called the Dufour or diffusion-thermo effect. Temperature gradients can also create mass fluxes, and this is the Soret or thermal-diffusion effect. Generally, the thermal-diffusion and the diffusion-thermo effects are of smaller-order magnitude than the effects prescribed by Fourier's or Fick's laws and are often neglected in heat and mass transfer processes. There are, however, exceptions.(ChennaKesavaiah et al, 2013) has been consideredradiation and Thermo - Diffusion effects on mixed convective heat and mass transfer flow of a viscous dissipated fluid over a vertical surface in the presence of chemical reaction with heat source,(Karunakar Reddy et al,2013) carried out of the work MHD heat and mass transfer flow of a viscoelastic fluid past an impulsively started infinite vertical plate with chemical reaction,(Rajaiah and Sudhakaraiah, 2015) depicted on radiation and Soret effect on unsteady MHD flow past a parabolic started vertical plate in the presence of chemical reaction with magnetic dissipation through a porous medium, (Ch Kesavaiah et al, 2013)has been considered the effects of radiation and free convection currents on unsteady Couette flow between two vertical parallel plates with constant heat flux and heat source through porous medium,(Rajaiah et al, 2014) explained in detailed on unsteady MHD free convective fluid flow past a vertical porous plate with Ohmic heating in the presence of suction or injection, (ChKesavaiah et al, 2012) revealed on radiation and mass transfer effects on moving vertical plate with variable temperature and viscous dissipation,(Satyanarayana et al, 2011) shown viscous dissipation and thermal radiation effects on an unsteady MHD convection flow past a semi-infinite vertical permeable moving porous plate, ChKesavaiah et al, 2011) expressed their view on effects of the chemical reaction and radiation absorption on an unsteady MHD convective heat and mass transfer flow past a semi-infinite vertical permeable moving plate embedded in a porous medium with heat source and suction. (Chenna Kesavaiah, 2022) explained heat and mass transfer effects over isothermal infinite vertical plate of Newtonian fluid with chemical reaction,(Chenna Kesavaiah, 2022) motivated study on influence of joule heating and mass transfer effects on MHD mixed convection flow of chemically reacting fluid on a vertical surface, (Bal Reddy, 2022) observed Anote on heat transfer of MHD Jeffrey fluid over a stretching vertical surface through porous plate.

In view of the above the objective of the present paper is radiation and magnetic field effects on unsteady flow past an accelerated isothermal infinite vertical plate in the presence of chemical reaction and heat source. The plate temperature is raised to T_w and the concentration level near the plate is also raised to C_w. The dimensionless governing equations are solved using perturbation technique. The velocity, temperature and concentration profiles are studied for different physical parameters by using MATLAB. 5362

FORMULATION OF THE PROBLEM

We consider unsteady radiative flow of a viscousincompressible fluid past a uniformly acceleratedisothermal infinite vertical plate with uniform massdiffusion and magnetic field in the presence of chemical reaction which takes place in the flow is assumed to be homogeneous and of first order with uniform magnetic field. Unsteady flow of a viscousincompressible fluid which is initially at rest andsurrounds an infinite vertical plate with temperature T_∞ and concentration C_∞. The x-axis is taken along the platein the vertically upward direction and the y-axis is takennormal to the plate. At time $t' \le 0$, the plate and fluid areat the same temperature T_∞. At time $t' > 0$, the plate isaccelerated with a velocity $u = \frac{u_0^3 t'}{\nu}$ in its own plane andthe temperature from the plate is raised to T_w *w*and theconcentration levels near the plate are also raised to C_w.It is assumed that the effect of viscous dissipation isnegligible in the energy equation and there is a first orderchemical reaction between the diffusing species and thefluid. The fluid considered here is a gray, absorbing emitting radiation but a non-scattering medium. Thenunder usual Boussinesq's approximation the unsteadylow is governed by the following equations:

$$\frac{\partial u^*}{\partial t^*} = g\beta\left(T^* - T_\infty^*\right) + g\beta^*\left(C^* - C_\infty^*\right) + \nu\frac{\partial^2 u^*}{\partial y^{*2}} - \frac{\sigma B_0^{\ 2}}{\rho}u^* \quad (1)$$

$$\rho C_p\frac{\partial T^*}{\partial t^*} = k\frac{\partial^2 T^*}{\partial y^{*2}} + \mu\left(\frac{\partial u^*}{\partial y^*}\right)^2 - \frac{\partial q_r}{\partial y^*} - Q_0\left(T^* - T_\infty^*\right) \quad (2)$$

$$\frac{\partial C^*}{\partial t^*} = D_M\frac{\partial^2 C^*}{\partial y^{*2}} - Kr^*\left(C^* - C_\infty^*\right) + D_T\frac{\partial^2 T^*}{\partial y^{*2}} \quad (3)$$

The initial and boundary conditions for the velocity, temperature and concentration fields are

$$u^* = 0, T^* = T_\infty^*, C^* = C_\infty^* \Big\} \quad for \ \ all\, t' > 0$$

$$\left.\begin{aligned} t^* > 0 : u = \frac{u_0^{\ 3} t'}{\nu}, \\ T^* = T_w^*, C^* = C_w^* \end{aligned}\right\} \quad at \quad y = 0 \quad (4)$$

$$\left.\begin{aligned} u^* \to 0, \ \ T^* \to T_\infty^* \\ C^* \to C_\infty^* \end{aligned}\right\} \quad as \quad y \to \infty$$

where u' is the velocity of the fluid along the plate in the x' - direction, t' is the time, g is theacceleration due to gravity, β is the coefficient of volume expansion, β^* is the coefficient ofthermal expansion with concentration, T_∞ is the temperature of the fluid near the plate, C' is thespecies concentration in the fluid near the plate, C'_∞ is the species concentration in the fluid faraway from the plate, ν is the kinematic viscosity, σ is the electrical conductivity of thefluid, B_0 is the strength of applied magnetic field, ρ is thedensity of the fluid, C_p is the specific heat at constant pressure, K is the thermal conductivity ofthe fluid, μ is the viscosity of the fluid, D is the molecular diffusivity.

The local radiant for the case of an optically thin gray gas is expressed by

$$\frac{\partial q_r}{\partial y^*} = -4a^*\sigma\left(T_\infty^4 - T^4\right) \quad (5)$$

It is assume that the temperature differences within the flow are sufficiently small such that T^4 may be expressed as a linear function of the temperature. This is accomplished by expanding T^4 in a Taylor series about T_∞ and neglecting higher-order terms, thus

$$T^4 \cong 4T_\infty^3 T - 3T_\infty^4 \quad (6)$$

By using equations (5) and (6), equation (2) reduces to

$$\rho C_p\frac{\partial T^*}{\partial t^*} = k\frac{\partial^2 T^*}{\partial y^{*2}} + \mu\left(\frac{\partial u^*}{\partial y^*}\right)^2 + 16a^*\sigma T_\infty^3\left(T^* - T_\infty^*\right) - Q_0\left(T^* - T_\infty^*\right) \quad (7)$$

eISSN1303-5150

On introducing the following non-dimensional quantities:

$$U=\frac{u^*}{u_0},Y=\frac{u_0 y^*}{\nu},\ t=\frac{t^* {u_0}^2}{\nu},\ Sc=\frac{\nu}{D}$$

$$\phi=\frac{\left(C^*-C_\infty^*\right)}{C_w^*-C_\infty^*},Gc=\frac{\nu\beta^* g\left(C_w^*-C_\infty^*\right)}{{u_0}^3}$$

$$Gr=\frac{\nu\beta g\left(T_w^*-T_\infty^*\right)}{{u_0}^3},\Pr=\frac{\mu C_p}{k}$$

$$Kr=\frac{Kr^*\nu}{{u_0}^2},\ Q=\frac{\nu^2 Q_0}{k{u_0}^2},\ \ M=\frac{\sigma {B_0}^2\nu}{\rho {u_0}^2} \quad (8)$$

$$Ec=\frac{u_0^2}{k\left(T_w^*-T_\infty^*\right)},\quad R=\frac{16a^*\nu^2\sigma T_\infty^3}{ku_0^2}$$

$$S_0=\frac{D_T\left(T_w^*-T_\infty^*\right)}{\nu\left(C_w^*-C_\infty^*\right)},\quad \theta=\frac{\left(T^*-T_\infty^*\right)_\infty}{T_w^*-T_\infty^*}$$

where Gr is the thermal Grashof number, Gc is modifiedGrashof Number, $\Pr$ is Prandtl Number, M is the magnetic field, Sc is Schmdit number, Kr is Chemical Reaction, S_0 is Soret number, ϕ is Heat source parameter respectively.

Introducing the above non dimensional quantities in equations (1) - (3) and using equation (7) reduces to

$$\frac{\partial U}{\partial t}=Gr\,\theta+Gc\,C+\frac{\partial^2 U}{\partial Y^2}-M\,U \quad (9)$$

$$\frac{\partial\theta}{\partial t}=\frac{1}{\Pr}\frac{\partial^2\theta}{\partial Y^2}+\frac{Ec}{\Pr}\left(\frac{\partial U}{\partial Y}\right)^2 -\frac{1}{\Pr}\left(R+Q\right)\theta+Q_l C \quad (10)$$

$$\frac{\partial\phi}{\partial t}=\frac{1}{Sc}\frac{\partial^2\phi}{\partial Y^2}-Kr\,\phi+S_0\frac{\partial^2\theta}{\partial Y^2} \quad (11)$$

The negative sign of Kr in the last term of the equation (11) indicates that the chemical reaction takes place from higher level of concentration to lower level of concentration.

The initial and boundary conditions in non-dimensional quantities are

$$U=0,\ \ \theta=0,\ \phi=0\ \ for\ all\ Y,\ t\le 0$$

$$t>0: U=t,\ \ \theta=1,\ \ \phi=1\quad at\ \ Y=0 \quad (12)$$

$$U\to 0,\theta\to 0,\phi\to 0\quad as\quad Y\to\infty$$

SOLUTION OF THE PROBLEM:

Equations (9) – (11) are coupled, non – linear partial differential equations and these cannot be solved in closed – form using the initial and boundary conditions (12). However, these equations can be reduced to a set of ordinary differential equations, which can be solved analytically. This can be done by representing the velocity, temperature and concentration of the fluid in the neighbourhood of the fluid in the neighbourhood of the plate as

$$U=U_0\left(y\right)+\varepsilon e^{nt}U_1\left(y\right)\ +o\left(\varepsilon^2\right)$$

$$\theta=\theta_0\left(y\right)+\varepsilon e^{nt}\theta_1\left(y\right)\ +o\left(\varepsilon^2\right) \quad (13)$$

$$\phi=\phi_0\left(y\right)+\varepsilon e^{nt}\phi_1\left(y\right)+o\left(\varepsilon^2\right)$$

Substituting (13) in equation (9) – (11) and equating the harmonic and non – harmonic terms, and neglecting the higher order terms of $0\left(\varepsilon^2\right)$, we obtain

$$U_0''-MU_0=-Gr\,\theta_0-Gc\,C_0 \quad (14)$$

$$U_1''-\left(M+n\right)U_1=-Gr\,\theta_1-Gc\,C \quad (15)$$

$$\theta_0''-\left(R+Q\right)\theta_0=-Ec\,{U_0'}^2 \quad (16)$$

$$\theta_1''-\left(R+Q+n\Pr\right)\theta_1=-2Ec\,U_0'U_1' \quad (17)$$

$$\phi_0''-Sc\,Kr\,\phi_0=-ScS_0\theta_0'' \quad (18)$$

$$\phi_1''-\left(Kr+n\right)Sc\phi_1=-ScS_0\theta_1'' \quad (19)$$

The corresponding boundary conditions can be written as

$$\left.\begin{array}{l}U_0=t,U_1=0,\theta_0=1\\ \theta_1=1,\ \phi_0=1,\ \phi_1=0\end{array}\right\}\quad at\quad y=0$$

$$\left.\begin{array}{l}U_0\to 0,U_1\to 0,\theta_0\to 0\\ \theta_1\to 0,\ \phi_0\to 0,\ \phi_1\to 0\end{array}\right\}\ as\ y\to\infty \quad (20)$$

The equations (14) - (19) are still coupled and non-linear, whose exact solutions are not possible. So we expand $U_0,U_1,\theta_0,\theta_1,\phi_0,\phi_1$ in terms $\left(f_0,\ f_1\right)$ of Ec in the following form, as the Eckert number is very small for incompressible flows.

eISSN1303-5150

$$f_0(y) = f_{01}(y) + Ec\ f_{02}(y)$$
$$f_1(y) = f_{11}(y) + Ec\ f_{12}(y) \quad (21)$$

Substituting (21) in Equations (14) - (19), equating the coefficients of Ec to zero and neglecting the terms in Ec^2 and higher order, we get the following equations.

$$U_{01}'' - MU_{01} = -Gr\,\theta_{01} - Gc\,\phi_{01} \quad (22)$$
$$U_{02}'' - MU_{02} = -Gr\,\theta_{02} - Gc\,\phi_{02} \quad (23)$$
$$U_{11}'' - (M+n)U_{11} = -Gr\,\theta_{11} - Gc\,\phi_{11} \quad (24)$$
$$U_{12}'' - (M+n)U_{12} = -Gr\,\theta_{12} - Gc\,\phi_{12} \quad (25)$$
$$\theta_{01}'' - (R+Q)\theta_{01} = 0 \quad (26)$$
$$\theta_{02}'' - (R+Q)\theta_{02} = -U_{01}'^{2} \quad (27)$$
$$\theta_{11}'' - (Q+R+n\Pr)\theta_{11} = 0 \quad (28)$$
$$\theta_{12}'' - (R+Q+n\Pr)\theta_{12} = -2U_{01}'U_{11}' \quad (29)$$
$$\phi_{01}'' - Sc\,Kr\,\phi_{01} = -ScS_0\theta_{01}'' \quad (30)$$
$$\phi_{02}'' - Sc\,Kr\,\phi_{02} = -ScS_0\theta_{01}'' \quad (31)$$
$$\phi_{11}'' - (Kr+n)Sc\phi_{11} = -ScS_0\theta_{11}'' \quad (32)$$
$$\phi_{12}'' - (Kr+n)Sc\phi_{12} = -ScS_0\theta_{12}'' \quad (33)$$

The respective boundary conditions are

$$\left.\begin{array}{lll} U_{01} = t, & U_{02} = 0, & \theta_{01} = 1 \\ \theta_{02} = 0, & \phi_{01} = 1, & \phi_{02} = 0 \\ U_{11} = 0, & U_{12} = 0, & \theta_{11} = 0 \\ \theta_{12} = 0, & \phi_{11} = 0, & \phi_{12} = 0 \end{array}\right\} y = 0 \quad (34)$$

$$\left.\begin{array}{l} U_{01} \to U_{02} \to \theta_{01} \to \theta_{02} \to 0 \\ \phi_{01} \to \phi_{02} \to U_{11} \to U_{12} \to 0 \\ \theta_{11} \to \theta_{12} \to \phi_{11} \to \phi_{12} \to 0 \end{array}\right\} y \to \infty$$

Solving equations (22) - (33) under the boundary conditions (34)we obtain the velocity, temperature and concentration distributions in the boundary layer as

$$\begin{aligned} U(y,t) = {} & A_1 e^{m_1 y} + A_2 e^{m_1 y} + A_3 e^{m_2 y} + A_4 e^{m_3 y} \\ & + Ec\{A_5\ e^{m_1 y} + A_6\ e^{2m_3 y} + A_7 e^{2m_1 y} \\ & + A_8\ e^{2m_1 y} + A_9\, e^{2m_2 y} + A_{10}\ e^{(m_1+m_3)y} \\ & + A_{11} e^{2m_1 y} + A_{12} e^{(m_1+m_3)y} + A_{13} e^{(m_2+m_3)y} \\ & + A_{14}\, e^{(m_1+m_2)y} + A_{15}\, e^{(m_1+m_3)y} + A_{16}\, e^{m_2 y} \\ & + A_{17} e^{m_1 y} + A_{18} e^{2m_3 y} + A_{19}\, e^{2m_1 y} \\ & + A_{20}\, e^{2m_1 y} + A_{21} e^{2m_2 y} + A_{22} e^{2m_1 y} \\ & + A_{23} e^{2m_1 y} + A_{24} e^{2m_1 y} + A_{25} e^{(m_1+m_2)y} \\ & + A_{26} e^{(m_1+m_2)y} + A_{27}\, e^{(m_1+m_2)y}\} \end{aligned}$$

$$\begin{aligned} \theta(y,t) = {} & e^{m_1 y} + Ec\{ J_1 e^{2m_3 y} + J_2 e^{2m_1 y} \\ & + J_3 e^{2m_1 y} + J_4 e^{2m_2 y} + J_5 e^{(m_1+m_3)y} \\ & + J_6 e^{2m_1 y} + J_7 e^{(m_1+m_3)y} + J_8 e^{(m_2+m_3)y} \\ & + J_9 e^{(m_1+m_2)y} + J_{10} e^{(m_1+m_2)y} + J_{11} e^{m_1 y}\} \end{aligned}$$

$$\begin{aligned} \phi(y,t) = {} & B_1 e^{m_1 y} + B_2 e^{m_2 y} + Ec\{B_{14} e^{m_2 y} \\ & + B_3 e^{m_1 y} + B_4 e^{2m_3 y} + B_5 e^{2m_1 y} \\ & + B_6 e^{2m_1 y} + B_7 e^{2m_2 y} + B_8 e^{2m_1 y} \\ & + B_9 e^{2m_1 y} + B_{10} e^{(m_1+m_3)y} + B_{11} e^{(m_1+m_2)y} \\ & + B_{12} e^{(m_1+m_2)y} + B_{13} e^{(m_1+m_2)y}\} \end{aligned}$$

Skin-friction:

We now calculate skin-friction from the velocity field. It is given in non-dimensional form as:

$\tau = -\left(\dfrac{\partial U}{\partial y}\right)_{y=0}$, where $\tau = -\dfrac{\tau'}{\rho U_0^{\,2}}$

$$= A_1 m_1 + A_2 m_1 + A_3 m_2 + A_4 m_3 + Ec\{A_5 m_1 + 2A_6 m_1 + 2A_7 m_1 + 2A_8 m_1 + 2A_9 m_2 + A_{10}(m_1+m_3) + 2A_{11} m_1 + (m_1+m_3)A_{12} + (m_2+m_3)A_{13} + (m_1+m_2)A_{14} + (m_1+m_3)A_{15} + + A_{16} m_2 + A_{17} m_1 + 2A_{18} m_3 + 2A_{19} m_1 + 2A_{20} m_1 + 2A_{21} m_2 + 2m_1 A_{22} + 2A_{23} m_1 + 2A_{24} m_1 + A_{25}(m_2+m_1) + A_{26}(m_1+m_2) + A_{27}(m_1+m_2)\}$$

Rate of heat transfer:

The dimensionless rate of heat transfer is given by

$$Nu = -\left(\frac{\partial \theta}{\partial y}\right)_{y=0}$$

$$= m_1 + Ec\{2J_1 m_3 + 2J_2 m_1 + 2J_3 m_1 + 2J_4 m_2 + (m_1+m_3)J_5 + 2J_6 m_1 + (m_1+m_3)J_7 + (m_2+m_3)J_8 + (m_1+m_2)J_9 + (m_1+m_2)J_{10} + J_{11} m_1\}$$

Sherwood number:

The dimensionless Sherwood number is given by

$$Sh = -\left(\frac{\partial \phi}{\partial y}\right)_{y=0}$$

$$= B_1 m_1 + B_2 m_2 + Ec\{B_{14} m_2 + B_3 m_1 + 2B_4 m_3 + 2B_5 m_1 + 2B_6 m_1 + 2B_7 m_2 + 2m_1 B_8 + 2B_9 m_1 + (m_1+m_3)B_{10} + (m_1+m_2)B_{11} + (m_1+m_2)B_{12} + (m_1+m_2)B_{13}\}$$

RESULTS AND DISCUSSION

The results for various parameters were discussed for the dimensionless governing equations. The velocity, temperature and concentration profiles are studied for different physical parameters through graphically.We assigned the following values for various parameters involving in flow problem, $\Pr = 0.72$, $Q = 1.0$, $Kr = 1.0$, $R = 1.0$, $M = 1.0$, $n = 0.5$, $S_0 = 1.0$, $Gr = 5.0$, $Gc = 5.0$, $t = 0.2$, $Sc = 0.84$, $Ec = 0.01$. The effect of thermal Grashof number on the velocity profiles is shown in figure (1). Form the plot increase in Grashof numbercontributes to the increase in velocity. Also it is noticed that as we move away from the plate the influence of Grashof number is not that significant.As shown in figure (2),as the mass Grashof number increases the velocity profiles is seen to be increasing. Also, it is seen that as we move far away from the plate it is seen that the effect of mass Grashof number is found to be not that significant.The effect of chemical reaction parameter decreases the velocity of the boundary layer thickness with increasing various values of chemical reaction parameter shown in figure (3). The influence of Magnetic field on the velocity profiles has been plot in figure (4). It is seen that the increase in the applied magnetic intensity contributes to the decrease in the velocity. Further, it is seen that the magnetic influence does not contribute significantly as we move away from the bounding surface.From figures(5) – (6), it is observedthat increases the radiation parameter and heat source parameter produces significant decrease. This is attributed to the thermal state of the fluid causing its velocity to decreases. The contribution of Soret number on the velocity profiles is noticed in figure (7), from this figure we observed that an increase in Soret number contributes the increase in the velocity field. This is due to that increase in the fluid temperature induces through the effect of thermal buoyancy more flow in the boundary layer causing the velocity of the fluid there to increase. Further, it is noticed that the velocity decreases as we move away from the plate which is found to be independent of Soret number. The influence of Schmidt number on velocity profiles has been illustrated in figure (8). It is observed that, while all other participating parameters are held constant and Schmidt numberis increased, it is seen that the velocity decreases in general. Further, it is noticed that as we move far away from the plate, the fluid velocity goes down. The velocity profiles for different values oftime studied and presented in figure (9). It is observed that the velocity increases with increasing values of the time. The temperature profiles decreases with increase in the value of the internal heat source parameter and radiation parameter increases the thermal boundary layer thickness shown in figures (10) & (11). Figure (12) show the influence of the chemical reaction parameter. Increasing the chemical reaction parameter produces a decrease in the species concentration. In turn, this causes the concentration buoyancy effects to decrease as chemical reaction parameter increases. The influence of Schmidt number on the concentration is illustrated in figure (13). It is observed that increase in Schmidt numbercontributes to decrease of concentration of the fluid medium. Further, it is seen that Schmidt numberdoes not contributes much to the concentration field as we move far away from the bounding surface. Knowing the velocity, temperature and concentration profiles, it is customary to study the skin-friction, Nusselt number and Sherwood number. The local as well as average values of skin-friction, Nusselt number and Sherwood number in dimensionless form are as follows: The Local values of the skin-friction, Nusselt number and Sherwood number for fixed parameters and are shown in tables (1) – (3), with the values of $\Pr = 0.72$, $Q = 1.0$, $Kr = 1.0$, $R = 1.0$, $M = 1.0$, $n = 0.5$, $S_0 = 1.0$, $Gr = 5.0$, $Gc = 5.0$, $t = 0.2$, $Sc = 0.57$, $Ec = 0.01$. Local skin-friction as function of the axial coordinate for different values of Soret number versus Grashof number. It is observed that with increasing values of Soret number the results increases, the Nusselt number shown for various values of radiation parameter versus Grashof numberwe observed that there is a fall down in Nusselt number with increasing radiation parameter, finally the Sherwood number for various values of chemical reaction parameter versus Grashof number, it is clear that an increasing values of chemical reaction parameter the results are decreases.

CONCLUSIONS:

The main conclusions of this study are as follows:

- Velocity profiles increases with increasing values of Grashof number, modified Grashof number, Soret number and time.
- The velocity profiles decreases with increasing values of magnetic field. So magnetic field can effectively be used to control the flow as well as chemical reaction parameter, heat source parameter, radiation parameter and Schmidt number.
- Temperature profiles decreases with increases in heat source parameter and radiation parameter.
- Concentration profiles decreases with increasing values of Schmidt number and chemical reaction parameter.
- The plate temperature is raised to T_w and the concentration level near the plate is also raised to C_w.

Table (1): Skin friction

S_0	τ
1.0	0.5412
2.0	0.6523
3.0	1.2532
4.0	1.5701

Table (2): Nusselt number

R	Nu
1.0	-2.6235
2.0	-3.1524
3.0	-3.5256
4.0	-4.6452

Table (3): Sherwood number

Kr	Sh
1.0	-0.64587
2.0	-0.89586
3.0	-0.95892
4.0	-1.52546

Appendix:

$m_1 = -\sqrt{R+Q},\ m_2 - \sqrt{KrSc},\ m_3 = -\sqrt{M}$

$m_4 = -\sqrt{Q+R+n\Pr}\ , m_5 = -\sqrt{(Kr+n)Sc}$

$m_6 = -\sqrt{M+n}\ , A_1 = -\dfrac{Gr}{m_2^2 - M}$

$A_2 = -\dfrac{GcB_1}{m_2{}^2 - M}\ , A_3 = -\dfrac{GcB_2}{m_4{}^2 - M}$

$A_4 = (t - A_1 - A_2 - A_3)\ , A_5 = -\dfrac{GrJ_{11}}{m_8^2 - M}$

$A_6 = -\dfrac{GrJ_1}{4m_6{}^2 - M},\ A_7 = -\dfrac{GrJ_2}{4m_2{}^2 - M}$

$A_8 = -\dfrac{GrJ_3}{4m_2{}^2 - M}\ , A_9 = -\dfrac{GrJ_4}{4m_4{}^2 - M}$

$A_{10} = -\dfrac{GrJ_5}{(m_2 + m_6)^2 - M}\ , A_{11} = -\dfrac{GrJ_6}{4m_2{}^2 - M}$

$A_{12} = -\dfrac{GrJ_7}{(m_2 + m_6)^2 - M}$

$A_{13} = -\dfrac{GrJ_8}{(m_4 + m_6)^2 - M}$

$A_{14} = -\dfrac{GrJ_9}{(m_2 + m_4)^2 - M}$

$A_{15} = -\dfrac{GrJ_{10}}{(m_2 + m_4)^2 - M}\ , A_{16} = -\dfrac{GcB_{14}}{m_{12}{}^2 - M}$

$A_{17} = -\dfrac{GcB_3}{m_8{}^2 - M}\ , A_{18} = -\dfrac{GcB_4}{4m_6{}^2 - M}$

$A_{19} = -\dfrac{GcB_5}{4m_2{}^2 - M}\ , A_{20} = -\dfrac{GcB_6}{4m_2{}^2 - M},$

$A_{21} = -\dfrac{GcB_7}{4m_4{}^2 - M}\ , A_{22} = -\dfrac{GcB_8}{(m_2 + m_8)^2 - M}$

$A_{23} = -\dfrac{GcB_9}{4m_2{}^2 - M}\ , A_{24} = -\dfrac{GcB_{10}}{(m_2 + m_6)^2 - M}$

$A_{25} = -\dfrac{GcB_{11}}{(m_4 + m_8)^2 - M}$

$A_{26} = -\dfrac{GcB_{12}}{(m_2 + m_4)^2 - M}$

$A_{27} = -\dfrac{GcB_{13}}{(m_2 + m_4)^2 - M}$

$$A_{28} = -\begin{pmatrix} A_5 + A_6 + A_7 + A_8 + A_9 + A_{10} + A_{11} \\ +A_{12} + A_{13} + A_{14} + A_{15} + A_{16} + A_{17} \\ +A_{18} + A_{19} + A_{20} + A_{21} + A_{22} + A_{23} \\ +A_{24} + A_{25} + A_{26} + A_{27} \end{pmatrix}$$

$J_1 = -\dfrac{m_6^2 A_4^2}{4m_6^2 - (R+Q)},$

$J_2 = -\dfrac{m_2^2 A_1^2}{4m_2^2 - (R+\phi)}$

$J_3 = -\dfrac{m_2^2 A_2^2}{4m_2^2 - (R+Q)},$

$J_4 = -\dfrac{m_4^2 A_3^2}{4m_4^2 - (R+Q)}$

$J_5 = -\dfrac{2m_2 m_6 A_1 A_4}{(m_2 + m_6)^2 - (R+Q)}$

$J_6 = -\dfrac{2m_2^2 A_1 A_2}{4m_2^2 - (R+Q)}$

$J_7 = -\dfrac{2m_2 m_6 A_2 A_4}{(m_2 + m_6)^2 - (R+Q)}$

$J_8 = -\dfrac{2m_4 m_6 A_3 A_4}{(m_4 + m_6)^2 - (R+Q)}$

$J_9 = -\dfrac{2m_2 m_4 A_1 A_3}{(m_2 + m_4)^2 - (R+Q)}$

$J_{10} = -\dfrac{2m_2 m_4 A_2 A_3}{(m_2 + m_4)^2 - (R+Q)}$

$$J_{11} = -\begin{pmatrix} J_1 + J_2 + J_3 + J_4 + J_5 \\ +J_6 + J_7 + J_8 + J_9 + J_{10} \end{pmatrix}$$

$$B_1 = -\frac{ScS_0}{m_2^2 - KrSc}\ B_2 = \left(1 - B_1\right),$$

$$B_3 = -\frac{ScS_0 m_8{}^2 J_{11}}{m_8{}^2 - ScKr}, B_4 = -\frac{4ScS_0 m_6{}^2 J_1}{4m_6{}^2 - ScKr}$$

$$B_5 = -\frac{4ScS_0 m_2{}^2 J_2}{4m_2{}^2 - ScKr}\ B_6 = -\frac{4ScS_0 m_2{}^2 J_3}{4m_2{}^2 - ScKr}$$

$$B_7 = -\frac{4ScS_0 m_4{}^2 J_4}{4m_4{}^2 - ScKr}$$

$$B_8 = -\frac{ScS_0\left(m_2 + m_8\right)^2 J_5}{\left(m_2 + m_8\right)^2 - ScKr}$$

$$B_9 = -\frac{4ScS_0 m_2{}^2 J_6}{4m_2{}^2 - ScKr}$$

$$B_{10} = -\frac{ScS_0\left(m_2 + m_6\right)^2 J_7}{\left(m_2 + m_6\right)^2 - ScKr}$$

$$B_{11} = -\frac{ScS_0\left(m_4 + m_6\right)^2 J_8}{\left(m_4 + m_6\right)^2 - KrSc}$$

$$B_{12} = -\frac{ScS_0\left(m_2 + m_4\right)^2 J_9}{\left(m_2 + m_4\right)^2 - KrSc}$$

$$B_{13} = -\frac{ScS_0\left(m_2 + m_4\right)^2 J_{10}}{\left(m_2 + m_4\right)^2 - KrSc}$$

$$B_{14} = -\begin{pmatrix} B_3 + B_4 + B_5 + B_6 + B_7 + B_8 \\ +B_9 + B_{10} + B_{11} + B_{12} + B_{13} \end{pmatrix}$$

REFERENCES

Chenna Kesavaiah D, Venkateswarlu B, Oluwole Daniel M: Radiative MHD Walter's Liquid-B flow past a semi-infinite vertical plate in the presence of viscous dissipation with a heat source, Engineering Transactions, 2021; 69(4): 373–401

Rajaiah M and Sudhakaraiah A: Unsteady MHD free convection flow past an accelerated vertical plate with chemical reaction and Ohmic heating, International Journal of Science and Research, 2015; 4 (2): 1503-1510

Rami Reddy G, Chenna Kesavaiah D, Venkata Ramana Musala and Bkaskara Reddy G: Hall effect on MHD flow of a viscoelastic fluid through porous medium over an infinite vertical porous plate with heat source, Indian Journal of Natural Sciences, 2021; 12 (68): 34975-34987

Chenna Kesavaiah D and Venkateswarlu B: Chemical reaction and radiation absorption effects on convective flows past a porous vertical wavy channel with travelling thermal waves, International Journal of Fluid Mechanics Research, 2020; 47 (2):153-169

Mallikarjuna Reddy B, D Chenna Kesavaiah D and Ramana Reddy G V: Radiation and diffusion thermo effects of viscoelastic fluid past a porous surface in the presence of magnetic field and chemical reaction with heat source, Asian Journal of Applied Sciences, 2019; 7 (5):597-607

Haranth Y and Sudhakaraiah A: Viscosity and Soret effects on unsteady hydromagnetic gas flow along an inclined plane, International Journal of Science and Research, (2015); 4 (2): 2650-2654

Srinathuni Lavanya and Chenna Kesavaiah D: Heat transfer to MHD free convection flow of a viscoelastic dusty gas through a porous medium with chemical reaction, International Journal of Pure and Applied Researches,2017; 3 (1):43 – 56

Mallikarjuna Reddy B, Chenna Kesavaiah D and Ramana Reddy G V: Effects of radiation and thermal diffusion on MHD heat transfer flow of a dusty viscoelastic fluid between two moving parallel plates, ARPN Journal of Engineering and Applied Sciences, 2018; 13 (22): 8863-8872

Chenna Kesavaiah D and Sudhakaraiah A: Effects of heat and mass flux to MHD flow in vertical surface with radiation absorption, Scholars Journal of Engineering and Technology, (2014);2 (2):219-225

Yeddala H, Sudhakaraiah A, Venkatalakshmi P and Sivaiah M: Finite difference solution for an MHD free convective rotating flow past an accelerated vertical plate, i-manager's Journal on Mathematics, 2016;5 (2): 34-44

Chenna Kesavaiah D, Satyanarayana P V, Sudhakaraiah A and Venkataramana S Natural convection heat transfer oscillatory flow of an elastico-viscous fluid from vertical plate, International Journal of Research in Engineering and Technology,2013; 2 (6): 959-966

Chenna Kesavaiah D, Satyanarayana P V: MHD and Diffusion Thermo effects on flow accelerated vertical plate with chemical reaction, Indian Journal of Applied Research, 2013; 3 (7): 310-314

Rajaiah M, Sudhakaraiah A, Varma S V K and Venkatalakshmi P: Chemical and Soret effect on MHD free convective flow past an accelerated vertical plate in presence of inclined magnetic field through porous medium, i-manager's Journal on Mathematics, 2015;4(1): 32-39

ChennaKesavaiah D, Satyanarayana P V and Venkataramana S: Radiation and Thermo - Diffusion effects on mixed convective heat and mass transfer flow of a viscous dissipated fluid over a vertical surface in the presence of chemical reaction with heat source, International Journal of Scientific Engineering and Technology, 2013; 2 (2): 56-72

Karunakar Reddy S, Chenna Kesavaiah D and Raja Shekar M N: MHD heat and mass transfer flow of a viscoelastic fluid past an impulsively started infinite vertical plate with chemical reaction, International Journal of Innovative Research in Science, Engineering and Technology,2013; 2 (4):973- 981

Rajaiah M and Sudhakaraiah A: Radiation and Soret effect on Unsteady MHD flow past a parabolic started vertical plate in the presence of chemical reaction with magnetic dissipation through a porous medium, International Journal of Science and Research, 2015; 4 (2):1608-1613

Damala Ch Kesavaiah, Satyanarayana P V and Sudhakaraiah A: Effects of radiation and free convection currents on unsteady Couette flow between two vertical parallel plates with constant heat flux and heat source through porous medium, International Journal of Engineering Research, 2013; 2 (2): 113-118

Rajaiah M, Sudhakaraiah A, Venkatalakshmi P and Sivaiah M: unsteady MHD free convective fluid flow past a vertical porous plate with Ohmic heating in the presence of suction or injection, International Journal of Mathematics and Computer Research, 2014; 2 (5): 428-453

ChKesavaiah D, Satyanarayana P V, Gireesh Kumar J and Venkataramana S: Radiation and mass transfer effects on moving vertical plate with variable temperature and viscous dissipation, International Journal of Mathematical Archive, 2012; 3 (8): 3028-3035

Satyanarayana P V,ChKesavaiah D and Venkataramana S: Viscous dissipation and thermal radiation effects on an unsteady MHD convection flow past a semi-infinite vertical permeable moving porous plate, International Journal of Mathematical Archive, 2011;2 (4): 476-487

ChKesavaiah D, Satyanarayana P V and Venkataramana S: Effects of the chemical reaction and radiation absorption on an unsteady MHD convective heat and mass transfer flow past a semi-infinite vertical permeable moving plate embedded in a porous medium with heat source and suction, Int. J. of Appl. Math. and Mech., 2011; 7 (1): 52-69

Chenna Kesavaiah D, Ramakrishna Goud T, Nookala Venu and Seshagiri Rao Y V. MHD effect on convective flow of dusty viscous fluid with fraction in a porous medium and heat generation, Journal of Mathematical Control Science and Applications, 2021; 7 (2): 393-404

Chenna Kesavaiah D, Ramakrishna Goud T and Seshagiri Rao Y V Nookala Venu. Radiation effect to MHD oscillatory flow in a channel filled through a porous medium with heat generation, Journal of Mathematical Control Science and Applications, 2019; 5 (2): 71-80

Chenna Kesavaiah D, Ramakrishna Goud T, Nookala Venu and Seshagiri Rao Y V. Analytical study on induced magnetic field with radiating fluid over a porous vertical plate with heat generation, Journal of Mathematical Control Science and Applications, 2017; 3 (2): 113-126

D. Chenna Kesavaiah, Mohd Ahmed, K. Venugopal Reddy, Dr. Nookala Venu (2022): Heat and mass transfer effects over isothermal infinite vertical plate of Newtonian fluid with chemical reaction,NeuroQuantology, Vol. 20 (20), pp. 957-967

D. Chenna Kesavaiah, K. Ramakrishna Reddy, Ch. Shashi Kumar, M. Karuna Prasad (2022): Influence of joule heating and mass transfer effects on MHD mixed convection flow of chemically reacting fluid on a vertical surface, NeuroQuantology, Vol. 20 (20), pp. 786-803

G. Bal Reddy, D. Chenna Kesavaiah, G. Bhaskar Reddy, Dr. Nookala Venu (2022): Anote on heat transfer of MHD Jeffrey fluid over a stretching vertical surface through porous plate,NEUROQUANTOLOGY, Vol. 20 (15), pp. 3472-3486

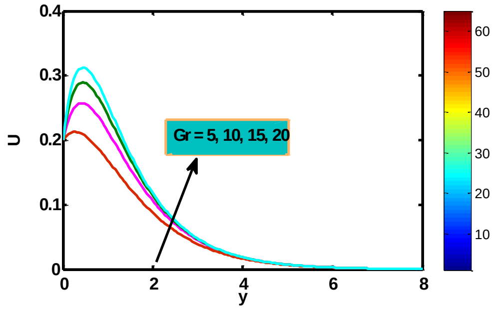

Fig. (1): Velocity Profiles for Gr

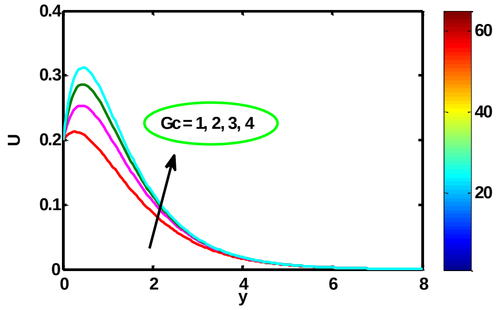

Fig. (2): Velocity Profiles for Gc

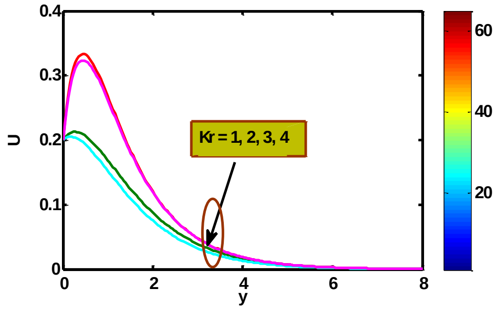

Fig. (3): Velocity Profiles for Kr

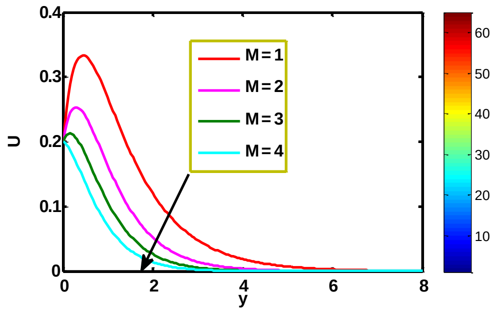

Fig. (4): Velocity Profiles for M

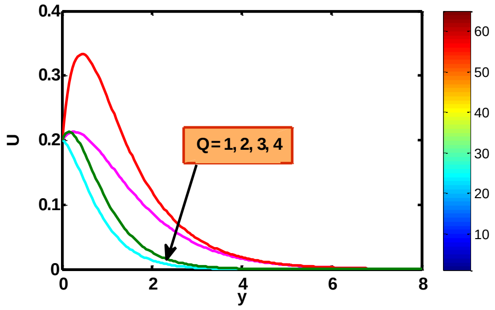

Fig. (5): Velocity Profiles for Q

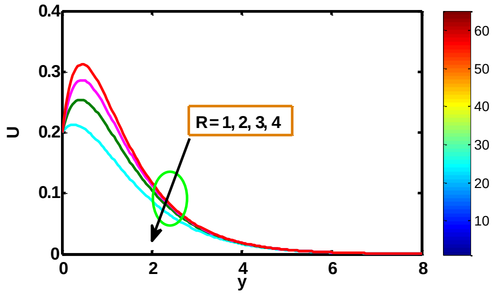

Fig. (6): Velocity profiles for R

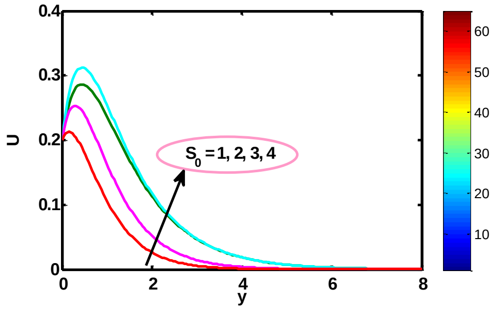

Fig. (7): Velocity Profiles for S_0

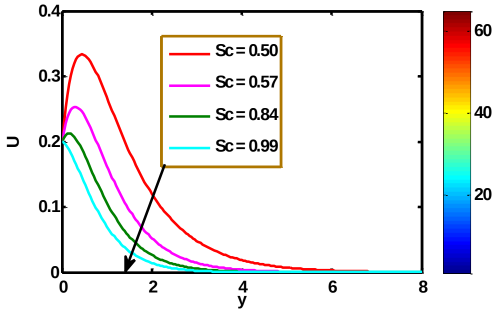

Fig. (8): Velocity Profiles for Sc

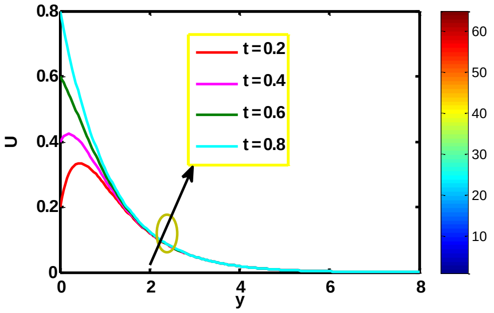

Fig. (9): Velocity Profiles for t

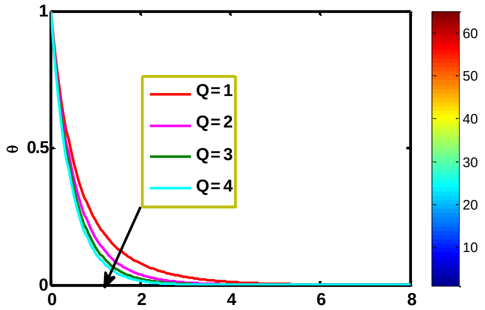

Fig. (10): Temperature Profiles for Q on y axis

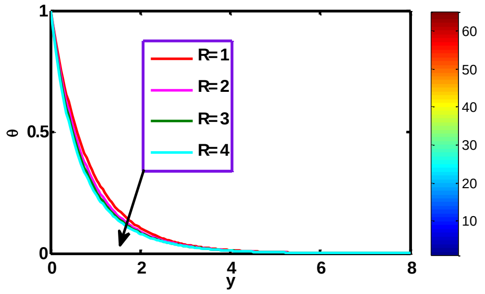

Fig. (11): Temperature Profiles for R

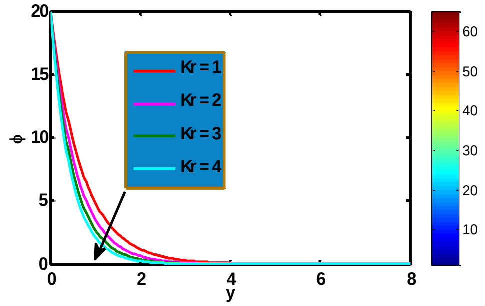

Fig. (12): Concentration Profiles for Kr

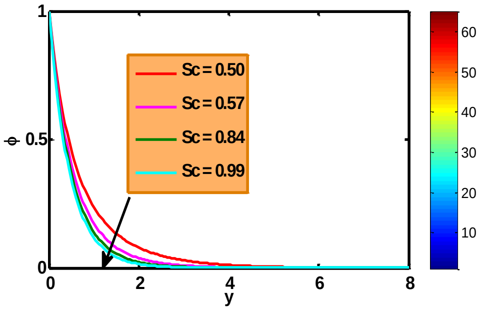

Fig. (13): Concentration Profiles for Sc

RADIATION AND MASS TRANSFER EFFECTS ON MHD MIXED CONVECTIVE FLOW FROM A VERTICAL SURFACE WITH HEAT SOURCE AND CHEMICAL REACTION

D. Chenna Kesavaiah[1], P. Govinda Chowdary[2], Ashfar Ahmed[3], B. Devika[4]

[1,2]Department of Basic Sciences & Humanities, Vignan Institute of Technology and Science, Deshmukhi (V), Pochampally (M), Yadadri-Bhuvanagiri (Dist), TS-508284, India

Email: chennakesavaiah@gmail.com & Email: chowdary.ratp@gmail.com

[3]Department of Mathematics, Malla Reddy Engineering College (Autonomous), Dulapally (V), Kompally (M), Medchal Malkajgiri (Dist), TS-500100, India
Email: ahmedashfaq02@gmail.com

[4]Department Mathematics, GITAM School of Science, GITAM (Deemed to be University), Bengaluru-562163, Karnataka, India
Email: dbalanna@gitam.edu

ABSTRACT

The effects of radiation and mass transfer on MHD mixed convection flow of a vertical plate with heat source/heat absorption and chemical reaction has been is discussed. The governing equations are transformed into a system of nonlinear ordinary differential equations by using suitable perturbation technique. Graphical results for the velocity, temperature and concentration profiles based on the numerical solutions are presented and discussed. We also discuss the effects of various parameters on the skin-friction coefficient and the rate of heat and mass transfer at the surface.

Keywords: Mass transfer, Radiation, MHD, Chemical reaction and Heat absorption

DOI Number: 10.14704/nq.2022.20.11.NQ66078 **NeuroQuantology 2022; 20(11): 821-835**

INTRODUCTION

For many mixed flows of practical importance in nature as well as in many engineering devices, the environment is thermally stratified. The discharge of hot fluid into enclosed regions often results in a stable thermal stratification with lighter fluid overlying denser fluid. The thermal stratification effects of heat transfer over a porous wedge are of interest in polymer extrusion processes, where the object, after passing through a die, enters the fluid for cooling below a certain temperature. Transport processes in porous media play a significant role in various applications, such as geothermal engineering, thermal insulation, energy conservation, petroleum industries, solid matrix heat exchangers, chemical catalytic reactors, and underground disposal of nuclear waste materials. In many transport processes in nature and in industrial applications, the heat and mass transfer with variable viscosity is a consequence of buoyancy effects caused by the diffusion of heat and chemical species. The study of such processes is useful for improving a number of chemical technologies, such as polymer production and food processing. In nature, the presence of pure air or water is impossible. Some foreign mass may be presented either naturally or mixed with air or water. A large amount of research work has been reported in this field. Particularly, the study of heat and mass transfer with chemical reactions is of considerable importance in the chemical and hydrometallurgical industries. In view of the above (Chenna Kesavaiah et. al, 2021) Radiative MHD Walter's Liquid-B flow past a semi-infinite vertical plate in the presence of viscous dissipation with a heat source, (Rami Reddy et. al, 2021): Hall effect on MHD flow of a viscoelastic fluid through porous medium over an infinite vertical porous plate with heat source, (Chenna Kesavaiah and Venkateswarlu, 2020) Chemical reaction and radiation absorption effects on convective flows past a porous vertical wavy channel with travelling thermal waves, (Mallikarjuna Reddy et. al. 2019) Radiation and diffusion thermo effects of viscoelastic fluid past a porous surface in the presence of magnetic field and chemical reaction with heat source, (Srinathuni Lavanya and Chenna Kesavaiah, 2017) Heat transfer to MHD free convection flow of a viscoelastic dusty gas through a porous medium with chemical reaction, (Mallikarjuna Reddy et. al. 2018): Effects of radiation and thermal diffusion on MHD heat transfer flow of a dusty viscoelastic fluid between two moving parallel plates, (Chenna Kesavaiah and Sudhakaraiah, 2014): Effects of heat and mass flux to MHD flow in vertical surface with radiation absorption, (Rajaiah et. al, 2015)Chemical and Soret effect on MHD free convective flow past an accelerated vertical plate in presence of inclined magnetic field through porous medium.

Convective flows with simultaneous heat and mass transfer under the influence of a magnetic field and chemical reaction arise in many transport processes both naturally and artificially in many branches of science and engineering applications. This phenomenon plays an important role in the chemical industry, power and cooling industry for drying, chemical vapour deposition on surfaces, cooling of nuclear reactors and petroleum industries. Changes in fluid density gradients may be caused by non-reversible chemical reaction in the system as well as by the differences in molecular weight between values of the reactants and the products. Some of the authors considered (Chenna Kesavaiah et. al, 2013) Natural convection heat transfer oscillatory flow of an elastico-viscous fluid from vertical plate, (Chenna Kesavaiah and Satyanarayana, 2013) MHD and Diffusion Thermo effects on flow accelerated vertical plate with chemical reaction, (Chenna Kesavaiah et. al, 2013) Radiation and Thermo - Diffusion effects on mixed convective heat and mass transfer flow of a viscous dissipated fluid over a vertical surface in the presence of chemical reaction with heat source, (Karunakar Reddy et. al, 2013) MHD heat and mass transfer flow of a viscoelastic fluid past an impulsively started infinite vertical plate with chemical reaction, Ch Kesavaiah et. al, 2013) Effects of radiation and free convection currents on unsteady Couette flow between two vertical parallel plates with constant heat flux and heat source through porous medium, (Rajaiah and Sudhakaraiah (2015) Unsteady MHD free convection flow past an accelerated vertical plate with chemical reaction and Ohmic heating, Ch Kesavaiah et. al. 2012): Radiation and mass transfer effects on moving vertical plate with variable temperature and viscous dissipation, Satyanarayana et. al.

2011): Viscous dissipation and thermal radiation effects on an unsteady MHD convection flow past a semi-infinite vertical permeable moving porous plate.

Chemical reactions can be modelled as either homogeneous or heterogeneous processes. This depends on whether they occur at an interface or as a single phase volume reaction. A homogeneous reaction is one that occurs uniformly throughout a given phase. On the other hand, a heterogeneous reaction takes place in a restricted area or within the boundary of a phase. In most cases of chemical reactions, the reaction rate depends on the concentration of the species itself. For example, the formation of smog is a first order homogeneous reaction. Consider the emission of nitrogen dioxide from automobiles and other smoke-stacks. This nitrogen dioxide reacts chemically in the atmosphere with unburned hydrocarbons (aided by sunlight) and produces peroxyacetylnitrate, which forms an envelop which is termed photo-chemical smog. Ch Kesavaiah et. al, 2011) Effects of the chemical reaction and radiation absorption on an unsteady MHD convective heat and mass transfer flow past a semi-infinite vertical permeable moving plate embedded in a porous medium with heat source and suction, (Haranth and Sudhakaraiah 2015) Viscosity and Soret effects on unsteady hydromagnetic gas flow along an inclined plane, Chenna Kesavaiah et. al, 2021) MHD effect on convective flow of dusty viscous fluid with fraction in a porous medium and heat generation, Rajaiah et. al. 2014) Unsteady MHD free convective fluid flow past a vertical porous plate with Ohmic heating In the presence of suction or injection, Chenna Kesavaiah et. al, 2019) Radiation effect to MHD oscillatory flow in a channel filled through a porous medium with heat generation, (Rajaiah and Sudhakaraiah 2015) Radiation and Soret effect on Unsteady MHD flow past a parabolic started vertical plate in the presence of chemical reaction with magnetic dissipation through a porous medium, Chenna Kesavaiah et. al, 2017): Analytical study on induced magnetic field with radiating fluid over a porous vertical plate with heat generation, (Beg et. al, 2009) Magnetohydrodynamic convection flow from a sphere to a non-Darcian porous medium with heat generation or absorption effects: network simulation.

The use of magnetic field that influences heat generation/absorption process in electrically conducting fluid flows has many engineering applications. For example, many metallurgical processes which involve cooling of continuous strips or filaments, which are drawn through a quiescent fluid. The properties of the final product depend to a great extent on the rate of cooling. The study of heat generation or absorption in moving fluids is important in problems dealing with chemical reactions and those concerned with dissociating fluids. Heat generation effects may alter the temperature distribution and this in turn can affect the particle deposition rate in nuclear reactors, electronic chips and semi conductor wafers. Although exact modelling of internal heat generation or absorption is quite difficult, some simple mathematical models can be used to express its general behaviour for most physical situations. Heat generation or absorption can be assumed to be constant, space-dependent or temperature-dependent. Aliakbar et. al, 2009) The influence of thermal radiation on MHD flow of Maxwellian fluids above stretching sheets, (Cortell, 2008) Effects of viscous dissipation and radiation on the thermal boundary layer over a nonlinearly stretching sheet, (Ibrahim et. al, 2008): Effect of the chemical reaction and radiation absorption on the unsteady MHD free convection flow past a semi infinite vertical permeable moving plate with heat source and suction, (Mahd, 2010): Effect of chemical reaction and heat generation or absorption on double-diffusive convection from a vertical truncated cone in a porous media with variable viscosity, (Makinde and Aziz, 2010): MHD mixed convection from a vertical plate embedded in a porous medium with a convective boundary condition, (Mohamed, 2009): Double-Diffusive convection-radiation interaction on unsteady MHD flow over a vertical moving porous plate with heat generation and Soret effects, (Pal and Talukdar 2010) Perturbation analysis of unsteady magnetohydrodynamic convective heat and mass transfer in a boundary layer slip flow past a vertical permeable plate with a thermal radiation and chemical reaction, (Patil and Kulkarni, 2008) Effects of chemical reaction on free convective flow of a polar fluid through a porous medium in the presence of internal heat generation. (Salem and Abd El-Aziz, 2008) Effect of Hall currents and chemical reaction on hydromagnetic flow of a stretching vertical surface with internal heat generation/absorption, (Samad and Mohebujjaman, 2009) MHD heat and mass transfer free convection flow among a vertical stretching sheet in presence of magnetic field with heat generation.

In spite of all the previous studies, the unsteady MHD mixed convection radiation and mass transfer for a heat generation/absorption with radiation absorption in the presence of a reacting species over a vertical plate has received little attention. Hence, the main objective of this chapter is to investigate the effects of radiation, chemical reaction, heat source/sink parameter of an electrically conducting fluid over vertical plate subjected to variable suction. The plate is assumed to be embedded in a uniform porous medium and moves with a constant velocity in the flow direction in the presence of a transverse magnetic field.

FORMULATION OF THE PROBLEM

We consider the mixed convection flow of an incompressible and electrically conducting viscous fluid and radiating fluid such that x^*-axis is taken along the plate in upwards direction and y^*-axis is normal to it. A transverse constant magnetic field is applied i.e. in the direction of y^*- axis. Since the motion is two dimensional and length of the plate is large therefore all the physical variables are independent of x^*. Let u^* and v^* be the components of velocity in x^* and y^* directions, respectively, taken along and perpendicular to the plate. The governing equations of continuity, momentum and energy for a flow of an electrically conducting fluid along a hot, non-conducting porous vertical plate in the presence of concentration and radiation is given by

$$\frac{\partial v^*}{\partial y^*} = 0 \tag{1}$$

$$v^* = -v_0 \text{ (Constant)} \tag{2}$$

$$\frac{\partial p^*}{\partial y^*} = 0 \Rightarrow p^* \text{ is independent of } y^* \tag{3}$$

$$\rho\left(v^*\frac{\partial u^*}{\partial y^*}\right) = \mu\frac{\partial^2 u^*}{\partial y^{*2}} + \rho g\,\beta(T^* - T_\infty) + \rho g\beta^*(C^* - C_\infty) - \sigma B_0^2 u^* \tag{4}$$

$$\rho C_p\left(v^*\frac{\partial T^*}{\partial y^*}\right) = k\frac{\partial^2 T^*}{\partial y^{*2}} - \frac{\partial q_r^*}{\partial y^*} - Q_0\left(T^* - T_\infty\right) + Q_l^*\left(C^* - C_\infty\right) \tag{5}$$

$$v^*\frac{\partial C^*}{\partial y^*}=D\frac{\partial^2 C^*}{\partial y^{*2}}-Kr^*\left(C^*-C_\infty\right) \qquad (6)$$

Here, g is the acceleration due to gravity, T^* the temperature of the fluid near the plate, T_∞ the free stream temperature, C^* concentration, β the coefficient of thermal expansion, k the thermal conductivity, P^* the pressure, C_p the specific heat of constant pressure, B_0 the magnetic field coefficient, μ viscosity of the fluid, q^* the radiative heat flux, ρ the density, σ the magnetic permeability of fluid V_0 constant suction velocity, ν the kinematic viscosity and D molecular diffusitivity.

The radiative heat flux q_r^* is given by equation (5) in the spirit of (Cogly et.al, 1968)

$$\frac{\partial q_r^*}{\partial y^*}=4(T^*-T_\infty)I \qquad (7)$$

where $I=\int_0^\infty K_{\lambda w}\frac{\partial e_{b\lambda}}{\partial T^*}d\lambda,\ K_{\lambda w}-$ is the absorption coefficient at the wall and $e_{b\lambda}$ is Planck's function, I is absorption coefficient

The boundary conditions are

$$\begin{aligned} &y^*=0\ :\ u^*=0,\quad T^*=T_w,\ C_\infty=C\\ &y^*\to\infty: u^*\to 0,\ T^*\to T_\infty,\ C^*\to C_\infty \end{aligned} \qquad (8)$$

Introducing the following non-dimensional quantities

$$u=\frac{u^*}{v_0},\ y=\frac{v_0 y^*}{\nu},\ M^2=\frac{B_0{}^2\nu^2\sigma}{v_0{}^2\mu},\ Sc=\frac{\nu}{D}$$

$$\theta=\frac{T^*-T_\infty}{T_w-T_\infty},\quad \Pr=\frac{\mu C_p}{k},\quad C=\frac{C^*-C_\infty}{C_w-C_\infty}$$

$$Gr=\frac{\rho\beta g\nu^2(T_w-T_\infty)}{v_0^3\mu},\qquad \phi=\frac{Q_0}{\rho C_p v_0^2} \qquad (9)$$

$$Gm=\frac{\rho\beta^* g(C-C_\infty)}{v_0^3},\qquad R=\frac{4\nu I}{\rho C_p v_0^2}$$

$$Kr=\frac{Kr^*\nu}{v_0^2},\qquad Q_l=\frac{Ql^*\left(C_w-C_\infty\right)\nu}{\rho C_p v_0^2\left(T_w-T_\infty\right)}$$

SOLUTION OF THE PROBLEM

In the equations (4), (5), (6) and (8), we get

$$\frac{\partial^2 u}{\partial y^2}+\frac{\partial u}{\partial y}-M^2u=-Gr\theta-GmC \qquad (10)$$

$$\frac{\partial^2\theta}{\partial y^2}+\Pr\frac{\partial\theta}{\partial y}-\left(R+\phi\right)\Pr\theta+Q_lC=0 \qquad (11)$$

$$\frac{\partial^2 C}{\partial y^2}+Sc\frac{\partial C}{\partial y}-ScKrC=0 \qquad (12)$$

where Gr is Grashof number, Gm is the mass Groshof number, $\Pr$ is Prandtl number, M is magnetic parameter, R is Radiation parameter, Sc is Schmidt number, ϕ is heat source parameter, Kr is Chemical reaction parameter, Q_l is the heat absorption parameter.

The corresponding boundary condition in dimensionless form are reduced to

$$\begin{aligned} &y=0:\quad u=0,\quad \theta=1,\ C=1\\ &y\to\infty: u\to 0,\ \theta\to 0, C\to 0 \end{aligned} \qquad (13)$$

The physical variables u,θ *and* C can be expanded in the power of $\left(\varepsilon<<1\right)$. This can be possible physically as ε for the flow of an incompressible fluid is always less than unity. This can be done by representing the velocity, temperature and concentration of the fluid in the neighborhood of the fluid in the neighborhood of the plate as

$$u = u_0(y) + \varepsilon e^{nt} u_1(y) + 0(\varepsilon^2) + ...$$
$$\theta = \theta_0(y) + \varepsilon e^{nt} \theta_1(y) + 0(\varepsilon^2) + ... \quad (14)$$
$$C = C_0(y) + \varepsilon e^{nt} C_1(y) + 0(\varepsilon^2) + ...$$

Using equation (14) in equations (10)–(12) and equating the coefficient of like powers of E, we have

$$u_0'' + u_0' - M^2 u_0 = -Gr\,\theta_0 - Gm\,C_0 \quad (15)$$
$$\theta_0'' + \Pr\,\theta_0' - (R+\phi)\Pr\theta_0 = -Q_l C_0 \quad (16)$$
$$C_0'' + Sc\,C_0' - KrC_0 = 0 \quad (17)$$
$$u_1'' + u_1' - M^2 u_1 = -Gr\,\theta_1 - Gm\,C_1 \quad (18)$$
$$\theta_1'' + \Pr\theta_1' - (R+\phi)\Pr\theta_1 = -Q_l C_1 \quad (19)$$
$$C_1'' + Sc\,C_1' - KrC_1 = 0 \quad (20)$$

The corresponding boundary conditions are

$$\begin{aligned} y = 0: &\quad u_0 = 0, u_1 = 0, \theta_0 = 1 \\ &\quad \theta_1 = 0, C_0 = 1, C_1 = 0 \\ y \to \infty: &\quad u_0 \to 0, u_1 \to 0, \theta_0 \to 0 \\ &\quad \theta_1 \to 0,\ C_0 \to 1, C_1 \to 0 \end{aligned} \quad (21)$$

Solving equations (15) to (20) with the help of (21), we get

$$u_0 = L_1 e^{m_2 y} + L_2 e^{m_6 y} + L_3 e^{m_2 y} + L_4 e^{m_{10} y}$$
$$\theta_0 = Z_1 e^{m_2 y} + Z_2 e^{m_6 y}$$
$$C_0 = e^{m_2 y}$$
$$u_1 = 0$$
$$\theta_1 = 0$$
$$C_1 = 0$$
$$u = L_1 e^{m_2 y} + L_2 e^{m_6 y} + L_3 e^{m_2 y} + L_4 e^{m_{10} y}$$
$$\theta = Z_1 e^{m_2 y} + Z_2 e^{m_6 y}$$
$$C = e^{m_2 y}$$

Skin – friction:

The skin-friction coefficient at the plate is given by

$$\tau = \left(\frac{\partial u}{\partial y}\right)_{y=0} = m_2 L_1 + m_6 L_2 + m_2 L_3 + m_{10} L_4$$

Heat Transfer:

The rate of heat transfer in terms of Nusselt number at the plate is given by

$$Nu = \left(\frac{\partial \theta}{\partial y}\right)_{y=0} = m_2 Z_1 + m_6 Z_2$$

Sherwood number

$$Sh = \left(\frac{\partial C}{\partial y}\right)_{y=0} = m_2$$

RESULTS AND DISCUSSION

Approximate solutions have been derived for the velocity, temperature field, concentration profiles, skin friction and Nusselt number using multi-parameter perturbation technique. The obtained results are discussed with the help of the graphs to observe the effect of various parameters like the thermal Grashof number (Gr), solutal Grashof number (Gm), the magnetic field parameter (M), absorption radiation parameter (Q_l), thermal radiation parameter (R), Prandtl number $(\Pr)$, heat absorption (ϕ), chemical reaction parameter (Kr) and Schmidt number (Sc) on the velocity, temperature and concentration profiles can be analyzed from Figures (1) - (17).

Velocity profiles:

Figure (1) shows the influence of thermal buoyancy force parameter Gr on the velocity. As can be seen from this figure, the velocity profile increases with increases in the values of the thermal buoyancy. We actually observe that the velocity overshoot in the boundary layer region. Buoyancy force acts like a favourable pressure gradient which accelerates the fluid within the boundary layer therefore the solutal buoyancy force parameter Gr has the same effect on the velocity as Gr. From figure (2) we observe that the effect of magnetic field (M) is results in decreasing velocity distribution across the boundary layer because of the application of transfer magnetic field will result a restrictive type force (Lorentz force) similar to drag force which tends to resist the fluid flow and thus reducing its velocity.

The effect of increasing the value of the absorption parameter (Q_l) on the velocity is shown in figure (3). We observe in this figure that increasing the value of the absorption of the radiation parameter due to increase in the buoyancy force accelerates the flow rate. Figure (4) depicts the effect of varying thermal radiation parameter (R) on the flow velocity. We observe that the thermal radiation enhances convective flow. Figure (5) illustrates the influence of heat absorption coefficient ϕ on the velocity. Physically, the presence of heat absorption (thermal sink) effect has the tendency in resulting in a net reduction in the flow velocity. This behaviour is seen from Figure (5) in which the velocity increases as ϕ increases. The hydrodynamic boundary layer decreases as the heat absorption effects increase. The velocity profiles for different values of solutal Grashof number (Gm) are described in figure (6). It is observed that an increasing in Gm leads to a rise in the values of velocity. In addition, the curves show that the peak value of velocity increases rapidly near the wall of the porous plate as soultal Grashof number increases, and then decays to the relevant free stream velocity. The influences of chemical reaction parameter (Kr) on the velocity profiles across the boundary layer are presented in Figure (7). We see that the velocity distribution across the boundary layer decreases with increasing of chemical reaction parameter. Figure (8) shows the velocity profiles across the boundary layer for different values of Prandtl number $(\Pr)$. The results show that the effect of increasing values of Pr results in a decreasing the velocity. For different values of the Schmidt number (Sc), the velocity profiles are plotted in figure (9). It is obvious that the effect of increasing values of Sc results in a decreasing velocity distribution across the boundary layer.

Temperature profiles:

The influence of heat absorption, Prandtl number, radiation absorption, thermal radiation chemical reaction parameter and Schmidt number on the temperature distribution is respectively, shown on figures (10) - (15). Figure (10) depicts the effects of heat absorption (ϕ) on the temperature distribution. It is observed that the boundary layer absorbs energy resulting in the temperature to fall considerably with increasing values of (ϕ). This is because when heat is absorbed, the buoyancy force decreases the temperature profile. Figure (11) temperature decreases with the increasing value of the Prandtl number (Pr). Prandtl number is very important for temperature profiles. It is clear that increasing Pr increases ϑ and the thickness of the thermal boundary layer. An increase Pr leads to a fall in the temperature. This emphasizes the influence of the injected flow in the cooling process. The effect of absorption of radiation parameter (Q_l) on the temperature profile is shown on figure (12). It is seen from this figure that the effect of absorption of radiation is to increase temperature in the boundary layer as the radiated heat is absorbed by the fluid which in turn increases the temperature of the fluid very close to the porous boundary layer and its effect diminishes far away from the boundary layer. From figure (13) we observe that the effect of thermal radiation (R) is to enhance heat transfer as thermal boundary layer thickness decreases with increase in the thermal radiation. We observe that the effect of radiation parameter (R) is to increase the temperature distribution in the thermal boundary layer. This is because the increase of *R* implies increasing of radiation in the thermal boundary layer, and hence increases the values of the temperature profiles in thermal boundary layer. Figure (14) is the graph of temperature profiles for different values of chemical reaction parameter (Kr). It can easily be seen that the thermal boundary layer release the energy which causes the temperature of the fluid to decreases with increase in the chemical reaction parameter (Kr). Lastly the effect of Schmidt number (Sc) on the temperature field is displayed in figure (15). We see that the temperature profiles decrease with increasing values of (Sc). This is because sucking decelerates fluid particles through the porous wall reducing the growth of the fluid boundary layer as well as thermal and concentration boundary layers.

Spices Concentration profiles:

The effect of reaction parameter Kr on the species concentration profiles for generative chemical reaction is shown in Figure 16. It is noticed for the graph that there is marked effect of increasing the value of the chemical reaction rate parameter Kr on concentration distribution in the boundary layer. It is clearly observed from this figure that the concentration of spices which is greater than 1 at the start of the boundary layer decreases slowly till it attains the minimum value of zero at the end of the boundary layer and this trend is seen for al the values of reaction parameter. Further, it is due to the fact that an increasing the value of the chemical reaction parameter Kr decreases the concentration of spices of the boundary layer. Schmidt number very important in concentration. Figure 17 gives the species concentration for different values of gasses like Sc it is observed that the concentration at all points in the flow field decreases exponentially with y and tends to zero as $y \to \infty$. A comparison of curves in the figure shows a decrease in concentration (C) with an increase in Sc Physically the increase of Sc means decrease of molecular diffusivity (D). That results in decrease of decrease of concentration boundary layer. Hence, the concentration of the species is higher for small values of Sc and lower for larger values of Sc. Figure (18) illustrates the effect of Prandtl number on the skin-friction of the fluid under consideration. As the Prandtl number decreases the ski-friction is found to be increasing. Figure (19) illustrates the effect of the Prandtl number on the Nusselt number of the fluid under consideration. As the Prandtl number increases, the Nusselt number decreases.

REFERENCES

Chenna Kesavaiah Damala, Venkateswarlu Bhumarapu, Oluwole Daniel Makinde. Radiative MHD Walter's Liquid-B flow past a semi-infinite vertical plate in the presence of viscous dissipation with a heat source, Engineering Transactions, 2021; 69 (4): 373–401

Rami Reddy G, Chenna Kesavaiah D, Venkata Ramana Musala and Bkaskara Reddy G. Hall effect on MHD flow of a viscoelastic fluid through porous medium over an infinite vertical porous plate with heat source, Indian Journal of Natural Sciences, 2021; 12 (68): 34975-34987

Chenna Kesavaiah D and Venkateswarlu B. Chemical reaction and radiation absorption effects on convective flows past a porous vertical wavy channel with travelling thermal waves, International Journal of Fluid Mechanics Research, 2020; 47 (2): 153-169

Mallikarjuna Reddy B, Chenna Kesavaiah D and Ramana Reddy G V. Radiation and diffusion thermo effects of viscoelastic fluid past a porous surface in the presence of magnetic field and chemical reaction with heat source, Asian Journal of Applied Sciences, 2019; 7 (5), 597-607

Srinathuni Lavanya and Chenna Kesavaiah D. Heat transfer to MHD free convection flow of a viscoelastic dusty gas through a porous medium with chemical reaction, International Journal of Pure and Applied Researches, 2017; 3 (1): 43 - 56

Mallikarjuna Reddy B, Chenna Kesavaiah D and Ramana Reddy G V. Effects of radiation and thermal diffusion on MHD heat transfer flow of a dusty viscoelastic fluid between two moving parallel plates, ARPN Journal of Engineering and Applied Sciences, 2018; 13 (22): 8863-8872

Chenna Kesavaiah D and Sudhakaraiah A. Effects of heat and mass flux to MHD flow in vertical surface with radiation absorption, Scholars Journal of Engineering and Technology, 2014; 2(2): 219-225

Rajaiah M, Sudhakaraih A, Varma S V K, and Venkatalakshmi P. Chemical and Soret effect on MHD free convective flow past an accelerated vertical plate in presence of inclined magnetic field through porous medium. i-manager's Journal on Mathematics, 2015; 4(1): 32-39

Chenna Kesavaiah D, Satyanarayana P V, Sudhakaraiah A, Venkataramana S. Natural convection heat transfer oscillatory flow of an elastico-viscous fluid from vertical plate, International Journal of Research in Engineering and Technology, 2013; 2 (6): 959-966

Chenna Kesavaiah D and Satyanarayana P V. MHD and Diffusion Thermo effects on flow accelerated vertical plate with chemical reaction, Indian Journal of Applied Research, 2013; 3 (7). 310-314

Chenna Kesavaiah D, P V Satyanarayana and S Venkataramana (2013): Radiation and Thermo - Diffusion effects on mixed convective heat and mass transfer flow of a viscous dissipated fluid over a vertical surface in the presence of chemical reaction with heat source, International Journal of Scientific Engineering and Technology, 2013; 2 (2), pp: 56-72

Karunakar Reddy S, D Chenna Kesavaiah D and Raja Shekar M N. MHD heat and mass transfer flow of a viscoelastic fluid past an impulsively started infinite vertical plate with chemical reaction, International Journal of Innovative Research in Science, Engineering and Technology, 2013; 2 (4): 973- 981

Damala Ch Kesavaiah, Satyanarayana and P V and Sudhakaraiah A. Effects of radiation and free convection currents on unsteady Couette flow between two vertical parallel plates with constant heat flux and heat source through porous medium, International Journal of Engineering Research, 2013; 2 (2): 113-118

Rajaiah M and Sudhakaraiah A. Unsteady MHD free convection flow past an accelerated vertical plate with chemical reaction and Ohmic heating, International Journal of Science and Research, 2015; 4 (2): 1503-1510

Ch Kesavaiah D, Satyanarayana P V, Gireesh Kumar J and Venkataramana S. Radiation and mass transfer effects on moving vertical plate with variable temperature and viscous dissipation, International Journal of Mathematical Archive, 2012; 3 (8): 3028-3035

Satyanarayana P V, Ch Kesavaiah D and Venkataramana S. Viscous dissipation and thermal radiation effects on an unsteady MHD convection flow past a semi-infinite vertical permeable moving porous plate, International Journal of Mathematical Archive, 2011; 2(4): 476-487

Ch Kesavaiah D, Satyanarayana P V and Venkataramana S. Effects of the chemical reaction and radiation absorption on an unsteady MHD convective heat and mass transfer flow past a semi-infinite vertical permeable moving plate embedded in a porous medium with heat source and suction, Int. J. of Appl. Math and Mech, 2011; 7 (1): 52-69

Haranth Y and Sudhakaraiah A. Viscosity and Soret effects on unsteady hydromagnetic gas flow along an inclined plane, International Journal of Science and Research, 2015; 4 (2): 2650-2654

Chenna Kesavaiah D, Ramakrishna Goud T, Nookala Venu, Seshagiri Rao Y V. MHD effect on convective flow of dusty viscous fluid with fraction in a porous medium and heat generation, Journal of Mathematical Control Science and Applications, 2011; 7 (2): 393-404

Rajaiah M, Sudhakaraiah A, Venkatalakshmi P and Sivaiah M. Unsteady MHD free convective fluid flow past a vertical porous plate with Ohmic heating In the presence of suction or injection, International Journal of Mathematics and Computer Research, 2014; 2 (5): 428-453

Chenna Kesavaiah D, Ramakrishna Goud T, Seshagiri Rao Y V, Nookala Venu (2019): Radiation effect to MHD oscillatory flow in a channel filled through a porous medium with heat generation, Journal of Mathematical Control Science and Applications, 2019;5 (2): 71-80

Rajaiah M and Sudhakaraiah A. Radiation and Soret effect on Unsteady MHD flow past a parabolic started vertical plate in the presence of chemical reaction with magnetic dissipation through a porous medium, International Journal of Science and Research, 2015; 4 (2): 1608-1613

Chenna Kesavaiah D, Ramakrishna Goud T, Nookala Venu, Seshagiri Rao Y V. Analytical study on induced magnetic field with radiating fluid over a porous vertical plate with heat generation, Journal of Mathematical Control Science and Applications, 2017; 3 (2): 113-126

Beg O A, Zueco J, Bhargava R and Takhar H S. Magnetohydrodynamic convection flow from a sphere to a non-Darcian porous medium with heat generation or absorption effects: network simulation, International Journal of Thermal Sciences, 2009; 48: 913-921

Aliakbar V, Alizadeh-Pahlavan A and Sadeghy K. The influence of thermal radiation on MHD flow of Maxwellian fluids above stretching sheets, Communications in Nonlinear Science and Numerical Simulation, Commun., 2109; 14 (3): 79-794.

Cortell R. Effects of viscous dissipation and radiation on the thermal boundary layer over a nonlinearly stretching sheet. Phys., Lett., A, 2008; 372: 631-636

F S Ibrahim, Elaiw A M and A A Bakar A A. Effect of the chemical reaction and radiation absorption on the unsteady MHD free convection flow past a semi infinite vertical permeable moving plate with heat source and suction. Communications in Nonlinear Science and Numerical Simulation, 2008; 13: 1056-1066

Mahd A. Effect of chemical reaction and heat generation or absorption on double-diffusive convection from a vertical truncated cone in a porous media with variable viscosity. International Communications in Heat and Mass Transfer, 201; 37: 548-554

Makinde O D and Aziz A. MHD mixed convection from a vertical plate embedded in a porous medium with a convective boundary condition. International Journal of Thermal Sciences, 2010; 49: 1813-1820

Mohamed R A. Double-Diffusive convection-radiation interaction on unsteady MHD flow over a vertical moving porous plate with heat generation and Soret effects, Applied Mathematical Sciences, 2009; 3 (13): 629-651.

A Pal and B Talukdar. Perturbation analysis of unsteady magnetohydrodynamic convective heat and mass transfer in a boundary layer slip flow past a vertical permeable plate with a thermal radiation and chemical reaction, Communications in Nonlinear Science and Numerical Simulation, 2010; 15: 1813-1830.

Patil P M and Kulkarni P S. Effects of chemical reaction on free convective flow of a polar fluid through a porous medium in the presence of internal heat generation. International Journal of Thermal Sciences, 2008; 47: 1043-1054

Salem A M and Abd El-Aziz M. Effect of Hall currents and chemical reaction on hydromagnetic flow of a stretching vertical surface with internal heat generation/absorption, Applied Mathematical Modelling, 2008; 32: 1236-1254.

Samad M A and Mohebujjaman M. MHD Heat and Mass Transfer Free Convection Flow among a Vertical Stretching Sheet in Presence of Magnetic Field with Heat Generation. Research Journal of Applied Science, Engineering and Technology, 2009; 1 (3): 98-106

Cogley A C, Vincenty W G and Gilles S E. AIAAJ, 1968; 6: 551

APPENDIX

$$m_2 = m_4 = -\left(\frac{Sc + \sqrt{Sc^2 + 4KrSc}}{2}\right),$$

$$m_6 = m_8 = -\left(\frac{\Pr + \sqrt{\Pr^2 + 4(R+\phi)\Pr}}{2}\right)$$

$$m_{10} = m_{12} = -\left(\frac{1+\sqrt{1+4M^2}}{2}\right)$$

$$Z_1 = -\frac{Q_l}{m_2^{\,2} + \Pr m_2 - (R+\phi)\Pr}$$

$$Z_2 = 1 - Z_1$$

$$L_1 = -\frac{Gm}{m_2^{\,2} + m_2 - M^2}$$

$$L_2 = -\frac{GrZ_2}{m_6^{\,2} + m_6 - M^2}$$

$$L_3 = -\frac{GrZ_1}{m_2^{\,2} + m_2 - M^2}$$

$$L_4 = -(L_1 + L_2 + +L_3)$$

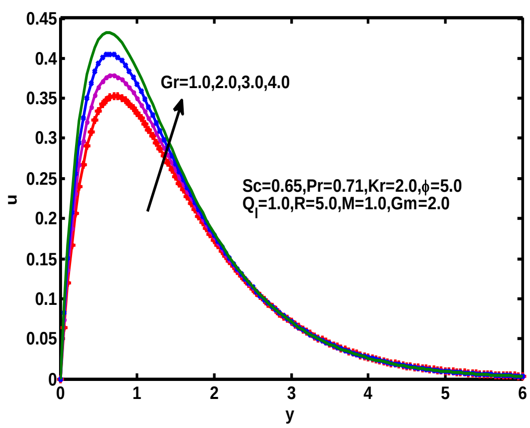

Figure 1: Velocity profiles for different values of Gr

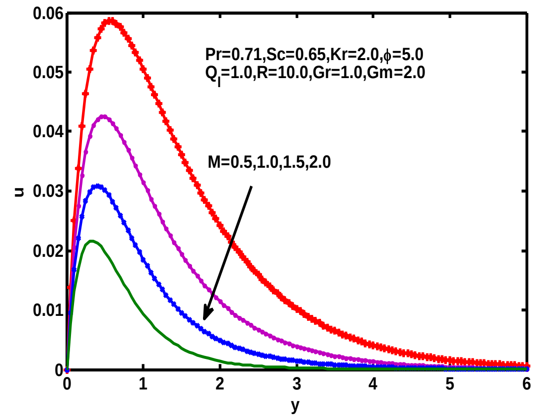

Figure 2: Velocity profiles for different values of M

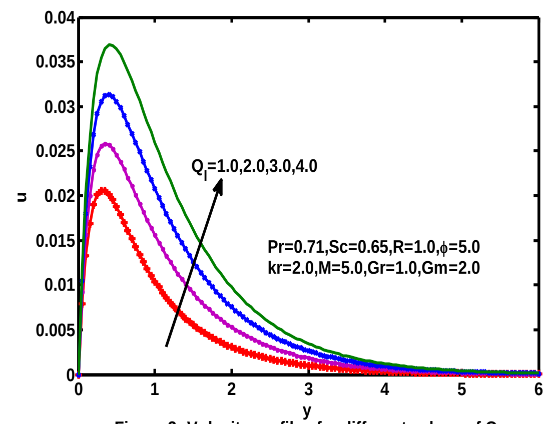

Figure 3: Velocity profiles for different values of Q_l

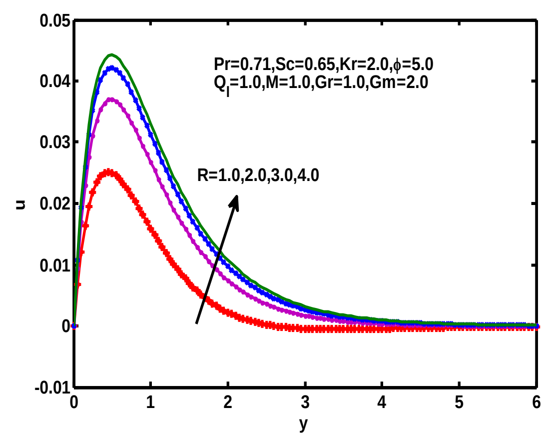

Figure 4: Velocity profiles for different values of R

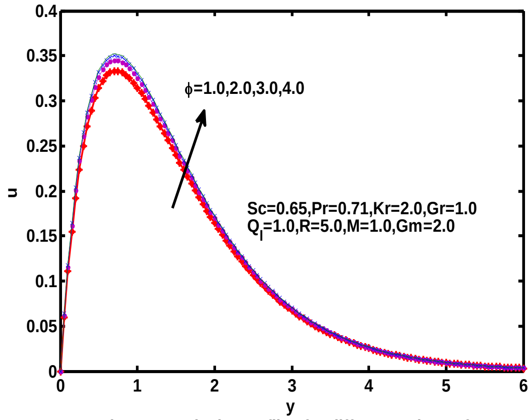

Figure 5: Velocity profiles for different values of ϕ

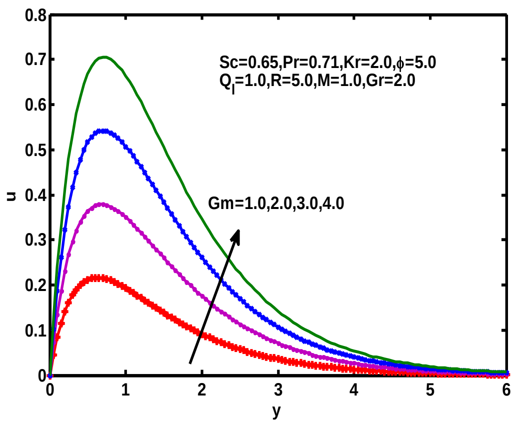

Figure 6:Velocity profiles for different values of Gm

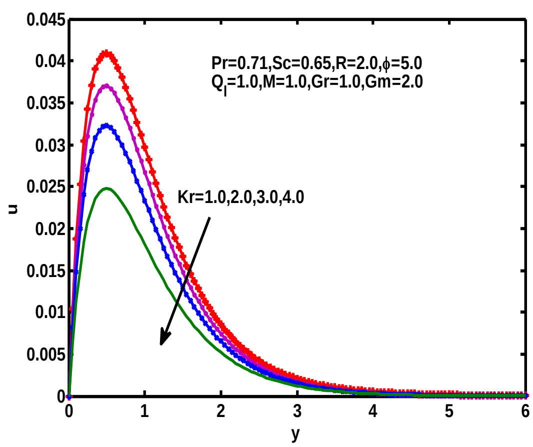

Figure 7: Velocity profiles for different values of Kr

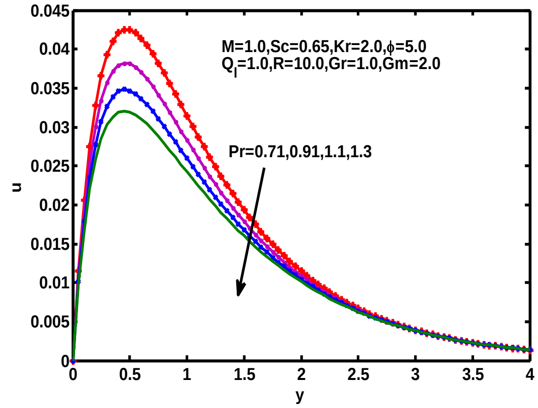

Figure 8: Velocity profiles for different values of Pr

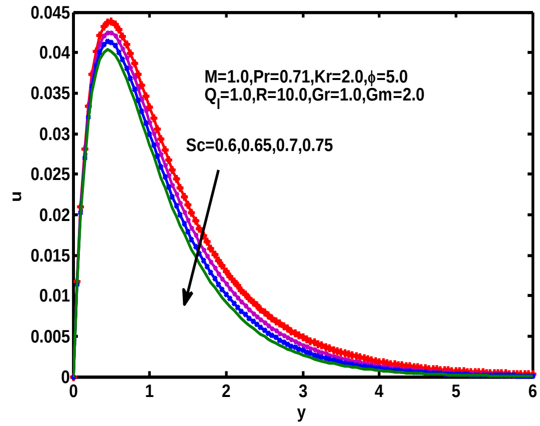

Figure 9: Velocity profiles for different values of Sc

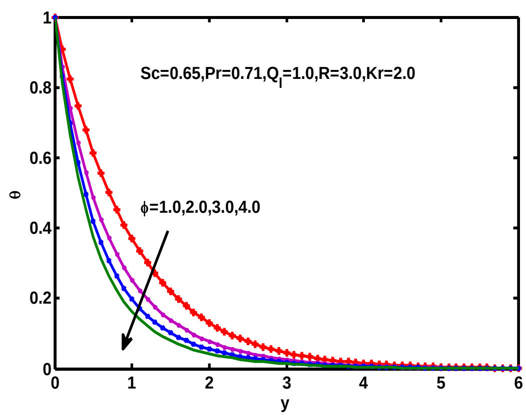

Figure 10: Temperature profiles for different values of ϕ

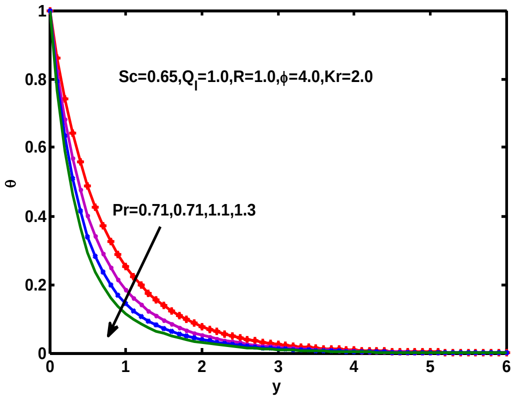

Figure 11: Temperature profiles for different values of Pr

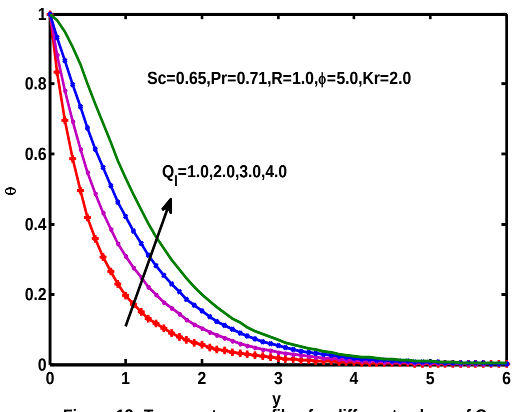

Figure 12: Temperature profiles for different values of Q_l

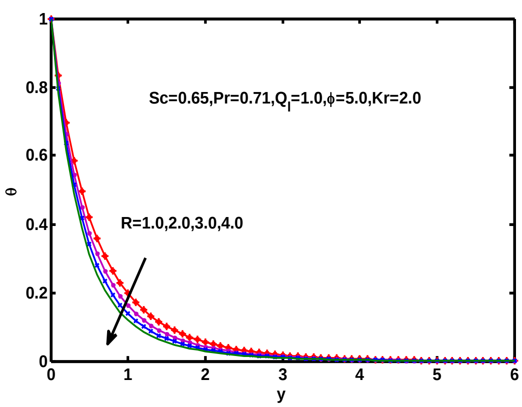

Figure 13: Temperature profiles for different values of R

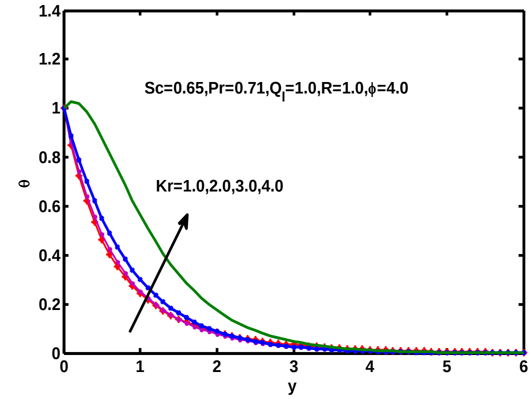

Figure 14: Temperature profiles for different values of Kr

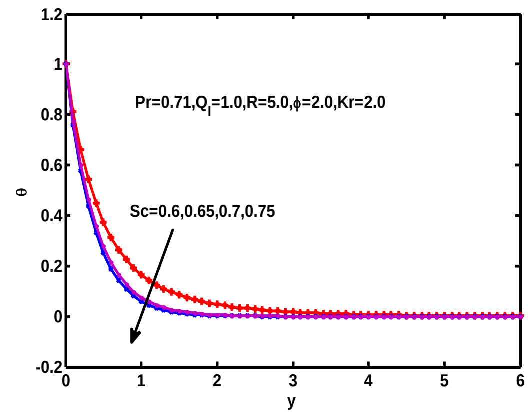

Figure 15: Temperature profiles for different values of Sc

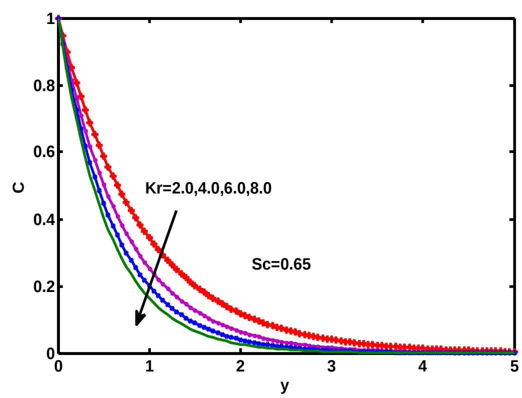

Figure 16: Concentration profiles for different values of Kr

eISSN 1303-5150

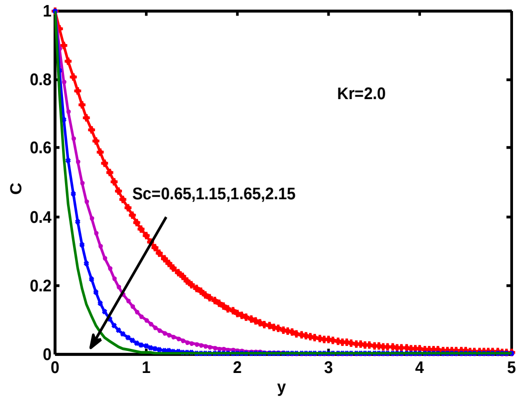

Figure 17: Concentration profiles for different values of Sc

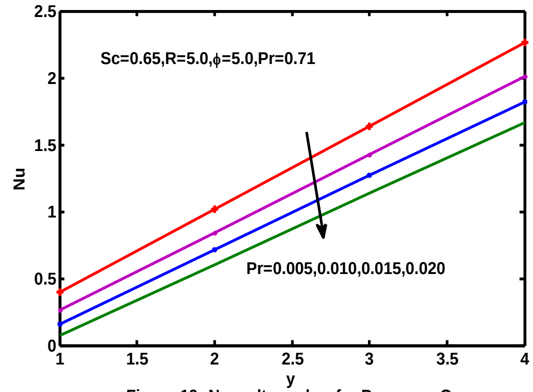

Figure 19: Nusselt number for Pr versus Q_l

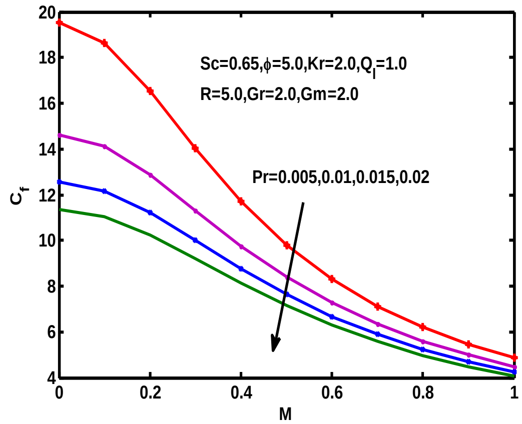

Figure 18: Skin friction for different values of Pr versus M

CHEMICAL REACTION AND MHD EFFECTS ON FREE CONVECTION FLOW OF A VISCOELASTIC DUSTY GAS THROUGH A SEMI INFINITE PLATE MOVING WITH RADIATIVE HEAT TRANSFER

D. Chenna Kesavaiah[1], P. Govinda Chowdary[2], M. Chitra[3], Dr. Nookala Venu[4]

[1, 2]Department of Basic Sciences & Humanities, Vignan Institute of Technology and Science, Deshmukhi (V), Pochampally (M), Yadadri-Bhuvanagiri (Dist), TS-508284, India
Email: chennakesavaiah@gmail.com & Email: chowdary.ratp@gmail.com

[3]Department of Mathematics, Malla Reddy Engineering College (Autonomous), Dulapally (V), Kompally (M), Medchal Malkajgiri (Dist), TS-500100, India
Email: muddasanichitra@gmail.com

[4]Department of Electronics and Communication Engineering,
Balaji Institute of Technology and Science (Autonomous), Narsampet, Warangal, TS -506331, India
Email: venunookala@gmail.com

ABSTRACT

The present paper is concerned with the study of MHD free convective flow of a viscoelastic (Kuvshinski type) dusty gas through a porous medium induced by the motion of a semi-infinite flat plate under the influence of radiative heat transfer moving with velocity decreasing exponentially with time and chemical reaction taking into an account. The expressions for velocity distribution of a dusty gas and dust particles, concentration profile and temperature field are obtained. The effect of Schmidt number (Sc), Magnetic field parameter (M), Chemical reaction parameter (Kr) and Radiation parameter (N) on velocity distribution of dusty gas and dust particles, concentration and temperature distribution are discussed graphically.

Keywords: Chemical reaction, MHD, Free convection, Radiative heat transfer, Dusty Gas
DOI Number: 10.14704/nq.2022.20.8.NQ44962 **NeuroQuantology 2022; 20(8): 9425-9434**

INTRODUCTION

The study of radiation in thermal engineering is of great interest for industry point of view. Many processes in thermal engineering areas occur at high temperature and radiative heat transfer becomes very important for the design of pertinent equipment. Nuclear power plants, gas turbines and the various propulsion devices for air craft, missiles, satellites and space vehicles are example of such engineering areas. In view of above some authors observed (Aboeldahab Emad 2000) has been studied radiation effect on heat transfer in an electrically conducting fluid at a stretching surface with uniform free stream, (Cortell 2006) shown a note on flow and heat transfer of a viscoelastic fluid over a stretching sheet, (Chenna Kesavaiah et. al. 2021) motivated study on radiative MHD Walter's Liquid-B flow past a semi-infinite vertical plate in the presence of viscous dissipation with a heat source, (Datti et. al. 2004) depicted MHD viscoelastic fluid flow over a non- isothermal stretching sheet, (Rami Reddy et.al. 2021) explained on hall effect on MHD flow of a viscoelastic fluid through porous medium over an infinite vertical porous plate with heat source, (Chenna Kesavaiah and B Venkateswarlu 2020) expressed in detailed on chemical reaction and radiation absorption effects on convective flows past a porous vertical wavy channel with travelling thermal waves, (Mallikarjuna Reddy et. al. 2019) has been considered the radiation and diffusion thermo effects of viscoelastic fluid past a porous surface in the presence of magnetic field and chemical reaction with heat source, (Srinathuni Lavanya and Chenna Kesavaiah 2017) observed that heat transfer to MHD free convection flow of a viscoelastic dusty gas through a porous medium with chemical reaction, (Mallikarjuna Reddy et. al. 2018) motivated study on effects of radiation and thermal diffusion on MHD heat transfer flow of a dusty viscoelastic fluid between two moving parallel plates, (Chenna Kesavaiah et. al. 2013) intended their plane in radiation and Thermo - Diffusion effects on mixed convective heat and mass transfer flow of a viscous dissipated fluid over a vertical surface in the presence of chemical reaction with heat source.

As for as dusty viscoelastic fluid is concerned, it is one of the multiphase flows. The particular importances in various engineering disciplines are heat transfer and flow attitude of viscoelastic fluid among parallel plates. In the aspects of these uses, the study of the perspective of boundary layers has been channeled to viscoelastic fluid. (Karunakar Reddy et.al. 2013) MHD heat and mass transfer flow of a viscoelastic fluid past an impulsively started infinite vertical plate with chemical reaction, (Ch Kesavaiah et. al. 2012) Radiation and mass transfer effects on moving vertical plate with variable temperature and viscous dissipation, (Satyanarayana et. al. 2011) Viscous dissipation and thermal radiation effects on an unsteady MHD convection flow past a semi-infinite vertical permeable moving porous plate, (Ch Kesavaiah et. al. 2011) Effects of the chemical reaction and radiation absorption on an unsteady MHD convective heat and mass transfer flow past a semi-infinite vertical permeable moving plate embedded in a porous medium with heat source and suction, (Edmundo et. al. 1998) Numerical model for radiative heat transfer analysis in arbitrary shaped axisymmetric enclosures with gases media, (Chenna Kesavaiah and Satyanarayana 2013) MHD and Diffusion Thermo effects on flow accelerated vertical plate with chemical reaction, (El-Hakiem 2000) MHD oscillatory flow on free convection-radiation through a porous medium with constant suction velocity, (Hossain et. al. 1999) The effect of radiation in free convection from a porous vertical plate, (Jae Hyun Park and Seung Wook Baek 2002): Non gray thermal radiation effects on the sound wave propagation in gasparticle two-phase medium, (Chenna Kesavaiah et. al. 2013) Natural convection heat transfer oscillatory flow of an elastico-viscous fluid from vertical plate, (Kee Soo Han et. al. 1991): Analysis of heat transfer in a pipe carrying two-phase gas-particle suspension, (Gretler and Regenfelder 2002) Similarity solution for laser-driven shock waves in a dust-laden gas with internal heat transfer effects.

The physical significance of Newtonian heating is discussed broadly in the literature. According to Newton's law of cooling, the rate of heat loss of a body varies directly to the distinction of temperature between the surrounding and the body. Newtonian heating performs a very decisive role in heat exchanger designing, associate heat transfer about fins, radiation of solar, heating and cooling processes of buildings, and in petroleum industries. The matter of the convection of heat in the cylinders invites a lot of researchers globally due to the enormous number of applications in wires coating and polymer fiber spinning. (Chenna Kesavaiah and Sudhakaraiah 2014) Effects of heat and mass flux to MHD flow in vertical surface with radiation absorption, (Makinde and Chinyoka 2010) Numerical investigation of transient heat transfer to hydromagnetic channel flow with radiative heat and convective cooling, (Mansour 1997) Forced convection-radiation interaction heat transfer in boundary layer over a flat plate submerged in a porous medium, (Ch Kesavaiah et. al. 2013) Effects of radiation and free convection currents on unsteady Couette flow between two vertical parallel plates with constant heat flux and heat source through porous medium, (Mbeledogu et. al. 2007) Unsteady MHD free convection flow of a compressible fluid past a moving vertical plate in the presence of radiative heat transfer, (Murthy et. al. 2004) Combined radiation and mixed convection from a vertical wall with suction/ injection in a non-darcy porous medium, (Muthukumarswamy and Kumar Senthil 2004) Heat and Mass transfer effect on moving vertical plate in the presence of thermal radiation, (Raptis et. al. 2004) Effect of thermal radiation on MHD flow,(Saffman 1962) On the stability of laminar flow of a dusty gas, (Seddeek and Abdelmeguid 2006) Effect of radiation and thermal diffusivity on heat transfer over a stretching surface with variable heat flux,

(Siddheshwar and Mahabaleswar 2005) Effects of radiation and heat source on MHD flow of a viscoelastic liquid and heat transfer over a stretching sheet, (Sujit Kumar Khan 2006): Heat transfer in a viscoelastic fluid flow over a stretching surface with heat Source/sink, suction/blowing and radiation, (Varshney Ram Prakash 2004) MHD free convection flow of a viscoelastic dusty gas through a porous medium induced by the motion of a semi- infinite flat plate moving with velocity decreasing exponentially with time, (Chenna Kesavaiah et. al. 2021) MHD effect on convective flow of dusty viscous fluid with fraction in a porous medium and heat generation.

In the present paper a proper sign for the normal stress modulus $\left(i.e.\alpha_1 \geq 0\right)$ is used and, as we will see the effects of viscous dissipation, uniform transverse magnetic field, internal heat generation/absorption and thermal radiation are included in the energy equation.

FORMULATION OF THE PROBLEM

Let the dusty gas to confine in the space $y > 0$ and the flow is produced by the motion of a semi – infinite flat plate moving with velocity $ve^{\lambda^2 t}$ in $x-$direction. The $x-$axis is taken along the plate and y is measured normal to it. Since the plate is semi infinite, all the physical quantities will be function of y and t only.

The gas is optically thin with a relatively low density and radiative heat flux is given by

$$\frac{\partial q}{\partial y} = 4\alpha^2\left(T_0 - T\right) \qquad (1)$$

Where *u* and *v* are the gas and the particle velocity, ν is the kinematic coefficient of viscosity of the gas, K_0 is the Stoke's resistance coefficient N_0 is the number density of the dust particles which is taken to be constant, *ρ* is the density of gas, *m* is the mass of a dust particle, K_T is the thermal conductivity and C_p is the specific heat at constant pressure.

According to Saffman,1 the equation of motion of dusty gas and dust particles along the $x-$axis with the body forces due to applied magnetic field, porous medium, concentration and radiation are given by:

$$\left(1+\eta\frac{\partial}{\partial t}\right)\frac{\partial u}{\partial t}=\nu\frac{\partial^2 u}{\partial y^2}+\frac{K_0N_0}{\rho}\left(1+\eta\frac{\partial}{\partial t}\right)(v-u)-\left(\frac{\sigma B_0}{\rho}+\frac{\nu}{K}\right)\left(1+\eta\frac{\partial}{\partial t}\right)u+g\beta(T-T_0)+g\beta'(C-C_0) \quad (2)$$

$$\frac{\partial v}{\partial t}=\frac{K_0}{m}(v-u) \quad (3)$$

$$\frac{\partial T}{\partial t}=\frac{K_T}{\rho C_p}\frac{\partial^2 T}{\partial y^2}-4\alpha^2(T_0-T) \quad (4)$$

$$\frac{\partial C}{\partial t}=D\frac{\partial^2 C}{\partial y^2}-Kr'(C-C_0) \quad (5)$$

Boundary conditions are:

$$\left.\begin{array}{l}u=ve^{\lambda^2 t},T=ve^{\lambda^2 t}\\ C=ve^{\lambda^2 t}\end{array}\right\}\quad at\quad y=0 \quad (6)$$
$$u\to 0,T\to 0,C\to 0\ \ at\quad y\to\infty$$

Solution of the problem

Let us introduce the non- dimensional variables,

$$u^*=\frac{u}{\nu},\qquad v^*=\frac{v}{\nu},\quad y^*=\frac{y}{(\nu\tau)^{\frac{1}{2}}}$$

$$t^*=\frac{t}{\nu},T=\frac{T-T_0}{T_\infty-T_0},C=\frac{C-C_0}{C_\infty-C_0}$$

The dimensionless forms of the equations (2)–(5) respectively are:

$$\left[1+\alpha_1\left(f+M+\frac{1}{K_1}\right)\right]\frac{\partial u}{\partial t}=\frac{\partial^2 u}{\partial y^2}+\alpha_1 f\frac{\partial v}{\partial t}+f(v-u)-Mu-\frac{1}{K_1}u+GrT+GmC \quad (7)$$

$$\frac{\partial v}{\partial t}=(v-u) \quad (8)$$

$$\frac{\partial T}{\partial t}=\frac{1}{Pe}\frac{\partial^2 T}{\partial y^2}-\frac{N^2}{Pe}T \quad (9)$$

$$\frac{\partial^2 C}{\partial y^2}-Sc\frac{\partial C}{\partial t}-KrSc=0 \quad (10)$$

where f is the mass-concentration of dust particles, M is the magnetic field parameter, N is radiation parameter, Gr is the thermal Grashof number, Gm is modified Grashof number α_1 is the visco-elastic parameter, Pe is the Peclet number, K_1 is the permeability parameter, N is radiation parameter , Kr is the Chemical reaction parameter and Sc is Schmidt number.

$$f=\frac{mN_0}{\rho},\quad \alpha_1=\frac{\eta}{\tau},\quad \frac{1}{K_1}=\frac{\nu\tau}{K},\quad M=\frac{m\sigma B_0{}^2}{K_0\rho}$$

$$Gm=\frac{\beta' g\tau(C-C_0)}{\nu},\qquad Gr=\frac{\beta g\tau(T-T_0)}{\nu}$$

$$Pe=\frac{\nu\rho C_p}{K_T},N^2=\frac{4\alpha^2\nu\tau}{K_T},Kr=\frac{Kr'\nu}{U_0{}^2},Sc=\frac{\nu}{D}$$

Boundary conditions (6) reduced to

$$\left.\begin{array}{l}u=ve^{\lambda^2 t},T=ve^{\lambda^2 t}\\ C=ve^{\lambda^2 t}\end{array}\right\}\quad at\quad y=0 \quad (11)$$
$$u\to 0,T\to 0,C\to 0\quad at\quad y\to\infty$$

Let the solutions of various profiles are:

$$u=F(y)e^{-\lambda^2 t} \quad (12)$$

$$v=G(y)e^{-\lambda^2 t} \quad (13)$$

$$T=H(y)e^{-\lambda^2 t} \quad (14)$$

$$C=W(y)e^{-\lambda^2 t} \quad (15)$$

The boundary conditions (11) reduced to:

$$\begin{array}{ll}H=1,F=1,W=1 & at\quad y=0\\ H\to 0,F\to 0,W\to 0 & at\ y\to\infty\end{array} \quad (16)$$

The equations (7)–(10) becomes with (12)–(15):

$$F''+\left(\alpha_2\lambda^2-M-\frac{1}{K_1}-f\right)F+(1-\alpha_1\lambda^2)fG=-GrH-GmH \quad (17)$$

$$(1-\lambda^2)G=F \quad (18)$$

$$H'' + \left(N^2 + \lambda^2 Pe\right)H = 0 \qquad (19)$$

$$W'' + \lambda^2 ScW - KrSc = 0 \qquad (20)$$

Eliminating G from (17) and (18)

$$F'' + n^2 F = -GrH - GmW \qquad (21)$$

The equations (19) and (20) give:

$$W = e^{-izy}$$

$$H = e^{-isy}$$

Equation (21) with boundary conditions (16) gives:

$$F = e^{-iny} + \frac{Gr\left(e^{-iny} - e^{-isy}\right)}{n^2 - s^2} - \frac{Gm\left(e^{-iny} - e^{-isy}\right)}{n^2 - s^2} \qquad (22)$$

Equation (18) with (22);

$$F = \frac{1}{\left(1-\lambda^2\right)}\left[\begin{array}{l} e^{-iny} + \dfrac{Gr\left(e^{-iny} - e^{-isy}\right)}{n^2 - s^2} \\ -\dfrac{Gm\left(e^{-iny} - e^{-isy}\right)}{n^2 - s^2} \end{array}\right] \qquad (23)$$

The velocity of dusty gas for equation (12) is:

$$u = \left[\begin{array}{l} e^{-iny} + \dfrac{Gr\left(e^{-iny} - e^{-isy}\right)}{n^2 - s^2} \\ -\dfrac{Gm\left(e^{-iny} - e^{-isy}\right)}{n^2 - s^2} \end{array}\right] e^{-\lambda^2 t} \qquad (24)$$

The velocity of dust particles with (13) is:

$$v = \frac{1}{\left(1-\lambda^2\right)}\left[\begin{array}{l} e^{-iny} \\ +\dfrac{Gr\left(e^{-iny} - e^{-isy}\right)}{n^2 - s^2} \\ -\dfrac{Gm\left(e^{-iny} - e^{-isy}\right)}{n^2 - s^2} \end{array}\right] e^{-\lambda^2 t} \qquad (25)$$

The concentration profile is:

$$C = e^{-izy}.e^{-\lambda^2 t}$$

The temperature field for dusty gas is:

$$\theta = e^{-isy}.e^{-\lambda^2 t}$$

Real part of *u* is:

$$u = \left[\begin{array}{l} \cos ny + \dfrac{Gr}{n^2 - s^2}\left(\cos ny - \cos sy\right) \\ -\dfrac{Gm}{n^2 - s^2}\left(\cos ny - \cos zy\right) \end{array}\right] e^{-\lambda^2 t}$$

Similarly, the real part of velocity of dust particle is:

$$v = \frac{1}{\left(1-\lambda^2\right)}\left[\begin{array}{l} \cos ny \\ +\dfrac{Gr}{n^2 - s^2}\left(\cos ny - \cos sy\right) \\ -\dfrac{Gm}{n^2 - s^2}\left(\cos ny - \cos zy\right) \end{array}\right] e^{-\lambda^2 t}$$

Real part of *C* is:

$$C = Cos\left(zy\right)e^{-\lambda^2 t}$$

Real part of ϑ is:

$$\theta = Cos\left(sy\right)e^{-\lambda^2 t}$$

RESULTS AND DISCUSSION

To examine the different behaviours of both the velocities, we need to inspect and understand the above-plotted graphs. These graphs give us the other physical conduct of different parameters like Schmidt number $\left(Sc\right)$, magnetic field parameter $\left(M\right)$ and radiation parameter $\left(N\right)$, chemical reaction parameter $\left(Kr\right)$ on velocity distribution of dusty gas and dust particles, concentration and temperature field is mainly emphasized. Analysis of each graphical representation is discussed separately. From figure (1) and (2) show that the concentration profiles for different values of Schmidt number and Chemical reaction parameter; it is observed that concentration decreases for increasing value of Schmidt number and Chemical reaction parameter; also time concentration is decreases for increasing value of y.

Temperature profile:

From figure (3) it is clear that the behaviour of radiation parameter N with temperature. This figure shows that there is a direct variation between radiation and temperature. It is the fact that by increasing the radiation parameter N, the kinetic energy is increasing and therefore decrease occurs in the temperature of the fluid.

Velocity profile for dusty gas:

Figures (4) – (6) represents that the velocity for dusty gas for various values of magnetic parameter, radiation parameter and Schmidt number for the fixed values of the $\lambda = 2.0,\ \alpha_1 = 1.0, \alpha_2 = 2.0,\ f = 1.0,$ $K^{-1} = 0.1, Gr = 10.0,\ Gm = 5.0,\ Sc = 0.6,$ $Pe = 0.71, t = 1.0$. Figures (4) show that the velocity for the dusty gas increases for increasing values of radiation number. The relation between magnetic parameter factor and fluid and dust particles velocities can be observed in figures (5), respectively. It is revealed from these graphs that the magnetic parameter is the decreasing function of the velocities of dust particles and fluid. Physically, greater magnetic parameter values enhance the drag forces called the Lorentz forces, which retards the flow. It is true that the fractional force is motivated to increase by increasing the magnetic parameter values, which contributes to confront the fluid flow and thus reduces its velocity; but the reverse effect observed from figure (6) for increasing values of Schmidt number.

Velocity profile for dust particles:

From figures (7) – (9) we observed that velocity of dust particles for fixed values of the $\lambda = 2.0,\ \alpha_1 = 1.0, \alpha_2 = 2.0,\ f = 1.0,$ $K^{-1} = 0.1, Gr = 10.0,\ Gm = 5.0,\ Sc = 0.6,$ $Pe = 0.71,\ t = 1.0$. From figure (7), we observed that the velocity of the dust particles increases for increasing value of magnetic parameter. Figure (8) corresponds to the behaviour of radiations parameter N on the velocity profiles of fluid and dust particles respectively. According to these graphs by increasing the radiation parameter the dust particles and fluid velocity are also increases. It is obvious that by increasing the radiation the temperature of the fluid increases which brings increase in kinetic energy and this why the dust particles and fluid velocity increases.

CONCLUSIONS

The results for temperature field, concentration profile and velocity distribution for both dusty gas and dust particles have been discussed graphically to clarify the impact of magnetic field parameter, radiation number etc. we conclude the following remarks:

- Concentration is decreasing for increasing values of Schmidt number and chemical reaction parameter.
- Temperature is decreasing for increasing values of radiation number.
- Velocity for both the dusty gas and dust particle is increasing for increasing values of radiation number and magnetic field parameter while decreasing for increasing values of Schmidt number.

APPENDIX

$$z = -\left(\frac{\lambda^2 Sc + \sqrt{\left(\lambda^4 Sc^2 + 4KrSc\right)}}{2}\right)$$

$$s = \sqrt{N^2 + \lambda^2 \mathrm{P}e}, \alpha_2 = \left\{1 + \alpha_1\left(M + \frac{1}{K_1} + f\right)\right\}$$

$$n^2 = \left[\frac{\alpha_2\lambda^2 - \lambda^2\left(\alpha_2 - \alpha_1 f + M + f + K^{-1}\right) + M + K^{-1}}{\lambda^2 - 1}\right]$$

REFRENCES

Aboeldahab Emad M: Radiation effect on heat transfer in an electrically conducting fluid at a stretching surface with uniform free stream, J. Phys. D., Appl. Phys., 2000; 33: 31-80

Cortell R: A note on flow and heat transfer of a viscoelastic fluid over a stretching sheet, Int. J. Non- Linear Mech., 2006; 41: 78–85.

Chenna Kesavaiah Damala, Venkateswarlu Bhumarapu, Oluwole Daniel Makinde: Radiative MHD Walter's Liquid-B flow past a semi-infinite vertical plate in the presence of viscous dissipation with a heat source, Engineering Transactions, 2021; 69 (4): 373–401

Datti P S, Prasad K V and Subhas Abel M, Ambuja Joshi: MHD viscoelastic fluid flow over a non- isothermal stretching sheet, Int. J. Eng. Sci., 2004; 42: 935–946

Rami Reddy G, Chenna Kesavaiah D, Venkata Ramana Musala and Bkaskara Reddy G: Hall effect on MHD flow of a viscoelastic fluid through porous medium over an infinite vertical porous plate with heat source, Indian Journal of Natural Sciences, 2021; 12 (68), 34975-34987

D Chenna Kesavaiah and B Venkateswarlu (2020): Chemical reaction and radiation absorption effects on convective flows past a porous vertical wavy channel with travelling thermal waves, International Journal of Fluid Mechanics Research, 2020; 47 (2): 153-169

Mallikarjuna Reddy B, D Chenna Kesavaiah D and Ramana Reddy G V (2019): Radiation and diffusion thermo effects of viscoelastic fluid past a porous surface in the presence of magnetic field and chemical reaction with heat source, Asian Journal of Applied Sciences, 2019; 7 (5): 597-607

Srinathuni Lavanya and D Chenna Kesavaiah: Heat transfer to MHD free convection flow of a viscoelastic dusty gas through a porous medium with chemical reaction, International Journal of Pure and Applied Researches, 2017; 3(1), 43 - 56

Mallikarjuna Reddy B, D Chenna Kesavaiah D and Ramana Reddy G V: Effects of radiation and thermal diffusion on MHD heat transfer flow of a dusty viscoelastic fluid between two moving parallel plates, ARPN Journal of Engineering and Applied Sciences, 2018; 13 (22), 8863-8872

Chenna Kesavaiah D, P V Satyanarayana P V and Venkataramana S: Radiation and Thermo - Diffusion effects on mixed convective heat and mass transfer flow of a viscous dissipated fluid over a vertical surface in the presence of chemical reaction with heat source, International Journal of Scientific Engineering and Technology, 2013; 2 (2): 56-72

Karunakar Reddy S, Chenna Kesavaiah D and Raja Shekar M N: MHD heat and mass transfer flow of a viscoelastic fluid past an impulsively started infinite vertical plate with chemical reaction, International Journal of Innovative Research in Science, Engineering and Technology, 2013; 2 (4): 973- 981

Ch Kesavaiah D, Satyanarayana P V, Gireesh Kumar J and Venkataramana S: Radiation and mass transfer effects on moving vertical plate with variable temperature and viscous dissipation, International Journal of Mathematical Archive, 2012; 3 (8), 3028-3035

Satyanarayana P V, Ch Kesavaiah D and S Venkataramana S: Viscous dissipation and thermal radiation effects on an unsteady MHD convection flow past a semi-infinite vertical permeable moving porous plate, International Journal of Mathematical Archive, 2011; 2(4): 476-487

Ch Kesavaiah D, Satyanarayana P V and Venkataramana S: Effects of the chemical reaction and radiation absorption on an unsteady MHD convective heat and mass transfer flow past a semi-infinite vertical permeable moving plate embedded in a porous medium with heat source and suction, Int. J. of Appl. Math and Mech., 2011; 7 (1): 52-69

Edmundo M Nune and Mohammad and Naragh H N: Numerical model for radiative heat transfer analysis in arbitrary shaped axisymmetric enclosures with gases media, Numerical Heat Transfer, 1998; 33 (5): 495 – 513

Chenna Kesavaiah D and Satyanarayana P V: MHD and Diffusion Thermo effects on flow accelerated vertical plate with chemical reaction, Indian Journal of Applied Research, 2013; 3 (7): 310-314

El-Hakiem M A: MHD oscillatory flow on free convection-radiation through a porous medium with constant suction velocity, J. of magnetism and magnetic materials, 2000; 220: 271 – 276

Hossain M A, Alim M A and Rees D A: The effect of radiation in free convection from a porous vertical plate, *Int. J. Heat and Mass transfer*, 1999; 42: 131

Jae Hyun Park and Seung Wook Baek: Non gray thermal radiation effects on the sound wave propagation in gasparticle two-phase medium, Journal of Quantitative Spectroscopy and Radiative Transfer, 2002; 73 (2-5), 397-407

Chenna Kesavaiah D, Satyanarayana P V, Sudhakaraiah A, Venkataramana S: Natural convection heat transfer oscillatory flow of an elastico-viscous fluid from vertical plate, International Journal of Research in Engineering and Technology, 2013; 2 (6): 959-966

Kee Soo Han, Hyung Jin Sung and Myung K yoon Chung: Analysis of heat transfer in a pipe carrying two-phase gas-particle suspension, International Journal of Heat and Mass transfer, 1991; 34 (1): 69-78

Gretler W and Regenfelder R: Similarity solution for laser-driven shock waves in a dust-laden gas with internal heat transfer effects, Fluid Dynamics Research, 2002; 30 (5): 293-313

Chenna Kesavaiah D and Sudhakaraiah A: Effects of heat and mass flux to MHD flow in vertical surface with radiation absorption, Scholars Journal of Engineering and Technology, 2014; 2(2): 219-225

Makinde O D and Chinyoka T: Numerical investigation of transient heat transfer to hydromagnetic channel flow with radiative heat and convective cooling, Communications in Nonlinear Science and Numerical Simulations, 2010; 15: 3919-3930

Mansour M A: Forced convection-radiation interaction heat transfer in boundary layer over a flat plate submerged in a porous medium, Applied Mechanical Engineering, 1997; 3: 405 – 413

Ch Kesavaiah D, Satyanarayana P V and Sudhakaraiah A: Effects of radiation and free convection currents on unsteady Couette flow between two vertical parallel plates with constant heat flux and heat source through porous medium, International Journal of Engineering Research, 2013; 2 (2): 113-118

Mbeledogu U I, Amakiri A R C and Ogulu A: Unsteady MHD free convection flow of a compressible fluid past a moving vertical plate in the presence of radiative heat transfer, Int. Journal of Heat and mass transfer, 2007; 50: 1668-1674

Murthy P V S N, Mukherjee S, Srinivasacharya D, Krishna P V S S R: Combined radiation and mixed convection from a vertical wall with suction/ injection in a non-darcy porous medium, Acta Mechanica, 2004; 168: 145 – 156

Muthukumarswamy R and Kumar Senthil G: Heat and Mass transfer effect on moving vertical plate in the presence of thermal radiation, Theoretical Applied Mechanics, 2004; 3: 35

Raptis A, Perdikis C and Takhar H S: Effect of thermal radiation on MHD flow, Appl. Math. Comput., 2004; 153: 645–649

Saffman P G: On the stability of laminar flow of a dusty gas, Journal of fluid mechanics, 1962; 13 (1): 120-129

Seddeek M A and Abdelmeguid M S: Effect of radiation and thermal diffusivity on heat transfer over a stretching surface with variable heat flux, Phys. Lett., 2006; A 348: 172–179

Siddheshwar P G, Mahabaleswar U S: Effects of radiation and heat source on MHD flow of a viscoelastic liquid and heat transfer over a stretching sheet, Int. J. Non-Linear Mech., 2005; 40: 807–820

Sujit Kumar Khan: Heat transfer in a viscoelastic fluid flow over a stretching surface with heat Source/sink, suction/blowing and radiation, Int. J. Heat Mass Transfer, 2006; 49: 628–639

Varshney N K and Ram Prakash: MHD free convection flow of a visco elastic dusty gas through a porous medium induced by the motion of a semi- infinite flat plate moving with velocity decreasing exponentially with time, Acta Ciencia Indica (India), 2004; XXX (2): 467-473

Chenna Kesavaiah D, Ramakrishna Goud T, Nookala Venu and Seshagiri Rao Y V: MHD effect on convective flow of dusty viscous fluid with fraction in a porous medium and heat generation, Journal of Mathematical Control Science and Applications, 2021; (7) 2: 393-404

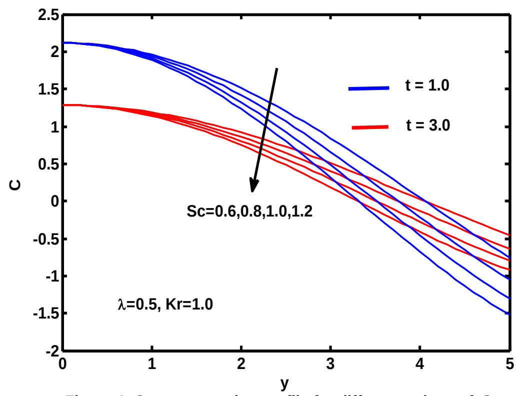

Figure 1. Concenentration profile for different values of Sc.

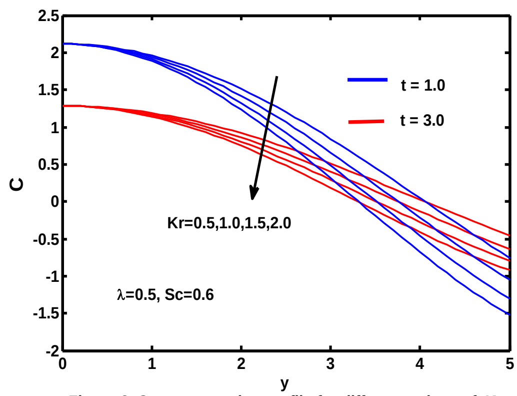

Figure 2. Concenentration profile for different values of Kr

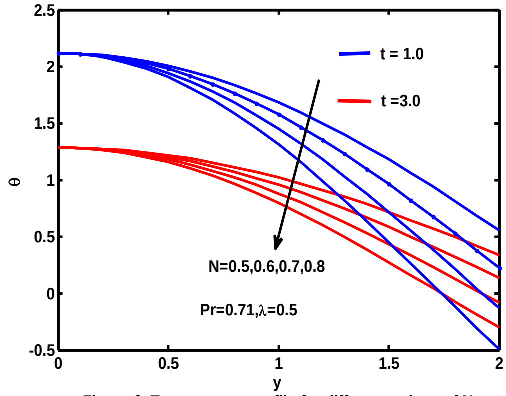

Figure 3. Temperature profile for diffrenet values of N

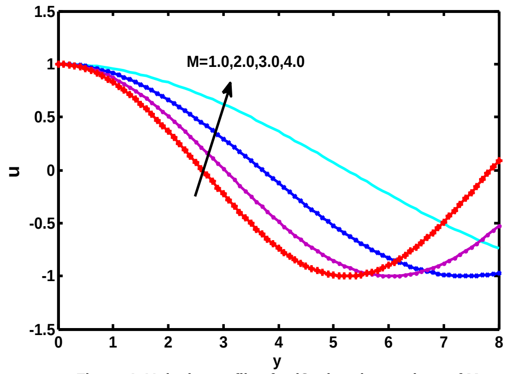

Figure 4: Velocity profiles for (Gas) various values of M

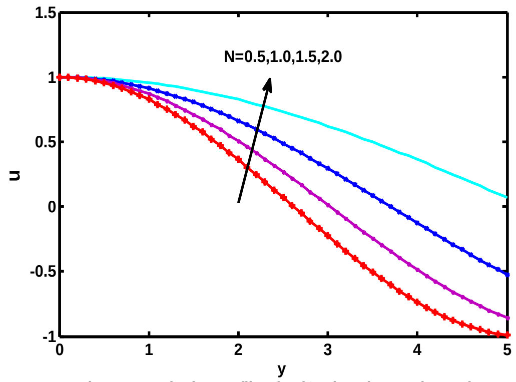

Figure 5: Velocity profiles for (Gas) various values of N

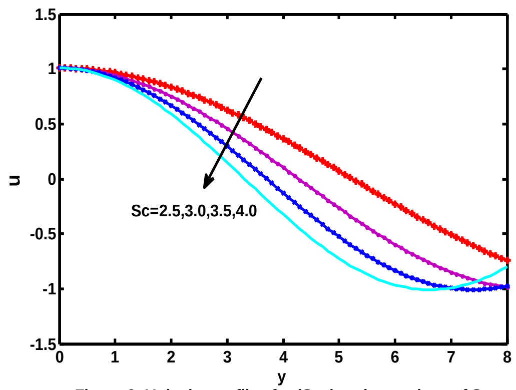

Figure 6: Velocity profiles for (Gas) various values of Sc

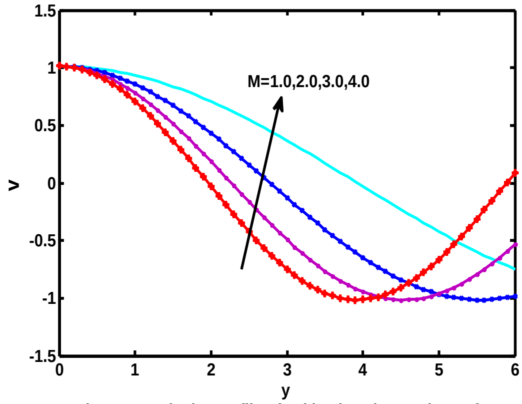

Figure 7: Velocity profiles for (dust) various values of M

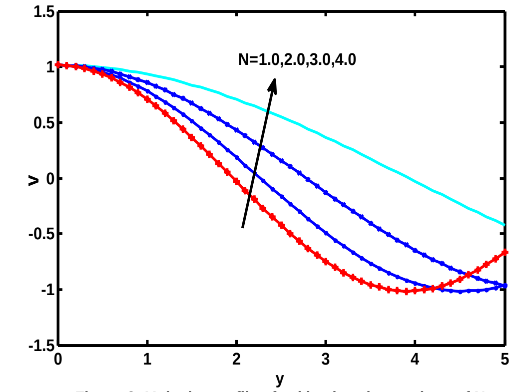

Figure 8: Velocity profiles for (dust) various values of N

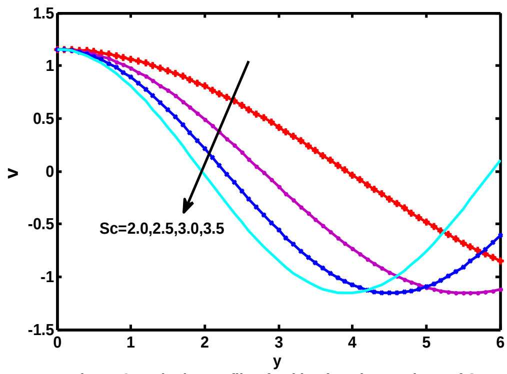

Figure 9: Velocity profiles for (dust) various values of Sc

Materials Today: Proceedings 64 (2022) 925–930

Contents lists available at ScienceDirect

Materials Today: Proceedings

journal homepage: www.elsevier.com/locate/matpr

Promotional effect of Ce on catalytic performance for the glycerol hydrogenolysis over Ni–Ce/RSAC catalyst

K. Subba Rao [a], Kishor Palle [b,*], S. Naga Gayatri [c], Narendra Phani Kumar [d], Kishore Kumar Angajala [e], V. Shanthi [b]

[a] Department of Chemistry(H&S), Malla Reddy Engineering College (Autonomous), Main Campus, Secunderabad, Telangana, India
[b] Department of Basic Science & Humanities, Muffakham Jah College of Engineering & Technology, Hyderabad, Telangana, India
[c] Department of Science and Humanities, MLR Institute of Technology, Hyderabad, Telangana, India
[d] Department of Science & Humanities, Nalla Narasimha Reddy Education Society's Group of Institutions, Hyderabad, Telangana, India
[e] Department of Humanities & Sciences, Vardhaman College of Engineering, Shamshabad, Hyderabad, Telangana, India

ARTICLE INFO

Article history:
Available online 15 June 2022

Keywords:
Impregnation
Catalyst
Reduction
Rice straw

ABSTRACT

Activated carbons are prepared from Rice Straw used for metal impregnation. Glycerol hydrogenolysis in aqueous medium was carried out on Ni–Ce/RSAC catalyst. In contrast by other metals, such as Cu, Sn, Zn, Al, Fe & Co, Ce demonstrated a markedly enhanced catalytic performance. For example, 80.5% conversion of glycerol could be accomplished at 300 °C under 5 MPa of H_2 with 6 h. XRD, H_2-TPR, TEM, NH_3-TPD, N_2 physisorption, and characterization were performed on the Ni–Ce/RSAC catalyst. It was found that adding Ce to Ni/RSAC catalyst highly affected reduction behavior.

1. Introduction

Biomass is an extensive and renewable energy source which is derived from all organic products generated through human and natural activity [1]. Biomass can be seen as one of the successful environmentally friendly alternatives for renewable energy and has drawn increasing interest [2]. Rice straw from the agricultural sectors in India and China is an extensive biomass product typically handled using conventional techniques like composting & incineration. Nevertheless, rice straw is not suitable for incineration because it contains tiny quantities of nitrogen for composting and a large amount of solid granules that produce smoke in the environment when incinerated [3].The rice straw may be used as being a green energy source as the abundant with volatile and combustible components. How this precious biomass material can be reused and recycled is a critical and essential but not easy work [4].

Glycerol, as the major derivative of the manufacture of biodiesel, is a viable raw material to add mass to high-value chemicals as of now being obtained from renewable possessions [1,2]. Propylene glycol (P.G) as well as ethylene glycol (E.G) are important chemical commodities for the manufacture of polymers and resins in addition to pharmaceutical, food, aesthetics, and efficient liquids [3]. From the viewpoint of sustainable chemistry, the instantaneous conversion of glycerol into P.G and E.G is very much attractive. The application of metal catalysts such as Ru, Pd, Rh & Pt etc. [3–8] having noble character and also metal catalysts such as Ni, Cu, etc. [9–15] having non-noble character has recently made significant progress. Promoters, like acid additives or metal promoters, are typically used to improve catalytic efficiency. Lingaiah and collaborators [3] stated to facilitate solid acids apparently enhanced the catalytic efficiency for the Ru/C catalyst and in addition with the purpose of the conversion of glycerol could be 44.6 %, particularly with Nb_2O_5 as a co-catalyst. Tomishige and his collaborators employed Amberlyst as a stabilizer, furthermore glycerol hydrogenolysis showed a tremendous promotional consequence. Ma & He [8] developed Re-modified Ru-supported catalyst furthermore reached glycerol conversion 56.9 % as well as 1, 2-PG with 47.2 % attained over Ru – Re / ZrO_2 support catalyst.

Cerium has attracted quite a lot of attention among the numerous promoters over the past few years as it has shown excellent promotion of results during hydrogenation reactions [16–21]. The Cerium impregnated Ruthenium supported SBA-15 produced

* Corresponding author.
E-mail address: nagagayathri@mlrinstitutions.ac.in (K. Palle).

https://doi.org/10.1016/j.matpr.2022.06.056
2214-7853/

superior cyclohexane products during benzene catalytic hydrogenation because the hydrophilicity of the catalyst was increased. After adding cerium to Ruthenium supported SBA-15 [16], the contact amongst Ce and Ru was improved. Ce-doped and Pd–B shapeless alloy catalyst has been applied to the similar reaction [17] furthermore incorporation for Ce possibly will upgrade Pd metal's distribution and electron density. Ce as the promoter was likewise employed in specific unsaturated aldehyde hydrogenation [18–21]. For example, in liquid-phase hydrogenation of furfural to furfural alcohol, Ce-promoted Ni – B catalyst has been used. A study showed that the species of cerium acted like support as well as Lewis acid [18]. W.Q. Yu et al. previously explained a new process for synthesizing the activated carbon (A.C) Ni / AC catalyst as support [14] also the catalyst has shown improved catalytic efficiency in support of aqueous glycerol hydrogenolysis than traditionally arranged. We have produced the Ce-promoted Ni / RSAC catalyst in this study and examined promotional impact of Ce on glycerol hydrogenolysis.

2. Experimental methods

2.1. Raw materials

Rice straw was obtained from Krishna district, Andhra Pradesh, India, which is cut into small pieces. They were immersed in 2 wt% Sodium hydroxide solution for 24 h toward take off the residue also water-dissolvable components. The rice straw was subsequently thoroughly cleaned with de-ionized water till the pH is 7 and afterward dried at 110 °C for 12 h.

2.2. Preparation of activated carbons

A cylindrical heater (tubular furnace) for carbonization furnished through temperature programmer was employed to prepare activated carbons. Weigh about 10 g of dried rice straw become heated in the furnace in the presence of nitrogen atmosphere at 10 °C/min from room temperature to 600 °C and maintained for an hour [22]. Following carbonization, the furnace was cool down to room temperature under continuous flow of nitrogen to avoid post oxidation process. Thus produced solids were washed with 1 M HCl followed by thorough washing by means of warm distilled water to expel chloride ions as well as other filtrates till the pH is impartial. The filtered solids had been desiccated at 110 °C for 10 h. This sample is designated as RSAC.

2.3. Activation by $(NH_4)_2HPO_4$

5 g of RSAC is first impregnated with 30 wt% $(NH_4)_2HPO_4$ and after that calcination at 250 °C underneath air for 2 h. The same sample is then at 600 °C in a nitrogen atmosphere for activation.

2.4. Preparation of Ni–Ce/RSAC catalyst

Ni–Ce/RSAC was prepared through wet- impregnation after that the Carbothermal reduction method was then treated with KBH_4 [14].11.5 g $Ni(NO_3)_2{\cdot}6H_2O$ and 0.5 g $Ce(NO_3)_3{\cdot}6H_2O$ were liquefied in 40 mL water and afterward, RSAC (40 mesh, Venkateswara Rice Mill, Telaprolu, Vijayawada) was soaked in the salt solution for day-and-night at room temperature and dried for 12 h at 110 °C. Carbothermal reduction of the above catalyst is introduced in a tubular furnace within flow N_2 (99.999% purity) at 600 °C for 2 h. After that, reduced sample is treated by using 2 M Potassium borohydride including 0.2 M NaOH allowed for constant magnificent. Further metal-promoted Ni/RSAC catalysts were organized to similar procedure, furthermore the entire the loading quantities of metal supports take place 1percentage in Ni-supported catalysts.

3. Results and discussion

3.1. BET analysis (Surface Area, pore volume and Pore size)

The specific surface area (SSA), aggregate pore volume & avg. pore diameters of Ni/RSAC &Ni-Ce/RSAC catalysts were showed in Table 1. Outcomes observed to the adding Ce into the Ni/RSAC catalyst modified the surface composition extensively. The BET surface area as well as the pore volume of Ni-Ce/RSAC had 946 m^2/g and 0.37 cm^3/g correspondingly, the two of which are diminished and distinguish with the Ni/RSAC catalyst. Pore size distribution is illustrated in Fig. 1.

The adding of cerium had clearly modified to the expected pore-structure of Ni/RSAC catalyst, moreover, therefore, average pore-size almost remained constant. These types of transforms has characterized by pores in RSAC being blocked with the integrated cerium particles.

3.2. X-Ray diffraction studies

The presence of Cerium and Nickel crystal phases within the Ni–Ce/RSAC catalysts had been studied using XRD analysis; moreover, thus these XRD patterns have been revealed in Fig. 2. Almost like Ni/A.C. catalyst, peak to show at the 2θ value of 23^0 had been recognized to the amorphouscarbon of RSAC support and 3-peaks approximately 43^0, 53^0, and 75.5^0 of 2θ had been allotted to metallic Ni [23]. High-intensity peak detected at the 2θ value of 44^0 has been measured to the metallic phase of Nickel. Ni crystalline size of Ni–Ce/RSAC was ca.16 nm through Ni as said by Scherrer's calculations. It is clear that there is no Ce crystalline phase becomes found in XRD patterns on behalf of Ni–Ce/RSAC catalyst through 1 %of Ce material. Ce particles may enormously spread on the catalyst while the substance of the cerium was lower. As a result, the signal of cerium particles is lesser than the inadequacy of the XRD detector. Consequently, Ni–Ce/RSAC catalysts with high cerium substance (3% and 10%) had developed to find out cerium particles in crystal phase. For Ni–Ce/A.C. catalyst with 3 %of cerium substance, found a novel peak at the 2θ of 28.50 that will be the standard peak of CeO_2 [24]. While cerium substance becomes promoted to10%, new peaks have been found at 28.50, 33.20, 47.50, and 56.60 of 2θ. Each one of those peaks belongs to crystal phase CeO_2 [24]. XRD patterns exposed to Cerium particles are present as CeO_2 in the Ni – Ce / RSAC catalyst. CeO_2 formation ought to have some impact on glycerol hydrogenolysis ' catalytic efficiency.

3.3. Ammonia-Temperature programmed desorption (NH_3-TPD)

The surface acidic characteristics of prepared Ni-Ce/RSAC catalyst were analyzed using NH_3-TPD. As per NH_3-TPD curves, acid amount has been determined, moreover the outcomes were revealed into Table 2. In the view of this study, acid quantity of Ni/RSAC activated carbon catalyst (168.4 μmol/g) is higher than that acid quantity of Ni–Ce/RSAC catalyst (238.6 μmol/g).Then

Table 1
Physico-chemical properties of Ni/RSAC and Ni–Ce (1%)/RSAC catalysts.

Catalyst	BET Surface area(m^2/g)	Pore Volume (cm^3/g)	Average Pore size (nm)
Ni/RSAC	1034	0.42	0.49
Ni-Ce/RSAC	946	0.37	0.50

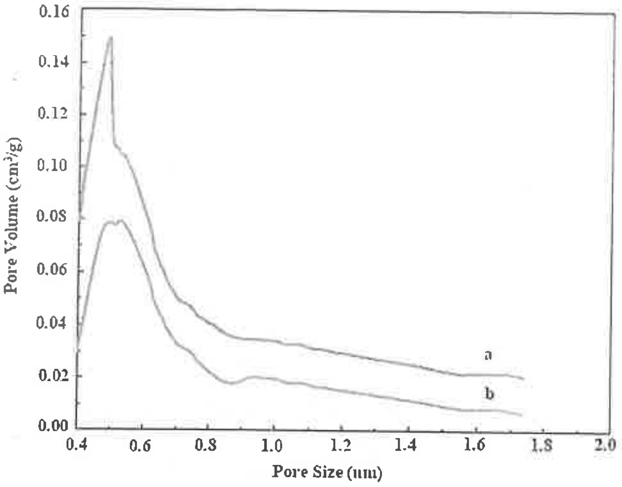

Fig. 1. Pore size distributions of (a) Ni /RSAC and (b) Ni–Ce (1%)/RSAC catalysts.

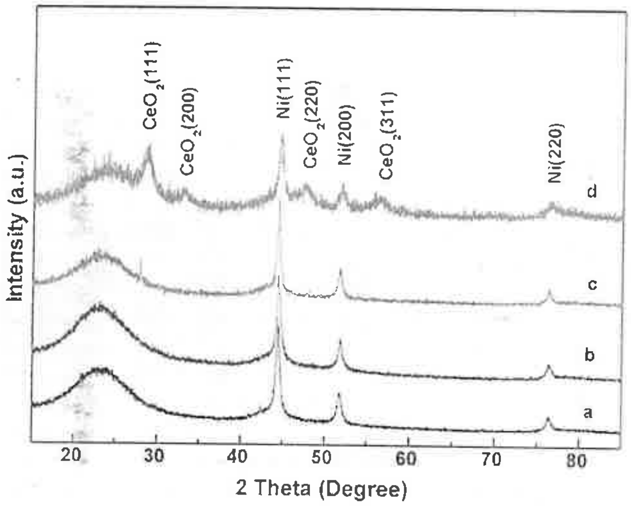

Fig. 2. XRD patterns of (a) Ni/RSAC, (b) Ni–Ce (1%)/RSAC, (c) Ni–Ce (3%)/RSAC and (d) Ni–Ce (10%) /RSAC.

Table 2
Acidity - NH_3-TPD Method.

Catalyst	Acidity by NH_3-TPD Method (μmol/g)
Ni/RSAC	168.4
Ni-Ce/RSAC	238.6

improved acid amount have been most expected toward the cerium components [25]. Alternatively, there is no outstanding enhancement in the acid amount due to a little portion of cerium.

3.4. H_2-TPR studies

Catalysts of Ni/RSAC and Ni–Ce/RSAC catalyst H_2-TPR curves has attained while illustrated in Fig. 3. It is clear that there is another H_2 consumption peak under 250 °C for the catalysts, that can have because of the dilution as a result of the gas liberation by decomposition of Nickel nitrate [26], or adsorption of H_2 on the support. Incredible dissimilarity in H_2-TPRcurves has been observed within the range of 250°–400 °C, which was correlated with the procedure of NiO reduction [27]. The peak approximately 360 °C has been extremely physically powerful for Ni/RSAC catalyst; furthermore, it approximately vanished for Ni–Ce/RSAC catalyst. The H_2-TPR peaks within range of 280 °C for Ni–Ce/RSAC catalyst grow to be significantly higher than that of Ni/RSAC catalyst. In favor of both samples, which can observe the maximum peak areas of the utilization of H_2 had been just about the same in the range of 250°–400 °C, that showed to facilitate the reduction temperature can be diminished after cerium pieces had added to the Ni/RSAC catalyst.

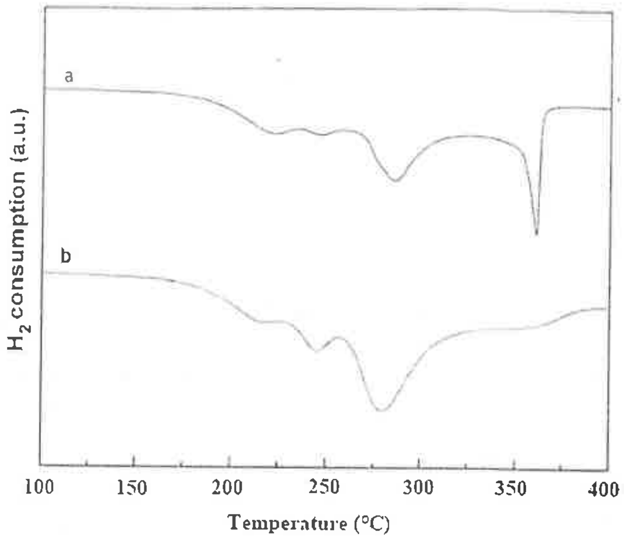

Fig. 3. H_2-TPR curves of samples to facilitate produced before carbothermal reduction of Ni/RSAC and (b) Ni–Ce (1%)/RSAC.

4. Catalyst activity studies

Glycerol Hydrogenolysis will have performed in autoclave reactor have with 600 mL capacity furnished through external temperature & magnificent regulator. The reactor survives at the beginning charged with 50 mL of aqueous glycerol solution (25 wt%) and 6.95 g of Ni–Ce/RSAC catalyst. Later, air is removed from the reactor, then it becomes heated at 200 °C and then rinsed with 5 MPa of H_2 (99.999%), and after that, time is noted. The pressure is constant as it providing H_2 throughout the reaction. The mixture had continuously stimulated to six hours, and the reactor becomes followed by cool down to room temperature. The yield had been recognized with using MS detector as well as quantized with the internal standard procedure by Agilent 4890D G.C. furnished by an FID detector and an HP-5 (30 m × 0.53 mm × 0.6 μm) capillary column. In the reaction toward the primarily adding of glycerol, the conversion is measured as the molar ratio of the consumed glycerol. Selectivity is characterized by the molar ratio of the product to the glycerol utilized during the reaction [9].

4.1. Activity of catalyst in the hydrogenolysis of glycerol

4.1.1. Activity study of Ni–Ce/RSAC and different metals influenced Ni/RSAC catalysts

Catalytic functionalities of Ni–Ce/RSAC as well as metal- promoted Ni/RSAC catalyst has been concentrated into the reactant hydrogenolysis of aqueous glycerol solution by following suitable conditions like 5 MPa of H_2 at 473 K. The outcomes have appeared into Table 3. Generally, the conversion of glycerol into E.G. as well as 1, 2-PG over those catalysts, and GC–MS distinguished by way of other products collectively along with methanol and ethanol. The glycerol conversion diminished later the adding of Sn otherwise Co into Ni/RSAC (41.2% glycerol conversion achieved through Ni/

Table 3
Catalytic Performance of glycerol hydrogenolysis over Ni/RSAC catalyst promoted using several metals.

Catalysts	Conversion (%)	Selectivity (%)	
		1,2-PG	EG
Ni-Ce/RSAC	80.5	53.8	10.6
Ni-Cu/RSAC	52.4	71.2	8.3
Ni-Co/RSAC	33.4	75.5	9.4
Ni-Sn/RSAC	32.6	59.6	5.2
Ni-Zn/RSAC	60.3	69.2	8.6
Ni-Al/RSAC	69.4	65.2	10.1
Ni-Fe/RSAC	62.2	65.6	7.8

a. All the reactions were carried out by 25 wt% glycerol aqueous Solution at 200 °C and 5 MPa H_2 for 6 h.
b. Further by-products simultaneously with CH_3OH and C_2H_5OH are identified by GC–MS.

RSAC [14]). Addition of Cu, Zn, Al & Fe into Ni/RSAC catalysts have somewhat advantages for the selectivity of 1, 2-PG; however; there is no improvement in the glycerol conversion. Conversely, while cerium has integrated with Ni/RSAC catalyst, the glycerol conversion was a lot of improved as of 41.2% toward 80.5%, with 53.4% selectivity of 1, 2-PG &10.6% selectivity of E.G. Then outcomes showed to the adding of cerium into Ni/RSAC catalyst possess a tremendous promoting impact during glycerol hydrogenolysis.

4.1.2. Influence of reaction time

Fig. 4 explain about impact of reaction time for glycerol hydrogenolysis over Ni–Ce/RSAC catalyst. During first two hours, glycerol quickly transformed, moreover conversion was 54.7%. As the reaction time extended toward 4 h, glycerol conversion was enhanced near 74.6% with an insignificant selectivity diminish for 1, 2-PG. when time enhanced, conversion gradually improved, and selectivity of E.G. & 1, 2-PG progressively became steady. While the reaction takes place in support of eight hours, the conversion of glycerol attained 85.1%. The above effects specified to the Ni–Ce/RSAC catalyst became incredibly successful to the hydrogenolysis reaction.

The entire reactions have been carried out by 25 wt% glycerol aqueous solutions at 200 °C and 5 MPa H_2 for 6 h.

4.1.3. Effect of reaction temperature and hydrogen pressure

The effect of temperature at the glycerol hydrogenolysis became studied at 150°, 180° and 200 °C, correspondingly (Fig. 5.). The conversion of glycerol slowly enhanced moreover the selectivity of E.G. or 1, 2-PG stayed generally steady. The effect of H_2 pressure on hydrogenolysis reaction is furthermore examined on the pressures 3, 5 &7 MPa(Fig. 6.). Glycerol conversion improved from 3to 5 MPa and after that stayed more or less steady. The selectivity of E.G. and 1, 2-PG has been continued by 10% and 60–70%, in that order. As a result, suitable temperature and pressure are essential toward comfort better production.

All the reactions were carried out by using 25 wt% glycerol aqueous solutions at 5 MPa H_2 for 6 h.

All the reactions were per-formed by 25 wt% glycerol aqueous solutions at 200 °C for 6 h-8 h.

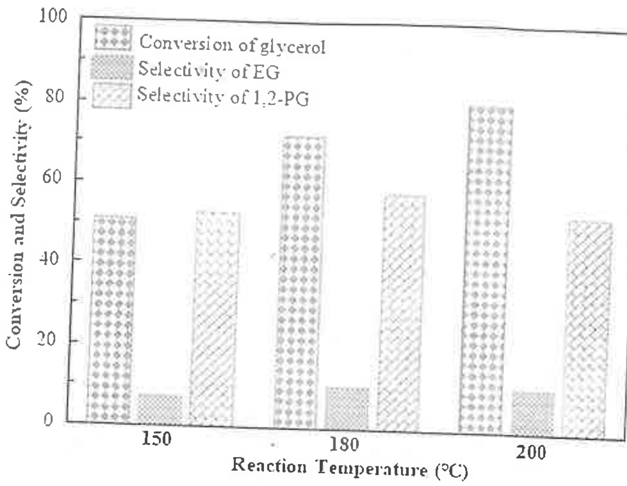

Fig. 5. Effect of temperature on Glycerol Hydrogenolysis.

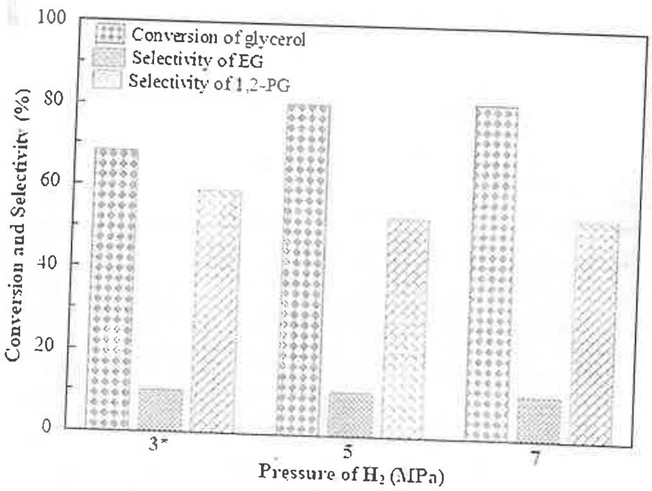

Fig. 6. Effect of H_2 pressure on Glycerol Hydrogenolysis.

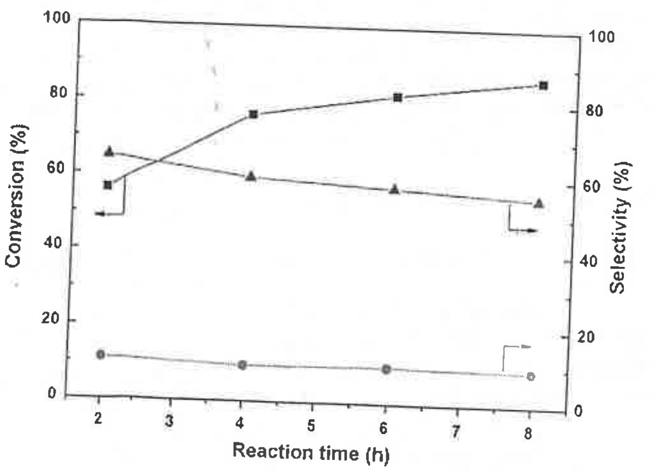

Fig. 4. Effect of reaction time on glycerol hydrogenolysis. Symbols: (■) glycerol conversion;(▲) 1, 2-PG selectivity and (●) EG selectivity.

4.1.4. Influence of glycerol concentration

It was examined influence of glycerol concentration moreover, findings exposed in Fig. 7. Conversion of glycerol diminished significantly as the glycerol concentration enhanced with similar conditions around 25 to 75 wt% Nevertheless, they observed that 32.8, 55.4 and 76.4 g of glycerol has been processed in that order, taking into account the extracted amount of glycerol. Material distribution has been nearly constant, and a related process has been found in the Ru-based catalyst compositions [3].

Entire reactions carried out at 200 °C & 5 MPa hydrogen for 6 h.

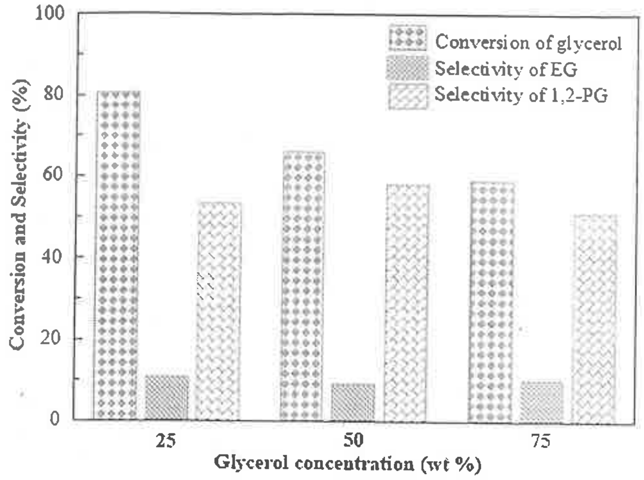

Fig. 7. Glycerol concentration Influence on its hydrogenolysis.

5. Proposed reaction pathways

The majority descriptions [3,12] and our latest effort [14] indicated to dehydration/ hydrogenation processes were used to carry out glycerol hydrogenolysis. After that, glycerol had been dehydrated to acetol and after that hydrogenated to 1, 2-PG. The Ni / RSAC catalyst utilized in earlier study [14] is a bi-functional catalyst comprising the performing of dehydration as well as hydrogenation; yet the effectiveness sustained to be increased.

To have a look at the hydrogenolysis of glycerol manner on the Ni–Ce/RSAC catalyst, we performed managed researches on glycerol dehydration and acetol hydrogenation (Fig. 8). The dehydration of uncontaminated glycerol has been carried out first in the N_2 atmosphere. Acetol became identified through G.C.–M.S. This suggested to the glycerol had been converted to acetol by dehydration above Ni-Ce/RSAC catalyst. Consequently, of acetol hydrogenation (10 wt% aqueous solutions) has been done by using suitable conditions like 5 MPa H_2 and 100 °C for one hour. The acetol conversion was almost 100%. The present outcomes destined with the aim of glycerol hydrogenolysis were achievable following toward the planned dehydration/hydrogenation process.

To additionally regard as the promoting effect with the adding of cerium within Ni/RSAC catalyst; we directed a similar procedure above Ni/RSAC catalyst by using similar conditions. From Fig. 8, it can be detected to acetol has been moderately changed over Ni/RSAC whilst hydrogenation of acetol has been carried out. Better conversion of acetol can be gotten while catalyzed with Ni–Ce/RSAC which is compared with Ni/RSAC in which Ni–Ce/RSAC was amazing regarding hydrogenation for acetol. This outcome consistent with the higher potential of Ni–Ce/RSAC and the development is associated with the being there of cerium.

6. Conclusion

This work shows that the cerium promoted Ni-Ce/RSAC catalysts has been shown an outstanding promotional effect on the aqueous glycerol hydrogenolysis. By using suitable conditions like 200 °C & 5 Mega Pascal (Mpa) of Hydrogen, conversion of 25%

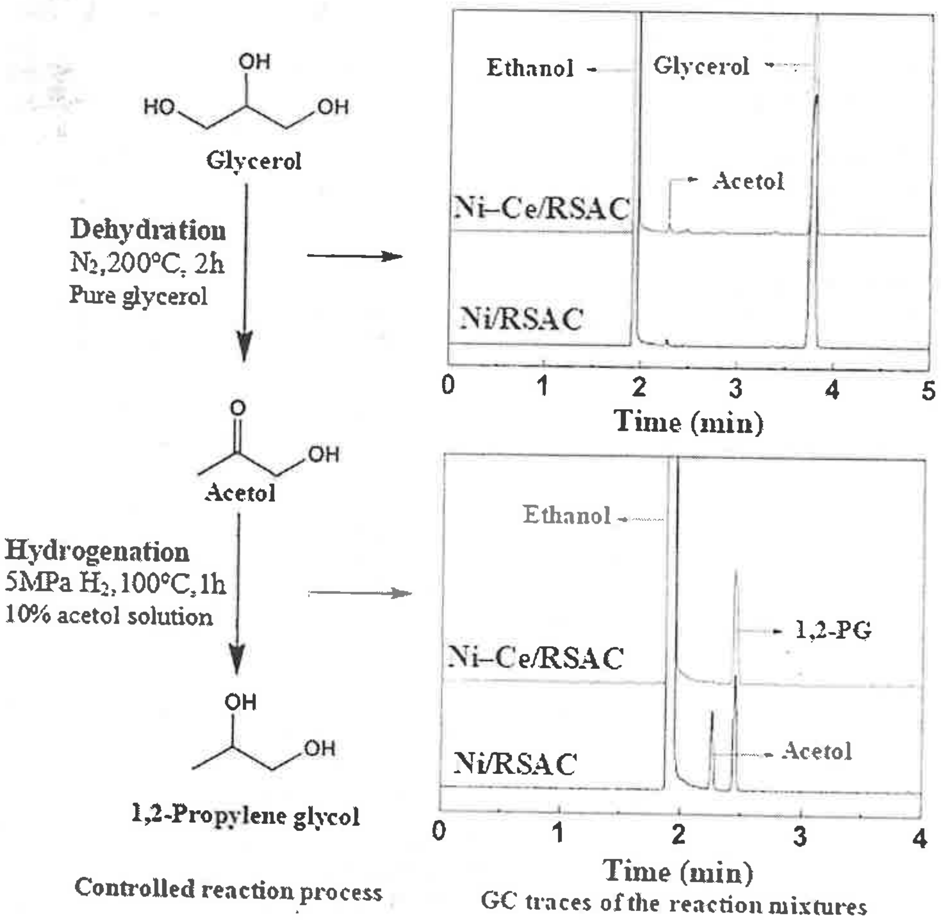

Fig. 8. Influence of cerium in Ni-Ce/RSAC for glycerol hydrogenolysis.

aqueous solution of glycerol is 80.5% in 6 hr than Ni–/RSAC catalyst. When cerium is added to the Ni/RSAC catalyst appreciably altered the reduction conduct. Supported at the managed researches, ourselves has been observed to cerium in Ni–Ce/RSAC catalyst might speed up acetol hydrogenation.

Declaration of Competing Interest

The authors declare that they have no known competing financial interests or personal relationships that could have appeared to influence the work reported in this paper.

Acknowledgement

The authors acknowledge Department of Science and Technology, New Delhi, India for sophisticated instrument facility.

References

[1] M. Pagliaro, R. Ciriminna, H. Kimura, M. Rossi, C.D. Pina, From glycerol to value-added products, Angew. Chem. Int. Ed. Engl. 46 (24) (2007) 4434–4440.
[2] C.H. Zhou, J.N. Beltramini, Y.X. Fan, G.Q. Lu, Chemo selective catalytic conversion of glycerol as a bio-renewable source to valuable commodity chemicals, Chem. Soc. Rev. 37 (2008) 527–549.
[3] Balaraju, V. Rekha, P.S. Sai Prasad, B.L.A. Prabhavathi Devi, R.B.N. Prasad, N. Lingaiah, Influence of solid acids as co-catalysts on glycerol hydrogenolysis to propylene glycol over Ru/C, catalysts, Appl. Catal. A: Gen. 354 (2009) 82–87.
[4] E.P. Maris, W.C. Ketchie, M. Murayama, R.J. Davis, Glycerol hydrogenolysis on carbon-supported Pt-Ru and Au-Ru bimetallic catalysts, J. Catal. 251 (2007) 281–284.
[5] E.P. Maris, R.J. Davis, Hydrogenolysis of glycerol over carbon-supported Ru and Pt catalysts, J. Catal. 249 (2007) 328–337.
[6] I. Furikado, T. Miyazawa, S. Koso, A. Shimao, K. Kunimori, K. Tomishige, Catalytic performance of RH/SiO_2 in glycerol reaction under hydrogen, Green Chem. 9 (2007) 582–588.
[7] T. Miyazawa, Y. Kusunoki, K. Kunimori, K. Tomishige, Glycerol conversion in the aqueous solution under hydrogen over Ru/C + an ion exchange resin and its reaction mechanism, Catal. 240 (2006) 213–221.
[8] L. Ma, D.H. He, Hydrogenolysis of Glycerol to Propanediols over Highly Active Ru–Re Bimetallic Catalysts, Top. Catal. 52 (2009) 834–844.
[9] M.A. Dasari, P.-P. Kiatsimkul, W.R. Sutterlin, G.J. Suppes, Low-pressure hydrogenolysis of glycerol to propylene glycol, Appl. Catal. A: General 281 (2005) 225–231.
[10] T.A. Werpy, J.G. Frye Jr., A.H. Zacher, D.J. Miller, Hydrogenolysis of 5-Carbon Sugars, Sugar Alcohols, and Compositions for Reactions Involving Hydrogen, US Patent 6, 2004,677, pp. 385.
[11] S. Wang, H.C. Liu, Selective hydrolysis of glycerol to propylene glycol on Cu-ZnO catalysts, Catal. Lett. 117 (2007) 62–67.
[12] Z.W. Huang, F. Cui, H.X. Kang, J. Chen, X.Z. Zhang, C.G. Xia, Highly dispersed silica-supported copper nanoparticles prepared by precipitation- gel method: A simple but efficient and stable catalyst for glycerol hydrogenolysis, Chem. Mater. 20 (2008) 5090–5099.
[13] A. Perosa, P. Tundo, Selective hydrogenolysis of glycerol with Raney Nickel, Ind. Eng. Chem. Res. 44 (23) (2005) 8535–8537.
[14] W.Q. Yu, J. Xu, H. Ma, C. Chen, J. Zhao, H. Miao, Q. Song, A remarkable enhancement of catalytic activity for KBH4 treating the Carbothermal reduced Ni/AC catalyst in glycerol hydrogenolysis, Catal. Commun. 11 (2010) 493–497.
[15] J. Zhao, W.Q. Yu, C. Chen, H. Miao, H. Ma, J. Xu, A bifunctional efficient catalyst for selective hydrogenolysis of glycerol, Catal. Lett. 134 (2010) 184–189.
[16] J.L. Liu, L.J. Zhu, Y. Pei, J.H. Zhuang, H. Li, H.X. Li, M.H. Qiao, K.N. Fan, Ce-promoted Ru/SBA-15 catalysts prepared by a "two solvents" impregnation method for selective hydrogenation of benzene to Cyclohexane, Appl. Catal. A: Gen. 353 (2009) 282–287.
[17] H. Li, J.L. Liu, H.X. Li, Liquid-phase selective hydrogenation of phenol to cyclohexanone over the Ce-doped Pd–B amorphous alloy catalyst, Mater. Lett. 62 (2) (2008) 297–300.
[18] H.X. Li, S.Y. Zhang, H.S. Luo, A Ce-promoted Ni-B amorphous alloy catalyst (Ni-Ce-B) for liquid-phase furfural hydrogenation to furfural alcohol, Mater. Lett. 58 (22–23) (2004) 2741–2746.
[19] J.C. Serrano-Ruiz, J. Luettich, A. Sepúlveda-Escribano, F. Rodriguez-Reinoso, Effect of the support composition on the vapor-phase hydrogenation of crotonaldehyde over Pt/CexZr1−xO2 catalysts, J. Catal. 241 (1) (2006) 45–55.
[20] A. Sepúlveda-Escribano, F. Coloma, F. Rodriguez-Reinoso, Promoting Effect of Ceria on the Gas Phase Hydrogenation of Crotonaldehyde over Platinum Catalysts, J. Catal. 178 (2) (1998) 649–657.
[21] S. Velu, M.P. Kapoor, S. Inagaki, K. Suzuki, Vapor phase hydrogenation of phenol over palladium supported on mesoporous CeO2 and ZrO2, Appl. Catal. A: Gen. 245 (2) (2003) 317–331.
[22] K. Subba Rao, B.N. Srinivas, A.K. Turaka, P. Kishore, Catalytic Functionalities of Ru Supported on Activated Carbons Prepared from Rice Straw for Glycerol Hydrogenolysis, IJIRSET 6 (9) (2017) 19476–19481.
[23] Y. Li, B.C. Zhang, X.W. Xie, J.L. Liu, Y.Y. Xu, W.J. Shen, Novel Ni catalysts for methane decomposition to hydrogen and carbon nanofibers, J. Catal. 238 (2) (2006) 412–424.
[24] M.B. Chong, D.G. Cheng, L. Liu, F.Q. Chen, X.L. Zhan, Deactivation of CeO_2 catalyst in the hydrogenation of benzoic acid to benzaldehyde, Catal. Lett. 114 (2007) 198–201.
[25] J.R. Sohn, D.C. Shin, Physicochemical and Catalytic Properties of NiSO4/CeO_2-ZrO_2 Catalyst Promoted with CeO_2 for Acid Catalysis, Bull. Korean Chem. Soc. 28 (8) (2007) 1265–1272.
[26] L.M.S. Silva, J.J.M. Orfão, J.L. Figueiredo, Formation of two metal phases in the preparation of activated carbon-supported nickel catalysts, Appl. Catal. A: Gen. 209 (1–2) (2001) 145–154.
[27] B. Mile, D. Stirling, M.A. Zammitt, A. Lovell, M. Webb, The location of nickel oxide and nickel in silica-supported catalysts: Two forms of "NiO" and the assignment of temperature-programmed reduction profiles, J. Catal. 114 (2) (1988) 217–229.

MRS Communications

https://doi.org/10.1557/s43579-022-00262-w

MRS Communications

Research Letter

Preparation of activated carbon from rice husk for CO_2 adsorption: Isotherm and artificial neural network modelling

Kishor Palle, Department of Chemistry, Muffakham Jah College of Engineering and Technology, Hyderabad, Telangana, India
G. K. Sivasankara Yadav, Department of Physics, Rayalaseema University College of Science, Kurnool, Andhra Pradesh, India
Sambhani Naga Gayatri, Department of Science and Humanities, MLR Institute of Technology, Hyderabad, Telangana, India; Present address: Department of Interdisciplinary Sciences, University Institute of Engineering and Technology (UIET), Guru Nanak University, Ibrahimpatnam, Hyderabad, India
Shanthi Vunguturi, Department of Chemistry, Muffakham Jah College of Engineering and Technology, Hyderabad, Telangana, India
P. Ramesh Babu, Department of Physics, Gokaraju Rangaraju Institute of Engineering & Technology, Hyderabad, Telangana, India
K. Subba Rao, Department of Chemistry (H&S), Malla Reddy Engineering College (Autonomous), Main Campus, Secunderabad, Telangana, India
Md. Mustaq Ali, Department of Mathematics (H&S), Malla Reddy Engineering College (Autonomous), Main Campus, Secunderabad, Telangana, India

Address all correspondence to Kishor Palle at **drkishorepalle@gmail.com**

(Received 24 July 2022; accepted 31 August 2022)

Abstract

A great deal of attention has been paid to the climate change greenhouse effect in recent years. Rice husk porous carbon adsorbent was made using a single step of KOH activation in this investigation. Carbon dioxide adsorption was studied by the generated activated carbon. For adsorption isotherm data, isotherm models such Freundlich, Langmuir, Hill, Temkin, and Dubinin-Rudeshkovich were utilised. Additionally, the capacity to adsorb CO_2 was predicted using artificial neural networks. Trial and error allowed us to choose the architecture with the best regression coefficient and the lowest mean-square error (MSE).

Introduction

Atmospheric CO_2 is currently 416 parts per million (ppm), which is 46.4% over pre-industrial levels. Fossil fuels, which will continue to be the most important source of human energy demand, will contribute to the trend of rising energy usage for a very long period.[1] As CO_2 quantities in the atmosphere increase, it is essential to create technology that can absorb CO_2 effectively.[2] A useful and significant method for reducing the rising CO_2 emissions from the use of fossil fuels is the collection and storage of CO_2 after the combustion of those fuels.[3] Adsorption is a suitable technology among those that have been proposed for the removal of carbon dioxide.[4] Adsorption technology has received a lot of attention recently with regard to preserving the environment and producing sustainable energy.[5] Adsorption utilising the materials extremely porous can show various advantages as carbon dioxide adsorbents, including consumption of lower energy, and has drawn the most interest among the many approaches.[6]

High CO_2 concentrations may be absorbed by a perfect CO_2 adsorbent, which also has great recyclability, is simple to renew, has a high CO_2 selectivity, is inexpensive, and has quick adsorption kinetics.[3,7] Metal–organic frameworks (MOFs), porous carbons and porous polymers are solid adsorbents that selectively absorb carbon dioxide at SATP (25°C, 1 bar), and they may provide a competitive alternative to amine-based solvents. Strong chemical and thermal stability, High pore volume and specific surface area and simple pore-structure manipulation are all characteristics of carbon porous materials.[8]

KOH is one of the primary activators used to create extremely porous carbon. Utilising activated rice husk carbon based on KOH (KOH-AC, 1439 m^2/g), Wang et al. created a low-cost CO_2 adsorbent. Under indoor circumstances, the adsorption rate of RHAC was 2.1 mmol/g at a lower concentration of carbon dioxide (2000–500 ppm).[1] Wang et al. produce carbon using chitosan as a precursor by combining hydrothermal treatment with light KOH activation. Despite having 1249m^2/g surface area, the AC produced from the salt-assisted hydrochar had the maximum CO_2 absorption (4.41 mmol/g). Huang et al. employed KOH in the initial phase of the conversion of garlic peel into hydrochar to synthesise activated carbon materials with high surface area and wide pores. With a surface area of 1262 m^2/g, activated carbon made by treating it with KOH at 800°C and a KOH/hydrochar ratio of 2 shows excellent pore structure.[9] To study the behaviour of CO_2 adsorption, Li et al. created biochars using 70% pine sawdust and 30% sewage sludge by KOH modification. Modified biochars demonstrated greater CO_2 adsorption capabilities than virgin biochars (35.5–42.9 mg/g), ranging from 136.7 to 182.0 mg/g.[10]

The nonlinear statistical model tool known as ANN was created in the 1980s, and today, people are employing it more and more frequently. The process is a useful tool for modelling these processes because it enables the modelling of inputs and outputs in intricate nonlinear systems.[11] To establish the link between variables, such as the dependency of estimated parameters on the adsorption mechanism, models used to explain the adsorption process should meet specific requirements. A great tool for this strategy is ANN, which can carry out mathematical operations for both linear and nonlinear systems.[12] ANN uses a learning mechanism to predict an output from an input. In that it can imitate the activities of the human brain while learning, ANN is similar to the human brain.[13]

Recently, there has been a huge interest in the ANN because of its ability to accurately anticipate complicated physical and chemical phenomena. The ANN model demands more attention to testing, validation, and data points for training and to train an ANN model, the required number of neurons cannot be calculated mathematically due to nonavailability of mathematical calculation. In terms of model accuracy, the ANN algorithm is equally important.

This paper investigated carbon dioxide adsorption on activated carbon samples, based on the previous explanation regarding natural gases. The study shows how artificial intelligence and neural network modelling may be used to forecast the adsorption capacity of the activated carbon samples stated above using various scope matrixes. With the finest applicable artificial intelligence approaches, the study may give helpful information about unconventional gas and activated carbon preparations for CO_2 adsorption and gas production.

To understand the activated carbons behaviour toward gas sorption in the subsurface, sorption analysis is normally performed traditionally at high-reservoir pressures and temperatures. The goal of doing high adsorption studies is to study supercritical CO_2 sorption and simulate field operational conditions.[14] Most practical research, additionally observations of adsorption analysis using equilibrium isotherm models, which are not always the most accurate. The majority of isotherm models have limitations in terms of pressure, porosity, and even temperature measurement. As a result, there is indeed a fundamental need for a more accurate and larger range of application modelling to improved understanding of the association between selectivity and sorption capacity and the porous medium examined, such as activated carbon.

At up to 200 bar working pressure, CO_2 adsorption analysis is frequently affected by the buoyancy effect, which must be compensated using the equation for other states. As a result, the measurement uncertainty is significantly enhanced.[15] Modifications in isothermal pressure conditions or weight of the sample are commonly used to estimate adsorption capacities, and these parameters and conditions are then correlated to modify the dominating factors and conditions. However, no research has coupled operational characteristics in the field with distribution of pores in a narrow porous medium for increased gas recovery evaluations and innovative uses.

The aim of this work is to examine the effectiveness of AC derived from rice husk as a convenient and cost-effective adsorbent for CO_2 adsorption. Here, an investigation at 273 K and 298 K for carbon dioxide adsorption is reported together with a thorough characterisation of the AC. Scanning electron microscopy (SEM), Fourier transforms infrared (FTIR), and Brunauer–Emmett–Teller (BET) have all been used to examine the characteristics of activated carbon produced chemically by activating carbon with KOH (SEM). For the purposes of this inquiry, the adsorption process was modelled using the Freundlich, Langmuir, Dubinin-Radushkevich (DR), Hill, and Temkin isotherm models. The ANN model was ultimately employed to estimate the adsorption capacity of carbon dioxide.

Materials and methods

Porous carbon synthesis

Rice Husk was collected from local rice mill. KOH is used for chemically activating biomass to produce activated carbon. The most effective and commonly used activator is KOH, as it can create a high total pore volume (especially micropores) and a large specific surface area.[1] For 24 h, the drying process was conducted at 100°C to remove any moisture from the biomass. During the four-hour calcination process, rice husks were heated at different temperatures and under different atmospheric conditions. A temperature of 10°C per minute was programmed, and a gas flow of 40 mL per minute was maintained.[16,17]

Activated carbon is the final product. The sample's powder was produced by crushing. In a single step, activation and carbonisation were applied. The precursor was submerged in an aqueous solution containing KOH for three hours. We impregnated biomass with KOH at a ratio of 1:2. The mixture was cooled after 24 h of heating at 100 degrees. The mixtures were activated for 60 min in a pure N_2 flow at 800°C after being dried for 24 h at 100°C. After being thoroughly cleaned with distilled water three times, the activated carbon was submerged in 1 M HCl and then rinsed once more to remove the chloride ions before being let to dry naturally. The final process was drying the AC for 12 h at 100°C.[18] Figure 1 shows the processes for making activated carbon.

Gas adsorption

A cylindrical reactor illustrated in Fig. S1 was used to examine the CO_2 adsorption capability of activated carbon made from rice husk. There is a cylindrical stainless steel reactor with a grid cell for exposing the CO_2 sample. The device's cylindrical shell is entirely sealed around the AC when it is installed there. The totally sealed cylindrical reactor was filled with 0.5 g of the manufactured porous carbon. Pure CO_2 is introduced into the chamber for 60 min. at 0°C and 25°C with a pressure of 0–1 bar to gauge the amount of gas absorbed.

The pressure needed to enter the mixing chamber with the CO_2 from the premium cylinder was determined using a pressure gauge and regulator. In addition to the electrical heat trace, a computer also continuously records the reactor's temperature and pressure.

Equation 1 is used to find the activated carbons adsorption capacity.

$$q = \frac{m_i - m_f}{w} = \left(\frac{VM_w}{Rw}\right)\left(\frac{P_i}{Z_i T_i} - \frac{P_f}{Z_f T_f}\right). \qquad (1)$$

$$Z = 1 + \frac{BP}{RT}. \qquad (2)$$

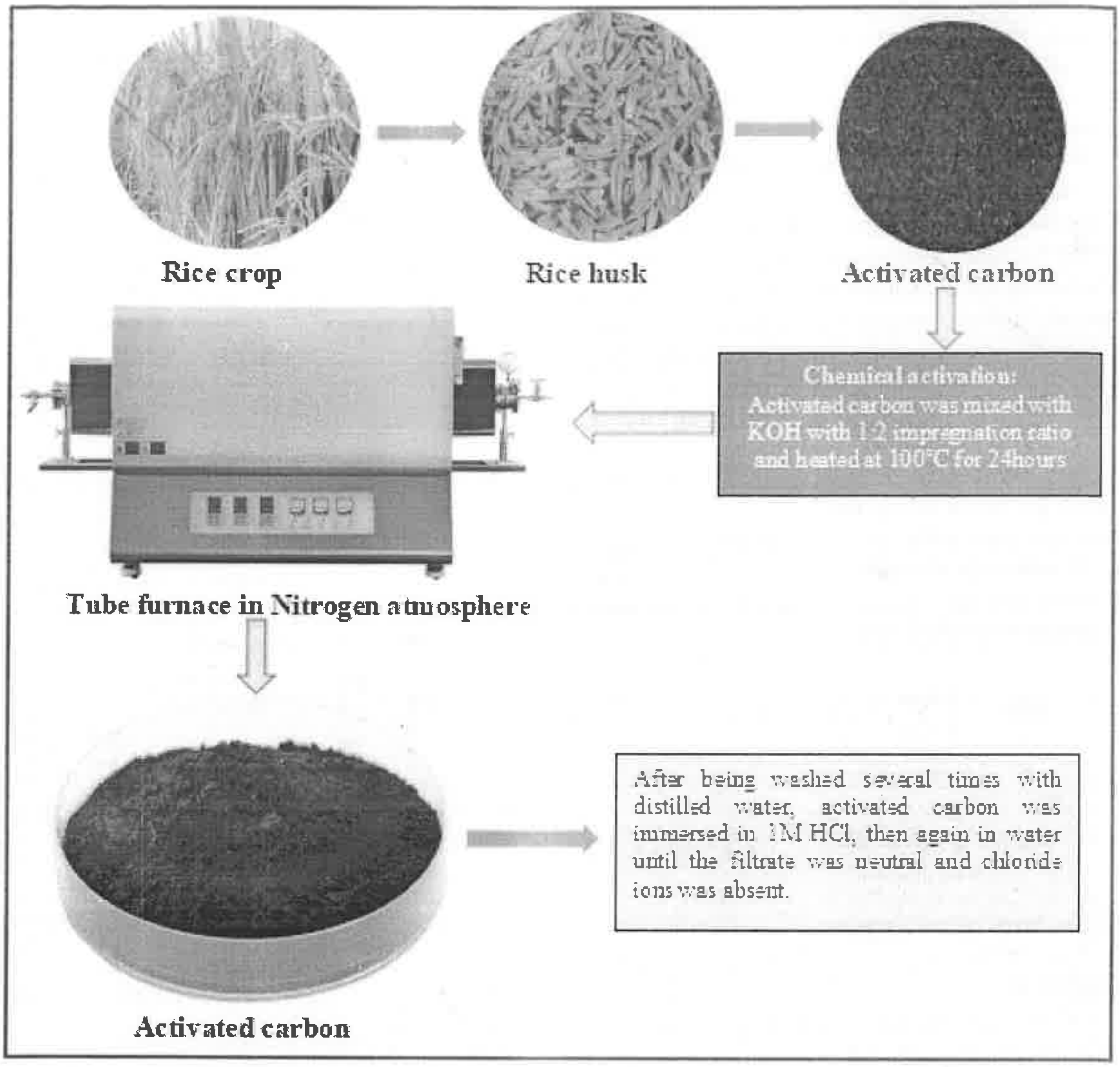

Figure 1. The preparation steps of activated carbon.

The subscripts 'i' denote initial condition and 'f' denote final condition. The variables are temperature (T), stand in for pressure (P), compressibility factor (Z), universal gas constants (R), reactor volume (V), and rice husk adsorbent mass (w). Based on the Virial equation (Eq. 2), the compressibility factor was calculated.[19]

Characterisation

A micrometric ASAP 2020 device captured the porous carbon's pore structure. Samples were degassed to constant weight under dynamic vacuum conditions for 2 h at 393 K in order to prepare them for adsorption–desorption studies. The structure and morphology of activated carbon are examined using a scanning electron microscope (SEM) [model: TESCAN Vega 3]. Functional groups on AC surfaces were found using a Perkin Elmer FTIR spectrometer.

ANN model

The idea behind the neural network is to emulate the actual human nervous system, which processes information in a complex, parallel, and nonlinear manner. A network design based on precise specifications connects the artificial neurons. A neural network (ANN) is a method that uses a sequence of three layers to translate inputs into meaningful outputs (Input layer, hidden layer, and output layer). Data are received by input layers, processed by hidden levels, and finally sent to the output layer. Every piece of data is processed by neurons in accordance with a certain activation function, such as sigmoid, tanh, linear, etc.[20] A weight value corresponds to each link. The neurons in the last layer of the hidden layer output the following equation[15]:

$$h_i = \sigma\left(\sum_{j=1}^{N} W_{ij}x_j + T_i^{hid}\right), \tag{3}$$

where N = number of input neurons, σ = activation function, W = weights, T^{hid} = threshold terms of the hidden neurons, x_j = inputs of the input neurons and.

A feed-forward radial base function (RBF) with a 2:10:1 architecture was used to simulate the CO_2 adsorption characteristics using activated carbon made from rice husk, as shown in Fig. S2. For the training sample, the data from the 38 data (70% training) and the 16 data (16% validation and 16% testing) were utilised, respectively. The buried layer neurons were activated by using the Tan-Sigmoid transfer function (tansig). Pressure and temperature were also used as input variables in the current investigation. A process response or output variable was formed by adsorption on the AC (The amount of CO_2 adsorbed). With the use of several designs and between 2 and 20 neurons, the ideal hidden layer of the ANN model was discovered. The statistical metric known as mean-square errors (MSE) is used to train ANN. The estimated MSE values are shown against the quantity of neurons in the hidden layer, as seen in Fig. S3. To obtain the least amount of mistake, 10 neurons in the intermediate layer were specifically chosen. Equations 4 and 5 were used, respectively, to determine MSE & correlation coefficient (R^2).[21]

$$\mathrm{MSE} = \frac{1}{N}\sum_{i=1}^{N}\left(Y_{\text{predicted}} - Y_{\text{real}}\right)^2, \tag{4}$$

$$R^2 = \sum_{i=1}^{N}\frac{\left(Y_{\text{predicted}} - Y_{\text{real}}\right)^2}{\left(Y_{\text{predicted}} - Y_{\text{mean}}\right)^2}. \tag{5}$$

Results and discussion

Pore size distribution and N_2 adsorption–desorption

On rice husk-derived activated carbons, CO_2 adsorption tests were performed at STP from 0–1.0 relative pressure (P/P_0). The progressive absorption of nitrogen at 77 K is shown in Fig. 2(a). The curve showed a high rise of 500 cm^3/g at low relative pressures ($P/P_0<0.02$) followed by a second fast rise up to 0.85 bar. The curvature then progressively grew until it reached 1 bar. These discoveries led to the conclusion that the material had micropores, which could be seen in the pattern of the pore size distribution [Fig. 2(b)]. There seems to be a slight hysteresis between absorption and desorption as a result of the big spaces trapping gas. The result was that the SBET volume and the volume of the micropores were 2458 m^2/g and 0.76 cm^3/g, respectively. This substance is more valuable than the majority of porous carbons.

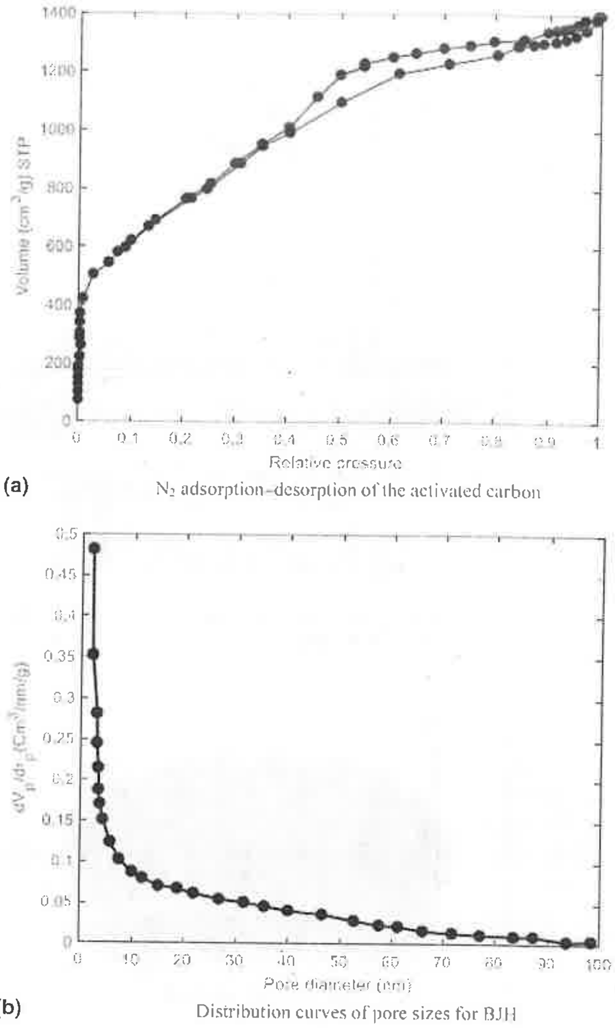

Figure 2. (a) N2 adsorption–desorption of the activated carbon. (b) Distribution curves of pore sizes for BJH.

Scanning electron microscopic analysis (SEM)

A scanning electron microscope (SEM) operating at 25 kV was used to analyse activated carbon made from rice husk. As observed in the SEM picture (Fig. S4), AC usually consists of a structure that is rather smooth with irregular holes on the surface.

Fourier transform infrared analysis (FTIR)

The adsorbent's FTIR spectrum is crucial for determining if the appropriate functional groups and bonds are present. The activated carbon made from rice husk may be seen in Figure S5 FTIR spectrum. hydroxyl group stretching in the presence of -OH evidenced by the peak at 3430 cm^{-1} is caused by. Methoxyl group molecular vibrations may be observed at a wavelength of 2924 cm^{-1}, which is related to the symmetric and asymmetric vibrations of C–H. Vibrations from the C–O are said to have a peak at 1057 cm^{-1}.[18]

Modelling of CO2 adsorption by ANN

To determine the adsorption capacity the Neural Network Toolbox from MATLAB 2017a is used. The artificial neural network used in the current study has two inputs, a hidden layer with 10 neurons inside of it, and one target output. Best correlation coefficient and lowest error(MSE) architecture were ultimately chosen after much trial and error. Figure 3(a)

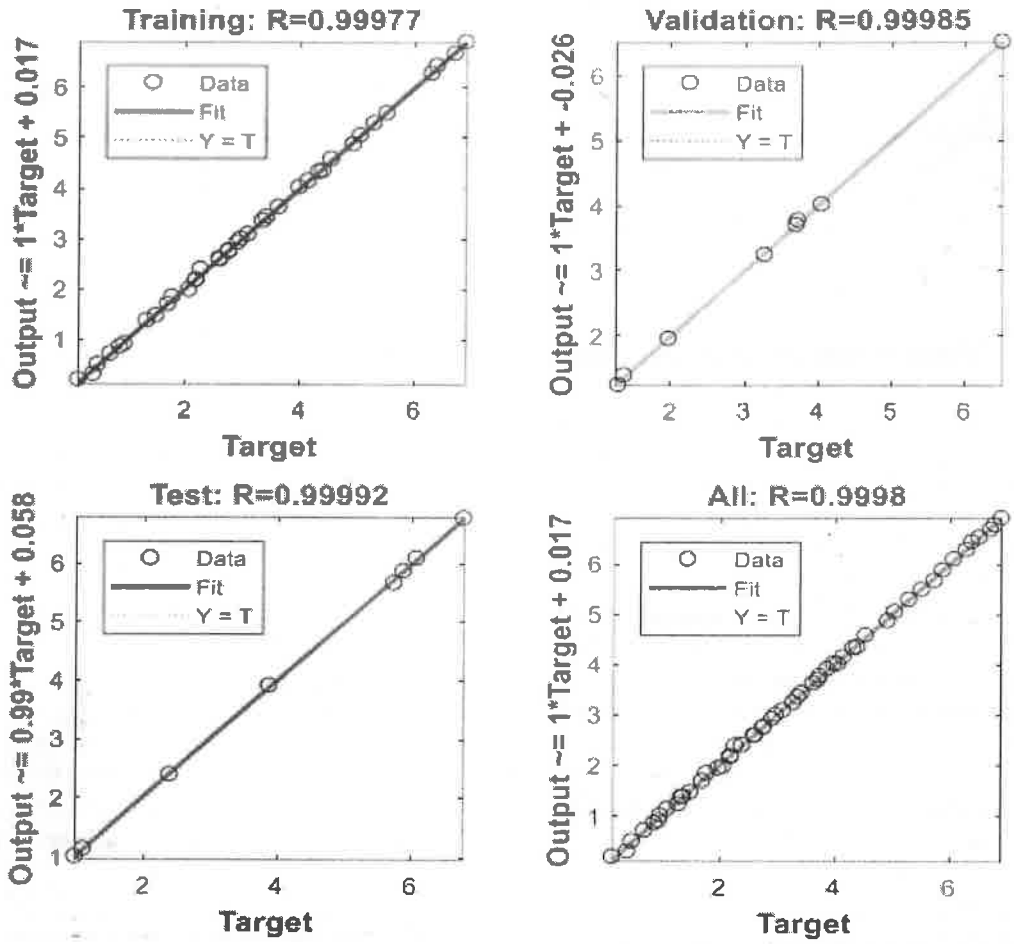

(a) ANN regression data for training, test and validation steps

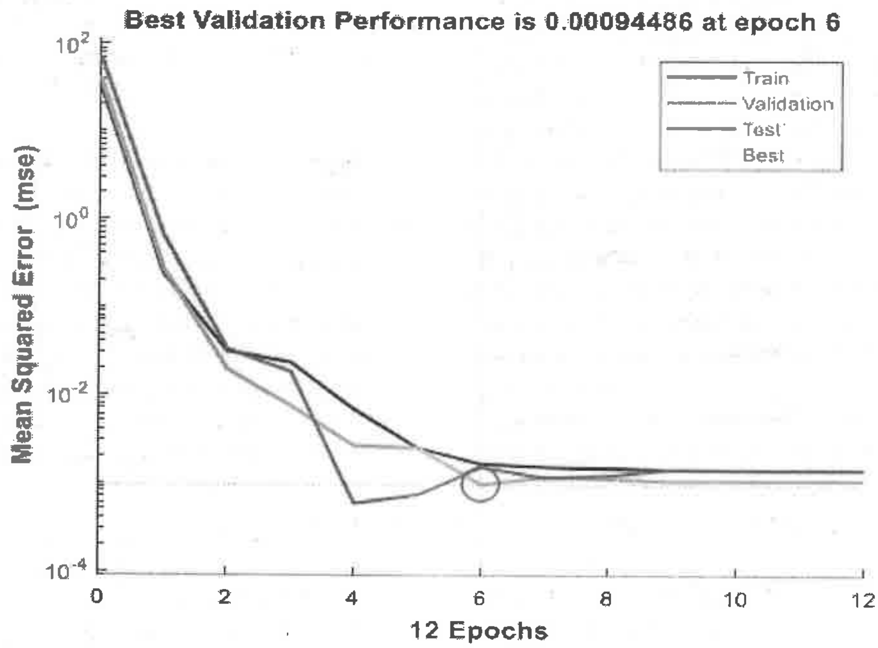

(b) The validation performance of the best ANN

Figure 3. (a) ANN regression data for training, test, and validation steps. (b) The validation performance of the best ANN.

displays the outcomes of the experiment and the CO_2-adsorbed output values of the neural network model. The determination of linear coefficient for entire set of data, according to the findings, was 0.9998. From the modelling data, ANN model can accurately estimate CO_2 adsorption on rice husk-activated carbon. The network obtains the greatest degree of validation according to the performance graph [Fig. 3(b)]. The outcomes of the ANN model for forecasting ANN weights are shown in Table AI based on the CO_2 adsorption network's optimal weight.[22]

The effect of temperature and pressure

Figure S6 depicts a CO_2 adsorption isotherm at 273 K and 298 K. The activation of rice husk-based activated carbon is significantly influenced by the isotherm. Figure S6 shows how as the adsorption temperature rises, the quantity of CO_2 that can be absorbed declines. Because adsorption is exothermic, its quantity reduces with rising temperature. It rises with pressure. The carbon dioxide adsorption comparison by several activated carbons are listed in Table S1. The present activated carbon from rice husk virtually performs the same as the others and reveals the outstanding carbon dioxide adsorption at 273 K and 298 K when the observed carbon dioxide adsorption capacity is compared to that reported in previous research, according to the comparison. The findings of this study can be utilised to create new rice husk-activated carbon that is efficient in absorbing CO_2.

Isotherm modelling

The adsorption rate of carbon dioxide depends on gas pressure. Figure 4 shows adsorption curve of carbon dioxide at atmospheric pressure and at temperature 273 and 298 K. The lower binding strengths of the carbon dioxide adsorbate and the Rice Husk-activated carbon can be used to explain why CO_2 adsorption capacity declines with increasing temperature in Fig. 4.[23] Additionally, the CO_2 adsorption capacity decreases at high temperatures, indicating an exothermic sorption process and the presence of physical sorption. Unlike chemisorption, which is mediated by a strong van der Waals force, physical adsorption relies on a weaker van der Waals force, which tends to break down as temperature rises.[23,24] Table S2 predicts the isotherm constants and associated R^2 values for the CO_2 adsorption using the regression approach.

The Hill isotherm is the best match for the adsorbent at 273 K based on the R^2 values in Table S2. (Fig. 4). Based on R^2 values, Table S2 demonstrates that Freundlich and

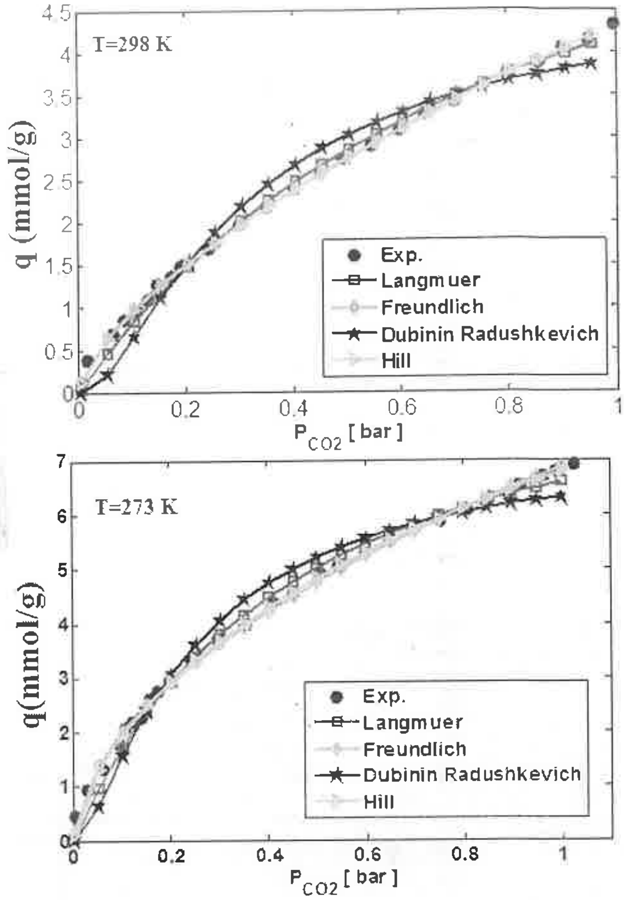

Figure 4. Experimental data and isotherm models at 273 K and 298 K for CO2 adsorption.

Hill isotherms (Fig. 4) are the best-fit models for the adsorption of activated carbon from rice husk at 298 K. According to the Freundlich model, carbon dioxide adsorption on the surface of activated carbons is multilayered rather than limited to a monolayer.[23] The Hill model is frequently used to describe how various species attach to homogenous surfaces.[25] Endothermic desorption is more beneficial at high temperatures, which lowers CO_2 adsorption capacity. According to Table S2's Freundlich constant, n, the CO_2 adsorption will be successful. The Dubinin-Radushkevich and Temkin isotherms are also helpful in providing information on A_T (heat of adsorption) and adsorption mean free energy(E). These are the energy parameters. The CO_2 adsorption process is entirely physical, as demonstrated by energy parameter values of 3 and 4 kJ/mol.[26]

Conclusion

KOH effectively activated and carbonised a carbon produced from biomass to obtain significant CO_2 adsorption capacity. At a holding temperature of 60 min, the activation was carried out above 800°C. Using scanning electron microscopy (SEM), Fourier transform infrared (FTIR), and Brunauer–Emmett–Teller (BET), the structure and characteristics of AC have been investigated. The total pore volume and BET surface area 2458 m^2/g and 0.76 cm^3/g respectively. With a strong CO_2 absorption of 6.76 mmol/g at 0°C and 1 pressure, this carbon exhibits. Lower binding strengths between the adsorbate and the activated carbon might be the cause of the declining CO_2 adsorption capability with rising temperature. At 289 k and 1 bar, AC-KOH had an adsorption capacity of 4.31 mmol/g. Based on R^2 values, Freundlich and Hill isotherms are the best-fit models for the activated carbon adsorbent at 298 K. The Hill isotherm is the model that fits the adsorbent at 298 K the best. Results indicate that the linear correlation coefficient for the entire set of data was 0.9998. The ANN outcomes demonstrated how well the neural network model could forecast CO_2 adsorption on activated carbon. The models' predictions of process performance were largely accurate, according to their findings.

Acknowledgments

The authors acknowledge financial support of this work from department of Chemistry, MJCET, which is operated and managed by Sultan-ul-Uloom Education society and also grateful to the Hon. Secretary, SUES, and Advisor-cum director, and department of CSE for programming data, MJCET, Hyderabad for their encouragement and support in completing this work successfully.

Data availability

The datasets generated and analysed during the current study are available from the corresponding author on reasonable request.

Declarations

Conflict of interest

On behalf of all the authors, the corresponding author states that there is no conflict of interest.

Appendix

See Table AI.

Table AI. The weights of RBF network with Levenberg–Marquardt algorithm.

Neuron	1	2	3	4	5	6	7	8	9	10
1W{1, 1}	−0.95205	−4.6498	−4.2967	−4.3362	−3.4764	−4.0559	−3.7245	1.1675	−2.4699	0.7053
	5.263	−0.65388	0.79438	−1.265	−3.5654	−0.59199	2.89	4.5297	−1.8386	−4.5716
b{1}	3.585	2.9496	2.56	1.1842	−0.26483	−0.79994	−1.1087	2.0934	−4.8113	4.2445
LW{1, 1}	−1.6906	0.45472	−0.08057	−0.06529	−1.9462	−0.1839	−0.67141	−0.22446	−0.92397	−0.21734
b{2}	−1.1291									

Supplementary Information

The online version contains supplementary material available at https://doi.org/10.1557/s43579-022-00262-w.

References

1. S. Wang, Y.R. Lee, Y. Won, H. Kim, S.E. Jeong, B.W. Hwang, A.R. Cho, J.Y. Kim, Y.C. Park, H. Nam, D.H. Lee, Development of high-performance adsorbent using KOH-impregnated rice husk-based activated carbon for indoor CO_2 adsorption. Chem. Eng. J. **21**, 135378 (2022)
2. Z. Khoshraftar, A. Ghaemi, Presence of activated carbon particles from waste walnut shell as a biosorbent in monoethanolamine (MEA) solution to enhance carbon dioxide absorption. Heliyon **8**(1), e08689 (2022)
3. H. Cui, J. Xu, J. Shi, S. You, C. Zhang, N. Yan, Y. Liu, G. Chen, Evaluation of different potassium salts as activators for hierarchically porous carbons and their applications in CO_2 adsorption. J. Colloid Interface Sci **1**(583), 40–49 (2021)
4. H. Pashaei, A. Ghaemi, Review of CO_2 capture using absorption and adsorption technologies. Iran. J. Chem. Chem. Eng. (2021)
5. M. Karimi, M. Shirzad, J.A. Silva, A.E. Rodrigues, Biomass/Biochar carbon materials for CO_2 capture and sequestration by cyclic adsorption processes: a review and prospects for future directions. J. CO2 Util **1**(57), 101890 (2022)
6. J. Serafin, M. Ouzzine, O.F. Cruz Jr., J. Sreńscek-Nazzal, I.C. Gómez, F.Z. Azar, C.A. Mafull, D. Hotza, C.R. Rambo, Conversion of fruit waste-derived biomass to highly microporous activated carbon for enhanced CO_2 capture. Waste Manag. **1**(136), 273–282 (2021)
7. M. Oschatz, M. Antonietti, A search for selectivity to enable CO_2 capture with porous adsorbents. Energy Environ. Sci **11**(1), 57–70 (2018)
8. C. Jin, J. Sun, Y. Chen, Y. Guo, D. Han, R. Wang, C. Zhao, Sawdust wastes-derived porous carbons for CO_2 adsorption. Part 1. Optimization preparation via orthogonal experiment. Sep. Purif. Technol. **276**, 119270 (2021)
9. G.G. Huang, Y.F. Liu, X.X. Wu, J.J. Cai, Activated carbons prepared by the KOH activation of a hydrochar from garlic peel and their CO_2 adsorption performance. N. Carbon Mater. **34**(3), 247–257 (2019)
10. K. Li, D. Zhang, X. Niu, H. Guo, Y. Yu, Z. Tang, Z. Lin, M. Fu, Insights into CO_2 adsorption on KOH-activated biochars derived from the mixed sewage sludge and pine sawdust. Sci. Total Environ. **25**, 154133 (2022)
11. L. Yin, W. Zheng, H. Shi, D. Ding, Ecosystem services assessment and sensitivity analysis based on ANN model and spatial data: a case study in Miaodao Archipelago. Ecol. Ind. **1**(135), 108511 (2022)
12. M. Ghaedi, N. Zeinali, A.M. Ghaedi, M. Teimuori, J. Tashkhourian, Artificial neural network- genetic algorithm based optimization for the adsorption of methylene blue and brilliant green from aqueous solution by graphite oxide nanoparticle. Spectrochim. Acta A **125**, 264–277 (2014)
13. J. Sarkar, Z.H. Prottoy, M.T. Bari, M.A. Al Faruque, Comparison of ANFIS and ANN modeling for predicting the water absorption behavior of polyurethane treated polyester fabric. Heliyon **7**(9), e08000 (2021)
14. F.A. Abdulkareem, E. Padmanabhan, Applied techniques for residual oil recovery from source rocks: a review of current challenges and possible developments. Can. Chem. Eng. **99**(1), 251–267 (2021)
15. D.K. Singh, K.S. Krishna, S. Harish, S. Sampath, M. Eswaramoorthy, No more HF: Teflon assisted ultrafast removal of silica to generate high-surface-area mesostructured carbon for enhanced CO_2 capture and supercapacitor performance. Angew. Chem. Int. Ed **55**, 2032–2036 (2016)
16. K. Palle, S. Vunguturi, S. N. Gayatri, et al., The prediction of CO_2 adsorption on rice husk activated carbons via deep learning neural network. MRS Commun. 1–7 (2022).
17. K. Palle, S. Vunguturi, K. Subba Rao, et al., Comparative study of adsorption isotherms on activated carbons synthesized from rice husk towards carbon dioxide adsorption. Chem. Pap. (2022)
18. M.O. Prakash, G. Raghavendra, S. Ojha, M. Panchal, Characterization of porous activated carbon prepared from arhar stalks by single step chemical activation method. Mater. Today **39**, 1476–1481 (2021)
19. H. Ramezanipour Penchah, A. Ghaemi, H. Godarziani, Eco-friendly CO_2 adsorbent by impregnation of diethanolamine in nanoclay montmorillonite. Environ. Sci. Pollut. Res. **28**(39), 55754–55770 (2021)
20. S. Kalam, U. Yousuf, S.A. Abu-Khamsin, U.B. Waheed, R.A. Khan, An ANN model to predict oil recovery from a 5-spot waterflood of a heterogeneous reservoir. J. Pet. Sci. Eng. **210**, 110012 (2022)
21. A. Hemmati, A. Ghaemi, M. Asadollahzadeh, RSM and ANN modeling of hold up, slip, and characteristic velocities in standard systems using pulsed disc-and-doughnut contactor column. Sep. Sci. Technol. **56**(16), 2734–2749 (2021)
22. S. Kolbadinejad, H. Mashhadimoslem, A. Ghaemi, M. Bastos-Neto, Deep learning analysis of Ar, Xe, Kr, and O_2 adsorption on activated carbon and zeolites using ANN approach. Chem. Eng. Process. Process Intensif. **170**, 108662 (2022)
23. N.A. Rashidi, S. Yusup, A. Borhan, Isotherm and thermodynamic analysis of carbon dioxide on activated carbon. Procedia Eng. **148**, 630–637 (2016)
24. A.S. Kovo, CO_2 capture using amine-impregnated activated carbon from *Jatropha curcas* shell. Br. J. Appl. Sci. Technol. **14**(4), 1 (2016)
25. G.K. Rajahmundry, C. Garlapati, P.S. Kumar, R.S. Alwi, D.V. Vo, Statistical analysis of adsorption isotherm models and its appropriate selection. Chemosphere **276**, 130176 (2021)
26. R.D.C. Soltani, M. Safari, A. Rezaee, H. Godini, Application of a compound containing silica for removing ammonium in aqueous media. Environ. Prog. Sustain. Energy **34**(1), 105–111 (2015)

Publisher's Note Springer Nature remains neutral with regard to jurisdictional claims in published maps and institutional affiliations.

MRS Communications (2022) 12:434–440

https://doi.org/10.1557/s43579-022-00197-2

MRS Communications

Research Letter

The prediction of CO_2 adsorption on rice husk activated carbons via deep learning neural network

Kishor Palle, and Shanthi Vunguturi, Department of Chemistry, Muffakham Jah College of Engineering and Technology, Hyderabad, Telangana, India
Sambhani Naga Gayatri, Department of Science and Humanities, MLR Institute of Technology, Hyderabad, Telangana, India
K. Subba Rao, Department of Chemistry (H&S), Malla Reddy Engineering College (Autonomous), Main Campus, Secunderabad, Telangana, India
P. Ramesh Babu, Department of Physics, Gokaraju Rangaraju Institute of Engineering & Technology, Nizampet Road, Hyderabad, Telangana, India
R. Vijay, Department of Physics, Usha Rama College of Engineering & Technology, Telaprolu, Vijayawada, Andhra Pradesh, India
Address all correspondence to Kishor Palle at **drkishorepalle@gmail.com**

(Received 2 May 2022; accepted 20 June 2022; published online: 30 June 2022)

Abstract
The carbon dioxide adsorption capacity of porous carbons prepared from rice husk with different textural properties varies greatly. It is widely accepted that greater CO_2 adsorption capacity is exhibited due to the existence of narrow micropores. This study investigates the relationship between carbon's textural characteristics and CO_2 adsorption. After training the neural network, the carbon dioxide adsorption capacity of unknown porous carbon was implicitly predicted by using the trained model. Surprisingly, when surface area, mesopore volume, and micropore volume are all utilized as input values, the predicted CO_2 adsorption values are well agreed with the experimental values.

Introduction
Rice husk is an important biomass resource in South Asia as well as in India and China. When compared to other agricultural Bio-wastes, rice husk is known for low utilization value as husk and highly utilized as ash that is mostly in the form of silica. Rice husk that is a layer protective for rice grain is the major by-product obtained from rice processing mill.[1]

Activated carbon can be synthesized from feed stock with high carbon and low inorganic content. The most common feed stocks used for the preparation of activated carbon are rice husk. During the activation method, the unique internal pore structure is created, that provides the activated carbon is outstanding adsorptive properties. Activated carbons have a variety of distinctive characteristics like large internal surface area, chemical properties, and good accessibility of internal pores.

In recent years, the concentration of carbon dioxide has increased rapidly in the atmosphere, leading to great concern for the environment. To improve carbon dioxide capture and storage, many technologies such as membrane separation and cryogenic as well as physical and chemical adsorption have been made. Among all these technologies, adsorption is regarded as the best method due to their high adsorption capacity, low cost, simplicity, low energy, demand, controllability, and other characteristics. Now a days, a lot of interest has shown in the development of porous carbons for the carbon dioxide adsorption, such as porous carbons,[2] metal–organic frameworks, mesoporous silica,[3] zeolites, microporous organic polymers, and covalent-organic frameworks. Currently, the best carbon dioxide capture adsorbents are carbon-based materials due to high surface area and pore volume, easy-to-design pore structure, fast adsorption–desorption kinetics, and low cost.[4]

Carbon-based porous materials have been synthesized in a variety of ways, and surface parameters obtained, which are surface area (SBET), micropore volume (V_{micro}), mesopore volume (V_{meso}), and so on, highly outstanding.[5] Much research effort has gone into developing a carbon-based porous material with a large SBET and high pore volume to improve CO_2 uptake.[5] The most efficient approaches are KOH activation and template-assisted methods. Xia et al., for example, utilized the zeolite as model to increase carbon-based microporous materials surface area & pore volume to achieve higher carbon dioxide adsorption (28.3 mmol g^{-1}) at 25°C.[6] Although it is widely acceptable that the most important factor in CO_2 adsorption is due to the existence of narrow micropores,[7] the carbon dioxide adsorption and pore structure relationship remains unknown. In general, it is obstruct that the development of advanced gas adsorbents and future-generation carbon-based adsorbents is due to the lack of structural–property relationship.

It has been numerous phenomenological efforts to fulfill this knowledge gaps. Particularly, past work by Clark, North, and colleagues has showed that V_{meso} has a surprising effect on CO_2 adsorption capacity via the nonlinear product term of V_{micro} and V_{meso} shown in Eq. (1). They demonstrated that CO_2 physisorption is the most common adsorption mechanism.[8] As shown in Eq. (1), partial least squares regression method was utilized to determine CO_2 adsorption.

$$M_{ads}^{CO_2} = 0.095 + 2.10 \times V_{micro} + 3.51 \times V_{micro} \times V_{meso}. \quad (1)$$

Although this regression equation can provide a reasonable fit, obtaining an ideal empirical formula using the method of regression polynomials is difficult. Furthermore, because this equation is linear, it is unable to find out and amend as database extends.[9] More importantly, according to Eq. (1), ordered carbon-based mesoporous materials without micropores the ability to do so should be very limited almost not to adsorb CO_2, which is unreasonable in some cases.

To recognize relation between different variables, Machine learning algorithms-enabled computers were used to render basic instructions, also for nonlinear interpolations.[10] By adjusting the synapse weights, artificial neural networks (NNs) can produce optimal results as machine learning algorithms. In each layer to form a Neural Network, Neurons ordered essentially be linked together.[11] A variety of uses have showed by DNNs (deep neural networks) with a variety of hidden layers to exceed state-of-the-art models.[12] Whereas the use of DNNs to chemistry-related issues is till now at beginning stage, the circumstances are rapidly changing.[12] To date, there has been much discussion about the relationship between the textural parameters of porous carbons and the corresponding CO_2 adsorption capacity. Despite the fact that textural parameters of porous carbon are well studied, little research has been carried out on the prediction of their behavior.

Materials and methods

Preparation of rice husk activated carbon (RHAC)

Rice husk gathered from rice mill near Telaprolu, Vijayawada, India, was cleaned exhaustively with distilled water to take off adhering soil and dust, and dried at 110°C overnight. Rice husks were calcined at different temperatures at different atmospheres for 4 h. The temperature was programmed as 10°C per minute and gas flow maintained at 40 mL per minute.[13] Flow chart of activated carbon is shown in Fig. S1.

BET surface area and pore volume

Table S1 summarizes Brunauer–Emmett–Teller surface area (S_{BET}), V_{micro}, and V_{meso} of various porous carbons samples synthesized in our laboratory. The predicted samples were MPC-400, MPC-600, and MPC-800, which were synthesized by the usage of increased hydrogen-bonding interaction method (in which mesoporous carbon materials pyrolyzed at temperatures of 400, 600, & 800°C, respectively). The total pore volume of all the as-synthesized mesoporous carbons (MPCs) was greater than 0.5 $cm^3\ g^{-1}$, but they exhibit very low micropore volume, showing that those samples were predominantly mesoporous materials. Type IV isotherm is also shown in Fig. 1(a) and (b) with remarkable hysteresis loops at relative pressure $P/P0 = 0.6–0.8$, indicating the presence of uniform mesoporosity. Furthermore, as shown in Table S1, as the temperature of pyrolysis raised, the SBET and total pore volume of the MPCs increased.

N_2 adsorption–desorption isotherms

In order to increase the scope of the predication, a commercial Dacro activated carbon (ACD), Rice husk activated carbon (RHAC), and VXC605 (Vulcan XC605) were selected as predicted samples. The S_{BET} of ACD in Table S1 was 625 $m^2\ g^{-1}$ with V_{micro} of 0.14 $cm^3\ g^{-1}$ & V_{meso} of 0.43 $cm^3\ g^{-1}$. At very low relative pressure, nitrogen adsorption–desorption isotherms of ACD sample showed a elevated beginning and a typical IV isotherm with a significant hysteresis loop, designating a different porous structure. RHAC, on the other hand, the sample with highest SBET value 1326 $m^2\ g^{-1}$ as mentioned in Table S1, displayed a typical I isotherm and Fig. 1(a) and (b), indicating that it was mainly microporous. Due to smallest surface area 55 $m^2\ g^{-1}$, the mesoporous material VXC605 had almost no micropore volume.

Deep learning neural network method

According to Clark, North, and colleagues' research, the V_{micro} and V_{meso} values were the influencing factor for CO_2

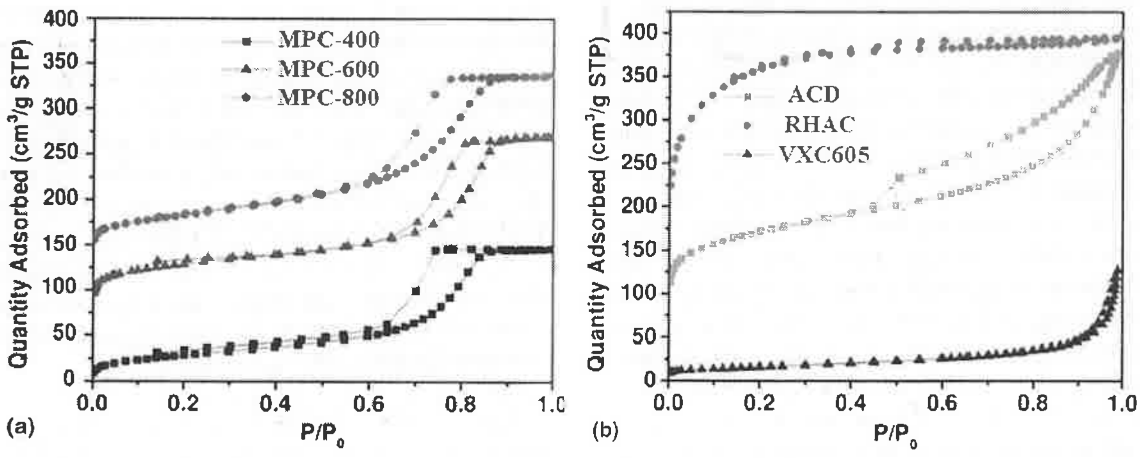

Figure 1. (a), (b) The predicted porous carbon materials N_2 adsorption–desorption isotherms at 77 K.

adsorption, as shown in Eq. (1).[8] According to other research, high surface area and narrow micropores in porous carbons contribute to higher CO_2 adsorption. To better understand the roles of SBET, V_{micro}, and V_{meso}, various variables taken out from input layer were selected as neurons, and sequentially send to hidden layers & output layer. Finally, for the prediction of carbon dioxide adsorption of 6 MPCs, the data taken from Neural Network were stored & transferred by using feed-forward process in our laboratory. Figure 2(a) depicts a typical NN construction; a neural network was mentioned as DNN when it has hidden layers more than one. Every line connecting two nodes describes weight, the relation between input–output values is pretended by the variation of these weights. In order to reduce error, the weights for each node of the NN were adjusted based on the output values of experimentation and calculation.

CO_2 adsorption prediction

According to Clark, North, and colleagues reported in Table S2,[8] with 12 known data points, we describe three NNs trained by using V_{micro}, V_{micro}–V_{meso}, and V_{micro}–V_{meso}–S_{BET} as the input neurons, respectively. On the basis of underlying relationship between textural properties and CO_2 adsorption, we apply the NNs to estimate the potential CO_2 adsorption uptakes of 6 porous carbon materials synthesized in our laboratory. In order to make predictions more extensively applicable, we screened 500 CO_2 adsorption data set of porous carbon materials at various conditions for adsorption, then developed a Deep learning Neural Network having 2 hidden layers based on adsorption conditions (pressure and temperature) & textural properties as training set.

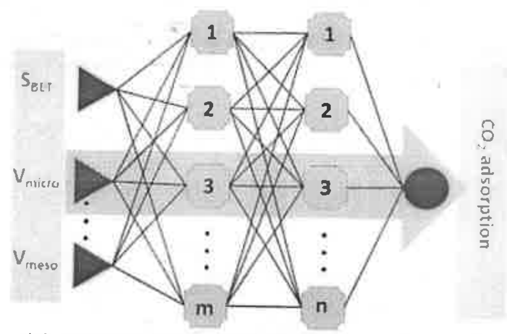

(a) Construction of ANN (artificial neural network)

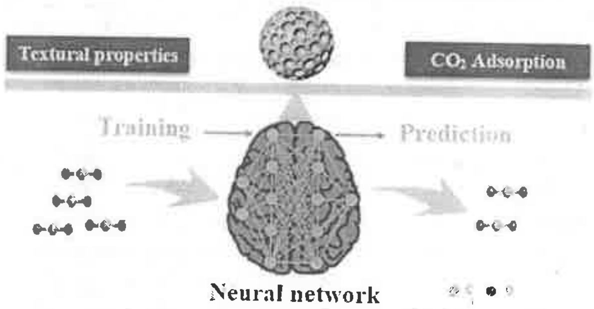

(b) Carbon dioxide adsorption prediction of porous carbon.

Figure 2. (a) Construction of artificial neural network (ANN). (b) Carbon dioxide adsorption prediction of porous carbon.

Whatever the synthesis method, specific structure, or raw materials of the porous carbon, deep learning technique was able to predict automatically the CO_2 adsorption capacity of 20 porous carbons which are randomly untrained. As shown in Fig. 2(b), this novel deep learning neural network approach has significant potential for predicting carbon dioxide adsorption capacities of porous carbons based on their textural properties.

Results and discussion

We selected twelve porous carbon data points in Table S2[8] that Clark, North, and colleagues had investigated as training objectives in order to establish a correlation among textural properties & CO_2 adsorption.[8] Using the same set of experimental conditions and the same 12 training objectives, the 6 predicted carbons in Table S1 were examined for their CO_2 adsorption properties. The samples were dried before being subjected to four cycles of pressurization to 5 bar with CO_2 for 0.5 h, followed by vacuum at 25°C until the mass did not change. To calculate the CO_2 adsorption capacity (mmol gm^{-1} CO_2 adsorbed), the mass change between the pressurization and vacuum processes was used. Figure 3(a) depicts avg. data prevailed from 4 cycles. The experimental values of MPC-400, MPC-600, MPC-800, ACD, RHAC, and VXC605 were 1.35, 2.01, 2.26, 2.78, 5.42, and 0.31 mmol g^{-1}, respectively. The first Neural Network (NN-1) was created, consisting of one input (V_{micro}), one output (CO_2 adsorption), and one hidden layer. The first neural network (NN-1) is created by including of one input (V_{micro}), one output (CO_2 adsorption), and one hidden layer. Figure 3(b) shows 12 training objectives correlation plot, with V_{micro} as the only input value. Data were fitted to 12 training objectives (12 black dots) using experimental and predicted data, and by taking V_{micro} as input value, the CO_2 adsorption was predicted using created first neural network NN-1.

However, there was a significant difference between experimental & predicted data from first neural network (6 blue dots in Fig. 4(b)), particularly for VXC605, ACD, and RHAC samples. Due to these results, to predict the CO_2 adsorption values of MPC materials, the first neural network NN-1 could not be used. These findings suggest that porous carbons micropore volume (V_{micro}) is not the only factor influencing CO_2 adsorption. Following that, input layer containing 2 neurons (V_{micro} and V_{meso}) was utilized for the creation of second Neural Network (NN-2). The optimized results in Fig. 3(c) show that prediction by NN-2 is better than NN-1, suggesting that mesopores are also responsible for CO_2 adsorption. However, predicted CO_2 adsorption value (2.35 mmol g^{-1}) of RHAC was less than that of experimental value of 5.42 mmol gm^{-1}.

We compared carefully the textural properties of RHAC & carbon dioxide adsorption data of twelve training samples to clarify the reason. From the data shown in Table S2, there is a similarity of V_{total} which is identified for RHAC (0.61 cm^3 g^{-1}) & ACN (Commercial Norit Activated Carbon) (0.60

Figure 3. (a) Carbon dioxide adsorption data of all the different samples. Experimental and estimated carbon dioxide data correlation from (b) NN-1 (V_{micro}), (c) NN-2 (V_{micro} &V_{meso}), & (d) NN-3 (SBET, V_{micro}, and V_{meso}). See text for details.

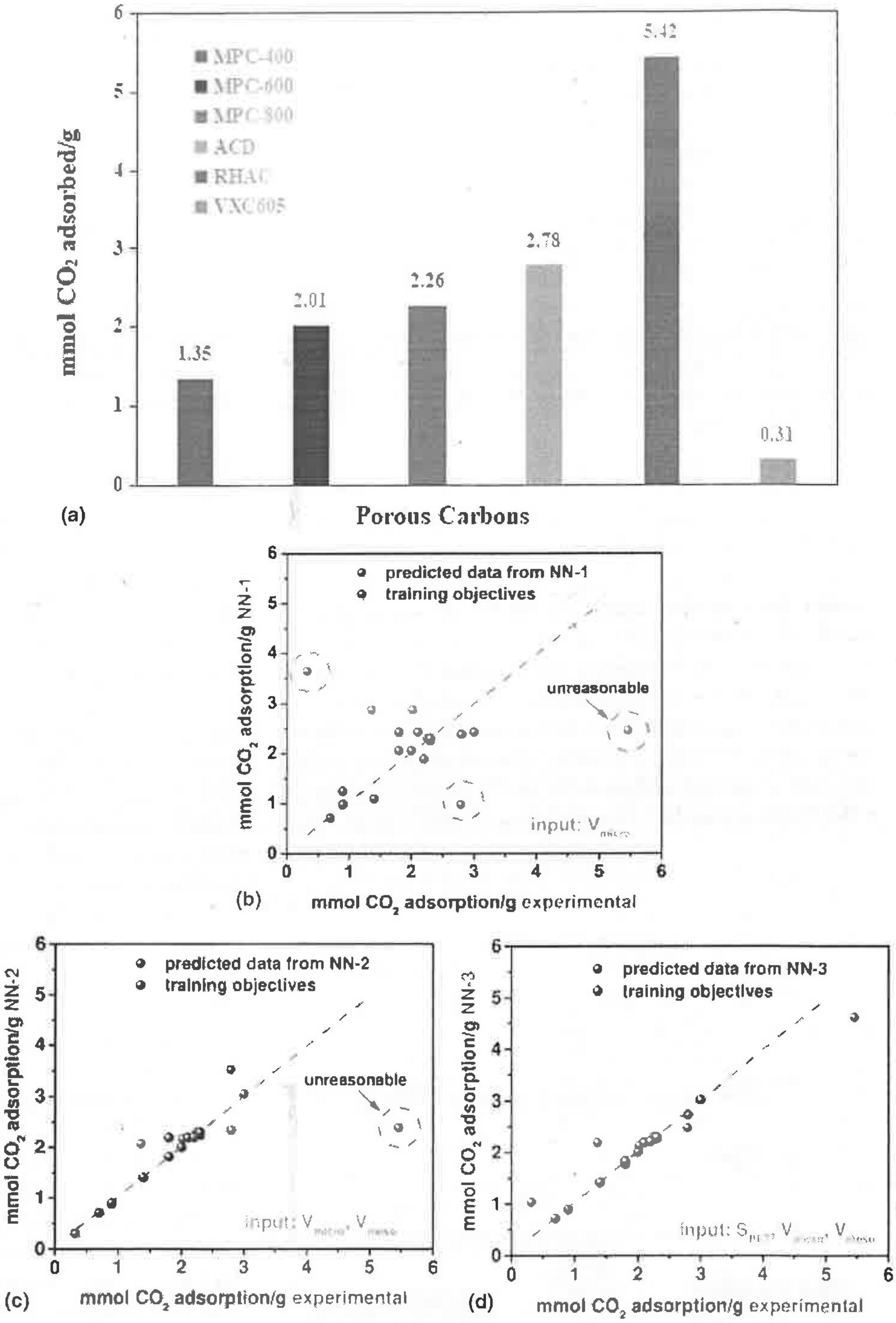

cm^3 g^{-1}).[8] ACN sample has 0.42 and 0.18 cm^3 g^{-1} micropore & mesopore volumes, respectively. In RHAC, the V_{total} was a little less than ACN, but the V_{micro} was almost same. According to these results, carbon dioxide adsorption values calculated by using Eq. (1) must be similar for RHAC and ACN. While ACN sample had a CO_2 adsorption capacity of 2.0 mmol g^{-1}, RHAC had CO_2 adsorption capacity of 5.42 mmol g^{-1} by practically which was very high. According to the NN-2 model, the predicted carbon dioxide adsorption value was 2.35 mmol g^{-1}, which is also very low than experimental carbon dioxide adsorption value 5.42 mmol g^{-1}, but it is similar to that of ACN sample. However, RHAC and ACN had similar pore volumes, but RHAC's SBET was 1326 m^2 g^{-1}, which was greater than ACN 798 m^2 g^{-1}. It was proposed that RHAC's greater CO_2 adsorption capacity compared to ACN was due to its larger surface area.

Then, a neural network with 3 neurons (SBET, V_{micro}, and V_{meso}) was utilized to train 12 samples. Some network structures with varying numbers of neurons and one hidden layer were investigated. As previously stated, the number of training and testing objectives was 12 and 6, respectively. A comparison of experimental and predicted values using this NN-3 model showed that NN model was accurate in predicting porous carbon's CO_2 adsorption. Figure 3(d) depicts the outcomes. The twelve training samples results collected from NN-3 were identified to be similar to the experimental result obtained (black dots). Following that, the SBET, V_{micro}, and V_{meso} values of 6 tested samples were selected as input values to test NN-3's predictive value. Interestingly, the prediction values from BPNN-3 for the six tested specimens were much similar to that of experimental values (blue dots) shown in Fig. 3(d).

Clark et al. proposed Eq. (1), which showed that V_{meso} has a surprising effect on CO_2 adsorption capacity via the nonlinear product term of V_{micro} and V_{meso}.[20] It is undeniable that Eq. (1) gives a elaborated correlation between CO_2 adsorption & textural properties for the first time. However, for carbonaceous materials, the scope of this application was extremely limited. According to Eq. (1), ordered mesoporous carbons almost without micropores should have less capacity to the adsorption of CO_2. Figure 3(a) shows mesoporous carbon with high CO_2 adsorption, indicating that Eq. (1) does not apply to such types of porous materials. Furthermore, we utilized this equation for the prediction of carbon dioxide adsorption values of porous materials in our laboratory and determined a significant difference between calculated and observed results.

To prevent the occurrence of using small data, we collected approximately 1020 CO_2 adsorption values data for various porous carbon materials shown in Table S3[8] at various adsorption temperatures and pressures.[8, 14–30] Because heteroatom N has shown to have a large effect on CO_2 adsorption ability, all porous carbons have been filtered without heteroatom N. In input layer, five neurons are temperature, pressure, mesopore volume, micropore volume, and surface area as depicted in Fig. S2.[8] We then trained a DNN with two hidden layers with 1000 samples of data as training data, followed by 20 data samples that we used for prediction. Additionally, we tested the accuracy of NN model's by using 1000 training samples taken random with leave-k-out method. To make predictions, the leave-k-out method selects k examples from the 1000 training samples dataset, after selection repeat the same process 1000/k times to create an entity of test cases. Generally, $k=1$ is used, and each case is treated as a test, a statistically significant communication of the neural network model's accuracy is provided by the avg. error/performance. For 1000 training samples, as seen in Fig. 4(a), phenomenal concordance was achieved among predicted and experimental values.

More interestingly, avg. error is 0.43 only which was shown for the dataset of 1000 training samples taken randomly in Figure S3[8] by the leave-one-out results. Thus, an invisible correlation has been found using a Deep Neural Network to transform input data (adsorption conditions and textural properties) for test case of the remaining 20 samples to instantaneously explore new interpretations for output data (CO_2 adsorption). Figure 4(b) confirms that this DNN is suitable for predicting CO_2 adsorption due to its highly improved prediction performance. We presume that the NN model's inaccuracy is totally acceptable for the range of regular experimental results.

Figure 4(c) depicts the CO_2 uptake, micropore, and mesopore volume correlation over 75 data points at 25°C temperature and 1 bar pressure conditions. The effects of micropore and mesopore volume on CO_2 adsorption were found to be significantly different. According to the findings, at room temperature and pressure, micropore volume primarily governs CO_2 adsorption in porous carbons, which is consistent with past research. For CO_2 adsorption, mesopore volume is also one of the important parameter.

Despite the fact that there is no clear role for mesopores in Fig. 4(c), a small quantity of mesoporosity did get better improvement in porous carbons' capacity to absorb CO_2. In comparison, as shown in Fig. 4(d), mesopores play a particularly significant role in CO_2 adsorption under high pressure, effectively explaining why high CO_2 adsorption at low pressure has always been attained under microporous carbons and extremely high CO_2 adsorption at high pressure can be achieved under stratified porous carbons.

Conclusion

In this research work, we build three neural network models (NNs) with V_{micro}, V_{micro}–V_{meso}, and V_{micro}–V_{meso}–SBET as input neurons & CO_2 adsorption ability as output neurons. Following that, the achieved NN was used to predict the CO_2 adsorption values of 6 porous carbon materials in our laboratory. Interestingly, the best agreement among both experimental and predicted values for CO_2 adsorption capacity is procured only when V_{micro}, V_{meso}, and SBET are used as input neurons at the same time. More pertinently, for over 1000 data samples taken from the past research work and our laboratory, suitable prediction of carbon dioxide adsorption capacity is given by trained DNN. The following are recommended findings: To begin, the large data investigation confirmed the significance of V_{meso} in controlling gas utilization, dispelling a lengthy false narrative that V_{micro} is now the only parameter controlling small molecule gas uptake. Second, SBET is a self-governing textural parameter that, when coupled with the other textural parameters, is used to determine gas–solid interactions thereby gas-adsorption abilities. Finally, carbon dioxide adsorption by solid adsorbents is predicated by complex interaction of textural characteristics, also selectivity of which could be predicted. This technique opens up a new pathway for the use of NNs in predicting the gas-adsorption capacities of activated carbon. This technology may also serve as a model for the progression of next-generation carbon adsorbent materials and advanced gas adsorbent materials.

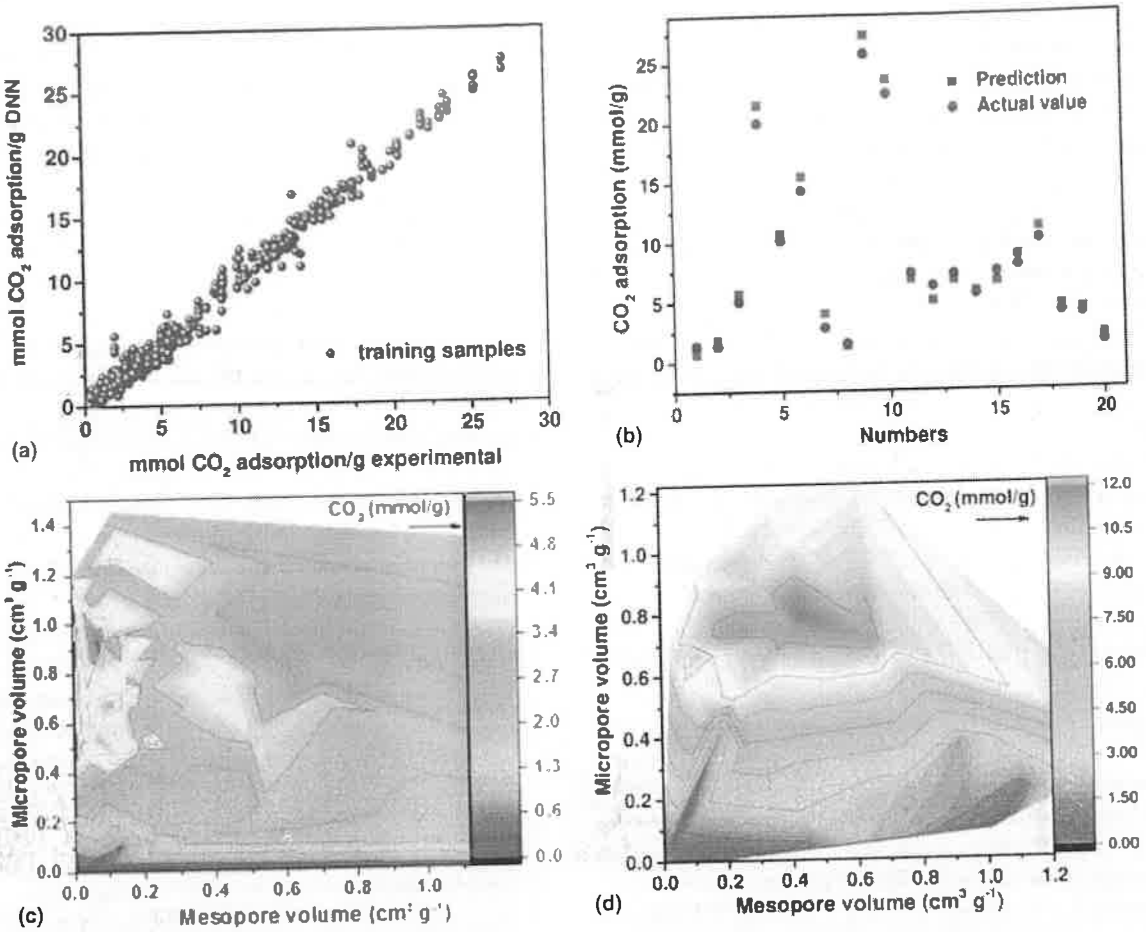

Figure 4. (a) Experimental and estimated CO_2 adsorption data correlation via deep learning neural network; (b) Average error of single sample VS training iterations of the random 1000 training samples; (c) CO_2 uptake, micropore, and mesopore volume correlation at 25°C temperature and 1 bar pressure conditions; (d) CO_2 uptake, micropore, and mesopore volume correlation at 25°C temperature and 5 bar pressure conditions.

Acknowledgments

The authors acknowledge financial support of this work from department of Chemistry, MJCET, which is operated and managed by Sultan-ul-Uloom Education Society and also grateful to the Hon. Secretary, SUES and Advisor-cum director and department of CSE for programming data, MJCET, Hyderabad for their encouragement and support in completing this work successfully.

Data availability

The datasets generated and analyzed during the current study are available from the corresponding author on reasonable request.

Declarations

Conflict of interest

On behalf of all the authors, the corresponding author states that there is no conflict of interest.

Supplementary Information

The online version contains supplementary material available at https://doi.org/10.1557/s43579-022-00197-2.

References

1. I. Nhapi, N. Banadda, R. Murenzi, C. Sekomo, U. Wali, Removal of heavy metals from industrial waste water using rice husks. Open Environ. Eng. J. **4**, 170–180 (2011)
2. M.G. Plaza, C. Pevida, A. Arenillas, F. Rubiera, J.J. Pis, CO_2 capture by adsorption with nitrogen enriched carbons. Fuel **86**, 2204–2212 (2007)
3. R. Serna-Guerrero, Y. Belmabkhout, A. Sayari, Further investigations of CO_2 capture using triamine-grafted pore-expanded mesoporous silica. Chem. Eng. J. **158**, 513–519 (2010)
4. Y. Li, B. Zou, C.W. Hu, M.H. Cao, Nitrogen-doped porous carbon nanofiber webs for efficient CO_2 capture and conversion. Carbon **99**, 79–89 (2016)
5. R. Wang, P. Wang, X. Yan, J. Lang, C. Peng, Q. Xue, Promising porous carbon derived from celtuce leaves with outstanding supercapacitance and CO_2 capture performance. ACS Appl. Mater. Interfaces **4**, 5800–5806 (2012)
6. J.J. He, J.W.F. To, P.C. Psarras, H.P. Yan, T. Atkinson, R.T. Holmes, D. Nordlund, Z.N. Bao, J. Wilcox, Tunable polyaniline-based porous carbon with ultrahigh surface area for CO_2 capture at elevated pressure. Adv. Energy Mater. **6**, 1502491 (2016)

7. H. Wei, S. Deng, B. Hu, Z. Chen, B. Wang, J. Huang, G. Yu, Granular bamboo-derived activated carbon for high CO_2 adsorption: the dominant role of narrow micropores. Chemsuschem **5**, 2354–2360 (2012)
8. G. Dura, V.L. Budarin, J.A. Castro-Osma, P.S. Shuttleworth, S.C. Quek, J.H. Clark, M. North, Importance of micropore-mesopore interfaces in carbon dioxide capture by carbon-based materials. Angew. Chem. Int. Ed. **55**, 9173–9177 (2016)
9. S.K. Sinha, M.C. Wang, Artificial neural network prediction models for soil compaction and permeability. J. Geotech. Geol. Eng. **26**, 47–64 (2008)
10. Y. Deng, M. Zhu, D. Xiang, X. Cheng, An analysis for effect of cetane number on exhaust emissions from engine with the neural network. Fuel **81**, 1963–1970 (2002)
11. S. Shakeri, A. Ghassemi, M. Hassani, A, Hajian, Investigation of material removal rate and surface roughness in wire electrical discharge machining process for cementation alloy steel using artificial neural network. Int. J. Adv. Manuf. Tech. **82**, 549–557 (2008)
12. K. Ryan, J. Lengyel, M. Shatruk, Crystal structure prediction via deep learning. J. Am. Chem. Soc. **140**(32), 10158–10168 (2018)
13. P. Kishore, A.K. Turaka, B.N. Srinivas, K. Subba Rao, Study of physical properties of bio-waste materials like rice husk ash prepared in different atmospheres and temperatures. Int. J. Recent Innov. Eng. Res. **2**(7), 26–31 (2017)
14. W. Travis, S. Gadipelli, Z. Guo, Superior post-combustion CO_2 adsorption from waste coffee ground derived carbons. RSC Adv. **5**, 29558–29562 (2015)
15. S.-Y. Lee, S.-J. Park, Determination of the optimal pore size for improved CO_2 adsorption in activated carbon fibers. J Colloid Interface Sci. **389**(1), 230–235 (2013)
16. M. Sevilla, A.B. Fuertes, CO_2 adsorption by activated templated carbons. J. Colloid Interface Sci. **366**(1), 147–154 (2012)
17. M. Sevilla, A.B. Fuertes, Sustainable porous carbons with a superior performance for CO_2 capture. Energy Environ. Sci. **4**, 1765–1771 (2011)
18. A. Wahby, J.M. Ramos-Fernandez, M. Martinez-Escandell, A. Sepulveda-Escribano, J. Silvestre-Albero, F. Rodriguez-Reinoso, High-surface-area carbon molecular sieves for selective CO_2 adsorption. Chemsuschem **3**, 974–981 (2010)
19. S.-M. Hong, S.W. Choi, S.H. Kim, K.B. Lee, Porous carbon based on polyvinylidene fluoride: enhancement of CO_2 adsorption by physical activation. Carbon **99**, 354–360 (2016)
20. M.E. Casco, M. Martínez-Escandell, J. Silvestre-Albero, F. Rodríguez-Reinoso, Effect of the porous structure in carbon materials for CO. Carbon **67**, 230–235 (2014)
21. J. Ludwinowicz, M. Jaroniec, Potassium salt-assisted synthesis of highly microporous carbon spheres for CO_2 adsorption. Carbon **82**, 297–303 (2015)
22. B. Adeniran, R. Mokaya, Low temperature synthesized carbon nanotube superstructures with superior CO_2 and hydrogen storage capacity. J. Mater. Chem. A **3**(9), 5148–5161 (2015)
23. G.K. Parshetti, S. Chowdhury, R. Balasubramanian, Biomass derived low-cost microporous adsorbents for efficient CO_2 capture. Fuel **148**, 246–254 (2015)
24. L. Estevez, D. Barpaga, J. Zheng, S. Sabale, R.L. Patel, J.G. Zhang, B.P. McGrail, R.K. Motkuri, Hierarchically porous carbon materials for CO_2 capture: the role of pore structure. Ind. Eng. Chem. Res. **57**, 1262–1268 (2018)
25. G. Srinivas, V. Krungleviciute, Z.-X. Guo, T. Yildirim, Exceptional CO_2 capture in a hierarchically porous carbon with simultaneous high surface area and pore volume. Energy Environ. Sci. **7**(1), 335–342 (2014)
26. G. Singh, I.Y. Kim, K.S. Lakhi, P. Srivastava, R. Naidu, A. Vinu, Single step synthesis of activated bio-carbons with a high surface area and their excellent CO_2 adsorption capacity. Carbon **116**(17), 448–455 (2017)
27. M. Sevilla, A.S.M. Al-Jumialy, A.B. Fuertes, R. Mokaya, Optimization of the pore structure of biomass-based carbons in relation to their use for CO_2 capture under low- and high-pressure regimes. ACS Appl. Mater. Interfaces **10**(2), 1623–1633 (2018)
28. G.P. Hao, W.C. Li, D. Qian, G.H. Wang, W.P. Zhang, T. Zhang, A.Q. Wang, F. Schüth, H.J. Bongard, A.H. Lu, Structurally designed synthesis of mechanically stable poly(benzoxazine-co-resol)-based porous carbon monoliths and their application as high-performance CO_2 capture sorbents. J. Am. Chem. Soc. **133**, 11378–11388 (2011)
29. N. Balahmar, A.S. Al-Jumialy, R. Mokaya, Biomass to porous carbon in one step: directly activated biomass for high performance CO_2 storage. J. Mater. Chem. A **5**, 12330–12339 (2017)
30. E. Hirst, A. Taylor, R. Mokaya, A simple flash carbonization route for conversion of biomass to porous carbons with high CO_2 storage capacity. J. Mater. Chem. A **6**, 12393–12403 (2018)

Chemical Papers
https://doi.org/10.1007/s11696-022-02371-1

ORIGINAL PAPER

Comparative study of adsorption isotherms on activated carbons synthesized from rice husk towards carbon dioxide adsorption

Kishor Palle[1] · Shanthi Vunguturi[1] · K. Subba Rao[2] · Sambhani Naga Gayatri[3] · P. Ramesh Babu[4] · Md. Mustaq Ali[5] · Ramesh Kola[6]

Received: 16 June 2022 / Accepted: 11 July 2022

Abstract

Rice husk was chemically activated with saturated KOH solution and the activation temperature was varied from 400 to 700 °C to generate activated carbons with different textural characteristics. Activated carbons were investigated for their ability to adsorb CO_2. We selected Langmuir, Freundlich, Sips and Radke-Prausnitz equations to fit the experimental CO_2 adsorption data. In order to determine the effect of using different error standards when calculating isotherm model parameters, an error analysis was conducted. The Radke-Prausnitz model shows the best fit to CO_2 adsorption and calculated adsorption capacity correlates closely with experimental data.

Keywords Rice husk · Activated carbon · Adsorption models · Error analysis · CO_2 adsorption

Introduction

Rice husk is an important biomass resource in South Asia as well as India and China. When compared to other agricultural Bio-wastes rice husk is known for low utilization value as husk and highly utilized as ash that is mostly in the form of silica. Rice husk that is a layer protective for rice grain is that the major by-product obtained from rice processing mill (Nhapi et al. 2011; Zhang et al. 2011).

Global warming has become major concern over the past few years. Increasing greenhouse gas concentrations caused the global average temperature to rise by about 1 °C every year. Among the gases responsible for the greenhouse effect, CO_2 plays the most significant role, since it stays in atmosphere for a significantly longer period of time. By 2020, CO_2 emissions will be over 36 billion tons, up from 2 billion tons in 1900 (Sai Bhargava Reddy et al. 2021). As the amount of harmful CO_2 in atmosphere continues to rise, this is critical for maintaining continued initiatives to minimize worldwide greenhouse gas emissions that cause climatic changes by developing and implementing impressive CO_2 capture methods.

Porous materials are a promising strategy to capture CO_2. In particular, advantages offered by carbon materials such as low desorption temperatures, rapid kinetics and high stability. Carbonaceous materials are very inexpensive if they are made with renewable resources or even waste. So researchers are trying to develop technologies that will enable carbon dioxide to be captured and stored, particularly adsorption technologies are treated as really promising at present (Singh et al. 2017). CO_2 capture is possible with the use of solid adsorbents, which have recently been studied: porous polymers (Sun et al. 2015), zeolites (Nguyen et al. 2016), monoliths (Günay et al. 2007), carbon nanotubes (Elmorsi

✉ Kishor Palle
drkishorepalle@gmail.com

1 Department of Chemistry, Muffakham Jah College of Engineering and Technology, Hyderabad, Telangana, India

2 Department of Chemistry (H&S), Malla Reddy Engineering College(Autonomous), Main Campus, Secunderabad, Telangana, India

3 Department of Science and Humanities, MLR Institute of Technology, Hyderabad, Telangana, India

4 Department of Physics, Gokaraju Rangaraju Institute of Engineering & Technology, Nizampet Road, Hyderabad, Telangana, India

5 Department of Mathematics (H&S), Malla Reddy Engineering College(Autonomous), Main Campus, Secunderabad, Telangana, India

6 Department of Chemistry, Chaitanya Bharathi Institute of Technology (A), Gandipet, Hyderabad, Telangana, India

Published online: 23 August 2022

2011), carbon nanosheets (Gong et al. 2014), metalloorganic structures (Zhang et al. 2017), activated carbons (Serafifin et al. 2017; Młodzik et al. 2016). In addition to the advantages mentioned above, carbonaceous materials appear to offer several particularly attractive advantages, including a low cost of production, high porosity, high surface area, readily controlled composition, an excellent chemical and thermal stability and high efficiency (Ayawei et al. 2015a; b).

According to equilibrium sorption isotherms, activated carbons adsorption ability and its efficiency can be predicted. An isotherm model with 2, 3, 4, and even 5 parameters are used to describe adsorption process (Elmorsi 2011; Schell et al. 2012a, b). For determining an isotherm of an adsorption and its constant, both experimentation and calculation values are needed. Langmuir, Freundlich, Sips and the Radke-Prausnitz equations were selected among the existing theoretical adsorption models for quantitative comparison of applicability of these models to fit CO_2 adsorption experiments. The amount of gas adsorbed as a function of pressure is defined by the following equations:

Langmuir isotherm

Various models have been developed to describe the adsorption of the gas–solid phase, the Langmuir isotherm being the simplest. A maximum adsorption capacity is also quantified and compared between different sorbents using this method. As described by Langmuir theory, adsorption take place at homogeneous sites in a monolayer of adsorbate. Once a site occupied by adsorbate, no further adsorption happen at that site. As a consequence, capacity of sorbent is limited to adsorb (Elmorsi 2011; Günay et al. 2007). By the following Eq. (1) Langmuir isotherm can be expressed:

$$q = \frac{q_{mL} b_L p}{1 + b_L p} \tag{1}$$

where q_{mL} = maximum adsorption capacity [mmol/g]; b_L = Langmuir constant [bar^{-1}]; p = pressure [bar]; q = adsorbed quantity under p pressure [mmol/g].

Freundlich isotherm

According to Eq. (2), Freundlich's model describes adsorption of different adsorption energies (Ayawei et al. 2015a, b) on heterogeneous surfaces.

$$q = k_F\, p^{n_F} \tag{2}$$

Sips isotherm

Activated carbon is commonly specified using the Sips model, which is typically applied for heterogeneous adsorbents like that (Delavar et al. 2010; Ning et al. 2012). At lower concentrations adsorbate, it becomes the Freundlich model, but Langmuir model is applicable for higher concentrations of adsorbate, it becomes the Langmuir model (Travis and Etnier 1981), then which is represented by Eq. (3):

$$q = \frac{q_{mS} b_S p^{n_S}}{1 + b_S p^{n_S}} \tag{3}$$

where q_{mS} = maximum adsorption capacity [mmol/g]; b_S = Sips constant [bar^{-1}]; n_S = heterogeneity factor.

Radke-Prausnitz isotherm

There are several significant characteristics of Radke-Prausnitz that accomplish an ideal selection for adsorption systems with low concentrations of adsorbate. It becomes a linear isotherm at lower adsorbate concentrations for an adsorption system, a Freundlich isotherm at high concentrations, and a Langmuir isotherm when the $n_{RP} = 0$. Another important property of this isotherm is that it fits a wide range of concentrations of adsorbate. Below is the Radke-Prausnitz Eq. (4) (Radke and Prausnitz 1972):

$$q = \frac{q_{mRP} b_{RP} p}{\left(1 + b_{RP} p\right)^{n_{RP'}}} \tag{4}$$

where q_{mRP} = maximum adsorption capacity [mmol/g]; b_{RP} = Radke-Prausnitz constant [bar^{-1}]; n_{RP} = Radke-Prausnitz model exponent.

The fitted isotherm was obtained by using a nonlinear optimization technique. Nonlinear regression can be a useful alternative to linear regression due to the flexibility it provides in fitting curves. As part of nonlinear regression, all the error functions should be diminished. During estimation if the error is small which indicates the prediction is more accurate. SNE(sum of the normalized error) is used to select most suitable set of parameters for all the isotherms based on their smallest error. Complete information of error functions was characterized by Eqs. (5)–(9) and are represented below:

Error function	Equations	References
Sum of the squares of the errors (SSE)	SSE $= \sum_{i=1}^{n} \left(q_{e,\mathrm{calc}} - q_{e,\exp}\right)_i^2$ (5)	Ho (2004)
Hybrid fractional error function (HYBRID)	HYBRID $= \frac{100}{1-p} \sum_{i=1}^{n} \left[\frac{\left(q_{e,\mathrm{calc}} - q_{e,\exp}\right)^2}{q_{e,\exp}} \right]_i$ (6)	Porter et al. (1999)

Error function	Equations	References
Average relative error function (ARE)	ARE $= \frac{100}{1-p}\sum_{i=1}^{n}\left(\frac{q_{e,calc}-q_{e,exp}}{q_{e,exp}}\right)_i$ (7)	Khan et al. (1997)
Marquardt's percent standard deviation (MPSD)	MPSD $= 100\sqrt{\frac{1}{n-p}\sum_{i=1}^{n}\left(\frac{q_{e,calc}-q_{e,exp}}{q_{e,exp}}\right)_i^2}$ (8)	Marquardt (1963)
Sum of the absolute errors function (SAE)	SAE $= \sum_{i=1}^{n}(q_{e,calc}-q_{e,exp})_i$ (9)	Ng et al. (2003)

where $q_{e,calc}$ = calculated adsorption capacity[mmol/g] $q_{e,exp}$ = experimentally measured adsorption capacity [mmol/g]

Because the goal of every error function would be to procure a different set of isotherm parameters, these seems to be hard to interpret directly.

It is also possible that another model sum of the normalized errors (SNE) will be recognized as the best based on various error functions. As a result, the error function chosen may have an effect on obtained parameters of the isotherm. The SNE can be used to compare essential parameters. The Sum of normalized errors function (SNE) (Ho 2004):

$$SNE = \sum_{i=1}^{n}\frac{f_i}{f_{i\max}} \tag{10}$$

The function with the least number SNE and the best-defined empirical results was chosen.

Aim of this work is to investigate CO_2 adsorption on rice husk activated carbons in connection to the investigation of the influence of the isotherm type as well as the model being used determine its parameters by the 2 and 3 parametric models on the calculations while discussing the error functions. The use of KOH as an activator has been the work's novelty. Solid-state carbon materials are presented in the literature. The new method synthesis of activated carbon and impregnation with KOH presented here is much simpler and inexpensive. The use of KOH as an activator was the work's novelty. All of the solid-state carbon sources described in the literature. The new method presented here for preparation of activated carbons and KOH impregnation is much simpler and less expensive.

Materials and methods

Preparation of rice husk activated carbon (RHAC)

Rice husk gathered from rice mill near Telaprolu, Vijayawada, India, was cleaned exhaustively with distilled water to take off adhering soil and dust, and dried at 110 °C overnight. Rice husks were calcined at different temperatures at different atmospheres for 4 h. The temperature was programmed as 10 °C per minute and gas flow maintained at 40 mL per minute (Kishore et al. 2017; Srinivas et al. 2017). Flow chart of activated carbon shown in Fig. 1. Digital images of rice crop, rice husk and its activated carbon were shown in Fig. 2.

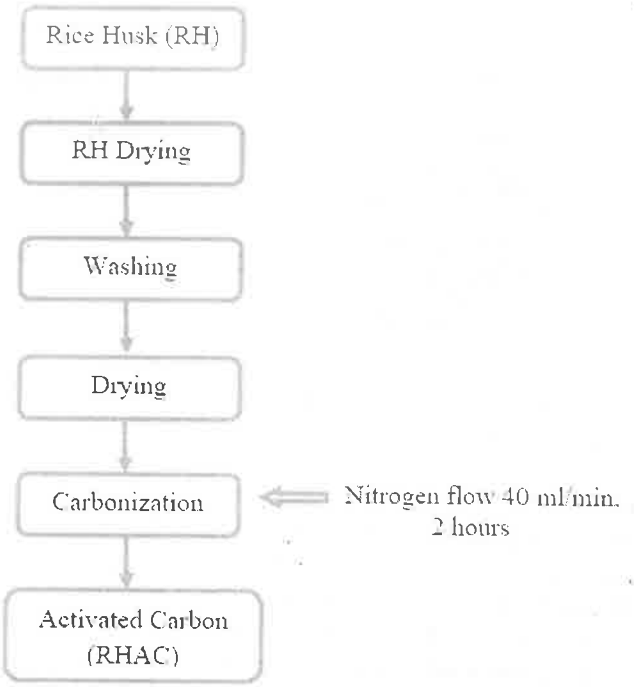

Fig. 1 Flow diagram of preparation of Activated carbon

Chemical activation by using KOH

Synthesized rice husk activated carbons was treated by KOH. Mass ratio of RHAC:KOH was equal to 1:1. Chemical activation of rice husk was carried out with the use of saturated KOH solution. The material was then vigorously mixed till rice husk activate carbon was clearly dissolved in KOH solution and then heated at room temperature about three hours. Following this, the impregnated materials were dried at 200 °C about 20 h in laboratory dryer. After the impregnation carbonization is carried out for synthesized activated carbons. In horizontal electric furnace tubular reactor was placed to carry out the process of physical activation between the range of 400–700 °C temperature, after this increase the temperature at a rate of 10 °C per minute to a predetermined value.The procedure was carried out in a nitrogen-carbon dioxide environment (flow rate of 18 dm^3/h, carbon dioxide flow rate of 5 dm^3/h). In all of the trials, the activation process parameters such as duration, N_2-CO_2 flow rate, and heating rate of furnace were the same. They were

Fig. 2 Digital images of rice crop, rice husk and activated carbon

thought, based on numerous prior studies, the optimal settings results assuring highest improvement of surface area of examined activated carbon materials.

To achieve a neutral reaction, activated carbons comprising with KOH or K_2CO_3 was washed with deionized water. These activated carbons were soaked with a 1 mol/dm³ HCl solution and left for 20 h after evaporation. Carbons were then washed with deionized water till the chloride ions being completely removed. The product was dried for 16 h at 110 °C. Synthesized activated carbons labelled as: RHAC-KOH-400, RHAC-KOH-500,RHAC-KOH-600, RHAC-KOH-700, where: RHAC is rice husk activated carbon, KOH is an activating agent and 400, 500, 600, 700 are activation temperatures. A pore size analyzer and sorption surface area (ASAP 2460, Micrometrics, Novcross, USA) instrument is used to analyse Nitrogen adsorption at − 196 °C for all activated carbon samples. For eliminating impurities of activated carbons, adsorption tests were proceeded by 12 h of heating at 250 °C at 1°/min heating rate under decreased pressure due to continual running of pump. The following characteristics defining the porous structure were acquired using N_2 sorption isotherms:

- Surface area (SBET) calculated using the BET equation and a partial pressure in the range of $p/p0 = 0.05–0.2$. This range was determined separately for each material in order to achieve linearity of function (11).
- Nitrogen vapours maximal adsorption at $p/p0 = 0.99$ is used to estimate total pore volume (Vp,N_2)

$$f\left(\frac{p}{p_0}\right) = \frac{1}{W\left(\frac{p}{p_0} - 1\right)} \tag{11}$$

where W = mass of gas adsorbed at a relative pressure p/p_0; p = nitrogen pressure; p_0 = 1.01 bar;

The DFT approach was used to analyse pores variety of mesopores and micropores (Vmic,N_2) utilizing N_2 analysis at − 196 °C temperature (density functional theory).

The Nitrogen adsorption isotherm at − 196 °C provides information regarding the micropore structure, partially macropores and mesopores. The CO_2 adsorption activities were performed using ASAP at 0 °C temperature and 1 bar pressure. To regulate the temperature of the experiment, the investigated were placed in a thermostat. The activated carbons were out-gassed for 12 h prior to the CO_2 adsorption tests at a temperature of 250 °C.

Results and discussion

Figure 3 depicts the findings of the N_2 adsorption–desorption isotherms of investigated activated carbons.The isotherms revealed that microporous materials exhibit high

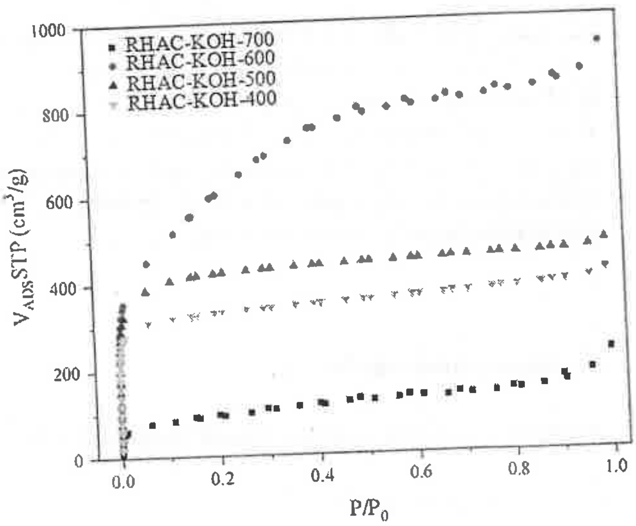

Fig. 3 Activated carbons nitrogen adsorption–desorption isotherms

N_2 adsorption at low relative pressure. It indicates larger micropore volume with narrow pore size distribution. The N_2 adsorption determined at − 196 °C temperature rose remarkably in all carbon materials as the activation temperature raised during the heat treatments, the carbon activated at maximum temperature (800 °C) exhibit lowest N_2 adsorption is the only one exception.

The N_2 adsorption isotherms belong to Type I for low pressure and Type IV for middle and higher ranges, according to the International Union of Pure and Applied Chemistry (IUPAC). The presence of a clearly developed hysteresis loop, which would be associated to capillary condensation in mesopores region, is a distinguishing Type IV isotherm characteristics. Type IV hysteresis loop is formed by isotherms. In mesopores, capillary condensation takes place between relative pressure range $p/p0 = 0.45–1$, indicating presence of mesopores in all four samples.

More detailed information about the structure of the adsorption over investigated samples may be obtained by analyzing the pore size distribution. An investigation of distribution of pore size for activated carbon materials based on N_2 adsorption was undertaken to examine correlation between pore size of analyzed carbon materials and of the activation process temperature. The pore distribution depicted in Fig. 4 demonstrates that all the activated carbon materials, additionally rather extensively developed microporosity, have advanced mesoporosity.

The selected approach offers information about porosity of pores with in ranging between 0.34 and 302 nm, according to adsorbate applied. Although, only holes up to 5 nm are shown in Fig. 4 since no bigger pores were found in the studied activated carbons.

Table 1 Activated carbons surface area, pore volume and micropore volume taken from nitrogen adsorption isotherms at − 196 °C

Sample	S_{BET} [m^2/g]	$V_{p,N2}$ [cm^3/g]	$V_{mic,N2}$ [cm^3/g]
RHAC-KOH-400	248	0.63	0.39
RHAC-KOH-500	576	0.72	0.52
RHAC-KOH-600	1074	1.42	0.45
RHAC-KOH-700	124	0.35	0.06

Table 1 shows the textural characteristics of all samples. In case of samples RHAC-KOH-400, RHAC-KOH-500, RHAC-KOH-600, with increasing activation temperature, greater surface areas and pore volumes were achieved. Moreover, as shown in Table 1, the trend differs for sample RHAC-KOH-700. High surface area (1074 m^2/g) achieved for RHAC-KOH-600 sample. The RHAC-KOH-500 carbon has shown highest micropore volume of 0.52 cm^3/g with excellent microporosity.

Activated carbon was tested at 0°C temperature under 1 bar pressure and adsorption of CO_2 was measured. In Fig. 5, we show the experimental CO_2 adsorption capacity at 0 °C.

A decrease in carbonization temperature was found to increase CO_2 adsorption capacity at 0 °C.

It is surprising that these results conflict with literature reports (Wang and Yang 2012) which show that efficiency of CO_2 adsorption increases by increasing specific surface area as well as volume of total pores. It follows that for synthesized activated carbons, pores whose diameters are in the range of 0.3 to 0.6 nm are the most important, while pores that are larger play an almost insignificant role. The results

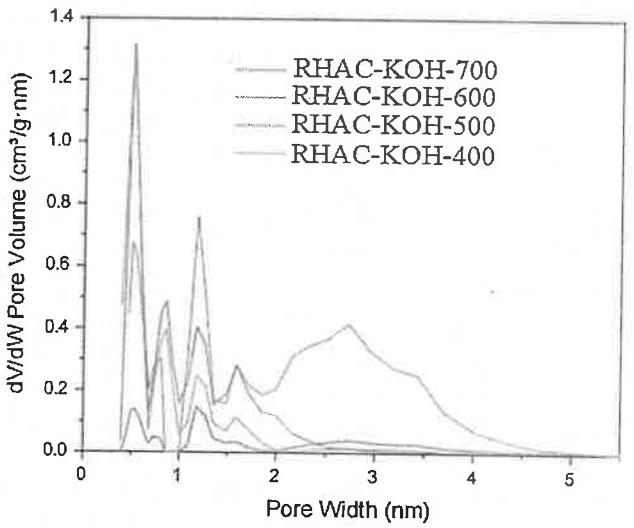

Fig. 4 Distribution of pores size of activated carbon materials

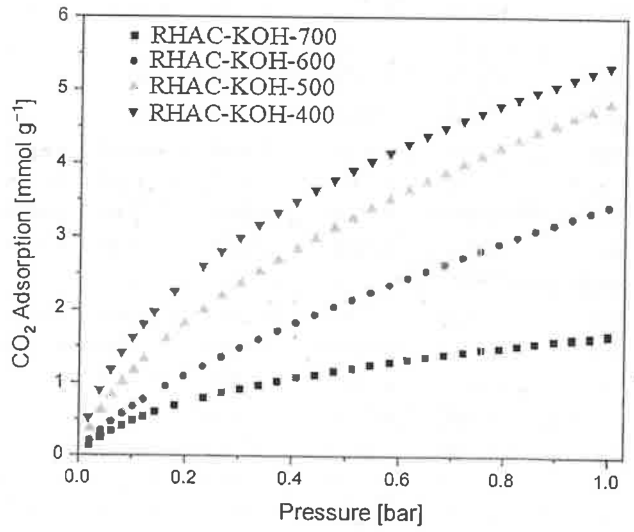

Fig. 5 Measured isotherms of adsorption of CO_2 at 0 °C

Table 2 Langmuir CO_2 adsorption of various activated carbons at 1 bar and 0 °C

Material	CO_2 adsorption at 0 °C [mmol/g]	References
Organic framework polymers	2.9	Li et al. (2013)
Activated carbon xerogels	4.9	Martin-Jimeno et al. (2015)
Mg and N-doped mesoporous carbon	3.7	Liu et al. (2021)
Waste wool-derived N-doped hierarchical porous carbon	3.7	Li et al. (2018)
Polyaniline-graphene oxides	3.2	Rodriguez-Garcia et al. (2019)
KOH activated carbon derived from rice husk	5.3	This work

Table 3 Langmuir isotherms constants with error analysis

	SSE	HYBRID	ARE	MPSD	SAE
RHAC-KOH-400					
q_{mL}	7.2707	6.7818	6.6419	6.1657	7.5580
b_L	2.4183	2.8826	2.9746	3.6483	2.1633
SSE	0.505	0.6586	0.7666	1.4430	0.5884
HYBRID	1.1769	0.9676	0.9984	1.3673	1.5786
ARE	5.9061	5.4549	5.4176	5.9606	6.4050
MPSD	11.1292	9.0957	8.9495	7.9138	12.8738
SAE	3.39919	3.9596	4.1155	5.5469	3.1862
SNE	3.4954	**3.3413**	3.4467	4.4115	3.9822
RHAC-KOH-500					
q_{mL}	.0398	7.2929	7.0237	6.3559	8.2289
b_L	1.39 8	1.6943	1.7979	2.2240	1.3194
SSE	0.2922	0.4024	0.5183	1.1479	0.3200
HYBRID	0.8823	0.7123	0.7452	1.0937	].()465
ARE	5.8638	5.4440	5.2:687	5.8189	6.1 97
MPSD	11.0699	8.9443	8.5690	7.5538	12.0371
SAE	2:.5697	3.1291	3.3528	4.6078	2.4829
SNE	3.5118	**3.3383**	3.4842	4.5691	3.8010
RHAC-KOH-600					
q_{mL}	7.2701	6.5517	6.2432	5.3984	7.7763
b_L	2.4183	1.0075	1.0685	1.3850	0.7605
SSE	0.5058	0.1395	0.1987	0.4368	0.1048
HYBRID	1.1769	0.3865	0.4222	0.6498	0.5752
ARE	5.9061	5.2092	5.1408	5.5799	6.0437
MPSD	11.1292	8.7370	8.5614	7.2350	11.6905
SAE	3.3992	1.8368	1.9745	2.9106	1.4299
SNE	4.9292	**2.7539**	2.9155	3.8141	3.1167
RHAC-KOH-700					
q_{mL}	2.3634	2.2 177	2.1264	2.0454	2.4152
b_L	2.1749	2.5319	2.7403	3.0590	2.0372
SSE	0.0354	0.0463	0.0669	0.0955	0.0392
HYBRID	0.2405	0.1916	0.2128	0.2700	0.3046
ARE	5.0117	4.5123	4.3913	4.6334	5.3820
MPSD	8.8630	6.8759	6.3129	5.7975	10.0703
SAE	0.9143	1.0524	1.1685	1.3988	0.8799
SNE	3.6249	**3.3866**	3.6769	4.3230	4.0390

Standard uncertainties of all constants are equal to 0.001, uncertainties of all errors equal to 0.0001 (0.5 level of confidence)

Table 4 Freundlich isotherms constants with error analysis

	SSE	HYBRID	ARE	MPSD	SAE
RHAC-KOH-400					
q	5.4205	5.4856	5.5150	5.5975	5.3964
b_F	1.5139	1.5354	0.5367	0.5603	0.5012
SSE	0.1401	0.1980	0.22:11	0.4431	0.1625
HYBRID	0.3874	0.2846	0.2923	0.4152	0.5647
ARE	3.2034	2.8662	2.8350	3.2776	3.6642
MPSD	7.2039	5.1631	5.1589	4.2316	8.8241
SAE	1.7629	2.1561	2.1921	3.0892	1.6738
SNE	3.2636	3.0160	3.0845	4.1093	3.9085
RHAC-KOH-500					
q	4.8747	4.9154	4.9327	4.9916	4.8676
b_F	0.6134	1.6293	0.6314	0.6487	0.6054
SSE	0.0351	0.0542	0.0638	0.1471	0.04 14
HYBRID	0.1387	0.09 6	0.1008	0.1565	0.1980
ARE	2.1842	1.9252	1.9129	2.2214	2.4765
MPSD	5.1089	3.6259	3.5209	2.8951	6.1199
SAE	0.8572	1.1171	1.1772	1.7416	0.7960
SNE	3.1485	2.8783	2.9663	4.1604	3.7383
RHAC-KOH-600					
q	3.4494	3.4629	3.4653	3.4932	3.44 6
b_F	0.7105	0.7184	0.7183	0.7294	0.7080
SSE	0.0025	0.0044	0.0045	0.0161	0.0027
HYBRID	0.0198	0.014 1	0.0142	0.0254	0.0243
ARE	1.0365	0.9412	0.9334	1.1573	1.1344
MPSD	2.6721	1.9611	1.9862	1.5462	2.9536
SAE	0.2122	0.3164	0.3168	0.5735	0.2036
SNE	3.1073	2.8550	2.8730	4.5235	3.4631
RHAC-KOH-700					
q	1.7039	1.7311	1.7350	1.7808	1.6913
b_F	0.5361	0.5655	0.5627	0.6016	0.5148
SSE	0.0199	0.0299	0.0293	0.0754	0.0257
HYBRID	0.2135	0.1537	0.1561	0.2358	0.3477
ARE	4.2889	3.8856	3.8502	4.5703	5.1219
MPSD	10.3752	7.3861	7.7001	5.9423	13.3000
SAE	0.6473	0.8396	0.8150	1.2886	0.5973
SNE	2.9977	2.8043	2.8004	4.0172	3.8045

Standard uncertainties of all constants are equal to 0.001, uncertainties of all errors equal to 0.0001 (0.5 level of confidence)

Table 5 Sips isotherms constants with error analysis

	SSE	HYBRID	ARE	MPSD	SAE
RHAC-KOH-400					
q_{mS}	14.5122	13.5991	13.6306	12.6177	13.6362
bs	0.5774	0.6389	0.6348	0.7201	0.6347
n_S	0.6698	0.6835	0.6811	0.6985	0.6823
SSE	0.0021	0.0032	0.0040	0.0084	0.0039
HYBRID	0.0079	0.0055	0.0063	0.0084	0.0062
ARE	0.3765	0.3752	0.3598	0.4799	0.3625
MPSD	1.1333	0.7660	0.8467	0.6191	0.7971
SAE	0.1846	0.2621	0.2434	0.4270	0.2415
SNE	3.4052	**3.1082**	3.2932	4.5463	3.2227
RHAC-KOH-500					
q_{mS}	22.6789	19.8826	19.9379	17.2029	17.4800
bs	0.2698	0.3190	0.3172	0.3856	0.3777
n_S	0.7046	0.7193	0.7165	0.7353	0.7366
SSE	0.0016	0.0025	0.0029	0.0073	0.0061
HYBRID	0.0076	0.0051	0.0059	0.0083	0.0091
ARE	0.4527	0.4383	0.4209	0.5216	0.5614
MPSD	1.2981	0.8558	0.9880	0.6795	0.7877
SAE	0.1736	0.2488	0.2427	0.3972	0.3692
SNE	3.2912	**2.9670**	3.1687	4.3638	4.3763
RHAC-KOH-600					
q_{mS}	42.7761	32.7762	32.7525	24.6378	24.7621
bs	0.0873	0.1168	0.1168	0.1609	0.1602
n_S	0.7457	0.7567	0.7550	0.7697	0.7728
SSE	0.0004	0.0006	0.0008	0.0022	0.0018
HYBRID	0.0031	0.0021	0.0023	0.0036	0.0043
ARE	0.3799	0.3564	0.3413	0.4385	0.4809
MPSD	1.1134	0.7421	0.8305	0.5790	0.7074
SAE	0.0834	0.1195	0.1201	0.2177	0.2004
SNE	3.0586	**2.7163**	2.9021	4.2867	4.3704
RHAC-KOH-700					
q_{mS}	4.0852	3.6207	3.6222	3.2118	3.9718
bs	0.6867	0.8426	0.8377	1.0460	0.7162
n_S	0.7222	0.7558	0.7507	0.7898	0.7249
SSE	0.0011	0.0017	0.0019	0.0044	0.0013
HYBRID	0.0130	0.0086	0.0095	0.0131	0.0135
ARE	0.9887	0.9161	0.8855	1.0281	0.%17
MPSD	2.6725	1.6678	1.8912	1.2971	2.7228
SAE	0.1519	0.2034	0.1936	0.2998	0.1507
SNE	3.6710	**3.2133**	3.3430	4.4471	3.7447

Standard uncertainties of all constants are equal to 0.001, uncertainties of all errors equal to 0.0001 (0.5 level of confidence)

of carbon dioxide adsorption on activated carbon materials generated from many carbon sources are summarized in Table 2.

According to IUPAC classification, all isotherms correspond to microporous adsorbents, which are characteristic of type I. The adsorption isotherms for CO_2 were derived from experimental data in each model.

As shown in Tables 3, 4, 5, and 6, based on SNE there are sets of parameters and error functions of CO_2 adsorption isotherm. The SNE was compared and therefore, the isotherm constants that fit the measured data the best were obtained. As shown in Tables 3, 4, 5, and 6, bolded letters denote the minimum SNE value for activated carbon of each isotherm, and underlined letters denote lowest SNE value and the set of optimal parameters of activated carbons of all the isotherms.

Table 3 shows the results of fitting parameters to the Langmuir model.

By utilizing different error functions, nonlinear regression was used to estimate the constants. The constants q_{mL} and b_L values have very high similarity. The Langmuir isotherm is not a useful model for the adsorption of CO_2 over all the activated carbon samples. Based on the SNE values, HYBRID is the best overall Langmuir fit across all 4 activated carbon materials.

In Table 4, we present the Freundlich isotherm constants and error functions.

The ARE give the best Freundlich fit for RHAC-KOH-700, and HYBRID for RHAC-KOH-400, RHAC-KOH-500, RHAC-KOH-600 according to SNE. In spite of this, the best Freundlich fit cannot be accepted.

The Set of parameters for fitting Sips model are represented in Table 5.

Based on the SNE, the HYBRID was the best fit for SIPs.

Table 6 represents isotherms constants and error functions of Radke-Prausnitz model.

Specifically, the SNE stipulated MPSD for RHAC-KOH-600, ARE for RHAC-KOH-700, and HYBRID for RHAC-KOH-400 & RHAC-KOH-500 provides the best Radke-Prausnitz fit. With respect to error functions, the three constants qmRP, bRP, and nRP are comparable. In all error functions only qmRP, bRP, nRP constants are approximate. The SNE is lowest for RHAC-KOH-400, RHAC-KOH-700 in all the established models. A rational approximation for optimal set of parameters is given by Radke-Prausnitz

Table 6 Radke-Prausnitz isotherms constants with error analysis

	SSE	HYBRID	ARE	MPSD	SAE
RHAC-KOH-400					
$q_{m\mathrm{RP}}$	6.0801	6.0346	6.0345	6.0045	6.1359
b_{RP}	7.1453	7.7204	7.7204	8.2684	6.5972
n_{RP}	0.6237	0.6114	0.6107	0.5990	0.6353
SSE	0.0018	0.0027	0.0029	0.0059	0.0027
HYBRID	0.0057	0.0038	0.0039	0.0055	0.012
ARE	0.3647	0.3350	0.3324	0.3670	0.4673
MPSD	0.9164	0.5601	0.5688	0.4408	1.4428
SAE	0.1993	0.2577	0.2611	0.3621	0.1 96
SNE	2.7259	**2.5733**	2.6215	3.5170	3.9580
RHAC-KOH-500					
$q_{m\mathrm{RP}}$	5.7020	5.6944	5.6881	5.6828	5.7173
b_{RP}	5.5569	5.5968	5.6404	5.6899	5.4427
n_{RP}	0.5016	0.5008	0.4998	0.4981	0.5042
SSE	0.0002	0.0001	0.0002	0.0002	0.0001
HYBRID	0.0002	0.0002	0.0002	0.0002	0.0003
ARE	0.0753	0.0656	0.0619	0.0651	0.0900
MPSD	0.1246	0.1044	0.0929	0.0871	0.2103
SAE	0.0511	0.0470	0.0491	0.0579	0.0456
SNE	2.9617	**2.5525**	2.7331	3.5854	3.8452
RHAC-KOH-600					
$q_{m\mathrm{RP}}$	4.0263	3.6978	3.7420	4.1119	4.0787
b_{RP}	5.8348	13.9867	11.7225	5.0523	5.3481
n_{RP}	0.3585	0.3127	0.3203	0.3718	0.3647
SSE	0.0001	0.0014	0.0009	0.0002	0.0001
HYBRID	0.0003	0.0058	0.0048	0.0004	0.0003
ARE	0.1371	0.5852	0.5081	0.1379	0.1231
MPSD	0.3185	1.3273	1.2821	0.1701	0.2063
SAE	0.0444	0.1795	0.1349	0.0708	0.0473
SNE	1.8140	4.0187	3.0246	**0.2076**	0.4890
RHAC-KOH-700					
$q_{m\mathrm{RP}}$	2.0027	1.8197	2.0092	2.0170	1.9999
b_{RP}	5.0158	12.7788	4.8565	4.7483	5.0536
n_{RP}	0.6512	0.5146	0.6605	0.6660	0.6503
SSE	0.0001	0.0133	0.0001	0.0002	0.0001
HYBRID	0.0005	0.0746	0.0005	0.0005	0.0006
ARE	0.2146	2.6605	0.1799	0.1885	0.2209
MPSD	0.4830	4.9792	0.2943	0.2309	0.5463
SAE	0.0402	0.5515	0.0480	0.0594	0.0388
SNE	0.2633	5.0000	**0.2306**	0.2450	0.2773

Standard uncertainties of all constants are equal to 0.001, uncertainties of all errors equal to 0.0001 (0.5 level of confidence)

equation. Figure 6. represents theoretical and experimental data of Radke-Prausnitz isotherms.

For empirical data analysis, the Radke-Prausnitz model is recommended. Based on Fig. 4, a similar conclusion can be reached. It seems that irrespective of the error function, the experimental isotherm suits rather well with the Radke-Prausnitz equation model.

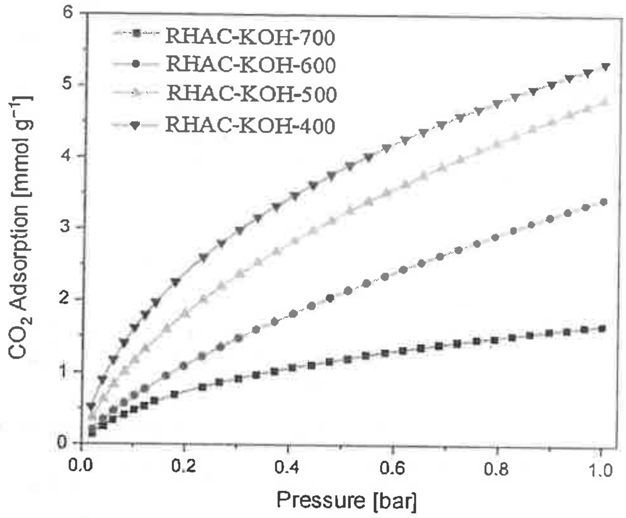

Fig. 6 Carbon dioxide adsorption isotherms at 0 °C. Based on lowest SNE, empirical results are expressed by symbols, lines were prevailed by Radke-Prausnitz model

Conclusions

The CO_2 adsorption findings at 0 °C on four activated carbons produced by using rice husk and treated with KOH solution suggest that these activated carbons may be useful for improving CO_2 adsorption. The measured specific surface area and pore volume is as large as 1074 m^2g^{-1} and 1.42 cm^3g^{-1} respectively, related to the activated carbon designated as RHAC-KOH-600. Interestingly, reduction in the carbonization temperature significantly increased the CO_2 adsorption ability at temperatures 0 °C. At 0 °C temperature and 1 bar pressure, activated carbon labelled as RHAC-KOH-400 shown highest CO_2 adsorption as 5.3 mmolg^{-1}. The equilibrium adsorption findings were calculated and analyzed using 4 distinct isotherms and 5 different optimization and error functions. The error function was compared using the sum of normalized errors, and the optimum isotherm equation was determined. The best estimation is provided by the Radke-Prausnitz model, because it is significant model for actual data.

Acknowledgements The authors acknowledge financial support of this work from department of Chemistry, MJCET, which is operated and managed by Sultan-ul-Uloom Education Society and also grateful to the Hon. Secretary, SUES and Advisor-cum director, and other colleagues of Chemistry department, MJCET, Hyderabad for their encouragement and support in completing this work successfully.

Data availability The data of the current study are available from the corresponding author on reasonable request.

Declarations

Conflict of interest On behalf of all the authors, the corresponding author states that there is no conflict of interest.

References

Ayawei N, Angaye SS, Wankasi D, Dikio ED (2015a) Synthesis, characterization and application of Mg/Al layered double hydroxide for the degradation of congo red in aqueous solution. Open J Phys Chem 5:56–70. https://doi.org/10.4236/ojpc.2015.53007

Ayawei N, Ekubo AT, Wankasi D, Dikio ED (2015b) Adsorption of congo red by Ni/Al—CO3: equilibrium, thermodynamic and kinetic studies. Orient J Chem 31:1307–1318. https://doi.org/10.13005/ojc/310307

Delavar M, Ghoreyshi AA, Jahanshahi M, Irannejad M (2010) Experimental evaluation of methane adsorption on granular activated carbon (GAC) and determination of model isotherm. Eng Technol 62:47–50

Elmorsi TM (2011) Equilibrium isotherms and kinetic studies of removal of methylene blue dye by adsorption onto miswak leaves as a natural adsorbent. J Environ Prot Ecol 2:817–827. https://doi.org/10.4236/jep.2011.26093

Gong J, Michalkiewicz B, Chen X, Mijowska E, Liu J, Jiang Z, Wen X, Tang T (2014) Sustainable conversion of mixed plastics into porous carbon nanosheets with high performances in uptake of carbon dioxide and storage of hydrogen. ACS Sustain Chem Eng 2:2837–2844. https://doi.org/10.1021/sc500603h

Günay A, Arslankaya E, Tosun I (2007) Lead removal from aqueous solution by natural and pretreated clinoptilolite: adsorption equilibrium and kinetics. J Hazard Mater 146:362–371. https://doi.org/10.1016/j.jhazmat.2006.12.034

Ho YS (2004) Selection of optimum sorption isotherm. Carbon 42:2115–2116. https://doi.org/10.1016/j.carbon.2004.03.019

Khan AR, Al-Bahri T, Al-Haddas A (1997) Adsorption of phenol based organic pollutants on activated carbon from multicomponent dilute aqueous solution. Water Res 31:2101–2112. https://doi.org/10.1016/S0043-1354(97)00043-2

Kishore P, Srinivas BN, Rao KS, Turaka AK, Prasad NBL (2017) Carbon dioxide adsorption studies of rice husk ash prepared in different atmospheres. Int J Recent Innov Eng Res 2(7):26–31. https://doi.org/10.15680/IJIRSET.2016.0608043

Li T, Sullivan JE, Rosi NL (2013) Design and preparation of a core–shell metal–organic framework for selective CO2 capture. J Am Chem Soc 135:9984–9987. https://doi.org/10.1021/ja403008j

Li Y, Xu R, Wang X, Wang B, Cao J, Yang J, Wei J (2018) Waste wool derived nitrogen-doped hierarchical porous carbon for selective CO_2 capture. RSC Adv 35:19818–19826. https://doi.org/10.1039/C8RA02701C

Liu B, Shi R, Ma X, Chen R, Zhou K, Xu X, Sheng P, Zeng Z, Li L (2021) High yield nitrogen-doped carbon monolith with rich ultra-micropores prepared by in-situ activation for high performance of selective CO2 capture. Carbon 181:270–279. https://doi.org/10.1016/j.carbon.2021.05.029

Marquardt DW (1963) An algorithm for least squares estimation of non-linear parameters. J Soc Ind Appl Math 11:431–441

Martin-Jimeno FJ, Suarez-Garcia F, Paredes JI, Martinez-Alonso A (2015) Activated carbon xerogels with a cellular morphology derived from hydrothermally carbonized glucose-graphene oxide hybrids and their performance towards CO_2 and dye adsorption. Carbon 81:137–147. https://doi.org/10.1016/j.carbon.2014.09.042

Młodzik J, Sre'nscek-Nazzal J, Narkiewicz U, Morawski AW, Wróbel RJ, Michalkiewicz B (2016) Activated carbons from molasses as CO_2 sorbents. Acta Phys Pol A 129:402–404. https://doi.org/10.1007/978-3-319-16901-9_29

Ng JCY, Cheung WH, McKay G (2003) Equlibrium studies for the sorption of lead from effluents using chitosan. Chemosphere 52:1021–1030. https://doi.org/10.1016/S0045-6535(03)00223-6

Nguyen TH, Gong H, Lee SS, Bae TH (2016) Amine-appended hierarchical Ca-A zeolite for enhancing CO_2/CH_4 selectivity of mixed-matrix membranes. Chem Phys Chem 17:3165–3169. https://doi.org/10.1002/cphc.201600561

Nhapi I, Banadda N, Murenzi R, Sekomo C, Wali U (2011) Removal of heavy metals from industrial waste water using rice husks. Open Environ Eng J 4:170–180. https://doi.org/10.2174/1874829501104010170

Ning P, Li F, Yi H, Tang X, Peng J, Li Y, He D, Deng H (2012) Adsorption equilibrium of methane and carbon dioxide on microwave-activated carbon. Sep Purif Technol 98:321–326. https://doi.org/10.1016/j.seppur.2012.07.001

Porter F, McKay G, Choy KH (1999) The prediction of sorption from a binary mixture of acidic dyes using single and mixed isotherms variants of the ideal adsorbed solute theory. Chem Eng Sci 54:5863–5885. https://doi.org/10.1016/S0009-2509(99)00178-5

Radke CJ, Prausnitz JM (1972) Adsorption of organic solutions from dilute aqueous solution on activated carbon. Ind Eng Chem Fundam 11:445–451. https://doi.org/10.1021/i160044a003

Rodriguez-Garcia S, Santiago R, Lopez-Diaz D, Merchan MD, Velazquez MM, Fierro JLG, Palomar J (2019) Role of the structure of graphene oxide sheets on the CO_2 adsorption properties of nanocomposites based on graphene oxide and polyaniline or Fe_3O_4-nanoparticles. ACS Sustain Chem Eng 7:12464–12473. https://doi.org/10.1021/acssuschemeng.9b02035

Sai Bhargava Reddy M, Ponnamma D, Sadasivuni KK, Kumar B, Abdullah AM (2021) Carbon dioxide adsorption based on porous materials. RSC Adv 11:12658–12681. https://doi.org/10.1039/D0RA10902A

Schell J, Casas N, Blom R, Spjelkavik AL, Andersen A, Hafizovic Cafka J, Mazzotti M (2012a) MCM-41, MOF and UiO-67/MCM-41 adsorpbents for pre-combustion CO_2 capture by PSA: adsorption equilibria. Adsorption 18:213–227. https://doi.org/10.1007/s10450-012-9395-1

Schell J, Casas N, Pini R, Mazzotti M (2012b) Pure and binary adsorption of CO2, H2, N2 on activated carbons. Adsorption 18:49–65. https://doi.org/10.1007/s10450-011-9382-y

Serafifin J, Narkiewicz U, Morawski AW, Wróbel RJ, Michalkiewicz B (2017) Highly microporous activated carbons from biomass for CO_2 capture and effective micropores at different conditions. J CO2 Util 18:73–79. https://doi.org/10.1016/j.jcou.2017.01.006

Singh G, Kim IY, Lakhi KS, Srivastava P, Naidu R, Vinu AB (2017) Single step synthesis of activated bio-carbons with a high surface area and their excellent CO_2 adsorption capacity. Carbon 116:448–455. https://doi.org/10.1016/j.carbon.2017.02.015

Srinivas BN, Kishore P, Rao KS, Kumar TA (2017) Preparation of surface modified activated carbons from rice husk and CO_2 adsorption studies. IOSR J Appl Chem 10:54–60

Sun LB, Kang YH, Shi YQ, Jiang Y, Liu XQ (2015) Highly selective capture of the greenhouse gas CO_2 in polymers. ACS Sustain Chem Eng 3:3077–3085. https://doi.org/10.1021/acssuschemeng.5b00544

Travis CC, Etnier EL (1981) A survey of sorption relationships for reactive solutes in soil. J Environ Qual 10:8–17. https://doi.org/10.2134/jeq1981.00472425001000010002x

Wang L, Yang RT (2012) Significantly increased CO_2 adsorption performance of nanostructured templated carbon by tuning surface area and nitrogen doping. J Phys Chem C 116:1099–1106. https://doi.org/10.1021/jp2100446

Zhang J, Fu H, Lv X, Tang J, Xu X (2011) Removal of Cu (II) from aqueous solution using the rice husk carbons prepared by the physical activation process. Biomass Bioenergy 35(1):464–472. https://doi.org/10.1016/j.biombioe.2010.09.002

Zhang K, Qiao Z, Jiang J (2017) Molecular design of zirconium tetrazolate metalorganic frameworks for CO_2 capture. Cryst Growth Des 17:543–549. https://doi.org/10.1021/acs.cgd.6b01405

ANSF
APPLIED AND NATURAL SCIENCE FOUNDATION

Journal of Applied and Natural Science
14(2), 450 - 458 (2022)
ISSN : 0974-9411 (Print), 2231-5209 (Online)
journals.ansfoundation.org

Review Article

Titanium dioxide electrospun nanofibers for dye removal- A review

Madhavi Konni
Department of Humanities and Science (Chemistry), Malla Reddy Engineering College (Autonomous), Secunderabad, Telangana, India
Bhavya Kavitha Dwarapureddi
Department of Environmental Science, School of Science, GITAM (Deemed to be) University, Visakhapatnam-45, India
Swathi Dash
Department of Environmental Science, School of Science, GITAM (Deemed to be) University, Visakhapatnam-45, India
Aman Raj
Department of Environmental Science, School of Science, GITAM (Deemed to be) University, Visakhapatnam-45, India
Manoj Kumar Karnena*
Department of Environmental Science, School of Science, GITAM (Deemed to be) University, Visakhapatnam-45, India

*Corresponding author. Email: manojkumarenviron@gmail.com

Article Info
https://doi.org/10.31018/jans.v14i2.3436
Received: April 5, 2022
Revised: May 25, 2022
Accepted: May 30, 2022

How to Cite
Konni, M. *et al.* (2022). Titanium dioxide electrospun nanofibers for dye removal- A review. *Journal of Applied and Natural Science,* 14(2), 450 - 458. https://doi.org/10.31018/jans.v14i2.3436

Abstract
Due to rapid urbanization and industrialization, water demand has increased worldwide. The availability of potable water is becoming more difficult in the global scenario. Hazardous pollution disposal by the industries to the nearest stream and search for the facile environmentally friendly technologies capable of treating these pollutants become more challenging. Effluent disposal consisting of the dyes without proper pre-treatment adversely affects the aquatic life and ecological system as they are carcinogenic and highly toxic. Dyes in the water are becoming a significant problem in the current scenario and attracted many researchers to research the current topic. Even though the conventional treatment options are available for treating polluted water, still they are not enough for the demand and supply. Thus, new state-of-the-art technologies are required to meet the demand and supply. Titanium dioxide nanofibers synthesized by electrospinning techniques have proven to be new nanomaterials gaining prominence in science. Several researchers are using these fibres by fabricating them into a thin film for pollutant removal and water treatment. They are gaining much importance as they perform best in treating water containing both organic and inorganic loads. The present review provides insights into the background and the origin of the electrospun nanofibers and preparation mechanisms. Further, we identified 25 widely used titanium dioxide electrospun nanofibers with various combinations in removing the dyes from the aqueous medium.

Keywords: Electrospinning, Nanofibers, Titanium dioxide, Wastewater treatment

INTRODUCTION

Surface water pollution by the organic dyes is commonly found due to the partially treated effluents released from the various industries (Khan *et al.,* 2019). Dyes are stable synthetic compounds resistant to photo light, microbial degradation and extreme temperature, and further, these are toxic and carcinogenic (Jose *et al.,* 2021; Khan et *al.,* 2022; Bölgen and Vaseashta, 2021). Several techniques have been employed to treat water and wastewater, including coagulation/ electrocoagulation, biological processes, oxidation, membrane technologies, phytoremediation, extraction techniques, etc. Still, none of them is proven efficient in removing all the pollutant parameters. (Nidheesh and Singh, 2017; Marinho *et al.,* 2021). During recent decades metal oxides of titanium were utilized chiefly in applying photocatalytic activity. The critical factor for widespread is its chemical stability and low cost of operation. However, using these substances in suspension to eliminate the catalyst in water is complicated, making usage of these oxides not economically viable

(Matsuzaw *et al.*,2008; Qi *et al.*,2021; Marinho *et al.*,2021); To deal with this problem, one of the alternatives is to functionalize the metal oxides with the catalyst nanoparticles, making the separation of water from pollutants easy as it is highly stable. Various techniques have been adopted to fabricate the different types of titanium oxide and catalyst films (Vella *et al.*,2010); nevertheless, the nanofibers fabricated by the electrospun technique are good examples of the next generation nanocatalysts (Altaf *et al.*,2020). As this method is versatile, it can fabricate polymers, composites, and inorganic materials from nanomaterials with controlled diameters (Armstrong *et al.*,2020). The nanofibers produced by the electrospun techniques have larger surface areas and high pore volume with interconnectivity favouring methods like water remediation, energy storage, and conversion (Song *et al.*, 2021; Marinho *et al.*, 2021). The research works related to titanium oxide nanofibers are increasing. These substances are highly potential in environmental applications compared to conventional catalysts due to their unique parameters, and these nanofibers help overcome water pollution-related problems (Xu *et al.*,2018; Pascariu *et al.*,2019; Marinho *et al.*, 2021). Indeed, the utilization of nanofibers fabricated by the oxides of titanium is already proven to be best in removing the pollutants than the nanoparticles produced (Altaf *et al.*,2020; Ehsani and Aroujalian, 2020). In this connection, the current review presents a history of electrospinning, techniques and applications of titanium dioxide nanofibers in dye removal.

BACKGROUND

Marinho *et al.* (2021) stated that before developing titanium dioxide nanofibers, several researchers conducted many studies for more than four centuries. Fig, 1 depicts the brief timeline of evolving electrospinning techniques until the first research publications regarding titanium dioxide nanofibers by an electrospun method in 2002. William Gilbert, in 1628 observed the changes in the shape of the water droplet when it encountered the external electrical field, and it was found to be the first record of electrospinning. Primarily, the spherical water drops attracted the amber piece and changed its shape to a cone, and this progression is called as "Taylor cone" (Gugulothu *et al.*,2018; Barhoum *et al.*,2019). Further in the next two centuries, variations in these shapes in contact with electrical charges were studied by many researchers. A researcher named Charles V. Boys in the year 1887 found that fibres can be fabricated by using a viscid liquid with the help of a dish connected with an electrical charge (Xue *et al.*,2019). After a few years, JF Cooley, in 1902, filed a patent in the USA titled "Apparatus for electrically dispersing fibres" with his observations and description about electrospinning (Cooley, 1902). Later in the twentieth century, electrospinning techniques were spread around the globe, primarily in the production of water filters and industrial applications. Doshi and Reneker 1995 reported electrospinning techniques with the usage of various polymers (Xue *et al.*,2019). These techniques are popularized and led to modern electrospinning concepts, which ushered in the production of ultrathin fibres having a diameter at a nanoscale level (Tucker *et al.*, 2012). The research rapidly disseminated the incorporation of metal oxides and metal nanoparticles into the fibres fabricated by electrospun methods. Many researchers described incorporating titanium dioxide nanofibers in 2001-2002. After that, the publications on electrospinning techniques have increased each year exponentially. It was

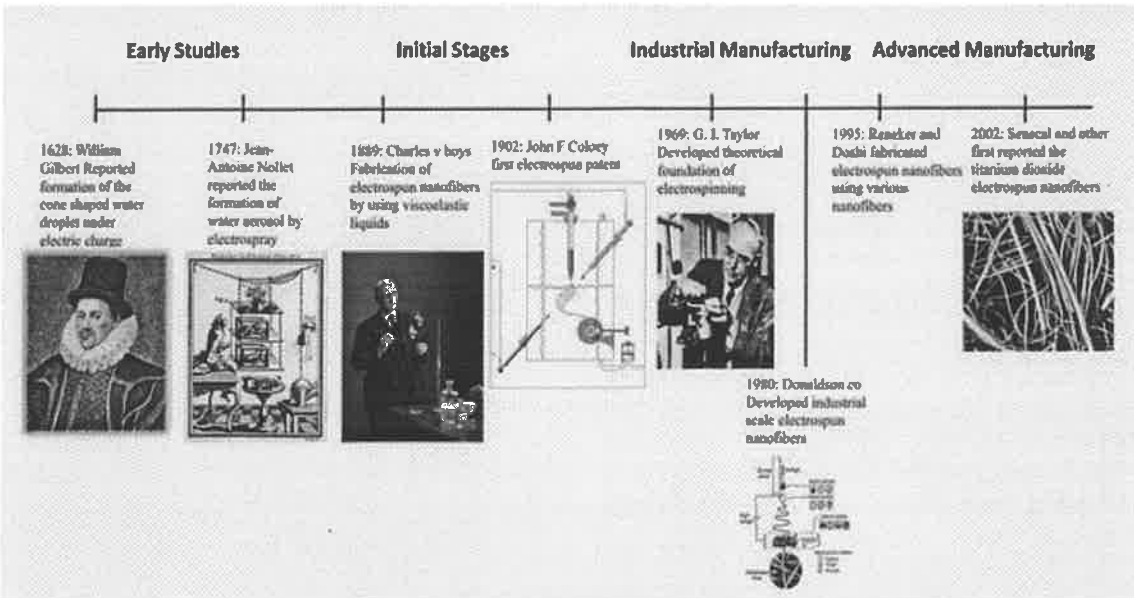

Fig. 1. *A brief timeline of electrospinning*

estimated that more than two hundred types of polymers had been fabricated into nanofibers by using electrospun techniques for several applications (Zhu *et al.*,2020). In addition, these nanofibers can be produced in larger volumes, allowing the manufacturing of more recent commercial goods; the present uses on-air/water filtration, biomedical products, and facial masks. In the meantime, the research organizations are developing innovative methods and compositions that provide specific functions in advanced applications (Barhoum *et al.*,2019; Marinho *et al.*,2021).

Process of Electrospinning

Electrospinning techniques are simple, have low operation costs, and continuously produce nanofibers in bulk production (Kim *et al.*,2021). The significant benefits of electrospinning are required simple equipment compositions and have high flexibility in nanofiber orientations (Liao *et al.*,2018). Thus, the electrospinning technique has gained much prominence in research worldwide (Istirohah *et al.*, 2019). Electrospraying is a technique that depends on the ejection of liquids from the jets under high voltage, and it is an electrohydrodynamic process. In the electrospraying technique, jets will break down the droplets to produce a particle, whereas, in the electrospinning process, the jet continuously makes the nanofibers. The liquids' viscosity and elasticity are the main features that determine the behaviour of the jets (Xue *et al.*,2019). The setup of the electrospinning process is simple and accessible by all laboratories, as shown in Fig. 2 (Marinho *et al.*,2021). The equipment configuration includes a power supply, an injection pump, and a sharp tip and collector. Nevertheless, different electrospinning designs were found worldwide, which provide for multiple needles with a jet (Démuth *et al.*,2016; SalehHudin *et al.*,2018), coaxial shape needles (Prado-Prone *et al.*, 2018), without needles (Ali *et al.*,2017), and liquid bath connected to a solid collector (Zhou *et al.*, 2009; Wu and Hong, 2016).
Different types of materials were used to prepare nanofibers by the electrospinning technique. However, organic polymer solutions were primarily used in electrospinning methods (Liao *et al.*, 2018). Alternative methods are introducing nanomaterial into the polymer solutions to produce nano functionalized fibres. This process has created many opportunities for researchers to test several combinations of nanoparticle-solvents-polymers to fabricate nanofibers for varied applications. One of the first reported research for the fabrication of titanium dioxide nanofibers used a composition of ethanol dissolved polyvinyl pyrrolidone and titanium tetraisopropoxide (Marinho *et al.*, 2021).

Titanium dioxide nanofibers in dye removal

Titanium dioxide materials have more significant advantages than other materials as they show higher photoactivity and higher stability (Wang *et al.*,2019). Indeed, titanium dioxides are the most used semiconductors for photocatalytic applications (Greenstein *et al.*,2021). Even though many researchers have studied these materials, most of the information related to titanium dioxide is related to its production in suspension or powder forms. Nevertheless, recycling these materials is a complex and costly process, as separating catalyst powder from liquids is difficult (Ananpattarachai and Kajitvichyanukul, 2016). This problem can be avoided by functionalizing titanium dioxide with active semiconductor nanoparticles; it eliminates the post-filtration step and allows the catalyst for reuse with more excellent stability. Several methods like chemical vapour deposition, sol-gel techniques, sputtering, physical vapour deposition, and sputtering, have fabricated titanium dioxide and catalyst supports (Sonawane *et al.*,2003). Moreover, materials like paper, ceramics, pumice stones, glass, and stainless steel are often tested as catalyst supports (Vella *et al.*, 2010). Electrospinning techniques are simple and economical methods for fabricating nanofibers continuously with even diameters with various compositions (Someswararao *et al.*, 2018). One dimensional nanomaterials also gained much prominence in research as titanium dioxide nanofibers due to their larger surface areas and photocatalytic activity (Pascariu *et al.*, 2019; Marinho *et al.*, 2021). Conventionally, the titanium oxide nanofibers are fabricated by electrospinning technique by incorporating titanium dioxide as a precursor with a polymer.
Further, the nanofibers are calcinated to change their amorphous phase to crystalline (Mahltig *et al.*,2007). Although titanium dioxide is used for calcination and precursors, nanofibers can be fabricated even by electrospinning methods using blended semiconductor fibres alone from them. The coaxial and dual electrospinning techniques are more effective for new nanofiber production. Luo *et al.* (2016) used the coaxial design to spin the titanium dioxide and polyvinyl alcohol nanoparticles concurrently.
Nevertheless, it is essential to note that nanofibers fabricated by polymeric solutions containing titanium dioxides might show instabilities, and both materials demixing can occur (Grothe *et al.*, 2018). However, with more excellent stabilities, titanium dioxide nanofibers by mixing polyetherimide and titanium dioxide nanopowder in dimethylformamide and tetrahydrofuran. The nanofibers fabricated are subjected to the cold plasma in nitrogen atmospheres to enhance their photocatalytic and adhesion properties. The material showed excellent photocatalytic activities for the discolouration of methylene blue with higher stability, and the same was tested for five cyclic performances. The alternative approach is to coat the purest electrospun nanofibers to the titanium dioxide after the electrospun process. Indeed, it is one of the first approaches for

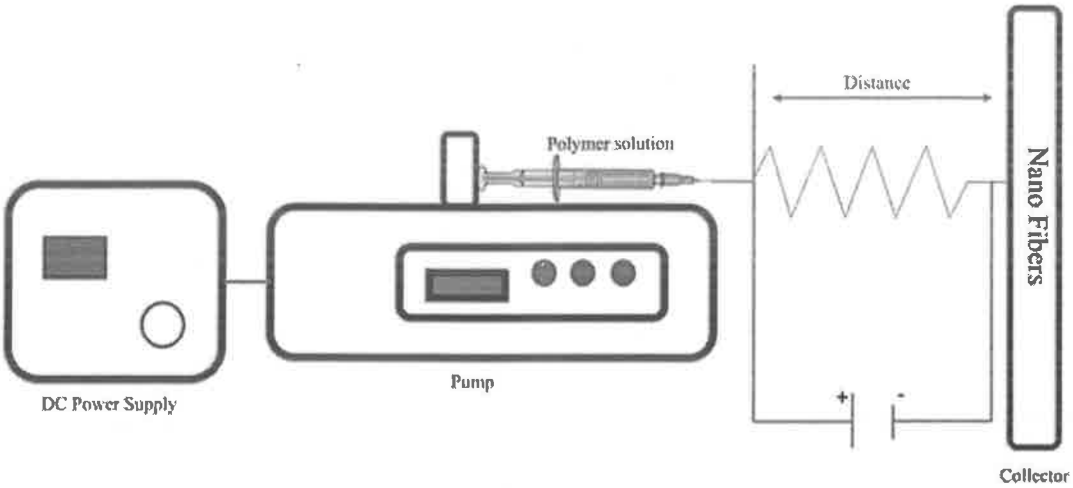

Fig. 2. *Diagrammatic representation of electrospinning device*

fabricating titanium dioxide nanofibers. Drew *et al.* (2003), synthesized the nanofibers using polyacrylonitrile by immersing them in a solution consisting of titanium dioxide. The structural properties of the pristine titanium dioxide nanofibers can be modified by adding transition-metal/nonmetals to form composites (Pascariu *et al.*,2019). Kudhier *et al.* (2018) compared the pristine and silver doped titanium nanofibers; the material's bandgap was decreased by adding silver to the titanium dioxide nanofibers, which enhanced the antibacterial activity. Correspondingly, titanium dioxide nanofibers were fabricated by doping with the graphitic carbon nitride to titanium dioxide in polymer solution adding urea. Heterojunctions are formed between the semiconductor materials due to graphitic carbon nitride with titanium dioxide enhancing the photocatalytic activity by suppressing the recombination charge (Tang *et al.*, 2018).

The properties of the nanofibers are mainly dependent on the polymer solutions utilized, working procedures and laboratory conditions (Pascariu *et al.*, 2019). Kim *et al.* (2018)stated that modified aluminium collectors would help in the unidirectional growth of nanofibers. The unidirectional nanofibers show higher crystallinity, act as electron transport, and enhance the nanofibers' optical/mechanical properties.

In recent years many techniques have been developed to treat water and wastewater. Several technologies have been examined to find better treatment options at lower costs (Chen *et al.*,2020). Generally, conventional technologies like coagulation, adsorption and biological processes are easily operated and involve lesser costs. Nevertheless, they have a disadvantage like sludge disposal and a longer duration of the water treatment (Bora *et al.*,2016). In contrast, ultrafiltration, photocatalytic degradation, and electrochemical methods involve initial high capital investment and energy; however, these methods have long-term advantages (Ortega *et al.*, 2017). Water and wastewater treatment methods are never unique or straightforward and need continuous improvement and different approaches (Song *et al.*,2017). In this regard, the titanium dioxide nanofibers fabricated by the electrospinning technique have more significant advantages for removing pollutants by the methods like membrane filtration, photocatalytic activity, and adsorption (Li *et al.*, 2014; Marinho *et al.*, 2021).

Titanium dioxide nanofibers are suitable adsorbents for eliminating heavy metals from the water as their surfaces consist of carboxyl, hydroxyl groups, etc. (Zhu *et al.*,2020). As hydrophilicity of the nanofibers is enhanced by titanium dioxide; further it also increases the stabilities, mechanical strength, and anti-smudge properties when they are utilized in the process of membrane filtration (Chen *et al.*, 2020). The surface roughness of the nanofibers is improved, which helps for the desalination of water (Pan *et al.*, 2019). Furthermore, the titanium dioxide photocatalytic properties also helped regenerate electrospun nanofibers. Li *et al.* (2014) conducted studies on the titanium dioxide electrospun nanofibers for dye removal and achieved removal percentages of 92 for methylene blue, 95 for the congo red and 52 for methyl orange. The pH of the solutions affects the charge of the titanium dioxide particles significantly. The zero-point charge is termed pH, where the surface of the particles is not charged. Singh *et al.*,2003 reported that the zero-point charge's commercial titanium dioxide nanoparticles pH is 6.2; beyond this value might negatively affect the catalysts and attract the other molecules.

On the other hand, the reactant adsorption phenomena are negatively affected and limit the reactions at higher temperatures, i.e., above 80°C; further, the oxygen concentration in the water decrease by increasing the temperatures. Thus, optimum temperatures for the reactions range from 20 to 80°C (Malato *et al.*,2016). Even though these methods seem to be promising as they

have a greater agglomeration tendency, they are challenging to separate from the aqueous medium; thus, usage of these methods is limited (Kumar *et al.*, 2014). However, doping of photocatalytic nanoparticles to the electrospun nanofibers is found to be an alternative for these limitations (Peng *et al.*, 2016). Comparing heterogeneous photocatalytic activity with membrane filtration to remove the toxic pollutants found that the titanium nanofibers show many advantages as they have the potency to degrade the contaminants compared to the membrane filtration and separate the solution phase easily. Li *et al.*, 2017 used Heteropolyacids and titanium dioxide nanoparticles for the composite and removed the methyl orange dye with an efficiency of 94%. Ramasundaram *et al.*, 2015 used Polyvinylidene fluoride and titanium dioxide nanoparticles to remove the Bisphenol A and removed the pollutants from the aqueous medium completely. Park *et al.* (2011) used silver, titanium dioxide and polyvinylpyrrolidone nanoparticles to prepare electrospun nanofibers and removed the methyl orange with an efficiency of up to 80%. In addition, traditional membrane separation methods only separate the pollutants concentrate; this method requires high energy for the operation to reduce the fouling of the membrane to maintain the constant flow (Gao *et al.*, 2020). Wang et al., 2018 prepared electrospun nanofibers by doping carbon nanofibers and removing the methylene blue dye with an efficiency greater than 57 %. Khan et al., 2022 synthesized titanium dioxide nanofibers by doping them with zinc and cadmium and tested them to remove the organic dyes. These electrospun titanium dioxide nano-

Table 1: Application of electrospun titanium dioxide nanofibers for dye removal

S. no	Nanofiber constituents	Dye	Dye removal (%)	References
1	Heteropolyacids and titanium dioxide	Methyl orange	94	Li *et al.*, 2017
2	Metal organic frame works, titanium dioxide and zinc	Rhodamine	92	Hou *et al.*, 2019
3	Polymethyl methacrylate and titanium dioxide	Methylene blue	100	Vild *et al.*, 2016
4	Polyvinylidene fluoride and titanium dioxide	Cimetidine	100	Ramasundaram *et al.*, 2015
5	Polyvinylidene fluoride and titanium dioxide	4- Chlorophenol	100	Ramasundaram *et al.*, 2015
6	Polyvinylidene fluoride and titanium dioxide	Bisphenol A	100	Ramasundaram *et al.*, 2015
7	Silver, titanium dioxide and polyvinylpyrrolidone	Methylene blue	100	Chang *et al.*,2009
8	Silver, titanium dioxide and polyvinylpyrrolidone	Methylene blue	80	Park *et al.*,2011
9	Titanium dioxide and bio-glass nanofibers	Methylene blue	60	Lian *et al.*,2018
10	Titanium dioxide and carbon nanofibers	Rhodamine B	80	Xu *et al.*, 2016
11	Titanium dioxide and cyanide nitrogen	RhB	96	Wang *et al.*, 2018
12	Titanium dioxide and graphene oxide	Propranolol	100	Gao *et al.*, 2020
13	Titanium dioxide and peroxyl acetyl nitrate	Isoproturon	90	Xie *et al.*, 2017
14	Titanium dioxide and polyvinylpyrrolidone	Methylene blue	90	Aghasiloo *et al.*,2019
15	Titanium dioxide and polyvinylpyrrolidone	Rhodamine	92	Wang *et al.*,2019
16	Titanium dioxide, zinc oxide and polyvinyl alcohol	Methyl orange	60	Ramos *et al.*,2020
17	Titanium dioxide, graphene oxide and polyvinyl acetate	Rhodamine	90	Seong *et al.*,2018
18	Titanium dioxide, graphitic carbon nitride and polyvinyl acetate	Rhodamine	90	Adhikari *et al.*,2016
19	Titanium dioxide, polyaniline and polyacrylonitrile	Methyl orange	90	Sedghi *et al.*,2017
20	Titanium dioxide, silver and peroxyl acetyl nitrate	Methylene Blue	99	Shi *et al.*, 2017
21	Titanium dioxide, silver and peroxyl acetyl nitrate	Methylene Blue	100	Panthi *et al.*, 2017
22	Zinc ferrite, titanium dioxide and polyvinylpyrrolidone	Methylene blue	100	Nada *et al.*,2017
23	Titanium dioxide, Zinc and Cadmium	Methylene blue	94	Khan *et al.*, 2022
23	Titanium dioxide, Zinc and Cadmium	Methyl orange	96	Khan *et al.*, 2022
25	Titanium dioxide and carbon nanofibers	Methylene blue	57	Wang *et al.*, 2018

fibers removed the methylene blue with an efficiency of 94% within 2 hours. Further, they have achieved 96 % removal of methyl orange with the same nanocomposites within 100 minutes.

In contrast, the utilization of titanium dioxide nanofiber proved that they are efficient in photocatalytic activities compared to the titanium dioxide nanoparticles.Table 1 depicts the list of titanium doped electrospun nanofibers to remove the dye from the aqueous medium. 1. Still, there is a need to conduct further research on these nanofibers for industrial and large-scale applications. Integrating academic research with the industries will help move the bench-scale operations to the industries that will benefit both. Further researchers should concentrate on the disadvantages of the solvents and fabrications procedure, and alternative green chemistry methods should be implemented to make the complete process sustainable.

Conclusion

The evolution in treating the water with various nanomaterials showed how the current research advances science. The literature showed that electrospun nanofiber's application in water and wastewater is efficient, and researchers have gained much prominence. Even though several bench-scale studies have proven that nanofibers are efficient in removing the organic and inorganic pollutants from the aqueous medium, further scaling up of studies is required to move these technologies to the water industries for larger-scale production and utilization. The cost expenditures in producing the electrospun nanofibers hinder their usage in developing countries like India. However, adopting these technologies in the water industry is reliable, reducing secondary unit treatment processes. Thus, these technologies must be adopted and utilized for water treatment to replace the associated costs linked with conventional water treatment units.

Conflict of interest

The authors declare that they have no conflict of interest.

REFERENCES

1. Adhikari, S. P., Awasthi, G. P., Kim, H. J., Park, C. H. & Kim, C. S. (2016). Electrospinning directly synthesized porous TiO_2 nanofibers modified by graphitic carbon nitride sheets for enhanced photocatalytic degradation activity under solar light irradiation. *Langmuir* 32(24): 6163-6175. doi: 10.1021/acs.langmuir.6b01085.
2. Aghasiloo, P., Yousefzadeh, M., Latifi, M. & Jose, R. (2019). Highly porous TiO2 nanofibers by humid-electrospinning with enhanced photocatalytic properties. *J Alloys Compd* 790: 257-265. doi: https://doi.org/10.1016/j.jallcom.2019.03.175
3. Ali, U., Niu, H., Aslam, S., Jabbar, A., Rajput, A. W. & Lin, T. (2017). Needleless electrospinning using sprocket wheel disk spinneret. *J Mater Sci* 52(12): 7567-7577. doi: https://doi.org/10.1007/s10853-017-0989-6
4. Altaf, A. A., Ahmed, M., Hamayun, M., Kausar, S., Waqar, M. & Badshah, A. (2020). Titania nano-fibers: a review on synthesis and utilities. *Inorganica Chimica Acta* 501: 119268. doi: https://doi.org/10.1016/j.ica.2019.119268
5. Ananpattarachai, J., & Kajitvichyanukul, P. (2016). Enhancement of chromium removal efficiency on adsorption and photocatalytic reduction using a bio-catalyst, titania-impregnated chitosan/xylan hybrid film. *J Clean Prod* 130: 126-136. doi: https://doi.org/10.1016/j.jclepro.2015.10.098
6. Armstrong, M., Nealy, S., Severino, C., Maniukiewicz, W., Modelska, M., Binczarski, M. & Stanishevsky, A. (2020). Composite materials made from glass microballoons and ceramic nanofibers for use as catalysts and catalyst supports. *J Mater Sci* 55(27): 12940-12952. doi: https://doi.org/10.1007/s10853-020-04956-1
7. Barhoum, A., Rasouli, R., Yousefzadeh, M., Rahier, H. & Bechelany, M. (2019). Nanofiber technologies: history and development. Handbook of nanofibers. Springer International Publishing, Cham, 3-43. doi: https://doi.org/10.1007/978-3-319-53655-2_54
8. Bölgen, N. & Vaseashta, A. (2021). Electrospun Nanomaterials: Applications in Water Contamination Remediation. *Water Safety, Security and Sustainability*, 197-213. doi: https://doi.org/10.1007/978-3-030-76008-3_8
9. Bora, A. J., Gogoi, S., Baruah, G., & Dutta, R. K. (2016). Utilization of co-existing iron in arsenic removal from groundwater by oxidation-coagulation at optimized pH. *J Environ Chem Eng* 4(3): 2683-2691. doi: https://doi.org/10.1016/j.jece.2016.05.012
10. Chang, S. H., Wang, K. S., Chao, S. J., Peng, T. H., & Huang, L. C. (2009). Degradation of azo and anthraquinone dyes by a low-cost Fe0/air process. *J Hazard Mater 166*(2-3): 1127-1133. doi: https://doi.org/10.1016/j.jhazmat.2008.12.021
11. Chen, H., Huang, M., Liu, Y., Meng, L., & Ma, M. (2020). Functionalized electrospun nanofiber membranes for water treatment: A review. *Sci Total Environ* 739: 139944. doi: https://doi.org/10.1016/j.scitotenv.2020.139944
12. Cooley, J. F. (1902). U.S. Patent No. 692,631. Washington, DC: U.S. Patent and Trademark Office.
13. Démuth, B., Farkas, A., Pataki, H., Balogh, A., Szabó, B., Borbás, E. & Nagy, Z. K. (2016). Detailed stability investigation of amorphous solid dispersions prepared by single-needle and high-speed electrospinning. *Int J Pharm*, 498 (1-2): 234-244. doi: https://doi.org/10.1016/j.ijpharm.2015.12.029
14. Drew, C., Liu, X., Ziegler, D., Wang, X., Bruno, F. F., Whitten, J. & Kumar, J. (2003). Metal oxide-coated polymer nanofibers. *Nano Lett* 3(2): 143-147. doi: https://doi.org/10.1021/nl025850m
15. Ehsani, M. & Aroujalian, A. (2020). Fabrication of electrospun polyethersulfone/titanium dioxide (PES/TiO2) composite nanofibers membrane and its application for photocatalytic degradation of phenol in aqueous solution. *Polym Adv Technol* 31(4): 772-785. doi: https://doi.org/10.1002/pat.4813
16. Gao, Y., Yan, N., Jiang, C., Xu, C., Yu, S., Liang, P. & Huang, X. (2020). Filtration-enhanced highly efficient pho-

tocatalytic degradation with a novel electrospun rGO@ TiO2 nanofibrous membrane: Implication for improving photocatalytic efficiency. *Appl Catal B* 268: 118737. doi: https://doi.org/10.1016/j.apcatb.2020.118737

17. Greenstein, K. E., Nagorzanski, M. R., Kelsay, B., Verdugo, E. M., Myung, N. V., Parkin, G. F., & Cwiertny, D. M. (2021). Carbon–titanium dioxide (C/TiO_2) nanofiber composites for chemical oxidation of emerging organic contaminants in reactive filtration applications. *Environmental Science: Nano* 8(3): 711-722. doi: https://doi.org/10.1039/D0EN00975J
18. Grothe, T., Böttjer, R., Wehlage, D., Großerhode, C., Storck, J. L., Juhász Junger, I. & Ehrmann, A. (2018). Photocatalytic properties of TiO2 composite nanofibers electrospun with different polymers. *Inorganic and Composite Fibers* 303-319. doi: 10.1016/B978-0-08-102228-3.00014-1
19. Gugulothu, D., Barhoum, A., Nerella, R., Ajmer, R. & Bechlany, M. (2018). Fabrication of nanofibers: electrospinning and non-electrospinning techniques. *Handbook of Nanofibers* 1-34. doi: https://doi.org/10.1007/978-3-319-53655-2_6
20. Hou, Y., Yan, S., Huang, G., Yang, Q., Huang, S., & Cai, J. (2020). Fabrication of N-doped carbons from waste bamboo shoot shell with high removal efficiency of organic dyes from water. *Bioresour Technol* 303, 122939. doi: https://doi.org/10.1016/j.biortech.2020.122939
21. Istirohah, T., Himmah, S. W. & Diantoro, M. (2019). Fabrication of aligned PAN/TiO2 fiber using Electric Electrospinning (EES). Mater Today Proc 13: 211-216. doi: 10.1016/j.matpr.2019.03.216
22. Jose, A., Pai, S. D. K. R., Pinheiro, D. & Kasinathan, K. (2021). Visible light photodegradation of organic dyes using electrochemically synthesized MoO3/ ZnO. *Environmental Science and Pollution Research*, 28 (37), 52202-52215. doi: https://doi.org/10.1007/s11356-021-14311-9
23. Khan, I., Sadiq, M., Khan, I. & Saeed, K. (2019). Manganese dioxide nanoparticles/activated carbon composite as efficient UV and visible-light photocatalyst. *Environmental Science and Pollution Research* 26(5): 5140-5154. doi: https://doi.org/10.1007/s11356-018-4055-y
24. Khan, S., Sadiq, M., Kim, D. S., Ullah, M. & Muhammad, N. (2022). TiO2 and its binary ZnTiO2 and ternary CdZnTiO2 nanocomposites as efficient photocatalysts for the organic dyes degradation. *Appl Water Sci* 12(6): 1-12. doi: https://doi.org/10.1007/s13201-022-01628-0
25. Kim, D., Noh, W. Jo, S., & Lee, T. S. (2021). Electrospun mesoporous silica nanofibers decorated with titanium dioxide nanoparticles for a repeatable photocatalysis. *Molecular Crystals and Liquid Crystals*, 1-16. doi: https://doi.org/10.1080/15421406.2021.1956761
26. Kim, J. H., Lee, J. H., Kim, J. Y., & Kim, S. S. (2018). Synthesis of aligned TiO2 nanofibers using electrospinning. *Appl Sci* 8(2): 309. doi: https://doi.org/10.3390/app8020309
27. Kudhier, M. A., Sabry, R. S., Al-Haidarie, Y. K. & Al-Marjani, M. F. (2018). Significantly enhanced antibacterial activity of Ag-doped TiO_2 nanofibers synthesized by electrospinning. *Mater Technol* 33(3): 220-226. doi: https://doi.org/10.1080/10667857.2017.1396778
28. Kumar, P. S., Sundaramurthy, J., Sundarrajan, S., Babu, V. J., Singh, G., Allakhverdiev, S. I., & Ramakrishna, S. (2014). Hierarchical electrospun nanofibers for energy harvesting, production and environmental remediation. *Energy Environ Sci* 7(10): 3192-3222. doi: https://doi.org/10.1039/C4EE00612G
29. Li, W., Li, T., Li, G., An, L., Li, F. & Zhang, Z. (2017). Electrospun H4SiW12O40/cellulose acetate composite nanofibrous membrane for photocatalytic degradation of tetracycline and methyl orange with different mechanism. *Carbohydr Polym* 168: 153-162.
30. Li, X., Chen, Y., Hu, X., Zhang, Y., & Hu, L. (2014). Desalination of dye solution utilizing PVA/PVDF hollow fiber composite membrane modified with TiO_2 nanoparticles. *J Membr Sci* 471: 118-129. doi: https://doi.org/10.1016/j.memsci.2014.08.018
31. Lian, H. & Meng, Z. (2018). A novel and highly photocatalytic "TiO2wallpaper" made of electrospun TiO2/bioglass hybrid nanofiber. *Mater Sci Semicond Process* 80: 68-73. doi: https://doi.org/10.1016/j.mssp.2018.02.019
32. Liao, Y., Loh, C. H., Tian, M., Wang, R. & Fane, A. G. (2018). Progress in electrospun polymeric nanofibrous membranes for water treatment: Fabrication, modification and applications. *Prog Polym Sci* 77: 69-94. doi: https://doi.org/10.1016/j.progpolymsci.2017.10.003
33. Luo, Y., Jia, Y., Zhang, D., & Cheng, X. (2016). Coaxial electrospinning method for the preparation of TiO2@ CdS/ PVA composite nanofiber Mat and investigation on its photodegradation catalysis. *Photochem Photobiol* 92(4): 515-522. doi: https://doi.org/10.1111/php.12591
34. Mahltig, B., Gutmann, E., Meyer, D. C., Reibold, M., Dresler, B., Günther, K. & Böttcher, H. (2007). Solvothermal preparation of metallized titania sols for photocatalytic and antimicrobial coatings. *J Mater Chem* 17(22): 2367-2374. doi: https://doi.org/10.1039/B702519J
35. Malato, S., Maldonado, M. I., Fernandez-Ibanez, P., Oller, I., Polo, I. & Sánchez-Moreno, R. (2016). Decontamination and disinfection of water by solar photocatalysis: The pilot plants of the Plataforma Solar de Almeria. *Materials Science in Semiconductor Processing* 42: 15-23.
36. Marinho, B. A., de Souza, S., de Souza, A. A. U. & Hotza, D. (2021). Electrospun TiO2 nanofibers for water and wastewater treatment: a review. *J Mater Sci* 56(9): 5428-5448. doi: https://doi.org/10.1007/s10853-020-05610-6
37. Nada, A. A., Nasr, M., Viter, R., Miele, P., Roualdes, S., & Bechelany, M. (2017). Mesoporous ZnFe2O4@ TiO2 nanofibers prepared by electrospinning coupled to PECVD as highly performing photocatalytic materials. *J Phys Chem C 121*(44): 24669-24677. doi: https://doi.org/10.1021/acs.jpcc.7b08567
38. Nidheesh, P. V. & Singh, T. A. (2017). Arsenic removal by electrocoagulation process: recent trends and removal mechanism. *Chemosphere* 181: 418-432. doi: https://doi.org/10.1016/j.chemosphere.2017.04.082
39. Ortega, A., Oliva, I., Contreras, K. E., González, I., Cruz-Díaz, M. R., & Rivero, E. P. (2017). Arsenic removal from water by hybrid electro-regenerated anion exchange resin/ electrodialysis process. *Sep Purif Technol* 184: 319-326. doi: https://doi.org/10.1016/j.seppur.2017.04.050
40. Pan, C. Y., Xu, G. R., Xu, K., Zhao, H. L., Wu, Y. Q., Su, H. C., & Das, R. (2019). Electrospun nanofibrous membranes in membrane distillation: Recent developments and future perspectives. *Sep Purif Technol.* 221: 44-63.

doi: https://doi.org/10.1016/j.seppur.2019.03.080

41. Panthi, G., Park, S. J., Chae, S. H., Kim, T. W., Chung, H. J., Hong, S. T. & Kim, H. Y. (2017). Immobilization of Ag3PO4 nanoparticles on electrospun PAN nanofibers via surface oximation: Bifunctional composite membrane with enhanced photocatalytic and antimicrobial activities. *Ind Eng Chem Res* 45: 277-286. doi: https://doi.org/10.1016/j.jiec.2016.09.035
42. Park, J. Y., Hwang, K. J., Lee, J. W., & Lee, I. H. (2011). Fabrication and characterization of electrospun Ag-doped TiO 2 nanofibers for photocatalytic reaction. *J Mater Sci* 46(22): 7240-7246. doi: https://doi.org/10.1007/s10853-011-5683-5
43. Pascariu, P., Airinei, A., Iacomi, F., Bucur, S. & Suchea, M. P. (2019). Electrospun TiO2-based nanofiber composites and their bio-related and environmental applications. *In Functional Nanostructured Interfaces for Environmental and Biomedical Applications* (pp. 307-321). Elsevier. doi: https://doi.org/10.1016/B978-0-12-814401-5.00012-8
44. Peng, S., Jin, G., Li, L., Li, K., Srinivasan, M., Ramakrishna, S. & Chen, J. (2016). Multi-functional electrospun nanofibres for advances in tissue regeneration, energy conversion & storage, and water treatment. *Chem Soc Rev* 45(5): 1225-1241. doi: https://doi.org/10.1039/C5CS00777A
45. Prado-Prone, G., Silva-Bermudez, P., Almaguer-Flores, A., García-Macedo, J. A., García, V. I., Rodil, S. E. & Velasquillo, C. (2018). Enhanced antibacterial nanocomposite mats by coaxial electrospinning of polycaprolactone fibers loaded with Zn-based nanoparticles. *Nanomed Nanotechnol Biol Med* 14(5): 1695-1706. doi: 10.1016/j.nano.2018.04.005.
46. Qi, W., Yang, Y., Du, J., Yang, J., Guo, L. & Zhao, L. (2021). Highly Photocatalytic Electrospun Zr/Ag Co-doped Titanium Dioxide Nanofibers for Degradation of Dye. *J Colloid Interface Sci* 603: 594-603. doi: https://doi.org/10.1016/j.jcis.2021.06.109
47. Ramasundaram, S., Son, A., Seid, M. G., Shim, S., Lee, S. H., Chung, Y. C. & Hong, S. W. (2015). Photocatalytic applications of paper-like poly (vinylidene fluoride)–titanium dioxide hybrids fabricated using a combination of electrospinning and electrospraying. *J Hazard Mater* 285: 267-276. doi: 10.1016/j.jhazmat.2014.12.004.
48. Ramos, P. G., Luyo, C., Sánchez, L. A., Gomez, E. D., & Rodríguez, J. M. (2020). The spinning voltage influence on the growth of ZnO-rGO nanorods for photocatalytic degradation of methyl orange dye. *Catalysts,* 10(6): 660. doi: https://doi.org/10.3390/catal10060660
49. SalehHudin, H. S., Mohamad, E. N., Mahadi, W. N. L. & Muhammad Afifi, A. (2018). Multiple-jet electrospinning methods for nanofiber processing: A review. *Mater Manuf Process* 33(5): 479-498. doi: https://doi.org/10.1080/10426914.2017.1388523
50. Sedghi, R., Moazzami, H. R., Davarani, S. S. H., Nabid, M. R. & Keshtkar, A. R. (2017). A one step electrospinning process for the preparation of polyaniline modified TiO_2/polyacrylonitile nanocomposite with enhanced photocatalytic activity. *J Alloys Compd* 695: 1073-1079. doi: https://doi.org/10.1016/j.jallcom.2016.10.232
51. Seong, D. B., Son, Y. R., & Park, S. J. (2018). A study of reduced graphene oxide/leaf-shaped TiO_2 nanofibers for enhanced photocatalytic performance via electrospinning. *J Solid State Chem* 266: 196-204. doi: https://doi.org/10.1016/j.jssc.2018.06.003
52. Shi, Y., Yang, D., Li, Y., Qu, J. & Yu, Z. Z. (2017). Fabrication of PAN@ TiO2/Ag nanofibrous membrane with high visible light response and satisfactory recyclability for dye photocatalytic degradation. *Appl Surf Sci* 426: 622-629. doi: https://doi.org/10.1016/j.apsusc.2017.06.302
53. Singh, H. K., Muneer, M. & Bahnemann, D. (2003). Photocatalyzed degradation of a herbicide derivative, bromacil, in aqueous suspensions of titanium dioxide. *Photochem Photobiol Sci* 2(2): 151-156. doi: https://doi.org/10.1039/B206918K
54. Someswararao, M. V., Dubey, R. S., Subbarao, P. S. V., & Singh, S. (2018). Electrospinning process parameters dependent investigation of TiO_2 nanofibers. *Results Phys* 11: 223-231. doi: https://doi.org/10.1016/j.rinp.2018.08.054
55. Sonawane, R. S., Hegde, S. G., & Dongare, M. K. (2003). Preparation of titanium (IV) oxide thin film photocatalyst by sol–gel dip coating. *Mater Chem Phys* 77(3): 744-750. doi: 10.1016/S0254-0584(02)00138-4
56. Song, P., Yang, Z., Zeng, G., Yang, X., Xu, H., Wang, L., & Ahmad, K. (2017). Electrocoagulation treatment of arsenic in wastewaters: A comprehensive review. *Chem Eng J* 317: 707-725. doi: https://doi.org/10.1016/j.cej.2017.02.086
57. Song, Y., Zhao, F., Li, Z., Cheng, Z., Huang, H. Yang, M. (2021). Electrospinning preparation and anti-infrared radiation performance of silica/titanium dioxide composite nanofiber membrane. *RSC Advances* 11(39): 23901-23907. doi: https://doi.org/10.1039/D1RA03917B
58. Tang, Q., Meng, X., Wang, Z., Zhou, J., & Tang, H. (2018). One-step electrospinning synthesis of TiO2/g-C3N4 nanofibers with enhanced photocatalytic properties. Appl Surf Sci 430: 253-262. doi: https://doi.org/10.1016/j.apsusc.2017.07.288
59. Tucker, N., Stanger, J. J., Staiger, M. P., Razzaq, H. & Hofman, K. (2012). The history of the science and technology of electrospinning from 1600 to 1995. *J Eng Fibers Fabr* 7(2_suppl), 155892501200702S10. doi: https://doi.org/10.1177/155892501200702S10
60. Vella, G., Imoberdorf, G. E., Sclafani, A., Cassano, A. E., Alfano, O. M. & Rizzuti, L. (2010). Modeling of a TiO_2-coated quartz wool packed bed photocatalytic reactor. *Appl Catal B* 96(3-4): 399-407. doi: 10.1016/j.apcatb.2010.02.037
61. Vild, A., Teixeira, S., Kühn, K., Cuniberti, G. & Sencadas, V. (2016). Orthogonal experimental design of titanium dioxide—Poly (methyl methacrylate) electrospun nanocomposite membranes for photocatalytic applications. *J Environ Chem Eng* 4(3): 3151-3158. doi: https://doi.org/10.1016/j.jece.2016.06.029
62. Wang, C., Hu, L., Chai, B., Yan, J. & Li, J. (2018). Enhanced photocatalytic activity of electrospun nanofibrous TiO2/g-C3N4 heterojunction photocatalyst under simulated solar light. *Appl Surf Sci* 430: 243-252. doi: 10.1016/j.apsusc.2017.08.036
63. Wang, T., Gao, Y., Tang, T., Bian, H., Zhang, Z., Xu, J., ... & Chu, X. (2019). Preparation of ordered TiO2 nanofibers/nanotubes by magnetic field assisted electrospinning and the study of their photocatalytic properties. *Ceram Int* 45 (11): 14404-14410. doi: 10.1016/j.ceramint.2019.04.158

64. Wu, J. & Hong, Y. (2016). Enhancing cell infiltration of electrospun fibrous scaffolds in tissue regeneration. *Bioact Mater* 1(1), 56-64. doi: https://doi.org/10.1016/j.bioactmat.2016.07.001
65. Xie, R., Zhang, L., Liu, H., Xu, H., Zhong, Y., Sui, X., & Mao, Z. (2017). Construction of CQDs-Bi20TiO32/PAN electrospun fiber membranes and their photocatalytic activity for isoproturon degradation under visible light. *Mater Res. Bull.* ,94, 7-14. doi: https://doi.org/10.1016/j.materresbull.2017.05.040
66. Xu, D., Li, L., He, R., Qi, L., Zhang, L., & Cheng, B. (2018). Noble metal-free RGO/TiO2 composite nanofiber with enhanced photocatalytic H2-production performance. *Appl Surf Sci* 434, 620-625. doi: https://doi.org/10.1016/j.apsusc.2017.10.192
67. Xu, Z., Li, X., Wang, W., Shi, J., Teng, K., Qian, X. & Liu, L. (2016). Microstructure and photocatalytic activity of electrospun carbon nanofibers decorated by TiO2 nanoparticles from hydrothermal reaction/blended spinning. *Ceram Int.* 42(13), 15012-15022. doi: 10.1016/j.ceramint.2016.06.150
68. Xue, J., Wu, T., Dai, Y., & Xia, Y. (2019). Electrospinning and electrospun nanofibers: Methods, materials, and applications. *Chem Rev.*, 119(8): 5298-5415. doi: https://doi.org/10.1021/acs.chemrev.8b00593
69. Zhou, F. L., Gong, R. H. & Porat, I. (2009). Three-jet electrospinning using a flat spinneret. *J Mater Sci* 44(20), 5501-5508. doi: 10.1007/s10853-009-3768-1
70. Zhu, F., Zheng, Y. M., Zhang, B. G. & Dai, Y. R. (2020). A critical review on the electrospun nanofibrous membranes for the adsorption of heavy metals in water treatment. *J Hazard Mater.*, 401, 123608. doi: https://doi.org/10.1016/j.jhazmat.2020.123608

International Journal of Surface Engineering and Interdisciplinary Materials Science
Volume 10 • Issue 1

Hydrogen Sorption Behaviors on Lithium Doped MIL@53-Al at Non-Cryogenic Temperatures

Madhavi Konni, Department of H&S (Chemistry), Malla Reddy Engineering College (Autonomous), Secunderabad, India*

https://orcid.org/0000-0002-2022-5528

Manoj Kumar Kamena, Department of Environmental Science, Institute of Sciences, GITAM University (Deemed), Visakhapatnam, India

https://orcid.org/0000-0001-9241-2990

Saratchandra Babu Mukkamala, Department of Chemistry, Institute of Sciences, GITAM University (Deemed), Visakhapatnam, India

ABSTRACT

The current research work reports the methods that have been developed to dope the lithium nanoparticles to the MIL@53-Al surface frameworks without inducing the structures. The prepared MIL@53-Al MOFs and Li/MIL/53-Al were characterized by XRD, TEM, SEM, BET, and TGA. The developed lithium doped MIL@53-Al and MIL@53-Al were measured for the hydrogen sorption capacities at 298 and 253 K under a pressure of 75 bar. The study reports revealed that sorption capacities of MIL@53-Al enhanced significantly due to the doping of lithium ions; however, doping of these ions should be controlled for obtaining good uptake capacities as the higher concentrations of lithium might damage the frameworks of the synthesized materials. The lithium doping enhances the hydrogen uptake from 1.37 to 1.75 wt % at 253 K and 75 bar pressure.

KEYWORDS

High-Pressure Adsorption, Hydrogen Storage, Lithium Doping, Metal-Organic Framework (MOF), MIL@53-Al

1. INTRODUCTION

The metal ions clusters and organic multidentate ligands form Metal-organic frameworks (MOFs), and these materials are highly crystalline and porous (Yaghi et al., 1995; Capková et al., 2020). MOFs emerged as potential materials for application in science like catalysis (Miao et al., 2019), storage (Jia et al., 2019), biomedical, and sensors (Shet et al., 2021; Kreno et al., 2012) from the past decade. MOFs can be changed into many varieties by altering the ligands or metal ions, as their structures can be tuned by changing the pore sizes. Additionally, MOFs consist of substantial surface areas and volumes, making them attractive hydrogen storage candidates (Broom et al., 2019; Hu & Zhang, 2010; Suh et al., 2012). Hydrogen storage might be crucial to achieving a hydrogen economy that can be used as a fuel carrier for the fuel cells. Even though many researchers study several materials for the storage application of hydrogen, to date, no material was achieved "DOE" ("US Department of Energy") targets, i.e., volumetric capacities (40 g/L) and gravimetric capacities (5.5 wt%) at the ambient

*Corresponding Author

DOI: 10.4018/IJSEIMS.302239

temperatures (Dai et al., 2020). MOFs and COFs (Covalent organic frameworks) are considered suitable sorption materials for hydrogen as they have significant surface areas and porosities. MOFs and COFs utilize weak Vander Waals interactions to enable reversible/fast discharge, which might store hydrogen.

Nevertheless, due to these interactions at ambient temperatures, significant amounts of hydrogen cannot be stored. According to the literature available, several researchers have been that at cryogenic temperatures, the hydrogen storage capacities have reached above 5.5 wt %; however, none of the studies said that hydrogen uptake capacities reached around two wt % at room temperature conditions (Wang et al., 2020; Guo et al., 2020; Kaye et al., 2007; Furukawa et al., 2007; Lin et al., 2009; Koh et al., 2009; Furukawa et al., 2010). Insertion of cations with alkaline nature to the MOFs Nano space has gained many researchers' attention to overcome the common storage problems associated with hydrogen storage. Specifically, cations like lithium are promising materials as these compounds have a lower molecular weight and provide an affinity for the molecules of hydrogen as they induce dipole interactions (Lochan and Head-Gordon, 2006). According to the literature available, the researchers have proposed several theoretical theories by doping lithium to COFs and MOFs to achieve a hydrogen storage wt % of 6 at ambient temperatures (Han & Goddard, 2007; Cao et al., 2009). Many research groups have been demonstrated the experiments by doping lithium with MOFs and revealed that these ions' doping enhanced the storage capacities of hydrogen at non-cryogenic temperatures (Mulfort & Hupp, 2007; Yang et al., 2008; Mulfort et al., 2009a; Mulfort et al., 2009b; Nouar et al., 2009; Himsl et al., 2009; Yang et al., 2009; Li et al., 2010; Xiang et al., 2011). These studies used MOFs consisting of specific functionalized groups such as hydroxyls to form lithium alkoxides by removing the protons with lithium cations (Mulfort et al., 2009b; Nouar et al., 2009). MOFs with specific functionalized groups are limited; thus, new methods like doping of lithium might be adopted to develop wide varieties of MOFs.

Composite MOFs are prepared to enhance hydrogen uptake capacities by doping carbonaceous materials (Yang et al., 2010). The developed composites materials have significant mechanical properties and moisture stabilization; It was also observed that doping of carbonaceous materials with transition metals enhanced hydrogen uptake capacities at room temperature. The enhancements in uptake capacities are attributed to the spillover mechanism - the MOFs act as secondary receptors consisting of a larger surface area for hydrogen atoms (Kolmann et al., 2008). Theoretical investigations have also been reported in the literature on the cation alkali metals doped to the MOFs consisting of organic linkers to the fullerenes and carbon nanotubes to enhance uptake capacities (Öztürk, 2021). Lithium cations are the most common materials doped to the MOFs as they can effectively donate the electrons to the linkers of MOF and these ions are easy to dope as they have low molar masses (Dalach et al., 2008). Some computational studies on the MOFs doped with lithium revealed that Li donates the electrons to MOFs' linkers and leads to the high binding energy of hydrogen, which exhibited a solid affinity for MOFs nearer to Li (Meng et al., 2013). Meng et al., 2013 reported that hydrogen sorption capacities in computational studies achieved at 298 K with a 100-bar pressure attained a weight of 4 wt% with a simulation doping lithium with IRMOF9. In the theoretical studies at ambient temperatures, MOFs and COFs doped with lithium also achieved a weight of 6% hydrogen (Klontzas et al., 2008). Klontzas et al., 2008 conducted theoretical calculations and reported that utilization of functionalized organic linkers consisting of lithium atoms showed enhanced MOFs' performance to store hydrogen. It was also found that enhanced hydrogen uptake capacities were observed in the experimental approaches. In his empirical studies (Li et al., 2010), Li et al., 2010 revealed that hydrogen uptake capacities in conjugated polymers (microporous) with lithium over 1 bar pressure at 77 K were a weight percent of 6.1; adopting these mechanisms to real-time applications are not possible due to inconsistent repeatability (Wang et al., 2020). Mulfort et al., 2019a reported enhanced uptake capacities of hydrogen over 1 bar pressure at 77 K, i.e., up to 75% in the MOFs doped with lithium than the pristine MOFs; further reported that the organic inkers might increase these capacities with functionalized groups (Himsl et al., 2009). Himsl et al. revealed that lowering the pressures enhanced the uptake capacities of hydrogen from a weight of 0.5 to 0.7% by the post-synthesis formation of lithium alkoxides in MIL-53 (Al) hydroxyl functionalized groups (Yang et al., 2009; Loiseau et al., 2004). By immersing MOF with

Computational FEM Application on Percutaneous Nephrolithotomy (PCNL) Minimum Invasive Surgery Through Needle Insertion Process

Ranjit Barua, Surajit Das, Pallab Datta and Amit RoyChowdhury (2022). *Advances in Computational Approaches in Biomechanics (pp. 210-222).*

www.igi-global.com/chapter/computational-fem-application-on-percutaneous-nephrolithotomy-pcnl-minimum-invasive-surgery-through-needle-insertion-process/300498?camid=4v1a

Design and Thermal Analysis of MgZrO3 Ceramic Coated I.C. Engine Piston Based on Finite Element Analysis (FEA)

Shailendra Kumar (2018). *Advanced Numerical Simulations in Mechanical Engineering (pp. 156-176).*

www.igi-global.com/chapter/design-and-thermal-analysis-of-mgzro3-ceramic-coated-ic-engine-piston-based-on-finite-element-analysis-fea/192998?camid=4v1a

Materials Today: Proceedings xxx (xxxx) xxx

Contents lists available at ScienceDirect

Materials Today: Proceedings

journal homepage: www.elsevier.com/locate/matpr

Surface investigation on aluminium composite by additive manufacturing process

P. Sellamuthu [a], P. Srinivas Reddy [b], R. Ramesh [c], M. Haritha Kiranmai [d], CH.LDS. Narayana Gupta [e], A. Daniel Das [f], Ram Subbiah [g,*]

[a] Department of Mechanical Engineering, Vinayaka Mission's Kirupananda Variyar Engineering College, Salem, Tamil Nadu, India
[b] Department of Mechanical Engineering, CVR College of Engineering, Hyderabad, India
[c] Department of Chemical Engineering, Adama Science and Technology University, Adama, Ethiopia
[d] Department of Humanities and Sciences, Gokaraju Rangaraju Institute of Engineering and Technology, Hyderabad, India
[e] Department of Humanities and Sciences, Malla Reddy Engineering College, Hyderabad, India
[f] Department of Mechanical Engineering, Karpagam Academy of Higher Education, Coimbatore, India
[g] Department of Mechanical Engineering, Gokaraju Rangaraju Institute of Engineering and Technology, Hyderabad, India

ARTICLE INFO

Article history:
Available online xxxx

Keywords:
Aluminium
Silicon carbide
Surface morphology
Material properties
Atomic force microscopy

ABSTRACT

In present days, additive manufacturing plays an essential role in manufacturing industries. The powder bed fusion techniques were used to fabricate the silicon carbide based aluminium composite. The synthesized aluminium composite has hardness of 220 BHN, tensile strength of 390 MPa, density of 6.34 g/cc and elongation of 12 %.Laser source is used to provide the heat source and melt the metal powders of aluminium 6063 and silicon carbide. The composition and characterization was analyzed through Energy dispersive X-ray (EDX) and scanning electron microscopy (SEM). The surface morphology was analyzed by atomic force microscopy (AFM). It was concluded that the synthesized aluminium composite has admirable material properties and surface characteristics. Surface with average surface roughness of 37.38 nm was observed from AFM. The average waviness is 35.41 nm.

Selection and peer-review under responsibility of 2nd International Conference on Sustainable Materials, Manufacturing and Renewable Technologies 2022 (i-SMART 2022).

1. Introduction

The quality of the material depends on fabrication methods and composition of alloying elements. The reliable, flexible and reduction of wastage are the salient features of additive manufacturing technique. Aluminium 6063 alloy is used in aerospace, automobile, sports equipments, doors and roofs. The quality characteristics and behavior of the aluminium composite were analyzed. The limitations and processing techniques of additive manufacturing methods were discussed [1]. The powder bed fusion working principle and its advantages were analyzed during fabrication of various materials. The quality of the materials and its characteristics were depends on the shape and size of the powder particles [2]. The working principle and reinforcement characteristics were analyzed in additive manufacturing of different materials [3]. The performance of additive manufacturing and its applications of industrial and automotive sectors were discussed. The material properties and its quality characteristics were enhanced by additive manufacturing process [4].

The morphology and surface characteristics were analyzed in different composites which were fabricated by additive manufacturing process. The observed results were compared to other conventional fabrication techniques [5]. The challenges and recent developments of powder bed fusion method and its industrial applications were studied [6]. Laser and electron beam was the suitable heat source and it's used to melt the materials with controlled temperature. The strengthening of layer formation and its mechanism were depends on the volume fraction of reinforcement to the alloys [7]. Industrial applications and thermo mechanical properties were enhanced due to the addition of silicon carbide particles [8].The effect of reinforcement and its behavior were investigated in aluminium composite. The microstructure behavior and its surface integrity were changed due to the addition of the reinforcement to the base alloy [9]. The quality of the composite and its performance characteristics were varied by different

* Corresponding author.
E-mail address: ramsubbiah20031985@gmail.com (R. Subbiah).

https://doi.org/10.1016/j.matpr.2022.07.249
2214-7853/
Selection and peer-review under responsibility of 2nd International Conference on Sustainable Materials, Manufacturing and Renewable Technologies 2022 (i-SMART 2022).

fabrication techniques and its composition [10–12]. The surface finish and morphology of the composite was depends on the chemical composition of different alloys and reinforcement strength between the different particles [15–17].

The present article is described about the surface analysis of synthesized silicon carbide based aluminium composite. The powder bed fusion technique was utilized to fabricate the composite. The characterization and its composition were analyzed through SEM and EDX. Based on the literature reviews, less concentration was given on additive manufacturing based aluminium composite. The surface investigation of the composite was not done by the researchers.

2. Materials and method

Aluminium 6063 and silicon carbide powders were used to fabricate the composite through additive manufacturing method. The size of the aluminium and silicon carbide powders were100μm and 50 μm respectively. The fine granular aluminium powders were used to produce the excellent surface structure of the material [18]. The other particles such as chromium, magnesium, copper, iron and titanium were added to the aluminium with one weight percentage. Powder bed fusion process was used to develop the aluminium composite and it's shown in Fig. 1. The sample of aluminium composite was shown in Fig. 2.

Powder bed fusion (PBF) plays an essential role in additive manufacturing process and works on the basic principle of material deposition method as well as three dimensional printing technologies. The different parameters such as laser melting, layer thickness, powders size were considered. Laser beam is used to melt the metal powders and make the metal powder in fusion stage [19]. A thin layer of the powder across the build surface was developed by roller. Powder bed fusion process was depending on size of the powders, heat source, layer height and quality of the metal powders [20]. The metal powders of aluminium and silicon carbide were spreaded over the bed and heat source was applied by laser. Due to laser beam, the powders were fused together and form the layer. The quality of the layer was depending on the solidification rate. The quality of surface finish and its performance were enhanced by powder bed fusion technique. The residual stresses and defect of the components were reduced by powder bed fusion method [21]. Tensile and hardness properties were greatly improved by powder bed fusion method of niobium with different melting conditions [22].

Fig. 2. Sample of aluminium composite.

3. Result and discussion

3.1. Characterization of composite

The morphology and material characterization were studied through SEM image and it's shown in Fig. 3. The morphology of the silicon carbide based aluminium composite has developed by powder bed fusion was better than casting process. The silicon carbide particles were strongly reinforced with aluminium alloy [13,14]. The excellent boding strength was developed between aluminium and silicon carbide. It means chemical bond embrace between atoms together in a material. It was confirmed by SEM image. The enlarge view of the silicon carbide were noted like cluster of particles. The matrix structure depends on the reinforcement and layer formation of the composite. The analyses of the material

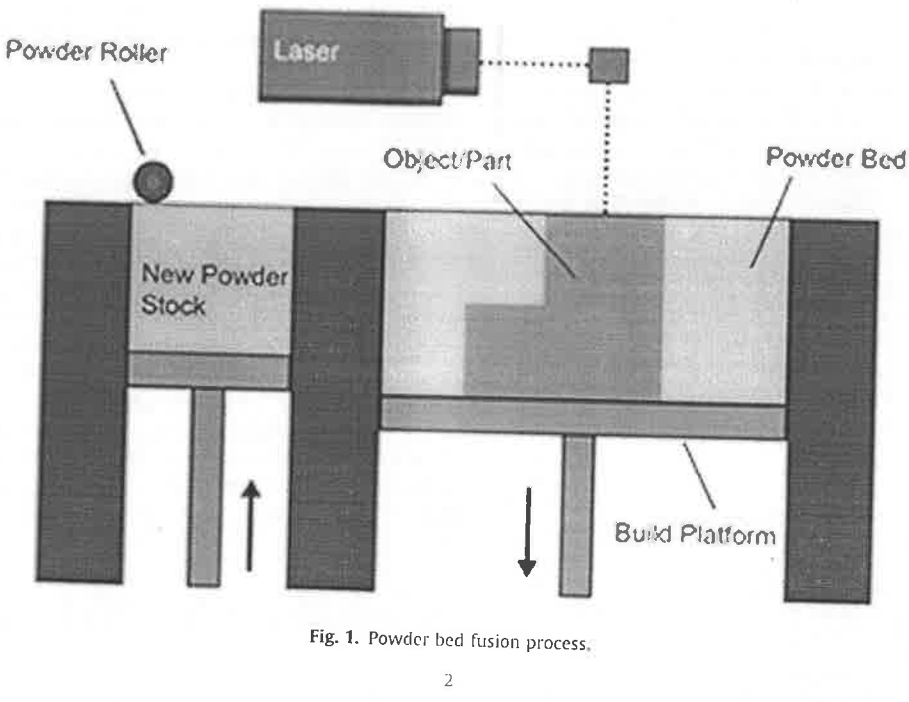

Fig. 1. Powder bed fusion process.

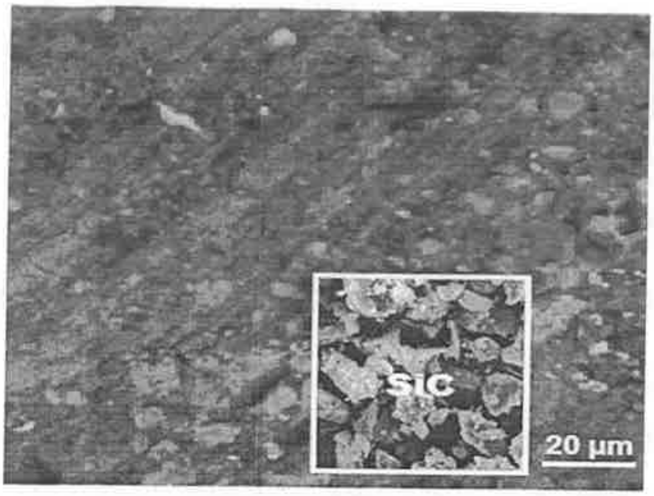

Fig. 3. SEM image of Al-SiC.

composition were validated through EDX and it's shown in the Fig. 4. Brinell hardness testing and universal testing machine was used to evaluate the hardness and tensile strength. Tensile test specimen was prepared as per ASTM E8 standard. Density was evaluated based on the Archimedes principle. The synthesized aluminium composite has the hardness of 220 BHN, tensile strength of 390 MPa, density of 6.34 g/cc and elongation of 12 %.

The alloying elements and its composition were given in the Table 1 based on the EDX analysis. The major elements were aluminium and silicon carbide. The other alloying elements were used to enhance the properties of the composite.

3.2. Surface topography

The surface characteristics of the synthesized aluminium composite were analyzed through atomic force microscopy and it's shown in Fig. 5. It was used to explain surface of the synthesized aluminium composite. It has smooth and less peak surface with silicon carbide particles. The peak valleys was varied and extruded in outer surface of the composite.

The average surface roughness is 37.38 nm observed from AFM. The surface plot of the silicon carbide based aluminium composite was shown in Fig. 6. The maximum height of the roughness is depends on the peak valleys of the surface. It has produced the maximum height of the roughness is 303.3 nm and it has produced

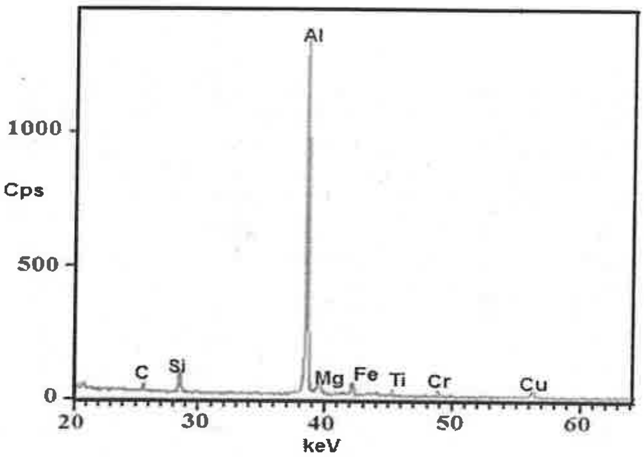

Fig. 4. EDX image of Al-SiC.

Table 1
Alloying elements of Al-SiC composite.

Elements	Wt.%
Al	98.0
Si	1.00
C	0.50
Fe	0.10
Ti	0.10
Mg	0.10
Cr	0.10
Cu	0.10

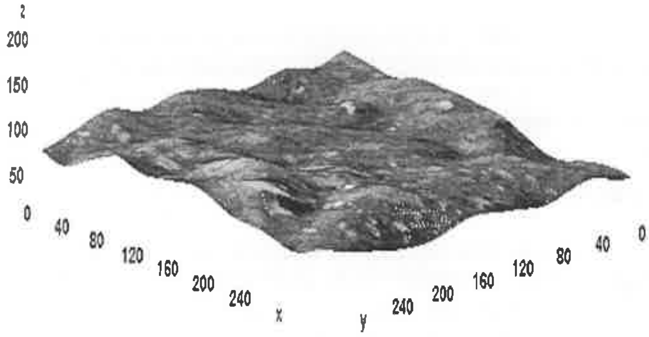

Fig. 5. AFM image of Al-SiC.

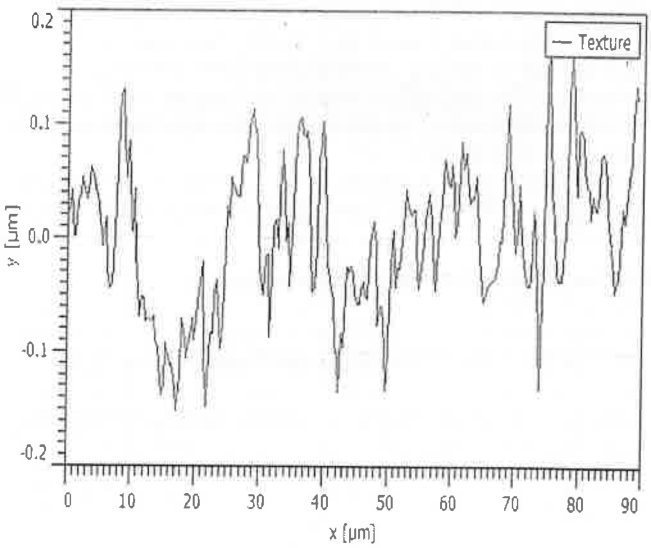

Fig.6. Surface plot of Al-SiC

Fig. 6. Surface plot of Al-SiC.

roughness peak height is 162.3 nm. The average heights of the surface roughness (218.2 nm) were varied. It depends on the composition of the alloying elements and interfacial bonding strength between aluminium and silicon carbide particles. The maximum peak to valley roughness is 303.7 nm. The average waviness is 35.41 nm. The surface analyses of different material were made with various parameters. The surface characteristics of the material were varied due to the alloying elements and fabrication technique [20]. Layer strength and reinforcement strength between the particles were used to enhance the surface characteristics [21]. The surface integrity and the effect of surface topography were analyzed in different materials using atomic force microscopy [22].

Table 2
Parameters of surface roughness.

Sl.no	Surface parameters	Values
1	Roughness average	37.38 nm
2	Root mean square roughness	19.22 nm
3	Maximum height of the roughness	303.3 nm
4	Maximum roughness valley depth	56.34 nm
5	Average maximum height of the roughness	218.2 nm
6	Average maximum roughness valley depth	48.19 nm
7	Average maximum roughness peak height	162.3 nm
8	Average maximum height of the profile	110.2 nm
9	Maximum peak to valley roughness	303.7 nm
10	skewness	0.3179
11	Kurtosis	5.821

The different surface roughness parameters were shown in Table 2. The surface roughness was affected by different ways like height of the roughness, valley depth, peak height, profile variation, valley roughness and waviness.

4. Conclusion

Based on the experimental investigation on surface analysis of synthesized silicon carbide based aluminium composite, the following points were added to the conclusion.

- The powder bed fusion technique was utilized to fabricate the composite. The characterization and its composition were analyzed through SEM and EDX.
- The morphology and surface characteristics were improved by powder bed fusion method and alloying composition.
- The interfacial bonding strength and material properties were enhanced. The synthesized aluminium composite has hardness of 220 BHN, tensile strength of 390 MPa, density of 6.34 g/cc and elongation of 12 %.
- Smooth surface with average surface roughness of 37.38 nm was observed from AFM. The average waviness is 35.41 nm.

CRediT authorship contribution statement

P. Sellamuthu: Conceptualization, Data curation. **P. Srinivas Reddy:** Formal analysis, Funding acquisition. **R. Ramesh:** Investigation, Methodology. **M. Haritha Kiranmai:** Project administration. **CH.LDS. Narayana Gupta:** Resources, Software, Supervision. **A. Daniel Das:** Validation, Visualization. **Ram Subbiah:** Writing – original draft, Writing – review & editing.

Data availability

Data will be made available on request.

Declaration of Competing Interest

The authors declare that they have no known competing financial interests or personal relationships that could have appeared to influence the work reported in this paper.

References

[1] R.J. Griffiths, M.E.J. Perry, J.M. Sietins, J. Mater. Eng. Perform. 28 (2019) 648–656.
[2] W.E. King, A.T. Anderson, R.M. Ferencz, N.E. Hodge, C. Kamath, S.A. Khairallah, A.M. Rubenchik, Appl. Phys. Rev. 2 (2015) 304–310.
[3] M. Dadkhah, M.H. Mosallanejad, L. Iuliano, Acta Metall. Sin. 34 (2021) 1173–1200.
[4] J.E. Spowart, N. Gupta, D. Lehmhus, J. Mater. Sci. 70 (2018) 272–274.
[5] M. Saravana Kumar, E. Mohan, S. Robinson, Silicon 14 (2022) 2695–2706.
[6] Y. Zhang, L. Wu, X.J. Guo, J. Mater. Eng. Perform. 27 (2018) 1–13.
[7] R. Kumar, R.G. Deshpande, B. Gopinath, J. Fail. Anal. Preven. 21 (2021) 525–536.
[8] A. Goyal, N. Yuvaraj, R. Butola, SN Appl. Sci. 2 (2020) 892–900.
[9] P. Garg, A. Jamwal, D. Kumar, K.K. Sadasivuni, C.M. Hussain, P. Gupta, J. Mater. Res. Technol. 8 (2019) 4924–4939.
[10] M. Balasubramanian, B. Stalin, S. Marichamy, K. Anandan, R. Subbiah, Mater. Today Proc. 33 (2020) 4677–4680.
[11] B. Chaitanya Kumar, P. Sri Charan, Kanishkar Jayakumar, D. Alankrutha, G. Sindhu, Ram Subbiah, Mater. Today Proc. 27 (2020) 1541–1544.
[12] T. Lakshmi Deepak, G. Ananda Mithra, K. Lokesh, B. Sai Chandra, R. Subbiah, Mater. Today Proc. 27 (2020) 1681–1684.
[13] K. Manjith Srinivas, S. Bharath, P.N.V. Krishna Chaitanya, M. Pramod, Ram Subbiah, Mater. Today Proc. 27 (2020) 1575–1578.
[14] A. Rohit Sai Krishna, B. Vamshi Krishna, T. Sashank, D. Harshith, Ram Subbiah, Mater. Today Proc. 27 (2020) 1555–1558.
[15] V. Ram Subbiah, G. Vinod Kumar, L. Prasanna, Mater. Today Proc. 26 (2020) 2946–2952.
[16] J. Anix Joel Singh, T. Vishnu Vardhan, J. Vairamuthu, B. Stalin, Ram Subbiah, Mater. Today Proc. 33 (2020) 4893–4896.
[17] L. Girisha, S. Sridhar, L.D. Tadepalli, M. Swetha, Ram Subbiah, S. Marichamy, Mater. Today: Proc. 45 (2020) 2105–2108.
[18] S. Alazov, A. Roberts, L. Wright, Prog. Addit. Manuf. 7 (2022) 289–314.
[19] T. Griemsmann, A. Abel, C. Hoff, Int. J. Adv. Manuf. Technol. 114 (2021) 305–317.
[20] A.G. Temiryazev, V.I. Borisov, S.A.J. Saunin, Synch. Investig. 8 (2014) 708–711.
[21] K.S. Ladutenko, A.V. Ankudinov, V.P. Evtikhiev, Tech. Phys. Lett. 36 (2010) 228–235.
[22] A. Carnini, H.A. Phillips, L.G. Shamrakov, D.T. Cramb, Can. J. Chem. 82 (2004) 113–120.

Materials Today: Proceedings xxx (xxxx) xxx

Contents lists available at ScienceDirect

Materials Today: Proceedings

journal homepage: www.elsevier.com/locate/matpr

Effect of parameters and surface analysis on eglin steel by shot blasting method

P. Srinivas Reddy [a], P. Ravi Kumar [a], D.V.S.S.S.V. Prasad [b], Bh. Saroja Rani [c], CH.LDS. Narayana Gupta [d], A. Daniel Das [e], Ram Subbiah [f,*]

[a] Department of Mechanical Engineering, CVR College of Engineering, Hyderabad, India
[b] Department of Mechanical Engineering, Aditya Engineering College, Surampalem, Andhrapradesh, India
[c] Department of Humanities and Sciences, Gokaraju Rangaraju Institute of Engineering and Technology, Hyderabad, India
[d] Department of Humanities and Sciences, Malla Reddy Engineering College, Hyderabad, India
[e] Department of Mechanical Engineering, Karpagam Academy of Higher Education, Coimbatore, India
[f] Department of Mechanical Engineering, Gokaraju Rangaraju Institute of Engineering and Technology, Hyderabad, India

ARTICLE INFO

Article history:
Available online xxxx

Keywords:
Shot blast
Eglin steel
Surface roughness
Taguchi method
Atomic force microscopy

ABSTRACT

The surface finish is progressively improved by shot blasting method. The present work describes the different factors of shot blasting process of eglin steel and their effect on surface roughness (Ra). The surface roughness were evaluated based on the different input constrains such as blasting angle, standoff distance (SoD) and blasting time. The surface topography of the eglin steel was analyzed before and after the shot blasting process using atomic force microscopy (AFM). The optimal shot blasting parameter is attained through Taguchi method. The effect of parameters on surface roughness and their contribution were validated by analysis of variance. It was concluded that the surface roughness was greatly improved after shot blasting process. The optimal surface roughness was performed at 900 mm of standoff distance, 60 degree of blast angle and blasting time of 50 s. The excellent surface was attained after shot blasting process of eglin steel with average roughness is 14.15 nm.

Selection and peer-review under responsibility of 2nd International Conference on Sustainable Materials, Manufacturing and Renewable Technologies 2022 (i-SMART 2022).

1. Introduction

The surface texture is improved and rust particles are removed by shot blasting method. Shot blasting process is applied in construction, railways, automotive and foundry industries. The surface finish of the eglin steel was enhanced from 44.15 nm to 14.15 nm using shot blasting method. Eglin steel has admirable material properties and its grain structure was used to increase the surface topography. The surface cleaning and enhancement of surface roughness were attained using shot blasting of different steels. The residual stresses and rust particles were completely removed by shot blasting process [1]. The improvement of surface roughness of steel sheet depends on the different input constrains such as shot velocity, flow rate of the steel balls and blasting time [2,3]. The microstructure of the surface and surface quality characteristics were analyzed during shot blasting of stainless steel. The surface properties were improved after shot blasting process [4]. The surface quality mainly depends on the distance between nozzle and work piece. The impact and surface finish of the material was depends on the standoff distance. The smaller standoff distance was made excellent surface finish during shot blasting process [5]. The different shot blasting factors and their effect on surface roughness were investigated in shot blasting of different steel grades [6]. The standoff distance and blast angle was produced the largest effect on surface roughness. The oxide and rust layer was completely removed by high velocity of steel balls [7]. The surface was strengthened by high velocity of steel balls and its impact. The morphology of the material structure was analyzed after shot blasting process [8,9]. The surface roughness experiment of the different materials were evaluated and it's depends on the composition of different alloying elements and metal removal of the different processes [10–14]. Taguchi optimization was used to increase the performance of the process and enhance the quality characteristics of responses. The correlation between input and output constrains were used to analyze the optimal responses and their effect [15–17].

* Corresponding author.
E-mail address: ramsubbiah20031985@gmail.com (R. Subbiah).

https://doi.org/10.1016/j.matpr.2022.07.248
2214-7853/
Selection and peer-review under responsibility of 2nd International Conference on Sustainable Materials, Manufacturing and Renewable Technologies 2022 (i-SMART 2022).

The aim of the paper is to enhance the surface finish of the eglin steel using shot blasting process. The present investigation is deals with the effect of factors on surface roughness using variance analysis and optimization of shot blasting parameters. The surface of the eglin steel was analyzed before and after the shot blasting process using AFM. The surface characteristics were enhanced using shot blasting method. Based on the literature reviews, surface investigation of eglin steel was not done by researchers.

2. Material and method

Eglin steel is a high strength and toughness steel which is consist of different alloying elements such as iron, carbon, manganese, silicon, chromium, molybdenum, tungsten, vanadium, copper and aluminium. The properties of the eglin steel have greatly improved by different composition alloying elements.

The oxide and rust layer were removed by shot blasting process. The blasting wheel plays an essential role in shot blasting machine. It consists of impeller wheel, control cage and spindle. Steel balls were used to clean the surface of materials with high velocity (60–80 m/s) of impact on the work piece. The eglin steel (Size: 100 × 80 × 5mm) was considered as the work piece. The surface roughness depends on the projection velocity and abrasive flow rate of steel balls. Due to rotation of the impeller blade, steel balls were thrown towards the eglin steel with high velocity and impact. The composition of eglin steel was shown in Table 1.

Table 1
Composition of Eglin steel.

Element	Weight %
Carbon (C)	0.16–0.35 %
Manganese (Mn)	0.85 %
Silicon (Si)	1.25 %
Chromium (Cr)	1.50–3.25 %
Nickel (Ni)	5.00 %
Molybdenum (Mo)	0.55 %
Tungsten (W)	0.70–3.25 %
Vanadium (V)	0.05–0.30 %
Copper (Cu)	0.50 %
Phosphorous (P)	0.015 %
Sulfur (S)	0.012 %
Calcium (Ca)	0.02 %
Nitrogen (N)	0.14 %
Aluminum (Al)	0.05 %
Iron (Fe)	Balance

3. Experimental results and discussion

The surface roughness were evaluated by the variation shot blasting input constrains such as standoff distance (300–900 mm), blasting angle (30–60°) and blasting time (50–150 s). The portable perthometer were used to measure the surface roughness of the eglin steel. The maximum range of the surface roughness is 150 μm. The surface roughness is indicated as Ra and expressed in micro meter as shown in Table 2. Eglin steel has medium surface roughness due to high strength and different alloying elements. Shot blasting was used to enhance its surface roughness. Surface roughness was increased with increase of input constraints of the shot blasting process due to metal erosion. The surface modification and material properties of the different alloys were enhanced using shot blasting process [18]. Surface morphology and its characteristics were improved by shot blasting process under different conditions [19].

3.1. Optimization method

The experimental investigation of surface analysis of eglin steel using shot blasting process was planned as per L_9 orthogonal array. Optimal surface roughness was attained through taguchi technique. Surface finish is the important factor in metal and manufacturing process. The smaller the better criterion was chosen to obtain the better rate of surface roughness. Signal to Noise ratio (SN) and means were calculated as per lower the better criterion. The effect of input factors on surface finish has linear relation with the different variables. Response of SN ratio and mean for shot blasting process was shown in Table 3. Based on SN ratio, standoff distance was played an essential role in surface roughness. Rate of metal erosion was increased with increase of standoff distance.

Fig. 1 shows the SN ratio effect for the shot blasting process. The better surfaces were developed when the surface roughness was at minimum level. The optimal surface roughnesses were performed

Table 2
Experimental result for surface roughness using shot blasting method.

S.No	Standoff distance (mm)	Blasting angle (°)	blasting time (Sec)	Ra (μm)
1	300	30	50	2.32
2	300	45	100	2.45
3	300	60	150	2.68
4	600	30	100	3.56
5	600	45	150	3.27
6	600	60	50	3.78
7	900	30	150	4.38
8	900	45	50	4.89
9	900	60	100	4.97

Table 3
Response of SN ratios and mean for shot blasting process.

SN ratios				Means		
Level	Standoff distance	Blasting angle	blasting time	Standoff distance	Blasting angle	blasting time
1	−7.885	−10.389	−10.882	2.483	3.420	3.663
2	−10.957	−10.620	−10.913	3.537	3.537	3.660
3	−13.514	−11.347	−10.561	4.747	3.810	3.443
Delta	5.629	0.957	0.352	2.263	0.390	0.220
Rank	1	2	3	1	2	3

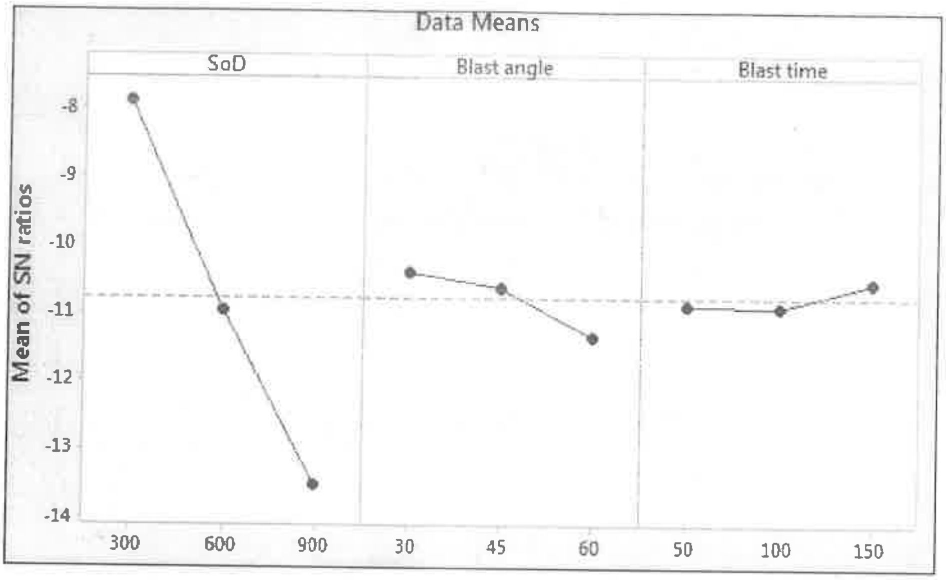

Fig. 1. SN ratio effect for shot blasting process.

Table 4
Variance analysis for shot blasting process.

Basis	DF	SS	MS	F	P	%
SoD	2	7.69629	3.84814	115.87	0.009	95.03
Blast angle	2	0.24042	0.12021	3.62	0.216	02.96
Blast time	2	0.09536	0.04768	1.44	0.411	01.17
Error	2	0.06642	0.03321	–	–	00.84
Total	8	8.09849	–	–	–	100

at 900 mm of standoff distance, 60 degree of blast angle and blasting time of 50 s. The optimal factor level of $A_3B_3C_1$ was preferred for shot blasting of eglin steel. The contribution of each factors on rate of metal removal were shown in Table 4. The effect of SoD, blast angle and blast time are 95.03 %, 2.96 % and 1.17 % respectively. The blasting time was produced the least effect on surface roughness.

3.2. Analysis of shot blasting surface

The surface after the shot blasting process were analyzed by atomic force microscopy and it's shown in Fig. 2. Less amount of peak valleys were observed on the shot blasting surface. The indentation of the steel balls on the surface was observed. The extrusion of the surface was based on the input constrains of the shot blasting surface process. From the AFM results, the average roughness of the surface is 14.15 nm. Maximum height of the roughness is 81.09 nm. Maximum roughness peak height is 74.8 nm. Average of the waviness is 7.15 nm. The surface texture was mainly depends on the standoff distance between the work piece and impact of the steel balls. AFM image for before shot blasting process was shown in Fig. 3. It has more peak valleys and rough surface. From the AFM results, the average roughness of the surface is 44.15 nm.

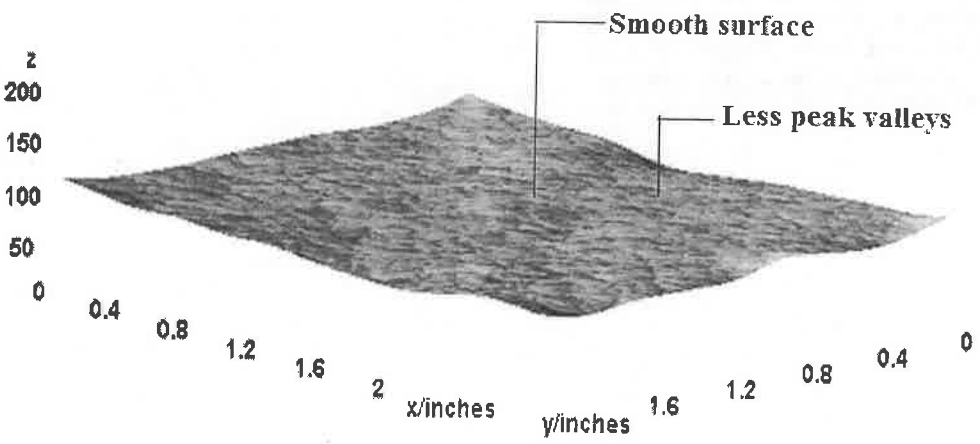

Fig. 2. AFM image for after shot blasting process.

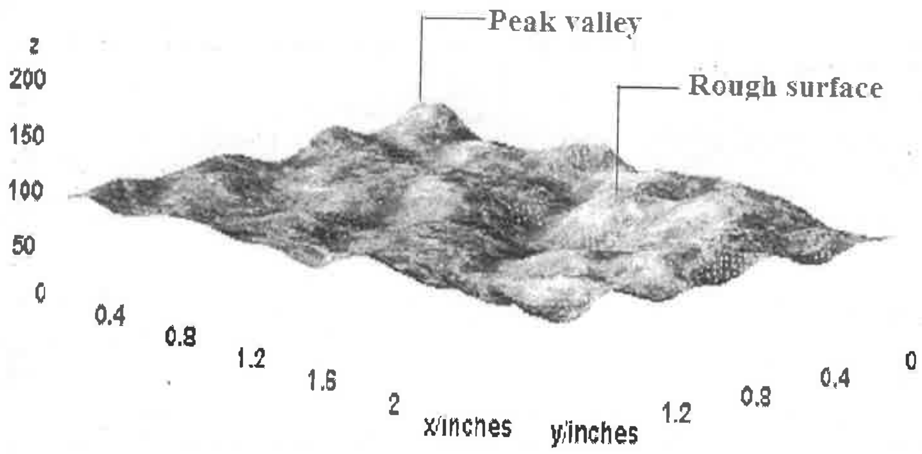

Fig. 3. AFM image for before shot blasting process.

4. Conclusions

The conclusions were drafted based on the experimental investigation of shot blasting parameters and surface analysis on eglin steel.

- The different factors of shot blasting process and their effect on surface roughness (Ra) were analyzed. The surface roughness of the eglin steel was depends on the standoff distance, blast angle and time.
- The optimal surface roughness was performed by taguchi method. It was found at 900 mm of standoff distance, 60 degree of blast angle and blasting time of 50 s.
- The effect of parameters on surface roughness and their contribution was validated by analysis of variance. The effect of SoD, blast angle and blast time are 95.03 %, 2.96 % and 1.17 % respectively.
- The surface characteristics were analyzed in eglin steel before and after the shot blasting process using atomic force microscopy (AFM). The excellent surface was attained after shot blasting process of eglin steel with average roughness is 14.15 nm.
- The surface finish of the eglin steel was enhanced after shot blasting process. The surface finish of the eglin steel was enhanced from 44.15 nm to 14.15 nm using shot blasting method.

CRediT authorship contribution statement

P. Srinivas Reddy: Conceptualization, Data curation. **P. Ravi Kumar:** Formal analysis, Funding acquisition. **D.V.S.S.S.V. Prasad:** Investigation, Methodology. **Bh. Saroja Rani:** . **CH.LDS. Narayana Gupta:** Resources, Software, Supervision. **A. Daniel Das:** Validation, Visualization. **Ram Subbiah:** Writing – original draft, Writing – review & editing.

Data availability

Data will be made available on request.

Declaration of Competing Interest

The authors declare that they have no known competing financial interests or personal relationships that could have appeared to influence the work reported in this paper.

References

[1] A. Malekahmadi, M. Honarpisheh, SN Appl. Sci. 2 (2020) 1593–1600.
[2] N.N. Ogarkov, E.Y. Zvyagina, Y.D. Zaletov, Steel Transl. 46 (2016) 847–850.
[3] F. Nazari, M. Honarpisheh, H. Zhao, Micron 132 (2020) 102–110.
[4] M. Walczak, M. Szala, Archiv. Civ. Mech. Eng. 21 (2021) 157–167.
[5] I. Rösler, Surf. Technol. 11 (2018) 50–60.
[6] N. Vu, A. Phan Chi Chinh, Appl. Mech. Mater. 1 (2017) 52–54.
[7] X. You, Z. Wang, Q. Wang, M. Cao, M. Shen, W. Huang, Metals 7 (2017) 517–527.
[8] B. Gerin, E. Pessarda, F. Morel, C. Verdub, Mater. Sci. Eng., A 686 (2017) 121–133.
[9] J. Yamabe, M.J. Kobayashi, Soc. Mater. Sci. 55 (2017) 301–308.
[10] M. Balasubramanian, B. Stalin, S. Marichamy, K. Anandan, Ram Subbiah, Mater. Today:. Proc. 33 (2020) 4677–4680.
[11] B. Chaitanya Kumar, P. Sri Charan, Kanishkar Jayakumar, D. Alankrutha, G. Sindhu, Ram Subbiah, Mater. Today Proc. 27 (2020) 1541–1544.
[12] T. Lakshmi Deepak, G. Ananda Mithra, K. Lokesh, B. Sai Chandra, R. Subbiah, Mater. Today:. Proc. 27 (2020) 1681–1684.
[13] K. Manjith Srinivas, S. Bharath, P.N.V. Krishna Chaitanya, M. Pramod, Ram Subbiah, Mater. Today Proc. 27 (2020) 1575–1578.
[14] A. Rohit Sai Krishna, B. Vamshi Krishna, T. Sashank, D. Harshith, Ram Subbiah., Mater. Today:. Proc. 27 (2020) 1555–1558.
[15] V. Ram Subbiah, G. Vinod Kumar, L. Prasanna, Mater. Today:. Proc. 26 (2020) 2946–2952.
[16] J. Anix Joel Singh, T. Vishnu Vardhan, J. Vairamuthu, B. Stalin, Ram Subbiah, Mater. Today:. Proc. 33 (2020) 4893–4896.
[17] L. Girisha, S. Sridhar, L.D. Tadepalli, M. Swetha, Ram Subbiah, S. Marichamy, Mater. Today:. Proc. 45 (2020) 2105–2108.
[18] B. Arifvianto, M.M. Suyitno, Int. J. Miner. Metall. Mater. 20 (2013) (2013) 788–795.
[19] H.R. Lashgari, C. Kong, E. Adabifiroozjaei, S. Li, Wear 1 (2020) 456–457.

Measurement: Sensors 24 (2022) 100491

Contents lists available at ScienceDirect

Measurement: Sensors

journal homepage: www.sciencedirect.com/journal/measurement-sensors

Floorplanning for thermal consideration: Slicing with low power on field programmable gate array

Subbulakshmi N [a,*], M. Pradeep [b], Pattem Sampath Kumar [c], Megavath Vijay kumar [d], Rajeswaran N [e]

[a] Department of CSE, IIT Guwahati, Assam, India
[b] Department of ECE, Shri Vishnu Engineering College for Women, Bhimavaram, Andhrapradesh, India
[c] Department of ECE, Malla Reddy Institute of Engineering and Technology, Maisammaguda, Secunderabad, Telangana State, India
[d] Department of Mechanical Engineering, Malla Reddy Engineering College, Maisammaguda, Secunderabad, Telangana State, India
[e] Department of EEE, Malla Reddy Institute of Engineering and Technology, Maisammaguda, Secunderabad, Telangana State, India

ARTICLE INFO

Keywords:
Floorplanning
Placement
Routing
Low power
Thermal based algorithms
Slicing tree graph
FPGA

ABSTRACT

In recent years, semiconductor manufacturers focus mainly on shrinking the size of the transistor in Integrated Circuits (ICs) so as to achieve the proliferation in speed and performance of the system. The RC delay is a negligible factor in the submicron technology when compared to a signal propagation delay, it is treated as a dominant factor which leads to many considerations that concerns the end of device scaling and it has accelerated the exploration for curious solutions beyond the perceived limits of current two Dimension (2D) devices. During the floorplan evaluation, heat aware floorplanning methods usually reflect the peak thermal consideration of wirelength and area. Various thermal prototypes which are used to calculate the temperature effects are used in the estimation of peak temperature in an efficient manner. The floorplanning process involves macro placement, partitioning of design, power planning and output ports placement. Various design parameters such as area, timing, power, slicing and performance are considered during the process of floorplanning. Several methods have been discussed on thermal optimization which includes thermal driven floorplanning, placement and routing in this paper. In this paper, different soft computing techniques and improve the results in all aspects are discussed to reduce the power and area and slicing with graph representations are presented. The floorplanning can be done and placements provide better results in this work when compared to other methods.

1. Introduction

Three-dimensional (3-D) integration that restores a large number of interconnects in 2D structures. In order to address this issue, 3D IC technologies could considerably diminish the interconnect length using multiple device layers arranged in a vertical manner [1]. Consequently, 3-D IC technologies define a comfortable approach to perform the System-on-Chip (SoC) model using incorporating different blocks such as logic circuits, memory devices, and mixed signal, radio frequency (RF), optoelectronic devices etc [2]. Various investigations have been done with the few bench mark circuits and from the results, it has been observed that the reduction in area and power is achieved and in addition, the same has been extended for the multiplier architecture which reports 60% reduction in area and 9% reduction in power. Among the various challenges, the most important that needs great focus is heat dissipation [2].

Power density is translated into heat directly and as a result of this, processors get too hot. The chip temperature has to be maintained below a certain limit and this could be done by the removal of the heat that has been generated by the processor. The cost of removal of heat increases as similar to the increase in power density and the decrease the temperature in the design might diminish the cooling system cost [3]. High temperature in the chip greatly affects its reliability. When the temperature is increased, the reliability of the chip is reduced exponentially. The leakage in the consumed power is estimated and it could be related with dynamic power consumption in the next few processes leakage and temperature are dependent on each other [3]. Consequently, the reduction in temperature could result in less leakage. The increase in power density of digital circuits leads to the dissipation in heat which is considered as a limiting factor in microprocessor design. The thermal

* Corresponding author.
E-mail address: lakshu.125@gmail.com (S. N).

https://doi.org/10.1016/j.measen.2022.100491
Received 22 July 2022; Received in revised form 19 September 2022; Accepted 26 September 2022
Available online 11 October 2022

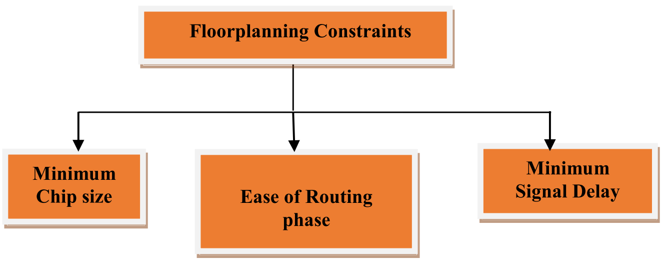

Fig. 1. Floorplanning design constraints.

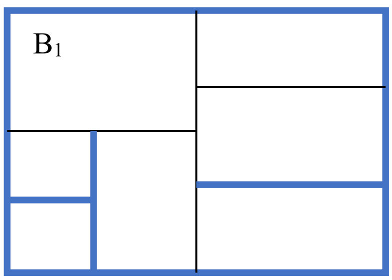

Fig. 2. Floorplanning.

profile of the spot gets increased due to the power dissipation in the IC at a specific place which might lead to the failure of an IC. From many research works, it has been observed that the thermal issues are considered to be the most predominant factor as the temperature is further considered as functions of cost in thermal aware floorplanning systems [4]. A hot block might be placed between cool units and thus it leads to the decrease in temperature due to the spreading of heat. The thermal pairing among most power consuming units might considerably affects thermal allocation in the entire design. These algorithms usually deliberate the maximum temperature when compared to area and wirelength during the floorplan calculation. Various methods that are used to work out the temperature effect are used in the estimation of peak temperature in an efficient manner [4].

The floorplanning process involves macro placement, partitioning of design, power planning and output ports placement. Various design parameters such as area, timing, power and performance are considered during the process of floorplanning. These assessments are computed at each and every step and this calculation depends on the feedback that has been acquired from the implementation team and RTL designers. During the hierarchical designs, iterations get increased as all the blocks are combined at top level at a later stage. In addition to the temperature control, power management also leads to decrease in power density [3]. Power reduction is inactive and in fact conflicts to power thermal manipulation.

Many research works have been done on thermal optimization which includes thermal driven floorplanning, placement and routing. The circuit operations might not be proper even when the complicated thermal-aware approach is done to augment the dissipation of heat. Hence, an algorithm is required for thermal profile-based placement and routing. The thermal profile might be reduced due to the mapping of different blocks with different supply voltage and thus, it leads to the reduction in thermal profile that might lead to the variations in critical path and therefore the conditions are checked to ensure the issues in timing. As a result, the whitespace and the ability to be routed in the architecture are increased.

2. Importance of floor planning

Physical implementation of VLSI circuits is floorplanning. It is defined as a process of insertion of blocks or macros in the chip or core area. This is done so as to identify the routing areas between the blocks. The size of die and creation of wire tracks for assignment of standard cells is decided by the floorplan. In addition, it also produces Power Ground (PG) connections and the I/O pin/pad assignment information has been determined. The floorplanning problem belongs to the NP-Hard problem class. This is due to the simplification of placement problem which is an overview of quadratic assignment problem which is treated as NP-Hard. A floorplan is denoted as 'F' and it is a part of a rectangle that is encircled by parallel and perpendicular line segments into rectangles. The basic block is a rectangle which is not subdivided by any line segment. Design constraints of floorplanning is shown in Fig. 1. The two floorplans of seven basic blocks are depicted in the below Fig. 2. Slicing is important factor in any floorplanning process. The line segments could be moved and the dimensions of the basic blocks could be chosen in order to optimize the layout. The floorplans depicted in the above figure are similar if for every pair of basic blocks, the above-below relation and left-right association of the blocks that are in pair looks the same in both the figures.

A. Slicing Floorplans

A slicing floorplan is symbolized using a rooted binary tree and it is termed as a slicing tree. The slicing tree and the skewed slicing tree of the slicing floorplan is shown in the Fig. 3.

B. Slice Tree Floorplan

A Slicing tree confines the order of the formation of the rectangle in which it has been identified that the division of the rectangle has been taken place recursively to achieve the final floorplan. However there exists multiple scaling tree that matches with the same floorplan which

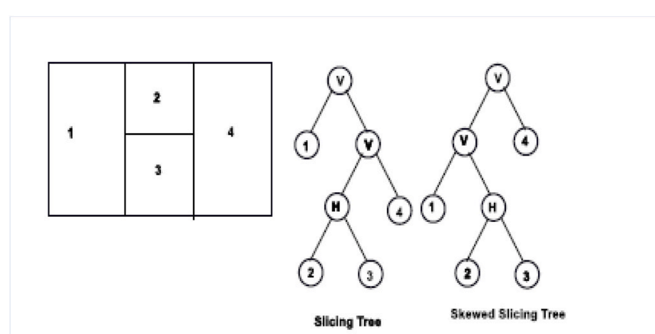

Fig. 4. Slicing tree and the Skewed slicing tree graph.

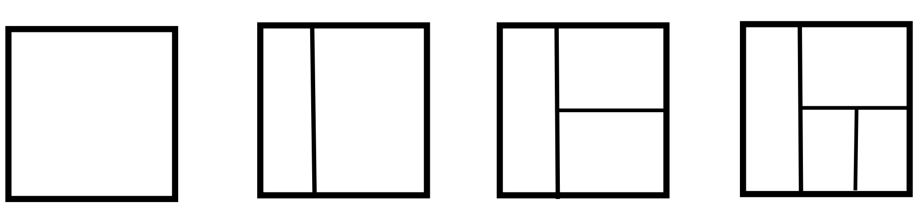

Fig. 3. Slicing Floorplan [1].

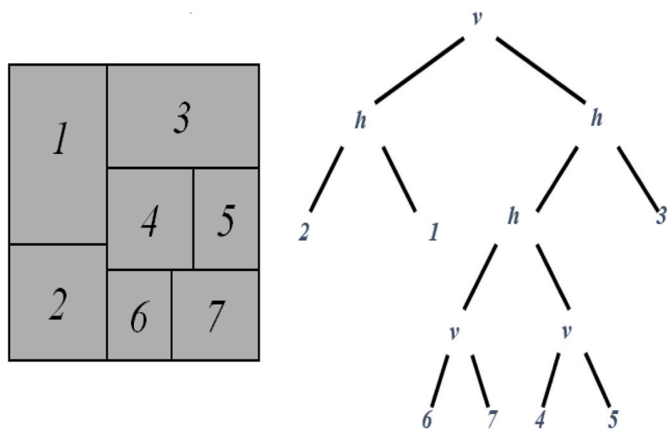

Fig. 5. Graph with horizontal and Vertical floorpalnning

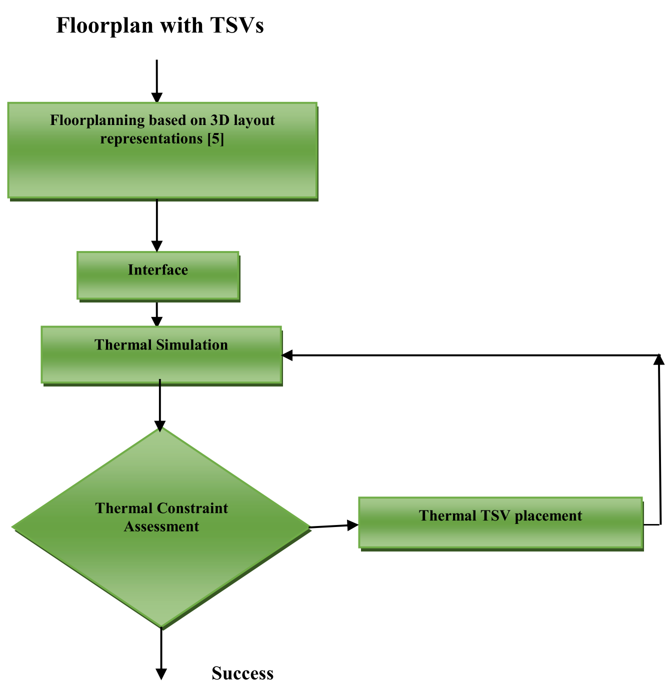

Fig. 6. Dynamic thermal management.

Table 1
Characteristics of floorplanning and placement [13].

Characteristics	Floorplanners	Floorplacers	Placers	Partitioners
Handling net weights	Yes	Yes	No	No
Scalable runtime	No	Yes	Yes	Yes
Scalable wirelength	No	Yes	Yes	N/A
Can handle large modules	Yes	Yes	No	Yes
Handling length bounds	Yes	Yes	Yes	No
Explicit non-overlapping constraints	Yes	Yes	No	No
Routing optimization	N/A	Yes	Yes	No
Can optimize orientation of modules	Yes	Yes	No	No

Table 2
Comparison based on floorplanning methods.

S. No	Floorplanning Type	Algorithm Used
1	Non-slicing is implemented	Hybrid Genetic Algorithm - Memetic Algorithm
2	Non-slicing is implemented	Genetic Algorithm is implemented
3	Non-slicing is implemented	Minimized size Min-Cut floorplacement algorithm
4	Deals with both Slicing and Non-slicing	PSO is implemented
5	Non-slicing is applied	Hybrid Simulated Annealing Algorithm
6	Non-slicing is done in this work.	Iterative POEMS (Prototypes Optimization with Evolved Improvement) algorithm
7	Deals with both Slicing and Non-slicing	Deterministic Lease Flexibility First Algorithm
8	Non-slicing is applied	Variable Order Ant System Optimization
9	Non-slicing is implemented	Hybrid Particle Swarm Optimization
10	Deals with both Slicing and Non-slicing	Hierarchical Congregated Ant Systems
11	Slicing is implemented	Based on Randomized Algorithm
12	Non-slicing is done in this work.	Scaled Log-Sum Exponential (sLSE) wirelength model
13	The author focused on Non-Slicing	Simulated Annealing is done in this work
14	The author worked on Non-Slicing	Dynamic Reduction algorithm is implemented Least Injury First Approach is used.
15	Deals with non-slicing	Implements Linear Programming and Simulated Annealing [9]

is stated in Fig. 4. A sub-class of slicing trees called skewed slicing trees that are fundamentally slicing trees also follows the rules. Floorplans could be categorized into two ways namely hierarchical or nonhierarchical. A hierarchical floorplan is defined as the recursive construction of patterns which are of fixed size for instance a horizontal slice or a vertical slice or a wheel. By default, the slicing floorplans are considered as hierarchical due to the increase in the complexity of circuits.

The properties of the slicing tree are stated as:

- Each internal node is denoted as either 'v' or 'h' which represents the vertical and horizontal slice respectively.
- Each leaf node gets matched to the basic room in the final floorplan
- The sub-tree at the left child of a 'V' node denotes the floorplan restricted in the left half of the room which was cut vertically into two and the sub-tree at the right child of a node represents the floorplan contained in the right half of the room that was cut into two.
- The sub-tree at the left child of a 'H' node denotes the floorplan restricted in the lower half of the room which was cut vertically into two and the sub-tree at the right child of a node represents the floorplan contained in the upper half of the room that was cut into two.

Fig. 5 explains the graph of vertical and horizontal floorplanning for a design. 2 and 1 are divided through horizontal partitioning. Another horizontal partitioning takes place for 3 and 4, 5, 6, 7. Again the second part of divided graph is vertically separated as 4, 5 and 6,7. This splitting mechanism is clearly explained in the floorplan graph. v is vertical partitioning and h is horizontal partitioning.

3D layout demonstrations show more advantages rather than 2D floorplanning methods. The runtime complexity of 3D corner block [5] shows more satisfactory when compared with other designs. The author proposes in order to adapt the developing more interconnects. The proposed approach works out towards the area optimization, wirelength and thermal distribution. Number of dies, and their respective summaries are restricted and thus it is required for manufacturing purposes [6].

Table 3
Advantages and Disadvantages of various algorithms [10].

Algorithm	Advantages	Disadvantages
Non-slicing Floorplan	• An efficient genetic search technique is used • An effective local search algorithm is used • Shows improvement rather than MDA and GA	- Static threshold bias search is used to reduce the performance of the algorithm
Non-slicing Floorplan	• Wirelength and area gets reduced in this approach	- GA takes much time for responding
Non-slicing Floorplan	• Enhanced B* trees are used so as to decrease the whitespace • Scalability and robustness of floorplacement is improved • Time consumption of running time and HPWL is low	- Slicing floorplan is not carried over in this approach - This approach does not consider about the area minimization
Non-slicing Floorplan	• Using this approach, discrete problems are solved. • Works both for slicing and non-slicing	- Performance gets decreased in the multi-objective floorplanning
Non-slicing Floorplan	• Dynamic threshold is used and thus search space is reduced • Improved bias search technique is used in this work • Area minimization over LFF, MA and PSO shows a great improvement	- This approach is not appropriate for slicing FP - Greedy technique might not produce the accurate solution - Parameters such as wirelength, power and other optimization factors are not considered
Non-slicing Floorplan	- Local search space is minimized with the help of GA	- Not feasible for slicing floorplan
Non-slicing Floorplan	- Aspect ratio varies from 1/3 to 3 for slicing floorplan	- The wirelength is not optimized for hard blocks
Non-slicing Floorplan	- The optimal solution is obtained by performing certain operations such as crossover and mutation - Shows better improvement over Hybrid Simulation Annealing	- Execution time is not optimized - Thermal and power optimizations are not considered
Non-slicing Floorplan	• This approach shows progress in reliability, convergence and scalability • Follows a simple bottom-up hierarchical floorplan construction	- The bottom-up approach could not control the white-space and the outline of a circuit - Communication latency is high
Non-slicing Floorplan	• This approach produces a variable aspect ratio • Power consumption is less • Uses MSV-aware floorplan approach	- Execution time is more - Non-slicing floorplan could not be solved in this approach
Non-slicing Floorplan	• Estimation for the interconnection wirelength is done and the method adapted to do this is very simple • Appropriate approximation of HPWL is done	- In this approach considerations were not allowed for parameters such as area, power and thermal optimizations - Not suitable for slicing floorplan
Non-slicing Floorplan	• Regularity constraints to the floorplanning for multicore processors • The area and wirelength is optimized in reasonable amount	- Time complexity of this algorithm is more - Regularity constraints is suitable only for multicore processors - Power and thermal optimizations are not taken into account
Non-slicing Floorplan	• Feasibility, non-inferiority, compactness and compacting algorithm	- Issues regarding the wirelength, power and thermal optimizations are not resolved
Non-slicing Floorplan	• Execution Time is very low • Power and Temperature optimal floorplan could be generated	- Issues regarding Area and Wirelength are not resolved
Non-slicing Floorplan	• Optimization factors such as congestion and interconnect reliability are taken into account	- Optimization of area and power are not included - Area and wirelength is slightly increased.
Non-slicing Floorplan	• Blockages are not handled • Wirelength-optimal floorplan is generated	- Area, power and thermal optimization is not considered - Solutions (N100, pch500, N200, N300, ami49, ami33) is not dealt
Slicing Floorplan	• The area of slicing floorplan could be optimized efficiently with the help of convex optimizer	- This approach does not work for non-slicing floorplan - Various optimization factors such as power, temperature and wirelength are not taken into account

Table 4
Results for AMI33 and AMI 49.

Number of Placement Constraints	Time (sec)	Wirelength 10^6	Type
4	18.0	0.0248	Floorplan Constraints method [24]
8	20.04	0.0252	
12	19.89	0.0252	
16	24.05	0.0252	
20	42.37	1.931	
22	357.39	1.467	
24	374.71	1.448	
2	16.23	0.0221	Proposed Floorplanning method
4	17.91	0.0258	
6	19.88	0.0214	
8	22.12	0.0223	
10	24.20	0.0269	
12	29.28	0.0482	
16	48.11	0.977	
18	223.99	1.280	

3. Classifications of floorplanning

C. Dynamic Thermal Management

Dynamic Thermal Management (DTM) have been designed so as to decrease the packaging cost of microprocessors. In this, there is no need to care about the performance limitations. DTM methods adjust on-chip temperature for high performance microprocessors and the temperature of the chip is monitored during run time. By means of DTM along with a cheap package, since these techniques control the on-chip temperature so as to circumvent the safe temperature. Various DTM techniques have been investigated such as dynamic voltage scaling, fetch throttling, clock gating and dynamic frequency scaling. Fig. 6 states the process of Dynamic thermal management.

Thermal management techniques [7] which propose for solving the issues related to hot spot continues to identify using semiconductor trades. The main objective of this is to maintain the multicore processor under a harmless temperature threshold whereas system is maintained in an efficient manner. Consequently, this method attains the reduction in temperature so as to retain the performance of the processor system. In order to manage the temperature of cores task scheduling is used as an alternative method. The principle of thermal-electrical duality has been employed in the Hotspot. This tool is utilized for various applications [8]. In the layer configuration, vertical layers are identified besides their physical properties.

D. Simulated Annealing and Analytic Formulation

The basic principle behind the simulated annealing-based floorplanning [9] is the illustration of geometric relationship among modules when analytical method deals with the absolute directly. Various methods are normalized polish expression, B-tree and sequence pair

Fig. 7. Alignment of the blocks in (a) horizontally and (b) vertically.

were implemented. Thoughse methods are effective, compatible and efficient in modelling geometric. Many researchers have directed their attention towards various major concerns such as power, temperature and reliability etc. Processor design together with frequency, leakage, cooling cost and performance throttling have been greatly affected by the thermal characteristics.

E. Wirelength-driven floorplanning

The word "data" is plural, Pure block-based designs: The floorplacer involves a modern floorplanner which serves the purpose of handling pure block based designs. This algorithm is able to dense units in a compact, optimization of block orientations are effective. The algorithm implements the concept of floorplanning while the block size is tiny. When block size is high, then first it initiates the process and the fixed-outline floorplanning for individual bins are done [13]. It is shown in the below Fig. 5 that illustrates the block design with 300 that has been placed. Partition that occurs due to the min cut partitioner can be visualized and these results taken from various values [11]. The algorithm proves to be scalable and effective in terms of wirelength minimization in spite of redundant bisection and showed their success of wirelength reduction and annealing floorplanning.

F. Free-shape rectilinear floorplanning

Embedded memories and pre-designed data paths [12] found to have maintained in the shapes of rectangular type. If shape is unknown and only when the area of a module is known and it could be predicted, then in this case there is an option to fix its rectangular shape. These kinds of limitations might be required since the blocks is possible but the interconnect optimization is not possible [13]. In few works, non-rectangular floorplanning has been done and previous works could be categorized based on the decision of the floorplanner. Annealing-based framework has been done in Ref. [13] and on the other hand the work in Ref. [18] resolves by proposed specific floorplanning. Mostly all modules are fixed in rectangle shapes but sometime L-, T- and U- shapes are also established [13]. Mostly rectangular shapes are taken into consideration since it is convenient in many perspectives due to the relative rigidity of fake grids and min-cut placement. Reduction in interconnect might lead to generation of other shapes. This is illustrated in Fig. 3a in which modules are color-coded.

G. Thermal-aware floorplanning with the help of genetic algorithms

Hung et al. proposed the thermal-aware floorplanning with the help of genetic algorithms [14]. In this proposed approach, the peak temperatures had been decreased by merging the area and thermal optimization technique and the provided floorplan had areas comparable with the traditional area-oriented techniques. In Ref. [3], the authors proposed an approach that consists of three features:

- Concentration is made on theoretical and simplified floorplanning where all the blocks have the same size.
- Sum of power numbers of a partial floorplan is used in the place of temperatures. The real temperature difference between different floorplans is calculated using Hotspot software.
- Simulated power numbers for SPEC2000 benchmarks is used instead of randomly generated power numbers
- Evaluation of different floorplans is done with the interconnection model.

Aseem Gupta et al. (2007) investigated various approaches on temperature dependent leakage power-aware floorplanning. The dynamic power block is taken into account to design a leakage-power floorplanner, so as to determine the individual unit temperatures. This in turn is used to predict the leakage power of the SoC. Optimization for power leakage is implemented and it is named as Leakage Aware Floorplanner (LEAF). A few considerations are needed in order to identify placement of blocks in the design. Ehsan K. Ardestani et al. investigated the thermal-aware floorplanning scheme with the aim of improving the performance measures and reliability. Thermal emergencies could be prevented by influencing the lateral heat transfer effects and decreasing the power density [15]. The heat transfer could be done by altering the floorplanning process. Resizing of functional blocks has been done in order to minimize the power density. From the observations, it is understood that the performance is improved by 8.8% and reliability is enhanced by 40% with the cost of area by 3% in the total chip area is obtained. Various thermal analyses have to be performed for 3D ICs in products. To perform a correct analysis 3D in thermal management ICs, an analytical methods for heat spread are needed. Jain Ankur et al. [10] investigated and deployed a finite element and analytical model of heat transfer for stacked 3D ICs. This model has been developed so as to disseminate the temperature for various heat resources. In addition, this model also addressed the issues due to the ICs that is treated as the air thermal resistance [17]. Thermal analysis that includes the structure of BEOL and identifying the location of all power sources in the layout is needed at a huge demand. The thermal outcome of various design iterations must involve thermal analysis and verification has to be done before sign-off.

H. Compact resistive thermal model

A compact resistive thermal model (CBA-T) [18] has been joined with the 3D floorplanning algorithm so as for obtaining better temperature optimization [16]. This algorithm has been simplified as CBA-T Fast to obtain a faster solution for 3D floorplanning. In addition, a hybrid (CBA-T Hybrid) which consists of resistive network and closed-form thermal model has been proposed to achieve a relation quality and run time. Comparison to the non-thermal driven floorplan, the CBA-T algorithm achieves reduction of 56% in maximum on-chip temperature with 9x runtime. The CBA-T fast algorithm shows a reduction on increase on-chip temperature of 40% with 2x runtime when comparison with the non-thermal driven 3D floorplanning. Finally, CBA-T hybrid method shows reduction by 50% with 3X runtime compared with CBA.

I. Multi-objective genetic algorithm

Pradeep Fernando and Srinivas Katkoori (2008) [10] considered a multi-objective genetic algorithm to obtain area and wirelength optimal floorplanning. The non-domination concepts are adapted for allocating the rank solutions. Two crossover operators that generate the floorplans from good sub-floorplans have been utilized by the author. From the comparison results, it is proven that wirelength of 18% and area of 4.6% and for MCNC, a saving of 26% wirelength is achieved.

J. Rectangle Packing Area Minimization Problem

Rectangle Packing Area Minimization Problem (RPAMP) is considered as a finding in the algorithms of VLSI [10] (see Table 1). This Rectangle Packing Problem (RPP) deals with the filling of a larger rectangle with various smaller rectangles. Kun He et al. (2015) solved this problem by proposing an algorithm namely Dynamic Reduction Algorithm (DRA). In this algorithm, the unused spaces have been minimized. In addition, it is altered to a series of incidence in rectangle by locating the range of the bigger shape. To solve RPP, Least Injury First (LIF) algorithm is used. At end result in DRA is proven to be effective and well-competent resolution, since area minimization has been done particularly on superior numbers of rectangular modules. Table 2 shows the comparison based on floorplanning methods and comparison of algorithms implemented along with various representations used in several research works.

4. Results and discussions

This paper focuses on floorplanning algorithms used in various applications. Most of the algorithms try to diminish hardware complexity to improve the system speed. The summary of various floorplanning techniques based on parameters such as type, classification, algorithms, etc. is presented in Table 2. Hence, these considerations paved the way for the devised algorithm used in this work. The main objectives that have been carried over in were.

- A multi-supply voltage islands for reducing the power dissipation has been created
- High heat profile blocks have been allotted at the edges and that are enclosed by cool profile blocks
- Allocation of white space around the hot spots has been done dynamically in order to decrease the heat that has been produced
- The dimensions of the soft blocks have been swapped, rotated and altered that can decrease in the wire length and hotspots in an IC. A review paper is discussed for the hearing aid device [20] and a VLSI design concept can be implemented based on the relevant design.

An efficient genetic search technique is implemented with effective local search algorithm. Floorplanning algorithm for optimal wirelength is implemented. Power and temperature optimal floorplan is generated. Non-slicing is implemented for Genetic algorithms, simulated annealing Dynamic reduction algorithm and Linear programming techniques [9]. Slicing is implemented for Randomized algorithm. Table .3 shows the advantages and disadvantages of various algorithms [16–18]. In order to carry out all the above mentioned features, the proposed algorithm carried out certain distinguished features such as Arrangement of blocks along with edges in the chip reduced the dissipated heat that occurred due to the blocks.

The supply voltage of that block has been reduced and moreover, the high switching activity block has also been identified. This has been tested with multiple blocks and therefore the thermal heat is thus reduced. It is also observed that the thermal profile of the block has been reduced with the help of modifications that has been carried over in the block. Accordingly, the white space allocation resulted in the augmentation and the congestion had been decreased in the routing. Based on those comparisons some of the algorithms are implemented in various placement constraints are stated in the Table 4. Set of Floorplanning bench mark data AMI 33 and AMI 49 are taken as inputs. Fig. 7 shows the alignment of the blocks in horizontally and vertically. Many low power techniques and optimization to achieve suitable implementations have been discussed in Ref. [19]. The Floorplanning with Minimum Wirelength is discussed in Ref. [20].

5. conclusions

In the middle of various parameters, temperature is considered as the most bedrock design since the temperature and the availability of the microprocessor are related directly whereas performance and power relate efficiency. The implementation of thermal management techniques profound a complex process. The ultimate aim is that the low power results in the reduction of temperature. The temperature distribution is measured with the help of temperature aware floorplanning. The floorplanning is found here the predominant factor in the complete design implementation flow. The macro placement has a potent impact on timing and congestion in design flow. In the view of remarked schedules, the determining factor decides a suitable/non-suitable floorplan. The proposed algorithm worked effectively for thermal profile-based placement and routing and different blocks have been mapped with different supply voltage so that the thermal profile has been reduced and this result in critical path variation and the conditions are verified to ensure the timing issues. The routing of the architecture and the whitespace has been increased. Moreover, the design for reducing the power has been synthesized again and the thermal profile equality involved scattering. An efficient algorithm may be proposed based on different soft computing techniques and improve the results in all aspects. Recent days, a number of critical architectures are proposed by different vendors that also may be included in benchmark circuit for testing placement and routing. Still, designing the low power and reduced temperature circuit with floorplanning algorithm is an open issue. The floorplanning can be done and placements provide better results in this paper.

CRediT authorship contribution statement

Subbulakshmi N: Conceptualization, Methodology, Software, Writing – original draft. **M. Pradeep:** Data curation, Writing – review &; editing. **Pattem Sampath Kumar:** Visualization, Investigation. **Megavath Vijay kumar:** Supervision, Writing – review &; editing. **Rajeswaran N:** Software, Resources, Validation.

Declaration of competing interest

The authors declare that they have no known competing financial interests or personal relationships that could have appeared to influence the work reported in this paper.

Data availability

No data was used for the research described in the article.

References

[1] Y.C. Chang, Y.W. Chang, G.M. Wu, S.W. Wu, B -trees: a new representation for nonslicing floorplans, in: Proc. 37th ACM, /IEEE Design Automation Conf., 2000.
[2] Andreas Thor Winther, Wei Liu, Nannarelli Alberto, Vrudhula Sarma, Thermal Aware Floorplanning Incorporating Temperature Dependent Wire Delay Estimation, Microprocessors and Microsystems, 2015.
[3] Puskar Budhathoki, Johann Knechtel, Andreas Henschel, M. Ibrahim Abe, Elfadel. "Integration of thermal anagement and floorplanning based on three-dimensional layout representations, in: 2013 IEEE 20th International Conference on Electronics Circuits and Systems (ICECS), 2013.
[4] Y. Yorozu, M. Hirano, K. Oka, Y. Tagawa, Electron spectroscopy studies on magneto-optical media and plastic substrate interface, in: IEEE Transl. J. Magn. Japan, Vol. 2, Pp. 740-741, August 1987 [Digests 9th Annual Conf. Magnetics Japan, 1982, p. 301.
[5] Zao Liu, Tailong Xu, S.X.-D. Tan, Hai Wang, Dynamic Thermal Management for Multi-Core Microprocessors Considering Transient Thermal Effects", 2013 18th Asia and South Pacific Design Automation Conference, ASP-DAC), 2013.
[6] T. Chen, Floorplanning", Electronic Design Automation, 2009.
[7] J.A. Roy, et al., Min-cut floorplacement, IEEE Trans. Comput. Aided Des. Integrated Circ. Syst. 25 (7) (7/2006) 1313–1326, https://doi.org/10.1109/TCAD.2005.855969.
[8] I.L. Markov, Unification of partitioning, placement and floorplanning, in: IEEE/ACM International Conference on Computer Aided Design 2004 ICCAD-2004 ICCAD-04, 2004.
[9] S. Magdy, Abadir. "LEAF: A System Level Leakage-Aware Floorplanner for SoCs", 2007 Asia and South Pacific Design Automation Conference, 01/2007.
[10] Ehsan K. Ardestani, Enabling power density and thermal-aware floorplanning, in: 2012 28th Annual IEEE Semiconductor Thermal Measurement and Management Symposium (SEMI-THERM), 03/2012.
[11] A. Jain, R.E. Jones, R. Chatterjee, S. Pozder, Analytical and numerical modeling of the thermal performance of three-dimensional integrated circuits, IEEE Trans. Compon. Packag. Technol. 33 (1) (2010) 56–63, https://doi.org/10.1109/TCAPT.2009.2020916.
[12] Zhihong Huang, Thermal modeling and design of 3D integrated circuits, in: 2008 11th Intersociety Conference on Thermal and Thermomechanical Phenomena in Electronic Systems, 05/2008.
[13] J. Cong, Jie Wei, Yan Zhang, A thermal-driven floorplanning algorithm for 3D ICs, in: IEEE/ACM International Conference on Computer Aided Design, 2004. ICCAD-2004, 2004.
[14] Kun He, Pengli Ji, Chumin Li, Dynamic reduction heuristics for the rectangle packing area minimization problem, Eur. J. Oper. Res. 241 (3) (2015) 674–685, https://doi.org/10.1016/j.ejor.2014.09.042.
[15] Xuan Zhang, Survey of Network Security Situation Awareness and Key Technologies, Lecture Notes in Electrical Engineering, 2014.
[16] X. Tang, D.F. Wong, Floorplanning with alignment and performance constraints, Proc. 39th ACM/IEEE Des. Autom. Conf. (2002) 848–853.
[17] F.Y. Young, D.F. Wong, H.H. Yang, Slicing floorplans with boundary constraints, IEEE Trans. Comput. Aided Des. 18 (Sept. 1999) 1385–1389.
[18] F.Y. Evangeline, Chris Young, C.N. Chu, M.L. Ho, Placement Cnstraints in Floorplan Design, IEEE Trans. Very Large Scale Integr. Syst. 12 (7) (JULY 2004).
[19] N. Subbulakshmi, R. Manimegalai, A survey of filter bank algorithms for biomedical applications, Proc. IEEE Int. Conf. Comput. Commun. Inform. (2014) 1–5.
[20] N. Subbulakshmi, R. Manimegalai, MFMW: modified floorplanning with Minimum wirelength, Int. J. Innovative Technol. Explor. Eng. 9 (2019).

Materials Science for Energy Technologies 5 (2022) 155–160

Contents lists available at ScienceDirect

Materials Science for Energy Technologies

journal homepage: www.keaipublishing.com/en/journals/materials-science-for-energy-technologies

One-dimensional numerical simulations of single-cylinder spark ignition engine fuelled H_2O based emulsion fuel, methanol blends, and gasoline conventional

Ufaith Qadiri

Malla Reddy Engineering College, Maisammaguda(H), Gundlapochampally Village,Medchal Mandal, Medchal-Malkajgiri District, Telangana State - Hyderabad 500100, India

ARTICLE INFO

Article history:
Received 17 December 2021
Revised 14 January 2022
Accepted 15 January 2022
Available online 20 January 2022

Keywords:
Avl Boost
Performance
Emissions
Micro-emulsions
combustion

ABSTRACT

In this work, we have used two types of renewable fuels for testing in one-dimensional simulation software and comparing its performance and emission characteristics with 100% Gasoline fuel. For this work, we have used ethanol 20%-H_2O 2%, and gasoline 90% based micro-emulsion fuel and blends of 20% Methanol in 80% Gasoline fuel as an Alternative fuel. This work is done computationally on one-dimensional licensed AVL Boost Simulation Software. The micro-emulsion fuel was prepared in the lab by adding ethanol as co-surfactant and H_2O as an additive in the blended fuel. The other alternative fuel Methanol blended 20% with Gasoline 80% is also used to test the performance and emission characteristics of multi-cylinder Spark Ignition Engine. This is a novel based work done to improve the performance and Emissions of 3- Cylinder Spark Ignition Engine. The performance parameters like power, Torque, BSFC, BMEP, showed better results & emissions like CO, HC, & NOx showed significant decrease as compared to conventional 100% Gasoline fuel. Micro-emulsion fuel were better in emissions particularly NOx, which showed 25% decreases than Methanol fuel. Also showed slightly better power & Torque output by 10% than Methanol blend. Both the renewable fuel were compared with gasoline 100%.

1. Introduction

In this present world of today, most of the researchers are working more and more towards reducing the harmful emissions and trying to meet the stringent emission regulations Euro VII. Presently internal combustion engine has very harmful effects on atmosphere due to severe pollution it creates. Thus, all research is focussed presently on Alternative fuels for reducing the emissions as much as possible. However, the fossil fuel reserves still remains the most demanded conventional fuel. Since the demand of fossil fuel is increasing day by day, so the need is to implement some better options in order to use the fuel in a way so that our demands can also be met with less emissions [1]. The harmful emissions that are coming out from vehicles change the air quality and has adverse effect on human life [2]. The emissions that are coming out from the vehicles are mostly carcinogenic in nature like Carbon monoxide, Hydrocarbon, and Nitrogen oxide emissions. Almost 20% of the Greenhouse gases worldwide are the result of harmful emissions from Petrol and Diesel Engines [3–5].

Consequently having the demand of fossil fuel for transportation sector, many countries support the researchers to work more towards the Alternative fuels in order to reduce the harmful emissions and help in preventing the diminishing of fossil fuel, which are getting depleted at an alarming rate [5]. Since Alternative, fuel has many advantages apart from supplying of energy. The main advantage of fossil fuel is that it helps in reducing the harmful emissions like CO, HC, and NOx [6–8].

Various types of Alternative fuels are in demand presently. However, Ethanol is considered as one of the best possible alternative fuel. Since Ethanol has better physicochemical properties as compared to other, existing fuels [9–12]. In the last many years, the Ethanol Fuel has gained lot of attention, since this fuel has successfully been tested in Spark Ignition Engine and it produces very less emissions when blended properly with gasoline fuel [13]. Many researchers have tested the ethanol fuel in Diesel Engine and Petrol Engine; however, there is some limitations in terms of percentage of ethanol in conventional gasoline engine. The maximum percentage of ethanol in gasoline should not exceed beyond

Peer review under responsibility of KeAi Communications Co., Ltd.

Production and hosting by Elsevier

E-mail addresses: ufaith.qadri@gmail.com, ufaithqadiri@mrec.ac.in

https://doi.org/10.1016/j.mset.2022.01.003
2589-2991/

20% in 80% gasoline engine, otherwise the engine will block and will be damaged, and cannot run further due to corrosive nature of ethanol fuel [14–16]. There are many advantages of ethanol fuel if used in proper percentage, since the ethanol fuel has higher octane no as compared to gasoline fuel that gives more power from the engine. The blended fuel can also tolerate higher pressures, which can prevent Knocking of engine. Most of the research work is based on ethanol/gasoline blended fuel used in spark ignition engine for emission control and improved performance [17–22]. However, very less work has been done on ethanol water based emulsion fuel and Methanol blended Gasoline fuel. Methanol is one of the renewable fuels that can be produced from feedstock, biomass, CO_2 and Hydrogen. Its usage in place of fossil fuels can prevent lot of harmful emissions like SO_2, NOX, and PM Etc. While interest in methanol-powered vehicles has decreased in developed countries, China has recently increased its efforts to promote methanol as a transportation fuel, primarily to reduce its dependence on imported petroleum. A variety of Chinese automakers provide methanol-powered vehicles, including cars, vans, Lorries, and buses that can run on M85 (85% methanol, 15% gasoline) and M100 (pure methanol), as well as methanol/gasoline blends with lower methanol percentages (SGS, 2020). GEM fuels (gasoline, ethanol, and methanol) and flexible-fuel cars (IRENA, 2019a; Olah et al., 2018; Schröder et al., 2020) are also accessible. The cost of these vehicles is comparable to that of regular autos. Blended Methanol successfully reduced the emissions particularly CO, and HC, and reduced NOx emissions too, but slightly lower than micro emulsion fuel. So water based emulsion fuel came into existence which successfully able to reduce harmful emissions particularly NOx [23–29].

This research work will contribute in reducing the harmful emissions that are coming out from the spark ignition engine. The novelty of this work is that micro emulsions fuel have not been tested in Spark Ignition engine in order to commercialize. In India, a lot more work still needs to be done for Methanol blended fuel and emulsion fuel, for reducing the emissions like HC, CO & NOx etc. In this work, the emulsion fuel that is the emerging alternative fuel for using in internal combustion engine can act as reducing emissions particularly NOx emissions. Since H_2O molecule present in the fuel will help in reducing the temperature inside the combustion chamber, which can finally reduce the pollutants.

2. Methodology

The methodology adopted in this contribution is using Alternative fuel micro-emulsion, Methanol Blends, and Conventional Gasoline fuel for checking and comparing the performance and Emission Characteristics of Spark Ignition Engine. This work will be performed computationally on AVL Boost Simulation Software using micro-emulsion fuel, Methanol blends with conventional gasoline fuel will also be checked on AVL Boost, and the performance and emission characteristics will be predicted on single cylinder Spark Ignition Engine. The composition used for micro-emulsion fuel is 90% Gasoline + 8% Ethanol + 2% H_2O and Methanol 10% + Gasoline 90% will also be checked on AVL Boost Software. Both Alternative fuels will be compared with the conventional Gasoline Engine. The performance and its emission characteristics will be predicted for both fuels and comparison will be drawn on results, in order to understand which fuel is more efficient both in terms of Emission characteristics and in terms of Performance.

3. Simulation setup

One-dimensional simulation set up has been implemented in this work. The licenced commercialized software AVL Boost is used in this contribution for predicting the performance and Emission Characteristics of Single cylinder Spark Ignition Engine. All the work has been done on this software for predicting the emissions, combustion, and performance using various Alternative fuels. This one-dimensional simulation software consists of connectors, inlet conditions, air filters, Catalytic Convertors, plenums, Resistances, system boundaries, injectors, and engine. All the parts of the engine are connected through connectors, which are present in the database of the software, and all the parts of the engine components are given some initial conditions and fuel supplied is also changed as per the requirements. The schematic representation of One-dimensional modelling is shown in Fig. 1. The load is varied from 10 to 100% and speed is kept constant at 2000 rpm. This commercialized software has many better options available to predict the performance and emission characteristics by varying various operating parameters like compression ratio, speed, spark timings, etc. This work was performed to find out which Alternative fuel is more efficient both in terms of performance and emission characteristics. Table 1 shows the properties of methanol and micro-emulsions and Table 2 shows the Engine Specifications (Figs. 2 and 3).

The Engine specifications that is used in this work are already mentioned in Table 2, and all those parameters were used for simulating the Single cylinder Spark Ignition Engine. Since this whole work is performed on One- dimensional Simulation software AVL boost, the engine load is varied by making injector of the engine as global parameter and is varied from 10% to 100% (Figs. 4 and 5).

4. Results and discussion

In plot3, the variation is showed between Methanol blends, micro-emulsions, and gasoline 100% fuel. This research showed that conventional 100% gasoline has highest power as compared to other two types of Alternative fuel. It can be seen that almost all the three types of fuel showed almost similar kind of trend that is increasing with increase in load. Since this work is to predict which fuel is more efficient both in terms of performance and emission characteristics. As the conventional gasoline, fuel has highest heating value, which ranges between 44 MJ and 46 MJ as compared to Methanol and Ethanol, which is 23 ML/kg & 29.7Ml/kg, so conventional gasoline fuel is comparatively more in power. The Gasoline fuel showed around 15% more power than Micro-emulsion fuel and around 20% more power than Methanol blend with Gasoline (Figs. 6 and 7).

Since torque is the measure of power output. Therefore, increase in power also increases torque. As the comparison is between micro-emulsion, Methanol Blend, and Conventional 100% gasoline fuel. Here it can be seen that the plot shows increasing trend with increase in load. Therefore, all the blended and emulsion fuel proved to be efficient in terms of Torque output and power. This can be justified with the fact that blended fuel Methanol and micro-emulsions contains gasoline in blended form, which adds to its calorific value, shows almost equal trend with other fuel, and proved to be efficient fuel. Although the slight variations for blended fuel and emulsion fuel is due to the fact that both contains alternative fuels Methanol 20%, and Ethanol 8% which slightly reduces its heating value and resulted in decrease of torque (Figs. 8 and 9).

In plot5, the variation is shown between BMEP and load percentage. This increase in BMEP is due to increase in load. As BMEP is the average pressure present in the engine. As the load increases, the pressure also increases. Since the number of cycles produced per unit, time also increases with increasing Load. This increase in cycles leads to increase in average pressure in the engine. For almost all the fuels, the pressure showed equal trend, but conventional 100% & gasoline fuel showed slightly more BMEP as com-

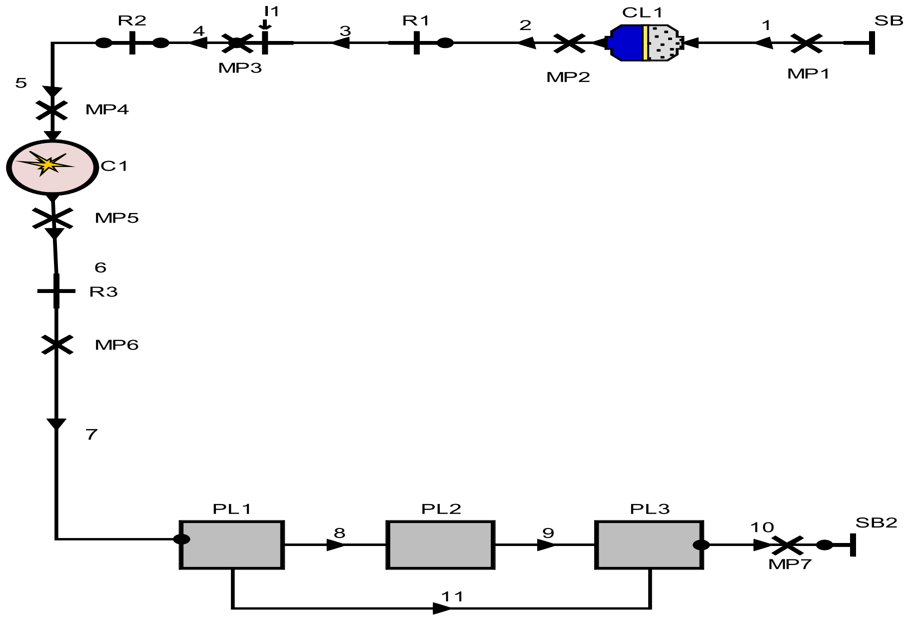

Fig. 1. Shows the schematic representation of One-dimensional AVL Boost Simulation Model.

Table 1
Shows the Properties of Methanol and Gasoline fuel.

Properties	Methanol	Gasoline
Chemical Formula	CH_3OH	C_8H_{18}
Stoichiometric Air/Fuel ratio	6.5	14.7
Auto Ignition Temperature C	500	300
Boiling Point C	65	25–215
Density kg/m3	0.794	0.742
Lower heating value MJ/kg	20.26	2.82
Research Octane No	110	90

Table 2
Shows the Description of Engine Test Rig.

Criteria	Description
Manufacturer	Briggs and Stratton
category	Air cooled 4 S
Stroke & Bore	61.91 mm to 64.09 mm
Compression ratio	9
Cooling System	Air Cooled
Horse Power	6.5
Displacement	206 cc
Ignition System	Magnetron Electronic

pared to blended methanol, and micro-emulsion fuel. This can be attributed to the fact that conventional gasoline fuel produce more power that leads to increase in its operating cycles which leads to the increase of BMEP (Fig. 10).

In plot 6 the variation of BSFC with load can be seen for blended Methanol, micro-emulsion, and Gasoline 100% fuel. The BSFC plot shows the variation for three types of fuels. In this plot, all the three types of fuels show equal type of trend for all the three fuels. For 100% gasoline, fuel at the starting load the 100% gasoline shows highest BSFC value and for other two fuels equal value of decreasing trend is shown too. This plot explains how with increase in load the BSFC value also decreases. This is due to reason that with increase in load the Air/Fuel mixture turns more towards the stoichiometric and leaner side results in decrease of fuel consumption. For all the types of fuels, the fuel consumption shows very good BSFC results. However, for micro-emulsion fuel, the BSFC resulted in much lower BSFC consumption, and proved to be the most efficient fuel in terms of consumption of Fuel. The possible reason for this decrease in BSFC is that micro-emulsion fuel contains more quantity of Gasoline fuel as compared to blended Ethanol fuel, which increases its Calorific Value resulted in less consumption of fuel for same loading conditions.

4.1. Emissions

In plot 7, the variation is shown for CO emissions with varying percentage load. The three types of fuel have been compared for carbon monoxide emissions with varying loads. In this plot, it can be seen that carbon monoxide emission showed almost equal kind of trend for all the three types of fuel. The highest fuel consumption is shown for conventional Gasoline fuel followed by blended Methanol, and Micro-emulsion fuel. The possible reason for this decrease in carbon monoxide emission is that emulsion fuel contains H_2O molecule that increases the oxygen supply in the combustion chamber results in oxidation of fuel and decreases the carbon monoxide emissions. Apart from decreasing the carbon monoxide emissions at lower loads, it can be further seen that at higher loads the carbon monoxide emissions increases, this is due to the reason that at higher loads the fuel mixture is getting less time for complete combustion of fuel because of more number of cycles operating per second which decreases time for complete oxidation of fuel molecule.

In Plot 8, the variation is shown between Hydrocarbon emissions and varying loads. In the Hydrocarbon plot, all types of fuels that are under investigation showed similar kind of trend. With increase in load, the blended 20% Methanol fuel showed improvement in Hydrocarbon emission as compared to conventional 100% gasoline fuel. However, water based emulsion fuel proved to be the most efficient fuel in terms of reduction in Hydrocarbon emissions. The possible reason for this decrease in hydrocarbon emission is that emulsion fuel contains H_2O that acts as an additive in fuel by promoting full combustion of fuel and thereby decreasing the emissions. Since hydrocarbon emission, mostly occur due to fuel, remain unburnt, goes through the crevices, and causes incomplete combustion results in more hydrocarbon emissions. Also with increase in load, the air/fuel mixture turns more towards the leaner side that increases the oxygen supply in the engine results in complete combustion of fuel and gives less hydrocarbon emissions.

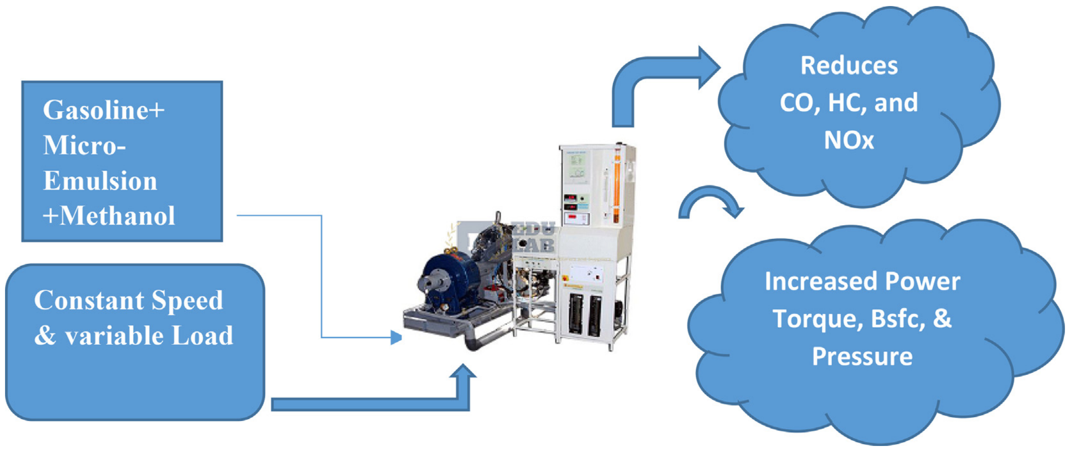

Fig. 2. Shows the schematic description of Alternative fuel blends to improve Emissions and Performance.

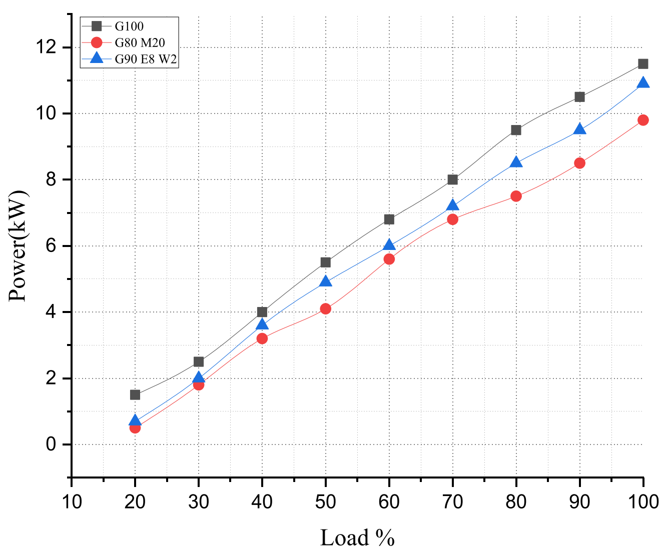

Fig. 3. Shows the variation of Power with load percentage for Gasoline 100 %, Methanol 20% blend & Micro-emulsion fuel.

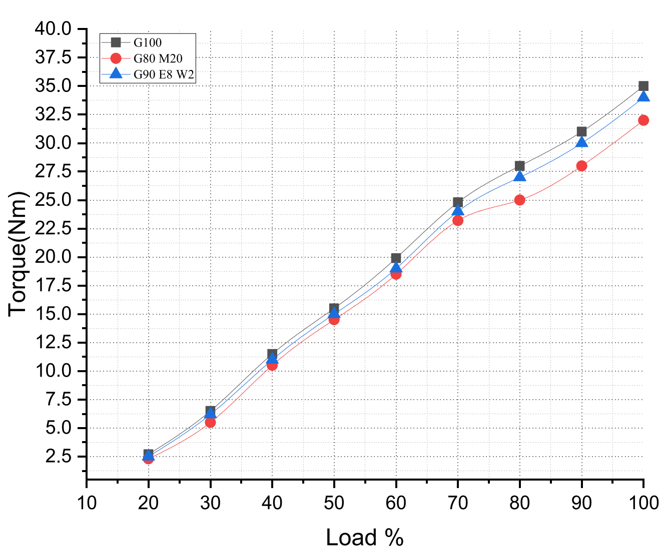

Fig. 4. Shows the variation of Torque with load percentage for Gasoline 100 %, Methanol 20% blend & Micro-emulsion fuel.

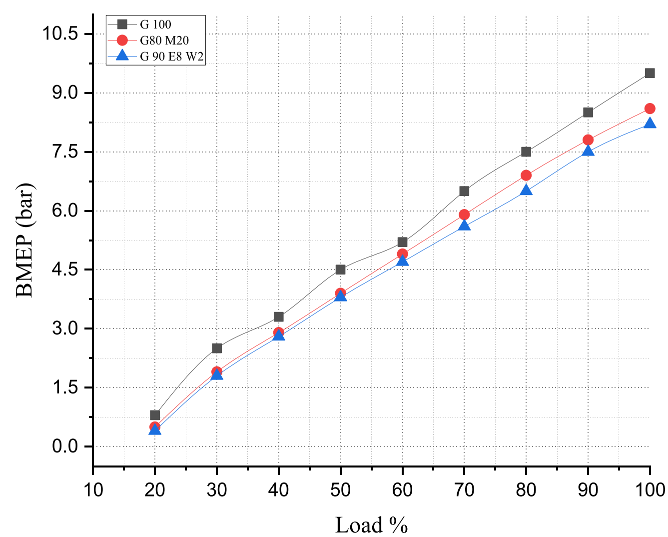

Fig. 5. Shows the variation of BMEP with load percentage for Gasoline 100 %, Methanol 20% blend & Micro-emulsion fuel.

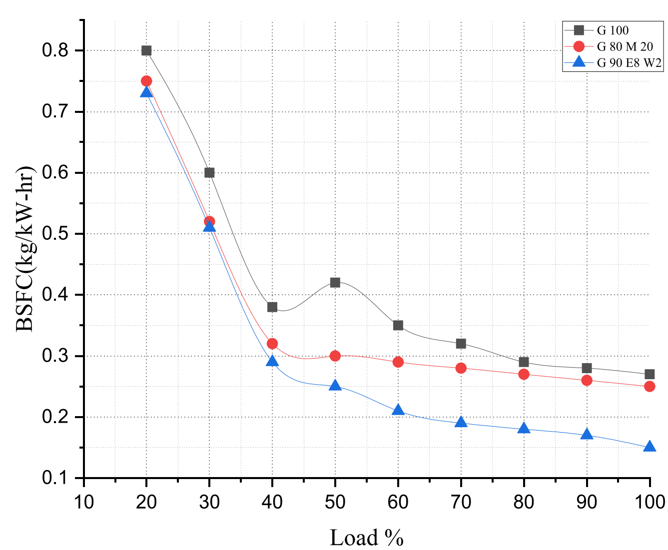

Fig. 6. Shows the variation of BSFC with load percentage for Gasoline 100 %, Methanol 20% blend & Micro-emulsion fuel.

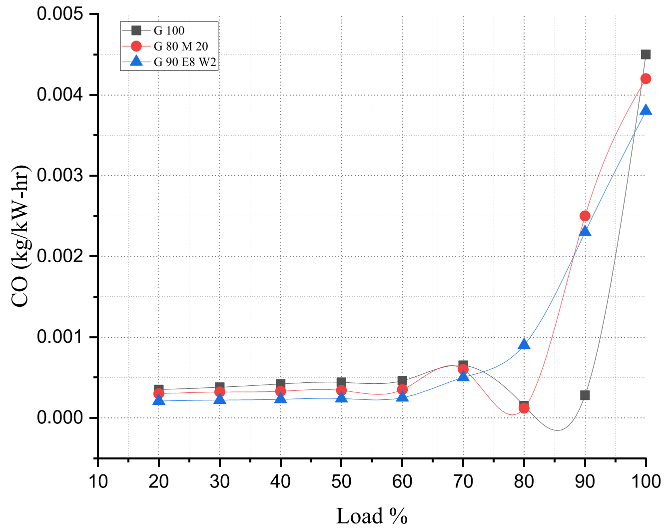

Fig. 7. Shows the variation of CO with load percentage for Gasoline 100 %, Methanol 20% blend & Micro-emulsion fuel.

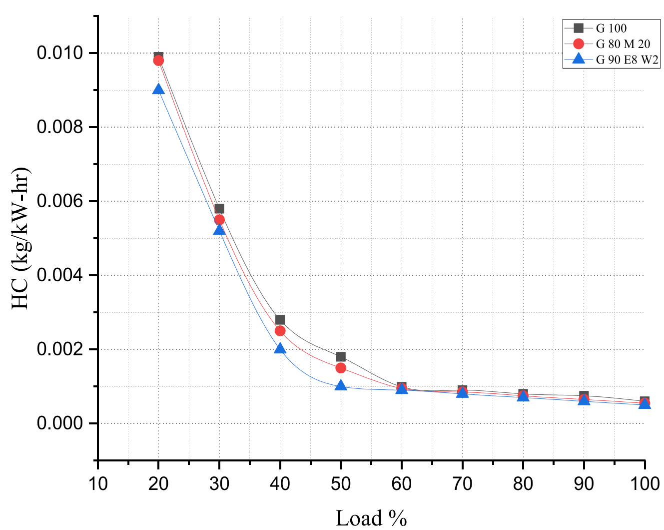

Fig. 8. Shows the variation of HC with load percentage for Gasoline 100 %, Methanol 20% blend & Micro-emulsion fuel.

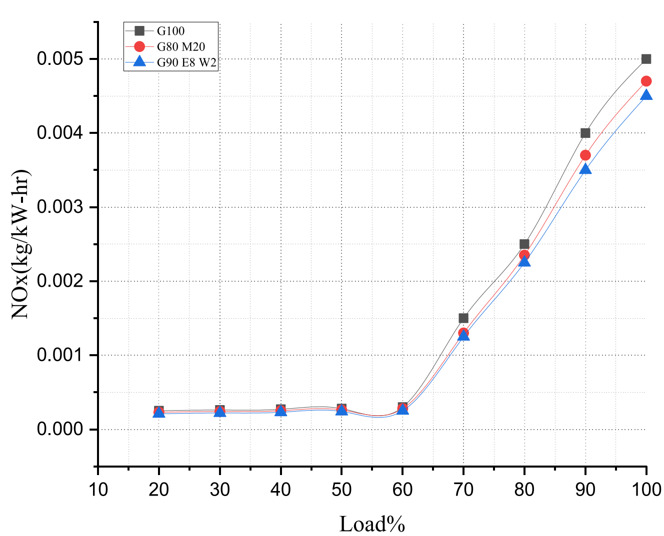

Fig. 9. Shows the variation of NOx with load percentage for Gasoline 100 %, Methanol 20% blend & Micro-emulsion fuel.

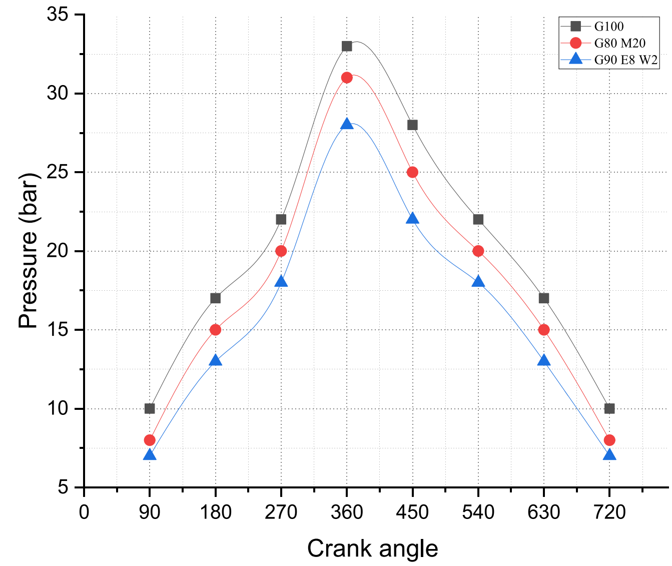

Fig. 10. Shows the variation of Pressure with load percentage for Gasoline 100 %, Methanol 20% blend & Micro-emulsion fuel.

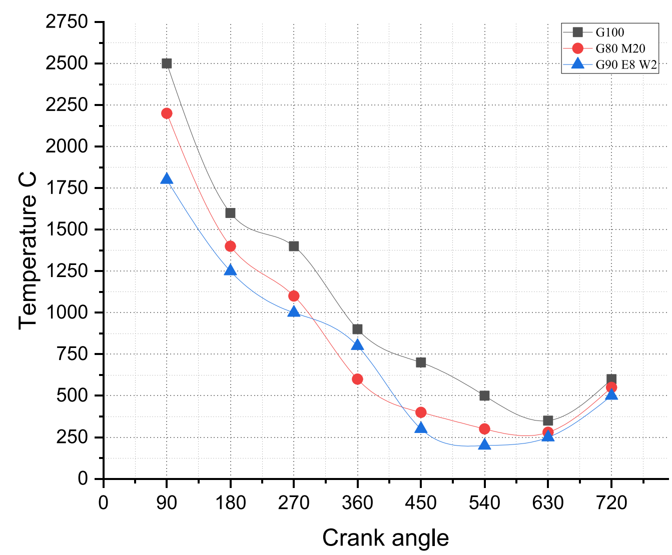

Fig. 11. Shows the variation of Temperature with load percentage for Gasoline 100 %, Methanol 20% blend & Micro-emulsion fuel.

In plot 9, NOx emissions has been predicted with varying loads. It can be seen that with increase in load the NOx emissions also start increasing. In addition, at lower loads, the NOx emissions showed fewer emissions and remained constant until the mixture turns more towards the stoichiometric and leaner side of the mixture. The possible reason for this decrease in NOx emissions at lower loads is due to the fact that at lower loads the temperature of the combustion chamber is less as compared at higher loads, which showed more NOx emissions because at higher loads the temperature inside the combustion chamber increases, because of more air supply and Nitrogen of air do not completely burn and remain unburnt that converts into NOx emissions. For emulsion, fuel the NOx emissions showed lower value of 25% less as compared to blended Methanol fuel and Conventional Gasoline fuel. This is due to the reason that emulsion fuel contains water molecule that lower the temperature of the combustion chamber results in lower value of NOx and proved to be the most efficient fuel.

In plot 10, the pressure variations can be seen with crank angle. The pressure of the combustion chamber shows increase with variation in crank angle. For conventional Gasoline fuel, the peak pressure is highest, followed by blended Methanol fuel, and micro-emulsions. The possible decrease of pressure for emulsion fuel is because emulsion fuel has slightly lower calorific value as compared to blended methanol and Conventional gasoline. So it lacks in showing more pressure inside the combustion chamber. For 100% gasoline fuel the peak pressure shows tremendous increase, which shows the capability of the fuel as high power.

The variation of pressure with varying crank angle is shown in Fig. 11. The temperature of all types of fuel start showing decreasing trend with crank angle variations. The temperature at the beginning is more. Since at the the start of the combustion the mixture is rich and due to lack of the air supply the air/fuel mixture does not burn completely and increases the temperature inside the combustion chamber which results in more temperature at the beginning, and when the mixture turns more towards the leaner side, complete combustion takes place, that reduces the temperature of the combustion chamber and the temperature level also decreases with crank angle variations.

4.2. Conclusions

In this contribution, various Alternative fuel blends have been compared with the 100% Gasoline fuel.

Following conclusions can be drawn from the above research contributions.

- Blended Methanol 20% with 80% Gasoline fuel has been used for performance evaluation and emission check on AVL Boost.
- Water based emulsion fuel that contains the composition of gasoline 90%, ethanol 8%, and H_2O 2% has been compared with 100% Gasoline fuel.
- Both Blended Methanol 20%, and emulsion fuel proved efficient fuel in terms of emission characteristics and performance.
- For Blended Methanol fuel with gasoline the emissions CO, HC, and NOx shows reduced value as compared to conventional 100% Gasoline fuel.
- Similarly, when water based emulsion fuel was compared with 100% gasoline fuel it proved to be the most efficient fuel in terms of both emission characteristics and performance.
- The emulsion fuel showed 10% lower value of CO emissions as compared to gasoline 100%.Also for HC and NOx emissions the NOx emissions also showed very much decrease. Therefore, the conclusions can be drawn that both Alternative Blended fuel, are efficient when performance and emission characteristics were compared with gasoline fuel.

Declaration of Competing Interest

The authors declare that they have no known competing financial interests or personal relationships that could have appeared to influence the work reported in this paper.

Acknowledgements

This work has been performed in Malla Reddy Engineering College Hyderabad. We are very thankful for providing the research environment to conduct this research work in your organization. We are also thankful to the co-authors of this paper who worked very hard for getting this work done in time limit.

References

[1] R. Saidur, E.A. Abdelaziz, A. Demirbas, M.S. Hossain, S. Mekhilef, A review on biomass as a fuel for boilers, Renew. Sustain. Energy Rev. 15 (5) (2011) 2262–2289.
[2] S.E. Hosseini, M.A. Wahid, Feasibility study of biogas production and utilization as a source of renewable energy in Malaysia, Renew. Sustain. Energy Rev. 19 (2013) 454–462.
[3] A. Liaquat, A. Kalam, H. Masjuki, M. Jayed, Potential emissions reduction in road transport sector using biofuel in developing countries, Atmos. Environ. 44 (2010) 3869–3877.
[4] P. Iodice, A. Senatore, G. Langella, A. Amoresano, Effect of ethanol-gasoline blends on CO and HC emissions in last generation si engines within the cold-start transient: An experimental investigation, Appl. Energy 179 (2016) 182–190.
[5] B.R. Kumar, S. Saravanan, Use of higher alcohol biofuels in diesel engines: A review, Renew. Sustain. Energy Rev. 60 (2016) 84–115.
[6] M. Mofijur, M.G. Rasul, J. Hyde, A.K. Azad, R. Mamat, M.M.K. Bhuiy, Role of biofuel and their binary (diesel-biodiesel) and ternary (ethanol-biodiesel-diesel) blends on internal combustion engines emission reduction, Renew. Sustain. Energy Rev. 53 (2016) 265–278.
[7] O. Awad, O. Ali, R. Mamat, A. Abdullah, G. Najafi, M.K. Kamarulzaman, I. Yusri, M. Noor, Using fusel oil as a blend in gasoline to improve SI engine efficiencies: A comprehensive review, Renew. Sustain. Energy Rev. 69 (2017) 1232–1242.
[8] Available online: https://www.thecropsite.com/articles/1781/biofuel-production-greater-shares-of-commodities-used/ (accessed on 20 March 2021).
[9] O.I. Awad, R. Mamat, T.K. Ibrahim, A.T. Hammid, I. Yusri, M.A. Hamidi, A.M. Humada, A. Yusop, Overview of the oxygenated fuels in spark ignition engine: Environmental and performance, Renew. Sustain. Energy Rev. 91 (2018) 394–408.
[10] P. Geng, E. Cao, Q. Tan, L. Wei, Effects of alternative fuels on the combustion characteristics and emission products from diesel engines: A review, Renew. Sustain. Energy Rev. 71 (2017) 523–534.
[11] S.T. Leong, S. Muttamara, P. Laortanakul, Applicability of gasoline containing ethanol as Thailand's alternative fuel to curb toxic VOC pollutants from automobile emission, Atmos. Environ. 36 (2002) 3495–3503.
[12] C. Flavin, J.L. Sawin, L. Mastny, M. Aeck, S. Hunt, A. Mac Evitt, P. Stair, J. Podesta, A. Cohen, B. Hendricks, American Energy: The Renewable Path to Energy Security; World watch Institute & the Center for American Progress: Washington, DC, USA, 2006.
[13] P. Iodice, A. Senatore, G. Langella, A. Amoresano, Advantages of ethanol-gasoline blends as fuel substitute for last generation SI engines, Environ. Prog. Sustain. Energy 36 (2017) 1173–1179.
[14] I. Coordinating, Intermediate-Level Ethanol Blends Engine Durability Study; Research Council: Alpharetta, GA, USA, 2012.
[15] Tester, F. Gas-Caused (E10) Engine Damage and Performance Issues. Available online: http://www.fuel-testers.com/list_e10_engine_damage.html (accessed on 25 September 2020). Energies 2021, 14, 4034 16 of 18
[16] P. Wróblewski, A. Iskra, Problems of Reducing Friction Losses of a Piston-Ring-Cylinder Configuration in a Combustion Piston Engine with an Increased Isochoric Pressure Gain, SAE Tech, Pap, 2020.
[17] J. Chong, A. Tsolakis, S. Gill, K. Theinnoi, S. Golunski, Enhancing the NO2/NOx ratio in compression ignition engines by hydrogen and reformate combustion, for improved after treatment performance, Int. J. Hydrog. Energy 35 (2010) 8723–8732.
[18] S. Shahir, H. Masjuki, A. Kalam, A. Imran, A. Ashraful, Performance and emission assessment of diesel–biodiesel–ethanol/bioethanol blend as a fuel in diesel engines: A review, Renew. Sustain. Energy Rev. 48 (2015) 62–78.
[19] B. Masum, H. Masjuki, A. Kalam, I.R. Fattah, S. Palash, M. Abedin, Effect of ethanol–gasoline blend on NOx emission in SI engine, Renew. Sustain. Energy Rev. 24 (2013) 209–222.
[20] A. Ganguly, P. Chatterjee, A. Dey, Studies on ethanol production from water hyacinth—A review, Renew. Sustain. Energy Rev. 16 (2012) 966–972.
[21] EthanolFeedstocks.Availableonline:http://www.afdc.energy.gov/fuels/ethanol_feedstocks.htm (accessed on 1 October 2015).
[22] I.M. Rizwanul Fattah, H.H. Masjuki, A.M. Liaquat, R. Ramli, M.A. Kalam, V.N. Riazuddin, Impact of various biodiesel fuels obtained from edible and non-edible oils on engine exhaust gas and noise emissions, Renew. Sustain. Energy Rev. 18 (2013) 552–567.
[23] Krishan Kumar, Studies on simulation of fuel Injection, Combustion and Gas Exchange Process in a Diesel Engine", Ph.D thesis, IIT Delhi.
[24] Krieger, R.B., Borman, G.L., The Computation of Apparent Heat Release for Internal Combustion Engines, ASME Paper66-WA/DG-4.
[25] karim,G.A and wierzba,I., "Comparative studies of methane and propane as Fuels for Spark Ignition and Compression Ignition engines," SAE 831196.
[26] Mathur,H.B, babu, M.K.G., Prasad,Y.N and Ved Singh, Evaluation of the performance and Emission Characteristics of a Bio-gas operated Diesel Engine,7th National Conference on I.C Engines and Combustion,R.E.C Surathkal, Karnataka, India.
[27] S. Verhelst, C.G.W. Sheppard, 3-zone thermodynamic modelling of spark-ignition engine combustion - An overview, Energy Convers. Manag. 50 (5) (2009) 1326–1335, https://doi.org/10.1016/j.enconman.2009.01.002.
[28] Francesco Duronio, Angelo De Vita, Alessandro Montanaro, Carlo Villante, Gasoline direct injection engines – A review of latest technologies and trends. Part 2, Fuel, Volume 265, 2020, 116947, ISSN 0016-2361, https://doi.org/10.1016/j.fuel.2019.116947.
[29] Y. Zhou, D. Yin, D. Wang, C. Zhang, Z. Yang, Experiment investigation of microemulsion enhanced oil recovery in low permeability reservoir, J. Mater. Res. Technol. 9 (4) (2020) 8306–8313.

ISSN: 0974-5823 Vol. 7 No. 6 June, 2022

International Journal of Mechanical Engineering

A Study on Tribological Properties of different Nanoparticles as additives in various Lubricants

Sri Deepthi Immaneni[a*], M. V. Varalakshmi[b], B. Saritha[c]

[a,c] Assistant professor, Department of Mechanical Engineering, Malla Reddy Engineering College (Autonomous), Hyderabad, Telangana

[b] Associate professor, Department of Mechanical Engineering, Malla Reddy Engineering College (Autonomous), Hyderabad, Telangana

Abstract:

This article deals on the prose review of the nanoparticles mixed with different base oils. The synthesis of few of the nanoparticels and its effect on friction and wear has been analyzed. It is been studied that the optimum concentration of the nanparticels in the base oils has given significant improvement in the friction co-efficient, scar diameter and the increasing life of rubbing components. The tribological behavior of different nanoparticles with different lubricants were reviewed,also,the review of tribological properties of WS_2 Nanorods, rare earth (REN) and $ZnAl_2O_4$ nanoparticles in base oils has been presented.

Keywords: WS_2 Nano rods, four ball tester, SEM, tribological properties.

1. Introduction

In industries, the mating mechanical components which work under high pressure, increases the temperature on the surfaces, to reduce this it requires lubrication. The increase in the temperature increases the wear between the mating surfaces which results in the failure of the components [33]. To minimize this failure traditional lubrication plays a chief in industries. In order to improve the life of these lubricants, additives like nanoparticles are used.

The addition of nanoparticles as additives to the base oil has reduced the friction and wear of the mating parts [34]. The nanoparticles of (1 to 100nm) based on the synthesis has shown considerable improvement [35]. The tribological properties of any components changes with the shape like spherical, cubic, nanotube, nanorods .etc..,Significant efforts have been directed for synthesis of nanoparticles by various methods like friction reduction, self reduction, hydrothermal..etc., the addition of some nanoparticles in base oil had not given good tribological properties due to its improper dispersion. To overcome this, additions of agents have been introduced for better results.

The concentration of nanoparticles as oil additives should also be considered for optimum results [38]. The tribological properties can be examined by performing test on various equipments like four ball testers, ball on disc, pin on disc, disc on disc etc., there are several factors that affect the tribological properties of the mating components.

2. Overview of Lubricants:

Lubrication is the traditional method to decrease the wear and friction between the rolling and sliding contact [39]. This develops a thin protective film between the contact surfaces. Flash point, pour point, viscosity index oxidization resistance and thermal stability are some of the factors that affect the lubrication performance [1-4].

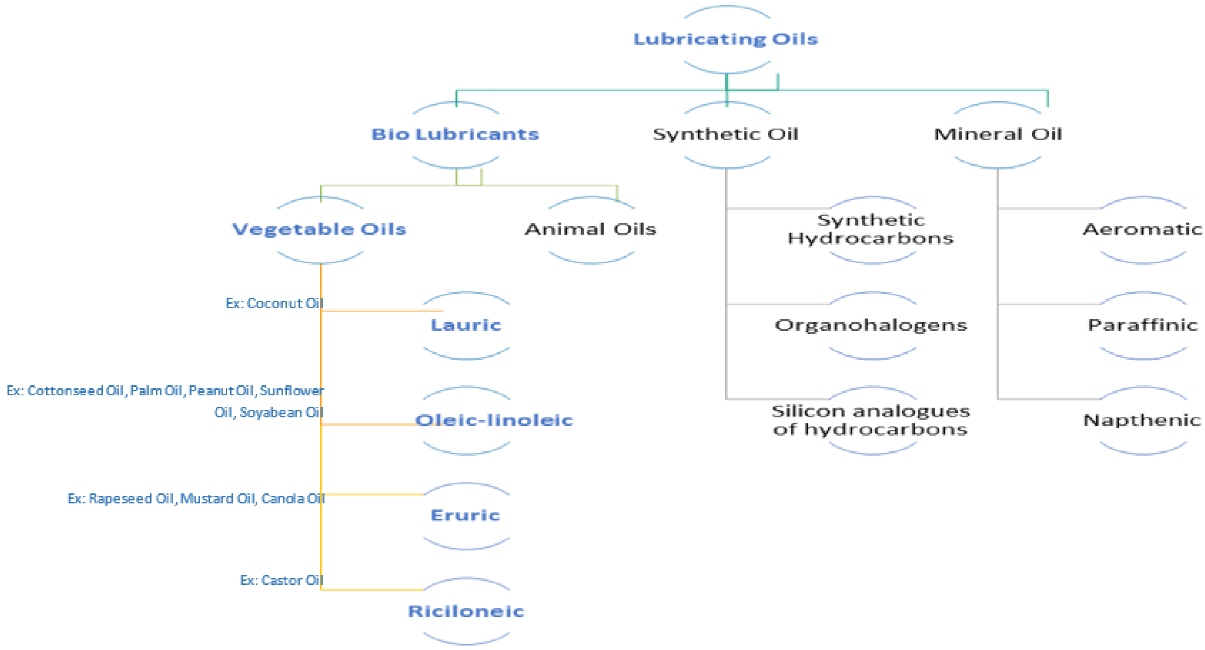

Fig 1: Classification of Lubricants

2.1 Mechanism of Nanoparticles in Lubricants

Mineral oils are formed by the fractional distillation of crude oils, hydrocarbons contribution to the mineral oils are considered to be the most important because of its chemical structures like naphthenic, aromatic and paraffinic[5]. Animal fats and vegetable oil come under bio lubricants [6]. Vegetable oils have glycerol and fatty acids which gives excellent lubricating and thermal properties [7]. Synthetic oils are man made lubricants which is the best alternative for mineral and bio lubricants due to its capability to withstand from extremely low to high temperature. To improve the tribological properties of the mating parts it is necessary to know the mechanism of the nanoparticles in lubrication, because, addition of these nanoparticles has showed good tribological properties [8].

In ball bearing mechanism the particles are usually spherical or quasi- spherical in shape which rolls between the mating surfaces to give better tribological properties [9-11]. Where as in tribo film formation mechanism an unstructured layer is formed on the mating surface which reduces the friction by the formation. [12-15]. At the wheel work piece interface the surface quality obtained by the nanofluids was found to be better due to the ball bearing and polishing affect [16].

In polishing effect mechanism, the nanoparticles will fill the gap in between the rough surface which was caused due to the rubbing action [40]. This mechanism smoothen the rough surface and hence called smoothing effect [17-19]. In mending effect mechanism the nanoparticles gets deposited in the grooves of the rough surface and reduce the roughness, which called a self repairing mechanism [20, 21].

2.2 Analysis of Nanolubricants (Synthesis):

L.L.Zhang has synthesized WS_2 nanorods as nano additives in lubricant by ball milling process which was carried out at ambient temperature by a planetary ball milling machine with a rotational speed of 450 rpm for 12 hrs which led to the formation of precursor nanosheets [22]. These nanosheets were synthesized by putting into autoclave filled with 80% of alcohol and maintained at 240^0C for 24 hrs followed by annealing process. These sheets were dispersed in the base oil by a sorbitol monoleate dispersing agent for the equal suspension in T-18 high dispersion machine for 20min [23].

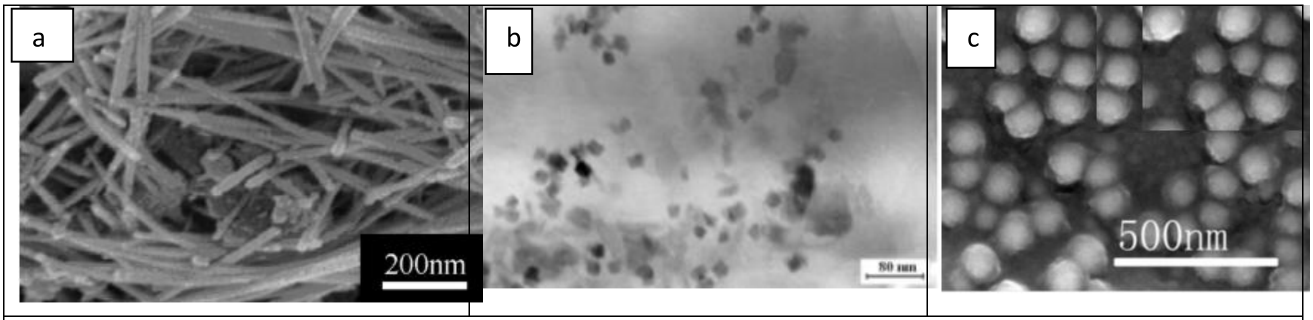

Fig 2. SEM images of a) WS_2 Nano rods [23] b)Rare earth[22] c) $ZnAl_2O_4$ nanoparticles [24]

Rende Liu has took a small portion of REN, VG26 lubricant and surface improving agent in a container and blended thoroughly. The Mixture was excited at 60°C in absolute alcohol and diluted aqueous hydrazine solution. The byproduct naphthenic acid was formed by putting triethylene tetra mine into the container. Finally the water is separated from the solution by using vacuum pump and the surface modified REN were obtained [22].

Xiaoyun Song prepared $ZnAl_2O_4$ nanoparticles by dissolving 1MZn (Ac)$_2$ 2H_2O and 2M Al (NO_3) 9H_2O into alcoholic solution by adding 0.3wt % of polyethylene glycol. Later ammonia was added to the solution to form a gel by mechanical stirring and ultrasonic dispersion which was then washed with alcohol for 3times [41]. The mixture of these two gels was put into an autoclave and fully stirred at 220^0 C for 24 hrs, further the as prepared $ZnAl_2O_4$ nanoparticles were mixed with different amount of oleic acid like 3, 6, and 9 %wt at different temperatures say 30^0, 70^0, 110^0C. By changing the percentage weight of oleic acid in $ZnAl_2O_4$ series of modified nanoparticles were formed [24].

3. Tribological properties:

L.L.Zhang investigated the friction and wear by using a four ball tester under varying loads like 170,245 and 320N for 30min. by using optical microscope with an accuracy ±0.01mm,the WSD of the steel balls were measured. Rende Liu evaluated the properties on MS-800 four ball tester under a load of 294N at 1450rpm for 30min near ambient temperature [25]. The author followed the ASME D2783 and ASME D4172 for measuring the COF, WSD and maximum non-seize load. Xiayun deliberate the WSD and COF of ZnAl2O4 nanoparticles in the base oil by two different test procedures wiz. Four ball tester and thrust ring test [26]. The test in the four ball tester was conducted under a load thrust ring at 1450rpm for 1800sec near 348K, while in thrust ring test it was under200N at 1200rpm for 1800sec near 348K.

S.No	Material	Size (nm)	Shape	Morphology	Lubricant	Tribology Test	Ref.
1	Cu	25	Nearly Spherical	TEM	PAO6	Block-on-Ring	[47]
2	Pb	2.2	Spherical	TEM	Liquid Paraffin	Pin-on-disc	[48]
3	CuO	5	Spherical like	TEM	Chemically Modified rapseed oil	Four-ball Tester	[49]
4	CuO	5	Spherical Like	TEM	Chemically modified palm oil	Piston ring-cylinder liner	[49]
5	WS_2	100	Spherical	AFM	Paraffin oil	Pin on disc	[36]
6	MoS_2	350	Layered	TEM	Surface Modified Coconut Oil	Four ball Tester	[42]
7	ZnO	11.7	Nearly Spherical	SEM	PAO6	Block On Ring	[48]

8	TiO2	80	Spherical	TEM	Liquid paraffin	Four Ball tester	[51]
9	Boron Nitride	70	Spherical	SEM	PAO10	Piston Skirt Cylinder Liner	[52]
10	ZrO_2/SiO_2 nano Composite	50-80	Nearly Spherical	TEM	Surface Modified machine oil	Thrust Ring	[50]
11	$Al2O_3/SiO_2$ Nanocomposite	70	Elliptical	TEM	Surface Modified Machine Oil	Thrust Ring	[53]
12	Nickel	20	Nearly Spherical	TEM	PAO6		[48]

Table: 1 Summary of different nanoparticles as additives and tribological properties studied by various researchers

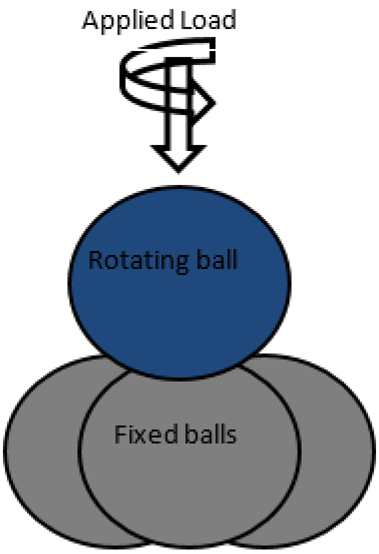

a. Four Ball tester

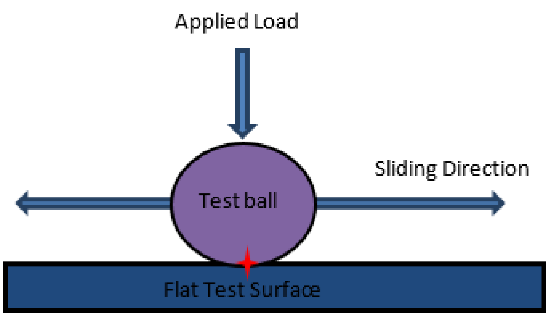

b. Ball On Flat test

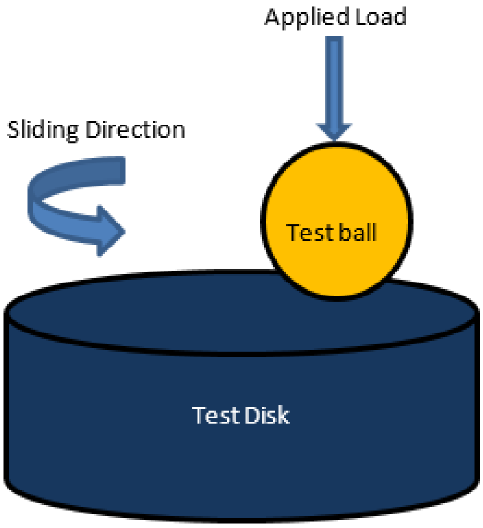

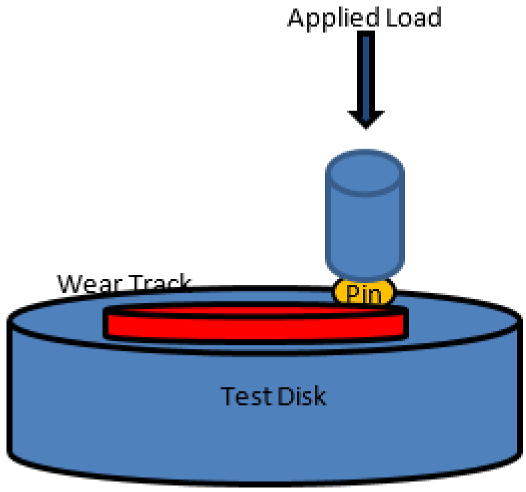

c. Ball On Disk **d. Pin On Disk**

Fig 3. Schematic diagrams of Tribological tests.

Four Ball tester:

As the name indicates it has four balls which operates in sliding or rotating motion. One ball rotates over the other three balls [27]. These balls are stainless steel and are coated with the lubricating film. The rotating ball rotates at a given speed under the applied load. The ball is rotated until it gets seized. This test is used to find the characteristics of the lubricant. This is operated under certain standards usually called as ASTM D-2266(Grease) or ASTM D-4172 (Oils) [28].

Ball on Flat Test:

In this experiment the ball made of steel is made to slide on the flat surface in to and fro motion. The size of the ball is taken as per the AISI standards [29]. The lubricating film passes between the ball and the flat surface [43]. Due to the friction between the rubbing surfaces, heat is produced leading to wear in the mating parts. [54]

Ball on Disk Test:

In this ball is in continuous contact with the disk and hence this is used for checking the mechanical component surfaces which are subject to sliding motion [30]. Its robust design can help in withstanding the high loads and with greater velocities and therefore can be used under various test conditions [44] .

Pin On Disc Test:

Pin On disc tribometer consists of a pin that is stationary loaded against a disc which is rotating. This is also one of the methods to characterize the wear properties and find the performance of the lubricants [31].

4. Morphology:

The author used SIRIONJY/T010-1996 SEM to examine the morphology ofWS_2 Nano rods as additives in the lubricant [32]. For rare earth nanoparticles the author investigated the tribological morphology by using Auger electro spectroscopy (AES) and XPS[46] . It was observed that the description of $ZnAl_2O_4$ nanoparticles with base oil by SEM with a FEI FEG quanta 250 microscope and XRD onD8Advance radiation.

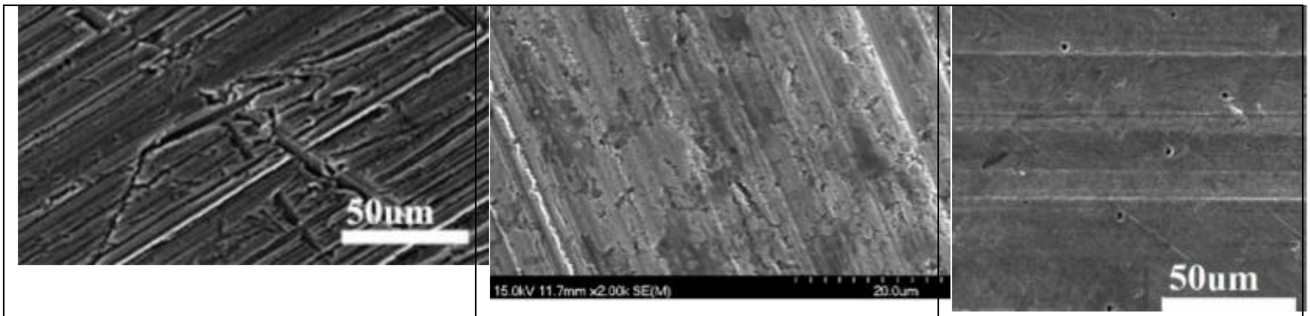

Fig 4. SEM Image of worn surface of a) Pure base oil b)Base oil with Ws_2 Nanorods[23] c) Base oil with $ZnAl_2O_4$ [24]

5. Conclusion:

This article exposes the exclusive evaluation on use of various nanoadditives for lubrication. The synthesis and characterization of nanoparticles in different shapes, size and based on method of preparation were analyzed. It was observed that the addition of nano additives in the lubrication with different concentrations gave improved results when compared pure lubricant. The WSD, COF and various tribological properties were improved in oil instance.

- The mating surfaces were improved in friction and wear when WS_2 nanorods along with the base oil were used.
- The improved REN showed excellent tribological properties when blended with the lubricant.
- $ZnAl_2O_4$ nanoparticles showed good tribological properties with optimum nanoparticle concentration.

Future work:

The investigations can be towards the procurement of new nanoadditive, which can be used as lubricants in various industrial and automotive applications. Nanoparticles with various base oils were used as the potential lubricants under suitable conditions.

References:

[1]. H.Mobarak, E.N. Mohamad, H.Masjuki, M.kalam, K.AlMahmud, M.Habibullah, A.Ashraful, "The prospects of bio lubricants as alternatives in automotives applications, renewable and sustainable energy reviews", vol,pp.34-43,2014,Doi:10.1016/j.rser.2014.01.062
[2]. Y.Hori, Hydrodynamic lubrication, spring japan,2006.
[3]. S.M.Hsu, R.Gates,"Boundary lubricating films: formation and lubrication mechanism", Tribology International, vol.38,iss,3pp.305-312,2005,Doi:10.1016/j.triboint.2004.08.021
[4]. E.Holglund, "Influence of lubricant properties on elasto hydrodynamic lubrication", Wea,Vol. 23,Iss.2,pp.176-184,1999, Doi:10.1016/s0043-1648(99)00143-x
[5]. W.Shafi, A.Raina,M.UI Haq, "Friction and wear characteristics of vegetable oils using nanoparticles sustainable lubrication", pp 27-43, Doi.org/10.1080/17515831.1435343
[6]. G.Stachowiak, A.Batchelor, "Engineering Tribology,Butterworth-Helnemann,2013.
[7]. N.Fox, G.Stachowiak, "Vegetable oil-based lubricants-A review of oxidation, Tribology International, Vol.40, Iss.7,pp.1035-1046,2007,Doi:10.1016/j.triboint.2006.10.001
[8]. E.O.Aluyor, K.O.Obahiagbon, M.Ori-jesu, Biodegradation of vegetable oils: A review, Scientific Research and Essaya, Vol.4, No.6,pp.543-548,2009.
[9]. F.Chinas-Castillo, H.Spikes, "Mechanism of action of colloidal solid dispersion", Journal of Tribology, Vol.125,Iss.3,pp.552-557,2003,Doi:10.1115/1.1537752#
[10]. L.Rapoport, V.Leshchinsky, M.Lvovsky, O.Nepomnyashchy, Y.Volvovik, R.Tenne, "Mechanism of friction of fullerenes", Industrial lubrication and tribology, Vol.54,Iss.4, pp.171-176,2002, Doi:10.1108/00368790210431727
[11]. Y.Y.Wu,W.C.Tsui, T.C.Liu, "Experimental analysis of tribological properties of lubricating oils withnanoparticle additives, wear, Vol.262, Iss.7-8, pp.819-825, 2007, Doi:10.1016/j.wear.2006.08.021

[12]. B.M.Ginzburg, L.A. Shibaev, O.F kirennko, A.A Sheplevskii, M.V. Baidakova, A.A Sitnikova, Antiwear effect of fullerence C 6 0 additives to lubricating oils,Russian Journal of applied chemistry, vol.75,iss.8, pp.1330-1335,2002,doi:10.1023/a:1020929515246

[13]. Z.XIaodong, F.Xun,S.Huaqiang,H.Zhengshui, Lubricating properties of Cyanex 302-modified MoS2 microspheres in base oil 500SN, Lubrication science, vol.19, iss,pp.71-79,2007,doi:10.1002/Is.32

[14]. W.Yu, H.Xie, A review on nanofluids:preparation, stability mechanisms, and applications Journal of nanomaterials, vol2012, pp.1-12, doi:10.1155/2012/435873

[15]. Z.S Hu, R.Lai, F.Lou, L. Wang, Z. Chen, G. Chen, J.X Dong, Preparation and tribological properties of nanometer magnesium borate as lubricating oil additive, Wear, vol.252,iss.5-6, pp.370-374,2002,doi:10.1016/S0043-1648(01)00862-6

[16]. Roshan Lal Virdi, Sukhpal singh Chatha, Hazoor Singh, " Experimental investigation on the tribological and lubrication behavior of minimum quantity lubrication technique in grinding of Inconel 718 alloy" Tribology International,153(2021)106581. Doi.org/10.1016/j.triboint.2020.106581

[17]. X.Tao, Z Jiazheng, X.Kang, "The ball-bearing effect of diamond nanoparticless as an additives," Journal of physics D: Applied physics, vol.29, no. 11, pp.2932,1966, Doi: 10.1088/0022-3727/29/11/029

[18]. T.sui, B.song, F.Zhang, Q.Yang, "Effect of particles size and ligand on the tribological properties of amino-functionalized hairy silica nanoparticles as an additive to polyalphaolefin", Journal of nanomaterials, vol.2015, pp.1-9,2015,Doi:10.1155/2015/49401

[19]. K.Lee, Y.Hwang, S.Cheong, L.Kwon, S.Kim, J.Lee, "Performance evalution of nano-lubrication of fullerence nanoparticles in refrigeration mineral oil", Current Applied Physics, Vol.9, iss.2,pp.e128-131,2009, Doi: 10.1016/j.cap.2008.12.054

[20]. G Liu, X.Li, B.Qin, D.Xxing, Y.Guo, R.Fan, Investigation of the mending effect and mechanism of copper nanoparticles on a tribologically stressed surface", Tribology Letter, vol.17,Iss.4,pp. 961-966,2004,Doi:10.1007/s11249-004-8109-6

[21]. H.Ahmadi, A.Rashidi, S.S.Mohtasebi, "Investigation of the anti-wear properties of nano additives on sliding bearings of internal combustion engines, international journal of precision engineering and manufacturing, vol.14, Iss.5, pp.805-809,2013,Doi:10.1007/s12541-013-0105-z

[22]. Rende Liu, Xicheng Wei, Dehua Tao,Yuan Zhao, " Study of preparations and triboplogical properties of rare earth nano particles in lubricating oil",Tribology International 43, 2010,PP 1082-1086.Doi:Doi:10.1016/j.triboint.2009.12.026

[23]. L.L.Zhang,J.P.Tu,H.M.Wu,Y.Z.Yang, "WS_2 Nanorods prepared by Self transformation process and their tribological properties as additives in base oil", Material sciences and engineering A,454-455(2007) 487-491.Doi:10.1016/j.msea.2006.11.072

[24]. Xiaoyun Song, Shaohua Zheng, Jun Zhang, Wei.Li, Qiang Chen, Bingqiang Cao, "Syntheisis of mono dispersed $ZnAl_2O_4$ nanoparticels as lubricating additives", Materials Research Bulliten,2012.Doi.org/10.1016/j.materresbull.2012.09.0.13

[25]. Roshan Lal Virdi, Sukhpal Singh Chatha, Hazoor Singh, " Experimental investigation on tribological and lubrication behavior of minimum quantity lubrication technique in grinding of Inconel 718 alloy", Tribology International 153(2021)106581. Doi.org/10.1016/j.triboint.2020.106581

[26]. Anurag singh, prashant Chauhan, Mamatha T.G, " A review on tribological performance of lubricants with nanoparticles additives", Materials Today: Proceedings, Doi.org/10.1016/j.matpr.2019.07.245

[27]. P.D.Srivyas, M.S.Charoo, "A review on tribological characterization of lubricants with nano additives for automotive applications", Vol.40. No.4(2018) 594-623, Doi:10.24874/ti.2018.40.04.08

[28]. Akbulut M (2012)" Nanoparticle-based lubrication systems".J powder Metall Min-2012.Doi:10.4172/2168-9806.1000e101.

[29]. Alves SM,Barros BS,Trajano MF,Ribeiro KSB,Moura E "Tribological Behaviour of vegetable oil-based lubricants with nanoparticels", Tribology International, Vol.65 (2013), pp:28-36, Doi.org/10.1016/j.triboint.2013.03.027

[30]. Asrul M,Zulkifli NWM,Masjuki HH,Kalam MA " Tribological Properties and lubricant mechanism of nanoparticle in engine oil".Procedia Eng, 68(2013) pp:320-325, Doi:10.1016/j.proeng.2013.12.186.

[31]. Chou R,Battez AH,Cabello JJ,Viesca JL,Osorio A,Sagastume A (2010)."Tribological Behaviour of polyalphaolefin with the addition of nickel nanoparticels".Tribol Int 43:2327-2332. Doi:10.1016/j.triboint.2010.08.006.

[32]. Y.Gerbig,S.I.-U.Ahmed,F.A.Gerbig,H.Haefke,"Suitabiloity of Vegetable oils as industrial lubricants",Journal of synthetic Lubrication,Vol.21,iss. 3, pp. 177-191,2004,doi:10.1002/jsl.3000210302.

[33]. V.Bakunin,A.Y.Suslov,G.Kuzmina,O.Perenago,"Recent achievements in the synthesis and application of inorganic nanoparticels as lubricant components ,Lubrication science,Vol.17,no.2,pp.127-145,2005,doi:10.1002/ls.3010170202

[34]. B.A.Kheireddin , "Tribological Properties of Nano particle based lubrication Systems" 2013.

[35]. M.Gulzar, H.H.Masjuki, M.A.Kalam, M.Varman, N.W.M.Zulkifli, R.A.Mufti & Rehan Zahid, " Tribological performance of nanoparticles as lubricating oil additives", Journal of Nanoparticle Research, 18(2016)

[36]. L.Rapoport,Y,Bilik,Y.Feldman,M.Homyonfer,S.Cohen,R.Tennen,"Hollow Nanoparticels of WS_2 as potential solid state lubricants",Nature,vol:387,Page No.791-793,1977.doi:10.1038/42910.

[37]. X.B.Wang, W.M.Liu, Nanoparticle-based lubricant additives,in Q.J. Wang ,Y.w.Chung,(Ed.): Encyclopeidia of Tribology,Springer,pp.2369-2376,2013.doi:10.1007/978-0-387-92897-5_1245.

[38]. N.G.Demas,E.V.timofeeva,J.L Routbort,G.R.Fenske,"Tribological effects of BN,MoS_2 Nanoparticels added to polyalphaolefin oil in piston skirt/cylinder liner tests",Tribology letters,vol.47,issue-1,pp 91-102,2012.doi:10.1007/s11249-012-9965-0.

[39]. B. Li, X. Wang, W. Liu, Q. Xue, Tribochemistry and antiwear mechanism of organic inorganic nanoparticles as lubricant additives, Tribology Letters, vol. 22, iss. 1, pp. 79-84, 2006, doi : 10.1007/s11249-005-9002-7.

[40]. N. Ohmac, J.M. Martin, S. Mori, Introduction to Micro and Nanotribology, in N. Ohmae, J.M. Martin, S. Mori, Micro and Nanotribology, ASME pp. 129-150, 2005,doi: 10.1115/1.802310.ch1.

[41]. L. Pena-Paras, J. Taha-Tijerina, L. Garza, D.Maldonado Cortes, R. Michalczewski, C. Lapray, Effect of Cuo, A10; nanoparticle additives on the tribological behavior of fully formulated oils, Wear, vol. 332-333, pp. 1256-1261, 2015, doi: 10.1016/j.wear.2015.02.038

[42]. C.P.Koshy, P.K. Rajendra Kumar, M.V. Thottackkad," Evaluation of the tribological and thermo-physical properties of coconut oil added with MoS_2 Nanoparticels at elevated tempretures",Wear,Vol.330, pp. 288-308,2015,doi: 10.1016/j.wear.2014.12.044.

[43]. H. Mobarak, E.N. Mohamad, H. Masjuki, M. Kalam, K. Al Mahmud, M. Habibullah, A. Ashraful, "The prospects of biolubricants as alternatives in automotive applications, Renewable and sustainable energy reviews", vol. 33, pp. 34-43, 2014, doi: 10.1016/j.rser.2014.01.062

[44]. S. Ma, S. Zheng, D. Cao, H. Guo, "Anti-wear, friction performance of ZrO2 nanoparticles as a lubricant additive", Particuology, vol. iss. 5, pp. 468-472 2010, doi: 10.1016/j.partic.2009.06.007.

[45]. P. Rabaso, F. Ville, F. Dassenoy, M. Diaby, P. Afanasiev, J. Cavoret, T. Le Mogne, "Boundary lubrication influence of the size and structure of inorganic fullerene-like MoS2 nanoparticles on friction and wear reduction", Wear, vol. 320, pp. 161-178, 2014, doi: 10.1016/j.wear.2014.09.001.

[46]. Z. Chen, X., Liu, Y. Liu, S. Gunsel, I. Luo, "Ultrathin Mos, nanosheets with superior extreme pressure property as boundary lubricants", scientific reports, vol. 5, Pp. 2015, doi: 10.1038/srep 12869.

[47]. G. Biresaw, A. Adhvaryu, S. Erhan "Friction properties of vegetable oils", Journal of the American Oil Chemists Society, vol. 80, iss. 7. pp. 697, 2003, doi: 10.1007/s11746-003- 0760-7.

[48]. S.J.Asadauskas, R.Kreivaitis ,G.Bikulcius, A.Griguceviciene, J.Padagurskas, " Tribological effects of Cu, Fe, Zn nanoparticels, Suspended in mineral, bio-based oils, Lubrication science,vol.28,no.3,pp.157-176,2016,doi:10.1002/ls.1307.

[49]. H.Masjuki,M.Maleque,A.Kubo,T.Nonaka,Palm oil,Mineral oil based lubricants-their tribological and emission performance, Tribology International, vol. 32, iss. 6,pp. 305-314,1999, doi:10.1016/S0301-679X(99)00052-3.

[50]. P.Nagendramma,S.Kaul, " Development of Ecofriendly/biodegradeable lubricants: An Overview" Renewable and sustainable energy reviews, vol. 16.iss 1, pp764-774,2012,doi: 10.1016/j.rser.2011.09.002.

[51]. H. Amiruddin, M. Abdullah, A. Idris, M. Gulzar, R.Zahid, " Study of tribological properties of lubricating oil blend added with graphene nanoplatelets" , Journal of Material research, vol.31, No. 13, pp 1932/1938, 2016, doi:10.1557/jmr.2016.24.
[52]. W.castro,J.M.perez, S.Z.Erhan,F.Caputo," A Study of the oxidation and wear properties of vegetable oils soyabean oil without additives", Journal of the American Oil Chemists Society,Vol.83, iss.1 pp.47-52,2006,doi:10.1007/s11746-006-1174-2.
[53]. S.Armugam,G.Sriram,"Effect of bio-lubricant and biodiesel-contaminated lubricant on tribological behavior of cylinder liner-piston ring combination", Tribology Transactions,vol.55,iss 4. pp.438-445,2012,doi:10.1080/10402004.2012.667517.
[54]. A.K.Rasheed,M.Khalid,A.Javed,W.Rashmi,T.C.S.M.Gupta,A.Chan, " Heat Transfer and tribological performance of graphene nano lubricant in an internal combustion engine", Tribology International,vol 103,pp.504-515,2016,doi:10.1016/j.triboint.2016.08.007.
[55]. D.H.Cho,Yze, " Comparision of scuffing life between uni directional and reciprocating sliding motion"Wear, vol.271(2011) pp.1637-1641.